NASA/CP-1998-206280

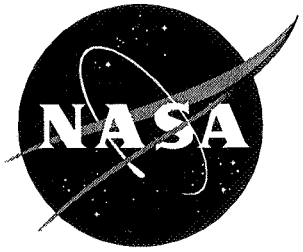

Stability Analysis of Plates and Shells

A Collection of Papers in Honor of Dr. Manuel Stein

Compiled by
Norman F. Knight, Jr.
Old Dominion University, Norfolk, Virginia

Michael P. Nemeth
Langley Research Center, Hampton, Virginia

January 1998

The NASA STI Program Office . . . in Profile

Since its founding, NASA has been dedicated to the advancement of aeronautics and space science. The NASA Scientific and Technical Information (STI) Program Office plays a key part in helping NASA maintain this important role.

The NASA STI Program Office is operated by Langley Research Center, the lead center for NASA's scientific and technical information. The NASA STI Program Office provides access to the NASA STI Database, the largest collection of aeronautical and space science STI in the world. The Program Office is also NASA's institutional mechanism for disseminating the results of its research and development activities. These results are published by NASA in the NASA STI Report Series, which includes the following report types:

- TECHNICAL PUBLICATION. Reports of completed research or a major significant phase of research that present the results of NASA programs and include extensive data or theoretical analysis. Includes compilations of significant scientific and technical data and information deemed to be of continuing reference value. NASA counter-part or peer-reviewed formal professional papers, but having less stringent limitations on manuscript length and extent of graphic presentations.

- TECHNICAL MEMORANDUM. Scientific and technical findings that are preliminary or of specialized interest, e.g., quick release reports, working papers, and bibliographies that contain minimal annotation. Does not contain extensive analysis.

- CONTRACTOR REPORT. Scientific and technical findings by NASA-sponsored contractors and grantees.

- CONFERENCE PUBLICATION. Collected papers from scientific and technical conferences, symposia, seminars, or other meetings sponsored or co-sponsored by NASA.

- SPECIAL PUBLICATION. Scientific, technical, or historical information from NASA programs, projects, and missions, often concerned with subjects having substantial public interest.

- TECHNICAL TRANSLATION. English-language translations of foreign scientific and technical material pertinent to NASA's mission.

Specialized services that help round out the STI Program Office's diverse offerings include creating custom thesauri, building customized databases, organizing and publishing research results . . . even providing videos.

For more information about the NASA STI Program Office, see the following:

- Access the NASA STI Program Home Page at ***http://www.sti.nasa.gov***

- Email your question via the Internet to help@sti.nasa.gov

- Fax your question to the NASA Access Help Desk at (301) 621-0134

- Phone the NASA Access Help Desk at (301) 621-0390

- Write to:
  NASA Access Help Desk
  NASA Center for AeroSpace Information
  800 Elkridge Landing Road
  Linthicum Heights, MD 21090-2934

NASA/CP-1998-206280

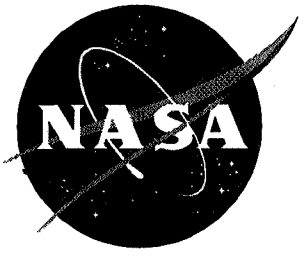

Stability Analysis of Plates and Shells

A Collection of Papers in Honor of Dr. Manuel Stein

Compiled by
Norman F. Knight, Jr.
Old Dominion University, Norfolk, Virginia

Michael P. Nemeth
Langley Research Center, Hampton, Virginia

Compilation of papers presented at
special sessions honoring Dr. Manuel Stein
during the 38th AIAA/ASME/ASCE/AHS/ASC
Structures, Structural Dynamics, and
Materials Conference held in
Kissimmee, Florida
April 7-10, 1997

National Aeronautics and
Space Administration

Langley Research Center
Hampton, Virginia 23681-2199

January 1998

Available from the following:

NASA Center for AeroSpace Information (CASI)
800 Elkridge Landing Road
Linthicum Heights, MD 21090-2934
(301) 621-0390

National Technical Information Service (NTIS)
5285 Port Royal Road
Springfield, VA 22161-2171
(703) 487-4650

Preface

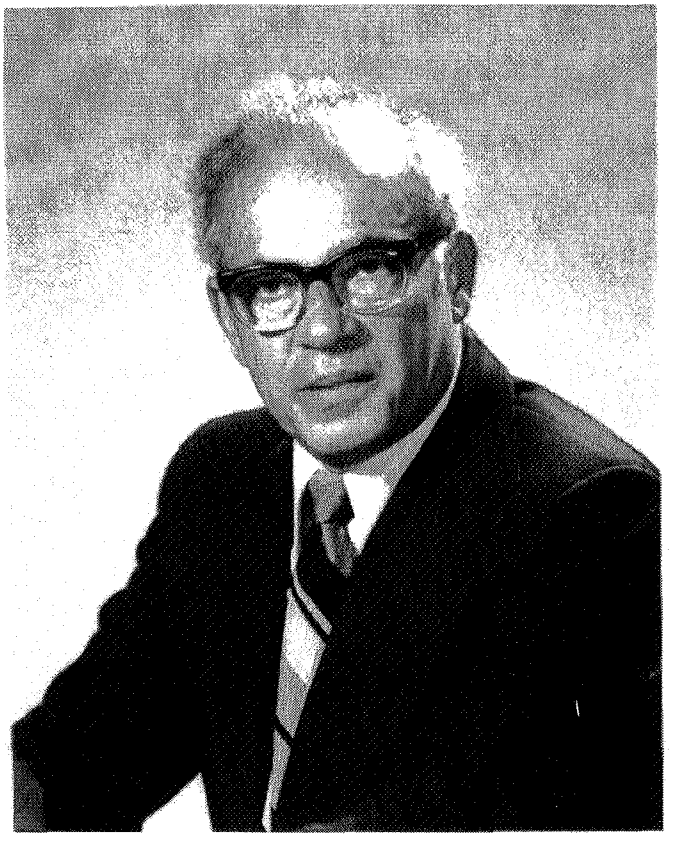

Dr. Manuel Stein
(1921–1991)

This special publication contains the papers presented at the special sessions honoring Dr. Manuel Stein during the 38th AIAA/ASME/ASCE/AHS/ASC Structures, Structural Dynamics, and Materials Conference held in Kissimmee, Florida, April 7–10, 1997. This volume, and the SDM special sessions, are dedicated to the memory of Dr. Manuel Stein, a major pioneer in structural mechanics, plate and shell buckling, and composite structures. Many of the papers presented are the work of Manny's colleagues and co–workers and either directly or indirectly, are a result of his influence on us.

Dr. Stein earned his Ph. D. in Engineering Mechanics from Virginia Polytechnic Institute and State University in 1958. He worked in the Structural Mechanics Branch at the NASA Langley Research Center from 1943 until 1989. In 1982, Dr. Stein was presented the NASA Exceptional Scientific Achievement Medal in recognition of exceptional contributions to structural mechanics through the development of fundamental analyses for the buckling and postbuckling behaviors of structures. Following his retirement in 1989, Dr. Stein continued his involvement with NASA as a Distinguished Research Associate.

Contents

MANUEL STEIN'S FIVE DECADES OF STRUCTURAL MECHANICS CONTRIBUTIONS (1944-1988)

Martin M. Mikulas
Professor, University of Colorado, Boulder CO
and
Michael Card
Research Engineer, Eagle Engineering, Hampton VA
and
Jim Peterson
Retired, NASA, Langley, Hampton VA
and
James Starnes
Branch Head, NASA, Langley, Hampton VA

Abstract

Manuel Stein went to work for NACA (National Advisory Committee for Aeronautics) in 1944 and left in 1988. His research contributions spanned five decades of extremely defining times for the aerospace industry. Problems arising from the analysis and design of efficient thin plate and shell aerospace structures have stimulated research over the past half century. The primary structural technology drivers during Dr. Stein's career included 1940's aluminum aircraft, 1950's jet aircraft, 1960's launch vehicles and advanced spacecraft, 1970's reusable launch vehicles and commercial aircraft, and 1980's composite aircraft. Dr. Stein's research was driven by these areas and he made lasting contributions for each. Dr. Stein's research can be characterized by a judicious mixture of physical insight into the problem, understanding of the basic mechanisms, mathematical modeling of the observed phenomena, and extraordinary analytical and numerical solution methodologies of the resulting mathematical models. This paper summarizes Dr. Stein's life and his contributions to the technical community.

Manual Stein's Life

Dr. Manuel Stein, a Virginia Polytechnic Institute and State University PhD graduate, understood the importance of higher education to an individual's development and maturity, as well as its importance to the prosperity of America. He constantly encouraged his family, friends, students, and colleagues to pursue advanced degrees. His basic philosophy of pursuing excellence at every opportunity not only affected people he interacted with, but also led to many of his own significant scientific achievements. These achievements led to both national and international recognition of Dr. Stein as an expert in the field of structural mechanics.

Dr. Stein also understood the importance and interaction of good citizenship and professional ethics. He always conducted business in a calm and friendly manner, and radiated a feeling of professionalism. He is remembered by his family, friends, and colleagues for his warmth, compassion, humility, friendliness towards others, and especially his sense of humor. Dr. Stein genuinely enjoyed helping people, especially young people. As a result, he mentored many students and co-workers during his nearly fifty-year-long career. A scholarship in his name has been established at Virginia Tech, endowed by his family, friends, and colleagues worldwide which celebrates the exceptional achievements of Dr. Stein and the high ideals he practiced on a daily basis.

Manuel Stein (1921-1991) was born November 27, 1921 in Monaca, Pennsylvania. He was the youngest of four children of Charles and Lena Stein, who had emigrated to the United States from Russia. The family operated Stein's Department Store and the family lived in the rooms above the

store. After attending primary and secondary schools in the area, he enrolled at the University of Pittsburgh. In 1943, he graduated with a Bachelor of Science in Mechanical Engineering.

Manual Stein's Career

After graduating from college in 1943, Dr. Stein moved to Hampton, Virginia to begin employment with the National Advisory Committee for Aeronautics (NACA) at Langley field. The NACA was the predecessor of the well-known National Aeronautics and Space Administration (NASA). The first 17 years of Dr. Stein's career (1944 - 1961) were spent working with and learning from the masters of structural mechanics. These individuals included such names as, Batdorf, Budiansky, Reissner, Seide, Libove, Houbolt, Hedgepeth, Sanders, Mayers, and others. Dr. Stein published 33 highly original technical papers during that time period with these individuals. The last 27 years of his career were spent with Dr. Stein pioneering new research areas, mentoring, and unselfishly transferring his immense knowledge to the next generations of structural mechanists. During this time period Dr. Stein published 38 technical papers, 20 of which were co-authored by next generation researchers. A complete list of his papers is given in the reference list at the end of this paper.

Dr. Stein's work during the early period of his career dealt with mathematical analysis and experimental investigation of the structural behavior of stiffened and unstiffened plates and shells. During this time, he contributed greatly to the development of a nondimensional parameter for characterizing buckling of curved plates and cylindrical shells. Another significant achievement during this period of his career was the formulation of a theory for stress analysis and buckling of sandwich plates and shells. Dr. Stein's theory became the basis for most of the analytical work performed in this area for the next thirty years.

Graduate study was highly encouraged by the management of the NACA. Thus, Dr. Stein completed an MS degree in Aeronautical Engineering from the University of Virginia in 1951. His thesis work dealt with the torsion and transverse bending behavior of cantilevered plates. This work was of great interest to the NACA in that it supported the national effort to develop swept-wing jet aircraft. A couple of years later, Dr. Stein became involved in analyzing low aspect ratio wing structures. He developed a method of analyzing these structures that led to his recognition as a national expert in the field of structural analysis. It was at this time that he met Bernice Malkin. They were married in 1953 and raised four children.

In 1958, President Dwight D. Eisenhower introduced the National Aeronautics and Space Act that created NASA to replace the NACA on a much grander scale. Also in 1958, Dr. Stein received a PhD degree in Applied Mechanics from VPI. His dissertation dealt with the postbuckling behavior of rectangular isotropic plates. This effort and his subsequent work in this area, led to major advancements in the understanding of buckling and postbuckling behavior of plate structures. His publications written on this topic during this period of his career are still both widely referenced today and considered to be benchmark publications by the technical community.

During the next several years, Dr. Stein developed a refined analysis for predicting buckling of pressurized unstiffened circular cylindrical shells loaded in compression. His work in this area supported the development of spacecraft launch vehicles such as the one used to put the first American astronaut, Alan Shepard, into space. His work focused attention on the effects of boundary conditions and prebuckling deformations on the collapse behavior of shell structures. Up until this time, these effects were thought to be unimportant. Dr. Stein's work, originally published in 1962, stimulated a great deal of interest and research in this area for nearly 25 years.

In the early 60's the state-of-the-art for predicting the buckling load and natural frequencies of stiffened cylinders was highly empirical. This commonly led to significant

errors in predicting the buckling load of stiffened cylinders with unprecedented geometry such as was common in the development of new and larger launch vehicles. For example, experimental buckling loads for Saturn class structures were found to be in error by greater than a factor of two from theoretical predictions. Dr. Stein led a group of researchers during that time period in the development of a rational analytical procedure for predicting the buckling of cylinders with eccentric stiffeners. This stiffened shell research coupled with Dr. Stein's research on effects of boundary conditions and prebuckling deformations resulted in highly accurate prediction methods for the analysis and design of high performance stiffened shell structures. These analytical developments helped keep the Nation's Apollo program on schedule and paved the way for modern stiffened shell analysis.

Although Dr. Stein's major contributions were in the field of structural stability of plates and shells, his basic mechanics knowledge resulted in original contributions to the fields of membrane mechanics, vibrations, flutter, and laminate mechanics. For example in the early 60's he and John Hedgepeth developed a theory for partly wrinkled membranes which for the first time permitted wrinkled membranes to be analyzed using traditional approaches. This theory has been subsequently experimentally verified and has been used for the rational analysis and understanding of complex behavior of advanced missions involving membranes over the past thirty years. This work supported the development of paragliders, parasails, ballutes, and other deceleration devices for recovery of orbital payloads. Dr. Stein also made significant contributions to the dynamic analysis of membrane structures. He obtained exact solutions for the arrest of a moving mass by a flat circular membrane, or a membrane strip, attached to the mass. This work contributed greatly to the design and evaluation of structural reinforcements for the radio tracking beacon installations on the Echo II passive communications satellite.

In the latter part of Dr. Stein's career, he analyzed the buckling and postbuckling behavior of laminated composite plates and shells. His work in this area led to the development of nondimensional parameters for characterizing the postbuckling behavior of orthotropic plates. In addition, he formulated a theory for the nonlinear behavior of thick composite plates and shells. Both of these activities continue to support the development of energy efficient commercial transport aircraft that are expected to be operating in the year 2000.

The breadth and depth of Dr. Stein's contributions led to his recognition as an international authority on buckling of plate and shell structures, and to him being awarded the NASA medal for exceptional scientific achievement. Dr. Stein presented numerous talks and published approximately 50 technical papers during his career. He regularly reviewed books and journal articles for organizations including the American Institute of Aeronautics and Astronautics, the American Society of Mechanical Engineers, and the McGraw-Hill Book Company. He also reviewed articles for the International Journal of Solids and Structures and the Journal for Computers and Structures. Dr. Stein was often consulted by researchers at NASA, at other government laboratories, by members of the armed forces, by faculty members, at universities, and by many aerospace companies for advice on the solution of difficult structural mechanics problems.

He was invited to present lectures at universities around the world. His large reservoir of knowledge and experience, together with his talents as an analyst, were very valuable assets which contributed to his own research as well as to the output of others through his consultation and advice. Recent publications from NASA refer to the Donnell-Stein and Batdorf-Stein Equations, acknowledging his impact in these areas.

Dr. Stein was a member of Sigma Xi, Sigma Lambda Tau, and an Associate Fellow of AIAA. He served as a member of the Board of Examiners for doctoral candidates at George Washington University, Virginia

Polytechnic Institute and State University, and the Indian Institute of Technology Kampur. He taught extension classes for George Washington University, Old Dominion University and the University of Virginia at NASA's facilities.

The Dr. Manuel Stein Scholarship established at VPI&SU is awarded annually to an outstanding student pursuing graduate studies in the Department of Engineering Science and Mechanics within the College of Engineering. Recipients of the Scholarship Award shall be selected annually by the Head of the Department upon the recommendation of the Department's Scholarship and Awards Committee. The criteria to be used in the selection of the recipient of the Scholarship Award shall be those so well-reflected in Dr. Stein's own lifetime of service to his profession and commitment to his colleagues and students: the potential for scholarly achievement in teaching and research and a demonstrated dedication to the welfare and well-being of others.

Gifts to the Dr. Manuel Stein Scholarship are placed in an endowed fund with only the annual earnings available for funding scholarship awards; earnings from the Fund qualify for such matching funds as may be provided by the Commonwealth of Virginia under the Virginia Graduate and Undergraduate Tuition Assistance Program.

Gifts to The Dr. Manuel Stein Scholarship should be made payable to the "Virginia Tech Foundation, Inc." and sent to:

The Dr. Manuel Stein Fund
Office of University Development
201 Pack Building
Blacksburg, Virginia 24061-0336

Summary

Although Dr. Stein made numerous outstanding technical advancements throughout his career, perhaps his most lasting legacy was the unselfish sharing of his immense technical knowledge and insight with numerous researchers at, and associated with the Langley research Center. Dr. Stein's contribution to the aerospace community is poorly measured by publication numbers, but must instead be evaluated by technical quality and significance and by the several generations of structural mechanists that he mentored, consulted with, or otherwise positively influenced. This paper commemorates the historical significance of the five decades of technical and mentoring contributions of Dr. Manuel Stein to the aerospace community. The paper includes a complete bibliography of Dr. Stein's research work for ready reference for future researchers.

Technical Papers by Manuel Stein

1. Rafel, Norman; Stein, Manuel; and Houbolt, John C.: Compressive Strength of Curved Plywood Panels with Internal Pressure. NACA Memo. Report, March 1944.

2. Batdorf, Samuel B.; Stein, Manuel; and Libove, Charles: Critical Combinations of Longitudinal and Transverse Direct Stress for an Infinitely Long Flat Plate with Edges Elastically Restrained Against Rotation. NACA WR L-49, April 1945.

3. Libove, Charles; and Stein, Manuel: Charts for Critical Combinations of Longitudinal and Transverse Direct Stress for Flat Rectangular Plates. NACA WR L-224, September 1945.

4. Kotanchik, Joseph N.; Weinberger, Robert A.; and Stein, Manuel: Comparison of the Effects of Machine-Gun Fire on Artificially Aged and Non-Aged Alclad 24S-T Sheet-Stiffener Panels. NACA Memo. Report L-5513a, September 1945.

5. Batdorf, Samuel B.; Schildcrout, Murry; and Stein, Manuel: Critical Stress of Thin-Walled Cylinders in Axial Compression. NACA TN 1343, June 1947.

6. Stein, Manuel; and Neff, John: Buckling Stresses of Simply Supported Rectangular Flat Planes in Shear. NACA TN 1222, March 1947.

7. Batdorf, Samuel B.; and Stein, Manuel: Critical Combinations of Shear and Direct Stress for Simply Supported Rectangular Flat Planes. NACA TN 1223, March 1947.

8. Batdorf, Samuel B.; Stein, Manuel; and Schildcrout, Murry: Critical Stress of Thin Walled Cylinders in Torsion. NACA TN 1344, June 1947.

9. Batdorf, Samuel B.; Stein, Manuel; and Schildcrout, Murry: Critical Combinations of Torsion and Direct Axial Stress for Thin-Walled Cylinders. NACA TN 1345, June 1947.

10. Batdorf, Samuel B.; Schildcrout, Murry; and Stein, Manuel: Critical Shear Stress of Long Plates with Transverse Curvature. NACA TN 1346, June 1947.

11. Batdorf, Samuel B.; Schildcrout, Murry; and Stein, Manuel: Critical Combinations of Shear and Longitudinal Direct Stress for Long Plates with Transverse Curvature. NACA TN, June 1947.

12. Batdorf, Samuel B.; Stein, Manuel; and Schildcrout, Murry: Critical Shear Stress of Curved Rectangular Panels. NACA Report 887, 1947. (Formerly TN 1349.)

13. Batdorf, S.B.; and Stein, Manuel: Discussion of "Stability of Thin Cylindrical Shells in Torsion," by R.G. Sturm. Proc. ASCE, October 1947.

14. Budiansky, Bernard; Connor, Robert W.; and Stein, Manuel: Buckling in Shear of Continuous Flat Plates. NACA TN 1565, April 1948.

15. Budiansky, Bernard; Stein, Manuel; and Gilbert, Arthur C.: Buckling of a Long Square Tube in Torsion and Compression. NACA TN 1751, November 1948.

16. Selde, Paul; and Stein, Manuel: Compressive Buckling of Simply Supported Plates and Longitudinal Stiffeners. NACA TN 1825, March 1949.

17. Stein, Manuel; and Fralich, Robert W.: Critical Shear Stress of Infinitely Long, Simply Supported Plate with Transverse Stiffeners. NACA TN 1851, April 1949.

18. Schildcrout, Murry; and Stein, Manuel: Critical Axial-Compressive Stress of a Curved Rectangular Panel with a Central Longitudinal Stiffener. NACA TN 1879, May 1949.

19. Schildcrout, Murry; and Stein, Manuel: Critical Combinations of Shear and Direct Axial Stress for Curved Rectangular Panels. NACA TN 1926, August 1949.

20. Stein, Manuel; and Yaeger, David J.: Critical Shear Stress of a Curved Rectangular Panel with a Central Stiffener. NACA TN 1972, October 1949.

21. Stein, Manuel; Sanders, J. Lyell, Jr.; and Crate, Harold: Critical Stress of Ring-Stiffened Cylinders in Torsion. NACA TN 1981, November 1949.

22. Stein, Manuel; and Mayers, J.: A Small - Deflection Theory for Curved Sandwich Plates. NACA TN 2017, February 1950.

23. Stein, Manuel: Torsion and Transverse Bending of Cantilever Plates. Thesis, University of Virginia, 1941.

24. Reissner, Eric; and Stein, Manuel: Torsion and Transverse Bending of Cantilever Plates. NACA TN 2369, June 1951.

25. Stein, Manuel: and Mayers, J.: Compressive Buckling of Simply Supported Curved Plates and Cylinders of Sandwich Construction. NACA TN 2601, January 1951.

26. Peters, Roger W.; and Stein, Manuel: Deflection of Delta Wings Having a Carry-Through-Bay Chord Smaller than the Wing Root Chord. NACA TN 2927, May 1953

27. Stein, Manuel; Anderson, J. Edward; and Hedgepeth, John M.: Deflection and Stress Analysis of Thin Solid Wings of Arbitrary Plan Form with Particular Reference to Delta Wings. NACA Report 1131, 1953. (Formerly TN 2621.)

28. Stein, Manuel; and Sanders, J. Lyell, Jr.: A Method for Deflection Analysis of Thin Low-Aspect-Ratio Wings. NACA TN 3640, June 1956.

29. Stein, Manuel: Postbuckling Behavior of Rectangular Plates. Dissertation, Virginia Polytechnic Institute, 1958.

30. Stein, Manuel: The Phenomenon of Change in Buckle Pattern in Elastic Structures. NASA TR R-39, 1959.

31. Stein, Manuel: Loads and Deformations of Buckled Rectangular Plates. NASA TR R-40, 1959.

32. Stein, Manuel: Behavior of Buckled Rectangular Plates. Journal of the Engineering Mechanics Division, Proceedings of the ASCE, April 1960.

33. Stein, Manuel; and Hedgepeth, John M.: Analysis of Partly Wrinkled Membranes. NASA TN D-813, July 1961.

34. Stein, Manuel: The Effect on the Buckling of Perfect Cylinders of Prebuckling Deformations and Stresses Induced by Edge Support. Included in the Collected Papers on Instability of Shell Structures, 1962. NASA TN D-1510.

35. Stein, Manuel: Arrest of a Moving Mass by an Attached Membrane. NASA TN D-1928, July 1963.

36. Stein, Manuel: The Influence of Prebuckling Deformations and Stresses on the Buckling of Perfect Cylinders. NASA TR-R-190, 1965.

37. Mikulas, Martin M., Jr.; and Stein, Manuel: Buckling of a Cylindrical Shell Loaded by a Pre-Tensioned Filament Winding. Technical Note, AIAA Journal, Vol. 3, March 1965, pp. 560-561.

38. McElman, John A.; Mikulas, Martin M., Jr.; and Stein, Manuel: Static and Dynamic Effects of Eccentric Stiffening of Plates and Cylindrical Shells. AIAA Journal, Vol. 4, No.5, May 1966, pp. 887-894.

39. Stein, Manuel; and McElman, John A.: Buckling of Segments of Toroidal Shells.

AIAA Journal, Vol. 3, No. 9, September 1965, pp. 1704-1709.

40. Stein, Manuel: An Incremental Procedure for Solution of Nonlinear Problems with Applications to Plates and Shells. NASA TN D-3765, December 1966.

41. Stein, Manuel: Some Recent Advances in the Investigation of Shell Buckling. AIAA Journal, Vol. 6, No. 12, December 1968, pp. 2339-2345.

42. Stein, Manuel: The Impact of the Computer on Shell Analysis. Conference on Computer Oriented Analysis of Shell Structures. AFFDL-TR-71-79, June 1971.

43. Stroud, W. Jefferson; Dexter, Cornelia B.; and Stein, Manuel: Automatic Preliminary Design of Simplified Wing Structures to Satisfy Strength and Flutter Requirements. NASA TN D-6534, December 1971.

44. Stein, Manuel: Design Problems of Shell Structures and the Impact of the Computer on Shell Analysis. Computers and Structures, Vol. 2, 1972, pp. 31-45.

45. Stein, Manuel; and Starnes, James H.: Numerical Analysis of Stiffened Shear Webs in the Postbuckling Range. Numerical Solution of Nonlinear Structural Problems. ASME, AMD-V.6, pp. 211, 223, 1973.

46. Stein, Manuel: Flutter of Panels on Discrete Flexible Supports. NASA TN D-7443, March 1974.

47. Housner, Jerrold M.; and Stein, Manuel: Flutter Analysis and Parametric Studies of the Buckling of Composite Orthotropic Compression and Shear Panels. NASA TN D-7996, October 1975.

48. Housner, Jerrold M.; and Stein, Manuel: Numerical Analysis and Parametric Studies of the Buckling of Composite Orthotropic Compression and Shear Panels. NASA TN D-7996, October 1975.

49. Housner, Jerrold M.; and Stein, Manuel: NASTRAN Modeling Accuracy Studies. Appendix D, Analytical and Experimental Vibration Studies of a 1/8-Scale Shuttle Orbiter; Pinson, Larry D.; Coordinator. NASA TN D-7964, October 1975.

50. Williams, Jerry G.; and Stein, Manuel: Buckling Behavior and Structural Efficiency of Open-Section Stiffened Composite Compression Panels. AIAA Journal, Vol. 14, No. 11, November 1976, pp. 1618-1626.

51. Stein, Manuel; and Housner, Jerrold M.: Application of a Trigonometric Finite Difference Procedure to Numerical Analysis of Compressive and Shear Buckling of Orthotropic Panels. "Computers and Structures," Vol. 9, pp. 17-25, 1978.

52. Stein, Manuel; and Williams, Jerry G.: Buckling and Structural Efficiency of Sandwich-Blade Stiffened Composite Compression Panels. NASA TP-1269, September 1978.

53. Stein, Manuel: Postbuckling of Orthotropic Composite Plates Loaded in Compression. AIAA Paper No. 82-0778, May 1982.

54. Stein, Manuel: Postbuckling of Long Orthotropic Plates in Combined Shear and Compression. AIAA Paper No. 83-0876, May 1983.

55. Stein, Manuel; and Stein, Peter A.: A Solution Procedure for Behavior of Thick Plates on a Nonlinear Foundation and Postbuckling Behavior of Long Plates. NASA TP 2174, September 1983.

56. Stein, Manuel: Postbuckling of Orthotropic Plates Loaded in Compression. AIAA Journal, Vol. 21, No. 12, December 1983.

57. Stein, Manuel: Analytical Results for Postbuckling Behavior of Plates in Compression and in Shear. NASA TM 85766, March 1984.

58. Nemeth, Michael P.; Johnson, E.R.; Stein, M.; and Kamat, M.P.: Buckling Behavior of Orthotropic Composite Plates with Centrally Located Cutouts, VPI-E-83-21, June 1983.

59. Stein, Manuel: Postbuckling of Long Orthotropic Plates Loaded in Combined Transverse Compression and Longitudinal Compression or Shear. AIAA Paper No. 84-0890, May 1984.

60. Stein, M.; and Jegley, D.C.: Effects of Transverse Shearing on Cylindrical Bending, Vibration and Buckling of Laminated Plates. AIAA Paper No. 85-0744, April 1985.

61. Stein, Manuel: Nonlinear Theory for Laminated and Thick Plates and Shells Including the Effects of Transverse Shearing. AIAA Paper No. 85-0671-CP, April 1985.

62. Stein, M.: Postbuckling of Long Orthotropic Plates in Combined Shear and Compression. AIAA Journal, Vol. 21, No. 5, May 1985, p. 788.

63. Stein, M.: Postbuckling of Long Orthotropic Plates Under Combined Loading. AIAA Journal, Vol. 23, No. 8, August

64. Stein, M.; and Bains, N.J.C.: Postbuckling Behavior of Longitudinally Compressed Orthotropic Plates with Three-Dimensional Flexibility. AIAA Paper No. 86-0976-CP, may 1986.

65. Stein, M.: Nonlinear Theory for Plates and Shells Including the Effects of Transverse Shearing. AIAA Journal, Vol. 24, No. 9, September 1986, p. 1937.

66. Stein, M.; and Jegley, D.C.: Effects of Transverse Shearing on Cylinder Bending, Vibration, and Buckling of Laminated Plates. AIAA Journal, Vol. 25., No. 1, January 1987, p. 123.

67. Stein, M.: Analytical Results for Postbuckling Behavior of Plates in Compression and in Shear. Aspects of the Analysis of Plate Structures, 1985, pp. 205-223.

68. Stein, Manuel: Effects of Transverse Shearing Flexibility on the Postbuckling of Plates Loaded by Inplane Shear. AIAA Paper No. 87-0866-CP, April 1987.

69. Stein, Manuel: Postbuckling of Eccentric Open-Section Stiffened Composite Panels. AIAA Paper No. 88-2215, April 1988.

70. Librescu, L.; and Stein, M.: The Use of Higher Order Theory in the Postbuckling Analysis of Shear Deformable Symmetrically Laminated Composite Plate Panels. ICAS Paper No. 88-5.2.4, August 1988.

SOME COMMENTS ON THE STATUS OF SHELL THEORY AT THE END OF THE 20TH CENTURY: COMPLAINTS AND CORRECTIVES

by
J. G. Simmonds
Institute of Applied Mathematics and Mechanics
University of Virginia, Charlottesville, VA 22903

Abstract

This review is divided into *complaints* and *correctives.* Complaints are directed at: sloppy refereeing and editing; authors who fail to read or acknowledge what others have done; the mis-naming or mis-crediting of results; the misunderstanding and misuse of the Kirchhoff hypothesis; inflated claims of accuracy based on overly-simplified benchmark problems; the failure to appreciate the inherent errors in various shell models; the failure to appreciate that the physical response and mathematical structure of shell theory are fundamentally different from 3-dimensional elasticity; and the irrelevance of *Cosserat-type* theories.

Correctives include a simple, straight-forward derivation of a general nonlinear dynamic shell theory with the following features: (1) the equations of motion and kinematics (and those of thermodynamics, if desired) are *exact* consequences of their 3-dimensional counterparts; (2) there are no asymptotic or series expansions through the thickness; (3) *all* approximations (including the Kirchhoff Hypothesis) occur in the constitutive relations; (4) in static problems, there is a *mixed* form of the governing equations involving a mixed-energy density and exhibiting remnants of the well-known static-geometric duality of linear theory which is numerically robust because the limiting cases of nonlinear membrane theory and inextensional bending theory fall out naturally. (These latter two special cases are known to produce numerical nightmares unless treated with great care); (5) all equations may be expressed in coordinate-free form (although, sometimes, a hybrid form is shown to be superior).

Introduction

This paper summarizes many of the ideas in a new chapter of the 2nd edition of *The Nonlinear Theory of Elastic Shells* by Professor Avinoam Libai of the Technion, Israel, and myself. The book is to be published by Cambridge University Press in 1997. Both Avinoam and I knew Manny—perhaps me better than he—and I hope that my efforts will reflect an approach to shell theory that would have pleased that generous and thoughtful soul. Manny didn't tolerate overly fancy theories or unnecessarily elaborate mathematics and neither do I, but given his sweet nature, he probably would not have voiced his complaints as blatantly as I shall.

Complaints

(1) Sloppy refereeing and editing. I continue to see in "reputable" journals—journals that libraries pay good money for—papers that I cannot believe ever passed under the gaze of a referee or a technical editor, much less that of the editor(s): poor English, well-known names misspelled, missing references, etc., abound. To my colleagues I say, "If your going to agree to serve on an editorial board, then edit!"

(2) Authors who fail to credit or mis-credit others. Ignorance of old or obscure papers can be forgiven; simple laziness or hubris cannot. How many times have I seen an author of a paper on the *statics* of plates refer to Reissner-Mindlin theory? All workers in this field should know that Reissner's pioneering paper[1] on a static theory of plate bending accommodating Poisson's three boundary conditions (instead of Kirchhoff's two) appeared in 1945 in the *J. Appl. Mech.*. Mindlin's paper[2], which extended Reissner's ideas (with full credit) to dynamic problems, appeared in the same journal six years later. Another example is the *simultaneous* and *independent* development of a consistent, linear, first-approximation theory of shells by Koiter[3] and Sanders[4] in 1959. Often, one sees Sanders' name dropped in references to this theory, especially on the other side of the Atlantic. This is ironic because the two men have been great friends for a long time, and both hold the other's work in high regard. (And I need hardly mention to this audience that Lyell wrote his famous report when he was a

colleague of Manny's in the Structures Division at NASA, Langley.)

(3) Misuse (and misunderstanding) of the Kirchhoff Hypothesis. I could cite hundreds of papers where this is introduced, *a priori*, as a kinematic hypothesis. Sometimes these papers will point out that the Kirchoff Hypothesis leads to an unacceptable physical conclusion, namely, that the transverse normal stresses in a thin shell are no longer small compared to the (usually) dominant in-plane stresses. I will argue later, as have many others, that the proper place for the Kirchhoff Hypothesis is in the *constitutive relations*.

A similar but more elaborate *a priori* kinematic hypothesis is dubbed

(4) Cosserat Theory. Who need it? I defy anyone to show me a physical phenomenon in shells which cannot be explained in a simpler, more straight-forward way by conventional shell theory (properly formulated and properly applied).

(5) Inflated or unjustified claims of accuracy of so--called "higher-order" shell theories. Very often, the accuracy of such theories—and I seem to see a new one each week—are checked against 3-dimensional elasticity solutions. But, almost invariably, *these so-called "benchmark solutions" satisfy boundary conditions of simple support.* What's wrong with this? Well, with conditions of simple support, there are no 3-dimensional boundary layers—boundary layers of width proportional to the structure's thickness. Indeed, there is now a substantial body of work (which certain camps continue to ignore) based on both specific examples and general considerations that demonstrate that, except in exceptional circumstances, one cannot refine the classical, first-approximation theory of shells without simultaneously evoking the 3-dimensional theory of elasticity to refine the boundary conditions.

(6) The intrinsic errors in plate and shell theories are often ignored in mathematical analyses. Three common instances: (a) many nonlinear theories assume a quadratic strain-energy density and thus, in effect, ignore strains compared to one in the constitutive relations. Yet, there have been analyses that have hinged on the presence of similar negligible terms in the final equations; (b) the von Kármán equations have been used to analyze deflections much greater than a plate's thickness, and (c) spectral and control analyses have proceeded as if plate or shell models were accurate for any wavelength.

(7) Solution techniques for 3-dimensional bodies are often ill-adapted to shells. Analysts, especially in the finite element literature, have often approached shell problems as they would 3-dimensional elasticity problems, namely via a displacement formulation. But a thin-walled structure is a different animal—physically and mathematically—from a body all of whose dimensions are comparable. Thus, approximate methods developed for the latter may be inefficient or inappropriate for the former. In the linear theory of shells, the well-known static-geometric duality yields a *mixed formulation* of the field equations—or of the associated variational principles—that is at once elegant and numerically robust. In the nonlinear theory, enough of this duality persists to suggest that one should work with the same dual pairs of variables that work so well in linear theory. *Displacement formulations in shell theory must be treated carefully.*

(8) The cult of the material mid-surface. In rigid-body dynamics, who would *not* write the equations of motion with respect to the center of gravity because it was not a material point or because it did not coincide with the geometrical center of the body? So why distinguish the geometrical midsurface of a shell? In fact, I will argue shortly that there is a unique and much more natural surface to work with—the *surface of mass* as Libai and I call it, the analog of the center of mass in rigid body dynamics.

Correctives

(1) Notation. A good notation should be sufficient unto the topic and reveal the underlying physics in as an uncluttered way as possible. At the same time it should facilitate analytical or numerical approximations. These sometimes conflicting demands call for a *flexible* notation—"Flexible bodies call for a flexible approach," was one of Koiter's bons mots—not a fanatical insistence that there is but one path to enlightenment. Thus, Libai and I freely mix *direct, hybrid,* and *component notation.* For example, in different places, we represent the membrane stress resultant tensor as $\mathbf{N}$, $\mathbf{N}^{\alpha}$, or $N^{\alpha\beta}$, as appropriate.

(2) The del operator. Let $\mathbf{y}$ be the *position* of a point on a surface $\mathcal{R}$ and let $\mathcal{F}$ be some function—scalar, vector, or tensor—of $\mathbf{y}$. The definition of the *differential of* $\mathcal{F}$

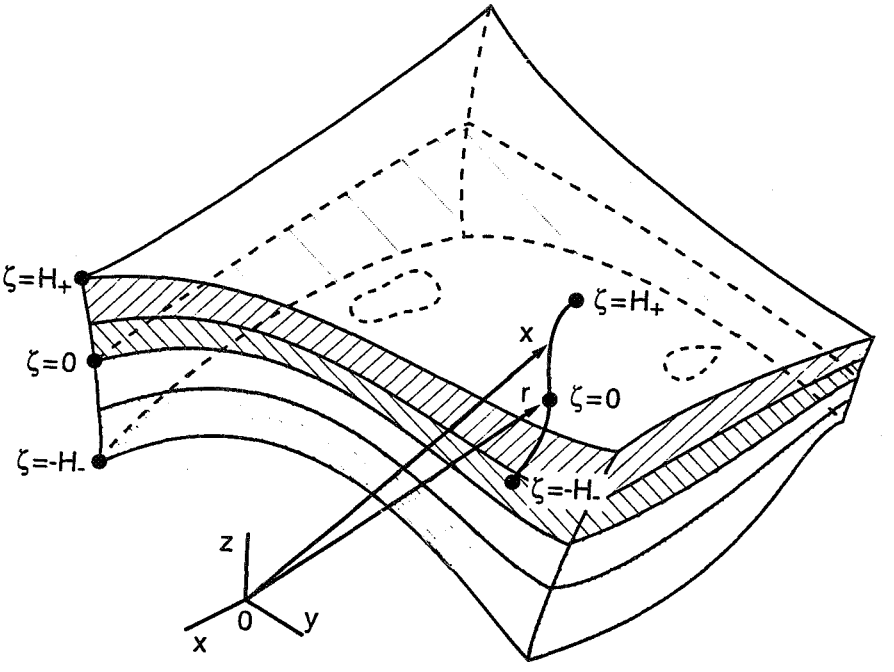

Fig. 1. Geometry of a general shell.

at **y** (when it exists) is analogous to the definition of the differential in elementary calculus; when the differential is a linear function of the independent variable dx, we write $df \equiv f'(x)dx$. In the more general case, we may write

$$d\mathcal{F} = d\mathbf{y} \bullet \nabla \mathcal{F}, \tag{1}$$

which defines (implicitly) the del operator ∇. This operator allows us to write local (differential) equations in coordinate-free form.

(3) Geometry. Why introduce surface or shell coordinates unnecessarily? The reference configuration of a general shell can be described simply as a 1-parameter family of smooth, non-intersecting surfaces, characterized by a (thickness-like) parameter ζ (a *foliation*). Thus, we may visualize a shell in its reference configuration as looking like a curved cake, made of layers of different ingredients of variable thicknesses, as in Fig. 1. Moreover, we may write the position of any particle within the reference configuration in the form

$$\mathbf{x} = \mathbf{x}(\mathbf{y}, \zeta) \ , \ \mathbf{y} \in \mathcal{R} \ , \ \zeta \in [-H_-, H_+] . \tag{2}$$

This representation can take us a long way before we must introduce surface coordinates and the associated concepts from differential geometry.

In a *motion* of the shell, the particle with position **x** moves to the *deformed position*

$$\bar{\mathbf{x}} = \bar{\mathbf{x}}(\mathbf{y}, \zeta, t) \ , \ \mathbf{y} \in \mathcal{R} \ , \ \zeta \in [-H_-, H_+] \ , \ 0 < t , \tag{3}$$

where t is time.

(4) The integral-impulse form of the equations of motion of a shell are exact consequences of those for a 3-dimensional continuum. Why integral forms? Because (a) they admit rougher solutions (e.g., shocks) than the *differential* equations of motion and (b) we may incorporate concentrated loads in a simple, natural way without having to summons the heavy machinery of distribution theory.

For a 3-dimensional continuum, we read off from Fig. 2

$$\int_{t_1}^{t_2} \left(\int_{\partial V} \mathbf{S} dA + \int_V \mathbf{f} dV \right) dt = \int_V \rho \dot{\bar{\mathbf{x}}} dV \Big|_{t_1}^{t_2} \tag{5}$$

and

$$\int_{t_1}^{t_2} \left(\int_{\partial V} \bar{\mathbf{x}} \times \mathbf{S} dA + \int_V \bar{\mathbf{x}} \times \mathbf{f} dV \right) dt = \int_V \bar{\mathbf{x}} \times \rho \dot{\bar{\mathbf{x}}} dV \Big|_{t_1}^{t_2} . \tag{6}$$

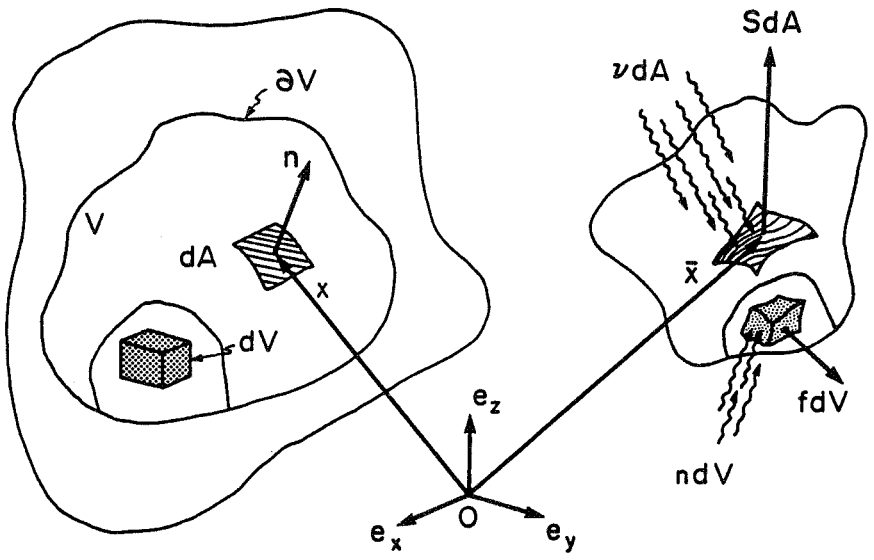

Fig. 2. Geometry of a 3-dimensional continuum.

The exact equations of motion for a shell follow by specializing (5) and (6) to shell-like bodies, i.e., to any structure that can be represented as in (2). Writing $dV = \mu dR d\zeta$, as in Fig. 3, we obtain immediately from (5)

$$\int_{t_1}^{t_2} \left(\int_{\partial R} \mathbf{N} ds + \int_R \mathbf{p} dR \right) dt = \int_R \mathbf{L} dR \Big|_{t_1}^{t_2} , \qquad \forall R \subseteq \mathcal{R} , \; t_1 < t_2 . \tag{7}$$

Here, with $\int_-^+ \equiv \int_{H_-}^{H_+}$ and $|_-^+ \equiv |_{H_-}^{H_+}$,

$$\mathbf{N} \equiv \int_-^+ \mathbf{S} \mu d\zeta = \mathbf{N}(\mathbf{y}, t; \boldsymbol{\nu}) \tag{8}$$

is the *stress resultant*, with $\boldsymbol{\nu}$ an outward unit normal to ∂R,

$$\mathbf{p} \equiv \mathbf{S}\mu^* |_-^+ + \int_-^+ \mathbf{f} \mu d\zeta = \mathbf{p}(\mathbf{y}, t) \tag{9}$$

is the *external force per unit area of* $\mathcal{R}$, and

$$\mathbf{L} \equiv \int_-^+ \dot{\bar{\mathbf{x}}} \rho \mu d\zeta = \mathbf{L}(\mathbf{y}, t) \tag{10}$$

is the *translational momentum* per unit area of $\mathcal{R}$.

Because the time derivative in (10) can be taken outside the integral, we can further decompose $\mathbf{L}$ by setting

$$\mathbf{L} = m \dot{\bar{\mathbf{y}}} , \tag{11}$$

where

$$m \equiv \int_-^+ \rho \mu d\zeta = m(\mathbf{y}) \tag{12}$$

is the *mass per unit area of* $\mathcal{R}$, and

$$\bar{\mathbf{y}} \equiv \int_-^+ \bar{\mathbf{x}} \rho \mu d\zeta / m = \bar{\mathbf{y}}(\mathbf{y}, t) \tag{13}$$

is a *weighted position.* Being the center of mass at time t of the differential column swept out by dR, we call $\bar{\mathbf{y}}(\mathbf{r}, t)$ the vector parametric equation of the deformed *surface of mass.* All the equations to follow are simplified if we now take the reference surface $\mathcal{R}$ to be the surface of mass so that $\bar{\mathbf{y}}(\mathbf{y}, 0) = \mathbf{y}$.

If we now introduce the *deviation* (from the surface of mass)

$$\mathbf{z} = \bar{\mathbf{x}} - \bar{\mathbf{y}} = \mathbf{z}(\mathbf{y}, \zeta, t) , \tag{14}$$

then (13) implies the *dynamic consistency condition,*

$$\int_-^+ \bar{\mathbf{z}} \rho \mu d\zeta = \mathbf{0} \tag{15}$$

and (6) applied to a shell-like body yields

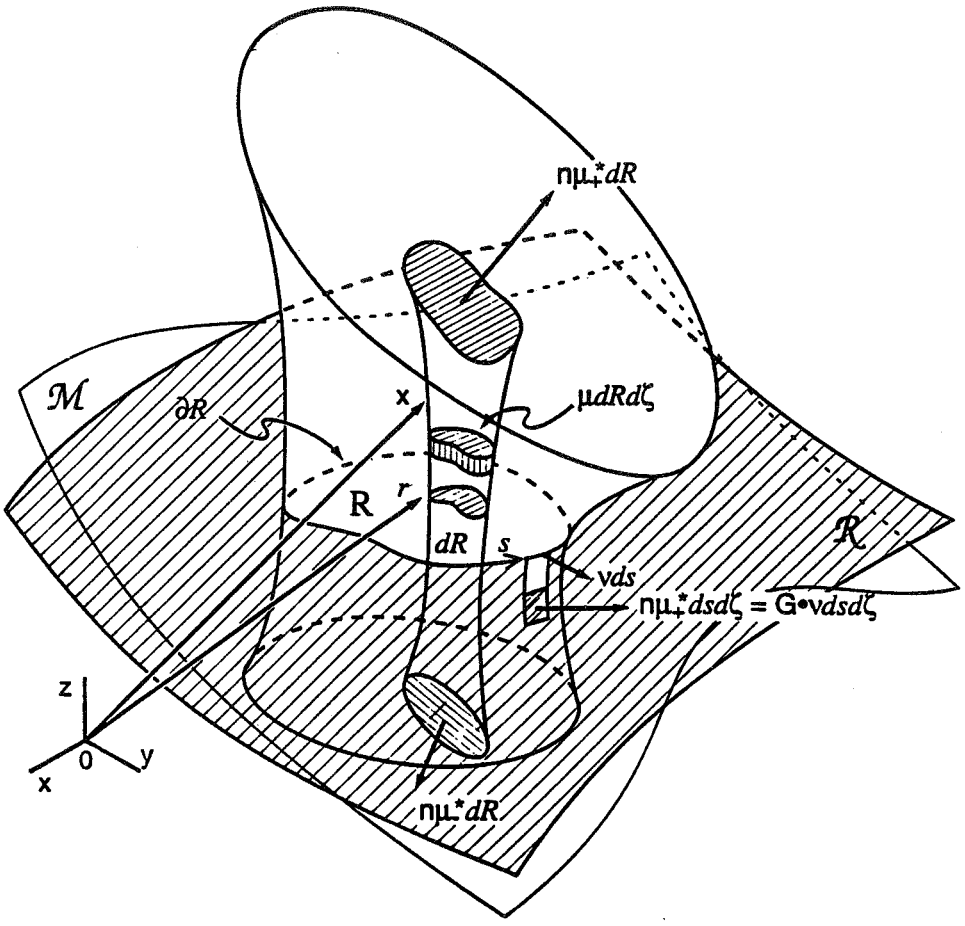

Fig. 3. Detailed geometry of an arbitrary volume of a shell.

$$\int_{t_1}^{t_2}[\int_{\partial R}(\bar{\mathbf{y}}\times\mathbf{N}+\mathbf{M})ds+\int_{R}(\bar{\mathbf{y}}\times\mathbf{p}+\mathbf{l})dR]dt = \int_{R}(\bar{\mathbf{y}}\times\mathbf{L}+\mathbf{R})dR\Big|_{t_1}^{t_2},\ \forall R\subseteq\mathcal{R},\ t_1<t_2, \tag{16}$$

where

$$\mathbf{M}\equiv\int_{-}^{+}\bar{\mathbf{z}}\times\mathbf{S}\mu d\zeta=\mathbf{M}(\mathbf{y},t;\mathbf{v}) \tag{17}$$

is the *stress couple*,

$$\mathbf{l}\equiv\bar{\mathbf{z}}\times\mathbf{S}\mu^*\Big|_{-}^{+}+\int_{-}^{+}\bar{\mathbf{z}}\times\mathbf{f}\mu d\zeta=\mathbf{l}(\mathbf{y},t) \tag{18}$$

is the *external couple per unit area of the reference surface* $\mathcal{R}$, and

$$\mathbf{R}\equiv\int_{-}^{+}\bar{\mathbf{z}}\times\dot{\bar{\mathbf{z}}}\rho\mu d\zeta=\mathbf{R}(\mathbf{y},t) \tag{19}$$

is the *rotational momentum per unit area of the reference surface* $\mathcal{R}$. Unlike what we found with (10), we cannot, in general, take the time derivative in (19) outside the integral sign. However, we may define a *spin* by setting

$$\mathbf{R}=I\boldsymbol{\omega}\ \text{ where }\ I\equiv\int_{-}^{+}\zeta^2\rho\mu d\zeta \tag{20}$$

may be called the *Kirchhoff inertia coefficient.*

(5) Local (differential) equations of motion for a shell. From 3-dimensional continuum mechanics, we have $\mathbf{S}=\mathbf{P}\bullet\mathbf{n}$, where $\mathbf{P}$ is the *1st Piola-Kirchhoff stress tensor*, and from Fig. 3 (and a little calculation) we have

$$\mu \mathbf{n} = \mathbf{G} \bullet \mathbf{v} \ , \ \mathbf{G} = -(\mathbf{b} \times \nabla \mathbf{x} \times \mathbf{x}_{,\zeta})^T . \tag{21}$$

Thus, from (8) and (17),

$$\mathbf{N} = \mathbf{N} \bullet \mathbf{v} \text{ and } \mathbf{M} = \mathbf{M} \bullet \mathbf{v} , \tag{22}$$

where

$$\mathbf{N} \equiv \int_{-}^{+} \mathbf{P} \bullet \mathbf{G} \, d\zeta = \mathbf{N}(\mathbf{y}, t)$$

and (23)

$$\mathbf{M} \equiv \int_{-}^{+} \bar{\mathbf{z}} \times \mathbf{P} \bullet \mathbf{G} \, d\zeta = \mathbf{M}(\mathbf{y}, t)$$

are *stress resultant and couple tensors*, respectively.

Since (7) and (16) must hold for all subregions of the reference surface and for all time intervals, it follows that if we insert (22) into these equations, assume sufficient smoothness in space and time, and apply the (surface) divergence theorem, we may conclude by a standard argument that the following local (differential) equations must hold at each point of $\mathcal{R}$ and at each time t:

$$\nabla \bullet \mathbf{N}^T + \mathbf{p} = m\dot{\mathbf{v}} \ , \ \nabla \bullet \mathbf{M}^T - (\mathbf{N} \bullet \nabla) \times \bar{\mathbf{y}} + \mathbf{l} = I\dot{\boldsymbol{\omega}} , \tag{24}$$

where $\mathbf{v} = \dot{\bar{\mathbf{y}}}$ is the shell *velocity*.

(6) The work identity. If we take the dot product of $(24)_1$ with $\mathbf{v}$ and the dot product of $(24)_2$ with $\boldsymbol{\omega}$, add the resulting expressions and integrate over an arbitrary subregion R of the reference surface, we obtain

$$\int_R \{(\nabla \bullet \mathbf{N}^T + \mathbf{p} - m\dot{\mathbf{v}}) \bullet \mathbf{v} + [\nabla \bullet \mathbf{M}^T - (\mathbf{N} \bullet \nabla) \times \bar{\mathbf{y}} + \mathbf{l} - I\dot{\boldsymbol{\omega}}] \bullet \boldsymbol{\omega}\} dR = 0 . \tag{25}$$

Removing spatial derivatives on $\mathbf{N}$ and $\mathbf{M}$ by using the divergence theorem, we obtain, with the aid of (22), the *Mechanical Work Identity*

$$\int_{\partial R} (\mathbf{N} \bullet \mathbf{v} + \mathbf{M} \bullet \boldsymbol{\omega}) ds + \int_R (\mathbf{p} \bullet \mathbf{v} + \mathbf{l} \bullet \boldsymbol{\omega}) dR \equiv [\tfrac{1}{2} \int_R (m\mathbf{v} \bullet \mathbf{v} + I\boldsymbol{\omega} \bullet \boldsymbol{\omega}) dR]^{\bullet} + \int_R [\mathbf{N}:(\nabla \mathbf{v} + \nabla \bar{\mathbf{y}} \times \boldsymbol{\omega}) + \mathbf{M}:\nabla \boldsymbol{\omega}] dR , \tag{26}$$

where $\partial R: \mathbf{y} = \mathbf{y}(s)$, $0 \le s \le L$ denotes the edge(s) of the shell, parameterized by arc length s.

(7) Conjugate strains. It would be tempting but incorrect to identify the tensors $\nabla \mathbf{v} + \nabla \bar{\mathbf{y}} \times \boldsymbol{\omega}$ and $\nabla \boldsymbol{\omega}$ in (26) as time derivatives of extensional and bending strains. To obtain proper expressions, let the spin $\boldsymbol{\omega}$ generate a *rotator* through the initial-value problem

$$\mathbf{Q}^{\bullet} = \boldsymbol{\omega} \times \mathbf{Q} \ , \ \mathbf{Q}(\mathbf{y}, 0) = \mathbf{1} . \tag{27}$$

Now imagine the surface gradient $\nabla \mathbf{y}^T = \nabla \mathbf{y}$ carried into $\nabla \bar{\mathbf{y}}$ by a rigid body rotation, represented by $\mathbf{Q}$, followed by a stretch, represented by the tensor $\mathbf{1} + \mathbf{e}$. That is,

$$\nabla \bar{\mathbf{y}}^T = (\mathbf{1} + \mathbf{e}) \bullet \mathbf{Q} \bullet \nabla \mathbf{y} \tag{28}$$

Following Ogden[5] (p.118), we call $\mathbf{e}$ the *Euler strain tensor*. According to Pietraszkiewicz[6], this strain measure was 1st introduced into shell theory by Alumae[7]. It can be shown—see Libai & Simmonds[8] for details—that

$$\nabla \mathbf{v} + \nabla \bar{\mathbf{y}} \times \boldsymbol{\omega} = (\mathbf{e}^* \bullet \mathbf{Q})^T . \tag{29}$$

Here, an asterisk (*) denotes the so-called *local* or *objective* time derivative, that is, the rate of change with respect to a reference frame that spins with angular velocity $\boldsymbol{\omega}$.

A bending strain tensor $\mathbf{K}$ can be introduced by setting

$$\nabla \mathbf{Q} = \mathbf{K} \times \mathbf{Q} . \tag{30}$$

It turns out—I again defer to Libai & Simmonds[8] for details—that

$$\nabla \boldsymbol{\omega} = \mathbf{K}^* + \boldsymbol{\omega} \times \mathbf{K} . \tag{31}$$

Thus, the integrand on the right side of (26)—the internal power (IP)—can be given the form

$$IP = \mathbf{N}:(\nabla \mathbf{v} + \nabla \bar{\mathbf{y}} \times \boldsymbol{\omega}) + \mathbf{M}:\nabla \boldsymbol{\omega} = \mathbf{n}:\mathbf{e}^* + \mathbf{m}:\mathbf{k}^* , \tag{32}$$

where $\mathbf{n} \equiv \mathbf{Q} \bullet \mathbf{N}^T$, $\mathbf{m} \equiv \mathbf{M} \bullet \mathbf{Q}^T$, and $\mathbf{k} \equiv \mathbf{Q} \bullet \mathbf{K}$.

Perhaps it is time to introduce hybrid notation and components. This could have been done earlier or could be delayed virtually indefinitely—it boils down to a question of taste: what notation seems simplest and the most revealing of the underlying mechanical ideas. Thus, if we assume that our reference surface $\mathcal{R}$ has the parametric representation

$$\mathcal{R}: \ \mathbf{y} = \mathbf{y}(\sigma^\alpha) \ , \ \sigma^\alpha \in D \ , \ \alpha = 1, 2 , \tag{33}$$

then, assuming $\mathcal{R}$ is smooth, we have the *covariant base vectors* and *unit normal*

$$\mathbf{y}_\alpha \equiv \mathbf{y}_{,\alpha} \ , \ \mathbf{b} = \frac{\mathbf{y}_1 \times \mathbf{y}_2}{|\mathbf{y}_1 \times \mathbf{y}_2|} = \tfrac{1}{2}\varepsilon^{\alpha\beta}\mathbf{y}_\alpha \times \mathbf{y}_\beta \ . \quad (34)$$

Here, $\varepsilon^{\alpha\beta}$ are the contravariant components of the surface permutation tensor. At any point of $\mathcal{R}$ where $|\mathbf{y}_1 \times \mathbf{y}_2| \neq 0$, the triad $\{\mathbf{y}_\alpha, \mathbf{b}\}$ forms a basis. We call

$$\{\mathbf{Y}_\alpha, \mathbf{B}\} \equiv \mathbf{Q} \bullet \{\mathbf{y}_\alpha, \mathbf{b}\} \quad (35)$$

the *spin basis*. If we resolve the resultant, couple, and strain tensors, first in terms of dyadic components and then in terms of surface tensor and vector components we have

$$\begin{aligned} \mathbf{n} &= \mathbf{Y}_\alpha \mathbf{N}^\alpha = N^{\alpha\beta}\mathbf{Y}_\alpha\mathbf{Y}_\beta + Q^\alpha \mathbf{Y}_\alpha \mathbf{B} \\ \mathbf{m} &= \mathbf{M}^\alpha \mathbf{Y}_\alpha = M^{\alpha\beta}\mathbf{Y}_\beta \times \mathbf{B}\mathbf{Y}_\alpha + M^\alpha \mathbf{B}\mathbf{Y}_\alpha \end{aligned} \quad (36)$$

$$\begin{aligned} \mathbf{e} &= \mathbf{E}_\alpha \mathbf{Y}^\alpha = E_{\alpha\beta}\mathbf{Y}^\beta\mathbf{Y}^\alpha + E_\alpha \mathbf{B}\mathbf{Y}^\alpha \\ \mathbf{k} &= \mathbf{Y}^\alpha \mathbf{K}_\alpha = K_{\alpha\beta}\mathbf{Y}^\alpha\mathbf{Y}^\beta \times \mathbf{B} + K_\alpha \mathbf{Y}^\alpha \mathbf{B} \ . \end{aligned} \quad (37)$$

Here, we have denoted the *direct product* of two vectors simply by **ab** instead of by the more cumbersome notation $\mathbf{a} \otimes \mathbf{b}$ (often favored in the literature).

In terms of these hybrid and component representations, the internal power (32) takes the form

$$\begin{aligned} IP &= \mathbf{N}^\alpha \bullet \dot{\mathbf{E}}^*_\alpha + \mathbf{M}^\alpha \bullet \dot{\mathbf{K}}^*_\alpha \\ &= N^{\alpha\beta}\dot{E}_{\alpha\beta} + Q^\alpha \dot{E}_\alpha + M^{\alpha\beta}\dot{K}_{\alpha\beta} + M^\alpha \dot{K}_\alpha \ . \end{aligned} \quad (38)$$

(8) All approximations in shell theory are made in the 1st Law of Thermodynamics (which is approximate anyway, in the sense that we can never account for all the forms of energy that flow into a shell—mechanical, thermal, chemical, electromagnetic, ...). Restricting myself to isothermal motions (which I do simply to save space—it is not at all necessary), I now *assume* that the left side of (26) represents the actual work done by the external environment on the piece of the shell represented by R.

Furthermore, we define a shell to be *elastic* if there exists a strain-energy density $\Phi(\mathbf{e}, \mathbf{k})$ such that the right side of (32) is equal to $\Phi^\bullet$. Since the strain rates can be assigned arbitrarily at any given event $(\mathbf{y}^*, t^*)$, it follows from (32) or (38) that

$$\mathbf{n} = \Phi_{,\mathbf{e}} \ , \ \mathbf{m} = \Phi_{,\mathbf{k}} \quad (39)$$

or

$$\begin{aligned} N^{\alpha\beta} &= \Phi_{,E_{\alpha\beta}} \ , \ Q^\alpha = \Phi_{,E_\alpha} \\ M^{\alpha\beta} &= \Phi_{,K_{\alpha\beta}} \ , \ M^\alpha = \Phi_{,K_\alpha} \ . \end{aligned} \quad (40)$$

Often, the shell equations may be cast into a more robust form if we use a *Legendre-Fenchel transformation* to introduce the *mixed-energy density*

$$\Psi(\mathbf{n}, \mathbf{k}) \equiv \inf_{\mathbf{e}} \{\Phi(\mathbf{e}, \mathbf{k}) - \mathbf{n}:\mathbf{e}\} \ . \quad (41)$$

If $\Phi(\mathbf{e}, \mathbf{k})$ is differentiable in $\mathbf{e}$ and grows faster than $O(\|\mathbf{e}\|)$ as $\|\mathbf{e}\| \to \infty$, then the stress-strain relations $(39)_1$ hold at any point(s) where the infimum in (41) is achieved. Furthermore, if $(39)_1$ can be solved for $\mathbf{e}$ as a function of $\mathbf{n}$ and $\mathbf{k}$ or, equivalently, if $(40)_1$ and $(40)_2$ can be solved for $E_{\alpha\beta}$ and E_α as functions of $N^{\alpha\beta}$, Q^α, $K_{\alpha\beta}$, and K_α, then it follows that

$$\mathbf{e} = -\Psi_{,\mathbf{n}} \ , \ \mathbf{m} = \Psi_{,\mathbf{k}}$$

or (42)

$$E_{\alpha\beta} = -\Psi_{,N^{\alpha\beta}} \ , \ E_\alpha = -\Psi_{,Q^\alpha} \ , \ M^{\alpha\beta} = \Psi_{,K_{\alpha\beta}} \ , \ M^\alpha = \Psi_{,K_\alpha} \ .$$

As is well known from the linear theory of shells, the use of a mixed-energy density together with the components of $\mathbf{n}$ and $\mathbf{k}$ (or Ψ) as unknowns leads, in general, to well-conditioned field equations in the sense that near inextensional bending ($\|\mathbf{e}\| \approx \mathbf{0}$) or near membrane behavior ($\|\mathbf{m}\| \approx \mathbf{0}$) does not lead to the cancellation of dominant terms.

(9) Integral and differential forms of the compatibility conditions. Consider *any* piecewise smooth curve ∂R, enclosing a subregion R on $\mathcal{R}$. If ∂R is parameterized by arc length s so that $\partial R : \mathbf{y} = \hat{\mathbf{y}}(s)$, $0 \le s \le L$, then

$$\int_{\partial R} \bar{\mathbf{y}}' ds = \mathbf{0} \ . \quad (43)$$

If we introduce the *unit tangent* to ∂R, $\boldsymbol{\tau} = \hat{\mathbf{y}}'(s) \equiv \mathbf{y}_\alpha \tau^\alpha$, then (43) can be written

$$\int_{\partial R} \boldsymbol{\tau} \bullet \nabla \bar{\mathbf{y}} ds = \int_{\partial R} \tau^\alpha \bar{\mathbf{y}}_\alpha ds = \mathbf{0} \ . \quad (44)$$

We now assume that there are no jumps (dislocations) in $\bar{\mathbf{y}}$ around any holes enclosed by ∂R. Thus, if the integrands in (44) are sufficiently smooth, we have, by Stokes' Theorem,

$$\int_R \mathbf{b} \bullet (\nabla \times \nabla \bar{\mathbf{y}}) dR = \int_R \varepsilon^{\beta\alpha} \bar{\mathbf{y}}_\alpha|_\beta dR = \mathbf{0} \ . \quad (45)$$

Further, if we assume that the integrands are spatially continuous, then, since R is arbitrary, we arrive at the *local* conditions

$$\mathbf{b}\bullet(\nabla\times\nabla\bar{\mathbf{y}})=\varepsilon^{\beta\alpha}\bar{\mathbf{y}}_{\alpha}|_{\beta}=\mathbf{0}\,. \tag{46}$$

It can be shown that, in terms of the extensional and bending strains, (46) may be given the form

$$\begin{aligned}\mathbf{b}\bullet[\nabla\times(\mathbf{e}\bullet\mathbf{Q})^{T}+(\mathbf{Q}:\mathbf{K})\mathbf{Q}^{T}-(\mathbf{Q}\bullet\mathbf{K}\bullet\mathbf{Q})^{T}]\\ =\varepsilon^{\beta\alpha}(\mathbf{E}_{\alpha}|_{\beta}+\mathbf{K}_{\beta}\times\mathbf{Y}_{\alpha})=\mathbf{0}\,.\end{aligned} \tag{47}$$

The economy of the hybrid notation is remarkable. Component forms of these equations may be found in Libai & Simmonds[8].

To obtain an additional strain compatibility condition, we note that, in analogy with (43), we also have

$$\int_{\partial R}\mathbf{Q}'ds=\int_{\partial R}\boldsymbol{\tau}\bullet\nabla\mathbf{Q}ds=\int_{\partial R}\tau^{\alpha}\mathbf{Q}_{,\alpha}ds=\mathbf{0}\,. \tag{48}$$

Following steps similar to those that led from (43) to (46), we are led to the local compatibility conditions

$$\bar{\mathbf{b}}\bullet[\nabla\times(\mathbf{K}\times\mathbf{Q})]=\varepsilon^{\beta\alpha}(\mathbf{K}_{\alpha}\times\mathbf{Q})|_{\beta}=\mathbf{0}\,. \tag{49}$$

If we carry out the differentiations in (49), we obtain terms involving $\nabla\mathbf{Q}$ or $\mathbf{Q}_{,\beta}$ which we re-express in terms of $\mathbf{Q}$ and $\mathbf{K}$ or $\mathbf{K}_{\beta}$. Thus, we obtain, after some further calculations, the following coordinate-free and hybrid form of our second strain compatibility condition:

$$\begin{aligned}\bar{\mathbf{b}}\bullet\{\nabla\times\mathbf{K}+2(\mathbf{K}:\mathbf{1})\mathbf{K}^{T}-2(\mathbf{K}^{T})^{2}+[\mathbf{K}^{2}:\mathbf{1}-(\mathbf{K}:\mathbf{1})^{2}]\mathbf{1}\}\\ =\varepsilon^{\beta\alpha}(\mathbf{K}_{\alpha}|_{\beta}+\tfrac{1}{2}\mathbf{K}_{\alpha}\times\mathbf{K}_{\beta})=\mathbf{0}\,.\end{aligned} \tag{50}$$

Again, the apparent simplicity of hybrid notation is remarkable. Component forms of this equation may be found in Libai & Simmonds[8]. In linear static theory, (50) is the kinematic dual of $(24)_1$.

(10) The rational finite rotation vector. The action of the rotator $\mathbf{Q}$, at any time and any position, is equivalent to a rotation through an angle $\beta(\mathbf{y},t)$ about a unit vector $\mathbf{e}(\mathbf{y},t)$. Of the several known representations of $\mathbf{Q}$ in terms of such a vector, the following has the advantage that it is *rational* in the components of $\boldsymbol{\psi}\equiv 2\tan(\beta/2)\mathbf{e}$:

$$\mathbf{Q}=P_{+}(\boldsymbol{\psi})[P_{-}(\boldsymbol{\psi})\mathbf{1}+\tfrac{1}{2}\boldsymbol{\psi}\boldsymbol{\psi}+\boldsymbol{\psi}\times\mathbf{1}]\,, \tag{51}$$

where

$$(1\pm\tfrac{1}{4}\boldsymbol{\psi}\bullet\boldsymbol{\psi})^{\pm1}P_{\pm}(\boldsymbol{\psi})\equiv 1\,. \tag{52}$$

The bending strain tensor $\mathbf{K}$ is defined implicitly in terms of $\nabla\mathbf{Q}$ by (30). Inserting (51) into this equation, we obtain from Libai & Simmonds[9] or Pietraszkiewicz & Badur[10] the following expressions for the bending strains in terms of $\boldsymbol{\psi}$:

$$\mathbf{K}=P_{+}(\boldsymbol{\psi})(\nabla\boldsymbol{\psi}-\tfrac{1}{2}\nabla\boldsymbol{\psi}\times\boldsymbol{\psi})$$

or (53)

$$\mathbf{K}_{\alpha}=P_{+}(\boldsymbol{\psi})(\boldsymbol{\psi}_{,\alpha}+\tfrac{1}{2}\boldsymbol{\psi}\times\boldsymbol{\psi}_{,\alpha})\,.$$

This expression, 1st given in component form by Simmonds & Danielson[11], represents the nonlinear extension of the bending strain in the Sanders-Koiter *linear* theory which, as Budiansky & Sanders[12] have emphasized, involves angles of rotation only. With the use of (53), (50) becomes satisfied identically. The spin turns out to have the equally simple representation

$$\boldsymbol{\omega}=P_{+}(\boldsymbol{\psi})(\dot{\boldsymbol{\psi}}+\tfrac{1}{2}\boldsymbol{\psi}\times\dot{\boldsymbol{\psi}})\,. \tag{54}$$

We note that in *static* theory, the dual of (53), which satisfies the homogeneous force equilibrium condition $(24)_1$ ($\mathbf{p}=\dot{\mathbf{v}}=\mathbf{0}$), is the stress function representation

$$\mathbf{N}^{T}=-\mathbf{b}\times\nabla\mathbf{F}\,. \tag{55}$$

(11) The Kirchhoff Hypothesis. Let us decompose $\mathbf{n}$ and $\mathbf{k}$ into symmetric and skew parts:

$$\mathbf{n}=\tfrac{1}{2}(\mathbf{n}+\mathbf{n}^{T})+\tfrac{1}{2}(\mathbf{n}-\mathbf{n}^{T})\equiv\bar{\mathbf{n}}+\hat{\mathbf{n}} \tag{56}$$

$$\mathbf{k}=\tfrac{1}{2}(\mathbf{k}+\mathbf{k}^{T})+\tfrac{1}{2}(\mathbf{k}-\mathbf{k}^{T})\equiv\bar{\mathbf{k}}+\hat{\mathbf{k}}\,. \tag{57}$$

Then the Kirchhoff Hypothesis is simply that the mixed-energy density $\Psi(\mathbf{n},\mathbf{k})$ depends only on $\bar{\mathbf{n}}$ and $\bar{\mathbf{k}}$. In terms of components, this means that

$$\Psi=\Psi(\bar{N}^{\alpha\beta},\bar{K}_{\alpha\beta})\,,\ \bar{N}^{\alpha\beta}=\tfrac{1}{2}(N^{\alpha\beta}+N^{\beta\alpha})\,,\ etc\,. \tag{58}$$

(12) Boundary conditions under the Kirchhoff Hypothesis. Under the Kirchhoff Hypothesis, $\bar{\mathbf{b}}=\mathbf{B}$ and $\boldsymbol{\omega}$ is no longer independent of the deformed position $\bar{\mathbf{y}}$. This means that along the edge of the shell we can no longer prescribe six boundary conditions, as the first integral on the left of (26) implies in unrestricted shell theory.

To deduce the proper *contracted* boundary conditions, we introduce the shell *displacement* $\mathbf{u}\equiv\bar{\mathbf{y}}-\mathbf{y}$. Then a unit tangent to $\partial\bar{R}$, the deformed image of the

shell boundary ∂R, is given by

$$\bar{\tau} = \lambda(\tau + \mathbf{u}'), \tag{59}$$

where

$$\lambda^2 \equiv 1 + 2\tau\bullet\mathbf{u}' + \mathbf{u}'\bullet\mathbf{u}' \tag{60}$$

and $\tau = \mathbf{y}'$ denotes a unit tangent to ∂R, the prime (') denoting differentiation with respect to arc length s along ∂R. With

$$\bar{\mathbf{v}} = \bar{\tau}\times\bar{\mathbf{b}}, \tag{61}$$

we have at every point of $\partial\bar{R}$ an orthonormal basis $\{\bar{\mathbf{v}}, \bar{\tau}, \bar{\mathbf{b}}\}$.

As Pietraszkiewicz[13] has pointed out, the spin $\bar{\boldsymbol{\omega}}$ of this deformed edge triad is *not* equal to $\boldsymbol{\omega}$. However, it is obvious (since spins obey the ordinary rules of vector addition, unlike finite rotation vectors) that $\bar{\boldsymbol{\omega}}$ and $\boldsymbol{\omega}$ differ only by a spin about $\bar{\mathbf{b}}$. But the Kirchhoff Hypothesis implies that $\mathbf{M}\bullet\bar{\mathbf{b}} = 0$; hence, $\mathbf{M}\bullet\boldsymbol{\omega} = \mathbf{M}\bullet\bar{\boldsymbol{\omega}}$.

The basic problem is now this: for deformations involving both large strains and large rotations, we want to introduce a scalar θ that we can call the *rotation of the edge*, but which can be expressed in terms of $\underline{\mathbf{u}}$ and its derivatives $\underline{\mathbf{u}}'$ and $\underline{\mathbf{u}}^\circ$ along and (outwardly) normal to ∂R. The following procedure, inspired by the work of Iura[14], Makowski & Pietraszkiewicz[15], and Pietraszkiewicz[16], accomplishes this goal.

Let $\bar{\boldsymbol{\psi}}$ denote the finite rotation vector that delivers $\{\bar{\mathbf{v}}, \bar{\tau}, \bar{\mathbf{b}}\}$ from its undeformed pre-image $\{\mathbf{v}, \tau, \mathbf{b}\}$. Then, in analogy with (54),

$$\bar{\boldsymbol{\omega}} = P_+(\bar{\boldsymbol{\psi}})(\dot{\bar{\boldsymbol{\psi}}} + \tfrac{1}{2}\bar{\boldsymbol{\psi}}\times\dot{\bar{\boldsymbol{\psi}}}) \tag{62}$$

so that

$$\mathbf{M}\bullet\boldsymbol{\omega} = \mathcal{M}\bullet\dot{\bar{\boldsymbol{\psi}}} \text{ on } \partial R, \tag{63}$$

where

$$\mathcal{M} \equiv P_+(\bar{\boldsymbol{\psi}})(\mathbf{M} + \tfrac{1}{2}\mathbf{M}\times\bar{\boldsymbol{\psi}}) \tag{64}$$

is an edge *pseudo-stress couple*.

The idea is now to express $\bar{\boldsymbol{\psi}}$ in terms of τ, $\bar{\tau}$, and the scalar $\theta \equiv \bar{\boldsymbol{\psi}}\bullet\tau = \bar{\boldsymbol{\psi}}\bullet\bar{\tau}$; in turn, $\bar{\tau}$ and θ can be expressed in terms of the edge displacement and its derivatives along and normal to the edge. From the analog of (51), it follows that

$$\bar{\tau} = P_+(\bar{\boldsymbol{\psi}})[P_-(\bar{\boldsymbol{\psi}})\tau + \tfrac{1}{2}\theta\bar{\boldsymbol{\psi}} + \bar{\boldsymbol{\psi}}\times\tau]. \tag{65}$$

Taking dot and cross products, we obtain

$$\bar{\boldsymbol{\psi}} = \frac{\theta(\tau+\bar{\tau}) + 2\tau\times\bar{\tau}}{1+\tau\bullet\bar{\tau}}, \quad \bar{\boldsymbol{\psi}}\bullet\bar{\boldsymbol{\psi}} = \frac{2[\theta^2 + 2(1-\tau\bullet\bar{\tau})]}{1+\tau\bullet\bar{\tau}}. \tag{66}$$

Thus,

$$\dot{\bar{\boldsymbol{\psi}}} = \left[\frac{\tau+\bar{\tau}}{1+\tau\bullet\bar{\tau}}\right]\dot{\theta} + \left[\frac{\theta\mathbf{1} - \bar{\boldsymbol{\psi}}\tau + 2\tau\times\mathbf{1}}{1+\tau\bullet\bar{\tau}}\right]\bullet\dot{\bar{\tau}}. \tag{67}$$

We now express $\dot{\bar{\tau}}$ and θ in terms of the displacement $\mathbf{u}$ and its derivatives $\mathbf{u}'$ and $\mathbf{u}^\circ$ along and normal to the edge. From (59),

$$\dot{\bar{\tau}} = \frac{\dot{\bar{\mathbf{y}}}'}{\lambda} - \frac{\dot{\lambda}\bar{\mathbf{y}}'}{\lambda^2} = \lambda^{-1}(\mathbf{1} - \bar{\tau}\bar{\tau})\bullet\dot{\mathbf{u}}'. \tag{68}$$

To express θ in terms of $\mathbf{u}'$ and $\mathbf{u}^\circ$, we use (66) and

$$P_+(\bar{\boldsymbol{\psi}})\bar{\boldsymbol{\psi}} = \tfrac{1}{2}(\tau\times\bar{\tau} + \mathbf{v}\times\bar{\mathbf{v}} + \mathbf{b}\times\bar{\mathbf{b}}), \tag{69}$$

to write

$$\frac{(1+\tau\bullet\bar{\tau})\theta}{1+\frac{1}{4}\theta^2} = \mathbf{v}\bullet\bar{\mathbf{b}} - \mathbf{b}\bullet\bar{\mathbf{v}}. \tag{70}$$

Thus,

$$\theta = \frac{2(\mathbf{v}\bullet\bar{\mathbf{b}} - \mathbf{b}\bullet\bar{\mathbf{v}})}{1+\tau\bullet\bar{\tau} + \sqrt{(1+\tau\bullet\bar{\tau})^2 - (\mathbf{v}\bullet\bar{\mathbf{b}} - \mathbf{b}\bullet\bar{\mathbf{v}})^2}}. \tag{71}$$

All terms on the right of (71) are obviously expressible in terms of $\mathbf{u}$, $\mathbf{u}'$, and $\mathbf{u}^\circ$.

With the aid of (67) and (68), we can now write the rate of work of the edge stress couples, (63), in the form

$$\mathbf{M}\bullet\boldsymbol{\omega} = \hat{\mathcal{M}}\dot{\theta} + \hat{\boldsymbol{\mathcal{M}}}\bullet\dot{\mathbf{u}}', \tag{72}$$

where

$$\hat{\mathcal{M}} \equiv \mathcal{M}\bullet\left[\frac{\tau+\bar{\tau}}{1+\tau\bullet\bar{\tau}}\right] \tag{73}$$

and

$$\hat{\boldsymbol{\mathcal{M}}} = \mathcal{M}\bullet\left[\frac{\theta\mathbf{1} - \bar{\boldsymbol{\psi}}\tau + 2\tau\times\mathbf{1}}{\lambda(1+\tau\bullet\bar{\tau})}\right]\bullet(\mathbf{1} - \bar{\tau}\bar{\tau}). \tag{74}$$

Finally, adding to the left side of the mechanical work identity (26) any external concentrated forces $\mathbf{F}_i$ acting at any corners $s = s_i$ of ∂R, inserting (32) and (72), integrating by parts along ∂R to remove the derivative on $\dot{\mathbf{u}}'$, and neglecting the rotary inertia (which incurs errors of the same order of magnitude as

those engendered by the Kirchhoff Hypothesis—see Timoshenko's now classic argument[17] of 1921 for the case of beams) as well as the external surface couple $\mathbf{l}$, we obtain the *reduced Kirchhoff mechanical work identity*

$$\sum(\mathbf{F}-[\hat{\mathcal{M}}])_i\bullet\dot{\mathbf{u}}_i+\int_{\partial R}(\mathcal{K}\bullet\dot{\mathbf{u}}+\hat{\mathcal{M}}\dot{\theta})ds+\int_R\mathbf{p}\bullet\dot{\mathbf{u}}dR$$
$$=(\int_R \tfrac{1}{2}m\dot{\mathbf{u}}\bullet\dot{\mathbf{u}}dR)^{\cdot}+\int_R(\mathbf{n}:\mathbf{e}^*+\mathbf{m}:\mathbf{k}^*)dR\,, \tag{75}$$

where

$$\mathcal{K}=\mathbf{N}-\hat{\mathcal{M}}' \tag{76}$$

is an *effective Kirchhoff edge stress resultant.*

Acknowledgements.

I owe much of my interest and approach to shell theory to the influence of the following colleagues, many of them close friends: Stu Antman, Ernst Axelrad, Bernie Budiansky, Don Danielson, A. L. Goldenveiser, Warner Koiter, Bob Leonard, Pierre Ladevèze, Avinoam Libai, Frithiof Niordson, V. V. Novozhilov, Wojciech Pietraszkiewicz, Eric Reissner, Lyell Sanders, Chuck Steele, Manny Stein, Clifford Truesdell, Roger Valid, Fred Wan. As you can see, Manny is in good company.

This research was supported by the U. S. Army Research Office under Grant DAAH04-94-G0189 and by the National Aeronautics and Space Administration under Grant NAG-1-1854.

References.

1. Reissner, E., The effect of transverse shear deformation on the bending of elastic plates. *J. Appl. Mech.* **12** (1945), A69-A77.
2. Mindlin, R. D., Influence of rotatory inertia and shear on flexural motions of isotropic, elastic plates. *J. Appl. Mech.* **18** (1951), 31-38.
3. Koiter, W. T., A consistent first approximation in the general theory of thin elastic shells. *Theory of Thin Elastic Shells*, Proc. Sympos. Delft, 1959 (W. T. Koiter, ed.), pp. 12-33. North-Holland, Amsterdam.
4. Sanders, J. L., Jr., An improved first-approximation theory for thin shells. NASA Rep. No. 24, 1959.
5. Ogden, R. W., *Non-Linear Elastic Deformations.* Halsted Press (John Wiley), New York, 1984.
6. Pietraszkiewicz, W., Geometrically nonlinear theories of thin elastic shells. *Adv. Mech.* **12** (1989), 52-130.
7. Alumae, N. A., Differential equations of equilibrium of thin shells in the post-critical state (in Russian). *Prikl. Mat. Mekh.* **13** (1949), 95-106.
8. Libai, A., and Simmonds, J. G., *The Nonlinear Theory of Elastic Shells,* 2nd ed., Cambridge University Press, 1997.
9. Libai, A., and Simmonds, J. G., Nonlinear elastic shell theory. *Adv. Appl. Mech.* **23** (1983), 271-371.
10. Pietraszkiewicz, W., and Badur, J., Finite rotations in the description of continuum deformation. *Int. J. Engr. Sci.* **21** (1983), 1097-1115.
11. Simmonds, J. G., and Danielson, D. A., Nonlinear shell theory with finite rotation and stress-function vectors. *J. Appl. Mech.* **39** (1972), 1085-1090.
12. Budiansky, B., and Sanders, J. L., Jr., On the "best" first-order linear shell theory. *Progress in Applied Mechanics* (Prager anniversary volume, D. C. Drucker, ed.). Macmillan, New York, 1963.
13. Pietraszkiewicz, P., Finite rotations in shells. *Theory of Shells,* Proc. 3rd I.U.T.A.M. Sympos., Tbilisi, 1978 (W. T. Koiter and G. K. Mikhailov, eds.). North-Holland, Amsterdam, 1980.
14. Iura, M., A generalized variational principle for thin elastic shells with finite rotations. *Int. J. Solids Struct.* **22** (1986), 141-154.
15. Makowski, J., and Pietraszkiewicz, W., Work-Conjugate boundary conditions in the nonlinear theory of thin shells. *J. Appl. Mech.* **56** (1989), 395-402.
16. Pietraszkiewicz, W., Work-Conjugate boundary conditions associated with the total rotation angle of the shell boundary. *J. Appl. Mech.* **60** (1993), 785-786.
17. Timoshenko, S. On the correction for shear of the differential equation for transverse vibration of prismatic bars. *Phil. Mag.* **41** (1921), 744-746.

EXPERIMENTAL STUDIES IN SHELL BUCKLING*

Josef Singer**

Abstract

Recent developments in shell buckling experiments are reviewed and related to earlier investigations. The motivation for buckling experiments on shells in the era of the digital computer, analysed by the author in two previous reviews, is re-examined and evaluated.

The historical development of shell buckling tests is briefly traced and the interaction of theory, experiments and numerical studies in developing better understanding of buckling and postbuckling phenomena is emphasized.

Some significant measurement problems are briefly discussed. The role of initial imperfections and their measurement is outlined, as well as the effect of boundary conditions. Nondestructive test methods for shell buckling are briefly mentioned.

Finally, areas of shell buckling experimentation that deserve attention in coming years are enumerated.

Introduction

In contrast to columns which have a neutral postbuckling path and plates which exhibit a stable postbuckling behavior, shells usually have a very unstable postbuckling behavior that strongly influences their buckling characteristics. Thin shells, however, are very efficient structures that can support very high buckling loads and hence their buckling and postbuckling have presented scientific and engineering challenges for decades. Extensive theoretical studies have clarified the phenomena, connected initial postbuckling behavior with imperfection sensitivity, have developed analysis procedures and established the imperfection sensitivity of some shell/load combinations. Unfortunately the impact of these modern methods of analysis on engineering practice has yet been very small, one reason being the scarcity of experimental investigations that were closely coordinated with theoretical studies, though thousands of shell buckling tests have been carried out.

The purpose of this paper is to sketch some of the dominant characteristics of shell buckling experiments and to discuss some examples of special interest. These examples are excerpts from a two-volume book, Buckling Experiments - Experimental Methods in Buckling of Thin-Walled Structures, by J. Singer, J. Arbocz and T. Weller, to be published by John Wiley and Sons later this year, many chapters of which are devoted to the buckling of shells.

Motivation for Experiments

Before embarking on experimental shell buckling studies or on a review of their highlights, it may be worth the while to reflect on the purpose of buckling experiments today, as was done by the author in his 1982 review[1].

With the rapid development in computers in the last decades the question of "why continue to do experiments?" has often been asked in many fields of applied mechanics. As the computational tools improved and expanded, the idea that computer simulations can replace the experiments has been voiced occasionally. For example, in the early sixties computer simulated experiments became popular and, in the excitement about their advantages and potential, their limitations were forgotten. For instance, Johnston in 1961 claimed[2]: "There are many advantages in simulated tests, carried out with the aid of a computer, in comparison with real tests in an actual testing machine. No machining is involved, no materials need be acquired, and there is no scatter in the test results! Moreover, the precision of results, although based on a simulated and idealized material, permits a study of details of behavior that is not possible in ordinary laboratory tests. It would be impossible to completely duplicate the observations that may be made on the basis of the simulated tests reported in this paper". It was forgotten that the simulation was so successful because *the physical phenomena in this case were well known* and had been extensively explored by very many real experiments. *New phenomena have still to be found and properly understood in physical tests*, before even the powerful computers of today can give a reliable simulation and then extend the range of parameters.

Another example in a similar vein was the false 1975 prediction for aerodynamics, on the wave of the

* This work has been sponsored in part by the Jordan and Irene Tark Aerospace Structures Research Fund.

** Professor Emeritus, Faculty of Aerospace Engineering, Technion - Israel Institute of Technology, Haifa 32000, Israel. Fellow

CFD achievements, that "Wind tunnels in 10 years will be used only to store computer print out".

Hence a scrutiny of the purpose of experiments in the computer era may be of value. The question was examined for shell buckling in two reviews in the eighties[1,3] and is now re-examined fifteen years later. One can enumerate eight primary motives:

a. Better Understanding of Buckling and Postbuckling Behavior and the Primary Factors Affecting It.

In addition to the buckling loads, careful experiments in which the parameters are varied one at a time, yield the behavior of the structure just before, at and after buckling, and accentuate the main parameters affecting this behavior. Such a philosophy of "research type experimental programs" had been strongly advocated for shells by Sechler[4] for many years, and was implemented in some test programs, for example in Ref. 5. Based on these observed parameters numerical schemes can be developed, verified, and can also be employed for "experiments on the computer" to extend the range of the parameters tested. One should remember that computer methods can converge to non-realistic behavior, unless the physical phenomena are well understood, or at least well described by appropriate experimentation, to permit reliable modelling.

b. to Find New Phenomena.

This reason is a direct extension of the first one and has already been stressed by Drucker[6,7], Sechler[4] and many others. In shell buckling and postbuckling experiments, the new phenomena are likely to be unexpected behavior patterns or mode interactions.

c. To Obtain Better Inputs for Computations.

The mathematical models employed in modern large multi-purpose computer programs can simulate real structures fairly closely for buckling, but the simulation depends very much on the input of correct boundary conditions, in particular joints or bonds, on material properties, imperfections, residual stresses and load applications. This has been emphasized by recent experience and definitely applies also to postbuckling. Often improved inputs can be obtained from appropriate nondestructive tests: for example, boundary conditions by vibration correlation techniques[8], imperfection shapes and amplitudes by imperfection scans[9], load transfer and eccentricities by strain measurements and vibration correlation techniques, residual stresses by X-ray techniques etc. Fully automated recording in experiments has begun and much closer interaction between test and computation is developing.

d. To Obtain Correlation Factors Between Analysis and Test and for Material Effects.

Even when large powerful programs are employed, test results may still differ considerably from predictions. These differences are partly due to inaccuracies of inputs and partly to variations in buckling and postbuckling behavior of the mathematical model and the structures tested. They can all be lumped for design purposes in a "correlation factor". The advantage of such a correlation factor is the overall correlation it provides for the designer, but its weakness is that it is completely reliable only for the structures tested. One can statistically evaluate a large number of tests to obtain overall lower bound correlation factors, called "knock-down" factors in the case of shells, but this results in very conservative design. Since many experiments are on laboratory scale shells, extensive studies comparing the results of laboratory scale and large scale tests are needed to reassure the experimenter and to guide the designer, in particular for dynamic loading. Correlation type experiments will therefore continue to be a major task of research and industrial laboratories for quite some time to come, as they provide the designer with essential correction factors which include the effects of new materials and manufacturing techniques and, to some extent, bridge the gap between the buckling and postbuckling behavior of the computation model and the realistic shell structures.

e. To Build Confidence in Multipurpose Computer Programs.

Extensive experimental verification is an essential element for confidence in a large computer program. This is therefore a primary motive for shell buckling and postbuckling experiments, which becomes more important, as the programs become more sophisticated and ambitious. Though some developers of programs have promoted and applied extensive experimental confirmation, as for example Bushnell in Ref. 10 for his BOSOR4 and 5 programs[11], or Almroth and Holmes[12] for the STAGS program[13], more correlations of the results obtained from computer programs with test results are required, as pointed out for instance in Ref. 14.

f. To Test Novel Ideas of Construction or Very Complicated Elements of a Structure.

Exploratory tests of new concepts have been used extensively by aeronautical, civil, mechanical and ocean engineers, and will continue to be an important tool. Furthermore, if the shell structure is elaborate and has many openings with complicated stiffening and load diffusion elements, model testing may sometimes even be less expensive and faster than computation with a large multipurpose program.

g. For Buckling Under Dynamic Loading and in Fluid-Structures Interaction Problems.

These are areas where computation is cumbersome, expensive, and difficult to interpret reliably. Experiments may therefore be preferable at this stage, though they too present many difficulties. Theory and numerical computations should follow these experiments closely, to reinforce and broaden the partial understanding of the phenomena that the experiments will provide.

h. For Certification Tests of Full Scale Shell Structures.

This is the typical industrial task which will continue till model experiments are sufficiently advanced and integrated with computation to eliminate the necessity for them. Here computerization of data acquisition and reduction has made great strides, and has significantly advanced the accuracy of measurement and interpretation.

Examination of these motives, originally proposed for shells at a Euromech Colloquium in 1980 (and published in 1982[1]) and recent experience reinforces the conclusion that the computer does not replace the experiments. It may change their purpose somewhat, it modifies the techniques, it broadens the capability to acquire results and it can use the experimental results to improve the computations. The presence of the computer in the experimental scene enhances and develops new techniques and capabilities. As pointed out by Birkemoe of the University of Toronto in 1994[15]: "High speed and high quality data acquisition, combined with on-line use of the data for control of the loading and/or response of a boundary condition, present a framework for improved experimental demonstration of stability limits in structures." Furthermore, "Improvements in user software for test environment continue to make ... computer control easier".

The experiment remains *an essential link* in the analysis also in the computer era, and its scope and usefulness are even greater today.

Historical Background

The earliest shell buckling tests were probably carried out in 1845-1850 by Fairbairn and Hodgkinson in England on thin-walled tubes under axial compression and bending, in connection with the design of the Britannia and Conway Tubular Bridges[16]. A few years later, Fairbairn[17,18] carried out extensive experimental studies on tubes under external pressure. The studies were undertaken "to determine the laws which govern the strength of cylindrical vessels exposed to uniform external force, and their immediate practical application in proportioning more accurately the flues of boilers ...". Fairbairn's reports were not only the first accounts of a comprehensive experimental program in shell stability (35 shells subjected to external pressure and 7 to internal pressure), but they, in particular his 1858 Royal Society paper[18], present a well documented discussion of a systematic and carefully planned study, that provides enlightening reading even today.

It is worth noting that for nearly half a century, Fairbairn's experiments, and the formula in which he summarized his results, were the basis of boiler design and the starting point for all the discussions on improved empirical formulae. There were vigorous debates in the 1860's, 70's and 80's, but very few and isolated experimental investigations till the beginning of the 20th century. The exception was an extensive series of tests of 18 circular wrought iron tubes, representing the geometries used in ship boilers, carried out at the German Navy Docks, Danzig in 1887-1882, which were discussed in detail by C. Bach, one of the leading German researchers in strength of materials at the time[19].

Bach began his paper on the Danzig experiments by pointing out that, though Fairbairn's test specimens were too small and weak to be relevant to practical designs in the 1880's, scientists and engineers in England, France, and in particular Germany, had been preoccupied for decades with mathematical processing of Fairbairn's results. This was also emphasized by the investigators at the beginning of the 20th century, especially Carman at the University of Illinois[20], and Stewart at the U.S. National Tube Company[21], who carried out very extensive systematic experimental studies of tubes under external pressure. Both Carman and Steward noted with surprise that an important problem, "the solution of which has not only great scientific interest

but also valuable technical applications, should remain for so many years with so little experimental work". (Both, however, overlooked the German Navy Danzig tests published more than a decade earlier.)

Carman's and Stewart's experiments covered a broad range of geometries. Carman tested 132 tubes in 1905-6 and Steward tested 514 tubes in 1902-4. Two comprehensive test programs indeed. Stewart's 1906 paper[21] represents a well planned experimental study, defining at the outset the factors on which the resistance of tubes to external pressures were assumed to depend, and investigating the influence of these factors. For example, "since it was anticipated that the out-of-roundness of the tube would exert a controlling influence on its behavior", an Autographic Calipering Apparatus was constructed and used to automatically record the divergence from roundness of tubes, at many stations along their length. From his experimental results, Stewart developed empirical formulae, charts and curves for designers, but his careful experimental investigation was actually only a broader and more modern version of Fairbairn's work of 50 years ago, without any innovative concepts.

Carman[20] on the other hand, tried to correlate his experimental results with "rational formulae", with the predictions of the theoreticians Bryan[22], Bassett[23] and others, who had attempted in the two preceding decades to treat this "difficult" problem of "the stability of an elastic system". Carman's tests at the turn of the century can therefore be considered as the first "research type experimental program" advocated by Sechler[4] seven decades later.

A decade later, in 1918, another such a research program, combining experiment and theory, was carried out by von Mises (and reported a decade later[24]). He tested a series of large thin-walled mild steel shells, of (R/t) = 400 (unusually thin for the period), loaded by hydrostatic pressure and found that the observed number of circumferential waves agreed very well with the predicted ones.

It may be point out here, that since the motivation for the study of the collapse of cylindrical shells under external pressure in the 19th century came primarily from the designs of steam-boiler flues and of similar larger pipes and containers and early in the 20th century from problems arising in the design of submarines or tunnel liners, nearly all the early experiments on shells were made on comparatively thick tubes and shells, which usually failed by plastic buckling, or due to yielding of the material, rather than by elastic instability. With the exception of the above mentioned 1918 von Mises test program, the experiments with very thin shells, where elastic buckling predominates, appeared only in the late twenties and thirties, with the widespread application of thin shells to airplane structures, in which buckling under axial compression gained prominence.

However, before discussing axial compression, the extensive studies of collapse of cylindrical shells under external pressure in the late twenties and early thirties, motivated primarily by submarine design, warrant a closer look, since they contributed significantly to the understanding of shell buckling and postbuckling behavior, in particular that of stiffened shells. Many of these studies were carried out at the U.S. Navy Experimental Model Basin in Washington D.C. (later called the David Taylor Model Basin) under the auspices of the ASME Special Research Committee on the Strength of Vessels Under External Pressure[25-27].

These experiments, carried out in 1929-1934, excel in their precision, care of execution and correlation and include 36 short and thin shells, in a wide range of geometries. For example, in Ref. 25 the importance of overall and local imperfections and the technique of their measurement is discussed, and the lack of recorded imperfection measurements is pointed out to be a primary weakness of previous experimental investigations. Also the essential requirements of geometrical and material similarity for reliable model tests are emphasized. Or Saunders and Windenburg's 1932 paper on the use of models[26] reports on what is probably the first systematic study of scaling problems and model manufacturing techniques for shells. This paper presents even today and outstanding account of the model approach with its associated problems.

The excellent DTMB tests and the two concurrent test programs of Tokugawa[28] and Sturm[29] laid the foundations for design and analysis of cylindrical stiffened shells under external pressure for many decades, actually to this very day.

Though thin-walled circular tubes under *axial compression* were tested already in 1846 by Fairbairn and Hodgkinson[16], their buckling was first recognized in the beginning of this century by "wrinkling" or "secondary flexure" in columns. In 1905-8 Lilly[30,31] carried out an extensive series of experiments on mild steel tubes at Trinity College in Dublin, Ireland, accompanied by a theoretical study. He showed clearly the "remarkable wave phenomena" that occur "in connection with secondary flexure" and that the load producing failure becomes smaller the larger (R/t), and stressed that "the true strength to compression of the tube is the

load which produces the wave formation". Lilly's experiments represent the first systematic study of elastoplastic buckling and collapse of axially compressed circular cylindrical shells.

Similar observations were made at the time also by other investigators. In the same period, the problem of wrinkling, buckling, or elastic instability, of circular cylindrical shells was also investigated theoretically by Lorenz[32] and others, yielding the main results of the classical linear theory. In practice, however, buckling of cylindrical shells under axial compression became important as their use in aircraft structures broadened, first as thin-walled columns and then in the stressed-skin construction of fuselages and wings, introduced in the late twenties and thirties (see Ref. 33). It soon became the central design problem of aerospace structures.

The first comprehensive series of experiments correlated with theoretical predictions were those carried out by Robertson[34,35], at the Royal Aircraft Establishment in 1915 and later at Manchester, but reported only a decade later. Four sets of short tubes, with (R/t)=5-500, made of different materials, were tested. Robertson emphasized the difference between the collapse behavior of thick tubes, which is determined by the material behavior (the yield stress), and that of thin tubes which is determined by elastic instability (buckling), indicating the different collapse patterns as well as the different autographic (stress-strain) diagrams and showing the transition value of (t/R) for the various sets of tubes.

The rapid growth of air transportation in the thirties and the associated development of semi-monoque aircraft shell structures motivated the careful experimental studies on cylindrical shells under compression of Lundquist[36] at NACA Langley and of Donnell[37] at the California Institute of Technology. Concurrently, the increased employment of thin-walled columns in civil engineering structures prompted an extensive study by Wilson and Newmark at the University of Illinois Engineering Experiment Station (for example Ref. 38). At about the same time, Flügge at the University of Göttingen, Germany, independently studied the stability of cylindrical shells and carried out experiments on shells under axial compression.

These comprehensive tests by many investigators covered a large range of geometries (R/t=35-1440 and L/R=0.25-32) as well as of materials and could therefore serve as a data base for designers.

Comparison of experimental buckling stresses with predictions by the then well known and accepted linear classical theory, which for a Poisson's ration of ν=0.3 can be written as

$$\sigma_{cl} = 0.605\, E(t/R) \qquad (1)$$

showed, however, great scatter, with experimental values being very much lower than the theoretical values, though failure in most of these relatively thin shells was due to elastic instability. The length of the cylinder was found to have very little effect on the buckling load, unless it was very short, and similarly the effect of end fixity was very small. The ratio of experimental to predicted buckling load or stress, later to be known as "knock down factor", $\rho = (\sigma_{exp} / \sigma_{cl})$ varied between 0.10-0.65, depended on the method of fabrication of the shells, and showed a definite tendency to decrease with increasing (R/t). This discrepancy between theory and experiment was too great to be accepted, it was a challenge to researchers and became the motivation for the development of large deflection theory for imperfect shells in the decades to come.

The engineers, however, could not wait and embarked on further testing programs. As a matter of fact, from the mid thirties to the late fifties, most shell buckling tests were for design data only and their results usually exhibit wide scatter and nonrepeatability (see also Ref. 39). In the last four decades, however, more careful experiments, more closely accompanied by analysis, have been carried out, that not only helped the understanding of buckling and postbuckling behavior, but also have began to influence the designers.

Buckling and Postbuckling Patterns

The perplexing behavior of thin cylindrical shells in axial compression, a pivotal problem in shell stability, has been studied for decades[40]. It is now well known that the main cause for the large difference between the predicted buckling load for a perfect shell and that observed in a typical test is the unstable initial postbuckling behavior of the shell and the resulting imperfection sensitivity. Furthermore, the buckling pattern predicted by classical linear theory for a perfect shell is a chessboard pattern, which differs considerably from the two-tier postbuckling pattern observed in a typical test. The theoretical chessboard pattern (which is really for an infinitely long shell) represents the high unstable initial buckling pattern and has never been observed directly in this form in an actual experiment. But high speed photography of very carefully performed axial compression tests, high speed recording of changes in

the photoelastic isoclinic patterns, and some experiments with mandrels inside the shells that restrict the buckle depth, have revealed traces of an unstable initial buckle pattern that (somewhat) resembles the chessboard pattern, predicted by classical theory, and have clearly shown the transition from an initial buckling pattern to another completely different postbuckling pattern.

In the sixties, a number of experimental studies of the unstable deformation states by high speed photography were carried out (see Refs. 43-49). At the Institut für Strukturmechanik of the German Aerospace Research Establishment (DLR) in Braunschweig, Esslinger and Meyer-Piening studied the buckling process on a number of axially loaded polyester (Mylar) cylindrical shells with a Fastax camera, having a maximum speed of 5200 frames per second (Refs. 45, 47 and 48). The thin shells had a radius of 100 mm, an (R/t)=394, and (L/R)=1.41-3.30.

The shells were tested in the rigid and precise deformation controlled test system RZ 100 of the DLR Braunschweig. For most of the high speed photography the slowest axial shortening of 0.039 mm/sec was applied. For the photography experiments the shells were sprayed with a silver paint which gave them a mat silvery tone and were placed in the test rig between special cylindrical distance pieces, to provide space for many lamps needed. The high light intensity needed posed some heating problems that required special attention.

Only about 0.3 seconds camera running time at sufficiently high speed was available for recording the buckling process. The starting of the control system, that operated the lamps and the film, had therefore to be fixed within less than 0.1 seconds. This emphasizes the camera timing problem in photographing the rapid elastic buckling process of a cylindrical shell, pointed out also by other investigators (for example in Ref. 42). Triggering the camera by the initiation of buckling is very difficult, since as the camera takes about half a second to reach its maximum speed, the buckling process (which, from initiation to the stable two-tier postbuckling pattern, takes about 5-30 ms, see Refs. 41, 43 or 49) would be completed long before that. If, however, the shell can be buckled several times at virtually the same axial load, (the automatic control of the RZ 100 system ensured here repeated identical loading speed), i.e. repeatability can be assured, as was the case of these Mylar shells (on account of the ability of Mylar to remain elastic for large strains), the camera could be synchronized with the expected initiation of buckling.

The buckling process for one of the longer Mylar shells, (L/R)=3.30, is shown in Fig. 1 (reproduced from Ref. 48) which presents selected frames from the high speed film covering the unstable initial post-buckling region, from just before buckling to the stable postbuckling equilibrium. Buckling commences here simultaneously at two points, at the bottom end and in the middle of the cylinder, as can be clearly seen in the second frame shown, 0.33 ms after the onset of buckling. Each of these buckles becomes the source of a growing unstable buckle pattern that spreads over the cylinder. The buckles in the middle region soon predominate in this shell, as can be seen from the 5th frame (0.83 ms) onwards, whereas the bottom buckles become weaker and eventually disappear. The buckles in this initial unstable postbuckling state are small rounded squares (see for example in the 3rd frame, 0.50 ms, or 5th frame, 0.83 ms) and can be considered to represent the chessboard pattern predicted by linear theory. As a matter of fact, with some imagination one can regard them as corresponding to a circumferential wave number n=18, as predicted from linear theory for "square" buckles. Many additional similar buckles appear around the initial ones till they cover a large part of the cylinder surface (as can be seen for example in the 9th frame, 1.5 ms, or the 10th one, 1.7 ms). Their shape is still roughly square, but they have become larger than the initial buckles, and in the 11th frame, at 2.3 ms, they correspond to a circumferential wave number n=13. From this point the shape of the buckles begin to change. They become more elongated in the axial direction, until the usual stable two-tier diamond pattern has evolved in the 15th frame, at 24 ms. By comparing, say the third frame at 0.50 ms with the 20th after 24 ms, one observes very clearly that the *initial unstable buckling pattern differs very significantly in shape and size from the stable postbuckling pattern* reached eventually, which is visible to the naked eye after the snap-through.

Similar conclusions were reached earlier by Tennyson (Refs. 41 and 43), who studied the initial buckling modes of circular cylindrical photoelastic shells subjected to axial compression, by recording the change in the 45° isoclinic patterns with high speed cameras. The shells were manufactured by spin-casting a liquid photoelastic plastic in a rotating apparatus, and had (R/t)≅100-400 and (L/R)≅2/5-4. They behaved completely elastically, permitting repeatable tests (as required for camera synchronization) and yielded buckling loads within

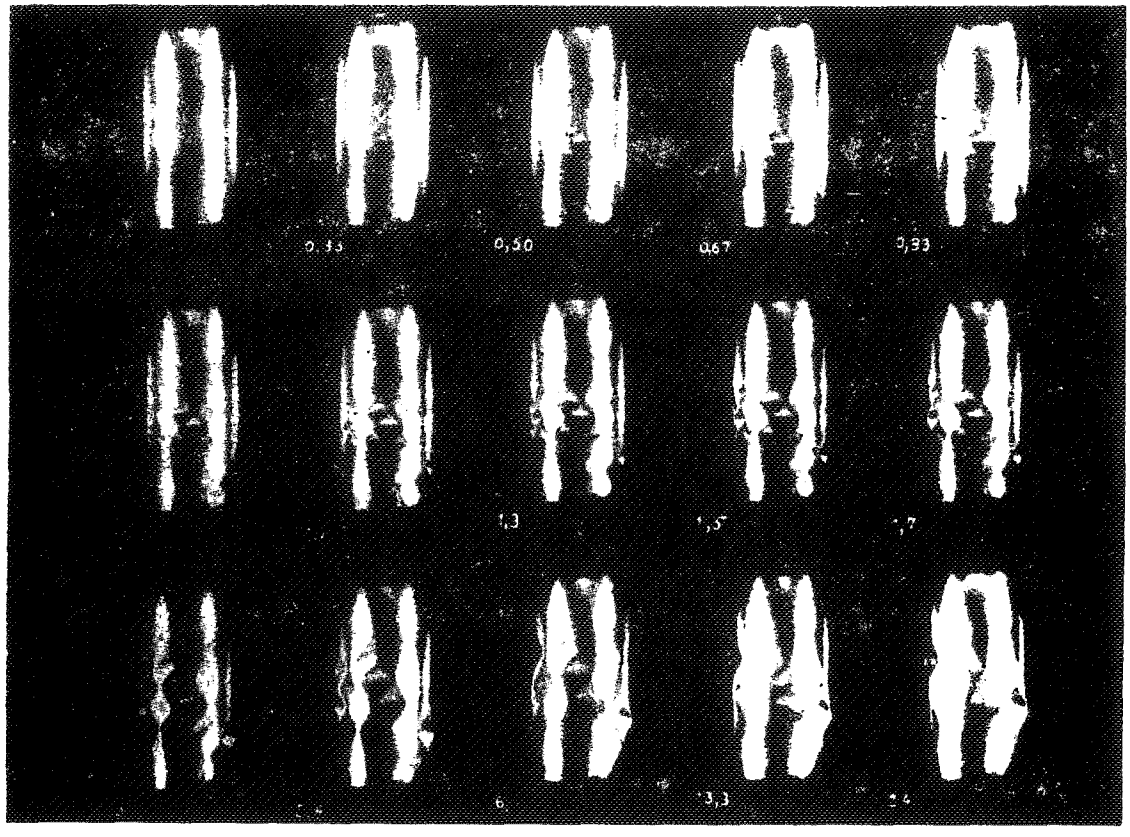

Fig. 1: High Speed Photography of Buckling Process

10-14% of the classical predicted values. The behavior he observed again emphasized the very significant difference between the unstable initial buckling pattern and the final stable postbuckling configuration, which one usually observes in tests. In additional studies[46] Tennyson reconfirmed these conclusions, that buckling initiation in an isotropic cylindrical shell under axial compression is a very localized phenomenon with an initial postbuckling pattern, which somewhat resembles the classical one and differs significantly from the large deflection postbuckling diamond shapes, into which the shell eventually deforms.

A similar process was observed in another high speed photography study carried out by Almroth, Holmes and Brush[44] at the Lockheed Palo Alto Research Laboratory. They tested very thin electro-deposited nickel cylindrical shells, (R/t)=857 and (L/R)=1.67, under axial compression, and photographed the buckling process on two of their specimens with a Fastax camera, at a shutter speed of about 8000 frames per second. The camera was also synchronized in these tests with the expected initiation of buckling obtained from an earlier test, to be repeated in the photographed one. In all the filmed tests, buckling initiated with a small local buckle about midway between the end plates. A series of similar small rounded buckles then propagated from the initial one circumferentially in a wedge-shaped manner, growing to a pattern that could perhaps be considered as representing a chessboard pattern. Later a different stable pattern of diamonds developed, each about twice the size of the initial rounded buckles.

In order to achieve repeatability of buckling tests on thin shells, a technique of restricting the inward buckle motion by a closely fitting internal mandrel was developed by Horton[50,51] at Stanford University and concurrently by Almroth, Holmes and Brush[44] at Lockheed Palo Alto. Electrodeposited nickel shells and thin-walled 7075-T6 aluminum alloy shells were used. In all these inward buckle restricted shells, a rounded buckle pattern appeared at buckling, which covered part of the shell, usually one or two rows of buckles extending around the circumference of the shell. When the load was increased after each buckling, as was done in the case of the nickel shells (see Ref. 50), the buckles spread row after row until the shell was entirely covered with a rounded pattern, that can be considered to somewhat resemble the theoretical chessboard pattern.

The important conclusions from the high speed photography studies and experiments with restricted buckle depth, are therefore that buckling initiates in a local unstable rounded pattern, which somewhat resembles the classical chessboard pattern, but which - after propagating circumferentially - transforms into an entirely different stable postbuckling pattern of diamonds of about twice the size of the initial rounded buckles. These studies of the buckling behavior clarify the phenomena: The onset buckling in an isotropic cylindrical shell under axial compression is a local occurrence and the buckling loads are therefore independent of the length of the shell (except of very short and very long shells), whereas the minimum postbuckling loads, and the corresponding postbuckling patterns, are strongly length dependent. On the other hand, initial geometric imperfections and disturbances will significantly influence the onset of buckling, and hence the buckling load, but will hardly affect the minimum stable postbuckling load.

The Influence of Initial Imperfections and Boundary Conditions

There exists a vast amount of literature on the influence of *initial imperfections* on the buckling of shells (see for example Refs. 1, 3, 9, 39, 52-54). Here the importance of this effect is only briefly recapitulated and it is stressed that the correlation between theory, imperfection measurements and buckling load is still incomplete (see Ref. 9). As pointed out in Ref. 9 and other papers (for example Refs. 52, 53, 55 or 56), semi-automated measurement techniques are available and an International Imperfection Data Bank has been initiated[55,56].

This data bank has to be further developed and enhanced in order to permit the introduction of a new buckling design method for imperfect shells outlined in Ref. 9, that will yield more efficient shells.

The effect of *boundary conditions* on the buckling of shells is also very significant, in particular for stiffened shells, where it may be as important as that of the imperfections (see for example Refs. 8 or 57). The definition of the actual effective boundary conditions, including load eccentricity, can be facilitated by application of vibration correlation methods[57].

This nondestructive vibration correlation technique[8,58] (VCT), consists essentially of an experimental determination of the lower natural frequencies for a loaded shell, and evaluation of equivalent elastic restraints that represent the boundary conditions. It is based on the similarity of the strong influence of axial and rotational restraints on free vibrations of stiffened shells, in particular for the lower natural frequencies whose mode shapes resemble the buckling modes, to that observed for buckling loads.

A coordinated international effort to collect additional imperfection data and correlate it with the relevant fabrication processes, with a concurrent effort to improve the definition of the actual effective boundary conditions, is essential to achieve significant improvements in the structural efficiency of shells (see Ref. 9).

Areas of Shell Buckling Experiments Deserving Attention in Coming Years

Due to the shortage of space and time, only few of the characteristics of shell buckling experiments have been reviewed. For a broader exposition one may turn to the surveys and references quoted.

In conclusion, the author feels that the *following areas* deserve careful attention and extensive efforts in the coming years:

a. Imperfection Data. The correlation between imperfection measurements, fabrication methods and buckling loads is still incomplete. The Imperfection Data Bank has to be further developed and enhanced in order to allow the introduction of new design methods based on it, that will result in more efficient shell structures.

b. Effect of Boundary Conditions. The definition of the actual effective boundary conditions including load eccentricity should be improved, by further development and applications of vibration correlation and other nondestructive techniques.

c. Material Imperfections and residual stresses should be given more attention to enlarge our knowledge of their effects.

d. Composites. Some tests on composite shells have been carried out in the last decade, but extensive experiments are required to further clarify their buckling and in particular their postbuckling behavior under different loading conditions. The effects of damage, delaminations and repeated buckling warrant additional study.

e. Load Distribution. More precise measurements are needed to assess the influence of load nonuniformities on shell buckling.

f. Load Interaction. New structural materials require re-evaluation of load interaction curves and how they are affected by boundary conditions.

g. Mode Interaction. Many theoretical studies have shown this to be one of the dangers of structural

optimization, but very few tests have been carried out. For stiffened shells this is of primary importance.

h. Buckling Due to Impact and Dynamic Loading. More systematic experiments are needed to supplement the earlier ones, mainly aimed at energy absorption devices.

i. Plastic and Elastic-Plastic Buckling. The extensive recent theoretical investigations should be evaluated, corroborated, and amplified by tests, to provide data for optimization studies.

References

1. Singer, J., "Buckling Experiments on Shells - a Review of Recent Developments", Solid Mechanics Archives, Vol. 7, 1982, pp. 213-313.
2. Johnston, B.G., "Buckling Behavior Above the Tangent Modulus Load", Journal of the Engineering Mechanics Division, American Society of Civil Engineers, Vol. 87, EM6, Paper 3019, Dec. 1961, pp. 79-99.
3. Singer, J., "The Status of Experimental Buckling Investigation of Shells", in: *Buckling of Shells*, Ramm, E., Ed., Proceedings of the State-of-the-Art Colloquium, Stuttgart, Springer-Verlag, Berlin, Heidelberg, New York, 1982, pp. 501-533.
4. Sechler, E.E., "The Role of Experimentation in Shell Research", in: *Mechanics Today*, Vol. 5, Nemat-Nasser, S., Ed., Pergamon Press, Oxford, 1980, pp. 439-449.
5. Singer, J., Arbocz, J., and Babcock, C.D., "Buckling of Imperfect Stiffened Cylindrical Shells under Axial Compression", AIAA Journal, Vol. 9, No. 1, 1971, pp. 68-75.
6. Drucker, D.C., "On the Role of Experiment in the Development of Theory", General Lecture, Proc. 4th U.S. National Congress of Applied Mechanics, ASME, 1962, pp. 15-33.
7. Drucker, D.C., "Thoughts on the Present and Future Interrelation of Theoretical and Experimental Mechanics", William M. Murrey Lecture 1967, Experimental Mechanics, Vol. 8, No. 3, 1968, pp. 97-106.
8. Singer, J., "Vibrations and Buckling of Imperfect Stiffened Shells - Recent Developments", in *Collapse: The Buckling of Structures in Theory and Practice*, Thompson, J.M.T. and Hunt, G.W., Eds., Cambridge University Press, Cambridge 1983, pp. 443-481.
9. Singer, J. and Abramovich, H., "The Development of Shell Imperfection Measurement Techniques", Thin-Walled Structures, Vol. 23, 1995, pp. 379-398.
10. Bushnell, D., "Thin Shells", in *Structural Mechanics Computer Programs, Surveys, Assessments and Availability*, Pilkey, W., Saczalski, K. and Schaeffer, H., Eds., University of Virginia Press, Charlottesville, VI, 1974, pp. 277-358.
11. Bushnell, D., "BOSOR 5 - Program for Buckling of Elastic-Plastic Complex Shells of Revolution Including Large Deflections and Creep", Computers and Structures, Vol. 16, 1976, pp. 221-239.
12. Almroth, B.O. and Holmes, A.M.C., "Buckling of Shells with Cutouts, Experiment and Analysis", International Journal of Solids and Structures, Vol. 8, 1972, pp. 1057-1071.
13. Almroth, B.O., Brogan, F.A. and Stanley, G.M., "Structural Analysis of General Shells, Vol. II: User Instructions for STAGSC", Lockheed Missiles & Space Co., Report LMSC-D633873, January 1979.
14. Buchert, K.P., "Practical Application of Shell Research", in: *Buckling of Shells in Offshore Structures*, Harding, J.E., Dowling, P.J. and Agelidis, N., Eds., Granada, London, 1982, pp. 257-283.
15. Birkemoe, P.C., "Stability: Direction in Experimental Research", Proceedings of SSRC 50th Anniversary Conference, Lehigh University, Bethlehem, Penn., June 1994, SSRC, Fritz Engineering Laboratory, 1994, pp. 349-357.
16. Clark, E., *The Britannia and Conway Tubular Bridges, With General Inquiries on Beams and on the Properties of Materials Used in Construction*, Vol. 1, Day and Son, Lincoln's Inn Fields, and John Weale, High Holborn, London, 1850.
17. Fairbairn, W., "On the Resistance of Tubes to Collapse", Report of the British Association for the Advancement of Science - 1857, Vol. 27, London 1857, pp. 215-219.
18. Fairbairn, W., "On the Resistance of Tubes to Collapse", Phil. Trans. of the Royal Society of London, Vol. 148, 1858, pp. 389-413.
19. Bach, C., "Die auf der kaiserlichen Werft in Danzig von 1887-1892 ausgeführten Versuche Über die Widerstandsfähikeit von Flammrohren" Zeitschrift des Vereines deutscher Ingenieure, Vol. 38, No. 23, 9 June 1894, pp. 689-696.

20. Carman, A.P., "Resistance of Tubes to Collapse", Physical Review, Vol. 21, 1905, pp. 381-387.
21. Steward, R.T., "Collapsing Pressure of Bessemer Steel Lap-Welded Tubes, Three to Ten Inches in Diameter", Trans. American Society of Mechanical Engineers, Vol. 27, 1906, pp. 730-822.
22. Bryan, G.H., "Application of the Energy Test to the Collapse of Long Thin Pipe Under External Pressure", Proceedings Cambridge Philosophical Society, Vol. 6, 1888, pp. 287-292.
23. Basset, A.B., "On the Difficulties of Constructing a Theory of the Collapse of Boiler Tubes", Philosophical Magazine, Vol. 34, No. 208, Sept. 1892, pp. 221-233.
24. Von Mises, R., "Der kritische Aussendruck für allseits belastete zylindrischer Rohre", Festschrift, Prof. Dr. A. Stodola, Orell Füssli Verlag, Zürich 1929, pp. 418-430.
25. Saunders, H.E. and Windenburg, D.F., "Strength of Thin Cylindrical Shells Under External Pressure", Trans. American Society of Mechanical Engineers, Vol. 53, APM-53-17a, 1931, pp. 207-218.
26. Saunders, H.E. and Windenburg, D.F., "The Use of Models in Determining the Strength of Thin-Walled Structures", Trans. American Society of Mechanical Engineers, Vol. 54, APM-54-25, 1932, pp. 263-275.
27. Windenburg, D.F. and Trilling, C., "Collapse by Instability of Thin Cylindrical Shells Under External Pressure", Trans. American Society of Mechanical Engineers, Vol. 56, APM-56-20, 1934, pp. 819-825.
28. Tokugawa, T., "Model Experiments on the Elastic Stability of Closed and Cross-Stiffened Circular Cylinders under Uniform External Pressure", Proc. World Engineering Congress, Tokyo, 1929, Vol. 29, 1931, pp. 219-279.
29. Sturm, R.G., "A Study of the Collapsing Pressure of Thin-Walled Cylinders", University of Illinois Engineering Experiment Station, Bulletin No. 329, Nov. 1941.
30. Lilly, W.E., "The Strength of Columns", Proceedings Institution of Mechanical Engineers, June 1905, Part 3 and 4, pp. 627-722.
32. Lilly, W.E., "The Design of Struts", Engineering (London), Vol. 85 Jan. 10, 1908, pp. 37-40.
32. Lorenz, R., "Achsensymmetrische Verzerrungen in dünnwandigen Hohlzylinder", Zeitschrift des Vereines Deutscher Ingenieure, Vol. 52, 1908, pp. 1706-1717.
33. Hoff, N.J., "Thin Shells in Aerospace Structures", Aeronautics and Astronautics, Vol. 5, Feb. 1967, pp. 26-45.
34. Robertson, A., "The Strength of Tubular Struts", Proceedings Royal Society of London, Vol. 121, Series A, 1928, pp. 558-585.
35. Robertson, A., "The Strength of Tubular Struts", Reports and Memoranda, R&M No. 1185, British A.R.C., July 1929.
36. Lundquist, E.E., "Strength Tests of Thin-Walled Duralumin Cylinders in Compression", NACA Report No. 473, June 1933.
37. Donnell, L.H., "A New Theory for the Buckling of Thin Cylinders Under Axial Compression and Bending", Trans. American Society of Mechanical Engineers, Vol. 56, AER-56-12, 1934, pp. 795-806.
38. Wilson, W.M. and Newmark, N.M., "The Strength of Thin Cylindrical Shells as Columns", University of Illinois Engineering Experiment Station, Bulletin No. 255, Feb. 1933.
39. Babcock, C.D., "Experiments in Shell Buckling", in *Thin-Shell Structures, Theory, Experiments and Design*, Fung, Y.C. and Sechler, E.E., Eds., Prentice-Hall, Englewood Cliffs, N.J. 1974, pp. 345-369.
40. Hoff, N.J., "The Perplexing Behavior of Thin Circular Cylindrical Shells in Axial Compression", Israel Journal of Technology, Vol. 4, No. 1, 1966, pp. 1-28.
41. Tennyson, R.C., "A Note on the Classical Buckling Load of Circular Cylindrical Shells Under Axial Compression", AIAA Journal, Vol. 1, No. 2, 1963, pp. 475-476.
42. Evensen, D.A., "High Speed Photographic Observation of the Buckling of Thin Cylinders", Experimental Mechanics, Vol. 4, No. 4, 1964, pp. 110-117.
43. Tennyson, R.C., "Buckling of Circular Cylindrical Shells in Compression", AIAA Journal, Vol. 2, No. 7, 1964, pp. 1351-1353.
44. Almroth, B.O., Holmes, A.M.C. and Brush, D.O., "An Experimental Study of the Buckling of Cylinders Under Axial Compression", Experimental Mechanics, Vol. 4, No. 9, 1964, pp. 263-270.
45. Esslinger, M. and Meyer-Piening, H.R., "Bericht über das Filmen des Beul - und Nachbeulverhaltens von dünnwandingen Kreiszylindern", Deutsche Luft- und Raumfahrt DLR Mitl. 69-07, June 1969.

46. Tennyson, R.C., "Buckling Modes of Circular Cylindrical Shells under Axial Compression", AIAA Journal, Vol. 7, No. 8, 1969, pp. 1481-1487.
47. Geier, B., "Die Hochgeschwindigkeits-Kinematographie als Hilfsmittel bei der Erforschung von Beulvorgängen bei dünnwandigen Kreiszylinderschalen", Research Film, Vol. 7, No. 2, 1970, pp. 128-135.
48. Esslinger, M., "Hochgeschwindigkeits-aufnahmen von Beulvorgang dünnwandiger, axialbelasteter Zylinder", Der Stahlbau, Vol. 39, No. 3, 1970, pp. 73-76.
49. Esslinger, M. and Geier, B., *Postbuckling Behavior of Structures*, CSIM Courses and Lectures, No. 236, Springer-Verlag, Wien, New York, 1975, pp. 122-124.
50. Horton, W.H. and Durham, S.C., "The Effect of Restricting Buckle Depth in Circular Cylindrical Shells Repeatedly Compressed to the Buckling Limit", SUDAER Report No. 174, Stanford University, California, Sept. 1963.
51. Horton, W.H. and Durham, S.C., "Imperfections, a Main Contributor to Scatter in Experimental Values of Buckling Load", International Journal of Solids and Structures, Vol. 1, 1965, pp. 59-72.
52. Arbocz, J. and Babcock, C.D., "Prediction of Buckling Loads Based on Experimentally Measured Initial Imperfections", in *Buckling of Structures*, Proceedings of IUTAM Symposium on Buckling of Structures, Harvard University, Cambridge, USA, June 17-21, 1974, Budiansky, B., Ed., Springer-Verlag, Berlin, 1976, pp. 291-311.
53. Arbocz, J., "Shell Stability Analysis: Theory and Practice", in *Collapse: The Buckling of Structures in Theory and Practice*, Thompson, J.M.T. and Hunt, G.W., Eds., Cambridge University Press, Cambridge, 1983, pp. 43-74.
54. Bushnell, D., *Computerized Buckling Analysis of Shells*, Martinus Nijhoff Publishers, Dordrecht, 1985.
55. Arbocz, J., "Imperfection Data Bank, a Means to Obtain Realistic Buckling Loads", in *Buckling of Shells*, Proceedings of a State-of-the-Art Colloquium, Stuttgart, Germany, 1982, Ramm, E., Ed., Springer, Berlin, Heidelberg, 1982, pp. 535-567.
56. Abramovich, H., Yaffe, R. and Singer, J., "Evaluation of Stiffened Shell Characteristics from Imperfection Measurements", Journal of Strain Analysis, Vol. 22, No. 1, 1987, pp. 17-23.
57. Singer, J. and Rosen, A., "Influence of Boundary Conditions on the Buckling of Stiffened Cylindrical Shells", in *Buckling of Structures*, Proceedings of IUTAM Symposium on Buckling of Structures, Harvard University, Cambridge, USA, June 17-21, 1974, Budiansky, B., Ed., Springer-Verlag, Berlin, 1976, pp. 227-250.
58. Weller, T., Abramovich, H. and Singer, J., "Application of Nondestructive Vibration Correlation Techniques for Buckling of Spot Welded and Riveted Stringer Stiffened Cylindrical Shells", Zeitschrift für Flugwissenschaften und Weltraumforschung, Vol. 10, No. 3, 1986, pp. 183-189.

Developments in Cylindrical Shell Stability Analysis

Norman. F. Knight, Jr.[1]
Old Dominion University
Norfolk, VA 23529–0247

James H. Starnes, Jr.[2]
NASA Langley Research Center
Hampton, VA 23681–0001

ABSTRACT

Today high–performance computing systems and new analytical and numerical techniques enable engineers to explore the use of advanced materials for shell design. This paper reviews some of the historical developments of shell buckling analysis and design. The paper concludes by identifying key research directions for reliable and robust methods development in shell stability analysis and design.

INTRODUCTION

Over the past four decades, much research has been focused on the buckling, collapse, and postbuckling behavior of cylindrical shells. This observation perhaps prompted Prof. Budiansky's statement in a review article that "Everybody loves a buckling problem" [1]. It also may have prompted Dr. Stein's acronym GOOSE (Get Out Of Shells – Everybody! [2]) because of the extreme competition and intensity of the research work.

The early work resolved several fundamental issues, especially the discrepancy between buckling loads computed with classical analysis methods and buckling loads observed experimentally for thin cylindrical shells loaded in axial compression. Seminal contributions were made by Lundquist [3], Donnell [4], von Karman and Tsien [5], and Koiter [6].

The 1940's through the 1960's were perhaps the heyday for classical shell stability research. Because of World War II, the distribution of many research contributions were restricted and often parallel efforts were being made in different countries. The work by Yoshimura [7] is one example of work that had limited distribution. The monumental work by Koiter [6] in his doctoral dissertation is another.

With the advent of the digital computer, computational methods began to be developed to address issues associated with structural collapse and postbuckling behavior. Notable collections of papers on this work include References [8–11]. With the computer available, additional terms in the series solutions were retained and computed, and their influence on the results was determined. The nonlinear partial differential equations for shell analysis were posed as discrete problems using finite difference approximations and numerical solutions were calculated. Energy formulations were developed. The development of the finite element method began in the 1960's. Questions still remained about which shell theory to use and which strains to consider.

The objectives of the present paper are to highlight selected aspects of cylindrical shell stability analysis that have developed over the past four decades, to identify the contributions of Dr. Manuel Stein to shell stability analysis, and to identify new directions and research thrusts for the coming years related to new aerospace vehicles as well as related to aircraft structural integrity. The scope of this paper is limited to elastic circular cylindrical shells subjected to axial compression. Much research has also been done in the areas of plastic buckling, thermal buckling, dynamic buckling, local instabilities, and non–conservative loading. Review of these areas is beyond the scope of this paper.

PREVIOUS REVIEWS

This paper takes extensive advantage of previous reviews of the field of shell buckling given by others. Some of the more notable reviews with extensive reference lists are briefly described herein.

In 1966 Budiansky and Hutchinson [12] presented a survey of some buckling problems for different shell geometries and loading conditions. They described the imperfection sensitive nature of the buckling problem and also the postbuckling behavior. This survey is primarily a survey of problems that Budiansky and Hutchinson had been involved with and limited analysis details are given. In 1979, Budiansky and Hutchinson [1] presented an updated review of buckling analysis advancements.

---

1. Professor, Department of Aerospace Engineering. Associate Fellow AIAA. Member ASME.
2. Head, Structural Mechanics Branch. Fellow AIAA.

In 1966 Hoff [13] presented a focused paper on buckling of cylindrical shells subjected to axial compression. Classical analysis methods are presented and reviewed. Hoff discussed the role of boundary conditions and imperfections on shell buckling as they relate to resolving the discrepancy between experimental and analytical results. Over 100 references are cited.

In 1968 Stein [14] presented a survey of different shell buckling problems. In this paper, Stein clearly demonstrated the need for using correct and consistent boundary conditions in the buckling calculations. The role of initial imperfections in shell buckling is again confirmed, and the equilibrium–bifurcation shell–buckling analysis approach is shown to be correct. Over 30 references are cited.

In 1970 Hutchinson and Koiter [15] reviewed postbuckling theory as related to elastic stability. Single–mode bifurcation behavior is described along with modal interaction. They reviewed the early postbuckling work and the influence of initial geometric imperfections. Over 200 references are cited.

In 1974 Sechler [16] presented a historical overview of the developments in shell research and design up to that time. Also in 1974, Babcock [17] presented a summary of experimental results and procedures for cylinder buckling, citing over 150 references.

In 1975 Tennyson [18] presented a review of "perfect" and imperfect composite cylinders. His review focused mainly on experimental results and correlation with analytical results. This review is perhaps the first for laminated composite cylinders and includes descriptions of experimental setups and results. Nearly 50 references are cited.

In 1983 Babcock [19] reviewed recent advances in shell buckling research associated with elastic and plastic buckling, dynamic buckling, experiments, and computations. His review focussed on modal interaction problems, localized buckling, contact buckling and buckle propagation. Over 70 references are cited.

In 1985 Bushnell [20] published a book entitled *Computerized Buckling Analysis of Shells* which described the fundamental shell equations and their numerical models for a wide range of shell problems. He also describes the structural behavior and characteristics of shell buckling, collapse and postbuckling response. Additional related information is available in several of his papers [21–23].

In 1986 Simitses [24] presented a review of buckling and postbuckling analysis for imperfect cylindrical shells. He described the work related to boundary conditions, prebuckling deflections, imperfections, load eccentricities, and material or constructional defects. Over 120 references are cited.

In 1990 Noor [25] presented an exhaustive list of over 400 books, monographs, and survey papers on shells. Research on various aspects of shell analysis (linear and nonlinear stress analysis, stability analysis, dynamics) are included in his bibliography. Key advances in analytical and computational models of shells are given by Noor, Belytschko, and Simo [26].

In 1996 Teng [27] presented a more recent review paper that primarily describes contributions in the past decade or so with a brief historical overview. He focuses on "real" structures with imperfections and nonuniform loading conditions. Localized effects caused by loads or geometric disturbances (e.g., dents) are described. This paper also has a rich listing of over 300 citations.

PROGRESS IN SHELL STABILITY

Key shell stability issues have been resolved over the past several decades. This progress may be broadly grouped in terms of: initial imperfections; prebuckling deformations; shell kinematics; composite shells; postbuckling behavior; modal interaction and mode jumping; finite element analysis; shell analysis codes; and modeling and simulation. Based on Sechler's equation for the production of papers relating to shells, it is estimated that approximately 1800 papers will appear in 1997 alone. An attempt has been made to be thorough but also concise, and apologies are extend to those authors not included in this review.

Initial Imperfections

In 1941 von Karman and Tsien [5] presented insight into the behavior of thin–walled isotropic circular cylinders subjected to axial compression. Their analysis indicated that a cylinder could jump from an unbuckled equilibrium configuration to an adjacent buckled equilibrium configuration at a load far below the classical buckling load and that any slight disturbance would suffice to trigger such a jump. Koiter [6] also investigated the influence of small deviations in shell geometry as related to shell stability. Later, Donnell and Wan [28] introduced initial imperfections into their analysis and concluded that initial imperfections were the principal reason for the discrepancy between buckling loads determined by classical analysis and those determined for test specimens.

Experimental and theoretical investigations of the effects of measured general imperfections on the buckling of cylinders were carried out by Arbocz and Babcock [29–30]. For global buckling, excellent correlation between the theoretical and experimental buck-

ling loads is reported. These investigations and others (e.g., Singer [31–33], Arbocz [34–35]) provided a better understanding of the buckling and postbuckling response of cylinders loaded in axial compression. Compilations of simplified procedures (e.g., [36–37]) empirically account for the effects of initial imperfections. These procedures yield conservative estimates of the buckling loads for isotropic and orthotropic cylinders.

Prebuckling Deformations

The effect of different in–plane boundary conditions on the stability of cylindrical shells loaded by axial compression has been studied by many investigators. The work of Hoff [38] and Nachbar and Hoff [39] demonstrated the influence of edge conditions, especially the free edge condition, on the buckling process. Stein [40–41] worked the more realistic problem of radially restrained edges in which the radial restraint is included from the onset of loading through the buckling process. This approach leads to nonuniform prebuckling deflections and stresses. Similar studies of finite length cylinders were performed by Almroth [42–43], and Sobel [44] who determined the importance of various edge conditions for the buckling of finite length cylinders.

Prebuckling deformations are also influenced by stiffener configuration and placement. The effect of stiffener eccentricity relative to the centerline of the shell wall was first pointed out by van der Neut [45]. Tests performed by Card [46] demonstrated the large effect stiffener eccentricity has on shell strength. The importance of this effect was then generally accepted. Block, Card, and Mikulas [47] were the first to show analytically that the eccentricity of stiffener placement strongly influences shell buckling behavior. Cylinders with external stiffeners exhibit significantly higher axial buckling loads than those with internal stiffeners. This effect was further studied by Block [48]. The effect of load eccentricity was studied by Weller et al. [49]. Singer and Rosen [50] developed an experimental technique to estimate the elastic support conditions for a shell buckling experiment.

Shell Kinematics

Shell theory was a topic of research in the past and continues to be pursued today. The popular Donnell theory [4, 51] is the most common theory even though it is not the most rigorous for general shell buckling problems. This theory gives accurate results for isotropic cylinders whose buckling modal displacements vary rapidly in circumferential coordinate. Dr. Stein's philosophy was that since buckling is a real physical phenomenon which occurs within the small deflection range, physical strains, rather than tensorial strains, should be used – large deflections are not an issue for the buckling case. The BUCLAP2 buckling analysis code described in Reference [52] is an example of his influence on the shell analysis community in the selection of strain–displacement relations to be used in analyses.

Extensions to shell theory to include nonlinear terms and transverse shear effects have been made by Loo [53] for Donnell theory as well as for additional shell theories developed, for example, by Koiter [54], Sanders [55–57], Budiansky and Sanders [58], Budiansky [59], Reissner [60], Naghdi [61–62], Simmonds [63–64], and Wempner [65–67] . In general, the nonlinear terms are not retained in the changes in curvature for small to moderate surface rotations [22].

Shell theory issues for stability and nonlinear analysis still remain. Researchers continue to review theoretical formulations and their computer implementations. Results of these reflections are available in several references, including Wempner [65], Bushnell [20], Ambartsumyan [68], Yamaki [69], Niordson [70], Librescu [71], Arbocz [72], and Palazotto and Dennis [73].

Composite Shells

Composite materials are used extensively in the design of automotive, aircraft, and space structures. Perhaps the first book on anisotropic shells is the one by Ambartsumyan [68]. The general formulation for laminated anisotropic plates and shells follows from the early work of Hildebrand et al. [74], Reissner and Stavsky [75], and Dong, Pister and Taylor [76] where the coupling between extension and bending is considered. Since then, numerous books and papers have been written on laminated composite and sandwich structures. The literature on composite structural mechanics has been reviewed by Bert and Francis [77], Hashin [78] and Chamis [79]. In addition, computational models for composite laminated and sandwich structures have been reviewed by Noor and Burton [80–81], Reddy [82], and Noor, Burton, and Bert [83] – each having an extensive list of references. Leissa [84] summarizes some results for the buckling of laminated structures.

In 1989 Kapania [85] presented a review of analysis methods and advances for laminated composite shells including finite element formulations. Assessment of various shell theories for linear stress analysis of cross–ply laminates is given in Reference [86] and for the buckling of cylindrical shells by Simitses et al. [87–88]. Because of the large number of parameters associated with laminated composite structures, it is often difficult to compare one design with another unless some non–dimensional parameters are used to char-

acterize the orthotropy and anisotropy of the laminate. Nemeth [89] has developed such parameters as extensions of the work of Batdorf [51] for isotropic cylinders and Stein [90] for orthotropic panels, and Nemeth refers to them as the Batdorf–Stein Z parameters. The effect of varying the laminate winding angle on the buckling load has been studied for various shell theories by Li et al. [91] and Jaunky and Knight [92]. Their findings confirm the need for a shell theory that is more robust than Donnell theory, since the lamination scheme definitely affects the shell buckling deflection pattern.

Limited work has been done on the design of postbuckled composite structures using detailed finite element models. Analysis tools for specific configurations and loading conditions have been used to design composite structures because of the inherent computational cost associated with performing a nonlinear finite element analysis within a design optimization procedure. Experimental studies of specific structural configurations indicate that substantial weight savings and improved structural behavior can be accomplished by exploiting the nonlinear response characteristics of composite structures. This feature provides the impetus for the development of robust and efficient nonlinear analysis methods for designing composite panels.

If the structure is designed to exploit its postbuckling stiffness, then effective design methods need to be developed and incorporated into the structural optimization procedures. Within the design optimization procedure, the values of the design parameters may vary. In composite structures, the number of design parameters may be large (e.g., Stroud [93]). Each change in a design variable requires a nonlinear analysis. The use of traditional nonlinear analysis methods within the design optimization procedure is unattractive, or more precisely, computationally uneconomical. From the designer's standpoint, performing nonlinear finite element analyses within the design optimization procedure limits the number of design configurations that can be assessed in a given amount of computer time. Preliminary design, analysis, and sizing tools with extensions to the postbuckling regime such as POSTOP (Dickson et al. [94–95]) and PANDA2 (Bushnell [96–99]) provide effective ways to search the design space and find near–optimal structural design configurations. These tools are based on advanced analytical formulations and take advantage of engineering approximations for many local buckling, postbuckling, and failure modes. Once an optimum solution is obtained, a nonlinear finite element analysis of the optimum panel design can be performed as demonstrated by Bushnell and Bushnell [99].

Postbuckling Behavior

Koiter's work [6] was the first application of initial postbuckling theory to cylinders subjected to axial compression. His work focused on determining the maximum load which can be supported before buckling is triggered and relating this load to the magnitude and forms of geometric imperfections. This approach led to Koiter's general nonlinear theory of stability. Kempner [100] extended the work of von Karman and Tsien [5] for cylinders by examining loading conditions based on dead weight versus a rigid testing machine.

Koiter [101] also studied the initial postbuckling behavior of isotropic cylindrical panels subjected to axial compression, suggesting that the behavior of a narrow curved panel in the advanced postbuckling stage approaches the behavior of a flat panel of equal width. His studies indicate that when the circumferential angle of a curved panel is sufficiently large, the postbuckling behavior is similar to that of a complete cylinder. Related research was also performed by van der Neut [102].

Application of a Rayleigh–Ritz type analysis based on a finite deflection theory including the effect of initial imperfections was introduced by Almroth [103] and Hoff, Madsen and Mayers [104] using trigonometric series for the displacement functions. Other studies of the buckling and postbuckling behavior of composite cylindrical panels and shells were extensions of the classical methods (e.g., Almroth [105], Khot [106], Budiansky [107], Seide [108], Koiter [109], Zhang and Matthews [110], Whitney [111], and Hui [112]). These studies considered the effects of stacking sequence, degree of anisotropy, and different material systems on the stability of cylindrical shells loaded by axial compression.

Stein [90, 113–116] contributed significantly to the understanding of postbuckling behavior of plates subjected to compression and shear as well as combined loading. His analysis is based on a series solution in one direction and an adaptive finite–difference–based two–point boundary–value problem "solver" in the other direction.

Traditionally the set of nonlinear algebraic equations resulting from the spatial discretization of the shell equations is solved using Newton–Raphson iteration (e.g., Bushnell [23]). The Newton–Raphson method is a solution technique based on linearizing the nonlinear equations, retaining only the leading term in a Taylor–series expansion about the last converged solution. Various forms of the Newton–Raphson algorithm are commonly used. The two most common are the full Newton–Raphson method and the modified Newton–

Raphson method. In the full Newton–Raphson method, the tangent stiffness matrix is formed and factored for every iteration and the residual force vector is formed for every iteration as part of the iterative procedure. Convergence is rapid but the computational cost is significant. For the modified Newton–Raphson method, only the residual force vector is formed for every iteration – the tangent stiffness matrix is not updated for every iteration. Instead, the tangent stiffness matrix is updated only at the beginning of each load step or perhaps only when convergence has not been attained after a specified maximum number of iterations. This method is very common, provides accurate solutions to many problems, and alleviates some of the computational cost of performing nonlinear finite element analysis without sacrificing accuracy or robustness for many structural mechanics problems.

Generally, the load level is incremented for each load step but held constant during the iterative process at that load level. In the arc–length control procedure of Riks [117], the load level is considered a variable within each iteration. The solution follows some specified path until convergence is attained. For a single degree of freedom system, this path may be in a plane normal to the tangent line at the beginning of the load step or the path may be an arc of a circle of a given radius (i.e., constant arc length). Since the load level is now a variable, an additional equation is needed. This equation is referred to as a constraint equation. To solve the original nonlinear system of equations with the constraint equation, *both* equations are linearized by considering the leading terms of the Taylor–series expansions about the last converged solution. This approach is robust and rigorous, and it avoids the root selection issue discussed by Crisfield [118] that arises from solving the quadratic form of the constraint equation.

Examination of Newton's method for isolated bifurcation problems reveals an alternative to the traditional incremental nonlinear analysis approach. Newton's method *differs* from the Newton–Raphson method in one fundamental way. Newton's method is a method for solving nonlinear differential equations by solving a sequence of linear differential equations in an iterative manner. The Newton–Raphson method is a incremental–iterative method for solving nonlinear algebraic equations by solving a sequence of linear algebraic equations in an iterative manner. These nonlinear algebraic equations arise from the spatial discretization of nonlinear differential equations. The form of Newton's method called parameter differentiation was further developed by Thurston [119] to solve problems with isolated bifurcation points. In the change of variables suggested by Thurston, the linear static solution for the membrane prebuckling stress state is used in combination with the first eigenpair associated with the linear bifurcation buckling problem. A postbuckling solution for a particular load level can be obtained directly without recourse to an incremental–iterative procedure. For example, a solution can be obtained directly at a load level where the maximum transverse deflection is as much as twice the panel thickness by using Newton's method with a linear combination of the linear pre–buckling stress solution and the linear bifurcation buckling mode shape. Hence, Newton's method provides an effective procedure for these problems provided the entire postbuckling response curve is not desired.

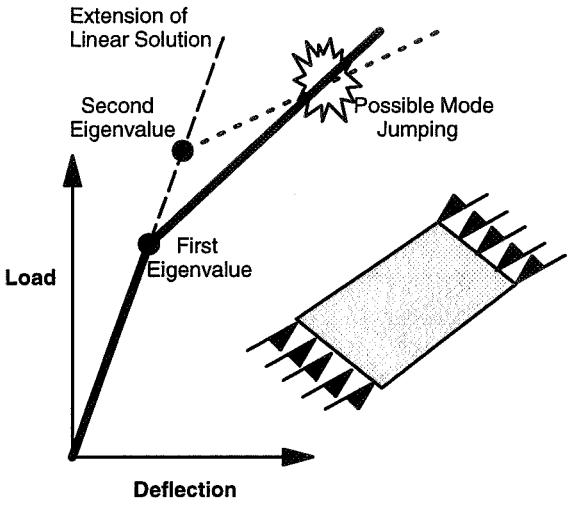

Fig. 1. Typical softening behavior exhibiting isolated critical points.

A softening structural behavior is related to a type of structural response which depends on the applied loading. This response, shown in Figure 1 for an axially compressed panel, is associated with buckling due to in–plane loads. Softening is generally related to a reduction in stiffness in the postbuckling regime without the response exhibiting a limit point. Buckling is associated with transitioning from one deformation mode to another (or an adjacent equilibrium configuration) at a common load level. That is, a perfect column loaded in compression will respond as a rod until the applied load reaches a critical value (the buckling load) at which time the lowest energy state becomes a beam bending mode. In this case, there exists a load level with two adjacent equilibrium configurations: one with a rod or membrane behavior and another with a beam or bending behavior. These critical values correspond to the eigenvalues of the structure based on a given stress state. Often these eigenvalues are isolated or spaced from one another. Such problems are not difficult to solve even though

the load–deflection curve generally does not exhibit a horizontal tangent. However, the buckling load does correspond to a critical value or eigenvalue which correspond to a point where the determinant to the tangent stiffness matrix is zero. As such, the nonlinear terms must be *triggered* in order to *jump* from the prebuckling path onto the adjacent equilibrium path. This triggering is usually done by incorporating the actual imperfect geometry of the structure (initial geometric imperfections) or by imposing a small lateral or eccentric load. In most practical nonlinear analyses of postbuckled panels, an initial imperfection in the form of a linear combination of one or more scaled local bifurcation buckling modes is used as a "trigger" in order to ease the transition from a prebuckled stable state to a post–locally–buckled stable state, that is, to enable the computed series of nonlinear equilibrium states easily to "turn the corner" labelled as "first eigenvalue" in Figure 1. The solution process usually continues smoothly in the postbuckled load range since the eigenvalues of the tangent stiffness matrix generally remain isolated rather than clustered together.

Modal Interaction and Mode Jumping

The buckling mode of a structure depends on a number of factors including geometric parameters such as shell thickness, shell radius, and shell length. Tvergaard [120] determined that the transition from an axisymmetric buckling mode to a diamond–shaped buckling mode is attributed to geometric effects associated with the cylinder thickness. Such behavior should be represented by the analysis tools used for cylinder design as the design space is searched.

The stability analysis of cylindrical shells involves an infinite number of repeated (or nearly identical) eigenvalues at the critical load. The postbuckling behavior, as shown in Figure 2, exhibits significant reduction in load carrying capability and many different unstable equilibriums paths are available before the lowest energy state is reached and stable equilibrium is re–established (e.g., Yoshimura [7]). Also in a design optimization procedure, a given panel structural design will generally evolve from one with an isolated bifurcation point to one with closely spaced eigenvalues. However, the form of Newton's method described previously in Reference [119] is for structures exhibiting isolated bifurcation points.

A softening structural behavior which exhibits a rapid reduction in load carrying capacity is generally associated with structural collapse and in shell structures occurs due to multiple or repeated eigenvalues. One example is a circular cylindrical shell subjected to axial compression as shown in Figure 2. In this case,

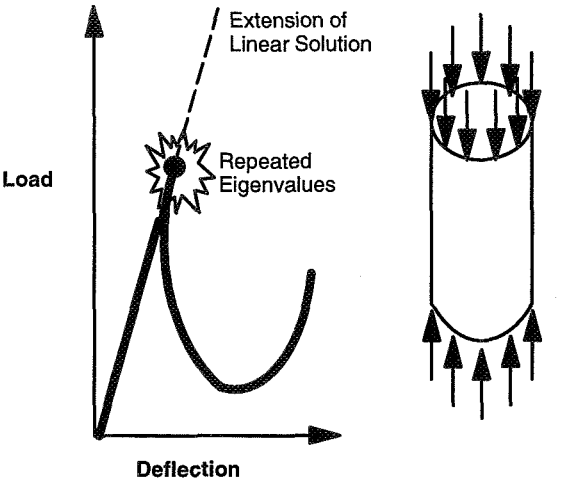

Fig. 2. Typical softening behavior exhibiting repeated eigenvalues and structural collapse.

multiple repeated eigenvalues or closely spaced eigenvalues cause difficulty in predicting the nonlinear structural response. In most cases, the nonlinear solutions along the unstable equilibrium path are not observable in the laboratory since they represent a dynamic event. However, analytically tracing this unstable branch using static analysis procedures may provide insight into the overall failure process and provide information useful for improving the design. In this unstable region, structural material failures often occur. The problem becomes even more complex since the geometry changes due to large deflections and rotations and changes in the material constitutive law due to local failures and/or inelastic behavior, or both.

The postbuckling behavior of structures is often characterized in terms of the postbuckling deformation pattern. In the postbuckling regime, two types of modal behavior occur as described by Bushnell [20] and Bushnell et al. [121]. One type is *modal interaction* which is defined as the interaction of long wavelength (general instability) buckling modes with one or more short wavelength (local instability) buckling modes (e.g., see Koiter [6], Tvergaard [122], Budiansky [107], Koiter and Pignataro [123], and van der Neut [124]). The other type is *mode jumping* or *mode switching* which is defined as the interaction between short wavelength buckling modes (e.g., Stein [125], Supple [126], and Riks et al. [127]). Mode jumping problems are dynamic problems wherein the stable equilibrium paths may not be statically connected [121, 127]. Associated with such a "jump" is an energy change which may be sufficient to cause localized damage leading to further complications in predicting the nonlinear shell response.

If a secondary critical point is reached (see Figure 1), then mode jumping may occur. At least one negative root is present in the tangent stiffness matrix. Such problems are generally referred to as "drop dead problems" since the nonlinear static solution procedure stops dead in its tracks. In such cases, the most likely cause of the numerical difficulties is the "mode switching" or "mode jumping" phenomenon that would lead to a new equilibrium configuration for the structure (e.g., see Riks et al. [127]). Further extensions to Newton's method for such *mode jumping* problems have been presented by Thurston, Brogan, and Stehlin [128]. These extensions require substantial software modifications to implement and user intervention to use. However for the case of isolated bifurcation points, Newton's method is readily adapted to existing finite element analysis systems. Alternatively, Riks et al. [127] have suggested that, at such a critical point, a transient dynamic analysis be initiated and continued until the inertia terms decay and a new stable equilibrium configuration is obtained. Examples are provided in Reference [121]. From this point, the nonlinear static analysis may proceed. For the solution procedure to proceed past such critical points on the response curve numerically, a transient dynamic analysis may be needed in order to "jump" to the next "stable" equilibrium configuration. Alternatively a new component of the initial buckling modal imperfection can be introduced corresponding to the critical eigenvector at the secondary branching point in Figure 1 in order to ease the transition to the tertiary branch.

Finite Element Analysis

The finite element method continues to evolve and mature. In the development of shell finite elements, basic issues still remain. These issues include element distortion sensitivity, geometry modeling and idealization, adaptive refinement and quality control, incorporation of interlaminar effects, and localized effects due to shell junctures and discrete changes in local stiffness (e.g., stiffener attachments, cutouts, variable thickness, local damage and delaminations). Gallagher [129] identified three formulation approaches that are still used in finite element codes. These approaches are the faceted shell approximation using flat elements, the isoparametric solid element approach to curved surface modeling, and the approach based on the use of a shell theory directly. MacNeal [130] has an excellent book on finite element design and element development. Other key references on shell elements for stability analysis include Hinton et al. [131], Hughes et al. [132], Stein et al. [133], Taylor [134], Noor et al. [26], Kratzig [135], Simo et al. [136], and Riks et al. [137]. Much research has been published in this area. Over 400 text books are available on the topic of finite element analysis, and space precludes any attempt to summarize these contributions within this paper.

Nonlinear finite element analysis procedures have been under development for more than three decades. Tremendous challenges are still being faced. Some of the fundamental work has been presented by Hartung [138], Hughes, Pifko, and Jay [132], and Hinton, Owen, and Taylor [131]. For these nonlinear problems, the interplay between various aspects of the problem and the analysis can become entangled causing analysts great difficulties in obtaining and verifying robust, accurate solutions. This interplay can include many contributors such as structural response, problem formulation, approximations, numerical solvers, iteration convergence, interpretation of results, boundary conditions, and loading. While many issues have been resolved, new issues have emerged as the computing technology and our understanding have evolved.

Most current commercial finite element codes provide a nonlinear analysis capability for both statics and transient dynamic problems (e.g., Hibbitt [139–140]). In most cases, the Newton–Raphson procedure is available and used as the default solution algorithm. In addition, some codes use the *full* Newton–Raphson method as their default method in order to provide robustness for novice users. Nonlinear problems are very difficult to solve. It is nearly impossible to anticipate all possible solution combinations that users may attempt. Users of nonlinear codes need to be especially cognizant of the structural problem being solved, options and defaults provided by the code developers, and thoroughly interrogate the computed results of the simulation.

Shell finite element development should continue to be an active area of research. Anomalies and pathological problems associated with many shell elements still remain. The intelligent use of the elements and thorough examination of the models and their predictions continues to be a major contributor to a successful finite element analysis.

Shell Analysis Codes

During the mid 1960's, the development of several shell analysis computer codes began. Only a few remain and continue to be widely used. In some cases, the digital computer was simply viewed as a *number cruncher* or *electronic calculator* for classical methods. New results based on series solutions and asymptotic methods became tractable for the first time (e.g., Stein [141]). Alternatively, numerical techniques based first on finite differences and then on finite elements began to appear. Symbolic computational tools are also

now available which remove some of the laborious mathematical analysis steps and expedites analytical investigations.

Shell of revolution analysis codes are very popular tools and continue to provide a basis for many shell design studies. FASOR developed by Cohen [142–143], BOSOR developed by Bushnell [144–146], and several shell of revolution analysis tools developed at NASA Langley [147–150] are the main general–purpose codes for shells of revolution.

To address issues associated with asymmetric response, general two– and three–dimensional shell analysis codes were developed. This advancement in the technology led to the "shell shoot out problems" posed by Hartung [151]. These problems continue to be used to test the nonlinear shell analysis capabilities of codes and elements. Nonlinear finite element analyses are readily performed using any one of several commercially available finite element software systems such as MSC/NASTRAN and HKS/ABAQUS. While stability and collapse analyses are available as analysis options, the more dominant sources of nonlinearity in mechanical component design problems are contact and localized material nonlinearities.

STAGS is focused primarily on shell analysis and solution procedures for shell problems. The STAGS code [152] has undergone continual development at Lockheed–Martin Palo Alto Research Center with sponsorship from NASA Langley, Wright–Patterson Air Force Base, and the Navy since the mid 1960's. Early versions, based on BOSOR experiences, are finite difference based (i.e., STAGS–A and STAGS– B), while the later versions are finite element based (i.e., STAGS–C and STAGS–C1). Today STAGS is perhaps the premier shell analysis code in the world.

Modeling and Simulations

Today analysts can easily model the spatial geometry of large complex systems and generate finite element models which easily exceed one million active degrees of freedom. Coupling these two facts with the availability of high–performance computing systems provides simulation capabilities which far exceed the capabilities available less than a decade ago.

Modeling and simulation of complex aerospace shell structures are perhaps the more challenging shell analysis tasks to date. Anderson [153] gave an overview of several shell problems facing the aerospace community in 1980. Following the Space Shuttle Challenger accident, the definition of large–scale nonlinear analysis changed as a result of the analyses performed on the solid rocket boosters (e.g., Knight et al. [154–155]). New designs for the Space Shuttle external tank and other cryogenic fuel tanks for hypersonic vehicles have also challenged the shell analysts (see Ko [156], Nemeth et al. [157] and Young and Rankin [158]). Other examples are also available.

Within the aircraft industry, composite fuselage shell analysis and aircraft structural integrity for metallic fuselage structures continues to challenge our ability to provide robust nonlinear analysis solutions. Examples of such work has been presented by Nagaswamy et al. [159], Starnes and Shuart [160], Starnes et al. [161], Budiman et al. [162], and Chamis et al. [163].

CURRENT THRUSTS

Current research thrusts are discussed briefly in this section as well as possible new directions in shell stability analysis. These thrusts are based on the authors' perception of the status of nonlinear shell stability and collapse analysis methods and the needs for future shell design tools. In addition, future directions and challenges in shell stability research are also identified by Arbocz [164].

Damage Tolerance and Structural Integrity

Damage tolerance and structural integrity represent recent and new research areas for shell analysts. Current simulations for metallic shells can incorporate elasto–plastic behavior and also allow for self–similar crack growth. Models which compute the crack growth path are only beginning to appear and need experimental verification followed by implementation in the analysis codes. Damage modeling and progression are also rich research areas for composite shells. The effects of localized damage caused by impact, manufacturing flaws, or local strength failures need to be assessed just as elasto–plastic behavior is for metallic shells.

In addition to these topics, the need to be able to simulate blast containment in cargo holds and fuel compartments is becoming critical. Having such analysis tools available will perhaps enable designers to devise structural concepts which would prevent tragedies caused by unexpected events.

Realistic Modeling and Loads Assessment

Realistic loading conditions and actual shell geometry modeling represent other research thrusts for shell analysts. Combined mechanical and thermal loads that exhibit time–dependent characteristics must now be considered in order to design the next generation of aerospace vehicles. Incorporation of actual manufacturing tolerances and thickness variations from a probabilistic sense needs to be addressed. Calladine [165] is investigating the influence of "locked in" initial

stresses due to the initial imperfection as well as imperfection associated with the "assumed–to–be–stress–free" case. These "locked in" stresses have a pronounced effect on the buckling performance unless precautions are taken to avoid them. Constitutive models for composite manufacturing procedures need to be developed and implemented into analysis codes.

Nonlinear Response Prediction

Nonlinear response prediction will continue to be a focussed research topic in the coming years. Analysis procedures for isolated bifurcation problems and even many elastic shell collapse problems can be solved with today's methods. New methods are needed to predict transient mode changes and discontinuous nonlinearities caused by crack growth and contact problems. These types of nonlinear problems are ever present in assessing residual strength and structural integrity.

Problem adaptive solution strategies and modeling procedures are needed and are generally only beginning to appear in the research literature (e.g., Lee and Belytschko [166]). Shell element formulations based on *p*–extensions will provide reliability and robustness to the numerical simulations. However, the interplay of shell geometry, imperfection modeling, discrete changes in stiffness, built–up structures, and so forth forms the basis for a rich research area for years to come.

Design Optimization

Optimization of structures for minimum–weight design and postbuckling strength generally always leads to a clustering of the eigenvalues. Sensitivity analyses of composite shells including anisotropy, imperfections and design changes are needed. One example of such work is that of Cohen and Haftka [167]. The design of shell structures continues to pose nonlinear analysis challenges as the lowest energy state at different load levels often leads to *mode jumping* (Bushnell, Rankin, and Riks [121]). Intelligent computational algorithms are needed that recognize the onset of *mode jumping* and automatically adapt the solution sequence. Hybrid analysis and optimization procedures such as the one posed by Bushnell and Bushnell [99] need to be developed further. These methods use advanced analytical procedures to search the design space and identify near–optimum configurations which are then analyzed using detailed nonlinear finite element models to verify the design. Incorporation of probabilistic models of manufacturing effects and imperfection characteristics should be made.

SUMMARY

Recent advances in structural analysis methods and computer technology have made it possible to solve structural stability and nonlinear shell analysis problems that were beyond the analysis state–of–the–art less than 5 to 10 years ago. Solution methods for modal interaction problems and transient response analyses coupled with nonlinear static analysis have made it possible to address nonlinear stability problems for large–scale, practical structural models of thin shell structures. The ability to integrate past limit points and to determine stable equilibrium solutions for nonlinear collapse problems have made it possible to analyze shell stability problems accurately. Large–scale finite element models of practical shell structures can now be analyzed in a reasonable amount of time. Structural engineers now have significantly improved analysis and design tools. High–fidelity models and corresponding analyses accurately represent the nonlinear response of many practical shell problems today, and improvements in solution algorithms and finite element modeling capabilities offer the potential for solving even more complicated structural response and failure problems in the future.

ACKNOWLEDGEMENT

The authors gratefully acknowledge Dr. Bushnell and Prof. Budiansky for reviewing the initial manuscript and providing insightful comments.

REFERENCES

1. Budiansky, B. and Hutchinson, J. W., "Buckling: Progress and Challenge," in *Trends in Solid Mechanics 1979*, Proceedings of the Symposium Dedicated to the 65th Birthday of W. T. Koiter, Delft University of Technology, June 13–15, 1979, J. F. Besseling and A. M. A. van der Heijden (editors), Delft University Press, 1979, pp. 93–116.

2. Walz, Joseph E., personal communication, 1996.

3. Lundquist, E. E., *Strength Tests of Thin–Walled Duralumin Cylinders in Compression*, NACA Report 473, 1933.

4. Donnell, L. H., "A New Theory for the Buckling of Thin Cylinders Under Axial Compression and Bending," *ASME Transactions,* Vol. 56, No. 11, November 1934, pp. 795–806.

5. von Karman, T. and Tsien, H.–S., "The Buckling of Thin Cylindrical Shells Under Axial Compression," *Journal of the Aeronautical Sciences,* Vol. 8, No. 8, June 1941, pp. 303–312.

6. Koiter, W. T., *On the Stability of Elastic Equilibrium*, Ph. D. Thesis (in Dutch), University of Delft, 1945. Also available in English translation as NASA TT F–10833, 1967 and AFFDL–TR–70–25, 1970.

7. Yoshimura, Y., *On the Mechanism of Buckling of a Circular Cylindrical Shell Under Axial Compression,* NACA TM 1390, July 1955.

8. Anon., *Collected Papers on Instability of Shell Structures –1962,* NASA TN–D–1510, December 1962.

9. Hartung, R. F. (editor), *Computer Oriented Analysis of Shell Structures,* Proceedings of a conference held in Palo Alto, CA, August 10–14, 1970, AFFDL–TR–71–79, 1971.

10. Fung, Y. C. and Sechler, E. E. (editors), *Thin–Shell Structures — Theory, Experiment, and Design,* Prentice–Hall, 1974.

11. Ramm, E. (editor), *Buckling of Shells*, Springer–Verlag, New York, 1982.

12. Budiansky, B. and Hutchinson, J. W., "A Survey of Some Bucking Problems," *AIAA Journal,* Vol. 4, No. 9, 1966, pp. 1505–1510.

13. Hoff, N., "The Perplexing Behavior of Thin Circular Cylindrical Shells in Axial Compression," *Israel Journal of Technology,* Vol. 4, No. 1, 1966, pp. 1–28.

14. Stein, M., "Some Recent Advances in the Investigation of Shell Buckling," *AIAA Journal,* Vol. 6, No. 12, December 1968, pp. 2339–2345. Also see comments by L. J. Hart–Smith on pp. 2459–2460 and author's reply on pp. 2460–2461 in the same volume.

15. Hutchinson, J. W. and Koiter, W. T., "Postbuckling Theory," *Applied Mechanics Review*, Vol. 23, No. 12, December 1970, pp. 1353–1366.

16. Sechler, E. E., "The Historical Development of Shell Research and Design," *in Thin–Shell Structures – Theory, Experiment, and Design,* Y. C. Fung and E. E. Sechler (editors), Prentice–Hall, Inc., Englewood Cliffs, NJ, 1974, pp. 3–25.

17. Babcock, C. D., "Experiments in Shell Buckling," in *Thin–Shell Structures: Theory, Experiment, and Design,* Y. C. Fung and E. E. Sechler (editors), Prentice–Hall, Englewood Cliffs, NJ, 1974, pp. 345–369.

18. Tennyson, R. C., "Buckling of Laminated Composite Cylinders: A Review," *Journal of Composites*, January 1975, pp. 17–24.

19. Babcock, C. D., "Shell Stability," *ASME Journal of Applied Mechanics*, Vol. 50, December 1983, pp. 935–940.

20. Bushnell, David, *Computerized Analysis of Shells*, Martinus Nijhoff Publishers, Kluwer Academic, Norwell, ME, 1985. Also available as AFWAL–TR–81–3049, Wright–Patterson AF Base, OH, June 1981.

21. Bushnell, David, "Buckling of Shells — Pitfall for Designers," AIAA Paper No. 80–0665, 1980.

22. Bushnell, David, "Computerized Analysis of Shells — Governing Equations," *Computers and Structures,* Vol. 18, No. 3, 1984, pp. 471–536.

23. Bushnell, David, "Static Collapse: A Survey of Methods and Modes of Behavior," *Finite Elements in Analysis and Design*, Vol. 1, 1985, pp. 165–205.

24. Simitses, G. J., "Buckling and Postbuckling of Imperfect Cylindrical Shells: A Review," *ASME Applied Mechanics Review,* Vol. 39, No. 10, 1986, pp. 1517–1524.

25. Noor, Ahmed K., "Bibliography of Monographs and Surveys on Shells,"*Applied Mechanics Reviews,* Vol. 43, No. 9, September 1990, pp. 223–234.

26. Noor, A. K., Belytschko, T., and Simo, J. C. (editors), *Analytical and Computational Models of Shells,* ASME CED–Vol. 3, 1989.

27. Teng, Jin Guang, "Buckling of Thin Shells: Recent Advances and Trends," *Applied Mechanics Review,* Vol. 49, No. 4, April 1996, pp. 263–274.

28. Donnell, L. H. and Wan, C. C., "Effect of Imperfections on Buckling of Thin Cylinders and Columns Under Axial Compression," *Journal of Applied Mechanics,* Trans. of ASME, Vol. 17, No. 1, March 1950, pp. 73–83.

29. Arbocz, J. and Babcock, C. D., Jr., "The Effect of General Imperfections on the Buckling of Cylindrical Shells," *Journal of Applied Mechanics,* Trans. of ASME, Vol. 36, No. 1, March 1969, pp. 28–38.

30. Arbocz, J. and Babcock, C. D., Jr., "Computerized Stability Analysis Using Measured Initial Imperfections," *Proceedings of the 12th Congress of the International Council of the Aeronautical Sciences,* Munich, Federal Republic of Germany, October 12–17, 1980, pp. 688–701.

31. Singer, J., *Buckling Experiments on Shells – A Review of Recent Developments,* TAE Report 403, Department of Aeronautical Engineering, Technion, Israel Institute of Technology, 1980.

32. Singer, J., "The Status of Experimental Buckling Investigations of Shells," in *Buckling of Shells*, E. Ramm (editor), Springer–Verlag, New York, 1982, pp. 501–534.

33. Singer, J. and Abramovich, H., "The Development of Shell Imperfection Measurement Techniques," *Thin–Walled Structures,* Vol. 23, No. 14, 1995, pp. 379–398.

34. Arbocz, J., "The Imperfection Data Bank, A Means to Obtain Realistic Buckling Loads," in *Buckling of Shells*, E. Ramm (editor), Springer–Verlag, New York, 1982, pp. 535–567.

35. Arbocz, J., *The Effect of Initial Imperfections on Shell Stability – an Updated Review,* Report LR–695, Delft University of Technology, September 1992.

36. Anon., *Buckling of Thin–Walled Circular Cylinders,* NASA SP–8007, August 1968.

37. Baker, E. H., Cappelli, A. P., Kovalevsky, L., Rish, F. L., and Verette, R. M., *Shell Analysis Manual,* NASA CR–912, 1965.

38. Hoff, N., *Buckling of Thin Shells*, SUDAER No. 114, Stanford University, November 1961. Also available as AFOSR TN–61–1422.

39. Nachbar, W. and Hoff, N., *On Edge Buckling of Axially–Compressed Circular Cylindrical Shells,* SUDAER 115, Stanford University, November 1961.

40. Stein, M., "The Effect on the Buckling of Perfect Cylinders of Prebuckling Deformations and Stresses Induced by Edge Support," in *Collected Papers on Instability of Shell Structures –1962,* NASA TN–D–1510, December 1962, pp. 217–225.

41. Stein, M., *The Influence of Prebuckling Deformations and Stresses on the Buckling of Perfect Cylinders,* NASA TR R–190, February 1964.

42. Almroth, B. O., "Influence of Edge Conditions on the Stability of Axially Compressed Cylindrical Shells," *AIAA Journal,* Vol. 4, No. 1, January 1966, pp. 134–140. Also available as NASA CR–161, April 1965.

43. Almroth, B. O., *Influence of Imperfections and Edge Constraint on the Buckling of Axially Compressed Cylinders,* NASA CR–432, April 1966.

44. Sobel, L. H., "Effects of Boundary Conditions on the Stability of Cylinders Subject to Lateral and Axial Pressures," *AIAA Journal,* Vol. 2, No. 8, August 1964, pp. 1437–1440.

45. van der Neut, A., *General Instability of Stiffened Cylindrical Shells Under Axial Compression,* Report S–314, National Luchvaartlab, Amsterdam, 1947.

46. Card, Michael F., *Preliminary Results of Compression Tests on Cylinders with Eccentric Longitudinal Stiffeners,* NASA TM X–1004, 1964.

47. Block, D. L., Card, M. F., and Mikulas, M. M., Jr., *Buckling of Eccentrically Stiffened Orthotropic Cylinders,* NASA TN D–2960, 1965.

48. Block, D. L., *Influence of Discrete Ring Stiffeners and Prebuckling Deformations on the Buckling of Eccentrically Stiffened Orthotropic Cylinders,* NASA TN D–4283, January 1968.

49. Weller, T., Singer, J. and Batterson, S. C., "Influence of Eccentricity of Loading on Stringer–Stiffened Cylindrical Shells," in *Thin–Shell Structures — Theory, Experiment, and Design,* Y. C. Fung and E. E. Sechler (editors), Prentice–Hall, 1974, pp. 305–324.

50. Singer, J. and Rosen, A., "The Influence of Boundary Conditions on the Buckling of Stiffened Cylindrical Shells," in *Buckling of Structures,* B. Budiansky (editor), Springer–Verlag, Berlin, 1976, pp. 227–250.

51. Batdorf, S. B., *A Simplified Method of Elastic–Stability Analysis for Thin Cylindrical Shells: I – Donnell's Equation,* NACA TN–1341, June 1947.

52. Viswanathan, A. V., Tamekuni, M., and Baker, L. L., *Elastic Stability of Laminated Flat and Curved, Long Rectangular Plates Subjected to Combined Inplane Loads,* NASA CR–2330, June 1974.

53. Loo, T. T., "An Extension of Donnell's Equations for Circular Cylindrical Shell," *Journal of Aeronautical Sciences,* Vol. 24, 1957, pp. 390–391.

54. Koiter, W. T., "A Consistent First Approximation in General Theory of Thin Elastic Shells," in *The Theory of Thin Elastic Shells,* North–Holland Publishing Company, Amsterdam, 1960, pp. 12–33.

55. Sanders, J. L., Jr., *An Improved First Approximation Theory for Thin Shells,* NASA Technical Report R–24, June 1959.

56. Sanders, J. L., Jr., "Nonlinear Theories for Thin Shells," *Quarterly of Applied Mathematics,* Vol. 21, No. 1, April 1963, pp. 21–36.

57. Sander, J. L., Jr., "Analysis of Circular Cylindrical Shells," *ASME Journal of Applied Mechanics,* Vol. 50, December 1983, pp. 1165–1170.

58. Budiansky, B. and Sanders, J. L., Jr., "On the 'Best' First–Order Linear Shell Theory," *Progress in Applied Mechanics – Prager Anniversary Volume*, Vol. 192, Macmillian, New York, 1963, pp. 129–140.

59. Budiansky, B., "Notes on Nonlinear Shell Theory," *Journal of Applied Mechanics,* June 1968, pp. 393–401.

60. Reissner, E., "Linear and Nonlinear Theory of Shells," in *Thin–Shell Structures — Theory, Experiment, and Design,* Y. C. Fung and E. E. Sechler (editors), Prentice–Hall, 1974, pp. 29–44.

61. Naghdi, P. M., "On the Theory of Thin Elastic Shells," *Quarterly of Applied Mathematics,* Vol. 14, No. 4, January 1957, pp. 369–380.

62. Naghdi, P. M. and Nordgren, R. P., "On the Nonlinear Theory of Elastic Shells Under the Kirchhoff Hypothesis," *Quarterly of Applied Mathematics,* Vol. 21, No. 1, April 1963, pp. 49–59.

63. Simmonds, J. G., "Recent Advances in Shell Theory," *Advances in Engineering Science,* NASA CP–2001, Vol. 2, 1976, pp. 617–626.

64. Simmonds, J. G. and Danielson, D. A., "Nonlinear Shell Theory with Finite Rotation and Stress–Function Vectors," *ASME Journal of Applied Mechanics*, Vol. 39, December 1972, pp. 1085–1090

65. Wempner, G. A., "A General Theory of Shells and Complementary Potentials," *ASME Journal of Applied Mechanics*, Vol. 53, December 1986, pp. 881–885.

66. Wempner, G. A., "Finite Elements, Finite Rotations and Small Strains of Flexible Shells," *International Journal for Numerical Methods in Engineering,* Vol. 5, 1969, pp. 117–153.

67. Wempner, G. A., "Shells: Mechanics and Approximations — Linear and Nonlinear Aspects," in *Computational Mechanics in Structural Engineering: Recent Developments and Future Trends,* F. Y. Cheng and F. Zizhi (editors), Elsevier, London, 1992, pp. 114–127.

68. Ambartsumyan, S. A., *Theory of Anisotropic Shells,* Moscow, 1961.

69. Yamaki, N., *Elastic Stability of Circular Cylindrical Shells,* North–Holland, Amsterdam, 1984.

70. Niordson, F. I., *Shell Theory,* North–Holland, Amsterdam, 1985.

71. Librescu, L. "Refined Geometrically Nonlinear Theories of Anisotropic Laminated Shells," *Quarterly of Applied Mathematics*, Vol. 45, No. 1, April 1987, pp. 1–22.

72. Arbocz, J., *Comparison of Level–1 and Level–2 Buckling and Postbuckling Solutions,* Report LR–700, Delft University of Technology, November 1992.

73. Palazotto, A. N. and Dennis S. T., *Nonlinear Analysis of Shell Structures,* AIAA, Washington, D. C., 1992.

74. Hildebrand, F. B., Reissner, E., and Thomas, G. B., *Notes on the Foundations of the Theory of Small Displacements of Orthotropic Shells,* NACA TN–1833, March 1949.

75. Reissner, E. and Stavsky, Y., "Bending and Stretching of Certain Types of Heterogeneous Aeolotropic Elastic Plates," *ASME Journal of Applied Mechanics,* Vol. 28, September 1961, pp. 402–408.

76. Dong, S. B., Pister, K. S., and Taylor, R. L., "On the Theory of Laminated Anisotropic Shells and Plates," *Journal of the Aerospace Sciences,* Vol. 29, August 1962, pp. 969–975.

77. Bert, Charles W. and Francis, Philip H., "Composite Material Mechanics: Structural Mechanics," *AIAA Journal,* Vol. 12, No. 9, September 1974, pp. 1173–1186.

78. Hashin, Z., "Analysis of Composite Materials — A Survey," *ASME Journal of Applied Mechanics,* Vol. 50, September 1983, pp.481–505.

79. Chamis, Christos C., "Mechanics of Composite Materials: Past, Present, and Future," *ASTM Journal of Composites Technology and Research,* Vol. 11, No. 1, Spring 1989, pp. 3–14.

80. Noor, A. K. and Burton, W. S., "Assessment of Shear Deformation Theories for Multilayered Composite Plates," *Applied Mechanics Review,* Vol. 42, No. 1, 1989, pp. 1–12.

81. Noor, A. K. and Burton, W. S., "Assessment of Computational Models for Multilayered Anisotropic Plates," *Computers and Structures,* Vol. 14, 1990, pp. 233–265.

82. Reddy, J. N. and Robbins, D. H., Jr., "Theories and Computational Models for Composite Laminates," *Applied Mechanics Review,* Vol. 47, No. 1, Part 1, 1994, pp. 147–169.

83. Noor, A. K., Burton, W. S. and Bert, C. W., "Computational Models for Sandwich Panels and Shells," *Applied Mechanics Review,* Vol. 49, No. 3, March 1996, pp. 155–199.

84. Leissa, A. W., *Buckling of Laminated Composite Plates and Shell Panels,* AFWAL–TR–85–3069, June 1985.

85. Kapania, R. K., "A Review on the Analysis of Laminated Shells,"*ASME Journal of Pressure Vessel Technology,* Vol. 111, May 1989, pp. 88–96.

86. Chandrashekhara, K. and Pavan Kumar, D. V. T. G., "Assessment of Shell Theories for the Static Analysis of Cross–Ply Laminated Circular Cylindrical Shells," *Thin–Walled Structures,* Vol. 22, 1995, pp. 291–318.

87. Simitses, G. J., Shaw, D., and Sheinman, I., "Stability of Cylindrical Shells by Various Nonlinear Shell Theories," *ZAMM*, Vol. 65, No. 3, 1985, pp. 159–166.

88. Simitses, G. J., Sheinman, I., and Shaw, D., "The Accuracy of Donnell's Equations for Axially–Loaded, Imperfect Orthotropic Cylinders," *Computers and Structures,* Vol. 20, No. 6, 1985, pp. 939–949.

89. Nemeth, M. P., "Nondimensional Parameters and Equations for Buckling of Anisotropic Shallow Shells," *ASME Journal of Applied Mechanics*, Vol. 61, September 1994, pp. 664–669.

90. Stein, M., "Postbuckling of Orthotropic Composite Plates Loaded in Compression," *AIAA Journal,* Vol. 21, No. 12, December 1983, pp. 1729–1735. Also available as AIAA Paper No. 82–0778, 1982.

91. Li, Yi–Wen, Elishakoff, I., Starnes, James H., Jr., and Bushnell, David, "Effect of the Thickness Variation and Initial Imperfection on Buckling of Composite Cylindrical Shells: Asymptotic Analysis and Numerical Results by BOSOR4 and PANDA2," *International Journal of Solids and Structures,* Vol. 34, No. 28, 1997, pp. 3755–3767.

92. Jaunky, Navin, and Knight, Norman F., Jr., "An Assessment of Shell Theories for Buckling of Circular Cylindrical Laminated Composite Panels," *International Journal of Solids and Structures,* to be submitted 1997.

93. Stroud, W. Jefferson, "Optimization of Composite Structures," in *IUTAM Proceeding for Mechanics of Composite Materials – Recent Advances*, Z. Hashin and C. T. Herakovich (editors), 1982, pp. 307–321. Also available as NASA TM–84544.

94. Dickson, J. N., Cole, R. T., and Wang, J. T. S., "Design of Stiffened Composite Panels in the Postbuckling Range," in *Fibrous Composites in Structural Design,* E. M. Lenoe, D. W. Oplinger, and L. L. Burke (editors), Plenum Press, New York, 1980, pp. 313–327.

95. Dickson, J. N. and Biggers, S. B., *POSTOP: Postbuckled Open–Stiffener Optimum Panels — Theory and Capability,* NASA CR–172259, 1984.

96. Bushnell, David, "Theoretical Basis of the PANDA Computer Program for Preliminary Design of Stiffened Panels Under Combined In–Plane Loads," *Computers and Structures,* Vol. 22, No. 4, 1987, pp. 541–563.

97. Bushnell, David, "PANDA2 — Program for Minimum–Weight Design of Stiffened, Composite Locally Buckled Panels," *Computers and Structures,* Vol. 25, 1987, pp. 469–605.

98. Bushnell, David, "Optimization of Composite, Stiffened, Imperfect Panels Under Combined Loads for Service in the Postbuckling Regime," *Computer Methods in Applied Mechanics and Engineering,* Vol. 103, 1993, pp. 43–114.

99. Bushnell, D. and Bushnell, W., "Minimum–Weight Design of a Stiffened Panel via PANDA2 and Evaluation of the Optimized Panel via STAGS," *Computers and Structures,* Vol. 50, No. 4, 1994, pp. 569–602.

100. Kempner, Joseph, "Postbuckling Behavior of Axially Compressed Circular Cylindrical Shells," *Journal of the Aeronautical Sciences,* Vol. 21, No. 5, May 1954, pp. 329–335, 342.

101. Koiter, W. T., *Buckling and Postbuckling Behavior of a Cylindrical Panel Under Axial Compression,* National Aeronautical Research Institute, Amsterdam, Report S–476, May 1956.

102. van der Neut, A., *Post Buckling Behaviour of Structures,* NATO AGARD Report 60, August 1956.

103. Almroth, B. O., "Postbuckling Behavior of Axially Compressed Circular Cylinders," *AIAA Journal,* Vol. 1, No. 3, March 1963, pp. 630–633.

104. Hoff, N., Madsen, W. A., and Mayers, J., "Postbuckling Equilibrium of Axially Compressed Circular Cylindrical Shells," *AIAA Journal,* Vol. 4, No. 1, January 1966, pp. 126–133.

105. Almroth, B. O., "Postbuckling Behavior of Orthotropic Cylinders Under Axial Compression," *AIAA Journal,* Vol. 2, No. 10, October 1964, pp. 1795–1799.

106. Khot, N. S., "Buckling and Postbuckling Behavior of Composite Cylindrical Shells Under Axial Compression," *AIAA Journal,* Vol. 8, No. 2, February 1970, pp. 1058–1062.

107. Budiansky, Bernard, "Theory of Buckling and Post–Buckling Behavior of Elastic Structures," *Advances in Applied Mechanics,* Vol. 14, 1974, pp. 1–65.

108. Seide, Paul, "A Reexamination of Koiter's Theory of Initial Postbuckling Behavior and Imperfection Sensitivity of Structures," in *Thin–Shell Structures — Theory, Experiment, and Design,* Y. C. Fung and E. E. Sechler (editors), Prentice–Hall, 1974, pp. 59–80.

109. Koiter, W. T., "Elastic Stability, Buckling and Post–Buckling Behaviour," in *Proceedings of the IUTAM Symposium on Finite Elasticity,* D. E. Carlson and R. T. Shield (editors), Martinus Nijhoff Publishers, The Hague, 1982, pp. 13–24.

110. Zhang, Y. and Matthews, F. L., "Postbuckling Behavior of Curved Panels of Generally Layered Composite Materials," *Composite Structures,* Vol. 1, No. 2, 1983, pp. 115–135.

111. Whitney, J. M., "Buckling of Anisotropic Laminated Cylindrical Plates," AIAA Paper No. 83–0979, May 1983.

112. Hui, D., "Asymmetric Postbuckling of Symmetrically Laminated Cross Ply, Short Cylindrical Panels Under Compression," *Composite Structures,* Vol. 3, 1985, pp. 81–95.

113. Stein, M., "Postbuckling of Long Orthotropic Plates Loaded in Combined Shear and Compression," *AIAA Journal,* Vol. 21, No. 5, May 1985, pp. 788–794.

114. Stein, M., "Postbuckling of Long Orthotropic Plates Under Combined Loading," *AIAA Journal,* Vol. 21, No. 8, August 1985, pp. 1267–1272.

115. Stein, M. and Bains, N. J. C., "Postbuckling of Longitudinally Compressed Orthotropic Plates with Three–Dimensional Flexibility," AIAA Paper No. 86–0976–CP, 1986.

116. Stein, M., "Nonlinear Theory for Plates and Shells Including the Effects of Transverse Shearing," *AIAA Journal,* Vol. 24, No. 9, September 1986, pp. 1537–1544. Also available as AIAA Paper No. 85–0671–CP, 1985.

117. Riks, E., *On the Numerical Solution of Snapping Problems in the Theory of Elastic Stability,* Stanford University, Report SUDAAR No. 401, 1970. Also available as AFOSR 70–2258TR.

118. Crisfield, M. A., "A Fast Incremental/Iterative Solution Procedure that Handles Snap–Through," *Computers and Structures,* Vol. 13, 1983, pp. 55–62.

119. Thurston, G. A., "Newton's Method–A Link Between Continuous and Discrete Solutions of Nonlinear Problems," in *Research in Nonlinear Structural and Solid Mechanics,* H. G. McComb and A. K. Noor (compilers), NASA CP–2147, 1980, pp. 27–48.

120. Tvergaard, Viggo, "On the Transition from a Diamond Mode to an Axisymmetric Mode of Collapse in Cylindrical Shells," *International Journal of Solids and Structures,* Vol. 19, No. 10, 1983, pp. 845–856.

121. Bushnell, David, Rankin, Charles R., and Riks, Eduard, "Optimization of Stiffened Panels in which Mode Jumping is Accounted for," AIAA Paper No. 97–1141, 1997.

122. Tvergaard, V., "The Sensitivity of a Wide Integrally Stiffened Panel under Compression," *International Journal of Solids and Structures,* Vol. 9, 1973, pp. 177–192.

123. Koiter, W. T. and Pignataro, M., *A General Theory for the Interaction of Local and Overall Buckling of Stiffened Panels,* WTHD 83, Department of Applied Mechanics, technical University of Delft, 1976.

124. van der Neut, A., "Mode Interaction with Stiffened Panels," in *Proceedings of the IUTAM Symposium on Buckling of Structures,* Harvard University, Spring–Verlag, 1976, pp. 117–132.

125. Stein, Manuel, *The Phenomenon of Change of Buckling Patterns in Elastic Structures,* NASA Technical Report R–39, 1959.

126. Supple, W. J., "Changes of Wave–Form of Plates in the Post–Buckling Range," *International Journal of Solids and Structures,* Vol. 6, No. 9, September 1970, pp. 1243–1258.

127. Riks, E., Rankin, C. C., and Brogan, F. A., "On the Solution of Mode Jumping Phenomena in Thin Walled Shell Structures," *Computer Methods in Applied Mechanics and Engineering,* 1997, to appear.

128. Thurston, G. A, Brogan, F. A., and Stehlin, P., "Postbuckling Analysis Using a General–Purpose Code," *AIAA Journal,* Vol. 24, No. 6, 1986, pp. 1013–1020.

129. Gallagher, R. H., "Applications of Finite Element Analysis," in *Advances in Computational Methods in Structural Mechanics and Design,* J. T. Oden, R. W. Clough, and Y. Yamamoto (editors), University of Alabama Press, Huntsville, Alabama, 1972, pp. 641–678.

130. MacNeal, R., *Finite Elements: Their Design and Performance*, Marcel Dekker, Inc., 1994.

131. Hinton, E., Owen, D. R. J., and Taylor, C. (editors), *Recent Advances in Nonlinear Computational Mechanics*, Pineridge Press, Swansea, 1982.

132. Hughes, T. J. R., Pifko, A., and Jay, A. (editors), *Nonlinear Finite Element Analysis of Plates and Shells,* ASME AMD–Vol. 48, 1981.

133. Stein, E., Wagner, W., and Wriggers, P., "Concepts of Modeling and Discretization of Elastic Shells for Nonlinear Finite Element Analysis," in *The Mathematics of Finite Elements and Applications VI – MAFELAP 1987,* J. R. Whiteman (editor), Academic Press Limited, 1988, pp. 205–232.

134. Taylor, R. L., "Finite Element Analysis of Linear Shell Problems," in *The Mathematics of Finite Elements and Applications VI – MAFELAP 1987,* J. R. Whiteman (editor), Academic Press Limited, 1988, pp. 191–203.

135. Kratzig, W. B., "Fundamentals of Numerical Algorithms for Static and Dynamic Instability Phenomena of Thin Shells," in *Computational Mechanics of Nonlinear Response of Shells,* W. B. Kratzig and E. Onate (editors), Springer–Verlag, Berlin, 1990, pp. 101–124.

136. Simo, J. C., Fox, D. D., and Rifai, M. S., "Formulation and Computational Aspects of a Stress Resultant Geometrically Exact Shell Model," in *Computational Mechanics of Nonlinear Response of Shells,* W. B. Kratzig and E. Onate (editors), Springer–Verlag, Berlin, 1990, pp. 31–55.

137. Riks, E., Brogan, F. A., and Rankin, C. C., " Numerical Aspects of Shell Stability Analysis," in *Computational Mechanics of Nonlinear Response of Shells,* W. B. Kratzig and E. Onate (editors), Springer–Verlag, Berlin, 1990, pp. 125–151.

138. Hartung, R. F., *Numerical Solution of Nonlinear Structural Problems,* AMD–Vol. 6, ASME, 1973.

139. Hibbitt, H. D., "Practical Aspects of Finite Element Computations in Solid Mechanics," *Applied Mechanics Review,* Vol. 39, No. 11, 1986, pp. 1678–1681.

140. Hibbitt, H. D., "Nonlinear Solid Mechanics from the Commercial Software Viewpoint," *Finite Elements in Analysis and Design,* Vol. 5, No. 1, 1993, pp. 3–10.

141. Stein, M., "The Impact of the Computer on Shell Analysis," in *Computer Oriented Analysis of Shell Structures,*Hartung, R. F. (editor), Proceeding of a conference held in Palo Alto, CA, August 10–14, 1970, AFFDL–TR–71–79, pp. 5–33.

142. Cohen, G. A., "FASOR — A Second Generation Shell of Revolution Code," *Computers and Structures,* Vol. 10, No. 1–2, 1978, pp. 301–309.

143. Cohen, G. A., *Computer Analysis of Ring–Stiffened Shells of Revolution,* NASA CR–2085, 1973.

144. Bushnell, David, *Stress, Stability, and Vibration of Complex Branched Shells of Revolution: Analysis and User's Manual for BOSOR4,* NASA CR–2116, October 1972.

145. Bushnell, David, "Stress, Stability, and Vibration of Complex Branched Shells of Revolution," *Computers and Structures,* Vol. 4, 1974, pp. 399–435.

146. Bushnell, David, "BOSOR5 – Program for Buckling of Elastic–Plastic Complex Shells of Revolution Including Large Deflections and Creep," *Computers and Structures,* Vol. 6, 1976, pp. 221–239.

147. Schaeffer, H. G., *Computer Program for Finite–Difference Solutions of Shells of Revolution Under Asymmetric Loads,* NASA TN D–3926, May 1967.

148. Stephens, Wendell B. and Robinson, Martha P., *Computer Program for Finite Difference Solutions of Shells of Revolution Under Asymmetric Dynamic Loading,* NASA TN D–6059, January 1971.

149. Heard, W. L., Jr., Anderson, M. S., and Chen, M. M., *Computer Program for Structural Analysis of Layered Orthotropic Ring–Stiffened Shells of Revolution (SALORS) — Linear Stress Analysis Option,* NASA TN D–7179, October 1973.

150. Anderson, M. S. and Heard, W. L., Jr., "New Generation Shell of Revolution Structural Code," in Proceedings of the Second Annual Engineering Mechanics Division Specialty Conference, North Carolina State University, Rayleigh, NC, May 23–25, 1977, pp. 253–256.

151. Hartung, R. F. and Ball, R. E., *A Comparison of Several Computer Solutions to Three Structural Shell Problems,* AFFDL TR–73–15, 1973.

152. Brogan, Frank A., Rankin, Charles C., and Cabiness, Harold D., *STAGS Manual,* Lockheed Missiles and Space Company, Report LMSC P032594, June 1994.

153. Anderson, M. S., "Practical Experience in Analysis of Aerospace Shell Structures," in *Theory of Shells,* W. T. Koiter and G. K. Mikhailov (editors), North–Holland, 1980, pp. 11–26.

154. Knight, Norman F., Jr., *Nonlinear Shell Analyses of the SRB/ETA Ring Interface,* NASA TM–89164, 1987.

155. Knight, N. F., Jr., Gillian, R. E., and Nemeth, M. P., "Nonlinear Shell Analysis of the Space Shuttle Solid Rocket Boosters," in *Computational Mechanics of Nonlinear Response of Shells,* W. B. Kratzig and E. Onate (editors), Springer–Verlag, Berlin, 1990, pp. 305–326.

156. Ko, William L., *Thermocryogenic Buckling and Stress Analyses of a Partially Filled Cryogenic Tank Subjected to Cylindrical Strip Heating,* NASA TM–4579, November 1994.

157. Nemeth, M. P., Britt, V. O., Collins, T. J., and Starnes, J. H., Jr., *Nonlinear Analysis of the Space Shuttle Superlightweight External Fuel Tank,* NASA TP–3616, December 1996.

158. Young, R. D. and Rankin, C. C., "Modeling and Nonlinear Analysis of a Large–Scale Launch Vehicle Under Combined Thermal and Mechanical Loads," AIAA Paper No. 96–1551–CP.

159. Nagaswamy, V., Pipkins, D. S., and Atluri, S. N., "An FEAM Based Methodology for Analyzing Composite Patch Repairs of Metallic Structures," in *Structural Integrity in Aging Aircraft,* C. I. Chang and C. T. Sun (editors), ASME AD–Vol. 47, 1995, pp. 273–300.

160. Starnes, James H., Jr. and Shuart, Mark J., "Composite Fuselage Shell Structures Research at NASA Langley Research Center," in *Ninth DoD/NASA/FAA Conference on Fibrous Composites in Structural Design,* J. R. Soderquist, L. M. Neri and H. L. Bohon (compilers), DOT/FAA/CT–92–25, Volume II, September 1992, pp. 631–657.

161. Starnes, J. H., Jr., Britt, V. O., Rose, C. A., and Rankin, C. C, "Nonlinear Response and Residual Strength of Damaged Stiffened Shells Subjected to Combined Loads," AIAA Paper No. 96–1555–CP, 1996.

162. Budiman, H. T., Henault, K., and Lagace, P. A., "Effects of Axial and Hoop Stiffeners on the Damage Propagation in Pressurized Composite Cylinders," AIAA Paper No. 96–1554–CP.

163. Chamis, C. C., Gotsis, P. K., and Minnetyan, L., "Damage Tolerance of Composite Pressurized Shells," AIAA Paper No. 96–1556–CP, 1996.

164. Arbocz, Johann, "Future Directions and Challenges in Shell Stability Research," AIAA Paper No. 97–1077, 1997.

165. Calladine, C. R., "Understanding Imperfection–Sensitivity in the Buckling of Thin–Walled Shells," *Thin–Walled Structures*, Vol. 23, 1995, pp. 215–235.

166. Lee, Sang–Ho and Belytschko, Ted, "H–Adaptive Methods for Nonlinear Dynamic Analysis of Shell Structures," *Shock and Vibration*, Vol. 2, No. 3, 1995, pp. 193–204.

167. Cohen, G. A. and Haftka, R. T., "Sensitivity of Buckling Loads of Anisotropic Shells of Revolution to Geometric Imperfections and Design Changes," *Computers and Structures,* Vol. 31, No. 6, 1989, pp. 985–995.

FUTURE DIRECTIONS AND CHALLENGES IN SHELL STABILITY ANALYSIS

by

Johann Arbocz*
Delft University of Technology
Faculty of Aerospace Engineering
The Netherlands

Abstract

An answer is sought to the question how comes that today, in 1997, after so many years of concentrated research effort, when it comes to designing buckling critical thin walled shells, one cannot do any better than using the rather conservative Lower Bound Design Philosophy of the sixties. It will be shown that with the establishment of Initial Imperfection Data Banks and the introduction of Probabilistic Design Procedures one has, what appears to be, a viable alternative that when used judiciously may lead step by step to improved shell design recommendations.

Introduction

In the sixties the engineering community was facing the urgent problem of having to devise reliable design procedures for both the ballistic missile program of the U.S. Air Force and the launch vehicles of the NASA space program. In these weight critical applications the structural optimization schemes often lead to buckling-critical designs. Facing a multiplicity of very complicated problems the different governmental agencies started large research programs dealing with shell stability.

Looking back at the results of each of these programs separately, one has to classify them as successful. The Lower Bound Design Philosophy [1], which was based on the results of the experimental programs, has provided generations of shell designers with a useful tool for successful shell designs.

---

* Professor of Aircraft Structures

The many publications dealing with different aspects of the Imperfection Sensitivity Theory [2,3] have improved our understanding of the different effects causing the sometimes wide scatter of buckling loads observed experimentally. With the introduction of ever faster workstations and supercomputers the current generation of the shell of revolution codes such as BOSOR-5 [4] and the general shell codes such as STAGS-2 [5] provide us with excellent tools needed for an accurate modelling of the collapse behavior of thin-walled shells.

However, it is very disturbing that, when it comes to determining the load carrying capability of a thin-walled shell structure then, also in 1997 the accounting for the uncertainties involved in every design is usually done by the above mentioned Lower Bound Design Philosophy, a very conservative deterministic procedure that has already been in use 70 years ago. That is, the uncertainties are accounted for by using an empirical "knockdown factor", which is so chosen that when it is multiplied with the calculated perfect shell buckling load a "lower bound" to all existing experimental data is obtained (see Fig. 1).

Deterministic vs Probabilistic Design Procedures

In principle, the use of empirical knockdown factors to account for the damaging effect of as yet unknown causes was and is a good engineering solution to a pressing problem. However, the question that immediately comes to one's mind is, where has the scientific community failed? How comes that today, in 1997, after so many years of concentrated research effort one cannot do any better, and this despite the enormously increased computational facilities provided by todays high powered computers? In this paper, while tracing

the developments related to the stability analysis of axially compressed cylindrical shells, special attention will be payed to the question whether it is possible to do better than the lower bound deterministic design philosophy and if yes, what does it take to achieve it?

Clearly, if for each application one could quantify and understand the "problem uncertainties" and their influence on the design variables, one would obtain a better engineered, better designed and ultimately a safer product. The reliability based design approach basically provides the means to achieve this goal. The collapse problem of axially compressed stiffened cylinders, say, can best be formulated in terms of a response (or limit state) function

$$g(\underset{\sim}{X}) = \Lambda_S(\underset{\sim}{X}) - \lambda \qquad (1)$$

where λ is a suitably normalized load parameter ($= P/P_C$, say), Λ_S is the random collapse load of the structure and the vector $\underset{\sim}{X}$ represents the random variables of the problem. The components of the random vector X_i may be Fourier coefficients of the initial imperfections and other parameters quantifying the uncertainties in the specified boundary conditions, the constitutive equation used to describe the nonlinear material behavior, thickness distribution, residual stresses, etc. Notice that the evaluation of the response function thus involves the solution of a complicated nonlinear structural analysis problem, represented by a detailed and possibly large finite element model. However, with todays computational resources this, in itself, should not pose any unsurmountable difficulties.

Clearly the response function $g(\underset{\sim}{X}) = 0$ separates the variable space into a "safe region" where $g(\underset{\sim}{X}) > 0$, and a "failure region" where $g(\underset{\sim}{X}) \leq 0$. The reliability $R(\lambda)$ - or the probability of failure $P_f(\lambda)$ can then be calculated as

$$R(\lambda) = 1 - P_f(\lambda) \qquad (2)$$

where

$$P_f(\lambda) = \text{Prob}\{g(\underset{\sim}{X}) \leq 0\} = \int\cdots\int_{g(\underset{\sim}{X})\leq 0} f_{\underset{\sim}{X}}(\underset{\sim}{x})\, d\underset{\sim}{x} \qquad (3)$$

and $f_{\underset{\sim}{X}}(\underset{\sim}{x})$ is the joint probability density function of the random variables involved

The credibility of this approach depends on two factors, the accuracy of the mechanical model used to calculate the limit state function and the accuracy of the probabilistic techniques employed to evaluate the multi-dimensional integral.

Comparing the two approaches in short, the Deterministic Design Procedure recommends the use of the following buckling formula

$$P_a = \leq \frac{\gamma}{F.S.} P_c \qquad (4)$$

where P_a = allowable applied load; P_c = lowest buckling load of the perfect structure, γ = "knockdown factor"; and F.S. = factor of safety. The empirical knockdown factor γ is shown for axially compressed isotropic shells in Fig. 1 as the lower bound curve to all available experimental data.

In the Probabilistic Design Procedure the improvements are sought in a more rational approach by the definition of the knockdown factor γ. The proposed new shell design procedure can be represented by the following formula

$$P_a \leq \frac{\lambda_a}{F.S.} P_c \qquad (5)$$

where λ_a = reliability-based improved (higher) knockdown factor, to be read from the appropriate reliability curve (see Fig. 2). If all the uncertainties involved in the problem such as initial imperfections, thickness variations etc. are covered by the random variables X_i, then the use of a factor of safety (F.S.) is unnecessary or one can use a factor of safety equal to one.

In the following the steps involved in the derivation of such a reliability-based improved (higher) knockdown factor λ_a will be discussed.

Characteristic Imperfection Distributions

In the beginning initial imperfection surveys were carried out on laboratory scale shells by the Caltech group [7,8] and others [9,10]. This was followed by complete imperfection surveys on large scale and full scale structures in different parts of the world [11,12,13]. Now-a-days practically in all shell buckling problems initial imperfections play an important role. However, when carrying out initial imperfection measurements one should always remember that Koiter's work [2,14] has shown that

the degree of imperfection sensitivity depends not only on the magnitude but also on the shape of the initial imperfections. Thus it is not sufficient to spot check the shell surface for the maximum imperfection amplitude by carrying out selected circumferential and/or axial scans. One must always provide for sufficient cross-reference data, so that later the individual scans can be pieced together to a complete surface map of the measured structure via numerical data reduction programs. The need for providing cross-reference data sometimes poses added complications but as has been shown in Ref. [15] on several examples in most cases the difficulties can be overcome rather routinely.

In all cases, where one attempts to measure the exact shape of a shell, before one can determine the initial imperfections one has to define the perfect cylinder. This is done by finding numerically the best-fit cylinder to the measured surface map assembled using the initial imperfection scans. Using the method of least-squares data reduction programs [7] can compute the eccentricities Y_1 and Z_1, the rigid body rotations ε_1 and ε_2 and the mean radius R (see Fig. 3) rather routinely. Finally, the measured radial displacements are recomputed with respect to the newly found "perfect" cylinder. These values are then used to prepare the 3-dimensional plots of the initial imperfections shown in Figures 4, 5 and 6.

In all cases the measured initial imperfections can be represented by one of the following two double Fourier series

$$\bar{W}(x,y) = t\sum_{k,\ell=0}^{N}\sum \cos k\pi\frac{x}{L}\left(A_{k\ell}\cos\ell\frac{y}{R} + B_{k\ell}\sin\ell\frac{y}{R}\right) \quad (6)$$

referred to as the half-wave cosine representation, and

$$\bar{W}(x,y) = t\sum_{k,\ell=0}^{N}\sum \sin k\pi\frac{x}{L}\left(C_{k\ell}\cos\ell\frac{y}{R} + D_{k\ell}\sin\ell\frac{y}{R}\right) \quad (7)$$

called the half-wave sine representation. Here R, L and t are shell radius, length and wall thickness; x and y are axial and circumferential coordinates; k and ℓ are integers denoting the number of axial half waves and the number of full waves in the circumferential direction, respectively. In all cases the measured imperfections are referred to the so-called "best fit" cylinders.

The adoption of a standard representation for the measured initial imperfections is necessary in order to be able to compare the different imperfection distributions that are associated with the different fabrication processes. Notice that in all cases the Fourier coefficients are normalized by the corresponding wall thicknesses of the shell bodies.

At the moment there are two Initial Imperfection Data Banks in existence, one at the Delft University of Technology [16] and one at the Technion in Haifa [9].

For a successful application of reliability based design methods the existence of data bases containing such experimentally measured initial imperfections, is very helpful, whereby the critical question is:

> *Can one associate characteristic initial imperfection distributions with a specified manufacturing process?*

That the answer to this question is an unconditional yes has been demonstrated very clearly in References [15,17], where characteristic imperfection distributions for different fabrications processes are shown.

Stochastic Stability Analysis

It has been demonstrated in References [15,17] that, indeed, one can associate characteristic initial imperfection distributions with the different fabrication processes. The question then arises:

> *Given a characteristic initial imperfection, distribution how does one proceed to incorporate this knowledge into a systematic design procedure?*

Since initial imperfections are obviously random in nature, the Probabilistic Design Procedure, described earlier by Eqs. 1-3, is one way to introduce the results of the experimentally measured initial imperfections into the analysis.

The proposed approach is based on the notion of a reliability function $R(\lambda)$, where by definition

$$R(\lambda) = \text{Prob}(\Lambda > \lambda) \tag{8}$$

and λ = normalized load parameter ($=P/P_c$) and Λ = normalized random buckling load.

As can be seen from Fig. 2, the knowledge of the reliability function permits the evaluation of the allowable load, defined as the load level λ_a for which the specified reliability is achieved, for a whole ensemble of similar shells produced by a given manufacturing process. Notice that the allowable load level λ_a is identical to the improved (higher) knockdown factor introduced in Eq. (5).

Turning now to the collapse problem of axially compressed cylinders with random initial imperfections one is faced with the evaluation of the multidimensional integral given by Eq. (3).

Whereas with todays advanced nonlinear finite element codes such as STAGS [5] and ABAQUS [18] the limit state function g(X) (if so desired) can be determined with great accuracy, the evaluation of the multidimensional integral, where the domain of integration depends on the properties of the limit state function, is still subject of detailed investigations. Since an exact numerical evaluation of this multidimensional integral is considered impractical, in the following it will be shown that by using the First-Order, Second-Moment Method [19,20] it is possible to develop a simple but rational method for checking the reliability of axially compressed shells using some statistical measures of the imperfections involved, and to provide an estimate of the structural reliability, whereby also the specified boundary conditions are rigorously enforced.

The use of the First-Order, Second-Moment Method involves linearization of the response function g(X) at the mean point and knowledge of the distribution of the random vector X. Calculations are relatively simple if X is normally distributed. If X is not normally distributed, an appropriate normal distribution has to be substituted instead of the actual one.

In the present case one is interested in knowing the reliability $R(\lambda)$ of the structure at any given load λ; that is, one wants to obtain

$$R(\lambda) = \text{Prob}(\Lambda_s > \lambda) = \text{probability that } \Lambda_s > \lambda \tag{9}$$

In this case the limit state or failure surface has the form given by Eq. (1)

$$Z(\lambda) = \Lambda_s - \lambda = \psi(X_1, X_2, \ldots, X_n) - \lambda = 0 \tag{10}$$

where Λ_s is the random buckling load and λ is the applied nondimensional deterministic load. It is apparent that in the absence of a straightforward deterministic relation connecting Λ_s and the X_i's an analytical solution is unfeasible. However, the first-order, second-moment analysis can be done numerically, as has been reported in Ref. 20 for a different problem.

To combine the use of numerical codes with the mean value first-order, second-moment method one needs to know the lower order probabilistic characteristics of Z. In the first approximation the mean value of Z is determined as follows:

$$\begin{aligned} E(Z) &= E(\Lambda_s) - \lambda \\ &= E[\psi(X_1, X_2, \ldots, X_n)] - \lambda \\ &\sim \psi[E(X_1), E(X_2), \ldots, E(X_n)] - \lambda \end{aligned} \tag{11}$$

This corresponds to the use of the Laplace approximation of the moments of nonlinear functions. The value of

$$\psi[E(X_1), E(X_2), \ldots, E(X_n)] \tag{12}$$

is calculated numerically by STAGS [21], the code that was chosen for the numerical work. It corresponds to the deterministic buckling load of the structure possessing mean imperfection amplitudes.

The variance of Z is given by

$$\text{Var}(Z) = \text{Var}(\Lambda_s) \sim \sum_{j=1}^{n} \sum_{k=1}^{n} \left(\frac{\partial \psi}{\partial \xi_j}\right) \left(\frac{\partial \psi}{\partial \xi_k}\right) \text{cov}(X_j, X_k) \tag{13}$$

where $\text{cov}(X_j, X_k)$ is the variance-covariance matrix. The calculation of the derivatives $\partial\psi/\partial\xi_j$ (or $\partial\psi/\partial\xi_k$) is performed numerically by using the following numerical differentiation formula at values of $\xi_j = E(X_j)$ [or $\xi_k = E(X_k)$]:

$$\frac{\partial \psi}{\partial \xi_j} = \frac{\psi(\xi_1, \ldots, \xi_{j-1}, \xi_j + \Delta\xi_j, \xi_{j+1}, \ldots, \xi_n) - \psi(\xi_1, \xi_2, \ldots, \xi_n)}{\Delta\xi_j} \tag{14}$$

Having obtained the quantities $E(Z)-E(\Lambda_s)-\lambda$ and Var(Z) one can estimate the probability of failure $P_f(\lambda)$ as

$$P_f(\lambda)=Pr(Z<0)=F_Z(0)=\int_{-\infty}^{o} f_Z(t)\,dt \qquad (15)$$

where $F_Z(t)$ is the probability distribution function of Z and $f_Z(t)$ is the probability density function of Z.

Assuming that the performance function Z is normally distributed, then

$$f_Z(t)=\frac{1}{\sigma_Z\sqrt{2\pi}}\exp[-\frac{1}{2}(\frac{t-a}{\sigma_Z})^2] \qquad (16)$$

where a = E(Z) and $\sigma_Z=\sqrt{Var(Z)}$. Further

$$F_Z(0)=\int_{-\infty}^{o} f_Z(t)\,dt=\frac{1}{2}+erf(-\frac{a}{\sigma_Z}) \qquad (17)$$

$$=\frac{1}{2}-erf(\frac{a}{\sigma_Z})=\phi(-\beta)$$

where $\beta=\alpha/\sigma_Z$ is the reliability index, $\phi(\beta)$ is the standard normal probability distribution function, and the error function $erf(\beta)$ is defined as

$$erf(\beta)=\frac{1}{\sqrt{2\pi}}\int_{o}^{\beta} e^{-t^2/2}dt \qquad (18)$$

Finally the reliability $R(\lambda)$ will be estimated as

$$R(\lambda)=1-P_F(\lambda)=1-Pr(Z<0) \qquad (19)$$

$$=1-F_Z(0)=\frac{1}{2}+erf(\beta)=\phi(\beta)$$

As can be seen from Eqs. 11 and 13, in order to be able to evaluate the mean value and the variance of the performance function Z, one must know the mean values and the variance-covariance matrix of the basic random variables X_i. Since in this case the basic random variables X_i represent the Fourier coefficients of the initial imperfections, the above statistical measures can only be evaluated if a sufficiently detailed initial imperfection data bank (see Refs. 16 and 22) is available.

Numerical Results

In the previous section the solution of the stochastic stability problem of Eq. (3) has been reduced to a series of n+1 deterministic buckling load analysis, where n is the number of random variables used.

To investigate the feasibility of using the first-order, second-moment method to make buckling load predictions, in Ref. [17] the integrally stringer stiffened aluminium alloy shells tested at Caltech in 1969, the so-called AS-shells were used. Based on the results of earlier investigations of the buckling behavior of the AS-2 shell [23], it was decided to use the following initial imperfection model for the collapse load calculations:

$$\bar{W}=tA_{2,0}\cos 2\pi\frac{x}{L} \qquad (20)$$
$$-t\sin\pi\frac{x}{L}\{\bar{\xi}_{1,2}\cos 2\theta+\bar{\xi}_{1,9}\cos 9\theta+\bar{\xi}_{1,10}\cos 10\theta$$
$$+\bar{\xi}_{1,11}\cos 11\theta+\bar{\xi}_{1,19}\cos 19\theta+\bar{\xi}_{1,21}\cos 21\theta\}$$

where $\bar{\xi}_{k\ell}=\sqrt{C_{k\ell}^2+D_{k\ell}^2}$ and $\theta=y/R$.

The mean values and the variance-covariance matrix of the 7 random variables were evaluated by ensemble averaging. An advantage of this method is that the statistical parameters of the initial imperfections are estimated from the real measurements of the shell profiles. The only assumption made is that the Fourier coefficients have a multivariate normal distribution.

In Ref. [17] the computation of the collapse loads with mean imperfections, needed to evaluate the derivatives $\partial\psi/\partial\xi_j$ numerically by using the formula given by Eq. (14), was done with a modified finite difference version of the well known code STAGS [21]. All numerical data used and the results of the numerical computations can be found in Ref. [17].

It has been shown in Ref. [24] that for stringer stiffened shells satisfactory correlation between theoretical predictions and experimental results requires the inclusion of both the initial imperfections and the appropriate elastic boundary conditions in the analysis. To illustrate this effect in Ref. [17] reliability functions were derived for SS-3 ($N_x=v=W=M_x=0$) and C-4 ($u=v=W=W_{,x}=0$) boundary conditions. The results of these calculations are displayed in Figures 2 and 7,

respectively. Notice that in Fig. 2 the buckling load λ is normalized by - 223.079 N/cm, the buckling load of the perfect AS-2 shell using nonlinear prebuckling and the SS-3 boundary conditions; whereas in Fig. 7 the normalizing factor used is -315.323 N/cm, the buckling load of the perfect AS-2 shell using nonlinear prebuckling and the C-4 boundary conditions.

Comparing the buckling loads predicted by Figs. 2 and 7 for a reliability of, say, 0.98 of $N_{SS-3}=-162.848$ N/cm and $N_{C-4}=-264.871$ N/cm with the experimental buckling load of $N_{exp}=-223.793$ N/cm, one notices that the calculated results seem to support the suggestion made in Ref. 24 that the experimental boundary conditions of the test setup used to buckle the AS-shells at Caltech [8] imposed some sort of elastic boundary conditions.

Effect of Boundary Conditions

Together with initial geometric imperfections general elastic supports [25] have been widely accepted as the explanation for the wide experimental scatter and the poor correlation between the predictions based on a linearized small deflection theory with SS-3 ($n_x=v=W=M_x=0$) boundary conditions and the experimental values shown in Fig. 1.

The effect of different combinations of in-plane boundary conditions on the stability of axially compressed perfect shells and shells with axisymmetric imperfections have been studied analytically and numerically by Hoff [25], Stein [26] and Almroth [27] among others. Recently Singer and his coworkers [28] have developed an experimental technique which makes it possible to estimate the degree of elastic support present in a particular test set-up.

To investigate the effect of elastic boundary conditions on the buckling load of the stringer stiffened shell AS-2, in Ref. [29] a rigorous solution is presented for the case of axially compressed stiffened cylindrical shells with general imperfections, where the edge supports are provided by symmetrical or unsymmetrical elastic rings. For the shell analysis the Donnell type nonlinear shell equations from Ref. [30] are used, whereas the ring analysis is based on Cohen's ring equations [31]. The circumferential dependence is eliminated by a truncated Fourier series. The resulting 2-point boundary value problem is solved numerically via the "Shooting Method" [32].

Modelling the elastic boundary conditions on the perfect AS-2 shell by symmetrically placed symmetrical rings with square cross sections one obtains the results shown in Fig. 8. It is interesting that even for this symmetrical case the stiffness matrix of the ring does not reduce to a diagonal matrix. Thus using a diagonal matrix to model ring supported elastic boundary conditions may lead to serious inaccuracies in the predicted critical load and buckling mode as has been pointed out in Ref. [33]. Returning to the results plotted in Fig. 8 it is clear that there is a critical size of the end ring below which the ring strain energy controls the buckling and the buckling mode is inextensional with n=2 full waves in the circumferential direction.

In a recent paper Arbocz et al [34] obtained a solution of the nonlinear anisotropic Donnell type imperfect shell equations, where the in-plane displacement boundary condition in the x-direction is varying in the circumferential direction, that is at x = 0

$$u=\bar{tu}_{01}\cos n\theta+\bar{tu}_{02}\cos 2n\theta+\bar{tu}_{03}\sin n\theta+\bar{tu}_{04}\sin 2n\theta \tag{21}$$

and at x = L

$$u=\bar{tu}_{L1}\cos n\theta+\bar{tu}_{L2}\cos 2n\theta+\bar{tu}_{L3}\sin n\theta+\bar{tu}_{L4}\sin 2n\theta \tag{22}$$

As can be seen from the results displayed in Fig. 9 the buckling load of the perfect AS-2 shell is very sensitive to an axial support varying in the circumferential direction.

Finally, it is interesting to look at the results shown in Fig. 10, where an a posteriori measurement of the flatness of the end-ring used to test the Caltech shells is displayed. In the authors opinion it is warranted to say that in the future we must pay more attention to provide an accurate definition of the boundary conditions at the shell edges if we want to achieve a better correlation between theoretical predictions and experimental results.

Conclusions and Future Developments

It has been demonstrated that if the collapse load of axially compressed stringer stiffened shells is calculated via a refined finite element model

capable of reproducing all the different buckling modes, and if the statistical characteristics of the geometric parameters, the correct boundary conditions and shape imperfections are taken into account adequately, then the First-Order Second-Moment Method probably will lead to an accurate and conservative prediction of the reliability function. If so desired a measure of the accuracy of this approach can be obtained by repeating the analysis using one of the Advanced Monte Carlo Simulation techniques such as Importance Sampling [35]. Once the shape of the reliability function $R(\lambda)$ is known, one can determine routinely the reliability based improved "knockdown factor" λ_a for any specified reliability.

For a successful application of reliability based design methods the existence of a data base containing, for instance, experimentally measured initial imperfections is very helpful. It can guide the users in choosing the appropriate probability density distributions for the input variables. If test data are not available, then the user must select probability density distributions based on his judgement. In such cases the availability of design software for calculating the parameter distribution sensitivities can be of great help in making the proper choice.

Before a large scale acceptance of reliability based probabilistic design methods by the engineering community is to occur, true reliability must be demonstrated and not simply estimated from engineering analysis. Thus it is not surprising that the first successful integration of probabilistic design methods with existing design processes have been accomplished in applications like the design of specific components of aircraft engines, where failure and failure rate data bases are available. It is also interesting to note that in the cases reported by Fox [36], the probabilistic approach was built around the existing design methodology and it is part of an integrated process rather than requiring the designer to make specific "stress analysis" runs and then entering the data and running the "probabilistic code" in an iterative loop. The probabilistic output is printed in addition to the normal deterministic output and it contains information about the model accuracy, so that the designer can decide wether or not the results from the probabilistic analysis are acceptable.

In all those applications where failure and failure rate data bases are as yet not available the probabilistic methods can best be utilized to great advantage as a design tool to help identify the sensitivities of problem parameters.

To facilitate the use of probabilistic methods in the design process of buckling critical structures one can best employ a hierarchical approach as proposed in Ref. [37]. In a hierarchical approach initially simple mechanical and stochastic methods of known accuracy are used to carry out the necessary parameter studies. This phase includes the evaluation of the sensitivity derivatives needed to decide which are the important random variables that must be included in the refined reliability calculations. Once the principal dimensions and the lay-out of the structure have been fixed, then the structural reliability of the final design should be calculated by carrying out a detailed analysis employing a refined finite element model to describe the mechanical behavior and an accurate reliability method to complete the probabilistic calculations.

The generation of reliability functions via the Advanced Monte Carlo Methods, which displays the degrading effect on the buckling load of the expected initial imperfection distribution characteristic of a given fabrication process, seems to offer the means of combining the Lower Bound Design Philosophy with the notion of Goodness Classes. Thus shells manufactured by a process, which produces inherently a less damaging initial imperfection distribution, will not be penalized because of the low experimental results obtained with shells produced by another process, which generates a more damaging characteristic initial imperfection distribution. The application of the Monte Carlo Method requires accurate and efficient deterministic buckling analysis capability especially for large initial imperfections.

It is anticipated that for applications where the total weight of the structure is one of the critical parameters (i.e. aerospace structures) there will be a chance for definite improvement in the design process with the help of the proposed new probabilistic design procedure, which involves a more effective use of the currently available nonlinear analysis capabilities. It is felt that the small added cost involved in carrying out the required initial imperfection surveys will be fully justified by the overall cost-savings and by producing improved and more reliable shell structures. The conventional lower bound approach

and the proposed new procedure will both be used until adequate experience has been developed by subsequent testing of shells designed by the new approach. It is not expected that the new approach would replace sound engineering judgement, only that this judgement would be guided by the rational use of the nonlinear shell analysis capability presently available.

It is encouraging to see that the need for detailed initial imperfection surveys on full scale and laboratory scale shells and the establishment of Initial Imperfection Data Banks is being recognized by more and more investigators [38,39]. It is this authors opinion that the existence of extensive data on characteristic initial imperfection distributions classified according to fabrication processes, the availability of the present generation nonlinear structural analysis codes, the stochastic stability approach via the reliability functions and the increased computational speed offered by the so-called super-computers will finally result in a series of improved design recommendations which will incorporate the latest theoretical findings and make them routinely accessible to the designers.

Acknowledgement

The research reported in this paper was supported in part by NASA Research Grant NAG 1 1826. Many helpful technical discussions with Drs. J.H. Starnes and M.P. Nemeth from NASA Langley Research Center are gratefully acknowledged.

References

1. Anon., "Buckling of Thin-Walled Circular Cylinders", NASA SP-8007, 1968.
2. Koiter, W.T., "On the Stability of Elastic Equilibrium", Ph.D. Thesis (in Dutch), TH-Delft, The Netherlands, H.J. Paris, Amsterdam, 1945; English translation NASA TTF-10, 1967, pp. 1-833.
3. Budiansky, B., and Hutchinson, J.W., "Dynamic Buckling of Imperfection Sensitive Structures", *Proceedings of the 11th IUTAM Congress*, edited by H. Görtler, Springer-Verlag, Berlin, 1964, pp. 636-651.
4. Bushnell, D., "BOSOR 5 - Program for buckling of elastic-plastic complex shells of revolution including large deflections and creep", Computers & Structures, Vol. 6, 1976, pp. 221-239.
5. STAGS Manual, Version 2.0, Lockheed Palo Alto Research Laboratories, March 1994, Palo Alto, California.
6. Weingarten, V.I., Morgan, E.J. and Seide, P., "Elastic Stability of Thin-Walled Cylindrical and Conical Shells Under Axial Compression", AIAA Journal, Vol. 3, No. 3, 1965, pp. 500-505.
7. Arbocz, J. and Babcock, C.D., Jr., "The effect of general imperfections on the buckling of cylindrical shells". Journal of Applied Mechanics, Vol. 36, No. 1, 1969, pp. 28-38.
8. Singer, J., Arbocz, J. and Babcock, C.D., Jr., "Buckling of imperfect stiffened cylindrical shells under axial compression", AIAA Journal, Vol. 9, No. 1, 1971, pp. 68-75.
9. Singer, J., Abramovitch, H. and Yaffe, R., "Initial imperfection measurements of integrally stringer-stiffened shells", TAE report No. 330, Technion, Haifa, Israel, 1978.
10. Walker, A.C. and Stridharan, S., "Buckling of compressed, longitudinally stiffened cylindrical shells", BOSS '79. *Proceedings 2nd International Conference on the Behaviour of Off-shore Structures*, Imperial College, London, 1979, Vol. 2, pp. 341-356.
11. Horton, W.H., "On the elastic stability of shells", NASA CR-145088, 1977.
12. Arbocz, J., Williams, J.G., "Imperfection surveys on a 10-ft diameter shell structure", AIAA Journal, Vol. 15, No. 7, 1977, pp. 949-956.
13. Sebek, R.W.L., "Imperfection surveys and data reduction of ARIANE interstages I/II and II/III", ir. thesis, TH-Delft, Department of Aerospace Engineering, 1981.
14. Koiter, W.T., "Elastic stability and postbuckling behavior", Proceedings Symposium Nonlinear Problems, University of Viscosin Press, Madison, 1963, pp. 257-275.
15. Arbocz, J., "The Imperfection Data Bank, a mean to obtain Realistic Buckling Loads", *Proceedings Buckling of Shells - A-state-of-the-Art Colloquium*, edited by E. Ramm, Springer Verlag, Berlin, 1982, pp. 535-567.
16. Arbocz, J. and Abramovitch, H., "The Initial Imperfection Data Bank at the Delft University of Technology - Part I", Report LR-290, Delft University of Technology, The Netherlands, 1979.
17. Arbocz, J. and Hol, J.M.A.M., "Collapse of Axially Compressed Cylindrical Shells with Random Imperfections", AIAA Journal, Vol. 29, No. 12, 1991, pp. 2247-2256.

18. ABAQUS Manual, Version 5-2, Hibbit, Karlsson & Sorensen Inc., 1991, Houston, Pennsylvania.
19. Elishakoff, I., Manen, S. van, Vermeulen, P.G. and Arbocz, J., "First-Order Second-Moment Analysis of the Buckling of Shells with Random Imperfections", AIAA Journal, Vol. 25, No. 8, 1987, pp. 1113-1117.
20. Karadeniz, H., Manen, S. van and Vrouwenvelder, A., "Probabilistic Reliability Analysis for the Fatigue Limit State of Gravity and Jacket Type Structures", *Proceedings of the Third International Conference on Behavior of Off-Shore Structures*, McGraw-Hill, London, 1982, pp. 147-165.
21. Almroth, B.O., Brogan, F.A., Miller, E., Zelle, F. and Peterson, H.T., "Collapse Analysis for Shells of General Shape", *User's Manual for the STAGS-A Computer Code*, Air Force Flight Dynamics Lab., Wright-Patterson AFB, AFFDL-TR-71-8, 1973.
22. Abramovitch, H., Singer, J. and Yaffe, R., "Imperfection Characteristics of Stiffened Shells - Group 1", TAE Rep. 406, Technion, Haifa, Israel, 1981.
23. Arbocz, J. and Babcock, C.D., "Utilization of STAGS to Determine Knockdown Factors from Measured Initial Imperfections", Report LR-275, TH-Delft, Dept. of Aerospace Engineering, The Netherlands, November 1978.
24. Arbocz, J., "Collapse Load Calculations for Axially compressed Imperfect Stringer Stiffened Shells", *Proceedings of the AIAA/ASME/ASCE/AHS 25th Structures, Structural Dynamics and Materials Conference*, May 14-18, Palm Springs, CA, AIAA, New York, pp. 130-139.
25. Hoff, N.J., "Buckling of Thin Shells", In: *Proceedings of an Aerospace Symposium of Distinguished Lectures in Honor of Theodore Von Karman on his 80th Anniversary*, 1961, pp. 1-42, Institute of Aerospace Sciences, New York.
26. Stein, M., "The Influence of Prebuckling Deformations and Stresses on the Buckling of Perfect Cylinders", NASA TR R-190, 1964.
27. Almroth, B.O., "Influence of Imperfections and Edge Constraint on the Buckling of Axially Compressed Cylinders", NASA, CR-432, April 1966.
28. Singer, J. and Rosen, A., "The Influence of Boundary Conditions on the Buckling of Stiffened Cylindrical Shells", In: *Proceedings IUTAM Symposium Buckling of Structures*, edited by B. Budiansky, Harvard University Cambridge, Mass., June 1974, pp. 227-50, Springer Verlag, Berlin, 1976.
29. Arbocz, J., Vermeulen, P.G. and van Geer, J., "The Buckling of Axially Compressed Imperfect Shells with Elastic Edge Conditions", In: *Buckling of Structures*, edited by I. Elishakoff, J. Arbocz and A. Libai, Elsevier Science Publishers B.V., Amsterdam, 1988.
30. Arbocz, J. and Sechler, E.E., "On the Buckling of Stiffened Imperfect Cylindrical Shells", AIAA Journal, Vol. 15, No. 11, 1976, pp. 1611-1617.
31. Cohen, G.A., "Computer Analysis of Ring-Stiffened Shells of Revolution", NASA, CR-2085, 1973.
32. Keller, H., "Numerical Methods for Two-Point Boundary Value Problems", Blaisdell Publishing Co., Waltham, Mass., 1968.
33. Dixon, S.C., Weeks, G.E. and Anderson, M.S., "Effect of Edge Restraint Coupling on Buckling of Ring-Supported Cylinders", AIAA Journal, Vol. 6, No. 8, 1968, pp. 1602-1604.
34. Arbocz, J., de Vries, J. and Hol, J.M.A.M., "On the Buckling of Imperfect Anisotropic Shells with Elastic Edge Supports under Combined Loading", Report LR-709, Delft University of Technology, Faculty of Aerospace Engineering, The Netherlands, May 1997.
35. Schuëller, G.I., Bucher, C.G., Bourgund, V. and Ouypornprasert, W., "On Efficient Computational Schemes to Calculate Structural Failure Probabilities", Probabilistic Engineering Mechanics, Vol. 4, No. 1, 1989, pp. 10-18.
36. Fox, E.P., "Methods of Integrating Probabilistic Design within an Organization's Design System using Box-Behnken Matrices", in: *Proceedings 34th AIAA/ASME/ASCE/AHS/ASC Structures, Structural Dynamics and Materials Conference*, April 19-22, 1993, La Jolla, California, USA, AIAA, pp. 714-723.
37. Arbocz, J. and Hol, J.M.A.M., "Shell Stability Analysis in a Computer Aided Engineering (CAE) Environment", in: Proceedings 34th AIAA/ASME/ASCE/AHS/ASC Structures, Structural Dynamics and Materials Conference, April 19-22, La Jolla, California, USA, pp. 300-314.
38. Grove, T. and Didriksen, T., "Buckling experiments on 4 large axial stiffened and 1 ring stiffened cylindrical shells", Det Norske Veritas Rep. 76-423, 1976.
39. Green, D.R. and Nelson, H.M., "Compression tests on large-scale, stringer stiffened tubes", in: *Proceedings Int. Conference Buckling of Shells in Offshore Structures*, P.J. Dowling and J.E. Harding (Eds.), April 23-24, 1981, Imperial College, London.

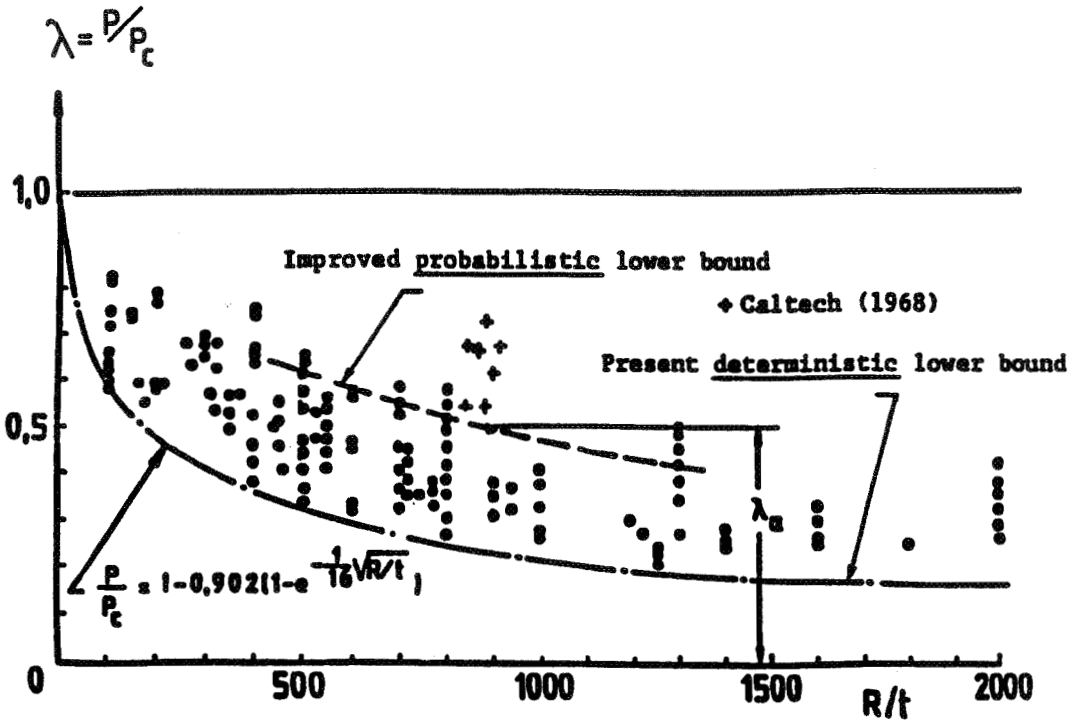

Fig. 1 Test data for isotropic cylinders under axial compression [6]

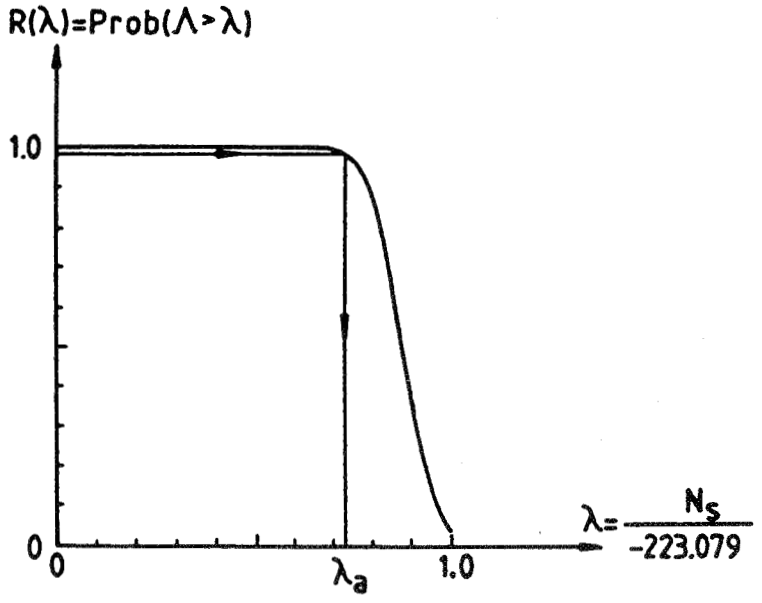

Fig. 2 Reliability curve calculated via the first-order, second-moment method (SS-3 boundary condition: $N_x = v = W = M_x = 0$) [17]

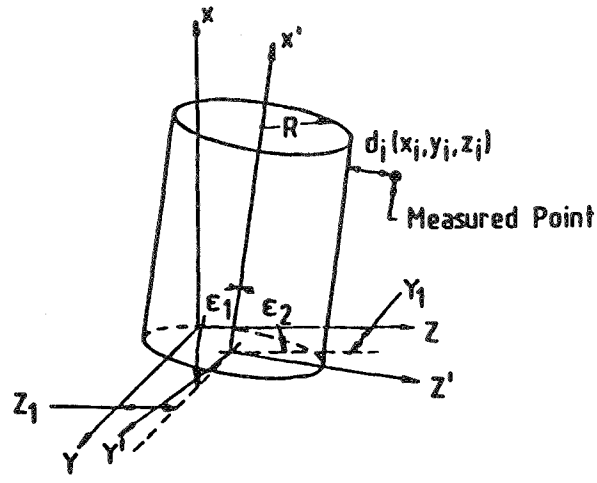

X,Y,Z Reference axis of traversing pick-up
X',Y',Z' Reference axis of best fit cylinder
d_i Normal distance from measured point to best fit cylinder

Fig. 3 Definition of the "perfect" cylinder [7]

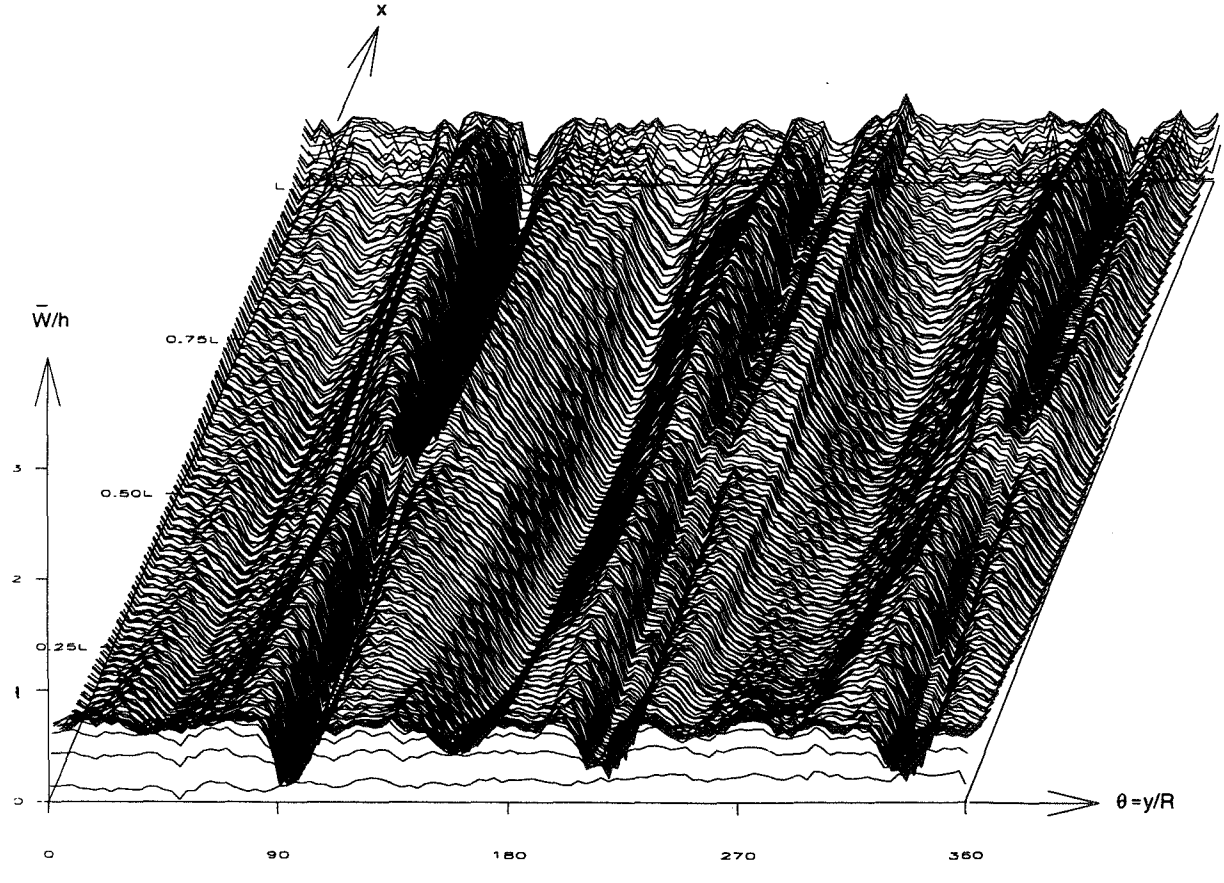

Fig. 4 Measured initial shape of aerospace shell X-1 [16]
(Radius: 1212.1 mm, length: 6454.1 mm, wall thickness: 1.549 mm)

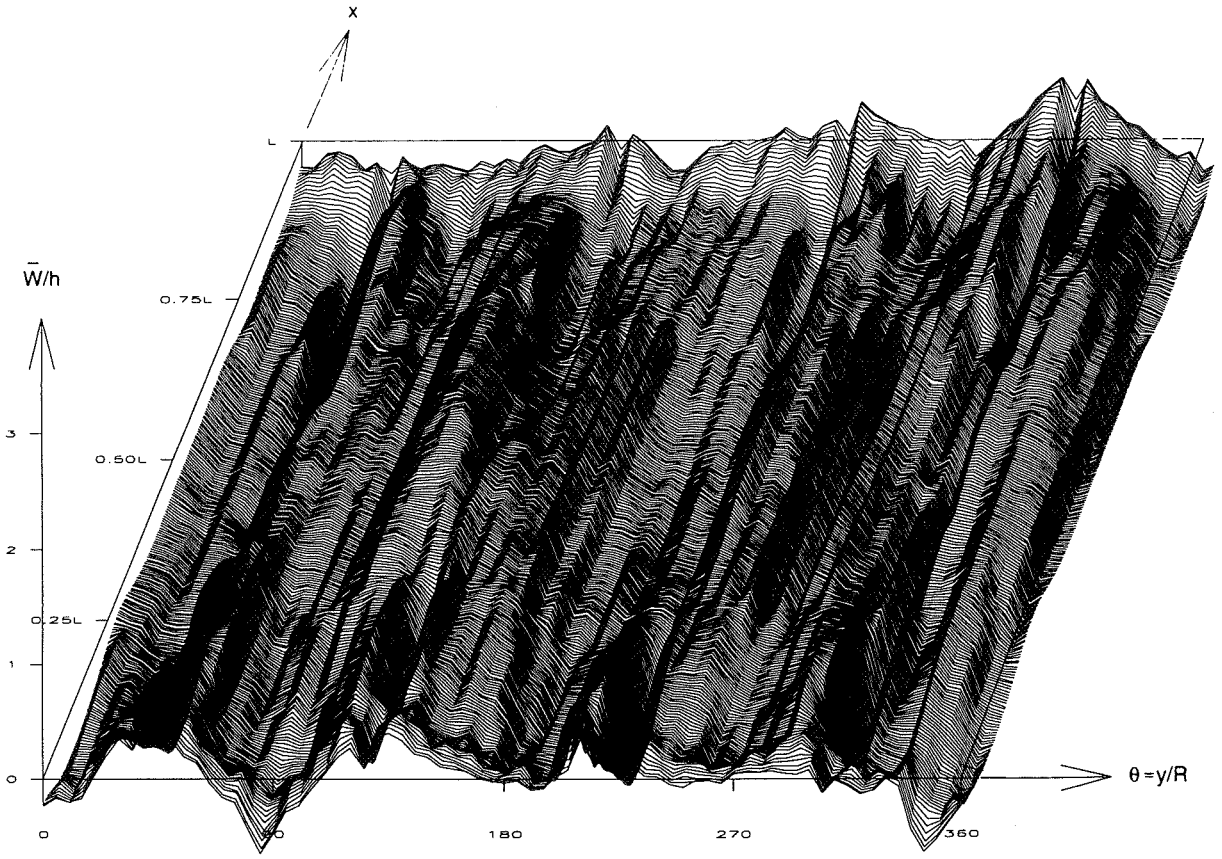

Fig. 5 Measured initial shape of aerospace shell X-2 [16]
(Radius 1527.4 mm, length: 6047.7 mm, mean wall thickness: 2.629 mm)

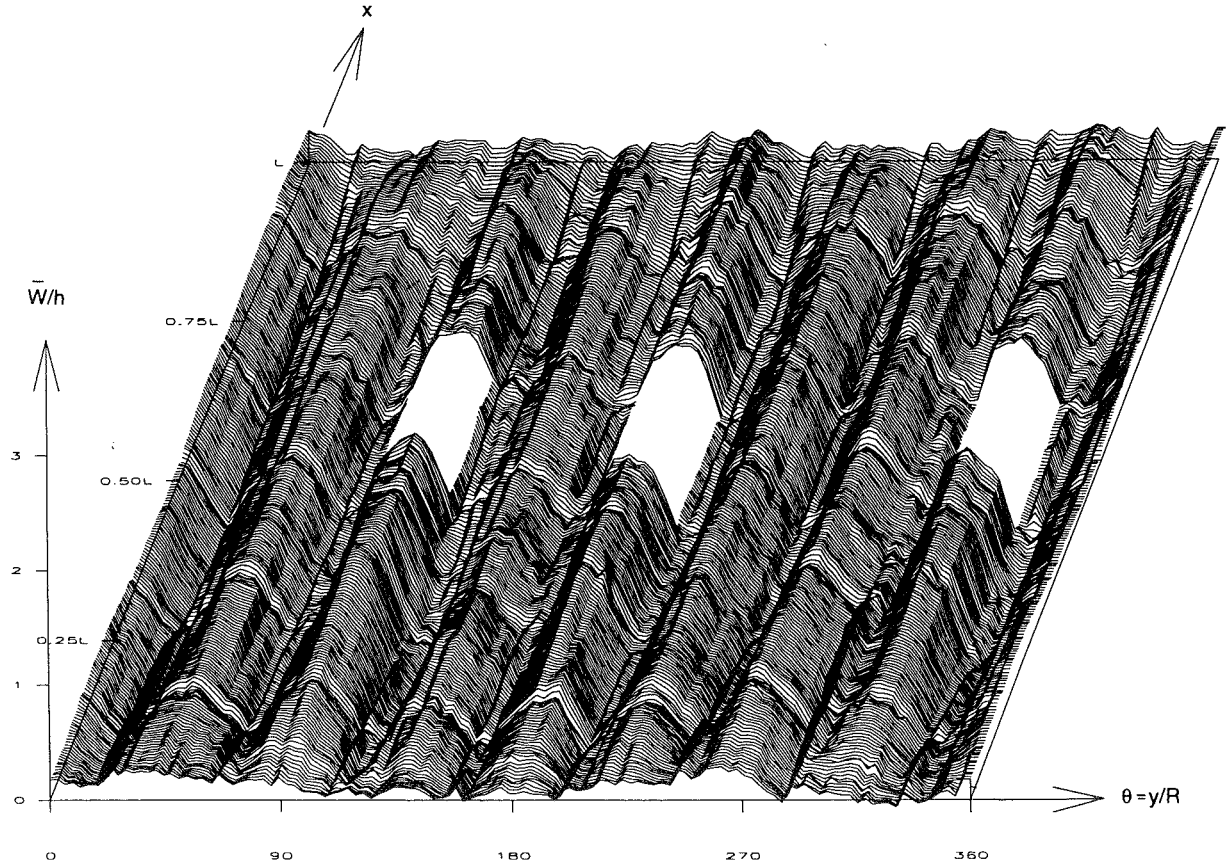

Fig. 6 Measured initial shape of an ARIANE interstage II/III shell [16]
(Radius: 1300.0 mm, length: 2730.0 mm, wall thickness: 1.2 mm)

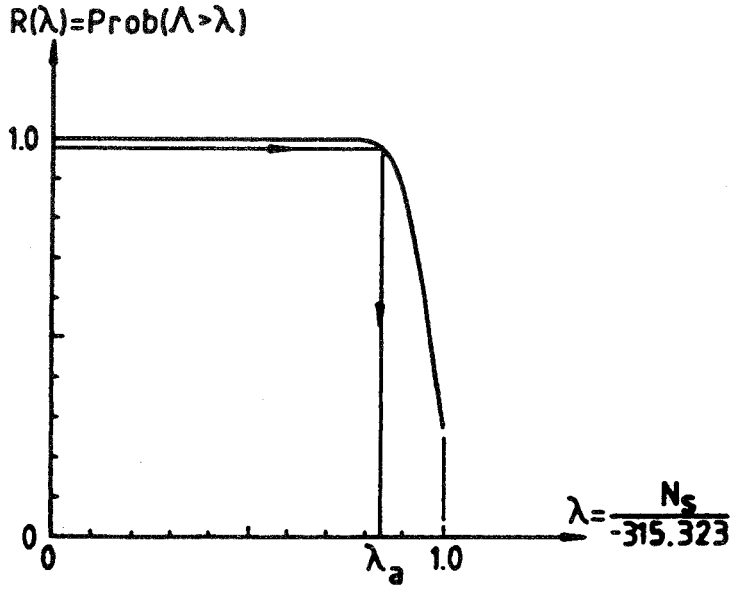

Fig. 7 Reliability curve calculated via the first-order, second-moment method (C-4 boundary conditions: $u = v = W = W_{,x} = 0$) [17]

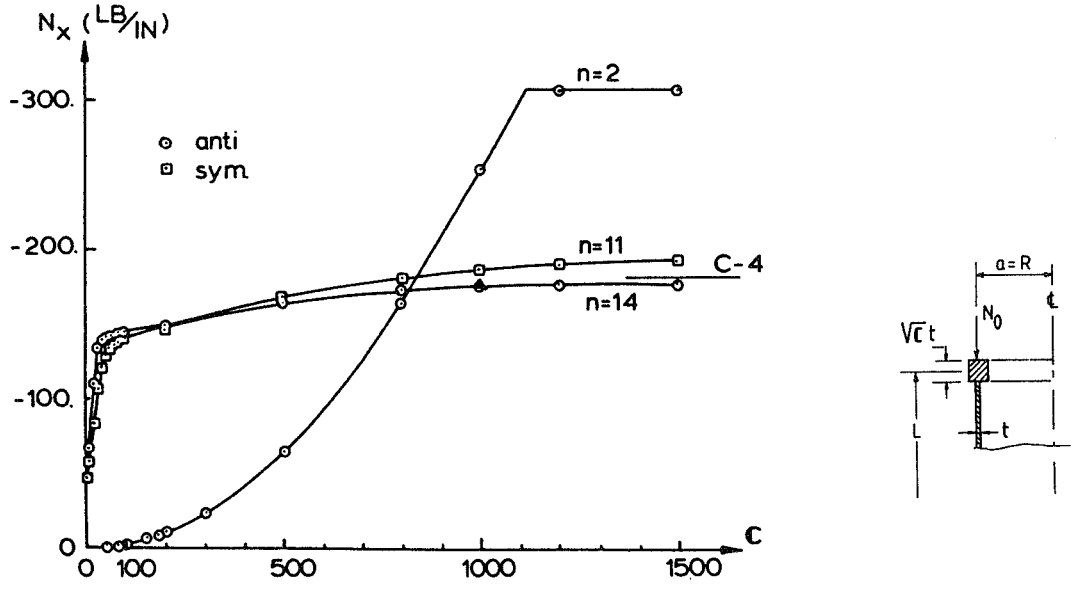

Fig. 8 Critical loads for perfect shell AS-2 supported by elastic end rings [29]

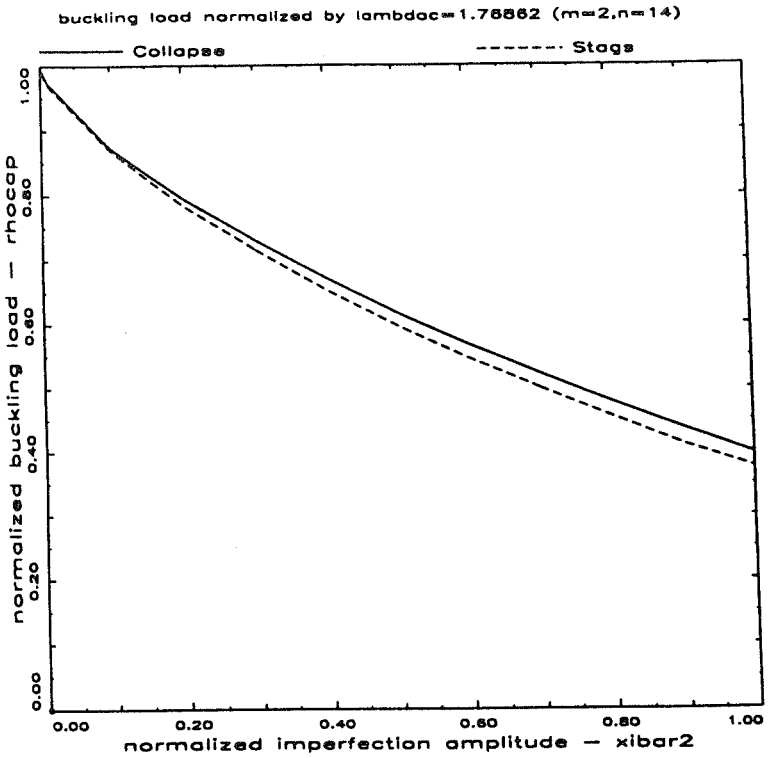

Fig. 9 Boundary imperfection sensitivity of shell AS-2 [34]
($u_{01}=u_{L1} \rightarrow$ antisymmetrical buckling mode; $\bar{\xi}_2=10u_{01}/t$)

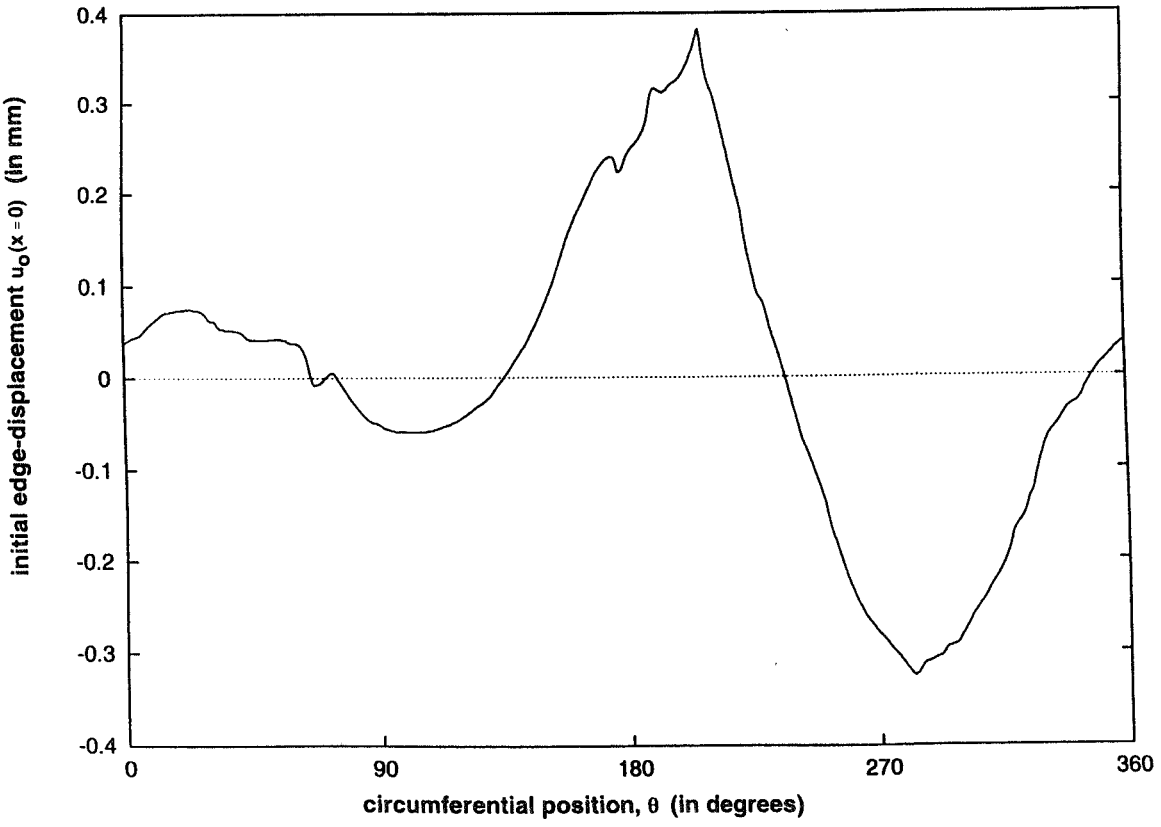

Fig. 10 Measured flatness of the Caltech end-ring (in mm)

Computational Tools for Stability Analysis

E. Riks[§] and C. C. Rankin[§§]

Structural stability analysis with general finite element codes is an outgrowth of a theory that was established during the last 100 years. In this paper, we intend to give an overview of the present capabilities in this field and this from the perspective of the development of the theory as it took place in the recent past.

1. Introduction

In the first part of this century, the stability analysis of structural components such as bars, struts and shells was mainly centered on the determination of the first bifurcation point in the prebuckling state of the structure under load. This type of analysis was thought to provide the prediction of the load carrying capacity of the structure.

It did not take long, however, before it was realized that the maximum load criterion developed on this basis was very unreliable because the actual load at which a given structure would fail could differ vastly from the computed value. This discrepancy between the theoretically determined failure load and the failure load of an actual structure was particularly large in the case of thin walled shell structures such as the thin walled cylindrical shell in compression. For example, the actual failure load of a thin walled cylindrical shell in compression could be as low as 10% of the value predicted by the bifurcation point. On the other hand, stiffened plate structures could often be loaded in excess of the bifurcation load determined by the theory.

Just at the end of the second world war, this perplexing behavior[1] was explained in general terms by Koiter[2,3], who showed that the actual behavior of a structure at the bifurcation load can be related to the stability properties of the bifurcation point itself. If the bifurcation point encountered is unstable, the failure load of the actual structure can be expected to occur below, and sometimes far below the bifurcation load. On the other hand, when the bifurcation point is stable, the structure can in general be loaded above the bifurcation load without detrimental after effects. But Koiter's theory not only provided an explanation of these peculiar differences in behavior, it also gave way to a new technique by which given problems could be analyzed. The latter corresponded to a perturbation method, whereby the initial post buckling behavior, the solutions of the bifurcation branches in the neighborhood of the bifurcation point could be determined. The theory also offered a means to predict the severity of the degradation of the failure load in the case the bifurcation point turned out to be unstable. The prediction took the form of a imperfection sensitivity relation, a lower bound, which expressed to what extent the actual failure load could drop in comparison to the theoretically determined bifurcation load this in dependence of the size of the imperfections.

The theory thus lead to the recognition that the stability behavior of mechanical systems cannot be understood properly without taking the essential non linearity of the problem into account. But it was specifically this nonlinear aspect, that made the practical application of the theory a difficult undertaking with the analytical methods that were available at that time. This is illustrated by the relatively small number of practical problems that were actually solved in the first two decades which followed the first appearance of the theory.

It was only after the emergence of the computer, that this situation gradually changed and it is this change that we intend to discuss in this paper.

2. Stability analysis in retrospect

2.1 Preliminaries

Classical stability theory, such as Koiter's is often cast in the frame work of a continuum model [2,3,4]. In this paper we will take an alternative and easier road by assuming that the governing equations are provided in discrete form, i.e., they are associated with an appropriate finite element model. This model approximates reality in its own way using the idea that the structure or solid is build from crystals or particles that are here modeled by finite elements.

[§]Delft University of Technology, The Netherlands.
[§§]Lockheed Martin, Palo Alto, California.

We assume that the structures to be considered are quasi conservative. This is to mean that the equations of equilibrium can be derived from a potential energy function but that, when transient phenomena come into play, we will introduce damping in order to make energy dissipation in terms of heat loss possible.

In the discrete setting of the finite element method, the state of a structure is determined by an N- dimensional vector **d**. For the loading of the structure we will make the distinction between live loads (external forces) that can be derived from an potential, and loads that are induced by prescribed displacements. In the general case, both types of loading can be applied simultaneously and for the time being we will assume that such a load system is varied by one intensity parameter, here denoted by λ. The potential energy function can then be written as:

$$P = P(\mathbf{d}, \lambda) \tag{1}$$

The brackets $(\mathbf{d}, \lambda)$ denote here that P is a function of **d** and λ, so as to avoid confusion with the symbols ([{ }]) which will be used to group algebraic terms. With the notation $P_{\mathbf{d}}$ for partial differentiation with respect to **d**, the governing equations are derived from the requirement that the potential energy attains a stationary value at equilibrium:

$$P = P_{\mathbf{d}}(\mathbf{d}, \lambda)\delta\mathbf{d} = [\mathbf{f}(\mathbf{d}, \lambda)]^T\delta\mathbf{d} = 0 \tag{2a}$$

which yields the N-dimensional set of equations:

$$\mathbf{f}(\mathbf{d}, \lambda) = 0 \tag{2b}$$

Please note that $\delta\mathbf{d}$ stands for an arbitrary variation of **d** while $P_{\mathbf{d}}$ is a notation for differentiation with respect to **d**, such that: $P_{\mathbf{d}}\delta\mathbf{d} = \frac{\partial P}{\partial \mathbf{d}}\delta\mathbf{d} = \frac{\partial P}{\partial d_i}\delta d_i$ (sum over i = 1,2,3,..., N). The vector valued function $\mathbf{f} = (P_{\mathbf{d}})^T$ and the displacement vector **d** are thus members of a linear space $\mathbb{R}_N$.
Equations (2) are nonlinear and are produced by the finite element model that is employed. An example of the possible structure of $\mathbf{f}(\mathbf{d}, \lambda)$ is given by:

$$\mathbf{f}(\mathbf{d}, \lambda) = -\lambda\mathbf{A} + \frac{1}{2}\mathbf{B}_{\mathbf{d}}\mathbf{d} + \frac{1}{3!}\mathbf{C}_{\mathbf{dd}}\mathbf{dd} + \frac{1}{4!}\mathbf{D}_{\mathbf{ddd}}\mathbf{ddd} \tag{3}$$

where the notation: **A**, $\mathbf{B}_{\mathbf{d}}\mathbf{d}$, $\mathbf{C}_{\mathbf{dd}}\mathbf{dd}$, etc. stands for: $\mathbf{A} = A_i\mathbf{e}_i$; $\mathbf{B}_{\mathbf{d}}\mathbf{d} = B_{ij}d_j\mathbf{e}_i$, $\mathbf{C}_{\mathbf{dd}}\mathbf{dd} = 3C_{ijk}d_jd_k\mathbf{e}_i$, etc.. (sum over i,j,k : 1,...N) and where $\mathbf{d} = d_i\mathbf{e}_i$; $\mathbf{e}_i$ (i = 1, ..., N) being the natural base vectors of the space $\mathbb{R}_N$ in which **d** and **f** are described*. These quantities **A**, $\mathbf{B}_{\mathbf{d}}\mathbf{d}$, $\mathbf{C}_{\mathbf{dd}}\mathbf{dd}$ etc., are also vectors in the space $\mathbb{R}_N$. The contraction of these vectors with another vector in $\mathbb{R}_N$ is written as $\mathbf{b}^T\mathbf{B}_{\mathbf{d}}\mathbf{d} = \mathbf{b}^T\mathbf{y}$ where $\mathbf{y} = \mathbf{B}_{\mathbf{d}}\mathbf{d}$. This is thus the same as the inproduct of two vectors **a** and **b**: $\mathbf{a}^T\mathbf{b}$.

2.2 Linearizations of the pre-buckling state
The deformation vector **d** is defined in such a way that when $\lambda = 0$; $\mathbf{d} = \mathbf{0}$. The deformation state that develops when λ is increased from zero is called the basic state or primary state and we will often label it by the subscript 1. We can write for this state:

$$\mathbf{d}_1 = \mathbf{d}_1(\lambda) \tag{4}$$

Struts and bars are three dimensional structures optimized to sustain loads that can be carried by axial stresses only. Shell and plate structures are three dimensional objects optimized to sustain loads that can be carried by in plane stresses only. Such optimization process leads usually to a deformation path (4) which can be approximated by

$$\mathbf{d}_1 = \mathbf{d}_1(\lambda) \approx \lambda\mathbf{d}_0' \tag{5}$$

where the solution vector $\mathbf{d}_0'$ is independent of λ. In this case the equations of equilibrium, which are still nonlinear, admit this linear solution, exactly or in good approximation:

$$\mathbf{f}(\lambda\mathbf{d}_0', \lambda) \cong 0 \tag{6}$$

in some range: $0 \le \lambda < \lambda^*$, where the bound λ^* is often determined by the requirement that the deformations, i.e. the -strains-, belonging to λ^* should remain small. Satisfaction of equations (2^b) by (5) thus means that:

$$\mathbf{f}(0,0) + \{\mathbf{f}_{\mathbf{d}}(0,0)\mathbf{d}_0' + \mathbf{f}_\lambda(0,0)\}\lambda + \frac{1}{2}\{\mathbf{f}_{\mathbf{dd}}(0,0)\mathbf{d}_0'\mathbf{d}_0' + 2\mathbf{f}_{\mathbf{d}\lambda}(0,0)\mathbf{d}_0' + \mathbf{f}_{\lambda\lambda}(0,0)\}\lambda^2 + O(\lambda^3) = 0 \tag{7}$$

from which it can be deduced that in this particular case:

$$\mathbf{f}_{\mathbf{d}}(0,0)\mathbf{d}_0' + \mathbf{f}_\lambda(0,0) = 0 \tag{8a}$$

$$\mathbf{f}_{\mathbf{dd}}(0,0)\mathbf{d}_0'\mathbf{d}_0' + 2\mathbf{f}_{\mathbf{d}\lambda}(0,0)\mathbf{d}_0' + \mathbf{f}_{\lambda\lambda}(0,0) \approx 0 \tag{8b}$$

etc., etc. Please note that the solution $\mathbf{d}_0'$ of (8^a) corresponds to the solution of linearized equations of elasticity.

---

* Equations can also be transcendental. It should be realized that in general, the function **f** is not computed from an expression in terms of the coëfficients Aij, Aijk etc. but that it is evaluated internally by the code. Please note that the continuum analogue to equations (2^b, 3) consists of a system of nonlinear partial differential equations with boundary conditions.

Of course, not all problems that are encountered can be treated in this way. When the solution (4) is truly nonlinear, the linearization (8^a) cannot longer be used. It is then necessary to replace the representation (5) by an expression that approximates (4) more adequately, for example, by a regular perturbation (Taylor) expansion of (4):

$$\mathbf{d}_1(\lambda) = \lambda \mathbf{d}_0' + \frac{1}{2}\lambda^2 \mathbf{d}_0'' + \frac{1}{3!}\lambda^3 \mathbf{d}_0''' + \ldots \qquad (9)$$

When a point $\mathbf{d}_a = \mathbf{d}_1(\lambda_a)$ of the nonlinear primary state (4) is known beforehand, linearization as an approximation device can still be used in the neighborhood of this particular point. The solution in a close neighborhood of $\mathbf{d}_a$ can then be represented by:

$$\mathbf{d}_L = \mathbf{d}_1(\lambda_a) + (\lambda_a - \lambda)\mathbf{d}_1'(\lambda_a) \qquad (10^a)$$

The equations that determine $\mathbf{d}_1'(\lambda_a)$ are:

$$\frac{d}{d\lambda}\{\mathbf{f}(\mathbf{d}_1(\lambda_a), \lambda_a)\} = \mathbf{f}_{\mathbf{d}}(\mathbf{d}_1(\lambda_a), \lambda_a)\mathbf{d}_1' + \\ + \mathbf{f}_\lambda(\mathbf{d}_1(\lambda_a), \lambda_a) = 0 \qquad (10^b)$$

where $(\,)' = \frac{d}{d\lambda}$. These equations determine the so called first "path derivative" of (4). As can immediately be verified, equations (8^a) are a special case of (10); i.e. for $\lambda_a = 0$.

In some present day finite element procedures, the approximation (10) is often used as a first step in the prediction of the point of (4) at which stability is lost. But in the beginning of this century, it was not possible to deal with the general case of a nonlinear primary state (4). This explains why elastic stability theory was predominantly occupied with problems that are characterized by a linearized primary state (5).

2.3 Neutral equilibrium and loss of stability

To determine the point of (4) at which loss of stability is expected to occur, two criteria were used. The first was based on the concept of neutral equilibrium[5-10]. According to this concept, if, at some specific value of the load $\lambda = \lambda_c$, next to the solution $\mathbf{d} = \mathbf{d}_1(\lambda_c)$, also a neighboring solution $\hat{\mathbf{d}} = \mathbf{d}_1(\lambda_c) + \Delta\mathbf{d}$ existed, -where the difference $\Delta\mathbf{d}$ is vanishingly small-, the point $\mathbf{d}_1(\lambda_c)$ was called a point of neutral equilibrium. A state of neutral equilibrium was thus coupled to the loss of uniqueness (in the small) of the solution (4) and this implies that the criterion for neutral equilibrium corresponds to a criterion for bifurcation. It was assumed that a structure that reached a state of neutral equilibrium would become unstable upon further loading so that at this state collapse would automatically follow.

The second approach to come to the prediction of the failure load was through the energy criterion. This criterion states that the equilibrium state of a structure is stable, if and only if, the potential energy of the structure in that state is a proper minimum. If this minimum does not exist, the structure is in an unstable state of equilibrium.

It now turns out that the potential energy function possess a minimum if the second variation of the energy function is positive definite. On the other hand, if the second variation is indefinite, no minimum exist. The search for the equilibrium state at which stability is lost can thus be based on the search for the point at which the second variation ceases becomes semi-positive definite. The transition point that divides the stable states of (4) from the unstable states is thus determined by a semi-positive definite second variation of the structure's potential energy.

Superficially, the two approaches lead to the same basic system of equations that defined this so called critical state $\mathbf{d}_c = \mathbf{d}_1(\lambda_c)$ and this coincidence is probably the reason that in elasticity, bifurcation and loss of stability are often taken (erroneously) to be identical concepts.

2.4 The condition for neutral equilbrium

The search for a state that is in neutral equilbrium is equivalent to the search of an equilbrium state at which one or more equilibrium paths $\mathbf{d}_1(\lambda)$, $\mathbf{d}_2(\lambda)$, $\mathbf{d}_3(\lambda)$, ... cross. Suppose that the crossing occurs at $\mathbf{d}_c = \mathbf{d}(\lambda_c)$. It then follows that in the neighborhood of $\mathbf{d}_c$ for λ: $\lambda_c - \varepsilon < \lambda < \lambda_c + \varepsilon$, $\varepsilon > 0$ at least two solutions exist: $\mathbf{d}_1(\lambda_c)$ and $\hat{\mathbf{d}}(\lambda_c) = \mathbf{d}_1(\lambda_c) + \Delta\mathbf{d}(\lambda)$. Substitution in equations (2^b) yields:

$$\mathbf{f}(\mathbf{d}_1(\lambda) + \Delta\mathbf{d}(\lambda), \lambda) = 0 \\ \mathbf{f}(\mathbf{d}_1(\lambda), \lambda) = 0 \qquad (11)$$

We assume when ε is small, $\Delta\mathbf{d}(\varepsilon)$ will also be small so that when $\varepsilon \to 0$, $\Delta\mathbf{d} \to 0$. Expansion of the first equation yields:

$$\mathbf{f}(\mathbf{d}_1(\lambda), \lambda) + \mathbf{f}_{\mathbf{d}}(\mathbf{d}_1(\lambda), \lambda)\Delta\mathbf{d} + O(\Delta\mathbf{d}^2) = 0 \\ \mathbf{f}(\mathbf{d}_1(\lambda), \lambda) = 0 \qquad (12)$$

Subtraction of these equations gives the equation for $\Delta\mathbf{d}$ when $\varepsilon \to 0$,

$$\mathbf{f}_{\mathbf{d}}(\mathbf{d}_1(\lambda), \lambda)\Delta\mathbf{d} = 0 \qquad (13)$$

which can be written in the form:

$$\mathbf{K}(\mathbf{d}_1(\lambda), \lambda)\mathbf{a} = 0 \\ \mathbf{K} = \mathbf{f}_{\mathbf{d}}(\mathbf{d}_1(\lambda), \lambda);\ \mathbf{a} = \Delta\mathbf{d} \qquad (14)$$

The equations of neutral equilibrium thus represent an eigenvalue problem, and the search for the state of neutral equilibrium is particular state ($\mathbf{d}_C$, λ_C) along (4) that admits a solution of (14) for the first time. Please note that in the case of a linear primary state (5), equations (14) read:

$$\mathbf{f_d}(\lambda \mathbf{d}_0, \lambda)\Delta \mathbf{d} = 0 \qquad (15^a)$$

or

$$\mathbf{K}(\lambda \mathbf{d}_0, \lambda)\mathbf{a} = 0$$
$$\mathbf{K} = \mathbf{f_d}(\lambda \mathbf{d}_0, \lambda);\ \mathbf{a} = \Delta \mathbf{d} \qquad (15^b)$$

2.5 The energy criterion for loss of stability

The energy criterion of stability dictates that an equilibrium state is stable if and only if the potential energy in that state is a proper minimum. This means that the state $\mathbf{d}_1 = \mathbf{d}_1(\lambda)$ is stable if it can be proved that:

$$\Delta P = P(\mathbf{d}_1(\lambda) + \Delta \mathbf{y},\ \lambda) - P(\mathbf{d}_1(\lambda),\ \lambda) > 0 \qquad (16)$$

for any vanishingly small, but otherwise arbitrary variations $\Delta \mathbf{y}$ in the space of degrees of freedom $\mathbb{R}_N$. If this property cannot be established, the equilibrium state $\mathbf{d}_1(\lambda)$ is unstable.

But the criterion as formulated above, is seldom used in this form. It is usually replaced by a weaker version which can be deduced from (16) if we expand the first term of (16) in a Taylor series:

$$\Delta P(\Delta \mathbf{y}) = P_{\mathbf{d}}(\mathbf{d}_1(\lambda), \lambda)\Delta \mathbf{y} +$$
$$+ \frac{1}{2} P_{\mathbf{dd}}(\mathbf{d}_1(\lambda), \lambda)\Delta \mathbf{y}\Delta \mathbf{y} + O(\Delta \mathbf{y}^3) - P(\mathbf{d}_1(\lambda), \lambda) > 0 \qquad (17)$$

Because $\mathbf{d}_1$ is an equilibrium state (see (2)), the leading term is identically zero so that there remains:

$$\Delta P(\Delta \mathbf{y}) = \frac{1}{2} P_{\mathbf{dd}}(\mathbf{d}_1(\lambda), \lambda)\Delta \mathbf{y}\Delta \mathbf{y} + O(\Delta \mathbf{y}^3) > 0 \qquad (18)$$

The inequality must be proved for arbitrary perturbations $\Delta \mathbf{y}$ which may be vanishingly small. It can now be shown that if

$$\Delta_2 P(\Delta \mathbf{y}) = \frac{1}{2} P_{\mathbf{dd}}(\mathbf{d}_1(\lambda), \lambda)\Delta \mathbf{y}\Delta \mathbf{y} \neq 0$$

for *all* arbitrary non zero choices of $\Delta \mathbf{y}$ in $\mathbb{R}_N$, the sign of ΔP will always be determined by the sign of $\Delta_2 P$ by taking the length of $\Delta \mathbf{y}$, $\|\Delta \mathbf{y}\|$ small enough. The notation $\| \ \|$ stands here for any appropriate vector norm. Thus, to ascertain that a given equilibrium state is stable, it is permissible to investigate the sign of the quadratic form $\Delta_2 P$ *provided* that $\Delta_2 P \neq 0$ for $\forall\ \Delta \mathbf{y} \in \mathbb{R}_N$; $\Delta \mathbf{y} \neq 0$.

Stability of the equilibrium state $(\mathbf{d}_1(\lambda), \lambda)$ is thus garanteed if:

$$\Delta_2 P(\Delta \mathbf{y}) = \frac{1}{2} P_{\mathbf{dd}}(\mathbf{d}_1(\lambda), \lambda)\Delta \mathbf{y}\Delta \mathbf{y} > 0 \qquad (19)$$

for all possible nonvanishing variations $\Delta \mathbf{y}$. On the other hand, if the quadratic form $\Delta_2 P$ takes a negative value for one or more choices of $\Delta \mathbf{y}$, say $\Delta \mathbf{y} = \Delta \mathbf{b}$, the potential energy differential ΔP will become negative for this perturbation taking $\|\Delta \mathbf{b}\|$ small enough. This means that P is not a minimum at $\mathbf{d}(\lambda)$ and the equilibrium state is then unstable.

There is, as one would expect, an intermediate case which occurs when the second variation is semi-positive definite, i.e., when $\Delta_2 P = 0$ for one, or possibly more choices of $\Delta \mathbf{y}$. In this situation, the second variation $\Delta_2 P$ does no longer determine the minimum or absence of the minimum of P. The analysis must then be carried out on ΔP in (17) taking into account the terms that are of higher order than $\Delta_2 P$.

The stability criterion which emerges on the basis of is the second variation $\Delta_2 P$ is attributed to Trefftz [11,12], see also [2]. Trefftz investigated the minimum of $\Delta_2 P$ by considering the problem:

$$\omega = \mathrm{MIN}\{\frac{\Delta P_2(\Delta \mathbf{y})}{\Delta \mathbf{y}^T \mathbf{T} \Delta \mathbf{y}}\} \qquad (20)$$
$$\forall \Delta \mathbf{y} \neq 0;\ \Delta \mathbf{y} \in \mathbb{R}_N$$

where $\mathbf{T}$ is a positive definite matrix so that the value of $\Delta_2 P$ is compared with that of a positive definite quadratic form $\Delta \mathbf{y}^T \mathbf{T} \Delta \mathbf{y}$. This variational problem leads to the set of equations:

$$[P_{\mathbf{dd}}(\mathbf{d}_1(\lambda), \lambda)\Delta \mathbf{y} - \omega \Delta \mathbf{y}^T \mathbf{T}]\delta \Delta \mathbf{y} = 0 \qquad (21^a)$$

which, with $\mathbf{a} = \Delta \mathbf{y}$ can be written as:

$$\mathbf{K}(\mathbf{d}_1(\lambda), \lambda)\mathbf{a} - \omega \mathbf{T}\mathbf{a} = 0 \qquad (21^b)$$

Thus according to Trefftz, stability of the state $\mathbf{d}_1$ is ensured if the solutions $\mathbf{a}(i)$ (i = 1, , N) of (21) yield: $\omega(i) > 0$ for all i: 1, .. N, while the equilibrium state $\mathbf{d}_1$ is unstable if one or more eigenvalues $\omega(i) < 0$.

Of particular interest is the case where the decision about stability is unsettled, i.e. when

$$\omega(1) = 0;\ \omega(i) > 0\ ;\ i > 1 \qquad (22^a)$$

In this situation the equations (21) admit a solution:

$$\mathbf{K}(\mathbf{d}_1(\lambda),\lambda)\mathbf{a} = 0 \qquad (22^b)$$

$$\mathbf{b}^T\mathbf{K}(\mathbf{d}_1(\lambda),\lambda)\mathbf{b} > 0;\ \mathbf{b}^T\mathbf{T}\mathbf{a} = 0 \qquad (22^c)$$

For simplicity, we will now assume that loss of stability only occurs for positive values of the load. By increasing the load slowly from zero the deformation state of the structure will follow the path $\mathbf{d}_1(\lambda)$ that we defined earlier. At first the equilibrium for $0 \le \lambda < \lambda_C$ is stable, so that ΔP_2 is positive along this first stretch of (4). But at the first instance that (22) is satisfied, thus at the lowest value of $\lambda = \lambda_C$ for which $\mathbf{K}$ becomes singular, the stability is no longer guaranteed by the second variation and the equilibrium state $\mathbf{d}_1(\lambda_C)$ is said to be on the stability limit. In elastic stability theory this particular state $\mathbf{d}_1(\lambda_C)$ is called a critical state. It signifies a boundary between states along $\mathbf{d}_1(\lambda)$ that are definitely stable, (for $0 \le \lambda < \lambda_C$) and definitely unstable (for $\lambda_C<\lambda<\lambda_C + \varepsilon$, where $\varepsilon > 0$).
As can be seen by inspection, equations (22) are identical in appearance to (15). But equations (22) are derived on the basis of the side condition (22^a) or (22^c) which was absent in the derivation of (15). The equations that determine the critical equilibrium states are thus more restrictive than the equations that determine the states of neutral equilibrium. However, from the practical point of view this difference is not of great significance because it is the first state $\mathbf{d}(\lambda_C)$ along the path (4) satisfying (22) or (15) which is of interest and it is this state that turns out to be identical for both criteria.

2.6 Linearization of the critical condition
As was mentioned in the foregoing, in the beginning of this century the failure load of an elastic structure was defined on the basis of equations (22) or (15). In practical applications, these equations were almost always simplified by assuming that the pre-critical state $\mathbf{d}_1(\lambda)$ could be linearized. This was due to the enormous difficulties that were connected with the analysis in the nonlinear case. The theory was thus only applicable for structures that possessed a linear pre-critical state.

For the linearized primary state, the critical condition is:

$$\mathbf{K}(\lambda\mathbf{d}_0,\ \lambda)\mathbf{a} = 0 \qquad (23)$$

which is still a nonlinear eigenvalue problem in terms of λ. Fortunately, optimized structures such as plates and shells often aloow the use of a simplification of (23). This is another linearization which follows from the expansion:

$$\mathbf{K}(\mathbf{0},0)\mathbf{a} + \mathbf{K}'(\mathbf{0},0)\mathbf{a}\lambda + O(\lambda^2) = 0 \qquad (24^a)$$

$\mathbf{K}'$ is here defined by:

$$\mathbf{K}' = \frac{d\mathbf{K}(\lambda\mathbf{d}_0,\ \lambda)}{d\lambda}\Big|_{\lambda=0} = \mathbf{f}_{\mathbf{d}\mathbf{d}}(0,\ 0)\mathbf{d}_0\mathbf{d}_0 + \mathbf{f}_{\mathbf{d}\lambda}(\mathbf{0},\ 0) \qquad (24^b)$$

and the higher order terms in (24^a) are then discarded. With the substitution $\mathbf{B} = -\mathbf{K}'$, these equations then appear as the linear eigenvalue problem:

$$\mathbf{K}(\mathbf{0},0)\mathbf{a} - \lambda\mathbf{B}'(\mathbf{0},0)\mathbf{a} = 0 \qquad (25)$$

The modes $\mathbf{a}(i)$ of (23) or (25), i = 1,2,3,.. are called the buckling modes. The mode $\mathbf{a}(1)$ that belongs to the smallest eigenvalue of (23),(25) $\lambda_1 = \lambda_C$ is the mode that belongs to the critical state. We see that a necessary condition for this critical load value is given by in the case (23):

$$\text{Det}\ \{\mathbf{K}(\lambda\mathbf{d}_0,\ \lambda)\} = 0 \qquad (26)$$

while in the linearized case (25) this condition reduces to:

$$\text{Det}\ \{\mathbf{K}(\mathbf{0},0) - \lambda\mathbf{B}'(\mathbf{0},0)\} = 0 \qquad (27)$$

It is of interest to note, that both conditions (26 or 27) can be seen to represent the condition for the intersection of a hyper surface in $\mathbb{R}_N$, -i.e. the stability boundary-, with the equilibrium curve $\mathbf{d} = \mathbf{d}_1(\lambda)$. In the first case (26), the hyper surface is formulated in the exact form, in the second case (27) it is linearized (in the sense of (24)). The intersection points for the smallest value of λ is the sought critical state of (4,5) or an approximation of this state. Even today, there seems to be some confusion about the proper formulation of the directional derivative $\mathbf{B} = -\mathbf{K}'$ defind by (24^b), as can be judged from a recent discussion about this subject in [13]

2.7 Stability of the critical states
The buckling criterion (23) or (14) determines a bifurcation point in the primary state of the structure. As discussed earlier, the bifurcation point represents the separation between the stable states of $\mathbf{d}_1(\lambda)$ (for $\lambda < \lambda_C$) and the unstable states (for $\lambda > \lambda_C$). It was thought at first that the passage through this point would inevitably lead to failure so that there appeared to be no need to carry the analysis any further. But it soon transpired that there was a great discrepancy between the point of failure as observed in practice, in experiments for example, and the point of failure as predicted by the theory. For example, the simply supported plate in compression[15,16,17,18] could be loaded beyond the buckling load into the postbuckling range without danger and this possibility was in fact exploited in the design of some aircraft structures[19] On the other hand, the thin walled cylindrical shell in compression always failed at loads far below the critical load predicted by the criterion (23), and sometimes, the discrepancy

amounted to a drop of nearly 90 %. The situation was clearly not very satisfactory and gave rise to efforts to come to grips with this anomaly.

It was Koiter[2] in the years leading up to 1945 who investigated this intriguing question in a general context. He came to the insight that the traditional concept of loss of stability was far too restricted and needed revision. Koiter began his investigation with an analysis of the stability of the critical states themselves because he suspected that the mysterious divergence in behavior was in some way related to the question whether the critical state is stable or not.

As we recall, at a critical state of equilibrium, the second variation (19) is semi-positive definite and in this case it fails to give a verdict about the existence or absence of a minimum of the potential energy in this state. The only way to get insight into this particular situation is then to go back to the strong form of the energy criterion (16). But before doing this we first write the energy increase ΔP as:

$$\Pi = \Pi(\Delta \mathbf{y}) = \Delta P =$$

$$= P(\mathbf{d}_1(\lambda) + \Delta \mathbf{y}, \lambda) - P(\mathbf{d}_1(\lambda), \lambda) \qquad (28)$$

For the time being, the load parameter can be dropped in this notation because we will consider the properties of Π at a fixed value of the load, i.e. at $\lambda = \lambda_C$. The expansion of (28) then gives:

$$\Pi = \frac{1}{2} P_{\mathbf{dd}}\Delta \mathbf{y}\Delta \mathbf{y} + \frac{1}{3!} P_{\mathbf{ddd}}\Delta \mathbf{y}\Delta \mathbf{y}\ \Delta \mathbf{y} + \frac{1}{4!} P_{\mathbf{dddd}}\Delta \mathbf{y}\Delta \mathbf{y}\ \Delta \mathbf{y}\Delta \mathbf{y} + O(\Delta \mathbf{y}^5)) \qquad (29)$$

Because we are at the critical state, the second variation is zero in the direction of the critical buckling mode **a**, whilie it is positive in any other direction. It seems useful therefore to use this direction as a reference in the evaluation of (29). This can be accomplished by the introduction of a change of basis that uses the buckling mode **a** as the principal base vector. It is introduced by:

$$\Delta \mathbf{y} = \mu \mathbf{a} + \mathbf{v} \qquad (30^a)$$

where the complement **v** to $\mu\mathbf{a}$ in this decomposition satisfies the orthogonality condition:

$$\mathbf{a}^T\mathbf{T}\mathbf{v} = 0 \qquad (30^b)$$

(see 20-21 for the meaning of **T**).

With this proposition we can now proceed to determine the minimum of the augmented function (for μ, **v**):

$$\Pi^* = \Pi(\mu, \mathbf{v}) + \kappa \mathbf{a}^T\mathbf{T}\mathbf{v} \qquad (31)$$

where κ is the Lagrange multiplier that is needed to introduce (30) as a constraint. The component **v** is thus in a subspace of $\mathbb{R}_N$ and, according to what transpired at (21), it has the property:

$$P_{\mathbf{dd}}(0)\,\mathbf{v}\,\mathbf{v} > 0 \qquad (32)$$

Koiter argued that it is admissible to look first for the minimum of Π^* on the plane Ω_μ: $\Delta \mathbf{y} = \mu \mathbf{a} + \mathbf{v}$; $\mathbf{a}^T\mathbf{T}\mathbf{v} = 0$ where the value of μ is considered fixed. If it can be established that this minimum exists and is given by $\Pi(\mu, \mathbf{V}(\mu))$ for $\mathbf{v} = \mathbf{V}(\mu)$; $0 < |\mu| < \varepsilon$ where ε is a positive constant, no matter how small, it follows that: $\Pi(\mu, \mathbf{V}(\mu)) < \Pi(\mu, \mathbf{v})$ for every $\mathbf{v} \neq \mathbf{V}$ that satisfies $\mathbf{a}^T\mathbf{T}\mathbf{v} = 0$. Consequently, if the minimum of Π along the solution $\Delta \mathbf{Y} = \mu \mathbf{a} + \mathbf{V}(\mu)$ satisfies $\Pi(\mu, \mathbf{V}(\mu)) > 0$ for some range of μ: $0 < |\mu| < \varepsilon$ it follows that $\Pi(\Delta \mathbf{y})$ is also positive for any vanishingly small variation of $\Delta \mathbf{y}$ around $\mathbf{d}_1(\lambda_C)$.
The minimum is thus determined by taking the stationary value of (31) with respect to **v** and κ. This yields the set of equations:

$$\begin{aligned} \mathbf{f}(\mu, \mathbf{v}) + \kappa \mathbf{T}\mathbf{a} &= 0 \\ \mathbf{a}^T\mathbf{T}\mathbf{v} &= 0 \end{aligned} \qquad (33)$$

in the (N+1) unknowns κ and **v**.

It can be shown that the system (33) is compatible in a small neighborhood of $\Delta \mathbf{y} = 0$ on the basis of the property (32) so that the solution for the function $\mathbf{v} = \mathbf{V}(\mu)$ can indeed be given.
The asymptotic solution of this problem for $\mu \to 0$ is carried out by setting:

$$\kappa = K(\mu) = \kappa^0 + \underline{\kappa}'\mu + \underline{\kappa}''\mu^2 + O(\mu^3)$$

$$\mathbf{v} = \mathbf{V}(\mu) = \underline{\mathbf{v}}^0 + \underline{\mathbf{v}}'\mu + \underline{\mathbf{v}}''\mu^2 + O(\mu^3) \qquad (34)$$

where $\underline{\mathbf{v}}$, $\underline{\kappa}$ is the shorthand for $\mathbf{v}(0)$, $\kappa(0)$. It turns out by inspection that $\kappa^0 = 0$; $\mathbf{v}^0 = \mathbf{v}' = 0$, so that the leading terms in this expansion are given by:

$$\kappa = \underline{\kappa}'\mu + \ldots; \quad \mathbf{v} = \underline{\mathbf{v}}''\mu^2 + \ldots \qquad (35)$$

The minimum $\Pi(\mu, \mathbf{V}(\mu))$ is thus a function defined along a curve $\mathbf{v} = \mathbf{V}(\mu)$ and is therefore only dependent on μ. Expansion of $\Pi(\mu, \mathbf{V}(\mu))$ around $\mu = 0$ gives:

$$\Pi = \frac{1}{3!}\Pi(0)^{(3)}\mu^3 + \frac{1}{4!}\Pi(0)^{(4)}\mu^4 + \ldots \qquad (36^a)$$

where

$$A_3 = \Pi(0)^{(3)} = P_{\mathbf{ddd}}\mathbf{aaa};\ A_4 = \Pi(0)^{(4)} = P_{\mathbf{dddd}}\mathbf{aaaa} - 12P_{\mathbf{dd}}\mathbf{v}''\mathbf{v}'' \qquad (36^b)$$

The displacement component $\underline{v}''$ is here determined by the (compatible) set of equations that follow from (33):

$$\begin{aligned} \mathbf{f_d}(0)\underline{v}'' + 2\underline{\kappa}'\mathbf{Ta} &= -\mathbf{f_{dd}}(0)\mathbf{aa} \\ \mathbf{a}^T\mathbf{T}\underline{v}'' &= 0 \end{aligned} \tag{37}$$

where **a** = the buckling mode given by (23).

It can now be concluded that if $A_3 = \Pi(0)^{(3)} \neq 0$ in the expansion (36^a), the critical state is unstable, because in that case the lower bound of the energy variation (36) will always take a negative value by taking μ small enough. A special case emerges when $\Pi(0)^{(3)} = 0$. In this situation, the lower bound of the energy function is again negative when $\Pi(0)^{(4)} < 0$. On the other hand if $\Pi(0)^{(4)} > 0$ it is positive for $|\mu| \rightarrow 0$ and this means that in this particular case the potential energy is still a minimum at the critical state. The summary of this evaluation is listed below:

If $A_3 \neq 0$; the critical state is unstable

If $A_3 = 0$; $A_4 < 0$; the critical state is unstable (38)

If $A_3 = 0$; $A_4 > 0$; the critical state is stable

Please note that when $A_3 = A_4 = 0$, the analysis must be continued to include the higher order coëfficient $\Pi^{(5)}$ etc., but this particular case is seldom encountered in elasticity.

With these results, we come to the conclusion that, - in a mathematical sense-, the critical states defined by (22) or (23) here are unstable in general. Only in the particular situation that $A_3 = 0$, there is a chance that stability of this point is retained. In the engineering practice, however, the case $A_3 = 0$ occurs very often which has to do with the presence of symmetry in the geometry of many structures, a property which is the result of attempts to reduce the weight of the structure as much as possible.

2.8 Postbuckling solutions

The preceding analysis is restricted to the intrinsic properties of the critical states themselves. To extent this analysis to the equilibrium branches that are connected with $\mathbf{d}_c = \mathbf{d}_1(\lambda_c)$. Koiter started again with the decomposition (30):

$$\mathbf{d} = \mathbf{d}_1(\lambda) + \mu\mathbf{a} + \mathbf{v}: \ \mathbf{a}^T\mathbf{T}\mathbf{v} = 0 \tag{39}$$

The potential energy increase from the pre-buckling state can then be written as:

$$\Delta P^* = P(\mathbf{d}_1(\lambda) + \mu\mathbf{a} + \mathbf{v}, \lambda) - P(\mathbf{d}_1(\lambda), \lambda) + -\kappa\mathbf{a}^T\mathbf{T}\mathbf{v} \tag{40}$$

where the side condition on **v** is again introduced via the Lagrange multiplier κ. The stationary value of ΔP^* which determines the equilibrium is first sought for arbitrary variations of **v** while μ is kept fixed. This variational process leads to the equations:

$$\delta\Delta P^* = 0$$

$$P(\mathbf{d}_1(\lambda) + \mu\mathbf{a} + \mathbf{v}, \lambda)_{\mathbf{d}}\delta\mathbf{v} - \kappa\mathbf{a}^T\mathbf{T}\delta\mathbf{v} - \delta\kappa\mathbf{a}^T\mathbf{T}\mathbf{v} = 0$$

$$\rightarrow \quad \begin{aligned} &\mathbf{f}(\mathbf{d}_1(\lambda) + \mu\mathbf{a} + \mathbf{v}, \lambda) - \kappa\mathbf{T}\mathbf{a} = 0 \\ &\mathbf{a}^T\mathbf{T}\mathbf{v} = 0 \end{aligned} \tag{41}$$

The resulting system is (N+1) dimensional while the number of variables it contains is (N+3). Two of these can thus be chosen as independent variables and it turns out to be of advantage to choose the bucklingmode amplitude μ and the load factor λ for this purpose.

The Jacobian of the system (41):

$$\mathbf{J} = \begin{bmatrix} \mathbf{f_d}(\mathbf{d}_c, \lambda_c) & \mathbf{Ta} \\ \mathbf{a}^T\mathbf{T} & 0 \end{bmatrix} \tag{42}$$

is nonsingular at λ_c and on the basis of continuity assumptions it is also nonsingular in a small neighborhood of the critical state $\mu = 0$, $\lambda = \lambda_c$. Consequently, according to the implicit function theorem, the system (40) is compatible in this neighborhood. Suppose that the solution is given by: $\mathbf{V} = \mathbf{V}(\mu, \Delta\lambda)$ $\{\Delta\lambda = \lambda - \lambda_c\}$; $K = K(\mu, \Delta\lambda)$, then it follows that the energy can be written as:

$$\Delta P^* = P(\mathbf{d}_1(\lambda) + \mu\mathbf{a} + \mathbf{V}(\mu, \Delta\lambda), \lambda) - P(\mathbf{d}_1(\lambda)\lambda) - K(\mu, \Delta\lambda)\mathbf{a}^T\mathbf{T}\mathbf{v} \tag{43}$$

so that there remains an expression in the variables λ and μ only, which in shorthand can be written as:

$$\Delta P^* = \Pi^*(\mu, \Delta\lambda) \tag{44}$$

The equilibrium states in the neighborhood of $\mathbf{d}_1(\lambda_c)$ are now described by the stationary value of Π^*:

$$\Pi^*(\mu, \Delta\lambda)_\mu\delta\mu = 0 \tag{45^a}$$

Koiter showed that for $|\Delta\lambda| \rightarrow 0$; $|\mu| \rightarrow 0$ the stability of the branches determined by this equation is determined by the sign of:

$$\Delta_2\Pi^* = \Pi^*(\mu, \Delta\lambda)_{\mu\mu}\delta\mu\delta\mu \tag{45^b}$$

The transformation process that makes use of the decomposition (39) leading to (41) and finally (45) is called the Liapunov-Schmidt reduction of the governing equations, see for example[20]. Koiter[2] found this reduction independently, using the principle of the

stationary value of the potential energy in more or less the same way it is described here, so that one could also call this method the Liapunov-Schmidt-Koiter reduction. The effectiveness of this method lies in the splitting of the governing equations in two parts. One part is large (41) and the other is small (45). The dimension of the latter corresponds to the multiplicity M of the the bifurcation point, which in the cases considered here is M = 1. The large system is compatible and can be linearized within some neighborhood of the critical state but the small system is singular which means that it cannot be linearized. The difficulty of the singularity of the original N-dimensional set of nonlinear equations is thus reduced to the difficulty of having to deal with a single singular nonlinear equation.

Lack of space prevents us to describe in what way the perturbation solution of (41), (43) and (45) is obtained. We only present the result. The asymptotic form of (43) turns out to be given by:

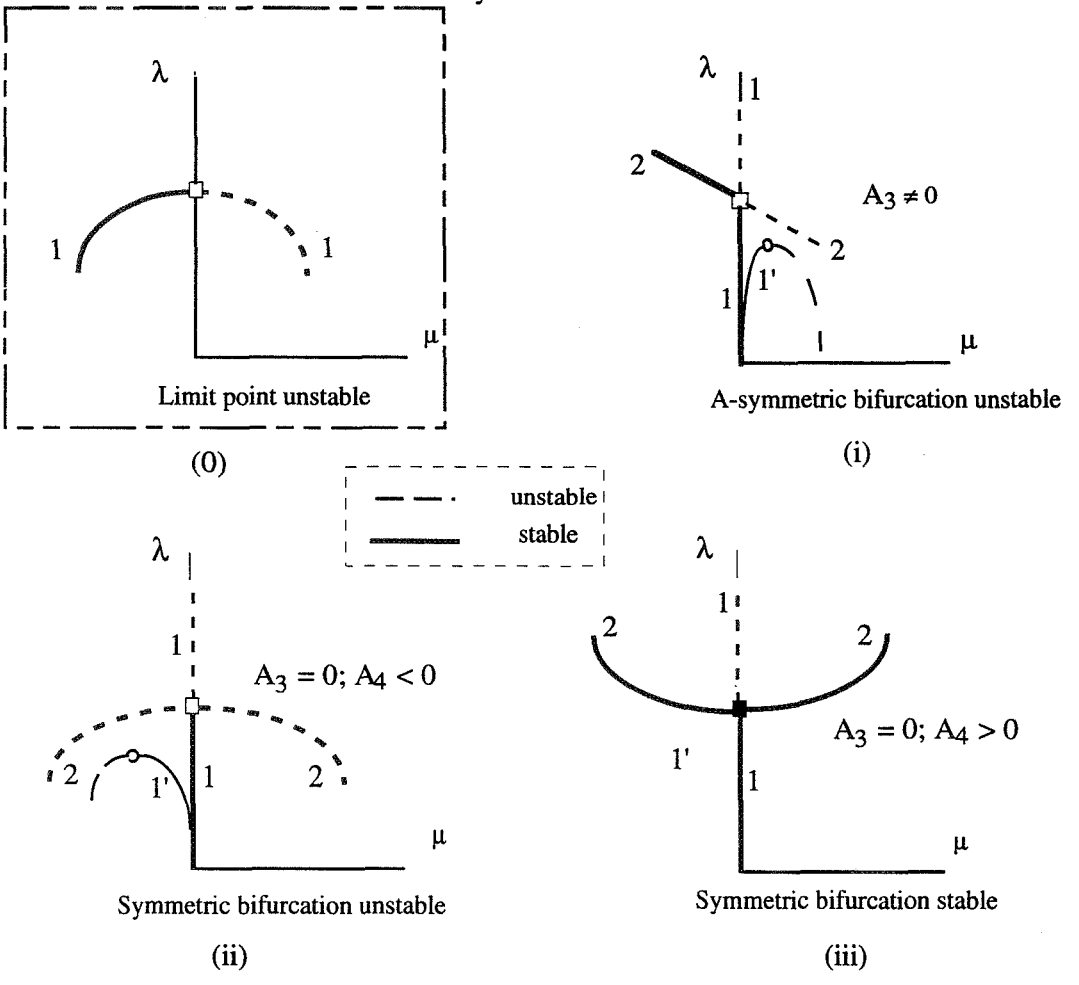

Figure 1 Classical results Koiter theory

$$\Delta P = \frac{1}{2} A_2'(\lambda-\lambda_c)\mu^2 + \frac{1}{3!} A_3\mu^3 + \frac{1}{4!} A_4\mu^4 \quad (46^a)$$

where: $A_2' = -\mathbf{a}^T(\mathbf{f_d})'\mathbf{a} = -\mathbf{a}^T\mathbf{K}'(\mathbf{d}_1(\lambda_c), \lambda)\mathbf{a}$;

$$(\mathbf{f_d})' = \mathbf{K}' = -\frac{d}{d\lambda}\{\mathbf{f_d}(\mathbf{d}_1(\lambda), \lambda)\}; \quad (46^b)$$

$$A_3 = P_{ddd}aaa;\ A_4 = [P_{dddd}aaaa - 2P_{dd}v''v''] \quad (46^c)$$

The equations that determine the solutions in the neighborhood of the bifurcation point $\mathbf{d}_1(\lambda_c)$ are then given by:

$$A_2'(\lambda-\lambda_c)\mu + \frac{1}{2} A_3\mu^2 + \frac{1}{3!} A_4\mu^3 = 0 \quad (47)$$

This, now classical result contains the essential information about the behavior of the solutions in the neighborhood of the critical states. The solutions are pictured in Figure 1, (i), (ii), and (iii). We refer to [2,3] for further details.

For simple bifurcation points, the solutions of (45) show that unstable points, defined by (38) have a descending branch 2 measured with respect to λ, while the stable bifurcation point (iii) has only ascending branches 2 for λ. Thus, for simple bifurcation points,

Koiter was able to show that stability of the bifurcation point meant only ascending branches (and the other way around) while unstable points always have at least one descending branch. This property becomes handy in interpreting numerical results as we will see in chapter 3.

2.9 Imperfection sensitivity

Structures are manufactured according to certain specifications but never meet these specifcations exactly. Before 1940 there was growing suspicion that these differences, even when they were very small and thus difficult to measure, could have a detrimental effect on the behavior of the structure near the buckling load. Koiter investigated the problem for shape (geometrical) imperfections and his analysis revealed that the most important influence (in an asymptotic sense) is to be expected from mode shapes that correspond to the buckling mode **a**. This follows, in part, from the structure of the energy function ΔP which is a quadratic form of the strain measures. The introduction of such an imperfection has the effect that the reduced form of the potential energy increase is changed to:

$$\Delta P^{\#} = -\varepsilon Q'(\lambda - \lambda_c)\mu + \frac{1}{2} A_2'(\lambda-\lambda_c)\mu^2 + \frac{1}{3!} A_3\mu^3 + \frac{1}{4!} A_4\mu^4 \qquad (48)$$

where we present the influence of the imperfections in the case that the primary state of the structure is linearized: $\mathbf{d}_1 = \lambda \mathbf{d}_0$. This new term $\varepsilon Q'(\lambda - \lambda_c)\mu$ is then the leading term in the expansion of ΔP with respect to ε, the amplitude of the imperfection $\mathbf{w}_0 = \varepsilon \mathbf{a}$. As follows from analysis of this modification (48), the influence of this initial geometrical perturbation of the structure is dramatic when the bifurcation points are unstable. This means that when $\varepsilon \neq 0$, structures fail at limit points rather than bifurcation points and this change of behavior takes place at loads far below the critical value that belongs to the original bifurcation point. In the case of a stable bifurcation point, the behavior also changes because the equilibrium path of the imperfect structure will smooth out the change in mode shape while the load is increasing, while for the perfect structure, it takes place in an abrupt way. (see Figure 1 where the imperfect paths are denoted by 1').

Among other examples, Koiter applied the theory in [2] to a simply supported plate in compression and the thin walled cylindrical shell in compression. The results of these investigations showed that the plate is governed by a stable bifurcation point (iii) in Figure 1, and the cylindrical shell by an unstable compound bifurcation point which, because it is unstable is very imperfection sensitive. He thus provided the explanation of why plates can be loaded beyond the bifurcation load and cylindrical shells fail miserably at loads λ^* below λ_c.

3. Numerical Computations

3.1. Computerized analysis

Of the two publications[2,3] that delivered this new theory, one was in Dutch and the other was so condensed that it took quite a while before its message filtered through. This was the reason that only after many years, in the sixties and beginning of the seventies, Koiter's theory became better known, only after it was reestablished, reformulated and further worked out by several scientist and engineers who were active in the field of solid mechanics. We can mention here for example the contributions of Sewell, Thompson and Hunt, and Budiansky [21,22,4]. These developments did not bring about any fundamental changes, but gave rise to alternative formulations and additional clarifications. On the level of practical applications some beautiful solutions appeared for a number of fundamental problems, see for example [23,24], but the solution of real world problems remained a difficult undertaking. The difficulty had to do with the circumstance that the perturbation equations were formulated as partial differential equations that defied solution except in the simplest of cases. Moreover, there was an additional difficulty. Problems that are dominated by a limit point behavior (Figure 1- (0) could not be solved by the analytical methods that were available at that time.

The advent of the computer brought considerable changes in this situation. It promoted the introduction of the finite element method and the development of numerical methods for the solution of ordinary nonlinear equations and ordinary differential equations that are produced by this approach.

In elastic stability analysis, two directions emerged as a result of this development. The first is aimed at an adaptation of the perturbation method to the computer environment [25-31]. This is thus a computerized analysis on the basis of the Koiter theory and corresponds to the solution of the governing equations of the type discussed in chapter 2. The second approach focuses on the global solution of the governing equations which is accomplished with the use of the so called continuation methods[32-38].We will now sketch this second approach which, it should be emphasised, has not changed the fundamentals of the existing theory, but which makes it possible to solve practical problems on a scale that was unheard of some thirty years ago.

3.2 The operational form of equilibrium equations

The equations of equilibrium were defined at (2) and the solutions of these equations can be written in the parametric form (4). For the computations that we want to describe here it is customary to introduce a evolution parameter σ which represents the progress of the deformation in a more general way:

$$\mathbf{d} = \mathbf{d}(\sigma)\,;\ \lambda = \lambda(\sigma) \qquad (49)$$

In the global computerized approach the solutions to the equations of equilibrium are obtained in a step by step fashion so that in terms of (49) the solutions to (2) are given as: $\mathbf{d} = \mathbf{d}(\sigma_i)$; $\lambda = \lambda(\sigma_i)$; (i = 1,2,3,...K). In this procedure, the definition of the general parameter σ changes with each step along (49), because its choice is adapted to the geometrical properties of the solutions that lay ahead.

The way this is accomplished in practice can be explained as follows. Suppose the last point computed is $(\mathbf{d}_k, \lambda_k) = (\mathbf{d}(\sigma_k), \lambda = \lambda(\sigma_k))$. To compute the new step $(\mathbf{d}_{k+1}, \lambda_{k+1}) = (\mathbf{d}(\sigma_k+\Delta\sigma_k), \lambda = \lambda(\sigma_k+\Delta\sigma_k))$ along (49), the numerical operations are conducted on an transformed set of equations that can be obtained by writing the new solution as: $\mathbf{d}_{k+1} = \mathbf{d}_k + \Delta\sigma_k\mathbf{n}_k + \mathbf{v}$; $\mathbf{n}_k^T\mathbf{v} = 0$; $\mathbf{n}_k^T\mathbf{n}_k = 1$. In most cases, the unit vector $\mathbf{n}_k$ is here a direction vector that is an approximation to the tangent to the path at $\mathbf{d}_k$, but other choices are also possible. The equations of equilibrium for this new step along (49) can be formulated using the augmented (potential) energy function:

$$P^* = P(\mathbf{d}_k + \Delta\sigma_k\mathbf{n}_k + \mathbf{v}; \lambda_{k+1}) - \kappa\mathbf{n}^T\mathbf{v} \quad (50)$$

Equilibrium is determined by the stationaryvalue of P^* with respect to $\Delta\sigma_k$, $\mathbf{v}$, κ, and this is enforced by:

$$\begin{aligned} \mathbf{n}^T\mathbf{f}(\mathbf{d}_1 + \Delta\sigma_k\mathbf{n} + \mathbf{v}; \lambda_{k+1}) &= 0 \\ \mathbf{f}(\mathbf{d}_1 + \Delta\sigma_k\mathbf{n} + \mathbf{v}; \lambda_{k+1}) - \mathbf{n}\kappa &= 0 \\ \mathbf{n}^T\mathbf{v} &= 0 \end{aligned} \quad (51)$$

This system is completely equivalent to (2) and it consists of (N+2) equations that govern (N+3) variables[&]. We can thus choose one of these variables as *independent variable* and it turns out to be of advantage to take $\Delta\sigma_k$ for this purpose. Writing $\mathbf{v} = \mathbf{d}_{k+1} - \mathbf{d}_k - \Delta\sigma_k\mathbf{n}_k$, and noting that the Lagrange multiplier $\kappa = 0$, equations (51) can be reduced to:

$$\begin{aligned} \mathbf{f}(\mathbf{d}_{k+1}; \lambda_{k+1}) &= 0 \\ \mathbf{n}_k^T(\mathbf{d}_{k+1} - \mathbf{d}_k) - \Delta\sigma_k &= 0 \end{aligned} \quad (52)$$

Consequently, the computational step from (k) to (k+1) is formulated by this set of equations, whereby $\Delta\sigma_k$ and the choice of $\mathbf{n}_k$ determines the distance between the two points along the path (49), see Figure 2.
The procedure thus operates on a system of equations:

$$\mathbf{F}(\mathbf{x}, \Delta\sigma) = 0; \mathbf{F} \in \mathbb{R}_N; \mathbf{x} \in \mathbb{R}_N \quad (53^a)$$

$$\mathbf{x} = \begin{Bmatrix} \mathbf{d}(\sigma) \\ \lambda(\sigma) \end{Bmatrix} \in \mathbb{R}_{N+1}; \mathbf{F} = \begin{Bmatrix} \mathbf{f}(\mathbf{d}; \lambda) \\ \mathbf{n}_k^T(\mathbf{d} - \mathbf{d}_k) - \Delta\sigma \end{Bmatrix} \quad (53^b)$$

where in this notation, the subscript k denotes the value of the solution of the previous step. In this way, equations (52) c.q. (53) present themselves as the operational form of the governing equations.

3.3 Solution of the equilibrium paths
A natural choice for the direction vector $\mathbf{n}$ is the tangent to the path at the previous step $\mathbf{x}_k$. It is defined by:

$$\frac{d}{d\sigma}\mathbf{F}(\mathbf{x}_k, \Delta\sigma) = 0 \rightarrow \mathbf{F}_{\mathbf{x}}(\mathbf{x}_k, 0)\mathbf{x}_k' - \mathbf{e}_{N+1} = 0 \quad (54)$$

But approximations to $\mathbf{x}_k'$ are also quite suitable. The stepping procedure now employs a predictor-corrector scheme that in its simplest form is based on the following three operational parts:

(i) Determine the step length $\Delta\sigma_{K+1}$ for the new step.

(ii) Determine the prediction for the new solution $\mathbf{x}_{k+1}$ on the basis of this choice.

(iii) Compute the new point $\mathbf{x}_{k+1}$, with a suitable corrector scheme

Once (iii) is successful, a new step can be undertaken.

We skip the discussion of (i), and briefly comment on (ii) and (iii). Very popular is the simple linear prediction:

$$\xi^0 = \mathbf{x}_k + \Delta\sigma\mathbf{n}_k. \quad (55)$$

ξ^0 Is thus a first approximation to $\mathbf{x}(\sigma_k+\Delta\sigma)$ and this starting value ξ^0 is then used in the corrector scheme (iii), the linear system of equations that are solved repeatedly:

$$\mathbf{A}^i\,\Delta\xi^i = -\mathbf{F}(\xi^i, \Delta\sigma) \; (i = 0, 1,...K) \quad (56)$$

$\mathbf{A}^i$ is here a suitable matrix operator which is usually derived in such a way that the method looks like Newton's method. In the case of Newton's method $\mathbf{A}^i$ is given by:

$$\mathbf{A}^i = \mathbf{F}_{\mathbf{d}}(\xi^i) \quad (57^a)$$

where $\mathbf{F}_{\mathbf{d}}(\xi^i)$ is the Jacobian of equations (52).
Another popular choice is:

$$\mathbf{A}^i = \mathbf{F}_{\mathbf{d}}(\xi^0) \quad (57^b)$$

[&] Please note the similarity of this formulation to equations (41)+(45[a]).

Details of this and other issues that concern the precise implementation of these choices can, for example, be found in [35-38] and [39]. A graphic representation of the way this procedure works is given in Figure 3.

The stepping procedure wich makes use of the scheme sketched above with the choice: $\mathbf{n}_k = \mathbf{x}'_k$ (or an approximation of $\mathbf{x}'_k$) is called (psuedo) arc-length continuation and it functions as a basic solution procedure in the computations that we describe here. But for stability analysis it is also necessary to have to ones disposal various additional computational devices, such as the control of the algorithm, the switch procedures for bifurcation analysis etc. etc. It would take too much space to describe them here. For these details we refer to the literature mentioned above.

3.4 Equations of motion

In the classical theory of elastic stability the loads are always applied in a quasi static fashion, i.e. the loads are considered to vary in time but only very slowly

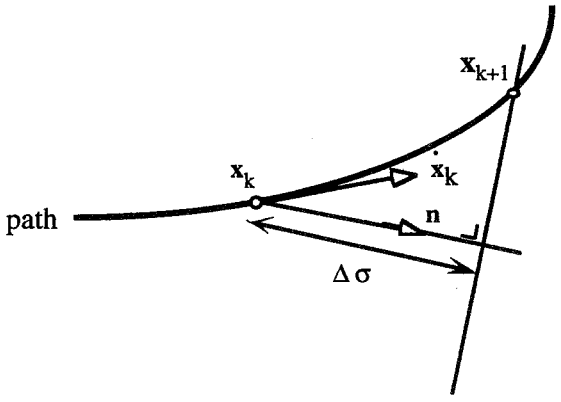

Figure 2 Principle path parameter

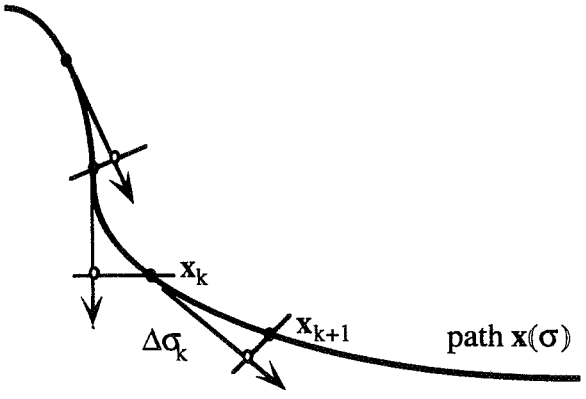

Figure 3 Continuation method

so that for the initial response, the fundamental state for example, inertia effects are neglected. Transient effects come into play only after the structure becomes unstable. But when stability is lost the structure is supposed to fail and this process is then no longer of interest from the practical point of view. Consequently, the classical stability analysis is carried out without resort to the analysis of the transient response of the structure.

In the philosophy of the present paper, this restriction to quasi static analysis is no longer necessary. We will therefore also consider the buckling process in terms of a transient response and this as a means to complete the analysis in a more satisfactory way. To introduce the transient aspect of the problem, we must also consider the solution of the equations of motion.

The equations of equilibrium were here derived from the principle of the stationary value of the potential energy function P. In the dynamic case, the equations of motion follow from the stationary value of the so called Lagrangian L:

$$L(\mathbf{d}, \dot{\mathbf{d}}, \lambda) = -T_2(\dot{\mathbf{d}}) + P(\mathbf{d}, \lambda) \qquad (58^a)$$

where P is the potential energy and T_2 is the kinetic energy of the system. The kinetic energy T_2 is here given by the quadratic form:

$$T_2 = \frac{1}{2}\dot{\mathbf{d}}^T\mathbf{M}\dot{\mathbf{d}} \qquad (58^b)$$

where $\dot{\mathbf{d}} = \frac{d\mathbf{d}}{dt}$ denotes the velocity of the generalized displacement $\mathbf{d}$ and $\mathbf{M}$ stands for the generalized mass matrix, which, in our case, will be considered to be symmetric and positive definite. Hamilton's principle states that the state of motion of the system is governed by the stationary value of the time integral of (58^a):

$$\delta \int_{t_1}^{t_2} L(\mathbf{d}, \dot{\mathbf{d}}, \lambda)\, d\tau = 0 \qquad (59)$$

where t_1 and t_2 denote the beginning and the end of the time interval during which the motion is studied. The variational process leads to the equations:

$$\mathbf{M}\ddot{\mathbf{d}} + \mathbf{f}(\mathbf{d}, \lambda) = 0 \qquad (60)$$

These equations hold for structural systems that are strictly conservative. However, for our applications it will be necessary to let the structural system dissipate energy during the snapping motions that we want to study. For this reason it is useful to introduce in the equations of motion the effect of some damping, by adding the term $\mathbf{C}\dot{\mathbf{d}}$, $\mathbf{C}$ being the damping matrix

(also considered to be symmetric here). Consequently, equations (60) are modified to:

$$\mathbf{M}\ddot{\mathbf{d}} + \mathbf{C}\dot{\mathbf{d}} + \mathbf{f}(\mathbf{d}, \lambda) = 0 \qquad (61)$$

With this modification, the structural systems that we consider here, are conservative if we restrict the behavior to the static domain. They are not longer conservative if the motion comes into play. This is the reason that we label this class of structures as *quasi conservative.*

3.5 Transient analysis

In this paper, the transient integration procedure used is a implicit multi-step method due to Park[40,41]. To sketch the idea behind Park's method we observe that the state of motion of the sytem under investigation can always be represented by the 2N dimensional vector:

$$\mathbf{z} = \mathbf{z}(t) = \begin{Bmatrix} \mathbf{d}(t) \\ \dot{\mathbf{d}}(t) \end{Bmatrix} \qquad (62)$$

With this formulation it is implied that we operate on the equations:

$$\mathbf{A}\dot{\mathbf{z}} + \mathbf{B}\mathbf{z} + \mathbf{F}(\mathbf{z}, \lambda) = 0 \qquad (63^a)$$

$$\mathbf{A} = \begin{bmatrix} \mathbf{C} & \mathbf{M} \\ \mathbf{M} & \mathbf{0} \end{bmatrix}; \mathbf{B} = \begin{bmatrix} \mathbf{0} & \mathbf{0} \\ \mathbf{0} & -\mathbf{M} \end{bmatrix}; \mathbf{F} = \begin{Bmatrix} \mathbf{f}(\mathbf{d}, \lambda) \\ \mathbf{0} \end{Bmatrix} \qquad (63^b)$$

The equations of motion in this form are of course completely equivalent to (61).

The transient response of the structure under load can thus be represented by a space curve symbolized by (62) in $\mathbb{R}^{2N+1}$. The task of the time integration procedure is to find this trajectory starting from some initial conditions $\mathbf{d}(t_1) = \mathbf{d}_0$, $\dot{\mathbf{d}}(t_1) = \dot{\mathbf{d}}_0$ for a load factor $\lambda(t)$ that is slowly varying. (The background to these initial conditions in our applications will be described later.) The trajectory is found by computing solutions to (63) in a step by step fashion using the time as path parameter.

Park's method can be seen as an averaging of two methods that are due to Gear [42,43,44] resulting in a modification that is in some respect superior to both of the original methods. We first introduce the basic ideas behind the Gear methods.

(i) *The second and third order methods of Gear*

Multi-step methods make use of previously determined solutions $\mathbf{z}_k$, $\mathbf{z}_{k-1}$, $\mathbf{z}_{k-2}$, $\mathbf{z}_{k-3}$ etc. in order to compute the new solution $\mathbf{z}_{k+1}$ ahead of $\mathbf{z}_k$.

To keep the discussion simple we assume here that the time step Δt between these configurations is kept constant. The evolution of $\mathbf{z}(t) = \mathbf{z}(t_k+\tau)$ can then be interpolated by a polynomial of the type:

$$\pi^{(n)}(t_k + \tau) = \mathbf{z}_k + \sum_{i=1}^{n} \mathbf{a}_i \tau^i \qquad (64)$$

where n depends on how many past solutions we want to take into account. These polynomials are determined by requiring:

$$\pi^{(n)}(t_k - i\Delta t) = \mathbf{z}_{k-i} \quad \text{for } i = 1,2,..,., n;$$
$$\pi^{(n)}(t_k + \Delta t) = \mathbf{z}_{k+1} \qquad (65)$$

In this way Gear developed a second order and third order method which are based on the polynomials:

$$\pi^{(2)}(t_k + \tau) = \mathbf{z}_k + \mathbf{a}_1\tau + \mathbf{a}_2\tau^2$$
$$\pi^{(3)}(t_k + \tau) = \mathbf{z}_k + \mathbf{b}_1\tau + \mathbf{b}_2\tau^2 + \mathbf{b}_3\tau^3 \qquad (66)$$

Enforcement of the compatibiliy equations (65) leads to expressions of the form:

$$\pi^{(2)}(t_k + \tau) = \mathbf{z}_k + \sum_{j=1}^{2} \Phi_j(\mathbf{z}_{k+1}, \mathbf{z}_k, \mathbf{z}_{k-1})\tau^j$$
$$\pi^{(3)}(t_k + \tau) = \mathbf{z}_k + \sum_{j=1}^{3} \Phi_j(\mathbf{z}_{k+1}, \mathbf{z}_k, \mathbf{z}_{k-1})\tau^j \qquad (67)$$

All the points $\mathbf{z}_i$ in these interpolations are known except the configuration $\mathbf{z}_{k+1}$ for the step $t_k \rightarrow t_k + \Delta t$. This configuration can now be determined by the requirement that the equations of motion should be satisfied at $t_k + \Delta t$, so that:

$$\dot{\mathbf{z}}_{k+1} = \dot{\pi}^{(n)}(t_k + \Delta t) = \sum_{j=1}^{n} j\Phi_j(\mathbf{z}_{k+1}, \mathbf{z}_k, \mathbf{z}_{k-1})\tau^{j-1} \qquad (68)$$

should satisfy (63). The explicit expressions of these equations and other details can be found in [41].

(ii) *Park's method*

Park's method relies on a linear combination of both predictors (67) and this results in an expression for the velocity $\dot{\mathbf{z}}_{k+1}$ that is given by:

$$\dot{\mathbf{z}}_{k+1} = [10\mathbf{z}_{k+1} - 15\mathbf{z}_k + 6\mathbf{z}_{k-1} - \mathbf{z}_{k-2}](6\Delta t)^{-1} \qquad (69)$$

Substitution in

$$\mathbf{A}\dot{\mathbf{z}}_{k+1} + \mathbf{B}\mathbf{z}_{k+1} + \mathbf{F}(\mathbf{z}_{k+1}, \lambda) = 0$$

leads to the set of equations (in $\mathbb{R}^{2N}$):

$$\mathbf{D}\mathbf{z}_{k+1} + \mathbf{r}(\mathbf{z}_k, \mathbf{z}_{k-1}, \mathbf{z}_{k-2}) + \mathbf{F}(\mathbf{z}_{k+1}, \lambda) = 0$$

$$\mathbf{D} = \frac{10}{6\Delta t}\mathbf{A} + \mathbf{B};\ \mathbf{r}(z_k, z_{k-1}, z_{k-2}) = -\frac{1}{6\Delta t}\mathbf{A}[15z_k - 6z_{k-1} + z_{k-2}] \tag{70}$$

The new value z_{k+1} is thus determined by this nonlinear set of equations and it can be solved by a suitable iteration method, Newton's method or the modified Newton's method for example.

The method looks very elaborate in view of the circumstance that it is developed in $\mathbb{R}_{2N}$, but it turns out that the nonlinear system (70) can be reduced to an N- dimensional set in terms of the unknown $\mathbf{d}_{k+1}$ from which all the other unknowns can be determined. In the STAGS code [45] which we will be using here, the method is equipped with a variable step size Δt_{k+1}. Park's method is just unconditionally stable[40-44] (in the numerical sense) and has, as a result of the use of past solutions in the construction of the next solution step, some measure of algorithmic damping, in particular in the high frequencies, as an inherent feature. The method shows a robust performance that is well suited to the type of problems that we are discussing here.

3.6 Global analysis

So far we only considered equations that depend on one parameter and this was the intensity λ of the load that is acting on the structure. In the practical situation, the behavior of a certain design must also be studied under variation of other parameters that represent among others, variable thicknesses, material constants, geometrical and material imperfections or also intensities of alternative load systems. This means that usually, for a specific design, many analyses must be carried out.

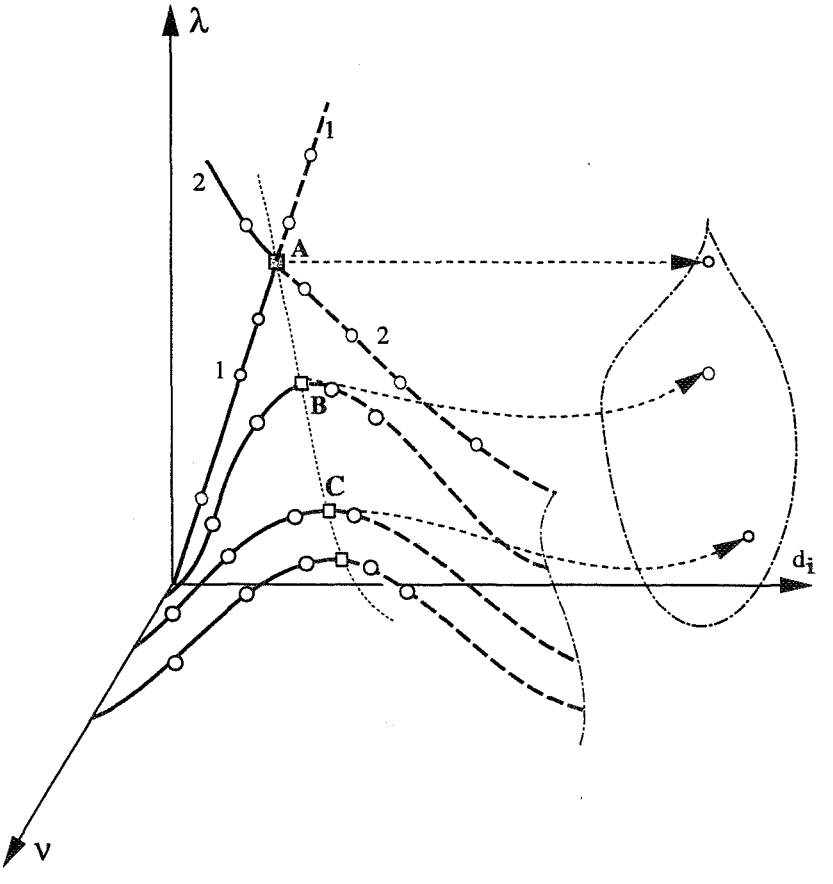

Figure 4 Global analysis

If the number of parameters Λ_i is M, the solutions to the equilibrium equations under variation of these parameters can be seen to span a M - dimensional surface in the space of the dependent and independent variables: $\mathbb{R}_{N+M}$. The evaluation of the behavior of the structure for a certain interval of these external parameters Λ_i corresponds to the determination of a patch of this equilibrium surface, the boundaries of which are determined by the range in which the parameters Λ_i are varied.
The simplest example of such an analysis that still brings out the multi-dimensional nature of this concept is pictured in Figure 4. The equilibrium surface is here a projection of a two dimensional surface in the space $\mathbb{R}_{N+2}$ to the space $\mathbb{R}_{1+2}$ of the solution to the set of equations:

$$\mathbf{f}(\mathbf{d}, \lambda, \nu) = 0; \mathbf{d} \in \mathbb{R}_N ; \lambda \in \mathbb{R}_1; \nu \in \mathbb{R}_1 \quad (71)$$

where **d** represents the deformation in then usual way, $\lambda \in \mathbb{R}_1$ is the load parameter and $\nu \in \mathbb{R}_1$, a design parameter or imperfection amplitude. To simplify the discussion, we will assume that ν is an imperfection parameter.

As the picture suggests, in this imaginary case, the solutions $[\mathbf{d}(\sigma), \lambda(\sigma)]$ exhibit for $\nu = 0$, a behavior that is governed by a bifurcation point (A) on a linear pre-buckling state, which is the intersection of the two solution branches 1, 2. For values of $\nu > 0$, this behavior erodes into what is called imperfect bifurcation. In the imperfect case, the solution branch of interest becomes unstable in a limit point; in (B) or (C) for example. The analysis of the load carrying capacity of the structure will in general be concerned with the determination of the paths that are defined by

$$[\mathbf{d}; \lambda] = [\mathbf{d}(\sigma_j, \nu_i)] \quad \sigma_j: 0 < \sigma_1 < \sigma_2 < .. ; \quad \nu_i: 0 < \nu_1 < \nu_2 < .. .$$

In the perfect case when $\nu = 0$, it is sufficient to compute the branch 1 up to and slightly beyond the bifurcation point A, and further to compute the branch 2 around A. This delivers information about the type of bifurcation. In the pictured situation, the bifurcation point is unstable and this feature tells us that the structure will collapse if it is loaded up to point A. It can also be deduced from the branches 1, 2 that the structure is imperfection sensitive. If ν represents the amplitude of the most dangerous imperfection for the structure, the sensitivity of the collapse load can be evaluated by computing the structural response for the case $\nu > 0$. If ν is not associated with this imperfection but is merely a design parameter, the collapse load of the structure may still be reduced when $\nu > 0$, but this may not be as drastic as in the case of imperfections that are chosen in the form of the buckling mode(s) that belong to the point (A).

The trace through the points (A), (B), (C), etc. represents a path of points at which the structure becomes unstable. This path gives information about the extent the collapse load of the structure is sensitive to variations in ν. It can be computed by tracing out the equilibrium paths that are defined by (71) when keeping ν fixed at $\nu = 0$, ν_1, ν_2, etc. and determining the limit points (B) , (C) etc.. It is also possible to compute this curve, the locus of limit points, directly by path following, starting from (A) using a special formulation that includes the critical condition that determines these special solutions [46,47].

In general, a structure that is loaded up to its stability limit will fail by undergoing a transient change of state. This transient process may lead to irreparable damage or even complete destruction but it may also lead to a state at which the structure is still serviceable so that more load can be applied. As it is not always possible to predict beforehand what the outcome of this process will be, the computational tools that are presently available allow us also to investigate the transient process [48,49]. This can be done with a suitable time integration method such as the one we described earlier. Examples of this possibility will be given in the sequel.

3.7 Local vs. global analysis

Iteration methods that are now the basic tools in the solution of the nonlinear governing equations thus enable us to obtain the solutions irrespective of the location of these solutions. The solutions have therefore a global character; i.e. they can be extended through the domain in which they are defined, and this without recourse to their accuracy. In contrast, the solutions based on the perturbation method (as discussed in chapter 3), are confined to a sub domain which is determined by the properties of the equations at the particular point in space at which the method is developed. For example, the computerized version of the analysis in Chapter 3 furnishes a means to compute an approximation of the surface shown in Figure 4 which is developed around the bifurcation point. This approximation becomes more and more accurate the closer we stay near this point but it becomes more and more inaccurate when we move away. Without further computation, it is not possible to assess the error; in other words the domain of validity is never known a-priory. For this reason we could call the perturbation method a local approximation method.

A method which also produces approximations in the sense described above is the linearized buckling analysis discussed in section 2.6. This method provides estimates for the location of the critical equilibrium states that lie ahead of the point at which the method is used.

Much has been said of perturbation methods in favor of continuation methods. The principal argument in favor is that perturbation methods are far less costly to use in terms of expenditure of computer resources, in particular, the computer time that is necessary to complete a certain well defined task in the analysis. Consequently, as the argument goes, perturbation methods are much more efficient. The question remains, however, whether this observation is really accurate, in particular, if also the cost of the analyst who is using these methods is taken into account. It is true that in general, continuation methods need more computation than perturbation methods but they also allow a much wider range of possibilities to be explored. For example, it remains to be seen whether the problem concerning the Engine Support of the Ariane V [50] or the External Fuel Tank of the Space Shuttle [51] could have been solved with these methods. The question of CPU time becomes simply irrelevant when the perturbation method fails to find the correct answer. A serious difficulty with the perturbation solutions is that the error of the approximation must always be assessed afterwards, while this is not an issue with the continuation method. Moreover, when the point at which the development must be carried out is nonlinear, recourse must be taken to a continuation procedure. We believe therefore that in view of the nature of the problems that arise in practice, the perturbation method is too restrictive in scope to be relied on as a single tool of analysis. The reduced volume of computations cannot really weigh against the advantages the flexibility of the continuation procedure offers, in particular, if the increasing power and diminishing costs of the computer are included in this evaluation. Nevertheless, the perturbation principle is of great importance in many instances because it can often be used as a first approximation or as an tool in the continuation process. Very useful in this respect is the buckling prediction mentioned above. Another example of such application is the predictor in the predictor-correction process.

4. Examples and Conclusion

4.1 Collapse behavior of a thin walled conical shell

To show the power of the procedures that we sketched in the previous chapter, we will now consider an example. This example concerns the simulation of an ultimate load test on a conical shell structure that functions as a support of a satellite during launch, see Figure 5. The dimensions of the shell† and its physical properties are given in the figure. The load case to be considered in the test is pure axial compression.

It is now observed that this loading can be introduced in two specific ways.

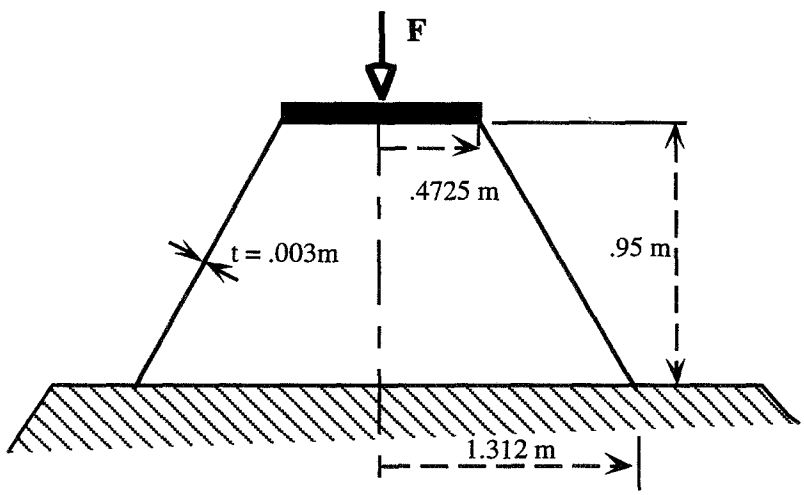

Data ring stiffener: I_y = 1.68E-7 m^4; I_z = 4.63E-8 m^4; A = 5.34E-4 m^2

Material: Youngs modulus, E = 7.E+10m^4 ; ν = 0.33

Base load Case A: $N_X = 3.33\ 10^3$ N/m; Case *B* : u = .605 10^{-3} m

Figure 5 The conical shell

The first, case *A*, is through a dead weight type of distributed load, which is applied along the generator at the top edge of the shell (this part of the shell is reinforced by a ring stiffener). The second case *B*, the loading is applied by means of a prescribed (uniform) displacement at the same edge of the shell. One realizes that these two options do not define the same problem and so that they will show a small difference

in the collapse load between, them but it is believed that the difference is so small that either option can be used for the certification of the shell. Another important difference that is expected to exist between the two options in load application concerns the behavior of the shell after collapse takes place. Dead weight loading implies an substantial surplus in potential energy that is available for conversion into kinetic energy of the shell during the collapse motion. In contrast, in the case of prescribed edge displacement, the potential energy that is available for conversion into kinetic energy cannot exceed the elastic energy which is stored just before collapse. This means that for practical reasons, the second option is to be preferred because this option promises to lead to much less damage of the shell after the test is completed. In the following we will calculate some of the responses of this test article in either situation and in this way verify to what extent these qualitative predictions ring true. To keep the analysis reasonably compact we will focus our attention mainly on the behavior of the perfect structure although we will also have a brief look at the influence of imperfections.

4.2 Branching diagram perfect shell

For convenience we will consider only half of the shell by taking a 180 degree segment into account. The base of the shell is considered to be fixed to the base of the testing facility (all displacements suppressed but not the rotations) while the ring stiffened edge at the top is unsupported. The analysis starts with an inspection of the location of the critical point in the perfect shell for the two loading cases:

A - line load applied to the top edge in the vertical direction. Nominal load is given in the Figure.

B- prescribed displacement in the vertical direction. Nominal load is given in the Figure.

The way this is done is by computing the basic state, which is an axisymmetric state of deformation, up to a certain value of the load that we expect to be close to the critical point $[\mathbf{d}_1(\lambda_k); \lambda_k]$ $\lambda_k < \lambda_c$ (k is the step number) and then conducting the eigenvalue analysis described at (23-25). Using the outcome of this calculation, the computation of the basic state can be continued with a few additional steps k+1, k+2 etc. so that we can approach the critical state very closely and repeat here the eigenvalue analysis. Incidentally, this is a procedure which is not automated in STAGS but which can be automated in a rather straight forward way[32,35,52]. The buckling modes that are computed at the point nearest to the critical state are stored to be used for the computation of the branch(es) of 1. Although the basic state is nonlinear and contains a limit point (not shown in the figure), the first critical state encountered is located well before the limit point so that we conclude that this point is a bifurcation point. We should thus be prepared to determine the branch(es) of this point.

The eigenvalue analysis, using the linearization (10) together with (21) at a point close to the bifurcation point, reveals that there at least three, -closely spaced- branches intersecting the basic equilibrium state $\mathbf{x}_1(\sigma)$. For the present analysis we are satisfied with computing only the first branch using the switch procedure [52,53] that is available in STAGS. The results of these computations are summarized in Figure 6. Figure 6[a] is the diagram for load case *A* and Figure 6[b] for load case *B*. Please note that the load factor in case *B* corresponds to the end-shortening of the shell and not the actual load that is acting on the edge.

It is clear that the bifurcation point $\mathbf{x}_c$ in either case is unstable, because the branches are descending. Moreover, the calculations reveal that branch 2 possess a bifurcation point at a very short distance from $\mathbf{x}_c$, followed by several others. This is an indication that the complete branching diagram in the neighborhood of $\mathbf{x}_c$ is rather intricate. Although we could attempt to compute this diagram, we will omit this here. In this paper, we are content with the knowledge that the clustering of bifurcation's is a sign that the shell will be very sensitive to imperfections.

Insight to the effect of the imperfection sensitivity on the buckling load can be gained, at least partially, by investigating how that branching diagram changes under the influence of geometrical imperfections. In STAGS, this can easily be done using some of the standard features of the code. We discuss this in the next section.

4.3 Imperfections

As a result of Koiters investigations, it is now well known[2,3,4] that initial geometrical imperfections have a strong detrimental effect on the buckling load of systems that are governed by an unstable bifurcation point. If the bifurcation point is simple and well separated from the other points further away along the basic state $\mathbf{x}_1(\sigma)$, the assessment of this influence is relatively easy. But in the present case, the behavior of the shell is dominated by three bifurcation points along $\mathbf{x}_1(\sigma)$ that are very closely spaced, indicating that there will be interaction between the buckling modes that are associated with these points. In this situation, the determination of a lower bound for the degradation of the load carrying capacity is more difficult. For a true compound bifurcation point, where many branches cross at $\mathbf{x}_c$, it is known that the branch of the steepest descent determines the most detrimental shape (again in an asymptotic sense, i.e., for a vanishing small amplitude of the imperfections)[4]. In the case studied here, the branches of $\mathbf{x}_1$ do not actually cross through one point, but we can compare it to a compound bifurcationpoint to some approximation.

† The structure and dimensions are based on a real design. Source: Fokker Space B.V., The Netherlands

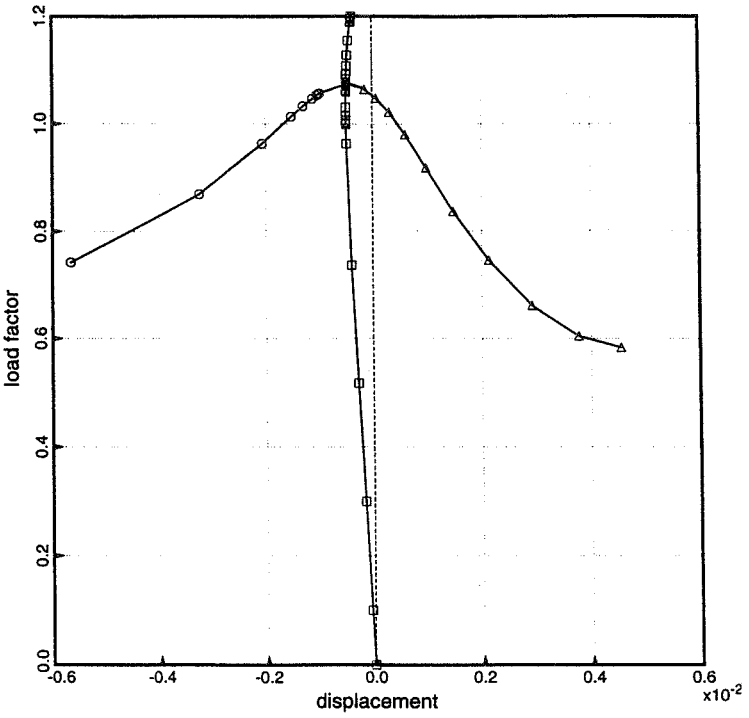

Figure 6[a] Branching diagram case *A*

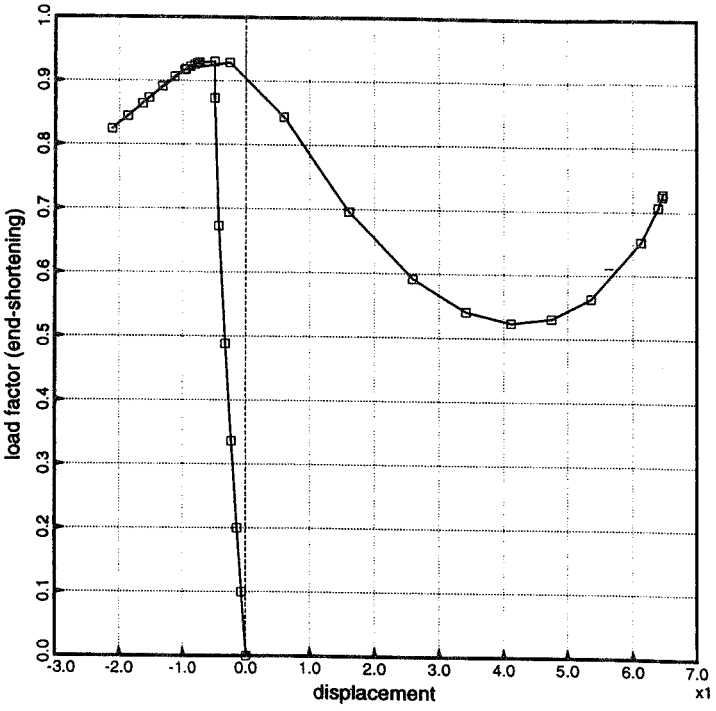

Figure 6[b] Branching diagram case *B*

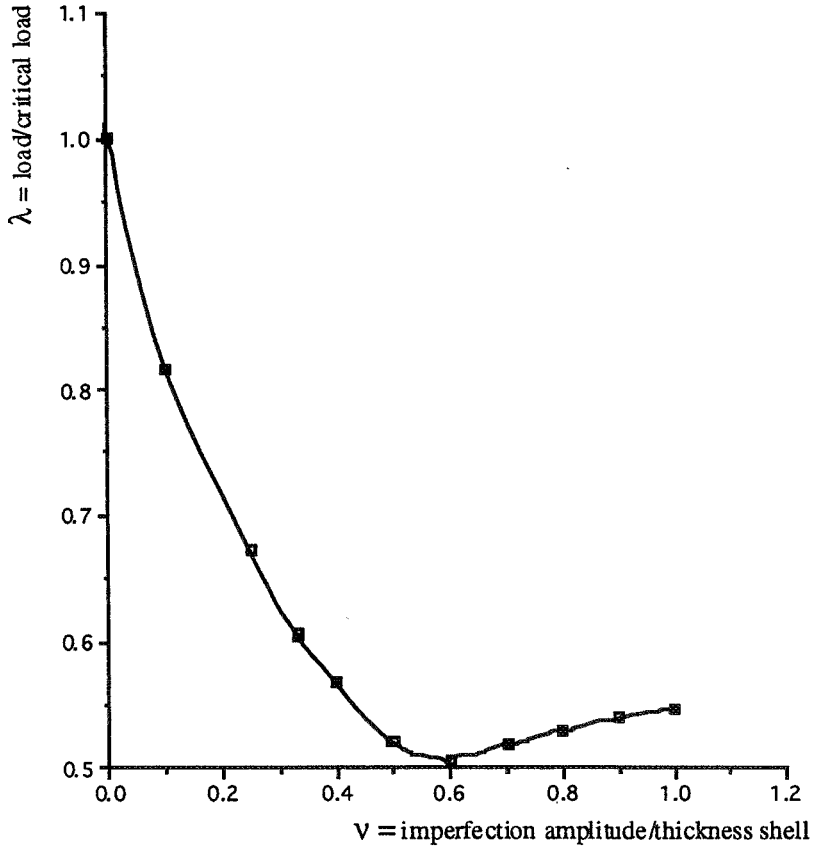

Figure 7 Load vs. Imperfection Amplitude

The steepest descent rule would then suggest that we should compute the branching behavior of the conus in more detail then is presented in figures 6^{a+b} so that we can get some idea which imperfections can be expected to be the most dangerous.

We decided not the follow this avenue because an analysis of this type is laborious and it therefore falls outside the scope of this paper. Here it will suffice to show how an imperfection sensitivity analysis can be carried out with the STAGS code. For this demonstration, we selected an initial imperfection which corresponds to the buckling mode associated with the first branch of $\mathbf{x}_1(\sigma)$. The analysis is restricted to case *A*. only.

With STAGS, the buckling modes calculated earlier can be used to perturb the original perfect geometry of the shell. To determine the collapse loads of these perturbed shells we used the standard path following method. This was done for several (increasing) values of the amplitude μ of the imperfection mode. The critical points in these cases $\mu = \mu_1 < \mu_2 < \ldots$ are limit points and, as expected, the corresponding limit loads are below the critical load of the perfect shell. The results of these calculations are summarized in Figure 7.

4.4 Collapse behavior perfect shells.
Transient analysis can be used to verify how violent collapse will take place once the shell has become unstable. We can inspect this behavior with the transient integration procedure that we sketched in chapter 3.

For the present discussion it suffices to restrict the analysis to the perfect shell in the two separate load cases that we considered before. The aim is to illustrate how the collapse mechanism differs between these two different loading cases.

We assume that the load is increased very slowly during the experiment. Because the equilibrium states of the structure are stable initially the response of the structure to this load is also characterized by gradual changes. This is what is called a quasi static behavior. However, as soon as stability of the equilibrium is lost, the transition of the deformation state of the structure that then takes place is not longer controled by the variation in the intensity of the load. The result is a very rapid change of deformation that takes place in such a short time span that the change in load during this process can be neglected.
Thus we imagine that the transient motion starts at an unstable equilibrium point just past the critical state $\mathbf{x}_C$ along $\mathbf{x}_1(\sigma)$ and that because of the extremely short duration of this process it can be percieved to have taken place under an load that is conatant. The precise indications of what initial conditions we should use to compute this motion are discussed in [48,49]. Here it suffices to mention that the unstable state $\mathbf{x}^* = \mathbf{x}_1(\sigma_C + \varepsilon)$ from which we start to compute the transient motion is first calculated with the path following method, using a relaxed convergence criterion so that the solution $\xi^* = \xi_1(\sigma_C + \varepsilon)$ for this state is deliberately somewhat out of equilibrium. The time integration of the motion ${}_t\mathbf{x} = \Psi(t)$ around or away from the equilibrium point $\mathbf{x}^*$ is now started with $\Psi(t=0) = \xi^*$, $\dot{\Psi}(t=0) = 0$ [f]. Because ξ^* is out of equilibrium, the motion will start and begin an oscillatory motion around $\mathbf{x}^*$. Because the apparent center of this motion, the equilibrium point $\mathbf{x}^*$ is unstable, the motion will eventually enter a state where the sum of the internal and external forces acting on the system pushes the system's configuration away from $\mathbf{x}^*$. The path the configuration $\Psi(t)$ is following thus leaves the neighborhood of the unstable equilibrium state $\mathbf{x}^*$ and eventually ends at some new stable equilibrium state, or, which is also quite possible, to a state of total destruction. The actual outcome depends simply on the problem at hand.

According to our calculations, in the case of dead weight loading, case *A*, exceeding the critical load λ_C results in the violent snapping motion that is pictured in Figure 8. In this case there is no doubt about the energy content of the motion. During the collapse process, the kinetic energy gain reaches about ten times the order of magnitude of the accumulated strain energy. On the other hand, in the case of prescribed end-shortening, case *B*, the snap that takes place is much milder, with a kinetic energy content of about one tenth of the accumulated strain energy. Also the change in deformation measured between state $\mathbf{x}^*$ and the end state $\mathbf{x}_E$ (which is a stable equilibrium state, step 1347) is considerably smaller. These results confirm the expectations about the collapse behavior of this shell expressed earlier: the case of dead weight loading is considerably more detrimental for the shell than the case of prescribed displacements when collapse occurs.

Remark
The transient analysis that we described in the foregoing is not really necessary for the assessment of the load carrying capacity of the cone problem. It was carried out here purely for the sake of demonstration. However, there are many practical problems, where the solution cannot be obtained without transient analysis. This is the case, for example, with so called mode jumping problems where structures suffer from a sequence of transient jumps in the deformation response when the load is slowly increased from zero,see [17,18, 5].

---

[f] A better way to start the calculations is to make use of the buckling modes associated with the bifurcation point $\mathbf{x}_c$, see [48,49]

4.5 Conclusion

The development of the computational methods for the analysis of the load carrying capacity of structural systems (which is determined by instability phenomena) can in our view be divided in three distinctive phases. The first phase took place in the period before WO II, and was primarily concerned with the formulation of the bifurcation buckling theory for systems that are linear or quasi linear. This phase established the general equations that determine the critical state of an elastic structure under load and the buckling modes that belong to this state.

In the second phase of the development, an initial post-buckling theory was established. With this important addition to the theory, the true nonlinear behavior of structural response in the neighborhood of buckling states could be analyzed as well as the effect that initial imperfections had on this behavior.

In the third phase of the development, the frontal solution (referred to as "brutal computerization" in [24]) of the nonlinear equations took a central place. This method has now become an addition and extension to the more traditional ways of computation. With this approach, the solutions that can be obtained are not restricted to a particular part of the solution domain, so that, together with that, it has turned into a very powerful tool for analysis for an amazingly wide range of structures that are encountered in practice.

step 64

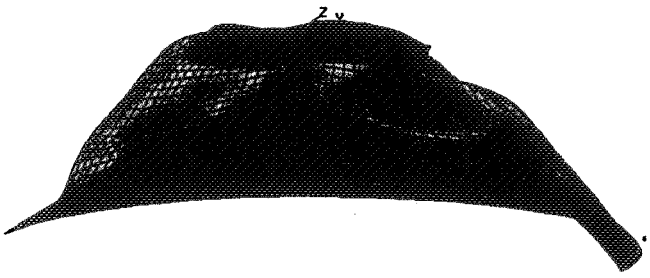

step 250

step 125

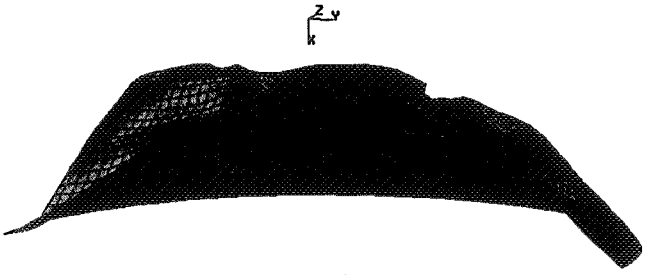

step 300

step 150

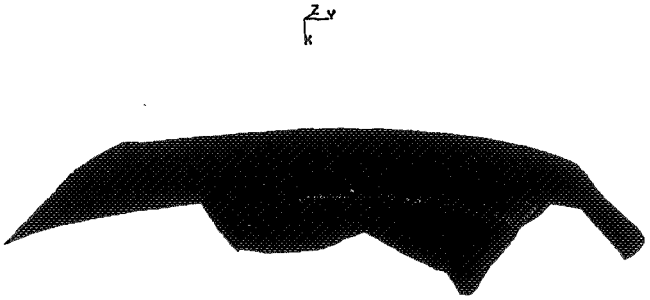

step 400

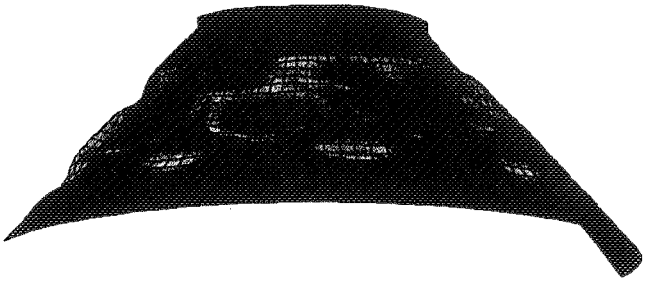

step 200

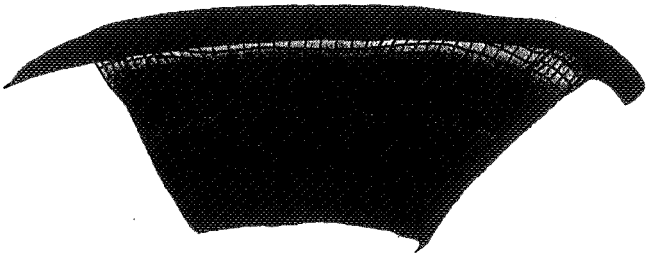

step 466

Figure 8. Collapse of the shell in case A

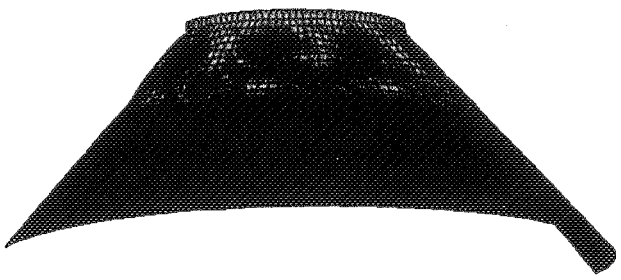

step 100

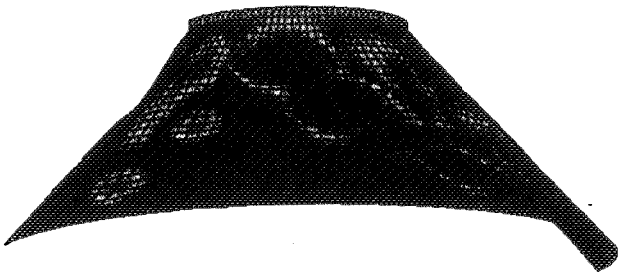

step 700

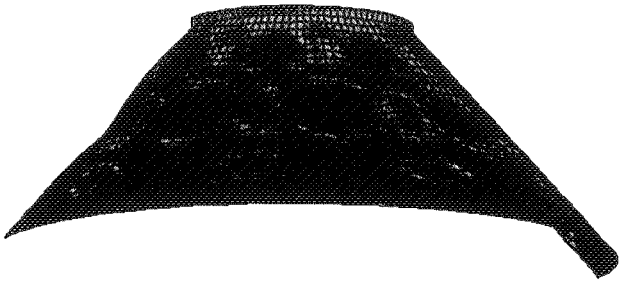

step 200

step 800

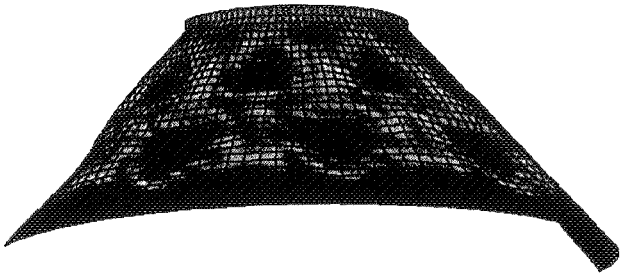

step 300

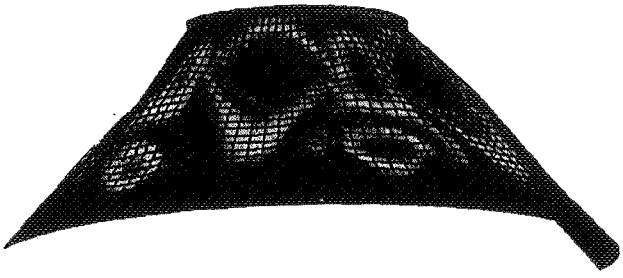

step 1000

step 500

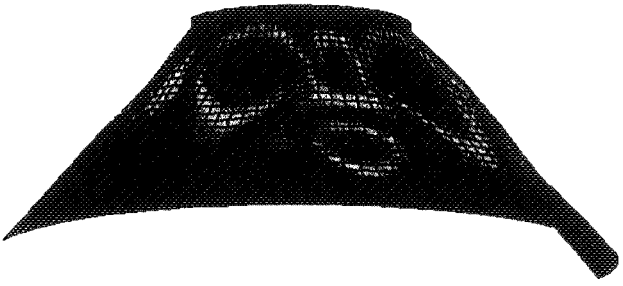

step 1347

Figure 9 Collapse of the shell in case B

[1] Hoff, N. J., The Perplexing behavior of Thin Circular Cylindical Shells in Axial Compression, The second Theodore von Kármán Memorial Lecture of the Israel Society of Aeronautical Sciences, Israel Journal of Technology, Vol. 4, no. 1, pp. 1-28, February 1966.

[2] Koiter, W.T. On the Stability of Elastic Equilibrium, H.J. Paris Publ., Amsterdam 1945, English translation: Report nr. AFFDL-TR-70-25, Air Force Flight Dynamics Lab., Wright Patterson AFB, OHIO,1970.

[3] Koiter W.T. "Elastic Stability and Post-Buckling Behavior, Proc. Symposium on Nonlinear Problems, (R.E. Langer Ed.), Univ. of Wisconsin Press, p. 257, 1963.

[4]. Budiansky, B., (1974). Theory of Buckling and Postbuckling of Elastic Structures, In: *Advances in Applied Mechanics* 14, C.S. Yih (Ed.), Academic Press, New York.

[5] Southwell R. V. (1913), On the general theory of Elastic stability, Phil. Trans. Roy. Soc. Lond., Ser. A, Vol. 213, p. 187.

[6] Biezeno C. B. and Hencky H., (1928), (1929), On the General Theory of Elastic Stability, Proc. Acad. Sci. Amst., Vol. 31 , p. 569; Vol. 32, p. 444

[7] Biot M. (1939), Théorie de l' Élasticité du Second Ordre avec Applications a la Théorie du Flambage, Ann. Soc. Scient. Bruxelles, t. LIX, série I , p 104.

[8] Biot M. (1939), Theory of elasticity with large displacements and rotations. Proc. 5. Int. Congr. Appl. Mech., Cambridge USA, p. 117.

[9] Biot M. (1939), Nonlinear theory of elasticity and the linearised case for a body under initial stress, Phil. Mag., ser. 7 Vol XXVII, p 468.

[10] Kappus R., Zur Elastiziteitstheorie endlicher Verschiebungen, Zeitrschr. für angew. Math. u. Mech., Bd. 19 (1939), p. 271 en 344.

[11] Trefftz E. (1930), Über die Ableitung der Stabilitätskriterien des elastischen Gleichgewichts aus der Elastizitatstheorie endlicher Deformationen. Proc. Int. Congr. Appl. Mech., Vol. III, Stockholm, p. 44.

[12] Trefftz E. (1933), Zur Theorie der Stabilitat des elastischen Gleichgewichts. Zeitschr. f. angew. Math. u Mech., Bd. 13, p. 160.

[13] Oñate E., Mathias W. T., Critical Displacement Approach for Predicting Structural Instability, CMAE, vol. 143, 1996, nos.,1-2, pp 135- 162.

[15] Trefftz E. and Marguerre K., Über die Tragfahigkeit eines langstbelasteten Plattenstreifens nach Überschreiten der Beullast, Zeitschr. f. angew. Math. u. Mech., Bd. 17 , p.85.

[16] Marguerre K.,(1937), Die mittragende Breite der gedruckten Platte, Luftfahrtforschung, Bd. 14 ,p. 121.

[17] Stein M., "Loads and Deformations of Buckled Rectangular Plates", NASA Technical Report R- 40, National Aeronautics and Space Administration, 1959.

[18] Stein M., "The Phenomenon of Change of Buckling Patterns in Elastic Structures", NASA Technical report R-39, National Aeronautics and Space Administration, 1959.

[19] Hoff N. J., (1967), Thin Shells in Aerospace Structures, 4th Von Karman Memorial Lecture, November 29, 1966, Printed in Astronautics and Aeronautics, February 1967.

[20] Golubitsky, M. and Schaeffer, D.(1985). Singularities and Groups in Bifurcation Theory, Volume I, Applied Mathematical Sciences, Springer Verlag, New York, Heidelberg, Tokyo.

[21] Sewell M. J. (1968), A general theory of Equilibrium Paths through Critical Points, I, II, Proc. Roy. Soc. A306, 201-223, 225-238.

[22] Thompson J.M.T., Hunt G.W., " A General Theory of Elastic Stability," John Wiley & Sons, Ltd., (1973).

[23] Hutchinson J. W. and Koiter W.T., Postbuckling Theory, Appl. Mech. Rev., 23, 1353-1366 (1970).

[24] Budiansky, B. and Hutchinson J. W., (1979). Buckling: Progress and Challenge, In: *Preprints of the Symposium "TRENDS IN SOLID MECHANICS 1997*, dedicated to the 65th birthday of W.T. Koiter, Delft University of Technology, June 13-15, 1979. Delft University Press, Delft, The Netherlands.

[25] Haftka R. T., Mallet R. H. Nachbar W., (1971) Adaptation of Koiter's Method to Finite Element Analysis of Snap through Buckling behavior, Int. J. Solids and Structures, Vol. 7, pp 1427-1447.

[26] Casciaro R. Aristodemo M., (1978) Perturbation Analysis of Geometrically Nonlinear Structures, Finite Elements in Nonlinear mechanics, eds. P.G. Bergan et al. TAPIR Publ. Trondheim, 1978 pp. 433-452.

[27] Carnoy E., (1980), Postbuckling Analysis of Elastics Structures by the Finite Element method, Computational Methods in Applied Mechanics and Engineering, Vol. 23, pp. 143-174.

[28] Casciaro R., Salerno G. and Lanzo A. D., (1992) Finite Element Asymptotic Analysis of Slender Elastic Structures: A Simple Approach, Int. J. Num. Meth. Eng. , Vol 35, 1397-1426.

[29] Azrar L., Cochelin B., Damil N. and Potier-Ferry M., (1993), An Asymptotic-Numerical Method to Compute the Post-Buckling Behaviour of Elastic Plates and Shells, Int. J. Numer. Methods Engng., Vol. 36, pp. 1251-1277.

[30] Lanzo A. D. and Garcea G. (1994), Koiter's Analysis of Thin Walled Structures by the Finite Element Approach", report N. 159, Dipartimento di Strutture, Universita' della Calbria, Italy.

[31] Bangemann T. R. (1975), Nonlinear Finite Element Treatment of Bifurcation in the Post-Buckling Analysis of Thin Elastic Plates and Shells, PhD Thesis, Department of Mathematics and Statistics, Brunel University.

[32] Riks E. (1973). The Incremental Solution of some Basic Problems in Elastic Stability, National Aerospace Laboratory, NLR, Report TR 74005 U.

[33] Rheinboldt W.C. (1977), Numerical Continuation Methods for Finite Element Applications, in: K.J. Bathe, J. T. Oden and W. Wunderlich eds. Formulations and Computational Algorithms in Finite Element Analysis (MIT Press, Cambridge, Mass. 1977) 599-631.

[34] Rheinboldt W.C. (1981), Numerical Analysis of Continuation Methods for Nonlinear Structural Problems, Computers & Structures Vol. 13, (103-113).

[35] Riks E. "Some Computational Aspects of the Stability Analysis of Nonlinear Structures", Comp. Meth. in Appl. Mech. in Engrg. Vol. 47 , 219-259, 1984.

[36] Riks E., "Progress in Collapse Analysis", Journal of Pressure Vessel Technology, Vol. 109/2 7 - 4 1, Febr.1987.

[37] Seydel R. (1989). From Equilibrium to Chaos, Practical Stability Analysis, Elsevier, New York-Amsterdam-London, ISBN 0-444-01250-8, .

[38] Riks E., Brogan F. A. and Rankin C.C. ,"Aspects of the Stability Analysis of Shells", International Conference of Computational Engineering Science, April 10 - 14, 1988, Atlanta. In : Static and Dynamic Stability of Shells, (W. B. Krätzig, E. Oñate eds.), Springer Series in Computational Mechanics, Springer -Verlag, Heidelberg, 1990.

[39] Crisfield M. A., (1997), Nonlinear Finite Element Analysis of Solids and Structures, Volume 2, John Wiley and Sons, Ltd, ISBN 0 471 95649 X.

[40] Park K. C.(1975).An improved stiffly stable method for direct integration of nonlinear structural dynamic equations, Journal of Applied Mechanics 42, 464-470.

[41] Park K. C.(1975). Evaluating Time Integration Methods for Nonlinear Dynamic Analysis, in: Finite Element Analysis for Transient Nonlinear Behavior, T. Belytschko, J. R. Osias and P. V. Marcal eds., Applied Mechanics Symposia Series (ASME New York).

[42] Gear, C. (1967), Numerical Integration of Stiff Ordinary Differential Equations, Report no. 221. Techn. Report., Department of Computer Science, University of Illinois.

[43] Belytschko T. and Hughes T. J. R. eds. (1983). Computational Methods for Transient Analysis, Volume 1, In the series of handbooks in Mechanics and Mathematical Methods, North Holland, ISBN 0444 864792.

[44] Argyris J., Mlejnek H. P. (1991). Dynamics of Structures, Texts on Computational Mechanics, Volume V, J. Argyris Editor, North Holland, Elseviers Publishers B.V., ISBN 0-444-89045-9.

[45] Rankin C.C. et al (1988). The STAGS User's Manual, NASA CONTRACTOR REPORT.

[46] Rheinboldt W.C. (1982), The Computation of Critical Boundaries on Equilibrium Manifolds, SIAM J. Numer. Anal. Vol. 19, no. 3.

[47] Eriksson A., (1994), Fold Lines for Sensitivity Analysis in Structural Stability, Comp. Meth. in Appl. Mech. in Engrg. Vol. 114, nos 1-2, pp. 55-77.

[48] Riks E., Rankin C.C. and Brogan F.A. (1996) "On the Solution of Modejump Phenomena in Thin Walled Shell Structures", Int. J. of Comp. Methods in Applied Mechanics and Engineering, Vol.136.

[49] Riks E., Rankin C.C., Computer Simulation of the Buckling Behavior of Thin Shells Under Quasi Static Loads., Computer Methods in Applied Mechanics, to appear.

[50] Vandepitte D., Riks E. (1992). Nonlinear Analysis of Ariane 5 Engine Frame, Report LR 678, Faculty of Aerospace Engineering, Delft University of Technology, Delft, The Netherlands.

[51] Nemeth M. P., Britt Vicky, Collin T. J. and Starnes J. H.(1996). Nonlinear Analysis of the Space Shuttle Super Light Weight External Fuel Tank. AIAA paper 96-1552-CP, 37thAIAA/ASME/ASCE/ AHS/ASC Structures, Structural Dynamics, and Materials Conference, April 15-17, Salt Lake City, UT, Collection of Technical Papers.

[52] Riks E. (1978), A Unified Method for the Computation of Critical Equilibrium States of Nonlinear Elastic Systems, Acta Technica Academia Scientarium Hungaricae, Tomus 87 (1-2), pp. 121-141, also as: NLR MP 77041 U, National Aerospace Lab., the Netherlands (1978).

[52] Thurston G.A.; Brogan F.A.; Stehlin P. (1985), Postbuckling Ana-lysis Using a General Purpose Code. AIAA Paper No. 85-0719-CP. Presented at the AIAA/ ASME/ AHS 26th Structures, Structural Dynamics, and Materials Conference, ORLANDO, FLORIDA, April 15-17.

[53] Rankin, C. C., and Brogan, F. A., Application of the Thurston Bifurcation Solution Strategy to Problems with Modal Interaction, AIAA Paper No. 88-2286 in Proceedings of the 29th Structures, Structural Dynamics, and Materials Conference Part 1 (1988), pp. 590--595.

[54] Bushnell D. Rankin C.C. and Riks E., (1997) Optimization of Stiffened panels in which Mode Jumping is Accounted for, This Proceedings, paper 97-1141.

PERSPECTIVE ON FINITE ELEMENTS FOR SHELL ANALYSIS

Dr. Richard H. MacNeal*

The MacNeal-Schwendler Corporation
Los Angeles, CA 90041

Abstract

The elastic stability analysis of complex structural models typically relies on finite element methods. The paper reviews the history of the development of finite elements for shell analysis from the earliest flat plate elements to current efforts, with emphasis on the gradual improvement of accuracy and robustness. The paper concludes with a discussion of design issues for higher order p elements.

Introduction

Finite elements are important tools for the analysis of structural stability, particularly as analysis models become larger and more detailed, approaching the complexity of actual structures. Thus it is that issues relating to finite elements—accuracy, robustness, performance, ease of use—take on significance for those who would analyze the elastic stability of structures. Also, since elastic stability primarily concerns itself with thin structures with plate-line and shell-like behavior, the issues of most concern are those relating to the corresponding plate and shell finite elements.

The analysis of structural stability contains a linear part and a nonlinear part. The nonlinear part can be as simple as a first-order geometric stiffness term employed in the calculation of buckling modes or as complicated as a large strain formulation of the basic equations. Here we will concern ourselves exclusively with the linear part. Paradoxically, experience has shown that the linear part is harder to get right and that it is responsible for the basic ills of finite elements—rigid body failure, patch test failure, spurious modes, and, above all, locking.

In this paper we will review the history of the development of (linear) plate and shell finite elements with emphasis on the gradual improvement of their accuracy and robustness. While the first plate bending element was introduced in 1961,[1] elements which are adequate for general shell analysis only became available in the 1970s. Table 1 outlines the chronology of plate and shell element development. Needless to say, research on the design of plate and shell elements continues to this day.

A simple shell problem which has become a standard for benchmarking shell elements is the Scordelis-Lo roof,[2] shown in Figure 1. Results for this example, with pre-1970 and post-1970 elements, are plotted in Figure 2. The improvements with time are evident and indicate a growing understanding of accuracy issues. For example, a comparison of the Ahmad shell element with and without reduced integration indicates that an issue of profound importance is operative here.

Kirchhoff Elements, 1961–1970

Coordinate directions and displacement definitions for a flat plate are shown in Figure 3. Finite elements for plates and shells employ the fundamental assumptions of first order plate theory which are that inplane displacements

$$u = u^m(x,y) - z\alpha(x,y) \qquad (1)$$

$$v = v^m(x,y) - z\beta(x,y) \qquad (2)$$

and the normal stress

$$\sigma_z = 0 \qquad (3)$$

The membrane part of displacement (u^m, v^m) is separable, for flat plates, from the bending part, (w, α, β). Finite elements to represent the membrane part have been available since 1956.[3] Credit for the earliest plate bending element goes

*Fellow

to Adini and Clough who published in 1961.[1] Theirs was a rectangular element with four corner nodes and three degrees of freedom (w, α, β) per node. It employed the Kirchhoff hypothesis, namely that the transverse shear strains

$$\gamma_{xz} = w_{,x} - \alpha$$
$$\gamma_{yz} = w_{,y} - \beta \qquad (4)$$

are null.

Long before the invention of finite elements, analysts used the Kirchhoff hypothesis to reduce the plate bending equations to a single fourth order partial differential equation in the lateral displacement, w. The virtue of the Kirchhoff hypothesis for the design of plate elements is that the designer needs only to specify w as a function of position since α and β can be computed by Equation 4.

In their element, Adini and Clough specified w as a twelve-term polynomial which allowed independent cubic variation of w on each edge. Specifically,

$$w = \left(1, y\right)\left(1, x, x^2, x^3\right) + \left(1, x\right)\left(1, y, y^2, y^3\right) \qquad (5)$$

where all distinct product terms have independent coefficients. The twelve independent coefficients were then specified in terms of the twelve corner displacements. The remaining work to make a finite element was to compute a stiffness matrix from the functional form of the strain energy implied by the assumed variation of w. See Reference 4, for example.

Early finite element designers also tried to develop a corresponding three-node triangle with nine degrees of freedom. They were confronted by the fact that a complete cubic has *ten* terms

$$1, x, y, x^2, xy, y^2, x^3, x^2y, xy^2, y^3 \qquad (6)$$

so that they had to eliminate one term. Unfortunately they could find no combination of terms which retained constant bending (the quadratic terms) and retained isotropy with respect to the element's geometry.

Developers of Kirchhoff elements also soon discovered that a completely satisfactory solution could not be achieved for *any* element with three degrees of freedom per node. Specifically, Irons and Draper,[5] 1965, discovered that an expression for w which assures uniqueness of the bending curvatures ($\chi_{xx}, \chi_{yy}, \chi_{xy}$) over the surface cannot assure slope continuity (continuity of $w_{,x}$ and $w_{,y}$) along the common edges of adjacent elements when only $w, w_{,x}, w_{,y}$ are prescribed at nodes.† Continuity of slope is important because without it a field of elements cannot correctly represent a state of constant bending curvature.

At this point three alternative courses presented themselves to the designers of Kirchhoff plate elements. They were:

1. Accept the *non-uniqueness* of curvature within an element in order to assure slope continuity.
2. Accept *discontinuity* of slope in order to assure uniqueness of curvature.
3. Add higher order derivatives of w, such as $w_{,xy}$, as nodal degrees of freedom.

All three courses of action have been used by element designers. It is clear from its description that the Adini-Clough rectangle uses the second alternative. The Clough-Tocher triangle,[6] 1965, which appeared in NASTRAN as the TRIA2 element, uses the first alternative. It consists of three subtriangles (see Figure 4) with nine displacement terms each, and enough constraints to eliminate the degrees of freedom at the common center node and to ensure internal slope continuity. The Fraeijs de Veubeke quadrilateral,[7] 1968, which Irons called the prettiest such element, also uses the first alternative. It has four subtriangles and preserves slope continuity.

The most interesting option is to add the second derivatives of w as nodal degrees of freedom so as to assure slope continuity and uniqueness of bending curvature. A three-node bending triangle constructed according to this option will have six degrees of freedom ($w, w_{,x}, w_{,y}, w_{,xx}, w_{,xy}, w_{,yy}$) per node for a total of eighteen. Since a complete quintic in x and y has twenty-one terms, we can design an element by deleting three terms from the complete quintic for w or by adding three degrees of freedom (such as normal slope at the midpoints of edges) to the element. 1968 and 1969 saw the publication of *seven* independent papers which described either the first approach,[8,9] or the second,[10,11,12] or both.[13,14]

Theoretically the element just described has a tremendous degree of accuracy but today it is

†An elementary proof will be found in Reference 4, pp 381-2.

mainly a curiosity. The reason for its lack of acceptance is the use of the second derivatives of w as nodal variables. Since they physically correspond to curvatures, how are they to be loaded and how are boundary conditions to be applied to them? They also prevent discontinuities in bending curvature at element corners such as would result from applied moments or changes in material properties.

Elements, such as those just described, which apply the Kirchhoff hypothesis à priori in the selection of a displacement field have long since passed from favor. In *discrete* Kirchhoff elements, separate fields are assumed for α and β and the Kirchhoff constraints ($\alpha = w_{,x}$, $\beta = w_{,y}$) are applied at discrete points to eliminate nodal variables. Early successful elements of this type include both triangles[15] and quadrilaterals[16] with minimum node counts and, most prominently, Irons' semiloof element,[17] 1976.

Lower Order Mindlin Elements, 1969–1990

While the designers of Kirchhoff elements were attempting to cope with fundamental limitations, progress was about to come from a different direction—which today we would call a paradigm shift—namely, extension of the isoparametric mapping concept to shell elements. Introduced with the Taig quadrilateral membrane element[18] in 1961, isoparametric mapping maps the interior of an irregular element into a standard shape (e.g., a curved quadrilateral into a square) and automatically preserves interelement displacement continuity in the process.‡ In 1966 Irons[19] extended the concept generally to elements of all dimensions and any number of edge nodes.

An important three-dimensional element made possible by Irons' work is the twenty-node solid brick which has nodes at the eight corners and at the midpoints of the twelve edges. In 1969 Ahmad[20] published a "degenerate" eight-node isoparametric shell element which was derived from the twenty-node brick by the procedure illustrated in Figure 5. The essential step, which corresponds precisely to the assumptions of plate/shell theory, is to replace the six translational degrees of freedom at corresponding points on the top and bottom surfaces of the solid by three translations (u, v, w) and two rotations (α, β) at their midpoint. Each of these five new displacement components is then interpolated from nodes to internal points by the same shape functions, expressed as functions of ξ, η, the parametric coordinates of points on the midsurface. Membrane strains, transverse shear strains, and bending curvatures are then computed from the displacement shapes in a manner entirely analogous to that used in the earlier plate elements but rendered more complicated by the curvature. Transverse shear strains are not set to zero as in the Kirchhoff elements which occasioned the application of a new name—Mindlin or Reissner–Mindlin—to the theoretical basis of the new element.

The new Ahmad element represented a giant step backward with respect to the representation of transverse displacement. Since α and β are now independent of w, the spatial representation of w in the eight-node element contains only eight terms rather than twenty-four. Nevertheless, Ahmad's element has the very important advantage that it is not subject to the fundamental limitations of the Kirchhoff elements and the less important advantages that it can include transverse shear deformation and that it fits neatly within the isoparametric formalism.

The new element also has problems of its own which soon revealed themselves. Referring to Figure 1, we note that the Ahmad shell element produces results which are not much better than those for the lower order Clough–Tocher triangle described earlier. Figure 1 also shows a dramatic improvement in results when "reduced order integration" is added to the Ahmad shell element. This result for the Ahmad element was published by Zienkiewicz, Too, and Taylor in 1971[21] without a fundamental explanation, but it proved to be fundamentally important for the future development of plate and shell elements.

One would not expect that changing the integration points for the Ahmad element from a 3 x 3 mesh of Gauss points to a 2 x 2 mesh would make all that difference. The explanation of the efficacy of reduced integration for the Ahmad curved shell element is not easy—it had to wait until 1982[22,23]—but reduced integration had already been understood and applied in 1969[24] to improve the accuracy of the isoparametric membrane quadrilateral. At bottom, the difficulty is that the element's shape or basis functions are unable to correctly interpolate higher order displacements states from nodal values. For example, the basis functions of the four node isoparametric quadrilateral, which are $(1, \xi, \eta, \xi\eta)$, are unable to represent a pure inplane bending state, $u = xy$, $v = -x^2/2$, even for a rectangular

‡In *isoparametric* mapping, the *same* basis functions are used to interpolate positions and displacements from nodal values.

element where $x = ac$, $y = b\eta$. In fact, for this case v is represented by its *alias*, $v = -a^2/2$, which has the correct value at nodes but not elsewhere. The only point at which the inplane shear strain, $\gamma_{xy} = u_{,y} + v_{,x}$, is correct is at the center, $\xi = \eta = 0$. This point happens to be the reduced order Gauss integration point for the four node quadrilateral. The other two strain components, ε_x and ε_y, are measured at the 2 x 2 Gauss points, giving rise to the term *selective* reduced-order integration.

If all three strain components in the last example are measured at the 2 x 2 Gauss points, the measured shear strains will be incorrect (they should be zero in the example). If the aspect ratio of the element is large, $a >> b$, the effect will be to greatly increase the strain energy, giving rise thereby to *shear locking*, a term which characterizes the greatly reduced displacements that will result.

Shear locking also appeared when shell element developers tried to apply the isoparametric formulation pioneered by Ahmad to three-node and four-node plate bending elements. Locking occurs because the lowest order bending state, $w = x^2$, is not representable by the basis set of the three-node element 1, x, y or by the basis set of the four-node element $1, \xi, \eta, \xi\eta$. The first paper which proposed a remedy, 1977,[25] for the quadrilateral case, used a single integration point for transverse shear strain. This unfortunately gave rise to *spurious strain-free modes* because the number of independent strain evaluations was insufficient to restrain these modes.

It was also soon discovered that the only places where the transverse shear strains are correctly computed for three-node and four-node elements when $w = x^2$ are at the midpoints of the edges. This discovery led to a new wrinkle in finite element theory—the direct assumed strain method—whereby transverse shear strains were computed at the midpoints of edges and interpolated to integration points. Between 1976 and 1982, Hughes[26,27] and MacNeal[22,28] independently published three- and four-node elements based on the direct assumed strain method. These elements have become the workhorses of finite element plate and shell analysis. Figure 1 shows that these elements, TRIA3 and QUAD4, have respectable accuracy.

The original Ahmad eight-node shell element avoids transverse shear locking in its most virulent form because its basis set can model quadratic terms. It suffers, however, from another form of locking known as *membrane locking* [23] because, when an element is curved, pure bending involves inplane displacements, measured in a Cartesian coordinate system, which are *cubic* functions of position. The remedy, reduced integration, works because the values of the membrane strains are correct at 2 x 2 Gauss integration points.

Attempts to apply reduced integration to the nine-node shell element fail because the additional five degrees of freedom at the center produce spurious modes. The period 1985–1990 saw the development of several approaches toward the elimination of locking and spurious modes for the nine-node element. While the nine-node shell element has some minor advantages over the eight-node element,[29] the chief motivation was probably just the challenge of a difficult task. One successful approach was extension of the direct assumed strain method from four to nine nodes, Park,[30] 1986. Another was the development of the *assumed strain hybrid method* in which a strain field with carefully selected low order terms is assumed in addition to a displacement field. The two fields are correlated using mixed variational principles[31,32] or constrained variational principles.[33,34] In another approach, *mode stabilization*,[35,36] high and low terms in the displacement field are separated and the low order terms are treated exactly while the high order terms are treated approximately. In its crudest form, mode stabilization gives just enough stiffness to the high order terms to avoid the appearance of spurious modes. Mode stabilization is a preferred method for nonlinear analysis because the restriction of accurate integration to the low order terms reduces computer time.

Higher Order Elements, 1988–

The extension of conventional element technology beyond bi-quadratic displacement shapes has been rare. Rhiu, Russell, and Lee,[37,38] 1989, 1990, have developed third-order degenerated shell elements with sixteen nodes which feature an assumed strain field to eliminate locking. The accuracy of these elements appears to be excellent.

A more important recent development has been the extension of p technology to shell elements. With the p method,[39] element displacements are designed to have a variable polynomial degree, p, which is selected at execution time. Conventional nodes with displacement degrees of freedom are placed at element corners. All higher degrees of freedom for $p \geq 2$ are defined as non-nodal

hierarchical variables along edges and in the element's interior. The designation *hierarchical* refers to the fact that such degrees of freedom can be added progressively without changing existing parts of the stiffness matrix.

The chief virtue of p elements is that they allow easy implementation of adaptive mesh refinement by increasing the polynomial degree of elements rather than by increasing the number of elements. It then becomes possible for the user to specify a desired level of accuracy and to let the computer program set the p level for the whole mesh or selectively for individual elements.

In perhaps the earliest paper on the application of p elements to shell analysis, Szabó and Sahrmann,[40] 1988, employed solid elements with $p = 1$ in the thickness direction and prescribed a zero value for Poisson's ratio to avoid locking. Their analysis of the Scordelis-Lo roof (Figure 1), demonstrated that reasonable convergence of displacements is achieved for a single element model with $p = 6$ in the direction of the midsurface.

The appearance of shell p elements in the technical literature has been slow. Leino, Pitkäranta, and Hakula at the Helsinki University of Technology have published reports[41,42] which show, among other things, that reduced integration produces significantly higher accuracy out to $p = 4$. Shell p elements are known to exist in two commercial finite element programs, Mechanica and MSC/NASTRAN. The development of practical shell p elements is labor intensive, which perhaps explains the slowness of their appearance in the open technical literature.

It may be worthwhile to comment on some of the features of the shell p elements in MSC/NASTRAN. There it is recognized that uniform accuracy does not require that all elements have the same p level, so that p is allowed to be different in every element and different in the ξ and η directions of a quadrilateral element. Along any common edge, however, the p values must be the same in adjacent elements to preserve displacement continuity.

The formulation of stiffness in p elements has generally followed the standard isoparametric formalism[¶] without special treatment to avoid locking. It has, in effect, been argued that locking is only a problem for $p = 1$ and $p = 2$ and that these low levels are unimportant and can be discarded. In MSC/NASTRAN we have taken the opposing view that $p = 1$ and $p = 2$ are important because many examples exist where accuracy requirements can be easily satisfied with low order elements over large regions of the structure. We have, accordingly, included variations of the antilocking devices described earlier for $p = 1$ and $p = 2$. This becomes complicated when one realizes that p may be different on all four edges of an element. We also employ reduced integration for $p \geq 2$.

One of the standard test problems for MSC/NASTRAN elements is the square plate with a clamped boundary condition shown in Figure 6. The standard thickness-to-length ratio for this surprisingly difficult test problem is $t / a = .0001$, chosen so small to emphasize any tendency toward transverse shear locking. Table 2 records the lateral deflection at the center for N, $p = 1, 2, 3, 4$, normalized to the correct solution. The results are quite poor, indicating a strong presence of locking even though several antilocking devices are used.

The results improve dramatically, as shown in Table 3, when the thickness-to-length ratio is increased. This is remarkable because, even at $t / a = .01$, the ratio of transverse shear flexibility to bending flexibility is exceedingly small. These results can be explained by noting that the Kirchhoff condition is effectively imposed at integration points by the small thickness, thereby imposing substantial distortion on higher modes which, because of aliasing, cannot satisfy the Kirchhoff condition. Relaxation of the Kirchhoff constraint, even to a slight degree, significantly relaxes distortion of the displacement shape.

Another conclusion which can be drawn from this example is that a minimum amount of transverse shear flexibility should be included in the elements, even for higher p values, to combat transverse shear locking. The older MSC/NASTRAN shell elements have, for a long time, included a minimum amount of transverse shear flexibility, called the residual bending flexibility,[43] which was originally introduced to reduce discretization error. The example shows, however, that residual bending flexibility is, and always has been, more valuable as an antilocking device.

Concluding Remarks

The long history of gradual improvements in the design of finite shell elements has been reviewed. Two major events have been noted: the change

[¶]Actually *sub*parametric in MSC/NASTRAN because only cubic edge geometry is allowed for $p \geq 3$.

Two major events have been noted: the change from Kirchhoff elements to Mindlin elements occurring about 1970, and the introduction of p technology which is ongoing. The first event was occasioned by the discovery of fundamental limitations in Kirchhoff elements. The second is occurring in response to the need to make structural analysis accessible to a wider user community through automation.

Along the way, progress has occurred by the process of detecting failure modes, discovering the reasons for failure, and devising fixes. Users of finite elements should be at least marginally aware of the failure modes in order to avoid disappointment.

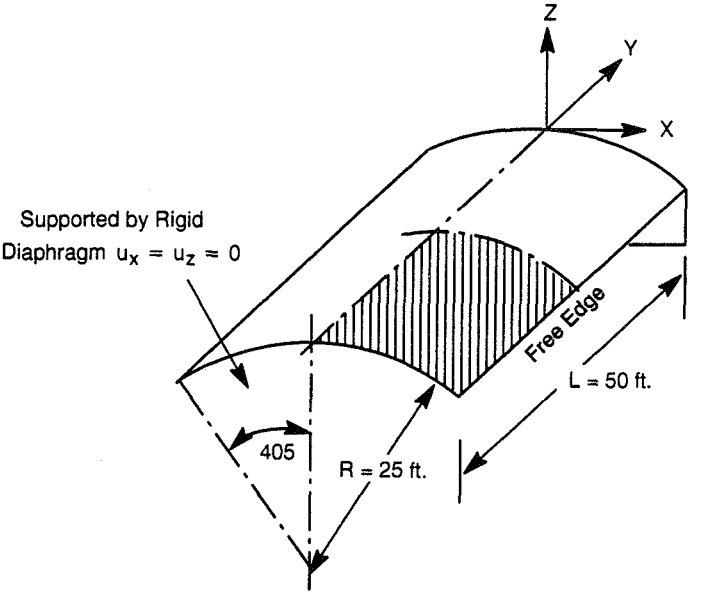

Figure 1. Shell Roof Under Gravity Load (the Scordelis-Lo Roof). Poisson's Ratio = 0. t = 3 in.

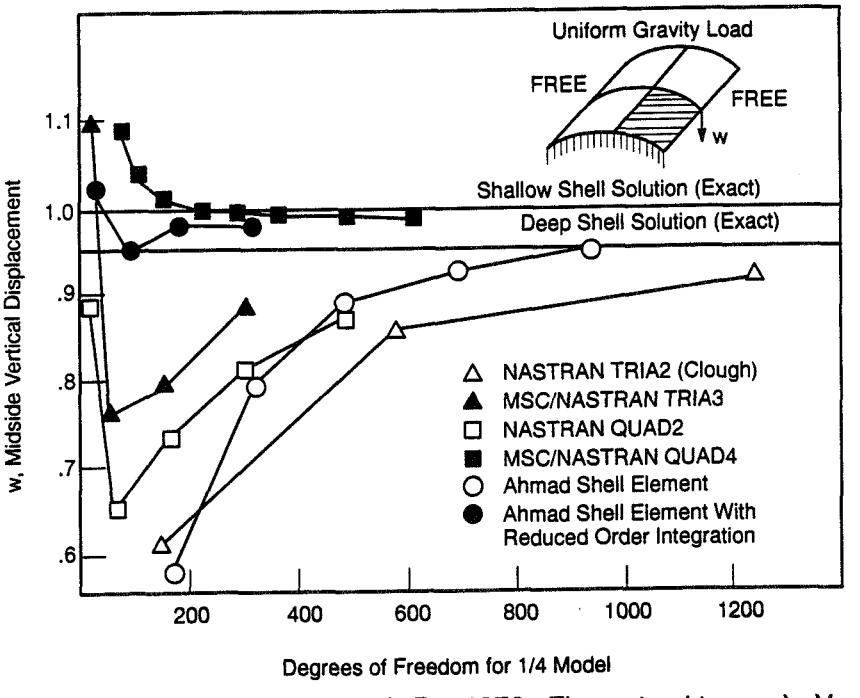

Figure 2. Scordelis-Lo Roof: Performance of Pre-1970 Elements (△, □, ○) Versus Post-1970 Elements(▲, ■, ●)

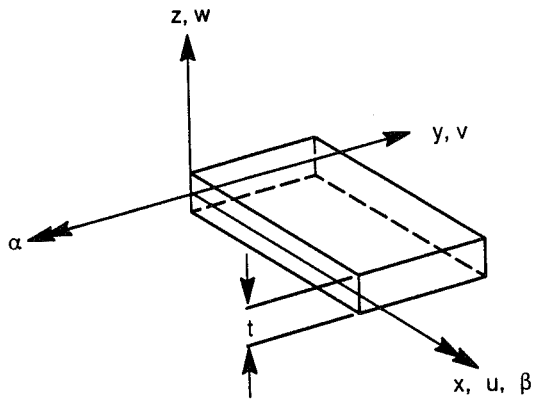

Figure 3. Coordinate Definitions for a Plate

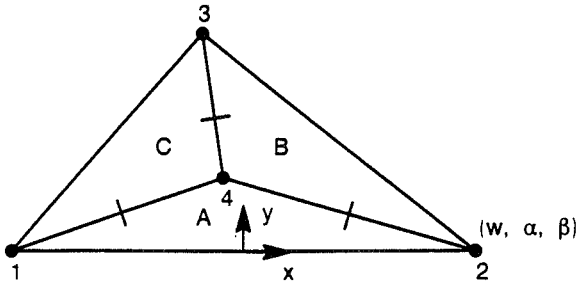

Figure 4. The Clough-Tocher Triangle

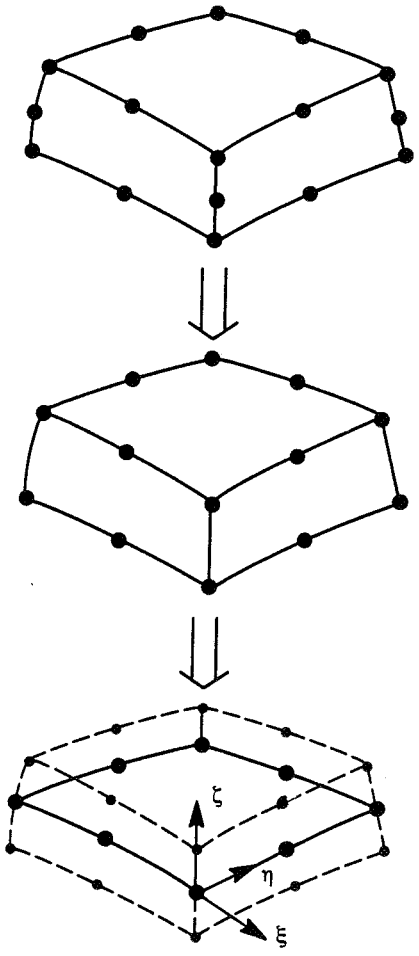

Figure 5. Degeneration of a Twenty-Node Brick Element into an Eight-Node Shell Element

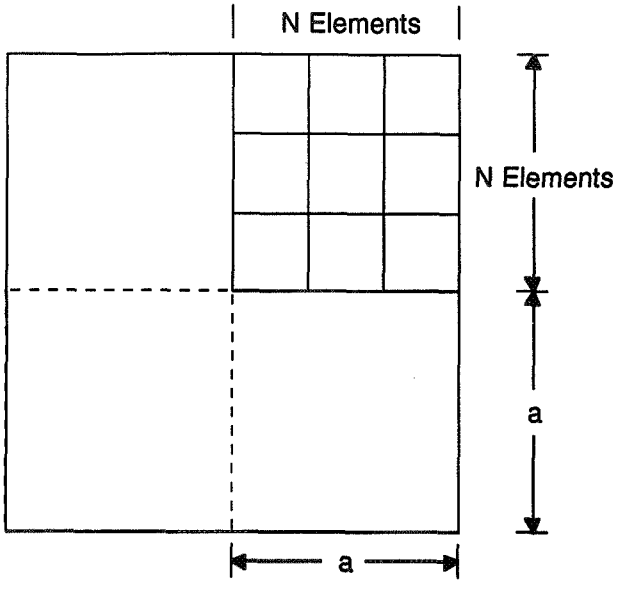

Figure 6. Clamped Square Plate
(Point Load at Center)

Table 1

Chronology of Plate and Shell Element Development

Element Development	Date
First membrane element	1956
First plate bending element	1961
Kirchhoff plate elements	1961–1970
Discrete Kirchhoff plate and shell elements	1969–
First Mindlin shell element (eight-node quadrilateral)	1969
Reduced integration	1971
Four-node quadrilateral, three-node triangle	1976–1982
Nine-node quadrilateral	1985–1990
Higher order shell elements	1988–

Table 2

Lateral Deflection at Center of a Clamped Square Plate with a Point Load at Center

N \ p	1	2	3	4
1	.00000	1.11607	.00001	.38940
2	.00001	.38308	.71086	.98198
3	.00005	.19744	.85764	.99394
4	.00029	.12684	.91864	.99767

N x N field of elements on quadrant. t/a = .0001.
Normalized to correct value.

Table 3

Accuracy Versus Thickness of Central Deflection of a Clamped Square Plate with Point Load at Center

Normalized to Correct Value

p	N	t/a = .0001	t/a = .001	t/a = .01
1	3	.00005	.00541	.33340
2	1	1.11607	1.11608	1.11663
2	2	.38308	.38432	.48697
2	3	.19744	.24164	.86304
2	4	.12684	.43630	.97361
3	1	.00001	.00115	.10203
3	2	.71086	.74251	.93456
3	3	.85746	.91375	.99154
4	1	.38940	.39590	.57622

REFERENCES

1. A. Adini and R. W. Clough, *Analysis of Plate Bending by the Finite Element Method* and Report to Natl. Sci. Foundation/USA, G7337, 1961.
2. A. C. Scordelis and K. S. Lo, "Computer Analysis of Cylindrical Shells," *J. Amer. Concr. Inst.*, 61, pp 539-61, 1961.
3. M. J. Turner, R. W. Clough, H. C. Martin, and L. J. Topp, "Stiffness and Deflection Analysis of Complex Structures," *J. Aeronautical Sci.*, 23, pp 803-23, p. 854, 1956.
4. R. H. MacNeal, *Finite Elements: Their Design and Performance*, Chapter 2, Marcel Dekker, New York, 1993.
5. B. M. Irons and J. K. Draper, "Inadequacy of Nodal Connections in a Stiffness Solution for Plate Bending," *J. AIAA*, 3, p. 5, 1965.
6. R. W. Clough and J. L. Tocher, "Finite Element Stiffness Matrices for Analysis of Plates in Bending," Proc. Conf. Matrix Methods in Struct. Mech., Air Force Inst. of Tech., Wright-Patterson AFB, Ohio, 1965.
7. B. Fraeijs de Veubeke, "A Conforming Finite Element for Plate Bending," *Intl. J. Solids Struct.*, 4, pp 95-108, 1968.
8. G. A. Butlin and R. Ford, "A Compatible Plate Bending Element," Univ. of Leicester Eng. Dept. Report, 68-15, 1968.
9. G. R. Cowper, E. Kosko, G. M. Lindberg, and M. D. Olson, "Formulation of a New Triangular Plate Bending Element," Trans. Canad. Aero-Space Inst., 1, pp 86-90, 1968 (see also N.R.C. Aero Report LR514, 1968).
10. B. M. Irons, "A Conforming Quartic Triangular Element for Plate Bending," *Intl. J. Numer. Methods Eng.*, 1, pp 29-46, 1969.
11. W. Bosshard, "Ein Neues Vollverträgliches Endliches Element für Plattenbiegung," Mt. Assoc. Bridge Struct. Eng. Bulletin, 28, pp 27-40, 1968.
12. W. Visser, "The Finite Element Method in Deformation and Heat Conduction Problems," Dr. W. Dissertation, T.H., Delft, 1968.
13. K. Bell, "A Refined Triangular Plate Bending Element," *Intl. J. Numer. Methods Eng.*, 1, pp 101-22, 1969.
14. J. H. Argyris, I. Fried, and D. W. Scharpf, "The TUBA Family of Plate Elements for the Matrix Displacement Method," *The Aeronautical J. R. Ae. S.*, 72, pp 701-9, 1968.
15. J. A. Stricklin, W. Haisler, P. Tisdale, and R. Gunderson, "A Rapidly Converging Triangular Plate Element," *J. AIAA*, 7, pp 180-1, 1969.
16. J. L. Batoz and M. Ben Tahar, "Formulation et Evaluation d'un Nouvel Elément Quadrilatéral à 12 D.L. pour la Flexion des Plaques Minces," Département de Génie Mécanique, Université de Technologie, Compiègne. France.
17. B. M. Irons, "The Semiloof Shell Element," *Finite Elem. for Thin Shells & Curved Members*, 11, pp 197-222, 1976.
18. I. C. Taig, "Structural Analysis by the Matrix Displacement Method," Engl. Electric Aviation Report No. 5017, 1961.
19. B. M. Irons, "Engineering Application of Numerical Integration in Stiffness Methods," *J. AIAA*, 14, pp 2035-7, 1966.
20. S. Ahmad, "Curved Finite Elements in the Analysis of Solid, Shell, and Plate Structures," Ph.D. Thesis, University of Wales, Swansea, 1969.
21. O. C. Zienkiewicz, J. Too, and R. L. Taylor, "Reduced Integration Technique in General Analysis of Plates and Shells," *Intl. J. Numer. Methods Eng.*, 3, pp 275-90, 1971.
22. R. H. MacNeal, "Derivation of Element Stiffness Matrices by Assumed Strain Distributions," *Nucl. Eng. Design*, 70, pp 3-12, 1982.
23. H. Stolarski and T. Belytschko, "Shear and Membrane Locking in Curved C^0 Elements," *Comput. Methods Appl. Mech. Engrg.*, 41, pp 279-96, 1983.
24. W. P. Doherty, E. L. Wilson, and R. L. Taylor, "Stress Analysis of Axisymmetric Solids Using Higher Order Quadrilateral Finite Elements," U. of Calif. Berkeley, Struct. Eng. Lab. Report SESM 69-3, 1969.
25. T. J. R. Hughes, R. L. Taylor, and W. Kanoknukulchai, "A Simple and Efficient Element for Plate Bending," *Intl. J. Numer. Methods Eng.*, 11, pp 1529-43, 1977.

26. T. J. R. Hughes and T. E. Tezduyar, "Finite Elements Based Upon Mindlin Plate Theory with Particular Reference to the Four-Node Bilinear Isoparametric Element," *J. Appl. Mech.*, pp. 587-96, 1981.

27. T. J. R. Hughes and R. L. Taylor, "The Linear Triangular Bending Element," *Mathematics of Finite Elem. and Appl. IV, MAFELAP 1981*, pp 127-42, 1982.

28. R. H. MacNeal, "The TRIA3 Plate Element," MacNeal-Schwendler Corp. Memo RHM-37, 1976.

29. R. H. MacNeal and R. L. Harder, "Eight Nodes or Nine?," *Intl. J. Numer. Methods Eng.*, 33, pp 1049-58, 1992.

30. K. C. Park and G. M. Stanley, "A Curved C^0 Shell Element Based on Assumed Natural-Coordinate Strains," *J. Appl. Mech.*, 53, pp 278-90, 1986.

31. J. J. Rhiu and S. W. Lee, "A New Efficient Mixed Formulation for Thin Shell Finite Element Models," *Intl. J. Numer. Methods Eng.*, 24, pp 581-604, 1987.

32. T. Y. Chang, A. F. Saleeb, and W. Graf, "On the Mixed Formulation of a Nine-Node Lagrange Shell Element," *Comput. Methods Appl. Mech. Engrg.* 73, pp 259-81, 1989.

33. H. C. Huang and E. Hinton, "A New Nine-Node Degenerated Shell Element with Enhanced Membrane and Shear Interpolation, *Intl. J. Numer. Methods Eng.*, 22, pp 73-92, 1986.

34. J. Jang and P. M. Pinsky, "An Assumed Covariant Strain Based Nine-Node Shell Element," *Intl. J. Numer. Methods Eng.*, 24, pp 2389-411, 1987.

35. T. Belytschko, W. K. Liu, J. S.-J. Ong, and D. Lam, "Implementation and Application of a Nine-Node Lagrange Shell Element with Spurious Mode Control," *Comput. Struct.*, 20, pp 121-8, 1985.

36. D. W. White and J. F. Abel, "Accurate and Efficient Nonlinear Formulation of a Nine-Node Shell Element with Spurious Mode Control," *Comput. Struct.*, 35, pp 621-41, 1990.

37. J. J. Rhiu and S. W. Lee, "A Sixteen-Node Shell Element with a Matrix Stabilization Scheme," *Comput. Mech.*, 3, pp 99-113, 1988.

38. J. J. Rhiu, R. M. Russell, and S. W. Lee, "Two Higher-Order Shell Finite Elements with Stabilization Matrix," *J. AIAA*, 28, pp 1517-24, 1990.

39. B. A. Szabó and A. K. Mehta, "p-Convergent Finite Element Approximations in Fracture Mechanics," *Intl. J. Numer. Methods Eng.*, 12, pp 551-60, 1978.

40. B. A. Szabó and G. J. Sahrmann, "Hierarchic Plate and Shell Models Based on p-Extension," *Intl. J. Numer. Methods Eng.*, 26, pp 1858-81, 1988.

41. Y. Leino and J. Pitkäranta, "On the Membrane Locking of h-p Finite Elements in a Cylindrical Shell Problem," Helsinki Univ. of Technology, Instit. of Mathematics Research Reports A311, June 1992.

42. H. Hakula, Y. Leino, J. Pitkäranta, "Pinched Shell of Revolution: Experimenets on High Order FEM," Helsinki U. of Tech., Inst. of Math. Research Reports, A346, April 1995.

43. R. H. MacNeal, "A Simple Quadrilateral Shell Element," *Comput. Struct.*, 8, pp 175-83, 1978.

FUTURE DIRECTIONS AND CHALLENGES FOR SHELL FINITE ELEMENT ANALYSIS

D. D. Fox & J. C. Nagtegaal

Hibbitt, Karlsson and Sorensen, Inc.

1080 Main Street, Pawtucket, RI 02860

Abstract

This paper gives a brief overview of some current issues and future challenges in finite element analysis of shells, with the emphasis on nonlinear effects.

- It discusses problems related to shell buckling, if the buckling is accompanied by other nonlinearities such as inelastic material behavior and contact constraints.
- It addresses the validity of traditional shell theory when applied to non-traditional materials, in particular short-fiber reinforced composites.
- It discusses shell element formulations and describes a non-traditional (though not exactly new) approach to formulation of shell elements, which may be relevant in the integration between CAD and FEA.

Various examples are included to illustrate the points made in the paper.

Introduction

The demand continues to grow for robust and accurate simulations of shell-like structures subjected to loading which causes nonlinear deformation. Increased computational resources and improved equation solver technologies have made it possible to solve large analysis problems in a reasonable amount of time. Linear shell problems with one million degrees of freedom can now be solved routinely on workstations, and nonlinear shell problems of a similar size can be solved effectively with explicit dynamics solution techniques. Nonlinear problems of a somewhat smaller size (but still large by most standards) can be solved effectively with implicit methods. However, it is not only size that counts; analysts want to obtain reliable solutions to more complex problems with less effort.

There is a growing need for the use of shell elements in applications that fall outside the scope of "classical" shell analysis, such as buckling instabilities induced by nonlinear material response (when elastic eigenvalue buckling predictions are inadequate) and contact constraints active prior to buckling or activated during the post-buckling phase. Such applications require sophisticated solution techniques capable of selecting the desired solution path near bifurcations and capable of handling discontinuities in the equilibrium path. Additional stabilizing forces may have to be added in such cases.

With the increasing use of non-traditional materials for structural applications, such as short fiber reinforced plastics and paper laminates, more complex material behavior in fairly thick shell structures needs to be taken into account. To facilitate the use of more complex material models (which may include failure models due to interlaminar shear and debonding) and to obtain more accurate solutions, it is desirable to avoid the classical plane stress assumption traditionally used in shell theory. A three-dimensional stress state can be introduced in a number of ways, for instance through resultant-based shell formulations that incorporate a thickness change degree of freedom and couple the membrane, transverse shear, and pinching force, or through sophisticated kinematic models that add as many additional degrees of freedom in the thickness direction as the analyst requires.

Finally, the growing sophistication of interactive modeling programs is likely to evolve traditional finite element programs into boundary value solvers, where the analyst does not interact directly with the finite element mesh. In such an environment, elements with non-traditional degrees of freedom (instead of the classical 4-node quadrilateral with 6 degrees of freedom per node) can be used, which may well re-invigorate interest in shell finite element technology.

Applications outside the scope of classical shell analysis

Classical applications of shell elements to aerospace problems typically involve linear static and dynamic analysis as well as eigenvalue buckling. In order to assess the load carrying capacity of structures after initial buckling, as well as to assess the imperfection sensitivity of structures, post-buckling analysis is quite helpful. This requires the introduction of special solution techniques, where one no longer determines the response of the structure to a given load, but tries to determine the loading path (or paths) of the structure together with the response. The initial proposal for such a method was made by Riks,[1] and the method has been popularized by many other important contributions.[2,3] The "traditional" Riks method works well for problems in which the "perfect" structure has been modified to change the bifurcation behavior into continuous "snap-

through" behavior and allows tracing of complex equilibrium paths. Many recent advances have been made that allow the method to deal with (local) bifurcations as well.

Consider for instance the simple elastic frame structure shown below, loaded by a vertical point force at the corner of the frame. Small geometric imperfections are introduced based on the first twenty buckling modes of the frame. Depending on whether the frame buckles inward or outward, a straightforward snap-through solution or a sequence of equilibrium shapes of ever increasing complexity is obtained, as shown in the figure. Although this is a rather academic example, it demonstrates the power of the Riks method.

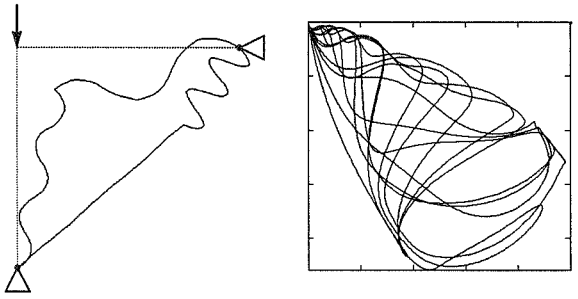

Simple frame subjected to point load, two unstable deformed shapes and the x-y path of the corner.

Since the Riks method has no concept of time or history (the solution advances forward by prescribed amounts in normalized displacement-load space), the method has obvious limitations when rate or history dependent material behavior is included. This limitation is particularly severe for rate dependent material behavior; "time" is in fact replaced by "arc length," which is a measure of the change in the solution, and hence the strain change per unit arc length is dimensionless. The situation is more subtle for history dependent behavior. Here, the material behavior is influenced by the solution *path*. The solution path is determined by the equilibrium equations but is not necessarily physically realistic because during part of the path the equilibrium will be unstable, and the actual physical behavior will be dynamic in nature. Nevertheless, it may be possible to obtain useful information from an elastic-plastic static post-buckling analysis.

A class of post-buckling problems that presents considerable difficulties involves buckling with inequality constraints. Consider the simple example shown below: a shell roof pressed down by a rigid indenter.

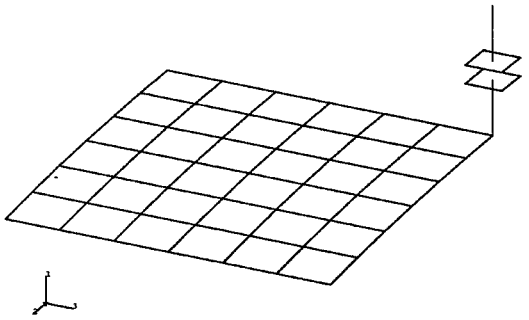

Shell roof with indenter.

The initial phase of the loading process is straightforward: the contact condition is activated, and the indenter presses the roof down. The analysis progresses smoothly as the load increases, and with either an applied displacement condition on the indenter (or with use of an arc length method) progresses even as the load decreases. However, problems start to develop as the load decreases further and reaches zero.

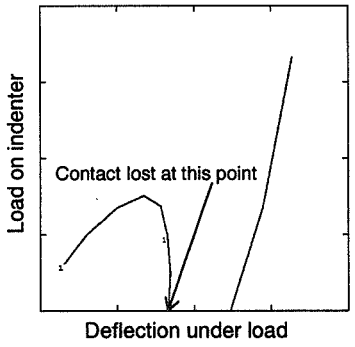

Load-displacement curve of shell roof with indenter.

At that point, contact between the indenter and the roof is lost, and it is no longer possible to control the solution with the load or the prescribed displacement of the indenter. In load-displacement space, this represents a discontinuity in the solution path that can only be bridged by adding additional forces on the roof. For instance, one can add inertia forces (and analyze the problem dynamically) or viscous forces (transforming it into a "diffusion type" problem). With elastic material behavior, the final state is the same in either case (since there are no history effects), but with history effects in the material the final state might show considerable dependence on the method used.

Another type of post-buckling problem that isn't readily solved with conventional methods is when the buckling mode is constrained by contact conditions. Consider for instance the simple Euler column shown below, which is

sandwiched between two rigid walls. Small imperfections are introduced in the geometry based on the buckling modes of the structure.

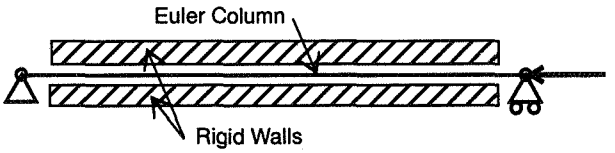

Geometry of Euler column and contact constraints.

The initial phase of the problem is straightforward: the column buckles and hits the wall. As the load increases, the contact zone widens, the contact pressure at the center of the zone decreases, and eventually the center of the zone loses contact. The axial force increases further and the free zone grows, and at a certain load the center zone starts to buckle away from the wall. Initially, the standard Riks algorithm can control this by lowering the applied load, but at a given point the column snaps away from the wall and the solution cannot be controlled by the applied load. At this stage the algorithm fails.

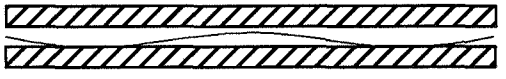

Buckled shape of Euler column just before static post-buckling analysis fails.

Problems of this nature can be solved by adding inertia or viscous damping. For this problem, the solution was obtained by adding viscous damping for motions in the direction transverse to the beam. The damping coefficient was chosen very small, so that the viscous forces had no influence on the solution during stable parts of the solution path. As soon as an instability develops, however, the velocity of the structure grows rapidly and the viscous damping terms become dominant. In order to prevent the solution from diverging, the increment size must be decreased dramatically so that the displacement increments remain small enough to obtain convergence. Typically, the increment size must be decreased by several orders of magnitude as long as the structure is in an unstable state. Obviously, a reliable automatic time stepping algorithm is essential for successful analysis. Hence, the load displacement curve typically shows certain "plateaus" where the applied force remains constant and the displacement changes, as shown below.

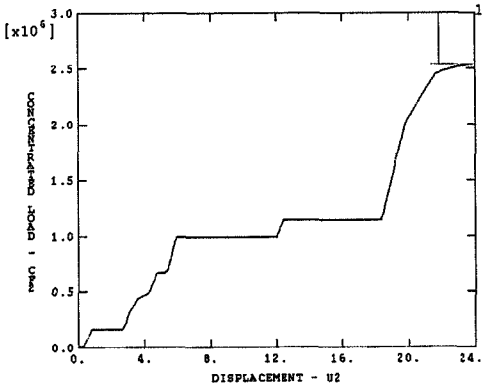

Load-displacement curve of Euler column.

After buckling in the first mode, the column subsequently buckles in the third mode, the fifth mode, and the seventh mode as shown below.

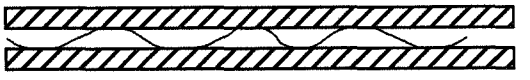

Buckled shape of Euler column after analysis with viscous damping.

Most of the examples shown here are simple beam problems. Similar difficulties occur with shells. In fact, in many cases shell problems will be harder than beam problems because even without contact constraints they are more prone to unstable post-buckling behavior.

A special but significant class of shell problems involving unstable behavior and contact constraints are springback problems. If a curved shell structure is created with a forming operation, the shell will be severely constrained by dies at the end of the forming operation and will not be stress free. Often, the shell will undergo considerable elastic or even plastic deformation when it is released from the tools.

An example of a simple forming problem, proposed as a benchmark problem at the 1993 Numisheet Conference,[4] with considerable springback is shown below. A flat plate is formed into a hat-shaped channel by pressing it between rigid dies. Subsequently, the dies are removed and the channels springs back significantly, as shown below.

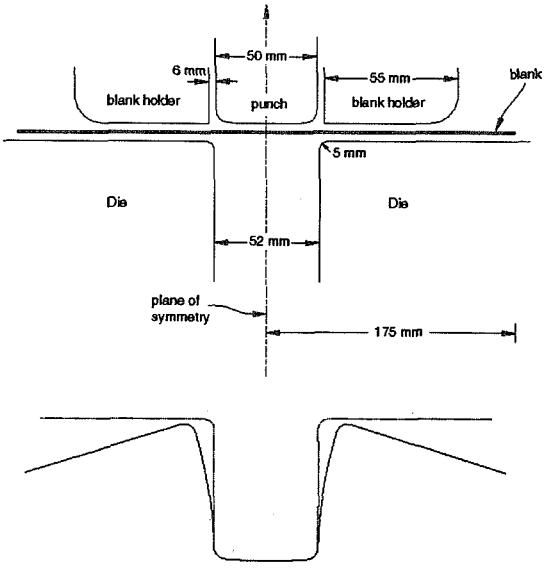

Forming and springback of hat-shaped profile.

Typically, the analysis of the forming process is done with an explicit dynamics code. For a simple 2-D example as shown above the analysis can also be done with a statics code, but experience has shown that for large, 3D forming operations the explicit dynamics approach is much more effective.[5] There are several reasons for this. One is that the forming problem is dominated by complex contact conditions, which are handled much easier by an explicit dynamics approach than by an implicit static approach. Another factor is that, due to the presence of the contact constraints, the bending of the blank is driven by the tools, and at the end of the forming process the blank is almost completely constrained.

The explicit dynamics method is much less suitable for the analysis of the springback process. In this phase of the process, the tools are removed and, after the initial part of the release, the deformation is no longer driven by tool motions. In particular, in the final stage of the release operation the blank is no longer constrained, and with an explicit dynamic method it will take many small time increments to damp out the vibrations and find the static solution. Hence, an implicit static analysis is more suitable for this phase of the process.

However, if the static analysis procedure is applied directly, the same kind of contact problems are experienced that make it so difficult to do the forming operation, particularly in the initial phase. Moreover, if there are significant compressive residual stresses in the blank, unstable contact problems as described earlier are likely to occur. Hence, it is attractive to do the static analysis without having to worry about contact constraints.

One possible way to create such a procedure would be to replace all nodal forces working on the blank due to contact and inertia effects by externally applied loads and to gradually decrease the external loads to zero. This procedure makes sure that the structure starts in static equilibrium at the beginning of the springback process. Unfortunately, there is no guarantee that the equilibrium is stable: in fact, we have seen in many practical examples that all or part of the blank has significant compressive stress after forming, and (local) buckling may occur after release of the contact constraints. In this situation, it is usually not possible to obtain solutions in a reliable manner without adding the same kind of viscous damping that was discussed earlier.

A more elegant method is to add the external forces in a manner that restores both equilibrium and stability. This is readily accomplished by adding the external loads in the form of an applied stress, equal and opposite to the stress existing in the blank. The total stress of in the blank is then the sum of the actual "material" stress σ^M and the "externally" applied stress σ^E:

$$\sigma^{TOT} = \sigma^M + \sigma^E$$

which is obviously zero to start. Hence, from a stability and equilibrium viewpoint, the initial state of the structure is stress-free and stable. Subsequently, the external stress is ramped down as part of the analysis step:

$$\sigma^E = -\sigma^M\left(1 - \frac{t}{t_s}\right),$$

where t_s is the duration of the analysis step, so that at the end of the step no externally applied stress remains and the proper static equilibrium is obtained. Moreover, if instabilities develop during the removal of the externally applied stress, they develop gradually and equilibrium can be controlled for instance with the Riks method. This procedure is described in more detail in Mercer et al.[6]

Of course, the path along which springback is obtained is not the exact path followed in the actual release process. This is particularly relevant if material nonlinearities such as plasticity occur during springback. Practical experience indicates, however, that active plasticity during springback is usually highly localized and driven by the state at the end of the

forming step, with little influence of the exact path followed. Hence, the approximate method presented here provides valuable information for design purposes.

As an example, consider the forming and springback of a gas turbine engine nozzle panel. The panel is made of Inconel 718, and is formed out of a flat plate in a single stamping operation. The forming analysis is carried out with ABAQUS/Explicit,[7] an explicit dynamics solver. The blank is modeled with a rectangular mesh of 18592 4-node quadrilateral shell element with a total of 113436 degrees of freedom. The shape of the plate is obtained by trimming the edges; this leads to edges that are rough, but this is not important since the precise solution near the edges is not relevant. The deformed finite element mesh is shown below.

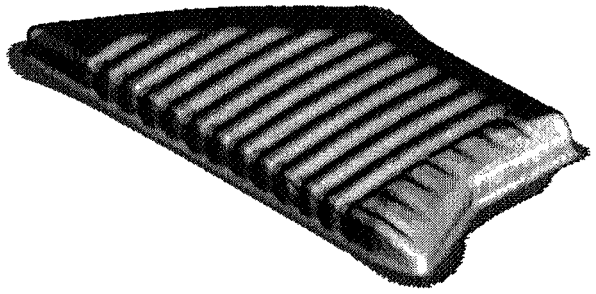

Mesh of gas turbine engine nozzle panel after stamping operation.

The deformed mesh and the stress state in the shell model are then imported in ABAQUS/Standard,[8] a general purpose nonlinear finite element program. The springback process is analyzed with the procedure described above. Contours of the displacements due to springback perpendicular to the panel are shown below. The total distortion is about 5% of the width of the panel or about 20 times the thickness of the panel wall. Other significant quantities, such as residual stresses, actual wall thickness, etc. are available from the analysis.

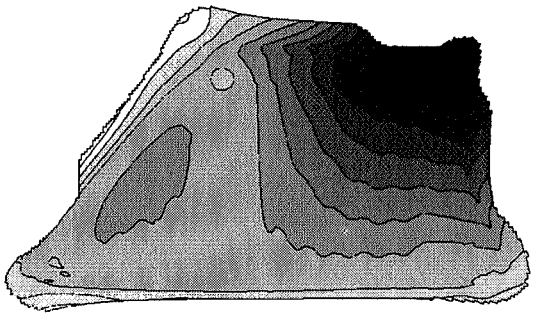

Springback displacements perpendicular to the panel after release.

Thick shells with complex material models

Designers are demanding ever-increasing performance from shell-like structures. In applications where weight, material cost, manufacturing constraints, or aesthetics force mechanical parts to be thin, shell-like structures are more likely to be the primary load-bearers at the same time that the thickness of these structures is being reduced. The finite element analyst, in turn, requires ever greater accuracy in problems with nonlinear deformation and complex material response, applications not traditionally amenable to shell element analysis. Such applications are many and range from fiber-filled thermoplastics in the automotive industry to paper laminates in packaging to honeycomb-core composites in aerospace applications.

Engineering thermoplastics design and manufacturing serves as an illustrative example of the high demands placed on finite element analysis of shell-like structures. The wide range of nonlinearities encountered in the material response, deformation level, and loading conditions and the importance of through the thickness variation and surface effects all contribute to the difficulty of the analysis.

Engineering thermoplastics are experiencing a dramatic rise in stiffness and strength due to research efforts by plastic part manufacturers and plastic resin suppliers. As a result, engineering thermoplastics are replacing metals in many applications where light weight, high strength plastic parts can be manufactured much less expensively than cast or machined metal parts. In the automotive industry many such examples exist. The figure below shows a glass-filled nylon air intake manifold.

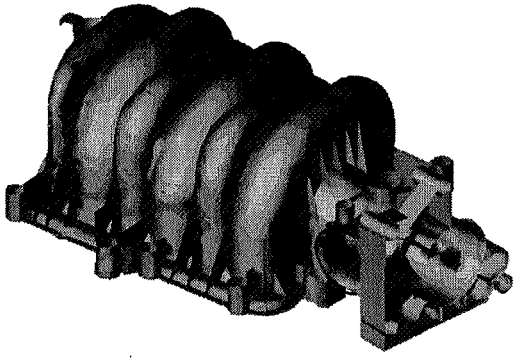

Shell element model of glass-filled nylon air intake manifold.

This part's operating environment is high temperature, so creep deformation is important; pressure cycling occurs between internal vacuum and zero gauge pressure, so fatigue life is important; during backfire conditions the internal pressure exceeds one atmosphere gauge pressure, so ultimate failure strength is important.

Other automotive applications include bumpers; radiator covers; (aesthetic) vertical side body panels; (structural) horizontal body panels; engine parts subjected to thermal and mechanical loading, such as cylinder head covers and cooling fans; suspension components; and complex assembly parts where hundreds of small metal features can be integrated into a single plastic part. In all of these applications injection-molded, fiber-filled engineering thermoplastic are being used for their high stiffness to weight ratio, low manufacturing costs, and good (yet complex) mechanical properties.

The typical design cycle for an injection-molded plastic part requires shell finite element analysis at several stages. At each of these stages the limits of validity of shell theory are tested.

In typical applications, the slender glass fibers imbedded in the resin have length to diameter ratio of 25, have overall length much less than the thickness of the part, and are used in volume fractions between 20 and 40 percent. If these fibers were fully aligned in the plane of shell, the resulting instantaneous elastic response would be orthotropic. However, during the injection-molding process a complex three-dimensional flow field is established that orients the glass fibers in all three directions. The nonzero thickness direction component of the fibers, together with the gradient in fiber density and direction through the thickness, make traditional plane stress constitutive assumptions invalid. A typical fiber orientation distribution through the thickness includes skin layers of highly aligned fibers surrounding a core of fibers which are nearly randomly aligned in all three directions as shown below.

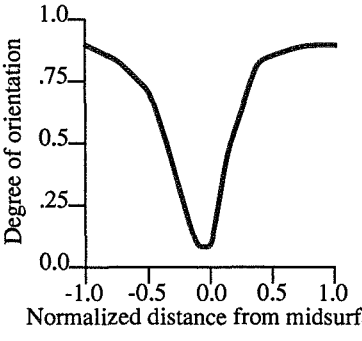

Fiber orientation distribution through the thickness of a glass-reinforced thermoplastic. High alignment near the surface, random orientation in the core.

After the resin-fiber mixture is injected into the mold and the mixture solidifies, the part is ejected from the mold while at high temperature. Rapid cooling coupled with through the thickness gradients in the temperature and viscoelastic relaxation of residual stresses lead to asymmetrical shrinking, overall warping, and local wrinkling of the part's surface. It is often the case that shrinkage and warpage is large enough to violate manufacturing tolerances or the surface imperfections are visible to the eye making the part unacceptable. In order to model such effects, a shell element analysis should include:

- three-dimensional state of stress allowing anisotropic material response with one direction of anisotropy in the thickness direction,
- high order kinematics to resolve gradients through the thickness,
- a nonlinear viscoelastic material description.

Assuming that dimensional tolerances and surface quality of the parts can be met, the part must then be analyzed for service thermomechanical loading, creep response, buckling load prediction, fatigue life, ultimate strength, failure due to impact loading, surface crack propagation, etc. Each of these analyses can require complex material response, large deformations, and nonlinearities in the loading or boundary conditions. In many instances, such as surface cracking, the response is dominated by three-dimensional effects or through the thickness variation that can not be captured with traditional shell element formulations. Although many of these analyses questions are difficult for three-dimensional continuum elements, shell element theory is particularly challenged by:

- three-dimensional, large strain, inelastic time dependent response,
- buckling load predictions of flexible structures with nonlinear material response,
- fatigue life predictions due to cyclic bending stresses,
- impact loading and failure for materials with high strain rate sensitivity,
- surface wrinkling and cracking.

Over the past several years numerous researchers have addressed some, but by no means all, of the deficiencies of classical shell theory. Within nonlinear, resultant-based shell theory Simo et al.[9] introduced a formulation which included the thickness change as a solution degree of freedom. This first order approximation allows the use of three-dimensional material response in resultant form for the membrane, transverse shear, and through-thickness stress resultants; however, the bending stress resultants remain an open question. The layerwise laminate theory of Reddy[10] allows an analyst-

defined number of kinematic variables through the thickness of the shell allowing for piecewise continuous distribution of transverse shear strains through the thickness. Other works rely on three-dimensional equilibrium and constitutive relations through out the shell's thickness; see for example Roy et al.[11] Such methods can be computationally expensive. A predictor-corrector approach is advocated by Noor et al.[12] whereby first-order shear deformable theory is used to predict the gross overall deformation, and three-dimensional equilibrium equations and constitutive relations are used to correct the solution through the thickness of the shell. In these efforts one or more limitation of classical shell theory can be removed; however, no general purpose effort has successfully addressed all of these deficiencies together.

Non-conventional shell element formulations and CAD

Creation of effective elements for analysis of curved shells has always been one of the biggest challenges for developers of finite elements. Even to this day, there is a steady stream of papers describing new elements and (real or imagined) improvements to existing elements formulations. Over the years, the understanding of the important issues for shell finite element design has steadily improved. Issues such as shear locking for thin shells and membrane locking for (doubly-)curved thin shells are now well understood and are discussed in many textbooks (see, for instance, Hughes[13]). The gradual emergence of a standard set of test problems for shell elements (such as the MacNeal/Harder set of linear problems[14] and the 'obstacle course' defined by Belytschko et al.[15]) have helped developers to evaluate new elements. The nonlinear test are limited: essentially, they only test geometric nonlinear behavior, and do not concern themselves with material nonlinearity or finite strains.

In the early days of finite elements, developers attempted to create elements based directly on classical shell theory; this required interpolation with C^1 continuous displacement fields, which turned out to be exceedingly difficult. Since the early days of finite elements, considerable progress in description of doubly curved surfaces has been made in the CAD world. The appearance and rapid increase in popularity of Non Uniform Rational B-Splines (NURBS) and NURBS based surfaces make it possible to define C^1 continuous surfaces with local support.[16,17] It is however not clear that these same approaches can be used effectively in finite element analysis. Although the support is local, it is not as strictly local as traditional finite elements, where the value inside the domain of an element is completely determined by parameters on the boundary and in the interior of the element. For NURBS, points in the vicinity of a element (but not necessarily on the boundary) help determine the interpolation inside the domain (see below).

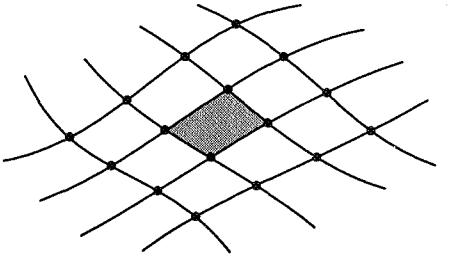

Local support for a NURBS surface.

There are certain CAD approaches, in particular Coons patches,[18] that have the strictly local support that is desirable in finite elements. However, such approaches, which were proposed in the early days of finite elements[19] (actually before the emergence of the Coons patch), require complex quantities on the boundary of the domain (such as the twist of the surface) to describe the interpolation, as well as a regular quadrilateral grid topology. Hence, it does not appear that the classical approach will make a comeback any time soon.

In virtually all modern finite elements, a two field approach is used: the displacements of the shell mid-surface and the rotation of the shell "normal" are interpolated independently with C^0 continuous functions. This approach is analogous to (Mindlin) thick shell theory, and hence many elements are based directly on this theory. The same interpolation principle with a different perspective leads to the "Discrete Kirchhoff" formulation. This thin shell formulation tries to enforce the Kirchhoff constraint at a few carefully chosen discrete points (and often in specific directions). The DK formulation may enrich the rotation field in the interior of the elements such that the discrete Kirchhoff constraint is applied exactly or may rely on a penalty approach to enforce the constraint; in the latter case, the element formulation is akin to the thick shell approach.

In either case, the rotation field is interpolated from the same nodal positions as the displacements. Most of the elements developed have actually 3 rotational degrees of freedom at each node, although there are some that have two rotation components around the tangents to the

shell. The advantage of this is that the "twist" or "drill" degree of freedom (rotation about the shell normal, not to be confused with the surface twist mentioned in the context of CAD surfaces) does not need to be considered. The disadvantage is that special precautions need to be taken at fold lines and intersections, and also at nodes that have single- or multi-point rotational constraints applied to them. It is fairly straightforward to solve these problems for geometrically linear analysis; it is a whole lot more difficult to address them effectively for geometrically nonlinear analysis with finite rotations.

In some formulations the drill degree of freedom has been put to good use to enrich the membrane field.[20] Quite a few publications have shown that the in-plane bending behavior of first order quadrilateral and triangular shells can be improved considerably with this enrichment, particularly if the elements are somewhat irregularly shaped. It appears, however, that an effective and robust formulation is only feasible for geometrically linear problems; for problems involving large rotations and certainly for problems involving large strains the approach appears to lose its robustness.

An alternative approach was proposed many years ago by Irons; he used displacement degrees of freedom at the usual corner and mid-edge positions and a single rotational degree of freedom at Gaussian positions along the edges, as shown below. Irons published this in the context of a rather complicated second order element, the so-called Semiloof[21] element. The element uses discrete, analytically enforced Kirchhoff constraints and in that sense it belongs to the discrete Kirchhoff family of elements.

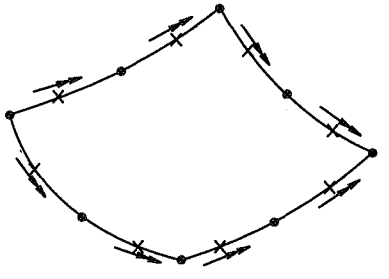

Semiloof element.

Although the element was implemented in a few commercial programs, particularly in the UK, it never attained worldwide popularity.

The interesting part of the approach is that the rotational degrees of freedom consist of rotations around the element edges, which correspond nicely to the natural boundary conditions for the shell. Hence, application of boundary conditions and edge moments is straightforward, and fold lines are dealt with naturally. First order elements can also be developed along these lines. The oldest element of this family is probably Morley's constant curvature plate bending triangle,[22] which has a single constant rotation around each edge, for a total of 12 degrees of freedom per element. As with most lower order triangles, the convergence characteristics of the element are rather poor, certainly as far as membrane behavior is concerned. A first order quadrilateral finite strain shell element with corner displacement and edge rotations was developed by Nagtegaal et al.,[23] as shown below. Although the element did perform well and was quite efficient, it did not become very popular. Part of the reason may well be that the element is simply different from what is perceived as the industry standard.

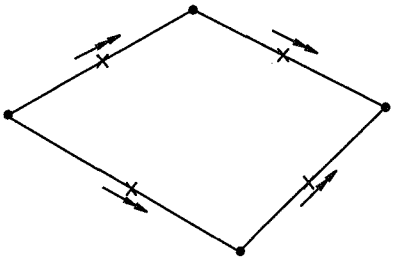

Four node element with edge rotations.

Elements of this type have a shortcoming: it is not straightforward to combine them with standard two-node beam elements for the analysis of stiffened shells. Either special beam elements or special multi-point constraints must be developed for easy combination of beams and shell, which takes away some of the advantages.

Nevertheless, it may well be worth reconsidering this kind of shell element. In particular with the ongoing integration of CAD and FEA, there is a trend to replace traditional finite element analysis with "push-button" automatic FEA analysis, particularly for traditional linear analysis. Typically, the analyst/design engineer will not deal with the finite element mesh but operate directly on the geometry. This integrated approach offers the possibility to define loads and constraints directly on the geometric model, and hence makes it possible to hide the details of the element formulation from the analyst/design engineer running the CAD system. Therefore, the choice of degrees of freedom for the shell element becomes irrelevant.

Closure

Although finite element analysis of shell structures is a mature field, there are still many advances left to be made in the areas of element design and analysis procedures. The growing use of high performance shell structures with non-conventional materials and the need for the analysis of strongly nonlinear phenomena, such as those that occur during the analysis of manufacturing processes or after structural buckling and collapse, present considerable challenges to finite element developers and analysts alike.

References

1. E. Riks, 'The application of Newton's method to the problem of Elastic Stability,' *J. of Appl. Mech.*, **39**, 1060-1066 (1972).
2. M.A. Crisfield, 'A fast incremental/iteration solution procedure that handles 'snap-through',' *Computers and Structures*, **13**, 55-62 (1981).
3. E. Ramm, 'Strategies for tracing the nonlinear response near limit points,' *Nonlinear finite element analysis in structural mechanics*, E. Wunderlich et al., eds., Springer-Verlag, Berlin (1981).
4. Proceedings of the 2nd International Conference, Numisheet '93, A.Makanouchi et al., eds., Isehara, Japan (1993).
5. J.C. Nagtegaal and L.M. Taylor, 'Comparison of implicit and explicit finite element methods for analysis of sheet forming processes,' *Proc. of the conf. on FE-sim. of 3-D sheet metal form. proc. (Numisheet '91)*, J. Reissner et al., eds., VDI Verlag, Duesseldorf (1991).
6. C.D. Mercer, J.C. Nagtegaal, and N. Rebelo, 'Effective application of different solvers to forming simulations,' *Proc. of the 5th Int. Conf. on Num. Meth. in Ind. Form. Proc., Numiform '95*, S-F. Shen and P.R. Dawson, eds., Ithaca, NY (1995).
7. ABAQUS/Explicit User's manual, Hibbitt, Karlsson and Sorensen, Inc. (1996).
8. ABAQUS/Standard User's manual, Hibbitt, Karlsson and Sorensen, Inc. (1996).
9. J.C. Simo, M.S. Rifai, and D.D. Fox, 'On a stress resultant geometrically exact shell model. Part IV: Variable thickness shells with through-the-thickness stretching,' *Comp. meth. appl. mech. engrg.*, **81**, 91-126 (1990).
10. J.N. Reddy, 'A generalization of two-dimensional theories of laminated composite plates,' *Commun. appl. numer. methods*, **3**, 173-180 (1987).
11. A.K. Roy and S.W. Tsai, 'Design of thick composite cylinders,' *Journal of pressure vessel technology*, **110**, 255-262 (1988).
12. A.K. Noor and J.M. Peters, 'A posteriori estimates for shear correction factors in multilayered composite cylinders,' *Journal of engineering mechanics*, **115**, no. 6, 1125-1244 (1989).
13. T.J.R. Hughes, 'The finite element method,' Prentice-Hall, Englewood Cliffs, NJ (1987).
14. R.H. MacNeal and R.L. Harder, 'A proposed standard set of problems to test finite element accuracy,' *J. finite elements in analysis & design*, **1**, 3-10 (1985).
15. T. Belytschko, B.L. Wong and H. Stolarski, 'Assumed strain stabilization procedure for the 9-node Lagrange shell element,' *Int. j. numer. methods eng.*, **28**, 285-414 (1989).
16. D.F. Rogers and J.A. Adams, 'Mathematical elements for computer graphics,' McGraw-Hill, New York (1990).
17. L Piegle and W. Tiller, 'The NURBS book,' Springer-Verlag, Berlin (1995).
18. S. Coons, 'Surfaces for computer-aided design of space forms,' *MIT proj. MAC*, MAC-TR-41 (1967).
19. F.K. Bogner, R.L. Fox, and L.A. Schmit, 'The generation of interelement-compatible stiffness and mass matrices by the use of interpolation formulae,' *Proc. Conf. Matrix Methods in Struct. Mech.*, Wright Patterson A.F. Base, OH (1965).
20. T.J.R. Hughes and F. Brezzi, 'On drill degrees of freedom,' *Comp. meth. appl. mech. engrg.*, **72**, 105-121 (1989).
21. B.M. Irons, 'The semiloof shell element,' *Finite elements for this shells and curved members*, D.G. Ashwell and R.H. Gallagher, eds., John Wiley, London (1976).
22. L.S.D. Morley, 'On the constant moment plate bending element,' *J. Strain Analysis*, **6**, 20-24 (1971).
23. J.C. Nagtegaal and J.G. Slater, 'A simple non-compatible thin shell element based on discrete Kirchhoff theory,' *Proc. winter ann. meeting ASME*, Washington, DC (1981).

Optimization of Stiffened Panels in which Mode Jumping is Accounted for

David Bushnell, Charles C. Rankin
Department H1-61, Building 255
Lockheed Martin Advanced Technology Center
3251 Hanover St., Palo Alto, California 94304

Eduard Riks
Aerospace Engineering Department
Delft University of Technology
The Netherlands

ABSTRACT

PANDA2 is a computer program for the minimum weight design of stiffened composite, flat or cylindrical, perfect or imperfect panels and shells subject to multiple sets of combined in-plane loads, normal pressure, edge moments and temperature. STAGS is a general nonlinear finite element code that is specifically designed to analyze especially difficult stability problems in shell structures. Weight optimization of stiffened panels can be particularly troublesome when local buckling is allowed to occur in the pre-collapse state. For these systems, designs may be affected by interaction between local modes, a mechanism that manifests itself as mode jumping and is difficult to characterize. In this paper we describe how in PANDA2 mode jumping is detected and suppressed in optimized panels. Two axially compressed blade stiffened panels optimized by PANDA2 for service in the far postbuckling regime were numerically tested by STAGS. Mode jumping was permitted to occur below the design load in the first panel and suppressed in the second. Results obtained by STAGS are in reasonably good agreement with predictions by PANDA2. The first panel exhibits mode jumping well below the design load. Application of STAGS to this panel reveals that even though the mode jump involves little change in potential energy it generates large amplitude oscillating stresses with significant stress reversal that might well cause fatigue and delamination. The oscillating stresses are caused by postbuckling lobes moving to and fro along the panel axis immediately after initiation of the mode jump.

INTRODUCTION

The PANDA2 code [1-3] is a fast interactive computer program that provides the user with the optimum design of stiffened panels of various shapes and materials including composite fabrications. Because of the particular nature of this code with its simplifying assumptions and the inherent nonlinear behavior of locally postbuckled panels, the results must be checked thoroughly by either an experiment or by an analysis with an independent general-purpose finite element code (or both). In PANDA2 it is easy to check the results with the robust finite element code STAGS because PANDA2 automatically translates its output design into model input for STAGS [4,5] The STAGS code can thus easily be used to check optimization designs that are produced by the PANDA2 user.

Weight optimization of stiffened panels designed for service in the local postbuckling regime can lead to a behavior dominated by mode interactions such as mode jumping [6-12] whereby the deformation state of the panel jumps from one mode shape to another as the load is increased. This phenomenon may or may not have a detrimental effect on the integrity of a panel, depending on the energy content of the jumps, on whether or not stresses oscillate significantly because of the jumps, and on the details of panel fabrication. For example, delamination in a composite panel can initiate or propagate as a result of mode jumps that release energy or otherwise alter the response significantly. Early fatigue failure might occur if the locations of maximum stress oscillate during the mode jumping. Consequently, the designer might want to prevent serious mode jumping from occurring in his design. To

provide this option, PANDA2 was equipped with a "prevent mode jump" constraint. We describe results of tests of this constraint here. For a description of previous work done on mode jumping in axially compressed plates the reader is referred to the excellent papers by Stoll [10,11].

Until recently it was very difficult to use STAGS to analyze panels in which mode jumping occurs before failure. This behavior, which is transient, cannot be analyzed with the traditional static path-following technique that the STAGS code employs [5]. This difficulty has recently been overcome by judicial combination of the path-following technique and transient integration methods. Now it is possible to check PANDA2 designs that exhibit mode jumping in their load-deformation response [8,9] A short description of the STAGS solution strategy is given here.

The objectives of this paper are:

1. To describe how the results from PANDA2 and STAGS compare for a stiffened panel optimized by PANDA2. The panel is designed to carry loads far in excess of the local buckling load of the panel skin.

2. To describe and evaluate the constraint condition in PANDA2 that is supposed to prevent serious mode jumping before the design load is reached.

3. To demonstrate the capability of STAGS to obtain the nonlinear collapse load of panels in which mode jumping occurs at loads below the design load.

THE PANDA2 PROGRAM

PANDA2 [1], which supersedes PANDA [2] but which contains many of the buckling algorithms from PANDA [3] finds minimum weight designs of laminated composite flat or curved cylindrical panels or cylindrical shells with stiffeners in one or two directions. Stiffeners can be blades, tees, angles, or hats. Truss-core sandwich panels [12] and stiffened sandwich panels with honeycomb or foam core [13] can also be handled, as well as isogrid-stiffened panels with added rings [14]. The panels or shells may have initial imperfections of the form of general, inter-ring, and local buckling modes [15]. The panels or shells can be loaded by as many as five combinations of in-plane loads, edge moments, normal pressure, and temperature. The material properties can be temperature-dependent. Local, inter-ring, and general buckling loads are calculated in PANDA2 with use of either closed-form expressions [3] or with use of discretized models [1] of panel cross sections. The discretized model is based on one-dimensional discretization similar to that used in the BOSOR4 computer code [16]. An analysis branch exists in which local post buckling of the panel skin is accounted for [17]. In this branch a constraint condition that prevents stiffener pop-off is introduced into the optimization calculations [1]. The postbuckling theory incorporated into PANDA2 is similar to that formulated by Koiter for panels loaded into the far-postbuckling regime [18].

PANDA2 can be run in five modes:

1. optimization,
2. simple analysis of a fixed design,
3. test simulation,
4. design sensitivity, and
5. load-interaction.

Optimization in PANDA2 is performed with use of the constraint-gradient-based ADS routines created by Vanderplaats and his colleagues [19,20]. There is a processor in the PANDA2 system called STAGSMODEL that automatically generates an input file for the STAGS computer program [21]. Thus, STAGS [4,5,22], which is a general purpose nonlinear finite element analyzer, can be used with reasonable ease to check the load-carrying capacity of stringer-stiffened panels optimized with PANDA2 [21,23].

MODE JUMPING

It has long been known that the optimization of plates, stiffened panels and other thin-walled structural components designed to carry compressive loads may lead to a panel behavior that is governed by clustered bifurcation points or compound bifurcation points [24]. By clustered bifurcation points we mean that along the pre-buckling equilibrium curve of the panel under load, bifurcations occur at values of the load that are very close together, see Fig. 1. It is also well known that under such conditions the equilibrium branches of these bifurcation points are intertwined and display secondary bifurcations. Some of these branches have stable parts, but most of them are unstable. This may, in general, imply imperfection sensitivity because the bifurcations may have become unstable. Improperly formulated automated panel optimization may therefore lead to

designs that fail long before the bifurcation load is reached, so that the computed design optimum does not in fact represent a feasible design [24].

With plates and stiffened panels that are only mildly curved in the transverse direction, the clustering sketched in Fig. 1 may still occur but it does not always lead to a direct lowering of the failure load. There are two subjects that have attracted attention in the literature which are associated with this clustering effect.

The first subject is called "mode interaction", defined as an interaction between a buckling mode of a long wave length with one or more modes of a short wavelength. Structures that exhibit mode interactions may be imperfection sensitive. They have been studied extensively in the literature [25-27].

The second subject is called "mode jumping", defined as interaction between mode shapes of short wave length and other so called "local modes" [6,7,10,11,28-32]. Structures that exhibit mode jumping (Stein's [6,7] is a perfect example) can be loaded above the initial buckling load as shown in Fig. 2a, in which stable equilibrium exists along branch *2*. This initial stable postbuckling phase is followed by a loss of stability as soon as a secondary bifurcation point is reached. Further loading will then result in a dynamic departure from branch *2* to a neighboring stable equilibrium branch *3*. During this transient event the mode shape changes from its current postbuckling form into a different form that belongs to the new stable tertiary branch. This branch may or may not be (statically) connected to the previous branch from which the jump started. The precise situation will depend on the structural configuration and loading. Further loading along stable branch *3* may then end with another jump to yet another stable branch *4* and so on (see Fig. 2a).

The above description of the jumping behavior pertains to a panel that exhibits true bifurcation points along the primary loading path because its geometry is perfectly symmetric. In reality, panels are slightly imperfect so that a modification of the behavior will be observed. First of all, the transition into the first stable buckling mode will occur gradually, such as shown in Fig. 6 of [17]. When the load is further increased, a jump may occur but this will then most likely take place from a limit point rather than a bifurcation point [8]. Even though bifurcations in the branching diagram of a panel will usually disappear when it is imperfect, the overall behavior most often resembles what occurs in the perfect panel. However, the jumps will not always correspond to the same mode changes and may occur at different values of the load from those of the perfect panel.

The jumps that occur in the way just described may not have enough energy content to damage the panel severely if they occur infrequently during service. On the other hand, mode jumping always involves an abrupt change in postbuckling local mode shape. Therefore, the locations of the peak postbuckling bending stresses, which may be substantial, shift along the length of the panel. At a given material point the peak stresses may oscillate during a mode jump, not because the postbuckling deflection lobes oscillate in a manner analogous to a modal vibration (standing waves), but because the lobes translate to and fro in the axial direction, a type of motion that can occur with only very small corresponding oscillation of the end shortening and therefore little change in potential energy. This phenomenon is exhibited in the examples provided here. If this happens repeatedly during service, fatigue could be a problem even if the energy content of the mode jump is low.

Experience with mode jumping indicates that the energy content of mode jumps increases with the jump number (with increasing load) to such a degree that irreparable damage may be sustained even on the first occurrence in service. Caution must be exercised when mode jumping is allowed in a design.

The analysis of a structure that exhibits such behavior is very demanding. In the literature there have been attempts to come to grips with some relatively simple examples of mode jumping, such as in an axially compressed plate strip [10,11,28-32]. Koiter's solution [33] for an infinitely long plate strip in compression for loads far in excess of the first bifurcation load serves as a constructive approximation to the mode jumping problem of a long plate. The report [33] precedes the report [18]. The former is restricted to axial compression only. The latter represents an extension to the combination of axial compression and shear. Koiter's solution [33] can be seen as the solution of the mode jumping problem of a plate strip of infinite length in which the changes in modeshape occur continuously with variation of the load. Koiter's work does not refer explicitly to the phenomenon of mode jumping. Koiter's method determines the stationary value of the potential energy from a response constructed with mode shapes that have continuously variable wavelengths in the axial direction (varying with load, not with axial

coordinate) and variable shapes in the transverse direction.

In PANDA2 the axial wavelength of the postbuckling pattern is also allowed to vary continuously with increasing load in a manner similar to that described by Koiter [33]. Variation of postbuckling deformation over the panel cross section is achieved in PANDA2 by expansion of the postbuckling displacement field in a power series of the critical local bifurcation buckling mode [17].

In the studies [11,28-32] a perturbation technique is applied to construct parts of the branching diagram in the neighborhood of the first two bifurcation points, by means of which the jumping phenomenon can be explored. The practical significance of this approach is rather restrictive, however, because it is very difficult to apply the technique to structures with a more complex geometry. Even if one considers brute-force computational techniques, such as path-following methods [34-36] for the solution of the nonlinear equations generated by finite element models, a complete solution of the branching diagrams of such cases seems to be out of the question.

For the designer a knowledge of the complete branching diagram of a panel that exhibits mode jumping is fortunately not very useful because this diagram is extremely difficult to analyze, especially when the number of interacting modes is large. On the other hand, the possibility to compute the load-deformation path of a panel in space and time and thus to simulate both the static and dynamic behavior of the panel under slowly increasing load offers useful information because it provides the load vs. end shortening relation, a means to compute the energy content of the jumps, and the states of the structure for every load step of the static phases of the analysis and every time step of the transient phases of the analysis. This is now done in STAGS through use of a combination of static path-following techniques and transient methods [8,9,37] described briefly in the section entitled "SIMULATION OF MODE JUMPING IN STAGS". For a stiffened panel that exhibits mode jumping the load vs. end-shortening diagram is similar to that plotted in Fig. 2b.

THE MODE JUMP CONSTRAINT IN PANDA2

Constraints on the design generated via PANDA2 include local buckling of stiffener segments, rolling of stiffeners, local, inter-ring, and general buckling, maximum displacement under pressure, maximum tensile or compressive stress along the fibers and normal to the fibers in each lamina, and maximum in-plane shear stress in each lamina, with stresses computed including load-induced amplification of all of the components of the initial imperfection as well as significant local postbuckling deformation.

A mode jump constraint with the identifying phrase

"Hi-axial-wave post-post-buckling of panel skin"

has been introduced into PANDA2. This constraint can be turned OFF or ON by the user. The purpose of the "mode jump" constraint, which is modeled as a static (bifurcation) event in PANDA2, is to prevent serious dynamic mode jumping from occurring in panels optimally designed for service in the far-local-postbuckling regime. By "serious" is meant mode jumping at loads well in excess of the initial local bifurcation buckling load but still below the design ultimate load. In PANDA2 the "mode jump" constraint, even when turned ON by the user, is activated only if the applied load is at least twice the initial local buckling load.

The following computational steps are used in PANDA2 to generate the "mode jump" constraint for each design evaluation (see Fig. A1):

1. The critical (lowest) local buckling load factor and mode shape are generated for the discretized skin-stringer panel module as described in [1]. The loading is uniform (N_{x0} in Fig. A1). In Fig. A1 the initial local buckling mode is indicated by the large-wave pattern labelled (a). This pattern has 3 axial halfwaves. Initial local buckling may occur at a load factor of 0.1, for example. That is, initial local buckling may occur at one tenth of the design ultimate load.

2. The post-local-buckling equilibrium state of the panel is computed as described in detail in [17]. (See Figs. 10 and 11, for example). In this state the 3-lobed pattern displayed in Fig. A1 would be extremely well developed.

3. The new distributions of the membrane stress resultants, N_x, N_y, N_{xy}, over the entire discretized cross section of the skin-stringer module are derived from the known post-local-buckled equilibrium state. The new distribution of N_x is qualitatively similar to that shown

in Fig. 24 of [1]: N_x is greatly diminished midway between stringers and increased near and in the stringers, as shown in Fig. A1, in which the new nonuniform distribution of axial load is labelled N_{x1}. In Fig. 2a the stresses, N_x, N_y, N_{xy}, belong to the branch *2*.

4. A "post-post" bifurcation buckling problem is set up and solved. This eigenvalue problem is entirely analogous to the initial local bifurcation buckling problem: Bifurcation buckling load factors are computed vs. number of axial halfwaves. However, in the "post-post" bifurcation buckling problem the new nonuniform distribution of N_x over the cross section of the panel module (called N_{x1} in Fig. A1) is used. *Local postbuckling deformations are ignored.* The new search over the number of axial halfwaves is conducted starting from $M = 2m_{crit)}$ where m_{crit} is the critical number of halfwaves determined for initial local buckling. The "post-post" bifurcation buckling mode with number of axial halfwaves, $m^*_{crit} >> m_{crit}$, in which m^*_{crit}, the number of axial halfwaves corresponding to the critical (lowest) "post-post" (secondary) bifurcation buckling eigenvalue, is assumed to be the mode that determines initiation of transfer to Branch 3 in Fig. 2a or Branch *2* in Fig. 2b. In Fig. A1 the critical secondary bifurcation buckling mode has nine axial halfwaves. Whereas the initial local buckling load factor corresponding to three axial halfwaves might be 0.1, the secondary bifurcation buckling load factor corresponding to nine axial halveaves might be 0.6, for example. The computation in PANDA2 corresponds to the determination of a bifurcation point in a fictitious prebuckling state of the panel in which the redistribution of N_x corresponding to the post buckling state at some point on Branch 2 in Fig. 2a is accounted for but buckling deflections are neglected. We hope that in this way we will obtain a good estimate of the load threshold beyond which a dynamic change in the number of axial halfwaves in the far post-locally-buckled state is likely. If this estimate is below the design load and significantly above the initial local buckling load we assume that "serious" mode jumping may take place, that is, the consequences for the structure may be dire.

5. Given the secondary buckling load factor, the "mode jump" margin is computed from the formula:

$$\text{margin} = (\text{secondary buckling load factor})/(\text{factor of safety}) - 1.0$$

6. Gradients of the "mode jump" constraint with respect to small perturbations of each of the decision variables are computed, just as with all other "behavioral" constraints such as general buckling and stress. Then Vanderplaats' ADS optimization routines [19] are called to generate a new design.

As with all behavioral constraints in PANDA2, the "mode jump" constraint is evaluated (for each design iteration or pass through the optimizer ADS) at the current design and at K neighboring (perturbed) designs in which K equals the number of decision variables in the problem. (In the rather simple case discussed in the section entitled "EXAMPLE" there are only three decision variables: height of the stringer, thickness of the panel skin, and thickness of the stringer.) The six steps outlined above (as well as any steps required to determine any other behavior, such as locally postbuckled state, general instability and stress) are traversed many, many times before a final optimum design is achieved. For each design iteration, constraint gradients are established from the difference in behavior (e.g. buckling load factor) at the perturbed design and at the current (unperturbed) design. The amount by which each decision variable is perturbed depends on the maximum sensitivity of behavior to that perturbation.

PANDA2 uses certain short-cuts to obtain perturbed behavior corresponding to each perturbed design. For example, PANDA2 uses buckling modes corresponding to the unperturbed design as starting vectors for iterations to extract the critical eigenvalues and mode shapes for the perturbed designs.

One can appreciate that for more complex panels, such as a laminated composite panel with both stringers and rings and with possibly multiple load sets, one must resort to all sorts of approximations, short-cuts, and "tricks" to obtain reasonably accurate predictions with as few calculations as possible. It is admitted that the "mode jump" predictor used in PANDA2 is a crude one (especially since only the redistribution of N_x, N_y, N_{xy} in the post-local-buckling regime is accounted for, with the effect of local normal deflections ignored). Its effectiveness should be tested through extensive application of PANDA2 and STAGS.

THE STAGS PROGRAM

STAGS (Structural Analysis of General Shells), is a shell finite element program with a strong bias towards stability analysis capabilities [4,5,22]. Apart from

having a good nonlinear shell modeling capability (small strain but arbitrarily large displacements and rotations), STAGS is also equipped with path-following techniques that make it possible to solve stability problems such as bifurcation buckling and collapse. The modeling capabilities include many design features that are frequently encountered in lightweight structures in the field of aero- and astronautics: a whole range of stiffener models, shell wall materials including composites, etc. In addition to the solution techniques for computing the static equilibrium branches of these models, STAGS also possesses robust transient time stepping methods. It is the unique availability of a combination of advanced static and transient solution strategies that proves most effective in the cases where mode jumping plays a role. We will discuss these particular types of calculations in the following section.

SIMULATION OF MODE JUMPING IN STAGS

As follows from the discussion in the section entitled "MODE JUMPING", the phenomenon of mode jumping is simply a collapse or snap buckling event as described by the theory of elastic stability: a transient change of deformation that occurs at a value of the load equal to or slightly in excess of the critical load that belongs to the bifurcation point or limit point. The only difference with the classical notion of collapse is that such a jump is not necessarily detrimental to the integrity of the structure. Damage depends on the frequency of occurrence during service of the structure, on the number and amplitude of stress oscillations precipitated by the jump and whether or not these oscillations involve stress reversal, and on the energy release associated with the jump, that is, the difference between the potential energy of the structure before and after the jump. In some plate structures for example the energy release can be so small that a series of successive jumps can perhaps be tolerated as the load increases up to and beyond a specified maximum (the design load).

According to the theory of elastic stability, collapse takes place at an unstable critical state of equilibrium [9,38,39] Unstable critical points in general are either a proper limit point (A) or unstable bifurcation points (B,C) in Fig. 3. Before such a point is reached (when the load is still below the critical value) the equilibrium is stable. At such a state a small externally applied perturbation will be counteracted by the structure in such a way as to restore the perturbed state to the original equilibrium state. A stable equilibrium point is therefore called a point of attraction.

When an unstable critical state is exceeded the property of restorative reaction forces is impaired. At this point there may be one or more particular perturbations from the equilibrium state that will induce a repellent reaction in the structure. The repellent force works in the direction of these special perturbations and thus initiates a motion that is divergent. The motion that develops in this way will gain momentum at a rate that depends on the amount of potential energy freed and converted into kinetic energy. In the actual situation and also in our simulations this motion is resisted by damping. Therefore, if a stable post-jump static equilibrium state exists at the load level corresponding to mode jumping, the kinetic energy will eventually decay. The motion will subside at another attractor, a stable equilibrium state that acts as a new focus for the orbit that the motion follows, such as Branch *3* in Fig. 2a..

The special direction of the perturbation that will best initiate the transient motion from the unstable critical state turns out to be given by the *buckling mode* associated with this state in the following sense: the perturbation should point to the *unstable* branch *1* of the limit point (Fig. 3A) or the unstable branch *2* that goes through the bifurcation point [8,9] (Figs. 3B,C). Please note that this figure, as well as Figs. 1 and 2, represents a *projection* of the general solution in an $N+1$ dimensional space of displacement variables N and the load intensity factor λ, to a 1+1 dimensional space of one displacement component and the load factor λ. In Fig. 3 the direction of the displacement component is the buckling mode, the amplitude of which is denoted μ.

To make use of these findings, we adopted in [8,9] the following computational strategy. We first compute the fundamental state of the panel previously optimized by PANDA2 using the standard path-following technique available in STAGS [35]. In Fig. 3 this computation is symbolically indicated by the small open circles along the primary paths denoted by *1* (an open circle is a solution point). Critical points that are part of these paths betray themselves in various ways, for example through sign changes of the determinant of the stiffness matrix or changes in the number of negative entries on the main diagonal of the factored stiffness matrix. It is possible with a simple technique to determine the critical states with some accuracy [34-36], but this is not always required in the type of analysis that we consider here. The identification of the type of critical

point, limit or bifurcation and stable or unstable, is more important.

In the case of a limit point the identification is trivial because in that case the load will reach and pass a maximum during the solution, an event that is easily monitored. In the case of a bifurcation point, the matter is slightly more complicated because a bifurcation point is a critical point that cannot in general be detected by observing the load factor. What usually happens is a change of sign in one or more of the diagonal terms of the factored stiffness matrix without a reversal of the sign of the path derivative of the load λ. However, to identify what type of bifurcation is encountered, we are required to conduct a calculation of the branch at the bifurcation point. This is possible in STAGS with the aid of a branch switch procedure [22]. Once small parts of the branches *2* in Fig. 3 are computed, we also know whether we have an unstable skew symmetric point (B) or an unstable symmetric point (C) or a stable symmetric point D.

After these preparations, we continue the analysis by computing the path that the actual structure follows. In the case of a stable symmetric point (D) the structure will follow one of the stable branches *2*. The switch procedure mentioned earlier acts to initiate such a computation. In this case we continue with the static path-following procedure because the structure does not jump at such a state but instead follows a different stable equilibrium branch. There is a gradual change of the deformation with increasing load. This happens in one of the cases explored here (Fig. 18a,b).

More interesting are the unstable states B and C. To conduct a simulation of the transient buckling process that starts from these points, we use an implicit transient time stepping procedure called Park's method [40]. To start the computations in a way that is in agreement with what we know about the properties of the unstable points, we assume initial conditions as indicated in Fig. 3 by the solid points with arrows:

1. In the case of the limit point (Fig. 3A), we start the time integration from an equilibrium point beyond the limit point by setting the load parameter to a value just above the limit load.

2. In the case of the unstable bifurcation points B and C, we take a point computed earlier on the unstable (descending) branch as the initial condition with the load again adjusted to a value that slightly exceeds the critical load. This type of initialization will insure that the structure will enter the post-jump orbit [8,9] if a stable post-jump equilibrium state exists at that load level.

In most simulations of this sort the limit point is the most frequently encountered point of loss of stability. This means that we can set up the initialization with almost no effort. In the case of a bifurcation point the procedure described above is appropriate but it sometimes needs branch switching [22] in order to find the descending branch *2*.

Often we can avoid the branch-switching calculations after crossing a critical point by taking advantage of slight numerical round-off errors in solutions computed with standard path-following methods. These tiny errors represent perturbations from the actual equilibrium state that usually contain enough of the critical bifurcation buckling modal component to turn a transient solution toward the unstable buckling modal direction. This means that we can also try, with some confidence, to start from the unstable points on the primary branch *1* just above the critical load, with the expectation that the system will gain momentum as energy is released. Experience has shown that this approach almost always works, although it may take more time for the system to gain momentum as compared with the procedure sketched earlier. It may also be very useful to add a small initial velocity proportional to the unstable mode, an option that is available in STAGS.

EXAMPLE

We present here a relatively simple example of a uniformly axially compressed, flat, blade-stiffened, steel panel that is optimized with PANDA2. Two alternative optimum designs are produced: PANEL I with the mode jump constraint OFF and PANEL II with the mode jump constraint ON.

The two optimum panel configurations thus obtained are then analyzed with STAGS to verify the reliability of the PANDA2 predictions.

The PANDA2 Optimization and analysis

Tables 1 and 2 provide the problem parameters and Figs. 4 - 14 display results from optimization and analysis of the optimized panel with PANDA2. The

following boundary conditions are used: the panel is clamped at the two axially loaded ends. Wide-column behavior [1] is assumed, that is, the behavior of the entire stiffened panel is modeled with use of a single skin-stringer module [1] with symmetry conditions applied midway between stringers. See Fig. 22(c) in [1] for example. In PANDA2 local buckling of the single module model is generated by forcing the normal displacement along one longitudinal edge to have the opposite sign from that along the opposite longitudinal edge (See Fig. 10).

Fig. 4 shows the evolution of the objective function (total panel weight) as a function of design iteration. For the first 15 design iterations the "mode jump" constraint, "Hi-axial-wave post-post-buckling of panel skin", was turned OFF. That is, the panel was optimized without regard to the probability of mode jumping occurring at some load between the initial buckling load and the design load. At Iteration No. 15 the local buckling load factor is very close to $\lambda_c = 0.1$ (buckling load = 0.1 x 5000 = 500 lb/in). The optimum design at this point is called "PANEL I".

At Iteration No. 15 the "mode jump" constraint was turned ON, and design iterations were continued with "mode jump" turned on until convergence to a somewhat heavier optimum design was achieved at Iteration No. 29. This second optimum design is called "PANEL II". Note that the weight of the panel increases significantly after the "mode jump" constraint is turned ON. The optimum weight with the "mode jump" constraint ON, 152 lbs., is about 20% higher than the optimum weight, 126 lbs., with the "mode jump" constraint turned OFF. Since this represents a considerable sacrifice, one must prove the necessity of turning ON the "mode jump" constraint. This is accomplished later by demonstrating via STAGS that at a load considerably less than the design ultimate load significant oscillations of peak stresses , with stress reversals, occur during a mode jump in the optimized panel with the "mode jump" constraint turned OFF (PANEL I).

Figure 5 displays the evolution of all margins less than unity during all design iterations. (NOTE: margin = design constraint - 1.) At Iteration No. 15 the design margins presented in Table 3 are critical or close to critical. No "mode jump" constraint is listed there because it is still turned OFF. The "mode jump" constraint appears in Fig. 5 only between Iterations 15 - 29, after it has been turned ON by the user of PANDA2. For those iterations the "mode jump" constraint is critical and therefore affects the evolution of the design.

In Table 3 are listed three margins that all represent models of general instability, Margins 6, 10, and 14. Margin 6 is computed from a single discretized module model analogous to that shown in Fig. 22(b) of [1]. The wide column buckling mode resembles that shown in Fig. 22(c) of [1], that is, the skin-stringer cross section is permitted to deform in this representation of general buckling. (In Fig. 22 of [1] the panel is TEE-stiffened; here the panel is blade-stiffened.). Margin 10 is computed from a wide column model in which the stringers are smeared out and Donnell's theory is used to compute the general buckling load factor from the theory set forth in [3]. Margin 14 is computed from the same model as Margin 10 except that Sanders' theory is used [14] rather than Donnell's theory.

Figures 6 and 7 show the evolution of the design.The primary effect of turning ON of the "mode jump" constraint at Iteration No. 15 is to cause the thickness of the panel skin to increase.This results in the initial local bifurcation buckling load being increased to such a degree that the panel as loaded by the design load, N_x = -5000 lb/in, is no longer far enough into its locally postbuckled state for the redistribution of N_x over the module cross section, as shown schematically in Fig. A1, to give rise to secondary bifurcation buckling (mode jumping) at a load below the design load.

Figures 8 - 14 show results obtained from PANDA2 used with the "test simulation" option, that is, an option in which the panel design is fixed and the applied axial load N_x is increased in steps. These results correspond to the optimized design at Iteration No. 15 (PANEL I: panel skin thickness = 0.057075 in.; stringer thickness = 0.16871 in.; stringer height = 1.6074 in.).

Figure 8 shows PANDA2's prediction of how the number of axial halfwaves in the local postbuckled pattern increases with N_x. PANDA2's treatment of number of axial halfwaves is similar to Koiter's [18,33]: the number of axial halfwaves computed in the postbuckling regime is permitted to vary continuously with load as if the panel were infinitely long. Details of how this is done in PANDA2 are given in [17]. The change in number of axial halfwaves from that at the bifurcation load (7 halfwaves in this case) to that at the design load, N_x = -5000 lb/in, (about 9.2 halfwaves in this case) is, of course, accounted for by PANDA2 during its computation of the stresses in the locally postbuckled panel. This predicted change in the number

of axial halfwaves is in reasonably good agreement with STAGS results, as will be shown later.

Figure 9 shows how the membrane tangent stiffness components, $C_{11}^{tan}, C_{22}^{tan}, C_{33}^{tan}$, in the panel skin decrease in the local postbuckling regime. This decrease in skin tangent stiffness is, of course, accounted for in the computation of the 6 x 6 integrated constitutive matrix C_{ij} that governs overall buckling of the locally postbuckled panel. In this way the interaction of long and short wavelength buckling modes of the type discussed in [25-27] is accounted for in PANDA2.

NOTE: PANDA2 uses the postbuckled state only at the MIDLENGTH of the panel in the computation of the tangent stiffness components, $C_{11}^{tan}, C_{12}^{tan}, C_{22}^{tan}, C_{33}^{tan}$. This limitation has significant consequences in the case of PANEL I, as will be discussed later in connection with Fig. 32. It is emphasized that PANDA2 is based on a theory in which it is assumed that all local behavior, such as the postbuckled state, varies trigonometrically along the entire length of the panel with no axial modulation of the short wavelength postbuckled lobes as they interact with overall axial bowing of the panel.

Figure 10 displays the deformed PANEL I module cross section for five values of axial compression. The deflection is amplified by a factor of eight. In a test the actual deformed panel skin would probably not exhibit the reversals in transverse curvature near the two longitudinal edges (midway between stringers: at abscissa coordinates 0 and 10 in Fig. 10) shown here for $abs(N_x)$ greater than 2000 lb/in. These reversals are doubtless a consequence of the limited expansion in PANDA2 of local postbuckling deflection in terms of local bifurcation buckling mode shape [17]. As written in Eq. (24) of [17] only two terms are used in this expansion, the linear and the cubic term. The consequence for design is not serious, it is thought, because the region of panel skin near the longitudinal planes of symmetry (midway between stringers) are under much less axial load in the far postbuckling regime than are the stringer and skin near the root of the stringer. Hence, critical stresses and strains are unlikely to occur in the region of panel skin where PANDA2's estimates of local postbuckling deflection are the least accurate.

Figure 11 shows a three-dimensional view of the local postbuckling deflection for a length of panel that spans one full axial wave of the post-local-buckling deflection pattern.

Figures 12 - 14 display axial, hoop (transverse to axial direction and in the plane of the panel skin), and in-plane shear strain components at the extreme fibers. The extremes of these values are later plotted in Figs. 26-28, which contain predictions from STAGS for PANEL I.

Note that up to Iteration No. 15 the "mode jump" constraint is turned OFF. Therefore, it is not included in the list of margins in Table 3 and of course does not affect the evolution of the optimum design up to Iteration No. 15. The design at Iteration No. 15 is judged by PANDA2 to be FEASIBLE because there are no significantly negative margins. (In PANDA2, designs are called FEASIBLE if all margins are greater than -0.01; designs are called ALMOST FEASIBLE if all margins are greater than -0.05; otherwise designs are called INFEASIBLE.)

After optimization with the "mode jump" constraint turned OFF, the PANDA2 user turns the "mode jump" constraint ON. At the zeroth iteration with the "mode jump" constraint ON (still at Iteration No. 15 in Figs. 4 - 7) the following margin is added to those just listed:

5 -3.19E-01 Hi-axial-wave post-post-buckling of panel skin -1; M=17 ; FS=1.0

The "mode jump" constraint is significantly negative. PANDA2 now rejects this design as INFEASIBLE because of the presence of this significantly negative margin. This margin is plotted in Fig. 5 starting at Iteration No. 15. Immediately after "mode jump" has been turned ON, PANDA2 finds that "post-post" bifurcation buckling occurs with $M = 17$ axial halfwaves and at a load factor of 1.0 - 0.319 = 0.681. Bifurcation buckling with use of the nonuniform N_x computed from the "Koiter branch" [17] of PANDA2 occurs at a load factor of about two thirds of the design ultimate load and with a mode shape that is analogous to that indicated by "(b)" in Fig. A1 (with 17 axial halfwaves rather than the 9 axial halfwaves shown schematically in Fig. A1). Design iterations are continued from Iteration 15 through Iteration 29 with the "mode jump" constraint turned ON, leading to a new, considerably heavier optimum design at Iteration No. 29 with the margins listed in Table 4.

This new, heavier design has a local buckling load factor of approximately $\lambda_c = 0.19$ (axial load = 0.19 x 5000 = 950 lb/in), almost twice that of the optimum

design obtained at Iteration No. 15 with "mode jump" turned OFF.

The STAGS analysis

In this section results from two STAGS analyses are reported:

1. a STAGS analysis of PANEL I, that is, the panel corresponding to the optimum design obtained with the mode jump constraint OFF (See Iteration No. 15 in Figs. 4, 6, 7). The values of the three decision variables at Iteration No. 15 are:

panel skin thickness	T(1) = 0.057075 in.
stringer thickness	T(2) = 0.16871 in.
stringer height	h = 1.6074 in.

2. a STAGS analysis of PANEL II, that is, the panel corresponding to the optimum design obtained with the mode jump constraint ON (See Iteration No. 29 in Figs. 4, 6, 7). The values of the three decision variables at Iteration No. 29 are:

panel skin thickness	T(1) = 0.075452 in.
stringer thickness	T(2) = 0.16256 in.
stringer height	h = 1.5896 in.

The STAGS finite element models are automatically generated with use of the PANDA2 data base via the PANDA2 processor called STAGSMODEL [21]. During execution of STAGSMODEL the user is prompted interactively for certain data. Among these prompts are the following two:

"Number of modules in the STAGS finite element model, NSTIF"

and

"Edges normal to screen (0) in-plane deformable; (1) rigid"

In the cases explored here the STAGSMODEL user's response to the "Number of modules..." prompt was "1". There is no anisotropy and no applied or Poisson-ratio-induced hoop resultant N_y nor in-plane shear resultant N_{xy}. The wide-column model is used to represent general instability. Therefore, a STAGS model with only a single module (one stringer with panel skin of width *b/2* on each side of the stringer, where *b* = stringer spacing) is sufficient to predict with reasonable accuracy what happens when the panel of axial length 50 inches and transverse length 100 inches is uniformly axially compressed.

NOTE: In both the PANDA2 and the STAGS models it is assumed that the two axially loaded "clamped" ends of the panel are free to undergo Poisson-ratio transverse expansion under the axial compression. Therefore, no membrane hoop compression, N_y, builds up in the neighborhoods of the ends of the panel as the axial load is applied.

In all cases explored here except one the STAGSMODEL user's response to the "Edges normal to the screen..." prompt was "0". All of the results in this paper except those corresponding to Fig. 33 were obtained with the "in-plane deformable" option, which is felt to be the more conservative (leading to earlier failure of the panel according to STAGS). Fig. 47 of [21] shows a comparison of deformations, with use of both "1" (Fig. 47a) and "0" (Fig. 47b) in response to the "Edges normal..." prompt, for a panel with three modules under combined axial compression and in-plane shear. For an axially compressed panel with use of only a single module in the STAGS model, the "(0) in-plane deformable" option might lead to significantly larger maximum normal displacements in the panel skin in the far post buckling regime predicted by STAGS than those predicted by PANDA2, seen during a test of a multi-module specimen, or seen in the internal bays of a multi-module STAGS model, especially if the panel skin has a large Poisson ratio such as would be the case for a panel skin with an angle-ply laminate with layup angle, $\theta = [\pm 45]_n$. A multi-module STAGS finite element model would require much, much more computer time because there would be far more finite elements in the model and the bandwidth of the stiffness matrix would be far greater than it is in the single-module model.

The following sequence of STAGS runs is performed for the analysis of each structure, such as PANEL I and PANEL II:

1. The critical local bifurcation buckling mode and eigenvalue is first determined from linear theory. This is done in order to obtain an imperfection shape for the static nonlinear STAGS run to follow and to provide a comparison with PANDA2 predictions of local bifurcation buckling.

2. A STAGS nonlinear static run or a series of runs is executed in order to load the panel as far as possible without having to conduct any special transient runs to follow dynamic mode jumping behavior. A typical series of such STAGS runs is listed in Table 2 of [21].

3. A series of STAGS nonlinear dynamic runs is executed in order to follow mode jumping and possibly to achieve post-jump static equilibrium. Damping constants are used in these runs so that convergence will be achieved to a stable post-jump state if any such state exists. The load factor is held constant during this series of transient runs at a level two per cent higher than the highest load factor for which STAGS obtained a converged solution in the previous series of nonlinear static runs.

4. A STAGS nonlinear static run or series of runs is executed from the post-jump stable state up to the collapse load, or to the next mode jump if there is one.

The "410" finite element was used throughout the STAGS analyses reported here.

STAGS results for PANEL I

Figures 15 - 32 pertain to this subsection. Fig. 15 shows the local critical buckling mode of two single-module STAGS models: Model 1 has finite elements fairly uniform in size throughout. Model 2 has very narrow finite elements in the panel skin near the stringer and a more refined mesh on one side of the stringer than on the other. The purpose of Model 2 is primarily to capture with more accuracy the extreme fiber post-local-buckling hoop stresses in the panel skin adjacent to the blade. These high hoop bending stresses result from the large change in hoop curvature under the blade, especially evident in Fig. 10. As will be seen later (Fig. 30) these high hoop bending stresses oscillate immediately after the mode jump.

PANDA2 predicts local buckling with seven axial halfwaves at a load factor close to 0.1. In the PANDA2 local buckling model the panel skin is assumed to be simply supported at the axially loaded ends even though the entire panel module (skin plus stringer) is clamped there. In the STAGS model the skin is clamped, except for transverse in-plane displacment v which allows Poisson-ratio expansion as mentioned previously. In-plane rotation of the stringer web is prevented. Allowing for these differences in boundary conditions in the PANDA2 and STAGS models, one sees that there is very good agreement between PANDA2 and STAGS for the buckling mode and load factor. (Also see Fig. 18a).

Figures 16 and 17 show the results of the first STAGS nonlinear static run on PANEL I with finite element Model 1. For this run a buckling modal imperfection amplitude of 0.005 inch was used. With use of nonlinear statics STAGS is unable to explore the region with load factor PA greater than 0.648 (Load Step 62). It appears that at a load factor of slightly more than 0.3 (Load Step 22) the panel experiences a gentle mode jump, that is, gentle enough that the Riks static path-following strategy can find equilibrium states for higher loads than the local peak at Load Step 22. The static solutions determined by STAGS beyond Load Step 62 appear to be on the same equilibrium curve as those covered between Load Step 42 and Load Step 62. It is therefore necessary to use the dynamic mode jumping strategy in order to determine the behavior of PANEL I for load factor, PA > 0.648.

The finite element Model 1 (Fig. 15a) was used to generate Fig. 18. Figure 18 displays edge-on views of the locally postbuckled PANEL I corresponding to five load steps during the initial static loading phase (a-e) and to the first static load step following the transient run and complete load relaxation (f). (Step 955 is the first static load step after the transient run for which the panel is in a state of static equilibrium. The load factor, PA = 0.6605 at Step 955). In Fig. 18 the amplitudes of the postbuckled normal displacements in the panel skin are the same in all six frames even though these frames correspond to different levels of applied load: a default option for deformation scaling, zero, was used in the input data required for the STAGS postprocessor, STAPL. This default causes the maximum displacement to be scaled to a certain fraction of the length of the undeformed structure. The purpose of this figure is not to demonstrate the growth or diminuation in the amplitude of the postbuckling deflection with changing applied load but rather to show how the number and position of axial halfwaves changes during loading.

Figure 18 contains several significant results:

1. Figure 18a demonstrates that the post-local-buckling mode from STAGS agrees well with that from PANDA2. While there are only six axial halfwaves along the length of the panel in the STAGS model rather than seven as predicted by PANDA2, the axial

wavelength of each of the halfwaves is close to one seventh of the panel length. There are regions near the clamped ends in the STAGS model where there is small deflection because in the STAGS model the panel skin cannot rotate about a normal to the plane of the paper. This rotation constraint is absent in the PANDA2 model of local buckling and postbuckling of the panel skin, as mentioned previously.

2. From Fig. 18b we see that there are seven axial halfwaves along the length of the panel rather than six, as displayed in Fig. 18a. Hence there has been a mode "jump" (transition from one equilibrium branch to another) in the sense that the postbuckling state has changed in a non-proportional way between Load Step No. 10 and Load Step No. 22. The number of axial halfwaves has increased in spite of the fact that the applied load increases monotonically between Load Step No. 10 and Load Step No. 22, as shown in Fig. 17. This "gentle" transition is the stable type shown in Fig. 3D.

3. In Figs. 18(a-c) the postbuckling lobes on either side of the stringer are in phase with respect to axial variation. These states are in agreement with the PANDA2 model, which, being based on a "strip" method, requires in the absence of in-plane shear loading and anisotropy of the panel skin, that the postbuckling lobes on either side of the stringer always be in phase with eachother with respect to the axial coordinate because discretized deflections of the type shown in Fig. 10 are assumed to vary trigonometrically in the axial direction and the nodal lines of the postbuckling lobes have zero slope [17]. Note that in Figs. 18(d-f) the postbuckling lobes are out of phase in the STAGS model even though the panel skin is isotropic and there is no applied in-plane shear loading N_{xy}. This difference in the PANDA2 and STAGS predictions affects the predictions of stress and strain distributions and locations and values of maximum stresses and strains.

4. From Figs. 18b and 18c we see that as the panel unloads between Load Step No. 22 and Load Step No. 42 (Fig. 17), there appears one additional axial half wave in the postbuckled state. In an experiment on this panel a gentle dynamic "mode jump" would probably occur near the load factor corresponding to Load Step 22. We did not have to resort to a special transient STAGS run in this case because the static path-following technique was capable of tracking the changes in state of the panel during this presumably mild mode jump.

5. From Figs. 18(d,e) we see that the phase discrepancy between postbuckled lobes on either side of the stringer increases as the applied load increases. The number of axial halfwaves remains the same.

6. From Figs. 18(e,f) we see that during the many-stepped transient phase the number of axial halfwaves jumps from 8 to 10. The postbuckled lobes on either side of the stringer remain out of phase. (More details about the change in pattern of postbuckling lobes during the transient phase will be given later for PANEL I in connection with the finite element Model 2).

7. Fair agreement is obtained between PANDA2 and STAGS for prediction of the increase in the number of axial halfwaves as the panel is loaded into its far postbuckled state. (Compare Figs. 8 and 18).

Figure 19 displays results from a series of STAGS dynamic runs. The initial load at Load Step 63 is set at 1.02 x 0.648 = 0.6605, slightly above the equilibrium branching, as shown schematically in Fig. 3. At Load Step 950 the dynamic behavior is judged to have decayed enough to permit resumption of static loading.

In this case a single post-transient nonlinear static run was required to bring the applied load to within 99 per cent of the design load (PA = 0.99). At this point STAGS was unable to continue in a static mode. From results obtained via the STAGS postprocessor STAPL, we were able to determine that the panel was in the process of collapsing. Hence, no additional STAGS runs were made for this case.

Figure 20 shows the complete load-end-shortening curve for Model 1 of PANEL I. The transient phase occurs at a single load factor, PA = 0.6605. This load level agrees reasonably well with PANDA2's prediction of "post-post" bifurcation: "post-post" bifurcation buckling load factor = -0.319 + 1=0.681. (See Fig. 5, the curve labeled "Hi-axial-wave post-post buckling of skin"; at Iteration No. 15 the "mode jump" margin is equal to -0.319). For PANEL I, PANDA2 predicts collapse at a load factor of 1.1 rather than the 0.99 from STAGS. Later an explanation is offered for this discrepancy.

Figure 21 shows the growth of postbuckling deflections before the mode jump, and Fig. 22 shows the same after the mode jump. Comparison of Fig. 21(d) with Fig. 22(a) reveals that during the mode jump one additional full wave appears in the locally buckled panel. Figure

22b shows that the panel is collapsing in an overall bowing mode in which the stringer is on the convex side.

Figures 16-22 all correspond to PANEL I with use of the finite element Model 1 displayed in Figs. 15a, 21 and 22. Since Fig. 10 exhibits a rather concentrated hoop (transverse) bending of the panel skin in the immediate neighborhood of the stringer, we decided to use a more refined finite element model, especially for the panel skin segment under and near the stringer. This more refined finite element model of PANEL I, called Model 2, is depicted in Fig. 15b and in Fig. 23.

As can be seen from Fig. 23 the maximum effective stress at the load factor, PA = 0.6875, is predicted by the STAGS Model 2 of PANEL I to be about 140 ksi. This very high effective stress is concentrated in extremely small regions in the panel skin very near the stringer. With Model 1 the maximum effective stress depicted in an analogous plot is about 110 ksi. The reduction in the peak effective stress is mostly caused by an averaging of results over each element required by the STAGS postprocessor STAPL to generate fringe plots and partly caused by Model 1's inability to capture the steep change in postbuckling hoop curvature change of the panel skin in the immediate neighborhood of the stringer.

Note that the maximum effective stress in Model 2 of PANEL I at load factor PA = 0.6875 is very, very high (140 ksi). As listed in Table 1, the allowable effective stress was set in this case to a very high number: 1000 ksi. Therefore, the examples explored here are impractical in a strict engineering sense. The allowable effective stress was set very high in order to avoid active stress constraints from forcing the panel skin thickness to increase so that the "mode jump" constraint does not become active, or only becomes active very near the design load. Early attempts at setting up a good example for use in this study of mode jumping ran into this problem. We wanted a panel optimized by PANDA2 with the "stop modejump" constraint turned OFF to exhibit serious mode jumping at a load considerably less than the design load. In order for this to happen the panel has to be optimized for service in the deep postbuckling regime. Very high local bending stresses are likely to occur in such panels. We therefore used the simple expedient of setting the allowable effective stress very high. We can, of course, still compare maximum stresses and strains obtained from PANDA2 and STAGS for this fictitious material. In future work on mode jumping, many, many examples, especially involving composite laminated panels, should be explored with use of realistic allowables for stress. Such a broad study is beyond the scope of this paper, which we regard as an introduction to optimization of panels in which mode jumping plays a significant role.

Figures 24 and 25 show the histories of the upper surface PANEL I skin hoop stress at the midlength of Model 1 (Fig. 24) and Model 2 (Fig. 25) in the finite element adjacent to the stringer where the maximum hoop stress occurs anywhere in the panel just before the transient phase of the analysis is initiated. With Model 1 the transient phase is conducted at a load factor, PA = 0.6605, and with Model 2 the transient phase is conducted at a load factor, PA = 0.7013. Both of these values of PA are two per cent above the maximum load factor for which STAGS was able to obtain a static solution. After correcting for the fact that the transient response phases of the STAGS analyses occur at slightly different load levels, we see from Figs. 24 and 25 that Model 2 predicts maximum hoop stress during the transient phase that is about 22 per cent higher than that that would be predicted with Model 1 at the same load level. Hence, the refinement in the finite element model is worthwhile.

It should be mentioned that in the initial static phase of the analysis the static path-following technique behaved quite differently for Models 1 and 2. With Model 1 a single static run was able to follow the the curve shown in Fig. 17 up to the maximum load factor, PA = 0.648, with use of only a single buckling modal initial imperfection, that shown in Fig. 15a. With Model 2 and use of the buckling modal initial imperfection shown in Fig. 15b, STAGS failed to obtain any static solution above a load factor of about 0.29. Before quitting at PA = 0.29, STAGS computed a buckling eigenvalue and eigenvector corresponding to the postbuckled state of the panel. The eigenvector, with an amplitude of 0.002 in., was used in addition to the original linear buckling mode shown in Fig. 15b as a new combined initial imperfection. Another static run was made starting from zero load. This time STAGS failed to find any static solution above a load factor of about 0.4. STAGS again computed a buckling mode at PA about 0.4, and this mode, with an amplitude of 0.0015, was added to the two previously determined buckling modes as a new combined initial imperfection. A final static run was then made from zero load. This time STAGS was able to follow the static equilibrium path, in 39 load steps, up to a load factor of 0.6875, at which point the transient phase of the analysis of Model 2 was initiated.

The technique of using multiple static nonlinear runs, accumulating with each failed run a new imperfection component or components and then starting over again at zero load, is described in Table 2, p 584 of [21]. This was the only way to entice STAGS to cover a complete load range in severely nonlinear and nearly singular systems before recent improvements [8,9].

Figures 26 - 28 show maximum strain components predicted from STAGS and PANDA2 for Model 2 of PANEL I. The PANDA2 points are read from Figs. 12-14. PANDA2 and STAGS agree well for maximum axial strain. For hoop strain and in-plane shear strain PANDA2 yields reasonably good agreement for load factors less than that for which the mode jump occurs. Beyond that STAGS predicts much more steeply increasing stresses with increasing load factor PA than does PANDA2. Most of the discrepancy is doubtless related to the fact that STAGS predicts a collapse load factor very close to 1.0 (Fig. 20), whereas PANDA2 predicts wide column buckling at a load factor very close to 1.1 (Margin No. 6 in Table 3). This discrepancy is explained later.

Fig. 29 is analogous to Fig. 18, except that Fig. 29 is based on finite element Model 2 rather than Model 1, and details of the change in postbuckling pattern are obtained only for the transient phase of computation. The six "snapshots" in Fig. 29 correspond to the six points indicated (a-f) in Fig. 30.

Each "snapshot" corresponds to a time for which the hoop stress plotted in Fig. 30 is at or near an extreme of its oscillation range. Careful inspection of the patterns in Fig. 29 reveals that what causes the oscillation of hoop stress plotted in Fig 30 are fairly small axial shifts in the buckling lobes. A given point anywhere along the panel length (except in the neighborhoods of the two ends) will "see" axial waves pass to and fro during the mode jump. The extreme fibers in the panel skin in the immediate neighborhood of the stringer will therefore experience alternate tension and compression in the hoop direction as the panel wall flexes during these repeated axial translations of the postbuckling lobes.

This type of behavior might very well cause delaminations in a composite panel or fatigue in any panel. Because of this oscillating behavior of stress, with significant repeated stress reversals, we strongly recommend that optimum designs be obtained from PANDA2 with the "prevent mode jump" switch always turned ON.

Figure 31 displays the end shortening of Model 2 of PANEL I during the transient phase. Note that the transient behavior is associated with very little change in energy: there is very little transient axial motion at the end of the panel and hence very little dynamic work done by the applied axial load N_x, particularly for times greater than about 50 milliseconds. In spite of this, there are significant oscillations of maximum hoop stress throughout the time spanning the transient phase of the analysis (Fig. 30). Hence, it is felt that panels designed for service in the post-local-buckling regime should ALWAYS be optimized with the "stop modejump" switch turned ON in PANDA2.

For PANEL I, PANDA2 predicts collapse (wide column buckling: Margin No. 6 in Table 3) at a load factor of 1.1 [NOTE: (buckling load factor) = (FS)*(Margin+1) in which FS means "factor of safety"]. STAGS predicts collapse of PANEL I at a load factor very close to unity. It is felt that the 10 percent discrepancy is caused by the fact that PANDA2 uses the postbuckled state only at the MIDLENGTH of the panel to generate the distribution of effective axial stiffness over the cross section of the discretized panel module. This distribution of postbuckled axial stiffness is used for computation of the wide column buckling load factor. Figure 22b shows the deformation pattern in PANEL I predicted by STAGS very near collapse. A plan view of this deformation pattern appears as an insert in Fig. 32. Note that there is considerable sidesway of the blade near the clamped ends. This sidesway leads to a loss of effective axial stiffness of the blade, especially near the tip of the blade. The loss of effective axial stiffness in the blade leads to considerable reduction in the effective overall "EI" of the wide column near the clamped ends. This local loss of overall "EI" is of course "seen" by the STAGS model whereas it is not "seen" by the PANDA2 model. At the midlength of the panel the amplitude of blade sidesway is greatly reduced because the panel bows in a direction such that the tip of the blade is under less axial compression than the root of the blade. Since PANDA2 uses the blade sidesway at the midlength of the panel in its computation of postbuckled effective axial stiffness, it yields a higher wide column buckling load factor than does STAGS.

Figure 32 shows axial bowing as predicted by PANDA2 and STAGS. The theory used by PANDA2 is explained in ITEM 82 of [41]. Axial bowing as predicted by STAGS increases very steeply for load factor, PA > 0.85, presumably because of the reduction in effective overall "EI" near the panel ends as

discussed in the previous paragraph. This difference in prediction of overall behavior of PANEL I for loads approaching the design load, PA = 1.0, doubtless accounts for the differing steepnesses of the curves from PANDA2 and STAGS for hoop and in-plane shear strain with increasing axial load plotted in Figs. 27 and 28, respectively. Fortunately, this type of discrepancy seems to occur only for panels loaded very far into the postbuckling regime. As will be seen later, a similar discrepancy in results between PANDA2 and STAGS does not exist for the panel optimized with the "prevent mode jump" constraint turned ON.

PANEL I was investigated again with use of STAGS. This time Lagrange constraints were introduced into the STAGS model that force the in-plane transverse displacement component v to vary linearly from one end of the panel to the other along the two unloaded (longitudinal) edges. This "straight-edges" model requires much more computer time than the model in which in-plane warping of the longitudinal edges is permitted because the bandwidth of the stiffness matrix increases from 144 to 364 for finite element Model 2. The load-end-shortening curve displayed in Fig. 33 requires about 20 hours on a DEC-ALPHA, half of that time spent for execution of about 700 time steps during the transient phase of computations. STAGS was able to track the static equilibrium curve up to a load factor, PA = 0.934 in a single run. The collapse load predicted with the "straight-edges" STAGS model is within one per cent of that predicted with the the earlier models in which in-plane edge warping was permitted.

STAGS Results for PANEL II

Figures 34 - 40 pertain to this section. PANEL II has dimensions corresponding to Iteration No. 29 in Figs. 6 and 7. This is the optimum design derived by PANDA2 with the "stop modejump" switch turned ON: panel skin thickness = 0.075452 in.; stringer thickness = 0.16256 in.; stringer height = 1.5896 in.

Figure 34 is analogous to Fig. 20. PANDA2 predicts mode jumping to occur at the design load, PA = 1.0 (Table 4, Margin No. 3). In the STAGS model an initial buckling modal imperfection amplitude of 0.007 in. was used. The imperfection shape is similar to those shown for PANEL I in Figs. 15a,b, except there is one less axial halfwave. Both PANDA2 and STAGS yield a linear bifurcation buckling load factor, PA = 0.19, for local buckling. In the initial nonlinear static run, STAGS was able to track the equilibrium curve to a load factor, PA = 1.094, well above the design load, PA = 1.0. Both PANDA2 and STAGS predict collapse of the panel at load factors close to 1.1, with PANDA2's prediction being the more conservative.

Figures 35 - 39 are analogous to Figs. 26 - 28. Two figures for each of hoop strain and in-plane shear strain are given because the location of maximum strain shifts along the length of the panel during the initial nonlinear calculations of static equilibrium. There is a "phase shift" of postbuckled lobes on either side of the stiffener as observed with PANEL I (Fig.18(a-e)). This "phase shift" is especially noticeable in Fig. 40.

Figure 40(a) depicts a distribution of upper surface hoop stress that very much resembles what one might expect from the postbuckling panel module deformation depicted in Fig. 10. for an isotropic panel with no in-plane shear loading. Because of the discontinuity in hoop curvature on either side of the stringer, which applies a line moment to the panel skin, there are equal and opposite hoop surface stresses in the panel skin on either side of the root of the stringer. These stress concentrations show up clearly along the midwidth of the STAGS model depicted in Fig. 40a. At the highest load attained in the nonlinear static analysis the postbuckled lobes on either side of the stringer have shifted in the axial direction relative to eachother so that the maximum compressive hoop stress now appears at the midlength of the panel. This maximum compressive hoop stress occurs on both sides of the stringer: there appears to be little discontinuity there, in sharp contrast to the state depicted in Fig. 40a. As mentioned previously, it is beyond the ability of PANDA2 to predict this kind of axial "phase shifting" behavior of the postbuckled lobes on either side of the stringer in the absence of anisotropy or applied in-plane shear loading.

From Figs. 40(c,d) it is seen that the distribution of in-plane shear stress in the panel skin, originally symmetric with respect to the midwidth of the panel module (Fig. 40c: the extreme fiber shear stress is symmetric because the normal displacements are antisymmetric, as shown in Fig. 10), becomes skewed as the load is increased (Fig. 40d). The maximum in-plane shear stress becomes much more concentrated in the far postbuckling regime. One can appreciate especially from Fig. 40d that, if mode jumps cause oscillatory axial shifting of the postbuckled lobes, significant cyclic extreme fiber stresses will occur at given material points in the structure. Again it is

emphasized that panels should therefore be designed to avoid mode jumping, that is, with the "stop modejump" switch turned ON in PANDA2.

CONCLUSIONS

In the foregoing we discussed a new feature in PANDA2 that makes it possible to prevent serious mode jumping from occurring in panels that are designed to function in the locally post-buckled state. Because PANDA2 uses a mode jump constraint that is based on a heuristic argument, it remains necessary to check optimum designs generated by PANDA2 with an analysis that is based on a more refined computational model such as provided by the finite element code STAGS. The method of conducting such an analysis is described in this paper.

The following conclusions are drawn from the results presented here, which are all obtained for a uniformly axially compressed, blade-stiffened steel panel with maximum stress constraints neglected:

1. PANDA2's model for the initiation of mode jumping is reasonably well confirmed by STAGS results for panels optimized by PANDA2:

   a. with the "prevent mode jump" switch turned OFF, that is, with mode jumping ignored during optimization, and

   b. with the "prevent mode jump" switch turned ON, that is, with a constraint condition that prevents mode jumping from occurring at a load below the design load.

2. Mode jumps, even if associated with very small changes in potential energy, can generate high-amplitude oscillations of stress components with significant stress reversals, especially the extreme fiber hoop stresses in the panel skin adjacent to the stringer. This oscillation might well cause fatigue failures and delaminations. Therefore, it is strongly recommended that the "prevent mode jump" switch always be turned ON during optimization with PANDA2.

3. The agreement between PANDA2 and STAGS for maximum extreme fiber strain in the far postbuckling range is acceptable for the purpose of preliminary design. PANDA2's predictions appear to be conservative provided that the load factor is not too close to the collapse load. We expect this will almost always be the case provided that the user turns the "prevent mode jump" switch ON before optimizing a panel.

4. Changes in the number of axial halfwaves in the locally postbuckled state can take place under monotonically increasing axial load.

5. The postbuckled lobes can shift by different amounts on either side of the stiffener even if the panel is isotropic and not subjected to any applied in-plane shear load. This phenomenon cannot be predicted by PANDA2. The differential axial shifting of course affects the locations of maximum stress and strain and probably their values.

6. Prevention of in-plane warping of the two longitudinal (unloaded) edges of the panel greatly increases the computer time required to explore a case but has little influence on the collapse load of the panel in the one case explored here.

7. A very refined finite element mesh is required in the panel skin in the neighborhood of the root of the stringer in order to capture steeply varying extreme fiber hoop stresses there.

8. Optimization with the "prevent mode jump" switch turned ON leads to panels that are approximately 20 percent heavier than those optimized ignoring mode jumping. The collapse loads of the heavier, safer panels as computed from STAGS and PANDA2 are in very good agreement.

SUGGESTIONS FOR FURTHER WORK

1. Additional results of a similar kind should be obtained for laminated composite panels. Realistic stress allowables should be used.

2. Cylindrical panels should be investigated.

3. Cases should be explored with initial buckling modal imperfections included in the PANDA2 models.

ACKNOWLEDGMENTS

The authors first wish to acknowledge the long-term contributions of Mr. Frank Brogan, a principal developer of the STAGS computer program since its infancy in the early 1960's. D. Bushnell wishes to express his appreciation for the continuing support of Dr. Ron Dotson and Mr. Bill Sable, Spacecraft Analysis Department (Dept. E4-20) in Lockheed-Martin Missiles and Space Satellite Systems Division. Dr. Charles Rankin and Professor Eduard Riks appreciate the sponsorship over many years of Dr. James Starnes, Jr, Head of the Structural Mechanics Branch of the NASA Langley Research Center, for the continuing development of advanced nonlinear methods as introduced into STAGS. Mr. Bill Bushnell wrote the software, PLOTPS, that generated all of the "x-y" plots in this paper. He also helped the authors provide the proper format of the paper for the AIAA and continues to support D. Bushnell in the maintenance of the PANDA2 computer program on several UNIX-based workstations. Bo Stehlin is one of the creators of the STAPL program, by means of which the plots of deformed panels and the fringe plots of stresses were generated.

REFERENCES

[1] Bushnell D., "PANDA2 - Program for minimum weight design of stiffened, composite, locally buckled panels," Computers and Structures, 25, 469-605, (1987).

[2] Bushnell, D., "PANDA - Interactive program for minimum weight design of stiffened cylindrical panels and shells", Computers and Structures, Vol. 16, pp. 167-185, 1983

[3] Bushnell, D., "Theoretical basis of the PANDA computer program for preliminary design of stiffened panels under combined in-plane loads," Computers and Structures, Vol. 27, No. 4, pp. 541-563 (1987)

[4] Almroth B. O. and Brogan F. A., "The STAGS Computer Code", NASA CR-2950, NASA Langley Research Center, Hampton, VA (1978).

[5] Rankin C. C., Stehlin P., and Brogan F. A., "Enhancements to the STAGS computer code". NASA CR 4000, NASA Langley Research Center, Hampton, VA., (1986).

[6] Stein M., "The Phenomenon of Change of Buckling Patterns in Elastic Structures", NASA Technical report R-39, National Aeronautics and Space Administration, (1959).

[7] Stein M., "Loads and Deformations of Buckled Rectangular Plates", NASA Technical Report R- 40, National Aeronautics and Space Administration, (1959).

[8] Riks, E., Rankin C. C., Brogan F. A., "On the solution of mode jumping phenomena in thin walled shell structures", First ASCE/ASM/SES Mechanics Conference, Charlottesville, VA, June 6-9, 1993, in: Computer Methods in Applied Mechanics and Engineering, Vol.136, (1996).

[9] Riks E.and Rankin C.C., "Computer Simulation of the Buckling Behavior of Thin Shells Under Quasi Static Loads", Archives of Computational Mechanics, to appear.

[10] Stoll, F. and Olson, S. E. "Finite element investigation of the snap phenomenon in buckled plates", Paper No. AIAA-97-1307, 38th AIAA SDM Conference, April 7-10 (1987).

[11] Stoll, F., "Analysis of the snap phenomenon in buckled plates", Int. J. Nonlinear Mechanics, Vol. 29, No. 2, 123-138 (1994).

[12] Bushnell, D., "Truss-core sandwich design via PANDA2", Computers and Structures, Vol. 44, No. 5, pp. 1091-1119 (1992)

[13] Bushnell, D., "Optimum design via PANDA2 of composite sandwich panels with honeycomb or foam cores", 38th SDM Conference, April (1997).

[14] Bushnell, D., "Recent enhancements to PANDA2", 37th AIAA Structures, Structural Dynamics and Materials Conference, April, 1996. Submitted to Finite Elements in Analysis and Design (1997).

[15] Bushnell, D. and Bushnell, W. D.,"Approximate method for the optimum design of ring and stringer stiffened cylindrical panels and shells with local, inter-ring, and general buckling modal imperfections", Computers and Structures, Vol. 59, No. 3, pp. 489-527 (1996)

[16] Bushnell, D.,"BOSOR4: Program for stress, buckling, and vibration of complex shells of

revolution," Structural Mechanics Software Series - Vol. 1, (N. Perrone and W. Pilkey, editors), University Press of Virginia, Charlottesville, 1977, pp. 11-131. See also Computers and Structures, Vol. 4, (1974) pp. 399-435; AIAA J, Vol. 9, No. 10, (1971) pp. 2004-2013; Structural Analysis Systems, Vol. 2, A. Niku-Lari, editor, Pergamon Press, Oxford, 1986, pp. 25-54, and Computers and Structures, 18, (3), (1984) pp. 471-536.

[17] Bushnell, D., "Optimization of composite, stiffened, imperfect panels under combined loads for service in the postbuckling regime", Computer Methods in Applied Mechanics and Engineering, Vol. 103, pp. 43-114 (1993)

[18] Koiter W.T., "Het schuifplooiveld by grote overschrijdingen van de knikspanning", ("The shear buckling mode at loads far above the critical value"), National Aerospace Laboratory, The Netherlands, Report X295, (1946).

[19] Vanderplaats, G. N., "ADS--a FORTRAN program for automated design synthesis, Version 2.01", Engineering Design Optimization, Inc, Santa Barbara, CA, January, 1987

[20] Vanderplaats, G. N. and Sugimoto, H., "A general-purpose optimization program for engineering design", Computers and Structures, Vol. 24, pp. 13-21, 1986

[21] Bushnell, D. and Bushnell, W. D., "Minimum-weight design of a stiffened panel via PANDA2 and evaluation of the optimized panel via STAGS", Computers and Structures, Vol. 50, no. 4, p569-602 (1994)

[22] Rankin, C. C., and Brogan, F. A., "Application of the Thurston Bifurcation Solution Strategy to Problems with Modal Interaction," AIAA Paper No. 88-2286 in Proceedings of the 29th Structures, Structural Dynamics, and Materials Conference Part 1 (1988), pp. 590--595.

[23] Bushnell, D. and Bushnell, W. D., "Optimum design of composite stiffened panels under combined loading", Computers and Structures, Vol. 55, No. 5, pp. 819-856 (1995)

[24] Thompson J.M.T., Hunt G.W., A General Theory of Elastic Stability, John Wiley & Sons, Ltd., (1973).

[25]. Tvergaard V., "The Sensitivity of a Wide Integrally Stiffened Panel under Compression," Int. Journ. Solids and Structures, Vol.9, 177 - 192 (1973).

[26]. Koiter W.T., Pignataro M., "A general Theory for the Interaction of Local and Overall Buckling of stiffened panels," WTHD 83, Department of Applied Mechanics, Technical University Delft, (1976).

[27]. Van der Neut A. "Mode Interaction with Stiffened Panels", Proc. IUTAM Symposium on Buckling of Structures, Harvard University, (1974), 117 - 132. Springer Verlag (1976).

[28]. Supple W. J. "Changes of Wave-Form of Plates in the Post-Buckling Range", Int. J. Solids Structures, Vol., pp. 1243-1258, (1970).

[29]. Nakamura T. Uetani K. "The Secondary Buckling and Post-Buckling Behaviours of Rectangular Plates", Int. J. Mech. Sci., Vol.21, pp. 265-286, (1979).

[30]. Schaeffer, D. and Golubitsky, M., "Boundary Conditions and Mode Jumping in the Buckling of a Rectangular Plate", Communications in Mathematical Physics, Vol. 69, pp. 209 - 236 (1979).

[31]. Golubitsky, M. and Schaeffer, D., "Singularities and Groups in Bifurcation Theory", Volume I, Applied Mathematical Sciences, Springer Verlag, New York, Heidelberg, Tokyo, (1985).

[32]. Suchy H., Troger H. and Weiss R. "A Numerical Study of Mode Jumping of Rectangular Plates", ZAMM Z. Angew.Math. u. Mech., Vol. 65, 2, pp. 71-78, (1985).

[33] Koiter W.T., "De meedragende breedte bij grote overschrijdingen van de knikspanning voor verschillende inklemmingen van de plaatranden," ("The equivalent width at loads far above the buckling load for various boundary conditions along the plate edges"), NLL report 287, National aerospace Laboratory, (1943).

[34] Riks E., "Some Computational Aspects of the Stability Analysis of Nonlinear Structures", Comp. Meth. in Appl. Mech. in Engrg. Vol. 47 , 219-259, (1984)

[35] Riks E., "Progress in Collapse Analysis", Journal of Pressure Vessel Technology, Vol. 109/27 - 41, Febr..(1987).

[36] Seydel R., "From Equilibrium to Chaos, Practical Stability Analysis", Elsevier, New York-Amsterdam-London, ISBN 0-444-01250-8, (1989).

[37] Riks E., Brogan, F. A. and Rankin C. C., "Aspects of the stability analysis of shells, Static and Dynamic Stability of Shells" (W. B. Kratzig and E. Onate, editors), Springer Series in Computational Mechanics, Springer Verlag, Heidelberg (1990).

[38] Koiter, W.T., "On the Stability of Elastic Equilibrium", H.J. Paris Publ., Amsterdam (1945), English translation: Report nr. AFFDL-TR-70-25, Air Force Flight Dynamics Lab., Wright Patterson AFB, OHIO, (1970).

[39] Koiter W.T., "Elastic Stability and Post-Buckling Behavior," Proc. Symposium on Nonlinear Problems, (R.E. Langer Ed.), Univ. of Wisconsin Press, p. 257, (1963).

[40] Park, K.C., "An Improved Stiffly Stable Method for the Direct Integration of Nonlinear Structural Dynamics," J. Appl Mech. Vol. 42, pp 464-470 (1975).

[41] Bushnell, D., .../panda2/doc/panda2.news, a continually updated file distributed with PANDA2 that contains a log of all significant modifications to PANDA2 from 1987 through the present.

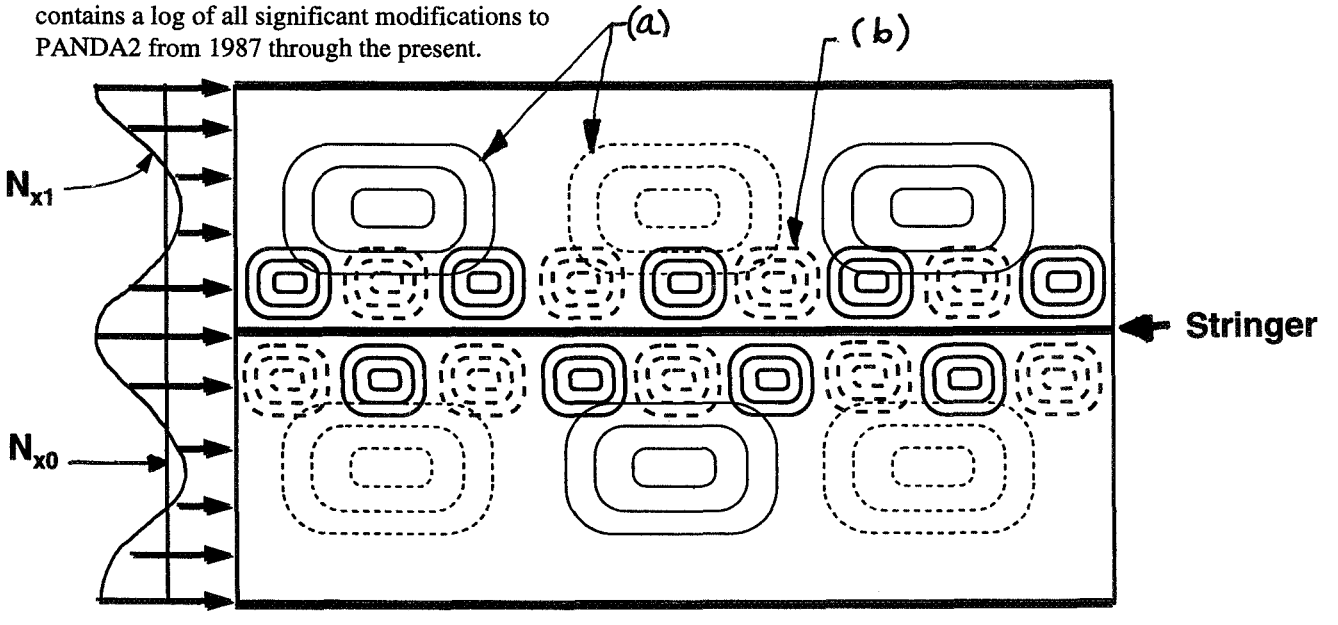

Fig. A1 Diagram for explanation of mode jumping constraint in PANDA2. Pattern (a) represents the initial buckling mode, obtained from a linear bifurcation buckling analysis in which the axial loading is uniform (Nx = Nxo). Pattern (b) represents secondary buckling, obtained from a linear bifurcation buckling analysis in which the axial loading, computed from the KOITER branch of PANDA2, is nonuniform (Nx = Nx1).

Table 1
INITIAL PANEL DIMENSIONS, MATERIAL PROPERTIES, AND LOADING

Axial length of panel	L = 50.0 in.
Transverse length of panel	B = 100.0 in.
stiffener spacing,	b = 10.0 in. (fixed in this example)
Initial height of stiffener,	h = 2.0 in. (decision variable)
Initial thickness of panel skin	t_1 = 0.1 in. (decision variable)
Initial thickness of blade	t_2 = 0.2 in. (decision variable)
Young's modulus	E = $30x10^6$ psi
Poisson's ratio	$\nu = 0.3$
Allowable effective stress	$1x10^6$ psi (set high to avoid active stress constraint)
Weight density of material	$\rho = 0.3$ lb/in^3
Applied axial load (the design load)	N_x =-5000.0 lb/in (ultimate load)

Table 2
MARGINS OF SAFETY FOR PANEL DESIGN

Local buckling	F.S. = 0.1 (local buckling permitted)
Wide column and general buckling	F.S. = 1.1
Effective stress	F.S. = 1.0

Table 3
MARGINS FOR OPTIMUM DESIGN AT ITERATION NO. 15 ("mode jump" turned OFF)

NO	VALUE	DEFINITION
1	1.58E-02	Local buckling from discrete model-1., M = 7 axial halfwaves; FS = 0.1
2	-1.30E-04	Local buckling from Koiter theory, M = 7 axial halfwaves; FS = 0.1
6	4.90E-03	(Wide column panel buckling load factor)/(F.S.) -1; FS = 1.1
7	-1.56E-03	(m=1 lateral-torsional buckling load factor)/(F.S.) -1; FS=1.1
10	1.80E-01	buck.(DONL); clamped general buck; M = 1;N = 1; slope=0.; FS = 1.1
14	1.80E-01	buck.(SANDERS); clamped general buck; M = 1;N = 1;slope=0.;FS = 1.1

Table 4
MARGINS FOR OPTIMUM DESIGN AT ITERATION NO. 29 ("mode jump" turned ON)

MAR. NO.	MARGIN VALUE	DEFINITION
1	9.13E-01	Local buckling from discrete model-1., M=6 axial halfwaves; FS = 0.1
2	8.95E-01	Local buckling from Koiter theory, M=6 axial halfwaves; FS = 0.1
3	-2.70E-03	Hi-axial-wave post-post-buckling of panel skin -1; M=12 ; FS = 1.0
4	5.24E-03	(Wide column panel buckling load factor)/(F.S.) -1; FS = 1.1
5	2.68E-01	(m=1 lateral-torsional buckling load factor)/(F.S.)-1; FS = 1.1
7	1.31E-01	buck.(DONL); clamped general buck; M=1; N=1; slope=0.; FS = 1.1
9	1.31E-01	buck.(SAND); clamped general buck; M=1; N=1; slope=0.; FS = 1.1

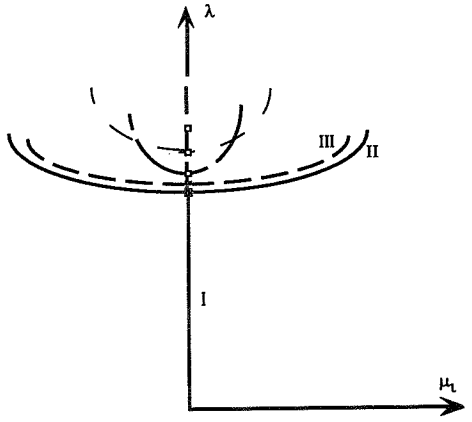

Fig. 1 Clustered bifurcation points

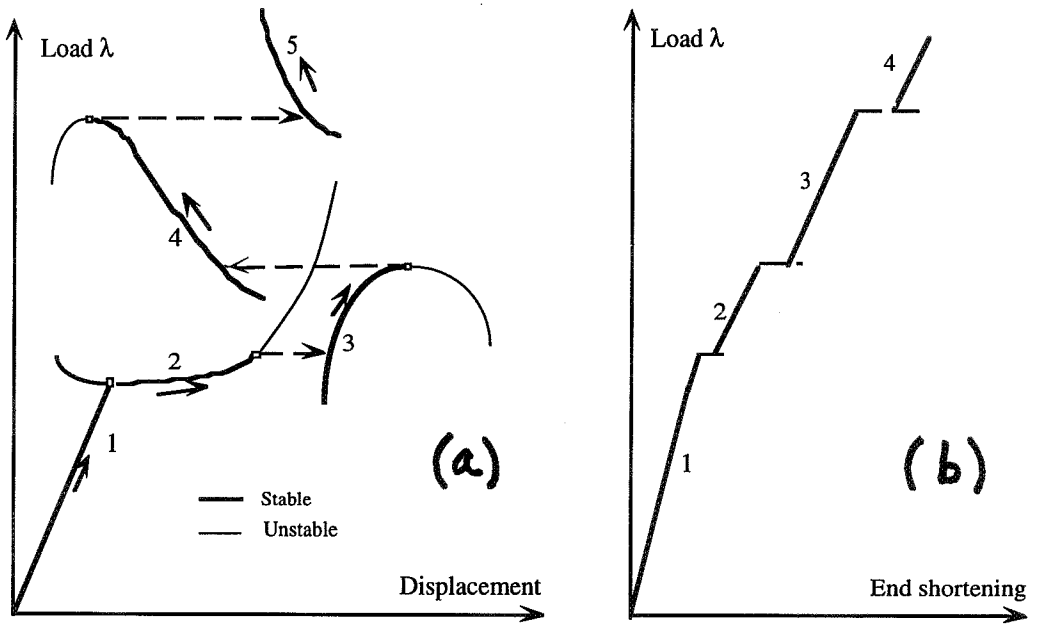

Fig. 2 (a) Mode jumping in general; (b) in axially compressed panels

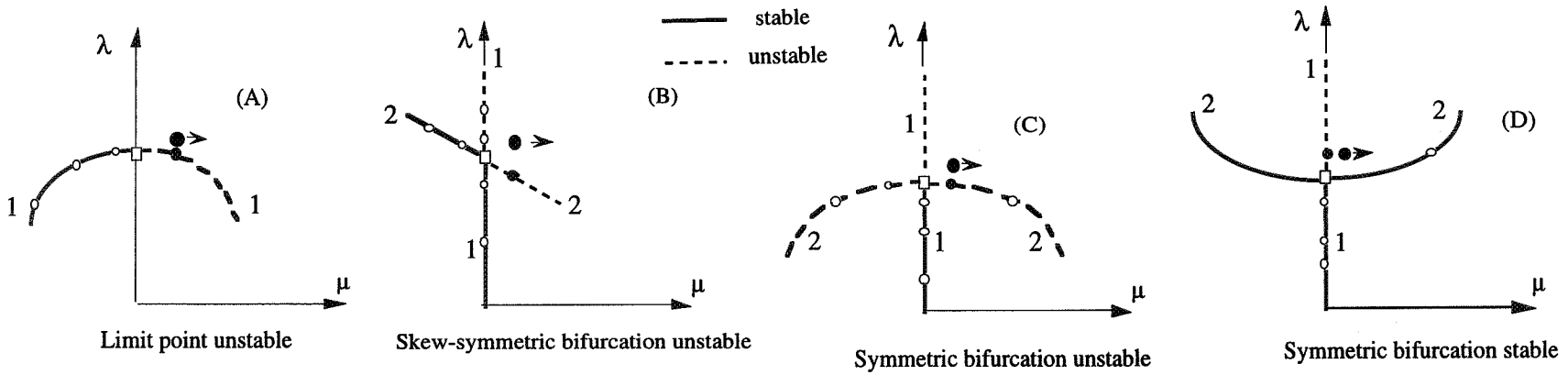

Fig. 3 Types of branching and initial conditions in STAGS for mode jumping

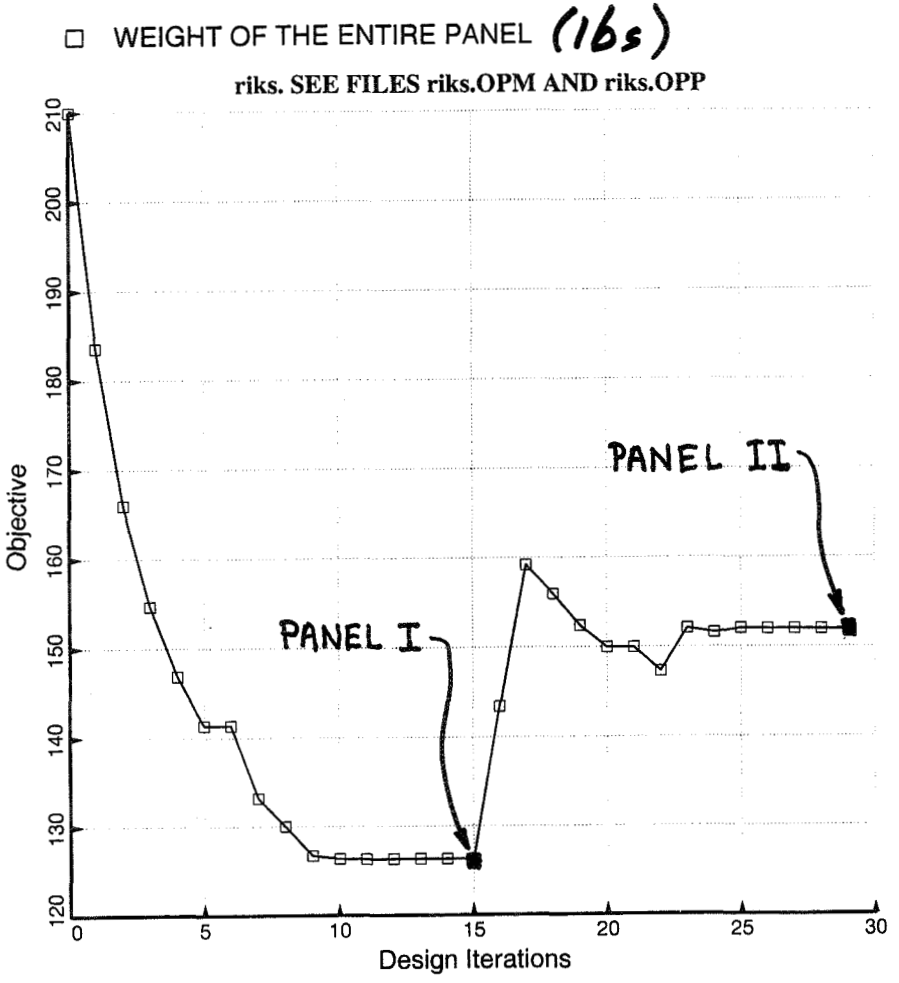

Fig. 4 Optimization in PANDA2 with "stop modejump" first turned OFF (Iterations 1 - 15), then turned ON (Iterations 15 - 29)

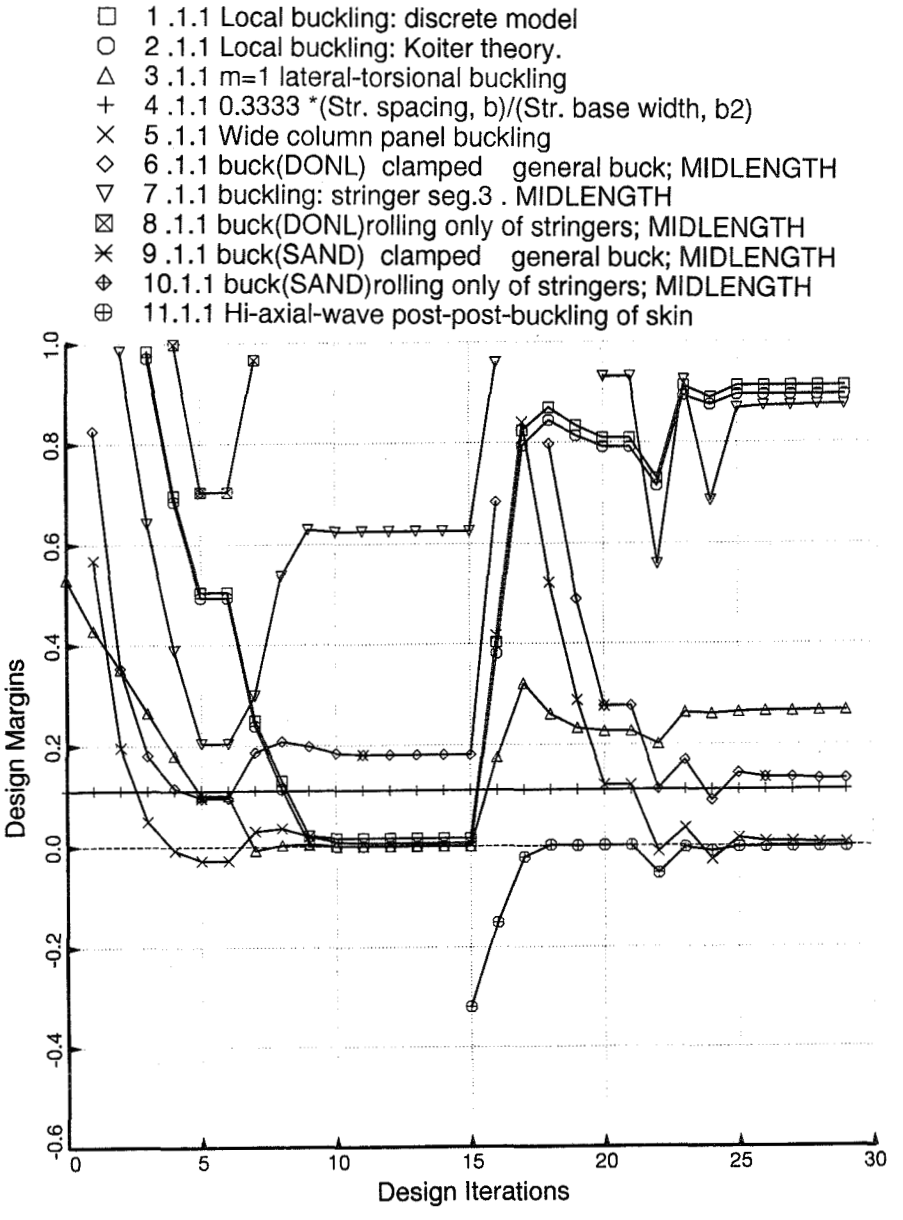

Fig. 5 Design margins during optimization with "stop modejump" first OFF, then ON

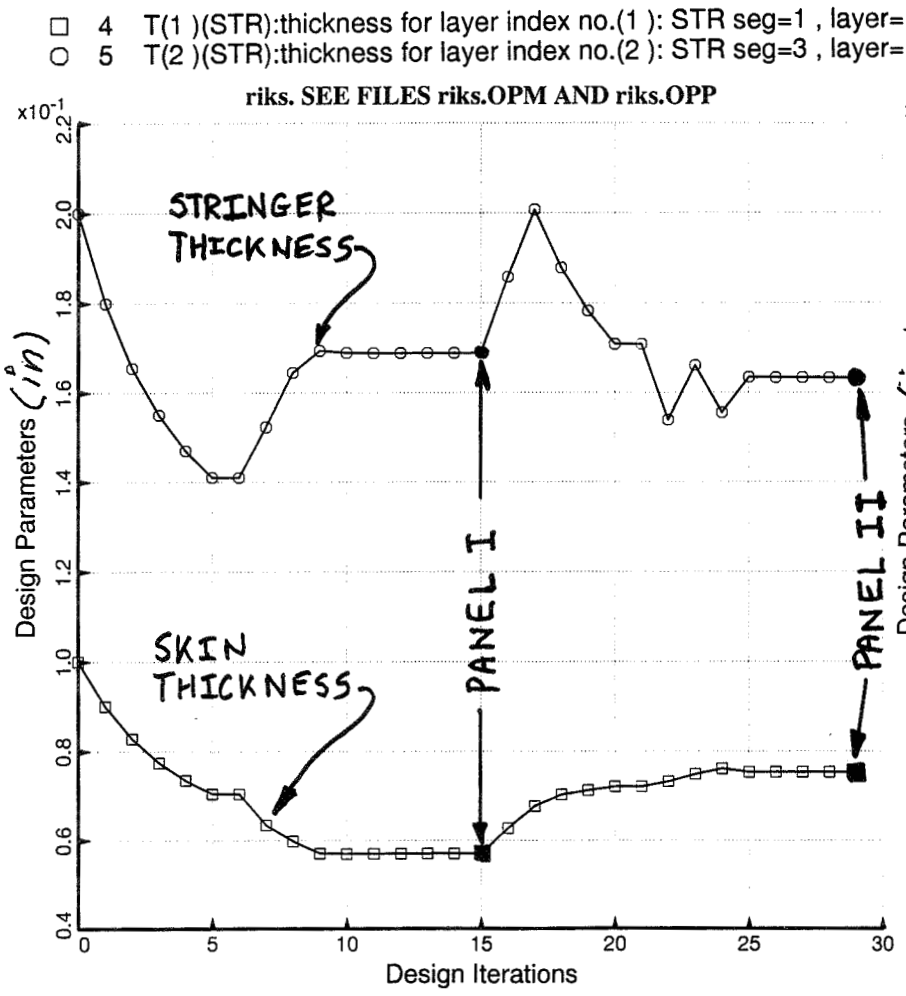

Fig. 6 Evolution of thicknesses with the "stop" modejump" constraint first turned OFF (Iterations 1-15), then ON (Iter. 15-29)

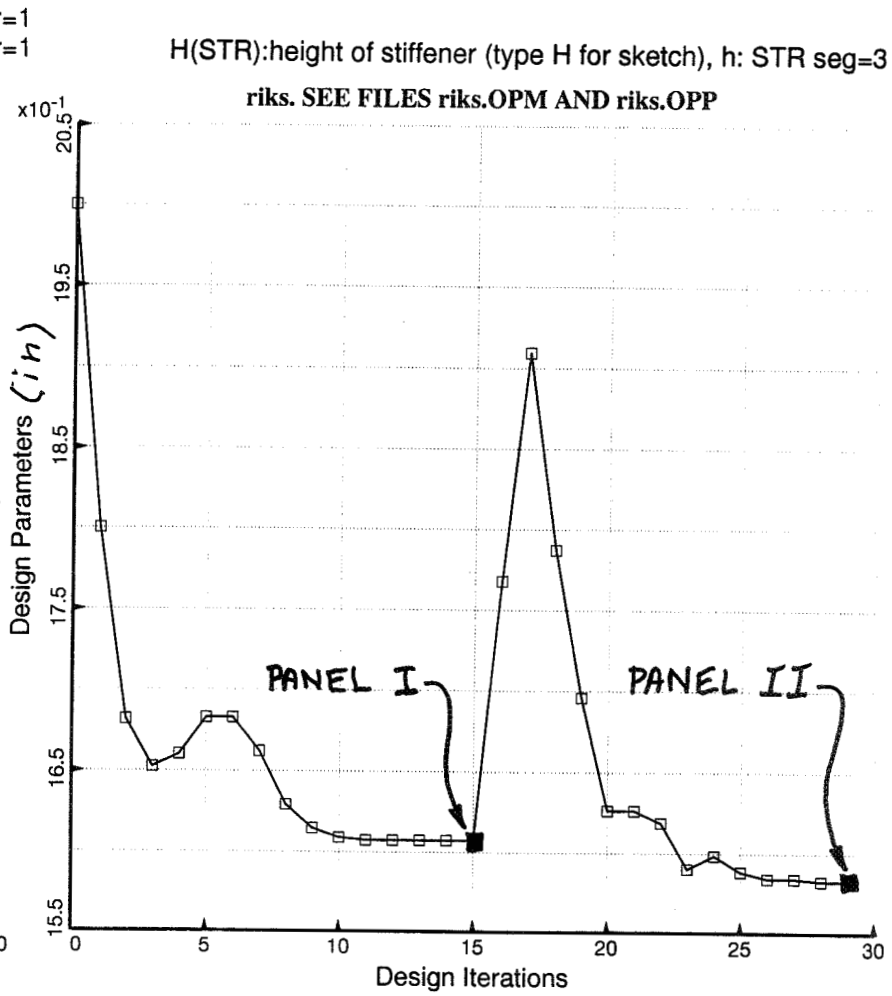

Fig. 7 Evolution of stringer height with the "stop modejump" constraint first turned OFF, then ON. The designs labelled PANEL I and PANEL II are analyzed with STAGS

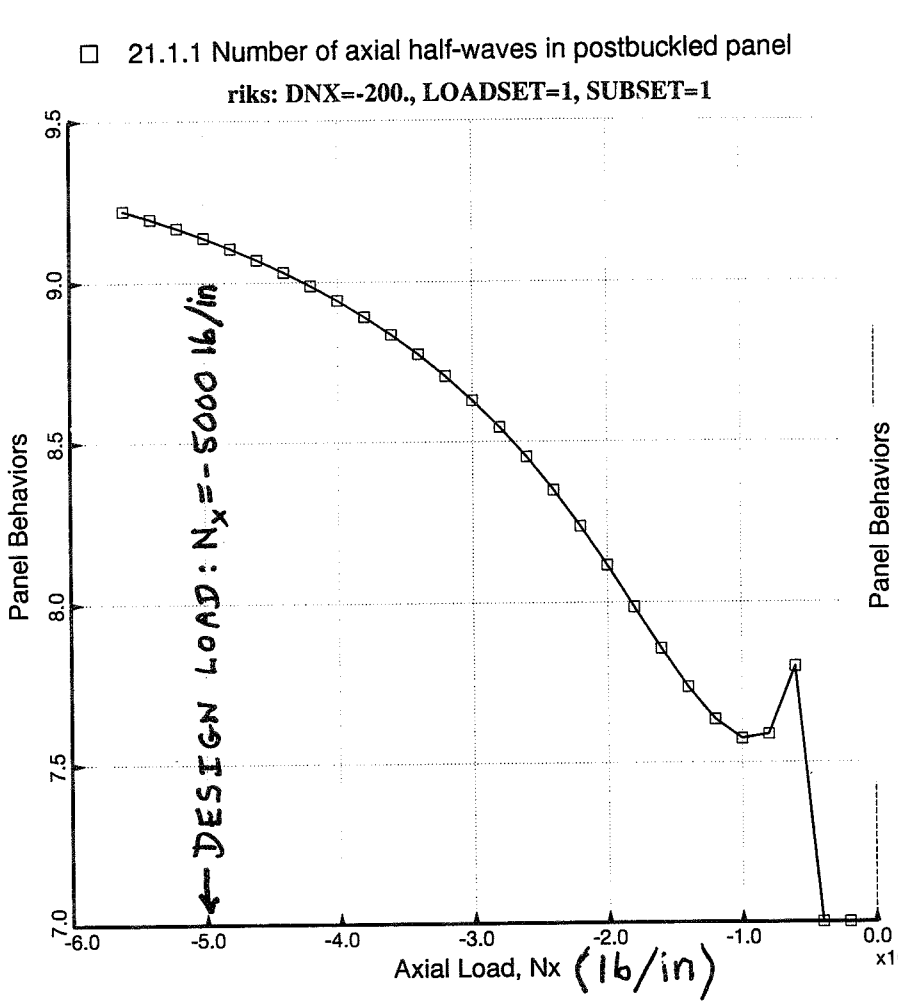

Fig. 8 Theory in PANDA2 [15] accounts for change in the number of axial halfwaves in the locally postbuckled loading regime

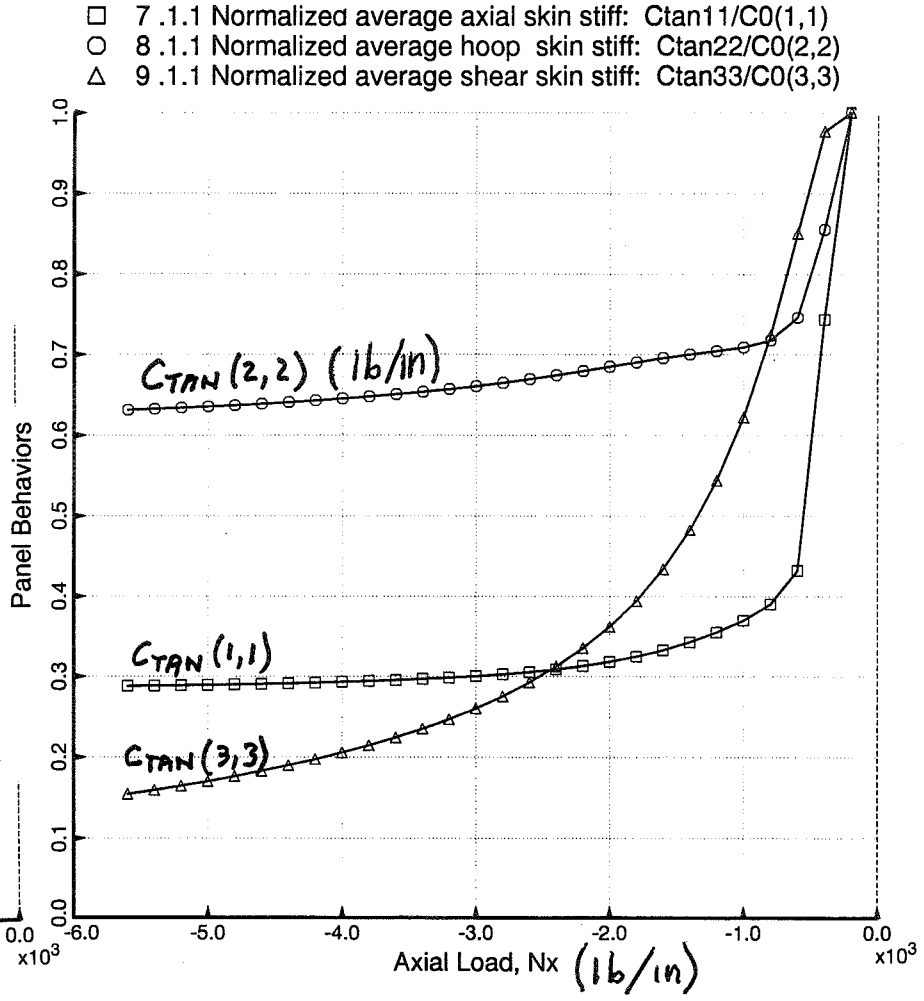

Fig. 9 Theory in PANDA2 [19] for wide column and general instability accounts for the change in effective membrane stiffness of a locally postbuckled panel. This is the "classical" long wave and short wave interaction effect.

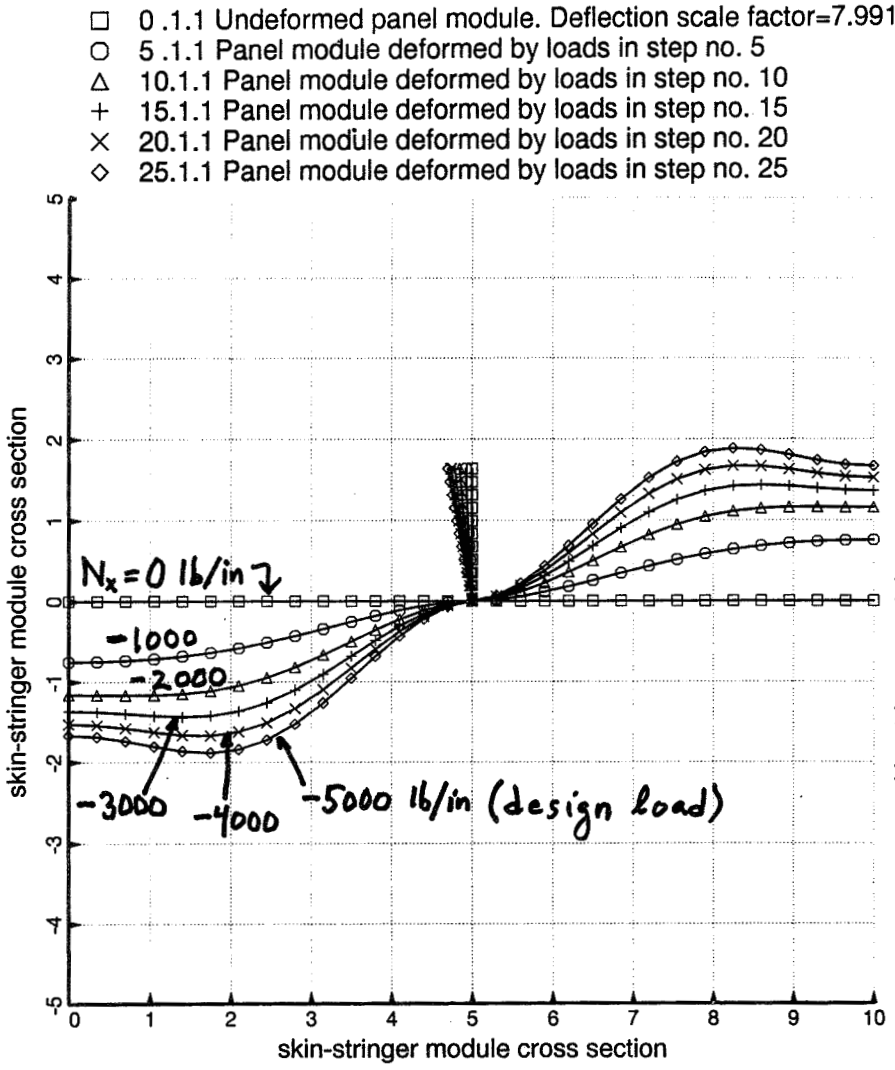

Fig. 10 PANDA2 prediction of locally postbuckled single discretized skin-stringer PANEL I module

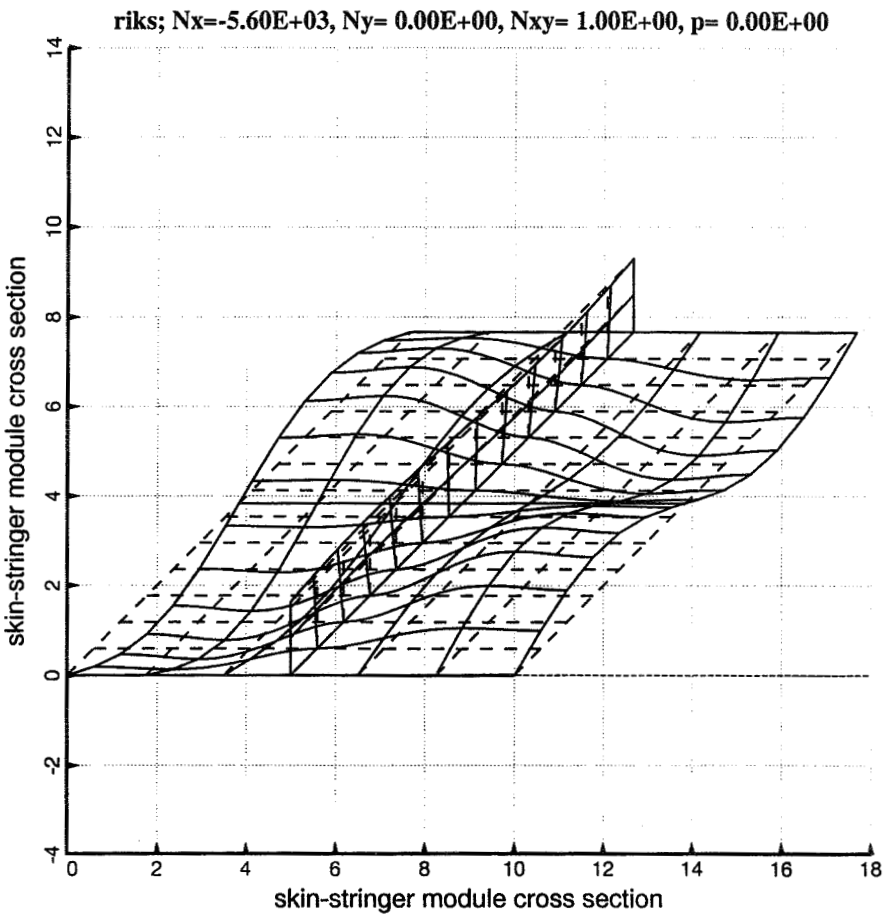

Fig. 11 PANDA2 prediction of locally postbuckled portion of PANEL I of length equal to one full axial wave of the deflection pattern

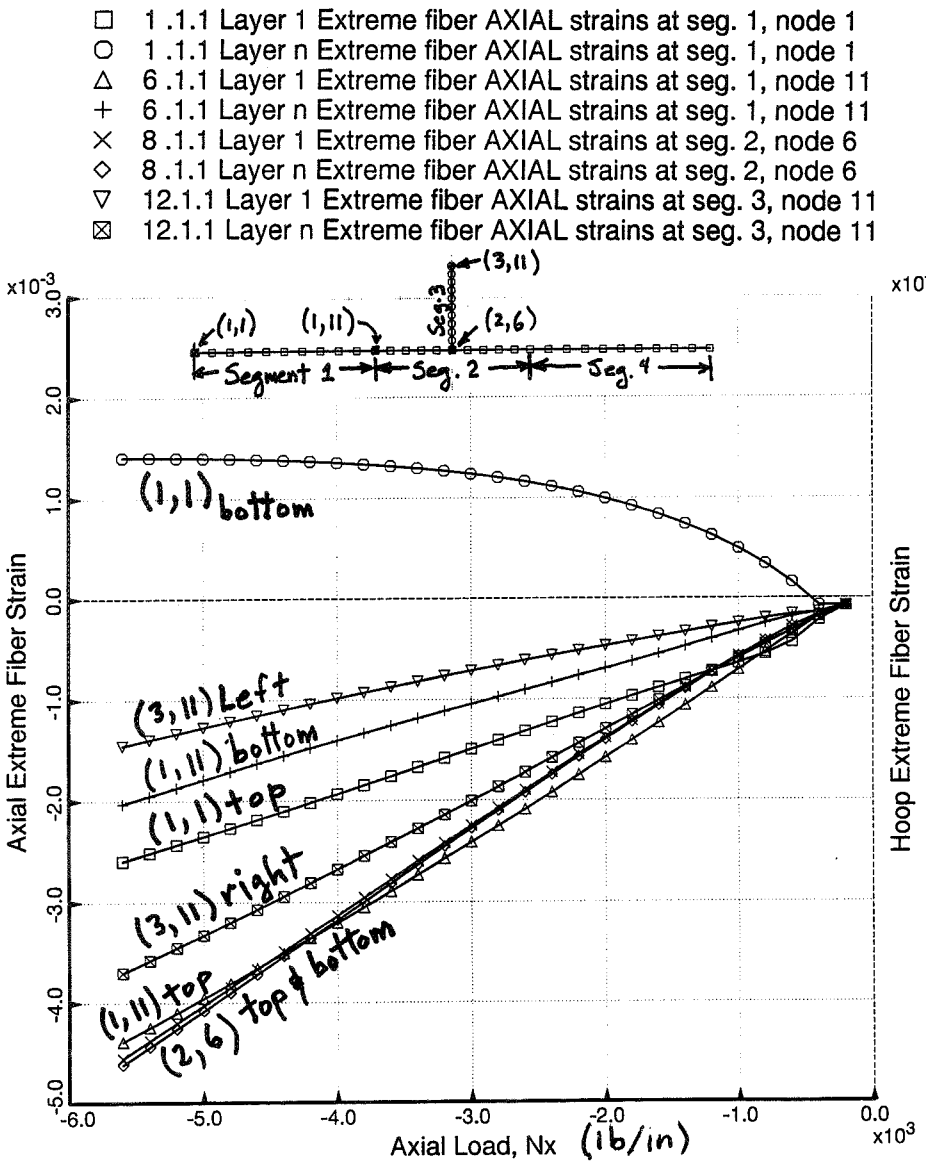

Fig. 12 PANDA2 prediction of axial strain in the surface fibers of the single PANEL I module

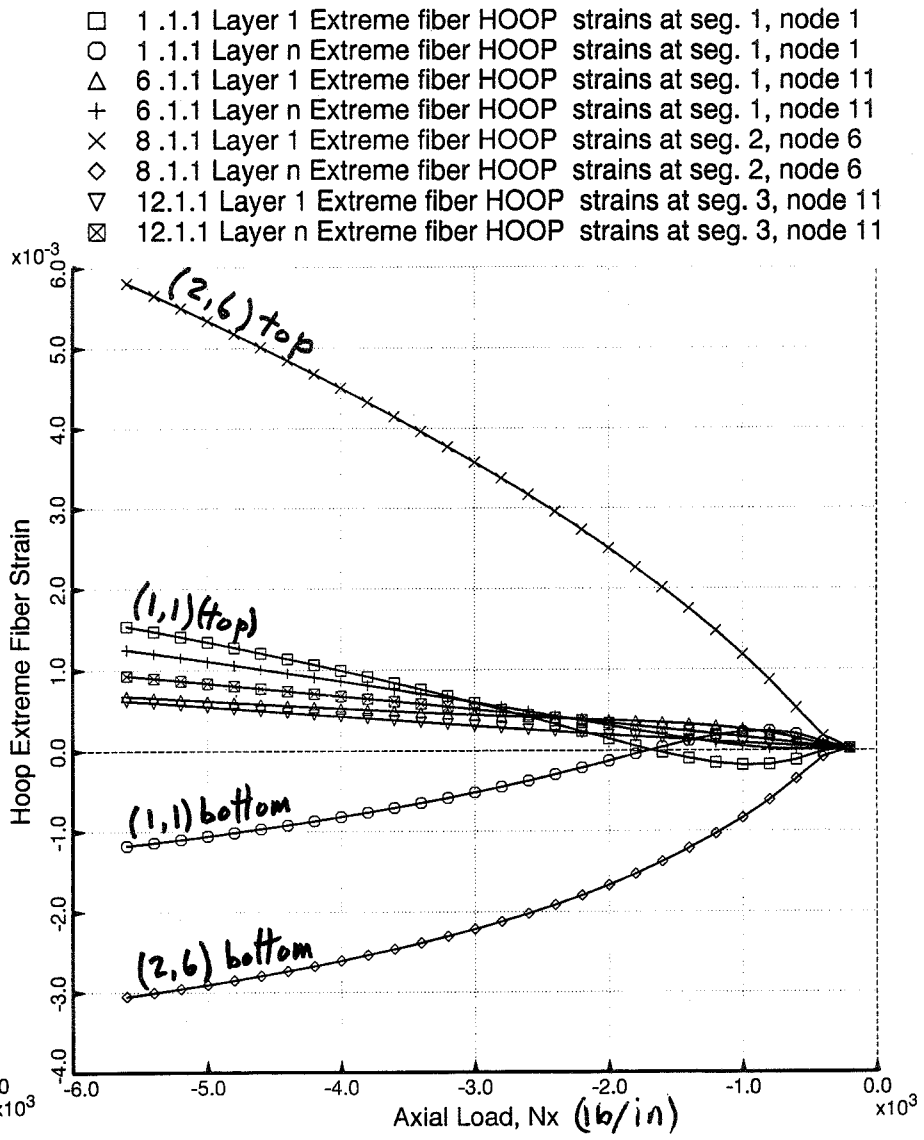

Fig. 13 PANDA2 prediction of hoop strain in the surface fibers of the single PANEL I module

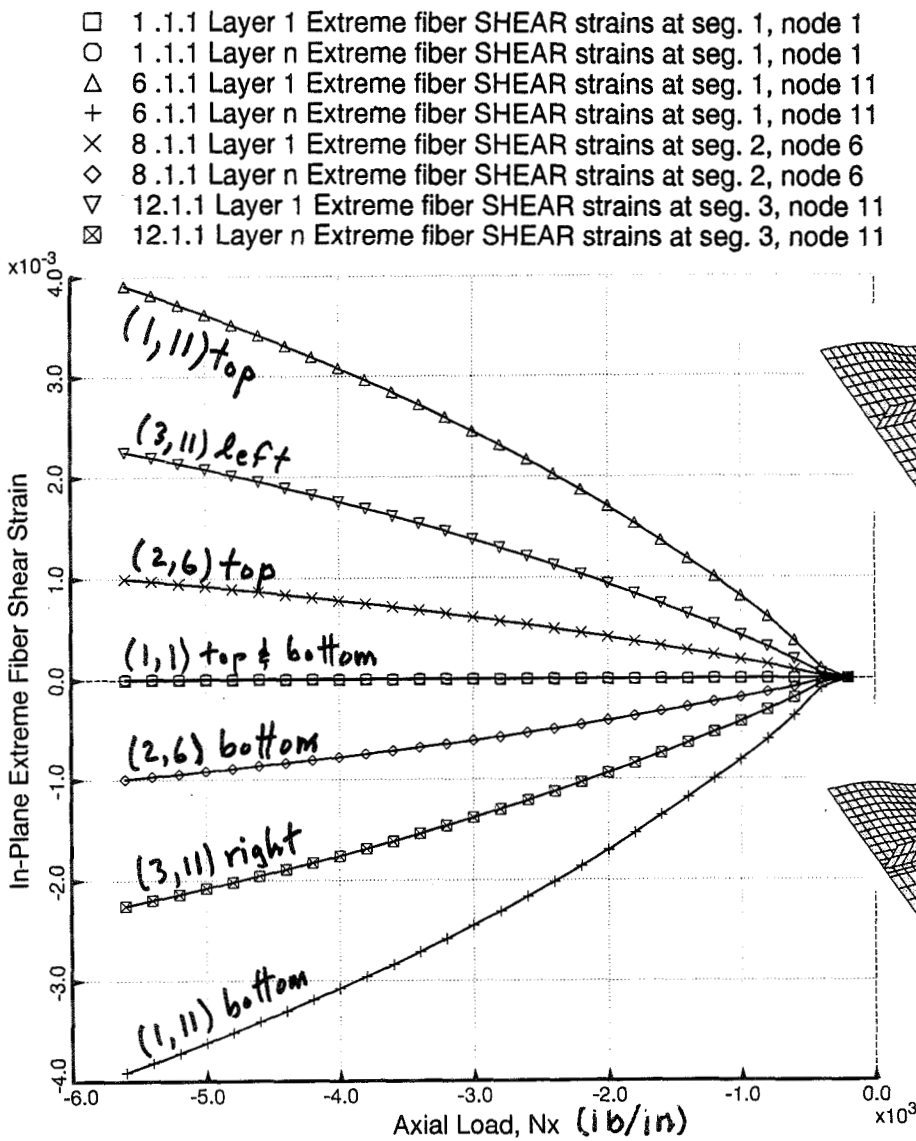

Fig. 14 PANDA2 prediction of in-plane shear strain in the surface fibers of the single PANEL I module

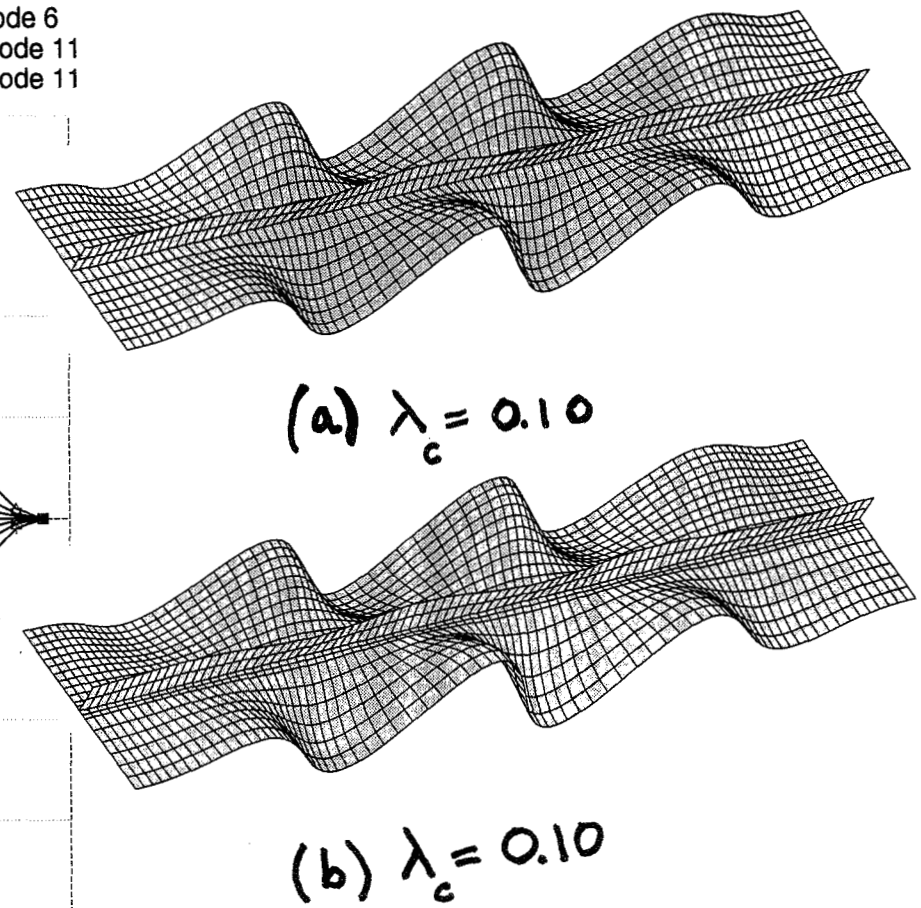

Fig. 15 Linear bifurcation buckling modes and load factors, lambda, for a single-module STAGS finite element model of the axially compressed PANEL I optimized with "stop modejump" OFF: (a) Model 1; (b) Model 2

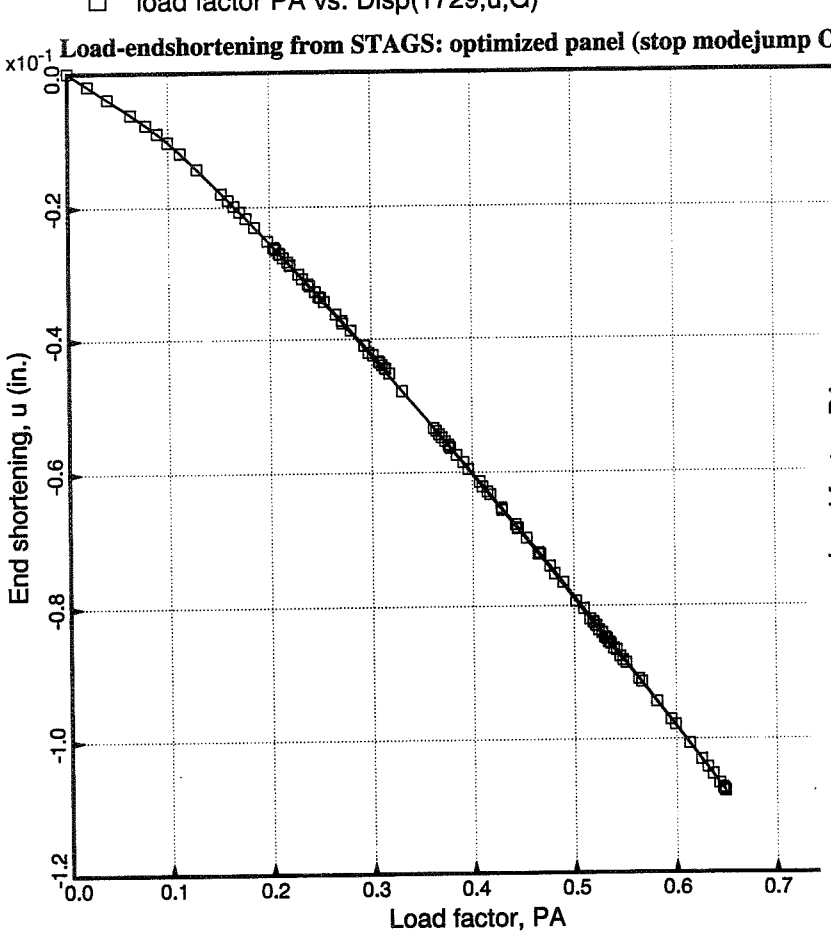

Fig. 16 Load-end-shortening curve for initial STAGS nonlinear static run of PANEL I. STAGS cannot obtain a static solution for a load factor higher than PA = 0.648.

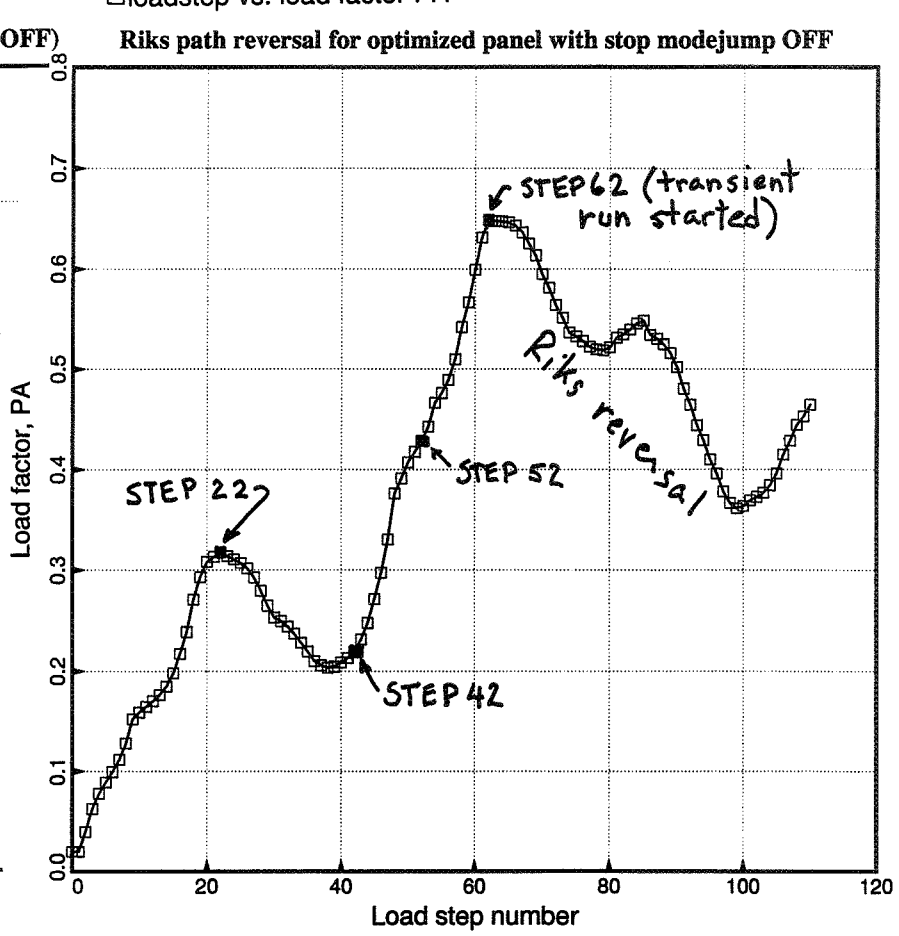

Fig. 17 Loading history showing successful static path-following during initial unloading and unsuccessful "Riks reversal" following attainment of maximum load factor at Step 62

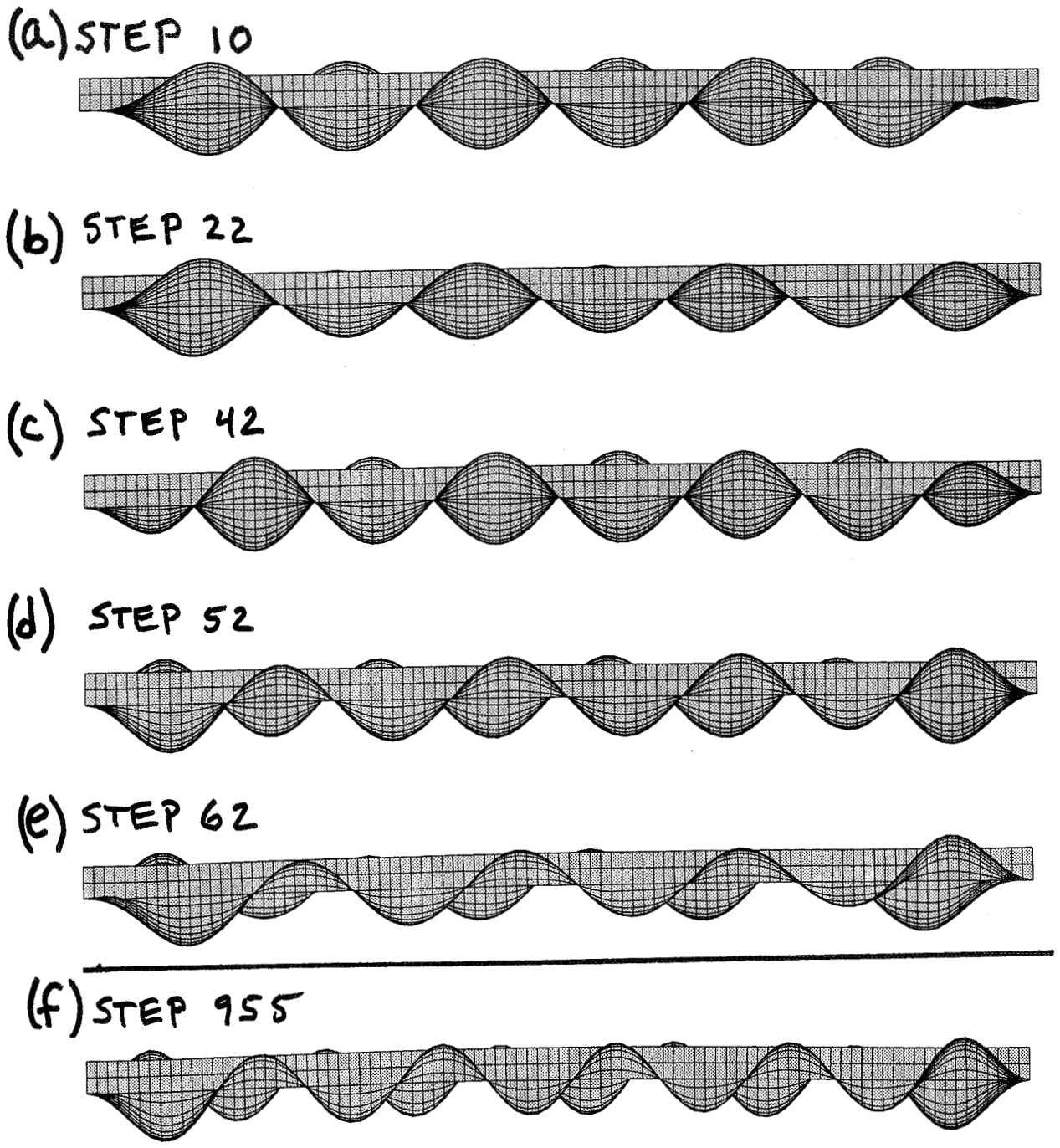

Fig. 18 Edge-on view of locally postbuckled PANEL I showing how the number of axial halfwaves changes during the initial static loading (a)-(e) and after the transient phase (f). The scale factors for deflection are different in each frame so that the maximum amplitudes are the same.

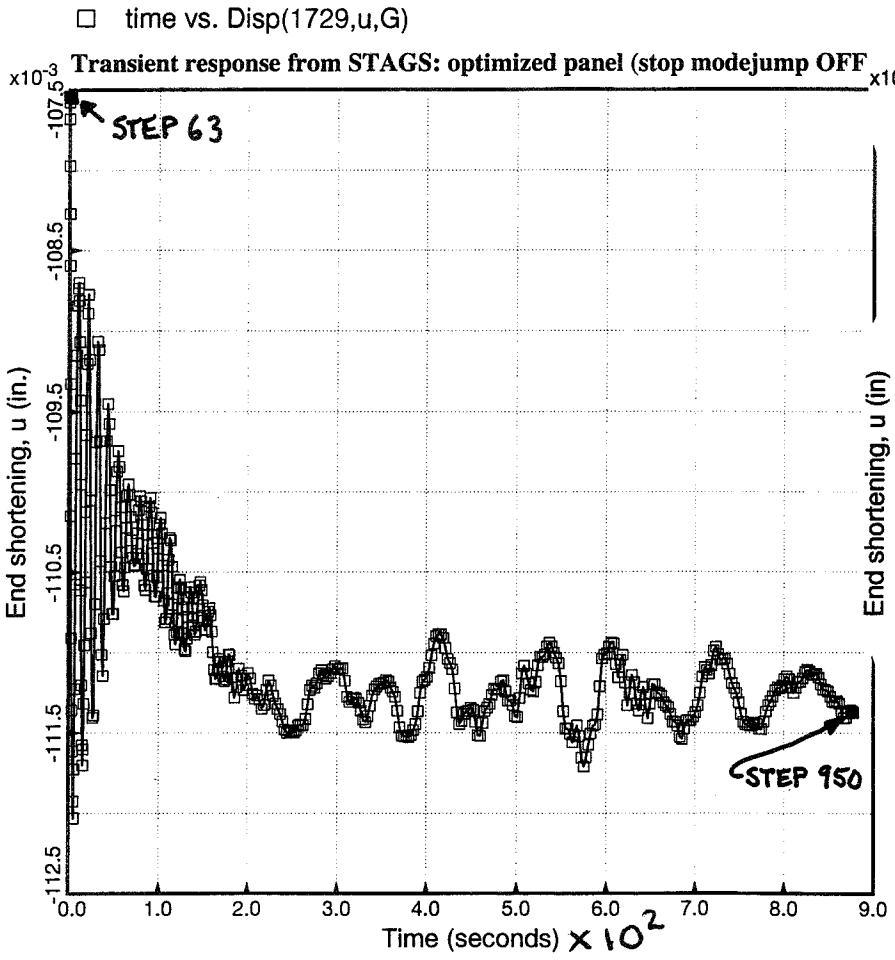

Fig. 19 End shortening during transient phase. The load factor PA is held constant at 0.6605. The maximum time in this frame is 0.09 sec.

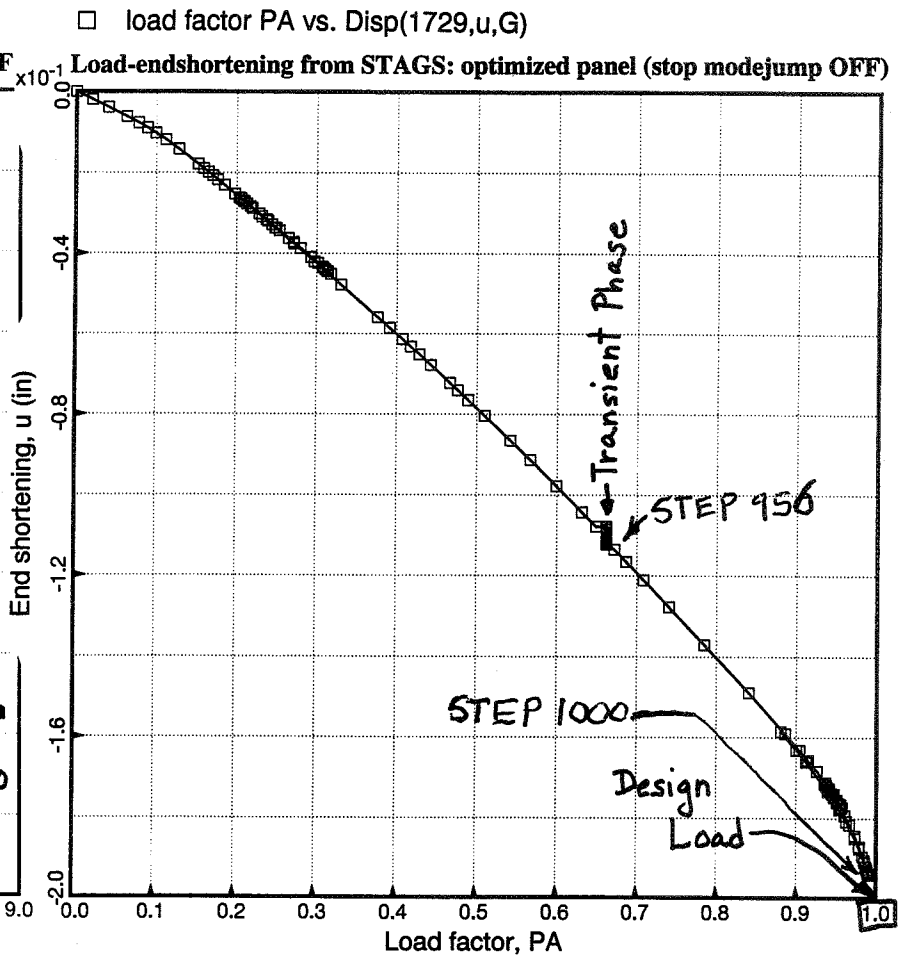

Fig. 20 Complete load-end-shortening curve for the STAGS simulation of what happens to PANEL I optimized by PANDA2 with "stop modejump" OFF

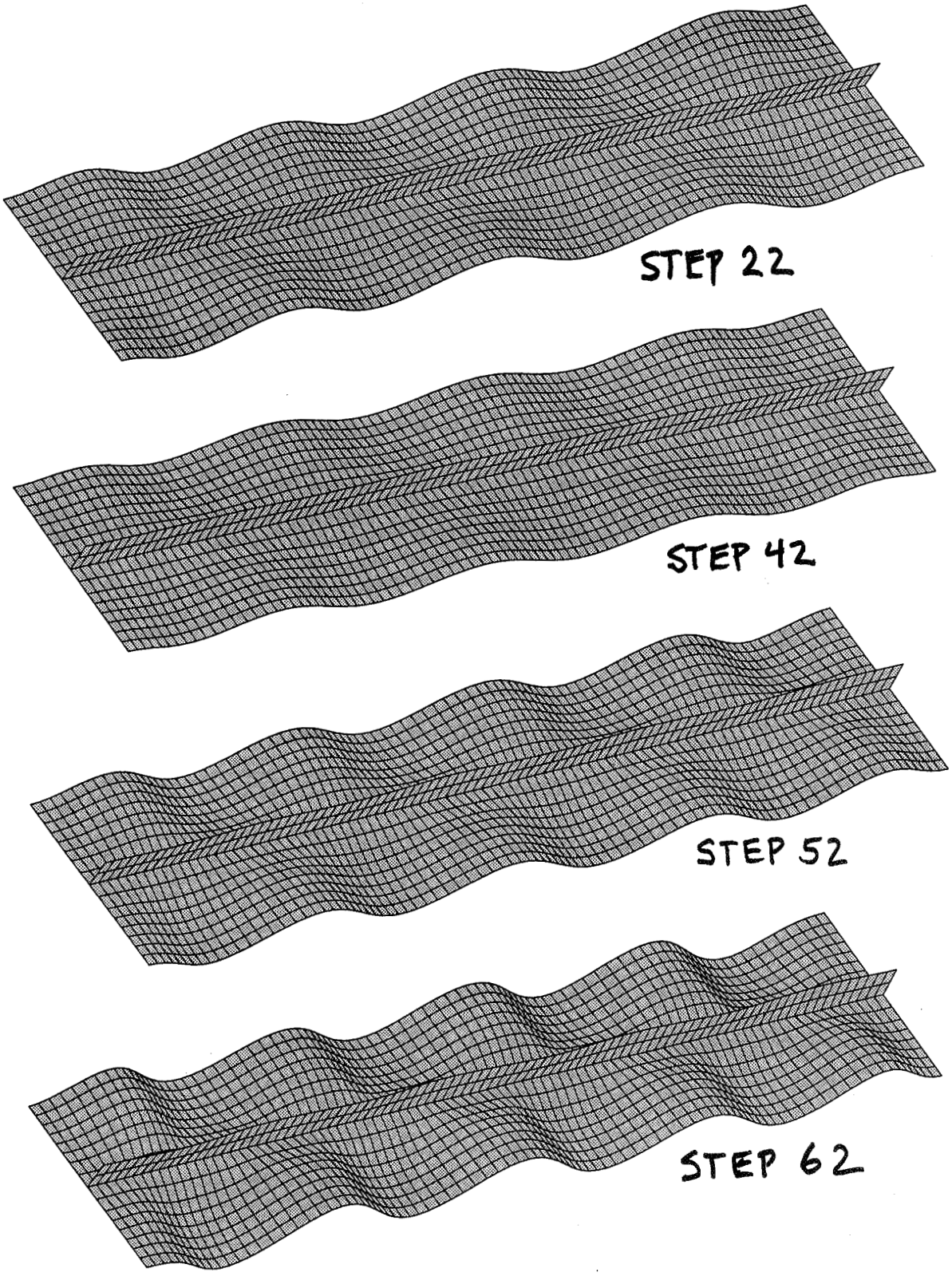

Fig. 21 View of postbuckling deformation of PANEL I during the initial static phase of loading. The same scale factor is used for all frames.

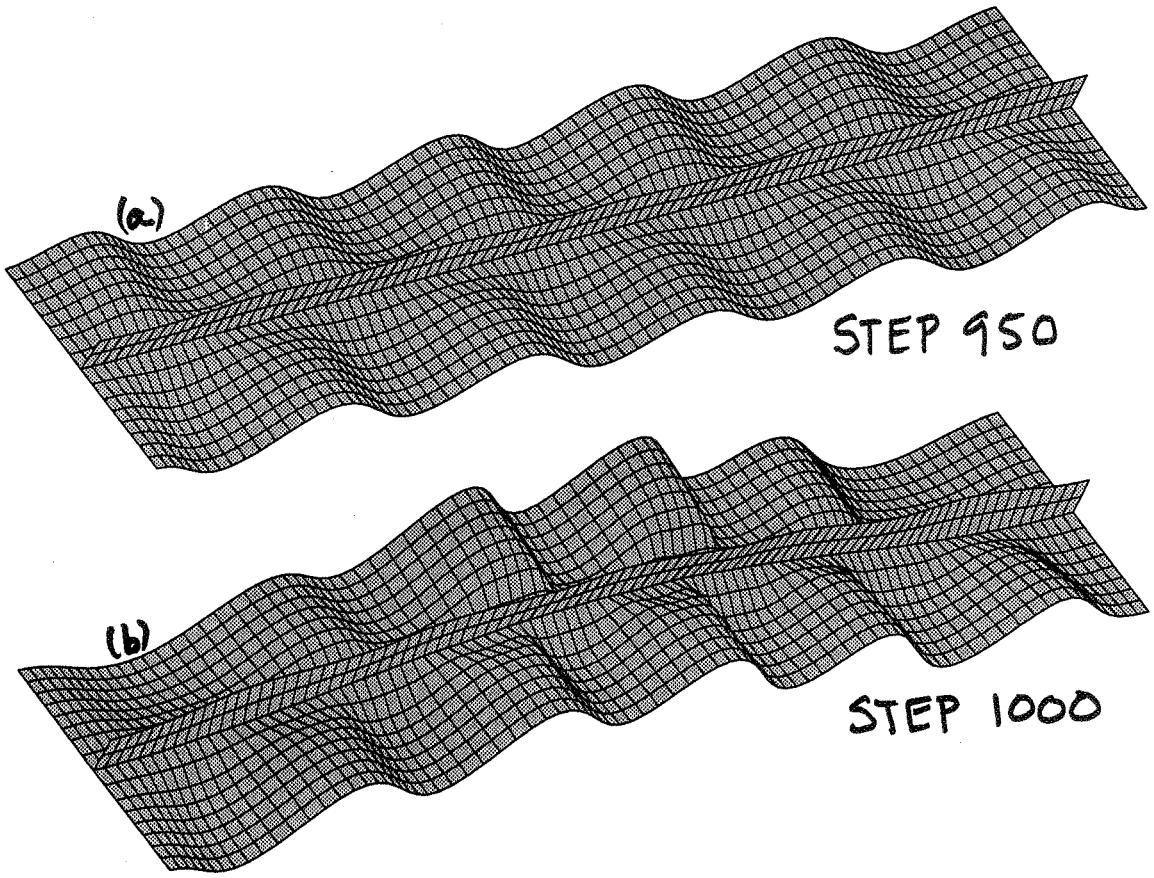

Fig. 22 View of postbuckling deformation of PANEL I at the start and end of the second static phase of loading: 0.660 < PA < 0.991

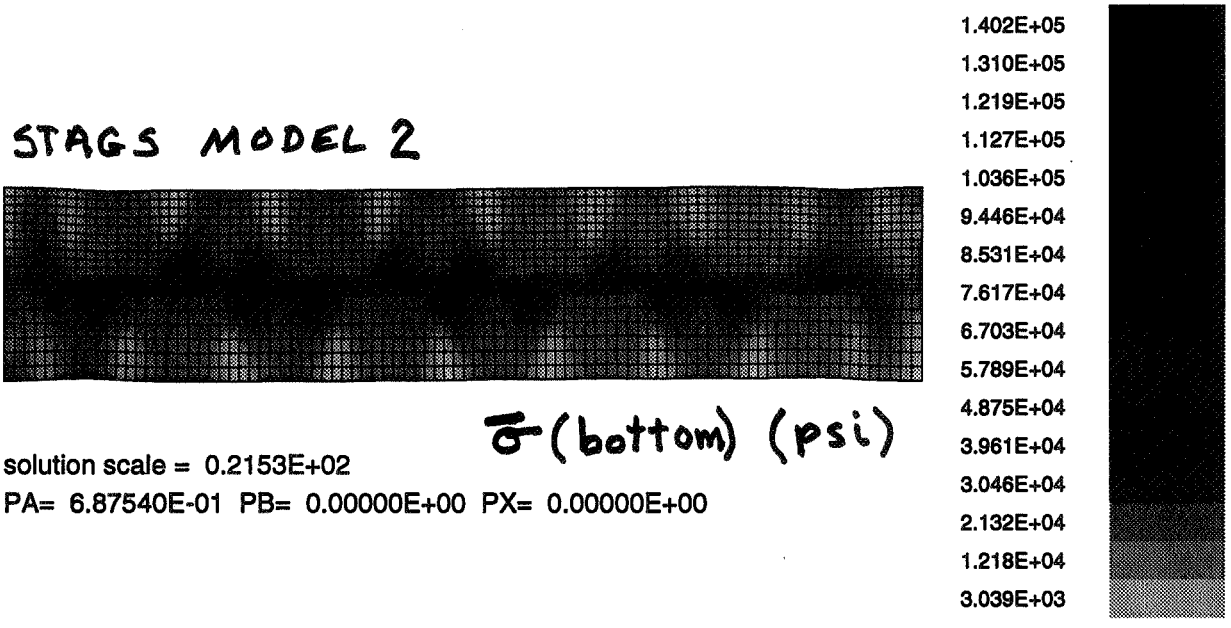

Fig. 23 Effective stress in PANEL I at the skin bottom surface at the load factor, PA = 0.6875, at end of initial static phase for STAGS Finite Element Model 2.

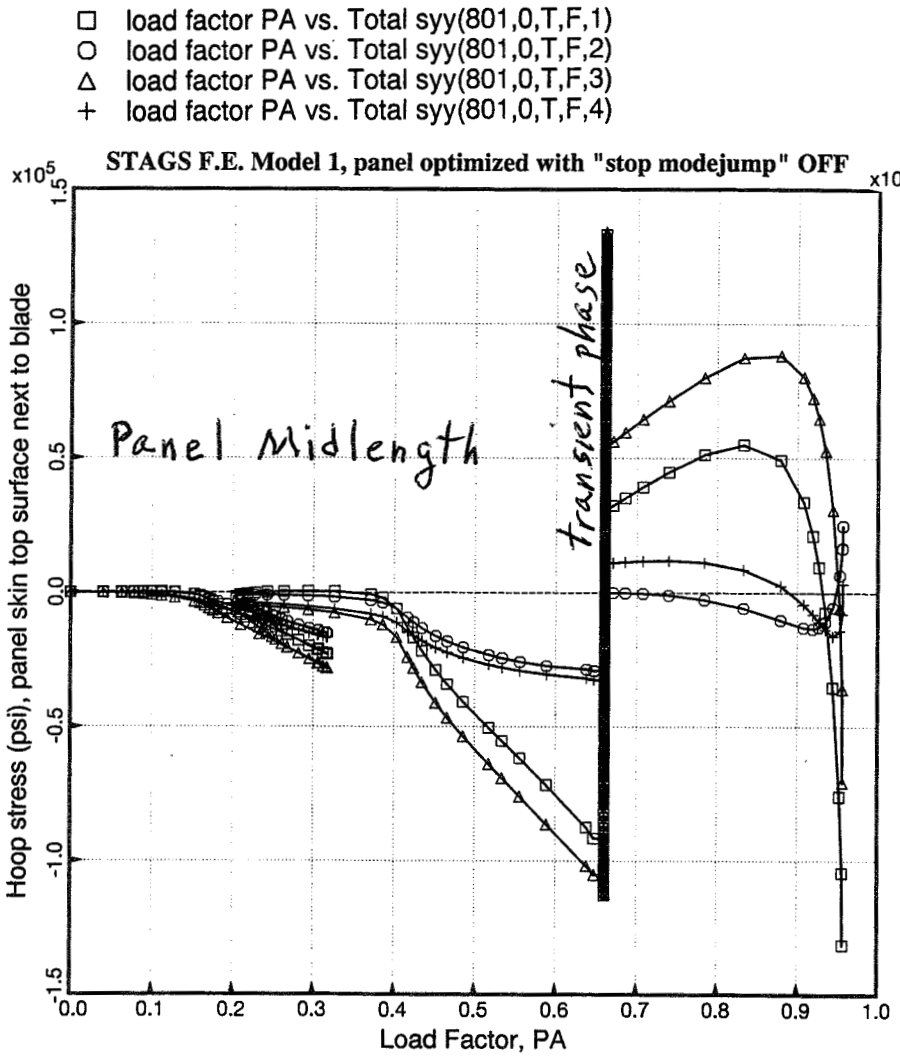

Fig. 24 History of hoop stress in PANEL I at the top surface of the panel skin next to the blade for the "unrefined" finite element Model 1

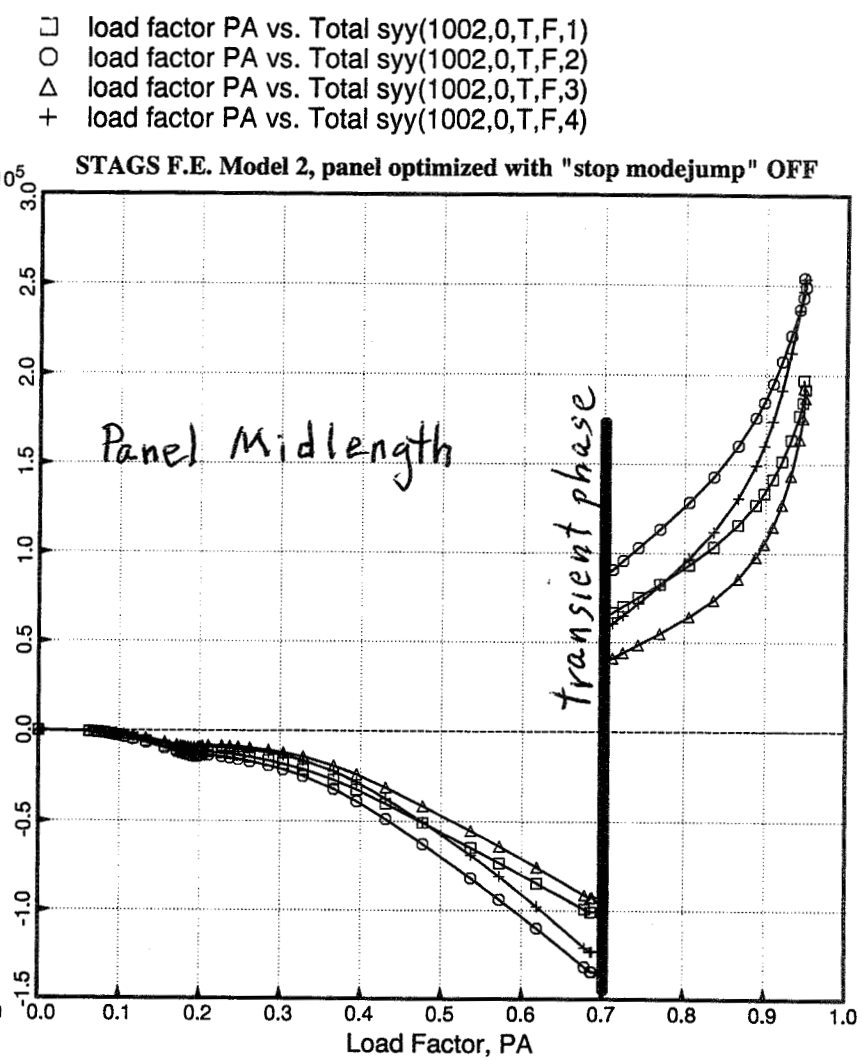

Fig. 25 History of hoop stress in PANEL I at the top surface of the panel skin next to the blade for the "refined" finite element Model 2

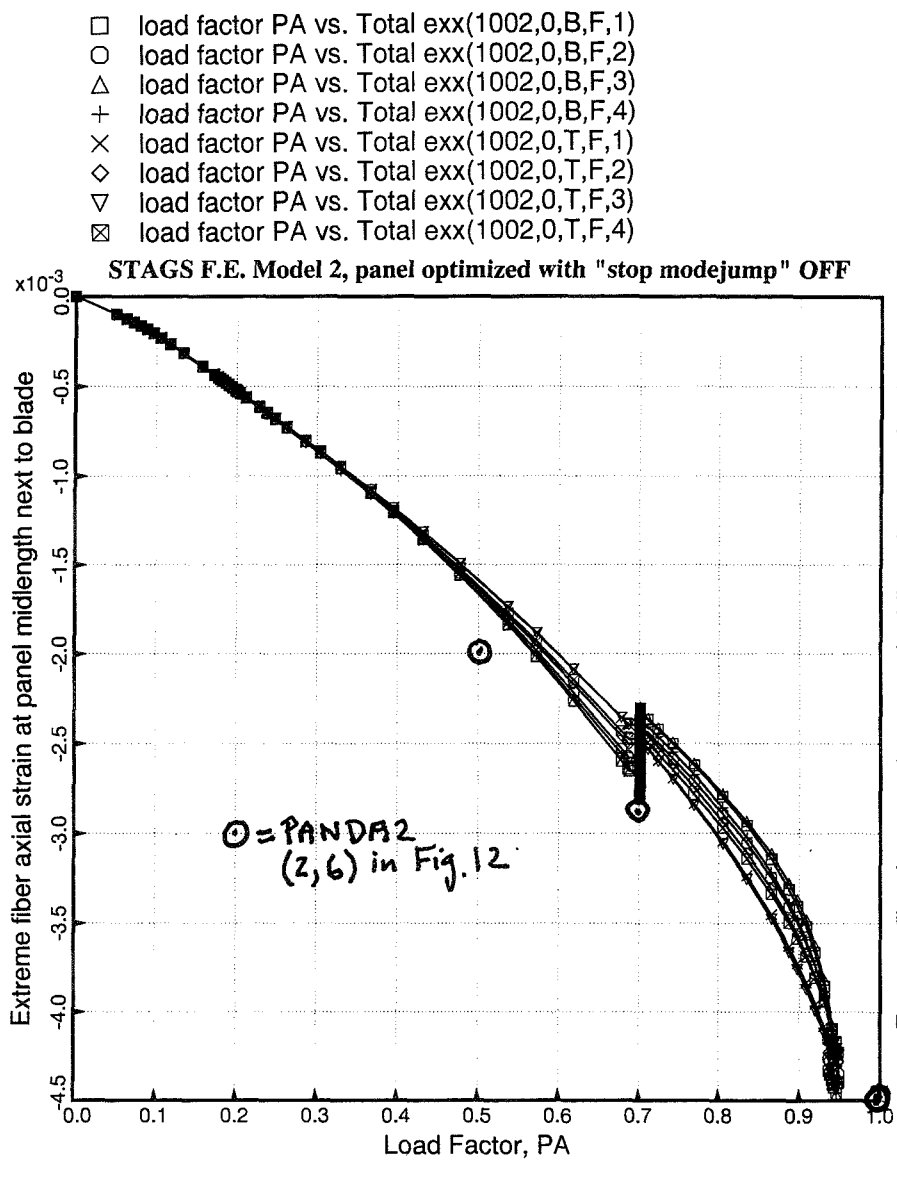

Fig. 26 History of axial strain in PANEL I at the top and bottom surfaces of the panel skin next to the blade. (Compare with Fig. 12)

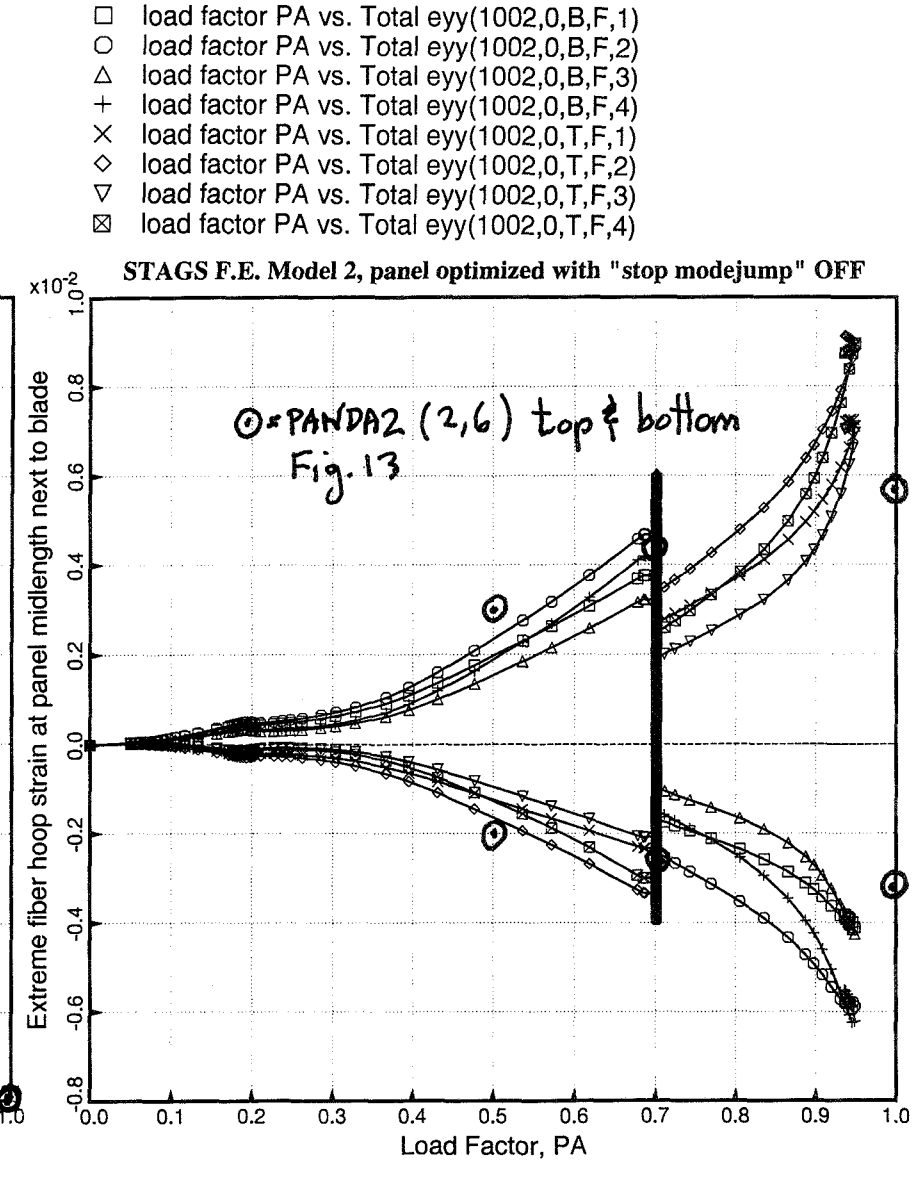

Fig. 27 History of hoop strain in PANEL I at the top and bottom surfaces of the panel skin next to the blade. (Compare with Fig. 13)

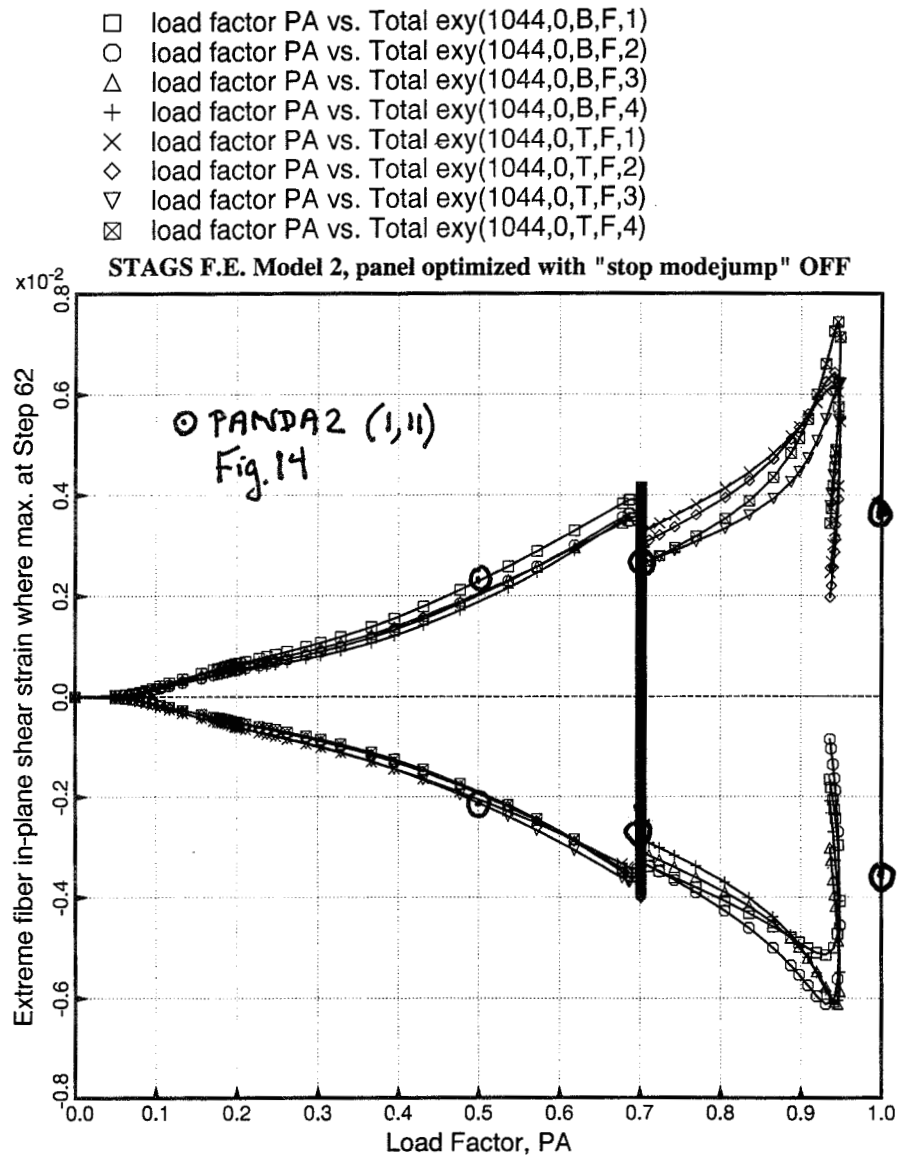

Fig. 28 History of shear strain in PANEL I at the top and bottom surfaces of the panel skin next to the blade. (Compare with Fig. 14)

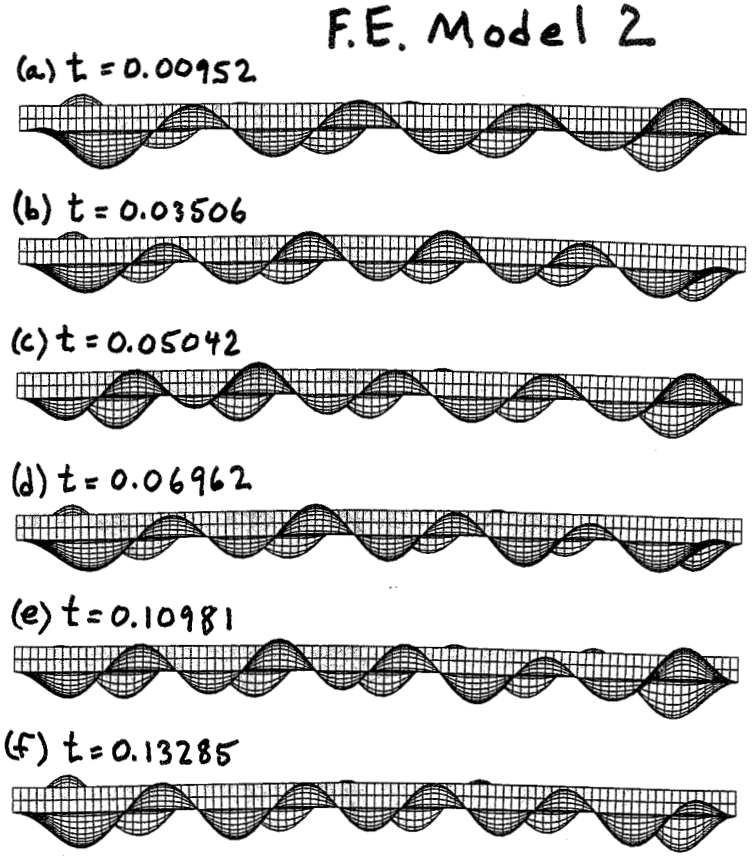

Fig. 29 Edge-on view of postbuckled PANEL I during transient phase at constant load factor PA = 0.7013. Each frame corresponds to a peak value of hoop stress in the next Fig.

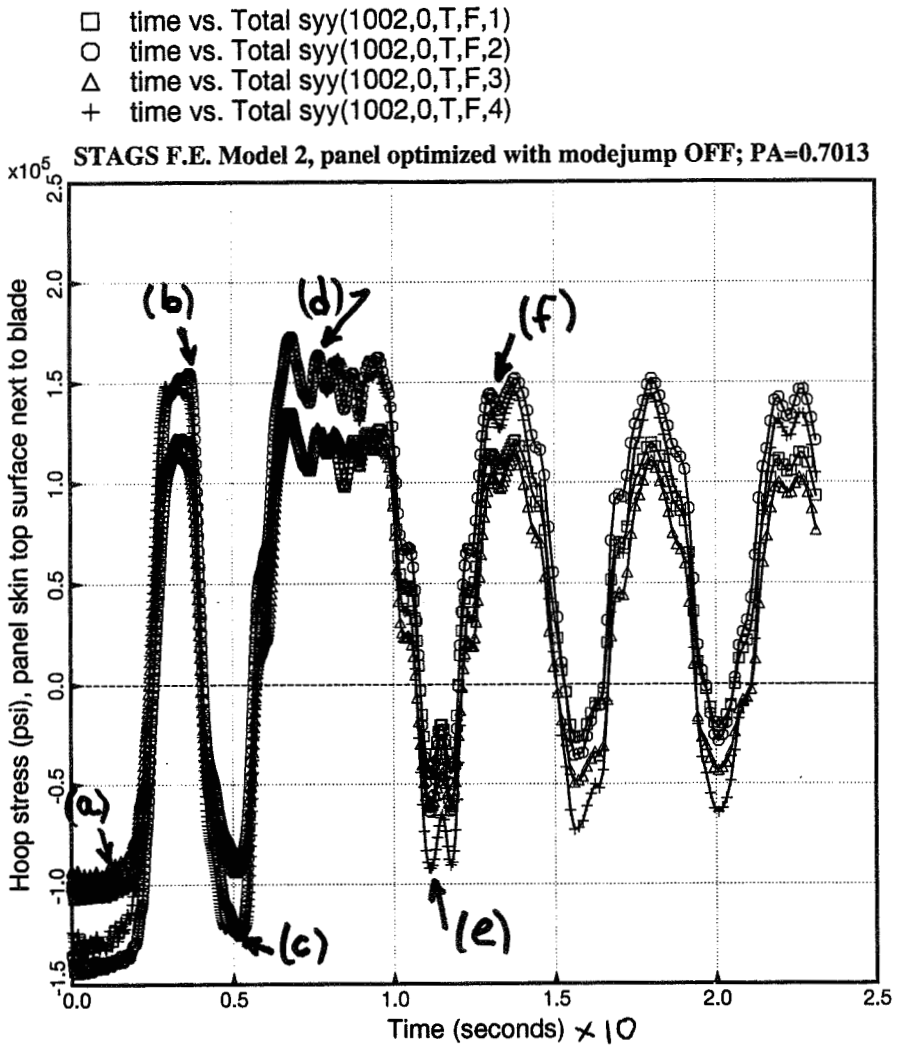

Fig. 30 Oscillations of maximum hoop stress during transient phase (dynamic mode jump). The callouts (a-f) refer to "snapshots" in the previous figure.

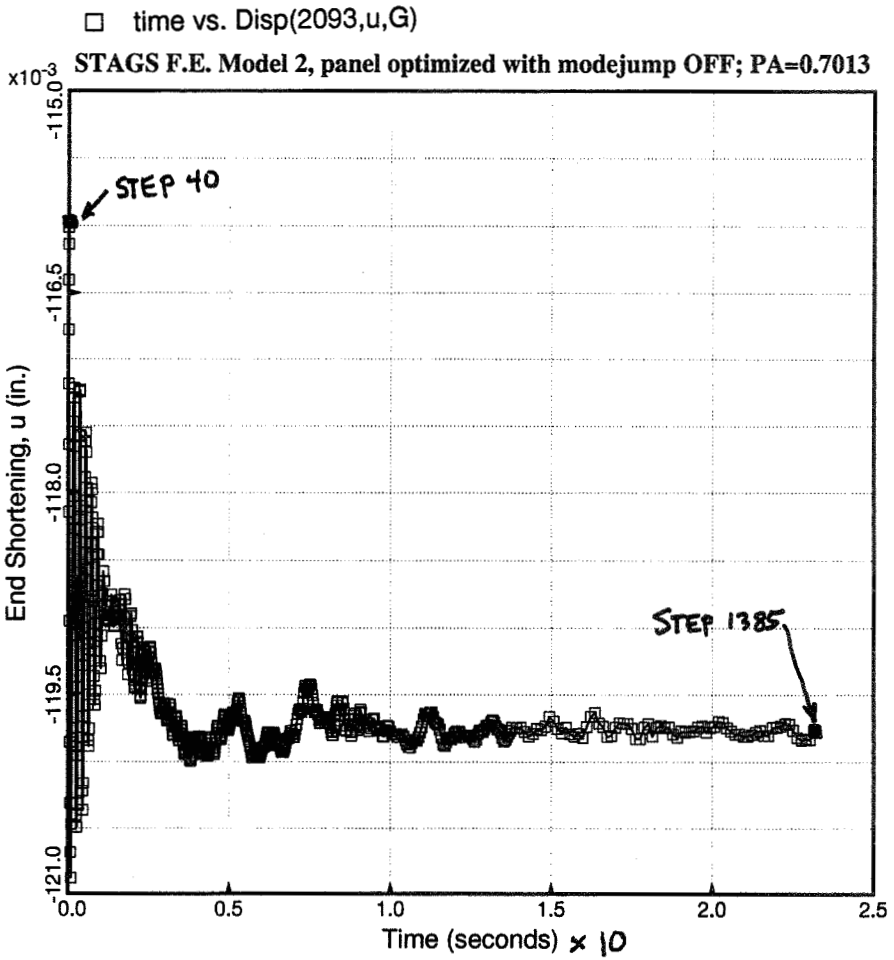

Fig. 31 End shortening during transient phase of PANEL I, Model 2. Although there are only very small changes in end shortening in the range 0.04 < Time < 0.23, there are large oscillations of the maximum hoop stress

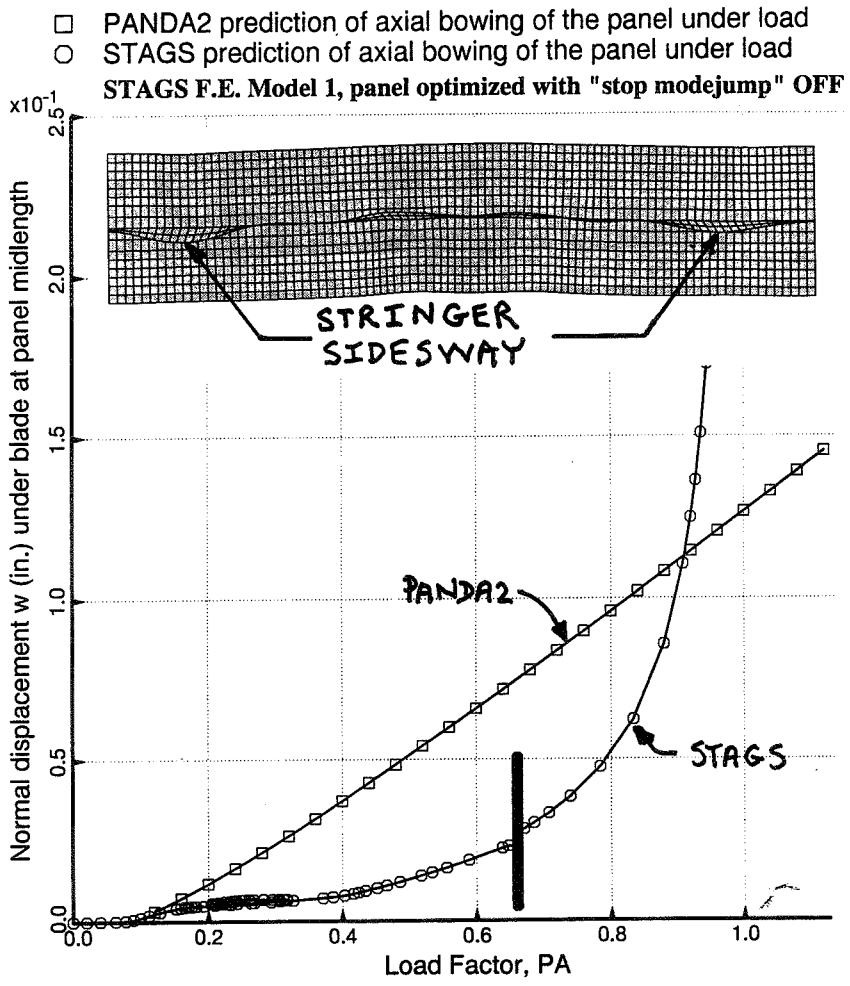

Fig. 32 Axial bowing at midlength of PANEL I predicted by STAGS and PANDA2. In this case PANDA2 does not include the effect of stringer sidesway near the clamped ends in the computation of wide column buckling.

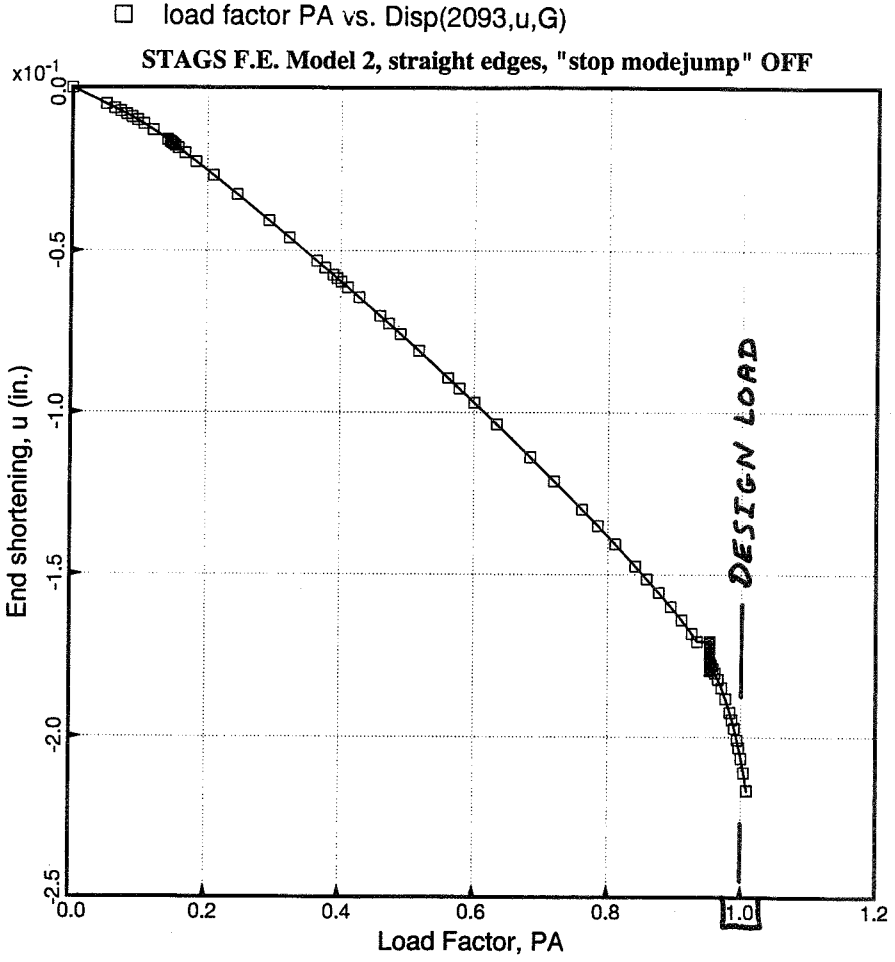

Fig. 33 Load-end-shortening curve for PANEL I. In the STAGS model the two longitudinal edges are prevented from in-plane warping in this case: displacement component v is restrained to vary linearly from one end of the panel to the other.

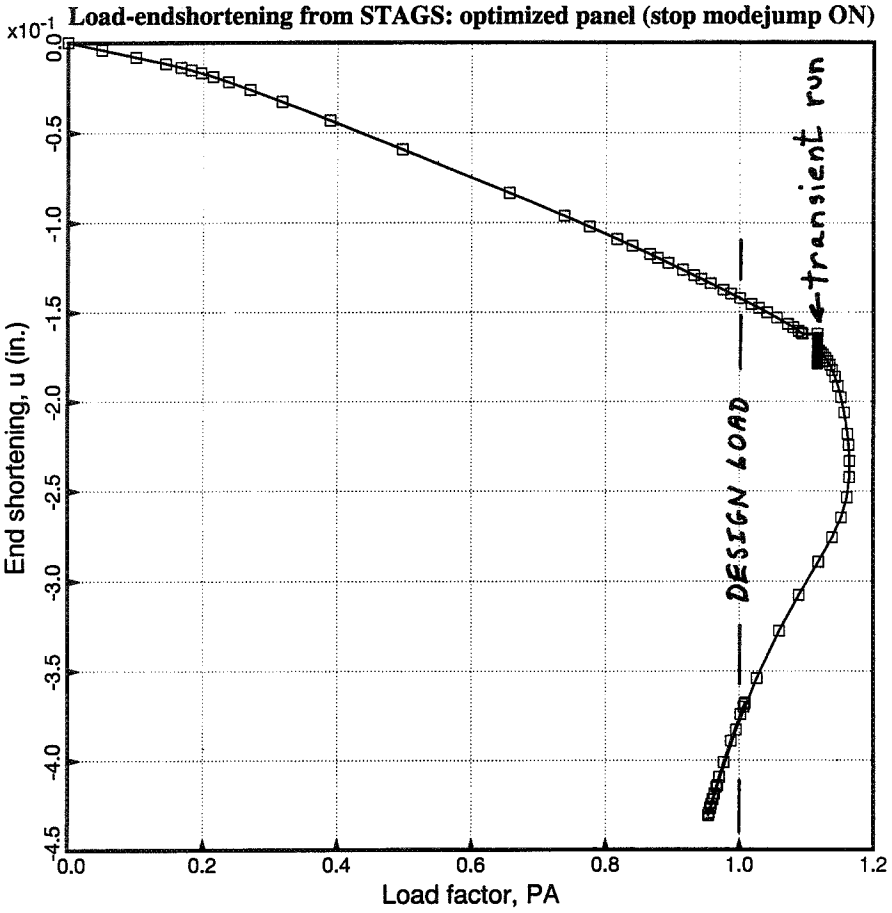

Fig. 34 Load-end-shortening curve for PANEL II, finite element Model 1. PANDA2 predicts mode jumping to occur at the design load.

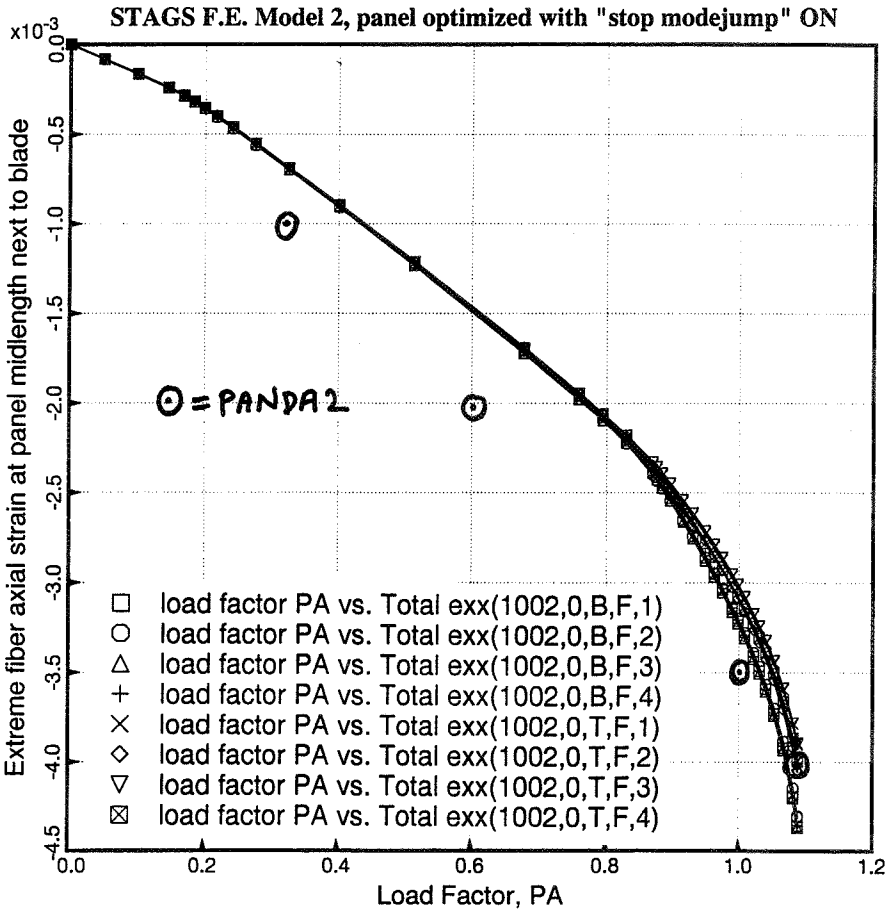

Fig. 35 History of axial strain in PANEL II at the top and bottom surfaces of the panel skin next to the blade.

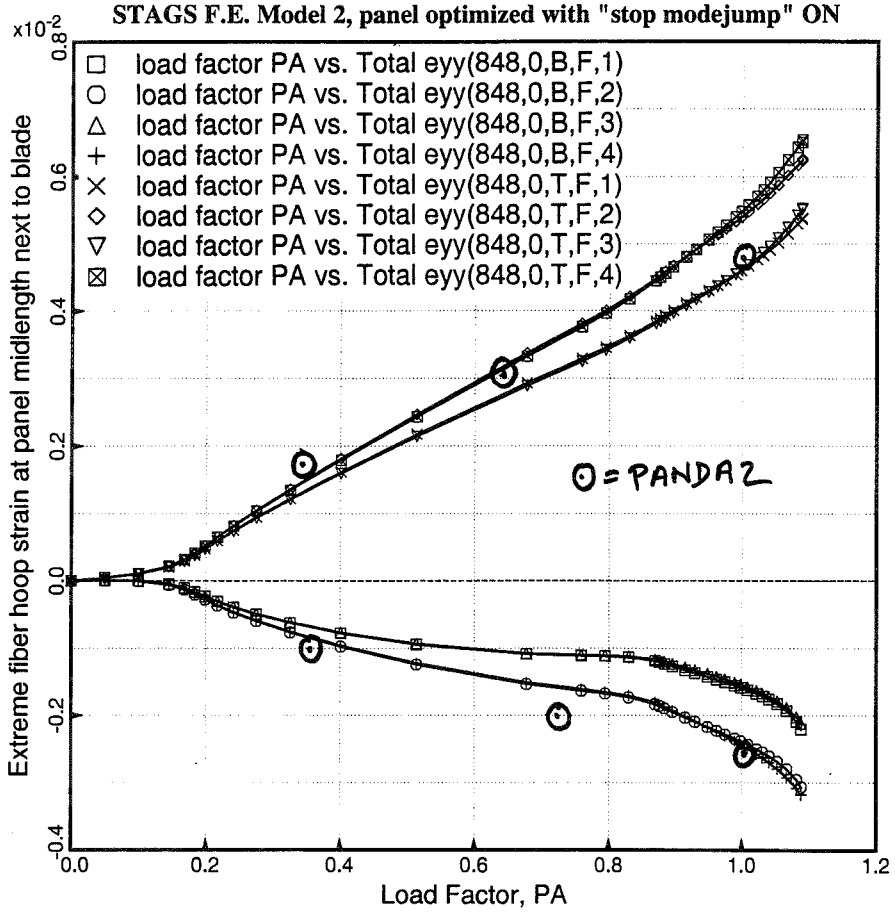

Fig. 36 History of hoop strain in PANEL II at the top and bottom surfaces of the panel skin next to the blade at the location on the axis of the panel where the maximum hoop strain occurs for load factor, PA < 0.6

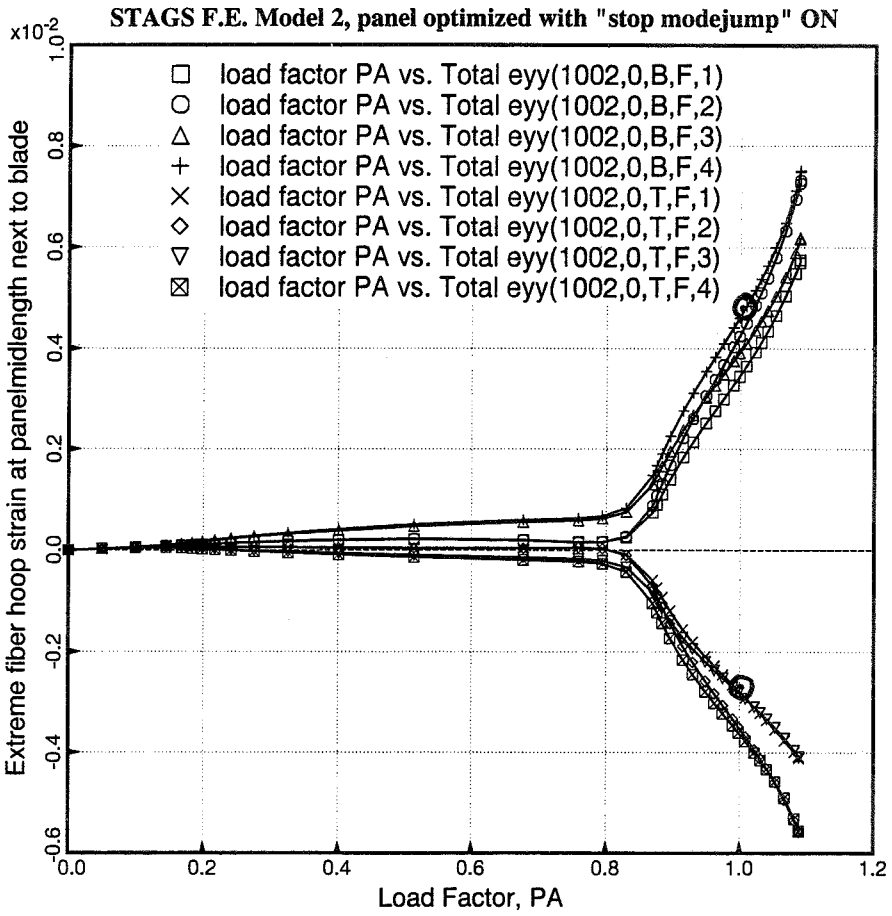

Fig. 37 History of hoop strain in PANEL II at the top and bottom surfaces of the panel skin next to the blade at the location on the axis of the panel where the maximum hoop strain occurs for load factor, PA > 0.9

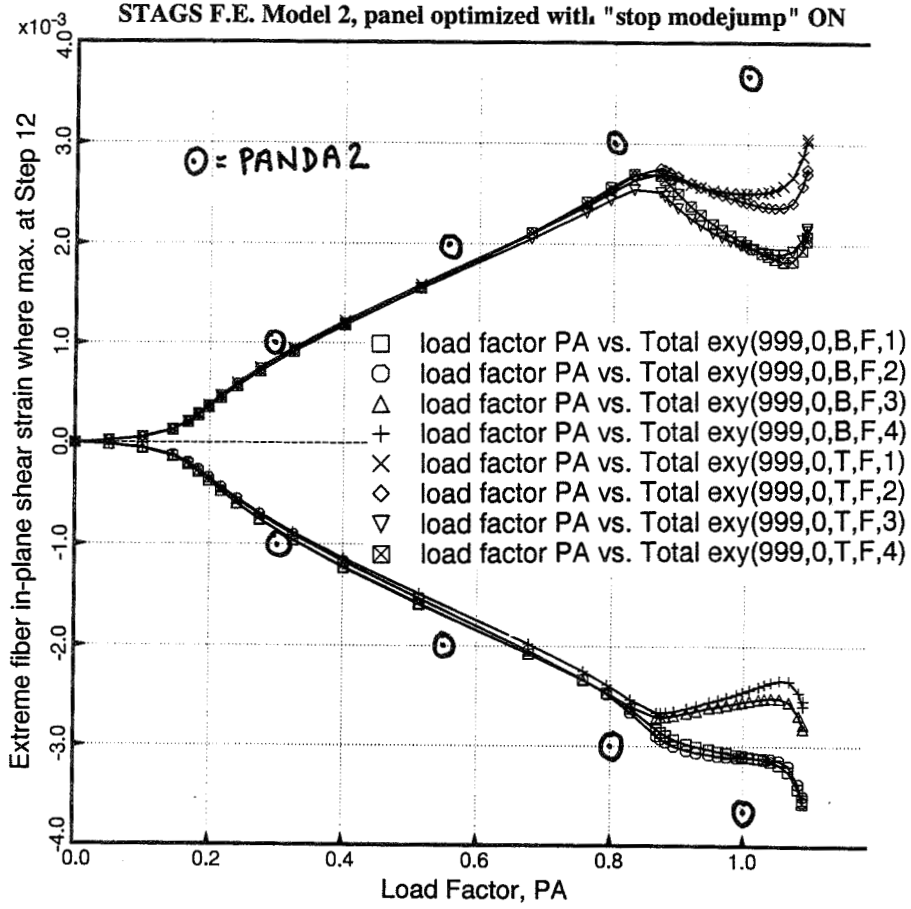

Fig. 38 History of shear strain in PANEL II at the top and bottom surfaces of the panel skin at the location nearest the panel midlength where the maximum shear strain occurs for load factor, PA < 0.6

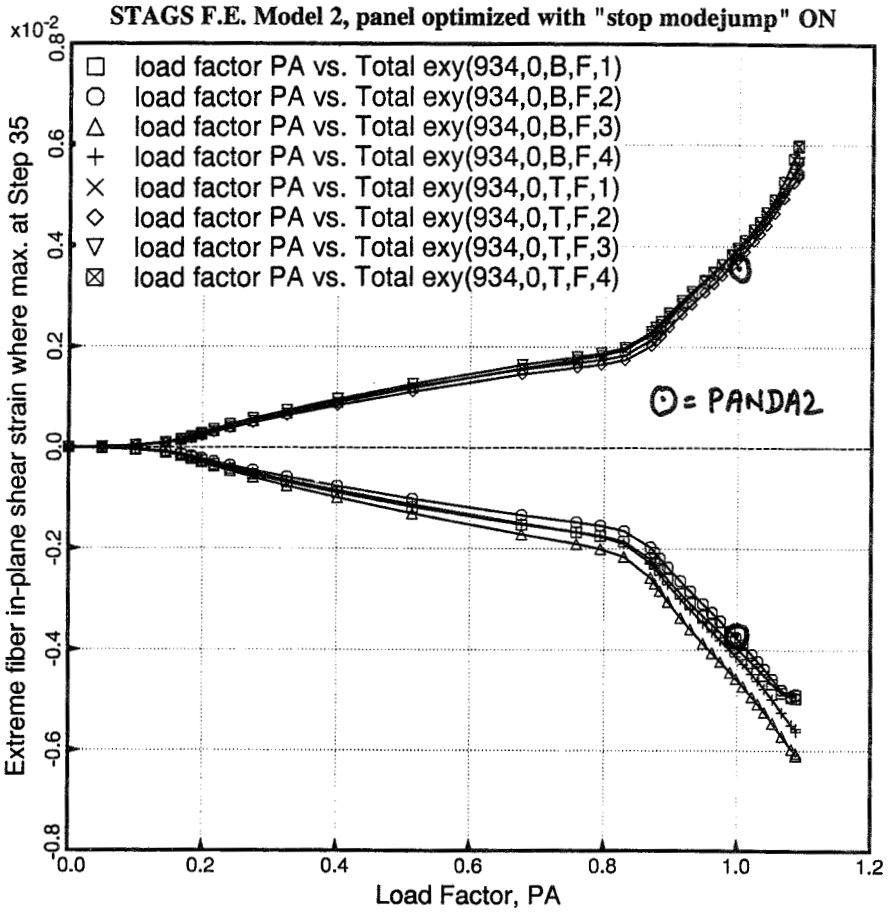

Fig. 39 History of shear strain in PANEL II at the top and bottom surfaces of the panel skin at the location nearest the panel midlength where the maximum shear strain occurs for load factor, PA > 0.9

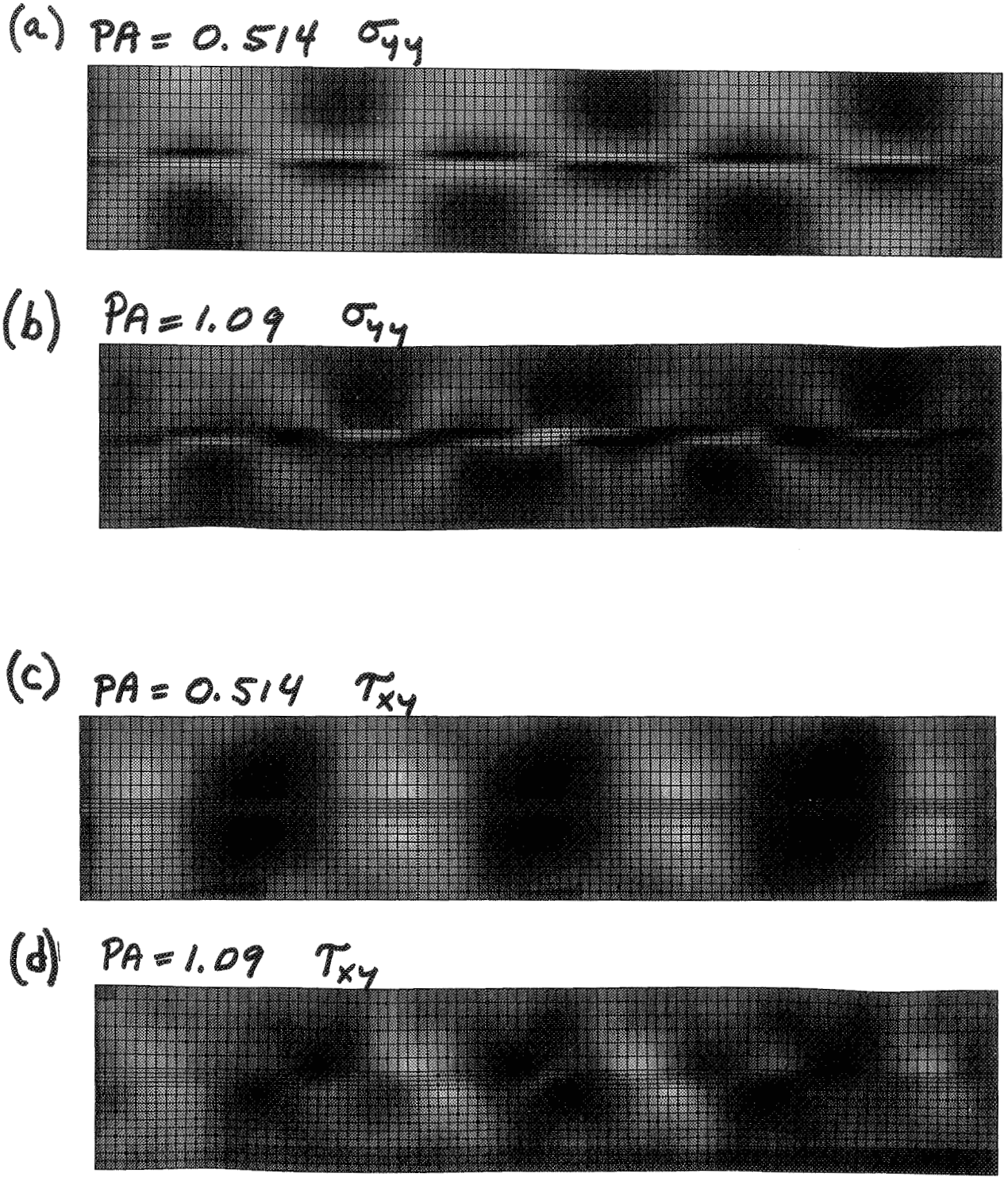

Fig. 40 Fringe plots of (a,b) hoop and (c,d) shear stress at the upper surface in the skin of PANEL II for two load factors. PANDA2 always predicts "in-phase" patterns of the types exhibited in (a) and (c). For load factors near and above the design load (PA=1.0), STAGS predicts relative shifting of the postbuckled lobes on either side of the stringer.

OPTIMUM DESIGN VIA PANDA2 OF COMPOSITE SANDWICH PANELS WITH HONEYCOMB OR FOAM CORES

David Bushnell
Senior Consulting Scientist (Retired)
Department H1-61, Building 255
Lockheed Martin Advanced Technology Center
3251 Hanover St., Palo Alto, California 94304

ABSTRACT

PANDA2 has been extended to handle panels with sandwich wall construction by inclusion of the following failure modes in addition to those previously accounted for: (1) face wrinkling, (2) face dimpling, (3) core shear crimping, (4) core transverse shear stress failure, (5) core crushing and tension failure, and (6) facesheet pull-off. Transverse shear deformation effects are included both for overall panel buckling and for local face sheet dimpling and face sheet wrinkling. The new PANDA2 code will optimize stiffened sandwich panels in which the stiffener segments as well as the panel skin may have sandwich wall constructions. The effects of panel buckling modal initial imperfections as well as initial face sheet waviness are accounted for during optimization cycles. The updated PANDA2 code will also handle optimization of a panel supported by an elastic Winkler foundation. Examples are presented for a uniformly axially compressed perfect and imperfect unstiffened panel without and with a uniform temperature gradient through the panel wall thickness. Initial face sheet waviness and initial overall buckling modal imperfections both have major influence on optimum designs of sandwich panels with honeycomb cores.

INTRODUCTION

Brief Review Of The Literature

Noor, Burton, and Bert [1] provide a recent survey of the state-of-the-art with regard to sandwich panels. Stein and his colleagues [2-4] have contributed several papers. The work reported here is based on earlier work by Vinson [5-7], Hoff and Mautner [8], Plantema [9], Hetenyi [10], and Bitzer and his colleagues at Hexcell Corporation [11-13]. The PANDA2 computer program for minimum weight design of unstiffened and stiffened flat and cylindrical panels and shells [14-20] is modified as described here. PANDA2 supercedes an earlier code PANDA [21] and contains algorithms adapted from BOSOR4 [22] in which the equations valid for branched shells of revolution are transformed to those valid for prismatic structures. PANDA2 will handle optimum designs of panels for which the panel skin stiffener module (module = one stiffener plus stiffener base plus panel skin on either side of the stiffener of total width equal to the stiffener spacing, as shown in Fig. 1) is in its locally postbuckled state (local buckling of the panel between adjacent stiffeners and of the stiffeners). The postbuckling theory in PANDA2 represents an extension of a theory first set forth by Koiter in 1946 [23]. Optimization is performed with use of the ADS software developed several years ago by Vanderplaats and his colleagues [24-25]. Although the examples presented here are for "classical" (non-composite) materials, PANDA2 will handle both regular and sandwich panels composed of laminated segments of advanced composite material [18,19]. PANDA2 consists of a "bundle" of executable processors, the most significant of which are:

BEGIN	(user supplies starting design, material properties, boundary conditions)
DECIDE	(user chooses decision variables and lower and upper bounds for optimization)
MAINSETUP	(user supplies loads, strategy parameters, type of analysis to be performed, etc.)
PANDAOPT	(mainprocessor execution is launched)

Fellow, AIAA

CHOOSEPLOT	(user chooses what to plot.)
DIPLOT	(plots are generated)
CHANGE	(user changes selected quantities)
SUPEROPT	(like PANDAOPT, except it attempts to find a global minimum-weight design [20])
STAGSMODEL	(a finite element model to be used in an execution of STAGS [17,26,27] is generated from an optimum design by PANDA2)

The purpose of the work on which this paper is based was to enhance PANDA2's capability to generate practical optimum designs of sandwich panels by inclusion of several new "sandwich-related" constraint conditions: face wrinkling, face dimpling, core shear crimping, core crushing, core normal tensile failure, face sheet pull-off, and core transverse shear stress failure. The very significant effects of initial face sheet wrinkling and initial buckling modal imperfections are included. This paper represents an abridged version of ITEM 271 in the file .../panda2/doc/panda2.news [29].

Meaning Of The Phrase, "Panel Module", And Other PANDA2 Jargon

In the following discussion, the terms "module segment" and "nodal point" are used. Also the terminology, "Iseg" and "Dseg", occurs. "Iseg" and "Dseg" represent two panel module segment numbering schemes: "Iseg" used primarily with input (Fig. 1a) and "Dseg" referring to segment numbering in a discretized single skin-stringer panel module (Fig. 1b).

As described in previous papers, a stiffened panel is considered by PANDA2 to be built up of a series of identical modules, each of which is divided into segments, as depicted in Figs. 1(a) and (b) for a hat-stiffened panel. Any or all of the module segments can be of sandwich wall construction. Different materials can be used in different segments of the module.

In the PANDA2 literature "x" is the axial coordinate (normal to the plane of the paper), "y" is the coordinate normal to "x" and lying in the plane of the panel skin, and "s" is a coordinate similar to "y": normal to "x" and lying in the plane of each segment of the panel module cross section, as shown in Fig. 9 on p 492 of [14]. In this paper "z" is the local through-thickness coordinate normal to the plane of each panel module segment.

NEW SANDWICH-RELATED BEHAVIORAL CONSTRAINT CONDITIONS INTRODUCED INTO PANDA2

Face Wrinkling

Face wrinkling is defined in the literature on sandwich shells as buckling of a face sheet supported on a continuous elastic foundation with a foundation modulus K (e.g. lb/in^3). See Eqs.(2,3) for K_{eff} which represents the effective stiffness of the sandwich core plus effective stiffness of the glue layer between the core and the face sheet. The elastic foundation modulus K relates normal displacement w of the face sheet to the pressure on that face sheet exerted by the core+glue material. The elastic foundation modulus depends on: 1. the thickness of the sandwich core, 2. the effective "normal-displacement" stiffness of the glue "layer" between a face sheet and the sandwich core, and, if the core is of honeycomb construction, on 3. the diameter of the honeycomb cell and 4. the thickness of the honeycomb cell wall. Three alternate formulas for face wrinkling are used in PANDA2:

(1) a formula based on Eq. (57) of [21] with the elastic foundation term added to a_{33} (Eq.(55f) of [21]; see Eq.(37) below)

(2) a formula presented by Vinson [5], Eq.(4)

(3) a formula first derived by Hoff and Mautner [8] and presented by Plantema [9], Eqs.(5,6).

PANDA2 uses (1) and the minimum face wrinkling load factor computed from either (2) or (3). There is no post-face-wrinkling analysis included in PANDA2.

Face Dimpling

Face dimpling is defined in the literature on sandwich shells as buckling of the face sheet over the diameter of a single cell of a honeycomb core. There is no post-face-dimpling analysis included in PANDA2.

Core Shear Crimping

Core shear crimping is defined as overall buckling of the sandwich wall in a short-wavelength mode in which transverse shearing of the core predominates, as shown

in Fig. 3, p 1692 of Vinson's paper [5], Eqs.(9-11).

Core Transverse Shear Stress Failure

Core transverse shear stress failure under transverse shear forces, Q_x and Q_y (e.g. lb/in) can occur when there is local bending of the panel, as is the case with axially compressed imperfect panels and panels subjected to normal pressure. This is not the same type of failure as "core shear crimping", a buckling phenomenon that can occur in a perfect, uniformly axially compressed flat panel for which the transverse shear forces Q_x and Q_y are zero. Rather, the new constraints for core failure under transverse shear forces Q_x and Q_y are analogous to stress constraints. New calculations for the transverse shear forces Q_x and Q_y are performed in PANDA2. It is assumed that the Q_x and Q_y are carried entirely by the sandwich core. The maximum values of Q_x and Q_y in each skin-stringer module segment, $Q_{x\max}$ and $Q_{y\max}$, are computed, and the corresponding maximum transverse shear stress components in the sandwich core, $\sigma_{13} = Q_{x\max} / t_{core}$ and $\sigma_{23} = Q_{y\max} / t_{core}$, in which t_{core} is the thickness of the sandwich core, are compared to allowables that are now provided by the PANDA2 user as input data in "look-up" tables of experimentally determined core shear failure stress as a function of core density obtained from sandwich core manufacturers such as the Hexcel Corporation [13]. Initial facesheet waviness often has a dramatic influence on the sandwich core transverse shear stress margins.

Core Crushing

Core crushing pressures are computed from the combined effects of axial and hoop curvature changes in each segment of the skin-stringer module which has a sandwich wall construction, applied normal pressure, amplification of initial facesheet waviness under load, and bending of initially imperfect stringer webs, especially stringer web bending along the lines of intersection of the stringer web with other parts of the skin-stringer panel module. The computed core crushing pressures are compared with allowables obtained, as in the case of sandwich core transverse shear stress allowables, from user-provided "look-up" tables. As is the case with core transverse shear stress, initial facesheet waviness has a dramatic influence on the sandwich core crushing margins.

Face Sheet Pull-off And Core Normal Tension Failure

Face sheet pull-off and core tension failure (tension in the core normal to the plane of the sandwich panel module segment) are computed with use of formulas from Plantema [9] and from Hetenyi [10]. Initial facesheet waviness, stiffener web root bending, and hoop bending of initially imperfect cylindrical sandwich panels play major roles.

Summary Of New Sandwich-related Design Margins

New design margins for a single segment of a panel module now appear in the PANDA2 output. These new "sandwich-related" margins are listed in Table.1. The margins with the string, "(VINSON)", are computed from Vinson's theory [5-7] The margins with the string "(HOFF)" are computed from a formula in Plantema's book [9]. PANDA2 uses only the minimum of the face wrinkling margins from "VINSON" and "HOFF". Therefore, both "VINSON" and "HOFF" face wrinkling margins never appear together for the same face sheet.

If more than one segment in a stiffened panel module consists of sandwich wall construction there can be many, many "sandwich-type" constraint conditions generated in a case. An example is presented in [29].

THEORY

Some details on the theories on which the "sandwich-related" constraint conditions just listed are based follow.

Overall Buckling Of The Sandwich Wall

The margin:

localbuck (VINSON) strng Iseg1 ....

is referred to by Vinson [5] as "Overall Instability" (of an unstiffened sandwich panel). Equations (2-6) in [5] govern. This mode of failure is called "localbuck" in PANDA2 because it represents buckling of a single segment of a skin-stringer module (panel skin or stringer web or under hat or hat crown) treated as a flat panel simply supported along all four edges. PANDA2 reserves the term "overall instability" or "general instability" to signify buckling in which the lines of intersection of stiffeners and panel skin displace normal to the panel skin in the buckling mode.

The "localbuck(VINSON)" margin provides a parallel prediction of what PANDA2 has always computed with analysis type IQUICK=1, that is, local buckling analysis of the panel module segments with use of Eq.(57) in [21] with subsequent "knockdown" as described in Section 8.2 of [14] to account for the effect of transverse shear deformation. For local buckling of the panel skin, the previously (and still) available PANDA2 margins that represent the same phenomenon as "localbuck(VINSON)" read:

buck.(DONL) simp-support local buck....

buck.(SAND) simp-support local buck....

in which the string "DONL" means "Donnell theory" and "SAND" means "Sanders theory".

For local buckling of various segments of the panel module other than the panel skin, the previously (and still) available PANDA2 margins that are analogous to the "localbuck(VINSON)" margin read:

buckling margin for stringer Iseg.3

in the case of the web of a T, J, or Hat stiffened panel, or

buckling margin for stringer Iseg.4

in the case of crown buckling in a Hat-stiffened panel. PANDA2's original local buckling constraints and Vinson's "localbuck(VINSON)" constraint are all still retained in the PANDA2 analysis because the effect of transverse shear deformation is handled differently in the two theories: in the original PANDA2 formulation the transverse shear deformation (t.s.d.) effect is applied as a "knockdown" factor as described in Section 8.2, pp495-496 in [14], whereas in Vinson's equations the effect of transverse shear deformation appears as quantities V_x and V_y in Eq.(3) of [5]. It is important that designs generated by PANDA2 survive the most conservative approximation of the buckling load factor obtained from various theories.

With use of analysis type IQUICK = 0 in PANDA2 (discretized single module model, see Figs. 3 - 5 on p.46 of [15]) the same local buckling phenomenon is identified by the phrase,

Local buckling from discrete model....

The "localbuck(VINSON)" margin is computed with the assumption that the module segment is flat and is simply supported along all four edges. Vinson uses certain coefficients in Eqs.(7) of [5] that depend on the number of axial halfwaves which he calls n. (In PANDA2 jargon this axial halfwavenumber is called m). If one assumes that there is only one-half wave across the width of the panel segment, then an explicit value for number of axial halfwaves m,

$$m = (a/b)(C_{55}/C_{44})^{1/4} \qquad (1)$$

results from minimization of the buckling load factor with respect to the number of axial halfwaves in the buckling mode. In Eq.(1) The quantity a is the axial length of the panel module segment (length between adjacent rings if the module represents a stringer), b is the "hoop" width of the panel module segment (for examples: stringer spacing, or width (height) of a stiffener web between the panel skin and outstanding flange, or width of the base or the crown of a hat), C_{55} is the "hoop" (y or s) bending stiffness of the sandwich (D_{22} in the usual laminated composite plate nomenclature), and C_{44} is the axial (x) bending stiffness of the sandwich (D_{11} in the usual nomenclature).

Strictly speaking the "localbuck(VINSON)" margin is valid only for uniaxial compression. However, in PANDA2 the application of Vinson's Eq.(2) in [5] is broadened to handle combined axial compression and in-plane shear in a panel skin because the "localbuck(VINSON)" buckling load factor (for the panel skin only) is "knocked down" by the same factor, FKNOCK(2), that accounts for in-plane shear and anisotropy in the computation of the local buckling margin obtained from the discretized single panel module model: "Local buckling from discrete model ".

Face Wrinkling

There are three margins for face wrinkling computed in PANDA2,

wrinkling; strng Iseg1....

wrinkling (VINSON);strng Iseg1....

wrinkling (HOFF);strng Iseg1....

The first, "wrinkling strng", is computed from Eq.(57) of [21] (knocked down as described above to account for t.s.d.), with a term added to a_{33} in Eq.(55f) of [21]

to account for the effect of the elastic foundation represented by the sandwich core [see Eq.(37) in the "BUCPAN2" entry in the section, IMPLEMENTATION...] , which is treated as a Winkler elastic foundation with stiffness EFOUND (e.g. lb/in^3):

$$EFOUND = K_{eff} = \frac{1}{\left(1/K_{glue} + 1/K_{core}\right)} \quad (2)$$

in which the elastic foundation modulus of the sandwich core, Kcore, is assumed by PANDA2 to be

$$K_{core} = E_{core}^{eff} / \left(0.5 t_{core}\right) \quad (3)$$

where E_{core}^{eff} is the effective elastic modulus of the sandwich core for displacements normal to the face sheets and t_{core} is the thickness of the sandwich core. The "wrinkling strng" margin is valid for arbitrary combinations of in-plane face sheet loads: N_x^{face}, N_y^{face}, N_{xy}^{face}.

The second face wrinkling margin, "wrinkling (VINSON)", is computed from Eq.(15) in Vinson's paper [5] or Eq.(60) in Vinson's paper [6] (same right-hand-sides in both Vinson equations). In PANDA2 the equation is written in terms of face sheet resultants (e.g. N_x^{face}) and coefficients C_{ij} of the 6 x 6 integrated constitutive law for each face sheet, which are available in SUBROUTINE BUCPAN, rather than in terms of stress and moduli, as is the case in Vinson's papers [5] and [6]. That is, in PANDA2 the critical face sheet resultants are given by:

$$N_x^{(face,crit)} = N_y^{(face,crit)} = N_{xy}^{(face,crit)} = t_{face}\left[0.667\left(E_{core}/t_{core}\right)\left(C_{11}^{face}C_{22}^{face}\right)^{1/2}\right]^{1/2} \quad (4)$$

in which C_{11}^{face} and C_{22}^{face} are the axial and hoop integrated stiffness coefficients for a face sheet, t_{core} is the thickness of the sandwich core, and t_{face} is the thickness of a face sheet.

The third face wrinkling margin, "wrinkling (HOFF)", is computed from a modified form of Eq.(10), p 43 of Plantema's book [9]:

$$N_x^{(face,crit)} = 0.5 t_{face}\left[\left(C_{11}^{face}/t_{face}\right)E_{core}G_{13}^{core}\right]^{1/3} \quad (5)$$

$$N_y^{(face,crit)} = 0.5 t_{face}\left[\left(C_{22}^{face}/t_{face}\right)E_{core}G_{23}^{core}\right]^{1/3} \quad (6)$$

$$N_{xy}^{(face,crit)} = N_y^{(face,crit)} \quad (7)$$

The VINSON (Eq. 4) and HOFF (Eqs. 5-7) models for face sheet wrinkling are based on completely different assumptions as to how the sandwich core behaves. In the VINSON model the core is similar to a Winkler elastic foundation. Face wrinkling is governed by the "spring" stiffness of the core normal to the face sheets (elastic modulus divided by the core thickness) and is independent of the transverse shear moduli of the core. In the HOFF model face wrinkling is regarded as a very local phenomenon that disturbs the core only in the neighborhood of the core-facesheet interface, decaying in the z-direction (normal to the face sheet) well before there is any interaction with the opposite face sheet. This local phenomenon is heavily influenced by the transverse shear moduli of the sandwich core. As mentioned previously, PANDA2 computes face wrinkling from both the VINSION and HOFF models, but bases the face wrinkling constraint only on that model which yields the smaller of the VINSION and HOFF face wrinkling load factors. The more critical of the two models is appropriately labelled in the list of design margins, as given, for examples, as Margins 8 and 12 in PART 3 of Table 3 and as Margins 9 and 14 in PART 4 of Table 17.

For combined in-plane loads, N_x^{face}, N_y^{face}, N_{xy}^{face}, the face wrinkling load factor (Eigenvalue) in PANDA2 corresponding to "wrinkling (VINSON)" is computed from

$$Eigenvalue = 1/[\left(N_x^{face}/N_x^{(face,crit)}\right)^2 + \left(N_y^{face}/N_y^{(face,crit)}\right)^2 + \left(N_{xy}^{face}/N_{xy}^{(face,crit)}\right)^2]^{1/2} \quad (8)$$

N_x^{face} is the largest negative axial resultant in the face sheet of the current module segment, N_y^{face} is the largest negative hoop resultant in the face sheet of the current module segment, and N_{xy}^{face} is the largest absolute value of N_{xy}^{face} in the segment. (See Table 14 for an example in which the face sheet resultants vary across the width of the panel module segment).

Face Sheet Dimpling

The face sheet dimpling load factor is governed by buckling of a simply-supported flat, square plate in which the hexagonal cell boundary is INSCRIBED. The length of one side of the square flat plate is 2*s, in which "s" is the width of one side of the regular hexagon of the honeycomb core. Equation [57] of [21], with subsequent "knockdown" to account for t.s.d., is used to compute the buckling load factor. Since the 2*s

x 2*s simply supported square plate is larger than the actual hexagonal plate that dimples, This procedure should yield a conservative estimate for dimpling, provided that the local transverse shear deformation in the face sheet is properly accounted for. PANDA2's dimpling margins are valid for any combination, N_x^{face}, N_y^{face}, N_{xy}^{face}, of in-plane loading in composite, anisotropic face sheets.

Core Shear Crimping

Core shear crimping is computed from Vinson's Eq.(12) in [5] which, for axial compression, can be expressed in the form:

$$N_x^{(total,crit)} = G_{13}^{core} t_{core} \tag{9}$$

and for hoop compression or in-plane shear can be expressed in the analogous forms:

$$N_y^{(total,crit)} = G_{23}^{core} t_{core} \tag{10}$$

$$N_{xy}^{(total,crit)} = \left(G_{13}^{core} G_{23}^{core}\right)^{1/2} t_{core} \tag{11}$$

in which the subscript "total" denotes the sum of the corresponding resultants in the two facesheets. The other variables, G_{13}^{core}, G_{23}^{core}, and t_{core}, represent the x-z and y-z transverse shear moduli and the core thickness, respectively. For combined loads an equation analogous to Eq.(8) is used.

New Configuration Constraints For Hexagonal Honeycomb Sandwich Core

For each panel module segment that is of hexagonal honeycomb core sandwich wall construction, two new constraint conditions of the following type have been added:

Face1 wavelength/celldiam;STR;Iseg=1...

Face2 wavelength/celldiam;STR;Iseg=1...

For each face sheet, the ratio

(face sheet wrinkling halfwavelength)/(1.732*s)

must be greater than or equal to 2.0 if the PANDA2 user indicates in "BEGIN" that he/she wants these constraints to be activated. In the expression above, the quantity "s" is the width of one side of the regular hexagonal honeycomb cell and 1.732*s is the flat-to-flat diameter of the hexagonal honeycomb cell. (1.732*s is called "cell size" in Hexcel Corporation's literature [11-13]). According to Plantema [9], the axial halfwavelength of the face wrinkles in an axially compressed sandwich plate is given by (face sheet wrinkling halfwavelength), L:

$$L = 1.26\pi\left[\left(C_{44}^{face}\right)^2 / \left(G_{xz}^{core} E_z^{core}\right)\right]^{1/6} \tag{12}$$

in which C_{44}^{face} is the axial bending stiffness of the face sheet (D11 in the usual composite material nomenclature), G_{xz}^{core} is the effective x-z transverse shear modulus of the sandwich core, and E_z^{core} is the effective modulus of the sandwich core for stretching of the core normal to the facesheet (z-direction).

The configuration constraint,

$$L/(1.732s) \geq 2.0 \tag{13}$$

in which L is the halfwavelength of the face sheet wrinkling mode of failure, was introduced into PANDA2 in order to force the honeycomb cell size to be small enough so that Plantema's equations for the effect of initial face sheet waviness, to be discussed in the next subsection, become valid for honeycomb core sandwich panels. If constraints of the type (13) are imposed, then in the analysis of the effect of initial face sheet waviness (an effect that is significant if the characteristic wavelength of this initial waviness is the same as that of the face wrinkling mode of instability, which is the assumption used in PANDA2) the honeycomb core can be "smeared out", that is, treated as a homogeneous continuum in the computation of certain "sandwich-related" stress constraints to be discussed later in the subsection entitled "Additional New Sandwich-Related Stress Constraints".

Often imposition of the configuration constraint (13) • does not significantly increase the optimum weight of a panel because the honeycomb cell wall thickness decreases in proportion to the honeycomb cell diameter. Also, small honeycomb cells are generally better than large cells because there are more surfaces for the facesheet-core adhesive to stick to, increasing the facesheet-core interface stress required to pull the facesheet from the core.

Effect Of Initial Face Sheet Waviness

For normal (z-direction) stress and x-z and y-z

transverse shear stress at the facesheet-core interface, Plantema (p 43, Eqs.(3) in [9]) gives the following equations as valid for a semi-infinite core:

$$\sigma_{z1} = \pi(w_0 / L)\left[1/(\lambda_1 - 1)\right]\left(G_{xz}^{core} E_z^{core}\right)^{1/2} \quad (14)$$

$$\tau_{xz1} = \pi(w_0 / L)\left[1/(\lambda_1 - 1)\right] G_{xz}^{core} \quad (15)$$

$$\tau_{yz1} = \pi(w_0 / L)\left[1/(\lambda_2 - 1)\right] G_{yz}^{core} \quad (16)$$

in which w_0 represents the amplitude of the initial face sheet waviness and L, the halfwavelength of the face wrinkling mode, is given above in Eq. (12). Plantema [9] writes that typical sandwich panels of good quality have $w_0 / L = 0.001$. In Eqs (14,15) λ_1 represents the load factor for face sheet wrinkling with all facesheet resultants, N_x^{face}, N_y^{face}, and N_{xy}^{face}, present. In Eq.(16) λ_2 represents the load factor for face sheet wrinkling with only the facesheet "hoop" resultant, N_y^{face}, present. The factors, $[1/(\lambda_i - 1)$, i=1,2], result from amplification of the initial face sheet waviness as the sandwich face sheets are subjected to destabilizing loads.

The stresses, σ_{z1}, τ_{xz1}, and τ_{yz1} play a significant role in the stress constraints to be discussed later in the subsection entitled "Additional New Sandwich-Related Stress Constraints".

Effect Of Web Root And Tip Bending

If the IQUICK=0 model option (discretized single skin-stringer panel module model [14]) is used in the PANDA2 processors, MAINSETUP and PANDAOPT, and if a stringer-stiffened sandwich panel has an initial imperfection in the form of its local buckling mode, significant local face sheet pull-off stresses can develop in the top face sheet of the stringer base due to growth of the initial buckling modal imperfection as the panel is loaded. See, for example, the local buckling mode of the tee-stiffened panel shown in Fig. 4(b) on p. 46 of [15]. There can be significant bending in the imperfect web at its root where it intersects the top face sheet of the stringer base. (This web root bending is what gives rise to stringer popoff, as displayed in Figs. 5 and 6 on p 477 of [14]). A concentrated line moment,

$$M_0 = C_{55}^{web} w_{,ss}^{web} \quad (17)$$

is therefore applied to the top face sheet of the stringer base. In Eq.(17) s is the width-wise coordinate in the web, identified in Fig. 9 on p 492 of [14].

If the stringer base is of sandwich construction, the line moment M_o gives rise to a normal displacement distribution $w(y)$ in the face sheet of the stringer base adjacent to the stringer web. This $w(y)$ is antisymmetric with respect to the line of intersection of the stringer web and the stringer base. This face sheet is supported by an elastic foundation with stiffness K. Hetenyi in his article on beams on elastic foundations [10] gives for the normal stress at the beam facesheet-foundation interface·

$$\sigma_{z2} = Kw = M_0 \lambda^2 e^{-\lambda y} \sin(\lambda y) \quad (18)$$

in which

$$\lambda = \left[K/\left(4C_{55}^{face}\right)\right]^{1/4} \quad (19)$$

Note that Hetenyi's formulas for a beam on an elastic foundation with a concentrated moment can be applied directly to the problem of a face sheet on an elastic foundation with a uniform applied line moment. Where Hetenyi uses EI for the bending stiffness of the facesheet of the beam, we can use C_{55}^{face} for the "hoop" bending stiffness of the top face sheet of the stringer base.

The maximum normal stress, σ_{z2}, occurs at a distance $y = \pi/(4\lambda)$ from the line of intersection of the web root with with the top facesheet of the stringer base. The quantity σ_{z2} in Eq.(18), with substitution of $y = \pi/(4\lambda)$, must be added to σ_{z1} generated from amplification of the the initial face sheet waviness, Eq.(14). These normal stresses contribute to the total normal stress tending to crush the core or tending to cause normal tensile failure in the core or tending to pull the facesheet from the core.

An analogous line moment occurs at the tip of a stringer web where it intersects the outstanding flange of a TEE-shaped stringer.

The formulas above are valid for a semi-infinite elastic foundation. PANDA2 accounts for the finiteness of the depth of the elastic foundation in the case of a sandwich wall by "knocking down" the sum, σ_{z1} plus σ_{z2} by a factor that depends on the ratio $(\pi/\lambda)/t_{core}$, in which t_{core} is the thickness of the sandwich core. If the ratio, $(\pi/\lambda)/t_{core}$, is less than unity the "knockdown"

factor is unity; if the ratio, $(\pi/\lambda)/t_{core}$, is greater than 3.0 the "knockdown" factor is zero; and the "knockdown" factor is assumed to vary linearly between these two limits.

What if the stringer web is a rather thick sandwich wall? Then, rather than a single applied line moment M_o, PANDA2 assumes that there are equal and opposite line loads $P_1 = N_y^{webface1}$ and $P_2 = N_y^{webface2}$, applied to the top face sheet of the stringer base where the two local web face sheet resultants, $N_y^{webface1}$ and $N_y^{webface2}$, occur. $P_1 = -P_2 = P = \pm N_y^{webface1}$ because there is zero net total hoop load $N_y^{totalweb}$ in the stringer web. Hetenyi [10] gives for the normal stress at the beam-foundation interface when the beam is subjected to a concentrated load:

$$\sigma_{z2} = Kw = 0.5P\lambda e^{-\lambda y}\left[\cos(\lambda y) + \sin(\lambda y)\right] \quad (20)$$

in which λ is given above by Eq. (19). Rather than compute the value of y for which the maximum absolute value of σ_{z2} occurs, in this case PANDA2 simply assumes the worst: that the two equal and opposite line loads, P_1 and P_2, applied by the two web face sheets to the top facesheet of the stringer base are far enough apart so that the maximum tensile or compressive normal stress, σ_{z2}, can with reasonable accuracy be given by

$$\sigma_{z2} = 0.5P\lambda \quad (21)$$

In order to generate conservative results, PANDA2 uses the following value for the line load P:

$$P = \pm\max\left[abs\left(N_y^{webface1}\right), abs\left(N_y^{webface2}\right)\right] \quad (22)$$

in which the superscripts "web face 1" and "web face 2" denote the maximum values anywhere in the stringer web face sheets rather than at the web face sheet roots only. This strategy also serves to smooth the optimization somewhat because very small changes in the dimensions of the stringer segments can sometimes lead to dramatic changes in the local buckling mode shape. An example of this behavior is displayed in Fig. 13 on p. 539 of [28]. The load factor for local buckling and the shape of the local buckling mode in the stringer web are the most significant determinants of σ_{z2}.

Additional New Sandwich-related Stress Constraints

Additional new sandwich-related stress constraints are also computed in SUBROUTINE BUCPAN of PANDA2. The new margins corresponding to these five additional "stress" constraints are identified in the PANDA2 output as listed in Table 2.

The "Iseg" number and the "Matl" number can be different from those listed in Table 2, of course, and "STR", which stands for "stringer", can just as well be "RNG", which stands for "ring"; and "MIDLENGTH", which corresponds to load Subcase 1, can just as well be "AT RINGS" or "PANEL END", which correspond to load Subcase 2 [17].

Sandwich core transverse shear stress constraints:

L-dir. sandwich core shear...

W-dir. sandwich core shear...

"L-dir" and "W-dir" are Hexcel Corporation jargon [11-13] denoting the major and minor sandwich core transverse shear stiffnesses, denoted in PANDA2 Gcxz and Gcyz, respectively. In PANDA2 "L-dir" always coincides with the x-z transverse shearing plane and "W-dir" always coincides with the y-z or s-z transverse shearing planes of each module segment, in which the coordinate "y" or "s" is in the plane of the panel module segment and normal to the x (axial) direction, as displayed in Fig. 9 on p. 492 of [14].

In order to compute the new sandwich core transverse shear stress constraints, transverse shear resultants, Q_x and Q_y (e.g. lb/in), must first be obtained at every nodal point in the panel skin-stringer discretized single module. These transverse shear resultants, Q_x and Q_y, are now computed in SUBROUTINE STRMID of the KOITER library in PANDA2 [15]. Q_x and Q_y are computed from the following equations for each discretized module segment:

$$Q_x = C_{44}w_{,xxx} + 3C_{46}w_{,xxy} + (C_{45} + 2C_{66})w_{,xyy} + C_{56}w_{,yyy} \quad (23)$$

$$Q_y = C_{46}w_{,xxx} + 3C_{56}w_{,xyy} + (C_{45} + 2C_{66})w_{,xxy} + C_{55}w_{,yyy} \quad (24)$$

in which $C_{44}, C_{45}, C_{46}, C_{55}, C_{56}, C_{66}$ are the integrated elastic constants for the module sandwich segment

(elements of the 3x3 D matrix in the usual nomenclature for laminated composite walls) and w is the normal displacement field obtained from the KOITER branch of PANDA2 as described in [15]. The "triple derivatives", $w_{,xxx}$, $w_{,xxy}$, , etc.,were not previously computed anywhere in PANDA2. Now the $W_{,xxx}$, $W_{,yyy}$, $W_{,xxy}$, $W_{,yyx}$ correponding to the local buckling mode W (Note: uppercase W!) used in the KOITER branch are computed in SUBROUTINE MODE (MODE library) by backward differencing of $W_{,xx}$ and $W_{,yy}$. The quantity W (cap w) denotes "normal local buckling modal displacement". The relation between w (lower case) and W (cap) is

$$w = fW \tag{25}$$

in which f is the amplitude quantity obtained by solution of the nonlinear equations for the four unknowns, f, "a", M, N, in the KOITER branch of PANDA2 [15]. (f represents the amplitude of the postbuckling normal displacement field, "a" represents a postbuckling modal flattening parameter, "M" represents the slope of the postbuckling nodal lines, and "N" is an axial wavelength parameter). Details about how the four unknowns, f, "a", M, and N, are determined in the KOITER branch are given in [15]. This postbuckling section in PANDA2 was very difficult to develop. It has been adjusted over a period of many years to increase its reliability.

PANDA2 computes (in SUBROUTINE STRMID) the maximum absolute values of the transverse shear stress components, Q_x / t and Q_y / t, where t is the total wall thickness of the module sandwich segment, for each skin-stringer module segment which has sandwich wall construction, then compares these two components of transverse shear stress with two user-provided allowable values for each sandwich core material used in the panel, as follows:

(sandwich core x-transverse shear stress constraint) =

$$\left[\tau_{xzcore}^{allowable} / \left(Q_x / t + \tau_{xz1}\right)\right] \tag{26}$$

(sandwich core y-transverse shear stress constraint) =

$$\left[\tau_{yzcore}^{allowable} / \left(Q_y / t + \tau_{yz1}\right)\right] \tag{27}$$

in which τ_{xz1} and τ_{yz1} are obtained from the analysis that accounts for initial face sheet waviness, Eqs. (15,16).

The $\tau_{xzcore}^{allowable}$ and $\tau_{yzcore}^{allowable}$ are obtained from user-provided "look-up" tables of values of core shear strength:

$\tau_{xzcore}^{allowable}$ vs core density (28)

and

$\tau_{yzcore}^{allowable}$ vs core density (29)

and

"knockdown factor for tau-allowable(core) vs core thickness" (30)

which originate in some published document such as Hexcel Corporation's [13]. An example of these user-provided "look-up" tables appears in Table 271.3 of ITEM 271 of [29].

Because the KOITER branch in PANDA2 does not handle transverse shear deformation effects in a rigorous manner but via "knockdown" factors for effective bending stiffnesses of panel skin and stringer web(s) based on Timonshenko beam factors computed as described in Section 8.2 of [14] and via a "knockup" factor for the amplitude f based on different values obtained for the local buckling load factor computed in the KOITER branch vs that computed from BOSOR4-type theory (See panda2.news ITEM 298 [29]), the values of the maximum transverse shear stresses, Q_x / t and Q_y / t, obtained in the KOITER branch may be unconservative. Therefore, alternative values of Q_x / t and Q_y / t are computed in SUBROUTINE STRCON as described in panda2.news ITEM 294 [29]. PANDA2 uses the maxima of the values of Q_x / t and Q_y / t as computed in SUBROUTINE STRMID and as computed in SUBROUTINE STRCON.

Sandwich core crushing/tensile failure:

Core crushing margin....

sandwichcore tension margin....

Core crushing or tensile failure can occur from the combination of sandwich core normal stresses generated from the following phenomena:

1. Initial face sheet waviness: inward or outward initial

face sheet waviness is amplified by the applied loading and tends to crush or pull apart the core locally [σ_{z1} in Eq. (14)].

2. Bending at the root and tip of a stringer web in a panel with a finite local buckling modal initial imperfection: amplification of the initial local buckling modal imperfection may be associated with significant concentrated line loads where the stringer web intersects other parts of the structure that may have sandwich wall construction. These line loads give rise to local normal stresses at the facesheet core interface [σ_{z2} in Eq.(18) or Eq.(21)].

3. Applied normal pressure to the panel skin: this pressure must be added to the other normal stress components tending to crush the core.

4. Deformation-induced core crushing or normal tension: Changes in curvature of initially flat panel segments always tend to crush the core. In the case of imperfect sandwich cylindrical panels and shells, curvature changes that increase the local hoop radius of curvature give rise to tension in the core normal to the face sheets.

The contributions of Items 1 and 2 to core crushing/tensile failure have already been discussed. Item 3 requires no discussion. Next, we will address the question of deformation-induced core crushing/tensile failure.

Part of the core crushing/tensile pressure is induced by the development of changes in axial and hoop curvature as an imperfect, thermally and mechanically loaded panel deforms. The deformation-induced core crushing or tensile pressure is assumed in PANDA2 to be given by

$$p_{inducedcrush} = N_x^{face} / R_1 + N_y^{face} / R_2 \qquad (31)$$

in which N_x^{face} is the axial resultant in the top face sheet caused by pure bending of the sandwich module segment about its neutral plane for axial bending; R_1 is the change in axial radius of curvature due to the pure bending (e.g. $w_{,xx} = 1/R_1$ in which w is the normal displacement resulting from pure bending)); N_y^{face} is the hoop resultant in the top face sheet caused by pure bending of the sandwich module segment about its neutral plane for hoop bending; and R_2 is the change in hoop radius of curvature due to the pure bending (e.g. $w_{,yy} = 1/R_2$). For orthotropic face sheets with no "B" terms in the 6 x 6 integrated constitutive matrix, N_x^{face} and N_y^{face} can be expressed in terms of the two normal strain components, ε_1^{face} and ε_2^{face}, at the top face sheet generated by pure axial and hoop bending, as:

$$N_x^{face} = C_{11}^{face}\varepsilon_1^{face} + C_{12}^{face}\varepsilon_2^{face} \qquad (32)$$

$$N_y^{face} = C_{12}^{face}\varepsilon_1^{face} + C_{22}^{face}\varepsilon_2^{face}$$

and the strain components, ε_1^{face} and ε_2^{face}, for pure bending can be written in the form:

$$\varepsilon_1^{face} = \left[0.5\left(t - t_{face}\right) - C_{14}^{total} / C_{11}^{total}\right] / R_1 \qquad (33)$$

$$\varepsilon_2^{face} = \left[0.5\left(t - t_{face}\right) - C_{25}^{total} / C_{22}^{total}\right] / R_2$$

in which t is the total thickness of the sandwich; t_{face} is the thickness of the top face sheet; and C_{ij}^{total} are elements of the integrated constitutive matrix for the entire sandwich wall. The ratio $-C_{14}^{total} / C_{11}^{total}$ represents the eccentricity of the neutral plane for axial (x) bending from the middle surface of the sandwich wall; $-C_{25}^{total} / C_{22}^{total}$ represents the same for "hoop" (y or "s") bending.

Equations (33) can be inserted into Eqs.(32), and the result can be inserted into Eq.(31) to yield the deformation-induced crushing pressure p_{crush} in terms of the axial and hoop curvature changes $1/R_1$ and $1/R_2$ (and $p_{tensile}$ in the case of initially curved sandwich panels with locally reduced curvature $1/R_2$).

In PANDA2 the maximum deformation-induced core crushing (tensile) pressure in each segment of the discretized skin-stringer single module is computed in SUBROUTINE GETEPS, which is called from SUBROUTINE STRTHK. In SUBROUTINE GETEPS the curvature changes, $1/R_1$ and $1/R_2$, are known. These curvature changes are associated with the local deformations normal to the module segment surface computed in the KOITER branch of PANDA2 [15] plus the local (prismatic) deformation that arises when a stringer-stiffened plate under normal pressure locally "wraps around" the line of intersection of the stringer web with the panel skin in the prebuckling phase (Figs. 56-58 in [14]).

As is true in the case of transverse shear stress components, Q_x / t and Q_y / t, discussed above, the

deformation-induced sandwich core crushing/ tensile pressure computed in SUBROUTINE GETEPS may be unconservative because this crushing/tensile pressure is derived from a displacement field determined from the KOITER branch in PANDA2, in which the effect of transverse shear deformation is accounted for in an approximate, possibly unconservative, manner. Therefore, an alternative value of the deformation-induced crushing/tensile pressure is also computed in SUBROUTINE STRCON as described in panda2.news ITEM 294 [29]. PANDA2 uses the maximum of the values of deformation induced crushing/tensile pressure calculated from the two alternative methods, as demonstrated in Parts 5a and 5b of Table 271.17 of ITEM 271 of [29].

Face Sheet Pull-Off

The constraints for face sheet pull-off are generated as described in the previous section. If PANDA2 perceives that the facesheet-core adhesive fails before the core, it identifies the corresponding normal tensile stress failure as "face sheet pull-off margin...." rather than as "sandwichcore tension margin....".

IMPLEMENTATION OF "SANDWICH" CAPABILITY IN PANDA2

PANDA2 permits analyses of sandwich walls with dissimilar face sheets and sandwich walls in which the in-plane loading in each face sheet may be different. Different loading in each of the two face sheets occurs in imperfect panels, thermally loaded panels with a temperature gradient through the sandwich wall, panels with applied external bending moments M_x and M_y, panels with applied normal pressure, and panels that are in their locally postbuckled states.

In each module segment (see Figs. 1(a,b) for definition of a "module segment") there may be only one "core": the user cannot "stack" sandwich walls. If there is a "core" there cannot also be an "external" elastic foundation. By "external" is meant a core-like (relatively soft) material as the extreme layer of a segment. If there is an "external" elastic foundation there cannot also be a sandwich "core". There can only be a single "external" elastic foundation; the user may not embed a segment wall between two elastic foundations.

The user provides input data for each segment laminate as previously. The "external" elastic foundation or the sandwich "core" layer in each segment is provided by the user simply as a layer of the wall, just like any other layer in that wall. Then the user provides properties for the various materials in the structure just as previously. Up to this point the input data required for the BEGIN processor are the same as previously.

After the user has provided all the material properties, PANDA2 automatically searches through the layers of each module segment in order to identify possible candidates as sandwich cores or "external" elastic foundations. This search is performed in SUBROUTINE PANEL of the BEGIN library. The criterion for candidacy of a module segment layer to be treated as an elastic foundation or as a sandwich core material appears in the following code fragment in the "BEGIN" processor:

```
ENORM = SQRT(E1L(J)**2 + E2L(J)**2)

IF (ENORM/EMAX.LT.0.001

.AND.TL(J).GT.0.5*TWALL) THEN

   (ask user for elastic foundation
   modulus or core properties)

ENDIF
```

in which J is the Jth layer in a module segment; E1L and E2L are the lamina elastic moduli for deformation parallel and normal to the Jth lamina fibers, respectively; EMAX is the maximum value of ENORM for the segment laminate; TL is the thickness of an individual segment layer; and TWALL is the total segment laminate thickness. If the user wants a certain segment layer to be treated as an "external" elastic foundation or as a sandwich core, then he/she must:

1. supply a thickness for that layer which is at least half the thickness of the entire wall and

2. the square root of the sum of the squares of the moduli for axial and hoop stretching of the core must be smaller than 0.001 times EMAX, where EMAX is the square root of the sum of the squares of the moduli of the material of that layer which has the maximum value of ENORM for any of the layers in that segment laminate.

If the soft candidate material corresponds to an extreme layer of a module segment (that is, this layer actually represents an external elastic foundation), then the previously user-provided thickness of that layer is

automatically reset to zero by PANDA2 so that in further PANDA2 processing that ("fake") layer does not contribute to the in-plane or bending stiffness of the segment laminate. NOTE: the weight of the elastic foundation is not included in PANDA2's computation of panel weight.

In order to implement the "sandwich/elastic foundation" capability into PANDA2, it was necessary to modify the PANDA2 prompt file, PROMPT.DAT, as listed in Table 271.1 of ITEM 271 of [29] and to modify the PANDA2 source code libraries, ARRAYS, BEGIN, BOSPAN, BUCKLE,... as described next.

ARRAYS

Introduce a new subroutine FOUNDA (taken from BOSOR4) which computes the contribution of the elastic foundation to the local finite element stiffness matrix. SUBROUTINE STABIL was modified.

BEGIN

Introduce new input data for sandwich core or external elastic foundation as called for in the modified PROMPT.DAT file (Table 271.1 of [29]). Reset previously user-supplied thickness for any layer representing an external elastic foundation to zero so that that "fake" layer will not affect in-plane or bending stiffness of the segment laminate. SUBROUTINE PANEL was modified.

BOSPAN

Introduce the elastic foundation modulus K into the BOSOR4 model of the panel generated via the PANDA2 processor, PANEL. SUBROUTINE SEGMNT was modified.

BUCKLE

Allow for a higher maximum allowable number of axial halfwaves in the local buckling model based on the discretized module. This is required because axially compressed plates on elastic foundations typically buckle into many, many axial halfwaves. SUBROUTINE LOCAL was modified. Also, include in SUBROUTINE CRIPPL (CRIPPL is called from SUBROUTINE STFEIG and performs local buckling of stiffener segments) the effect of an external elastic foundation, EFOUND=K^i. New quantities that govern the buckling load factors for stiffener segments are given for an "internal" stiffener segment by the following expressions. (An "internal" segment is a segment that is supported along both longitudinal edges by other stiffener segments or by the panel skin):

The new expression for the critical number of axial halfwaves m_i in the ith locally buckled stiffener segment is given by:

$$m_i = \left[\left(K^i + C^i_{55}F^2\right)/C^i_{44}\right]^{1/4}(\ell/\pi) \tag{34}$$

NOTE: m_i in Eq.(34) (a wavenumber) is equal to the value of what is called "m_i" in Eq.(69) of [21] mu.ltiplied by ℓ/π. The first term in the numerator on the right-hand side of Eq. (71) in [21] becomes

$$NUM_1 = 2\left[C^i_{44}\left(K^i + C^i_{55}F^2\right)\right]^{1/2} + \left(C^i_{45} + 2C^i_{66}\right)F \tag{35}$$

In Eqs.(34-35) the quantity F is given by $(\pi/b_i)^2$, where b_i is the width of the ith module segment. The quantity ℓ is the length between stiffeners. It was also necessary to modify SUBROUTINE WEBBUK (see panda2.news ITEM 121 [29]) to account for an elastic foundation. The simple modification is:

$$C44M4 = \left(C^i_{44}m_i^4 + K^i\right)/\left(C^i_{44}C^i_{55}\right)^{1/2} \tag{36}$$

This simple modification holds because the elastic foundation modulus, K_i, called "EFOUND" in SUBROUTINE WEBBUK, contributes a "w-type" term to the strain energy analogous to the term $C^i_{44}m_i^4$ that represents the strain energy for axial bending. (See the similar kind of addition of EFOUND to the coefficient a_{33} in SUBROUTINE EIGREG).

Also, in the case of hat stiffeners and truss-core sandwich panels, any elastic foundation that occurs as the first layer under the hat or as the first layer in the lower face sheet of a truss-core sandwich configuration is handled as if the elastic foundation material (called "FOAM" in the revised SUBROUTINE OBJECT) fills the hat or, in the case of a truss-core panel, fills the space between the lower and upper face sheets. The

contribution of this "FOAM" is included in the computation of panel weight in SUBROUTINE OBJECT.

In addition, because of the extreme sensitivity of the sandwich core maximum transverse shear stress constraints to the local buckling mode shape predicted for the skin-stringer discretized module, it was necessary to introduce some iterative refinement in SUBROUTINE LOCAL, as described in panda2.news ITEM 301 [29].

BUCPAN1

Compute buckling load factors corresponding to the new "sandwich-related" constraints listed above in the section entitled "SUMMARY OF NEW SANDWICH-RELATED MARGINS". A list of the new code is included in Table 271.2 of ITEM 271 of [29]. Most of the modifications in PANDA2 required for implementation of the "sandwich" capability occur in SUBROUTINE BUCPAN.

BUCPAN2

Introduce the elastic foundation modulus term, EFOUND=K^i, into the coefficient a_{33} (see Eq. 55f, p. 553 of [21]). This term accounts for both the face wrinkling phenomenon in a sandwich wall as well as local buckling of the module segment with an "external" elastic foundation. SUBROUTINE EIGREG was modified as follows:

```
A33 = C22*2.*FCUR/R**2 +
2.*C24*MSUM*FCUR/R
+2.*C25*NSUM*FCUR/R +C44*(M14+M24)
+C55*(N14+N24)
+(2.*C45+4.*C66)*(N12*M12+M22*N22) +
PREB + 2.*EFOUND/C11SVE                (37)
```

in which the FORTRAN variables, FCUR, MSUM, NSUM, M14,...PREB, etc., are defined in SUBROUTINE EIGREG. NOTE: The elastic foundation modulus, EFOUND, is divided by C11SVE because the coefficients of the integrated constitutive law for the sandwich wall, [Cij, i,j=1,6], are normalized by C11SVE.

GETCIJ

Compute integrated 6x6 constitutive matrices, C_{ij}^{face1}, C_{ij}^{face2} corresponding to the local segment laminates that comprise face sheet 1 and face sheet 2 of each skin-stringer module segment judged by PANDA2 to be a sandwich wall. Compute face sheet laminate thicknesses, t_{face1}, t_{face2} Compute effective transverse shear stiffnesses, $G_{13}^{face1}, G_{23}^{face1}, G_{13}^{face2}, G_{23}^{face2}$, of the two face sheets. Modifications were made to SUBROUTINES GETCIJ and OUTCIJ.

KOITER

Introduce the elastic foundation contribution to the strain energy in a manner analogous to that done in ARRAYS and in BUCPAN2. The new terms associated with the elastic foundation contribution might well appear (for ease of implementation into PANDA2) in association with Eqs. (3) and (4), pp. 50 and 51, of [15], for the panel skin and the stringers, respectively. The strain energy of the elastic (Winkler) foundation is given by:

$$U_{foundation} = 0.5\int Kw^2 dA \qquad (38)$$

which, for the panel skin, will cause to be added a term analogous to that in the first line of Eq.(45), p 62, [15], in which the coefficent, $4N^2D_{11}^{*i}$, is replaced by $0.25K$.. For the stringer the new contribution is analogous to the first term in Eq.(47), p. 62, [15], with the coefficient, $4N^2C_{44}^i$, replaced by $0.25K$. SUBROUTINES EPSAVE, EIGKOI, GETBK, ENERGY were modified.

Also, SUBROUTINE KOIT2 was modified as described in panda2.news ITEM 298 [29] in order to compensate for the lack of a rigorous theory in the KOITER branch for the transverse shear deformation effect.

SUBROUTINE STRMID was modified to compute transverse shear forces, Q_x and Q_y (e.g. lb/in), at every nodal point in the discretized single panel skin-stringer module where the stresses are calculated. [See Eqs. (23-25)]. The maximum transverse shear stresses in

each module segment, $Q_{x\max}$ and $Q_{y\max}$, are also computed. Later $Q_{x\max}$ and $Q_{y\max}$ are used, along with the user-provided "look-up" tables for allowable values, to generate constraint conditions for transverse shear stress failure of sandwich cores. [See Eqs.(26) - (30)].

MODE

It was necessary to modify SUBROUTINE MODE to compute the "triple" derivatives of W ($W_{,xxx}$; $W_{,xxy}$; $W_{,yyx}$; $W_{,yyy}$) needed for computation of transverse shear forcess, Q_x and Q_y, and maximum transverse shear stresses, $Q_{x\max}/t$ and $Q_{y\max}/t$, corresponding to the growth of buckling modal initial imperfections. The $Q_{x\max}/t$ and $Q_{y\max}/t$ are required for building the constraint conditions involving the maximum allowable x-z and y-z transverse shear stress components in the sandwich core in each panel module segment.

It was necessary to modify SUBROUTINE OUTPRS in order to compute the "triple" derivatives, WXXXGL and WYYYGL ("GL" for "global), which are required for inclusion of the maximum x-z and y-z transverse shear stress components in the sandwich core of an unstiffened flat sandwich panel subjected to normal pressure.

The absolute values of the transverse shear stress components from growth of the buckling modal imperfections are added to those from normal pressure before the "L"-direction (x-z) and "W"-direction (y-z) sandwich core transverse shear stress constraints are calculated.

In addition, it was necessary to modify SUBROUTINE MODE to compute buckling modal derivatives for the "long-wavelength bending-torsion" mode, in order to compute the "triple" derivative ($W_{,yyy}$) required for computation of sandwich core transverse shear stress, in case the "long-wavelength bending-torsion" mode generates values of QXXMAX/t, QYYMAX/t that are greater in absolute value than the previously computed $Q_{x\max}/t$ and $Q_{y\max}/t$. (See panda2.news ITEM 302 [29] for more details).

PANCOM

Face wrinkling and dimpling mode shapes had to be initialized and new constraint phrases for "localbuck.", face wrinkling, face dimpling, and core shear crimping had to be introduced. SUBROUTINES PANCOM and RECORD were modified. New margins are recorded, as listed above in the section entitled "SUMMARY OF NEW SANDWICH-RELATED MARGINS" and in Part 3 of Table 6, for example.

SETUPC

Previously, the properties of materials used in the panel segment layers were assumed to be fixed. Because the length "s" of one side of the hexagonal cell of the honeycomb core and the thickness "tc" of the honeycomb cell wall can now be decision variables, the properties, G_{13}^{core}, G_{23}^{core}, ρ_{core}, E_{core} derived from these dimensions must now be recomputed every time the design is changed. Also, the effective elastic foundation modulus, EFOUND, of a sandwich core now depends upon the thickness of the core as well as on the dimensions "s" and "tc" of a honeycomb cell. For these reasons, SUBROUTINE SETUPC of the CONMAN library had to be extensively modified. (SUBROUTINE SETUPC takes the current values of the decision variables and design parameters and inserts them into their proper places in labelled common blocks).

STRAIN

The prebuckling in-plane resultants in the two face sheets of each module segment are computed from the already-computed stresses in the particular lamina of which the face sheets are composed. These face sheet resultants, N_x^{face}, N_y^{face}, N_{xy}^{face}, are called (FNXF1, FNXF2), (FNYF1, FNYF2), (FNXYF1, FNXYF2), respectively, in which "F1" and "F2" signify "face sheet 1" and "face sheet 2", respectively. A rather gross approximation is used in this part of PANDA2: Within any one face sheet of a given module segment, the

minimum N_x^{face} and minimum N_y^{face} (maximum compressive values) for that face sheet and segment are combined with the maximum absolute value of N_{xy}^{face} in that face sheet and segment. This extreme set $[N_x^{face}, N_y^{face}, N_{xy}^{face}]$ (from the point of view of stability) is assumed to be uniform over the entire segment. See Table 14 and associated discussion for an example. This "worst" approximation will always be conservative and may perhaps be too conservative in cases for which there is significant local bending caused by post-local buckling deformations or prebuckling bending in the neighborhoods of stiffeners, such as the "hungry horse" phenomenon described on p. 495 of [19]. PANDA2 will handle cases in which the $[N_x^{face}, N_y^{face}, N_{xy}^{face}]$ are different in each of the two face sheets of a segment.

SUBROUTINES STRTHK and GETEPS in the STRAIN library were also modified to compute the deformation-induced sandwich core crushing pressure. (See discussion above associated with Eqs.(31) - (33)).

SUBROUTINE STRCON was modified to compute x-z and y-z transverse shear deformation stresses corresponding to deformations: $w_{,xxx}$, $w_{,xxy}$, $w_{,yyx}$, $w_{,yyy}$, which are now calculated for imperfect panels in SUBROUTINE CURIMP of the STRUCT library.

STOGET

Introduce new labelled common blocks as listed and defined in Table 271.2 of ITEM 271 of [29].

STRUCT

Certain quantities are initialized and new output is provided for the in-plane resultant set (N_x, N_y, N_{xy}) in each face sheet of each module segment judged by PANDA2 to be of sandwich wall construction. SUBROUTINE CURIMP, which predicts curvature changes and twist, $w_{,xx}, w_{,yy}, w_{,xy}$, in loaded imperfect panels, was modified to calculate also the deformations, $w_{,xxx}$, $w_{,xxy}$, $w_{,yyx}$, $w_{,yyx}$, required for later computation of transverse shear forces, Q_{x2} and Q_{y2}, in SUBROUTINE STRCON of the STRAIN library. In SUBROUTINE SKIN the axisymmetric prebuckling transverse shear deformation, $w_{,xxx}$, is computed corresponding to the "hungry horse" [19] inter-ring deformations.

EXAMPLE: UNIFORMLY AXIALLY COMPRESSED, SIMPLY-SUPPORTED SANDWICH PLATE WITH TITANIUM FACESHEETS AND ALUMINUM HONEYCOMB CORE

Summary

Tables 3 - 18 and Figs. 2-12 pertain to this section. The case is named "vinson" in honor of Professor Jack Vinson of the Department of Mechanical and Aerospace Engineering at the University of Delaware. The sandwich plate is unstiffened. The IQUICK = 0 (discretized) analysis [14,15] is used to obtain the results. In all of the examples the panel is subjected to uniform axial compression, N_x = -5000 lb/in. First a perfect sandwich panel is optimized; then a sandwich panel with only initial face sheet waviness is optimized; then a sandwich panel with both initial face sheet waviness and a buckling modal initial imperfection is optimized; finally an imperfect (face sheet waviness plus initial buckling modal imperfection) sandwich panel with a uniform through-thickness temperature gradient in addition to the uniform axial compression is optimized.

Input Data

Table 271.3 of ITEM 271 in [29] lists the input data file, vinson.BEG, for the PANDA2 "BEGIN" processor. This input corresponds to an unstiffened, simply-supported, sandwich plate 100 inches long and 20 inches wide, with titanium face sheets and aluminum honeycomb core. The following material properties were used:

titanium face sheets:

E=17.4*10^6 psi; ν =0.3; α =9.0*10^{-6}/deg.

ρ = 0.16 lb/in^3, $\sigma_{eff}^{allowable}$ = 120 ksi

aluminum honeycomb core material:

E =10.0*10^6 psi; ν =0.3; α = 0;

ρ = 0.10 lb/in^3 , $\sigma_{eff}^{allowable}$ = 40 ksi

Facesheet pull-off allowable= 40 lb/in.

The decision variables in the optimization are as follows:

T(1) = thickness of top face sheet

T(2) = thickness of honeycomb core

T(3) = thickness of bottom face sheet (Can be different from T(1)

s(2) = length of one side of regular hexagonal honeycomb core cell

tc(2)= thickness of wall of honeycomb cell wall

The decision variables "s" and "tc" have subscript "2" rather than "1" because these variables are associated with a material type and the the sandwich core is designated as "material type 2" in Table 271.3 of ITEM 271 of [29].

The lower bound of decision variable no. 4:

s(2): Length of one side of the hexagon

is set equal to 0.03608 in. because this corresponds to the smallest diameter honeycomb cell (1.732*s = 1/16th in.) fabricated in aluminum by the Hexcel Corporation, according to Table 13 in [13]. The lower bound of decision variable no. 5:

tc(2): Thickness of honeycomb cell wall

is likewise set equal to 0.0007 in.

In the starting design, the thickness of each face sheet is 0.03 inch and the thickness of the core is 0.5 inch. The initial values for the dimensions of a honeycomb cell are s = 0.5 inch and tc = 0.002 inch. Material No. 1 represents the material of the face sheets and Material No. 2 represents the material of the sandwich core. Table 271.3 of ITEM 271 of [29] contains a table of core crushing and L-direction and W-direction transverse shear stress allowables as functions of core density from [13], as well as other "look-up" tables for sandwich-related phenomena. These tables are not repeated here in order to save space.

The "INPUT DATA" section of ITEM 271 of [29] provides detail about how the PANDA2 user should provide initial values corresponding to the material type for the sandwich core, how PANDA2 uses these data to elicit further responses from the user concerning other properties of the sandwich core, and how PANDA2 converts the "sandwich-related" input data to data presented to the user in the output files. This information is deleted here to save space.

Results For Perfect Panel

Note that initially the honeycomb core configuration constraint, Eq.(13), is turned OFF and the initial face sheet waviness ratio w_0 / L is set equal to zero. This is NOT recommended procedure for designing sandwich panels, but is done here for demonstration purposes. These factors have a major influence on the size of the cells of the optimized honeycomb core and therefore on the values of the "dimpling" and "wrinkling" margins.

In order to obtain an optimum design with PANDA2, the PANDA2 mainprocessor, invoked via the command "PANDAOPT", is first executed five times in succession in this particular case. This series of five executions generates a file called vinson.OPP, the end portion of which appears as Parts 1 and 2 of Table 3.

Part 3 of Table 3 lists the design margins that correspond to the optimum design listed in PART 2. Margins for buckling, wrinkling, dimpling, and core shear crimping are computed from equations of the type:

Buckling margin = (buckling load factor)/(f.s.) - 1.0 (39)

in which "f.s." denotes "factor of safety". Margins for stress are computed from equations of the type:

Stress margin = (allowablestress)/(stress*f.s.) - 1.0 (40)

Critical margins, that is, margins near zero, affect the evolution of the design in the neighborhood of the optimum. Note that at the optimum design the margin associated with sandwich core shear crimping (margin no. 9 in this case) is not critical.

Because the panel is perfect and there is no prebuckling bending, the top and bottom face sheets behave

identically; therefore the wrinkling and dimpling margins for face sheet 1 are essentially the same as those for face sheet 2.

Margins 7 and 11 are obtained from the theory of [21] with the core represented as an elastic foundation as described in the discussion associated with Eq.(37), and with the effect of local transverse shear deformation in each facesheet included as described in Section 8.2 of [14]. Margins 8 and 12 are obtained from the Hoff-Mautner theory [8] as presented by Plantema [Eq.(5-7)]. No margins are listed in this case corresponding to the Vinson theory for face wrinkling because PANDA2 only chooses the most critical of the margins from EITHER the Hoff-Mautner [8] or the Vinson [5] theories.

Margins 10 and 13 are obtained from the theory of [21] for a simply supported square facesheet (no elastic foundation) with sides of length 2*s and with the local facesheet transverse shear deformation effect included as described in Section 8.2 of [14].

The design is deemed FEASIBLE even if there are some negative margins, provided that the absolute values of each negative margin is less than 0.01. If all negative margins are between -0.01 and -0.05, then the design is deemed ALMOST FEASIBLE. Designs with one or more negative margins less than -0.05 are deemed NOT FEASIBLE.

Note that margins 1, 2, 5, 6, and 14 in this case represent five predictions for the same phenomenon: overall buckling of the unstiffened panel. These margins are listed in Table 4. The three margins, 1, 2, and 6, are termed "local buckling" in PANDA2 because only the panel skin buckles. Phrases such as "overall buckling" or "general buckling" are reserved for buckling in which the lines of intersection of stiffener webs with the panel skin deflect in the buckling mode. Since there are no stiffeners in this example "local" buckling and "general" buckling point to the same phenomenon. The two margins, 1 and 2, are computed from the theories presented in [14] and [15]. The two margins, 5 and 14, are termed "general buckling" because the entire panel buckles. These two margins are computed with use of the theories presented in [21] and [20] (Donnell theory and Sanders theory, respectively), modified to account for transverse shear deformation as described in Section 8.2 of [14].

Ideally the five margins listed in Table 4 should all have the same value because they represent the same phenomenon. There is a significant discrepancy between the three margins, 1, 2, and 6, because the effect of transverse shear deformations (t.s.d.) is significant in this case and because the t.s.d. effect is handled differently in each of the three theories included in PANDA2 that lead to Margins 1, 2 and 6. Margin No. 1 is computed from a theory in which the transverse shear deformation effect is accounted for in the computation of the "Local buckling from discrete model" margin via a "knockdown" factor based on Timoshenko beam theory adjusted for a multiaxial stress field, as described in Sections 8.2 and 19.4 of [14], which most likely leads to conservative designs (see Fig. 25 in [14]). Margin No. 2 is computed from a theory implemented in the KOITER branch of PANDA2 in which the transverse shear deformation effect is accounted for by knocking down the bending stiffnesses by the Timoshenko factor. This is generally an unconservative method when the "knockdown" factor to compensate for transverse shear deformation effects is signficantly less than unity. However, note that the local deformations of imperfect panels with local buckling modal imperfections are computed including a strategy described in panda2.news ITEM 298 [29] which is intended to compensate for the lack of a rigorous transverse shear deformation theory in the KOITER branch of PANDA2. Margin No. 6 is computed from Vinson's theory as set forth in Eqs(2-6) of [5].

As will be seen from results to be presented later, the discrepancy between the buckling load factors from the various t.s.d. approximations diminishes for the more realistic cases in which the honeycomb core cell configuration constraint, Eq.(13), is active and there is initial face sheet waviness.

The two stress margins, Margin No. 3 and Margin No. 4, are calculated in two different subroutines of PANDA2, the first in SUBROUTINE STRTHK, which computes stresses corresponding to deformations obtained from the KOITER branch [15] of PANDA2, and the second in SUBROUTINE STRCON, which computes stresses from a much simplified theory in which it is assumed that initial buckling modal imperfections grow hyperbolically, as described in [19].

The results displayed in Figs. 2-12 for Design Iterations 0-20 show how the panel weight (the Objective) (Fig. 2), the Design Margins (Figs. 3-8), and the Design Parameters (Figs. 9-12) evolve during design iterations performed while the cell size constraint, Eq.(13), is turned OFF, there is no initial face sheet waviness

($w_0 / L = 0$), and there is no initial buckling modal imperfection ($w_{imp} = 0$). The results plotted at Iteration No. 20 correspond to those listed in Table 3.

The writer has found through exercise of PANDA2 for sandwich panels that very often the optimum design is not unique. Even in this very simple case of a perfect, unstiffened, uniformly axially compressed sandwich panel the optimum design is not unique. Different combinations of honeycomb cell size and cell wall thicknesses, "s" and "tc", affect the panel weight only slightly but have a major effect on the "dimpling" margins. Parts 4 - 7 in Table 3 demonstrate.

Following the initial optimization, the PANDA2 processor "CHANGE" was used to generate a new starting design with smaller values for hexagonal cell side width "s" and cell wall thickness "tc". The new starting values for "s" and "tc" are listed in Part 4 of Table 3. All other dimensions remain as listed in Part 2 of Table 3.

Part 5 of Table 271.9 in ITEM 271 of [29] lists the optimization cycles resulting from four successive executions of PANDAOPT. Part 6 of Table 3 lists the new optimum design and panel weight. Note that although the panel weights from the two optimizations, 1.437E+01 in Part 2 and 1.440E+01 in Part 6, are the same to three significant figures, the two corresponding sets of "s" and "tc" are quite different:

After the first optimization (Part 2):

s(2)=2.361E-01, tc(2)=9.508E-04

After the second optimization (Part 6):

s(2)=1.757E-01, tc(2)=7.000E-04

All margins remain essentially the same after the second optimization (Parts 3 and 7) except the two face dimpling margins,

After the first optimization (Part 3):

10 -6.34E-04 dimpling of face 1

13 -6.34E-04 dimpling of face 2

After the second optimization (Part 7):

10 7.84E-01 dimpling of face 1

13 7.84E-01 dimpling of face 2

It is emphasized that for a design to be optimum all the margins need not be critical.

Vinson computes "optimum" design dimensions, "hc" (core thickness), "d" (inscribed diameter of hexagonal honeycomb cell), "tc" (thickness of cell wall), and "tf" (thickness of face sheet) from Eqs.(34 - 37) in [5]. For the panel with dimensions "a" x "b" = 100 x 20 in. and with titanium face sheets and aluminum core the "optimum" design from Vinson's Eqs.(34-37) is listed in Part 1 of Table 5. Corresponding to Vinson's "optimum" design PANDA2 obtains panel weight and design margins as listed in Parts 2 and 3 of Table 5. The word, optimum, is enclosed in quotation marks in this section because Vinson's "optimum" weight is considerably heavier than PANDA2's optimum: PANDA2 optimum = 14.37 lb; Vinson "optimum" = 20.75 lb. At the Vinson "optimum" the core crimping constraint is critical and the effective stress constraint is not (PART 3 of Table 5). In contrast, at the PANDA2 optimum the opposite holds (Part 3 of Table 3).

Note that the following three margins computed from Vinson's theory (Vinson's "optimum" design):

6 -4.08E-02 localbuck (VINSON)....

8a-5.06E-04 wrinkling (VINSON)....

9 -2.94E-03 corecrimp (VINSON)....

are critical and that the margin

10 2.07E-01 dimpling of face 1

is somewhat higher than that computed by Vinson's Eq.(17). Vinson's Eq. (17) is not used in PANDA2 because it yields predictions for face sheet dimpling that are inconsistant with the classical Timoshenko equation for buckling of a square simply-supported plate of width and length b:

$$N_x^{crit} = 4\pi^2 E t^3 / \left[12(1-\nu^2)b^2\right] \quad \text{(Timoshenko) (41)}$$

For an isotropic material, Vinson's Eq.(17) is:

$$N_x^{dimpling} = 2Et^3 / \left[(1-\nu^2)d^2\right] \quad \text{(Vinson) (42)}$$

For $b = d$, the Timoshenko formula predicts a dimpling load more than 50 per cent higher than that

obtained from Vinson's formula. If we set b in the Timoshenko formula equal to 2*s, where s is the length of one side of the regular hexagonal honeycomb cell, then we are assuming that the dimpling load factor is governed by buckling of a simply-supported flat, square plate in which the hexagonal cell boundary is INSCRIBED. Since this 2*s x 2*s simply supported square plate is larger than the actual hexagonal plate that dimples, it seems that such a procedure should yield a conservative estimate for dimpling, provided that transverse shear deformation effects are accounted for in a conservative manner.

Insertion of Vinson's "optimum" dimensions, 2*s = 2*0.40144 = b and face sheet thickness t = 0.031617 (PART 1 of Table 5) and elastic modulus E = 17.4 x 10**6 psi and Poisson ratio ν = 0.3 into the Timoshenko formula leads to N_x^{crit} = 3084 lb/in. Since the total applied axial compression, N_x = 5000 lb/in, is shared equally in this particular example by the two equal face sheets, a dimpling margin of 3084/2500 - 1 = 0.233 is indicated for each face sheet if the effect of transverse shear deformation is neglected. Since the width/thickness ratio of the titanium face sheet over the dimple diameter in the Vinson "optimum" is about 25, transverse shear deformation effects are not significant for dimpling in this example.

The actual dimpling margin computed by PANDA2 is 0.207, as listed above and in Part 3 of Table 5. Therefore, PANDA2's dimpling computations are consistent with the Timoshenko formula for uniform axial compression, with a slightly lower margin than that just computed from the Timonshenko formula because there is a very small but finite effect of transverse shear deformation in the dimpling face sheet.

PANDA2's dimpling margins are valid for any combination, N_x, N_y, N_{xy}, of in-plane loading in composite, anisotropic face sheets because Eq.(57) on p. 553 of [21] is used for the computation.

If the same dimensions and properties are plugged into Vinson's Eq.(17), a dimpling margin very close to zero is obtained. This is to be expected, of course, because the "optimum" dimensions listed in PART 1 of Table 5 were derived from Vinson's equations, (34-37 of [5]), that require all four margins, localbuck (VINSON), wrinkling (VINSON), corecrimp (VINSON), and dimpling (VINSON), to be zero. Note that what Vinson calls "Overall Instability" on p. 1691 of [5] is called by PANDA2 "localbuck (VINSON)...".

Note that according to PANDA2, Vinson's "optimum" design is not feasible, since several margins are significantly negative, as follows:

5 -3.15E-01 buck.(DONL)....

8b-2.82E-01 wrinkling (HOFF)....

12b-2.82E-01 wrinkling (HOFF)....

18 -3.15E-01 buck.(SAND)....

Table 6 was generated after optimization with the "switch" for enforcement of the honeycomb core configuration constraint, Eq.(13), changed from "OFF" to "ON". As is to be expected, the effect of this constraint is to make the cell diameter, 1.732*s, and the depth of the sandwich core, T(2), significantly smaller. The optimum panel weight increases from 14.37 lbs to 15.33 lbs, about 6.7 per cent. In the case of a perfect panel without any initial face sheet waviness this increase in weight is unnecessary. However, once we allow for initial face sheet waviness, then the "(facewrinkle halfwavelength)/celldiam > 2" constraint should always be turned on in order to ensure that the Plantema and Hetenyi theories described above are valid. That is, it is valid to represent the honeycomb core as an elastic continuum when computing the maximum facesheet-core interface normal and shear stresses generated by amplification of the initial face sheet waviness as load is applied to the panel.

Note that with the"(facewrinkle halfwavelength)/celldiam > 2" constraint turned on, the five margins that all represent overall buckling of this unstiffened panel are in reasonably close agreement, as demonstrated in Table 7. This is because the effect of transverse shear deformation is much smaller: the honeycomb core of the optimized panel is much stiffer under transverse shearing loads because the "(facewrinkle halfwavelength)/celldiam > 2" constraint was turned on before optimization, thereby forcing the cell size, 1.732*s, and the core depth, T(2), to become significantly smaller in this example.

The results displayed in Figs. 2-12 for Design Iterations 21-44 show the evolution of the design and margins of the perfect panel ($w_0 / L = 0$, w_{imp}=0) with Eq.(13) turned ON. One can see from Fig. 3 that forcing the honeycomb cells to become smaller (see Fig. 11) results in a decrease in the discrepancy among the five models of overall panel buckling. The honeycomb core becomes thinner and has a higher transverse shear

stiffness. Hence, transverse shear deformation effects are less dramatic than for the design at Iteration No. 20. Figures 7 and 8 show the large effect on wrinkling and dimpling margins: at the new optimum design at Iteration No. 44 the wrinkling, dimpling, and core shear crimping margins are not at all critical (Margins 7,9,10,11,12, 14, and 15 listed in Part 3 of Table 6).

Initial Face Sheet Waviness, $w_0 / L = 0.001$; Panel Otherwise Perfect

Table 8 presents a list of margins for the design at Interation No. 44 (Part 2 of Table 6):

T(1)=0.02087; T(2)=0.6137; T(3)=0.02087; s(2)=0.06766; t_c(2)=0.0007

but with the initial face sheet waviness, w_0 / L, increased from zero to 0.001, a value that Plantema [9] writes is typical for "smooth wings". Most of the margins remain essentially the same. Those that are significantly affected by the introduction of finite initial face sheet waviness, $w_0 / L = 0.001$, are the core crushing margin, the x-z ("L-direction") core transverse shear stress margin, and the core tensile stress margin. (Compare Margins 16 and 17 in Table 6 with Margins 16 and 17 in Table 8 and note the new margin, Margin No. 19, in Table 8). With $w_0 / L = 0.0$ there are essentially zero core crushing and tensile stresses and x-z transverse shear stresses in the perfect panel. With $w_0 / L = 0.001$ there is significant core crushing stress and core tension stress as predicted from the Plantema equation, Eq.(14), and significant x-z ("L-direction") sandwich core transverse shear stress as predicted from the Plantema equation, Eq.(15).

With the print index, NPRINT = 2, in the vinson.OPT file (see Table 271.6 in ITEM 271 of [29]), PANDA2 lists the facesheet-core interface z-normal and x-z and y-z transverse shear stresses in the panel with initially wavy facesheets:

Action of web tending to crush the core or pull off the facesheet of Seg. 1: SIGWEB = σ_{z2} = 0.0000E+00 (no stringer in this case)

Stress from web and initial waviness, matl= 2: SIGTOT=SIGWEB+σ_{z1}=247.12 psi; τ_{xz1}=108.53 psi; τ_{yz1}= 0.0294 psi

---

SIGWEB is generated from bending at the root of an initially imperfect stringer web (the imperfection has the shape of the local buckling mode, such as shown in Fig. 4b of [15]), as identified in the discussion associated with the Hetenyi equations, Eqs.(18 or 21). SIGWEB is zero in this case, of course, because there are no stringers. SIGTOT is equal to SIGWEB + σ_{z1}, in which σ_{z1} is obtained from the Plantema equation, Eq.(14). τ_{xz1} and τ_{yz1} are obtained from the Plantema Eqs.(15,16). σ_{z1}, τ_{xz1}, and τ_{yz1} arise from amplification of the initial facesheet waviness as the panel is compressed.

Table 9 lists the optimization cycles (Part 1), the optimum design (Part 2), and the corresponding margins (Part 3) for the panel with initial face sheet waviness, $w_0 / L = 0.001$, and with the constraint, (face sheet wrinkling halfwavelength)/(1.732*s) > 2.0 turned ON. From Table 10 it is seen that with this more realistic case, at the optimum design the five margins, all of which represent the same phenomenon (overall buckling of this unstiffened sandwich panel), are now within a few per cent of eachother.

Also note that Margin No. 19 from Table 8,

19 1.71E+00 sandwichcore tension...

has been replaced by a differently worded margin in Table 9:

19 2.55E+00 face sheet pull-off...

This happened because PANDA2 tests for both tensile failure in the adhesive as well as tensile failure in the sandwich core material, using whichever yields the smaller margin. (In this case neither is critical).

Note that the face sheet wrinkling, face sheet dimpling, and core shear crimping margins are far from being critical at the optimum design.

The results displayed in Figs. 2-12 for Design Iterations 45-52 show the evolution of the design and margins of the panel with initial face sheet waviness, w_0 / L =

0.001, with Eq. (13) turned ON, and with no buckling modal initial imperfection (w_{imp}=0). Inclusion of a finite (small) value for w_0 / L results in a slight increase in panel weight (Fig. 2), a further decrease in the discrepancy among the five "overall panel buckling" margins (Fig. 3), a new critical margin: core crushing (Fig. 5), a somewhat thinner honeycomb core (Fig. 10), and a somewhat thicker honeycomb cell wall (Fig. 12).

In order to see what happens when initial face sheet waviness is present, but the constraint condition, (face sheet wrinkling halfwavelength)/(1.732*s) > 2.0 is turned OFF, the PANDA2 "CHANGE" processor was first used to set the sandwich hexagonal honeycomb core dimensions "s" and "t_c" to about four times their optimum values given in Part 2 of Table 9 and then the panel was re-optimized. The motivation behind this exploration was primarily to see how much influence on panel weight the presence of the "wrinkling/celldiameter" constraint has for a case in which a reasonable level of initial facesheet waviness is present.

The results for the final optimum design are listed in Table 11. Note that the panel weight is essentially unaffected. The difference between 16.12 lbs (Part 2, Table 9) and 16.16 lbs (Part 1, Table 11) is in the optimization "noise" level. At the two optimum designs, the second with much bigger honeycomb cells, the ratio s/t_c is about the same. Hence, margins governing overall stress and buckling of the unstiffened panel, core crushing, core shear crimping, face sheet wrinkling, and sandwich core transverse shear stress are essentially unaffected by the more than threefold increase in the size of the honeycomb cells. The margins for face sheet dimpling and face sheet pull-off are dramatically affected by the change, the face dimpling margin because of the much larger diameter of the honeycomb cells and the face sheet pull-off margin because there is much less core surface area for the facesheet-core interface adhesive to bond to. Table 12 highlights the quantities that are dramatically different at the two different optima listed in Tables 9 and 11.

Note from Part 2 of Table 11 that PANDA2 prints out a warning message in the *.OPM file if the half wavelength of the face wrinkling instability mode is smaller than the diameter of the hexagonal honeycomb cell.

Imperfect Panel (Face Sheet Waviness + Initial Buckling Modal Imperfection)

In the simple example above, the sandwich panel is not loaded into its postbuckled state. Since the panel is "perfect" in the overall sense ("perfect" in quotes means there is initial face sheet waviness, w_0 / L, but that there is no initial overall buckling modal initial imperfection) and since the axial loading is uniform axial compression at the neutral plane, there is no overall bending of the panel under the axial compression and therefore the resultants in the two face sheets are equal to eachother and uniform. In a more elaborate case it may happen that, for one reason or another, a panel skin that is of sandwich construction will experience, in addition to initial face sheet waviness, considerable bending between stiffeners. In such a case the face sheet resultants, N_x^{face}, N_y^{face}, N_{xy}^{face} (called simply "Nx, Ny, Nxy" for lack of enough width in Table 14) may vary considerably over the width of the panel skin between stringers and may be very different on the bottom face sheet ("facesheet 2") than they are on the top facesheet ("facesheet 1").

PART 2 of Table 9 lists thicknesses and honeycomb core dimensions "s" and "t_c" for the optimized panel with face sheet waviness, w_0 / L = 0.001, but otherwise perfect (zero overall buckling modal initial imperfection). Suppose the same optimized "perfect" panel with the same applied axial compression, Nx = -5000 lb/in, now has a buckling modal initial imperfection with amplitude w_{imp}= 0.1 in. Reference [19] describes how the effects of initial buckling modal imperfections are handled in PANDA2.

Table 13 lists the margins for the imperfect panel (initial face sheet waviness + overall initial buckling modal imperfection) with the same dimensions as the "perfect" panel (see Part 2 of Table 9, no further optimization yet). Several margins are now significantly negative because there is now considerable overall bending in the imperfect panel, with a result that the face sheets are no longer optimally loaded, each by a uniform axial compression, N_x^{face} = -2500 lb/in. Because of the overall bending of the panel as the initial buckling modal imperfection is amplified by the applied axial compression, the face sheets experience considerably more local axial compression than N_x^{face} = -2500 lb/in. Also present now in the face sheets are significant local hoop compression N_y^{face} and in-plane

shear N_{xy}^{face}. Hence, the face sheets now experience combined in-plane loads, N_x^{face}, N_y^{face}, N_{xy}^{face}, with the maximum local compressive N_x^{face} now considerably exceeding -2500 lb/in. These "extra" local membrane loads in the face sheets of the imperfect sandwich panel cause several of the margins to become significantly negative. The design listed in Table 9 is no longer feasible because of the added overall initial buckling modal imperfection.

Table 14 shows a schematic of the unstiffened sandwich panel with segment and nodal point numbering (PART 1) and the actual distributions across the width of the panel and "worst" values of facesheet resultants, sandwich core transverse shear stress components, and deformation-induced core crushing pressures for the "PERFECT" (PARTs 2 and 3) and the IMPERFECT (PARTs 4 and 5) panel. The face sheet resultants, N_x^{face}, N_y^{face}, and N_{xy}^{face} are called here "Nx, Ny, Nxy" for lack of sufficient width. In this table,"x" is the axial coordinate and "y" is the "hoop" coordinate or (for stringer segments, if any) the "s" coordinate called out in Fig. 9 on p. 492 of [14].

In PANDA2 an unstiffened panel is modelled as shown in Fig. 6, p. 48 of [15]. The unstiffened panel is modelled in a manner analogous to that for a single discretized module of a blade-stiffened panel: symmetry conditions are imposed along the two longitudinal (unloaded) edges which are located midway between adjacent stringers, and constraint conditions are introduced to force the local buckling pattern to be approximately antisymmetric about the line of intersection of the stringer root with the panel skin. The buckling modal displacements of the unstiffened panel are artificially constrained to be antisymmetric at the midwidth (except for the axial displacement u), as shown in Fig. 6 of [15]. To repeat: the pattern of normal displacements w in an axially compressed panel with a buckling modal initial imperfection resembles that shown in Fig. 6 of [15]: symmetry conditions are applied along the two longitudinal (unloaded) edges of the panel and antisymmetry (classical simple support) conditions are applied at the panel midwidth. Admittedly, this is an unusual way to model a simply supported unstiffened flat plate. It is done this way in PANDA2 so that the same program code can be applied to both unstiffened and stringer-stiffened panels.

PART 2a of Table 14 lists face sheet resultants across the width of the "PERFECT" panel, and PART 2b lists the "worst" resultants from the point of view of stability. The "worst" resultants in a given panel module segment are assumed by PANDA2 to be uniform over that entire module segment for the purpose of calculation of face wrinkling, face dimpling, and core shear crimping load factors. In the case of the "PERFECT" panel the actual and assumed values are practically the same because the actual distributions are essentially uniform. (PANDA2 introduces a tiny imperfection amplitude when the user specifies no imperfection; that is why there is a small nonuniformity of N_x^{face}, N_y^{face}, and N_{xy}^{face} across the width of the panel as listed in PART 2a).

Parts 3a and 3b give the width-wise distributions of x-z and y-z sandwich core transverse shear stresses and the "worst" values for the "PERFECT" panel. (The values are nonzero because of the tiny imperfection amplitude automatically supplied by PANDA2 in this case).

PART 4a of Table 14 lists face sheet resultants across the width of the IMPERFECT panel, and PART 4b lists the "worst" resultants. Note that in this case the "worst" axial resultant Nx and hoop resultant Ny occur at the same points, but that the "worst" in-plane shear resultant Nxy occurs at different locations. Even so, PANDA2 assumes that all "worst" resultants in each module segment occur over that entire module segment. This is a conservative approximation. In this case the relatively small initial imperfection (amplitude = 0.1 in., which is about 16 per cent of the total panel thickness) has a huge effect because the panel dimensions correspond to the optimized "PERFECT" panel, for which buckling is almost critical as can be seen from the first margin listed in Part 3 of Table 9. Therefore, the initial buckling modal imperfection is greatly amplified by the applied load, with the result that very large additional face sheet resultants are generated in this particular case.

PARTs 5a and 5b of Table 14 list the actual distributions of sandwich core transverse shear stresses in the x-z and y-z planes for the imperfect panel. Again, the "worst" values are very large because of the extreme amplification of the buckling modal initial imperfection.

Because of the almost perfect antisymmetry of the buckling modal imperfection in this case, the top and bottom face sheets experience essentially the same "worst" face sheet resultants. That is why in the optimum design (Table 15) the top and bottom face

sheets have the same thickness even though these two thicknesses are allowed to be independent decision variables.

Table 15 lists the final optimum design of the panel with initial face sheet waviness, $w_0 / L = 0.001$, and with initial buckling modal imperfection amplitude, $w_{imp} = 0.1$ in. Of course the re-optimized panel is somewhat heavier than that optimized without any initial buckling modal imperfection (Part 2 of Table 9). Note that the two face sheet thicknesses of the optimized imperfect panel are still equal. This is because both bottom and top face sheets "see" the same "worst" ("worst" = most destablizing) local membrane load combination, N_x^{face}, N_y^{face}, N_{xy}^{face}.

PANDA2 uses the "worst" face sheet prestress state in the computation of face wrinkling, face dimpling, and core crimping because these are all very local phenomena. It turns out that at the optimum design, face wrinkling, face dimpling, and core shear crimping are no longer critical in this case, as can be seen from the margins listed in PART 4 of Table 15. The optimized imperfect panel is about 19 per cent heavier than the optimized "perfect" panel (panel with initial face sheet waviness, $w_0 / L = 0.001$, but with zero overall initial buckling modal initial imperfection.

The results displayed in Figs. 2-12 for Design Iterations 53-69 show the evolution of the design and margins of the panel with initial face sheet waviness, $w_0 / L = 0.001$, with Eq. (13) turned ON, and with a buckling modal initial imperfection, $w_{imp} = 0.1$ in. Inclusion of the buckling modal initial imperfection causes the panel to become significantly heavier (Fig. 2), the five "overall panel buckling" constraints to become non-critical (Fig. 3), both estimates of effective stress (Margins 3 and 4) to become critical (Fig. 4), the added presence of "L-direction" and "W-direction" sandwich core transverse shear stress margins that are not too far above critical values (Fig. 5), a significant increase in face sheet thickness (Fig. 9), a significant increase in honeycomb core thickness (Fig. 10), and an increase in thickness of the honeycomb cell wall (Fig. 12). Also, note that the evolution of several of the margins is much more "jumpy" than was the case for earlier design iterations performed with $w_{imp} = 0$ (Figs. 3, 5,10). This "jumpiness" is caused primarily by the high sensitivity of imperfect panel tangent stiffness components, $C_{11}^{tan}, C_{22}^{tan}, C_{33}^{tan}$, with a result that with each design iteration the buckling modal initial imperfection w_{imp} is amplified by a different amount, giving rise to different stresses tending to crush the core or cause the core to fail in transverse shear.

Imperfect Panel With Through-thickness Temperature Gradient

Tables 16 - 18 list results for which there exist an initial face sheet waviness, $w_0 / L = 0/001$, an initial buckling modal imperfection with amplitude $w_{imp} =$ 0.1 in., and a temperature gradient through the thickness of the sandwich that is uniform over the entire simply supported panel. The overall dimensions and properties of the panel are the same as listed in the previous tables.

These results represent a case in which the optimum design has different thicknesses in the top and bottom facesheets of the sandwich panel. This case is the same as that for the imperfect panel (the panel with both initial face sheet waviness, $w_0 / L = 0.001$, and initial overall buckling modal imperfection, $w_{imp} = 0.1$ in.), except that now a uniform through-thickness thermal gradient has been added to the axial loading. The material properties are assumed to be independent of the temperature. The simply supported panel has nonzero thermal stresses in the facesheets because it is much longer than it is wide. If the bottom face sheet ("surface opposite stringer" in PANDA2 jargon even though there is no stringer in this case) is heated more than the top face sheet, which is the case corresponding to Tables 16 and 17, then before any axial load is applied to the sandwich plate, the bottom face sheet will be in axial compression and the top face sheet will be in axial tension due to the through-thickness thermal gradient. There are also smaller Poisson-ratio-induced hoop thermal stresses in the face sheets. This "thermal prestress" will cause the bottom face sheet to become thicker than the top face sheet during optimization cycles.

Note that in this example the thermal loading is considered to be part of "Load Set A", that is, the thermal loading is treated in the same way as the axial compression: thermal stresses, like the stresses from axial compression, are multiplied by the buckling eigenvalue (load factor) in the formulation of the bifurcation buckling problem.

Table 16 corresponds to the previously optimized imperfect panel, that is, the panel without any through-thickness thermal gradient (dimensions listed in the

heading: the same panel as that identified in PART 4 of Table 15). Listed in Table 16 are the face sheet resultants of the imperfect panel with the applied axial load of -5000 lb/in and WITHOUT the thermal gradient (PART 1), the face sheet resultants of the imperfect panel with both the applied axial load of -5000 lb/in plus the thermal gradient (PART 2), and the margins when both the applied axial load and thru-thickness thermal gradient are present (PART 3). Note that the presence of the thru-thickness thermal gradient causes the effective stress margin of the bottom face sheet (layer 3) and the core crushing margin to become significantly negative: the optimum design obtained previously for the imperfect panel without the thru-thickness thermal gradient is no longer feasible if a through-thickness temperature gradient is present.

Table 17 lists results after optimization with the through-thickness thermal gradient present and with the bottom face sheet hotter than the top face sheet. As is to be expected from the results listed in Part 2 of Table 16 (bottom facesheet has higher destabilizing resultants than top facesheet), the bottom facesheet in the optimized design is much thicker than the top facesheet.

Global optima can be sought via the PANDA2 processor SUPEROPT [20]. This was done for this case with two thermal gradient options:

1. bottom face sheet hotter than top face sheet and

2. top face sheet hotter than bottom face sheet.

The results are listed in Table 18. It is seen that the optimum weights for the two cases are about the same as that listed in Table 17 and are practically the same for each of the two loading cases, as they should be. Presumably these are both very near the global optimum design.

Note that the optimum designs in PARTs 1 and 2 of Table 18 are not perfectly "symmetrical" with respect to which of the face sheets is the hotter. That is, all dimensions of the optimized designs should be the same except that the upper and lower face sheets should be exchanged. However, the lack of "symmetry" of the globally optimized designs with respect to which of the two face sheets is hotter is small, essentially in the "noise level" within which different designs display essentially the same weight and feasibility.

CONCLUSIONS

Several new "sandwich-related" constraints have been added to the PANDA2 program. PANDA2 has been exercised for an axially compressed unstiffened sandwich panel which has initial face sheet waviness as well as a buckling modal initial imperfection. The face sheets of the sandwich panel need not be the same. A case involving optimization of an imperfect axially compressed panel with a uniform through-thickness temperature gradient, for which the optimum design has face sheets of unequal thickness, displays appropriate behavior.

If a buckling modal imperfection is present, overall buckling of the unstiffened panel is no longer critical (Fig. 3, Iterations 53-69). Rather, core crushing becomes critical and L-direction and W-direction core transverse shear stresses become nearly critical (Fig. 5, Iterations 53-69).

Face sheet dimpling and face sheet wrinkling become critical at optimized designs only if the honeycomb cell size constraint, Eq. (13), is turned OFF (Figs. 6 and 7, Iterations 21-44).

If initial face sheet waviness, w_0/L, is nonzero, the weight of optimum designs is hardly affected by the presence or absence of the honeycomb cell size constraint, Eq. (13). Therefore, it is best always to obtain optimum designs with Eq. (13) turned ON and with a non-zero value for w_0/L (Tables 9 and 11).

Optimization of sandwich panels with realistic assumptions, that is, with the honeycomb cell size constraint, Eq. (13) turned ON and with use of nonzero initial face sheet waviness, w_0/L, leads to minimum-weight designs for which the various approximations used in PANDA2 for including the effect of transverse shear deformations (t.s.d.) are in reasonably good agreement (Fig. 3, Iterations 40-50).

ADDITIONAL WORK NEEDED

PANDA2 should be exercised for a wide variety of stiffened composite panels in which the various segments have sandwich wall construction.

Optimum designs obtained via PANDA2 should be checked by using STAGS to find collapse loads. The STAGS models should include, if possible, segments in which face sheet wrinkling, core crushing, core crimping, and core transverse stress failure as well as

the effects of initial face sheet waviness, are predictable. As of this writing it is not possible to use STAGS to check "sandwich" designs generated via PANDA2.

More work needs to be done in PANDA2 on the effect of transverse shear deformation., especially in the routines that deal with the discretized panel module model and the routines that deal with stiffener rolling.

ACKNOWLEDGMENTS

The author wishes to express his appreciation for the continuing support of Dr. Ron Dotson and Mr. Bill Sable, Spacecraft Analysis Department (Dept. E4-20) in Lockheed Martin Missiles and Space Satellite Systems Division. Mr. Bill Bushnell helped the author provide the proper format of the paper for the AIAA and continues to support the author in the maintenance of the PANDA2 computer program on several UNIX-based workstations. Professor Jack Vinson, Center for Composite Materials at the University of Delaware provided helpful comments and enthusiastic support while the work was in progress. Dr. Frank Weiler helped the author produce the tables in two-column format.

REFERENCES

[1] Noor, A. K., Burton, W. S., and Bert, C. W., "Computational models for sandwich panels and shells", Applied Mechanics Reviews, Vol. 49, No. 3, March 1996

[2] Stein, M. and Mayers, J., "A small deflection theory for curved sandwich plates", NACA Report 1008, 1951

[3] Stein, M. and Mayers, J., "Compressive buckling of simply supported curved plates and cylinders of sandwich construction, NACA TN-2601, 1952

[4] Stein, M. and Williams, J. G., "Buckling and structural efficiency of sandwich-blade stiffened composite compression panels," NASA Technical Paper 1269, September 1978

[5] Vinson, J. R., "Optimum design of composite honeycomb sandwich panels subjected to uniaxial compression", AIAA Journal, ol. 24, No. 10, October 1986

[6] Vinson, J. R., "Comparison of optimized sandwich panels of various constructions subjected to in-plane loads", Proceedings of First International Conference on Sandwich Constructions, Stockholm Sweden, pp 23-49, of SANDWICH CONSTRUCTIONS I, edited by K-A Olsson and R. P. Reichard, June 1989

[7] Vinson, J. R., "Analysis and optimization of composite and metallic sandwich cylindrical shells", Proceedings of Second International Conference on Sandwich Constructions, SANDWICH CONSTRUCTIONS II, Florida, March 1992

[8] Hoff, N. J. and Mautner, S. E., "The buckling of sandwich-type panels," Journal of Aerospace Sciences, Vol. 12, pp 285-297, July 1945

[9] Plantema, F. J., SANDWICH CONSTRUCTION, John Wiley, 1966

[10] Hetenyi, M., "Beams on Elastic Foundation", Chapter 3 of HANDBOOK OF ENGINEERING MECHANICS, edited by W. Flugge, McGraw-Hill, 1962

[11] Bitzer, T. N., "Aluminum honeycomb flatwise tensile strengths", Hexcel Corporation, Dublin, California, Report LSR 932480, January 1988

[12] Anon. "The basics of bonded sandwich construction", Hexcel Corporation, Dublin, California, Report TSB 124, January 1988

[13] Anon. "Mechanical properties of honeycomb material", Hexcel Corporation, Dublin, California, Report TSB 120, January 1988

[14] Bushnell, D., "PANDA2-Program for minimum weight design of stiffened, composite, locally buckled panels", Computers and Structures, Vol. 25 (1987) pp. 469-605.

[15] Bushnell, D., "Optimization of composite, stiffened, imperfect panels under combined loads for service in the postbuckling regime", Computer Methods in Applied Mechanics and Engineering, Vol. 103, pp 43-114 (1993)

[16] Bushnell, D., "Truss-core sandwich design via PANDA2", COMPUTERS AND STRUCTURES, Vol. 44, No. 5, pp 1091-1119 (1992)

[17] Bushnell, D. and Bushnell, W. D., "Minimum-weight design of a stiffened panel via PANDA2 and evaluation of the optimized panel via STAGS",

Computers and Structures, Vol. 50, no. 4, p569-602 (1994)

[18] Bushnell, D. and Bushnell, W. D., "Optimum design of composite stiffened panels under combined loading", Computers and Structures, Vol. 55, No. 5, pp 819-856 (1995)

[19] Bushnell, D. and Bushnell, W. D.,"Approximate method for the optimum design of ring and stringer stiffened cylindrical panels and shells with local, inter-ring, and general buckling modal imperfections", Computers and Structures, Vol. 59, No. 3, pp. 489-527 (1996)

[20] Bushnell, D., "Recent enhancements to PANDA2" 37th AIAA Structures, Structural Dynamics and Materials Conference, April, 1996. Submitted to Finite Elements in Analysis and Design

[21] Bushnell, D., "Theoretical basis of the PANDA computer program for preliminary design of stiffened panels under combined in-plane loads," Computers and Structures, Vol. 27, No. 4, pp 541-563 (1987)

[22] Bushnell, D., "BOSOR4: Program for stress, buckling, and vibration of complex shells of revolution," Structural Mechanics Software Series - Vol. 1, (N. Perrone and W. Pilkey, editors), University Press of Virginia, Charlottesville, 1977, pp. 11-131. See also Computers and Structures, Vol. 4, (1974) pp. 399-435; AIAA J, Vol. 9, No. 10, (1971) pp. 2004-2013; Structural Analysis Systems, Vol. 2, A. Niku-Lari, editor, Pergamon Press, Oxford, 1986, pp. 25-54, and Computers and Structures, 18, (3), (1984) pp. 471-536.

[23] Koiter, W. T., "Het Schuifplooiveld by Grote Overshrijdingen van de Knikspanning," Nationaal Luchtvaart Laboratorium, The Netherlands, Report X295, November 1946 (in Dutch)

[24] Vanderplaats, G. N., "ADS--a FORTRAN program for automated design synthesis, Version 2.01", Engineering Design Optimization, Inc, Santa Barbara, CA, January, 1987

[25] Vanderplaats, G. N. and Sugimoto, H., "A general-purpose optimization program for engineering design", Computers and Structures, Vol. 24, pp 13-21, 1986

[26] Almroth, B. O. and Brogan, F. A., The STAGS Computer Code, NASA CR-2950, NASA Langley Research Center, Hampton, VA (1978).

[27] Rankin, C. C., Stehlin, P.and Brogan, F. A.Koiter, W. T., Enhancements to the STAGS computer code. NASA CR 4000, NASA Langley Research Center, Hampton, VA (1986).

[28] Bushnell, D., "Nonlinear equilibrium of imperfect, locally deformed stringer-stiffened panels under combined in-plane loads", Computers and Structures, Vol. 27, No. 4, pp 519-539 (1987)

[29] Bushnell, D., .../panda2/doc/panda2.news, a continually updated file distributed with PANDA2 that contains a log of all significant modifications to PANDA2 from 1987 through the present.

Table 1 New margins computed by PANDA2 especially for sandwich walls

```
FOR FACE SHEET NO. 1 (top or leftmost face sheet):
   wrinkling; strng Iseg1 ; MID;face 1; M=313;N=2;slope=0.;FS=1.
   wrinkling (VINSON);strng Iseg1 ; MID;face 1; M=309;FS=1.
   wrinkling ( HOFF );strng Iseg1 ; MID;face 1; M=309;FS=1.
   dimpling;  strng Iseg1 ; MID;face 1; M=1;N=1;slope=0.;FS=1.
   Face1 wavelength/celldiam;STR;Iseg=1 ;Matl=2 ;MIDLENGTH;FS=1.

FOR FACE SHEET NO. 2 (bottom or rightmost face sheet):
   wrinkling; strng Iseg1 ; MID;face 2; M=313;N=2;slope=0.;FS=1.
   wrinkling (VINSON);strng Iseg1 ; MID;face 2; M=309;FS=1.
   wrinkling ( HOFF );strng Iseg1 ; MID;face 2; M=309;FS=1.
   dimpling;  strng Iseg1 ; MID;face 2; M=1;N=1;slope=0.;FS=1.
   Face2 wavelength/celldiam;STR;Iseg=1 ;Matl=2 ;MIDLENGTH;FS=1.

FOR ENTIRE SANDWICH WALL OR SANDWICH CORE OR BOTH FACESHEETS
   localbuck (VINSON);strng Iseg1 ;MID; local buck.; M=5;FS=1.1
   corecrimp (VINSON);strng Iseg1 ;MID; core crimping;FS=1.
   Core crushing margin;STR;Iseg=1 ;Matl 2 ;MIDLENGTH;FS=1.
   sandwichcore tension margin;STR;Iseg=1 ;Matl 2 ;MIDLENGTH;FS=1.
   L-dir. sandwich core shear;STR;Iseg=1 ;Matl 2 ;MIDLENGTH;FS=1.
   W-dir. sandwich core shear;STR;Iseg=1 ;Matl 2 ;MIDLENGTH;FS=1.
   face sheet pull-off margin;STR;Iseg=1 ;Matl 2 ;MIDLENGTH;FS=1.
```

Table 2 Additional new sandwich-related stress margins

```
   L-dir. sandwich core shear;STR;Iseg=1 ;Matl 2 ;MIDLENGTH;FS=1.
   W-dir. sandwich core shear;STR;Iseg=1 ;Matl 2 ;MIDLENGTH;FS=1.
   Core crushing margin;STR;Iseg=1 ;Matl 2 ;MIDLENGTH;FS=1.
   sandwichcore tension margin;STR;Iseg=1 ;Matl 2 ;MIDLENGTH;FS=1.
   face sheet pull-off margin;STR;Iseg=1 ;Matl 2 ;MIDLENGTH;FS=1.
```

Table 3 INITIAL OPTIMIZATION OF PERFECT PANEL:

1. No initial face sheet waviness;
2. "(face sheet wrinkling halfwavelength)/(1.732*s) > 2.0" constraint condition turned OFF

NOTE: 1. and 2. are NOT recommended practice but are done here for the purposes of demonstration.

PART 1: Original optimization

SUMMARY OF STATE OF THE DESIGN WITH EACH ITERATION

ITERATION NO.	WEIGHT OF PANEL	LOAD SET NO.-> DESIGN IS...	FOR EACH LOAD SET.... (IQUICK; NO. OF CRITICAL MARGINS) 1	2	3	4	5	
1	2.6001E+01	FEASIBLE	(0; 0)	(0; 0)	(0; 0)	(0; 0)	(0; 0)	
2	2.3366E+01	FEASIBLE	(0; 2)	(0; 0)	(0; 0)	(0; 0)	(0; 0)	
3	2.1934E+01	FEASIBLE	(0; 4)	(0; 0)	(0; 0)	(0; 0)	(0; 0)	
4	2.1003E+01	FEASIBLE	(0; 4)	(0; 0)	(0; 0)	(0; 0)	(0; 0)	
5	2.0314E+01	FEASIBLE	(0; 4)	(0; 0)	(0; 0)	(0; 0)	(0; 0)	
6	1.9788E+01	FEASIBLE	(0; 5)	(0; 0)	(0; 0)	(0; 0)	(0; 0)	
						PANDAOPT		
7	1.9788E+01	FEASIBLE	(0; 4)	(0; 0)	(0; 0)	(0; 0)	(0; 0)	
8	1.8623E+01	FEASIBLE	(0; 4)	(0; 0)	(0; 0)	(0; 0)	(0; 0)	
9	1.7654E+01	FEASIBLE	(0; 4)	(0; 0)	(0; 0)	(0; 0)	(0; 0)	
10	1.6941E+01	FEASIBLE	(0; 4)	(0; 0)	(0; 0)	(0; 0)	(0; 0)	
11	1.6398E+01	FEASIBLE	(0; 4)	(0; 0)	(0; 0)	(0; 0)	(0; 0)	
12	1.5973E+01	FEASIBLE	(0; 5)	(0; 0)	(0; 0)	(0; 0)	(0; 0)	
						PANDAOPT		
13	1.5973E+01	FEASIBLE	(0; 4)	(0; 0)	(0; 0)	(0; 0)	(0; 0)	
14	1.5078E+01	FEASIBLE	(0; 6)	(0; 0)	(0; 0)	(0; 0)	(0; 0)	
15	1.4445E+01	FEASIBLE	(0; 6)	(0; 0)	(0; 0)	(0; 0)	(0; 0)	
16	1.4404E+01	FEASIBLE	(0; 8)	(0; 0)	(0; 0)	(0; 0)	(0; 0)	
17	1.4373E+01	FEASIBLE	(0; 8)	(0; 0)	(0; 0)	(0; 0)	(0; 0)	<-optimum
18	1.4395E+01	FEASIBLE	(0; 9)	(0; 0)	(0; 0)	(0; 0)	(0; 0)	
						PANDAOPT		
19	1.4395E+01	FEASIBLE	(0; 8)	(0; 0)	(0; 0)	(0; 0)	(0; 0)	
						PANDAOPT		
20	1.4395E+01	FEASIBLE	(0; 8)	(0; 0)	(0; 0)	(0; 0)	(0; 0)	

PART 2: Optimum design of perfect panel, no initial facesheet waviness;
(face sheet wrinkling halfwavelength)/(1.732*s) > 2.0 constraint condition turned OFF; Started from design with s(2)=0.5, tc(2)=0.002

VALUES OF DESIGN VARIABLES CORRESPONDING TO MINIMUM-WEIGHT DESIGN

VAR. NO.	STR/ RNG	SEG. NO.	LAYER NO.	CURRENT VALUE	DEFINITION
1	SKN	1	1	2.087E-02	T(1)(SKN):thickness for layer index no.(1)
2	SKN	1	2	8.218E-01	T(2)(SKN):thickness for layer index no.(2)
3	SKN	1	3	2.087E-02	T(3)(SKN):thickness for layer index no.(3)
4	SKN	1	0	2.361E-01	s(2)(SKN):Length of one side of the hexagon
5	SKN	1	0	9.508E-04	tc(2)(SKN):thickness of honeycomb cell wall

CORRESPONDING VALUE OF THE OBJECTIVE FUNCTION:

VAR. NO.	STR/ RNG	SEG. NO.	LAYER NO.	CURRENT VALUE	DEFINITION
		0	0	1.437E+01	WEIGHT OF THE ENTIRE PANEL

PART 3: Margins after original optimization; no initial facesheet waviness;
(face sheet wrinkling halfwavelength)/(1.732*s) > 2.0 constraint condition turned OFF;

BUCKLING LOAD FACTORS FOR LOCAL BUCKLING FROM KOITER v. BOSOR4 THEORY:
Local buckling load factor from KOITER theory = 1.4376E+00
Local buckling load factor from BOSOR4 theory = 1.0998E+00

MARGINS FOR CURRENT DESIGN: LOAD CASE NO. 1, SUBCASE NO. 1

MAR. NO.	MARGIN VALUE	DEFINITION
1	-1.76E-04	Local buckling from discrete model-1.,M=5 axial halfwaves;FS=1.1
2	3.07E-01	Local buckling from Koiter theory,M=6 axial halfwaves;FS=1.1
3	1.55E-03	eff.stress:matl=1,SKN,Dseg=2,node=11,layer=3,z=0.4345; MID.;FS=1.
4	3.08E-03	eff.stress:matl=1,SKN,Iseg=1,allnode,layer=3,z=0.4345;-MID.;FS=1.
5	1.76E-03	buck.(DONL);simp-support general buck;M=5;N=1;slope=0.;FS=1.1
6	1.75E-01	localbuck (VINSON);strng Iseg1 ;MID; local buck.; M=5;FS=1.1
7	1.47E-01	wrinkling ;strng Iseg1 ; MID;face 1; M=313;N=2;slope=0.;FS=1.
8	2.08E-03	wrinkling (HOFF);strng Iseg1 ; MID;face 1; M=310;FS=1.
9	9.57E-01	corecrimp (VINSON);strng Iseg1 ;MID; core crimping;FS=1.
10	-6.34E-04	dimpling ;strng Iseg1 ; MID;face 1; M=1;N=1;slope=0.;FS=1.
11	1.47E-01	wrinkling ;strng Iseg1 ; MID;face 2; M=313;N=2;slope=0.;FS=1.
12	2.06E-03	wrinkling (HOFF);strng Iseg1 ; MID;face 2; M=310;FS=1.
13	-6.34E-04	dimpling ;strng Iseg1 ; MID;face 2; M=1;N=1;slope=0.;FS=1.
14	1.76E-03	buck.(SAND);simp-support general buck;M=5;N=1;slope=0.;FS=1.1

PART 4: "CHANGE" processor used to restart from different values of hex cell side width "s" and hex cell thickness "tc"; vinson.CHG

```
      n          $ Do you want a tutorial session and tutorial output?
      y          $ Do you want to change any values in Parameter Set No. 1?
      4          $ Number of parameter to change (1, 2, 3, . .)
 0.8000000E-01   $ New value of the parameter(restart hex side width, s)
      y          $ Want to change any other parameters in this set?
      5          $ Number of parameter to change (1, 2, 3, . .)
 0.7000000E-03   $ New value of the parameter(restart hex cell thickness, tc)
      n          $ Want to change any other parameters in this set?
      n          $ Do you want to change values of "fixed" parameters?
      n          $ Do you want to change values of allowables?
```

```
PART 5: Another optimization of perfect panel with "s" and "tc" reset via
        the PANDA2 processor called "CHANGE" to "s" = 0.08, "tc"=0.007 in.;
        1. no initial face sheet waviness;
        2. (face sheet wrinkling halfwavelength)/(1.732*s) > 2.0 constraint
            condition turned OFF;
        (Results from optimization cycles are omitted here to save space.
        See Part 5 of Table 271.9 in ITEM 271 of [29])
```

```
PART 6: New optimum design; no initial face sheet waviness;
        (face sheet wrinkling halfwavelength)/(1.732*s) > 2.0 constraint
         condition turned OFF;
          SUMMARY OF INFORMATION FROM OPTIMIZATION ANALYSIS
 VAR. DEC. ESCAPE LINK. LINKED   LINKING    LOWER     CURRENT     UPPER  DEFINITION
  NO. VAR.  VAR.  VAR.    TO    CONSTANT    BOUND      VALUE     BOUND0
   1   Y      Y     N      0    0.00E+00  1.00E-03 2.0910E-02  5.00E-01    T(1)
   2   Y      Y     N      0    0.00E+00  1.00E-01 8.2862E-01  4.00E+00    T(2)
   3   Y      Y     N      0    0.00E+00  1.00E-03 2.0910E-02  5.00E-01    T(3)
   4   Y      N     N      0    0.00E+00  3.61E-02 1.7568E-01  3.00E+00    s(2)
   5   Y      Y     N      0    0.00E+00  7.00E-04 7.0000E-04  1.00E-01   tc(2)

   CURRENT VALUE OF THE OBJECTIVE FUNCTION:
 VAR. STR/ SEG. LAYER   CURRENT
 NO.  RNG  NO.   NO.     VALUE            DEFINITION
            0     0   1.440E+01   WEIGHT OF THE ENTIRE PANEL
```

```
PART 7: Margins after second optimization; no initial facesheet waviness;
        (face sheet wrinkling halfwavelength)/(1.732*s) > 2.0 constraint
         condition turned OFF;

 BUCKLING LOAD FACTORS FOR LOCAL BUCKLING FROM KOITER v. BOSOR4 THEORY:
  Local buckling load factor from KOITER theory =  1.4389E+00
  Local buckling load factor from BOSOR4 theory =  1.0991E+00

 MARGINS FOR CURRENT DESIGN: LOAD CASE NO. 1, SUBCASE NO. 1
 MAR. MARGIN
 NO.  VALUE                    DEFINITION
 1 -8.10E-04 Local buckling from discrete model-1.,M=5   axial halfwaves;FS=1.1
 2  3.08E-01 Local buckling from Koiter theory,M=6   axial halfwaves;FS=1.1
 3  2.12E-03 eff.stress:matl=1,SKN,Dseg=2,node=11,layer=3,z=0.4352; MID.;FS=1.
 4  3.66E-03 eff.stress:matl=1,SKN,Iseg=1,allnode,layer=3,z=0.4352;-MID.;FS=1.
 5  1.12E-03 buck.(DONL);simp-support general buck;M=5;N=1;slope=0.;FS=1.1
 6  1.75E-01 localbuck (VINSON);strng Isegl ;MID; local buck.; M=5;FS=1.1
 7  1.44E-01 wrinkling ;strng Isegl ; MID;face 1; M=313;N=2;slope=0.;FS=1.
 8 -5.24E-04 wrinkling ( HOFF );strng Isegl ; MID;face 1; M=309;FS=1.
 9  9.50E-01 corecrimp (VINSON);strng Isegl ;MID; core crimping;FS=1.
10  7.84E-01 dimpling  ;strng Isegl ; MID;face 1; M=1;N=1;slope=0.;FS=1.
11  1.44E-01 wrinkling ;strng Isegl ; MID;face 2; M=313;N=2;slope=0.;FS=1.
12 -5.36E-04 wrinkling ( HOFF );strng Isegl ; MID;face 2; M=309;FS=1.
13  7.84E-01 dimpling  ;strng Isegl ; MID;face 2; M=1;N=1;slope=0.;FS=1.
14  1.12E-03 buck.(SAND);simp-support general buck;M=5;N=1;slope=0.;FS=1.1
```

Table 4 Five margins computed in PANDA2 which, for the special case of the unstiffened flat panel, denote the same phenomenon: Overall panel buckling. Perfect panel, no initial waviness, Eq. (13) constraint turned OFF.

```
 1 -1.76E-04 Local buckling from discrete model-1.,M=5   axial halfwaves;FS=1.1
 2  3.07E-01 Local buckling from Koiter theory,M=6   axial halfwaves;FS=1.1
 5  1.76E-03 buck.(DONL);simp-support general buck;M=5;N=1;slope=0.;FS=1.1
 6  1.75E-01 localbuck (VINSON);strng Isegl ;MID; local buck.; M=5;FS=1.1
14  1.76E-03 buck.(SAND);simp-support general buck;M=5;N=1;slope=0.;FS=1.1
```

Table 5 Results from PANDA2 for the optimum design obtained via Vinson's Eqs (34 - 37), pp1694-5, AIAA J., Vol. 24, 1986 [5]

```
PART 1:
   VINSON'S OPTIMUM DESIGN DERIVED FROM EQS(34-37) in [5]
 LOWER    CURRENT    UPPER       DEFINITION
 BOUND     VALUE     BOUND
1.00E-03 3.1617E-02  5.00E-01    T(1 )(SKN):thickness for layer index no.(1)
1.00E-01 1.2946E+00  4.00E+00    T(2 )(SKN):thickness for layer index no.(2)
1.00E-03 3.1617E-02  5.00E-01    T(3 )(SKN):thickness for layer index no.(3)
3.61E-02 4.0144E-01  3.00E+00    s(2 )(SKN):Length of one side of the hexagon
2.00E-04 5.2367E-04  1.00E-01   tc(2 )(SKN):Thickness of honeycomb cell wall
```

```
PART 2
 ******************* DESIGN OBJECTIVE ******************
  CORRESPONDING VALUE OF THE OBJECTIVE FUNCTION:
 VAR. STR/ SEG. LAYER   CURRENT
 NO.  RNG  NO.   NO.     VALUE            DEFINITION
            0     0   2.075E+01   WEIGHT OF THE ENTIRE PANEL (Vinson's Optimum)
```

```
PART 3:
 MARGINS FOR CURRENT DESIGN: LOAD CASE NO. 1, SUBCASE NO. 1
 MAR. MARGIN
 NO.  VALUE                    DEFINITION
 1  3.88E-01 Local buckling from discrete model-1.,M=5   axial halfwaves;FS=1.1
 2  1.70E+00 Local buckling from Koiter theory,M=8   axial halfwaves;FS=1.1
 3  5.14E-01 eff.stress:matl=1,SKN,Dseg=2,node=11,layer=3,z=0.6789; MID.;FS=1.
 4  5.18E-01 eff.stress:matl=1,SKN,Iseg=1,allnode,layer=3,z=0.6789;-MID.;FS=1.
 5 -3.15E-01 buck.(DONL);simp-support general buck;M=5;N=1;slope=0.;FS=1.1
 6 -4.08E-02 localbuck (VINSON);strng Isegl ;MID; local buck.; M=5;FS=1.1
 7 -1.39E-02 wrinkling ;strng Isegl ; MID;face 1; M=153;N=1;slope=0.;FS=1.
 8a-5.06E-04 wrinkling (VINSON) strng Isegl ; MID;face 1; M=141;FS=1.
 8b-2.82E-01 wrinkling ( HOFF );strng Isegl ; MID;face 1; M=141;FS=1.
 9 -2.94E-03 corecrimp (VINSON);strng Isegl ;MID; core crimping;FS=1.
10  2.07E-01 dimpling  ;strng Isegl ; MID;face 1; M=1;N=1;slope=0.;FS=1.
11 -1.39E-02 wrinkling ;strng Isegl ; MID;face 2; M=153;N=1;slope=0.;FS=1.
12a-5.08E-04 wrinkling (VINSON) strng Isegl ; MID;face 2; M=141;FS=1.
12b-2.82E-01 wrinkling ( HOFF );strng Isegl ; MID;face 2; M=141;FS=1.
13  2.07E-01 dimpling  ;strng Isegl ; MID;face 2; M=1;N=1;slope=0.;FS=1.
14  5.90E+04 Core crushing margin;STR;Iseg=1 ;Matl 2 ;MIDLENGTH;FS=1.
15  4.12E+00 L-dir. sandwich core shear;STR;Iseg=1 ;Matl 2 ;MIDLENGTH;FS=1.
16  4.10E+00 W-dir. sandwich core shear;STR;Iseg=1 ;Matl 2 ;MIDLENGTH;FS=1.
17  2.19E+02 (Max.allowable ave.axial strain)/(ave.axial strain) -1; FS=1.
18 -3.15E-01 buck.(SAND);simp-support general buck;M=5;N=1;slope=0.;FS=1.1
```

Table 6 MORE OPTIMIZATION OF PERFECT PANEL: EQ.(13) CONSTRAINT TURNED ON
1. No initial face sheet waviness;
2. (face sheet wrinkling halfwavelength)/(1.732*s) > 2.0 constraint condition turned ON

```
PART 1: Optimization (omitted here to save space. See Table 271.9 in
        ITEM 271 of [29])
```

```
PART 2: Optimum design of perfect panel, no initial facesheet waviness;
        (face sheet wrinkling halfwavelength)/(1.732*s) > 2.0 constraint
        condition turned ON.
  VALUES OF DESIGN VARIABLES CORRESPONDING TO MINIMUM-WEIGHT DESIGN
 VAR. STR/ SEG. LAYER   CURRENT
 NO.  RNG  NO.   NO.     VALUE            DEFINITION
  1   SKN   1     1   2.087E-02    T(1 )(SKN):thickness for layer index no.(1)
  2   SKN   1     2   6.137E-01    T(2 )(SKN):thickness for layer index no.(2)
  3   SKN   1     3   2.087E-02    T(3 )(SKN):thickness for layer index no.(3)
  4   SKN   1     0   6.766E-02    s(2 )(SKN):Length of one side of the hexagon
  5   SKN   1     0   7.000E-04   tc(2 )(SKN):thickness of honeycomb cell wall

  CORRESPONDING VALUE OF THE OBJECTIVE FUNCTION:
```

```
 VAR. STR/ SEG. LAYER    CURRENT
 NO.  RNG  NO.    NO.      VALUE            DEFINITION
            0      0   1.531E+01   WEIGHT OF THE ENTIRE PANEL
-------------------------------------------------------------------------------

PART 3: Margins after optimization; no initial facesheet waviness;
        (face sheet wrinkling halfwavelength)/(1.732*s) > 2.0 constraint
         condition turned ON;
        vinson.OPM (abridged)

 BUCKLING LOAD FACTORS FOR LOCAL BUCKLING FROM KOITER v. BOSOR4 THEORY:
  Local buckling load factor from KOITER theory =  1.2219E+00
  Local buckling load factor from BOSOR4 theory =  1.1000E+00

 MARGINS FOR CURRENT DESIGN: LOAD CASE NO. 1, SUBCASE NO. 1
 MAR. MARGIN
 NO.  VALUE                  DEFINITION
  1 -4.65E-06 Local buckling from discrete model-1.,M=5   axial halfwaves;FS=1.1
  2  1.11E-01 Local buckling from Koiter theory,M=5   axial halfwaves;FS=1.1
  3  2.26E-03 eff.stress:matl=1,SKN,Dseg=2,node=11,layer=3,z=0.3283; MID.;FS=1.
  4  2.81E-03 eff.stress:matl=1,SKN,Iseg=1,allnode,layer=3,z=0.3283;-MID.;FS=1.
  5  2.97E-03 buck.(DONL);simp-support general buck;M=5;N=1;slope=0.;FS=1.1
  6  6.39E-02 localbuck (VINSON);strng Isegl ;MID; local buck.; M=5;FS=1.1
  7  1.09E+00 wrinkling ;strng Isegl ; MID;face 1; M=445;N=1;slope=0.;FS=1.
  8  2.12E-03 Facel wavelength/celldiam;STR;Iseg=1 ;Matl=2 ;MIDLENGTH;FS=1.
  9  8.90E-01 wrinkling ( HOFF );strng Isegl ; MID;face 1; M=426;FS=1.
 10  2.77E+00 corecrimp (VINSON);strng Isegl ;MID; core crimping;FS=1.
 11  8.88E+00 dimpling  ;strng Isegl ; MID;face 1; M=1;N=1;slope=0.;FS=1.
 12  1.09E+00 wrinkling ;strng Isegl ; MID;face 2; M=445;N=1;slope=0.;FS=1.
 13  2.12E-03 Face2 wavelength/celldiam;STR;Iseg=1 ;Matl=2 ;MIDLENGTH;FS=1.
 14  8.90E-01 wrinkling ( HOFF );strng Isegl ; MID;face 2; M=426;FS=1.
 15  8.88E+00 dimpling  ;strng Isegl ; MID;face 2; M=1;N=1;slope=0.;FS=1.
 16  1.21E+06 Core crushing margin;STR;Iseg=1 ;Matl 2 ;MIDLENGTH;FS=1.
 17  2.35E+02 L-dir. sandwich core shear;STR;Iseg=1 ;Matl 2 ;MIDLENGTH;FS=1.
 18  1.40E+02 W-dir. sandwich core shear;STR;Iseg=1 ;Matl 2 ;MIDLENGTH;FS=1.
 19  1.44E+02 (Max.allowable ave.axial strain)/(ave.axial strain) -1; FS=1.
 20  2.97E-03 buck.(SAND);simp-support general buck;M=5;N=1;slope=0.;FS=1.1
===============================================================================
```

Table 7 Five margins computed in PANDA2 which, for the special case of the unstiffened flat panel, denote the same phenomenon: Overall panel buckling. This table is analogous to Table 4.

```
===============================================================================
  1 -4.65E-06 Local buckling from discrete model-1.,M=5   axial halfwaves;FS=1.1
  2  1.11E-01 Local buckling from Koiter theory,M=5   axial halfwaves;FS=1.1
  5  2.97E-03 buck.(DONL);simp-support general buck;M=5;N=1;slope=0.;FS=1.1
  6  6.39E-02 localbuck (VINSON);strng Isegl ;MID; local buck.; M=5;FS=1.1
 20  2.97E-03 buck.(SAND);simp-support general buck;M=5;N=1;slope=0.;FS=1.1
===============================================================================
```

Table 8

```
     Margins before optimization; Initial facesheet waviness, w0/L = 0.001;
     (face sheet wrinkling halfwavelength)/(1.732*s) > 2.0 constraint
      condition turned ON;
     vinson.OPM file (abridged) corresponding to the optimum design found
     for no initial facesheet waviness:
     T(1)=0.02087; T(2)=0.6137; T(3)=0.02087; s(2)=0.06766; tc(2)=0.0007
===============================================================================
 MARGINS FOR CURRENT DESIGN: LOAD CASE NO. 1, SUBCASE NO. 1
 MAR. MARGIN
 NO.  VALUE                  DEFINITION
  1 -4.27E-03 Local buckling from discrete model-1.,M=5   axial halfwaves;FS=1.1
  2  1.06E-01 Local buckling from Koiter theory,M=5   axial halfwaves;FS=1.1
  3  1.18E-03 eff.stress:matl=1,SKN,Dseg=2,node=11,layer=3,z=0.3277; MID.;FS=1.
  4  1.73E-03 eff.stress:matl=1,SKN,Iseg=1,allnode,layer=3,z=0.3277;-MID.;FS=1.
  5 -1.30E-03 buck.(DONL);simp-support general buck;M=5;N=1;slope=0.;FS=1.1
  6  5.93E-02 localbuck (VINSON);strng Isegl ;MID; local buck.; M=5;FS=1.1
  7  1.09E+00 wrinkling ;strng Isegl ; MID;face 1; M=445;N=1;slope=0.;FS=1.
  8  1.06E-04 Facel wavelength/celldiam;STR;Iseg=1 ;Matl=2 ;MIDLENGTH;FS=1.
  9  8.87E-01 wrinkling ( HOFF );strng Isegl ; MID;face 1; M=426;FS=1.
 10  2.76E+00 corecrimp (VINSON);strng Isegl ;MID; core crimping;FS=1.
 11  8.83E+00 dimpling  ;strng Isegl ; MID;face 1; M=1;N=1;slope=0.;FS=1.
 12  1.09E+00 wrinkling ;strng Isegl ; MID;face 2; M=445;N=1;slope=0.;FS=1.
 13  1.06E-04 Face2 wavelength/celldiam;STR;Iseg=1 ;Matl=2 ;MIDLENGTH;FS=1.
 14  8.87E-01 wrinkling ( HOFF );strng Isegl ; MID;face 2; M=426;FS=1.
 15  8.83E+00 dimpling  ;strng Isegl ; MID;face 2; M=1;N=1;slope=0.;FS=1.
 16 -5.79E-01 Core crushing margin;STR;Iseg=1 ;Matl 2 ;MIDLENGTH;FS=1.
 17  3.48E-01 L-dir. sandwich core shear;STR;Iseg=1 ;Matl 2 ;MIDLENGTH;FS=1.
 18  1.34E+02 W-dir. sandwich core shear;STR;Iseg=1 ;Matl 2 ;MIDLENGTH;FS=1.
 19  1.71E+00 sandwichcore tension margin;STR;Iseg=1 ;Matl 2 ;MIDLENGTH;FS=1.
 20  1.44E+02 (Max.allowable ave.axial strain)/(ave.axial strain) -1; FS=1.
 21 -1.30E-03 buck.(SAND);simp-support general buck;M=5;N=1;slope=0.;FS=1.1
===============================================================================
```

Table 9 OPTIMIZATION OF PANEL WITH SOME INITIAL FACE SHEET WAVINESS:
1. Initial face sheet waviness, w0/L = 0.001;
2. (face sheet wrinkling halfwavelength)/(1.732*s) > 2.0 constraint condition turned ON

```
===============================================================================
PART 1: Optimization, starting from optimized panel obtained with the
        initial face sheet waviness, w0/L = 0.0 and with the constraint:
          (face sheet wrinkling halfwavelength)/(1.732*s) > 2.0
        turned ON. Starting design:
        T(1)=0.02087; T(2)=0.6137; T(3)=0.02087; s(2)=0.06766; tc(2)=0.0007
        In this case the initial face sheet waviness, w0/L = 0.001.

        SUMMARY OF STATE OF THE DESIGN WITH EACH ITERATION
 ITERA   WEIGHT                          FOR EACH LOAD SET....
 TION      OF                    (IQUICK; NO. OF CRITICAL MARGINS)
 NO.     PANEL      LOAD SET NO.->  1       2       3       4       5
                    DESIGN IS...
 ------------------------------------------------------PANDAOPT
   1 1.5312E+01   NOT FEASIBLE  (0; 7)  (0; 0)  (0; 0)  (0; 0)  (0; 0)
   2 1.7321E+01   NOT FEASIBLE  (0; 1)  (0; 0)  (0; 0)  (0; 0)  (0; 0)
   3 1.7220E+01      FEASIBLE   (0; 1)  (0; 0)  (0; 0)  (0; 0)  (0; 0)
   4 1.6282E+01      FEASIBLE   (0; 5)  (0; 0)  (0; 0)  (0; 0)  (0; 0)
   5 1.6118E+01  ALMOST FEASIBLE(0; 8)  (0; 0)  (0; 0)  (0; 0)  (0; 0)
   6 1.6130E+01  ALMOST FEASIBLE(0; 9)  (0; 0)  (0; 0)  (0; 0)  (0; 0)
 ------------------------------------------------------PANDAOPT
   7 1.6130E+01  ALMOST FEASIBLE(0; 8)  (0; 0)  (0; 0)  (0; 0)  (0; 0)
   8 1.6191E+01      FEASIBLE   (0; 8)  (0; 0)  (0; 0)  (0; 0)  (0; 0)
 ------------------------------------------------------PANDAOPT
   9 1.6191E+01      FEASIBLE   (0; 8)  (0; 0)  (0; 0)  (0; 0)  (0; 0)<-optimum
         Initial face sheet waviness, w0/L = 0.001 and with the constraint:
         (face sheet wrinkling halfwavelength)/(1.732*s) > 2.0 turned ON
-------------------------------------------------------------------------------
PART 2: Optimum design of panel, Initial facesheet waviness, w0/L=0.001;
        (face sheet wrinkling halfwavelength)/(1.732*s) > 2.0 constraint
        condition turned ON.
  VALUES OF DESIGN VARIABLES CORRESPONDING TO ALMOST FEASIBLE DESIGN
 VAR. STR/ SEG. LAYER   CURRENT
 NO.  RNG  NO.   NO.     VALUE            DEFINITION
  1    SKN   1     1   2.084E-02    T(1 )(SKN):thickness for layer index no.(1)
  2    SKN   1     2   5.774E-01    T(2 )(SKN):thickness for layer index no.(2)
  3    SKN   1     3   2.084E-02    T(3 )(SKN):thickness for layer index no.(3)
  4    SKN   1     0   5.709E-02    s(2 )(SKN):Length of one side of the hexagon
  5    SKN   1     0   8.920E-04   tc(2 )(SKN):thickness of honeycomb cell wall

  CORRESPONDING VALUE OF THE OBJECTIVE FUNCTION:
 VAR. STR/ SEG. LAYER   CURRENT
 NO.  RNG  NO.   NO.     VALUE            DEFINITION
```

```
           0     0   1.612E+01   WEIGHT OF THE ENTIRE PANEL
-------------------------------------------------------------------------------
PART 3: Margins after optimization; Initial facesheet waviness, w0/L=0.001;
        (face sheet wrinkling halfwavelength)/(1.732*s) > 2.0 constraint
         condition turned ON;

 BUCKLING LOAD FACTORS FOR LOCAL BUCKLING FROM KOITER v. BOSOR4 THEORY:
  Local buckling load factor from KOITER theory =  1.1814E+00
  Local buckling load factor from BOSOR4 theory =  1.1065E+00

 MARGINS FOR CURRENT DESIGN: LOAD CASE NO. 1, SUBCASE NO. 1
 MAR. MARGIN
 NO.  VALUE                DEFINITION
  1  5.90E-03 Local buckling from discrete model-1.,M=5   axial halfwaves;FS=1.1
  2  7.40E-02 Local buckling from Koiter theory,M=5   axial halfwaves;FS=1.1
  3  2.31E-03 eff.stress:matl=1,SKN,Dseg=2,node=11,layer=3,z=0.3096; MID.;FS=1.
  4  2.77E-03 eff.stress:matl=1,SKN,Iseg=1,allnode,layer=3,z=0.3096;-MID.;FS=1.
  5  9.26E-03 buck.(DONL);simp-support general buck;M=5;N=1;slope=0.;FS=1.1
  6  4.81E-02 localbuck (VINSON);strng Isegl ;MID; local buck.; M=5;FS=1.1
  7  1.64E+00 wrinkling ;strng Isegl ; MID;face 1; M=490;N=1;slope=0.;FS=1.
  8  2.39E-03 Face1 wavelength/celldiam;STR;Iseg=1 ;Matl=2 ;MIDLENGTH;FS=1.
  9  1.51E+00 wrinkling ( HOFF );strng Isegl ; MID;face 1; M=491;FS=1.
 10  4.42E+00 corecrimp (VINSON);strng Isegl ;MID; core crimping;FS=1.
 11  1.13E+01 dimpling  ;strng Isegl ; MID;face 1; M=1;N=1;slope=0.;FS=1.
 12  1.64E+00 wrinkling ;strng Isegl ; MID;face 2; M=490;N=1;slope=0.;FS=1.
 13  2.41E-03 Face2 wavelength/celldiam;STR;Iseg=1 ;Matl=2 ;MIDLENGTH;FS=1.
 14  1.51E+00 wrinkling ( HOFF );strng Isegl ; MID;face 2; M=491;FS=1.
 15  1.13E+01 dimpling  ;strng Isegl ; MID;face 2; M=1;N=1;slope=0.;FS=1.
 16  6.70E-04 Core crushing margin;STR;Iseg=1 ;Matl 2 ;MIDLENGTH;FS=1.
 17  1.81E+00 L-dir. sandwich core shear;STR;Iseg=1 ;Matl 2 ;MIDLENGTH;FS=1.
 18  3.09E+02 W-dir. sandwich core shear;STR;Iseg=1 ;Matl 2 ;MIDLENGTH;FS=1.
 19  2.55E+00 face sheet pull-off margin;STR;Iseg=1 ;Matl 2 ;MIDLENGTH;FS=1.
 20  1.44E+02 (Max.allowable ave.axial strain)/(ave.axial strain) -1; FS=1.
 21  9.26E-03 buck.(SAND);simp-support general buck;M=5;N=1;slope=0.;FS=1.1
===============================================================================
```

Table 10 Five margins computed in PANDA2 which, for the special case of the unstiffened flat panel, denote the same phenomenon: Overall panel buckling. This table is analogous to Tables 4 and 7.

```
===============================================================================
  1  5.90E-03 Local buckling from discrete model-1.,M=5   axial halfwaves;FS=1.1
  2  7.40E-02 Local buckling from Koiter theory,M=5   axial halfwaves;FS=1.1
  5  9.26E-03 buck.(DONL);simp-support general buck;M=5;N=1;slope=0.;FS=1.1
  6  4.81E-02 localbuck (VINSON);strng Isegl ;MID; local buck.; M=5;FS=1.1
 21  9.26E-03 buck.(SAND);simp-support general buck;M=5;N=1;slope=0.;FS=1.1
===============================================================================
```

Table 11 OPTIMIZATION OF PANEL WITH w0/L = 0.001 AND EQ.(13) TURNED OFF:
1. Initial face sheet waviness, w0/L = 0.001;
2. (face sheet wrinkling halfwavelength)/(1.732*s) > 2.0 constraint condition turned OFF

```
===============================================================================
PART 1: Optimum design of panel, Initial facesheet waviness, w0/L=0.001;
        (face sheet wrinkling halfwavelength)/(1.732*s) > 2.0 constraint
        condition turned OFF.
  VALUES OF DESIGN VARIABLES CORRESPONDING TO FEASIBLE DESIGN
 VAR.  STR/ SEG.  LAYER    CURRENT
 NO.   RNG  NO.    NO.      VALUE          DEFINITION
  1    SKN   1      1   2.084E-02    T(1 )(SKN):thickness for layer index no.(1)
  2    SKN   1      2   5.760E-01    T(2 )(SKN):thickness for layer index no.(2)
  3    SKN   1      3   2.084E-02    T(3 )(SKN):thickness for layer index no.(3)
  4    SKN   1      0   2.069E-01     s(2 )(SKN):Length of one side of the hexagon
  5    SKN   1      0   3.289E-03   tc(2 )(SKN):thickness of honeycomb cell wall
```

```
  CURRENT VALUE OF THE OBJECTIVE FUNCTION:
 VAR.  STR/ SEG.  LAYER    CURRENT
 NO.   RNG  NO.    NO.      VALUE          DEFINITION
           0      0   1.616E+01   WEIGHT OF THE ENTIRE PANEL
-------------------------------------------------------------------------------
PART 2: Warning issued by PANDA2 when the constraint
        (face sheet wrinkling halfwavelength)/(1.732*s) > 2.0
        is badly violated.
 ***** WARNING Iseg= 1, Iloop= 1: ******
 Face1 wrinkle halfwavelength is less than the honeycomb cell diameter.
 (face1 wrinkle halfwavelength)/(cell diameter)=  5.6723E-01
 ***** WARNING Iseg= 1, Iloop= 1: ******
 Face2 wrinkle halfwavelength is less than the honeycomb cell diameter.
 (face2 wrinkle halfwavelength)/(cell diameter)=  5.6725E-01
-------------------------------------------------------------------------------
PART 3: Margins after optimization; Initial facesheet waviness, w0/L=0.001;
        (face sheet wrinkling halfwavelength)/(1.732*s) > 2.0 constraint
         condition turned OFF.
 MARGINS FOR CURRENT DESIGN: LOAD CASE NO. 1, SUBCASE NO. 1
 MAR. MARGIN
 NO.  VALUE                DEFINITION
  1 -5.27E-05 Local buckling from discrete model-1.,M=5   axial halfwaves;FS=1.1
  2  6.72E-02 Local buckling from Koiter theory,M=5   axial halfwaves;FS=1.1
  3 -1.97E-04 eff.stress:matl=1,SKN,Dseg=2,node=11,layer=3,z=0.3088; MID.;FS=1.
  4  2.91E-04 eff.stress:matl=1,SKN,Iseg=1,allnode,layer=3,z=0.3088;-MID.;FS=1.
  5  3.30E-03 buck.(DONL);simp-support general buck;M=5;N=1;slope=0.;FS=1.1
  6  4.16E-02 localbuck (VINSON);strng Isegl ;MID; local buck.; M=5;FS=1.1
  7  1.62E+00 wrinkling ;strng Isegl ; MID;face 1; M=490;N=1;slope=0.;FS=1.
  8  1.50E+00 wrinkling ( HOFF );strng Isegl ; MID;face 1; M=492;FS=1.
  9  4.42E+00 corecrimp (VINSON);strng Isegl ;MID; core crimping;FS=1.
 10  2.91E-01 dimpling  ;strng Isegl ; MID;face 1; M=1;N=1;slope=0.;FS=1.
 11  1.62E+00 wrinkling ;strng Isegl ; MID;face 2; M=490;N=1;slope=0.;FS=1.
 12  1.50E+00 wrinkling ( HOFF );strng Isegl ; MID;face 2; M=492;FS=1.
 13  2.91E-01 dimpling  ;strng Isegl ; MID;face 2; M=1;N=1;slope=0.;FS=1.
 14  6.25E-04 Core crushing margin;STR;Iseg=1 ;Matl 2 ;MIDLENGTH;FS=1.
 15  1.79E+00 L-dir. sandwich core shear;STR;Iseg=1 ;Matl 2 ;MIDLENGTH;FS=1.
 16  2.93E+02 W-dir. sandwich core shear;STR;Iseg=1 ;Matl 2 ;MIDLENGTH;FS=1.
 17 -1.63E-04 face sheet pull-off margin;STR;Iseg=1 ;Matl 2 ;MIDLENGTH;FS=1.
 18  1.44E+02 (Max.allowable ave.axial strain)/(ave.axial strain) -1; FS=1.
 19  3.30E-03 buck.(SAND);simp-support general buck;M=5;N=1;slope=0.;FS=1.1
===============================================================================
```

Table 12 Comparison of certain results from Tables 9 and 11, which correspond to two different optimum designs found with PANDA2. The two different optima are essentially the same design except for "s", the hexagonal cell side width, and "tc" the cell wall thickness. The ratio, s/tc, is approximately the same for both optima.

```
===============================================================================
From Table 9  (Eq.(13) turned ON): optimized "s" and "tc" and certain margins:
  4    SKN   1      0   5.709E-02     s(2 )(SKN):Length of one side of the hexagon
  5    SKN   1      0   8.920E-04    tc(2 )(SKN):thickness of honeycomb cell wall

 11  1.13E+01 dimpling  ;strng Isegl ; MID;face 1; M=1;N=1;slope=0.;FS=1.
 15  1.13E+01 dimpling  ;strng Isegl ; MID;face 2; M=1;N=1;slope=0.;FS=1.
 19  2.55E+00 face sheet pull-off margin;STR;Iseg=1 ;Matl 2 ;MIDLENGTH;FS=1.
-------------------------------------------------------------------------------
From Table 11 (Eq.(13) turned OFF): optimized "s" and "tc" and certain margins:
  4    SKN   1      0   2.069E-01     s(2 )(SKN):Length of one side of the hexagon
  5    SKN   1      0   3.289E-03    tc(2 )(SKN):thickness of honeycomb cell wall

 10  2.91E-01 dimpling  ;strng Isegl ; MID;face 1; M=1;N=1;slope=0.;FS=1.
 13  2.91E-01 dimpling  ;strng Isegl ; MID;face 2; M=1;N=1;slope=0.;FS=1.
 17 -1.63E-04 face sheet pull-off margin;STR;Iseg=1 ;Matl 2 ;MIDLENGTH;FS=1.
===============================================================================
```

Table 13 Margins for IMPERFECT panel with same dimensions as the optimized "perfect" panel. Buckling modal imperfection amplitude, W0=0.1 in. t(face)=0.02084, t(core)=0.5774, s=0.05709, tc=0.000892 in.
1. Initial face sheet waviness, w0/L = 0.001;
2. (face sheet wrinkling halfwavelength)/(1.732*s) > 2.0 constraint condition turned ON
3. Buckling modal imperfection amplitude, W0 = 0.1 in.

MARGINS FOR CURRENT DESIGN: LOAD CASE NO. 1, SUBCASE NO. 1

MAR. NO.	MARGIN VALUE	DEFINITION
1	3.95E-04	Local buckling from discrete model-1.,M=5 axial halfwaves;FS=1.1
2	6.90E-02	Local buckling from Koiter theory,M=5 axial halfwaves;FS=1.1
3	-3.80E-01	eff.stress:matl=1,SKN,Dseg=1,node=9,layer=3,z=0.3095; MID.;FS=1.
4	7.88E+06	eff.stress:matl=2,SKN,Dseg=2,node=1,layer=2,z=0.2887; MID.;FS=1.
5	-2.41E-01	eff.stress:matl=1,SKN,Iseg=1,allnode,layer=1,z=-0.3095;-MID.;FS=1.
6	3.73E-03	buck.(DONL);simp-support general buck;M=5;N=1;slope=0.;FS=1.1
7	2.75E-01	localbuck (VINSON);strng Iseg1 ;MID; local buck.; M=5;FS=1.1
8	3.05E-01	wrinkling ;strng Iseg1 ; MID;face 1; M=403;N=3;slope=0.6811;FS=1.
9	3.18E-02	Facel wavelength/celldiam;STR;Iseg=1 ;Matl=2 ;MIDLENGTH;FS=1.
10	6.88E-02	wrinkling (HOFF);strng Iseg1 ; MID;face 1; M=490;FS=1.
11	6.34E-01	corecrimp (VINSON);strng Iseg1 ;MID; core crimping;FS=1.
12	3.84E+00	dimpling ;strng Iseg1 ; MID;face 1; M=1;N=1;slope=0.132;FS=1.
13	3.05E-01	wrinkling ;strng Iseg1 ; MID;face 2; M=403;N=3;slope=0.6811;FS=1.
14	3.18E-02	Face2 wavelength/celldiam;STR;Iseg=1 ;Matl=2 ;MIDLENGTH;FS=1.
15	6.88E-02	wrinkling (HOFF);strng Iseg1 ; MID;face 2; M=490;FS=1.
16	3.84E+00	dimpling ;strng Iseg1 ; MID;face 2; M=1;N=1;slope=0.132;FS=1.
17	-9.56E-01	Core crushing margin;STR;Iseg=1 ;Matl 2 ;MIDLENGTH;FS=1.
18	-9.02E-01	L-dir. sandwich core shear;STR;Iseg=1 ;Matl 2 ;MIDLENGTH;FS=1.
19	-7.76E-01	W-dir. sandwich core shear;STR;Iseg=1 ;Matl 2 ;MIDLENGTH;FS=1.
20	-8.32E-01	face sheet pull-off margin;STR;Iseg=1 ;Matl 2 ;MIDLENGTH;FS=1.
21	1.30E+02	(Max.allowable ave.axial strain)/(ave.axial strain) -1; FS=1.
22	3.73E-03	buck.(SAND);simp-support general buck;M=5;N=1;slope=0.;FS=1.1

Table 14 Facesheet resultants in the "perfect" and imperfect sandwich panel. Buckling modal imperfection amplitude, W0 = 0.1 in; Initial face sheet waviness, w0/L = 0.001 t(face)=0.02084, t(core)=0.5774, s=0.05709, tc=0.000892 in.

PART 1 Unstiffened Sandwich Panel "module"

```
      Seg. No. 1-.        simple support-.              .-Seg. No. 2
                  .                      .              .
Symmetry b.c.-->==========================   ==========================<-sym.
Nodal Point---->1    3    5    7    9    11  1             6             11
                !<------------  Entire panel width, CIRC  ------------>!
```

PART 2 Face sheet resultants across panel width: "PERFECT" PANEL

PART 2a: actual distributions across the width of the panel

Positive Imperfection...(imperfection is essentially zero)

FORCE RESULTANTS IN SANDWICH FACESHEETS FROM KOITER THEORY (SUB. STRTHK)

Seg. Node	Top (or leftmost) facesheet 1			Bottom (or rightmost) facesheet 2		
Dseg,i	Axial, Nx	Hoop, Ny	Shear, Nxy	Axial, Nx	Hoop, Ny	Shear, Nxy
1, 1	-2.5023E+03	-2.3500E+00	1.2504E+01	-2.4976E+03	2.3381E+00	1.2496E+01
1, 3	-2.5022E+03	-2.2384E+00	1.2111E+01	-2.4977E+03	2.2265E+00	1.2889E+01
1, 5	-2.5019E+03	-1.9116E+00	1.1759E+01	-2.4981E+03	1.8999E+00	1.3241E+01
1, 7	-2.5014E+03	-1.3965E+00	1.1478E+01	-2.4986E+03	1.3847E+00	1.3521E+01
1, 9	-2.5007E+03	-7.3963E-01	1.1297E+01	-2.4993E+03	7.2774E-01	1.3703E+01
1,11	-2.5000E+03	5.2333E-03	1.1235E+01	-2.5000E+03	-1.7042E-02	1.3765E+01
2, 1	-2.5000E+03	5.2333E-03	1.1235E+01	-2.5000E+03	-1.7042E-02	1.3765E+01
2, 6	-2.4983E+03	1.6634E+00	1.1608E+01	-2.5016E+03	-1.6752E+00	1.3392E+01
2,11	-2.4976E+03	2.3381E+00	1.2496E+01	-2.5023E+03	-2.3500E+00	1.2504E+01

PART 2b: "worst" values; used by PANDA2 to build face wrinkling, face dimpling and core shear crimping constraint conditions

FORCE RESULTANTS IN SANDWICH FACESHEETS FROM KOITER THEORY (SUB. STRTHK)
ASSUMED TO BE UNIFORM OVER SKIN-STRINGER MODULE SEGMENTS; USED FOR CONSTRAINTS

Segment	Top (or leftmost) facesheet 1			Bottom (or rightmost) facesheet 2		
Iseg	Axial, Nx	Hoop, Ny	Shear, Nxy	Axial, Nx	Hoop, Ny	Shear, Nxy
SKN 1	-2.5023E+03	-2.3500E+00	1.2504E+01	-2.5023E+03	-2.3500E+00	1.3765E+01

PART 3 Transverse shear stress in sandwich core across panel width: "PERFECT" PANEL

PART 3a: actual distributions across the width of the panel (omitted here in order to save space. See Table 271.14 of ITEM 271 in [29].

PART 3b: "worst" values; used by PANDA2 to build x-z ("L"-direction) and y-z ("W"-direction) sandwich core transverse shear constraints and deformation-induced core crushing constraint

DEFORMATION-INDUCED PRESSURE TENDING TO CRUSH THE CORE (COMPUTED IN SUB. STRTHK) AND MAXIMUM TRANSVERSE SHEAR STRESSES (COMPUTED IN SUB. STRMID) ON THE "X" AND "Y" SIDES OF THE SANDWICH CORE

Segment Iseg	Crushing pressure	X-transverse shear stress	Y-transverse shear stress
SKN 1	7.1154E-05	5.4852E-01	5.5839E-01

PART 4 Face sheet resultants across panel width: IMPERFECT PANEL

PART 4a: actual distributions across the width of the panel

Positive Imperfection...(Imperfection amplitude = 0.1 inch)

FORCE RESULTANTS IN SANDWICH FACESHEETS FROM KOITER THEORY (SUB. STRTHK)

Seg. Node	Top (or leftmost) facesheet 1			Bottom (or rightmost) facesheet 2		
Dseg,i	Axial, Nx	Hoop, Ny	Shear, Nxy	Axial, Nx	Hoop, Ny	Shear, Nxy
1, 1	-4.0338E+03	-2.6805E+03	1.7473E+01	1.3948E+03	2.6805E+03	7.5266E+00
1, 3	-4.0453E+03	-2.5678E+03	-4.3158E+02	1.1323E+03	2.5678E+03	4.5658E+02
1, 5	-4.0359E+03	-2.2255E+03	-8.3892E+02	4.0126E+02	2.2255E+03	8.6392E+02
1, 7	-3.8947E+03	-1.6539E+03	-1.1709E+03	-6.4145E+02	1.6539E+03	1.1959E+03
1, 9	-3.4980E+03	-8.8535E+02	-1.3896E+03	-1.7751E+03	8.8534E+02	1.4146E+03
1,11	-2.7739E+03	1.4293E+01	-1.4661E+03	-2.7825E+03	-1.4306E+01	1.4911E+03
2, 1	-2.7739E+03	1.4293E+01	-1.4661E+03	-2.7825E+03	-1.4306E+01	1.4911E+03
2, 6	-9.4079E+01	1.9674E+03	-1.0168E+03	-3.9900E+03	-1.9674E+03	1.0418E+03
2,11	1.3948E+03	2.6805E+03	7.5266E+00	-4.0338E+03	-2.6805E+03	1.7473E+01

Negative Imperfection...(Imperfection amplitude = 0.1 inch)

FORCE RESULTANTS IN SANDWICH FACESHEETS FROM KOITER THEORY (SUB. STRTHK)

Seg. Node	Top (or leftmost) facesheet 1			Bottom (or rightmost) facesheet 2		
Dseg,i	Axial, Nx	Hoop, Ny	Shear, Nxy	Axial, Nx	Hoop, Ny	Shear, Nxy
1, 1	1.3948E+03	2.6805E+03	7.5266E+00	-4.0338E+03	-2.6805E+03	1.7473E+01
1, 3	1.1323E+03	2.5678E+03	4.5658E+02	-4.0453E+03	-2.5678E+03	-4.3158E+02
1, 5	4.0126E+02	2.2255E+03	8.6392E+02	-4.0359E+03	-2.2255E+03	-8.3892E+02
1, 7	-6.4145E+02	1.6539E+03	1.1959E+03	-3.8947E+03	-1.6539E+03	-1.1709E+03
1, 9	-1.7751E+03	8.8534E+02	1.4146E+03	-3.4980E+03	-8.8535E+02	-1.3896E+03
1,11	-2.7825E+03	-1.4306E+01	1.4911E+03	-2.7739E+03	1.4293E+01	-1.4661E+03
2, 1	-2.7825E+03	-1.4306E+01	1.4911E+03	-2.7739E+03	1.4293E+01	-1.4661E+03
2, 6	-3.9900E+03	-1.9674E+03	1.0418E+03	-9.4079E+01	1.9674E+03	-1.0168E+03
2,11	-4.0338E+03	-2.6805E+03	1.7473E+01	1.3948E+03	2.6805E+03	7.5266E+00

PART 4b: "worst" values; used by PANDA2 to build face wrinkling, face dimpling and core shear crimping constraint conditions

FORCE RESULTANTS IN SANDWICH FACESHEETS FROM KOITER THEORY (SUB. STRTHK)
ASSUMED TO BE UNIFORM OVER SKIN-STRINGER MODULE SEGMENTS; USED FOR CONSTRAINTS

Segment	Top (or leftmost) facesheet 1			Bottom (or rightmost) facesheet 2		
Iseg	Axial, Nx	Hoop, Ny	Shear, Nxy	Axial, Nx	Hoop, Ny	Shear, Nxy
SKN 1	-4.0453E+03	-2.6805E+03	1.4911E+03	-4.0453E+03	-2.6805E+03	1.4911E+03

PART 5 Transverse shear stress in sandwich core across panel width: IMPERFECT PANEL

PART 5a: actual distributions across the width of the panel

TRANSVERSE SHEAR STRESSES IN SANDWICH CORE FROM KOITER THEORY (SUB.STRTHK)

Seg. Node	x-z transverse shear stress	y-z transverse shear stress
Dseg, i	Qx(i,Dseg)/Tx(j)	Qy(i,Dseg)/Tx(j)

```
  1,  1          6.3017E+02                  2.3818E+01
  1,  2          6.2321E+02                  6.4027E+01
  1,  3          6.0234E+02                  1.5305E+02
  1,  4          5.6759E+02                  2.4217E+02
  1,  5          5.1911E+02                  3.3007E+02
  1,  6          4.5735E+02                  4.1444E+02
  1,  7          3.8319E+02                  4.9202E+02
  1,  8          2.9807E+02                  5.5903E+02
  1,  9          2.0402E+02                  6.1154E+02
  1, 10          1.0365E+02                  6.4621E+02
  1, 11          1.1774E-07                  6.6068E+02

  2,  1          1.1775E-07                  6.6856E+02
  2,  2          1.0365E+02                  6.5408E+02
  2,  3          2.0402E+02                  6.2707E+02
  2,  4          2.9807E+02                  5.8175E+02
  2,  5          3.8319E+02                  5.2133E+02
  2,  6          4.5735E+02                  4.4951E+02
  2,  7          5.1911E+02                  3.7001E+02
  2,  8          5.6759E+02                  2.8595E+02
  2,  9          6.0234E+02                  1.9962E+02
  2, 10          6.2321E+02                  1.1229E+02
  2, 11          6.3017E+02                  2.4403E+01

PART 5b: "worst" values; used by PANDA2 to build x-z ("L"-direction) and
         y-z ("W"-direction) sandwich core transverse shear constraints
         and deformation-induced core crushing constraint
 DEFORMATION-INDUCED PRESSURE TENDING TO
 CRUSH THE CORE (COMPUTED IN SUB. STRTHK) AND MAXIMUM
 TRANSVERSE SHEAR STRESSES (COMPUTED IN SUB. STRMID)
 ON THE "X" AND "Y" SIDES OF THE SANDWICH CORE
  Segment      Crushing     X-transverse   Y-transverse
    Iseg       pressure     shear stress   shear stress
 SKN  1     9.3920E+01      6.3017E+02     6.6856E+02
================================================================================
```


Table 15 Optimization of IMPERFECT Titanium/Aluminum Sandwich Panel
Amplitude of the buckling modal imperfection, W0 = 0.1 in.
1. Initial face sheet waviness, w0/L = 0.001;
2. (face sheet wrinkling halfwavelength)/(1.732*s) > 2.0
constraint condition turned ON
3. Buckling modal imperfection amplitude, W0 = 0.1 in.

```
================================================================================
PART 1: Optimization (omitted here to save space. See Table 271.15 in
        ITEM 271 of [29])
--------------------------------------------------------------------------------
PART 2  Optimum design, IMPERFECT panel
  VALUES OF DESIGN VARIABLES CORRESPONDING TO ALMOST FEASIBLE DESIGN
 VAR. STR/ SEG. LAYER   CURRENT
 NO.  RNG  NO.   NO.     VALUE          DEFINITION
  1   SKN   1     1   2.379E-02    T(1 )(SKN):thickness for layer index no.(1)
  2   SKN   1     2   7.453E-01    T(2 )(SKN):thickness for layer index no.(2)
  3   SKN   1     3   2.379E-02    T(3 )(SKN):thickness for layer index no.(3)
  4   SKN   1     0   6.464E-02    s(2 )(SKN):Length of one side of the hexagon
  5   SKN   1     0   1.133E-03   tc(2 )(SKN):thickness of honeycomb cell wall
--------------------------------------------------------------------------------
PART 3  Objective, IMPERFECT panel
  CORRESPONDING VALUE OF THE OBJECTIVE FUNCTION:
 VAR. STR/ SEG. LAYER   CURRENT
 NO.  RNG  NO.   NO.     VALUE          DEFINITION
        0     0   1.925E+01   WEIGHT OF THE ENTIRE PANEL
--------------------------------------------------------------------------------
PART 4 Margins at the optimum design, IMPERFECT panel
 MARGINS FOR CURRENT DESIGN: LOAD CASE NO. 1, SUBCASE NO. 1
 MAR. MARGIN
 NO.  VALUE              DEFINITION
  1  8.48E-01 Local buckling from discrete model-1.,M=5   axial halfwaves;FS=1.1
  2  1.02E+00 Local buckling from Koiter theory,M=5   axial halfwaves;FS=1.1
  3  1.77E-02 eff.stress:matl=1,SKN,Dseg=2,node=11,layer=3,z=0.4078; MID.;FS=1.
  4 -3.60E-03 eff.stress:matl=1,SKN,Iseg=1,allnode,layer=1,z=-0.4078;-MID.;FS=1.
  5  8.54E-01 buck.(DONL);simp-support general buck;M=5;N=1;slope=0.;FS=1.1
  6  9.62E-01 localbuck (VINSON);strng Isegl ;MID; local buck.; M=5;FS=1.1
  7  1.34E+00 wrinkling ;strng Isegl ; MID;face 1; M=417;N=2;slope=0.132;FS=1.
  8  6.19E-04 Facel wavelength/celldiam;STR;Iseg=1 ;Matl=2 ;MIDLENGTH;FS=1.
  9  1.39E+00 wrinkling ( HOFF );strng Isegl ; MID;face 1; M=450;FS=1.
 10  4.90E+00 corecrimp (VINSON);strng Isegl ;MID; core crimping;FS=1.
 11  9.37E+00 dimpling  ;strng Isegl ; MID;face 1; M=1;N=1;slope=0.05;FS=1.
 12  1.34E+00 wrinkling ;strng Isegl ; MID;face 2; M=417;N=2;slope=0.132;FS=1.
 13  6.19E-04 Face2 wavelength/celldiam;STR;Iseg=1 ;Matl=2 ;MIDLENGTH;FS=1.
 14  1.39E+00 wrinkling ( HOFF );strng Isegl ; MID;face 2; M=450;FS=1.
 15  9.37E+00 dimpling  ;strng Isegl ; MID;face 2; M=1;N=1;slope=0.05;FS=1.
 16 -1.33E-02 Core crushing margin;STR;Iseg=1 ;Matl 2 ;MIDLENGTH;FS=1.
 17  1.78E-01 L-dir. sandwich core shear;STR;Iseg=1 ;Matl 2 ;MIDLENGTH;FS=1.
 18  3.77E-01 W-dir. sandwich core shear;STR;Iseg=1 ;Matl 2 ;MIDLENGTH;FS=1.
 19  1.58E+00 face sheet pull-off margin;STR;Iseg=1 ;Matl 2 ;MIDLENGTH;FS=1.
 20  1.61E+02 (Max.allowable ave.axial strain)/(ave.axial strain) -1; FS=1.
 21  8.54E-01 buck.(SAND);simp-support general buck;M=5;N=1;slope=0.;FS=1.1
================================================================================
```

Table 16 Effect of temperature gradient through the thickness:
1. Initial face sheet waviness, w0/L = 0.001;
2. (face sheet wrinkling halfwavelength)/(1.732*s) > 2.0
constraint condition turned ON
3. Amplitude of the buckling modal imperfection, W0 = 0.1 in.
t(face)=0.02379, t(core)=0.7453, s=0.06464, tc=0.001133 in.
is the optimum found with zero temperature gradient.

```
                y   $ Is there any thermal "loading" in this load set?
bottom face--> 400  $ Temperature rise, panel skin, surface opposite stringer
   top face--> 000  $ Temperature rise, panel skin, upper surface
                n   $ Is the thermal loading part of Load Set B?
================================================================================
PART 1
      FORCE RESULTANTS IN SANDWICH FACESHEETS AFTER CALL TO SUB. STRCON
       (IMPERFECT PANEL, NO THERMAL GRADIENT THROUGH PANEL THICKNESS)
 Segment   Top (or leftmost) facesheet 1      Bottom (or rightmost) facesheet 2
  Iseg    Axial, Nx   Hoop, Ny   Shear, Nxy   Axial, Nx   Hoop, Ny   Shear, Nxy
 SKN  1 -3.1111E+03 -5.9808E+02  3.3798E+02 -3.1111E+03 -5.9808E+02  3.3798E+02
--------------------------------------------------------------------------------
PART 2
      FORCE RESULTANTS IN SANDWICH FACESHEETS AFTER CALL TO SUB. STRCON
     (IMPERFECT PANEL, INCLUDING THERMAL GRADIENT THROUGH PANEL THICKNESS)
 Segment   Top (or leftmost) facesheet 1      Bottom (or rightmost) facesheet 2
  Iseg    Axial, Nx   Hoop, Ny   Shear, Nxy   Axial, Nx   Hoop, Ny   Shear, Nxy
 SKN  1 -2.4078E+03 -3.6908E+02  3.3798E+02 -3.8144E+03 -8.2707E+02  3.3798E+02
--------------------------------------------------------------------------------
PART 3   Margins INCLUDING thermal gradient. Design is the optimum design
         found with no thermal gradient, imperfect panel: PART 2, Table 271.15
         t(face)=0.02379, t(core)=0.7453, s=0.06464, tc=0.001133 in.
 MARGINS FOR CURRENT DESIGN: LOAD CASE NO. 1, SUBCASE NO. 1
 MAR. MARGIN
 NO.  VALUE              DEFINITION
  1  7.64E-01 Local buckling from discrete model-1.,M=5   axial halfwaves;FS=1.1
  2  9.25E-01 Local buckling from Koiter theory,M=5   axial halfwaves;FS=1.1
  3 -1.70E-01 eff.stress:matl=1,SKN,Dseg=2,node=11,layer=3,z=0.3964; MID.;FS=1.
  4 -1.86E-01 eff.stress:matl=1,SKN,Iseg=1,allnode,layer=3,z=0.3964;-MID.;FS=1.
  5  7.70E-01 buck.(DONL);simp-support general buck;M=5;N=1;slope=0.;FS=1.1
  6  8.71E-01 localbuck (VINSON);strng Isegl ;MID; local buck.; M=5;FS=1.1
  7  2.02E+00 wrinkling ;strng Isegl ; MID;face 1; M=418;N=2;slope=0.1757;FS=1.
  8  1.15E-03 Facel wavelength/celldiam;STR;Iseg=1 ;Matl=2 ;MIDLENGTH;FS=1.
  9  2.06E+00 wrinkling ( HOFF );strng Isegl ; MID;face 1; M=446;FS=1.
 10  4.54E+00 corecrimp (VINSON);strng Isegl ;MID; core crimping;FS=1.
 11  1.25E+01 dimpling  ;strng Isegl ; MID;face 1; M=1;N=1;slope=0.06;FS=1.
```

```
12  9.29E-01 wrinkling ;strng Isegl ; MID;face 2; M=417;N=2;slope=0.11;FS=1.
13  1.15E-03 Face2 wavelength/celldiam;STR;Iseg=1 ;Matl=2 ;MIDLENGTH;FS=1.
14  9.10E-01 wrinkling ( HOFF );strng Isegl ; MID;face 2; M=446;FS=1.
15  7.18E+00 dimpling  ;strng Isegl ; MID;face 2; M=1;N=1;slope=0.04;FS=1.
16 -3.48E-01 Core crushing margin;STR;Iseg=1 ;Matl 2 ;MIDLENGTH;FS=1.
17 -6.61E-02 L-dir. sandwich core shear;STR;Iseg=1 ;Matl 2 ;MIDLENGTH;FS=1.
18  2.49E-01 W-dir. sandwich core shear;STR;Iseg=1 ;Matl 2 ;MIDLENGTH;FS=1.
19  7.53E-01 face sheet pull-off margin;STR;Iseg=1 ;Matl 2 ;MIDLENGTH;FS=1.
20  1.62E+02 (Max.allowable ave.axial strain)/(ave.axial strain) -1; FS=1.
21  7.70E-01 buck.(SAND);simp-support general buck;M=5;N=1;slope=0.;FS=1.1
```

Table 17

Optimization of IMPERFECT Titanium/Aluminum Sandwich Panel
WITH through-thickness temperature gradient as specified
in the heading of Table 271.16.
1. Initial face sheet waviness, w0/L = 0.001;
2. (face sheet wrinkling halfwavelength)/(1.732*s) > 2.0
   constraint condition turned ON
3. Amplitude of the buckling modal imperfection, W0 = 0.1 in.
Starting design:
 t(face)=0.02379, t(core)=0.7453, s=0.06464, tc=0.001133 in.
is the optimum found with zero temperature gradient.
Bottom face sheet HOT.

PART 1: Optimization (omitted here to save space. See Table 271.17 in ITEM 271 of [29])

PART 2 Optimum design with buckling modal imperfection (W0=0.1 in.) plus thermal gradient as specified in the heading of Table 16: bottom face sheet HOT.

VALUES OF DESIGN VARIABLES CORRESPONDING TO FEASIBLE DESIGN

VAR. NO.	STR/ RNG	SEG. NO.	LAYER NO.	CURRENT VALUE	DEFINITION
1	SKN	1	1	1.485E-02	T(1)(SKN):thickness for layer index no.(1)
2	SKN	1	2	7.778E-01	T(2)(SKN):thickness for layer index no.(2)
3	SKN	1	3	3.780E-02	T(3)(SKN):thickness for layer index no.(3)
4	SKN	1	0	4.061E-02	s(2)(SKN):Length of one side of the hexagon
5	SKN	1	0	7.000E-04	tc(2)(SKN):thickness of honeycomb cell wall

PART 3 Objective, IMPERFECT panel WITH thermal gradient
CORRESPONDING VALUE OF THE OBJECTIVE FUNCTION:

VAR. NO.	STR/ RNG	SEG. NO.	LAYER NO.	CURRENT VALUE	DEFINITION
		0	0	2.098E+01	WEIGHT OF THE ENTIRE PANEL

PART 4 Margins at the optimum design, IMPERFECT panel WITH thermal gradient
Bottom face sheet HOT

```
BUCKLING LOAD FACTORS FOR LOCAL BUCKLING FROM KOITER v. BOSOR4 THEORY:
 Local buckling load factor from KOITER theory =  2.0947E+00
 Local buckling load factor from BOSOR4 theory =  1.9288E+00

MARGINS FOR CURRENT DESIGN: LOAD CASE NO. 1, SUBCASE NO. 1
MAR. MARGIN
NO.  VALUE                 DEFINITION
 1  7.53E-01 Local buckling from discrete model-1.,M=5   axial halfwaves;FS=1.1
 2  9.04E-01 Local buckling from Koiter theory,M=5   axial halfwaves;FS=1.1
 3  2.13E-02 eff.stress:matl=1,SKN,Dseg=2,node=11,layer=3,z=0.2457; MID.;FS=1.
 4 -6.42E-04 eff.stress:matl=1,SKN,Iseg=1,allnode,layer=3,z=0.2457;-MID.;FS=1.
 5  7.59E-01 buck.(DONL);simp-support general buck;M=5;N=1;slope=0.;FS=1.1
 6  8.52E-01 localbuck (VINSON);strng Isegl ;MID; local buck.; M=5;FS=1.1
 7  1.48E+00 wrinkling ;strng Isegl ; MID;face 1; M=595;N=1;slope=0.2737;FS=1.
 8 -1.45E-04 Facel wavelength/celldiam;STR;Iseg=1 ;Matl=2 ;MIDLENGTH;FS=1.
 9  1.61E+00 wrinkling (VINSON);strng Isegl ; MID;face 1; M=711;FS=1.
10  4.79E+00 corecrimp (VINSON);strng Isegl ;MID; core crimping;FS=1.
11  1.24E+01 dimpling  ;strng Isegl ; MID;face 1; M=1;N=1;slope=0.0917;FS=1.
12  1.96E+00 wrinkling ;strng Isegl ; MID;face 2; M=304;N=3;slope=0.0817;FS=1.
13  1.55E+00 Face2 wavelength/celldiam;STR;Iseg=1 ;Matl=2 ;MIDLENGTH;FS=1.
14  1.44E+00 wrinkling ( HOFF );strng Isegl ; MID;face 2; M=279;FS=1.
15  2.36E+01 dimpling  ;strng Isegl ; MID;face 2; M=1;N=1;slope=0.03;FS=1.
16 -2.45E-03 Core crushing margin;STR;Iseg=1 ;Matl 2 ;MIDLENGTH;FS=1.
17  1.75E-01 L-dir. sandwich core shear;STR;Iseg=1 ;Matl 2 ;MIDLENGTH;FS=1.
18  3.00E-01 W-dir. sandwich core shear;STR;Iseg=1 ;Matl 2 ;MIDLENGTH;FS=1.
19  3.39E+00 sandwichcore tension margin;STR;Iseg=1 ;Matl 2 ;MIDLENGTH;FS=1.
20  1.80E+02 (Max.allowable ave.axial strain)/(ave.axial strain) -1; FS=1.
21  7.59E-01 buck.(SAND);simp-support general buck;M=5;N=1;slope=0.;FS=1.1
```

Table 18

Optimized designs for IMPERFECT panel WITH thermal gradient
obtained from SUPEROPT
(See [20] and panda2.news ITEMs 151,152,194, [29] for SUPEROPT)
Thermal gradient: temperature rise in one facesheet = 400 deg.
temperature rise in the other facesheet = 0.0 deg.
 1. Initial face sheet waviness, w0/L = 0.001;
 2. (face sheet wrinkling halfwavelength)/(1.732*s) > 2.0
    constraint condition turned ON
 3. Amplitude of the buckling modal imperfection, W0 = 0.1 in.
 Starting design:
  t(face)=0.02379, t(core)=0.7453, s=0.06464, tc=0.001133 in.
 is the optimum found with zero temperature gradient.

PART 1 Optimum design obtained from SUPEROPT for bottom facesheet temperature rise = 400 deg., top facesheet = 0 deg.

VALUES OF DESIGN VARIABLES CORRESPOND. TO ALMOST FEASIBLE DESIGN

VAR. NO.	STR/ RNG	SEG. NO.	LAYER NO.	CURRENT VALUE	DEFINITION
1	SKN	1	1	1.489E-02	T(1)(SKN):thickness for layer index no.(1)
2	SKN	1	2	7.782E-01	T(2)(SKN):thickness for layer index no.(2)
3	SKN	1	3	3.749E-02	T(3)(SKN):thickness for layer index no.(3)
4	SKN	1	0	4.075E-02	s(2)(SKN):Length of one side of the hexagon
5	SKN	1	0	7.000E-04	tc(2)(SKN):thickness of honeycomb cell wall
		0	0	2.088E+01	WEIGHT OF THE ENTIRE PANEL

PART 2 Optimum design obtained from SUPEROPT for bottom facesheet temperature rise = 0 deg., top facesheet = 400 deg.

VALUES OF DESIGN VARIABLES CORRESPOND. TO ALMOST FEASIBLE DESIGN

VAR. NO.	STR/ RNG	SEG. NO.	LAYER NO.	CURRENT VALUE	DEFINITION
1	SKN	1	1	3.802E-02	T(1)(SKN):thickness for layer index no.(1)
2	SKN	1	2	7.431E-01	T(2)(SKN):thickness for layer index no.(2)
3	SKN	1	3	1.480E-02	T(3)(SKN):thickness for layer index no.(3)
4	SKN	1	0	4.023E-02	s(2)(SKN):Length of one side of the hexagon
5	SKN	1	0	7.000E-04	tc(2)(SKN):thickness of honeycomb cell wall
		0	0	2.089E+01	WEIGHT OF THE ENTIRE PANEL

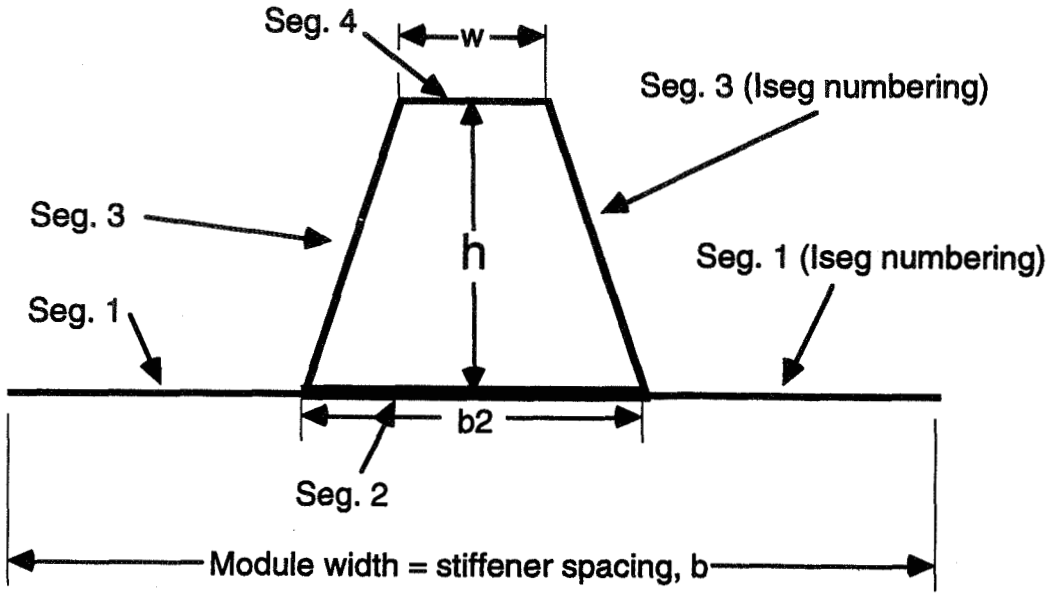

Segment numbering for single module model, "Iseg" numbering

(a)

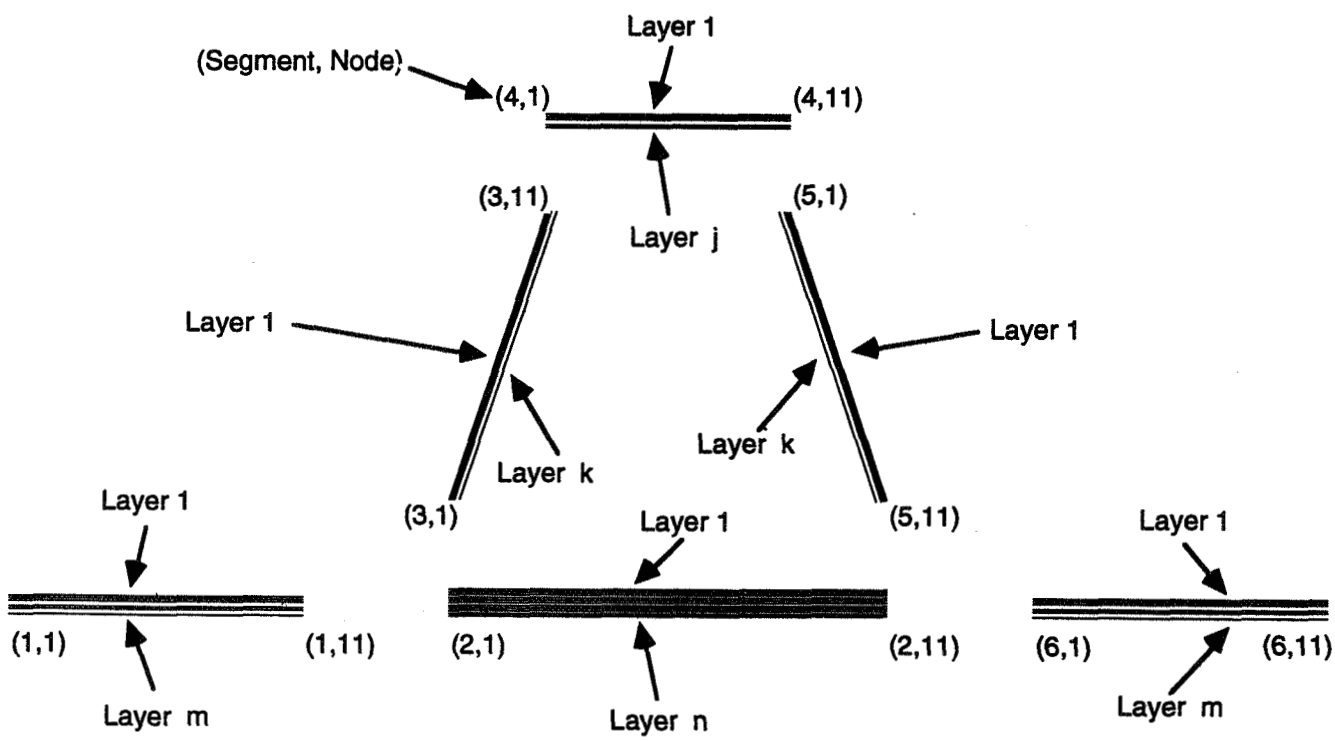

Segment numbering for single module model, "Dseg" numbering

(b)

Fig. 1 Single module model of panel: (a) Numbering of module segments for input data and PANDA type [21] models, (b) Segment numbering for discretized single module

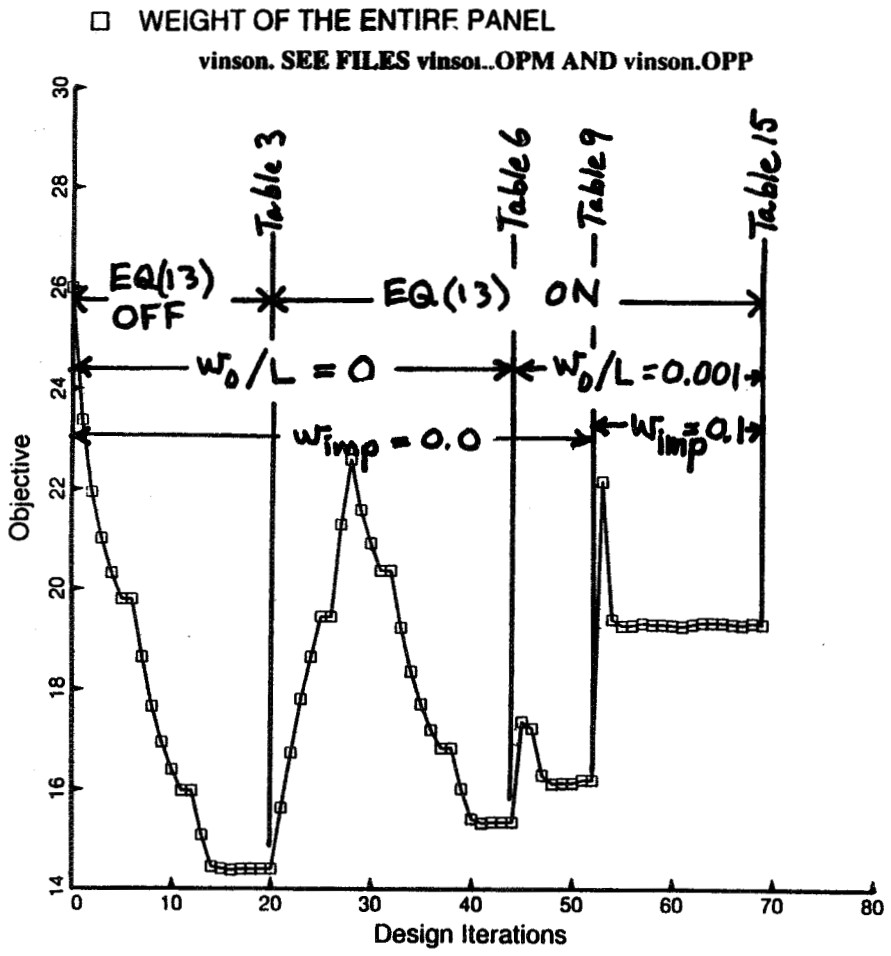

Fig. 2 Panel weight during optimization cycles

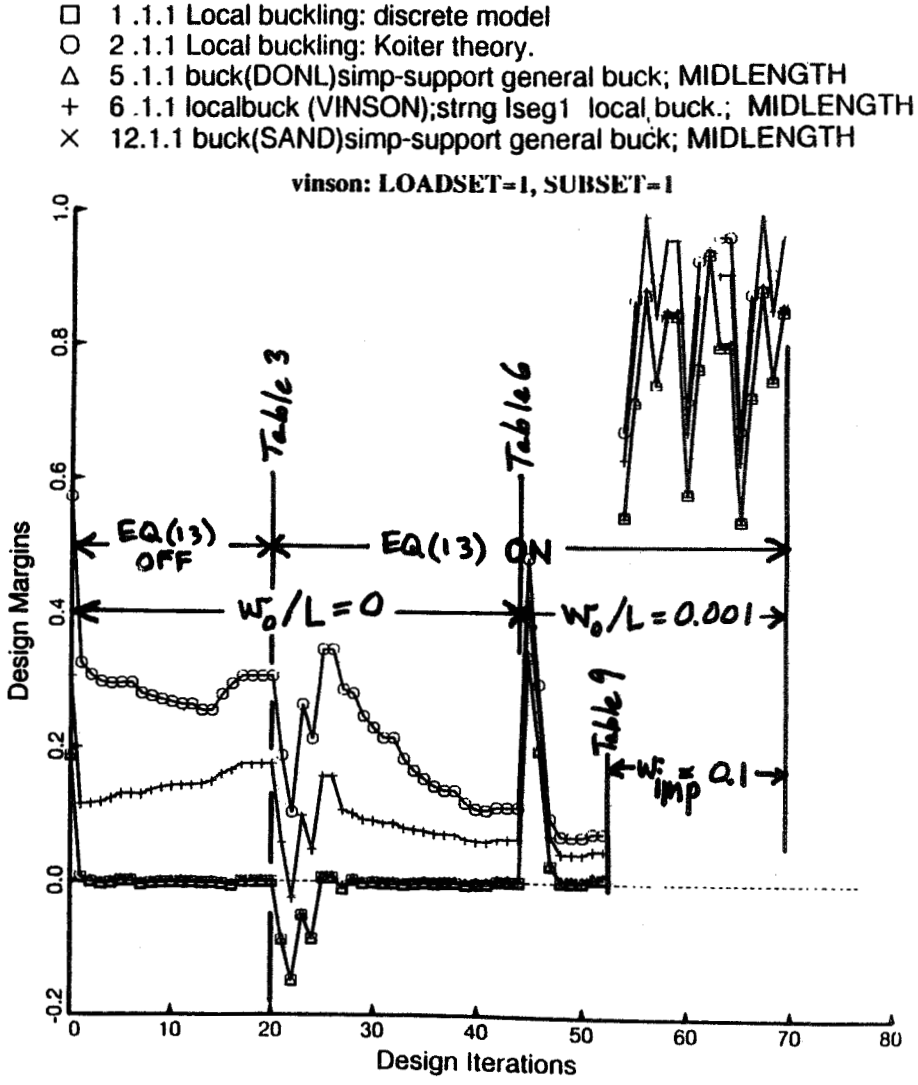

Fig. 3 The five margins that predict overall buckling of the unstiffened panel

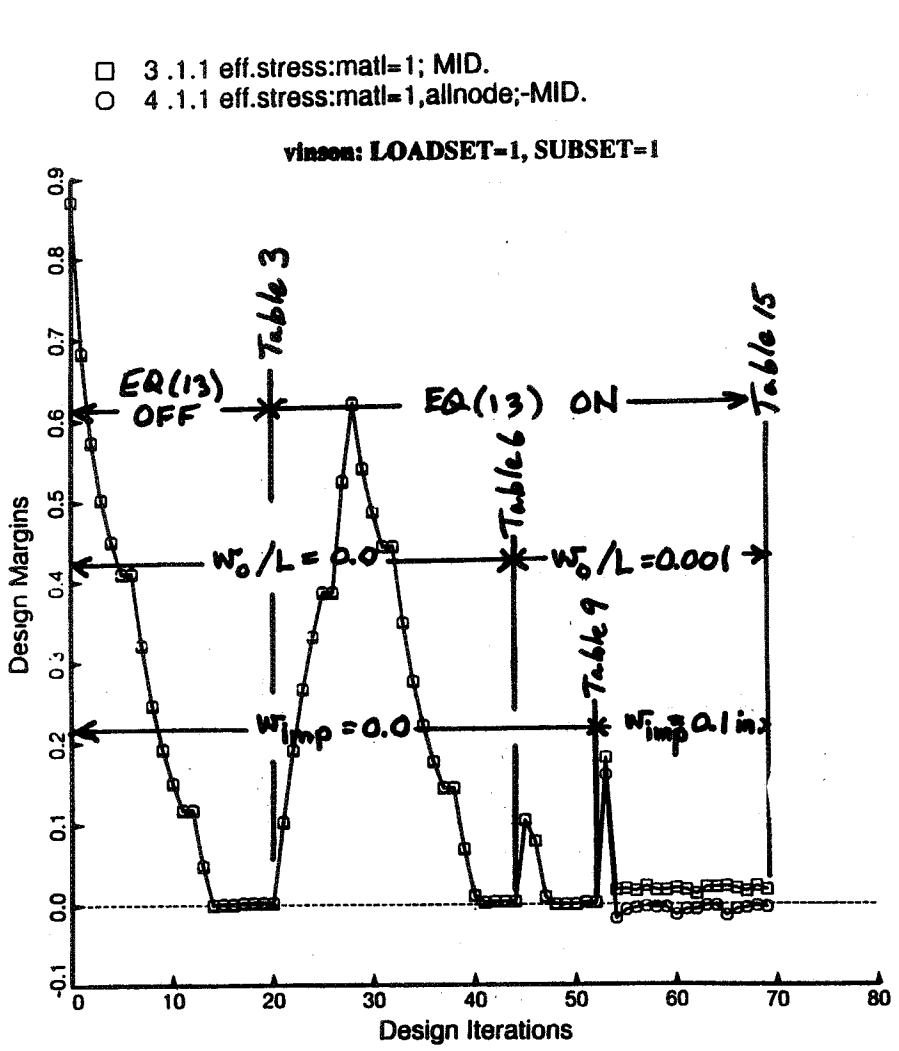

Fig. 4 Effective stress margins

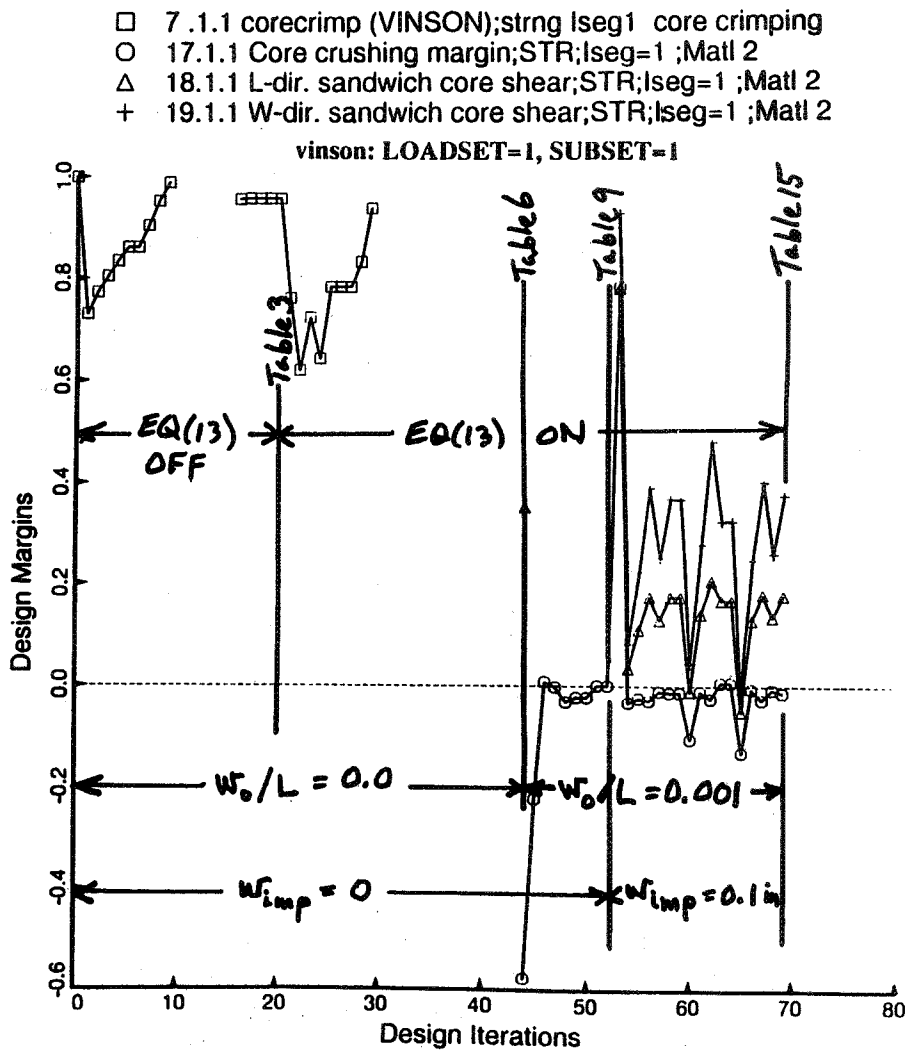

Fig. 5 Margins for sandwich core crimping, crushing, and L- and W-direction transverse shear stress

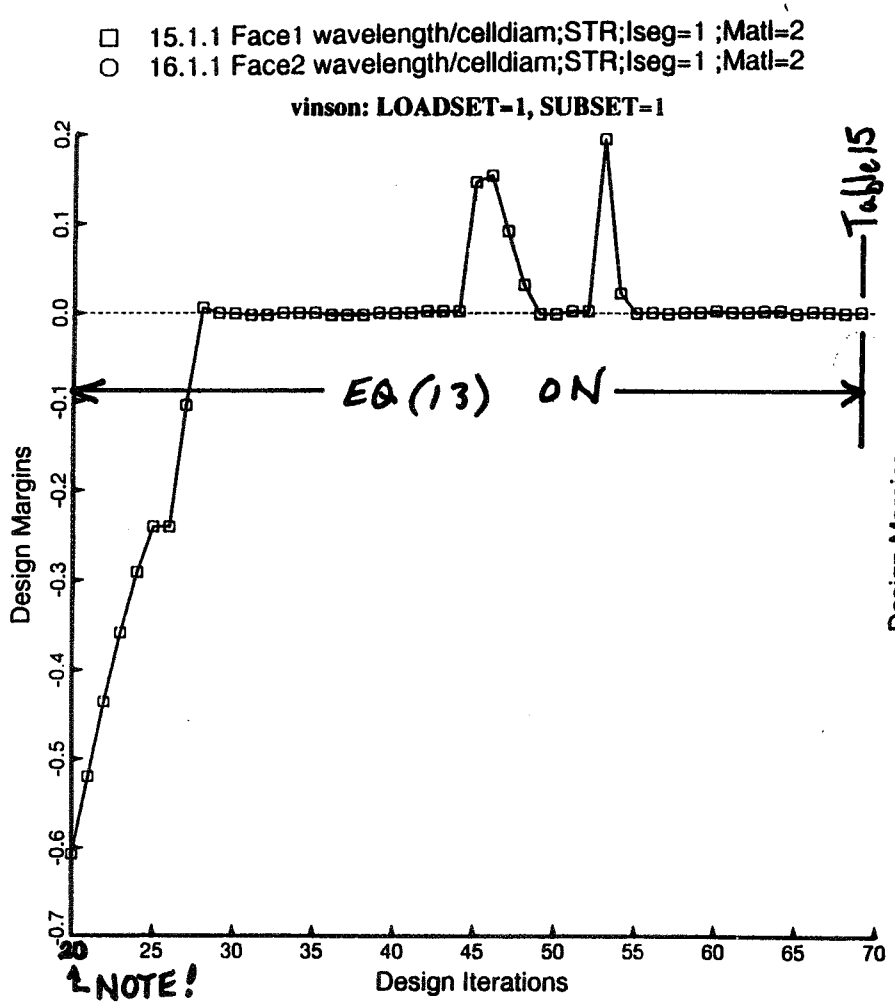

Fig. 6 Margins for honeycomb cell size constraint: (face sheet wrinkling halfwavelength)/(1.732*s) > 2

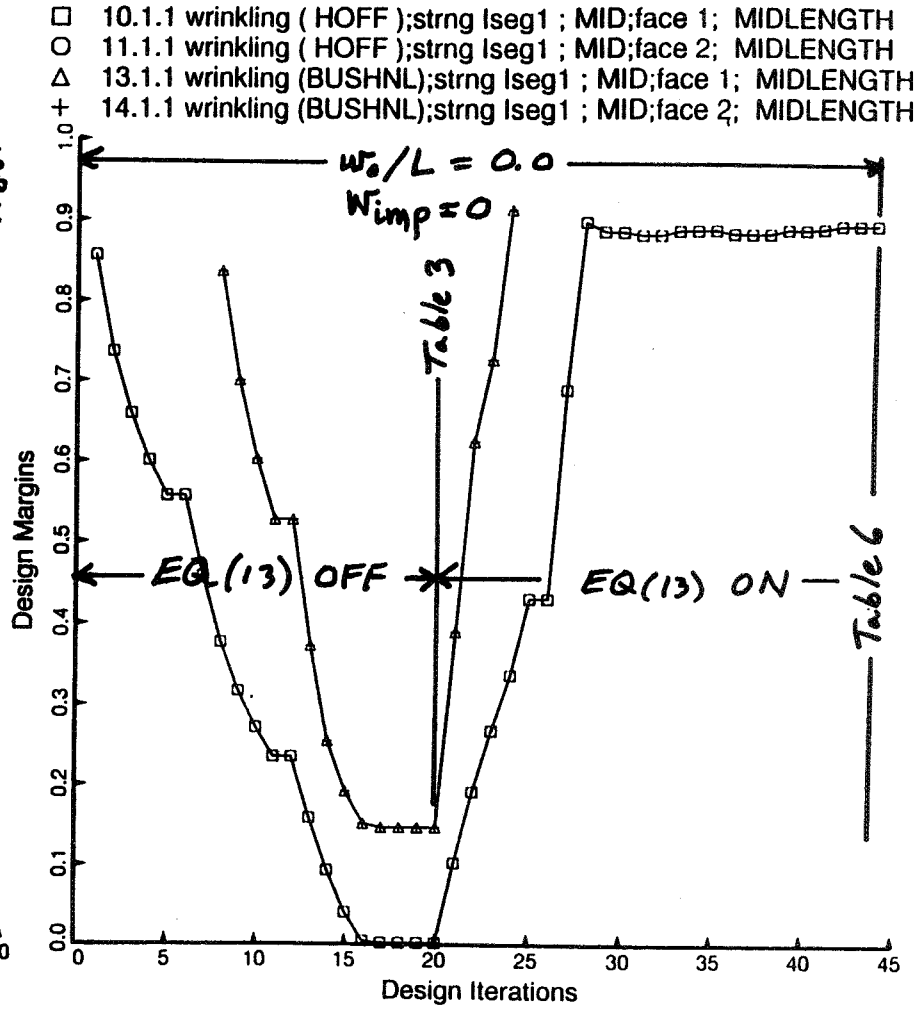

Fig. 7 Margins for face sheet wrinkling

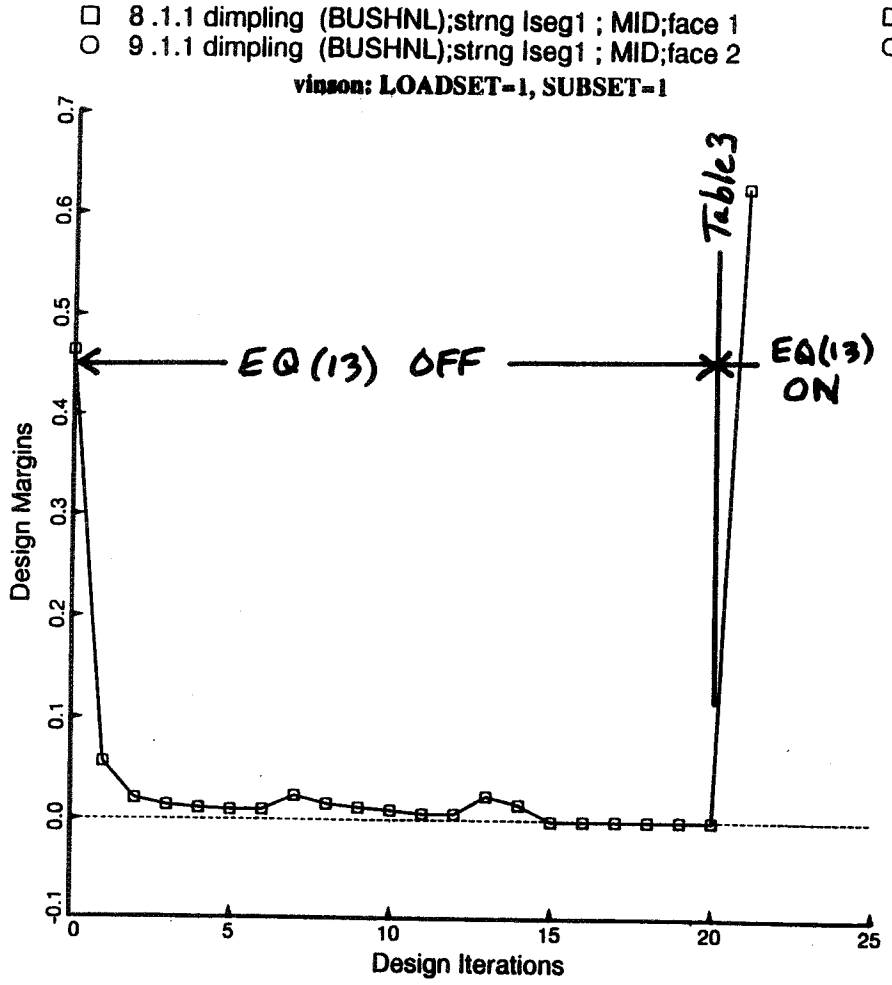

Fig. 8 Margins for face sheet dimpling

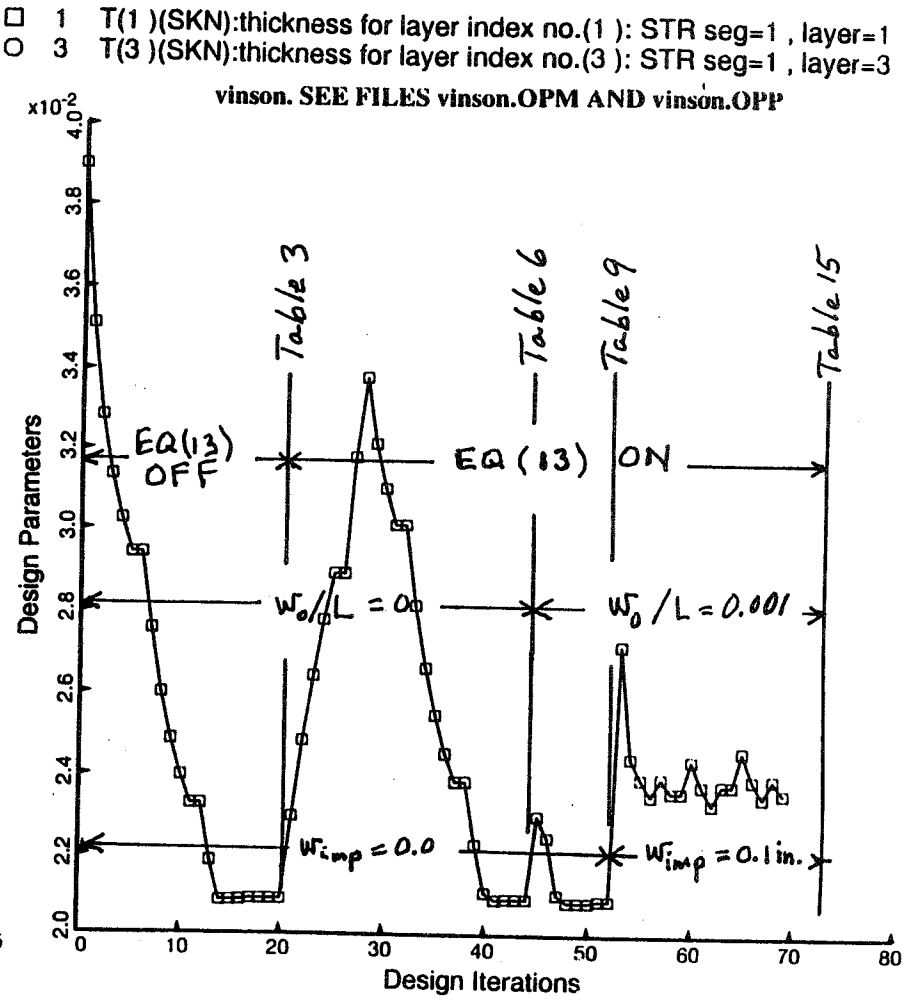

Fig. 9 Evolution of face sheet thickness

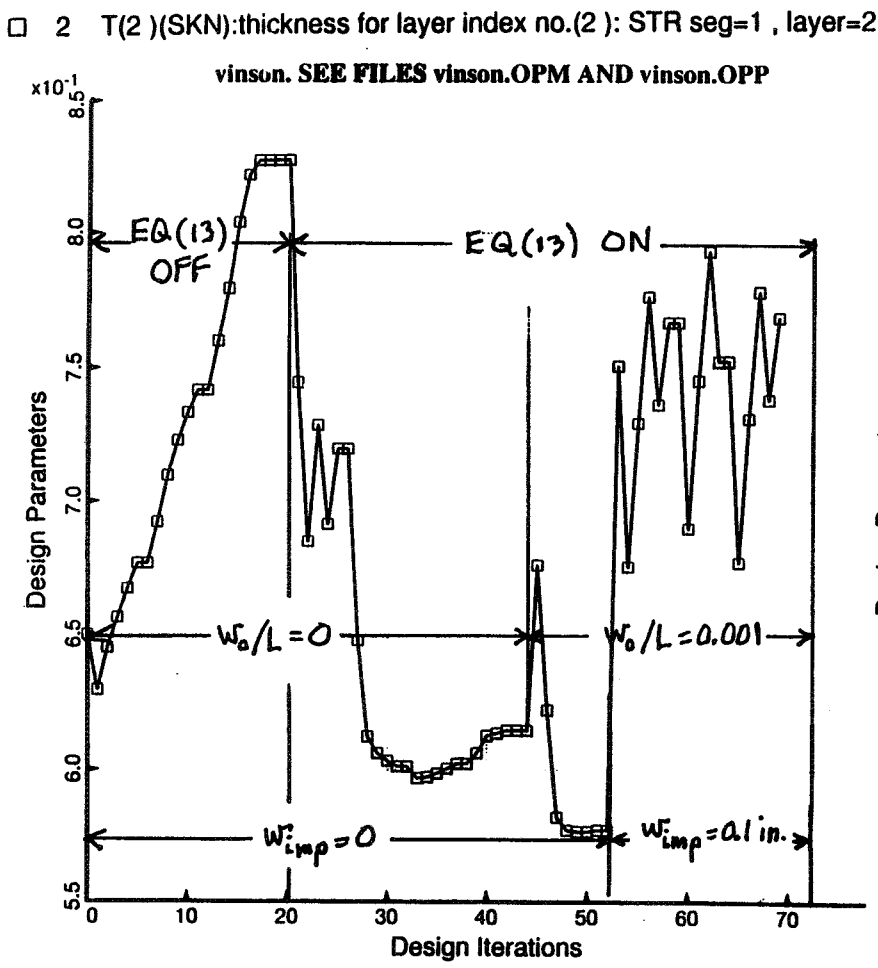

Fig. 10 Evolution of honeycomb core thickness

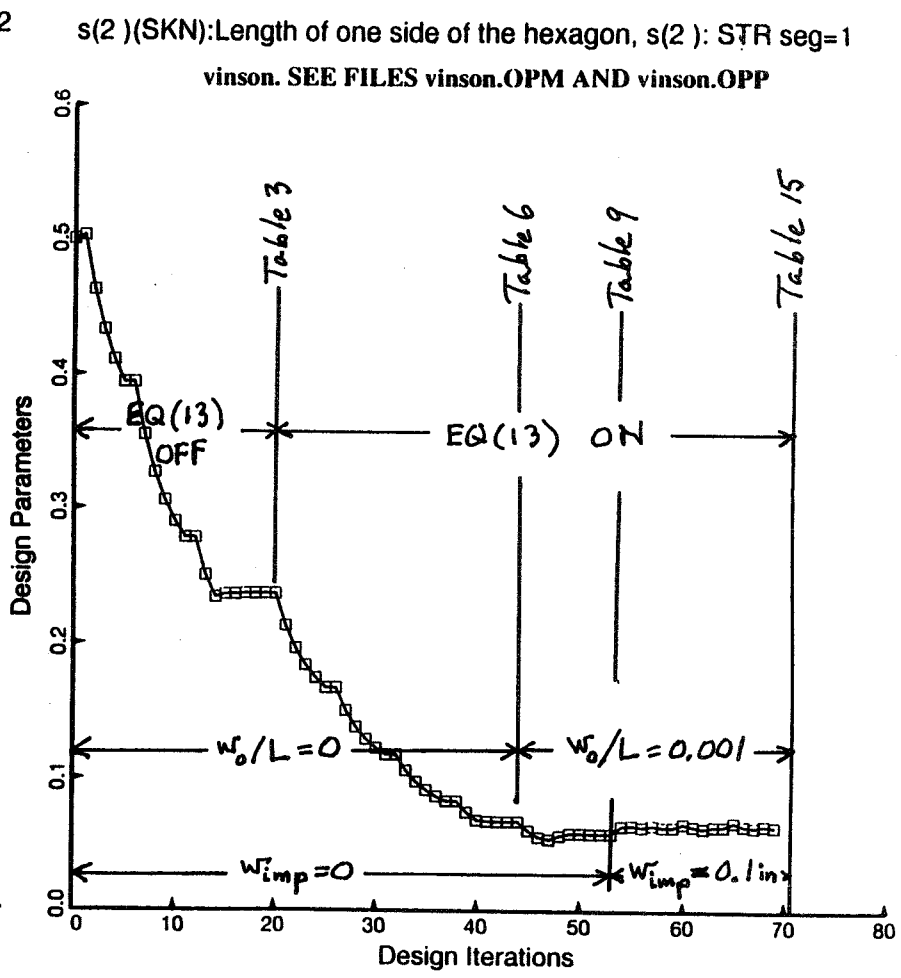

Fig. 11 Evolution of width of one side of hexagonal honeycomb cell

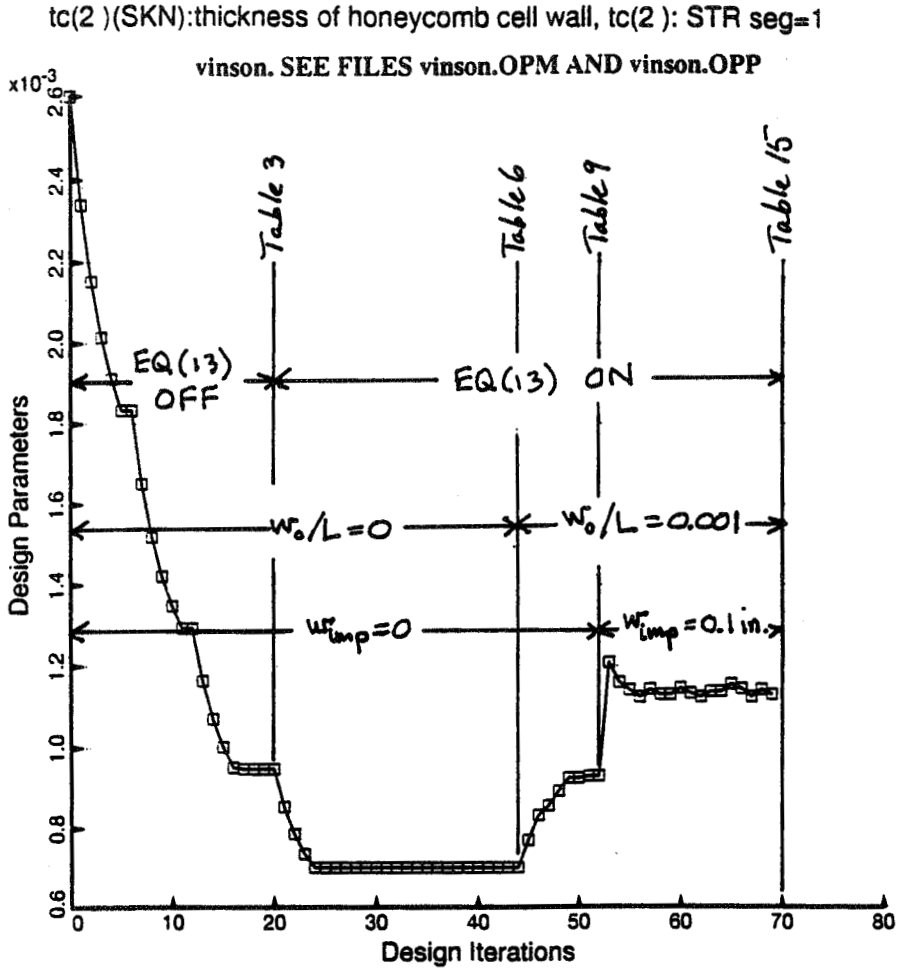

Fig. 12 Evolution of thickness of honeycomb cell wall

A MULTI-MODE RANDOM IMPERFECTION MODEL IN SHELL STABILITY ANALYSIS

A.R. STAM

FACULTY OF AEROSPACE ENGINEERING
DELFT UNIVERSITY OF TECHNOLOGY
THE NETHERLANDS

MARCH, 1997

ABSTRACT

It is generally accepted that the load carrying capacity of cylindrical shells is highly dependent on the presence of initial imperfections, amongst other factors, such as boundary conditions and plasticity effects. In order to be able to design reliable cylindrical shells a so called 'knock down' factor is used. This 'knock down' factor is in this context only theoretically dependent on geometry parameters. Therefore, in order to be able to explain the empirical buckling load scatter, one needs to incorporate this scatter into the parameters of the shell model. Then the quantified scatter of the parameters allows a probabilistic approach.

LIST OF SYMBOLS

R	— Radius.
L	— Length.
t	— Thickness.
ν	— Poisson ratio.
E_s	— Modulus of elasticity stringers
d_s	— Stringer pitch.
e_s	— Stringer eccentricity.
A_s	— Stringer area.
I_s	— Moment of inertia stringer.
J_s	— Torsional constant.
G	— Shear modulus.
$g(\vec{X})$	— Limit state function.
p_f	— Probability of failure.
J	— Jacobian function for transformation.
$\mathcal{R}_\Lambda$	— Reliability function of λ.
λ	— Normalized buckling load.
η	— Path parameter.
$\overline{\xi}_{\mathrm{ax}_i}$	— Axisymmetric imperfection amplitude of wave number i.
$\overline{\xi}_{\mathrm{as}_j}$	— Asymmetric imperfection amplitude of wave number j.
Λ	— Random buckling load.
$\phi_{\vec{X}}(\vec{x})$	— Probability density function of random variable $\vec{X}$.
$\Phi_\Lambda(\lambda)$	— Cumulative distribution function of random variable Λ.

1 INTRODUCTION

In the past quite a number of empirical results of buckling tests have been collected. When displaying these normalized buckling loads against the geometry factor $\frac{R}{t}$ one obtains Fig. 1. The lower

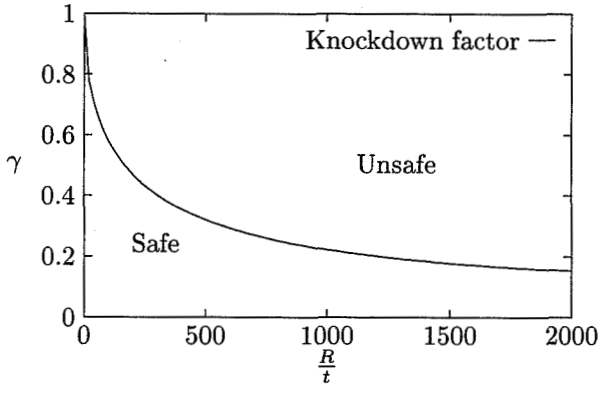

Figure 1: Emipical results and 'knock down' factor.

bound curve to 'all' experimentallly determined normalized buckling loads guarantees that failure will not occur when a design is based on a normalized buckling load below this line.

The conservativeness of this curve can be explained by the omission of any information about design uncertainties of the shell other than the experimentally obtained buckling load.

One of the main causes of decreasing buckling loads can be ascribed by the presence of initial shape imperfections. In general one does not know anything about the modes or amplitudes of the initial imperfections when presented in a Fourier series. For any $\frac{R}{t}$ the 'form' of the imperfection pattern depends on the production process [1].

With respect to this statement one could argue to introduce a so called improved 'knock down' factor when extra information on the shell is available, for a particular series of shells. Then the extra available information must be included in the analysis. This information is about the uncertainties in the parameters in the analysis. The uncertainties will be represented by statistical properties.

Considering this reliability approach, one is able to 'raise' the conventional 'knock down' curve such that it is suitable for design for that particular series of shells. This improved 'knock down' factor can be calibrated by the old one by assuming that for a particular $\frac{R}{t}$ a buckling load distribution is available. Then the lower bound curve specifies a currently accepted reliability level.

In order to arrive at the improved 'knock down' factor, the following steps must be set. First, one has to identify the geometric imperfection pattern with respect to the 'perfect' shell geometry. Second, distributions, when one uses a Fourier series expansion, of the coefficients have to be determined. Third a distribution of the buckling load has to be determined, either theoretical or empirical.

By assuming (experimental) or knowing (theoretical) the type of buckling load distribution, one can position the improved 'knock down' factor curve under the constraint that the probability of failure is the same as in the conventional 'knock down' curve. The interpretation of the probability of failure here is formally not correct. It should be interpreted here as the required stiffness of the shell expressed in terms of axial loading that should at least have a level above the 'knock down' curve. Shells that do not satisfy this requirement will fail at a load level lower than the required ones.

The transformation of the conventional 'knock down' curve into levels of acceptable probability of failure results in Fig. 2, under the assumption that the buckling load distribution, per level of $\frac{R}{t}$, is normal. Then the integration of this probability density function from minus infinity to the 'knock down' curve is the currently accepted measure of safety under the assumptions made here, Fig. 2, for a selected $\frac{R}{t}$. In order to determine the 'improved knock down factor' for a shell with a typical $\frac{R}{t}$ one must use the statistical information of the parameters under consideration to obtain a new probability density function based on this specific information. Then the location $\hat{\lambda}$ of the 'raised' 'knock down' factor can be found by integration of this 'new' probability density function from minus infinity to the level of p_f previously accepted.

$$\hat{p}_f = \int_{-\infty} \hat{\lambda}\phi_{\hat{\Lambda}}(t)dt \qquad (1)$$

where the $\hat{}$ refers to the 'new' set of statistical properties. It has to be noticed that the assumption of normality substitutes the notion of non-failure in the case of application of the knock down factor with that of a probability of failure, without changing the state of the model. It has to be proven from experimental data whether or not the assumption of the distribution being normal is valid. Possibly a bounded probability function is necessary.

It can be argued that the assumption of an unbounded probability density function is valid since the likeliness of occurrence of an experimental buckling load level under the knock down curve is very small, but present. However this approach, the assumption of normality of the probability density function, will be persued in this paper. Wether one should better use a bounded probability density function must await further experimental evidence.

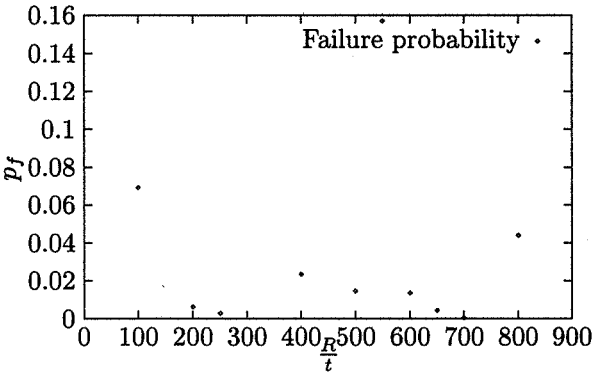

Figure 2: Accepted levels of probability of failure based on experimental data and lower bound curve.

The mean values and standard deviations of the obtained distributions per level of $\frac{R}{t}$ are given in Fig. 3 and Fig 4. From Fig. 3 it can be seen

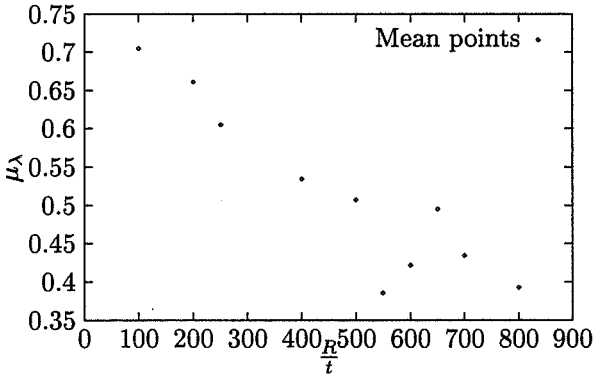

Figure 3: Calculated mean value of normal probability density function per level of $\frac{R}{t}$.

that the expected value of the assumed probability density function decreases with increasing level

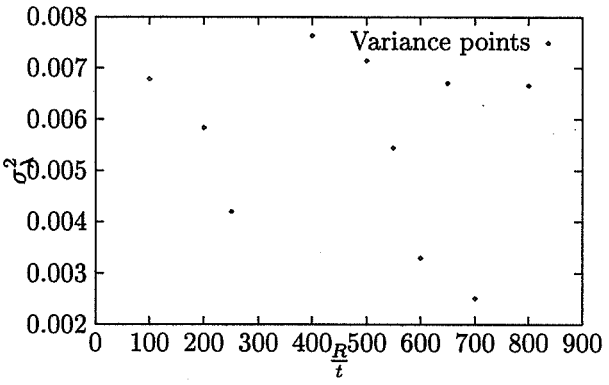

Figure 4: Calculated variance of normal probability density function per level of $\frac{R}{t}$.

of $\frac{R}{t}$, whereas the standard deviation is fluctuating strongly within certain bounds. The probability of failure displayed in Fig. 2 is also rather constant within certain bounds. If these results are representative for the complete shell population being tested, it can be concluded that under the presence of the same deviations in the shell, for an increasing level of $\frac{R}{t}$, the the shell becomes more responsive for the same level of the normalized applied load.

When using the reliability approach the main objective is to find, the allowable load level for a specified probability of failure. This means solving the equation

$$\lambda = \Phi_{\Lambda}^{-1}(p_f) \tag{2}$$

with

$$\Phi_{\Lambda}(\Lambda) = \int_{-\infty}^{\lambda} \phi_{\vec{X}}(\vec{t}) \frac{1}{|J(\Lambda, \vec{t})|} d\vec{t} \tag{3}$$

Where $J(\Lambda, \vec{t})$ is the Jacobian function for the transformation of the random variables from the input space $\vec{X}$ to the output space Λ. The formulation of the original problem described by Eq. 2 is in general very difficult and mostly not solvable. This equation enforces an iterative solution procedure on top of the evaluation of a multi dimensional integral in order to obtain a continuous solution of $\lambda(p_f)$. Therefore the problem is often formulated as

$$p_f = \int_{-\infty}^{\lambda} \phi_{\Lambda}(t) dt \tag{4}$$

$$= \int_{g(\Lambda,\vec{X})\leq 0} \cdots \int \phi_{\vec{X}}(\vec{t}) d\vec{t} \tag{5}$$

The function $g(\Lambda, \vec{X})$ is the limit state function, which separates the failure and non-failure region, in the input space. The limit-state function can be typed as

$$g(\Lambda, \vec{X}) = H(\vec{X}) - \Lambda \tag{6}$$

since the loading is not necessarily random.

Direct integration is not an alternative since generally the design space is large dimensional and the integration domain is difficult to describe in the design space. Therefore approximations will be used to obtain the reliability level of a defined structure.

2 Multi-mode shell stability analysis

The problems encountered in the field of stability of continuous systems are complicated. This phenomenon was already studied by Poincaré. Later, static stability of shell structures was investigated successfully by many schools.

The stability of an equilibrium state can be evaluated with the Trefftz criterion

$$\begin{aligned} \text{Equilibrium: } \delta V &= 0 \\ \text{Stability: } \delta^2 V &\geq 0 \end{aligned}$$

where V represents the potential energy functional of the system under consideration. If this last equation is not satisfied, higher order variations will have to be evaluated. The failure of the shell in the case of a perfect cylinder will be bifurcation. In general, the presence of asymmetric imperfections enforces the failure to be collapse. However, axisymmetric imperfections only do not necessarily reduce a bifurcation point into a limit point (collapse).

It was Koiter in 1945 who studied the structural stability for a continuous system in an axisymmetric configuration. Koiter was the first to recognize the sensitivity of the buckling load with respect to the initial imperfections. First, his general theory of small Gaussian curvature or theory of quasi-shallow shells showed the reduction of buckling load for small initial imperfections. Second, the special theory of small finite deflections or theory of shallow shells provided an estimate for the buckling load as a function of the imperfection amplitude, which was even more significant [2].

Later the effect of more than one imperfection mode was investigated, and also the significance of higher order theories has been discussed and developed.

The behavior of the cylindrical shell with a combination of a series of axisymmetric and asymmetric imperfection modes can best be explained as a result of the nonlinear interaction of specific modes. This interaction of modes, which occurs at certain wave number combinations, is more harmful than the contribution of the individual modes acting alone.

In shell stability analysis the simplest case to consider is the cylindrical shells with one imperfection mode. However, as already suggested the possible coupling of modes needs to be incorporated into the analysis in order to obtain a better model for the behavior of the shell.

The nonlinear approach is based on the Kármán-Donnell equations with a stress-free imperfection shape $\overline{W}$.This set of equations is derived, starting from the potential energy of the system. Then the first variation of the potential energy leads to the equilibrium equations. By introducing an Airy stress function F the in-plane equilibrium equations are satisfied identically. In order to solve for the unknown stress field F and the unknown displacement field in the radial direction W one needs besides the out-of-plane equilibrium equation a second equation, the so-called compatibility equation.

The equilibrium and compatibility equations are respectively

$$L_{A^*}(F) - L_{B^*}(W) = -\frac{1}{R}W_{,xx} - \frac{1}{2}L_{NL}(W, W + 2\overline{W}) \quad (7)$$

$$L_{B^*}(F) + L_{D^*}(W) = \frac{1}{R}F_{,xx} + L_{NL}(F, W + \overline{W}) \quad (8)$$

where W and $\overline{W}$ are positive inward. The linear differential operators $L_{A^*}()$, $L_{b^*}()$, $L_{D^*}()$ and the nonlinear operator $L_{NL}(S,T)$ are defined in [3].

Applying Galerkin's method and satisfying the natural boundary conditions, the solution of the algebraic equations for the buckling load will be an upper bound.

The partial differential equation will be reduced to a set of non-linear algebraic equations via Galerkin's method. In order to formulate the residues to be minimized the two fields functions for the stresses $F(x,y)$ and the displacements $W(x,y)$ will be substituted, together with the field function of the initial imperfection amplitude.

Here the initial radial imperfection amplitude is given by

$$\overline{W} = t\sum_{i=1}^{N_{\mathrm{ax}}} \overline{\xi}_{\mathrm{ax}_i} \cos\frac{n_i\pi x}{L} + t\sum_{j=1}^{N_{\mathrm{as}}} \overline{\xi}_{\mathrm{as}_j} \sin\frac{m_j\pi x}{L} \cos\frac{\ell_j}{R}(y - \tau_K x) \quad (9)$$

where n_i is the integer describing the number of axial half waves, m_j the integer describing the the number of axial half waves in the asymmetric mode and ℓ_j the integer describing the number of circumferential full waves.

For the response radial displacement function the following form is assumed

$$W = t\xi_0 + t\sum_{i=1}^{N_{\mathrm{ax}}} \xi_{\mathrm{ax}_i} \cos\frac{n_i\pi x}{L} + t\sum_{j=1}^{N_{\mathrm{as}}} \xi_{\mathrm{as}_j} \sin\frac{m_j\pi x}{L} \cos\frac{\ell_j}{R}(y - \tau_K x) \quad (10)$$

where Khot's skewedness parameter τ_K allows for buckling mode shapes of anisotropic laminated shells. The parameter ξ_0 describes the uniform radial extension of the shell due to the axial load. The assumed displacement satisfies approximately SS-3 boundary conditions.

The approach as mentioned above yields the following set of nonlinear algebraic equations in terms of the unknown amplitudes ξ_{ax_i} and ξ_{as_j} referring to the axisymmetric and asymmetric imperfection amplitude respectively.

$$\varepsilon_i^{(1)} = \overline{A}_{22}^* \alpha_{m_j}^2 F_i - \frac{1}{2}\frac{t}{R}\left(\overline{B}_{21}^* \alpha_{m_i}^2 + 1\right)\xi_{\mathrm{ax}_i} - \frac{ct}{8R}\sum_{j=1}^{N_{\mathrm{as}}} \xi_{\mathrm{as}_j}\left[\sum_{k=1}^{N_{\mathrm{as}}} \beta_{n_k}^2 \left(\xi_{\mathrm{as}_k} + 2\overline{\xi}_{\mathrm{as}_k}\right)\delta_{ijk}\right] = 0 \quad (11)$$

$$\varepsilon_j^{(1)} = \overline{T}_{56_j} F_j + \frac{1}{4}\frac{t}{R}\overline{T}_{34_j}\xi_{\mathrm{as}_j} + \frac{1}{4}\frac{c}{\pi}\frac{t}{R}\sum_{k=1}^{N_{\mathrm{as}}} \xi_{\mathrm{as}_k}\left(\sum_{l=1}^{N_{\mathrm{as}}} \left[\xi_{\mathrm{as}_l} + 2\xi_{\mathrm{as}_l}\right]\Theta_{ikl}\right) + \frac{1}{4}\frac{ct}{R}\sum_{i=1}^{N_{\mathrm{ax}}} \alpha_i^2 \xi_{\mathrm{ax}_i}\left[\sum_{k=1}^{N_{\mathrm{ax}}} \beta_{n_k}^2 \left(\xi_{\mathrm{as}_k} + 2\overline{\xi}_{\mathrm{as}_k}\right)\delta_{ijk}\right] + \frac{1}{4}\frac{ct}{R}\sum_{k=1}^{N_{\mathrm{as}}} \beta_{n_k}^2 \xi_{\mathrm{as}_k}\left[\sum_{i=1}^{N_{\mathrm{ax}}} \alpha_{m_i}^2 \left(\xi_{\mathrm{ax}_i} + 2\overline{\xi}_{\mathrm{ax}_i}\right)\delta_{ijk}\right] = 0 \quad (12)$$

And from the equilibrium equations

$$\varepsilon_i^{(2)} = 2\frac{R}{t}\left(\overline{B}_{21}^* \alpha_{m_i}^2 + 1\right)F_i + \overline{D}_{11}^* \alpha_{m_i}^2 \xi_{\mathrm{ax}_i} - 2\overline{\lambda}\left(\xi_{\mathrm{ax}_i} + \overline{\xi}_{\mathrm{ax}_i}\right) + c\frac{R}{t}\sum_{j=1}^{N_{\mathrm{as}}} F_j\left[\sum_{k=1}^{N_{\mathrm{as}}} \beta_{n_k}^2 \left(\xi_{\mathrm{as}_k} + \overline{\xi}_{\mathrm{as}_k}\right)\delta_{ijk}\right] = 0 \quad (13)$$

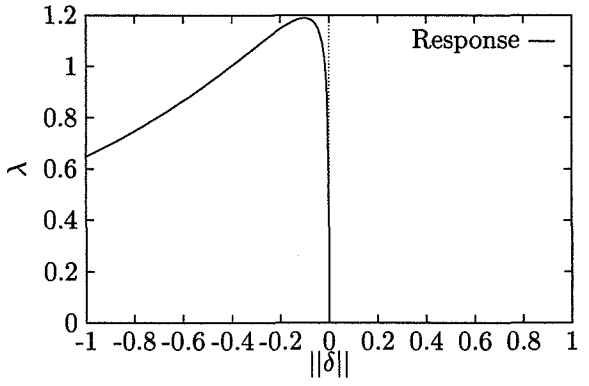

Figure 5: Response curve of axially loaded AS-2 shell.

$$\varepsilon_j^{(2)} = \overline{T}_{12_j}\xi_{\mathrm{as}_j} + \frac{R}{t}\overline{T}_{34_j}F_j - \left[\left(\alpha_{m_j}^2 + \alpha_{p_j}^2\right)\overline{\lambda} + 2\beta_{n_j}\left(\alpha_{m_j} - \alpha_{p_j}\right)\overline{\tau} + 2\beta_{n_j}^2\overline{p}\right]\left(\xi_{\mathrm{as}_j} + \overline{\xi}_{\mathrm{as}_j}\right) - 2c\frac{R}{t}\sum_{i=1}^{N_{\mathrm{ax}}}\alpha_i^2 F_i\left[\sum_{k=1}^{N_{\mathrm{as}}}\beta_{n_k}^2\left(\xi_{\mathrm{as}_k} + \overline{\xi}_{\mathrm{as}_k}\right)\delta_{ijk}\right] - 2c\frac{R}{t}\sum_{k=1}^{N_{\mathrm{as}}}\beta_{n_k}^2 F_k\left[\sum_{i=1}^{N_{\mathrm{ax}}}\alpha_i^2\left(\xi_{\mathrm{ax}_i} + \overline{\xi}_{\mathrm{ax}_i}\right)\delta_{ijk}\right] - 2\frac{c}{\pi}\frac{R}{t}\sum_{k=1}^{N_{\mathrm{as}}}F_k\left[\sum_{l=1}^{N_{\mathrm{as}}}\left(\xi_{\mathrm{as}_l} + \overline{\xi}_{\mathrm{as}_l}\right)\Theta_{jkl}\right] = 0 \quad (14)$$

where the coupling conditions are given by

$$\delta_k^j = \begin{cases} 1 & \text{for } n_j = n_k, \\ 0 & \text{otherwise} \end{cases} \quad (15)$$

$$\delta_{j+k}^i = \begin{cases} 1 & \text{for } m_i = m_j + m_k, \\ 0 & \text{otherwise} \end{cases} \quad (16)$$

$$\delta_{|j-k|}^i = \begin{cases} 1 & \text{for } m_i = |m_j - m_k|\ , \\ 0 & \text{otherwise} \end{cases} \quad (17)$$

And finally

$$\delta_{ijk} = \left[\delta_{j+k}^i - \delta_{|j-k|}^i\right]\delta_k^j \quad (18)$$

This set of equations, Eqs.(11,12) and (13,14), will be written as $\vec{f}(\vec{\xi}, \vec{\overline{\xi}}, \lambda)$. Notice that for the sake of simplicity the row vectors $\vec{\xi} = [\xi_1, \ldots, \xi_N]$ and $\vec{\overline{\xi}} = [\overline{\xi}_1, \ldots, \overline{\xi}_N]$ have been introduced.

In the set of algebraic equations the F-functions contain the terms $\vec{\overline{\xi}}$ and λ [4]. Since multiple solutions are available for selected values of $\overline{\xi}_{\mathrm{ax}_i}$ and $\overline{\xi}_{\mathrm{as}_j}$ the path following method is a useful tool for the response analysis. In Fig. 5 the trace of a typical response curve for the AS-2 shell is given. The

ID	n_i	m_j	ℓ_j
$i=1$	2	—	—
$j=1$	—	1	2
$j=2$	—	1	9
$j=3$	—	1	10

Table 1: Imperfection mode properties of AS-2 shell.

imperfection properties of the AS-2 shell are listed in Table 1. And the geometric properties are given in Table 2.

The response curve has been obtained by applying a continuation procedure to the set of nonlinear algebraic equation given in Eqs.(11); (14). By introducing a path parameter via an auxiliary equation the response curve can be described in the solution space as

$$\vec{f}(\vec{\overline{\xi}}, \vec{\xi}, \lambda) = 0 \quad (19a)$$

$$h(\vec{\overline{\xi}}, \vec{\xi}, \lambda) - \eta = 0 \quad (19b)$$

3 Shape of response surface

The shape of the response surface can be described in an exact manner only by solving the original deterministic set of equations. In order to be able to follow traces on the response surface the original set of non-linear algebraic equations has to be extended by a constraint that enforces to trace of solutions to be on the response surface. Since the domain of interest consists of limit points only, the set of equations can be reformulated as

$$\begin{aligned} \vec{f}(\vec{\overline{\xi}}, \vec{\xi}, \lambda) &= 0 \\ \Gamma(\vec{\overline{\xi}}, \vec{\xi}, \lambda) &= 0 \\ h(\vec{\overline{\xi}}, \vec{\xi}, \lambda) - \eta &= 0 \end{aligned}$$

Where $\Gamma(\vec{\overline{\xi}}, \vec{\xi}, \lambda) = 0$ enforces the determinant of the stiffness matrix to be zero, yielding a limit-point. Γ can also be interpreted as an eigenvalue problem with the lowest eigenvalue being zero. For larger problem this last formulation is easier to solve in combination with the Newton corrections. This set of equation can be solved with the path following method, [5], [6]. The solution of traces on the response surface for several limit load levels is given in Fig. 6. The traces on the response surface of both an axisymmetric and an asymmetric imperfection mode in the multidimensional design space is shown in Fig. 7.

It might become clear that the response surface contains quite a lot of symmetry. For a general response analysis this property can be interpreted as

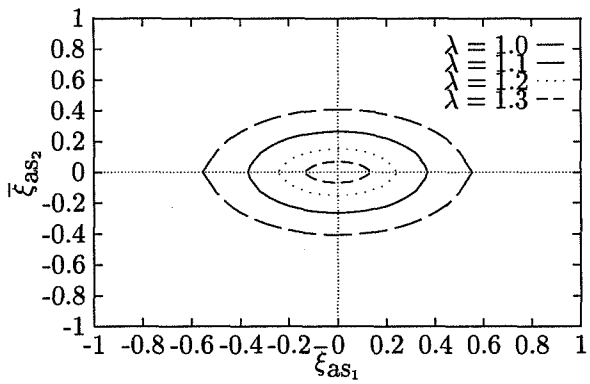

Figure 6: Trace on response surface for two asymmetric modes for several limit load levels of an AS-2 shell.

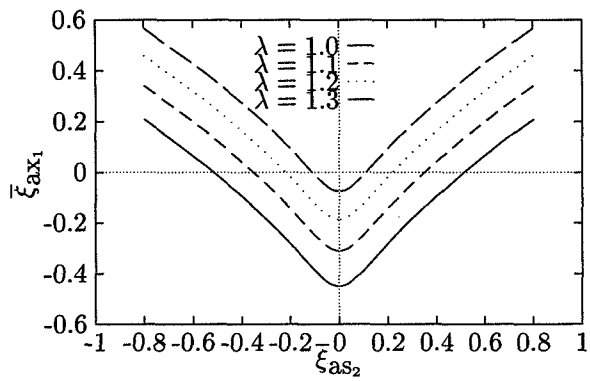

Figure 7: Trace on response surface for both an axisymmetrix and an asymmetric mode for several limit load levels of an AS-2 shell.

an indifference of the sign of the imperfection amplitude. However, with respect to reliability analysis, this multiple symmetry hampers the development of an 'easy to use' algorithm.

4 Response surface methodology

In order to be able to estimate the probability of failure in practical problem one has in general to rely on simulation methods. However, the 'exact' response surface is not practical in employing this simulation procedure. Therefore approximate response surfaces will have to be used. Quite a number of methods of fitting an approximate response surface to the 'exact' response surface are available, a few are useful.

First of all one has to realize that the response surface will be used for simulation purposes. Although, in general, approximate response surfaces are not global fits, the selection of the design points is dictated by moments of the distributions of the random variables. This is to avoid incorrect response outside the domain of validity.

Second the effort of obtaining the approximate response surface has to be taken into consideration also. When the number of random design variables is increased, not only the number of evaluations of the deterministic buckling load increases, but also the effort of obtaining a limit point from the deterministic analysis increases dramatically.

A solution to efficiently determining an approximate response surface will be done via a so called multi-factor design [7]. It turned out that varying only one factor at the time might lead to a completely wrong approximate response surface. In this way some coefficients of approximation might not be determined at all. Therefore it became clear that it was necessary to use 'blocked' designs.

In order to reduce the number of experiments or function evaluations for generating a response surface, generally incomplete factorial designs are employed. As will become clear, there are many types of incomplete factorial designs. The concepts of an incomplete factorial-type design are applicable to general polynomials. In most of the cases one is considering a factorial-type design with a p-level of evaluation points.

A full or complete factorial design, or a polynomial approximation in the most complete form usually requires

$$\frac{(i+r)!}{i!r!} \tag{19}$$

coefficients to be estimated, where i is the number of design dimensions, and r the design order (order of approximating polynomial).

When one uses a incomplete factorial-type design, the highest degree of polynomial that may be fitted to the observations from a p-level factorial is $p-1$. Thus generally, a p^k factorial design is a design of order $p-1$, with k the number of factors or in other words the design dimensions. In this way one can calculate the redundancy factor with respect to the complete factorial as

$$\frac{p^k k!(p-1)!}{(k+p-1)!} \tag{20}$$

It can be shown that via the use of an incomplete factorial design a large reduction of the number of observations can be achieved.

In situations where the experimental error variance is not so large as to require large numbers of observations to obtain the necessary precision, designs having small redundancy factors are desirable. However, in practice small redundancy design are not frequently employed because they do not provide residual degrees of freedom necessary in order to do adequate testing of the obtained response surface.

R	4.00
L	5.50
t	0.00774
ν	0.3
E	$1.00e^{-7}$
d_s	0.3163
e_s	-0.01326
A_s	$0.1238e^{-2}$
I_s	$0.36137e^{-7}$
J_s	$0.1188e^{-6}$
G	$3.84615e^{6}$

Table 2: Geometric properties of AS-2 shell.

The overall analyses can be done in standardized levels. These levels can be obtained by the following scaling, as defined previously

$$x_{iu} = \frac{(\xi_{iu} - \overline{\xi})}{S_i} \tag{21}$$

where i refers to the design number, and

$$S_i = \sqrt{\sum_{u=1}^{N} \frac{(\xi_{iu} - \overline{\xi})^2}{N}} \tag{22}$$

For the standardization the following identities hold

$$\sum_{u=1}^{N} x_{iu} = 0 \tag{23}$$

and

$$\sum_{u=1}^{N} x_{iu}^2 = \frac{N}{c} \tag{24}$$

Thus the level at which one wants to evaluate the function to be fitted can easily be obtained from

$$\xi_{iu} = \overline{\xi} + S_i x_{iu} \tag{25}$$

S_i can be seen as sort scaling factor for the 'spread' of the design points in the design space. The general idea about the incomplete factorial designs is that one reduces to variance in the design with respect to the response parameter. The least one wants is, as mentioned, a constant variance, i.e. the error in the approximate response is independent of the position on the response surface. The maximum reduction of variance can be obtained when one creates a situation in which the matrix $[X]^T[X]$ becomes an diagonal form. Then the design is orthogonal. This orthogonality can be obtained quite easily for a first order polynomial design, by standardizing the design. Then the coefficients are functionally independent, and the smallest variance design is obtained.

Deriving a second order orthogonal design is a bit more elaborate. First one has to transform the second order polynomial of the independent variables to a set of orthogonal polynomials. This transformation provides a set of conditions which the coefficients of the second order polynomial has to satisfy, such that the transformed design matrix is orthogonalized [8] and [9].

It has to be noticed that orthogonality is referred to as orthogonality in a particular direction of the design. It can be shown that the uncorrelatedness of the coefficients can not be maintained in general when the design is being rotated in the design space. Therefore one can only assure that the variance of the first order terms is constant, whereas the variance of the higher order and coupling terms varies with the rotation of the origin [8].

An example of response surface designs that is orthogonal and has low redundancy is the so called Box-Behnken design. The designs are characterized by the property of blocked orthogonality, and uses the properties of incomplete blocked design. This property is very admirable in a response surface design method. The 3-level Box-Behnken design matrices are generated via a certain combination of 2-level factorial designs with incomplete blocks [10], [11].

The quality of the response surface via the Box-Behnken design procedure will be demonstrated by the application to the above mentioned AS-2 shell with 4 initial geometric imperfections. The center point of the design will be at the average of the design variables and the variation in levels will be 3 times the standard deviation.

For a 4 dimensional design the Box-Behnken design matrix takes the form

$$\begin{bmatrix} \pm1 & \pm1 & 0 & 0 \\ 0 & 0 & \pm1 & \pm1 \\ 0 & 0 & 0 & 0 \\ \cdots & \cdots & \cdots & \cdots \\ \pm1 & 0 & 0 & \pm1 \\ 0 & \pm1 & \pm1 & 0 \\ 0 & 0 & 0 & 0 \\ \cdots & \cdots & \cdots & \cdots \\ \pm1 & 0 & \pm1 & 0 \\ 0 & \pm1 & 0 & \pm1 \\ 0 & 0 & 0 & 0 \end{bmatrix} \tag{26}$$

Here the ±1 requires all combinations of levels of the design variables to be evaluated, meaning 4 designs per row. Design matrices for higher dimensions are given in [12]. With this design matrix one needs to evaluate 27 deterministic responses in order to determine 15 coefficients.

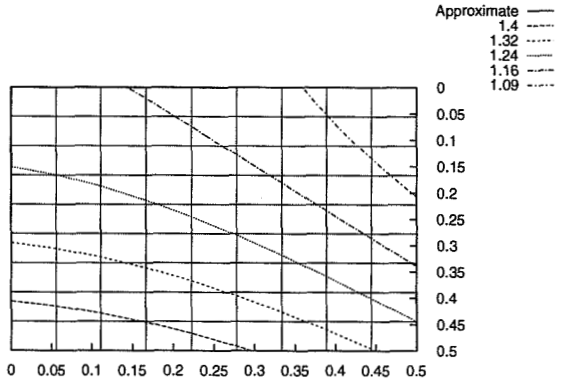

Figure 8: Approximate response surface for an axisymmetric and an asymmetric imperfection mode.

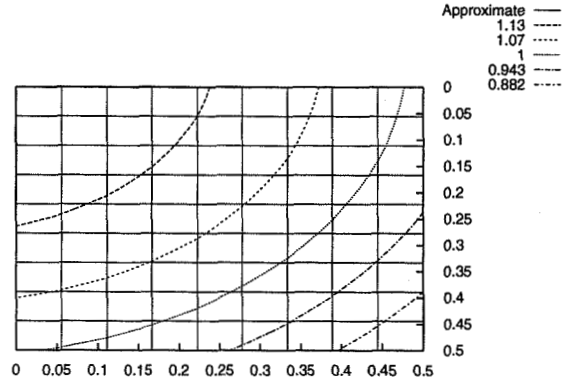

Figure 9: Approximate response surface for two asymmetric imperfection modes.

5 Approximation of the response surface

The previously stated technique of determining an approximate response surface will be demonstrated with a 4 mode imperfection model defined according to table 1, for an AS-2 shell.

This approach of using approximate response surfaces allows the determination of the probability of failure per λ-level based on the mean values of the amplitudes. With or without correlation between the random variables, one needs to evaluate in advance the region in the multi dimensional design space that would contribute significantly to the probability of failure.

Based on the variance of the individual random variables and their correlation one could initially guess which part of the design space could contribute most at a specific buckling load level.

6 Discontinuities

One of the main restrictions with respect to the application of the Box-Behnken response surface methodology with respect to stability analysis is the presence of 'ridges' in the design space. These ridges are introduced by the presence of the axisymmetric imperfection modes.

It can easily be seen that for small amplitudes of the asymmetric imperfection modes the 'spread' of the design points is dictated by the 'distance' available to the $\overline{\xi}_j = 0$ line.

A solution to this problem might be the used of selected scale factors per design dimension. This alternative, however, would undermine the concept of the Box-Behnken approach, i.e. the approximation error distributed over the design space would not be constant for the selected region. Contrary to that, there will be a large dispersion in the error level over the response surface in the selected domain.

It might, however, be considered that a small mean value of a design variable would in general mean that the variance of that random variable will be small also. The argument with respect to production processes is quite reasonable because there will in general be some sort of quality control, that do not allow these 'strange' occurrences to happen.

7 Monte Carlo simulation

The determination of the probability of failure can be done in several ways. One can try to solve the partial differential equations given by Eqs. 7 and 8 with stochastic coefficients. The difficulty then is that this randomness reduces to possible solutions to this set of equations drastically.

An alternative is to solve the deterministic problem and apply a transformation of the random properties of the input space to the random properties of the output space. Also this procedure is only feasible for one or two random variables in the physical problem, when one considers only the exact statistical transformation. Of course approximate methods such as the First Order Second Moment method could be used.

For general applications and especially for multi dimensional problems Monte Carlo simulation is most efficient. One can use either 'brute force' Monte Carlo simulation, i.e. that the complete domain of the random variables will be sampled. However, more efficient methods are available, such as

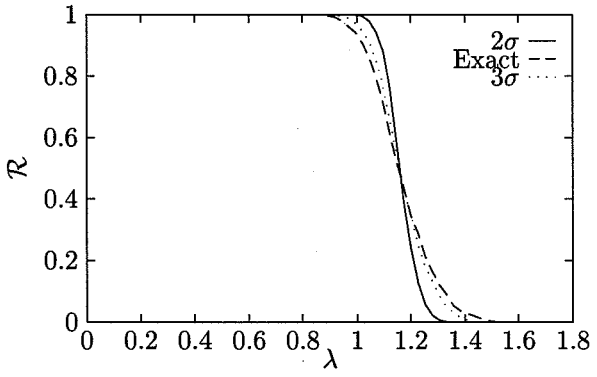

Figure 10: Reliability curves obtained via the different methods.

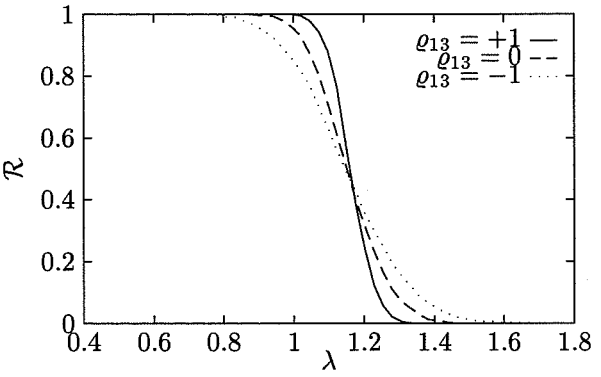

Figure 11: The effect of correlation between two of the asymmetric random variables.

importance sampling, or directional simulation [13]. The efficiency of importance sampling comes from the fact that the simulation will be concentrated near the most probable point, or when evaluated in the standard normal space, the β-point, i.e. the shortest distance from the limit-state function to the origin in this standard normal space.

The importance sampling procedure is available via ISPUD (Importance Sampling Procedure Using Design points). First a Lagrange type optimization procedure in the standard normal space will be employed, and then importance sampling will be used to evaluate the probability of failure. It is important to consider the extra variable that is available, the shape of the weight function used during the sampling procedure [14].

The advantage of the 'brute force' Monte Carlo approach is that one is able to sample throughout the complete domain of the random variable. The disadvantage of using the approximate response surface method or ISPUD, is again the desired knowledge of the largest failure volume. Since ISPUD also uses an approxiamte response surface description for importance sampling the results are expected to be quite similar. When one evalutes the probability of failure for a load level of $\lambda = 1.0$ as described above ISPUD provides $p_f = 0.16$. This is close to the estimate with an approximate response surface with the design points situated at plus and minus 2σ.

In order to demonstrate the performance of the approximate response surface described by the Box-Behnken design procedure, the probability of failure will be calculated via Monte Carlo simulation. In order to justify the quality of the obtained results also 'brute force' Monte Carlo simulation will be used.

From Fig. 10 it can be seen that the selection of the design points has quite a significant influence on the eventual probability of failure. The curve labeled 3σ suggests that the plus and minus levels of the design points are situated at respectively plus and minus three times the standard deviation. The curve labeled 2σ deviates due to the fact that the insecure selection of the design points enforces a large amount of samples to extrapolate the approximate response.

8 Correlation

From deterministic stability analysis it is known that the response of cylindrical shells including multiple geometric imperfection modes is quite different from that if each of the modes is taken individually. This nonlinear coupling in the mechanical model ensures the quite unpredictable behavior of the shells. In the context of reliability analysis the effect of coupling can be demonstrated in terms of the probability of failure variation, with the variation of the linear statistical dependence of the random variables incorporated in the reliability analysis. In Fig. 11 the effect of correlation of $\overline{\xi}_{\mathrm{ax}_1}$ and $\overline{\xi}_{\mathrm{a}3_3}$ indicated as ϱ_{13} on the global behavior of the shell is shown.

9 Conclusions

These preliminary result of the reliability evaluation with approximate response surfaces appear to be quite useful. The main variables that influence the analysis significantly are a combination of

- The quality of the response surface. Both the approximation function and the mechanical model used for the evaluation of the design points, are important.

- The effect of correlation. Identification of the principle contributor the the probability of failure is possible.

- Spurious design points. Design points that are automatically evaluated but do not have a meaning in the context of reliability evaluation. The effect of axisymmetric imperfection modes do introduce these typical 'ridges' in the response surface.

References

[1] J. Arbocz. The imperfection data bank, a mean to obtain realistic buckling loads. In E. Ramm, editor, Buckling of Shells A-Sate-of-the-Art Colloquium, pages 535–567, Berlin, 1982. Springer-Verlag.

[2] W.T. Koiter. The effect of axisymmetric imperfections on the buckling of cylindrical shells under axial compression. Koninklijke Academie van Wetenschappen, 1963.

[3] J. Arbocz. The effect of initial imperfections on shell stability — an updated review. LR 695, Faculty of Aerospace Engineering, Delft University of Technology, september 1992.

[4] J. Arbocz, M. Potier-Ferry, J. Singer, and V. Tvergaard. Lecture notes in physics; Buckling and Post-buckling, pages 83–142. Springer-Verlag, 1985.

[5] E. Riks and C.C. Rankin. A note on the computation of the imperfection sensitivity of the collapse load of elastic structures. M 698, Department of Aerospace Engineering, Delft University of Technology, october 1994.

[6] E. Riks. On formulations of pathfollowing techniques for structural stability analysis. LR 676, Department of Aerospace Engineering, Delft University of Technology, february 1992.

[7] G.E.P. Box. The exploration and exploitation of response surfaces: Some general considerations and examples. Biometrics, 10(1):16–60, 1954.

[8] G.E.P. Box and J.S. Hunter. Multi-factor experimental designs for exploring response surfaces. Ann. Math .Stat., 28(1):195–241, 1957.

[9] G.E.P. Box. Multi-factor desings of first order. Biometrica, 39:49–57, 1952.

[10] E.P. Fox. Methods of integrating probabilistic design within an organization's design system using box-behnken matrices. In AIAA/ASME/ASCE/AHS/ASC Structures, Structural Dynamics and Materials Conference, pages 714–723, 1993.

[11] E.P. Fox. The Pratt & Whitney probabilistic design system. In AIAA/ASME/ASCE/AHS/ASC Structures, Structural Dynamics and Materials Conference, pages 1075–1085, 1994.

[12] G.E.P. Box and D.W. Behnken. Some new three level designs for the study of quantitative variables. Technometrics, 2(4):455–475, 1960.

[13] G.I. Schuëller and R. Stix. A critical appraisal of methods to determine failure probabilities. Structural Safety, 4:293–309, 1987.

[14] U. Bourgund and C.G. Bucher. (ISPUD) Importance Sampling Procedure Using Design points. Universität Innsbruck, institut für Mechanik, november 1986. Innsbruck.

NONLINEAR RESPONSE OF THIN CYLINDRICAL SHELLS WITH LONGITUDINAL CRACKS AND SUBJECTED TO INTERNAL PRESSURE AND AXIAL COMPRESSION LOADS

James H. Starnes, Jr.* and Cheryl A. Rose†
NASA Langley Research Center
Hampton, Virginia 23681-0001

Abstract

The results of an analytical study of the nonlinear response of a thin unstiffened aluminum cylindrical shell with a longitudinal crack are presented. The shell is analyzed with a nonlinear shell analysis code that maintains the shell in a nonlinear equilibrium state while the crack is grown. The analysis accurately accounts for global and local structural response phenomena. Results are presented for internal pressure, axial compression, and combined internal pressure and axial compression loads. The effects of varying crack length on the nonlinear response of the shell subjected to internal pressure are described. The effects of varying crack length on the prebuckling, buckling and postbuckling responses of the shell subjected to axial compression, and subjected to combined internal pressure and axial compression are also described. The results indicate that the nonlinear interaction between the in-plane stress resultants and the out-of-plane displacements near a crack can significantly affect the structural response of the shell. The results also indicate that crack growth instabilities and shell buckling instabilities can both affect the response of the shell as the crack length is increased.

Introduction

Transport fuselage shell structures are designed to support combinations of internal pressure and mechanical flight loads which can cause the structure to have a geometrically nonlinear structural response. These shell structures are required to have adequate structural integrity so that they do not fail if cracks occur in service. The structural response of a shell structure with a local crack is influenced by the local stress and displacement gradients near the crack and by the internal load distribution in the shell. Local fuselage skin displacements near a crack can be large compared to the fuselage skin thickness, and these displacements can couple with the internal stress resultants in the shell to amplify the magnitudes of the local stresses and displacements near the crack. This nonlinear response must be understood and accurately predicted in order to determine the structural integrity and residual strength of a fuselage structure with damage. Recent studies (e.g., Refs. 1-4) have shown that the stiffness and internal load distributions in a shell will change as a crack grows in the shell, and these changes will affect the local stress and displacement gradients near the crack. These studies show that the structural response and structural integrity of a shell with a crack can be studied analytically by the use of a nonlinear structural analysis procedure that can model crack growth in the shell.

Typical nonlinear analysis results presented in Ref. 3 indicate that different combinations of applied loads can cause different responses for a stiffened shell with a long crack. The magnitudes of the stress-intensity factors associated with a long crack in a stiffened fuselage shell are affected significantly by different combinations of internal pressure and bending loads. The results in Ref. 3 indicate that the magnitude of the crack-opening stress-intensity factor for a shell subjected to internal pressure and an axial tension load is less than the magnitude of the corresponding stress-intensity factor for internal pressure only. The results also indicate that the magnitude of the crack-opening stress-intensity factor for a shell subjected to internal pressure and an axial compression load is greater than the magnitude of the corresponding stress-intensity factor for internal pressure only. The magnitude of this stress-intensity factor for an axial compression load and internal pressure is greater than the corresponding magnitudes of the other two loading conditions because the nonlinear coupling between the axial compression stresses and the out-of-plane displacements near the crack amplifies the magnitudes of the local stresses and displacements.

The magnitudes of the mechanical loads used in the studies described in Refs. 3 and 4 are representative of loads that do not buckle the skin of the fuselage. Fuselage shells are usually designed to allow the fuselage skin to buckle above a specified design load that is less than the design limit load for the shell. During the design of the fuselage, it is assumed that the design limit load can occur anytime during the service life of the aircraft. As a result, a long crack could exist in the fuselage shell after a considerable amount of flight service, and loading conditions could occur that cause the shell with the long crack to buckle. Most nonlinear response and residual strength analyses that have been conducted to date for fuselage shells with long cracks have been limited to an unbuckled fuselage shell response.

*Head, Structural Mechanics Branch. Fellow, AIAA.
†Aerospace Engineer, Structural Mechanics Branch. Member, AIAA.

The present paper describes the results of a nonlinear analytical study of the effects of internal pressure loading, axial compression loading and combined pressure and axial compression loading on the prebuckling, buckling and postbuckling responses of a typical thin, unstiffened aluminum cylindrical shell with a longitudinal crack. Predicted prebuckling and initial postbuckling deformation patterns and stress resultant distributions are presented for the different loading conditions and crack lengths. The effect of crack length on the initiation of stable tearing and unstable crack growth is discussed. The nonlinear analysis procedure used in the study is also described.

Shell Model and Analysis Procedure

Shell Model

The geometry of the shell analyzed in this study is described in figure 1a. The shell has a 9.0-inch radius, a 0.040-inch-thick wall, and is 36.0 inches long. A longitudinal crack is located at $\theta = 0^o$ and at the shell midlength. The initial crack length ranges from 1.0 to 4.0 inches. The shell is a typical laboratory-scale cylindrical shell and is made of 2024-T3 aluminum alloy. The Young's modulus, E, for the aluminum alloy is equal to 10 msi and Poisson's ratio is equal to 0.3. The yield stress for the material is 50 ksi and the ultimate stress is 72 ksi.

The loading conditions considered in the study include internal pressure, axial compression and combined internal pressure and axial compression. The maximum value of the applied internal pressure considered is 143 psi. This pressure is the pressure required to cause the shell with a 1.0-inch-long crack to fail due to internal pressure loading only. Internal pressure values equal to 25 psi and 50 psi are considered for the combined loading cases. The magnitudes of the axial compression loads are increased from zero to the maximum axial load that the shell can support with a longitudinal crack.

Nonlinear Analysis Procedure

The nonlinear response of the shells was studied numerically using the STAGS (STructural Analysis of General Shells) nonlinear shell analysis code.[5] STAGS is a finite element code for analyzing general shells and includes the effects of geometric and material nonlinearities in the analysis. The code uses both the modified and full Newton methods for its nonlinear solution algorithms, and accounts for large rotations in a shell by using a co-rotational algorithm at the element level. STAGS has static and transient analysis capabilities that can be used to predict local instabilities and modal interactions that occur due to destabilizing mechanical loads, such as an applied compression or shear load. The Riks pseudo arc-length path following method[6, 7] is used to continue a solution past the limit points of a nonlinear response.

STAGS can perform crack-propagation and residual-strength analyses, and can represent the effects of crack growth on nonlinear shell response. A node-release method and a load-relaxation technique are used to extend the length of a crack while the shell is in a nonlinear equilibrium state.[2] The forces necessary to hold the nodes together along the path of new crack growth are calculated with this method. These forces are relaxed as the crack is extended, and a new equilibrium state is calculated which corresponds to the longer crack. The changes in the stiffness matrix and the internal load distribution that occur during crack growth are accounted for in the analysis, and the nonlinear coupling between internal forces and in-plane and out-of-plane displacement gradients that occurs in a shell are properly represented. Results from STAGS calculations include strain-energy-release rates and stress-intensity factors [2, 8] that can be used to calculate the residual strength of a damaged shell. The crack-tip-opening-angle (CTOA) criterion[9] is used to determine when elastic-plastic stable-tearing crack growth will occur.

Both geometric and material nonlinearities are included in the analysis for the pressure only condition. The plasticity theory used to represent the material nonlinearities is the White-Besseling theory. The finite element model used in the analysis for this load case is shown in figure 1b. Symmetry conditions are applied along the edges $\theta = 0^o$ and $\theta = -180^o$ and along the edge $x = 18$ inches. Internal pressure is simulated by applying a uniform lateral pressure to the shell wall and an axial tensile force to the ends of the shell, with multi-point constraints to enforce uniform end displacement. Initial crack lengths of 1.0-4.0 inches are defined in the model. A high level of mesh refinement is required around the crack tip to predict accurately yielding at the crack tip, and crack extension. Crack extension occurs when the crack-tip opening angle is equal to 4.9^o.

The finite element model used for the axial compression and combined internal pressure and axial compression loading conditions is shown in figure 1c. The mesh is refined around the crack to represent the local stress and displacement gradients associated with the crack, and a slightly courser mesh is used for the rest of the shell to represent the deformation modes associated with the nonlinear response and buckling of the shell. For the combined load case, the axial compression and internal pressure loads are applied in STAGS using two independent load states. The internal pressure load is simulated in the same manner as for the pressure only case, and axial compression is applied to the ends of the shell by specifying an axial force, and a uniform end displacement.

The prebuckling response of the shells for these two loading conditions was determined using the nonlinear quasi-static analysis capability in STAGS. The initial, unstable, postbuckling response of the shells was predicted using the nonlinear transient analysis option of

the code. The transient analysis was initiated from an unstable equilibrium state just beyond the buckling point, by incrementing the end displacement. The transient analysis was continued until the kinetic energy in the system went to zero. A load relaxation analysis was conducted from the point of zero kinetic energy to establish a stable equilibrium state. The stable postbuckling response of the shells was computed using the standard nonlinear, static analysis option.

Results and Discussion

The results of an analytical study of the nonlinear response of a thin unstiffened aluminum cylindrical shell with a longitudinal crack are presented in this section. Results have been generated for three loading conditions that include: internal pressure only; axial compression only; and combined internal pressure and axial compression loads. Results have been generated for longitudinal cracks at shell mid-length with initial crack lengths of 1.0, 2.0, 3.0 and 4.0 inches. Typical results are presented to illustrate the effects of crack length on shell response for the applied loading conditions studied. The effects of varying crack length on the prebuckling, buckling and postbuckling responses of the shell are discussed.

Internal Pressure Loads

The effects of increasing the internal pressure in the shell on the total crack growth or crack extension is shown in figure 2a for shells with initial crack lengths of 1.0, 2.0, 3.0, and 4.0 inches. These results indicate that the internal pressure can be increased until yielding occurs in the material near the crack tips, and then stable tearing of the shell wall occurs that causes the total crack length to increase. Unstable crack growth or fracture of the shell wall occurs when the slope of the curve in figure 2a becomes zero, which means that a small increase in pressure causes a very large crack extension to occur. The results for an initial crack length of 1.0 inch indicate that stable tearing initiates when the internal pressure is approximately 113 psi and unstable crack growth occurs when the internal pressure is approximately 143 psi. The difference between the internal pressure required to initiate stable tearing and the internal pressure that causes unstable crack growth is approximately 30 psi for the 1.0-inch initial crack length. The results for an initial crack length of 2.0 inches indicate that stable tearing initiates when the internal pressure is approximately 51 psi and unstable crack growth occurs when the internal pressure is approximately 79 psi. The difference between the internal pressure required to initiate stable tearing and the internal pressure that causes unstable crack growth for this initial crack length is 28 psi. The difference between the internal pressure required to initiate stable tearing and the internal pressure that causes unstable crack growth for the 3.0- and 4.0-inch initial crack lengths is approximately 24 psi and 21 psi, respectively. These results indicate that the difference in internal pressure between the initiation of stable tearing and unstable crack growth decreases as the initial crack length increases. The effect of increasing the initial crack length on the internal pressure required to initiate stable tearing of the shell wall and to cause unstable crack growth is shown in figure 2b. The lower curve represents initiation of stable tearing and the upper curve represents unstable crack growth. These results indicate that the internal pressure required to initiate stable tearing and unstable crack growth decreases as the initial crack length increases.

Contour plots of the hoop stress resultants in the shell with the 3.0-inch initial crack length are shown on the corresponding deformed shapes of the shell in figure 3. Figure 3a shows the entire finite element model used in the analysis and defines the magnified region shown in figures 3b-d. Results are shown in figure 3b for an internal pressure of 21 psi which is less than the pressure required to initiate stable tearing. The results in figure 3c are for an internal pressure of 44 psi after some stable tearing has occurred. The results in figure 3d are for an internal pressure of 54 psi which causes unstable crack growth to occur. The darker and lighter regions in the figures correspond to higher and lower values of the hoop stress resultant, respectively. The increase in the size of the darker regions indicates the increase in the size of the local region with higher values of the hoop stress resultant. The axial and hoop stress resultants near the crack tip have high values, and these stress resultants increase in magnitude as the pressure increases until the material yields and stable tearing occurs. The modulus of the material is reduced as the material yields, and the effective stiffness of the shell is reduced locally in the plastic zone. The shell is stable until unstable crack growth occurs.

The results in figure 3 also indicate that large outward radial displacements occur in the neighborhood of the crack because of internal pressure. The response associated with these radial displacements is often referred to as "crack bulging" in the literature. The maximum values of the radial displacements near the crack increase as the initial crack length increases, when the magnitude of the internal pressure is slightly less than the internal pressure required to initiate stable crack growth. The values of this maximum radial displacement, w_{max}, normalized by the shell thickness, t, are $w_{max}/t = 0.46$, 1.58, 2.29 and 2.69 for the 1.0-, 2.0- 3.0- and 4.0-inch-long cracks, respectively. These displacements are greater than or equal to the shell thickness for crack lengths greater than or equal to 2.0 inches, and represent large displacements in the context of nonlinear thin shell theory.

Axial Compression Loads

A summary of the effects of axial compression

loads on the load-shortening results of shells with initial crack lengths of 1.0, 2.0, 3.0 and 4.0 inches is shown in figure 4a. The symbols in the figure represent the initial buckling loads for the shells with different crack lengths. The applied load, P, and the resulting end-shortening displacement, u, in figure 4a are normalized by the classical values for the buckling load P_{cr}, and the buckling end displacement u_{cr} for a shell without a crack. These results were obtained by increasing the axial compression load until the initial buckling load was determined using the nonlinear static analysis capability in STAGS. The effect of increasing the initial crack length on the initial buckling load of the shell is shown in figure 4b. The response of the shell is unstable for loads greater than or equal to the buckling load and, as a result, the axial load decreases after initial buckling occurs. The initial postbuckling response is determined by using the transient analysis capability in STAGS. The transient analysis is continued until the kinetic energy in the system is equal to zero. A time history of the change in the kinetic energy for a typical analysis is shown in figure 5. Once a stable equilibrium state is determined from the transient analysis, the nonlinear static analysis is resumed until another local buckling mode or the general or overall instability mode occurs. The results shown in figure 4a indicate that the magnitude of the initial buckling loads for the shell deceases as the initial crack length increases. The values of the normalized initial buckling loads are P/P_{cr} = 0.88, 0.59, 0.49 and 0.43 for the 1.0-, 2.0- 3.0- and 4.0-inch-long cracks, respectively. The axial compression loads for the stable postbuckling equilibrium states are much lower in value than the initial buckling loads.

The maximum values of the radial displacements near the crack increase as the initial crack length increases, for axial compression loads that are slightly less than the initial buckling load. The value of this maximum radial displacement, w_{max}, normalized by the shell thickness, t, is w_{max}/t = 0.2, 1.2, 2.1 and 3.0 for the 1.0-, 2.0- 3.0- and 4.0-inch-long cracks, respectively. These prebuckling displacements are greater than or equal to the shell thickness for crack lengths greater than or equal to 2.0 inches, and represent large displacements in the context of nonlinear thin shell theory.

The postbuckling deformation pattern for the cylinder with a 2.0-inch-long crack is shown in figure 6. The hoop and axial stress resultant distributions near the crack are shown on the right of the figure. The darker regions on the figures represent higher values of the stress resultants and the lighter colors represent lower values of the stress resultants. These results show that the crack has a relatively small, but noticeable, effect on the displacement pattern and the stress resultants. For the longer 3.0- and 4.0-inch-long cracks, the radial displacements near the crack are large relative to the shell thickness, and the initial buckling of the shell is a local buckling mode that is followed by a stable local postbuckling response before the shell buckles into its general instability mode. A typical example of the prebuckling radial displacement pattern for the 3.0-inch-long crack is shown in figure 7a. The hoop and axial stress resultant distributions near the crack are shown on the right of the figure. The darker regions on the figure represent higher values of the stress resultants and the lighter regions represent lower values of the stress resultants. These results indicate that the crack has a significant and noticeable effect on the prebuckling displacement pattern and stress resultants. The stable postbuckling deformation shape is shown in figure 7b. The hoop and axial stress resultants near the crack are shown on the right of the figure. The deformation pattern in figure 7b indicates that the shell deforms into a local pattern with high circumferential curvature that apparently stiffens the skin near the crack enough longitudinally to stabilize the shell and to increase the amount of axial compression load that can be supported by the shell after initial local buckling occurs.

The results of the analysis indicate that the stress-intensity factors associated with the crack are affected by the load level and the shell equilibrium state. Typical results for the 4.0-in.-long initial crack length indicate that the stress-intensity factors K_I and k_I, which correspond to in-plane crack-opening mode and the crack-bending mode, respectively, are small in value for axial compression loads up to approximately 75% of the initial buckling load. The stress-intensity factor K_I begins to increase from a negligibly small value for the axial compression load that corresponds to u/u_{cr} = 0.30 to a value of 21.0 ksi$\sqrt{in.}$ for an applied load that is slightly less than the initial buckling load. This stress-intensity factor then decreases to a value of 11.5 ksi$\sqrt{in.}$ at the initial buckling load that corresponds to u/u_{cr} = 0.44. This stress-intensity factor then increases up to a value of 30.5 ksi$\sqrt{in.}$ in the postbuckling load range for an applied load that corresponds to u/u_{cr} = 0.62. The stress-intensity factor k_I is very small up to initial buckling and then rapidly increases to a value of 105.4 ksi$\sqrt{in.}$ when initial buckling occurs. This stress-intensity factor further increases up to a value of 107.4 ksi$\sqrt{in.}$ in the postbuckling load range for an applied load that corresponds to u/u_{cr} = 0.62. These results suggest that a significant amount of local bending occurs near the crack tip at buckling and this local bending continues to increase in the postbuckling load range.

Combined Internal Pressure and Axial Compression Loads

A summary of the effects of combined internal pressure and axial compression loads on the buckling loads for shells with initial crack lengths of 1.0, 2.0, 3.0 and 4.0 inches is shown in figure 8 for 25 and 50 psi of internal pressure. These results indicate that the initial

buckling load of the shell increases as the internal pressure increases for a given crack length. The initial buckling load increases because of the tensile hoop stress resultants near the crack which tend to stabilize the shell. The results also indicate that the buckling load decreases as the crack length increases for a given pressure. The values of the normalized initial buckling loads are P/P_{cr} = 0.98, 0.75, 0.67 and 0.63 for the 1.0-, 2.0- 3.0- and 4.0-inch-long cracks, respectively, for 25 psi of internal pressure; and are P/P_{cr} = 1.12, 0.92, 0.83 and 0.77 for the 1.0-, 2.0- 3.0- and 4.0-inch-long cracks, respectively, for 50 psi of internal pressure.

The maximum values of the radial displacements near the crack for axial compression loads slightly less than the corresponding initial buckling load increase as the crack length increases. The value of this maximum radial displacement, w_{max}, normalized by the shell thickness, t, is w_{max}/t = 1.0, 2.7, 4.6, and 6.5 for the 1.0-, 2.0-, 3.0- and 4.0-inch-long cracks, respectively, for 25 psi of internal pressure; and is w_{max}/t = 1.3, 3.6, 5.8 and 7.9 for the 1.0-, 2.0- 3.0- and 4.0-inch-long cracks, respectively, for 50 psi of internal pressure. A typical example of the prebuckling radial displacement pattern for the 4.0-inch-long crack is shown in figure 9 for 50 psi of internal pressure. These results indicate that increasing the internal pressure changes the prebuckling-deformation results significantly compared to the results for axial compression with no internal pressure.

Concluding Remarks

The results of an analytical study of the effects of a longitudinal crack on the nonlinear response of a thin unstiffened aluminum cylindrical shell subjected to internal pressure, axial compression, and combined internal pressure and axial compression loads are presented. The results indicate that the nonlinear interaction between the in-plane stress resultants and the out-of-plane displacements near a crack in a thin shell can significantly affect the structural response of the shell. Large local stress and displacement gradients exist near a crack in the shell for all loading conditions considered in the study. The results indicate that the nonlinear response of the shell depends on the loading condition applied to the shell and the initial crack length. The magnitude of the internal pressure required to initiate stable tearing in a shell subjected to internal pressure decreases as the initial crack length increases. The magnitude of the internal pressure required to cause unstable crack growth in a shell also decreases as the initial crack length increases. The initial buckling load of a shell subjected to axial compression decreases as the initial crack length increases. Initial buckling causes general instability or collapse of the shell for shorter initial crack lengths. Initial buckling is a stable local response mode for longer initial crack lengths. This stable local buckling response is followed by a stable postbuckling response, which is followed by general or overall instability of the shell. The results for combined internal pressure and axial compression indicate that the initial buckling load of the shell increases as the magnitude of the internal pressure increases, but decreases as the initial crack length increases. Increasing the internal pressure tends to increase the initial buckling load of a shell with a crack, but it also increases the local stresses near the crack and decreases the crack length that initiates stable tearing and unstable crack growth in the shell.

References

[1]Riks, E., "Bulging Cracks in Pressurized Fuselages: A Numerical Study," NLR MP 87058 U, NLR National Aerospace Laboratory, The Netherlands, September 1987.

[2]Rankin, C. C., Brogan, F. A., and Riks, E., "Some Computational Tools for the Analysis of Through Cracks in Stiffened Fuselage Shells," Computational Mechanics, Springer International, Vol. 13, No. 3, December 1993, pp. 143-156.

[3]Starnes, James H., Jr., Britt, Vicki O., and Rankin, Charles C., "Nonlinear Response of Damaged Stiffened Shells Subjected to Combined Internal Pressure and Mechanical Loads," AIAA Paper 95-1462, April 1995.

[4]Starnes, James H., Jr.; Britt, Vicki O.; Rose, Cheryl A.; and Rankin, Charles, C.: "Nonlinear Response and Residual Strength of Damaged Stiffened Shells Subjected to Combined Loads," AIAA Paper No. 96-1555, April 1995.

[5]Brogan, F. A., Rankin, C. C., and Cabiness, H. D., "STAGS User Manual," Lockheed Palo Alto Research Laboratory, Report LMSC P032594, 1994.

[6]Riks, E., "Some Computational Aspects of the Stability Analysis of Nonlinear Structures," Computational Methods in Applied Mechanics and Engineering, Vol. 47, pp. 219-259, 1984.

[7]Riks, E., "Progress in Collapse Analysis," Journal of Pressure Vessel Technology, Vol. 109, 1987, pp. 27-41.

[8]Riks, E., Brogan, F. A., Rankin, C. C., "Bulging of Cracks in Pressurized Fuselages: A Procedure for Computation," in Analytical and Computational Models of Shells, Noor, A. K., Belytschko, T., and Simo, J. C., Editors, The American Society of Mechanical Engineers, ASME-CED Vol. 3, 1989.

[9]Newman, J. C., Jr., Dawicke, D. S., Sutton, M. A. and Bigelow, C. A., "A Fracture Criterion for Widespread Cracking in Thin-Sheet Aluminum Alloys," Proceedings of the ICAF 17th Symposium, 1993.

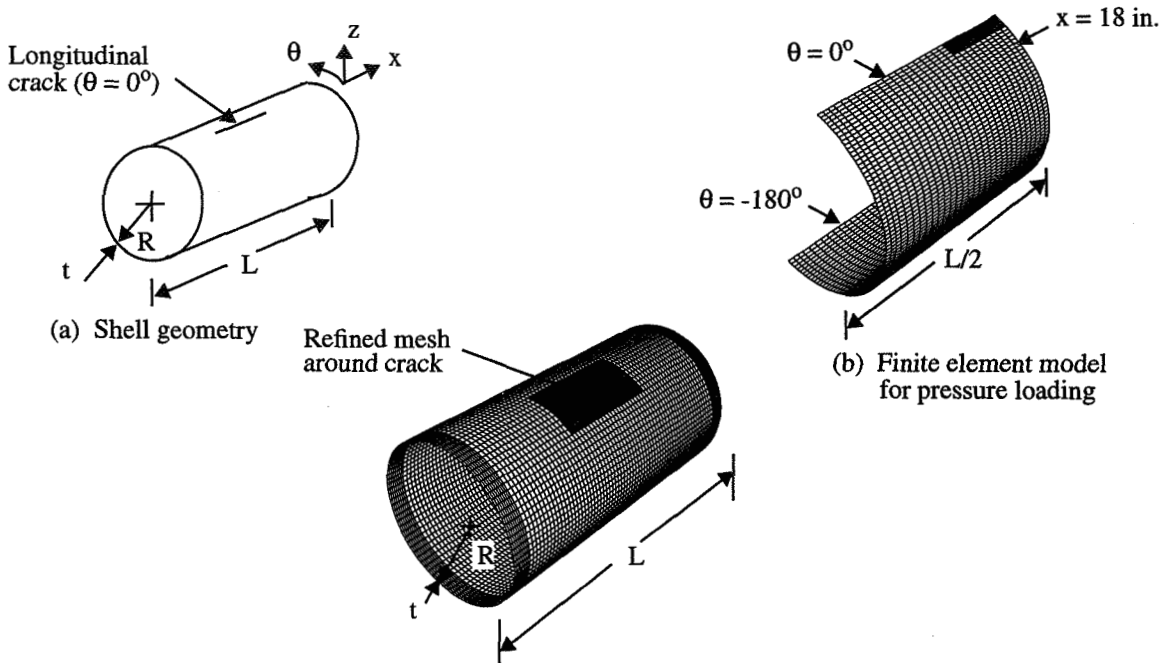

(a) Shell geometry

(b) Finite element model for pressure loading

(c) Finite element model for axial compression and combined loading

Figure 1. Shell geometry and finite element models.

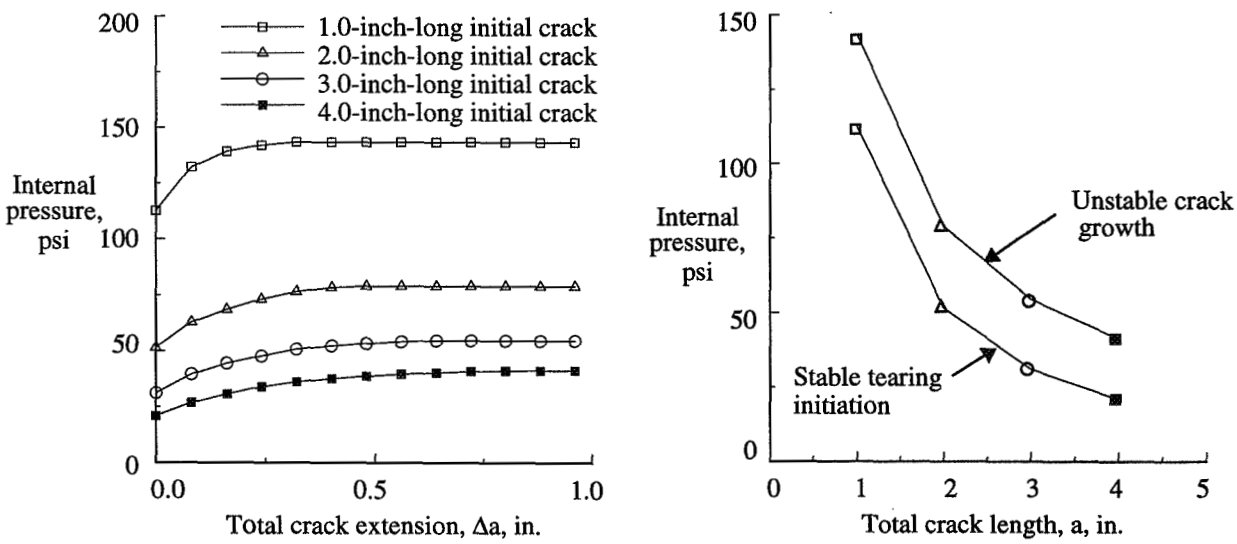

(a) Crack extension

(b) Initial stable tearing and unstable crack growth

Figure 2. Effect of increasing internal pressure on crack extension, initial stable tearing and unstable crack growth for different initial crack lengths.

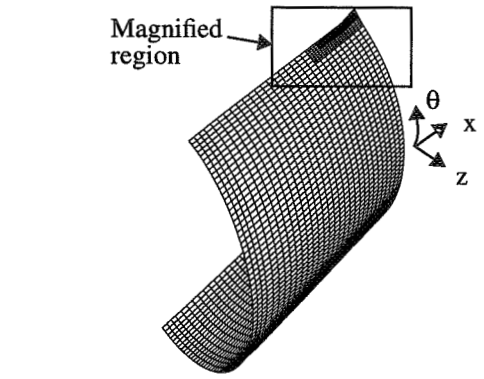

(a) Shell deformations, internal pressure = 44 psi

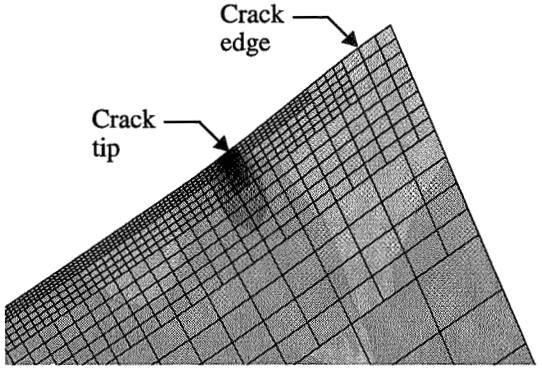

(b) No stable tearing, internal pressure = 21 psi

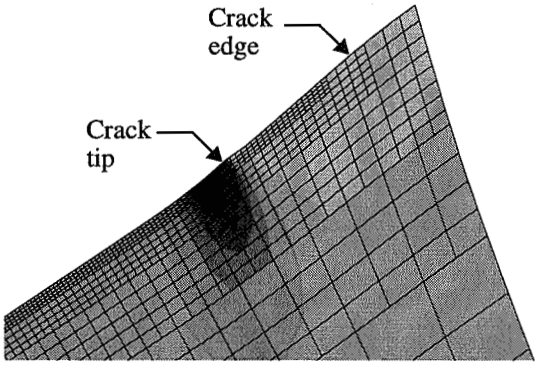

(c) Stable tearing, internal pressure = 44 psi

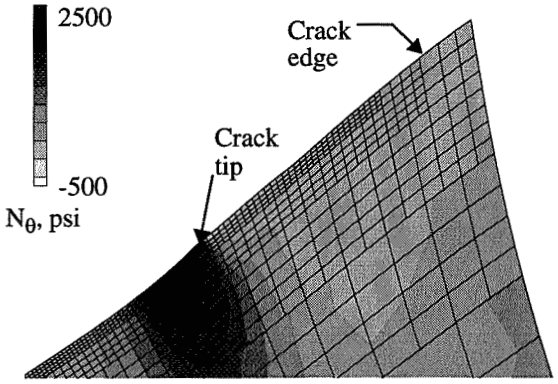

(d) Unstable tearing, internal pressure = 55 psi

Figure 3. Deformed shell and hoop stress resultants for a cylinder with 3.0-inch initial crack length and subjected to internal pressure.

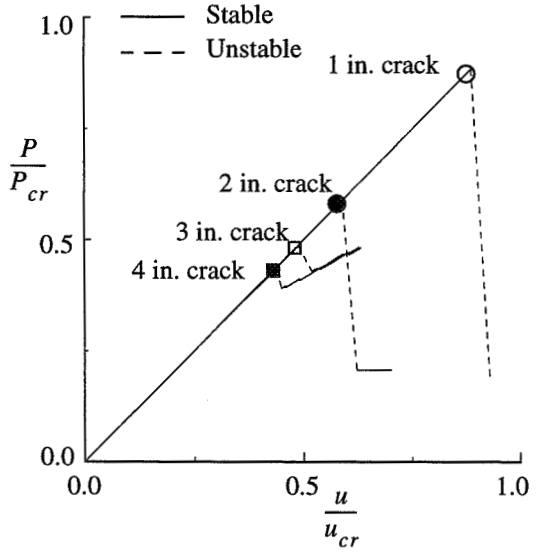

(a) Load-shortening response

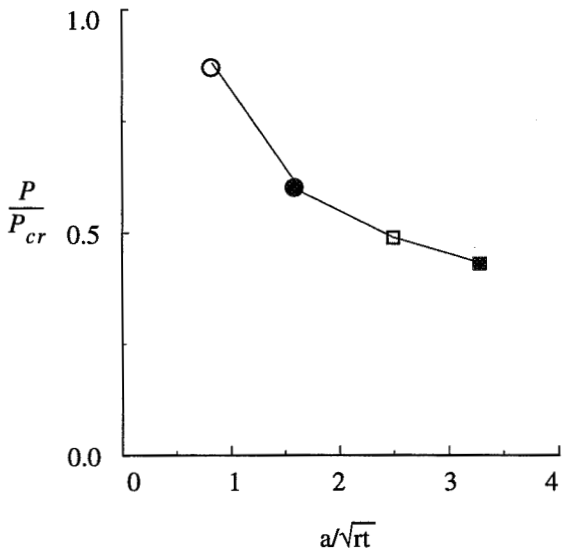

(b) Initial buckling load

Figure 4. Effect of initial crack length on the response of a shell subjected to axial compression.

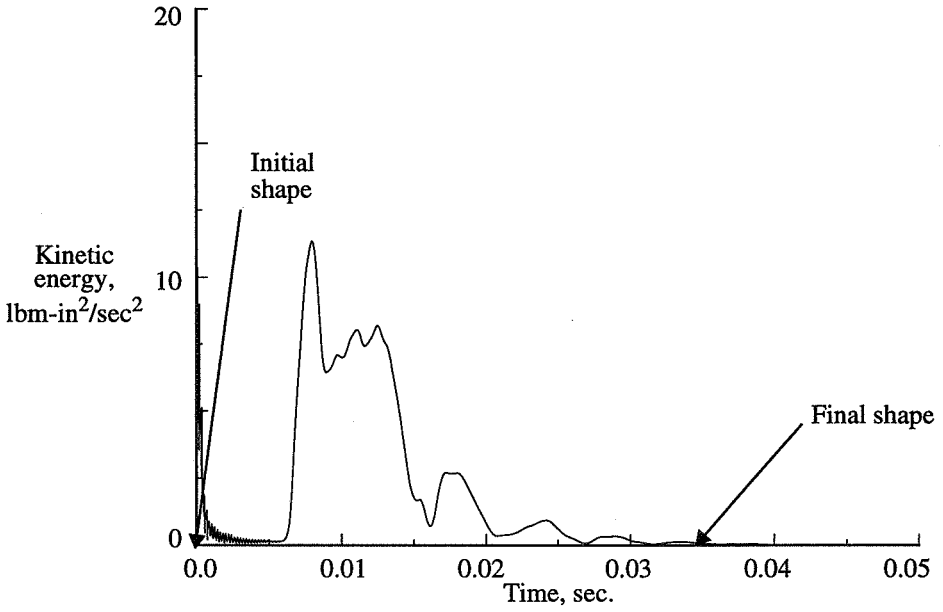

Figure 5. Kinetic energy time history for the unstable buckling reponse of a shell with a 3.0-inch-long crack and subjected to axial compression.

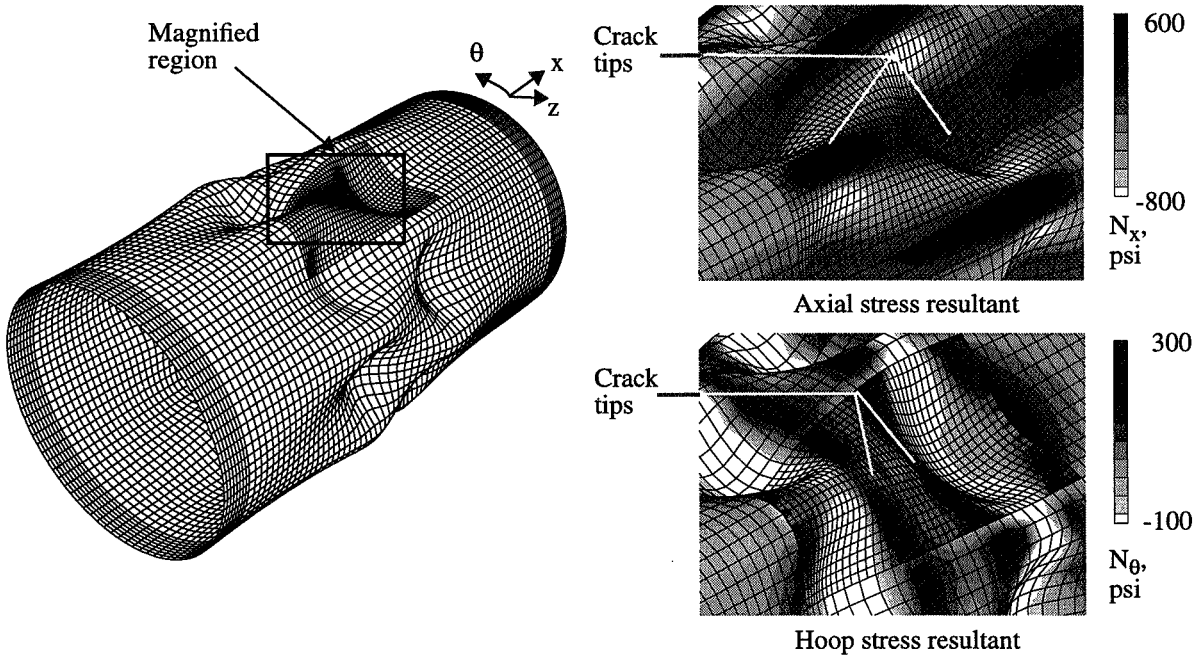

Figure 6. General instability deformation pattern for a shell with a 2.0-inch-long crack and subjected to axial compression.

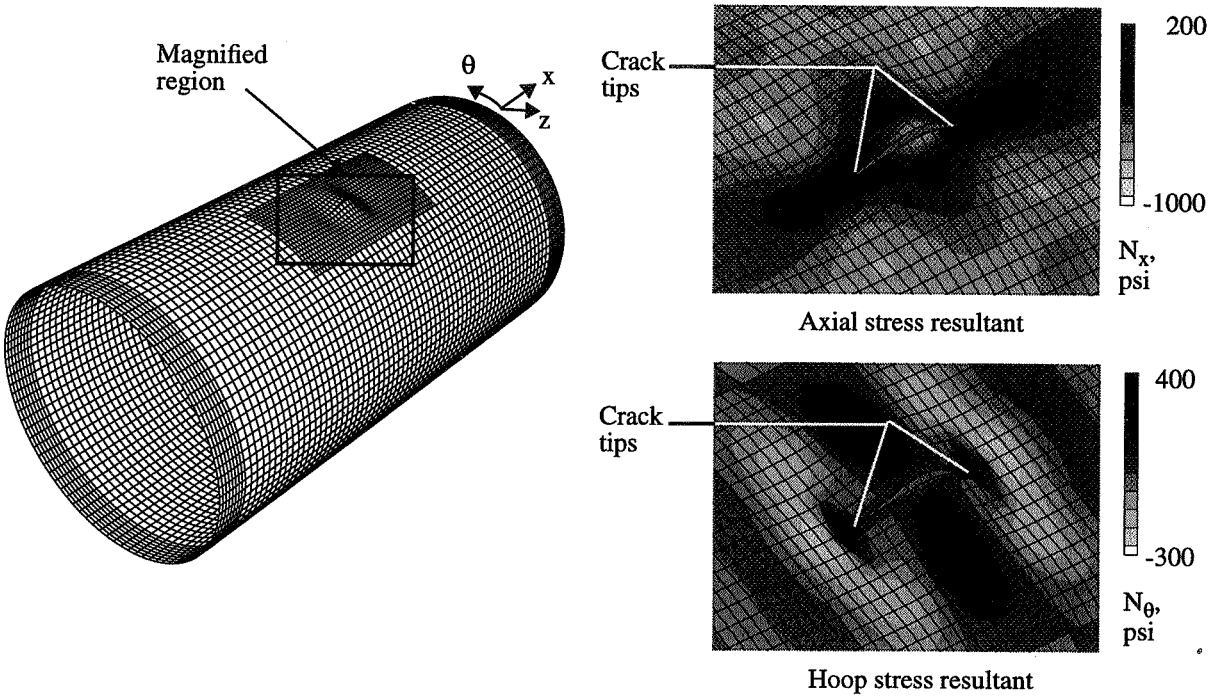

(a) Prebuckling deformation pattern just before initial buckling

Figure 7. Prebuckling and postbuckling deformation patterns for a shell with a 3.0-inch-long crack and subjected to axial compression.

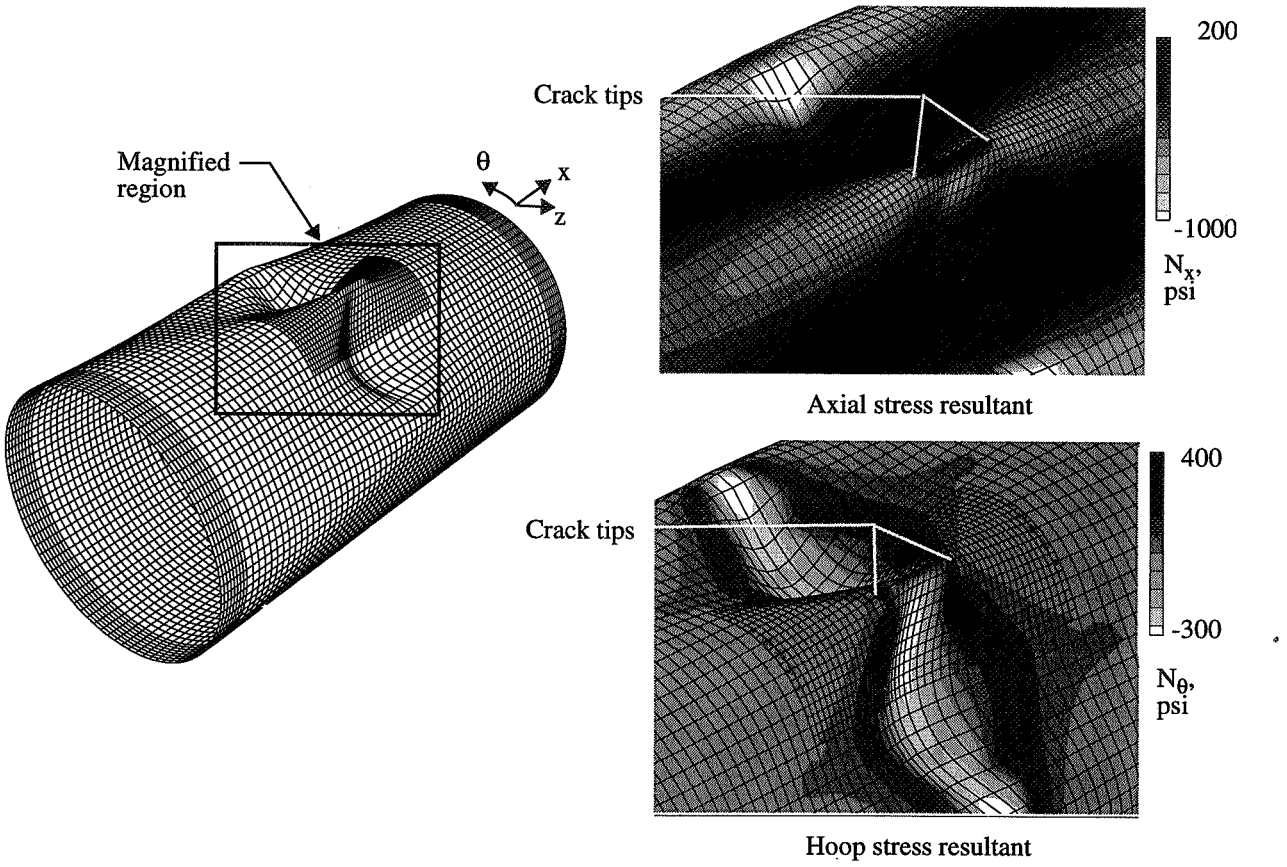

(b) Stable postbuckling deformation pattern

Figure 7. Concluded.

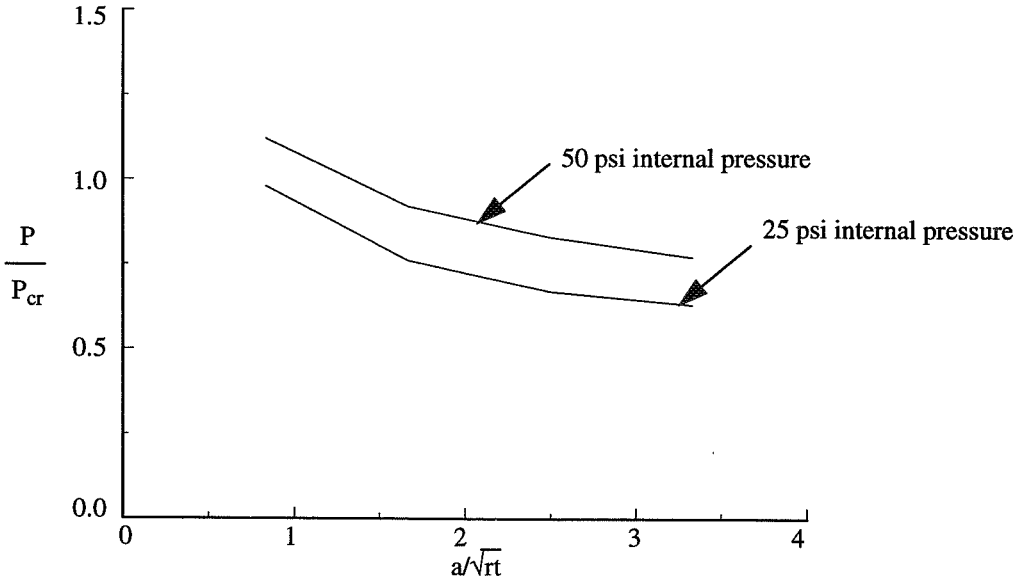

Figure 8. Effect of internal pressure on initial buckling load.

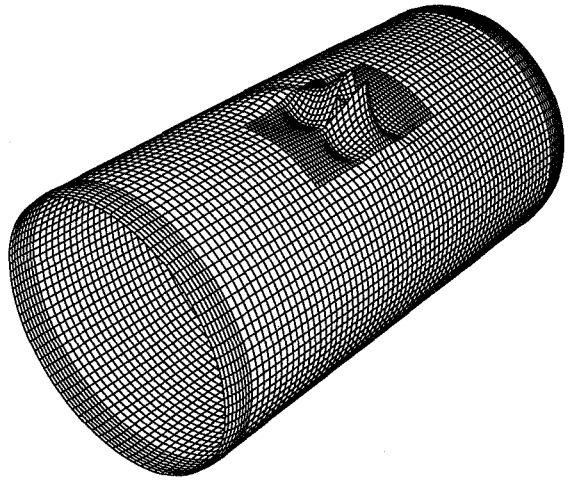

Figure 9. Prebuckling defornation pattern for a shell with a 4.0-inch-long crack and sujbected to axial compression and 50 psi internal pressure.

COMPOSITE SHELL STRUCTURES AND THEIR BEHAVIOR

Jack R. Vinson*
Mechanical Engineering
University of Delaware
Newark, DE 19716

ABSTRACT

The behavior of shell structures is discussed and illustrated by the consideration of a circular cylindrical shell subjected to axially symmetric loads, composed of specially orthotropic materials. The particular characteristics of shell behavior are discussed, including the fact that away from structural, material and load discontinuities shells behave as membranes. Only in well-defined areas close to structural, material and load discontinuities are bending stresses superimposed on the membrane stresses. For these bending boundary layers (BBL) stresses can exceed membrane values by factors of two or more.

Also presented are equations for the same shell in which the shell wall materials are mid plane asymmetric. In this case the governing equations differ from the mid-plane symmetric case. However a perturbation solution is presented which utilizes the solutions of the symmetric case, and the bending boundary layer for the asymmetric material shell is also defined.

INTRODUCTION

Shell structures involve very complicated, lengthy equations which are further lengthened when the shell is composed of an anisotropic material such as many fiber reinforced composite materials. Added to that is the fact that for many structures composed of composite materials in which the fibers are in the plane of the mid-surface, the effects of transverse shear deformation should be included, complicating and lengthening the equations compared to the classical theory.

However, for the simplest to the most involved form, the equations for shells involve certain characteristics which distinguish them from the equations and behavior of other structural components. In shells of any kind, the shell would like to deform in a membrane state of stress and deformation, wherein the deformation solutions are the particular solutions of the partial differential governing equations, usually easy to solve. In the case of membrane behavior, the stresses are uniform across the shell wall thickness, and usually found by a judicious use of free body diagrams.

However, close to any structural discontinuity, such as a simply supported, clamped or other restricted edge, adjacent to a hole, or an abrupt change in wall thickness or material, there exists a bending boundary layer (BBL). In this BBL, the stresses can exceed the membrane stresses by factors of two, three or more, due to the superposition of the bending stresses on the membrane stresses that exist throughout the shell. Obviously in the region of the BBL, the deformations are "wavy", and the curvatures are proportional to the bending stresses.

Thus, all of the complications, the maximum stresses, the areas of interest, and the sources of bad design all reside in the bending boundary layer region of composite shell structures and shells in general.

A. E. H. Love[1] wrote the first paper on shell theory in 1888, and as recently as January 1997, an interesting if not quite accurate quote says that for shells "all you need is LOVE". [2] Relatively little was done in advancing shell theory until the great emphasis in this area emanated from the needs of World War II, and shortly afterwards the advent of the missile and space ages. Many of this century's great researchers concentrated their efforts on shell structures during this period including Timoshenko[3], Reissner[4,5], Flügge[6,7], Goldenveizer[8], Vlasov[9], Naghdi[10], Hoff[11], Novozhilov[12], Kraus[13], Leissa[14], Dym[15], and the one we honor here, Manny Stein. In fact the golden era of shell theory was in the 1940's-1970's. More recently, nonlinear shell theory has been chromicled by Libai and Simmonds[16] and Palazotto and Dennis[17]. Most recently the increasing use of composite anisotropic materials and sandwich construction has resulted in continued sophisticated developments.

---

* H. Fletcher Brown Professor of Mechanical and Aerospace Engineering. Fellow, AIAA; Fellow, ASME; Member, ASC.

Certainly Manny Stein contributed significantly to this overall area of thin walled plate and shell structures as referenced in papers throughout this Conference.

In the limited space available, an attempt will be made to incorporate a few items of interest, which include "something old, something new...".

Equations are given for analyzing and designing circular cylindrical specially orthotropic shells subjected to axially symmetric static loads. The equations are very useful for treating an often met structure-load situation. They also clearly define the bending boundary layer discussed earlier. These equations may also be used to analyze the same shells composed of sandwich construction.

Next, the equations are generalized to handle the case of mid-plane asymmetry wherever bending-stretching coupling occurs through the B matrix terms. This coupling, often avoided, provides an opportunity to improve the structural behavior of shells, and may reduce the peel stresses and/or improve the shear stress distribution in adhesively bonded joints. By including the B matrix effect, the shell equations are dramatically altered.

Finally these mid plane asymmetric shell equations can be solved straightforwardly by using a perturbation technique.

This perturbation technique allows one to exploit all of the more conventional shell solutions, while RTM, SRIM and other advanced manufacturing techniques allow us to incorporate the B matrix effects into the manufacture of shell structures, either throughout the shell or at least in the bending boundary layer. The latter may reduce the overall maximum stress levels significantly. This is an area of current research by the author.

ANALYSIS

For the simplest case, consider a circular cylindrical shell of length L, radius to the middle of the shell wall R, and wall thickness h, as shown in Figure 1. Also, consider that Love's First Approximation holds:

$$h / R << 1 \qquad (1)$$

The equations of equilibrium in this case are well known:

$$\frac{\partial N_x}{\partial x} + \frac{1}{R}\frac{\partial N_{\theta x}}{\partial \theta} + q_x = 0 \qquad (2)$$

$$\frac{\partial N_{x\theta}}{\partial x} + \frac{1}{R}\frac{\partial N_\theta}{\partial \theta} + \frac{Q_\theta}{R} + q_\theta = 0 \qquad (3)$$

$$\frac{\partial Q_x}{\partial x} + \frac{1}{R}\frac{\partial Q_\theta}{\partial \theta} - \frac{1}{R}N_\theta + p(x,\theta) = 0 \qquad (4)$$

$$\frac{\partial M_x}{\partial x} + \frac{1}{R}\frac{\partial M_{x\theta}}{\partial \theta} - (Q_x - m_x) = 0 \qquad (5)$$

$$\frac{\partial M_{x\theta}}{\partial x} + \frac{1}{R}\frac{\partial M\theta}{\partial \theta} - (Q_\theta - m_\theta) = 0 \qquad (6)$$

where the N quantities are in-plane stress resultants, the Q quantities are transverse shear resultants the M quantities are stress couples, p (x,θ) is the radially distributed load per unit surface area, the q and m quantities are the surface shear stresses and the moments caused by the surface shear stresses.

For the simplest case of classical theory the admissible deflections are:

$$u(x,\theta,z) = u_o(x,\theta) + z\beta_x(x,\theta) \qquad (7)$$

$$v(x,\theta,z) = v_o(x,\theta) + z\beta_\theta(x,\theta) \qquad (8)$$

where u, v and w are displacements in the axial, circumferential, and radial directions respectively, u_o and v_o are mid-surface displacements, β_x and β_o are rotations, and ξ is the distance measured from the shell wall mid-surface. For the classical case of no transverse shear deformation, the relations between the rotations and displacement are prescribed to be

$$\beta_x + \frac{\partial w}{\partial x} = 0 \qquad (9)$$

$$\beta_\theta + \frac{1}{R}\frac{\partial w}{\partial \theta} - \frac{v_o}{R} = 0 \qquad (10)$$

If the shell is composed of composite materials, the constitutive equations can be written most succinctly as:

$$\begin{bmatrix} N_x \\ N_\theta \\ N_{x\theta} \\ M_x \\ M_\theta \\ M_{x\theta} \end{bmatrix} = \begin{bmatrix} A_{11}A_{12}2A_{16}B_{11}B_{12}2B_{16} \\ A_{12}A_{22}2A_{26}B_{12}B_{22}2B_{26} \\ A_{16}A_{26}2A_{66}B_{16}B_{26}2B_{66} \\ B_{11}B_{12}2B_{16}D_{11}D_{12}2D_{16} \\ B_{12}B_{22}2B_{26}D_{12}D_{22}2D_{26} \\ B_{16}B_{26}2B_{66}D_{16}D_{26}2D_{66} \end{bmatrix} \begin{bmatrix} \varepsilon_x^{\,o} \\ \varepsilon_\theta^{\,o} \\ \varepsilon_{x\theta}^{\,o} \\ \kappa_x \\ \kappa_\theta \\ \kappa_{x\theta} \end{bmatrix} \quad (11)$$

where the A_{ij}, B_{ij} and D_{ij} quantities are extensional stiffness, bending-stretching coupling stiffness, and flexural stiffness matrix quantities respectively. They are defined as follows:

$$A_{ij} = \sum_{k=1}^{N} (\overline{Q}_{ij})_k \left[h_k - h_{k-1}\right], [i,j = 1,2,6] \quad (12)$$

$$B_{ij} = \frac{1}{2}\sum_{k=1}^{N} (\overline{Q}_{ij})_k \left[h_k^2 - h_{k-1}^2\right], [i,j = 1,2,6] \quad (13)$$

$$D_{ij} = \frac{1}{3}\sum_{k=1}^{N} (\overline{Q}_{ij})_k \left[h_k^3 - h_{k-1}^3\right], [i,j = 1,2,6] \quad (14)$$

Equation (11) can be used whether the shell is a laminate, a homogeneous material, a sandwich, and whether the materials are isotropic or anisotropic.

AXIALLY SYMMETRIC CASE

Again, for the simplest case, consider that the applied load p(x) is axially symmetric, and that its fourth derivation with respect to x is zero, that the composite material is specially orthotropic and mid plane symmetric, i.e., ( )16 = ( )26 = Bij = 0, and that there are no surface shear stresses. In that case, the governing equations can be written as:

$$\frac{d^4w}{dx^4} + 4\varepsilon^4 w = \frac{1}{D_{11}}\left[p(x) - \frac{\upsilon_{\theta x}}{R} N_x\right], \quad (15)$$

$$\frac{d^2u_o}{dx^2} + \frac{\nu_{\theta x}}{R}\frac{dw}{dx} = 0 \quad (16)$$

where D_{11} is the flexural stiffness quantity in the axial direction, p(x) the axially symmetric distributed radial load, N_x the axial in plane load per unit circumference (a constant quantity determined by a free body diagram) and ε is found by the use of the following equation:

$$\varepsilon^4 = \frac{3(1-\nu_{x\theta}\nu_{\theta x})}{h^2R^2}\left(\frac{D_{22}}{D_{11}}\right) \quad (17)$$

It is seen that the lateral deflection can be obtained by solving (15), and that the in-plane axial deflection can be obtained subsequently. It is also seen that (15) is analogous to the equation for a beam on an elastic foundation. From (15) the lateral deflection is found to be

$$\begin{aligned} w(x) = {} & \frac{M_o}{2\varepsilon^2} D_{11}\, e^{-\varepsilon x}(Sin\ \varepsilon x - Cos\ \varepsilon x) \\ & - \frac{Q_o}{2\varepsilon^3 D_{11}} e^{-\varepsilon x} Cos\ \varepsilon x + \frac{M_L}{2\varepsilon^3 D_{11}} e^{-\varepsilon(L-x)} \\ & \left[Sin\varepsilon(L-x) - Cos\ \varepsilon(L-x)\right] + \\ & \frac{Q_L}{2\varepsilon^3 D_{11}} e^{-\varepsilon(L-X)} Cos\ \varepsilon(L-x) \\ & + \frac{1}{4\varepsilon^4 D_{11}}\left[p(x) - \frac{\nu_{\theta x} N_x}{R}\right] \end{aligned} \quad (18)$$

In (18) if $d^2p/dx^2 = 0$, then $M_O = M_X(0)$ and $M_L = M_X(L)$. Also in (17) if $d^3p/dx^3 = 0$, then $Q_O = Q_X(0)$ and $Q_L = Q_X(L)$. In those cases M_O and M_L are the edge moments and the Q_O and Q_L are the edge shear resultants. Otherwise, they are simply boundary value constants to be determined by solving the equations representing the boundary conditions.

BENDING BOUNDARY LAYER

The particular advantage of using the solution in the form of (18) is because one can take advantage of the unique behavior of shell structures. In (18) each term in the homogeneous solution contains trigonometric terms which oscillate between ± 1, multiplied by an exponential term with a negative exponent, i.e., an exponential decay. If one stipulates that when $e^{-\varepsilon X} \leq 0.006$ or $e^{-\varepsilon(L-X)} \leq 0.006$, that quantity is negligible, then each term in the homogeneous solution is negligible whenever

$$x > 4\sqrt{Rh(D_{11}/D_{22})^{1/2}}$$
$$(L-x) > 4\sqrt{Rh(D_{11}/D_{22})^{1/2}} \qquad (19)$$

The significance of (19) is that (18) reduces to only the last term, i.e., the particular solution, whenever one is seeking w(x) or any other dependent variable in locations specified by (19), i.e. outside the bending boundary layer. One can show that in general the particular solution is the membrane solution wherein there are no stress couples M_X or M_θ or transverse shear resultants, Q_X, i.e., the shell is in a state of membrane stress and deformation. For long shells that region can be significantly large.

It is only near the ends, i.e., near to structural discontinuities that the homogeneous part of the solution is significant, and in that case, bending stresses and shear stresses proportional to M_X and Q_X are important. Thus, this region is called the bending boundary layer (BBL) whose distance away from constrained ends is given by:

Bending Boundary

$$Layer\ Length = 4\sqrt{Rh(D_x/D_\theta)^{1/2}} \qquad (20)$$

The implications are most important including:

1. bending and shear stresses only exist in the BBL, otherwise the shell is in a state of membrane stress.

2. It can be shown that the BBL also exists around a load discontinuity be it a concentrated load, a ring load, stringer load, etc. Beyond the BBL the shell is in a state of membrane stress.

3. Outside of the BBL in a laminated shell wherein $d^2\ p/dx^2=0$. All interlaminar shear stresses are zero. Here, the implications are significant due to the expense and effort spent in NDE investigations over entire shell surfaces.

4. The length of the BBL is so small that even a "tuna fish can" is a long shell, i.e., L > (BBL).

5. In a shell structure composed of many segments, whenever a segment is longer than the BBL, then at x = 0, one can ignore the M_L and Q_L terms in (18), and at x=L one can ignore the M_O and Q_O terms in satisfying the boundary conditions at that edge. That is to say that for many shells the boundary conditions at each end are uncoupled from the boundary conditions at the other end, with great savings in an effort to obtain boundary value constants and overall solutions.

6. The (BBL) for an anisotropic shell is dependent upon the material properties. If the axial flexural stiffness D_{11} is greater than the circumferential flexural stiffness D_{22}, then the BBL is longer than for an isotropic material or a shell with a "hoop" wrap.

This behavior is almost unique to shells and does not exist in beams, plates or rings. Only in beams on an elastic foundation does this phenomenon exist.

DETERMINATION OF STRESSES

If the shell wall under consideration is made of one lamina or a unidirectional laminate the in-plane stresses are determined easily from

$$\sigma_i = \frac{N_i}{h} + \frac{M_i z}{h^3/12} \quad (i = x, \theta) \qquad (21)$$

which is the same form for plate and beam structures.

However for any other laminated shell, one must determine the in-plane stresses lamina by lamina and the stress values must be compared to the material strength allowable. In this case

$$\begin{bmatrix}\sigma_x\\ \sigma_\theta\end{bmatrix}_k=\begin{bmatrix}Q_{11}Q_{12}\\ Q_{12}Q_{22}\end{bmatrix}_k\begin{bmatrix}\varepsilon_x^0\\ \varepsilon_\theta^0\end{bmatrix}+z\begin{bmatrix}Q_{11}Q_{12}\\ Q_{12}Q_{22}\end{bmatrix}\begin{bmatrix}\kappa_x\\ 0\end{bmatrix}$$

$$where\ \varepsilon_x^o=\frac{duo}{dx},\varepsilon_\theta^o=w/R,\kappa_x=-d^2w/dx^2,$$

$$and\ Q_{11}=E_{11}/\left(1-\nu_{12}\nu_{21}\right),$$

$$Q_{22}=E_{22}\left(1-\nu_{12}\nu_{21}\right),\ and\ Q_{12}=\nu_{21}Q_{11}=\nu_{12}Q_{22}\ .$$

(22)

Finally the above equations can also be used to obtain the solutions from a shell composed of a sandwich construction , where for a symmetric sandwich the face thickness is t_f, the core depth is h_c. In sandwich construction of honeycomb and foam core, it is usually assumed all of the in-plane and bending loads are resisted by the faces alone. In that case the stresses are given by

$$\sigma_i=\frac{N_i}{2t_f}+\frac{M_i}{t_f h_c}\ (i=x,\theta) \qquad (23)$$

In the governing equations (15) and (18), D_{11} for the sandwich is

$$D_{11}=\tfrac{1}{2}E_{11}t_f h_c^{\,2} \qquad (24)$$

If the sandwich faces are laminates in which the stresses must be determined in each lamina, then the use of (14) can be made wherein one assigns a k number to each face lamina and also the core itself in a straightforward manner.

SHELLS WITH MID PLANE ASYMMETRY

With composite material laminates the stacking sequences can be selected for the stiffness matrix of (11) to be asymmetric with respect to the shell wall midsurface. In that case the $B_{ij} \neq 0$. Moreover with resin transfer molding (RTM), SRIM and other new manufacturing techniques it is easy to introduce preforms which are asymmetric if there is an advantage in doing so. In such cases if the A, B and D matrix quantities are constant, the governing equations for the lateral deflection w(x) is found to be:

$$\left[\frac{A_{11}D_{11}-B_{11}^{\,2}}{A_{11}}\right]\frac{d^4w}{dx^4}+\frac{2A_{12}B_{11}}{A_{11}R}\frac{d^2w}{dx^2}+\frac{1}{R^2}\left[\frac{A_{11}A_{22}-A_{12}^{\,2}}{A_{11}}\right]w=p(x)-\frac{A_{12}}{A_{11}}\frac{N_x}{R} \qquad (25)$$

It is seen that the coefficient of the first term is the well known reduced flexural stiffness, D_θ, often used in analyzing asymmetric beams. To simplify (25) define

$$D_e=\frac{A_{11}D_{11}-B_{11}^{\,2}}{A_{11}},\ \bar{p}(x)=p(x)-\frac{A_{12}}{A_{11}}\frac{N_x}{R} \qquad (26)$$

$$4\varepsilon^4=\frac{1}{D_e R^2}\left[\frac{A_{11}A_{22}-A_{12}^{\,2}}{A_{11}}\right] \qquad (27)$$

Using these, (25) becomes

$$\frac{d^4w}{dx^4}+\frac{2}{Rh}\left(\frac{A_{12}}{A_{11}}\right)\frac{B_{11}h}{D_e}\frac{d^2w}{dx^2}+4\varepsilon^4 w=\frac{1}{D_e}\bar{p}(x). \qquad (28)$$

where the numerator and denominator of the second term have been multiplied by the shell wall thickness h.

The second term appears only because of the asymmetry resulting in a non-zero B matrix term B_{11}. Were the shell symmetric it would have the same form as (15).

Consider the coefficient of the second term to be small, i.e., less than unity, such that a small parameter α can be defined as:

$$\alpha=\frac{2A_{12}}{A_{11}}\frac{B_{11}\,h}{D_e} \qquad (29)$$

As an illustration, even in a construction in which two laminae of the same thickness are bonded together, one of aluminum and one of steel, even then $\alpha<1$.

Equation (27) is now written as:

$$\frac{d^4w}{dx^4}+\frac{2\alpha}{Rh}\frac{d^2w}{dx^2}+4\varepsilon^4 w=\frac{1}{De}\bar{p}(x) \quad (30)$$

Consider the following form of solution:

$$w(x)=\sum_{n=0}^{\infty} w_n(x)\alpha^n \quad (31)$$

Upon substituting this into (29), and collecting like powers of the perturbation parameter α, it is seen that

$$\frac{d^4w_o}{dx^4}+4\varepsilon^4 w_o=\frac{1}{D_e}\bar{p}(x) \quad (32)$$

$$\frac{d^4w_n}{dx^4}+4\varepsilon^4 w_n=\frac{-2}{Rh}\frac{d^2w_{n-1}}{dx^2},\ n\geq 1 \quad (33)$$

Thus, a perturbation solution of the asymmetric shell can be made in terms of known solutions of the simpler mid plane symmetric shell. It is also seen that a bending boundary layer exists, analogous to that for the mid-plane symmetric shell, obtainable from (20).

It can be shown that for $\alpha<1$, (31) is another form of the exact solution for (30) and (25).

CONCLUSIONS

Solutions for the circular cylindrical shell made of specially orthotropic materials, including laminates and sandwich construction, subjected to axially symmetric states loads have been presented. In the case of mid-plane symmetry, the solutions show that the shell behaves as a membrane except in regions close to any structural, material or load discontinuity wherein those regions there exists a bending boundary layer wherein bending stresses are superimposed upon the membrane stresses, and the sum of the stresses may exceed the membrane stress values by factors of two to thrree or more.

The governing equation for the lateral deflection of the same shell having mid-plane asymmetry is also presented. This equation is different in form from the symmetric shell. It is also shown that in the asymmetric case, the bending boundary layer qualities of the shell behavior remain.

REFERENCES

1. Love, A. E. H., "The Small Free Vibrations and Deformation of a Thin Elastic Shell", Philosophical Transactions of the Royal Society of London, Vol. 17, pp. 491-546, 1888.

2. Epstein, Marcello, verbal presentation at the Pan American Conference on Applied Mechanics - V, San Juan, Puerto Rico, January 2-4, 1997.

3. Timoshenko, S. and Woinowsky-Krieger, S., Theory of Plates and Shells, Mcgraw Hill Publishing Company, numerous editions.

4. Reissner, E., "A New Derivation of the Equations for the Deformation of Elastic Shells", American Journal of Mathematica, 63, pp. 177-184, 1941.

5. Reissner, E., "On the Theory of Thin Elastic Shells", H. Reissner Anniversary Colume, J.W. Edwards, Ann Arbor, 1949, pp. 231-247.

6. Flügge, W., "Statik und Dynamik der Schalen", Edwards Brothers, Inc., AnnArbor, 1943.

7. Flügge, W., "Stresses in Shells", Springer-Verlag, Berlin, 1962 (2nd Ed.).

8. Goldenveizer, A.L., "Theory of Thin Shells", Pergamon Press, New York, 1961.

9. Vlasov, V.S., "Basic Differential Equations in General Theory of Elastic Shells", NASA.TM 1241, 1951.

10. Naghdi, P. M., "A survey of Recent Progress on the Theory of Elastic Shells", Applied Mechanics Review, Vol. 9, No. 9, 365-368, September 1956.

11. Hoff, N. J., "Buckling of a Thin Cylindrical Shell Under Hoop Stresses Varying in the Axial Direction", Journal of Applied Mechanics, Vol. 24, pp. 405-412, 1957.

12. Novozhilov, V.V., "Theory of Thin Shells", E.P. Noordhoff, Ltd., Groningen, The Netherlands, 1959.

13. Kraus, H., "Thin Elastic Shells", John Wiley & Sons, Inc., New York, 1967.

14. Leissa, A.W., "Vibrations of Shells", NASA SP-288, U.S. Government Printing Office, 1973.

15. Dym, C.L., "Introduction to the Theory of Shells", Pergamon Press, Glasgow, 1974.

16. Libai, A. and J.G. Simmonds, "The Nonlinear Theory of Elastic Shells", Academic Press, 1988.

17. Palazotto, A.N. and S.T. Dennis, "Analysis of Nonlinear Shell Structures", American Institute of Aeronautics and Astronautics, 1991.

18. Vinson, J. R., "The Behavior of Shells Composed of Isotropic and Composite Materials", Kluwer Academic Publishers, Dordrecht, 1993.

19. Vinson, J.R., and Sierakowski, R. L., "The Behavior of Structures Composed of Composite Materials", Martinus Nijhoff Publishers (Now Kluwer Academic Publishers), Dordrecht, 1987.

DESIGN OF PANELS HAVING POSTBUCKLING STRENGTH

M. S. Anderson*
Eagle Aeronautics, Newport News ,VA

Abstract

The VICONOPT computer program for analysis and design of prismatic plate assemblies based on initial buckling has been modified to allow buckling to occur at loads less than the design load while having residual strength based on an approximate estimate of the overall buckling load assuming reduced stiffnesses of the buckled plate elements. A nonlinear analysis by the finite element code STAGS of a panel designed in this manner is in reasonable agreement with the simplified approximate analysis. The paper gives the results of a design study comparing the mass of panels designed to buckle at different load levels less than the design load for both aluminum and composite construction.

Introduction

The VICONOPT computer code[1] is capable of optimum design of panels that are formed from a prismatic assembly of flat plates. The analysis used guarantees that buckling will not occur at loads less than the design value. A simple extension to the code has been made that allows panel designs with initial buckling loads at some prescribed fraction of the design load with a choice of the plate elements that will initiate buckling. (For example the skin of a stringer stiffened panel.) In this paper, the basis of the method is described, the accuracy of the design load calculation is assessed by a nonlinear analysis of a particular final design, and the characteristics of panels designed at different buckling loads relative to the design load are presented.

In reviewing the research accomplished by Manuel Stein over his long career, it centered on the different theoretical components that make the VICONOPT computer code possible. Thirty four papers on buckling alone and eighteen papers on postbuckling were found. The list includes five papers on the fundamental theory required for buckling analysis with emphasis on transverse shear deformation and four papers on the implication of buckling analysis on design. The transverse shear deformation theory used in VICONOPT[2]. is essentially that of Stein[3]. In addition Manny worked with the Lockheed group in monitoring contractual efforts on buckling and postbuckling analysis contained in the BOSOR and STAGS computer codes.. He also made significant contributions to the Boeing group in developing exact buckling analysis capability for plate assemblies that is closely related to the fundamental analysis contained in VICONOPT.

*Research Engineer, Associate Fellow AIAA

Basis of the Method

The analysis in VICONOPT is based on exact stiffness matrices for each plate element that is undergoing a sinusoidal deformation in the length direction of the panel. The plate stiffness matrix is a transendental function of the inplane loading and the axial wavelength of the deformation. The analysis is performed over a range of axial half-wavelengths that usually cover the range from a value less than the width of the smallest plate to a value equal to the length of the panel. The lowest load found is the critical buckling load for the panel. This discrete sinusoidal wavelength solution which is the VIPASA option in the program is exact for orthotropic panels without shear loading. For anisotropic panels or any with shear loads, this procedure results in skewed nodal lines so that results are valid only for long panels relative to the critical wavelength. Finite length panels can be treated by the VICON option where several wavelengths are combined that satisfy desired constraints such as zero deflection at panel ends. For optimization, any plate width or layer thickness can be a design variable and will be changed by the program to minimize the mass while carrying the design load. For panels designed to have post-buckling strength, two modifications have been made to the basic method. First, for local buckling (considered to be all half-wavelengths less than the panel length), the inplane loads in any plate designated by the user to initiate buckling is reduced by the fraction of the desired buckling load to the design load. when calculating the stiffness matrix for that plate. Second, for general or overall buckling (considered to be the half-wavelength equal the panel length), the inplane stiffnesses of any plate designated by the user to initiate buckling is reduced by a fraction that is input by the user. This fraction as determined by analysis in the literature for single plates is of the order of .5 for metal plates. An innovative method of determining the reduced stiffness was developed by Dr. Stein in his doctoral dissertation and applied in a study[4] of changes in buckle patterns in the postbuckling range .

The longitudinal loads in each plate are determined in VICONOPT as the sum of a linear portion N_l and for local buckling, a nonlinear portion

N_p due to pressure loads or imperfections. The linear portion is obtained by a simple stress analysis considering the entire panel cross-section as a beam subject to an axial load and end bending moments . This analysis is done twice, once with the full properties of all the plates and once for the reduced properties in the plates chosen to initiate buckling. The linear portion of the longitudinal load in each plate at the design loading is then taken as

$$N_l = r_l N_{le} + (1 - r_l) N_{lb} \qquad (1)$$

where r_l is the fraction of the design load at which buckling is to occur. The additional subscript e indicates the result of the analysis with full stiffnesses and the additional subscript b indicates the result of the analysis using reduced stiffnesses for the buckled plates. Equation (1) is correct for axial loads only but is only approximate if bending is present.

The nonlinear portion of the longitudinal loading is determined from the beam-column formula. Two values are again calculated, N_{pe} based on full properties for all plates and N_{pb} based on reduced properties of the buckled plates. A summary of the various conditions and the expression used for the axial loading N is as follows.

Local buckling, buckled plate

$$N = r_l N_{le} + r_l N_{pe} \qquad (2)$$

Local buckling, nonbuckling plates

$$N = r_l N_{le} + (1 - r_l) N_{lb} + N_{pb} \qquad (3)$$

General buckling, all plates

$$N = N_l = r_l N_{le} + (1 - r_l) N_{lb} \qquad (4)$$

Equation (3) is the best estimate of the plate loading at the design load and therefore is used in any material strength design requirement. Equation (2) is the correct loading in the buckled plates at the load level buckling is specified to occur. However, plates not designated to buckle must sustain the full loading given by equation (3) which gives higher loadings than a complete elastic analysis. Because these loadings are higher than that which occurs at the load level that initiates buckling, the actual buckling load would be somewhat higher than that specified by the user. Since this is a secondary effect associated with the edge restraint between the buckled plates and the unbuckled plates, this difference is usually small. Finally it is assumed that the general overall mode with loadings given by equation(4) is a column mode that is not affected by bending moments so no nonlinear terms are added for this case. There is also an option to use the general buckling load in the beam column formula rather than the column load calculated from the moment of inertia of the cross-section when calculating N_{pe} and N_{pb} used in equations (2) and (3).

The above changes to the code result in essentially no change in the time required to do a given optimization problem so no penalty is incurred for designing panels having postbuckling strength.

Evaluation of the Method

In the early stages of the development of the method, a zee-stiffened panel was designed to buckle at two thirds of the design load with the skin initiating the buckling. The dimensions of the panel, the design loading and material properties used are shown in figure 1. The design was based on a panel length of 30 inches with simply supported ends and classical plate theory was used in all theoretical calculations. The plate elements forming the skin were the only ones chosen to initiate buckling at two thirds of the design load. It was assumed that the inplane stiffness of the skin after buckling was .5 of its initial value. At this time, the stress analysis was based on the full properties of all the plate elements as equations (2-4) were not yet implemented in the code. The resulting design was analyzed in the postbuckling range with the STAGS[5] nonlinear code. Prescribing boundary conditions that allow the ends to remain moment free during the nonlinear STAGS analysis is very difficult if not impossible. Therefore the panel was assumed to be twice as long and boundary conditions of uniform end displacement with no rotation of individual plates was imposed for this and all subsequent STAGS analysis. The collapse load was found to be about 90% of the design load. Examination of the deformation pattern showed that after initial buckling, the overall panel mode began to develop with appreciable deflection. This deformation pattern caused additional bending from the beam column effect of the axial load which caused premature collapse in the area of the stiffeners. A new design was made where an initial imperfection was introduced as a design requirement. This results in additional bending moments that the panel must sustain similar to those found in the STAGS analysis. The load shortening curve for this panel as determined with STAGS is shown in figure 2. Two cases are shown: one for an initially perfect panel and one for a panel with an imperfection the shape of the clamped column buckling mode. The amplitude was twice that used for the design with simply supported ends. This results in the same imperfection for the middle 30 inch length as was used in the design. The limit load for this latter case is 9% higher than the design load which indicated the proposed method had potential as being a reasonable approximation The analysis of this panel by the current version of the program where equations(2)-

(4) have been implemented shows the critical load to be 102% of the design load.

Effect of Initial Buckling Load and Post-buckling Stiffness on Panel Mass

A parametric study was made of the effect on panel mass of varying the initial buckling load and post buckling stiffness for the configuration and design conditions shown in figure 1. The results for the aluminum design are shown in figure 3 where panel mass is shown as a function of the initial buckling load as given by r_l and the postbuckling stiffness as given by r_s (ratio of inplane stiffnesses after buckling to their original value)..No minimum gage requirement was imposed and the thickness variables were allowed to be continuous. The value $r_l = 1$ corresponds to a panel that buckles at the design load and its mass is not a function of r_s. For values of r_l less than one, the mass continues to be fairly insensitive to r_s especially at the higher values of r_l. This indicates that a conservative assumption could be made on r_l without too great a mass penalty and there would be greater confidence that the panel capability would equal or exceed the design load. The results also show that significant mass savings can be obtained by allowing the panel to buckle at low loads which has been a result of several investigators working on this problem. A similar study was done on a composite panel with the design variables and material properties shown in figure 1. The results of this study are shown in figure 4. No requirement on minimum ply thickness was imposed. Also there was no requirement that there be an integer number of plies of a given thickness. The mass of the composite panel is about 60% of the mass of the aluminum panel for all initial buckling conditions.

It was found that for panels designed to buckle at low loads relative to the design load, little or no margin existed for the overall buckling mode. Such a situation can make a panel very sensitive to imperfections because of the beam column effect. A study was made where the column buckling load used in the beam column formula was the actual overall buckling load. This forces the overall buckling load to be higher than the design load since the bending moment approaches infinity as the column buckling load is approached. This increased requirement increased the mass of the designs modestly. The results for a stiffness factor of .5 are shown in figure 5 where mass is plotted against the buckling load level for the composite panel using the two different assumptions on the beam column formula. A complete nonlinear analysis of designs from the two methods would be required to judge the adequacy of either approach.

Concluding Remarks

A method of designing panels having prescribed postbuckling strength has been developed. The method is based on a modification of the design code VICONOPT that allows certain user selected component plates of a panel structure to buckle at some fraction of the design load and then have reduced stiffness for the overall panel buckling mode. The modifications to the code to accomplish this result have little impact on computer time so designs can be made rapidly with all the efficiency of the original VICONOPT program. Using the STAGS computer code for nonlinear response to analyze a panel designed to buckle at two thirds the ultimate load showed reasonable agreement with the simplifying assumptions of the analysis. A study of the effect of allowing buckling to occur at less than the ultimate load showed that mass savings of over one third are possible over a nonbuckling design for both metal and composite panels. Further work is required to evaluate the method for shear loaded panels or any other design condition requiring the use of the VICON analysis capability of the program.

References

1. Williams, F. W., Kennedy, D., and Anderson, M. S., "VICONOPT: Program for exact vibration and buckling analysis or design of prismatic plate assemblies," AIAA Journal, Vol. 29, no. 11, 1991, pp. 1927-1928.

2. Stein, Manuel, and Mayers, J.: "A small-deflection theory for curved sandwich plates," NACA TN 2017, February, 1950.

3. Anderson, M. S. and Kennedy, D.: "Inclusion of transverse shear deformation in the exact buckling and vibration analysis of composite plate assemblies," NASA CR 4510, May 1993.

4. Stein, Manuel: "The phenomenon of change in buckle pattern in elastic structures," NASA TR R-39, 1959.

5. Brogan, F. A., Rankin, C. C., and Cabiness, H. D.: "STAGS users manual," Lockheed Palo Alto Research Laboratory, Report LMSC P032594, 1994.

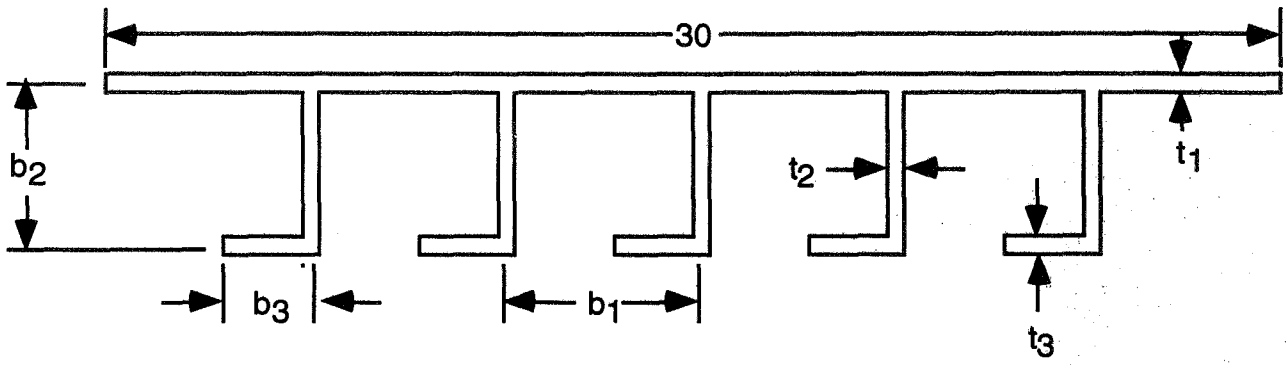

Design Conditions:

Simply Supported ends and Lateral Edges	
Axial Load	45000 lbs
Amplitude of Sinusoidal Imperfection	.03 in
Plates forming skin with dimension b_1 designated to initiate buckling	

Dimensions:

Length	30 in
b_1	5 in

Design Variables

Aluminum design:	b_2, b_3, t_1, $t_2 = t_3$
Graphite Epoxy Design:	b_2, b_3, and all five ply thicknesses

Wall Lay-up for Graphite Epoxy

t_1	45,-45,0/S	(Two independent ply thicknesses)
t_2	45,-45/S	(One independent ply thickness)
t_3	45,-45.0/S	(Two independent ply thicknesses)

Material Properties:

Isotropic Aluminum

E=10.5 x 10^6 psi Poisonn's Ratio = .32 Density =.1 lb/in^3

Graphite Epoxy

E_{11}=21.5 x 10^6 psi, E_{22}=1.35 x 10^6 psi, E_{12}=.75 x 10^6 psi

Major Poisson's Ratio = .3026, Density =.057 lb/in^3

Classical Plate Theory used in all theoretical calculations.

Figure 1. Stiffened panel and design conditions.

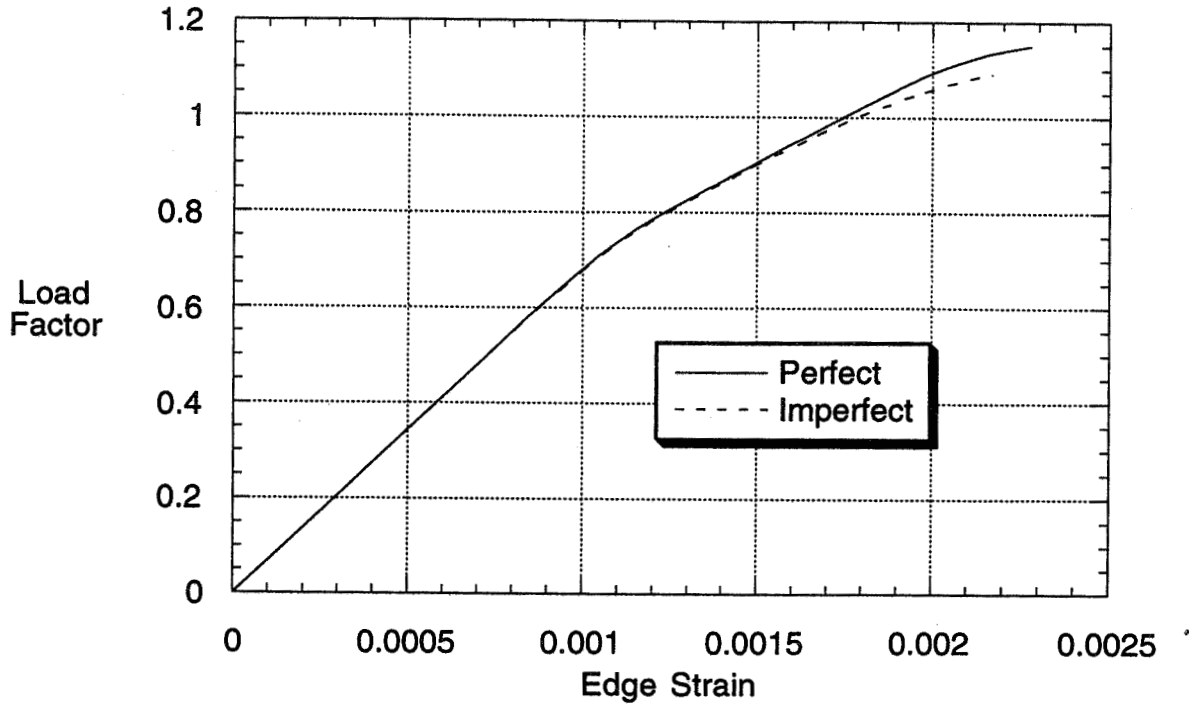

Figure 2 STAGS load shortening curve for aluminum Z-Stiffened panel designed to buckle at two thirds design load.

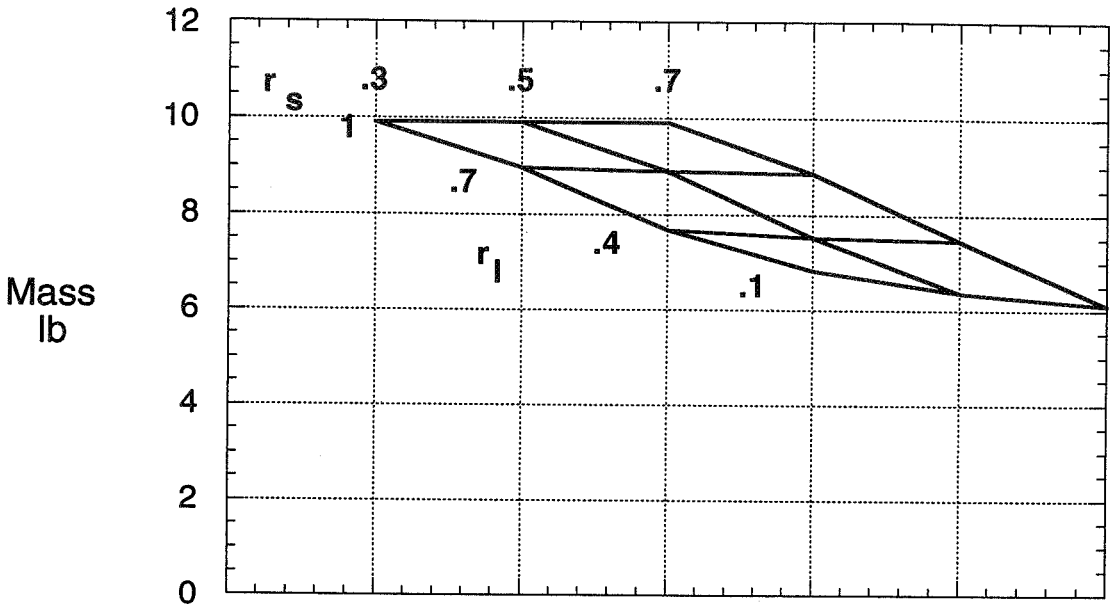

Figure 3 Effect of buckling load and postbuckling stiffness on the mass of aluminum Z-stiffened panel.

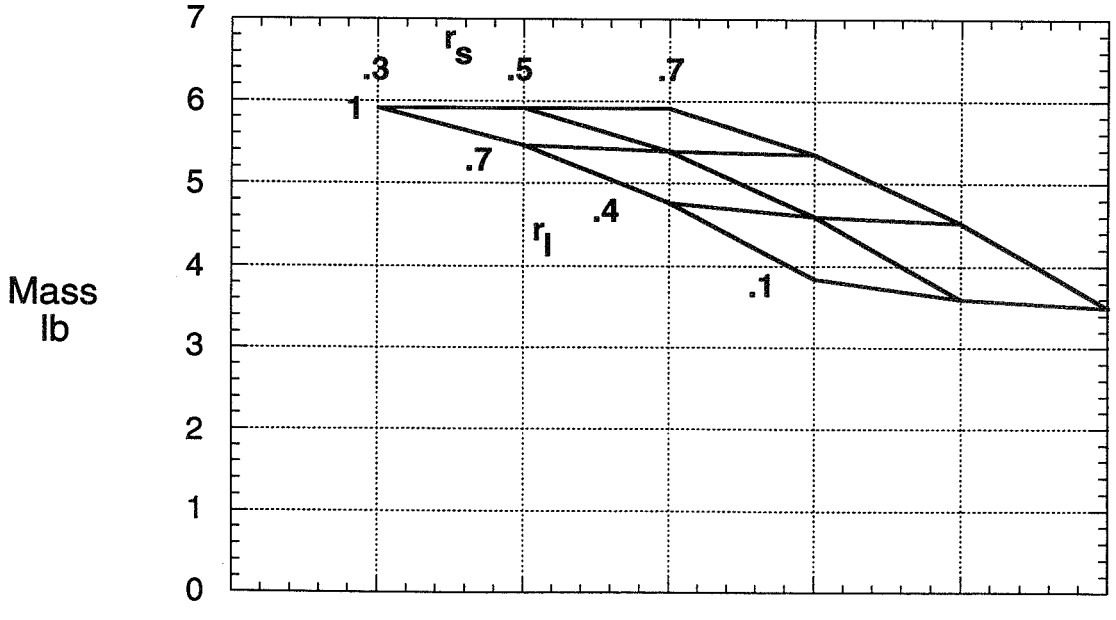

Figure 4 Effect of buckling load and postbuckling stiffness on the mass of composite Z-stiffened panel

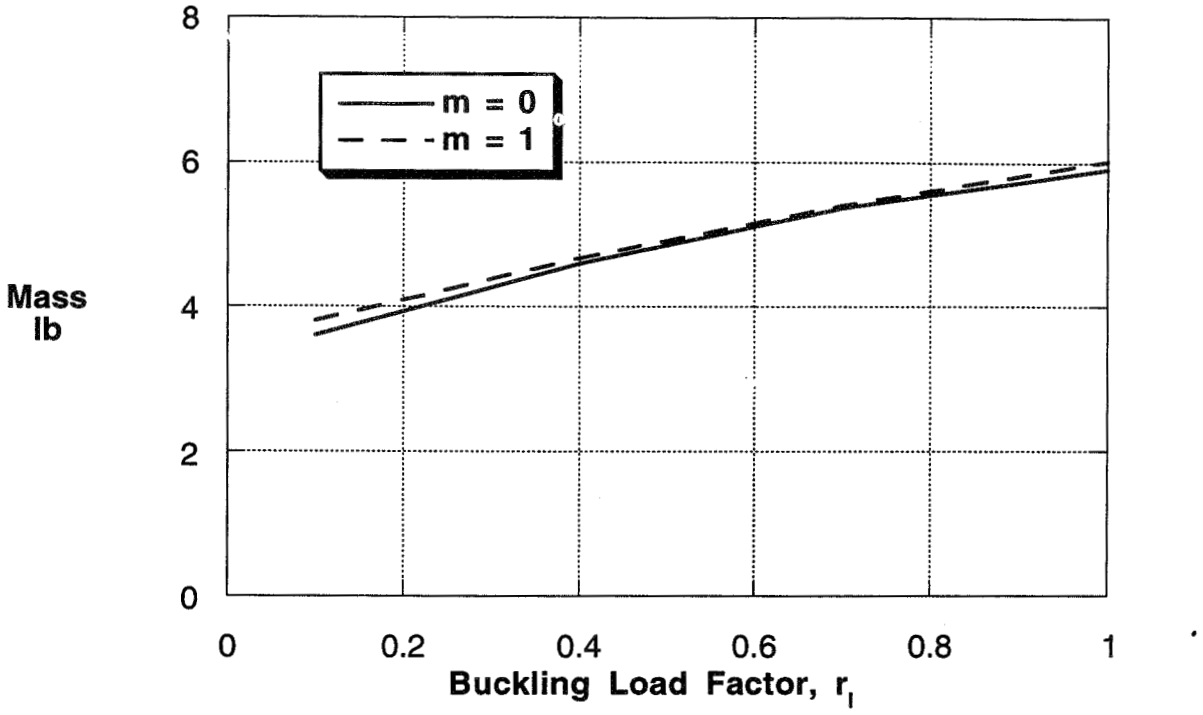

Figure 5 Effect of assumptions in beam-column formula on mass of composite panels. Calculated Euler load is used for m = 0 and the overall buckling mode from VICONOPT is s used for m =1.

COLLAPSE OF COMPOSITE CYLINDERS IN BENDING

Hannes P. Fuchs*
General Motors Research and Development Center
Warren, Michigan

James H. Starnes, Jr.**
NASA Langley Research Center
Hampton, Virginia

Michael W. Hyer***
Virginia Polytechnic Institute and State University
Blacksburg, Virginia

Abstract

This paper summarizes the results of a numerical and experimental study of the collapse behavior of small-scale graphite-epoxy cylindrical shells subjected to overall bending loads, and in one case, an initial internal pressure. Shells with quasi-isotropic and orthotropic inplane stiffness properties are studied. Numerical results from geometrically nonlinear finite element analyses and results from experiments using a specially-built apparatus indicate that extensive stable postbuckling responses occur. Orthotropy influences the buckling values and the extent to which the bending moment decreases after buckling. Material damage is observed to initiate in the vicinity of the nodal lines of the postbuckled deflection patterns. Numerical results indicate that the magnitudes of the shear stress resultants are greatest in these nodal regions. Failure of the internally pressurized cylinder is catastrophic.

Introduction

The response and failure characteristics of composite shell structures subjected to typical in-flight loads must be well understood before advanced composite materials can be used effectively for transport aircraft fuselage structures. The primary flight loads experienced by a typical transport fuselage structure are overall bending and internal pressure. Because the costs associated with full-scale fuselage experimentation and analysis are quite significant, a study of small-scale cylinders subjected to bending and pressure loads is justified. Previous papers[1-7] present expanded discussions of results of just such an investigation, and this paper summarizes those discussions, the emphasis here being on buckling, postbuckling, and collapse behavior.

For the investigation a special fixture was designed to load small-scale cylinders into the postbuckling range of response. The geometrically nonlinear responses of the cylinders were studied numerically with the use of the finite-element program STAGS[8]. Geometric imperfections were included in the STAGS analyses by using analytical representations of the measured surface shapes of the cylinders. The present paper describes the cylinder specimens, the loading apparatus, the finite-element model, and the predicted and measured responses, In addition, comments on failure of the cylinders are presented.

Test Specimens, Apparatus, and Procedure

A number of cylindrical shells with a nominal diameter of 12-in. were fabricated on an aluminum mandrel using unidirectional Hercules, Inc. AS4/3502† pre-impregnated graphite-epoxy tape. The specimens were eight-plies thick and had $[\mp 45/0/90]_S$, $[\mp 45/0_2]_S$, or $[\mp 45/90_2]_S$ stacking sequences, 0 deg. being the axial direction. All but one of the test specimens were 12 in. long and had length-to-radius ratios of two and radius-to-thickness ratios equal to approximately 160. The one exception, not discussed here (see ref. 4), had a length-to-radius ratio of five. The cylinders tested were C-scanned for imperfections, and other than small ply overlaps and gaps, there were no major imperfections in the cylinders discussed here. Internal and external fiberglass-epoxy tabs were attached to the ends of the specimens using a wet lay-up procedure. The tabs were cured at room temperature. The test specimen identification codes, laminate stacking sequences, average wall thicknesses, H, and radius-to-thickness ratios, R/H, are summarized in Table 1. The average mechanical properties for the cylinder specimens are summarized in Table 2, where is should be mentioned that specimen QP1, the pressurized specimen, was made in a slightly different fashion and at a later date. Note in Table 1 that specimen A1 is stiffer inplane in the axial direction than in the circumferential, or hoop, direction, specimens A2 and A3 are stiffer inplane in the hoop direction than in the axial direction, and specimens Q1, Q2, and QP1 are quasi-isotropic with respect to inplane stiffnesses. All specimens have anisotropic bending stiffness properties, i.e., have nonzero values of D_{16} and D_{26}.

The shell geometry and kinematics are defined in fig.1a. The midsurface radius, test length, and wall thickness of the

*Senior Research Engineer, Member, AIAA
**Head, Structural Mechanics Branch, Fellow, AIAA.
***Professor, Engineering Science and Mechanics

†Identification of commercial products and companies in this paper is used to describe the test materials adequately. The identification of these commercial products does not constitute endorsement, expressed or implied, of such products by the authors or their employers.

shell are identified in this figure as R, L, and H, respectively. The kinematic quantities u°, v°, and w° represent the axial, circumferential, and radial displacements, respectively, of the midsurface, whereas β_x°, β_θ°, and β_z° represent the two inplane rotations, and the normal rotation, respectively, of the midsurface. Applied bending and internal pressure loads are indicated in fig.1b. The ends of the shells were constrained to remain clamped and circular. Bending was induced by applying the known rotation angle Ω to the ends of the shell. The corresponding bending moment is represented by M and the nominal strain on the compressive side of the shell is represented by ε. For the internally pressurized case the ends of the shell were allowed to expand freely in the axial direction by means of slotted pin supports. For the no-pressure case the ends were axially restrained. The shells were painted white with a black grid on the compression side to improve visualization of the observed deflection patterns.

The test apparatus is illustrated in fig. 2a. The bending loads were applied symmetrically to the shell specimen by rotating the moment arms about the pivot pins, where the rotation of the moment arms was controlled by the vertical motion of two hydraulic jacks. The pressure supplied to the jacks, and hence the bending moment applied to the shell, was measured by a load cell. The internal pressure in the shell was supplied by a high pressure nitrogen tank that was controlled by a regulator. Details of the shell specimen and the endfittings are shown in fig. 2b. The internal and external fiberglass tabs on the specimen ends and a low-temperature melting-point alloy, used as a potting compound, provided the means to attach the shells to aluminum end-rings. The end-rings were then bolted to the test fixture moment arm in order to apply the bending rotations to the shell. This arrangement was designed to assure that the ends of the shell specimen were clamped and remained circular. Internal pressure was maintained in the shell through the two end plates with O-ring seals. The pressure line was attached to one end of the specimen and an instrumentation plug was attached to the other end. Strains were measured at a number of locations inside and outside the cylinder with strain gages. Deflections of the cylinders and rotations of the end moment arms were measured with direct current differential transformers. The shapes of the outer surfaces of the cylinders were measured after they had been mounted in the end-rings using the potting compound, but before they were bolted to the fixture moment arms.

For the bending tests with no internal pressure, the fixture moment arms were rotated by increasing the pressure in the jacks. Data were acquired from the no-load condition until the end of the test, which in some cases was the point of no load after unloading from a postbuckling condition. As the jack load was increased, still and moving video were used to record additional information regarding shell response, particularly the deformation of the black grid scribed on the compression side of the shells. When the cylinders developed postbuckling response, the jack pressure was held constant and the postbuckling deflection patterns were outlined, by hand, on the surface of the shell. Loading was then continued and other patterns developed, and/or material failure occurred. At that point, the cylinders were unloaded. Upon unloading they generally snapped back close to their original circular shape. In several cases the cylinders were loaded multiple times. For the case of the additional internal pressure loading, a 100 psi internal pressure was first applied, then the jack load was increased to buckling, postbuckling, and, as will be seen, sudden failure of the cylinder. Though an 8 psi pressure would be representative of a transport fuselage, the smaller diameter cylinders required a higher pressure to simulate the same circumferential stress resultant.

Analysis

For each shell the measured initial shape of the outer surface was assumed to represent the shape of the midsurface, and the thickness of the wall was assumed to be constant. Analytic representations of these shapes, based on Fourier series, were used in the analyses. The 4-noded STAGS 410 element was chosen to model the shells, with 510 transition elements being used when needed. Various mesh densities were used, ranging from 23,800 degrees of freedom to 12,300. The most efficient model had a finer mesh on the compression side of the cylinder than on the tension side. The kinematic boundary conditions applied to the finite element model for the bending-only case are shown in fig. 3. The boundary conditions enforced a clamped condition on the ends of the shell and rotated the plane containing the ends of the shell by the applied rotation angle Ω. For the case of additional internal pressure, a uniformly distributed radial load p was applied to the cylinder walls and the ends of the shell were displaced axially an additional amount

$$u_p = \frac{pRL}{2E_x H}(1 - 2\nu_{x\theta}), \tag{1}$$

where E_x and $\nu_{x\theta}$ are the laminate's effective axial inplane modulus and effective inplane Poisson's ratio measuring contraction in the circumferential direction when loaded in the axial direction.

With STAGS the responses up to buckling were calculated using the applied end rotation as an incrementally-applied loading parameter. An arc-length projection, or path-parameter strategy, was used to compute the responses beyond buckling. With this strategy the incrementally applied loading parameter is replaced with an increment of arc-length along the solution path, which is then used as an independent loading parameter. The arc-length increments were automatically adjusted by STAGS as a function of the solution behavior. With this approach, the highly unstable nature of postuckling could be studied.

Results

The response of the cylindrical shells is characterized by the moment-rotation responses of the shells. First, details of the numerically predicted postbuckling responses will be presented for the orthotropic $[\mp 45/0_2]_S$ shell subjected to only end rotation in order to illustrate the features of the complex predicted postbuckling equilibrium path. Next, the predicted and measured moment-rotation responses for this loading will be discussed and compared for the shell specimens representing the three levels of inplane orthotropy. The predicted and measured end rotation and moment results are normalized by the classical values of the buckling end rotation Ω_{cr} and buckling moment M_{cr}. The classical buckling values are summarized in Table 3 for all six shells. The compressive buckling ε_{cr} strain was introduced because it was often easier to measure experimentally than the end rotations. These classical buckling quantities were computed from the relations

$$M_{cr} = \pi R^2 N_{cr} = 2\pi R\sqrt{E_\theta H D_{11}} \qquad (2)$$

and

$$\Omega_{cr} = \frac{M_{cr}L}{2E_xI} = \frac{L}{2R}\cdot\varepsilon_{cr}, \qquad (3)$$

where D_{11} is the axial bending stiffness of the laminate, E_θ is the laminate's effective circumferential inplane modulus, and E_xI is the effective bending stiffness of the shell. The quantity N_{cr} represents the axial force resultant associated with the axisymmetric buckling of a right circular cylindrical shell subjected to axial compression. Equations 2 and 3 indicate that laminate orthotropy and shell geometry affect the classical buckling values. Continuing with the discussion of results, typical observed postbuckling deflection patterns will be described, and the observed material damage will be discussed. The analysis and observation of the internally pressurized case will be discussed where appropriate.

Initial Shape Imperfections

For completeness, a typical measured shape imperfection is shown in fig. 4, illustrating the radial deviation from a best-fit right circular cylinder. The imperfection amplitude is shown as a function of the shell surface coordinates and is normalized by the wall thickness. The maximum deviation from the best-fit cylinder was found to be less than 60% of the wall thickness. As can be seen, a slight out-of-roundness coupled with local deviations characterize the imperfection.

Predicted Response of Orthotropic Shell

To illustrate the features of the numerically predicted postbuckling equilibrium path, the moment-end rotation response and associated deflection patterns will be discussed for the axially stiff $[\mp 45/0_2]_S$ shell *A1*. The moment-rotation relation is shown in fig. 5. The extensive postbuckling response of this shell is indicated in the figure by a number of scallop-shaped branches beyond the buckling point. The buckling point is labeled as point *A*, the maxima of the individual branches are labeled as points *C*, *E*, *G*, and *I*, and the minima are labeled as points *B*, *D*, *F*, and *H*. Each branch of the postbuckling path features both a stable segment (e.g., *B-C*, *D-E*, etc.) and an unstable segment (e.g., *A-B*, *C-D*, etc.), as shown in the inset of the figure. Point *B* represents the minimum postbuckling moment. The slope of each adjacent stable segment decreases somewhat as the postbuckling response develops, indicating a reduction in the effective bending stiffness of the shell, E_xI, due to a change in the overall shape of the shell. As can be seen in the inset, the unstable segments of the postbuckling paths nearly coincide with the previous stable segments of the postbuckling path at the maximum points, indicating that the maximum points are points of unstable equilibrium.

Before proceeding, it is important to be sure fig. 5 is properly interpreted. In this study the intent was to control end rotation Ω. With this situation, referring to fig. 5, as the end rotation was increased from zero, the moment-rotation relation should move from the origin to point *A*. At point *A* the solution would lose stability and, since Ω was being controlled, the response should jump vertically downward from the solution at point *A* to a solution on path *BC*. With a further increase in Ω, the solution should move up stable path *BC* towards point *C*. At point *C* the solution again would again lose stability, but since Ω was being controlled, the solution would jump vertically downward to path *DE*. This downward jumping would occur at subsequent peaks, *E*, *G*, etc. On the other hand, if the moment *M* was being controlled, as the moment was increased from zero, the solution would move from the origin to point *A*. At point A, since there would be a loss of stability, the solution would move horizontally to path *FG*. With a further increase in moment, the solution would move up path *FG* and upon reaching point *G*, would jump to path *HI*. The difference in the actual path for rotation control as opposed to moment control is quite important. Also important is the fact that the jump from point *A* to path *BC*, for example, would actually be a dynamic event.

The deflection patterns corresponding to the first buckling mode relative to point *A* and postbuckling equilibrium solutions at points *C* and *I* in fig. 5 are shown in fig. 6a-c to illustrate the progression of deformation with increasing end rotation. The buckling pattern associated with point *A* indicates a short wavelength buckling mode, where skewing of the buckling mode can be attributed to the presence of the anisotropic laminate bending terms D_{16} and D_{26}. The predicted postbuckling deflection patterns are distinctly different from the buckling deflection patterns and have large inward local buckles on the compression side of the shell. As end rotation increases, the formation of new inward local buckles coincides with the reduction in the effective postbuckling bending stiffness as the response progresses through the scallop-shaped branches of the moment-rotation response. It is important to realize that these predicted shapes are based on imperfections specific to these shells. Similar cylindrical shells but with different imperfection characteristics would most likely result in different

moment-rotation relations and different deformation patterns.

The addition of initial internal pressure had a substantial influence on the predicted deformation response (see ref. 7). It is hypothesized that the internal pressure eliminated much of the initial overall out-of-roundness, and even having an influence on the local deviations from the prefect case.

Predicted and Measured Response Comparison

As a summary of the buckling behavior, the predicted and measured buckling end rotations and predicted and measured buckling moments are shown in Table 3. The quantities Ω_{cr}^{fep} and Ω_{cr}^{feimp} are the buckling end-rotations computed with a STAGS finite-element analysis assuming perfect and imperfect geometry, respectively. The quantity Ω_{cr}^{exp} is the measured value. The nomenclature for the moments is similar. For cylinder QP1 columns 5, 6, 9, and 10 include the influence of the internal pressure. As can be seen from the table, for the unpressurized cases the ranking of the end rotations by laminate stacking arrangement was predicted correctly by the two finite-element analyses as well as the simple classic prediction, laminate A1 requiring the least rotation to cause it to buckle. Also, imperfections almost always reduced the predicted end rotation. The addition of the internal pressure for the quasi-isotropic case greatly increased the predicted end rotation in the presence of imperfections, specifically about 40%. Finally, the measured end rotation was always less than any of the predictions. From Table 3 it can be concluded that the ranking as regards absolute magnitude of buckling moment for the pressurized case was accurately predicted by the finite element analyses, but not by the classical prediction. The axially stiff cylinder had the lowest buckling moment predicted by the finite-element analyses, and the lowest observed, and the quasi-isotropic cylinder had the highest, both predicted and observed. For the unpressurized cases the measured buckling moment was always less than predicted. Finally, with imperfections accounted for, internal pressure increased the predicted buckling moment about 35%, and the measured buckling moment was greater than the predicted moment by about 5%.

The predicted and measured moment-rotation responses for the unpressurized cases are compared in figs. 7a and b, respectively, for three specimens which represent the three levels of orthotropy, namely specimens Q2, A1, and A3. Buckling associated with each of these shells is identified by the filled symbols in these figures and the values of Ω/Ω_{cr} and M/M_{cr} at buckling are indicated in parentheses. The scallop-shaped features of the predicted postbuckling response discussed in the previous section can be observed in fig. 7a for the case of the three representative specimens. The progression of the predicted postbuckling deflection patterns for the shell specimens *Q2* and *A3* was similar to the progression shown in fig. 6 for specimen *A1*. The major difference among the predicted responses for each of the three shells is the relative difference between the value of the minimum postbuckling moment and the corresponding buckling moment. This relative difference is defined by the difference in the bending moments corresponding to points *A* and *B* in the moment-rotation response shown in fig. 5, and could represent a reduction in buckling capacity due to imperfections other than the included geometric imperfections. This reduction would be caused by the moment-rotation relation jumping to point *B* from the primary path as the loading increased from the origin toward *A*, the moment never reaching the predicted buckling value at *A*. The variation of this relative difference from cylinder to cylinder indicates the influence of laminate orthotropy, and to some extent, the effect of a particular measured shape imperfection on each shell. Table 4 summarizes the predicted reduction in bending moment for these cylinders, namely, the difference in the moments at points *A* and *B*. The implication in Table 4 is that in practice the axially stiff cylinder would be least influenced by imperfections not already included in the analysis.

The measured moment-rotation responses are summarized in fig. 7b. The broken lines in this figure indicate a transition between the unstable buckling point, *A*, and a stable postbuckling configuration. This transition is, as mentioned before, a dynamic event and is accompanied by an audible "popping" sound often interpreted as "buckling." The figure indicates that considerable postbuckling responses occurred in the experiments before the cylinders failed. It is important to note that the measured moment - rotation relations do not resemble the predicted moment - rotation relations, nor do they resemble the rotation-control vertical jumps or the moment-control horizontal jumps that were alluded to earlier. This is due to the difficulty of producing perfectly rigid fixtures, and producing loading systems based on hydraulics or kinematics (screw-driven) that can respond instantaneously. So what actually occurs is that *both* the moment level and the degree of rotation change immediately after point *A* of fig. 5.

Although for the reasons just discussed the measured and predicted moment-rotation responses do not, overall, compare well, it is apparent that similar trends are indicated. The prebuckling slopes coincide in both figs. 7a and b. Also, the ranking of the normalized buckling moments as a function of laminate orthotropy follows predictions, with the axially stiff cylinder having the largest normalized buckling moment and the hoop stiff cylinder having the smallest normalized buckling moment. This would seem to indicate that the prediction of the influence of geometric imperfections is accurate.

It was implied earlier that the reduction in buckling capacity in the experiments, relative to the finite-element predictions, could possibly be identified with the moment-rotation relation moving from the origin in fig. 5 directly to point *B* instead of going to the buckling value at point *A*. Table 4 summarizes the percent difference in experimental vs. predicted buckling moment, and it is seen that the differences do not correlate well with the differences in moment between point *A* and point *B*. The difference between predicted and experimental buckling moment is much less than

the difference between points *A* and *B*, leading to the conclusion that the inclusion of the geometric imperfection provides an accurate accounting of cylinder behavior, but all influences are not completely accounted for.

The predicted and measured moment-rotation relations for the pressurized case are shown in fig. 8. The normalization is with respect to the definitions in eq. 2, the unpressurized case. As a result, buckling occurs when these parameters are greater than one, indicating that pressurization increases the buckling load relative to the no-pressure case. One of the no-pressure quasi-isotropic cases previously discussed is indicated on the figure so the influence of internal pressure is better gaged. The predictions indicate that pressurization to 100 psi would increase the buckling moment by 35%. Observations indicate the increase was closer to 53%.

The value of the reduction in moment after buckling is an important parameter. For many designs, the buckling moment should be decreased by this value and the reduced value used as ultimate moment capacity. Interestingly, for these shells the reduction in moment appeared to be somewhat a function of laminate orthotropy. Table 5 summarizes the decrease in moment after buckling as measured from the experiments. It is seen that the axially stiff case, though having the lowest absolute buckling moment capacity, also had the lowest decrease in capacity after buckling. Interestingly, both the prediction and the observation indicate that the reduction in moment after buckling was considerable less if there was internal pressure. From the previous section the case of internal pressure was predicted to exhibit a 12% drop, whereas experimentally the decrease was 2%.

Observed Postbuckling Deflection Patterns and Material Damage and Failure

Two representative observed postbuckling deflection patterns are illustrated in fig. 9. The deflection patterns are presented in the form of outlines of the inward local buckles on the compression side of the shells and are shown as a function of the coordinates x and θ. The symmetric and asymmetric patterns in this figure correspond to the $[\mp 45/0_2]_S$ and $[\mp 45/90_2]_S$ shells, respectively. The $[\mp 45/0_2]_S$ shell exhibited a symmetric deflection pattern and correlated well with the predicted postbuckling deflection pattern (see fig. 6). The observed deflection patterns for the remaining shells correlated fairly well with the corresponding predicted deflection patterns.

In most cases local material damage was not apparent immediately following the transition from buckling to postbuckling. However, as the applied rotation was increased throughout the postbuckling range and the size of the inward local buckles grew larger and became more distinct, local material damage was observed in the vicinity of the nodal lines of the postbuckling deflection pattern. Ultimate failure of the shell specimens is attributed to an interlaminar shear failure mode which initiated along the nodal lines of the postbuckling deflection pattern. This experimental observation is supported by the STAGS analysis results. A magnified view of the deformations for the pressurized case in the vicinity of typical inward local buckles is shown in fig. 13. In this figure shading indicating the magnitude of the shear stress resultants Q_x and Q_θ are superimposed on the deformed finite element model. The results in this figure indicate that the magnitude of the induced shear stress resultants is greatest in the regions of the nodal lines of the postbuckling deflection pattern, indicating likely interlaminar shear failure locations.

Regions of visible material damage, observed both before and after ultimate failure, are indicated in fig. 9. Material damage in the $[\mp 45/0_2]_S$ shell *A1* and $[\mp 45/0/90]_S$ shells *Q1* and *Q2* (not shown) shells was confined to regions in the vicinity of the nodal lines of the deflection patterns. Material damage in the two $[\mp 45/90_2]_S$ shells *A2* and *A3* was initiated along the nodal lines of the deflection patterns and propagated along the circumferential direction during ultimate failure, as shown in fig. 9b. The severity of the observed material damage appears to be related to the relative magnitude of the buckling rotation Ω_{cr} (see Table 3). Equations (1) and (2) indicate that the buckling rotations are dependent on laminate orthotropy, thereby linking the laminate orthotropy to the severity of the observed material damage. A secondary deflection pattern occurred for the $[\mp 45/0_2]_S$ shell, possibly due to the localized material failure indicated in fig. 9a. The measured moment-rotation response for this shell, shown in fig. 7b, indicates that a reduction in bending stiffness is associated with the observed secondary deflection pattern.

Failure of the pressurized cylinder was quite dramatic. After buckling, loading of the pressurized cylinder increased until the material damage occurred. The damage caused a leak in the cylinder and simultaneously the nitrogen gas pressure was released in explosive fashion. Figure 11 shows a sequence of events when applying increasing moment to the pressurized cylinder. Careful examination of fig. 11b reveals a local buckle near the left end of the compression side of the shell. The local buckle appears to be in the form of a single half-wave in the axial direction, with the deformations oriented radially inward. Figure 11c shows the shell at the instant in time just after the failure event initiated, the nitrogen gas venting rapidly. Figure 11d shows the failed cylinder.

Concluding Remarks

A numerical and experimental study was conducted to investigate the buckling and postbuckling behavior of 8-ply thin-walled graphite-epoxy cylindrical shells loaded by end rotation, with and without internal pressure. The study indicated that the magnitude of the buckling end rotation depended on laminate orthotropy, and complex multi-branched postbuckling equilibrium paths were predicted. Internal pressure significantly increased the buckling end rotation. Each branch on the postbuckling path represented a unique deflection pattern that was distinctly different from the predicted buckling patterns and had large inward local

deformations on the compression side of the shell. Laminate orthotropy was predicted to influence the postbuckling path and in particular, the magnitude of the minimum postbuckling moment relative to the buckling moment. The shear stress resultants were found to be most severe in the regions of the nodal lines of typical local deformations of the postbuckling deflection patterns.

Extensive postbuckling responses occurred in the tests. Large inward local deformation appeared on the compression side of the shell specimens after buckling occurred, similar to those predicted by the numerical analysis. The reduction in moment in the experiments relative to the predicted values did not correlate with the magnitude of the minimum postbuckling moment relative to the buckling moment. The reduction in moment after buckling was observed to depend on cylinder orthotropy. Material damage was evident in the postbuckling loading range. Ultimate failure appeared to initiate along nodal lines of the local buckles of the postbuckling deflection patterns. The observed failure locations correlated well with typical predicted locations of high values of the shear stress resultants, suggesting that local interlaminar shear stresses are large enough to initiate failure. With internal pressure, failure was catastrophic.

Acknowledgments

The work reported on herein was supported by the Structural Mechanics Branch of the NASA Langley Research Center through the NASA-Virginia Tech Composites Program, Grant NAG-1-343, and also through a National Research Council Fellowship. The support of all organizations is greatly appreciated.

References

[1]Fuchs, H.P., Hyer, M.W., "The bending response of thin-walled laminated composite cylinders," *Composite Structures*, 22, 1992, 87-107

[2]Fuchs, H. P., Hyer, M. W., "The nonlinear bending response of thin-walled laminated composite cylinders," AIAA Paper No. 92-2230CP, *Proceedings of the 33rd AIAA/ASME/ASCE/AHS/ASC Structures, Structural Dynamics, and Materials Conference*, Dallas, TX, April 13-15, 1992, 70-78.

[3]Fuchs, H. P., Starnes, J. H., Jr., Hyer, M. W., "Prebuckling and collapse response of thin-walled composite cylinders subjected to bending loads," *Proceedings of the 9th International Conference on Composite Materials*, Vol. 6, Madrid, Spain, July 12-16, 1993, 410-417.

[4]Fuchs, J. P., "Numerical and experimental investigation of the bending response of thin-walled composite cylinders," Ph.D. Dissertation in Engineering Mechanics, Virginia Polytechnic Institute and State University, September, 1993, University Microfilms, Ann Arbor, MI, order number 9403851.

[5]Fuchs, H.P., Hyer, M.W., "Numerical and experimental investigation of the collapse response of thin-walled graphite-epoxy cylindrical shells loaded in bending," AIAA Paper No. 94-1608-CP, *Proceedings of the 35rd AIAA/ASME/ASCE/AHS/ASC Structures, Structural Dynamics, and Materials Conference*, Hilton Head, SC, April 18-20, 1994, 2308-2314.

[6]Fuchs, H.P., Hyer, M.W., "The nonlinear prebuckling response of short thin-walled laminated composite cylinders in bending," *Composite Structures*, 34, 1996, 309-324

[7]Fuchs, H.P., Starnes, J.H., Jr., Hyer, M.W., "Numerical and experimental investigation of the collapse response of a quasi-isotropic graphite-epoxy cylindrical shell subjected to bending and internal pressure loads," Buckling and Postbuckling of Composite Structures, ed. A.K. Noor, AD-41, PVP-293, available ASME, pp. 73-94,

[8]Almroth, B. O., Brogan, F. A. "The STAGS Computer Code," NASA CR-2950, 1980

Table 1 - Geometry of Test Specimens

I.D. code	Laminate	R, in.	R
Q1	$[\overline{+}45/0/90]_S$	0.0374	160.2
Q2	$[\overline{+}45/0/90]_S$	0.0375	160.0
A1	$[\overline{+}45/0_2]_S$	0.0381	157.5
A2	$[\overline{+}45/90_2]_S$	0.0369	162.5
A3	$[\overline{+}45/90_2]_S$	0.0358	167.5
QP1	$[\overline{+}45/0/90]_S$	0.0394	152.2

Table 2 - Graphite-Epoxy Mechanical Properties

	E_1, Msi	E_2, Msi	G_{12}, Msi	ν_{12}
Q1 - A3	23.4	1.75	1.03	0.285
QP1	22.1	1.64	0.95	0.289

Table 3 - Classical, Computed, and Measured Buckling End Rotations and Moments

I.D. Code	Laminate	Ω_{cr}, deg	Ω_{cr}^{fep}, deg	Ω_{cr}^{feimp} deg	Ω_{cr}^{exp} deg	M_{cr}, lb-in	M_{cr}^{fep}, lb-in	M_{cr}^{feimp}, lb-in	M_{cr}^{exp}, lb-in
Q1	$[\mp 45/0/90]_S$	0.207	0.212	0.197	0.172	139,550	143,310	132,570	110,660
Q2	$[\mp 45/0/90]_S$	0.207	0.212	0.193	0.183	139,998	142,900	130,130	119,280
A1	$[\mp 45/0_2]_S$	0.098	0.105	0.107	0.092	95,809	103,870	104,590	89,390
A2	$[\mp 45/90_2]_S$	0.484	0.437	0.415	0.344	144,378	134,100	125,390	99,040
A3	$[\mp 45/90_2]_S$	0.465	0.430	0.391	0.361	140,298	132,530	118,320	102,980
QP1	$[\mp 45/0/90]_S$	0.2181	- -	0.207[1] 0.292[2]	- 0.279[2]	147,100[1] -	- -	139,745[1] 189,759[2]	- 198,585[2]

1 - no pressure, 2 - pressure, - not determined

Table 4 - Reduction in Buckling Moment

I.D. code	Laminate	$\frac{M_A - M_B}{M_A}$	$\frac{M_{cr}^{feimp} - M_{cr}^{exp}}{M_{cr}^{feimp}}$
Q1	$[\mp 45/0/90]_S$	44.4%	16.5%
Q2	$[\mp 45/0/90]_S$	42.7%	8.33%
A1	$[\mp 45/0_2]_S$	20.9%	14.5%
A2	$[\mp 45/90_2]_S$	48.0%	21.0%
A3	$[\mp 45/90_2]_S$	53.0%	12.9%
QP1	$[\mp 45/0/90]_S$	-	-4.6%

- not determined

Table 5 - Reduction in Moment after Buckling as Measured from Experiments

I.D. code	Laminate	ΔM
Q1	$[\mp 45/0/90]_S$	41.2%
Q2	$[\mp 45/0/90]_S$	43.8%
A1	$[\mp 45/0_2]_S$	16.7%
A2	$[\mp 45/90_2]_S$	41.7%
A3	$[\mp 45/90_2]_S$	44.1%
QP1	$[\mp 45/0/90]_S$	2%

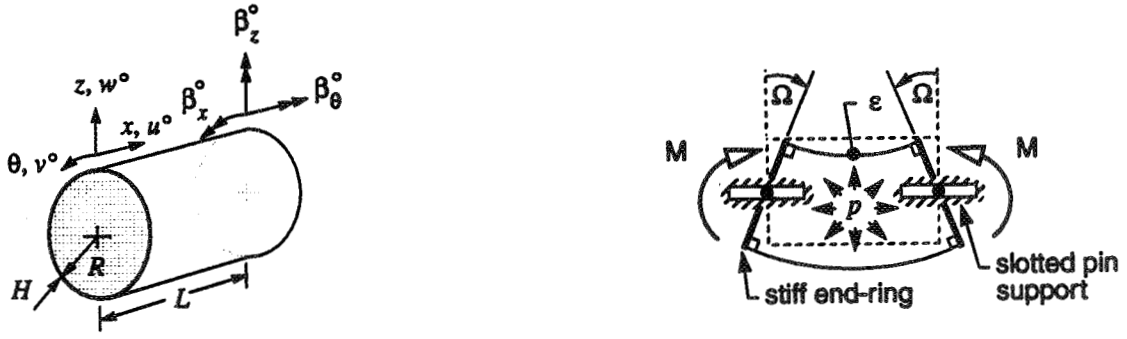

a - Geometry and kinematics

b - Loading.

Fig. 1 - Problem description

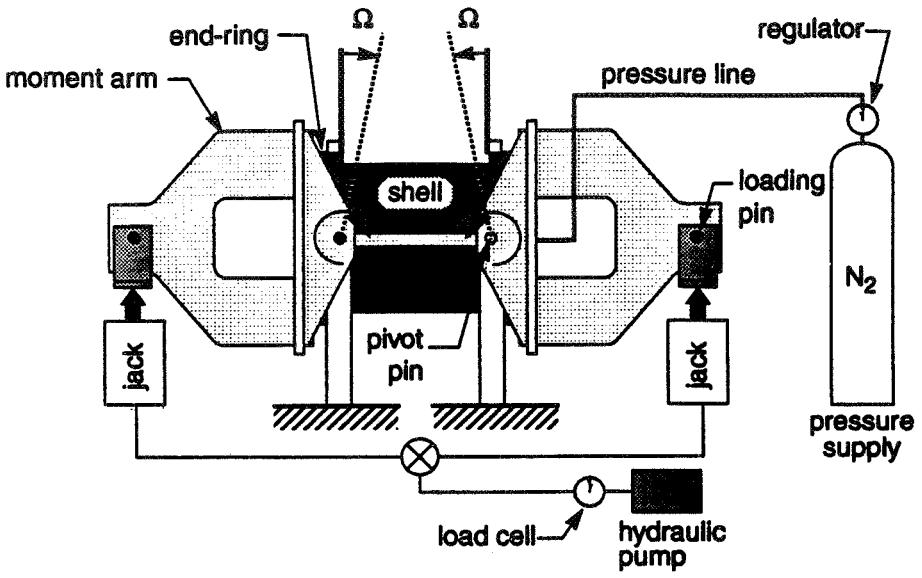

(a) - Apparatus schematic (side view)

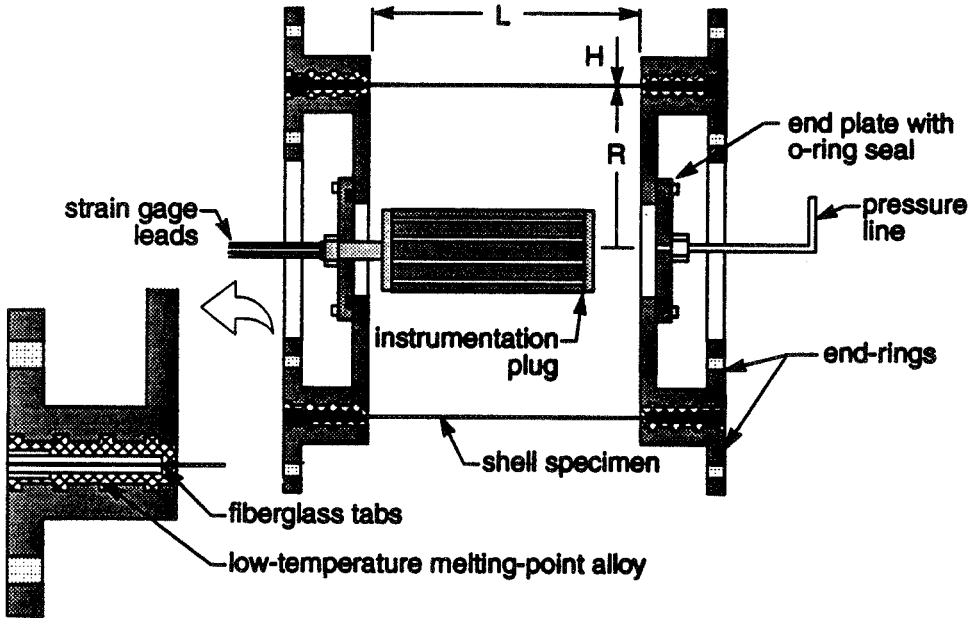

(b) - Specimen and end fitting schematic

Fig. 2 - Test apparatus and cylinder specimen

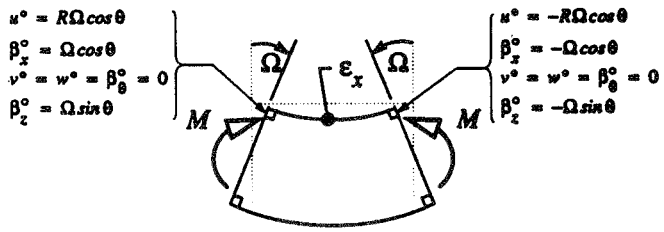

Fig. 3 - Bending boundary conditions

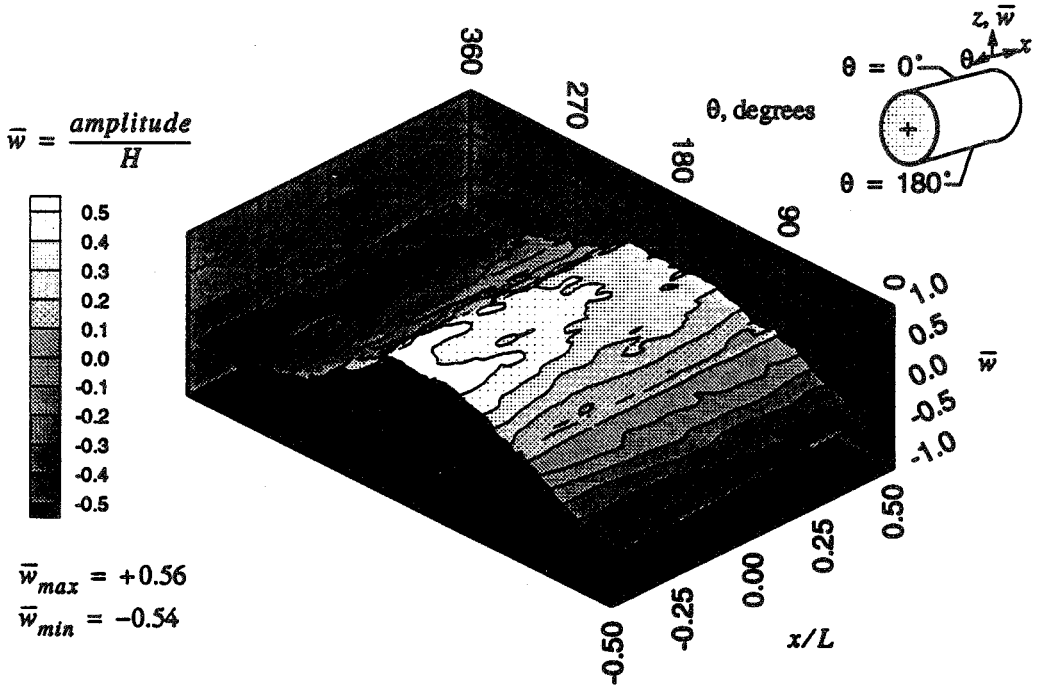

Fig. 4 - Analytic representation of measured outer surface shape imperfection

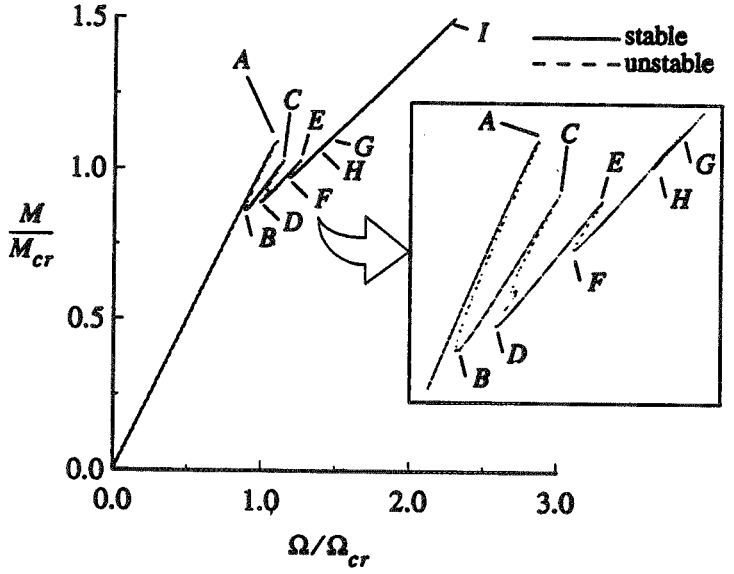

Fig. 5 - Features of computed moment - rotation relation for $[\mp 45/0_2]_S$ specimen A1

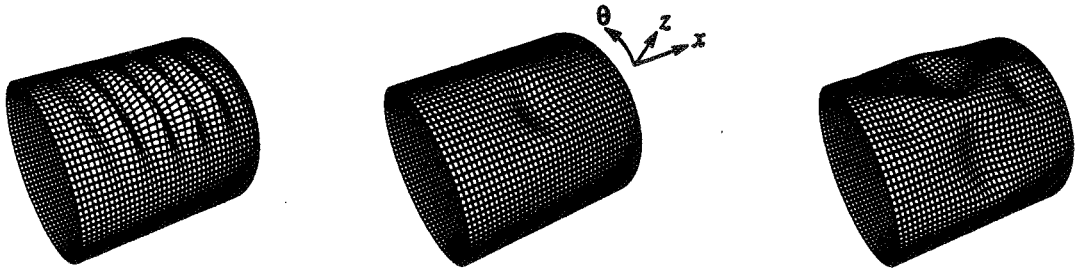

(a) - Buckled relative to A **(b) - Postbuckled at C** **(c) - Postbuckled at I**

Fig. 6 - Deflection patterns for $[\mp 45/0_2]_S$ specimen A1

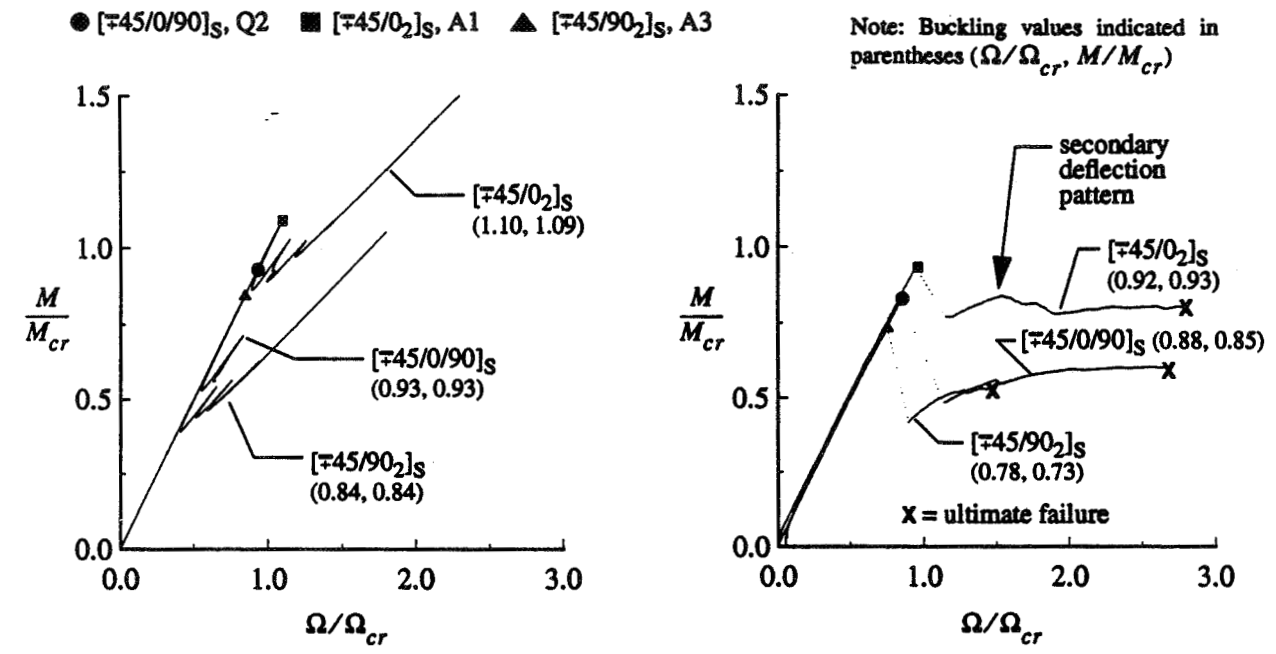

(a) - Predicted (b) - Measured

Fig. 7 - Representative moment - rotation relations, no-pressure case

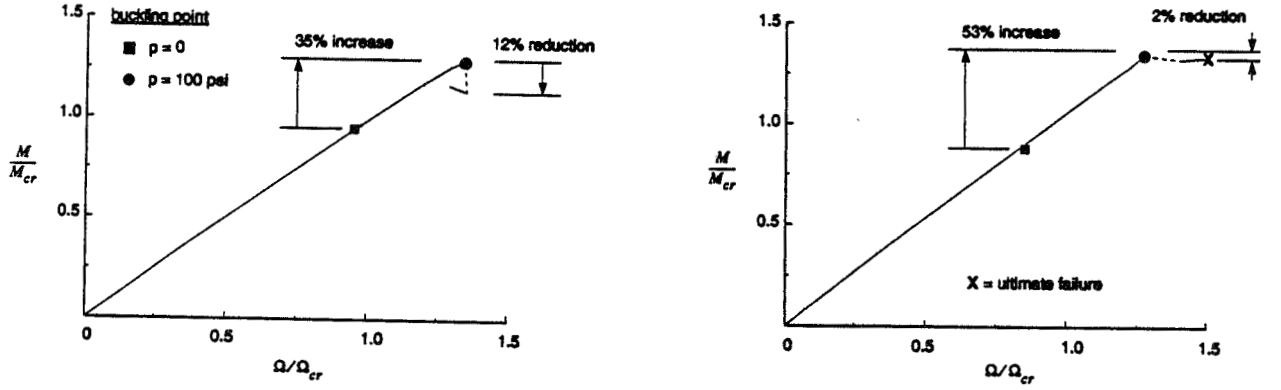

(a) - Predicted (b) - Measured

Fig. 8 - Moment - rotation relation, internal pressure case

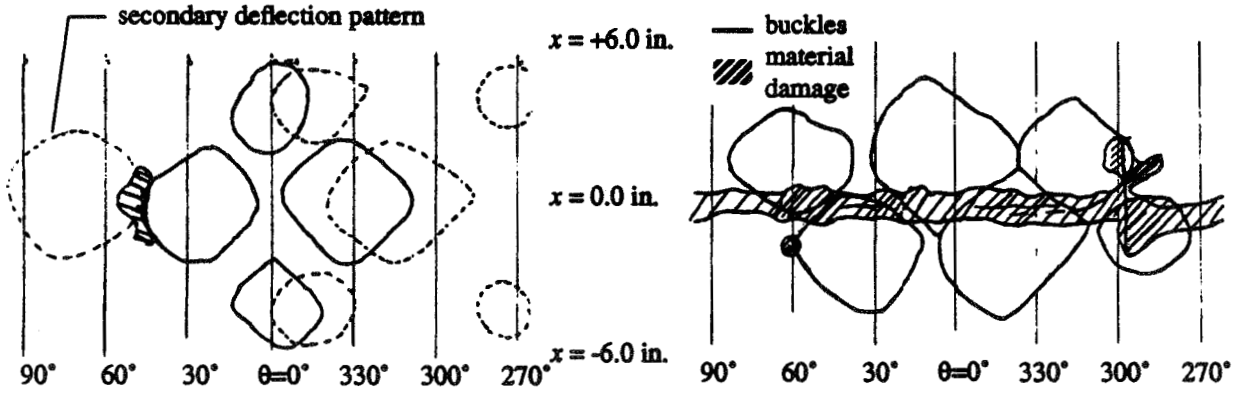

(a) - Symmetric pattern for[∓45/02]S specimen A1 (b) -Unsymmetric pattern for[∓45/902]S specimen A3

Fig. 9 - Typical observed postbuckling patterns

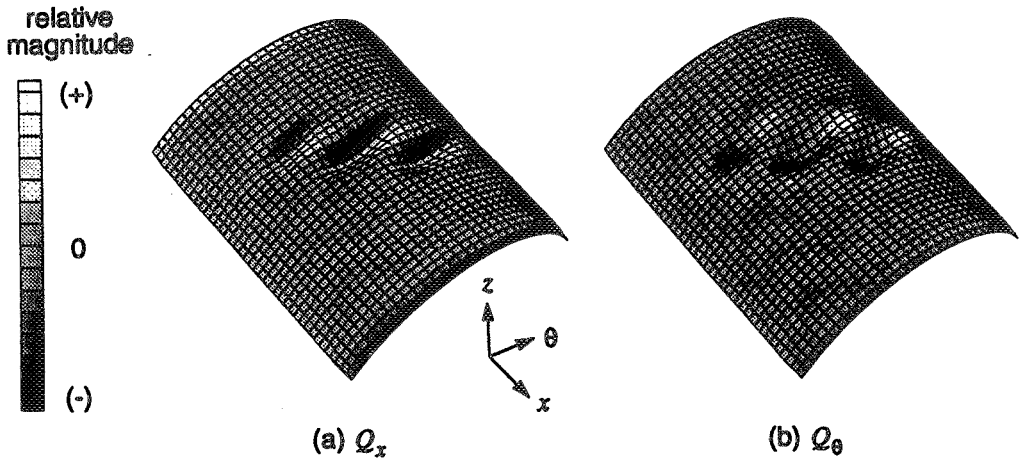

Fig. 10 - Shear stress resultant magnitudes

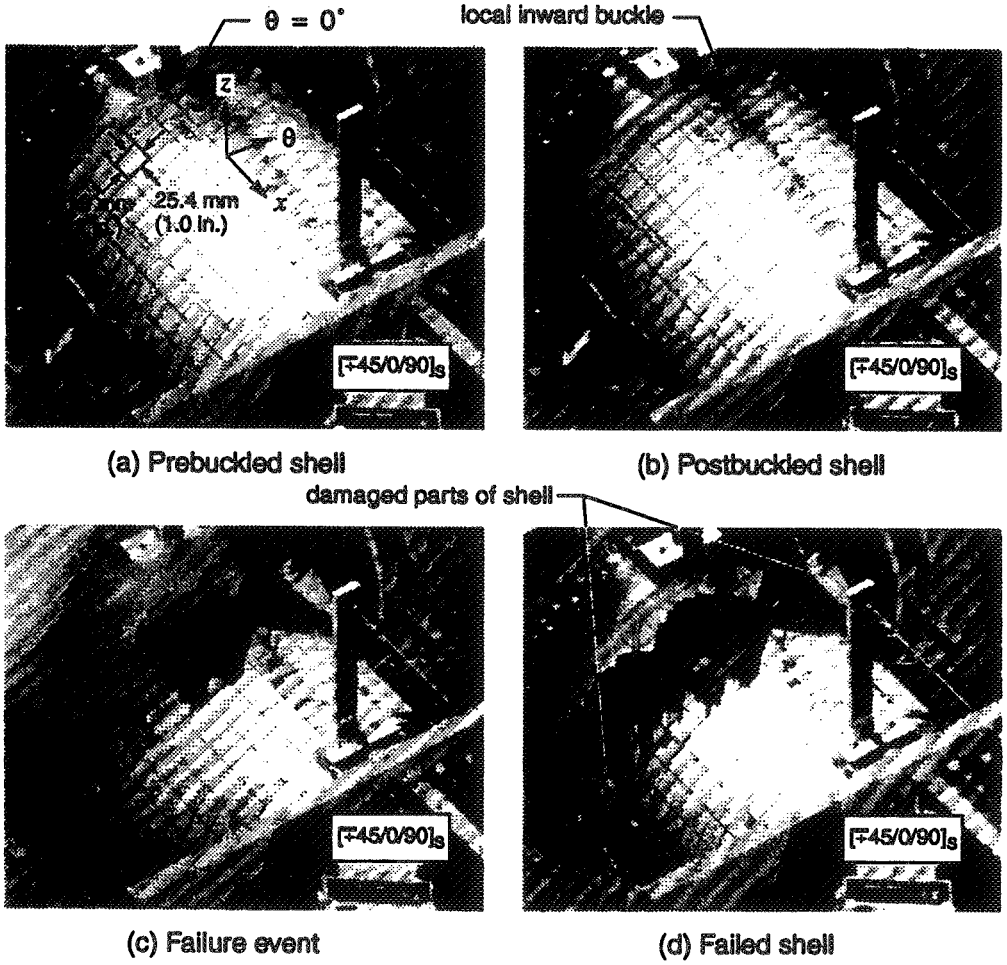

Fig. 11 - Sequence of events observed during testing of internal pressure case

How to Introduce the Imperfection Sensitivity Concept into Design 2*

Isaac Elishakoff
Department of Mechanical Engineering
Florida Atlantic University
Boca Raton, FL 33431-0991

ABSTRACT

The previous review on stochastic buckling of structures was written by Amazigo in 1976. The present review summarizes some of the developments which took place in recent two decades. A brief overview is given of the effect on uncertainty in the initial geometric imperfections, elastic moduli, applied forces, and thickness variation. For the benefit of the thinking reader, the review has a critical nature.

Present essay should be viewed as a direct continuation of our previous paper (1983) with the same title. In order not to repeat what was covered there, it appears instructive to read it although not necessarily prior to dwelling on this article. Accordingly the title is appended with the serial number. It is not promised that the third review will follow since the university science, both fortunately and unfortunately, stands on three things: relevance, interest, and grants.

1. INTRODUCTION

The general theory of buckling and postbuckling behavior of elastic structures and its principle essence-the imperfection-sensitivity theory was worked out by Koiter (1945, 1963). Further contributions were provided by Budiansky and Hutchinson (1964), Stein (1968), Arbocz (1985) and other investigators. For a bibliography the reader may consult, for example, with the review articles by Budiansky and Hutchinson (1966), Hutchinson and Koiter (1970), Stein (1972), Budiansky (1974), Budiansky and Hutchinson (1979), Koiter (1976, 1985), Arbocz (1990, 1997), and Knight and Starnes (1997).

There are many other investigations dealing with the chism that exists between the theoretical analyses and the experimental results. Most unfortunately, the experimental results "misbehave" their way and do not match the theoretical predictions. In these circumstances it was not unnatural to look for the uncertainty as a responsible factor for the scatter in experimental results. One conceptually understands that there exist no two identical shells produced even by the same manufacturing procedure. Motivated by this idea, the investigators could ascribe the scatter in buckling loads to the scatter in initial imperfections.

Next step made was to identify uncertainty with randomness and to utilize the probabilistic methods. We find the first hints of these thoughts in the paper by Hoff (1949):

"...The nature and the magnitude of the disturbance must be established from a statistical investigation of the conditions under which the structural element or part of machinery will be used. The safety of the system can be safeguarded if it is made stable for all disturbances which have a probability greater than a required minimum."

This idea, apparently independently, was pursued by Bolotin (1958). He postulated, in brief, that the buckling load λ of a structure can be

expressed as a deterministic function of a finite number of parameters $\bar{\xi}_i$, representing the initial imperfections:

$$\lambda = \varphi(\bar{\xi}_1, \bar{\xi}_2, \ldots, \bar{\xi}_N) \qquad (1)$$

where N is the number of terms taken in expansions. we also assume that we are given the function φ, as well as the joint probability density

$$f_{\bar{X}}(\bar{\xi}_1, \bar{\xi}_2, \ldots, \bar{\xi}_N) = Prob\left[\bigcap_{i=1}^{N} (\bar{\xi}_i \le \bar{X}_i \le \bar{\xi}_i + \Delta\bar{\xi}_i)\right] \qquad (2)$$

of random initial imperfection vector, denoted by $X = (\bar{X}_1, \bar{X}_2, \ldots, \bar{X}_N)^T$, i.e., the probability that the random components $\bar{X}_i$ of the vector $\bar{X}$ will belong to the interval $(\bar{\xi}_i, \bar{\xi}_i + \Delta\bar{\xi}_i)$, where $\Delta\bar{\xi}_i$ is an increment. Due to assumed randomness of the initial imperfection, the associated buckling load turns out to be also a random variable, denoted by Λ. Note that the random variables are denoted by capitals, whereas the possible values they can take on are identified by lower-case notation. Bolotin (1958) applied this method to a cylindrical panel under uniform compressive load along its curved edges, with the initial imperfections represented by a single normally distributed amplitude parameter. A single-term Galerkin approximation yielded an equation of type (1). Conceptually such an one-term analysis is quite straightforward. Once relation of type (1) is obtained, and the probability density of the initial imperfection $\bar{X}_{i_0}$ is specified or assumed (i_0 is the index of the governing initial imperfection parameter) one calculates the reliability of the structure. The reliability at preselected load level α is defined as the probability that the structure will not buckle prior to α, or, in other words, it will live beyond "age" of α:

$$R(\alpha) = Prob(\Lambda \ge \alpha) \qquad (3)$$

Having determined the reliability of the structure, one proceeds with its design as follows. One should specify a codified reliability r, i.e. the level of reliability below which the performance of the structure is declared as an unacceptable one. The probabilistic design criterion demands

$$R(\alpha) \ge r \qquad (4)$$

Combining Eqs. (3) and (4) results in

$$R(\alpha) = Prob(\Lambda \ge \alpha) \ge r \qquad (5)$$

Inequality (5) leads to a possibility to solve some basic problems of stochastic buckling. If the left and right sides of Eq. (4) are known then one can check if the probabilistic design criterion (4) is met, or it is violated. If some probabilistic characteristic of the initial imperfection, say, its variance $d_{i_0}^2$, is unspecified, one can calculate its maximum admissible level $\max d_{i_0}$, such that the design criterion is satisfied. The value $\max d_{i_0}$ is obtained by solving an equation

$$R(\alpha) = Prob(\Lambda \ge \alpha \,|\, \max d_{i_0}) = r \qquad (6)$$

Solution of this type of problems may then be introduced in the quality control process; if the variance of the initial imperfection exceeds $\max d_{i_0}$ the structure is declared unacceptable. The third problem consists in determining the design load α_r, such that if $\alpha \le \alpha_r$ then the reliability will not be less than r.

The reliability of the symmetrically behaving structure at the nondimensional load level α can be rewritten as

$$R(\alpha) = Prob\left[-\bar{\xi}_1(\alpha) \le \bar{X}_{i_0} \le \bar{\xi}_1(\alpha)\right] \qquad (7)$$

where $\bar{\xi}_1(\alpha)$ is the value at which the limit load equals α. This implies that $\bar{\xi}_1(\alpha)$ satisfies an equation:

$$\lambda = \varphi(\bar{\xi}_1) = \alpha \qquad (8)$$

Hence

$$\bar{\xi}_1(\alpha) = \varphi^{-1}(\alpha) \tag{9}$$

If, for example $\bar{X} \equiv \bar{X}_{i_0}$ is a random variable having a normal distribution with zero mean and mean-square deviation d_{i_0}

$$f_{\bar{X}}(\bar{x}) = \frac{1}{\sqrt{2\pi d_{i_0}}} \exp\left[-\frac{\bar{x}^2}{d_{i_0}^2}\right] \tag{10}$$

Then the reliability becomes:

$$R(\alpha) = Prob\left[-\varphi^{-1}(\alpha) \le \bar{X} \le \varphi^{-1}(\alpha)\right]$$

$$= 2erf\left[\frac{\varphi^{-1}(\alpha)}{2d_{i_0}}\right], \quad erf(x) = \frac{1}{\sqrt{2\pi}} \int_0^{\infty} \exp\left[-\frac{t^2}{2}\right] dt \tag{11}$$

This enables one to find the probabilistic design load α_r, such that if $\alpha = \alpha_r$ than the least reliability of the structure equals r:

$$\alpha_r = \varphi\left[2d_{i_0} erf^{-1}\left(\frac{r}{2}\right)\right] \tag{12}$$

Probability based knockdown factor (P.K.F.) is defined then as

$$P.K.F. = \frac{\alpha_r}{P_{c\ell}} \tag{13}$$

where $P_{c\ell}$ is the classical buckling load.

In order to illustrate the stochastic imperfection sensitivity concept let us consider a simple structure, namely, a column on a nonlinear elastic foundation

$$EI\frac{d^4w}{dx^4} + P\frac{d^2w}{dx^2} + k_1 w - k_3 w^3 = -P\frac{d^2\bar{w}}{dx^2} \tag{14}$$

where $\bar{w}(x)$ = initial imperfection, $w(x)$ - additional deflection, P = axial load, k_1 and k_3 = nonlinear spring coefficients of the foundation. The buckling of the perfect column on a linear foundation is a textbook problem (e.g. Timoshenko and Gere, 1961). The imperfect column on a nonlinear softening elastic foundation exhibits imperfection sensitivity in that the limit load the structure is able to support may turn out to be far less than the buckling load of perfect, linear, counterpart. Application of the Galerkin method for the column that is simply supported at its ends yields in a single-term approximation the following equation, derived by Fraser (1965) in his Ph.D. dissertation:

$$(1-\lambda)^3 = \frac{81}{32} s \bar{\xi}_m^2 \lambda^2 \tag{15}$$

where $\bar{\xi}_m$ = initial imperfection amplitude associated with m half-sine waves in axial direction, λ = nondimensional limit load, s is a value depending on the physical parameters of the system.

This type of analysis can also be demonstrated on the imperfection sensitivity of a shell with a non-axisymmetric periodic imperfections, studied by Koiter (1963):

$$w_0(x) = gh\left[\cos\frac{i_c \pi x}{L} + 4\cos\frac{i_c \pi x}{2L}\cos\frac{i_c \pi y}{2L}\right] \tag{16}$$

where x = axial coordinate, y = circumferential coordinate, g = non-dimensional initial imperfection amplitude, i_c = the number of half-waves at which the associated perfect shell buckles, L = shell length, h = shell thickness. Koiter (1963) arrived at the following equation relating the buckling load with the initial imperfection amplitude:

$$(1-\lambda)^2 + 6cg\lambda = 0 \tag{17}$$

when $\lambda = P_{\ell im}/P_c$, where $P_{\ell im}$ is the limit load, P_c = classical buckling load of the perfect shell, $c = \sqrt{3(1-\nu^2)}$.

The analysis which is based on a single-term approximation is quite similar in its general spirit but not in its particulars to the asymptotic analysis developed by Koiter (1945, 1963) and Budiansky and Hutchinson (1964). The asymptotic expressions or the equations based on a single-term Galerkin approximations can be utilized for understanding the disastrous influence of initial imperfections on the load-carrying capacity of the structure.

As far as the probabilistic considerations are concerned, we are looking for highly reliable performance, associated with the probability of failure, say 10^{-4} or even less. Realizing this, one immediately should cast a doubt on the possibility that the highly simplified expressions (which, however, are of *extreme* importance to capture the physical phenomenon itself) would accurately predict the required high reliability. In other words, simplified expressions may be unusable to calculate extremely small probabilities of failure. But this is exactly what the society demands, namely small, if not vanishing, unreliability.

It was perfectly valid to utilize a single-term Galerkin approximation in Bolotin's (1958) early work. Analogously, application of Koiter's (1963) asymptotic expressions by Thompson (1967), Roorda (1972) and Hansen and Roorda (1973) served a purpose of illustrating the reliability approach in imperfection-sensitive structures (see also Augusti, 1974). Yet it appears that an industrial designing firm, for example, cannot use such expressions in order to justify the reliability calculations with required extremely small probabilities of failure; taking into account additional terms in Galerkin expansion or additional terms in asymptotic expansions, may significantly alter the resulting probabilities of failure, and invalidate the designs proposed on the basis of single-term or asymptotic approximations. Yet, some very recent works still utilize the deterministic asymptotic expansions for reliability calculations (see, e.g., Cederbaum et al 1996).

We must assume that these fine points were perfectly understood by some investigators quite early, since they did not follow the deterministic single-term or asymptotic methodologies, in conjunction with treating the imperfection amplitude as a random variable.

2. STUDIES BASED ON ERGODICITY ASSUMPTION

In his review paper Amazigo (1976) stresses, relating to the equation (1) postulated by Bolotin (1958):

"It is however a nontrivial problem to obtain on (1) and perform the above analysis for $N > 2$, say. It is this difficulty that limits the effectiveness of this method."

Instead of utilizing the concept of the random variable, as in works by Bolotin (1958) and Thompson (1967), the scholars of the Harvard group correctly decided to adopt the theory of random functions, identifying the initial imperfections as random fields with specified probabilistic characteristics, namely, the mean initial imperfection function and the autocorrelation function. Apparently first such studies dealing with imperfection sensitive structures were undertaken by Frazer (1965) and Frazer and Budiansky (1969). They studied the imperfect column on a nonlinear elastic foundation. The length of the column was taken to be infinity. The following assumptions were made about the initial imperfection field : (a) they were considered to form a weakly homogeneous random field, (b) the assumption of ergodicity of this field was also introduced.

Weak homogeneity implies that the mean initial imperfection function is a constant, whereas the autocorrelation function depends only on the difference $x_2 - x_1$, where x_1 and x_2 are spatial coordinates. Hence the mean square value of a homogeneous random function is constant too. The weak homogeneity, or insensitivity to the shift of initial cross-section of reference is possible for infinite domains. Therefore, possibly, the infinite length assumption was adopted. For solving the problem Fraser and Budiansky (1969) resorted to the classical method of stochastic linearization and the additional assumption, that the *output* random field, namely the additional deflection of the column, was ergodic too. The main conclusion derived in the paper was that each infinite column in the ensemble has the *same, deterministic buckling load*, which depends on the autocorrelation function of the initial imperfection *alone*, not on a particular realization of

any of them. In his review Amazigo (1976) comments on the ergodicity assumption:

"The method...based on the ergodicity hypothesis leads to the conclusion that the structure will buckle statically or dynamically at the corresponding (deterministic- I.E.) load... with probability 1. This result may appear paradoxical. However, to dispel the apparent contradiction we note that no matter how the origin of an infinitely long column is defined the buckling load for such columns with imperfections $\overline{w}(x) = \sin(x + \phi)$ *is independent of* ϕ *and hence independent of any probabilistic distribution we may assign to* ϕ*."*

Authors probably themselves did not anticipate the above surprising result. Thus, several other methods have been applied. Stochastic linearization was utilized in the paper by Amazigo et al (1971), method of truncated hierarchy was employed by Amazigo (1969), method of perturbation was used in the papers by Amazigo (1971, 1974), whereas in his review paper Amazigo (1976) employed an extension of Poincare's perturbation method in the context of the dynamic buckling load. Invariably, for infinite structures with ergodic initial imperfections the deterministic buckling load either static or dynamic,resulted.

Later von Slooten and Soong (1972) (see also the discussion of it), and Fersht (1968) in Ph.D. dissertation again arrived at a deterministic buckling loads. As Fersht (1974) remarked:

"This [ergodicity-I.E.] assumption substantiates a considerable simplification in the solution of the problem independently of the method of approximation used."

Not discussing the question of validity of the assumption or the final results, as well as their practicality, Fersht (1974) noted: "*Qualitatively, the results obtained are as anticipated.*" It was also correctly concluded that,

"...perhaps a more difficult task would be to justify the results obtained."

It appears to us that the source of the above paradoxal result stems from the fact that the authors assumed the ergodicity not only of the *input* field, but also of the *output* field. This assumption allowed to facilitate the analytical solutions that were derived. In order to check the validity of such an assumption Scheurkogel et al (1981) undertook an investigation of a model system, which allowed to obtain closed-form solution. Then the same problem was solved by invoking the ergodicity assumption. A control parameter k was introduced so that one could study the changing behavior of the system as the control parameter was varied. It turned out that, in general, the output of the system was *inergodic*. At some value of the parameter, namely, $k = 2$, the ergodicity assumption yielded a result coinciding with the response obtained exactly. This implies that sometimes the error may not affect the estimate of the system's response (the ergodicity assumption constituted a "good" error)! In two distinctive ranges of variation of parameter k the behavior turned out to be of different nature. For $0 \leq k < 2$ the ergodicity assumption introduced a small error of the order of one percent. Yet, for $2 < k \leq 4$ the ergodicity assumption led to large errors. In particular, when k tends to 4, the ergodicity-based solution is finite, whereas the exact solution is unbounded. As is seen, extreme caution must be exercised when invoking the ergodicity assumption: the differential equation itself, rather than an analyst, should be given a freedom to decide if the output is ergodic or not.

Closely related conclusions were arrived at in another investigation (Scheurkogel et al, 1985) which investigated a specific applied mechanics problem, in which Bolotin (1971) also utilized an ergodicity assumption.

3. MONTE CARLO METHOD

Although the present writer was not a stranger to the stochastic buckling, through the works by Bolotin (1958), Makarov (1970) and Leizerakh (1969) the more deep interest into this subject was prompted rather incidentally. During the academic year 1977/78, Professor B. Budiansky was supposed to spend a sabbatical year at the Department of Aerospace Engineering of the Technion-Israel Institute of Technology. Head of the Structures Group, Professor J. Singer recommended me to investigate some problems which may generate an interest of the distinguished sabbatical visitor. Without taking an obligation to do so I decided to study some of the works of Professor B. Budiansky in more detail.

Amongst others, I read several elegant articles of Budiansky and Hutchinson devoted to the imperfection sensitivity of structures. When reading the article by Frazer and Budiansky (1969) about the buckling of a column with stochastic imperfections, their result struck me: the realizations of the columns are different, yet they all share the same, deterministic buckling load! Yes, this load did depend on the probabilistic characteristic of the imperfection, yet it was *shared* by all other columns by unity probability. Interestingly this load depended upon the single value of the spectral density of initial imperfections, and was independent, otherwise, on the spectral content of the field.

To illustrate this point let us reproduce the formulas for *deterministic* buckling loads derived for shells. Amazigo (1969) obtained following expression for the static buckling load of a circular cylindrical shell:

$$(1-\lambda_s)^{7/2} = \frac{9\pi c^2}{2\sqrt{2}} S(1) \qquad (18)$$

where $S(1)$ is the power spectral density of the imperfection spectrum $S(\omega)$ evaluated at the frequency corresponding to the classic asymmetric buckling mode, $\omega = 1$. Later on, Amazigo and Budiansky (1972) presented a modified formula

$$(1-\lambda_0)^{7/2} = \frac{9\pi c^2}{2\sqrt{2}} S(1)\lambda_s^2 \qquad (19)$$

According to the authors, this formula should provide a more accurate estimate for λ_s, the buckling load of the imperfect shell. Tennyson et al (1971) proposed to evaluate S(1) by utilizing the power spectral density corresponding to an exponentially cosine autocorrelation function

$$S(\omega) = \frac{\Delta^2 \zeta (\omega^2+\zeta^2+\gamma^2)}{\pi[\omega^4+2(\zeta^2-\gamma^2)\omega^2+(\zeta^2+\gamma^2)^2]} \qquad (20)$$

where Δ^2 = mean square value of the imperfection. By setting $\omega = 1$, $\zeta = 0.2$ and $\gamma = 1$, they obtained

$$S(1) = 2.52\Delta^2/\pi, \qquad (21)$$

with Eq. (19) taking a form

$$(1-\lambda_s)^{\frac{7}{2}} = \frac{9c^2}{2\sqrt{2}} (2.52\Delta^2)\lambda_s^2 \qquad (22)$$

Amazigo and Budiansky (1969) cautioned that the use of Eq. (19) will lead to incorrect results of the actual power spectral density does not peak near $\omega = 1$.

Yet, it appeared to the present writer that the very constancy of the buckling load should have been questioned. It was decided that instead of pursuing some new, purely analytic approach, in addition to what was already undertaken at Harvard, it would be nice to perform an experiment. Yet, where should one get numerous realizations, a thought occurred, of the real columns on nonlinear elastic foundations? If not in a real laboratory, then may be in the virtual one, on the computer? Thus the idea occurred to study the Frazer-Budiansky problem by the Monte Carlo simulation.

The idea did not seem to be very fancy or even new. Indeed, Frazer (1965) himself already has performed the Monte Carlo analysis of a column on a nonlinear foundation. Yet, most unfortunately, he limited himself with a single-term approximation. Such an analysis leads, once this assumption is made, to a closed-form solution, given in Eq. 11, for the reliability. Naturally, one does not need the Monte Carlo solution if the exact solution is at hand, unless one wants to illustrate the validity of the Monte Carlo solution in the particular case that is capable of the exact solution. Once the confidence is gained through such a comparison, if it is favorable, one resorts to the multi-mode Monte Carlo solution where the exact solution is unavailable. The Monte Carlo method had to be combined with the multi-mode approximation, rather than with a single-term approximation performed by Frazer (1965).

Multi-term Monte Carlo simulation was suggested by Hansen (1977) in his probabilistic analysis of randomly imperfect shells. However, the analysis performed could be characterized as an unbalanced one: a detailed analytical analysis was

superimposed with somewhat naive probabilistic analysis. The assumption was made that all the Fourier coefficients used in the series expansion were *identically* distributed. Namely, each Fourier coefficient was taken as a normally distributed variable with the same variance. This assumption in essence corresponds to the "white-noise" autocorrelation function of the initial imperfections. Thus, the analysis did not allow the information on general autocovariance function. Indeed, there exists no compelling reason for initial imperfections to be a spatial "white noise." Some other investigators too, although in a dynamic context, essentially followed Hansen-type analysis. They neglected correlations between the various Fourier coefficients, although adopted the nonconstant variances (with a new term coined for such imperfections: "grey noise" (Lindberg, 1983).

It was realized by this writer that the simulation analysis should start from the multi-dimensional probability densities; the correlation analysis must start from the mean function and the autocorrelation function, and end up with the variance-covariance matrix of initial imperfection's Fourier coefficients or of any other random variables, stemming for the suitable discretization. This matrix, in general case, must be a fully populated one: not a diagonal one with identical (Hansen, 1977) or different (Lindberg, 1993) elements. In order to study the Frazer-Budiansky model structure the present writer developed a general simulation procedure for solving the stochastic boundary value problems (Elishakoff, 1979).

This simulation procedure was applied to several probabilistic problems; the impact buckling of a column (Elishakoff 1978), Hoff's problem of buckling of a column in a testing machine (Elishakoff, 1980) and to the Frazer-Budiansky problem (Elishakoff, 1979). In a latter paper a column of *finite* length was studied because of several reasons: (1) an assumption of infinite length may simplify the analytical analysis but may complicate the numerical one, (2) the structures utilized and analyzed by engineers (fortunately) do not posses with the infinite length, (3) the nonlinear column on nonlinear elastic foundation in previous studies was not analyzed in terms of the edge-effect method to justify for looking for interior solutions (as those associated with the infinite structure), and corrective edge effect solutions. Moreover, why should one make an assumption of infinite length if the Monte Carlo solution for realistic finite-length shells is easier? In the study Elishakoff (1979), for each realization buckling load was determined numerically by transforming the nonlinear algebraic equations to the numerically solved ordinary differential equations. The adopted method of Qiria (1951) and Davidenko (1953) is similar to the arc-length method of Riks (1979), as was communicated to this writer by Professor W. T. Koiter. Reliability of the column was calculated. Following conclusions were drawn:

(1) Monte Carlo solution yields results that are practically coincident with the exact solution, when the latter is obtainable for the single term approximate problem. This demonstrates that the Monte Carlo solution may exhibit a better performance than the various statistical tests may forecast.
(2) A single-term Galerkin approximation is not sufficient to accurately predict the structural reliability; depending on the system's parameters, various degrees of approximation but higher than one must be achieved in order the reliability estimates to be accurate.
(3) Design buckling load associated with high reliability may significantly deviate from the average buckling load.
(4) When the length of the column increases the variance of the buckling load decreases.

The latter conclusion may represent a link with the result of Frazer and Budiansky (1969) who concluded that for an infinite column the buckling load was a deterministic quantity. However, for the realistic finite column the buckling load depends on the particular realization of the initial imperfection function, which in turn depends on the probabilistic measures (mean and autocorrelation function) of the initial imperfections.

In a later analysis, Day (1980) showed that in some simple cases the ergodicity assumption may even be dispensed with for the evaluation of the *mean buckling load*. Yet the analyses yielding mean buckling load alone could hardly be considered practical. Each of us may remember various, sometimes entertaining, objections to average

quantities, and they will not be recapitulated here. Anyway, the knowledge of the average buckling load is insufficient for probabilistic design of structures undergoing buckling.

The development of a general simulation procedure for initial imperfections with given mean and autocorrelation functions pinpointed the way of introducing the initial imperfection sensitivity into design. It involves three main items:

(a) Development of accurate deterministic (analytical or numerical) tools, for buckling load prediction.
(b) Compiling extensive experimental information on imperfections, boundary conditions, elastic properties, scatter in loads etc., in view of deriving mean functions, and their autocorrelation functions of random fields, and assessing their distributions.
(c) Utilization of the Monte Carlo analysis through simulating brothers and sisters (but not perfect clones!) of the experimentally measured structures.

This writer was humbled to read in several publications of Arbocz (1981, 1982, 1987):

"It was not until 1979, when Elishakoff published his reliability study... that a method has been proposed, which made it possible to introduce the results of imperfection surveys into the analysis."

Clearly, the future of the shell buckling analysis is identified by Arbocz in his recent articles with the notion of stochasticity (see, e.g., 1997).

In accordance with the recommendation of Professor W. T. Koiter, the early study (1979) was generalized to include both the quadratic and cubic nonlinearities of the elastic foundation (Elishakoff, 1985).

4. RELIABILITY OF SHELLS OR HOW THE BEAUTIFUL THEORIES HAVE TO COMPLY WITH UGLY FACTS

In order to proceed further, it is instructive to review first some other deterministic developments. Fortunately, some investigators of thin shells were interested with experimental analyses.

Arbocz (1968) devoted his Ph.D. dissertation to the careful experimental measurements of initial imperfections of shells designed and manufactured in the laboratory of the California Institute of Technology. In 1968 and 1969 Arbocz and Babcock reported their results on buckling experiments. They measured initial imperfections and the prebuckling growth of electroplated isotropic shells via automated scanning mechanisms. Singer et al (1971) reported results of analogous imperfection surveys on integrally machined ring-stiffened as well as stringer-stiffened shells. These studies provided a data for possible correlation of experimental buckling results with the theoretical or numerical prediction of the buckling loads. Such a correlation study would establish a feasibility of direct incorporation of the initial imperfection measurements into the (deterministic) theoretical procedure or the numerical code, with attendant direct comparison between the results. These results were reported by Babcock (1974) and Arbocz (1974) and other authors.

It was indicated by Arbocz (1974, p. 238), that

"Results of initial correlation studies seem to indicate that it may be possible to predict the buckling load of the structure to within +10% using a two-mode imperfection model with quadratic terms only, if the size of the measured harmonies is less than 20% of the wall thickness and the lowest classic eigenvalue is located within the region of the lower-order modes."

There were "better" results reported too, in the literature. Arbocz (1974, p. 236) in Table 5, reports the result by Hofmeister (1972) when *both* the experimental and the theoretical buckling loads of myler, normalized to the classical buckling load, constituted 0.52. Such a perfect coincidence is an exception, rather than an already achieved goal. Usually, when such a coincidence takes place one wonders if it was by pure chance, and if either experiment or the theory evaluation were properly conducted. For example, the following question arises: Were there myler shells analyzed as isotropic or orthotropic ones? (Singer, 1997).

Experimental verification of Koiter's special theory has been given by Tennyson and Muggeridge (1969). They tested a series of photoelastic plastic circular shells containing an axisymmetric imperfection. The specimens were manufactured by

the special spin-casting technique to produce near perfect cylinders. Experimental points all were within about 10% of Koiter's special theory; remarkably, in some cases the error was of order of 2%. For a stringer-stiffened shell AS-2, Arbocz (1981) reported value produced by a computer code STAGS (30 node model) of 243.8 N/cm, whereas the experimental value 226.3 N/cm was about 7% off. For shell A8, Arbocz (1981) reported a nondimensional experimental buckling load 0.66, whereas the theoretical prediction constituted 0.69. For shell designated AB-6, the experimental nondimensional buckling load constituted 0.75 whereas the theoretical estimate was 0.72 (Singer, 1983, Table 27.5). In parallel, Makarov (1969) performed extensive measurements of the initial imperfections profiles at the Moscow Power Engineering Institute in view of studying their statistical characteristics.

Being encouraged with the mere possibility of the relatively good correlation between the experimental and numerical results (and hopefully even a better one once the boundary conditions could be *closely* identified), it occurred to the present author that the probabilistic analysis must be tied with the numerical and experimental developments in a hybrid manner. The experimental developments in Caltech, Technion, University of Toronto, and the Moscow Power Engineering Institute influenced present writer's thinking in parallel to trying to investigate the effects of the ergodicity assumption suggested at Harvard. In 1975, Professor J. Arbocz, then a Senior von Humboldt Fellow of the DFVLR in Federal Republic of Germany, delivered a series of lectures in the Israel Institute of Technology's Aeronautical Department. The titles of the lectures were:

(a) "Prediction of Buckling Loads Based on Experimentally Measured Initial Imperfections" (4.23.1975).
(b) "Some Problems Associated with Data Handling When Measuring Initial Imperfections" (4.28.1975).
(c) "Accurate Numerical Methods for Computing the Buckling Load of Axially Compressed Imperfect Cylindrical Shells" (4.30.1975).

Listening to these "deterministic" lectures carefully , this writer thought that time was ripe to apply probabilistic methods, but in a different setting than before. Following year, in 1976 at the IUTAM Congress in Delft I have informed Professor Arbocz that I had some ideas to impart a "soul of uncertainty" into the available deterministic numerical codes and experimental data. He requested that I communicate my ideas in writing, for their close inspection and possible cooperation.

This was a time when Professor Budiansky's arrival to the Technion accelerated my interest in the imperfection-sensitivity concept. It was quite natural that I gave a preference to spending my first sabbatical year ("Why should I refuse this 'capitalistic' luxury?") at the Delft University of Technology, rather than elsewhere. A weekly seminar in the Department of Technical Mechanics, to which Professor W. T. Koiter lectured at least five times during that year, was extremely stimulating, along with the atmosphere of an unusual courtesy and good will, and the excellent technical support conditions. My host, Professor J. Arbocz met me with extreme encouragement and honesty: *"I certainly do not believe a thing in probability theory, but you can try to convince me that it makes sense!"*

First thing of business became to analyze the initial data banks just compiled (Arbocz and Abramovich, 1979). Two group of shells, designated as A-shells and B-shells, respectively, were statistically analyzed (Elishakoff and Arbocz, 1982) from the compiled data bank. Estimated variances of the measured initial imperfections were plotted as functions of the axial coordinate for group of A-shells (see Fig. 7 in Elishakoff and Arbocz, 1981) and B-shells (see Fig. 10). These variances were *not constant*, implying that the experimental initial imperfections can not be treated as a weakly homogeneous random field, let alone an ergodic one. This demonstrated, that the works based on the ergodicity hypothesis could not be characterized as practical. The fact that in another collection of shells, measured at the Moscow Power Engineering Institute, the experimental data did not contradict to the assumption of the weak homogeneity of initial imperfections of circular cylindrical shells in the circumferential direction (Makarov, 1969, 1970) appears to be surprising, since the latter shells had a seam.

The experimental results neither supported the assumption made by Hansen (1977), namely, that the Fourier coefficients of initial imperfections were statistically independent and distributed identically. Nor the imperfections constituted a "grey" noise as suggested by Lindberg (1993). Thus, statistical analysis of real shells vividly illustrated that *none* of specialized assumptions made in the literature about the probabilistic pattern of the initial imperfections were justified. It should be immediately noted, to "protect" authors of above studies, that these assumptions were made not arbitrarily: these assumptions either enabled the theoretical treatments of various kinds (work performed at Harvard university), or reduced the computational effort (work performed at Moscow Power Engineering Institute or University of Toronto).

One may clearly recognize the appropriateness of the quotation, which, as Professor J. Arbocz informed me, was exhibited on the wall in the office of Professor E. Sechler, in Caltech:

"The great tragedy of Science - the slaying of a beautiful hypothesis by an ugly fact" (Thomas Henry Huxley, 1825-1895).

Thus, the assumption of homogeneity in axial direction, employed in the West, as well as its counterpart on the homogeneity in the circumferential direction utilized in the East, did not prove to be viable hypotheses. In addition, dealing with infinitely long shells in conjunction with the hypothesis of ergodicity diverted an attention of the investigators from the main goal of the reliability of the structure, which can be utilized for design purposes. On the other hand, single-term Galerkin approximations, although did concentrate on the reliability, could not catch the reality properly, since too much was neglected.

As this junction it appears instructive to recapitulate the assessment of an study by Miller and Hedgepeth (1979) from the review in buckling by Budiansky and Hutchinson (1979):

"The intermediate situation, in which not a few but also not very many modes must be considered to have stochastic imperfections, has been addressed in [50] (i.e. by Miller and Hedgepeth, 1979 - I.E.), when the problem of a lattice column with random imperfections in the individual members is tackled. Through the use of effective approximations results for the means and variances of buckling loads are estimated, with accuracies confirmed by Monte Carlo calculations."

Indeed, dealing with the *finite* structure, on one hand, and the ability to determine *both* the mean values and variances of the buckling loads in the multimodal setting was a major step, yet the paper by Miller and Hedgepeth (1979) did not address the main issue of reliability determination; reliability, rather than first and second moments can be utilized in design. One may argue that the Gaussian assumption of buckling loads would yield the reliability once the first and second moments were calculated. Such an assumption would be incorrect, for the probability density is highly skewed (see, eg. Figs. 5.27 and 11.9, Elishakoff 1983) as both the single-or multi-mode analyses would clearly demonstrate.

Special simulation procedure (Elishakoff, 1979) was applied to shells with axisymmetric imperfections (Elishakoff and Arbocz 1982) as well as to shells with general nonaxisymmetric imperfections (Elishakoff and Arbocz 1985). The assumption of uncorrelatedness of some of the Fourier coefficients adopted in the latter paper, was dispensed with in later study (Elishakoff, 1988).

Next step in the analysis, following the Monte Carlo simulation of the "brothers" and "sisters" of experimentally measured shells, is the performance of the buckling calculations of each simulated shell by the special procedures. These procedures include special theory by Koiter (1963) for asymmetric shells, multimode analysis of Arbocz and Babcock (1976), the finite element method (Ernst, 1979) for the general non-axisymmetric shells, as well as other analytical studies or numerical codes, like STAGS, etc.

Once large amount of realizations were at hand, the reliability of the shells was possible to compute as the fraction of shells that did not fail prior to predetermined load level. This "*Assume As Little As Possible*" approach, if not yet "*Assume Nothing*" method in dealing with the problem directly combined three major ingredients, which were previously unconnected: theoretical, numerical and experimental sides of the buckling research.

Previous paper, under the same title as this one (1983), presented the following course of action

for choosing the gap between the theory and the practice:

"... introduction of the initial-imperfection concept into design calls for:
(1) Further development of combined analytical, numerical and experimental tools for predicting the buckling loads under deterministic imperfections (the deterministic analysis being one of the cornerstones of the Monte Carlo method), with appropriate establishment of the accuracy so vital for the reliability prediction,
(2) compilation of extensive experimental information on imperfection-sensitive structures, classified according to the manufacturing process, with a view to finding their mean and autocovariance functions.
With the above developments in analytical, numerical and experimental tools and compilation of experimental information, the Monte Carlo method is a promising means for narrowing the present chasm between the theory and practice."

5. HOW TO CORROBORATE THE MONTE CARLO ANALYSIS?

Monte Carlo method is applied by the investigators when the exact solution is not available. Yet, some other approximate methods may be available to tackle the stochastic boundary value problems in question. Once such an approximate solution is obtained, the investigators, almost invariably, check it versus the Monte Carlo simulation. But both methods are approximate in their nature. Which one is preferable in these circumstances? Usually investigators think that the non-Monte-Carlo method is the preferable one as a "cheaper" technique. Yet, such a premise calls for a reexamination.

Two considerations are of importance in this respect. The Monte Carlo simulation technique is an universal tool, applicable, for example, for small or large deviations of random variable or functions involved. The other approximate techniques invariably have limited areas of application. They may be effective, for example, when coefficients of variations are small. When we perform both the Monte Carlo analysis and the other, approximate evaluation, which method *checks* the other then?

Usually, researchers "promote" their own approximate technique; then, as they maintain, they compare it with the Monte Carlo method, since the exact solution is unavailable. Yet, they check the method of a restricted range of application with the one of a wider validity. It appears then reasonable to claim that in the general case the Monte Carlo method should be used, as an universal technique. Yet, since it is in essence a computerized experimental method, the other, approximate analytical techniques should be utilized to check it. Such a conclusion may appear to be paradoxal, at the first sight. Yet, for a specific set of parameters one approximate method may be of validity; for other sets of parameters other method may prove to be applicable. Both should be in vicinity of the results furnished by the Monte Carlo method, although in different ranges. It becomes obvious that the general method is being checked by methods of limited applicability. Analogous view is shared by Professor Shinozuka (1996).

It appears to be a must to confront the results delivered by the Monte Carlo method by different analytical-numerical techniques which may be effective in specific ranges of variation of parameters. One such method is a second-order second moment method. For its detailed exposition the reader may consult with the paper by Hasofer and Lind (1974), and numerous later texts. This method has been extended by Elishakoff et al (1987) to include nonlinear buckling of shells with initial imperfections treated as random functions.

The cornerstone of the method is the availability of a deterministic state equation

$$Z = Z(X_1, X_2, \ldots, X_N) \qquad (23)$$

where $Z(\ldots)$ is a *performance function*. Its nature depends on the type of the structure and the limit state considered. According to the definition the equation

$$Z = 0 \qquad (24)$$

determines the failure boundary. The inequality

$$Z < 0 \qquad (25)$$

implies failure, whereas the inequality

$$Z > 0 \qquad (26)$$

indicates a successful performance. *Zeroth-order* second moment method requires linearization of the

function Z at the *mean* points $E(X_i)$ and the knowledge of the distribution function of random vector X. Calculations are relatively straightforward if X is normally distributed. If X is not normally distributed, an appropriate transformation must be made.

In the case under investigation, we are interested in knowing the reliability of the structure at any given load λ, i.e.

$$R(\lambda) = Prob(\Lambda \geq \lambda) \tag{27}$$

where Λ is the random buckling load. A function Z can then be defined as follows:

$$\begin{aligned} Z(\lambda) &= \Lambda - \lambda \\ &= \varphi(X_1, X_2, \ldots, X_N) - \lambda \end{aligned} \tag{28}$$

where λ is the applied deterministic load, $\varphi(X_1, X_2, \ldots, X_N)$ is the relationship whose knowledge was postulated by Bolotin (1958), as per Eq. 1. However, when such a relationship is not available analytically, we can visualize that the availability of the numerical code is *equivalent* to the knowledge of this function. To combine numerical codes developed for example, by Arbocz and Babcock (1980) with the zeroth order or first-order second-moment method, we need to know the lower order probabilistic characteristics of Z. In the first approximation, for small variances and covariances if X_j, we have:

$$\begin{aligned} E(Z) &= E(\Lambda) - \lambda \\ &= E[\varphi(X_1, X_2, \ldots, X_N)] - \lambda \\ &\simeq \varphi[E(X_1), E(X_2), \ldots, E(X_N)] - \lambda \end{aligned} \tag{29}$$

The variance of Z is given:

$$\begin{aligned} Var(Z) &= Var(\Lambda) \\ &\simeq \sum_{j=1}^{N} \sum_{k=1}^{N} \left[\frac{\partial \varphi}{\partial X_j}\right]_0 \left[\frac{\partial \varphi}{\partial X_k}\right]_0 Cov(X_j, X_k) \end{aligned} \tag{30}$$

where $Cov(X_j, X_k)$ is a covariance of components X_j and X_k of initial imperfections, determined through experimental measurements. Calculation of the derivatives $(\partial \varphi / \partial X_j)$ at mean values of the arguments $X_{j0} = E(X_j)$ is performed numerically. Having estimated $E(Z)$ and Var(Z) one obtains the estimate for the probability of failure at the load level λ:

$$\begin{aligned} P_f(\lambda) &= Prob(Z<0) = \Phi(-\beta) \\ \Phi(x) &= \frac{1}{2} + erf(x) \end{aligned} \tag{31}$$

where

$$\beta = E(Z)/\sigma_Z \tag{32}$$

where σ_Z is the mean square deviation of Z

$$\sigma_Z = \sqrt{Var(Z)} \tag{33}$$

Numerical analysis for the unstiffened circular cylindrical shells were reported by Elishakoff et al (1987), and showed a good correlation with the Monte Carlo method. More accurate method is the first-order second moment method, or, as it is universally referred to the *Level 2* method. In the buckling context it is performed as follows (Elishakoff, 1984): For simplicity we consider, a problem involving two initial imperfection parameters X_j and X_k, forming a random vector X. Through the initial imperfection data banks one obtains the mean values $E(X_j)$, $E(X_k)$ and the variance covariance matrix

$$[C] = \begin{bmatrix} Var(X_j) & Cov(X_j, X_k) \\ Cov(X_j, X_k) & Var(X_k) \end{bmatrix} \quad (34)$$

We denote the vector of *basic variables* by Y, they have zero means and unity variances. Then

$$X = C^{1/2}Y + E(X) \quad (35)$$

whence

$$Y = \left[C^{1/2}\right]^{-1} \left[X - E(X)\right] \quad (36)$$

and $C^{1/2}$ is the square root of a positive-definite matrix C. For every realization of Y we find immediately the realization of X, and via the computer programs developed by Arbocz and Babcock (1980) we determine the buckling load. This allows one determine the failure boundary for fixed values of α

$$Z = \alpha - \lambda = 0 \quad (37)$$

How to find the failure boundary? This can be done as follows: One specifies the direction

$$\ell = (i\cos\gamma + j\sin\gamma)\ell \quad (38)$$

At the top of the vector we check if the boundary load exceeds α. If it does not, we enlarge the length of the vector and repeat the procedure. If the buckling load still does not exceed α, we continue the process. If the buckling load is in access of α, we multiply the length of the vector by a number less than unity and repeat the process till we reach the point at which buckling loads is nearly α, within demanded accuracy. Then we rotate the vector ℓ, by changing the angle γ, and repeat the process. This allows one to find the failure boundary. Then the smallest distance to the failure boundary, in case there are no multiple points with the same minimum distance, is determined from the origin of the coordinates to the failure boundary. The distance is denoted by β_{HL} as a Hasofer-Lind index. The probability of failure is given by Eq. (30), where β is replaced by β_{HL}. This procedure (Elishakoff, 1984) awaits for its numerical implementation for buckling of structures.

The zeroth-order second moment method has been applied by Arbocz and Hol (1991) and by Arbocz (1997) for integrally stringer- stiffened shells. Computationally it is much less expensive than the direct Monte Carlo method. Yet the latter is applicable for *arbitrary* coefficients of variation, whereas the former is valid only for *small* variation of the initial imperfection amplitudes. This basic premise may not hold true for many cases reported in the initial imperfection data banks. In addition, the reliability estimates furnished by the zeroth-order and first order second moment reliability estimates may be quite substantial.

It appears that the methods developed in past two decades in collaboration with Professor J. Arbocz illustrate that the *imperfection*-sensitivity concept can be introduced into practice. This will allow the theoretical findings to be directly introduced into codes, instead of well known "knockdown factors."

It should be stressed, that in the methods developed we do not try to match the known knockdown factors; if this were the case probabilistic methods would not have a predictive power, and would only constitute a "forecasting of the past." Yet, one must emphasize that the extremely intelligent effort are needed for probabilistic method to be implemented into practice: it needs sophisticated measurement devices to measure initial imperfection profiles. Fortunately, this is possible, as was shown in various laboratories in different parts of the world. Then the results of the measurement have to be statistically interpreted, in view of checking hypotheses on their distribution. If Fourier coefficients are involved, the *joint* probability distributions are needed rather than the *marginal* ones. The probabilistic analysis must be superimposed with the accurate deterministic analysis, based on either FEM or the multimode Galerkin approximations. If the mean square deviations of initial imperfections are small in comparison with their mean values, one can use the zeroth-order or the first- order second- moment method; if the coefficient of variation is moderate or large, it appears that one should use the Monte Carlo method. If the direct realization of this technique is employed, without variance reduction techniques, one may need the supercomputer environment or massively parallel computing facility, to perform sufficient amount of

Monte Carlo simulations for determining sufficiently small probabilities of failure with acceptable accuracy.

But let us try to contradict ourselves: May be we have neglected some important facets of the problem? For example, what about the boundary conditions? This problem is discussed in the following section.

6. CORRECT MODELLING OF BOUNDARY CONDITIONS IN AN EXTREMELY NON-TRIVIAL TASK

In order to be able to determine small probabilities of failure, one needs extremely accurate deterministic theories. Buckling load calculations naturally involve satisfaction of the boundary conditions. How to be able to model them sufficiently accurately? For beams, the determination of the boundary conditions appears to be a treatable task. Studies by Horton et al (1969) and by Sweet et al (1976, 1977) may support such a conclusion. For shells their determination appears to be an extremely complex task. When considering the effect of boundary conditions the existing studies predict relatively small influence of the boundary conditions for isotropic unstiffened shells (Almroth, 1966), if the movement of the edges in circumferential direction is restrained. However, the influence of these is significant for stiffened shells, as was demonstrated by Arbocz and Sechler (1976). Buckling loads for the specific integrally stiffened shell XS-1 with SS-3 and SS-4 boundary conditions, respectively, were 141.6 lb/in and 184.5 lb/in. Yet, for the same shell with C-3 and C-4 boundary conditions the buckling loads were, respectively 161.6 lb/in and 204.0 lb/in. Experimental data on stiffened shell buckling were reported by Singer et al (1971). As authors mention (p. 72, right column)

"The details of the end ring supports for the shell (Fig. 4) (not reproduced here - I.E.) were examined to find the effect of the elastic constraints. It was found that the experimental end conditions were rigid enough to consider the shell fully clamped (C-4)."

Elishakoff et al (1992) write

"...the boundary conditions on the experiment were neither "purely" C-3 nor "purely" C-4. Therefore, in order to meaningfully compare the experimental and analytical results on the buckling loads, more realistic conditions should be incorporated in the analysis with attendant probabilistic analysis."

Recall that SS-3 boundary conditions stipulate that

$$N_x = v = w = M_x = 0 \qquad (39)$$

whereas SS-4 boundary conditions require

$$u = v = w = M_x = 0 \qquad (40)$$

where u, v and w are axial, circumferential and transverse displacements, respectively, N_x = axial load, M_x = bending moment. It was suggested in the latter reference to consider following mixed boundary conditions, denoted SS-34:

$$\alpha N_x + \beta u = v = w = M_x = 0 \qquad (41)$$

These generalized boundary conditions are reducible to the boundary conditions given in Eqs. (39) and (40). Specifically, for $\alpha = 0$ and nonzero β, the boundary condition reduces to Eq. (40), whereas for $\beta = 0$ and nonzero α we recover Eq. (39). For non-zero α, the boundary condition 40 is rewritten as

$$N_x + K_x u = 0 \ , \ K_x = \beta/\alpha \qquad (42)$$

In order to accommodate the best resemblance with the experimental realization of boundary conditions K_x in Eq. (42) should be treated as a function of the circumferential coordinate θ. The following dependence was chosen

$$K_x(\theta) = \begin{cases} K_1 \ , \ for \ \theta_{2i} \le \theta \le \theta_{2i+1} \\ K_2 \ , \ for \ \theta_{wi+1} \le \theta \le \theta_{2i+2} \end{cases} \qquad (43)$$

where serial number i varies between zero to eight, $\theta_0 = 0°$, $\theta_{18}=360°$. In addition, $K_2 << K_1$. This implies that the shell is attached to the apparatus with nine relatively strong springs with stiffness K_1 and nine relatively weak springs with stiffness K_2.

It should be stressed that the uniform axial springs have been considered in the shell buckling, in linear setting, by Singer (1962). Nonuniform boundary conditions along the circumference, in the context of boundary imperfections, were first treated by Hoff and Soong (1967) with identical non-

uniformity at both edges of the shell; if this nonuniformity can be characterized as a boundary imperfection, one can say that they considered "perfect imperfections." This assumption has been abandoned by Stavsky et al (1988) and Sabag et al (1989) who considered realistic "imperfect imperfections," i.e. nonidentical imperfections on shell's two edges.

Although the problem of nonuniform support conditions for nonlinear, imperfect shells was formulated by Elishakoff et al (1992), the numerical results yet have to be reported. This latter paper led to more appreciation of difficulties in modeling of "true" boundary conditions. Recently another close look at the realization of boundary conditions in experimental setting was undertaken (Arbocz, 1997). We hope that computer experts in Professor J. Arbocz's group, at the Delft University of Technology will enable a close correlation between experimental results reported by Singer et al (1971) and the numerical findings, based on nonuniform boundary conditions as suggested here. Once this is performed the nagging questions (of the pseudo-skeptics in ourselves) will still remain. Here is their partial list:

(a) Is there a scatter in the values of the axial spring K_x?

(b) If the answer is yes, then how to model K_x as a random variable or as a one-dimensional random field?

(c) If K_1 and K_2 may be treated as random variables, how to determine experimentally their probabilistic characteristics, like their mean values $E(K_1), E(K_2)$, variances $Var(K_1), Var(K_2)$ and even more importantly, their covariance $Cov(K_1, K_2)$?

(d) Moreover, how to find their joint probability distribution, for performing rigorous probabilistic analysis?

(e) How to predict, on-line, the boundary conditions in the service environment, when possibly the connections between different parts of the system are changed or damaged?

Probabilistic modeling does not appear to be the most suitable method to answer the last question. It was shown by Elishakoff and Fang (1995) that a non-probabilistic convex modeling may turn out to be a suitable method to provide partial answers due to partial information available. In particular, one can attempt to determine the convex sets to which the spring constants belong, rather than their exact deterministic values, or their probabilistic characteristics.

A trivial conclusion of this section is that the rigorous modeling of boundary conditions is a highly non-trivial task. A less transparent conclusion lies in recognition of the fact that special *identification* techniques are needed to be developed for direct incorporation of the boundary conditions in the analysis; for example in the deterministic setting it is important to closely approximate the axial spring coefficient K_x as a function of the circumferential coordinate. In the probabilistic setting, one needs to identify the probabilistic characteristics of the random field $K_x(\theta)$. In convex modeling one has only to determine the set to which K_x belongs. Effective deterministic codes are needed to be developed to incorporate variation of $K_x(\theta)$ in the numerical analysis. The problem is not resolved even then: In other shells, with different set of unknown boundary conditions, additional spring constants may be needed, enormously complicating the analysis .

7. PROBABILITY IS NOT A MAGIC WAND

As we see, in the probabilistic setting the imperfection sensitivity concept may appear to be nice and dandy. Yet does probabilistic methods solve the problem in its entirely? Do probabilistic methods have disadvantages, or they constitute a panacea for fully closing the chasm between the theory and practice?

In order to provide a partial reply to this question, let us recapitulate that once the probability of failure is determined, we must design the ensemble of shells. This is done by requiring that the reliability should be not less than some preselected value r. Some investigators adopt, without providing a justification, a value of allowable probability of failure $P_{f,all} = 1 - r = 0.02$. Yet, it appears not easy to convince top management that, following frequency interpretation of probability, nearly 2 in every 100 realizations of the structure may fail. As Freudenthal (1956, p. 435) remarks, the problems is

engineers."

As Grandori (1991) writes:

"The concept of structural safety will not leave the "realm of metaphysics" unless we device a method for justifying the choice of risk acceptability level."

Initial imperfection data banks, even when compiled, still may contain *insufficient* information for rigorous probabilistic processing of all the variables. In these circumstances researchers "randomize" the problem by assigning the probability distributions. By doing so they try to "make something our of nothing," and create the illusion of availability of information, while in actuality it is lacking.

Is such a procedure a necessary evil, and should one just live with it? At least many investigations felt uncomfortable with this situation. Freudenthal (1956, p. 386) writes:

"Ignorance of the cause of variation does not make such a variation random."

Although Freudenthal recognizes, as this quotation may demonstrate, that the probability must not be a single game in the town, he did not provide with any alternative to it. Yet, this noble selfcriticism, of the "own" methods, appears worthy of following.

This and numerous other considerations led Ben-Haim and Elishakoff (1989) to develop a method which represents an alternative to the probabilistic treatment of the problem. The method is referred to as a *convex modeling*. The name comes from the realization of the fact that the most inequalities, describing the range of variations of uncertain variables, constitute convex sets. Since the variables are defined by their ranges of variation only, rather than by the probability densities, the following questions can be posed:

(a) What is the maximum buckling load the structure may experience when initial imperfections vary in a convex set?

(b) What is the minimum buckling load the structure may attain in these circumstances?

Once these questions are answered, it is prudent to use the minimum buckling load as a design load, to be on the safe side.

Such an analysis was performed by Ben-Haim and Elishakoff (1989). Initial imperfection vector X was represented as a sum of a nominal vector X_0 and the deviation vector ζ. The deviation was postulated to fall in the following ellipsoidal set:

$$Z(\chi,\omega)=\left\{\zeta:\sum_{i=1}^{N}\frac{\zeta_i}{\omega_i^2}\le\chi^2\right\} \qquad (44)$$

where the size parameter χ and the semi-axes $\omega_1,\omega_2,\ldots,\omega_N$ are based on experimental data, obtainable from the initial imperfection data banks. The lowest buckling load which can be obtained from any of the shells in the ensemble described by Eq. (44) is expressed formally as the minimum of expression (1) on the set Z:

$$\mu(\chi,\omega)=\min_{\zeta\in Z(\chi,\omega)}\varphi(X_0+\zeta) \qquad (45)$$

Hence $\mu(\chi,\omega)$ is the buckling load of the "weakest" shell in the ensemble Z which is constructed to represent a realistic range of shells. The limit load for an imperfection vector $X_0+\zeta$, to the first order of ζ, is

$$\varphi(X_0+\zeta)=\varphi(X_0)+\sum_{i=1}^{N}\frac{\partial\varphi(X_0)}{\partial X_i}\zeta_i \qquad (46)$$

Thus the problem (45) is replaced by the following one:

$$\mu(\chi,\omega)=\min_{\zeta\in Z(\chi,\omega)}\left[\varphi(X_0)+\phi^T\zeta\right] \qquad (47)$$

where

$$\phi^T=\left[\frac{\partial\varphi(X_0)}{\partial X_1},\frac{\partial\varphi(X_0)}{\partial X_2},\ldots,\frac{\partial\varphi(X_0)}{\partial X_N}\right] \qquad (48)$$

where the superscript T stands for matrix transportation. The minimum buckling load is given by the formula (Ben-Haim and Elishakoff, 1989):

$$\mu(\chi,\omega) = \varphi(X_0) - \chi\left[\sum_{i=1}^{N}\left(\omega_i \frac{\partial\varphi(X_0)}{\partial X_i}\right)^2\right]^{1/2} \quad (49)$$

From this relation one recognizes that the significant reduction in the buckling load results from large sensitivity of the nominal buckling load to Fourier coefficients, whose semiaxes in the imperfection ellipsoid are large. We also recognize that the minimum buckling load depends linearly on the overall size χ of the imperfection ellipsoid, and nonlinearly on its shape parameters $\omega_1, \omega_2, \ldots, \omega_N$ and on the partial derivatives $\partial\varphi(X_0)/\partial X_i$. The values partial derivatives have been borrowed from the previous, probabilistic study by Elishakoff et al (1987).

Whereas the formula (49) is a first-order approximation, the second order approximation has also been written explicitly in terms of the Hessian matrix with elements $\partial^2\varphi(x_0)/\partial\zeta_i\partial\zeta_j$. The result is not recapitulated here.

It also appeared interesting to define the variations of the imperfections in terms of a radial tolerance on the shape of the shell. Manipulations which are not reproduced here lead to the following expression of the buckling load in terms of the imperfection deviation

$$\varphi\big(X_0 + \zeta(\xi,\theta)\big) = \varphi(X_0) + \int_0^{2\pi}\int_0^{\pi}\zeta(\xi,\theta)S(\xi,\theta)\,d\xi d\theta \quad (50)$$

where $S(\xi,\theta)$ is a combination of the trigonometric functions with coefficients that depend on the elements of the vector $\partial\psi(X_0)/\partial\zeta_i$; for details one may consult with Ben-Haim and Elishakoff (1989, 1990). Close examination of Eq. (50) reveals that the greatest reduction in the buckling load is obtained from the imperfection profile which switches between its extreme values $\hat{\zeta}$ and $-\hat{\zeta}$, where $\hat{\zeta}$ is the radial tolerance. The minimum buckling load for the ensemble of shells with radial tolerance $\hat{\zeta}$ reads:

$$\mu(\hat{\zeta}) = \min_{|\zeta| < \hat{\zeta}}\left[\varphi(X_0+\zeta(\xi,\theta))\right] = \varphi(X_0) - \hat{\zeta}\int_0^{2\pi}\int_0^{\pi}|S(\xi,\theta)|\,d\xi d\theta \quad (51)$$

Suppose now that one wishes to construct a radial tolerance for which the minimum buckling load takes on value λ_0. Then one chooses $\hat{\zeta}$ as follows

$$\hat{\zeta} = \frac{\mu(\hat{\zeta}) - \varphi(X_0)}{\int_0^{2\pi}\int_0^{\pi}|S(\xi,\theta)|\,d\xi d\theta} \quad (52)$$

This approach allows one to theoretically determine the knockdown factor within the convex modelling (C.K.F.). It is defined as the ratio of the minimum buckling load to the classical buckling load:

$$C.K.F. = \frac{1}{P_{cl}}\left\{\varphi(X_0) - \chi\left[\left[\sum_{i=1}^{N}\omega_i\frac{\partial\varphi(X_0)}{\partial X_i}\right]^2\right]^{1/2}\right\} \quad (53)$$

for ellipsoidal modelled initial imperfections, and

$$C.K.F. = \frac{1}{P_{cl}}\left\{\varphi(X_0) - \hat{\zeta}\int_0^{2\pi}\int_0^{\pi}|S(\xi,\theta)|\,d\xi d\theta\right\} \quad (54)$$

for the shells with radial tolerance (compare with Eq. 13 defining K.F. within the probabilistic modelling). This knockdown factor is anticipated to be *above* the ones which are provided by the NASA monographs (1969). This would imply that the existing NASA

monographs may be providing too conservative estimates of K.F., and thus *penalizing* carefully designed shells. As we see a convex, non-probabilistic modeling of uncertainty, provides theoretical means of determining the K.F.

For other applications of this method the reader may consult with papers by Elishakoff and Ben-Haim (1990), Lindberg (1992), Ben-Haim (1993) and Pantelides (1995). The critical contrast between the probabilistic and convex modeling was undertaken by Elishakoff, Cai and Starnes (1993).

It was shown that in many realistic circumstances, convex modeling of uncertainty and the probabilistic analysis yield close results. This partially answers the following question: Which analysis is superior, probabilistic or convex modeling? Another facet of the problem is the fact that the convex modeling is both conceptually *simpler* and computationally *less expensive* than the probabilistic analysis. This may suggest, in accordance with the law of parsimony, or *Ockham's razor* that the convex modeling is advantageous over the probabilistic analysis. In words of columnist Charles Krauthammer (1997) Ockham's razor

"...states, in essence, that when confronted with two or more explanations for the phenomenon, we assume that the more compact, less complicated, simple one must be correct."

One cannot accept this assertion as a "totally" true one: why the correct analysis must be simpler too? On the other hand, why discard the simple analysis? Simple and complicated analyses usually have different ranges of applicability (the latter may include the former). Yet, it appears that the analysts should pursue the non-probabilistic, convex modeling of uncertainty with much more energy, especially when sufficient information is *unavailable* for *substantiating* probability densities used. If the past experience is of any guidance, this very situation is prevailing in most cases. Thus, we conjecture that the use of set-theoretical models will attract more and more investigators in the future.

8. OPTIMIZATION AND ANTI-OPTIMIZATION CAN BE COMBINED

Non-probabilistic models of uncertainty in essence look for *worst* designs under uncertainty constraints. One determines the minimum buckling load that the structure may experience when uncertain parameters (initial imperfections, elastic moduli, or other properties) vary within some sets. The ranges within which uncertainties vary, are the only quantities that are known; the probability densities may be not known due to the lack of sufficient information, to construct an accurate probabilistic model. This situation is somewhat opposite to what we are looking in classical optimization of structures, which looks for the *best* designs. It appeared natural, therefore, to the present writer to coin a term *anti-optimization* for such an analysis under uncertainty (1991). It includes as particular cases convex modeling (including interval analysis or ellipsoidal modeling) as well as non-convex, set-theoretical modeling.

Optimization and anti-optimization techniques can be meaningfully combined. Indeed, one is interested in *maximizing* the *minimum* buckling load the structure can carry due to uncertainty in the system. Such analyses were performed by Adali et al (1994) and Adali et al (1997). Zhu et al (1996) developed a novel technique to enclose experimentally available information into the ellipsoid of the minimum volume, in an N-dimensional space of initial imperfections.

9. THE STARNES PROBLEMS

When the new solutions of old problems appear at sight, the desire develops for solving other untoucned problems. Dr. J. H. Starnes, Jr. of NASA has posed several pertinent problems in the buckling uncertainty context. Only some of these will be discussed here.

First of all, the effect of thickness variation and its influence on the buckling of thin cylindrical shells was posed. To the best of our knowledge, there were no studies in this field. The first naive thought that comes to the mind is as follows: since the worse imperfections are co-configurational to the buckling mode of the perfect shells, so too, the shell thickness variations in the form of this classical buckling mode must be of significance. Subsequent investigation showed that this anticipation was premature. Koiter et al (1994a) illustrated that the nondimensional classical buckling load varies as

$$\lambda=1-\frac{1}{2}\nu\epsilon-\frac{832+464\nu-23\nu^2}{512}\epsilon^2 \qquad (55)$$

where ν is Poisson's ratio, ϵ = the amplitude of the deviation of the shell thickness from the uniformity

$$h=h_0[1-\epsilon\cos(p_0x/R)] \qquad (56)$$

with R = radius, x = axial coordinate, $p_0=[2cR/h_0]^{1/2}$ is the wave number in the axisymmetric buckling node of a shell with uniform thickness h_0, $c=[3(1-\nu^2)]^{1/2}$. The parameter ϵ is taken to be positive in order to achieve a detrimental effect by a "thinning" of the wall thickness in the region around $x=0$ where the flexural energy dominates. However, if the thickness variation is

$$h=h_0\left[1-\epsilon\cos(2p_0x/R)\right], \qquad (57)$$

then the classical buckling load becomes

$$\lambda=1-\epsilon-\frac{25}{32}\epsilon^2, \qquad (58)$$

i.e. reduction of the critical load factor below unity by ϵ. The associated buckling nodes are the non-symmetric mode

$$w=\cos\frac{mx}{R}\cos\frac{ny}{R} \qquad (59)$$

in the case $p=2p_0$, and the axisymmetric mode

$$w(x)=\cos\frac{p_0x}{R} \qquad (60)$$

in the case $p=2p_0$.

This situation is not unlike parametric resonance in the *time-dependent* problems. Here, as it were, we have case of the *space-wise* parametric resonance. The effect of both thickness variation and the initial imperfections was studied by Koiter et al (1994b).

In the case $p=p_0$ the equation for the critical load factor is governed by an equation

$$(1-\lambda)\left(1-\frac{1}{2}\nu\epsilon-\lambda\right)-\frac{3c}{2}\lambda\mu=0 \qquad (61)$$

(μ = initial imperfection parameter) whereas for the case $p=2p_0$ the critical load factor is found from the equation

$$(1-\lambda)(1-\epsilon-\lambda)-\frac{3c}{2}\lambda\mu=0 \qquad (62)$$

A semi-analytical and semi-numerical technique was also developed by Koiter et al (1994b). It was constructed in such a manner that for the shells with initial imperfections, in absence of the thickness variations, Koiter's (1963) results of the shells with constant thickness are uncovered. The "perturbative" solution from Koiter's (1963) work is obtained numerically via the Godunov-Conte method (Elishakoff and Charmats, 1977). It is remarkable that some specially laminated composite shells exhibit the same behavior as the isotropic shells (Li et al, 1995).

Second problem posed by Dr. J. Starnes is as follows: elastic moduli of homogeneous and composite structures my exhibit considerable scatter, with attendant lack of sufficient volume of information to justify the probabilistic analysis. How to incorporate the uncertainty into the design criteria? This problem has been resolved within the non-probabilistic, convex modeling. Experimental data (Goggin, 1973) was first enclosed by the four-dimensional box

$$E_i^L\le E_i\le E_i^U,\ (i=1,2,3,4) \qquad (63)$$

where the superscript L denotes lower bound, while the superscript U indicates the upper bound. Then an ellipsoid of minimal volume was constructed that contained the entire box of data. Semi-axis of the ellipsoid were determined analytically using the technique of Lagrange multipliers. Subsequently, either the convex modeling (Elishakoff, Li and Starnes, 1994) or the nonlinear programming methods (Li et al, 1996) were employed to determine the minimum buckling load due to the uncertainty in

the elastic moduli.

Additional set of problems of interest involve the phenomenon of localization of the buckling modes due to small disorder. This may explain the localized buckling patterns in the real structures (Pierre and Plaut, 1989; Nayfeh and Hawwa 1994a; Li, Elishakoff and Starnes, 1995; Ariaratnam and Xie, 1996) or provide a mechanism for the passive control (Nayfeh and Hawwa 1994b; Elishakoff, Li and Starnes, 1997). The problem of mode localization is often posed in a probabilistic setting (see, e.g., Lin, 1996 and bibliography, in vibration problems) when *all* the spans have a misplacement in the supports. Theoretically one can visualize such a situation, arguing that it is never possible to place *any* of the supports exactly at a specific location. Yet, deterministic analysis of general multi-span structure with a *single* perturbation produces the localization phenomenon (Li et al, 1996). Random misplacements with quite large variance $\sigma_x = 0.1$ in Fig. 9.3.6 and $\sigma_x = 0.5$ in Fig. 9.3.7 (Lin and Cai, 1995) would pinpoint to a poor workmanship; in the latter circumstance one may not need a probabilistic analysis, but rather changing the manufacturing process, or maybe the manufacturing organization itself. One should note that the experimental measurements to justify an assumption that all supports are misplaced are presently unavailable.

Many more practical problems are awaiting for their solutions. Indeed, "everybody loves the buckling problems," as Budiansky and Hutchinson (1980) maintain. May be, in the multiplicity of journals, there could be a new section introduced "Not Yet Solved Buckling Problems for Industry." This may make a contact between the 'buckling-lovers' and those who deal with variety of buckling problems in their everyday professional lives.

10. WHAT NEXT?

We do not have a crystal ball to predict the future development which will take place in the shell buckling research. Yet some summarizing appears to be in order.

Probabilistic methods did not escape making a fetish from the computer. There are numerous sessions at the conferences devoted to solely the computational side of stochastic mechanics, often, if not almost always, in full detachment from experimental data or information. Such a situation, in actuality was advocated long ago, by Johnston (1961) quite early:

"There are many advantages in simulated tests, carried out while with the aid of a computer, in comparison with real tests in an actual testing machine. No machining is involved, no materials need be acquired, and there is no scatter in the test results! Moreover, the precision of results, although based on a simulated and idealized material, permits a study of details of behavior that is not possible in ordinary laboratory tests. It would be impossible to completely duplicate the observations that may be made on the basis of the simulated tests..."

To this claim Singer (1997) responds, referring to deterministic problems:

"It was forgotten that the simulation was so successful because the physical phenomena in this case were well known and had been extensively explored by very many real experiments. New phenomena have still to be found and properly understood in physical test, before even the powerful computers of today can give a reliable simulation and then extend the range of parameters."

Indeed, as Arbocz (1991) mentions:

"...if one is unable to reproduce numerically the experimentally observed buckling process quite accurately, then it is of questionable value to use the same deterministic computational models repeatedly for statistical predictions."

Probabilistic methods require information about the probabilistic characteristics of modeled quantities. Hence one incorporate a probabilistically modeled uncertainty into design, if one is lacking experimental data. This statement appears to be quite innocent, yet there are many papers, including those regularly published in the Proceedings of the AIAA/ASME/ASCE/AHS/ASC Structural Dynamics conferences where far-going assumptions are made about the probability densities (for the general description of some of these problems see, e.g. Chamis, 1992). No explicit interest is expressed in the joint probability densities. Yet, as it was illustrated by Elishakoff and Hasofer (1996) reliability estimates may change considerably depending on *different* joint distributions possessing the same *marginal* ones. This fact is still awaiting its recognition by the community of extremely energetic researchers in stochastic mechanics, especially in apparent absence of the experimental data.

Without input experimental data one will need to make assumptions about the *joint* probability density of involved parameters. One can visualize a situation in which a data could be predicted from the theoretical considerations; if such a lucky situation is absent, the assumed data may be very far from the real data. An often quoted GIGO ("garbage in-garbage out") situation may prevail in such unfortunate circumstances.

Some researchers maintain that the Monte Carlo technique must be viewed as a means of last resort. The fact that the second- moment method developed by Elishakoff et al (1987) yields results in close vicinity to the ones which were predicted by the Monte Carlo method, may suggest that the second moment method is superior to the Monte Carlo technique. Arbocz (1991) writes

"Initially we have used... the Monte Carlo procedure to derive the reliability function R(λ). What always disturbed me with this approach was the large number of deterministic buckling load calculations that had to be done in order to define the shape of the reliability function R(λ) accurately."

Two comments appear to be instructive in this regard. First of all classical theorems maintain that the accuracy of the Monte Carlo predictions increase as $1/\sqrt{M}$ where M is the number of simulations. Yet, when one compares the reliabilities in benchmark cases when exact solution is available, one clearly observes that the actual situations are much more optimistic, and good comparisons are obtainable with not excessively volume of the data. The main point however is that approximate, non-Monte-Carlo methods may be valid only for small coefficients of variation of variables involved. In case of the elastic moduli, for example, variations may be substantially large and the second moment analysis may turn out to be extremely inaccurate.

It appears that the methodology developed by Elishakoff et al (1987) should not be oversold. Indeed, one still needs to perform the so called *Level 2* analysis for A- and B-shells. However, cautious researchers could anticipate some numerical difficulties. As Bouyssy and Rackwitz (1995 p. 1047) write

"...for large models and high dimension of the uncertainty vectors these methods involve considerable numerical effort in the gradient-based search of the design point. Moreover, multiple most likely failure points and highly nonlinear failure surface may be present. As an alternative, simulation methods have been proposed. Amongst these conditional sampling appears most suitable, because it does not require a priori knowledge on the important region(s) and can retain the advantages of FORM [first-order reliability method- I.E.]."

Conditional simulation technique was utilized by Li et al (1995) for studying the reliability of columns on nonlinear elastic foundation, in presence of the random initial imperfections and random axial load. Yet, As Bouyssy and Rackwitz (1995 p. 1053) mention:

"The method of conditional expectation is suitable if and only if the conditional failure probability is not too sensitive with respect to generated variables...The studied example as well as other simple ones and more complex ones clearly indicate that conditional sampling methods can be unreliable, especially if adaptive schemes are implemented. Their efficiency depends strongly on the starting conditions for the simulations if the dimension of the simulated vector is not high. That conditional sampling schemes with or without adaptive sampling densities can be unreliable. is most disturbing."

Response surface methodology may appear to be attractive to reduce the computational cost of the direct Monte Carlo method, as is suggested by several investigators. Yet, as Bucher et al (1989, p.12) stress:

"Obviously, since the interpolating procedure must cover combinations of different variables to ensure the quality of the RS (response surface-I.E.), the number of basic random variables should not be too large. This fact limits the method to cases with less than, say 20, random variables unless some mixed terms can be neglected. Without or with few mixed terms the method is suitable for up to 100 variables. Significant advantages over direct simulation techniques may be anticipated for cases with very complex systems and rather low number of variables."

It appears that even if response surface methodology will enable to reduce the computational cost by the order of magnitude or less, still, to find extremely small probability of failure, one must perform substantial number of simulations. We should not be too pessimistic in this regard; the observers of the past progress cannot agree with Graf's (1990) postulate: *"Every computer is too small."* Indeed, as Rogers reports (1996),

"Code-named Option Red, it [the fastest computer in the world-I.E.] will fill 85 locker size cabinets and 1,600 square feet at Sandia National Laboratories in Albuquerque, N. M. It has 600

gigabytes of memory, two terabytes-that's 2 trillion bytes of disc space and a peak capacity of 1.8 trillion operations per second."

Anyway, it appears that till the deterministic analysts will embrace the idea of uncertainty for the design, fastest computers will be uniformly available. The question is if the probabilistic methods are the must for uncertainty modeling? As we have seen above, the answer to this question is negative. In addition to probabilistic methods, there are other, viable, approaches. One such a method is a convex modeling.

In this era of tendency towards the total (and, quite often, arbitrary) randomization of the engineering problems one feels relieved when reading the philosophy adopted at NASA Langley Research Center (Nemeth and Starnes, 1997):

"The reliability of shell design procedures can be improved by using these more accurate deterministic analysis tools so long as the dimensions and properties are known to an acceptable level of accuracy. If the dimensions and properties of the shell are not well known, then the design process can include the effects of these uncertainties by coupling a probabilistic analysis with the deterministic analysis...This hybrid approach will retain the accuracy of deterministic analysis and include a probabilistic analysis for the uncertainties in the design problems."

We should bear in mind that if one does not know something, that quantity should not necessarily be modeled as a random one! (The notion of probability as a mental construct may yet turn out to be nonexistent). Hence we take a liberty of suggesting that the probabilistic analysis be utilized *only* for those variables for which *sufficient* experimental information will be available. Otherwise, in the presence of the scant data or lack of information, the convex modeling of uncertainty, and in general, *antioptimization* method will prove as more useful than the probabilistic one. It can be easier understood by both engineers, who should perform the job, and by the top management; it is also easier to implement than the probabilistic method. One thing is clear, to paraphrase Einstein's famous quotation, so far as the model of an engineering problem with scatter refers to reality, it is not certain; and so far as it is certain, it does not refer to reality.

11. CONCLUSION

We have highlighted some misconceptions, mistakes or misuses of probabilistic methods in buckling of structures as a learning experience. As an Chinese proverb maintains, "Through mistakes we can learn the truth." Thus, these mistakes and their critical analysis become a path which enables us to formulate more rigorously questions, and provide more insightful answers, than before (as G. K. Chesterton maintained, "It isn't that they can't see the solution. It is that they can't see the problem"). Additional reason of emphasizing the past errors in to (a) warn against repeating them by beginning researchers or engineers, (b) to allow researchers to learn from others' mistakes, rather than committing them themselves; (c) to demonstrate that even in modern non-judgmental society some decisions and judgements must be made, not to get lost in the available literature, on one hand, or not to be over-attracted by the computer's possibilities, on the other. The latter is especially unfortunate, since overzealous researchers are often declaring all variables (except, happily, universal constants) to be random; then by pushing the computer button one can choose any marginal distribution desired, from the list of the available ones; thus, the quick estimates of probabilistic parameters are furnished. This naive probabilistic research consumes minds and resources, which could be more usefully utilized. Links with the experimental data, hypotheses testing subroutines about joint probability density are not only absent, but not even dreamt about.

This essay clearly shows that closing the chasm between theory and practice is not an impossible task. It can be dealt with several alternative avenues. The probabilistic methods do not seem to have a monopoly on the truth about uncertainty. Conceptually and computationally simpler approaches are possible, especially when the data is scarce. In some instances hybrid approaches may be of use.

The problem is not declared as closed. Whereas knockdown factor disregards the available theoretical knowledge, its introduction was not a bad idea, since it provided with safe designs. Still, it somehow mixes "apples" and "oranges," i.e. structures produced by various manufacturing methods, with different degrees of workmanship, and produces universal criteria discarding the specific manufacturing process.

It is time now to *differentiate* the knockdown factors for different manufacturing methods, and produce new guidelines for NASA and other agencies. It appears to this writer that the research should concentrate on several directions:

(1) Accumulation of data for statistical analysis to check the nature of the distribution of random initial imperfections, elastic moduli, thickness variations, load variations etc.

(2) Development of techniques of the identification of boundary conditions, which may turn out to have a nonuniform nature. When limited data is provided, the problem of identification may be replaced by establishment of local modifications in boundary conditions, during the use of the structure, via convex modeling.

(3) Development of finite element codes in stochastic setting, incorporating uncertain imperfections, elastic moduli, boundary conditions, thickness variation, and loading conditions development of buckling post processors to commercially available codes like NASTRAN, ADINA, ALGOR, DIANA, etc.

Granting agencies generously supported the buckling research in the Sixties and Seventies. In this post-Sputnik- and post-Cold- War era buckling research cannot be abandoned. At least "small" group of researchers should be continuously supported to develop basic ideas for solving practical problems. The present writer, for example, envisions a single NASA Research Center which is assigned to carry out the buckling research in a concentrated manner through possibly, "NASA Buckling Institute." This Institute would pose problems and challenges, of both practical and theoretical nature. Relatively small annual grants of $60K-$70K, or, if hopefully the university overheads will be totally eliminated or reduced to the unavoidable minimum of 5%, the grants of size of $40K-$50K, but for *several years* without the constant fear of interruption, would provide a sound basis for both retaining knowledge and advancing it. Thus we could one day maintain that the imperfection sensitivity concept is finally introduced into the design practice, in a routine manner.

12. ACKNOWLEDGEMENT

The financial support provided by NASA Langley Research Center, through Grant NAG-1-1310 is gratefully acknowledged. Opinions, findings and recommendations expressed in this study are those of the author and do not necessarily reflect the views of the sponsor. Author gratefully acknowledges fruitful discussions and/or cooperations with following colleagues: J. Arbocz, Y. Ben-Haim, V. V. Bolotin, B. Budiansky, D. Bushnell, G. Q. Cai, J. van Geer, J. Kalker, W. T. Koiter, S. Krenk, S. van Manen, B. P. Makarov, V. M. Leizerakh, Y. W. Li, A. Scheurkogel, M. Shinozuka, J. Singer, J. H. Starnes, Jr., Y. Stavsky, W. J. Stroud, R. C. Tennyson, W. D. Verduyn, P. G. Vermeulen, L. P. Zhu and others over the recent decades on various imperfection sensitivity related topics. The full responsability for any flaw(s) in this essay rests solely upon the author.

REFERENCES

Adali S., Elishakoff I., Richter A. and Verijenko V.E. Optimal Design of Symmetric Angle-Ply Laminates for Maximum Buckling Load with Scatter in Material Properties, *Fifth AIAA/USAF/NASA/ISSMO Symposium on Multidisciplinary Analysis and Optimization*, Panama City Beach, AIAA Press, pp. 1041-1045, 1994.

Adali S., Richter A. and Verijnko V.E., Minimum Weight Design of Symmetric Angle-Ply Laminates with Incomplete Information on Initial Imperfections, *Journal of Applied Mechanics*, Vol. 64, 90-96, 1997.

Almroth B.O., Influence of Imperfections and Edge Constraint on the Buckling of Axially Compressed Cylinders, *NASA CR-432*, 1966.

Amazigo J. C., Buckling under Axial Compression of Long Cylindrical Shells with Random Axisymmetric Imperfections, *Quarterly of Applied Mechanics*, Vol. 26, 537-566, 1969.

Amazigo J. C., Buckling of Stochastically Imperfect Columns on Nonlinear Elastic Foundations, *Quarterly of Applied Mathematics*, Vol. 29, 403-409, 1971.

Amazigo J. C., Buckling of Stochastically Imperfect Structures, *Buckling of Structures* (B. Budiansky, ed.), Springer Verlag, pp. 172-182, Berlin, 1976.

Amazigo J.C., Asymptotic Analysis of the Buckling of Externally Pressurized Cylinders, with Random Imperfections, *Quarterly of Applied Mathematics*, Vol. 31, 429-442, 1974.

Amazigo J. C., Budiansky B. and Carrier G. F., Asymptotic Analysis of the Buckling of Imperfect Columns on Nonlinear Elastic Foundation, *International Journal of Solids and Structures*, Vol. 6, 1341-1356, 1971.

Amazigo J. C., and Budiansky B., Asymptotic Formulas for the Buckling Stresses of Axially Compressed Cylinders with Localized or Random Axysymmetric Imperfections, *Journal of Applied Mechanics*, Vol. 39, 179-184, 1972.

Anon., Buckling of Thin-Walled Circular Cylinders, NASA SP-8007 1868.

Arbocz J., The Effect of General Imperfections on the Buckling of Cylindrical Shells, *Ph.D. Thesis*, California Institute of Technology, Pasadena, 1968.

Arbocz J., The Effect of Initial Imperfections on Shell Stability, *Thin-Shell Structures*, (Y.C. Fung and E. E. Sechler, eds.), Prentice-Hall, Inc., Englewood Cliffs, pp. 205-245, 1974.

Arbocz J., The Imperfection Data Bank, a Means to Obtain Realistic Buckling Loads, *Buckling of Shells, A State-of-the Art Colloquium* (E. Ramm, ed.), University of Stuttgart, pp. 10.1-10.33, 1982.

Arbocz J., Recent Developments in Shell Stability Analysis, *Mechanika Teoretyczna i Stosowana*, Vol. 25, 523-540, 1987.

Arbocz J., Post-Buckling Behaviour of Structures: Numerical Techniques for More Complicated Structures, *Buckling and Postbuckling* (J. Arbocz, M. Potier-Ferry, J. Singer and V. Tvergaard), Springer, Verlag, Berlin, pp. 83-142, 1987.

Arbocz J., Towards an Improved Design Procedure for Buckling Critical Structures, *Buckling of Shell Structures, on Land in the Sea and in the Air* (J.F. Jullien, ed.), Elsevier Applied Science, London, pp. 270-276, 1991.

Arbocz J., Present and Future of Shell Stability Analysis, *Zeitschrift fuer Flugwissenschaften und Weltraumforschung*, Vol. 5, 335-348, 1991.

Arbocz J., Future Directions and Challenges in Shell Stability, *38th AIAA/ASME/ASCE/AHS/ASC Structures, Structural Dynamics, and Materials Conference and Exhibit*, AIAA Paper 97-1077, pp. 1949-1962, 1997.

Arbocz J. and Abramovich H., The Initial Imperfection Data Bank at the Delft University of Technology, Part 1, *Report LR-290*, Department of Aerospace Engineering, Delft University of Technology, Dec. 1979.

Arbocz J. and Babcock C. D., Experimental Investigation of the Effect of General Imperfections on the Buckling of cylindrical Shells, *NASA CR-1163*, 1968.

Arbocz J. and Babcock C. D., The Effect of General Imperfections on the Buckling of Cylindrical Shells, *Journal of Applied Mechanics*, Vol. 36, 28-38, 1969.

Arbocz J. and Babcock C. D. Jr., Prediction of Buckling Loads Based on Experimentally Measured Initial Imperfections, *Buckling of Structures* (B. Budiansky, ed.), Springer Verlag, Berlin, pp. 291-311, 1976.

Arbocz J. and Babcock C.D., Computerized Stability Analysis using Measured Initial Imperfections, *12th Congress of the International Council of the Aeronautical Sciences*, Münich, pp. 688-701, 1980.

Arbocz J. and Elishakoff I., Stochastic Stability Analysis of Axially Compressed Cylindrical Shells, *Buckling of Shells in Offshore Structures* (J.E. Harding, P.J. Dowling and N. Agelidis, eds.), Granada, London, pp. 413-423, 1982.

Arbocz J. and Hol J.M.A.M., Collapse of Axially Compressed Cylindrical Shells with Random Imperfections, *AIAA Journal*, Vol. 29, 2247-2256, 1991.

Arbocz J. and Sechler E.E., On the Buckling of Stiffened Imperfect Cylindrical Shells, *AIAA Journal*, Vol. 14, 1611-1617, 1976.

Ariaratnam S.T. and Xie W.-C., Buckling Mode Localization in Randomly Disordered Continuous Beams using a Simplified Model, *Chaos, Solitons and Fractals*, Vol. 7, 1127-1144, 1996.

Augusti G., Probabilistic Treatments of Column Buckling Problems, *Stochastic Problems in Mechanics*, University of Waterloo Press, pp. 255-274, 1974.

Babcock C.D., Jr., Experiments in Shell Buckling, *Thin-Walled Structures* (Y.C. Fang and E. E. Sechler, eds.), Prentice Hall, Inc., Englewood Cliffs, pp. 345-369, 1974.

Ben-Haim Y., Convex Models of Uncertainty in Radial Pulse Buckling of Shells, *Journal of Applied Mechanics*, Vol. 60, 683-688, 1993.

Ben-Haim Y. and Elishakoff I., *Convex Models of Uncertainty in Applied Mechanics*, Elsevier Science Publishers, Amsterdam, 1990.

Besseling J.F., Ernest L.J. and van der Werff K., Geometrical and Physical Nonlinearities: Some Developments in the Netherlands, *Computer Methods in Applied Mechanics and Engineering*, Vol. 17/18, 131-157, 1979.

Bolotin V. V., Statistical Methods in the Nonlinear Theory of Elastic Shells, *Izvestija Akademii Nauk SSSR, Otdelenie Tekhnicheskikh Nauk*, No. 3, 1958. English translation: NASA TTF-85, pp. 1-16, 1962.

Bolotin V. V. *Application of Methods of Theory of Probability and Theory of Reliability in Analysis of Structures*, Izdatelstvo Literatury po Stroitelstvu, Moscow, 1971 (in Russian).

Bouyssy V. and Rackwitz R., On Conditional Sampling to Assess the Reliability of Offshore Jacket Platforms, *Applications of Statistics and Probability* (Lemaire M., Favre J-L., and Mébarki A., eds.), A.A. Balkema, Rotterdam, pp. 1047-1053, 1995.

Bucher C.G., Chen Y.M. and Schuëller G.I., Time-Variant Reliability Analysis Utilizing Response Surface Approach, *Reliability and Optimization of Structural Systems* (P. Thoft-Christensen, ed.), Springer Verlag, Berlin, pp. 1-14, 1989.

Budiansky B. and Hutchinson J.W., Dynamic Buckling of Imperfection Sensitive Structures, *Proceedings of the Eleventh International Congress of Applied Mechanics*, (Görtler M., ed.), pp. 636-651, Münich, 1964.

Budiansky B., Theory of Buckling and Postbuckling Behavior of Elastic Structures, *Advances in Applied Mechanics*, Vol. 14, Academic Press, New York, pp. 1-65, 1974.

Budiansky B., Theory of Buckling and Post-Buckling Behavior of Elastic Structures, *Advances in Applied Mechanics*, Academic Press, Vol. 14, pp. 1-65, 1974.

Budiansky B. and Hutchinsen J.W., A Survey of Some Buckling Problems, *AIAA Journal*, Vol. 4, 1505-1510, 1966.

Budiansky B. and Hutchinson J.W., Buckling: Progress and Challenges, *Trends in Solid Mechanics* (J.F. Besseling and A.M.A. van der Heijden, eds.), Delft University Press and Sijtholff & Noordhoff International Publishers, Delft, pp. 93-116, 1979.

Cederbaum G. and Arbocz J., On the Reliability of Imperfection-Sensitive Long Isotropic Cylindrical Shells, *Structural Safety*, Vol. 18, 1-9, 1996.

Cedermbaum G. and Arbocz J., Reliability of Shells via Koiter Formulas, *Thin-Walled Structures*, Vol. 24, 173-187, 1996.

Chamis C.C., Probabilistic Structural Analysis Methods for Space Propulsion System Components, *Probabilistic Engineering Mechanics*, Vol. 2, 100-110, 1987.

Davidenko D.F., On a Method of Numerical Solution of the Systems of Nonlinear Equations, Proceedings of the USSR Academy of Sciences, Vol. 88, 601-602, 1953 (in Russian).

Day W. B., Buckling of a Column with Nonlinear Restraints and Random Initial Imperfections, *Journal of Applied Mechanics*, Vol. 47, 204-205, 1980.

Elishakoff I., Impact Buckling of Thin Bar via Monte Carlo Method, *Journal of Applied Mechanics*, Vol. 45, 586-590, 1978.

Elishakoff I., Buckling of a Stochasically-Imperfect Finite Columns on a Nonlinear Elastic Foundation-A Reliability Study, *Journal of Applied Mechanics*, Vol. 46, 411-416, 1979.

Elishakoff I., Simulation of Space-Random Fields for Solution of Stochastic Boundary-Value Problems, *Journal of Acoustical Society of America*, Vol. 65, 399-403, 1979.

Elishakoff I., Hoff's Problem in a Probabilistic Setting, *Journal of Applied Mechanics*, Vol. 47, 1-6, 1980.

Elishakoff I., *Probabilistic Methods in the Theory of Structures*, Wiley, New York, 1983.

Elishakoff I., Personal Communication to J. Arbocz, Jan. 12, 1984.

Elishakoff I., Reliability Approach to the Initial Imperfection Sensitivity, *Acta Mechanics*, Vol. 52, 122-128, 1985.

Elishakoff I., How To Introduce the Imperfection Sensitivity Concept into Design, *Collapse* (J. M. T. Thompson and G. W. Hunt, eds.), Cambridge University Press, pp. 345-357, 1985.

Elishakoff I., Stochastic Simulation of an Initial Imperfection Data Bank for Isotropic Shells with General Imperfections, *Buckling of Structures: Theory and Experiment* (I. Elishakoff, J. Arbocz, C.D. Babcock, Jr. and A. Libai, eds.), Elsevier, Amsterdam, pp. 195-210, 1988.

Elishakoff I., An Idea of Uncertainty Triangle, *The Shock and Vibration Digest*, Vol. 22, No. 10, p. 1, 1991 (Editorial).

Elishakoff I. and Arbocz J., Monte Carlo Method for the Reliability of Compressed Structures with Random Imperfections, *Proceedings of the Danish Engineering Academy of Sciences* (O. Ditlevsen, ed.), Lyngby, pp. 389-424, 1982.

Elishakoff I. and Arbocz J., Reliability of Axially Compressed Cylindrical Shells with Random Axisymmetric Imperfections, International *Journal of Solids and Structure*, Vol. 18, 563-585, 1982.

Elishakoff I., Arbocz J. and Starnes J.H., Jr., Buckling of Stiffened Shells with Random Initial Imperfections, Thickness and Boundary Conditions, *33rd AIAA/ASME/ASCE/AHS/ASC Structures, Structural Dynamics, and Materials Conference*, Dallas, pp. 95-100, 1992.

Elishakoff I. and Ben-Haim Y., Dynamics of a Thin Shell under Impact with Limited Deterministic Information on Its Initial Imperfections, *Structural Safety*, Vol. 8, 103-112, 1990.

Elishakoff I., Cai G.Q. and Starnes J. H. Jr., Non-linear Buckling of a Column with Initial Imperfection via Stochastic and Non-Stochastic Convex Models, *International Journal of Non-Linear Mechanics*, Vol. 29, 71-82, 1994.

Elishakoff I. and Charmats M., Godunov-Conte Method for Solution of Engineering Problems and Its Applications, *Journal of Applied Mechanics*, Vol. 44, 776-779, 1977.

Elishakoff I. and Fang J. J., Diagnosis of Local Modifications in the Boundary Conditions of a Rectangular Plate via Convex Modeling, *Computer Methods in Applied Mechanics and Engineering*, Vol. 124, 303-319, 1995.

Elishakoff I. and Hasofer A.M., Detrimental or Serendipitous Effect of Human Error on Reliability of Structures, *Computer Methods in Applied Mechanics and Engineering*, Vol. 129, 1-7, 1996.

Elishakoff I., Li Y.W. and Starnes J. H. Jr., A Deterministic Method to Predict the Buckling Load Variability due to Uncertain Elastic Moduli, *Computer Methods in Applied Mechanics and Engineering*, Vol. 111, 155-1667, 1994.

Elishakoff I., Li Y.W. and Starnes J.H., Jr., Passive Control of Buckling Deformation via Anderson Localization Phenomenon, *Chaos, Solitons and Fractals*, Vol. 8, 59-75, 1997.

Elishakoff I. and Nordstrand T., Probabilistic Analysis of Uncertain Eccentricities in a Model Structure. *Proceedings of the Sixth International Conference on Applications of Statistics and Probability in Civil Engineering*, (L. Esteva and S. E. Ruiz, eds.), Vol. 1, pp. 250-256, Mexico City, 1991.

Elishakoff I., van Manen S., Vermuelen P. and Arbocz, J., First-Order Second-Moment Analysis of the Buckling of Shells with Random Imperfections, *AIAA Journal*, Vol. 25, 1113-1117, 1987.

Ernst L.J., A Finite Element Approach to Shell Problems, *Ph.D. Thesis*, WTHD-114, TH Delft, Department of Mechanical Engineering, 1979.

Fersht R. S., Buckling of Cylindrical Shells with Random Imperfections, *Ph.D. Thesis*, California Institute of Technology, Pasadena, 1968.

Fersht R.S., Buckling of Cylindrical Shells with Random Imperfections *Thin Shell Structures: Theory, Experiment and Design* (Y.C. Fung and E. E. Sechler, eds.), Prentice-Hall, Englewood Cliffs, pp. 325-341, 1974.

Frazer W. B., Buckling of a Structures with Random Imperfections, Ph.D. Thesis, Division of Engineering and Applied Sciences, Harvard University, 1965.

Frazer W. B. and Budiansky B., The Buckling of a Column with Random Initial Deflection, *Journal of Applied Mechanics*, Vol. 36, 232-240, 1969.

Freudenthal A.M., *Selected Papers*, ASCE Press, New York, 1981.

Goggin P.R., The Elastic Constants of Carbon-Fiber Composites, *Journal of Material Science*, Vol. 8, 233-244, 1973.

Graf J., *Murphy's Computer Law*, Souvenir Press, London, p. 28, 1990.

Grandori G., Paradignes and Falsification in Earthquake Engineering, *Meccanica*, Vol. 26, 17-21, 1991.

Hansen J., Influence of General Imperfections in Axially Loaded Cylindrical Shells, *International Journal of Solids and Structures*, Vol. 11, 1223-1233, 1975.

Hansen J., General Random Imperfections in the Buckling of Axially Loaded Cylindrical Shells, *AIAA Journal*, Vol. 15, 1250-1256, 1977.

Hansen J. S. and Roorda J., Reliability of Imperfection Sensitive Structures, *Stochastic Problems in Mechanics* (S. T. Ariaratman and H. H. E. Leipholz, eds.), Waterloo University Press, pp. 229-242, 1973.

Hansen J. S. and Roorda J., On the Probabilistic Stability Theory for Imperfection Sensitive Structures, *International Journal of Solids and Structures*, Vol. 10, 341-359, 1974.

Hasofer A.M. and Lind N.C., Exact and Invariant Second-Moment Code Format, *Journal of Engineering Mechanics*, Vol. 100, 111-121, 1974.

Hoff N. J., *Dynamic Criteria and Buckling*, Engineering Structures Supplement, Butterworth Scientific Publications, London, 1949.

Hoff N. J., The Perplexing Behavior of Thin Circular Cylindrical Shells in Axial Compression, *Israel Journal of Technology*, Vol. 4, 1-28, 1966.

Hoff N.J. and Soong T.T., Buckling of Axially Compressed Circular Cylindrical Shells with Non-Uniform Boundary Conditions, *Proceedings of the Symposium of Thin-Walled Steel Structures - Their Design and Use in Building*, University College of Swansea, pp. 61-80, 1967.

Hofmeister L. D., Computer Codes to Predict Axial Buckling Loads of Initially Imperfect Cylindrical Shells, *TRW SDR-72-7*, 1972.

Horton W.H., Craig J.I. and Struble D.E., A Simple, Practical Method for the Experimental Determination of the End Fixity of a Column ,

Proceedings of the 8th Symposium on Space Technology and Science, Tokyo, pp. 269-280, 1969.

Hutchinson J.W. and Koiter W.T., Postbuckling Theory, *Applied Mechanics Reviews*, Vol. 23, 1353-1366, 1970.

Ikeda K., Murota K. and Elishakoff I., Reliability of Structures Subject to Normally Distributed Initial Imperfections, *Computers and Structures*, Vol. 59, 463-469, 1996.

Johnston B.G., Buckling Behavior Above the Tangent Modulus Load, *Journal of Engineering Mechanics Division*, Vol. 87, 79-99, 1961.

Ikeda K., Murota K. and Elishakoff I., Reliability of Structures Subjected to Normally Distributed Initial Imperfections, *Computers and Structures*, Vol. 59, 463-469, 1996.

Koiter W.T., Elastic Stability and Postbuckling Behavior, *Proceedings, Symposium on Nonlinear Problems*, University of Wisconsin Press, Madison, pp. 257-275, 1963.

Koiter W. T., The Effect of Axisymmetric Imperfections on the Buckling of Cylindrical Shells under Axial Compression *Koninklijke Nederlandse Akademie van Wetenoschappen (Proceedings of the Netherland's Academy of Sciences)*, Amsterdam, Series 13, Vol. 13, Vol. 66, No. 5, pp. 265-279, 1963.

Koiter W. T., On the Stability of Elastic Equilibrium (in Dutch), Thesis, Delft University, H. J. Paris; Amsterdam; English translations: (a) NASA TT-F-10, 833, 1967; (b) AFFDL-TR-70-25, 1970.

Koiter W.T., Current Trends in the Theory of Buckling, *Buckling of Structures* (B. Budiansky, ed.), Springer, pp. 1-16, 1976.

Koiter W. T., Elishakoff I., Li Y.W. and Starnes J. H. Jr., Buckling of an Axially Compressed Cylindrical Shell of Variable Thickness, *International Journal of Solids and Structures*, Vol. 31, 797-805, 1994.

Koiter W. T., Elishakoff I., Li Y. W. and Starnes J. H. Jr., The Combined Effect of the Thickness Variation and Axisymmetric Initial Imperfection on the Buckling of the Isotropic Cylindrical Shell under Axial Compression, *Proceedings, 35th AIAA/ASME/ASCE/AHS/ASC Structural Dynamics and Materials Conference*, Hilton Head, AIAA, pp 277-289, 1994.

Krauthammer Ch., Make it Snappy, *Time*, p. 89, July 21, 1997.

Leizerakh V.M., Statistical Analysis of Random Imperfections in Cylindrical Shells via Computers, *Proceedings of the Moscow Power Engineering Institute, Dynamics of Strength of Machines*, Moscow, 1969 (in Russian).

Li Y.W., Elishakoff I. and Starnes J.H., Jr., Buckling Mode Localization on a Multi-Span Periodic Structure with a Disorder in a Single Span, *Chaos, Solitons and Fractals*, Vol. 5, 955-969, 1995.

Li Y.W., Elishakoff I., Starnes J. H. Jr., and Shinozuka M., Nonlinear Buckling of a Structures with Random Imperfection and Random Axial Compression by a Conditional Simulation Technique, *Computers and Structures*, Vol. 56, 59-64, 1995.

Li Y.W., Elishakoff I. and Starnes J.H., Jr., Effect of the Thickness Variation and Initial Imperfection on the Buckling of Composite Cylindrical Shells, *Computers and Structures*, Vol. 56, 65-74, 1995.

Li Y.W., Elishakoff I., Starnes J.H., Jr. and Shinozuka M., Prediction of Natural Frequency and Buckling Load Variability due to Uncertainty in Material Properties by Convex Modelling, *Fields Institute Communications*, Vol. 9, 139-154, 1996.

Lin Y.K., Dynamics of Disordered Periodic Structures, *NOISE-CON 99, Progress in Noise Control for Industry* (Cuschieri J.M., Glegg S.A.L. and Yeager D.M., eds.), Noise Control Foundation, Poughkeepsie, NY, pp. 15-34, 1994.

Lin Y.K. and Cai G.Q., *Probabilistic Structural Dynamics*, McGraw Hill, New York, p. 439, 1995.

Lindberg H.E., An Evaluation of Convex Modelling for Multimode Dynamic Buckling, *Journal of Applied Mechanics*, Vol. 59, 929-936, 1992.

Makarov B. P., Statistical Analysis of Stability of Imperfect Cylindrical Shells, *Proceedings of Seventh All-Union Conference on the Theory of Plates and Shells*, Dnepropetrovsk, pp. 387-391, 1969 (in Russian).

Makarov B.P., Statistical Analysis of Imperfect Cylindrical Shells, *Raschety na Prochnost (Strength Analysis)*, Vol. 15, "Mashinostroenie" Publishing House Moscow, 1969 (in Russian).

Makaroff B. P., Statistical Analysis of Nonideal Cylindrical Shells, *Izvestiya Akademic Nauk SSR, Mekhanika Tverdogo Tela*, Vol. 5, No. 1, 97-104, 1970 (in Russian).

Miller R. K. and Hedgepeth J. M. The Buckling of Attice Columns with Stochastic Imperfections *International Journal of Solids and Structures*, Vol. 15, 73-89, 1979.

Myers R.H. and Montgomery D.C., *Response Surface Methodology: Process and Product Optimization Using Designed Experiments* Wiley, New York. 1995.

Nayfeh A.H. and Hawwa M.A., Buckling Mode Localization in Multi-Span Columns, *35th AIAA/ASME/ASCE/AHS/ASC Structures, Structural Dynamics, and Materials Conference*, Hilton Head, pp. 2117-2123, 1994a.

Nayfeh A.H. and Hawwa M.A., The Use of Mode Localization in the Passive Control of Structural Buckling, *AIAA Journal*, Vol. 32, 2131-2133, 1994b.

Nemeth M. and Starnes J.H., Jr., The NASA Monographs on Shell Stability Design Recommendations - Present Status and Future Directions, *38th AIAA/ASME/ASCE/AHS/ASC Structures, Structural Dynamics, and Materials Conference and Exhibit*, Kissimmee, Part 4, pp. 2639-2652, 1997.

Pantelides C. P., Buckling and Post-Buckling of Stiffened Elements with Uncertainty, *Thin-Walled Structures*, Vol. 26, 1-17, 1996.

Pantelides C. P., Stability of Elastic Bars on Uncertain Foundations using a Convex Model, *International Journal of Solids and Structures*, Vol. 33, 1257-1269, 1996.

Pierre C. and Plaut R.H., Curve Veering and Mode Localization in a Buckling Problem, *Journal of Applied Mathematics and Physics*, Vol. 40, 758-761, 1989.

Qiria V. S., Motion of the Bodies in Resisting Media, Proceedings of Tbilisi State University, Vol. 44, 1-20, 1951 (in Russian).

Rackwitz R., Structural Reliability Methods - Solutions and Problems in Probability Integration, *Sixth International Conference on Applications of Statistics and Probability in Civil Engineering*, Vol. 3, General Reports, Esteva L. and Ruiz S.E., eds., UNAM, Ciudad Universitaria, Mexico City, pp. 65-78, 1991.

Rajagopalan K., *Finite Element Buckling Analysis of Stiffened Cylindrical Shells*, A. A. Balkema, Rotterdam, 1993.

Riks E., An Incremental Approach to the Solution of Snapping and Buckling Problems, *International Journal of Solids and Structures*, Vol. 15, 524-551, 1979.

Rogers A., Getting Faster by the Second, *Newsweek*, pp. 86-88, 1996.

Roorda J., Buckling of Shells: An Old Idea with New Twist, *Journal of Engineering Mechanics Division*, Vol. 98, 531-538, 1972.

Roorda J., *Buckling of Elastic Structures*, University of Waterloo Press, 1980.

Rosenblueth E., Here and Henceforth, *Sixth International Conference on Applications of Statistics and Probability in Civil Engineering*, Vol. 3, General Reports, Esteva L. and Ruiz S.E., eds., UNAM, Ciudad Universitaria, Mexico City, pp. 81-94, 1991.

Sabag M., Stavsky Y. and Greenberg J.B., Buckling of Edge-Damaged Cylindrical Composite Shells, *Journal of Applied Mechanics*, Vol. 65, 121-126, 1989.

Scheurkogel A., Elishakoff I. and Kalker J., On the Error That Can Be Induced by an Ergodicity Assumption, *Journal of Applied Mechanics*, Vol. 48, 654-656, 1981.

Scheurkogel A. and Elishakoff I., On the Ergodicity Assumption in an Applied Mechanics Problem, *Journal of Applied Mechanics*, Vol. 52, 133-136, 1985.

Shinozuka M., Private Communication, August 1996.

Singer J., The Effect of Axial Constraint on the Instability of Thin Circular Cylindrical Shells under Uniform Axial Compression, *International Journal of Mechanical Science*, Vol. 4, 253-258, 1962.

Singer J., Vibrations and Buckling of Imperfect Stiffened Shells - Recent Developments, *Collapse* (J.M.T. Thompson and G.W. Hunt, eds.), Cambridge University Press, pp. 443-479, 1983.

Singer J., Private communication, July 1997.

Stam A.R., Stability of Imperfect Cylindrical Shells with Random Properties, *37th AIAA/ASME/ASCE/AHS Structures, Structural Dynamics & Materials Conference*, Vol. 3., pp. 1307-1315, AIAA, Washington, D.C., 1996.

Singer J., Experimantal Studies in Shell Buckling, *38th AIAA/ASME/ASCE/AHS/ASC Structures, Structural Dynamics, and Materials Conference and Exhibit*, AIAA Paper 97-1075, pp. 1922-1932, 1997.

Singer J., Abramovich H. and Yaffe R., Initial Imperfection Measurements of Integrally Stringer-Stiffened Cylindrical Shells, *TAE Report* 330, Department of Aeronautical Engineering, Technion-Israel Institute of Technology, Dec. 1978.

Singer J., Arbocz J. and Babcock C.D., Buckling of Imperfect Stiffened Cylindrical Shells under Axial Compression, *AIAA Journal*, Vol. 9, 68-75, 1971.

Stam A.R., Stability of Imperfect Cylindrical Shells with Random Properties, *37th AIAA/ASME/ASCE/AHS Structures, Structural Dynamics & Materials Conference*, Vol. 3., pp. 1307-1315, AIAA, Washington, D.C., 1996.

Stam A.R., 38th AIAA/ASME/ASCE/AHS Structures, Structural Dynamics & Materials Conference, Kissimee, pp. , AIAA, Washington, D.C., 1997.

Stavsky Y., Greenberg J.B. and Sabag M., Buckling of Edge-Damaged Filament-Wound Composite Cylindrical Shells under Combined Torsion/Axial Load, *Journal of Composite Structures*, Vol. 13, 21-34, 1988.

Stein M., Some Recent Advances in the Investigation of Shell Buckling, *AIAA Journal*, Vol. 6, 2239-2245, 1968.

Stein M., Design Problems of Shell Structures and the Impact of the Computer on Shell Analysis, *Computers and Structures*, Vol. 2, 31-45, 1972.

Stroud W.J., Davis D.D., Jr., Maring L.D., Krishnamurthy T. and Elishakoff I., Reliability of Stiffened Structural Panels: Two Examples, *Reliability Technology* (T.A. Cruse, ed.), ASME Press, New York, pp. 199-216, 1992.

Sweet A.L., Genin J. and Mlakar P.F., Vibratory Identification of Beam Boundary Conditions, *Journal of Dynamical Systems, Measurement and Control*, Vol. 98, 387-394, 1976.

Sweet A.L., Genin J. and Mlakar P.F., Determination of Column-buckling Criteria Using Vibratory Data, *Experimental Mechanics*, 385-392, 1977.

Tennyson R. C. and Muggeridge D. B., Buckling of Axisymmetric Imperfect Circular Cylindrical Shells under Axial Compression, *AIAA Journal*, Vol. 7, 2127-2131, 1969.

Tennyson R. C. and Muggeridge D. B. and Caswell R. D., New Design Criteria for Predicting Buckling of Cylindrical Shells under Compression *Journal of Spacecraft Rockets*, Vol. 8, 1062-1067, 1971.

Thompson J. M. T., Towards a General Statistical Theory of Imperfection Sensitivity in Elastic Post-Buckling, *Journal of Mechanics of Physics and Solids*, Vol. 15, 413-417, 1967.

Timoshenko S.P. and Gere J.M., *The Theory of Elastic Stability*, McGraw Hill, New York, 1961.

Van Slooten R.A. and Soong T.T., Buckling of a Long Axially Compressed Thin Cylindrical Shell with Random Initial Imperfections, *Journal of Applied Mechanics*, Vol. 39, 1066-1072, 1972.

Verduyn W.D. and Elishakoff I., A Testing Machine for Statistical Analysis of Small Imperfect Shells, *Proceedings of the Seventh International Conference on Experimental Stress Analysis* (A. Betser, ed.), Ayalon Press, Haifa, pp. 545-557, 1982.

Videc B. P. and Sanders J. L., Jr., Application of Khasminskii's Limit Theorem to the Buckling Problem of a Column with Random Initial Deflections, *Quarterly of Applied Mathematics*, Vol. 39, 422-428, 1976.

Zhu L.P., Elishakoff I. and Starnes J.H., Jr., Derivation of Multi-Dimensional Ellipsoidal Convex Model for Experimental Data, *Mathematics of Computation and Modelling*, Vol. 24, 103-114, 1996.

THERMOMECHANICAL POSTBUCKLING OF SHELLS*

Liviu Librescu*
Virginia Polytechnic Institute and State University
Blacksburg, VA 24061-0219

A number of issues involving the postbuckling of doubly-curved panels exposed to a non-uniform temperature field and subjected to a system of mechanical loads are considered in this paper. Effects played by transverse shear, initial geometric imperfections, membrane and thickness-wise temperature gradient, tangential edge constraints, linear/non-linear elastic foundation are incorporated and their implications on the non-linear response behavior of shells are discussed. Issues related with the delay of the occurrence of the snap-through buckling, alleviation of its intensity and even with its removal are addressed and remarks on conditions rendering a curved panel insensitive to initial geometric imperfections are included. Results on small vibration of shells about sub- and postcritical ranges are provided and structural modeling issues playing a non-negligeable role towards a reliable prediction of the postbuckling behavior of shells under complex loading conditions are discussed. Results on non-linear response of flat reinforced panels subjected to thermomechanical loads are also presented. Finally, problems not covered by this article are briefly indicated.

Introduction, Scope and Contents

The static and dynamic behavior of mechanically and thermally loaded flat and curved panels is a problem of considerable relevance in the design and development of supersonic/hypersonic vehicles, of future reusable space transportation systems, launch vehicles and of advanced propulsion systems.

During their missions, the structure of flight vehicles have to withstand severe aerodynamic, aeroacoustic and thermomechanical loads. The temperatures involved are likely to range from the extreme lows of cryogenic fuels and radiation to space, to the highs associated with aerodynamic heating, heat from propulsion unit and radiation from the sun.

In spite of the increased flexibility which is likely to characterize the structure of next generation of advanced flight vehicles, they have to be able to fulfill a multitude of missions in complex environmental conditions and feature an expanded operational envelope. The same is valid with the reusable space vehicles, which, for evident reasons, require a prolongation of their operational life, without impairing upon the security of flight.

A problem of evident importance towards the rational design of advanced supersonic/ hypersonic flight vehicles lies on the possibility to accurately determine the load carrying capability of their structure. Moreover, a better understanding of conditions yielding an enhancement of the load carrying capacity, can dramatically contribute to the increase in performance of these flight vehicles.

For curved panels such an investigation has a special relevance. Indeed, in contrast to flat panels which experience a considerable amount of additional load-carrying capability in the postbuckling range, the curved panels exhibit a highly unstable postbuckling behavior, manifested by snap-through jumps toward a state of stable equilibrium.

Such a snapping phenomenon is manifested in both the static case (i.e. in the case e.g. of the temperature/compressive load vs. transverse deflection behavior) and of the dynamic case (i.e. of eigenfrequency vs. temperature/compressive load interaction). In addition, the load carrying capacity of curved panels is imperfection sensitive.

It appears evident that reduction of the intensity of the snapping phenomenon as well as of the sensitivity to initial geometric imperfection is a matter of considerable importance toward a prolonged use of curved panels in the postbuckling range, without impairing upon their structural integrity.

One of the modern trends in the construction of advanced flight vehicles capable of operating in a high temperature environment, consists of the ongoing incorporation in their structure of advanced composite materials.

However, as a result of this trend and for a reliable determination of their load carrying capacity, a careful assessment of the implications played by a number of non-classical effects is required. One of these is related with the transverse shear flexibility featured by advanced composites, and, in this connection, the problem of adequacy of Love-Kirchhoff shell model when dealing with thermomechanical load carrying capacity has to be addressed.

Another effect which was identified as the main cause of the large discrepancies between the

* Dedicatd as a modest homage to the memory of the distinguished scientist Dr. Manuel Stein.

* Professor, Dept. of Engineering Science and Mechanics

experimental and theoretical predictions of buckling loads, and which can affect dramatically the load carrying capabilities of curved structures exposed to thermomechanical loading is the initial geometric imperfection.

The recent developments related with solid-propellant rocket motors, as well as the interest of specialists for developing further efficient thermal protection systems for space transportation vehicles have intensified the need for a better understanding of the postbuckling response of geometrically perfect/imperfect shells continuously supported by elastic media and subjected to combined thermomechanical loadings. This is an issue which will also be addressed in this paper.

Determination of frequency-temperature interaction in the pre/postbuckling ranges of curved panels featuring transverse shear flexibility, initial geometric imperfection and subjected to mechanical pre-loadings, is of prime importance towards a reliable prediction of the aeroelastic behavior, thermoacoustic fatigue as well as of the dynamic response under time dependent external excitation of supersonic/hypersonic flight vehicle structures. It should be pointed out that between structural behaviors described in terms of frequency-temperature and temperature-deflection interactions, there is a close correlation. Due to its heuristic importance, this correlation will be emphasized and its features discussed.

Another factor which becomes relevant in the context of *multilayered* plates and shells composed of advanced composite materials is of a modeling nature. This is related with the non-fulfillment of the continuity requirement of transverse shear stresses at the layer interfaces. As was revealed in a number of recent papers, the violation of this requirement can result in unavoidable errors in the evaluation of the load carrying capacity of laminated composite structures. These errors can even be exacerbated when large jumps in transverse shear moduli from layer to layer are experienced. This issue will be also addressed in this paper.

Having in view the permanent importance of stiffened panels in the construction of space vehicles, several results addressing the problem of thermomechanical load carrying capacity of *flat* reinforced panels will be supplied.

Finally, related issues, not covered by the present paper, but of current importance for the problem at hand will be briefly mentioned.

In spite of the considerable practical importance of this problem, the literature devoted to the thermomechanical postbuckling of shells, in general, and of the ones previously mentioned, in particular, is very limited. The most comprehensive survey papers available to date, (see Refs. 1-5), fully reveal this reality. Part of the results presented in this paper have been obtained in different contexts by this author and his co-workers and reported in a number of papers published (see Refs. 6-11) or presented in different conferences (see Refs. 12-16). Appropriate references to these results are indicated. Other results included here have not appeared or been discussed previously in the literature.

Shell Geometry. Governing Equations

The answer to the previously mentioned problems requires the development and solution of the nonlinear system of equations associated with the theory of shells incorporating the above mentioned non-classical effects.

To this end, consider the case of doubly-curved shallow panels of uniform thickness h. Assume that the structure is symmetrically laminated of $2m+1, (m = 1, 2, ...)$, elastic layers whose materials exhibit transversely -isotropic properties, the surfaces of isotropy being parallel at each point to the reference surface of the panel. Consideration of this particular anisotropy in our study is important in several respects: a) it enables one to emphasize in a more comprehensive way the effects played by the transverse shear flexibility, b) materials exhibiting this type of anisotropy, (such as the ones featured by the pyrolitic graphite and its alloys), play a great role in the thermal protection of aerospace vehicles and, as a result, they are used in the design of missile, reentry vehicle structures and engine nozzles (see e.g. Refs. 17 and 18), and finally, c) it provides a continuum model for the honeycomb type structures used as a filler in the sandwich type panels.

It is supposed that the layers are in perfect bond so that no slip between two contiguous layers may occur.

The points of the 3-D space of the panel are referred to a set of curvilinear normal system of coordinates, x^i, where $x^\alpha (\alpha = 1, 2)$ denote the coordinates tangent to the reference surface, x_3 denotes the coordinate normal to the planes tangent to the mid-surface, where $x^3 = 0$ defines the reference surface σ (coinciding with the mid-surface of the mid-layer).

In the forthcoming developments, the conditions pertinent to the theory of shallow shells are invoked. As a result of their adoption (see e.g. Ref. 19) it results that: i) the normal base vectors $\mathbf{g}_i$ tangent to the space coordinates coincide to $\mathbf{a}_i$ at the surface $x_3 = 0$, ii) the metric tensors associated with the system of coordinates on σ and with its projection on the plane P are the same and, iii) the curvature tensor of the reference surface behaves as a constant in the differentiation operation. In spite of mathematical simplifications implied by the adoption of the shallow shell theory, the obtained results are rather general, being applicable to large categories of aeronautical structures. Moreover, this theory enables one to cast the geometrically non-linear equations of shells in a form representing the generalized counterpart of the classical von-Kármán-Mushtari-Marguerre large deflection theory. Such a form of the governing equations was proven to be of an exceptional importance in the related buckling and post-buckling studies. Towards obtaining the governing equations in such a form, the various steps indicated in a number of previous papers (see e.g. Refs. 6, 10-12 and 20-25) have to be followed.

Without repeating these steps, we record here their final form which is:

$$
\begin{aligned}
&D u_3 \Big|_{\alpha\beta}^{\alpha\beta} - c^{\alpha\omega} c^{\beta\rho} \Big\{ b_{\alpha\beta} F_{|\omega\rho} + \left(u_{3|\alpha\beta} + \overset{\circ}{u}_{3|\alpha\beta} \right) F_{|\omega\rho} \\
&- \left(\frac{B+C}{S} - \delta_A \frac{M}{S} \right) \left(b_{\alpha\beta} F_{|\omega\rho} \right. \\
&\left. + \left(u_{3|\alpha\beta} + \overset{\circ}{u}_{3|\alpha\beta} \right) F_{|\omega\rho} \right) \Big|_{\sigma}^{\sigma} \Big\} \qquad (1a) \\
&- \left[P_3 - \left(\frac{B+C}{S} - \delta_A \frac{M}{S} \right) P_3 \Big|_{\sigma}^{\sigma} \right] \\
&+ m_o \left\{ \ddot{u}_3 - \frac{B+C}{S} + \delta_A \left(\frac{R}{m_o} - \frac{M}{S} \right) \right] \ddot{u}_3 \Big|_{\alpha}^{\alpha} \Big\} \\
&- \Pi \overset{1}{T} \Big|_{\alpha}^{\alpha} = 0,
\end{aligned}
$$

$$
\begin{aligned}
&(\tilde{b} + \tilde{c}) F \Big|_{\lambda\pi}^{\lambda\pi} + \frac{1}{2} \left(u_3 |_{\rho}^{\rho} u_3 |_{\lambda}^{\lambda} - u_3 |_{\rho}^{\lambda} u_3 |_{\lambda}^{\rho} \right) \\
&+ \left(\overset{\circ}{u}_3 |_{\pi}^{\pi} u_3 |_{\alpha}^{\alpha} - \overset{\circ}{u}_3 |_{\alpha}^{\pi} u_3 |_{\pi}^{\alpha} \right) + \left(2H u_3 \Big|_{\pi}^{\pi} - b_{\lambda}^{\beta} u_3 \Big|_{\beta}^{\lambda} \right) \\
&+ 2\delta_A \tilde{d} \left(u_3 \Big|_{\lambda}^{\lambda\rho} u_3 \Big|_{\rho} + u_3 |_{\rho}^{\lambda} u_3 |_{\lambda}^{\rho} + \overset{\circ}{u}_3 |_{\pi}^{\rho\pi} u_3 |_{\rho} + \right. \\
&\left. + u_3 \Big|_{\pi}^{\rho\pi} \overset{\circ}{u}_3 \Big|_{\rho} + 2 \overset{\circ}{u}_3 |_{\pi}^{\rho} u_3 |_{\rho}^{\pi} \right) + \tilde{\Lambda} \overset{\circ}{T} \Big|_{\alpha}^{\alpha} = 0, \qquad (1b)
\end{aligned}
$$

and

$$
\phi - \frac{C}{S} \phi |_{\sigma}^{\sigma} = 0. \qquad (1c)
$$

In Eqs. (1) $u_3 (\equiv u_3(x^\omega, t)$ and $\overset{\circ}{u}_3 (\equiv \overset{\circ}{u}_3(x^\omega)$ denote the transversal deflection measured from the imperfect surface in the positive, inward direction, and the stress-free initial geometric imperfection, respectively, $F (\equiv F(x^\omega, t))$ denotes the Airy's potential function $c^{\alpha\beta}$ is the two-dimensional permutation symbol while in Eq. (1c), $\phi (\equiv \phi(x^\omega, t))$ denotes a potential function associated with the transverse shear rotations. In addition, D, B, C, R, $\tilde{\Lambda}$, Π, $\tilde{b}$, and $\tilde{c}$ denote stiffness quantities; M, S and $\tilde{d}$ stand for the transverse shear stiffness quantities of the composite structure These quantities are recorded in Refs. 6, 24 and 25. In addition $(\cdot)|_{\alpha}^{\alpha}$ and $(\cdot)\Big|_{\alpha\beta}^{\alpha\beta}$ denote the 2-D Laplace and biharmonic operators, respectively, while $H (\equiv (1/R_1 + 1/R_2)/2))$, denotes the average curvature of the shell mid-surface, where R_1 and R_2 are the principal radii of curvature of σ. In the same equations $\overset{\circ}{T}\left(\equiv \overset{\circ}{T}(x^\omega)\right)$ and $\overset{1}{T}\left(\equiv \overset{1}{T}(x^\omega)\right)$ define the membrane and thicknesswise temperature distributions, respectively, in whose terms the 3-D temperature field is expressed as

$$
T(x^\omega, x^3) = \overset{\circ}{T}(x^\omega) + x^3 \overset{1}{T}(x^\omega). \qquad (2)
$$

In turn, $\overset{\circ}{T}$ and $\overset{1}{T}$ are expressed in terms of the temperature distributions at $x^3 = \pm h/2$, namely of $T_i (\equiv T(x^\omega, x^3 = h/2))$ and $T_e (\equiv T(x^\omega, x^3 = -h/2))$ as:

$$
\overset{\circ}{T}(x^\omega) = (T_i + T_e)/2, \qquad \overset{1}{T}(x^\omega) = (T_i - T_e)/h. \qquad (3)
$$

It can easily be shown that, depending on whether T_e or T_i is held fixed at a certain temperature level (e.g. at $70°F$), $\overset{1}{T}(x^\omega)$ can be expressed as $h\overset{1}{T} = 2(\overset{\circ}{T} - T_e)$ or $h\overset{1}{T} = 2(T_i - \overset{\circ}{T})$ respectively. These expressions are used in the generation of the numerical results.

In addition to these notations, $P_3 (\equiv P_3(x^\omega, t))$ entering Eq. (1a) is defined as

$$
P_3(x^\omega, t) = p_3 - \left(\overline{K}_1 u_3 + \overline{K}_3 u_3^3 \right), \qquad (4)
$$

where $p_3 (\equiv p_3(x^\omega))$ denotes the distributed lateral pressure while $\overline{K}_1$ and $\overline{K}_3$ are the linear and cubic moduli of the Winkler's foundation respectively.

The governing equations (1) include the effects of: *i)* transverse shear deformation and transverse normal stress; *ii)* large deflection (in the sense of the von Kármán large deflection theory); *iii)* initial geometric imperfections, *iv)* fulfill the conditions of the absence of shear tractions on the external bounding surfaces of the shell, and, *v)* enables one to consider the case when the shell is supported by a linear/nonlinear elastic foundation.

In the expressions of stiffness quantities $E, G(\equiv E/2(1+\nu)), \nu, \lambda$ denote the Young's modulus, shear modulus, Poisson's ratio and thermal compliance coefficient characterizing the thermoelastic properties parallel to the surface of isotropy, while E', G', ν' and λ' are the counterpart properties perpendicular to the surface of isotropy.

Specialization of governing equations for $\delta_A = 0$, and $\delta_H = 0$ and replacement in the stiffness quantities S and M of transverse shear moduli $G'_{(k)}$ by $K^2 G'_{(k)}$ (where K^2 denotes a transverse shear correction factor), the first order transverse shear deformation (FSDT) counterpart of the present theory is obtained. The classical von Kármán-Mushtari-Marguerre shell theory can be easily obtained from the FSDT variant of the governing equations by considering $G'_{(k)} \to \infty$. For the case of a single layer shell, in the stiffness quantities $h_{(m+1)} \to h/2$ and $\sum_{r=1}(\cdot) \to 0$ should be considered.

The governing equation (1c) of the Helmholtz type defines the boundary layer effect. Its solution is characterized by a rapid decay when proceeding from the edges towards the interior of the shell. Although uncoupled in the governing equations, the unknown function ϕ remains coupled with the other two functions, F and u_3, in the equations expressing the boundary conditions (in number of five at each edge).

As was previously shown, (see e.g. Ref. 21), for simply supported boundaries, the function ϕ can be rendered decoupled in the boundary condition, and as a result, the boundary layer equation (1c) in conjunction with these boundary conditions admits the trivial solution $\phi \equiv 0$.

Thermomechanical Postbuckling of Shallow Panels With Rectangular Planform

The previously displayed equations are used to study the postbuckling of simply-supported symmetrically laminated doubly curved panels with rectangular planform, $(\ell_1 \times \ell_2)$ exposed to a temperature rise $T\left(x^{\omega}, x^3\right)$ and subjected to compressive edge loads and a lateral pressure. We will refer the points of σ to a Cartesian orthogonal system of coordinates assumed to be parallel to the panel edges.

Consideration related with the identical fulfillment of the *out of plane* boundary conditions and implementation of initial geometric imperfections yielding the most critical postbuckling behavior (see e.g. Ref. 26) suggest the following representations:

$$\left\{ \begin{array}{c} u_3(x_1, x_2; t) \\ \overset{o}{u}_3(x_1, x_2) \end{array} \right\} = \left\{ \begin{array}{c} w_{mn}(t) \\ \overset{o}{w}_{mn} \end{array} \right\} \sin \lambda_m x_1 \sin \mu_n x_2,$$

$$\left\{ \begin{array}{c} \overset{o}{T}(x_1, x_2, x_3) \\ \overset{1}{T}(x_1, x_2, x_3) \\ p_3(x_1, x_2) \end{array} \right\} = \left\{ \begin{array}{c} \overset{o}{T}_{mn} \\ \overset{1}{T}_{mn} \\ p_{mn} \end{array} \right\} \sin \lambda_m x_1 \sin \mu_n x_2, \qquad (5a-c)$$

where $\lambda_m = m\pi/l_1$; $\mu_n \equiv n\pi/l_2$.

The **tangential** boundary conditions are satisfied on an average. To this end, the potential function F is represented as:

$$F(x_\alpha, t) = F_1(x_\alpha, t) - \frac{1}{2}((x_2)^2 N_{11} + (x_1)^2 N_{22}). \quad (6)$$

Here $F_1(\equiv F_1(x_\alpha, t))$ is a particular solution of Eq. (1b) (determined in conjunction with Eqs. (5), while N_{11} and N_{22} denote the normal edge loads (considered positive in compression).

In the case of the panel loaded in the direction of the x_1-coordinate only,the remaining edges being unloaded and immovable, the condition for the immovable edges $x_2 = 0$, ℓ_2 may be expressed in an average sense as (see, e.g. Refs. 20, 27),

$$\int_0^{\ell_1} \int_0^{\ell_2} u_{2,2} dx_1 dx_2 = 0, \qquad (7)$$

where $u_2(\equiv u_2(x_1, x_2, t)$ denotes the tangential displacement parallel to the x_2 -coordinate. This equation yields the fictitions edgeload N_{22} for which the edges $x_2 = 0, \ell_2$ remain immovable.

In addition to these extreme tangential edge restraint conditions, the case of *partially moveable* opposite unloaded edges $x_\alpha = 0, \ell_\alpha$ is considered. Following Refs., 7, 10, 15 and 20, a measure of the partial moveability of edges $x_\alpha = 0, \ell_\alpha$ in terms of the stiffness parameter λ_α is defined. As was shown in the indicated references, moveable and immoveable edges $x_\alpha = 0, \ell_\alpha, (\alpha = 1, 2)$ correspond to $\lambda_\alpha = 0$ and $\lambda_\alpha = 1$, respectively.

Partially moveable edges at $x_\alpha = 0, \ell_\alpha$ are defined by $0 < \lambda_\alpha < 1$. As in the case of immoveable edges, also in this case, for a specific value of λ_α, the necessary edge load $N_{\alpha\alpha}$ rendering the edges $x_\alpha = 0, \ell_\alpha$ partially moveable has to be determined.

In the case when the shell is supported on the inner surface by a Winkler linear/nonlinear foundation, the governing equation (1a) has to be considered in the sense of Eq. (4).

Following the procedure developed in Refs. 6–10, the displacement expansions given by Eq. (5) are substituted into the Eq. (1b) and $F_1(x_1, x_2)$ is obtained by solving the resulting linear nonhomogeneous partial differential equation. The remaining governing equation, Eq. (1a), is converted, via Galerkin's method, into a set of nonlinear ordinary differential equations. This procedure yields the following set of $M \times N$ nonlinear ordinary differential equations governing the postbuckling behavior

$$A_{rs}\ddot{w}_{rs} + R_{rs}w_{rs} + p_{rs}B_{rs} + P_1\left[w_{rs}, \overset{\circ}{w}_{rs}, \tilde{L}_{11}, \tilde{L}_{22}, \overline{K}_1\right] + \hat{P}_1\left[w_{rs}, \overset{\circ}{w}_{rs}, \overset{\circ}{T}_{rs}, \overset{1}{T}_{rs}\right] + P_2\left[w_{rs}^2, \overset{\circ}{w}_{mn}\right] + P_3\left[w_{rs}^3, \overset{\circ}{w}_{mn}, K_3\right] = 0. \qquad \sum_{r,s} \qquad (8)$$

The symbol $\sum_{r,s}$ indicates that there is no summation over the indices, r and s, where $r = 1, 2, \ldots, M$ and $s = 1, 2, \ldots N$. In Eqs. (8), $\hat{P}_1$, P_2 and P_3 are linear, quadratic, and cubic polynomials of the unknown modal amplitudes w_{rs}, respectively, the coefficients A_{rs}, B_{rs}, and R_{rs} are constants that depend on the material and geometric properties of the shell, $\tilde{L}_{11}\left(\equiv N_{11}\ell_1^2/\pi^4 D\right)$ and $\tilde{L}_{22}\left(\equiv N_{22}\ell_1^2/\pi^4 D\right)$ is the normalized forms of tangential edge loads, $\hat{p}(\equiv p_{11}\ell_1^4(Dh))$ the dimensionless lateral pressure amplitudes while $K_1\left(\equiv \overline{K}_1\ell_1^4/\pi^4 D\right)$ and $K_3\left(\equiv \overline{K}_3\ell_1^2/\pi^4 D\right)$ are the dimensionless moduli of the Winkler's foundation.

Vibrational Behavior in the Pre- and Postbuckling Ranges

We will restrict our attention to *small* vibrations $\overline{\overline{w}}_{mn}(t)$ about the static equilibrium position $\overline{w}_{mn}$. In this case the vibration amplitude can be represented as

$$w_{mn}(t) = \overline{w}_{mn} + \overline{\overline{w}}_{mn}(t), \qquad (9)$$

where the time-dependent part $\overline{\overline{w}}_{mn}$ is considered small as compared to $\overline{w}_{mn}$ and $\overset{\circ}{w}_{mn}$, in the sense of

$$\overline{\overline{w}}_{mn}^2 \ll \left(\overline{w}_{mn}, \overset{\circ}{w}_{mn}\right). \qquad (10)$$

The dependence of the static part of Eqs. (9) (defining the mean equilibrium position of the shell) upon the compressive edge loads, lateral pressure and the thermal field can be determined from the governing equations, (Eqs. (8)), by discarding the inertia terms. The equation of motion for small vibrations of the composite shell with respect to this position can be obtained by substituting Eq. (9) into Eqs. (8), where the order of magnitude stipulated by Eqs. (10) should be enforced.

In such a way, the equation of vibration about the equilibrium position is obtained as

$$A_{mn}\ddot{\overline{\overline{w}}}_{mn} + D_{mn}\overline{\overline{w}}_{mn} = 0, \qquad (11)$$

where $D_{mn} \equiv D_{mn}\left(\overline{w}_{mn}, \overline{w}_{mn}^2, \overline{w}_{mn}^3, \overset{\circ}{w}_{mn}, p_{mn}, \overset{\circ}{T}_{mn}, \overset{1}{T}_{mn}\overline{K}_1, \overline{K}_3\right)$ and the coefficient A_{mn} contain all the information about the thermo-mechanical and geometrical properties of the structure.

Employment in Eq. (11) of the representation

$$\overline{\overline{w}}_{mn}(t) = \tilde{w}_{mn}\exp\left(i\omega_{mn}t\right) \qquad (i = \sqrt{-1}) \qquad (12)$$

and keeping in mind that $\overline{w}_{mn}$ is obtainable from the static counterpart of Eq. (8), Eq. (11) in conjunction with Eq. (12) provides the interaction between the vibration frequency and the compressive, lateral and thermal loads in the pre- and postbuckling ranges (for the perfect panels) and in the pre- and post-limit ranges (for the geometrically imperfect ones).

Numerical Illustrations

A range of applications involving the postbuckling of simply supported curved panels exposed to thermomechanical loads is considered. The considered panels exhibit a square planform projection of side length $\ell_1 = \ell_2 = \ell$ and consist of either a single or three layers in which the constituent materials feature transversely-isotropic thermoelastic properties.

For single layer panels, in all numerical results, the following input data characterizing the associated thermoelastic material properties have been considered

$$\nu = \nu' = 0.2, \quad \lambda/E = -1.15 \times 10^{-5}\text{in/in/}^\circ\text{F}, \quad \lambda/\lambda' = 1.4286, \quad \text{and} \quad E/E' = 5.$$

For the three-layer panels one assumes that the core layer is twice as thick as each of the face-layers. In addition, throughout these results it was assumed

that the elastic moduli and thermal compliance coefficients are defined in terms of non-dimensional ratios as:

for the face-layers

$$(E/E')_f = 5;\ \ (E/G')_f = 10\ \ (\lambda/\lambda')_f = 1.4286,$$
$$(\lambda/E)_f = -1.15 \times 10^{-5}\text{in/in/}^\circ\text{F}$$

and for the core-layer

$$(E/E')_c = 2;\ \ (E/G')_c = 30\ \ (\lambda/\lambda')_c = 1.21413,$$
$$(\lambda/E)_c = -4.8875 \times 10^{-5}\text{in/in/}^\circ\text{F}.$$

It was also postulated that $E_f/E_c = 10$.

In these expressions the indices f and c identify the affiliation of respective quantities to the face and core layer, respectively. The considered numerical data reflect the fact that the core layer is more shear-deformable than the face layers, a behavior which is commonly valid in sandwich type constructions.

The effect of the positive and negative Gaussian curvature $K(\equiv\ (R_1R_2)^{-1})$ upon the nonlinear behavior of doubly curved panels of fixed $l_1/R_1 = 0.1$, subjected to a thickness-wise temperature variation is shown in Figs. 1a and 1b. One assumes that the temperature amplitude on the upper face of the panel is held fixed ($T_e = 70^0F$). For the panel featuring a negative Gaussian curvature ($K < 0$), the temperature rise is associated with a continuous increase of the positive transverse deflection. In contrast to this behavior, for panels of positive Gaussian curvature, with the increase of l_2/R_2, the non-linear behavior evolves from a critical one, characterized by a snap-through buckling until a benign one, characterized by a continuous upward increase of the transverse deflection. As Fig. 1a reveals, for $l_2/R_2 = 0.026$, the panel experiences a buckling bifurcation, followed, by the further increase of the temperature, by a snapping of high intensity. However, for $l_2/R_2 > 0.026$, the panel experiences a benign non-linear behavior. Associated with this case, Figure 1b depicting the associated frequency-temperature interaction reveals a similar trend. In other words, Fig. 1b reveals that only for the cases $l_2/R_2 = 0.026$ and $l_2/R_2 = 0.01$ one obtains a buckling bifurcation and a limit temperature, respectively. At the same time, Fig. 1b reveals that for the panels of $K < 0$, a steeper increase of the fundamental eigenfrequency is experienced as compared to the case of panels of a positive Gaussian curvature, characterized by $l_2/R_2 > 0.026$. Figures 2a and 2b constitute the counterparts of Figs. 1a and 1b, respectively, obtained when, in contrast to the case in Figs. 1, the temperature amplitude of the internal bounding surface is held fixed ($T_i = 70^0F$). The results reveal a reversal of trends as compared to those in the previous figures, in the sense that in this case, for $K > 0$, the increase of l_2/R_2 results in a benign temperature-deflection behavior, whereas for $K < 0$, in the case of panels characterized by $(-0.3 \leq l_2/R_2 \leq -0.1)$, the response evolves from a stable behavior characterized by a monotonous increase of the positive inward deflection followed, with the temperature rise, by an unstable response, characterized by the occurrence of the snapping phenomenon, until a benign one featuring a continuous increase of the negative deflection with the temperature rise. In this case, for the panel characterized by $l_2/R_2 = -0.23$, a buckling bifurcation becomes apparent. The frequency-temperature interaction corresponding to this case and depicted in Fig. 2b, reveals that the panels of $K > 0$ feature a larger fundamental frequencies than their negative Gaussian curvature panel counterparts.

An assessment of the effect of the immoveability of two opposite unloaded edges of a spherical cap subjected to the compressive pre-load $\tilde{L}_{11} = 3$ and a non-uniform through thickness temperature rise, with $T_e = 70°F$, can be inferred from Figs. 3 and 4. While in Figs. 3 the unloaded edges of the considered three-layer panel are freely moveable, in Fig. 4 these are immoveable. Figure 3a shows that in these conditions, for the panel characterized by $(0.03 > l/R \geq 0)$ a benign postbuckling behavior is experienced, followed in the curvature range $(054 \geq l/R \geq 0.03)$ by the existence of a limit temperature and (for $l/R = 0.054$)again, by a buckling bifurcation while in the range $l/R > 0.054$, by a benign nonlinear behavior. The frequency-temperature interaction of the case considered in Fig. 3a is depicted in Fig. 3b. This plot reveals the existence of the buckling bifurcation and of the limit temperatures at the points where the frequencies become zero valued quantities. Moreover, it reflects the same features as its static counterpart, such as the existence of a strong snap-through dynamic jump for the panel characterized by $l/R = 0.054$, when the temperature increases beyond the respective critical temperature, and also in the cases when limit-temperatures are featured. In the case of immoveable unloaded edges, (see Fig. 4a) in contrast to the trend in Figs. 3, a significant decay in the buckling bifurcation temperature featured by this the very shallow panel

is experienced. However, for curvatures l/R larger than the critical one (i.e. $l/R > 0.025$), the panel exhibits a benign non-linear behavior. Compared with the behavior emerging from Fig. 3a, in the present case it results that there is a larger range of curvature ratios for which a benign temperature - deflection dependence is reached. Fig. 4b reveals similar features as the ones occuring in the static case.

The effect of a biaxial compressive preload $L_R(\equiv \tilde{L}_{22}/\tilde{L}_{11}$ where $L_R = 0$ when $\tilde{L}_{22} = 0)$. and of a predetermined pressure on the non-linear behavior of a circular cylindrical panel subjected to a through the thickness temperature rise is shown in Figs. 5. The results reveal that, for the considered pressure amplitude ($\hat{p} = 2$), and depending on the magnitude of L_R, a large transition form a benign non-linear behavior (occurring in the range $(0.05 \geq L_R \geq 0)$, a limit temperature (in the range $(0.9 > L_R \geq 0.5)$, a thermal buckling for $L_R = 0.9$, followed finally, by a benign behavior for $L_R > 0.9$ is experienced. The same feature results also from Fig. 5b.

The effect of initial geometric imperfections is illustrated in Figs. 6. The results show that for the considered panel, in the considered range of the initial geometric imperfection amplitudes the panel features a large transition from a benign non-linear behavior (in the range $0.2 \geq \delta_0 \geq 0.6$); to a behavior characterized by a limit temperature (for $(-0.06 < \delta_0 < 0.2)$); a buckling bifurcation (for $\delta_0 = -0.06$) and finally, to a benign non-linear behavior for $\delta_0 < -0.06$. The dynamic counterpart of this plot, i.e. Fig. 6b reflects the same trend.

The non-linear response of a geometrically perfect three-layer spherical cape subjected to a non-uniform through thickness temperature rise, whose edges $x_1 = 0, l_1$ are perfectly moveable while the edges $x_2 = 0, l_2$ partially moveable is depicted in Figs. 7.

This plot shows that the degree of edge restraints of two opposite edges can play a considerable role towards enhancement of the non-linear response of the panel. This implies that is possible to eliminate the snap-through buckling at all, or at least to attenuate its intensity by properly selecting the degree of the edge restraint. Figure 7b reveals also that, in parallel with the enhancement of the load carrying capacity, the proper selection of the degree of the edge restraint results also in the possibility to improve the dynamic behavior by eliminating the possibility of occurrence of the dynamic snap-through and by ensuring that the fundamental eigenfrequencies feature a continuous increase with the temperature rise.

Figure 8 depicts the non-linear behavior of a geometrically perfect three-layer spherical cape resting on a non-linear Winkler foundation when subjected to lateral pressure rise and the fixed temperature amplitudes ($T_i = 500^0F$ and $T_e = 70^0F$).

The results reveal that both the linear and non-linear foundation moduli can contribute to the enhancement of the load carrying capacity of the panel, specifically, in the case of a hardening type foundation (characterized by $K_3 > 0$).

Another factor playing a non-negligeable role on the load carrying capacity of laminated panels is related with that of the structural modelling. In this sense, it should be stressed that all previous results have been obtained on the basis of a higher order shear deformation theory (see Refs. 21, 23, 28 and 29) of laminated shells fulfilling the condition of zero tractions on its external bounding surfaces.. Within that theory, while the kinematic continuity conditions are fulfilled, the static ones related with the continuity of transverse shear stresses across the laminae interfaces are violated.

With the exception of a few results dealing with the implication of such a violation on the response quantities obtained within a linear theory of laminated plates/shells (see Ref. 30) or on their postbuckling under mechanical loads (see Ref. 16), no results on the topic of the present article can be found in the specialized literature.

In the paper Refs. 16 and 30 it was shown that in the case of the fulfillment of both the kinematical and static continuity conditions at the layer interfaces, *the form* of governing equations remains similar to that obtained when the *static continuity* conditions are violated, (i.e. with Eqs. (1)). As it was shown in Refs. 16 and 30, the only difference occurs in the stiffness quantities.

The relationships between the stiffness quantities proper to the model based upon the non-fulfillment of static continuity conditions (Model 1), and based upon their fulfillment (Model II), have been indicated in the above mentioned papers. Figures 9 depict the non-linear behavior of a three-layer slightly imperfect spherical cape of various l/R, and as a special case, of its flat plate counterpart, when subjected to a fixed biaxial compressive pre-load ($L_R = 0.1$ and $\tilde{L}_{11} = 0.75\tilde{L}_{11}$), the temperature amplitude at the upper bounding surface being

fixed, ($T_e = 70^0 F$). In addition to the combined effects of both the compressive edge loads and of the temperature rise on the non-linear behavior of the panel, the results show that the difference between the predictions provided by the two models is really insignificant. However this situation is not general, in the sense that in some instances, significant differences in the predictions based on the two models can occur. In the case where significative jumps in the transverse shear moduli, or/and in the thickness of two contiguous layers are experienced, important differences in the predictions based on the two models can be expected to occur. In such a case, Model I can result in under/overestimations of the accurate predictions provided by the Model II.

Finally, Fig. 10 depicts the non-linear response of geometrically perfect/imperfect orthogonally reinforced *flat* panels subjected to a membrane temperature rise and a lateral pre-load. The results show that even in the case of a geometrically perfect panel subjected only to a membrane temperature rise, the panel does not feature buckling bifurcation. This is a direct result of the inherent structural non-symmetry featured by reinforced panels [31]. Due to this structural non-symmetry, a bending-stretching coupling in the constitutive equations and further, in the governing equations is induced. The response behavior depicted in Fig. 10 reflects this reality.

Conclusions

A number of issues related with the thermomechanical postbuckling of shells have been addressed. Moreover, due to the considerable practical importance of this area of research, the mode interaction, initial imperfection in the geometry and property of constituent materials, enhancement of the thermomechanical load carrying capacity of curved panels via the tailoring technique, implications of temperature-dependent properties of constituent materials, reinforced shells under thermomechanical loading systems, effects of interfacial imperfections on thermomechanical load carrying capability of laminated composite shells are likely to constitute topics of intense research in the years to come.

Acknowledgements

Parts of the results presented herein have been obtained during a research sponsored by NASA Langley Research Center, Grant NAG-1-1300. The author expresses his deep appreciation to Drs. J.H. Starnes, Jr. and M.P. Nemeth. for stimulating technical discussions and encouragement throughout this work.

Special thanks are also due to Drs. W. Lin and M.A. Souza for useful discussions on a number of topics contained in this article.

References

1. Ziegler, F. and Rammerstorfer, F.G., "Thermoelastic Stability," *Thermal Stresses III*, Vol. 3, (R.B. Hetnarski, Ed.), Chapter 2, pp. 108-189, Amsterdam, New York, Oxford, Tokyo, North Holland, 108-189, 1989.
2. Tauchert, T.R., "Thermally Induced Flexure, Buckling and Vibration of Plates," *Appl. Mech. Rev.*, 44 (8), 347-360, 1991.
3. Noor, A.K. and Burton, W.S., "Computational Models for High-Temperature Multilayered Composite Plates and Shells," *Appl. Mech. Rev.*, 45 (10), 414-446.
4. Thornton, E.A., "Thermal Buckling of Plates and Shells," *Appl. Mech. Rev.*, Vol. 46, 485, 1993.
5. Argyris, J. and Tenek, L., "Combined Steady-state Nonlinear Heat Transfer/Thermal Postbuckling Configurations in Unstiffened and Stiffened Laminated Composite Plates and Shells," to appear in the 25th anniversary issue of *Comput. Method. Appl. Mech. Eng.*, 1997.
6. Librescu, L. and Souza, M.A., "Postbuckling of Geometrically Imperfect Shear-Deformable Flat Panels Under Combined Thermal and Compressive Edge Loadings," *Journal of Applied Mechanics*, Trans. ASME, Vol. 60, 526-533, 1993.
7. Librescu, L., Lin, W., Nemeth, M.P., and Starnes, Jr., J.H., "Thermomechanical Postbuckling of Geometrically Imperfect Flat and Curved Panels Taking Into Account Tangential Edge Constraints," *Journal of Thermal Stresses*, **18**, 465-482, 1995.
8. Librescu, L., Lin, W., Nemeth, M.P. and Starnes, Jr., J.H., "Vibrational of Geometrically Imperfect Flat and Curved Panels Subjected to Thermal and Mechanical Loads," *Journal of Spacecraft and Rockets*, Vol. 33, No. 2., March-April, pp. 285-291, 1996.
9. Librescu, L., Lin, W., Nemeth, M.P. and Starnes, Jr., J.H. "Effects of a Thermal Field on Frequency-Load Interaction of a Geometrically Imperfect Shallow Curved Panel," *AIAA Journal*, Vol. 34, No. 1, January, pp. 166-177, 1996.
10. Librescu, L. and Lin, W., "Vibration of Thermomechanically Loaded Flat and Curved Panels Taking into Account Geometric Imperfections and Tangential Edge Restraints," *International*

Journal of Solids and Structures, Vol. 34, 17, 1997.

11. Librescu, L. and Lin, W., "Thermomechanical Postbuckling of Plates and Shells Incorporating Non-classical Effects," in *Thermal Stresses*, IV (R.B. Hetnarski, Ed), Elsevier Science, B.V., 379-452, 1996.
12. Librescu, L., Lin., W., Nemeth, M.P., and Starnes, Jr., J.H., "Classical Versus Non-Classical Postbuckling Behavior of Laminated Panels Under Complex Loading Conditions," *Non-Classical Problems of the Theory and Behavior of Structures Exposed to Complex Environmental Conditions*, AMD-Vol. 164 (L. Librescu, ed.), 169-182, 1993.
13. Librescu, L., Lin, W., Nemeth, M.P., and Starnes, Jr., J.H., "Vibration of Geometrically Imperfect Laminated Flat and Shallow Curved Panels Subjected to Heating and a System of Mechanical Loadings," *Tenth DoD/NASA/FAA Conference on Fibrous Composites in Structural Design*, Report No. NAWCAD WAR-94096 60, II, IX-51-IX-64, 1994.
14. Librescu, L., Lin, W., Nemeth, M. and Starnes, Jr.J.H., "Effects of a Thermal Field on Frequency-Load Interaction of Geometrically Imperfect Shallow Curved Panels," AIAA Paper 94-1342, *AIAA/ASME/ASCE/AHS/ASC 35th Structures, Structural Dynamic and Material Conference*, April 28-30, Hilton Head, SC, 1994a.
15. Librescu, L., Lin, W., Nemeth, M.P., and Starnes, Jr., J.H., "Effects of Tangential Edge Constraints on the Thermal Postbuckling of Flat and Curved Panels Subjected to Thermal and Mechanical Loads," *Buckling and Postbuckling of Composite Structures*, AD-Vol. 41, PVP-Vol., Ed. A.K. Noor, ASME, 55-69, 1994.
16. Librescu, L., and Lin, W., DiScuiva, M. and Icardi, U. "Postbuckling of Laminated Composite and Sandwich Plates and Shells: On the Significance of the Fulfillment of Static Interlayer Continuity Conditions," ICAS Preceedings, 1996, Vol. 2, 20th Congress of the International Council of the Aeronautical Science, Sorrento, Napoli, Italy 8-13 Sept. 1996, Paper ICAS-96-5.11.2, pp. 2710-2721 (an improved version of this paper is under press in *Computer - Methods in Applied Mechanics and Engineering*).
17. Garber, A.M., "Pyrolitic Materials for Thermal Protection Systems," *Aerospace Engineering*, January, 126-137, 1963.
18. Woods, P.H., "Pyrolitic Graphite for High Pressure, High Temperature Applications," AIAA Paper 76-605, 2805-2823, 1976.
19. Green, A.E. and Zerna, W., *Theoretical Elasticity*, Clarendon, Oxford, 1968.
20. Librescu, L., *Elastostatics and Kinetics of Anisotropic and Heterogeneous Shell Type Structures*, Noordhoff, Leyden, The Netherlands, 1975.
21. Librescu, L. and Stein, M., "A Geometrically Nonlinear Theory of Transversely-Isotropic Laminated Composite Plates and its Use in the Postbuckling Analysis," *Thin-Walled Structures-Special Aerospace Structures*, **11**, 177-201, 1990.
22. Librescu, L. and Stein, M., "Postbuckling of Shear Deformable Composite Flat Panels Taking Into Account Geometrical Imperfections," *AIAA J.*, **30**(5), 1352-1360, 1992.
23. Librescu, L. and Chang, M.Y., "Imperfect Sensitivity and Postbuckling Behavior of Shear-Deformable Composite Doubly-Curved Shallow Panels," *Intl. J. Solids Struct.*, **29**(9), 1065-1083, 1992a.
24. Librescu, L. and Chang, M.Y., "Vibration of Compressively Loaded Shear Deformable Flat Panels Exhibiting Initial Geometric Imperfections," *AIAA Journal*, **30**(11), 2793-2795, 1992b.
25. Librescu, L. and Chang, M.Y., "Effects of Geometric Imperfections on Vibration of Compressed Shear Deformable Laminated Composite Curved Panels," *Acta Mechanica*, 96, 203-224, 1993.
26. Seide, P., "A Reexamination of Koiter's Theory of Initial Postbuckling Behavior and Imperfection Sensitivity of Structures," *Thin Shell Structures: Theory, Experiment and Design*, (Edited by C.Y. Fung and E.E. Sechler), pp. 59-80, Prentice-Hall, New Jersey.
27. Librescu, L., "Aeroelastic Stability of Orthotropic Heterogeneous Thin Panels in the Vicinity of the Flutter Critical Boundary," Part I and Part II, respectively, *Journal de Mécanique*, 4, 51-76, **6**, 132-152, 1965, 1967.
28. Reddy, J.N. and Liu, C.F., "A Higher-Order Theory for Geometrically Nonlinear Analysis of Composite Laminates," NASA Contr. Rept. 4056, March, 1987.
29. Librescu, L. and Reddy, J.N., "A Few Remarks Concerning Several Refined Theories of Anisotopic Laminated Plates," *Int. J. Engng. Sci.*, **27** (5), 515-527, 1989.
30. Librescu, L. and Lin, W., "Two Models of Shear Deformable Laminated Plates and Shells and Their Use in Prediction of Global Response Behavior," *European Journal of Mechanics/Solids*

6, 1095-1120, 1996.

31. Librescu, L. and Souza, M.A. "Non-Linear Response of Geometrically Imperfect Stiffened Flat Panels Under Thermomechanical Loads" *Journal of Thermal Stresses* (in press)

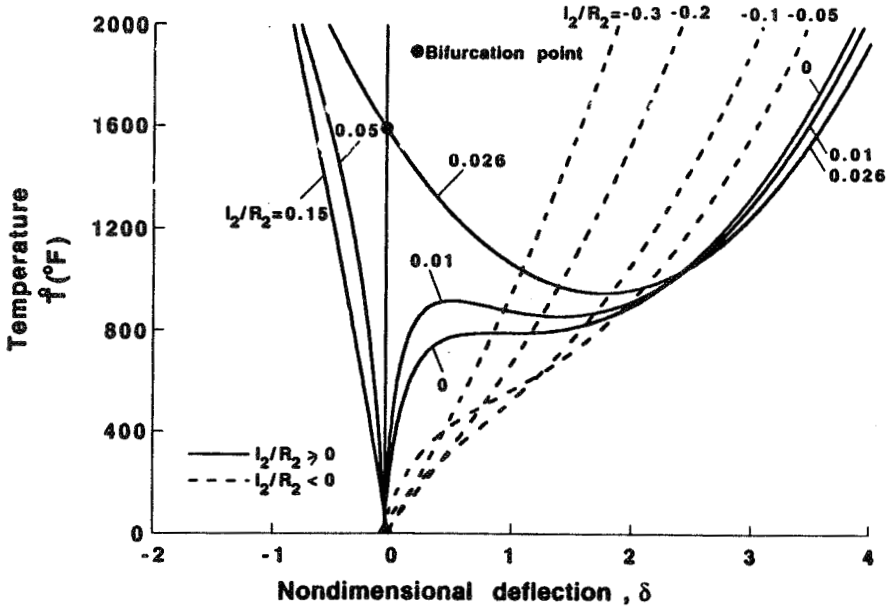

Fig. 1a Influence of the curvature parameter ℓ_2/R_2 upon temperature-transverse deflection dependence of doubly-curved three layer panels. Non-uniform through thickness temperature, ($T_e = 70°F$), $\ell_1/R_1 = 0.1, \ell_1/h = 100$.

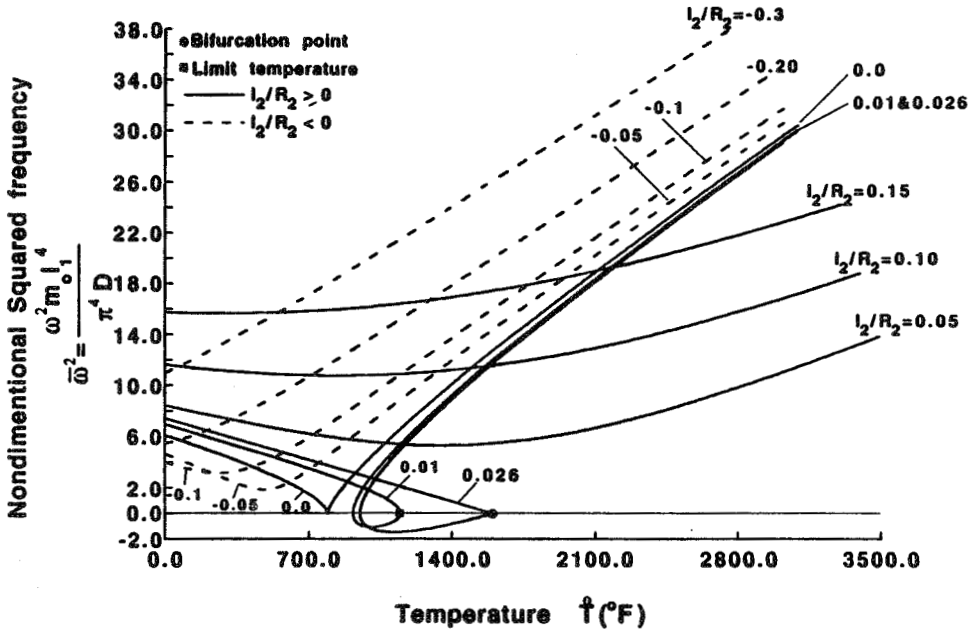

Fig. 1b Fundamental frequency (squared)-temperature interaction for the case described in Fig. 1a.

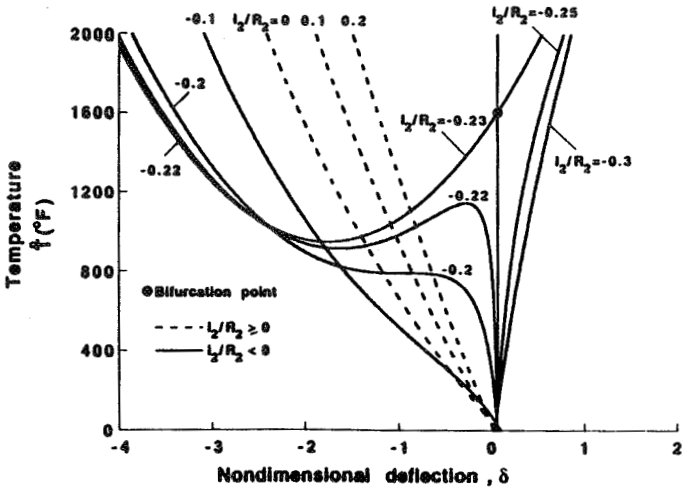

Fig. 2a Influence of the curvature parameter ℓ_2/R_2 on temperature-transverse deflection dependence of doubly curved three layer panels. Non-uniform through thickness temperature ($T_i = 70°F$). In the remaining, the data are similar to the ones in Figs. 1.

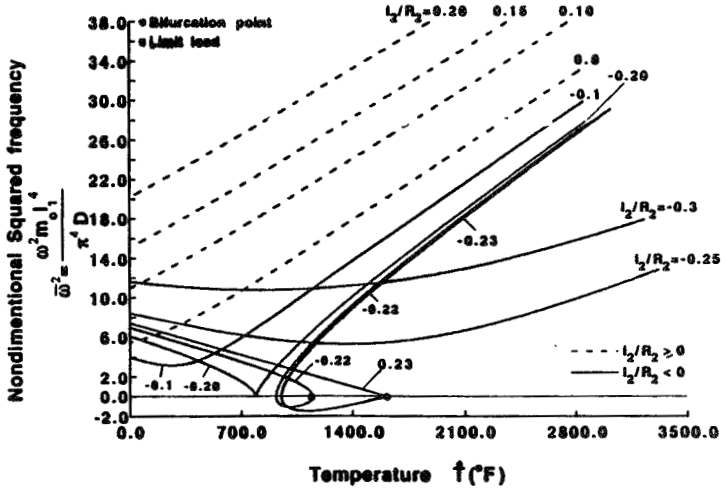

Fig. 2b Fundamental frequency (squared)-temperature interaction for the case described in Fig. 2a.

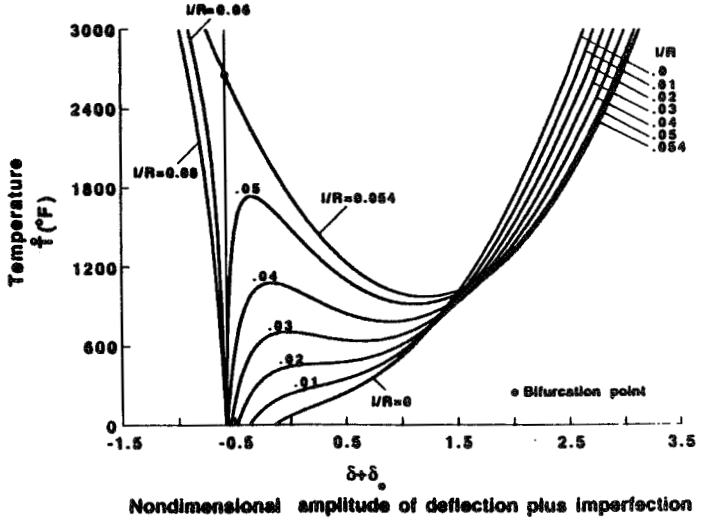

Fig. 3a Temperature-transverse deflection response in a three-layer geometrically-perfect spherical cape whose unloaded edges are freely moveable. Non-uniform through thickness temperature ($T_e = 70°F$), $\ell_1/h = 60, \tilde{L}_{11} = 3$.

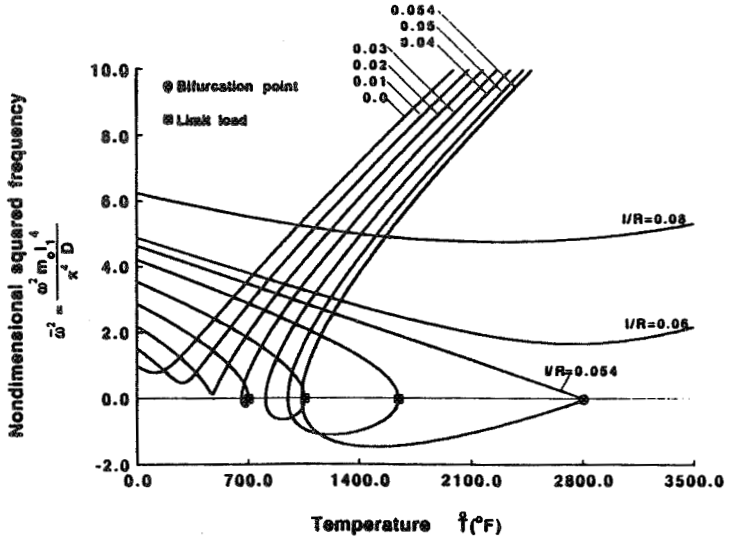

Fig. 3b Fundamental frequency-temperature interaction for the spherical cape described in Fig. 3a.

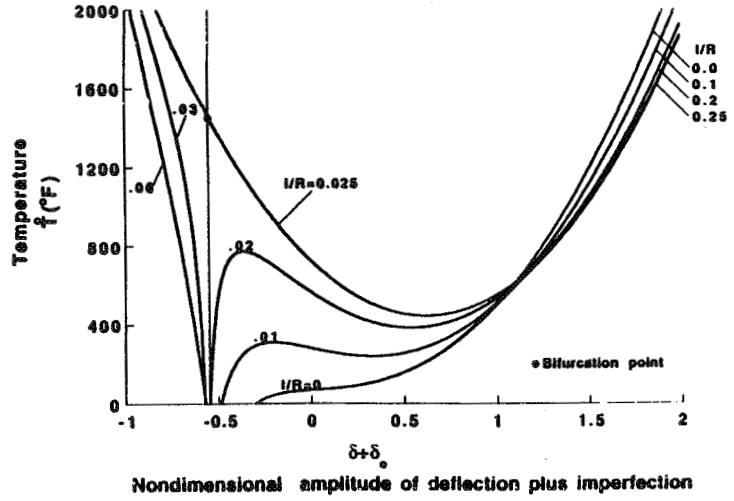

Fig. 4a Temperature-transverse deflection response in a three-layer geometrically perfect spherical cape whose unloaded eges are immoveable. The remaining data are similar to the ones in Fig. 3a.

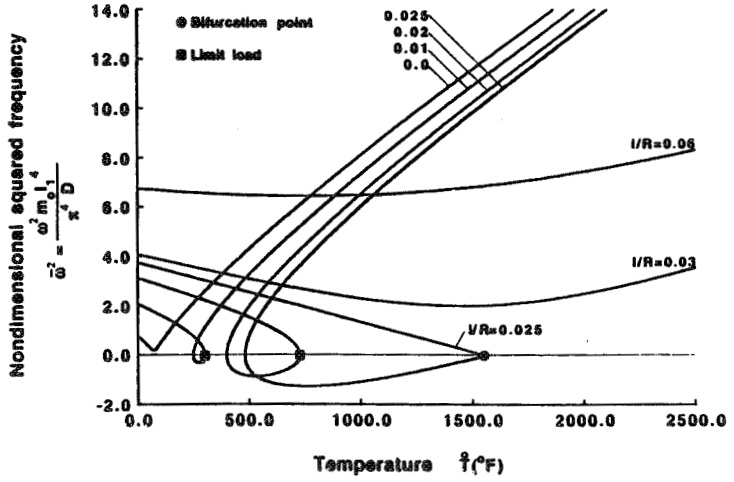

Fig. 4b Fundamental frequency (squared)-temperature interaction for the case described in Fig. 4a.

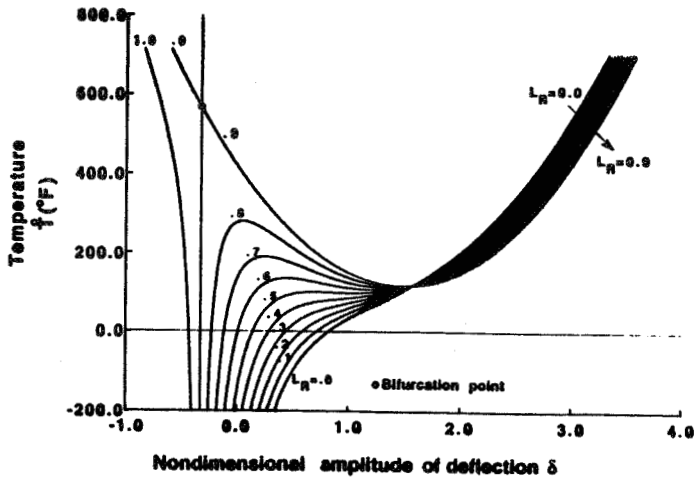

Fig. 5a Effect of a compressive biaxial pre-load of ratio L_R on temperature-transverse deflection response of a three-layer geometrically perfect circular cylindrical panel. Non-uniform through thickness temperature $T_e = 70°F)$, $\ell_1/h = 120, \ell_1/R_1 = 0, \ell_2/R_2 = 0.08, \tilde{L}_{11} = 2, \hat{p} = 2$.

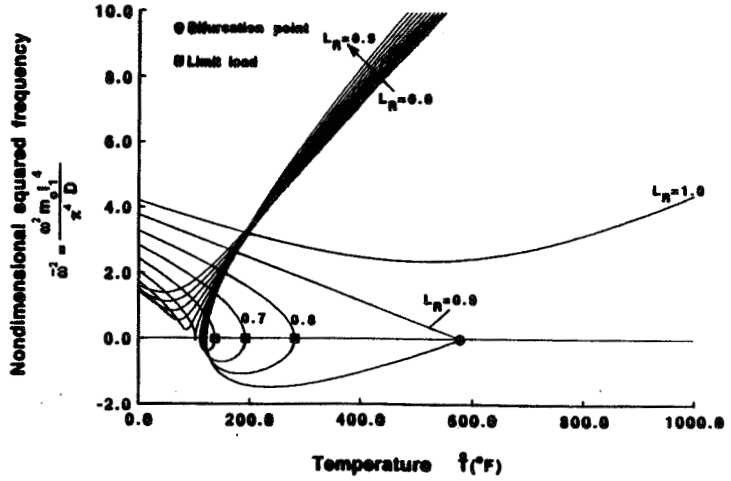

Fig. 5b Fundamental frequency (squared)-temperature interaction for the circular cylindrical panel described in Fig. 5a.

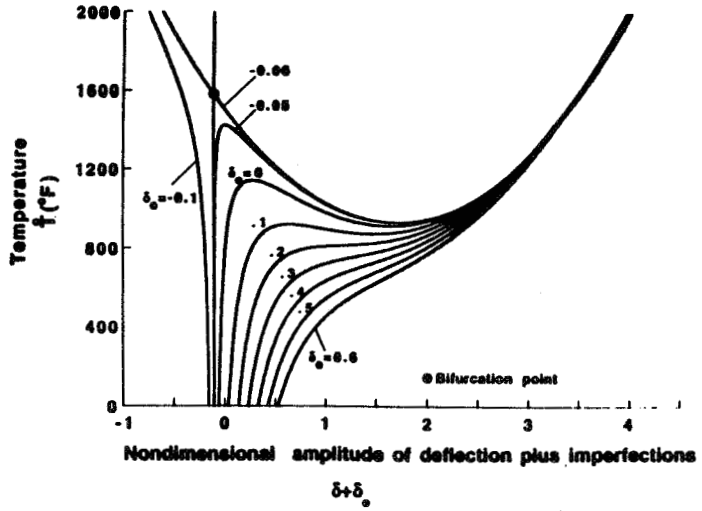

Fig. 6a Effect of initial geometric imperfection on the temperature-deflection response of a very shallow spherical cape. Non-uniform through thickness temperature $(T_e = 70°F), \ell_1/h = 100, \ell_1/R_1 = \ell_2/R_2 = 0.06$.

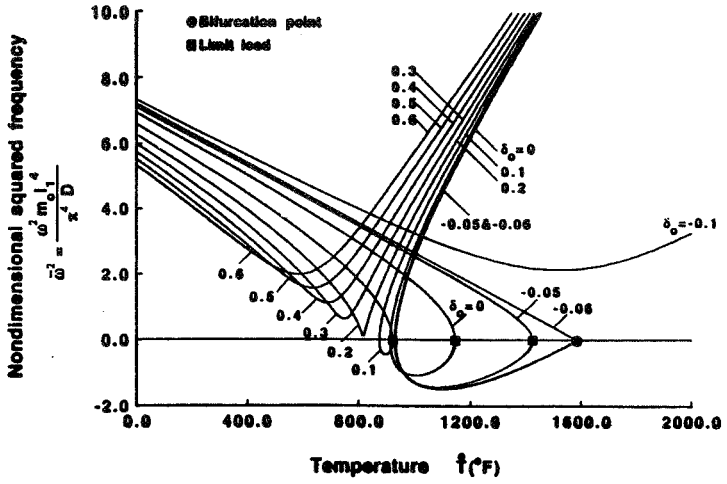

Fig. 6b Fundamental frequency (squared)-temperature interaction for the special case described in Fig. 6a.

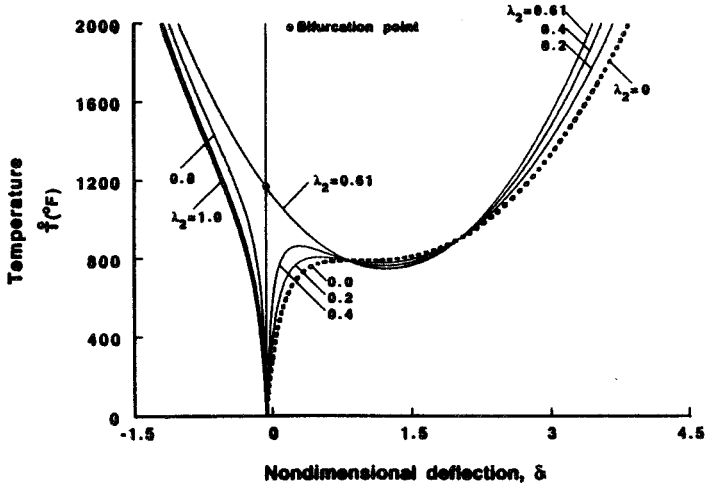

Fig. 7a Effects of tangential edge constraints on temperature-transverse response of a geometrically perfect very shallow three-layer spherical cape. Non-uniform through thickness temperature $(T_e = 70°F), \ell_1/h = 100, \ell_1/R_1 = \ell_2/R_2 = 0.05, \lambda_1 = 0.$

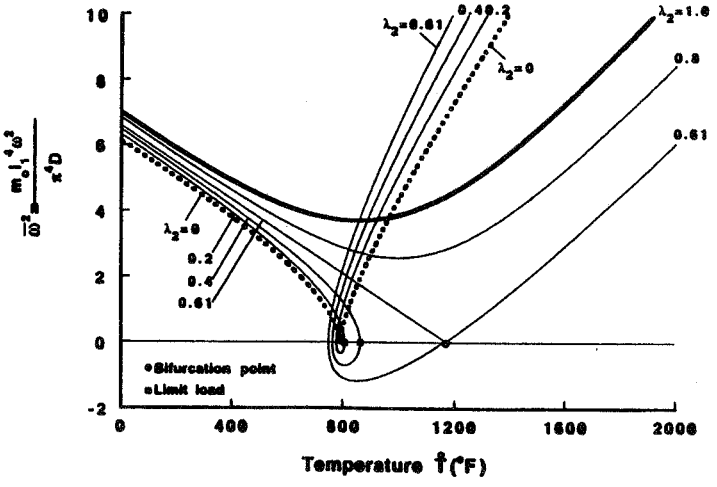

Fig. 7b Fundamental frequency (squared)-temperature interaction for the panel described in Fig. 7a.

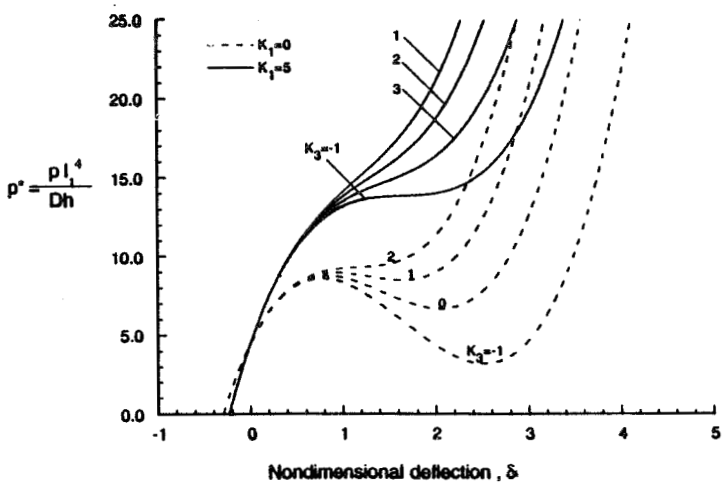

Fig. 8 Influence of the linear and non-linear Winkler foundation moduli on pressure- deflection response of a geometrically perfect three-layer spherical cape exposed to a pre-determined non-uniform through thickness temperature field ($T_e = 70°F, T_i = 500°F$). All edges are immoveable, $\ell_1/R_1 = \ell_2/R_2 = 0.1. \ell_1/h = 100$.

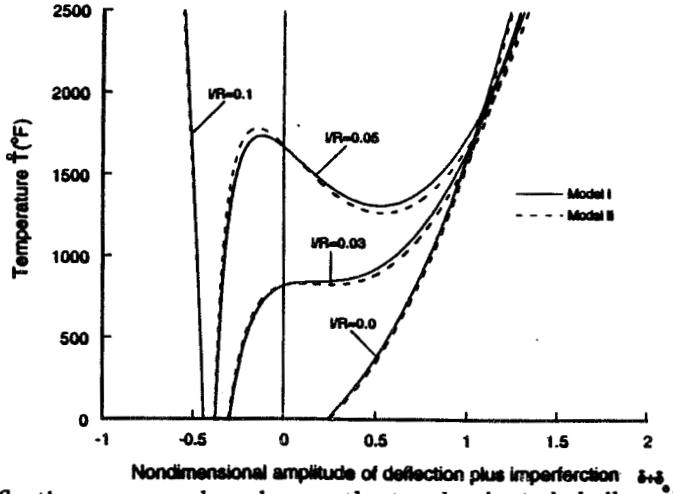

Fig. 9a Temperature-deflection response based upon the two laminated shell models, Model I and Model II, for a three-layer spherical cape of various curvatures ℓ/R. Non-uniform through thickness temperature variation ($T_e = 70°F$), $L_R = 0.1; \ell_1/h = 30, \tilde{L}_{11} = 0.75(\tilde{L}_{11}); E_f = E_c; E_f/G'_f = 10; E_c/G'_c = 30, \delta_0 = 0.05$.

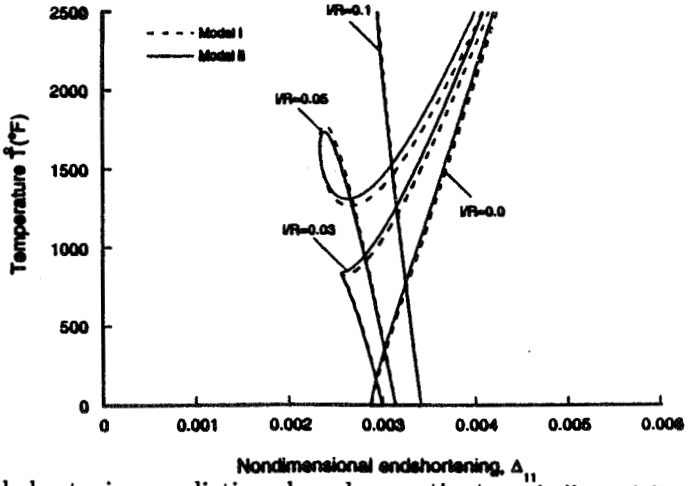

Fig. 9b Temperature-end shortening predictions based upon the two shell models as described in Fig. 9a.

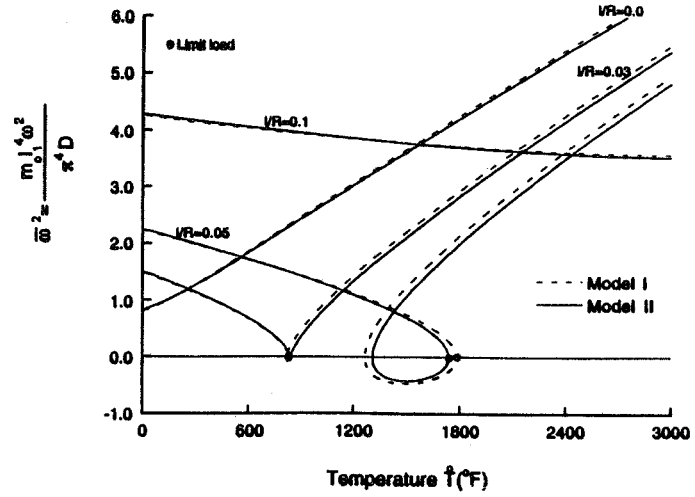

Fig. 9c Fundamental frequency-temperature interaction for the case described in Figs. 9a and 9b.

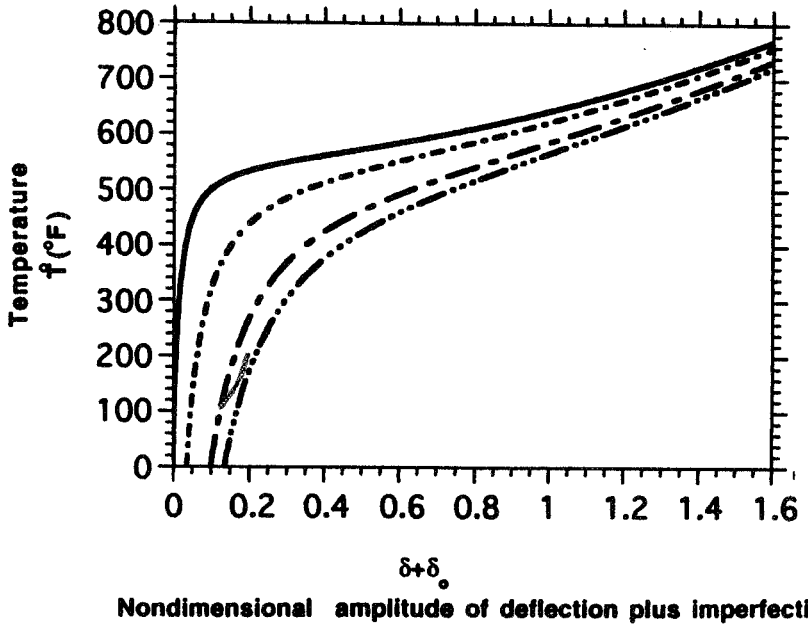

Fig. 10 Typical temperature-deflection response for a geometrically perfect/imperfect rectangular biaxially reinforced flate panel subjected to a membrane temperature rise and a lateral preload, $\ell_1/h = 50$. The various curves in the graph are characterized by selected values of the amplitudes of initial geometric imperfection δ_o and lateral pressure $\hat{p}$, in the sequence $(\delta_0; \hat{p})$ as: ——(0;0);—— - ——(0.10;0);- - - - -(0.0;40);——···——(0.10;40) Herein δ_o is the dimensionless amplitude of the initial geometric imperfection while $\hat{p}$ the dimensionless amplitude of the external lateral load.

DYNAMIC STABILITY OF SHELL STRUCTURES

George J. Simitses and Ala Tabiei*
Department of Aerospace Engineering and Engineering Mechanics
University of Cincinnati, Cincinnati, OH 45221-0070

Abstract

This paper deals with the response of structures subjected to time dependent loads. The primary emphasis is on the stability and collapse of shell configurations of different construction materials. Criteria of stability and approaches employed by various investigators for establishing critical conditions are reviewed and discussed. One of the goals of the paper is to review the literature for dynamic buckling of shell configurations. Moreover, since the term dynamic stability encompasses many classes of problems and many physical phenomena, the concentration in the present paper will be on suddenly loaded shell structures. In addition, the employed methodologies for such problems, including criteria for and estimates of critical conditions are presented. Finally, whenever applicable, important effects and influences of various parameters are identified.

Introduction

Stability of motion has concerned researchers for many years in many fields of engineering. Stability criteria are developed for structures under dynamic loads, controlled theory of motion, fluid-solid interaction, and combustion. In structural mechanics, dynamic stability has received considerable attention in the past forty years. Several studies have been conducted by many investigators on structural systems which are dynamically loaded. In these studies, several attempts have been made to define critical conditions and to develop methodologies for estimating critical conditions.

One particular class of dynamic loads consists of constant magnitude loads applied suddenly over a finite length of time, including extreme cases of ideal impulse loads and loads of constant magnitude and finite duration. These types of loads can be considered as idealization of blast loads in which pressure load is built up in a very short time. Then, the pressure returns to ambient pressure during a time called decay time. The decay time is extremely small, but in few cases, when repeated explosions take place it is possible for the decay time to be large and decay rate to be small. One of the common representation of blast loads (ideal impulse) is the step function model. This model can be employed if the time of step load is much smaller than the period of free oscillations for the structural configuration under consideration. A comprehensive literature review and discussion of the various dynamic stability phenomena can be found in the review articles by Simitses[1] and Herrmann[2] and in the book by Simitses[3]. All structural configurations, when acted upon by quasi-static loads, respond in a certain manner. When these systems are acted upon by sudden loads their response can be classified in one of the following groups:

Parametric resonance: the system tend to oscillate in the mode in which it is excited and then passes on to another distinctly different mode with increasing amplitude. Examples are symmetric shallow arch loaded suddenly by a symmetric transverse load, and column loaded by an in-plane load.

Nonlinear oscillation: a system simply oscillate about the near static equilibrium position under suddenly applied load.

Escaping motion response: systems, when acted upon by sudden loads will experience extremely large amplitude oscillations about a far static equilibrium point or divergent motion. This type of behavior can be found for structural configurations that exhibit snap-through buckling when loaded quasi-statically.

The methodologies developed by various investigators are for structural configurations that exhibit snap-through buckling and can be classified in the following three groups:

1. Equation of motion approach (Budiansky-Roth[4]). The equations of motion are numerically solved for various load parameter values to obtain the system response. The load parameter value at which there exists a large change in the response is called critical.
2. Total energy-phase plane approach (Hsu[5]). Critical conditions are related to characteristics of the system's phase plane, and the emphasis is on

---

* Professor and Interim Dean of Engineering
Fellow of AIAA and Assistant Professor, member of AIAA respectively.

establishing sufficient conditions for stability (lower bounds) and sufficient conditions for instability (upper bounds).

3. Total potential energy approach (Hoff[6]/Simitses[7]). Critical conditions are related to characteristics of the system's total potential. Through this approach the lower and upper bounds of critical conditions are established. This last approach is applicable to conservative systems only.

The equation of motion approach is the most popular approach for dynamic buckling analysis since it is very easy to implement in numerical and finite element methods. This methodology can be applied to complex geometries if the finite element technique is employed in the analysis. Several commercial finite element codes available in the market have the capability to perform dynamic buckling analysis. These codes can be characterized in two categories, implicit and explicit codes. In general the Newton-Raphson and Newmark methods are used to solve equations of motion to obtain dynamic response for implicit codes like, ANASYS, ABAQUS/ STANDARD, NASTRAN, etc. Explicit codes like DYNA3D, ABAQUS/ EXPLICIT, etc., employ the finite difference method to descretize time in equations of motion to obtain dynamic response. Almost all commercial finite element codes that are capable of dynamic analysis can perform the analysis for systems made of isotropic as well as anisotropic materials.

In the ensuing section a historical review is presented in a way that complements the presentation included in chapters 8 (The Shallow Spherical Cap) and 9 (Thin Cylindrical Shells) of the book by Simitses[3].

Demonstration examples are presented in later sections as well as a discussion of several effects such as duration time, static preloading as well as of shell structural parameters.

Historical Review

In the case of shell configurations, the first studies reported in the western literature appeared in the early 1960's. The two most commonly dealt with configurations are those of the shallow spherical shell (cap) and the cylindrical shell. Several studies are cited in Chapters 8 and 9 of Reference 3. In this section, some of the studies will be repeated but the effort will concentrate on discussing those that appear prior to 1990 but not reported in Reference 3 and those that appear in the literature since 1990.

Spherical Caps and Domes

The first reported studies dealing with spherical caps are those of Suhara[8], Budiansky and Roth[4] and Humphreys and Bodner[9]. Suhara treated the case of sudden pressure of infinite duration, Budiansky and Roth the case of uniform pressure applied suddenly for a finite time and Humphreys and Bodner the case of ideal impulse (uniform pressure but extremely small duration). In all of these studies, it was assumed that the response of the shallow cap is axisymmetric. This, of course, limited the applicability of the results to small shell rise parameter values. Moreover, it was assumed that the material of the caps is metallic (isotropic). Several studies, that followed, removed the assumption of axisymmetric response. In addition, a few experimental studies were reported also and both of these groups are discussed in chapter 8 of Reference 3.

From the late 1970's to date several studies have appeared which deal with dynamically loaded caps and domes (a) in the presence of holes, (b) of various shapes, (c) of different construction materials (orthotropic, anisotropic and stiffened) and (d) with various support conditions.

Dumir et al[10] reported critical conditions for an orthotropic spherical cap with elastically restrained edges. The same authors[11] studied the effect of the presence of a circular hole on the critical conditions for an orthotropic shallow cap. In both studies they assumed axisymmetric shell response. Dumir and Khatri[12] studied static and dynamic buckling of a cylindrically orthotropic truncated shallow conical cap with clamped edges. They also considered the effect of the presence of a free circular hole and a hole plugged by a rigid central mass. They assumed axisymmetric response and they computed static and dynamic critical load for both isotropic and orthotropic truncated shallow conical shells. Jain and Nath[13] extended previous work (Refs. 10 and 11) and reported critical conditions for cylindrically orthotropic spherical caps with and without holes, supported by a Winkler-Pasternak elastic foundation. The edges are either clamped or simply supported and the loading is a sudden load of finite duration. Saigal et al.[14] studied dynamic buckling of elastic shells in the presence of initial geometric imperfections by using a 48-degree-of-freedom doubly curved quadrilateral imperfect thin-shell finite element. They assessed the imperfection sensitivity of a spherical shell, a spherical cap and a hemispherical dome. Young and Liaw[15] extended the previous work to include the effect of plasticity. They also studied the effect of viscous damping. Ross and Johns[16] reported on a theoretical and experimental investigation of the dynamic buckling and vibration of thin-walled plastic

domes of various ellipsoidal shapes under extended water pressure.

Fu and Liu[17] studied the dynamic buckling of a shallow spherical shell by including transverse shear effects. They assumed axisymmetric response and they computed critical loads in the presence of a circular hole and for various elastically restrained edge conditions. Mu et al.[18] employed a finite difference scheme to study the response of shallow spherical caps to axisymmetric impact loads. They investigated the effect of change of the loading area on the dynamic critical load. They concluded that the critical impact load increases with increasing loading area. Lee et al.[19] employed a finite element scheme and reported critical conditions for clamped spherical caps under uniform step loading. Ganapathi and Varadan[20] employed the Budiansky -Roth criterion and derived critical conditions for clamped laminated spherical caps, subjected to sudden loads. They performed parametric studies in order to assess the effect of shell geometry, material properties, number of layers, and stacking sequence on the dynamic critical load.

Cylindrical Shells

Dynamic buckling of cylindrical shells subjected to suddenly applied axial compression of constant magnitude and infinite duration was first studied by Volmir[21] where a two-degree-of-freedom system was modeled and the Galerkin method was employed. Roth and Klosner[22] applied the potential energy method and treated the problem as a four-degree-of-freedom system which they studied numerically. Several contributions of the early years are discussed in Chapter 9 and Ref. 3. In the last ten years or so, investigators dealt with dynamic stability of cylindrical shells by addressing questions of imperfection sensitivity, of non-linear material behavior, of orthotropic and laminated construction, of experimental validation, etc. In the remainder of this section, a discussion of these works is presented.

Lindberg et al.[23] reported an experimental and theoretical investigation of dynamic buckling of thin cylindrical shells under oscillating stress waves following axial impact. Bogdanovich[24] dealt with dynamic buckling of stiffened and unstiffened laminated orthotropic cylindrical shells. Stiffening was treated as smeared (for ribs plus struts and as discrete (for ribs only). Kirkpatrick and Holmes[25] investigated the effect of initial imperfections on the dynamic critical conditions (pulse) of a thin metallic cylindrical shell, subjected to an impulsive external load applied with explosives. Lindberg[26] reported on dynamic buckling of cylindrical shells with uncertain imperfections subjected to symmetric radial impulsive loads.

Shaw et al.[27] reported on the dynamic buckling of an imperfect, laminated, cylindrical shell under axial and torsional sudden loads, applied individually or in combination. The sudden load is modeled as a step function. They employed both the total potential energy approach[6,7] and the Budiansky-Roth approach[4] and they concluded that the total potential energy approach yields conservative results (a lower bound is established through this approach). Mustafa et al.[28] studied dynamic buckling of tubes submerged in water and subjected to an axisymmetric external pressure pulse. They assumed axisymmetric behavior and they employed the finite element method. They included material non-linearities in their solution scheme (FE Code ABAQUS). The dynamic collapse behavior of composite cylindrical shells and panels subjected to a transverse point load was addressed by Palazotto and his research collaborators in a series of papers[29-32]. The behavior of undamped cylindrical shells of varying radii are analyzed with a finite element formulation that incorporates all nonlinear Green strain terms in the in-plane directions. Characterization of the chaotic nature of the post collapsed shells are explored.

Gilat and Aboudi[33] reported on the dynamic buckling of viscoplastic plates and shells by employing a unified theory of plasticity. They included the effects of applied loading rate, material rate sensitivity and transverse shear deformation. The same authors[34] dealt with application to metal matrix composites by using similar solution techniques and assessing the effect of the same parameters as in Ref. 33. More recently, Schokker et al.[35] studied the dynamic buckling of ring stiffened (on the inside) laminated composite, cylindrical shells under sudden hydrostatic pressure. In addition Kounadis and Sophianopoulos[36] analyzed the dynamic buckling response of a spring-mass, geometrically imperfect, dissipative model with three-degrees-of-freedom to simulate a relatively deep cylindrical panel under step loading.

Finally, there exist several efforts[37-46] reported in the literature that deal with dynamic buckling or collapse of cylindrical shell configurations, of various constructions but primarily metallic, subjected to seismic loads or under explosion conditions. The main interest in these studies is safety associated with structural configurations that house nuclear powerplants.

In the next section, a few examples of dynamic stability under sudden loads are presented. These applications have been investigated by the senior author and his research collaborators.

Effect of Static Preloading

One can identify several systems that fall in the category of initially load-free or idealized as initially load-free structures, which are subjected to sudden dynamic loads. Examples of this category may include, buildings, storage bins, and surface vehicles which are subjected to blast loads. It is also realistic for one to identify several structural systems which are initially statically preloaded and subsequently subjected to sudden dynamic loads. Consider, for example, a submarine operating at some depth smaller than the maximum allowable (the one corresponding to the design pressure). This implies that the submarine is statically preloaded by a pressure smaller than the design pressure. Subsequently, the system is subjected to a sudden blast load. This additional loading is the dynamic load, which can be idealized as an ideal impulse or a sudden load of finite duration. Another example is an aircraft at a level unaccelerated flight (static preloading) subjected to a sudden blast or gust (dynamic load).

To the best knowledge of the authors, no work has been reported on this topic in the literature for shells or shell-like structures. Several simple models have been presented in Ref. [3] for both "ideal impulsive" as well as "infinite duration" loads. In all cases, the response pattern is the same. If one considers the case of a statically preloaded structural system acted upon by a sudden load of infinite duration, then the critical dynamic load varies from the value corresponding to the case of no preloading down to zero when the amount of static preloading equals the static critical load.

Results for three models, taken from Ref. [3], are presented both in tabular and graphical forms (see table 1. and figure 1.). The first two systems correspond to one-degree-of freedom models, while the third system corresponds to a two-degree-of freedom model. The numbers reported for systems I and II are theoretical predictions of the dynamic critical conditions of the models, while the numbers reported for system III represent lower bounds of the dynamic critical conditions. The numbers reported were arrived at by employing the Total Potential Energy approach (see Ref. 3). In the table, p_o denotes the amount of static preloading, p_{crs} the value of the static critical load and p_{crd} denotes the level of the critical dynamic conditions[1]. In chapter 4 of Ref. 3, the interested reader can find results and discussion of the case of the ideal impulse load case. It is seen from table 1 and figure 1 that the critical dynamic load decreases in an almost linear manner with increasing static preloading. This observation is very significant in the design of dynamically loaded systems. Analysis with zero static preloading are much simpler in execution, especially when employing the Total Potential Energy approach, than analysis in the presence of static preloading.

It is recommended that this observation be verified for shell-like configurations, especially for submarine configurations.

Table 1. Effect of Static Preloading

SYSTEM I		SYSTEM II		SYSTEM III	
P_o/P_{crs}	P_{crd}/P_{crs}	P_o/P_{crs}	P_{crd}/P_{crs}	P_o/P_{crs}	P_{crd}/P_{crs}
0.000	0.961	0.000	0.993	0.000	0.780
0.781	0.196	0.366	0.628	0.657	0.218
0.885	0.103	0.419	0.665	0.739	0.166
0.964	0.030	0.524	0.471	0.821	0.093
1.000	0.000	1.000	0.000	1.000	0.000

Applications to Cylindrical Shells

In all cases to be discussed in this section the equations of motions approach is employed. The simplicity of this method has made it a popular method in the recent years. The method consists of solving the equation of motion (stated below) by a transient dynamic analysis.

$$MD'' + CD + KD = R(t)$$

where M is the mass matrix, C the damping matrix, K the stiffness matrix, R the load vector, and D'', D', D are the nodal acceleration, velocity and displacement respectively. At any time these equations can be thought of as a set of static equilibrium equations that take into account inertia and damping forces.

As demonstration examples (see Ref. 48) the ANSYS[49] computer code is employed to obtain the dynamic response of a metallic and a laminated shell subjected to suddenly applied axial compression, bending moment, and lateral pressure. The Newmark[50] time integration scheme is employed to solve these equations at discrete time points. The time increment between successive time points is called the integration time step. Since the response can be thought of as a combination of modes, the time step should be able to resolve the highest mode that can contribute to the response. It has been found that using approximately twenty points per period of the highest frequency of interest results in a reasonably accurate solution. The natural frequencies and mode shapes can be determined by modal analysis using the finite element method. To obtain the dynamic critical load of

[1] for the case of constant load applied suddenly with infinite duration.

an imperfect cylindrical shell under certain load condition, the following steps are followed:

- Calculate frequencies of shell under each load parameters and determine the integration time step.
- Solve the equation of motion for different load parameter and obtain the dynamic response.
- Determine the critical load according to the equation of motion approach.

Some finite element codes use the central difference method for integrating the equations of motion to obtain the dynamic response. For most cases both numerical integration methods (central difference and Newmark) yield approximately the same dynamic response as depicted in figure 2. Figure 2 shows the displacement of a point on the midsection of laminated cylindrical shell subjected to lateral pressure. The critical load is obtained by iterating on the applied load until escaping motion occurs as shown in figure 3.

Figure 4 shows the critical dynamic axial compression for a metallic cylinder for two imperfection amplitudes (a=.1 and .5) and different load durations. It is observed that critical load approaches that of infinite duration once the loading time is relatively long. Figure 5 shows the critical dynamic axial compression and bending for a laminated shell. The same observations can be made.

Acknowlegments

The senior author acknowledges the contributions of his former student, Dr. X. Huyan. Computing support was provided by the Ohio Super Computer Center. Part of the work, reported herein, was supported by the Office of Naval Research. Dr. Y. D. S. Rajapakse is the scientific officer of the project and this support is gratefully acknowledged.

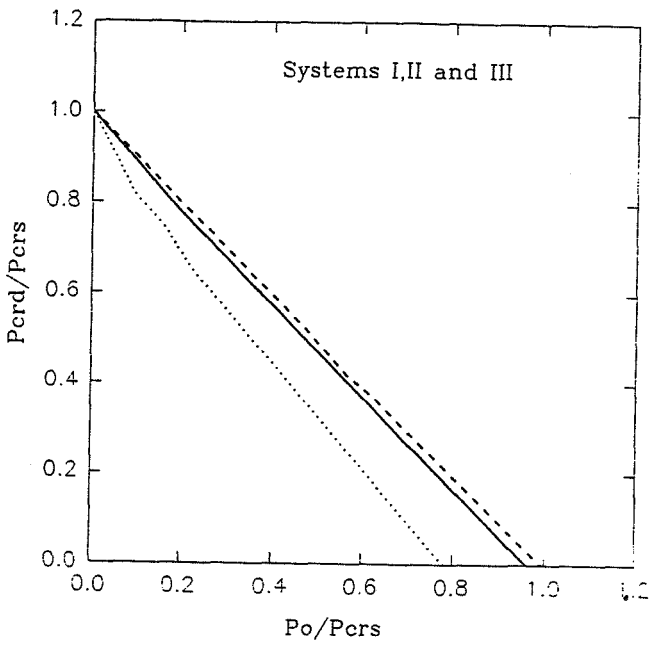

Figure 1. Effect of Static Preloading

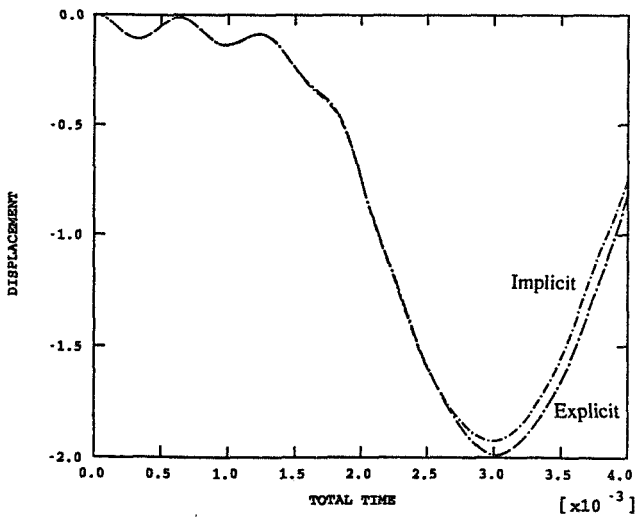

Figure 2. Cylindrical Laminted Shell Subjected to Suddenly Applied Lateral Pressure

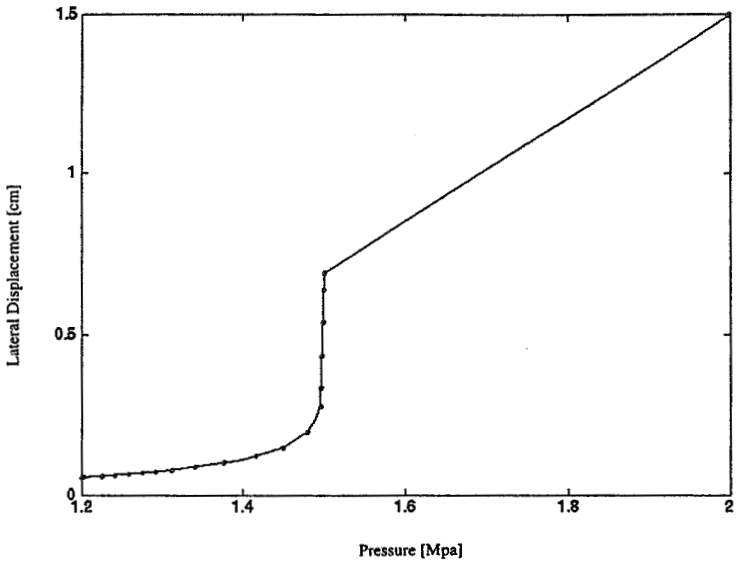

Figure 3. Displacement of Shell Mid-Section versus Suddenly Applied Lateral Pressure

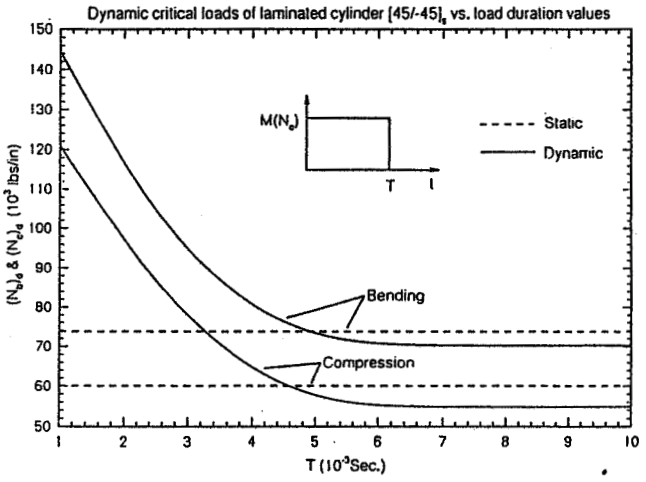

Figure 5. Dynamic Critical Load for Laminated Cylinder

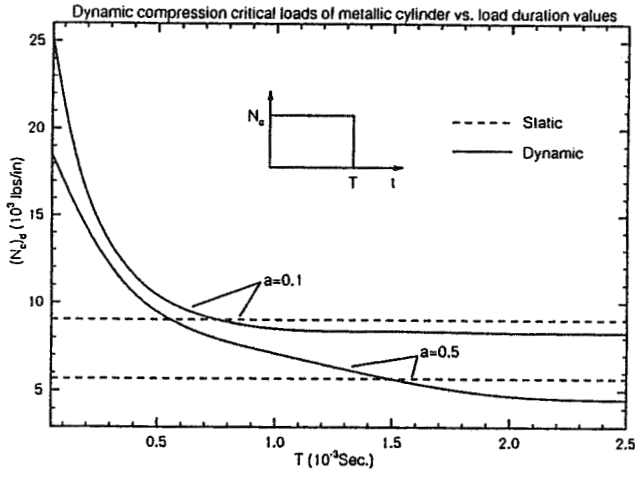

Figure 4. Dynamic Critical Load for Metallic Cylinder

References

1. Simitses, G.J., "Instability of Dynamically-Loaded Structures," Appl. Mech. Rev., Vol. 40, No. 10, 1987, pp. 1403-1408.
2. Herrmann, G., "Stability of Equilibrium of Elastic Systems Subjected to Non-conservative Forces," Appl. Mech. Rev., Vol. 20, No. 1, pp. 103-108.
3. Simitses, G.J., Dynamic Stability of Suddenly Loaded Structures, Springer-Verlag, New York, 1990.
4. Budiansky, B., and Roth, R.S., "Axisymmetric Dynamic Buckling of Clamped Shallow Spherical Caps ," in Collected Papers on Instability of Shell Structures. NASA TN D-1510, Washington, DC, 1962, pp. 597-606.
5. Hsu, D.S., "Equilibrium Configurations of a Shallow Arch of Arbitrary Shape and Their Dynamic Stability Character," Int. J. Nonlinear Mechanics, Vol. 3, 1968, pp. 113-136.
6. Hoff, N.J., "Dynamic Stability of Structures" in Dynamic Stability of Structures (edited by G. Herrmann) Pergamon Press, New York, 1967.
7. Simitses, G.J., "On the Dynamic Buckling of Shallow Spherical Caps," J. Appl. Mech., Vol. 41, No. 1, 1974, pp. 299-300.
8. Suhara, J., "Snapping of Shallow Spherical Shells Under Static and Dynamic Loadings," ASRL TR 76-4, Aeroelastic and Structures Research Laboratory, Cambridge, MA, June 1960.
9. Humphreys, J.S. and Bodner, S.R., "Dynamic Buckling of Shells Under Impulsive Loading," ASCE J of Eng. Mech. Division, Vol. 88, 1962, pp. 17-36.
10. Dumir, P.C., Nath, Y. and Gandhi, M.L., "Nonlinear Axicymmetric Static and Dynamic Buckling of Orthotropic Shallow Spherical Caps with Elastically Restrained Edges," Acta Mechanica, Vol. 52, 1984, pp. 93-106.
11. Dumir, P.C., Gandhi, M.L. and Nath, Y., "Axisymmetric Static and Dynamic Buckling of Orthotropic Shallow Spherical Caps with a Circular Hole," Computers and Structures, Vol. 19, No. 6, 1984, pp. 725-736.
12. Dumir, P.C. and Khatri, K.N., "Axisymmetric Static and Dynamic Buckling of Orthotropic Truncated Shallow Conical Caps," Computers and Structures, Vol. 22, No. 3, 1986, pp. 335-342.
13. Jain, R.K. and Nath, Y., "Dynamic Buckling of Orthotropic Spherical Caps Supported by Elastic Media," AIAA J., Vol. 25, No. 4, 1987, pp. 630-633.
14. Saigal, S., Yang, T.Y. and Kapania, R.K., "Dynamic Buckling of Inperfection Sensitive Shell Structures," J of Aircraft, Vol. 24, No. 10, 1987, pp. 719-724.
15. Yang, T.Y. and Liaw, D.G., "Elastic-Plastic Dynamic Buckling of Thin-Shell Finite Elements with Asymmetric Imperfections," AIAA J., Vol. 26, No. 4, 1988, pp. 479-486.
16. Ross, C.T.F. and Johns, T., "Dynamic Buckling of Thin-Walled Domes Under External Water Pressure," Res Mechanica: Int'l J. of Struct. Mech. and Mat'ls Sci., Vol. 28, No. 1-4, 1989, pp. 113-137.
17. Fu, Y.-M. and Liu, X.-H., "Nonlinear Dynamic Response and Dynamic Buckling of Shallow Spherical Shells with Circular Hole," Applied Math and Mech (English edition), Vol. 13, No. 2, 1992, pp. 159-171.
18. Mu, J.-C., Wu, W.-Z. and Yang, G.-T., "Numerical Calculation of Dynamic Buckling of a Thin Shallow Spherical Shell Under Impact," Applied Math and Mech (English edition), Vol. 13, No. 2, 1992, pp. 125-134.
19. Lee, Y.J., Lin, H.J. and Liou, Y.J., "Dynamic Buckling Strength of Spherical Caps," Computers and Structures, Vol. 48, No. 3, 1993, pp. 517-521.
20. Ganapathi, M. and Varadan, T.K., "Dynamic Buckling of Laminated Anisotropic Spherical Caps," J. Appl. Mech. ASME, Vol. 62, No. 1, 1995, pp. 13-19.
21. Volmir, A.S., "On the Stability of Dynamically Loaded Cylindrical Shells," Dokl. Acad. Nauk SSSR, Vol. 123, No. 5, 1958, pp. 806-808, (in Russian); translated in Soviet Physics Doklady, Vol. 3, 1958, pp. 1287-1289.
22. Roth, R.S. and Klosner, J.M., "Nonlinear Responses of Cylindrical Shells Subjected to Dynamic Axial Loads," AIAA J., Vol. 12, No. 10, 1964, pp. 1788-1794.
23. Lindberg, H.E., Rubin, M.B. and Schwer, L.E., "Dynamic Buckling of Cylindrical Shells from Oscillating Waves Following Axial Impact," Int'l J Solids and Struct., Vol. 23, No. 6, 1987, pp. 669-692.
24. Bogdanovich, A.E., "Nonlinear Problems of the Dynamic Buckling of Reinforced Laminar Cylindrical Shells," Soviet Applied Mechanics (English translation of Prikladnaya Mekhanika), Vol. 22, No. 8, 1986, pp. 745-753.
25. Kirkpatrick, S.W. and Holmes, B.S., "Effect of Initial Imperfections on Dynamic Buckling of Shells," ASCE J. of Eng. Mech., Vol. 115, No. 5, 1989, pp. 1075-1093.
26. Lindberg, H.E., "Evaluation of Convex Modeling for Multimode Dynamic Buckling," ASME J. Appl. Mech., Vol. 59, No. 4, 1992, pp. 929-936.

27. Shaw, D., Shen, Y.L. and Tsai, P., "Dynamic Buckling of an Imperfect Composite Circular Cylindrical Shell," Computers and Structures, Vol. 48, No. 3, 1993, pp. 467-472.
28. Mustafa, B., Al-Hassani, S.T.S. and Reid, S.R., "Axisymmetric Dynamic Buckling of Submerged Cylindrical Shells," Computers and Structures, Vol. 47, No. 3, 1993, pp. 399-405.
29. Palazotto, A., Chien, L. and Taylor, W., "Stability Characteristics of Laminated Cylindrical Panels Under Transverse Loading," AIAA J., Vol. 30, No. 6, 1992, pp. 1649-1653.
30. Forral, A. and Palazotto, A., "A Finite Element Model Considering Nonlinear Dynamically Load Composite Plates and Shells," Int'l J. for Engng. Analysis and Design, Vol. 1, 1994, pp. 379-393.
31. Greer, J. and Palazotto, A., "Some Nonlinear Response Characteristics of Collapsing Composite Shells," AIAA J., Vol. 32, No. 9, 1994, pp. 1935-1938.
32. Greer, J. and Palazotto, A., "Nonlinear Dynamics of a Simple Shell Model with Chaotic Snapping Behavior," ASCE, J. of Engng. Mech., Vol. 121, No. 6, 1995, pp. 753-761.
33. Gilat, R. and Aboudi, J., "Dynamic Buckling of Viscoplastic Plates and Shells Under Cylindrical Bending," J. Sound and Vibr., Vol. 174, No. 3, 1994, pp. 323-334.
34. Gilat, R. and Aboudi, J., "Dynamic Buckling of Metal Matrix Composite Plates and Shells Under Cylindrical Bending," Composite Structures, Vol. 28, No. 4, 1994, pp. 459-469.
35. Schokker, A., Sridharan, S. and Kasagi, A., "Dynamic Buckling of Composite Shells," Computers and Structures, Vol. 59, No. 1, 1996, pp. 43-53.
36. Kounadis, A.N. and Sophianopoulos, D.S., "Nonlinear Dynamic Buckling of a Cylindrical Shell Panel Model," AIAA J., Vol. 34, No. 11, 1996, pp. 2421-2428.
37. Combescure, A., "Static and Dynamic Buckling of Large, Thin Shells Design Procedure, Computation Tools, Physical Understanding of the Mechanisms," Nuclear Engineering and Design, Vol. 92, No. 3, 1986, pp. 339-354.
38. Nagashima, H., Kokubo, K., Takayamagi, M., Saitoh, K. and Imaoka, T., "Experimental Study on the Dynamic Buckling of Cylindrical Tanks," Int'l J of JSME, Vol. 30, No. 263, 1987, pp. 737-746.
39. Fujita, K., Ito, T. and Wada, H., "Experimental Investigation on the Dynamic Buckling of a Cylindrical Shell due to Seismic Escitation. (1st Report: Plastic Buckling due to Bending Load)," Trans. of JSME, Part C, Vol. 55, No. 515, 1989, pp. 1634-1637.
40. ("2nd Report: Influence of FSI on Elastic Buckling due to Shear Load)," Trans. of JSME, Part C., Vol. 56, No. 525, 1990, pp. 1101-1107.
41. Nagashima, H., Kokubo, K., Takayanagi, M. and Saitoh, K., "Experimental Study on Dynamic Buckling of Cylindrical Tanks (3rd Report: Buckling Modes under Static Lateral and Axial Load, and Harmonic Excitation)," Trans. JSME Part A, Vol. 55, No. 517, 1989, pp. 1992-1997.
42. Liu, W.K., Dhen, Y.-J., Tsukimori, K. and Uras, R.A., "Recent Advances in Dynamic Buckling Analysis of Liquid-filled Shells," ASME J. Pressure Vessel Tech. Vol. 113, No. 2, 1991, pp. 314-320.
43. Uras, R.A. and Liu, W.K., "Dynamic Buckling of Liquid-filled Shells Under Horizontal Excitation," J. Sound and Vibr., Vol. 141, No. 3, 1990, pp. 389-408.
44. Fujita, K., Ito, T. and Wada, H., "Experimental Study on the Dynamic Buckling of a Cylindrical Shell due to Seismic Excitation (Plastic Buckling due to Bending Load)," Int'l J of JSME, Series 3, Vol. 34, No. 3, 1991, pp. 339-344.
45. Hisada, T., Noguchi, H., Kanakami, T., Nakalongawa, T. and Tai, K., "Safety Study on Dynamic Buckling of Reactor Containment Vessels,", Trans of JSME, Part A, Vol. 59, No. 557, 1993, pp. 203-210.
46. Tsukimori. K., Liu, W.K. and Uras, R.A., "Formulation of Dynamic Stability of Fluid-filled Shells," Nuclear Engineering and Design, Vol. 142, 1993, pp. 267-297.
47. Nakagama, M., Fukuyama, M., Ishahama, K., Ikenchi, H., Hagiwara, Y. and Akiyama, H., "Pseudo-dynamic Buckling Experiments on Thin Cylindrical Shells under Biaxial Seismis Loads," Nuclear Engineering and Design, Vol. 157, No. 1-2, 1995, pp. 27-36.
48. Huyan, X., and Simitses, G. J., "Dynamic Buckling of Imperfect Cylindrical Shells Under Axial Compression and Bending Moment", Proceeding of the AIAA/ASE/ASCE/ASC/AHS 37th SDM Conference, Part 3, 1996, pp. 1333-1433; also to appear in AIAA J.
49. Swanson J., ANSYS user manual, Ver 5.1, 1995.
50. Newmark, N. M., "A Method of Computation for Structural Dynamics", ASCE J. of Engineering Mechanics Division, Vol. 85, pp. 67-94, 1959.

PLASTIC BUCKLING OF PLATES AND SHELLS

David Durban*
Faculty of Aerospace Engineering
Technion, Haifa 32000, Israel

Abstract

Theoretical predictions of plastic buckling loads admit an appreciable constitutive sensitivity which has centered on the controversy between the J_2 versions of flow and deformation theories (the plastic buckling paradox). A recent study on plastic buckling of annular plates in pure shear has shown that deformation theory predicts critical loads which are considerably below the predictions obtained with the flow theory. Comparison with experimental data for different metals shows a good agreement with the deformation theory results over a wide range of geometries. A different aspect of that constitutive sensitivity is provided by the case of plastic buckling of a rectangular plate under biaxial loads. the main finding of that study is the existence of an optimal loading path for the deformation theory model. Buckling loads attained along that loading path -- specified by particular compression/tension ratios -- are the highest possible over the entire space of loading histories . By contrast, no similar optimum has been found with the flow theory. The influence of boundary conditions on plastic buckling of axially compressed circular cylindrical shells is examined in detail along with a comparison with available test results.

1. Introduction

Studies of plastic buckling of plates and shells have been dominated for nearly half a century by the controversy about the appropriate model of material behaviour in the plastic range. The two competing J_2 theories (though other models are now available) may predict buckling loads which differ by up to an order of magnitude: J_2 flow theory gives critical loads that are higher than those obtained from the corresponding deformation theory, but the latter model usually agrees better with experimental data. A classical observation in this context is the plastic buckling of the cruciform column, examined experimentally by Gerard and Becker[1], where test results agree quite well with deformation theory predictions, but are consistently below flow theory results. That controversy, known as the plastic buckling paradox, has been discussed (for an authoritative review see Hutchinson[2]) in many papers and it is not the purpose of this report to repeat the usual arguments in favour or against each theory. We shall rather concentrate on recent research performed in the aerospace structures group, in the faculty of aerospace engineering at the Technion[3,4], on plastic buckling of plates and shells. Since only part of that work is available in English[5,6,7] it is felt that a unified if condensed presentation of the essential results would be beneficial to researchers and engineers working on problems of plastic buckling.

This paper summarizes investigations of three problems of buckling in the plastic range with a detailed comparison between critical loads predicted by the two competing J_2 theories. In two of the problems (the annular plate in shear and the axially compressed circular cylindrical shell) the validity of theoretical predictions is assessed against available experimental data.

2. Annular Plate in Pure Shear

The first example to be considered here is that of an annular plate in pure shear (Fig. 1). In-plane torsion of annular plates is a common technique for determining the stress-strain characteristics of metal plates. However, the possibility of out-of-plane plastic buckling may impose a limit to the applicability of that test.

The plate has an inner radius a, outer radius b, constant thickness h and is submitted to uniform shear stresses along the boundaries r=a,b. The only active stress component within the plate has the statically determined radial profile

$$\tau_{r\theta} = \frac{\lambda h^2}{24 r^2} \qquad (2.1)$$

where λ is the load parameter and the factor of 24 is introduced for convenience.

*Member, AIAA

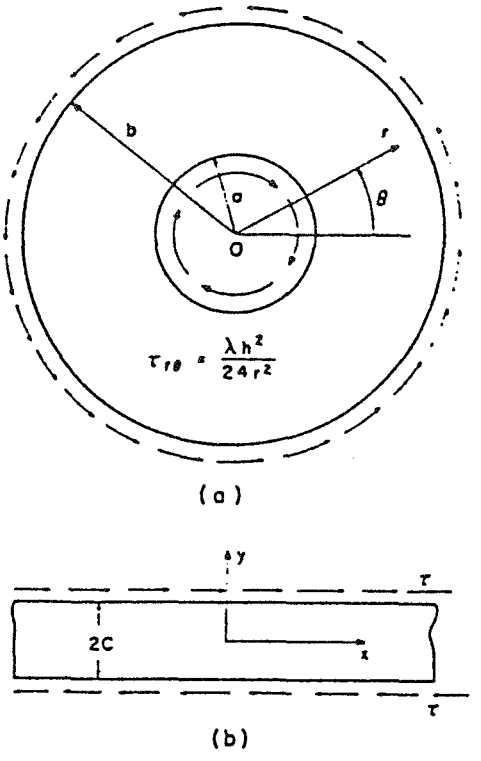

Fig. 1 (a) Notation for the annular plate, (b) the limiting problem of a long narrow panel. The thickness in both cases is h.

The constitutive relations that govern the onset of buckling, within the framework of linear buckling analysis, are

$$\dot{\sigma}_{rr} = E_{rr}\dot{\varepsilon}_{rr} + E_{r\theta}\dot{\varepsilon}_{\theta\theta} \tag{2.2}$$

$$\dot{\sigma}_{\theta\theta} = E_{r\theta}\dot{\varepsilon}_{rr} + E_{\theta\theta}\dot{\varepsilon}_{\theta\theta} \tag{2.3}$$

$$\dot{\tau}_{r\theta} = 2G_{r\theta}\dot{\varepsilon}_{r\theta} \tag{2.4}$$

wnere the stress rates are denoted by $(\dot{\sigma}_{rr}, \dot{\sigma}_{\theta\theta}, \dot{\tau}_{r\theta})$, the strain rates by $(\dot{\varepsilon}_{rr}, \dot{\varepsilon}_{\theta\theta}, \dot{\varepsilon}_{r\theta})$ and $(E_{rr}, E_{\theta\theta}, E_{r\theta}, G_{r\theta})$ are the instantaneous moduli of the material. The superposed dot can be understood as a small increment in time or as differentiation with respect to a time like parameter.

Inserting relations (2.2)-(2.4) in the standard plate buckling equation, results in the differential equation[3,6]

$$\frac{1}{r}\left[r\left(E_{rr}K_{rr} + E_{r\theta}K_{r\theta}\right)\right]_{,rr} - \frac{1}{r}\left(E_{r\theta}K_{rr} + E_{\theta\theta}K_{\theta\theta}\right)_{,r} + \frac{4}{r^2}\left(rG_{r\theta}K_{r\theta}\right)_{,r\theta} + \frac{1}{r^2}\left(E_{r\theta}K_{rr} + E_{\theta\theta}K_{\theta\theta}\right)_{,\theta\theta} - \frac{\lambda}{r^2}K_{r\theta} = 0 \tag{2.5}$$

where the rates (increments) of change in curvature during buckling are related to the out-of-plane velocity $w(r,\theta)$, at the onset of buckling, by

$$K_{rr} = w_{,rr} \quad K_{r\theta} = \left(\frac{w_{,\theta}}{r}\right)_{,r} \quad K_{\theta\theta} = \frac{w_{,r}}{r} + \frac{w_{,\theta\theta}}{r^2} \tag{2.6}$$

The boundary data which supplements the buckling equation (2.5) is either that of a clamped edge, namely

$$w = 0 \qquad w_{,r} = 0 \tag{2.7a}$$

or the simply supported edge conditions

$$w = 0 \quad w_{,rr} + \left(\frac{E_{r\theta}}{E_{rr}}\right)\frac{w_{,r}}{r} = 0 \tag{2.7b}$$

The instantaneous moduli in (2.2)-(2.4) depend on the particular constitutive model employed in the analysis. Earlier work is available for the linear elastic isotropic[8] and orthotropic[9] materials where the instantaneous moduli in (2.5) remain constant. In the elastoplastic range, however, the instantaneous moduli are stress dependent and the solution of the governing equation is more complicated.

Here we shall use the two small strain versions of the elastoplastic J_2 model. First we have the flow theory with

$$\dot{\sigma}_{ij} = 2G\dot{\varepsilon}_{ij} + \lambda_E\delta_{ij}\dot{\varepsilon}_{kk} - 3\left(G - G_T\right)\frac{S_{ij}S_{k\ell}\dot{\varepsilon}_{k\ell}}{\sigma_e^2} \tag{2.8}$$

where G, λ_E are the usual elastic Lamé constants, S_{ij} is the stress deviator, σ_e is the Mises effective stress (in our problem $\sigma_e = \sqrt{3}\tau_{r\theta}$), and G_T is the tangent shear modulus given by

$$\frac{1}{G_T} = \frac{1}{G} + 3\left(\frac{1}{E_T} - \frac{1}{E}\right) \tag{2.9}$$

where E is the elastic modulus and E_T is the tangent modulus of the uniaxial stress-strain curve (and a known function of σ_e). The instantaneous moduli associated with (2.8) in pure shear follow as

$$E_{rr} = E_{\theta\theta} = \frac{E}{1-\nu^2} \qquad E_{r\theta} = \frac{\nu E}{1-\nu^2}$$

$$G_{r\theta} = G_T = G(1 - R_T) \tag{2.10}$$

where

$$R_T = \frac{1-\eta_T}{1-\left(\frac{1-2\nu}{3}\right)\eta_T} \qquad \eta_T = \frac{E_T}{E} \tag{2.11}$$

and ν stands for the elastic Poisson ratio. Inserting the moduli (2.10)-(2.11) in (2.5) and using definitions (2.6) gives the differential equation for buckling

$$\nabla^4 w - \frac{2(1-\nu)}{r^2}\left[rR_T\left(\frac{w_{,\theta\theta}}{r}\right),r\right],r - \frac{S}{r^2}\left(\frac{w_{,\theta}}{r}\right),r = 0 \tag{2.12}$$

where S is given by

$$S = \frac{1-\nu^2}{E}\lambda \tag{2.13}$$

The second constitutive model employed in this study is the J_2 deformation theory with the appropriate rate version

$$\dot{\sigma}_{ij} = 2G_S\dot{\varepsilon}_{ij} + \lambda_S\delta_{ij}\dot{\varepsilon}_{kk} - 3(G_S - G_T)\frac{S_{ij}S_{k\ell}\dot{\varepsilon}_{k\ell}}{\sigma_e^2} \tag{2.14}$$

where (G_S, λ_S) are the secant moduli defined by

$$G_S = \frac{E_S}{2(1+\nu_S)} \qquad \lambda_S = \frac{\nu_S E_S}{(1+\nu_S)(1-2\nu_S)} \tag{2.15}$$

ν_S is the plastic Poisson ratio

$$\nu_S = \frac{1}{2} - \left(\frac{1}{2} - \nu\right)\frac{E_S}{E} \tag{2.16}$$

and E_S is the secant modulus of the uniaxial stress-strain curve. The instantaneous moduli generated by the deformation theory (2.14) for the pure shear state of stress are

$$E_{rr} = E_{\theta\theta} = \frac{E_S}{1-\nu_S^2} = \bar{E}_S \qquad E_{r\theta} = \nu_S\bar{E}_S$$
$$G_{r\theta} = G(1-R_T) \tag{2.17}$$

Thus, by comparison with (2.10) we find that the instantaneous moduli of the deformation theory are smaller than those obtained from the flow theory (except $G_{r\theta}$ which remains unchanged). Combining (2.17) with (2.5) gives the buckling equation according to the deformation theory in a form which is similar to but less elegant than (2.12).

Turning to the numerics, we have to solve an eigenvalue system governed by a partial differential equation (2.12) -- or its deformation theory counterpart -- along with the associated boundary data, (2.7a) or (2.7b), imposed at r=a,b. The objective is to determine the smallest eigenvalue S (or λ) for which a non-trivial solution becomes possible.

The method of solution assumes that the normal velocity (displacement increment) during buckling can be put in the form

$$w = \mathrm{Re}\left\{\phi(r)e^{im\theta}\right\} \quad m \text{ integer} \tag{2.18}$$

where the eigenfunction $\phi(r)$ is to be determined. The governing differential equation is now reduced to a fourth order ordinary differential equation for $\phi(r)$ which can be solved, along with the proper boundary conditions, by available numerical schemes. Sample calculations were performed for three materials represented by the Ramberg-Osgood relation

$$\varepsilon = \frac{\sigma_e}{E} + K\left(\frac{\sigma_e}{E}\right)^n \tag{2.19}$$

where n, K are material constants. The radial profile of the effective stress follows from (2.1) and (2.13) as

$$\sigma_e = \frac{\sqrt{3}}{24}\left(\frac{E}{1-\nu^2}\right)\left(\frac{h}{r}\right)^2 S \tag{2.20}$$

Figures 2(a)-2(b) show the variation of the critical eigenvalue S_{cr} with the thickness ratio h/(b-a) for three metals. The uniaxial tension curve is described by (2.19) with the following material constants:

commercial Al: E=68700MPa ν=0.3 $K=1.27\cdot10^{10}$ n=3.72
AL 2014 T6: E=69000MPa ν=0.33 $K=6.08\cdot10^{31}$ n=15.62
ST AISI 4340: E=201000MPa ν=0.28 $K=7.61\cdot10^{54}$ n=27.6

Buckling loads were computed for the radii ratio b/a=4.18, with the two J_2 theories, and for clamped and simply supported plates. Comparison is made also with purely elastic buckling where both theories coincide.

Initially, for sufficiently thin plates, both theories predict the known linear elastic results: S_{cr}=88.3 for the clamped plate[8] and S_{cr}=52.7 for the simply-supported plate[9]. For thicker plates, however, where buckling occurs in the elastoplastic range, there is a considerable departure of the S_{cr} versus h/(b-a) curves from the purely elastic values. The most striking finding that emerges from the curves displayed in Figs. 2(a)-2(b) is the increasing difference, as the plate is getting thicker, in the prediction of S_{cr} obtained from the two J_2 theories. As expected, the deformation theory gives lower eigenvalues than the flow theory, but the extent of the difference between

the corresponding eigenvalues is not common in plastic buckling analysis. That difference appears to increase with the hardening parameter 1/n. Similar results were obtained[3] for the two cases of mixed boundary conditions with one edge clamped and the other simply-supported. The critical loads for these cases fall between the corresponding results of Figs. 2(a) and 2(b), and are somewhat higher when the inner boundary is clamped in comparison with a clamped outer boundary.

We proceed now with a comparison of the results of our theoretical analysis with the experimental data reported recently by Bauer[10,11]. In these tests several annual plates, with clamped boundaries, were subjected to in-plane torsion. the onset of buckling was determined by tracing the torsion-twist history and observing the formation of a buckling waves pattern. Critical loads were measured for a few metals over a wide range of geometries.

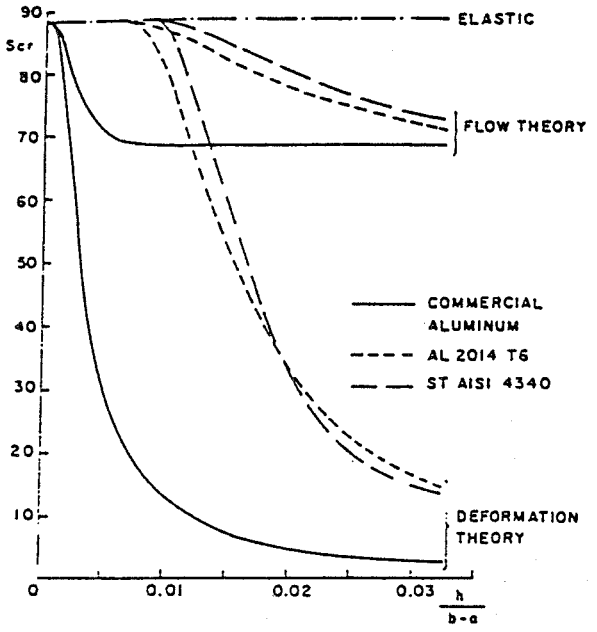

Fig. 2(a) Critical eigenvalues for clamped annular plates, b/a=4.18.

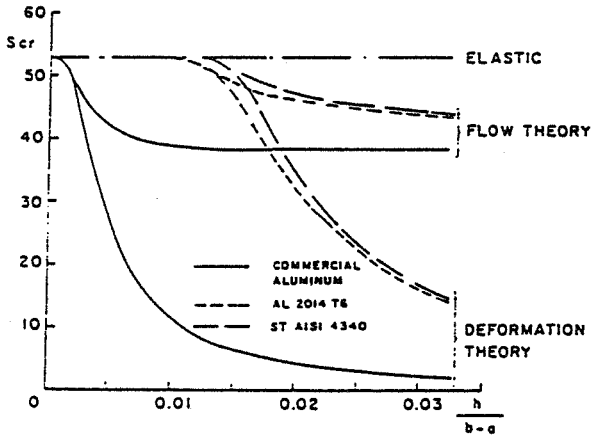

Fig. 2b Critical eigenvalues for simply supported annular plates, b/a=4.18.

Figures 3(a) -3(c) display the experimental values for the critical torsion moment M_{cr} along with the corresponding theoretical predictions obtained from the two J_2 theories. Also shown in Figs. 3(a)-3(c) is the background curve for purely elastic buckling. The critical torsion moment is related to eigenvalue (2.13) by the expression

$$M_{cr} = \frac{\pi E h^3}{12(1-\nu^2)} S_{cr} \qquad (2.21)$$

The stress-strain curves of the tension test for the metals used in the experiments can be described by (2.19) with the following constants:

CuZn36:	E=114400MPa	ν=0.33	$K=1.75\cdot10^5$
	n=2.4		
AL 98.7W:	E=70000MPa	ν=0.33	$K=8.95\cdot10^{11}$
	n=4.46		
ST 1403:	E=210000MPa	ν=0.3	$K=3.7\cdot10^{12}$
	n=4.9		

It is clearly seen from Figs. 3(a)-3(c) that the deformation theory predictions are generally in good agreement with the measured values for M_{cr}. Flow theory, by contrast, predicts buckling loads which are considerably above the experimental results. The difference between the critical torsion moments obtained from the two theories is emphasized more in Fig. 4 which shows the ratio M_{cr} (theoretical)/M_{cr} (experimental), for all three metals on a common scale.

It is certainly possible that unavoidable initial imperfections will reduce the maximum load

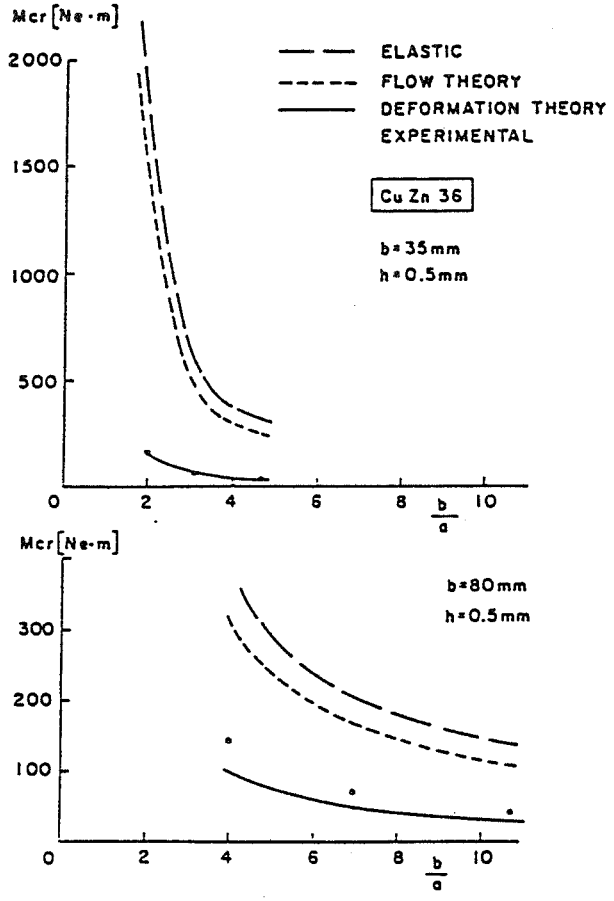

Fig. 3(a) Critical torsion moment for CuZn36, clamped boundaries.

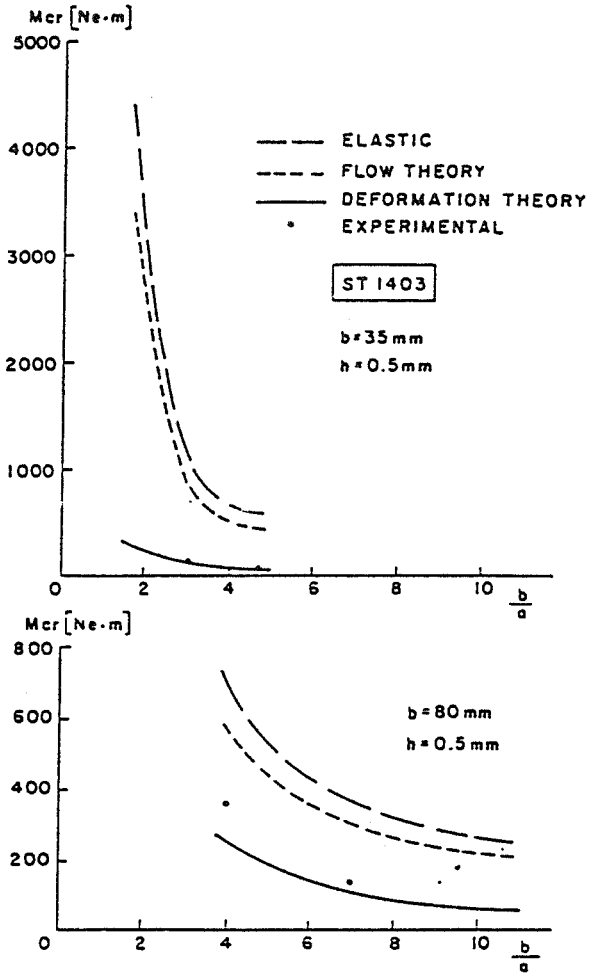

Fig. 3(c) Critical torsion moment for ST 1403, clamped boundaries.

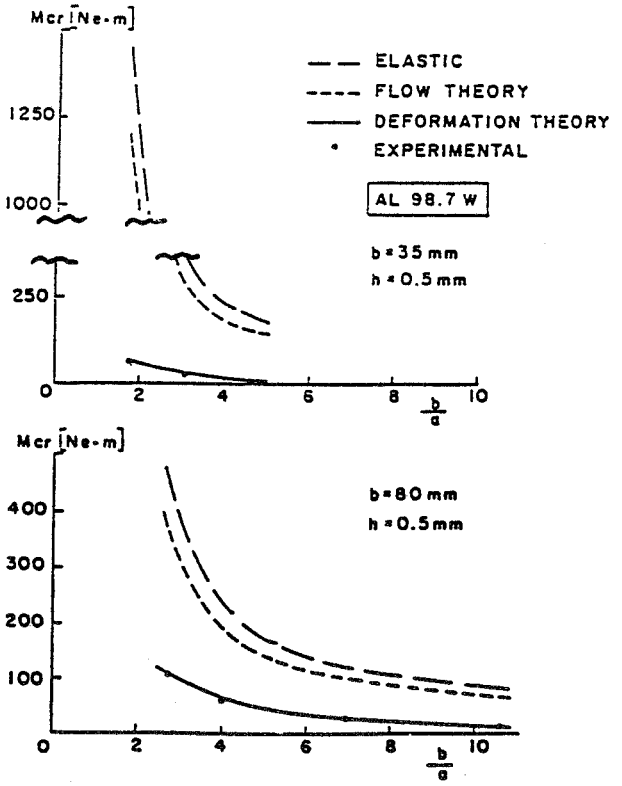

Fig. 3(b) Critical torsion moment for Al 98.7W, clamped boundaries.

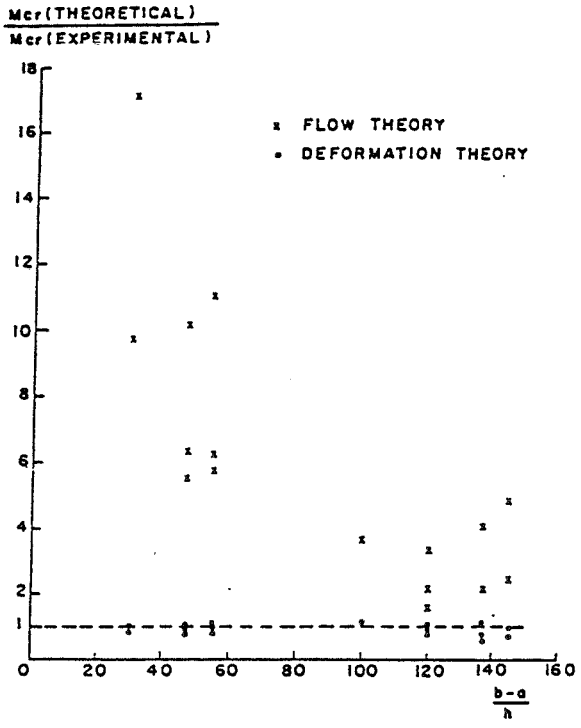

Fig. 4. The ratio M_{cr} (theoretical)/M_{cr}(experimental) for both theories, clamped boundaries.

prediction obtained from the flow theory[2]. But from a purely practical point of view, the deformation theory analysis of the bifurcation loads appears to be of sufficient reliability. The extent of the difference in the critical eigenvalues predicted by the two theories - for thick plates the ratio between the critical moments can reach an order of magnitude (Fig. 4) - provides a strong example of the "plastic buckling paradox".

When the annular plate (Fig. 1(a)) becomes very narrow, with a→b, we may expect the critical load to approach that of a long strip (Fig. 1(b)) under uniform shear along the boundaries. The solution of the strip problem is fairly simple since, unlike the plate problem, the prebuckling field is homogeneous with $\tau_{xy} \equiv \tau$. The buckling equation is simply

$$\frac{h^2}{12}\left[E_{xx}w_{,xxxx}+2\left(E_{xy}+2G_{xy}\right)w_{,xxyy}+E_{yy}w_{,yyyy}\right] -2\tau w_{,xy}=0 \qquad (2.22)$$

where $\left(E_{xx}, E_{xy}, E_{yy}, G_{xy}\right)$ are, with the usual notation, the instantaneous moduli of the material. These moduli are here exactly as in (2.10) for the flow theory, and as in (2.17) for the deformation theory, except for the transformation of the (r, θ) directions to the (y, x) directions.

The boundary conditions at the edges y=±c are taken as either clamped or simply-supported and we write the solution of (2.22) in the form

$$w = \mathrm{Re}\left\{f(y)e^{i\gamma\frac{x}{c}}\right\} \qquad (2.23)$$

where γ is an unknown parameter. The boundary conditions can now be written as

$f=0 \quad f'=0$ at a clamped edge (2.24a)

$f=0 \quad f''=0$ at a simply-supported edge (2.24b)

where here (and throughout this section) the prime denotes differentiation with respect to y. Inserting (2.23) in (2.22) we get the ordinary differential equation

$$E_{yy}f''''-2\left(\frac{\gamma}{c}\right)^2\left(E_{xy}+2G_{xy}\right)f'' -i\left(\frac{\gamma}{c^3}\right)\lambda^* f'+\left(\frac{\gamma}{c}\right)^4 E_{xx}f=0 \qquad (2.25)$$

where

$$\lambda^* = 24\left(\frac{c}{h}\right)^2\tau \qquad (2.26)$$

Since the coefficients of (2.25) are homogeneous we can put the solution for f(y) in the form

$$f=\sum_{p=1}^{4}A_p\exp\left(i\frac{\alpha_p}{c}y\right) \qquad (2.27)$$

where α_p are the four roots of the characteristic equation

$$E_{yy}\alpha^4+2\gamma^2\left(E_{xy}+2G_{xy}\right)\alpha^2+\gamma\lambda^*\alpha+\gamma^4E_{xx}=0 \qquad (2.28)$$

and A_p are the four integration constants. Compliance with the boundary conditions (2.24a) or (2.24b) leads to a system of four algebraic equations for constants A_p. The requirement for a nontrivial solution of that system gives the eigenvalue equation for the critical load at which the strip will buckle.

Calculations were made with a few metals (the same as those of Figs. 2(a)-2(b)) represented by relation (2.19). The solution procedure is essentially the same as for the annular plate problem, except that parameter γ of (2.23) is here continuous. Results for the critical load parameter

$$S^*_{cr}=\frac{1-\nu^2}{2E}\lambda^*_{cr}=\frac{3(1-\nu^2)}{E}\left(\frac{2c}{h}\right)^2\tau_{cr} \qquad (2.29)$$

are shown in Figs. 5(a)-5(b) for three different metals. The behavior of S^*_{cr} with increasing thickness is similar to what we have seen for the annular plate in Figs. 2(a)-2(b). In the elastic range, for thin panels, we recover the results of Southwell and Skan[12]: $S^*_{cr}\approx 22.18$ for the clamped panel and $S^*_{cr}\approx 13.21$ for the simply-supported panel. In the plastic range S^*_{cr} decreases with h/2c and there is again a con-siderable difference in the eigenvalues predicted by the two theories.

Comparison of the critical stresses for the clamped annular plate and the clamped long panel is shown in Fig. 6 for two different materials. The eigenvalues for the annular plate represent in Fig. 6 the critical shear stress at the inner boundary through the parameter

$$T_{cr}=\frac{3(1-\nu^2)}{E}\left(\frac{b-a}{h}\right)^2\tau_{cr}(r=a) \qquad (2.30)$$

The curves for the shear panel show the variation of S^*_{cr} from (2.29) with the thickness ratio h/2c. In calculating the annular plate curves we have assumed that h/a is maintained constant so that T_{cr} from (2.30) can be determined for every value of b/a. The variation of T_{cr} with h/(b-a) is shown in Fig. 6 for decreasing values of b/a. It can be clearly seen that T_{cr} approaches asymptotically S^*_{cr} as b/a→1 (implying that b-a→2c for the same thickness). T_{cr} is always higher than S^*_{cr} and the deformation theory curves are closer to the shear panel asymptotes in

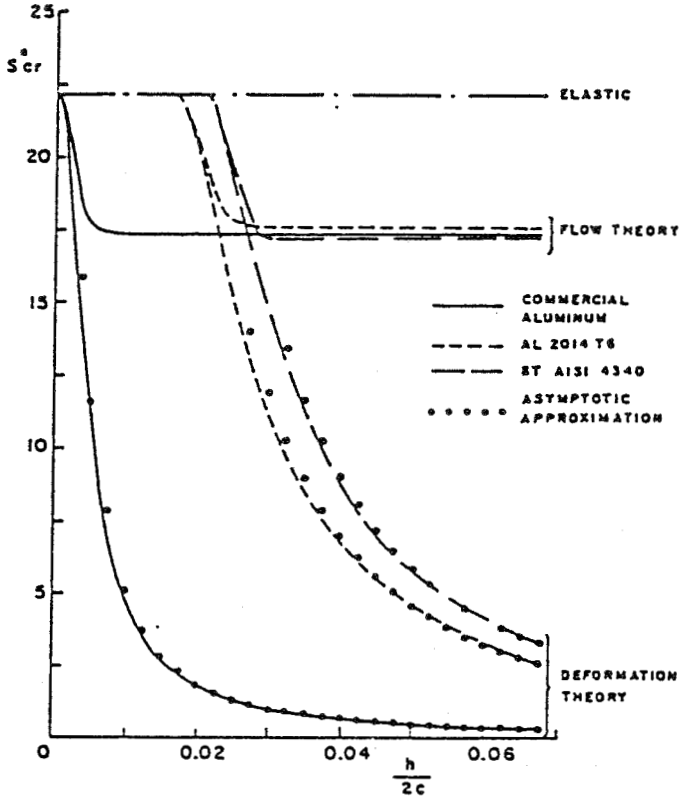

Fig. 5(a) Critical eigenvalues for clamped panels.

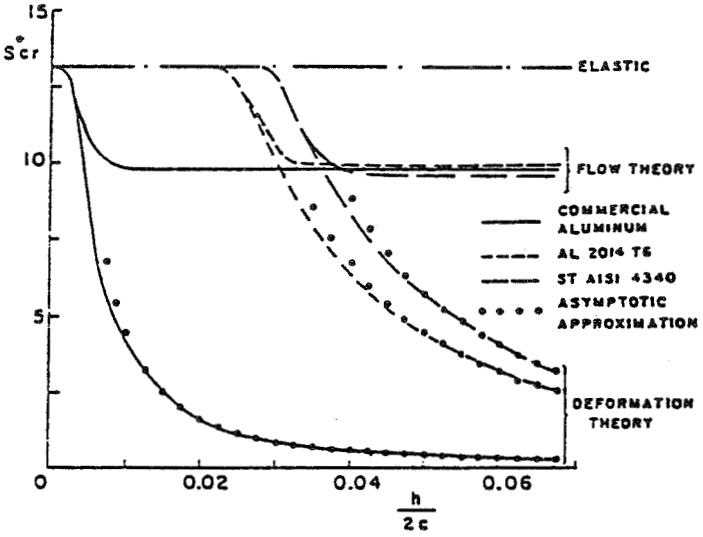

Fig. 5(b) Critical eigenvalues for simply-supported panels.

comparison with the flow theory and purely elastic curves.

It is worth noting that with the deformation theory and for the pure power law approximation of (2.19) it is possible to derive an asymptotic approximation for the critical load parameter, viz.

$$S^*_{cr} = B\left(\frac{h}{2c}\right)^{-\frac{2(n-1)}{n}} \qquad (2.31)$$

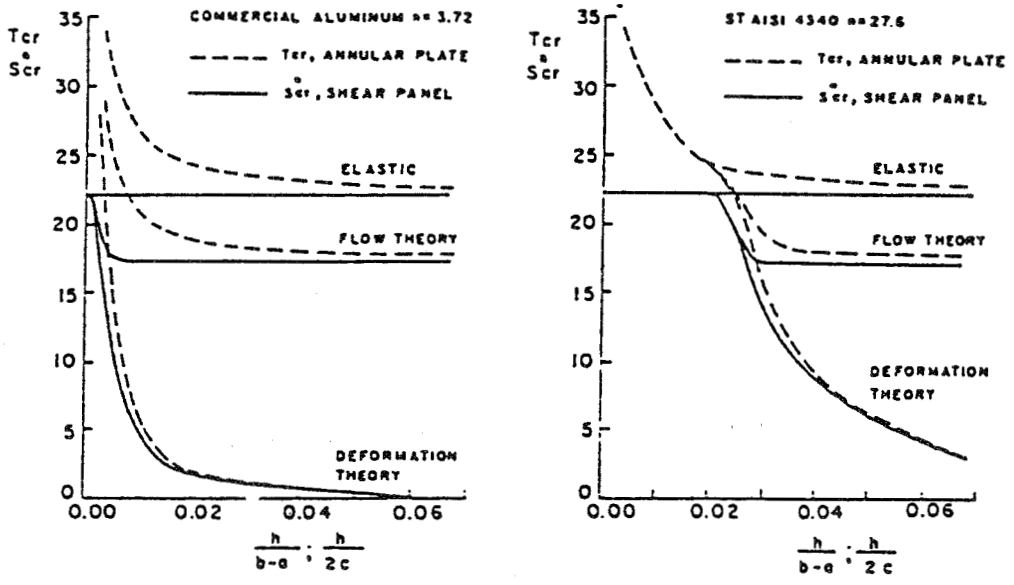

Fig. 6 Comparison of critical eigenvalues for the clamped annular plate (T_{cr}) and the clamped long panel (S^*_{cr}); the curves of the annular plate are computed with h/a=0.002.

where B depends on material properties and boundary data. Comparison of (2.31) with the exact solution shows an excellent agreement (Figs. 5(a)-5(b)) in the plastic range. It is interesting that essentially the same expression as (2.31) can be derived from the approximate analysis of Stowell who used a one term approximation for w in conjunction with a minimum principle and the deformation theory. Stowell[13] has compared his theoretical predictions with experimental measurements of Gerard[14] on the buckling of 24S-0 aluminum alloy shear panels. the agreement of the test data with the deformation theory predictions, over the range of thickness ratio $2c/h \approx 45 \div 103$, reveals essentially the same picture as in Fig. 4 of the present paper.

3. Rectangular Plate Under Biaxial Loads

Our second example is a rectangular plate of length a, width b, and uniform thickness h (see Fig. 7) which is subjected to axial compression $\sigma_y = -P$ along with axial tension $\sigma_x = \xi P$ where ξ is a fixed parameter. Thus, with ξ=0 we have simple axial compression, while $\xi = -1$ describes equibiaxial compression.

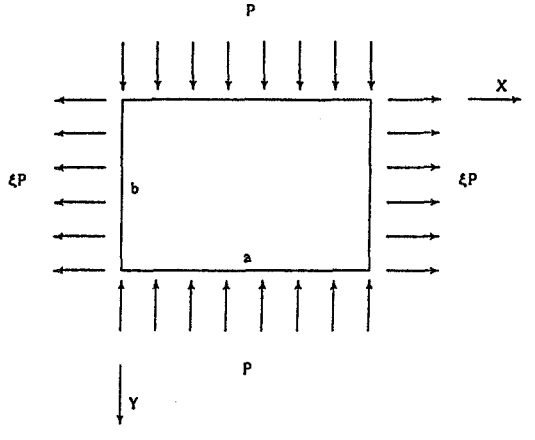

Fig. 7 Notation for rectangular plate.

With w denoting the out of plane velocity during buckling we have the plate buckling equation[4,5]

$$\frac{h^2}{12}\left[E_{xx}w_{,xxxx}+2\left(E_{xx}+2G_{xy}\right)w_{,xxyy}+E_{yy}w_{,yyyy}\right] -\xi P w_{,xx}+P w_{,yy}=0 \qquad (3.1)$$

where $(E_{xx}, E_{xy}, E_{yy}, G_{xy})$ are the instantaneous moduli of the plane-stress constitutive relations (2.2)-(2.4) with the transformation $(r,\theta) \rightarrow (y,x)$.

Equation (3.1) is supplemented by eight boundary conditions - two on each side of the plate. Taking the boundaries x=0,a as an example, we have for simple supports

$$w = 0 \qquad w_{,xx} = 0 \qquad (3.2a)$$

while for clamped edges

$$w = 0 \qquad w_{,x} = 0 \qquad (3.2b)$$

Similar conditions are imposed along the perpendicular boundaries y=0,b.

Specifying (2.8) and (2.14) for the present problem, with $\sigma_1 = \sigma_x$, $\sigma_2 = \sigma_y$ and $\sigma_z = 0$, it is convenient to redefine the instantaneous moduli as

$$\mu_{11} = E_{xx} \quad \mu_{22} = E_{yy} \quad \mu_{12} = E_{xy} + 2G_{xy} \qquad (3.3)$$

Thus, with the flow theory we get[4,5]

$$\mu_{ij} = \frac{4G(G+\lambda)-(G-G_T)[(2G+3\lambda)\Sigma_i\Sigma_j-G(\Sigma_i-\Sigma_j)^2+\frac{4}{3}G]}{2G+\lambda-\frac{1}{3}(G-G_T)(\Sigma_1+\Sigma_2)^2} \qquad i,j=1,2 \qquad (3.4)$$

while for the deformation theory we find[4,5]

$$\mu_{ij} = \frac{4G_S(G_S+\lambda_S)-(G_S-G_T)[(2G_S+3\lambda_S)\Sigma_i\Sigma_j-G_S(\Sigma_i-\Sigma_j)^2+\frac{4}{3}G_S]}{2G_S+\lambda_S-\frac{1}{3}(G_S-G_T)(\Sigma_1+\Sigma_2)^2} \qquad i,j=1,2 \qquad (3.5)$$

The effective stress is now given by

$$\sigma_e^2 = \left(1+\xi+\xi^2\right)P^2 \qquad (3.6)$$

and the normalized prebuckling stresses, $\Sigma_i = \sigma_i / \sigma_e$ i=1,2, are

$$\Sigma_1 = \frac{\xi}{\sqrt{1+\xi+\xi^2}} \qquad \Sigma_2 = -\frac{1}{\sqrt{1+\xi+\xi^2}} \tag{3.7}$$

To sum up, for given plate geometry, boundary conditions, material properties (μ_{ij}) and loading program (ξ), we seek the smallest value of P for which Eq. (3.1) admits a non trivial solution. That eigenvalue is identified with the critical load which causes buckling of the plate. Any uniaxial stress strain relation can be implemented in this analysis. The examples presented later were calculated with the Ramberg-Osgood elastoplastic formula (2.19).

The simplest solution of (3.1) is obtained for simply supported boundaries, namely $w = w_{,xx} = 0$ at x=0,a, and $w = w_{,yy} = 0$ at y=0,b. These constraints are met with the velocity field

$$w = A\sin\left(\frac{m\pi x}{a}\right)\sin\left(\frac{n\pi y}{b}\right) \qquad m,n = 1,2,\ldots \tag{3.8}$$

where A is an arbitrary constant. Inserting (3.8) in (3.1) we get the eigenvalue equations

$$\left[2G+\lambda-\frac{1}{3}(G-G_T)(\Sigma_1+\Sigma_2)^2\right]\left(\xi m^2-\beta^2 n^2\right)P$$

$$+\alpha\left\{\frac{4}{3}G(2G+3\lambda+G_T)(m^2+\beta^2n^2)^2\right.$$

$$-(G-G_T)\left[(2G+3\lambda)(m^2\Sigma_1+\beta^2n^2\Sigma_2)^2\right.$$

$$\left.\left.-2\beta^2m^2n^2G(\Sigma_1-\Sigma_2)^2\right]\right\}=0 \tag{3.9}$$

for the flow theory, and

$$\left[2G_S+\lambda_S-\frac{1}{3}(G_S-G_T)(\Sigma_1+\Sigma_2)^2\right]\left(\xi m^2-\beta^2 n^2\right)P$$

$$+\alpha\left\{\frac{4}{3}G_S(2G_S+3\lambda_S+G_T)(m^2+\beta^2n^2)^2\right.$$

$$-(G_S-G_T)\left[(2G_S+3\lambda_S)(m^2\Sigma_1+\beta^2n^2\Sigma_2)^2\right.$$

$$\left.\left.-2\beta^2m^2n^2G_S(\Sigma_1-\Sigma_2)^2\right]\right\}=0 \tag{3.10}$$

for the deformation theory. The geometrical parameters (α,β) are defined by

$$\alpha = \frac{\pi^2h^2}{12a^2} \qquad \beta = \frac{a}{b} \tag{3.11}$$

When $G_T = G_S = G$ and $\lambda_S = \lambda$ we recover from both (3.10) and (3.11) the linear elastic buckling equation

$$\frac{(1-\nu^2)P}{\alpha E} = \frac{\beta^2n^2+m^2}{\beta^2n^2-\xi m^2} \tag{3.12}$$

Accordingly, we shall refer to the nondimensional buckling parameter (not to be confused with the Ramberg-Osgood constant in (2.19))

$$K = \frac{(1-\nu^2)P}{\alpha E} \tag{3.13}$$

as a suitable measure of the critical loads. Notice that the smallest eigenvalues of (3.9)-(3.10) should be minimized with respect to the wave numbers (m,n).

We turn now to the case where the boundaries x=0,a are simply supported, (3.2a), but the compressed sides are clamped. It is convenient here to locate the origin of the (x,y) axes at the center of the boundary x=0 (see Fig. 8) so that the clamped boundary conditions read

$$w = 0 \quad w_{,y} = 0 \quad \text{at} \quad y = \pm\frac{b}{2} \tag{3.14}$$

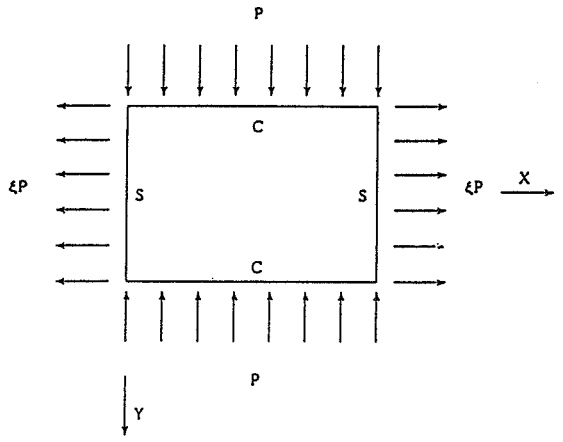

Fig. 8 Rectangular plate. S-simple support, C-clamped boundary.

The buckling mode is now written in the form

$$w = A\sin\left(\frac{m\pi x}{a}\right)f(y) \qquad m = 1,2,\ldots \tag{3.15}$$

where f(y) is to be determined. The field (3.15) complies with the boundary data (3.2a), and when substituted in (3.1) results in the ordinary differential equation

$$\frac{h^2}{12}\left[\mu_{11}\left(\frac{m\pi}{a}\right)^4 f - 2\mu_{12}\left(\frac{m\pi}{a}\right)^2 f'' + \mu_{22} f''''\right]$$

$$+\xi P\left(\frac{m\pi}{a}\right)^2 f + Pf'' = 0 \quad , \quad (\cdot)' = \frac{d(\cdot)}{dy} \qquad (3.16)$$

The solution of this equation has a symmetric part

$$f_1(y) = D_2 \sinh\left(\pi\gamma_1 \frac{y}{a}\right) + D_4 \sinh\left(\pi\gamma_3 \frac{y}{a}\right) \qquad (3.17)$$

and an antisymmetric part

$$f_2(y) = D_1 \cosh\left(\pi\gamma_1 \frac{y}{a}\right) + D_3 \cosh\left(\pi\gamma_3 \frac{y}{a}\right) \qquad (3.18)$$

where $D_i (i = 1,...4)$ are integration constants and (γ_1, γ_3) are the characteristic roots of (3.10) as determined from the equation

$$\alpha\mu_{22}\gamma^4 + \left(P - 2\mu_{12}\alpha m^2\right)\gamma^2 + \alpha\mu_{11}m^4 + \xi P m^2 = 0$$
$$m=1,2,... \qquad (3.19)$$

This equation has four roots labeled as $\pm\gamma_1$ and $\pm\gamma_3$. We skip here much of the algebra involved in the analysis, and for more details one should consult the original thesis[4], or the forthcoming report[15].

The standard technique of compliance with boundary conditions (3.14) and the requirement for a nontrivial solution leads to the eigenvalue equations. For symmetric buckling modes (3.17) we get

$$\gamma_3 \tanh\left(\frac{\pi}{2\beta}\gamma_3\right) - \gamma_1 \tanh\left(\frac{\pi}{2\beta}\gamma_1\right) = 0 \qquad (3.20)$$

while for antisymmetric modes (3.18) we have

$$\gamma_3 \tanh\left(\frac{\pi}{2\beta}\gamma_1\right) - \gamma_1 \tanh\left(\frac{\pi}{2\beta}\gamma_3\right) = 0 \qquad (3.21)$$

The solution of (3.20)-(3.21) provides the critical buckling parameter (3.13). Both modes have to be considered in the calculations along with a minimization procedure with respect to the wave number m.

Proceeding along similar lines we can solve the problem when the compressed sides are simply supported and the other edges clamped. Here we move the origin of the coordinates to the center of the side y=0, so that at y=0,b $w = w_{,yy} = 0$ while at $x = \pm\frac{a}{2}$ $w = w_{,x} = 0$. A solution is now sought in the form

$$w = Ag(x)\sin\left(\frac{n\pi y}{b}\right) \qquad (3.22)$$

and the eigenvalue equations follow as

$$\gamma_3 \tanh\left(\frac{\pi}{2}\beta\gamma_3\right) - \gamma_1 \tanh\left(\frac{\pi}{2}\beta\gamma_1\right) = 0 \qquad (3.23)$$

for symmetric modes, and

$$\gamma_3 \tanh\left(\frac{\pi}{2}\beta\gamma_1\right) - \gamma_1 \tanh\left(\frac{\pi}{2}\beta\gamma_3\right) = 0 \qquad (3.24)$$

for antisymmetric modes.

The characteristic roots $\pm\gamma_1$ and $\pm\gamma_3$ are determined by the transcendental equation

$$\alpha\beta^2\mu_{11}\gamma^4 - \left(\xi P + 2\mu_{12}\alpha\beta^2 n^2\right)\gamma^2$$
$$+\alpha\beta^2\mu_{22}n^4 - Pn^2 = 0 \qquad n=1,2,... \qquad (3.25)$$

Solution procedure parallels that of the previous problem including minimization with respect to wave numbers n.

Critical stresses were evaluated numerically by solving the eigenvalue equations (3.9)-(3.10), (3.20)-(3.21) and (3.23)-(3.24) for the different boundary conditions. The solution is straightforward though care has to be exercised in handling the complex roots of (3.19) and (3.25). As we have said already, the numerical routine includes a searching technique to trace the smallest eigenvalue (3.13).

Results for aluminum AL 7075-T6 are shown in Fig. 9 for simply supported plates with α=0.001 and β=1. The Ramberg-Osgood parameters (2.19) for that metal are $K=3.94\cdot10^{21}$, n=10.9, and the elastic constants are given by $E=7.24\cdot10^{10}$Pa, ν=0.32.

Initially, for low values of ξ both theories are in agreement, but with increasing load ratio flow theory predicts increasingly higher values of K as compared to the deformation theory. Furthermore, the deformation theory predicts an optimal buckling load at a specific value of ξ. That behavior is more emphasized in Figs. 10-11 which display the gradual transition from the elastic range (with α=0.0001) to the deep plastic range (α=0.002) by increasing the plate's thickness.

When the plate is more narrow (increasing β) optimal buckling is attained by biaxial compression (see Fig. 12). It is interesting therefore that there exists a critical value of plate aspect ratio (β) for

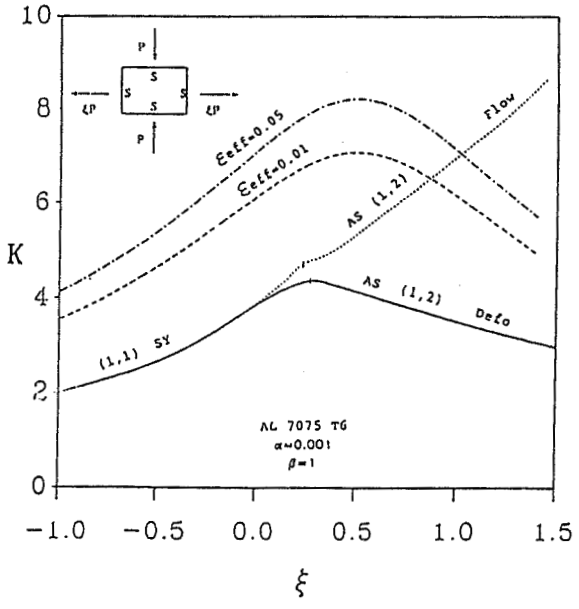

Fig. 9 Variation of buckling parameter with load ratio.

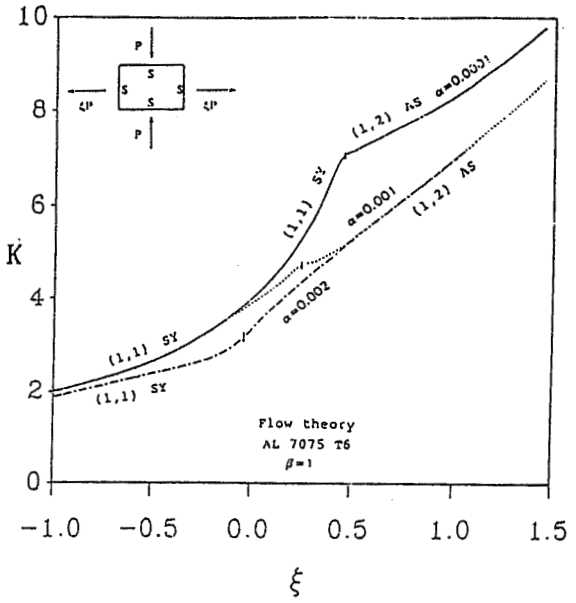

Fig. 11 Influence of plate thickness. Flow theory.

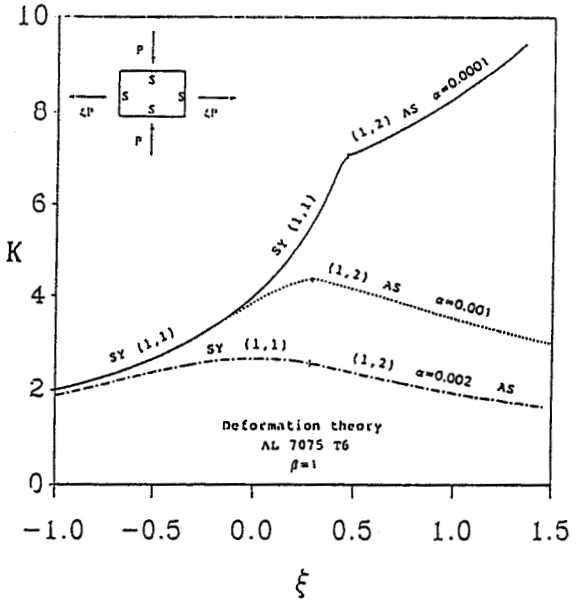

Fig. 10 Influence of plate thickness. Deformation theory.

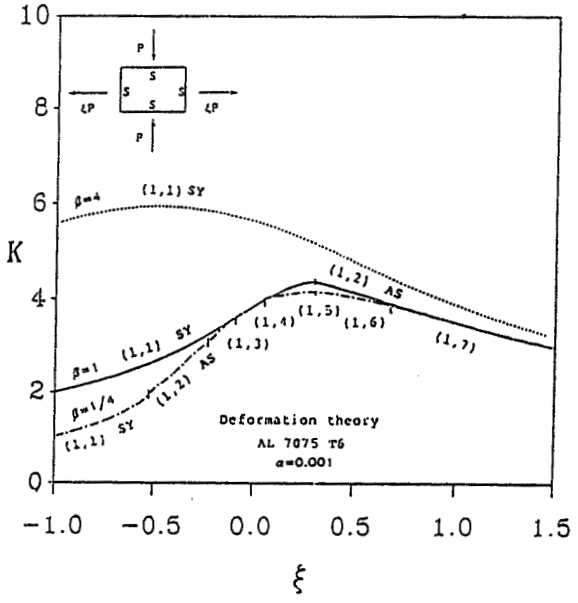

Fig. 12 Influence of plate dimensions. Deformation theory.

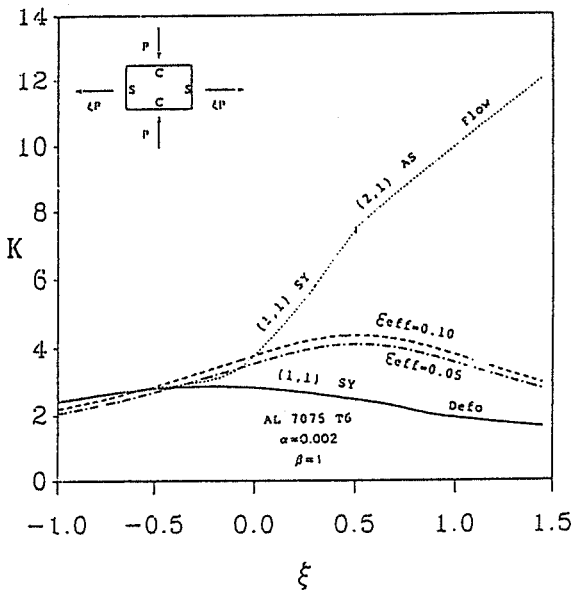

Fig. 13 Buckling with two clamped boundaries.

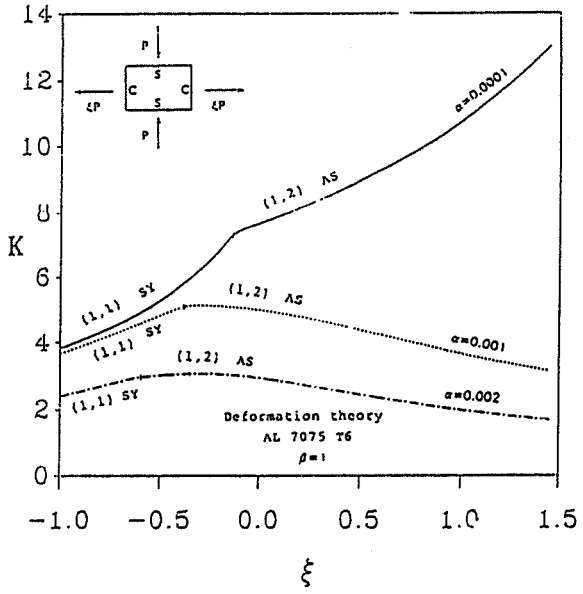

Fig. 14 Influence of plate thickness. Deformation theory. Two boundaries are clamped.

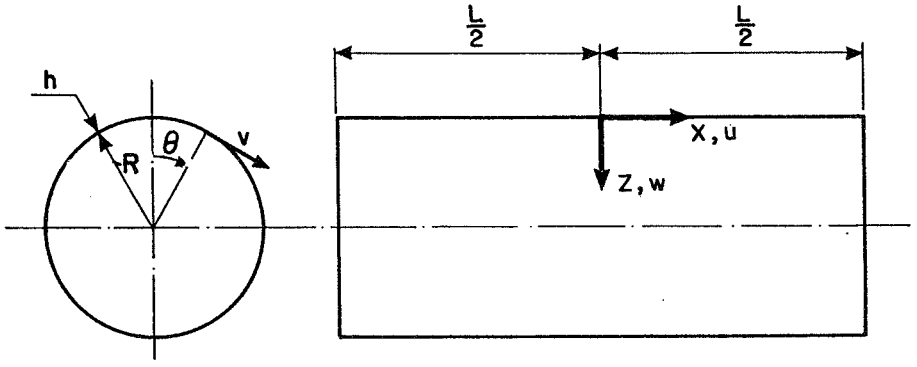

Fig. 15 Geometry and notation ror circular cylindrical shells.

which the highest buckling load is obtained in purely uniaxial compression (ξ=0). This observation can be helpful in optimal design of stiffness spacing.

Results for the other boundary conditions reveal a similar picture. Of course, clamped plates buckle at higher loads in comparison with simply supported plates, but the contrast between flow and deformation theories remains very much the same (see Figs. 13 and 14).

4. Circular Cylindrical Shell in Axial Compression

The third problem considered in this paper has to do with plastic buckling of an axially compressed circular cylindrical shell[3,7] with various end conditions. Thus, with the notation of Fig. 15 we consider a circular cylindrical shell subjected to uniform axial compression σ_{x0}. Denoting the length of the shell by L and its radius by R it is convenient to introduce a non-dimensionalized (with respect to R) axial coordinate x so that the loaded edges are defined by $x = \pm L/2R$. The axial stress resultant is then given by

$$N_{x0} = \sigma_{x0} h = -\frac{Eh}{g^2}\rho \tag{4.1}$$

where h is the shell's thickness, ρ the load parameter (eigenvalue) and

$$g^2 = \sqrt{3(1-\nu^2)}\,\frac{R}{h} \tag{4.2}$$

The instantaneous moduli of (2.2)-(2.4), with r replaced by x, are given here by

$$E_{xx} = H_T \frac{\bar{\eta}_T + 3}{4} \qquad E_{\theta\theta} = H_T \bar{\eta}_T$$
$$E_{x\theta} = H_T \frac{\bar{\eta}_T + 2\nu - 1}{2} \qquad G_{x\theta} = G \tag{4.3}$$

where

$$H_T = \frac{4E}{(5-4\nu)\bar{\eta}_T - (1-2\nu)^2} \qquad \bar{\eta}_T = \frac{E}{E_T} \tag{4.4}$$

for the J_2 flow theory, and by

$$E_{xx} = H_S \frac{\bar{\eta}_T + 3\bar{\eta}_S}{4} \qquad E_{\theta\theta} = H_S \bar{\eta}_T$$
$$E_{x\theta} = H_S \frac{\bar{\eta}_T + 2\nu - 1}{2} \qquad G_{x\theta} = G_S \tag{4.5}$$

where

$$H_S = \frac{4E}{(3\bar{\eta}_S + 2 - 4\nu)\bar{\eta}_T - (1-2\nu)^2} \qquad \bar{\eta}_S = \frac{E}{E_S} \tag{4.6}$$

for the J_2 deformation theory. Notice that all moduli are in fact known functions of the effective stress

$$\sigma_e = -\sigma_{x0} = \frac{E}{g^2}\rho \tag{4.7}$$

Denoting by (u,v,w) the nondimensionalized (with respect to R) mid-plane velocities (in directions x,θ,z, respectively) during buckling, we have the Donnell type equations[3,7]

$$E_{xx}u_{,xx} + G_{x\theta}u_{,\theta\theta} + (E_{x\theta} + G_{x\theta})v_{,x\theta} - E_{,x\theta}\,w_{,x} = 0 \tag{4.8a}$$

$$(E_{x\theta} + G_{x\theta})u_{,x\theta} + G_{x\theta}v_{,xx} + E_{\theta\theta}v_{,\theta\theta} - E_{\theta\theta}w_{,\theta} = 0 \tag{4.8b}$$

$$E_{xx}w_{,xxxx} + 2(E_{x\theta} + 2G_{x\theta})w_{,xx\theta\theta} + E_{\theta\theta}w_{,\theta\theta\theta\theta}$$
$$-12\left(\frac{R}{h}\right)^2 [E_{x\theta}u_{,x} + E_{\theta\theta}(v_{,\theta} - w)] + 4E_0 g^2 \rho w_{,xx} = 0 \tag{4.8c}$$

where

$$E_0 = \frac{E}{1-\nu^2} \tag{4.9}$$

Equations (4.8) are supplemented by the conditions along the boundaries $x = \pm L/2R \equiv \pm 1$. For simply supported boundaries we have the four variants

$$\begin{aligned}
&\text{SS1: } w = \dot{M}_x = \dot{N}_x = \dot{N}_{x\theta} = 0\\
&\text{SS2: } w = \dot{M}_x = u = \dot{N}_{x\theta} = 0\\
&\text{SS3: } w = \dot{M}_x = \dot{N}_x = v = 0\\
&\text{SS4: } w = \dot{M}_x = u = v = 0
\end{aligned} \tag{4.10}$$

where $\dot{M}_x$, $\dot{N}_x$, $\dot{N}_{x\theta}$ are the usual stress rate resultants. These conditions can be expressed directly in terms of the velocities, namely,

$$\begin{aligned}
&\text{SS1: } w = w_{,xx} = E_{xx}u_{,x} + E_{x\theta}v_{,\theta} = u_{,\theta} + v_{,x} = 0\\
&\text{SS2: } w = w_{,xx} = u = v_{,x} = 0\\
&\text{SS3: } w = w_{,xx} = u_{,x} = v = 0\\
&\text{SS4: } w = w_{,xx} = u = v = 0
\end{aligned} \tag{4.11}$$

A second set of boundary conditions which will be investigated here contains the four possibilities of clamped edges. These conditions, designated by CL1-CL4, are identical to these in Eqs. (4.11) except that the requirement $w_{,xx} = 0$ is replaced by the obvious condition that $w_{,x} = 0$.

The homogeneous system of differential equations (4.8) and boundary conditions (4.11), or CL1-CL4, has a non-trivial solution only for discrete eigenvalues of the load parameter ρ. The smallest eigenvalue ρ_{cr} determines the critical buckling load from Eq. (4.1). Note that the instantaneous moduli depend on ρ according to expressions (4.3) and (4.5).

For sufficiently thick shells the buckling mode is axially symmetric. In that case there is no θ-dependence and the velocity v vanishes identically. Equations (4.8) take now the simplified form

$$E_{xx}u_{,xx}-E_{x\theta}w_{,x}=0 \qquad (4.12a)$$

$$E_{xx}w_{,xxxx}-12\left(\frac{R}{h}\right)^2\left(E_{x\theta}u_{,x}-E_{\theta\theta}w\right)$$
$$+4E_0g^2\rho w_{,xx}=0 \qquad (4.12b)$$

The simply supported boundary conditions (4.11) are reduced to

$$\text{SS1, SS3: } w=0\ \ w_{,xx}=0\ \ u_{,x}=0 \qquad (4.13a)$$
$$\text{SS2, SS4: } w=0\ \ w_{,xx}=0\ \ u=0 \qquad (4.13b)$$

with similar expressions for the clamped boundaries (CL1, CL3) and (CL2, CL4) except that $w_{,xx}=0$ is replaced by $w_{,x}=0$.

Available experimental data[16,17,18] indicates that plastic buckling of axially compressed circular cylindrical shells is dominated by the axially symmetric mode. It appears therefore worthwhile to present a separate analysis for these particular modes which are governed by Eqs. (4.12). The method of solution is fairly standard: For boundary conditions SS1, SS3 of (4.13a) we recover the known results, due to Batterman[17],

$$\rho=\frac{2\sqrt{1-\nu^2}}{[(5-4\nu)\bar{\eta}_T-(1-2\nu)^2]^{1/2}} \quad \text{(flow theory)(4.14)}$$

$$\rho=\frac{2\sqrt{1-\nu^2}}{[(3\bar{\eta}_S+2-4\nu)\bar{\eta}_T-(1-2\nu)^2]^{1/2}}$$

(deformation theory) (4.15)

provided that the shell parameter $L/\sqrt{Rh}$ is sufficiently large. In the elastic range where $\bar{\eta}_T=\bar{\eta}_S=1$ we get from (4.14)-(4.15) the classical result $\rho=1$. For incompressible solids $(\nu=\frac{1}{2})$, relations (4.14)-(4.15) simplify to

$$\rho=\bar{\eta}_T^{-\frac{1}{2}} \qquad \text{(flow theory)}$$

$$\rho=(\bar{\eta}_T\bar{\eta}_S)^{-\frac{1}{2}} \quad \text{(deformation theory)} \qquad (4.16)$$

Parameters $\bar{\eta}_T$, $\bar{\eta}_S$ depend on ρ according to the uniaxial stress-strain response function. In the deep plastic range, where it is permissible to neglect the plastic part of (2.19) we have the useful asymptotic power law approximations

$$\rho=\left(\frac{1}{nK}\right)^{\frac{1}{n+1}}g^{\frac{2(n-1)}{n+1}} \quad \text{(flow theory)} \qquad (4.17)$$

$$\rho=\left(\frac{1}{\sqrt{n}K}\right)^{\frac{1}{n}}g^{\frac{2(n-1)}{n}} \quad \text{(deformation theory)} \quad (4.18)$$

where g is given by (4.2) with $\nu=\frac{1}{2}$. Better approximations which account for the effect of ν can be extracted from (4.14)-(4.15) by assuming that in the plastic range $\bar{\eta}_T>>1$ and $\bar{\eta}_S>>1$. This leads to the improved power law asymptotic approximations

$$\rho=\left(\frac{4(1-\nu^2)}{(5-4\nu)nK}\right)^{\frac{1}{n+1}}g^{\frac{2(n-1)}{n+1}} \quad \text{(flow theory)} \quad (4.19a)$$

$$\rho=\left(\frac{2\sqrt{1-\nu^2}}{\sqrt{3n}K}\right)^{\frac{1}{n}}g^{\frac{2(n-1)}{n}}$$

(deformation theory) (4.19b)

with g expressed by Eq. (4.2).

Buckling stresses predicted by the flow theory are consistently higher than those obtained from the deformation theory. This is evident from Eqs. (4.14)-(4.15) since both $\bar{\eta}_T$ and $\bar{\eta}_S$ increase with ρ beyond their initial elastic value $\bar{\eta}_T=\bar{\eta}_S=1$.

The buckling loads for boundary conditions SS2 and SS4, and those for clamped boundaries CL1, CL3 and CL2, CL4 are determined from the roots of transcendental eigenvalue equations. Similarly, the general solution of Eqs. (4.8) is reduced to specific eigenvalue equations, for each boundary condition, which take the form of transcendental algebraic equations for ρ. The numerical procedure for locating the smallest buckling load is detailed in[3,7] and here we shall give only the final results.

Sample calculations of the buckling loads were performed for three different materials and over a range of shell geometries. The metals considered here are characterized by the Ramberg-Osgood relation (2.19) with the same specifications as in Figs. 2(a)-2(b).

The length to thickness ratio has been kept constant at the value of L/h=200 while the radius to thickness ratio varied from R/h=2000 to R/h=10.

Figure 16 shows the dependence of the critical eigenvalues on h/R for all cases of simple supports. Initially, for sufficiently thin shells, we recover the known elastic values of ρ=0.5 for cases SS1-SS2, and ρ=1 for cases SS3-SS4. For thicker shells, however, there is a considerable decrease in the values of ρ_{cr} with increasing h/R. There is no significant difference between the eigenvalues with boundary conditions SS1 and SS2, and a similar agreement exists for conditions SS3 and SS4. Deformation theory predicts eigenvalues that are below those obtained with the flow theory. The differences in the critical eigenvalues evaluated from these two theories apepar to decrease with increasing n. The lowest values of ρ for cases SS1-SS2 were obtained with one circumferential wave, while in cases SS3-SS4 the dominant buckling mode is axially symmetric.

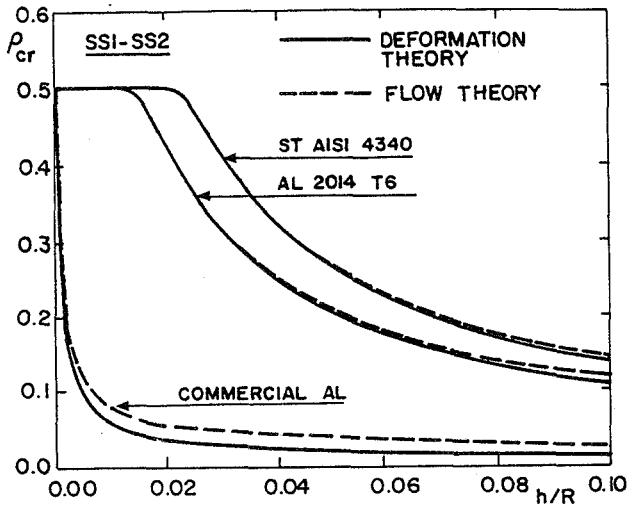

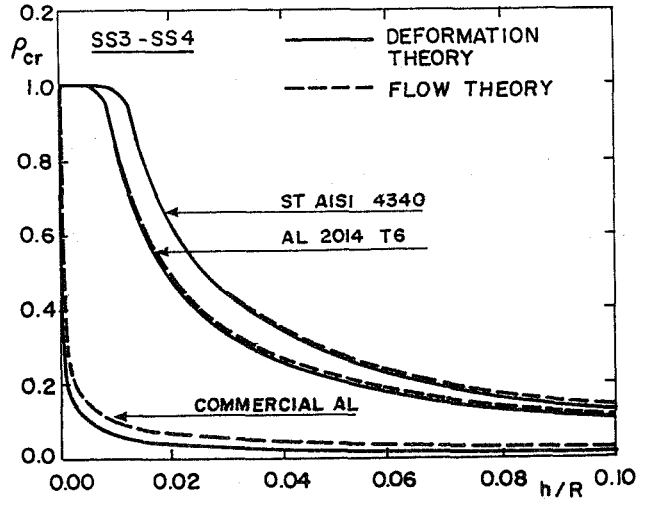

Fig. 16 Critical eigenvalues for simply supported boundaries.

Critical eigenvalues for clamped boundary conditions are practically identical for all four cases CL1-CL4 (Fig. 17), and are virtually equal to the SS3-SS4 results. Here again deformation theory predicts lower buckling loads than those obtained from the flow theory, but the difference decreases with increasing n. The eigenmodes are axially symmetric in the deep plastic range and with one circumferential wave in the initial plastic phase.

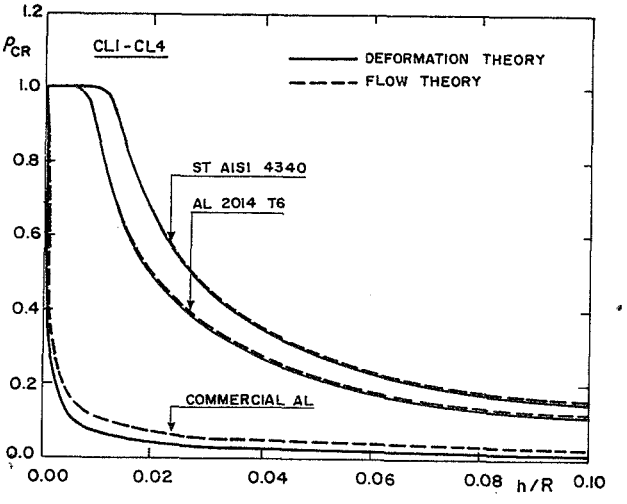

Fig. 17 Critical eigenvalues for clamped boundaries.

An interesting observation that emerges from our numerical study is the decreasing difference among the buckling loads, for the various boundary conditions, as the shell becomes thicker. This is illustrated in Fig. 18 where the dependence of the critical eigenvalues on h/R is shown for cases SS1-SS2, SS3-SS4 and CL1-CL4. These results are for AL 2014 T6 and with the deformation theory, but essentially the same picture is revealed with the flow theory. A similar observation is valid for commercial AL and ST AISI 4340 from the data of Figs. 16 and 17. It is possible though that conditions SS1-SS2 will give about half the buckling load of conditions SS3-SS4 and CL1-CL4 in the early plastic phase as has been shown by the analysis of Storakers[19] for semi-infinite shells with boundary conditions SS1 and SS3.

In the plastic range we have the SS3 asymptotic power law approximation (4.19b) which gives for the AL 2014 T6, with $\nu = \frac{1}{2}$,

$$\rho \approx 0.0135\left(\frac{R}{h}\right)^{0.936} \qquad (4.20)$$

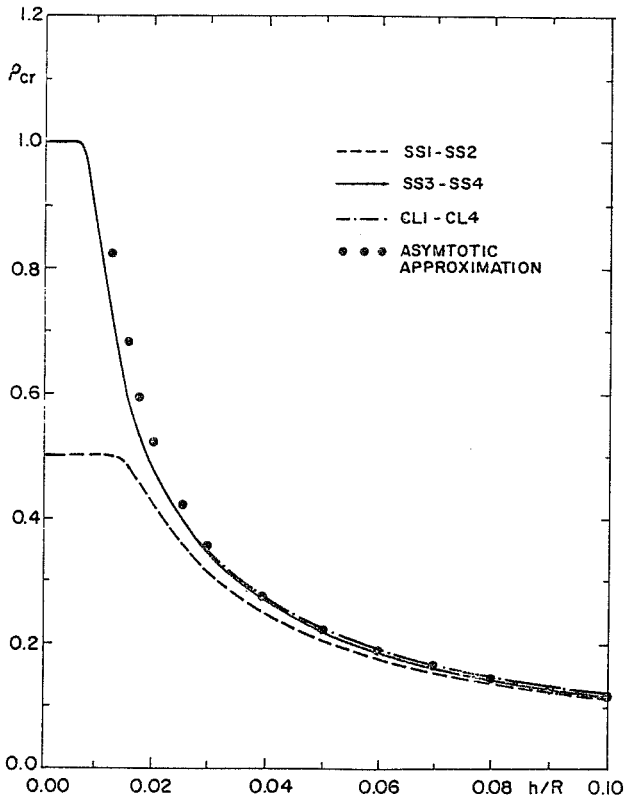

Fig. 18 Critical eigenvalues for simply supported and clamped boundaries according to the deformation theory.

This relation agrees quite well with the exact numerical results in the plastic range (Fig. 18).

A comparison of the present theoretical predictions with the experimental results of Lee is displayed in Fig. 19. The tests were performed with simply support (SS3) cylindrical shells, made of AL 3003-0 with the material parameters E=70000 MPa, ν=0.32, $K=2.48\times10^{10}$, n=4.10. The dominant buckling mode was axially symmetric. Agreement with deformation theory appears to be quite good (Fig. 19), while flow theory considerably overestimates the buckling stress. The improved asymptotic approximations (4.19) are given here by (in psi)

$$\sigma = 56572\left(\frac{R}{h}\right)^{-0.392} \quad \text{(flow theory)} \qquad (4.21a)$$

$$\sigma = 22149\left(\frac{R}{h}\right)^{-0.244} \quad \text{(deformation theory)} \qquad (4.21b)$$

These formulae appear to be good approximations of the more accurate theoretical results (Fig. 19).

Comparison with the buckling tests by Batterman[17] is shown in Fig. 20. The data here is for simply supported Al 2024-T4 shells with the material parameters E=70000 MPa, ν=0.32, $K=1.68\times10^{27}$,

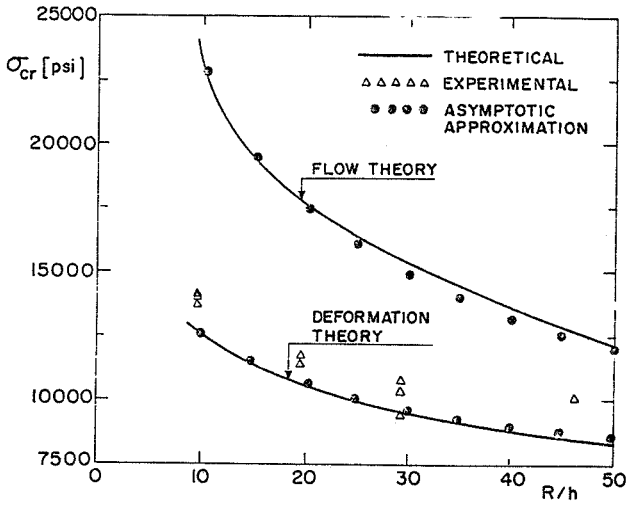

Fig. 19 Comparison with the experimental results of Lee.

n=13.03. Buckling in the plastic range was axially symmetric. The small difference between the theoretical results of the flow and deformation theories reflects the influence of the power law exponent n.

Experimental data on axially symmetric buckling is reported also by Sobel and Newman[18] for four ST 304 shells. The material parameters are E=221470 MPa, ν=0.27, $K=4.74\times10^{23}$, n=8.64. The radius to thickness ratio was nearly constant (R/h=18.5), with different values of L/R, and the average measured buckling stress was σ_{cr} = 46.1 kip. By comparison, for axially symmetric buckling with simply supported (SS3) boundaries, flow theory predicts an average critical load of σ_{cr}=54.2 kip while deformation theory gives σ_{cr} = 44.1 kip. For axially symmetric buckling with the CL3 conditions we have σ_{cr} = 55.9 kip (flow theory) and σ_{cr} = 44.5 kip (deformation theory).

It may be concluded that, in comparison with plastic buckling in shear, the plastic buckling paradox is less manifested for axially compressed circular cylindrical shells. The difference between the buckling loads predicted by the flow and deformation theories is appreciable only at low values of the power law exponent n.

5. Concluding Remarks

Plastic buckling of thin walled structures is still a lively subject of theoretical[20,21,22] and experimental[23,24] investigations. While the controversy surrounding the plastic buckling paradox has not been

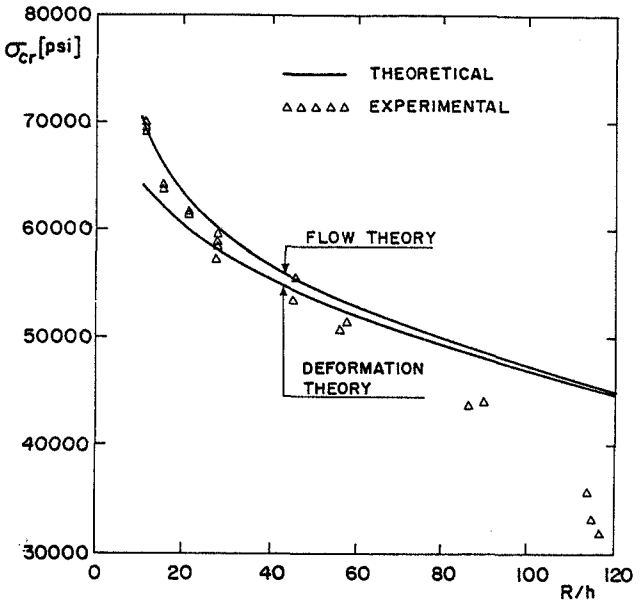

Fig. 20. Comparison with the experimental results of Batterman.

completely resolved, it may be safely argued that critical load predictions which are based on the J_2 deformation theory are in reasonably good agreement with test results, while J_2 flow theory predictions consistently overestimate experimental data for buckling stresses. Thus, it may well be the case that if an agreed upon plastic theory will ever be found its final incarnation will resemble and in fact be close to the present day version of the J_2 deformation theory.

Acknowledgement

This research was supported by the fund for promotion of research at the Technion.

6. References

1. Gerard, G. and Becker, H., "Handbook of structural stability: Part I - Buckling of flat plates", Nat. Adv. Comm. Aeronaut. Tech. Note 3781, 1957.
2. Hutchinson, J.W., "Plastic buckling", in *Advances in Applied Mechanics*, Ed. C.S. Yih, Vol. 14, pp. 67-144, Academic Press, 1974.
3. Ore, E., "Elastoplastic buckling of thin walled structures under non-uniform loads", D.Sc. Research Thesis (in Hebrew), Technion, Haifa, 1989.
4. Zuckerman, Z., "Optimization of elastoplastic buckling", M.Sc. Research Thesis (in Hebrew), Technion, Haifa, 1992.
5. Durban, D., "Plastic buckling of rectangular plates under biaxial loading", in *Buckling of Structures - Theory and Experiment*, Eds. Elishakoff et al., pp. 183-194, Elsevier, 1988.
6. Ore, E. and Durban, D., "Elastoplastic buckling of annular plates in pure shear", *J. Appl. Mech.*, **56**, pp. 644-651, 1989.
7. Ore, E. and Durban, D., "Elastoplastic buckling of axially compressed circular cylindrical shells", *Int. J. Mech. Sci.*, **34**, pp. 727-742, 1992.
8. Dean, W.R., "The elastic stability of an annular plate", *Proc. Roy. Soc. Lond.*, **A106**, pp. 268-284, 1924.
9. Durban, D. and Stavsky, Y., "Elastic buckling of polar orthotropic annular plates in shear", *Int. J. Solids Structures*, **18**, pp. 51-58, 1982.
10. Bauer, M., "Faltenbildung beim ebenen torsionsversuch", Ingenieur-Archiv, **57**, pp. 39-50, 1987.
11. Bauer, M., Doctoral Thesis, Stuttgart University, 1988.
12. Southwell, R.V. and Skan, S.W., "On the stability under shearing forces of a flat elastic strip", *Proc. Roy. Soc. Lond.*, **A105**, pp. 587-607, 1924.
13. Stowell, E.Z., "Critical shear stress of an infinitely long plate in the plastic region", NACA TN No. 1681, 1948.
14. Gerard, G., "Critical shear stress of plates above the proportional limit", *J. Appl. Mech.*, **15**, pp. 7-12, 1948.
15. Durban, D. and Zuckerman, Z., "Elastoplastic buckling of rectangular plates in biaxial compression", in preparation.
16. Lee, L.H.N., "Inelastic buckling of initially imperfect cylindrical shells subjected to axial compression", *J. Aero. Sci.*, **29**, pp. 87-95, 1962.
17. Batterman, S.C., "Plastic buckling of axially compressed cylindrical shells", *AIAA J.*, **3**, pp. 316-325, 1965.
18. Sobel, L.H. and Newman, S.Z., "Plastic buckling of cylindrical shells under axial compression", *J. Pressure Vessel Technol.*, **102**, pp. 40-44, 1980.
19. Storakers, B., "On the buckling of axisymmetric thin elastic-plastic shells", *Int. J. Solids Structures*, **11**, pp. 1329-1346, 1975.
20. Tugcu, P., "Plate buckling in the plastic range", *Int. J. Mech. Sci.*, **33**, pp. 1-11, 1991.
21. Tugcu, P., "On plastic buckling predictions", *Int. J. Mech. Sci.*, **33**, pp. 529-539, 1991.
22. Li, S. and Reid, S.R., "The plastic buckling of axially compressed square tubes", *J. Appl. Mech.*, **59**, pp. 276-282, 1992.
23. Giezen, J.J., Babcock, C.D. and Singer, J., "Plastic buckling of cylindrical shells under biaxial loading", *Experimental Mechanics*, **31**, pp. 337-343, 1991.
24. Blachut, J., Galletly, G.D. and James, S., "On the plastic buckling paradox for cylindrical shells", *Proc. Inst. Mech. Engrs*, **210**, pp. 477-488, 1996.

ANALYSIS OF CURVED SANDWICH PANELS SUBJECTED TO COMBINED TEMPERATURE GRADIENT AND MECHANICAL LOADS

Ahmed K. Noor, James H. Starnes, Jr., and Jeanne M. Peters
NASA Langley Research Center
Hampton, Virginia

Abstract

The results of a detailed study of the nonlinear response of curved sandwich panels with composite face sheets and subjected to a temperature gradient through-the-thickness combined with mechanical loadings are presented. The analysis is based on a first-order shear-deformation Sanders-Budiansky type theory with the effects of large displacements, moderate rotations, transverse shear deformation and laminated anisotropic material behavior included. A mixed formulation is used with the fundamental unknowns consisting of the generalized displacements and the stress resultants of the panel. The nonlinear displacements, strain energy, principal strains, transverse shear stresses, transverse shear strain energy density, and their hierarchical sensitivity coefficients are evaluated. The hierarchical sensitivity coefficients measure the sensitivity of the nonlinear response to variations in the panel parameters, the effective properties of the face sheet layers and the core, and the micromechanical parameters. Numerical results are presented for cylindrical panels subjected to combined pressure loading, edge shortening or extension, edge shear and a temperature gradient through the thickness. The results show the effects of variations in the loading and the panel aspect ratio, on the nonlinear response and its sensitivity to changes in the various panel, effective layer and micromechanical parameters.

Nomenclature

$[\mathbf{A}],[\mathbf{B}],[\mathbf{D}],[\mathbf{A}_s]$	matrices of the extensional, bending-extensional coupling, bending and transverse shear stiffnesses of the panel, see Eqs. A.10 and A.11 - Appendix A
a_{ij}, c_{ik}	coefficients relating panel stiffnesses to effective properties of individual layers, and micromechanical (constituent) properties, respectively - see Eqs. 3 and 4
b_{jk}	coefficients relating effective layer properties to the micromechanical properties - see Eq. 4
E_L, E_T	effective elastic moduli of the individual face sheet layers in the direction of fibers and normal to it, respectively
E_c	elastic modulus of the core material
E_{1f}, E_{2f}	elastic moduli of the fibers in the longitudinal and transverse directions
E_{1c}, E_{2c}	effective elastic moduli of the core in the x_1 and x_2 directions
E_m	elastic modulus of the matrix
$[\mathbf{F}]$	linear flexibility matrix of the panel, see Eqs. B.2 - Appendix B
G_{LT}, G_{TT}	effective shear moduli of the individual face sheet layers in the plane of the fibers and normal to it, respectively
G_c	shear modulus of the core material
G_{12f}, G_m	shear moduli of the fibers and matrix
$G_{12c}, G_{13c}, G_{23c}$	effective shear moduli of the core in the x_1-x_2, x_1-x_3 and x_2-x_3 planes
$\{\mathbf{G(Z)}\}$	vector of nonlinear terms of the panel, see Eqs. 1
$\{\mathbf{H}\}$	vector of stress-resultant parameters
$h_\ell, h_{\ell-1}$	distances from the top and bottom surfaces of the ℓth layer to the middle surface
h	total thickness of the sandwich panel
$h^{(c)}$	core thickness
$[\mathbf{K}]$	global linear structural matrix, see Eqs. 1

L_1, L_2 side lengths of the panel in the x_1 and x_2 coordinate directions

M_1, M_2, M_{12}, M_{21} bending stress resultants

$\left.\begin{matrix}\{\mathbf{M}(\mathbf{X}, \overline{\mathbf{X}}_e)\}, \\ \{\mathbf{N}(\mathbf{H}, \mathbf{X}, \overline{\mathbf{X}}_e)\}\end{matrix}\right\}$ subvectors of nonlinear terms, Eqs. B.3 - Appendix B

N_t, N_s total axial force and total shear force on the curved edges of the panel

N_1, N_2, N_{12} in-plane (extensional) stress resultants

NL total number of layers in the panel

$\{\mathbf{N}\}, \{\mathbf{M}\}$ vectors of in-plane and bending stress resultants, see Eqs. A.1 - Appendix A

$\{\mathbf{N}_\mathrm{T}\}, \{\mathbf{M}_\mathrm{T}\}$ vectors of thermal forces and moments in the panel, see Eqs. A.1 - Appendix A

p intensity of uniform pressure loading

Q_1, Q_2 transverse shear stress resultants

$\{\mathbf{Q}\}$ vector of transverse shear stress resultants

$\{\mathbf{Q}^{(1)}\}, \{\mathbf{Q}^{(2)}\}, \{\mathbf{Q}^{(3)}\}$ vectors of normalized mechanical loads, mechanical strains and thermal strains, see Eqs. 1

$[\overline{\mathbf{Q}}]^{(\ell)}, [\overline{\mathbf{Q}}_s]^{(\ell)}$ matrices of the extensional and transverse shear stiffnesses of the ℓth layer of the panel (referred to the x_1, x_2, x_3 coordinate system)

q_e applied edge displacement

q_T thermal strain parameter associated with $\{\mathbf{Q}^{(3)}\}$

R radius of curvature of the middle surface of the panel

$[\mathbf{S}_1], [\mathbf{S}_2]$ linear strain-displacement matrices associated with the free nodal displacements, $\{\mathbf{X}\}$, and the constrained (prescribed nonzero) edge displacements, $q_e\{\overline{\mathbf{X}}_e\}$

T_t, T_b temperature changes at the top and bottom surfaces

U total strain energy of the panel

$\overline{U}$ strain energy density (energy per unit surface area) of the panel

$\overline{U}_{sh}$ transverse shear strain energy density (per unit surface area) of the panel

$\hat{U}_{sh}$ transverse shear strain energy density per unit volume

u_1, u_2, w displacement components in the coordinate directions, see Fig. 1

v_f fiber volume fraction

$\{\mathbf{X}\}$ vector of free (unknown) nodal displacements

$\{\overline{\mathbf{X}}_e\}$ normalized vector of constrained (prescribed nonzero) edge displacements

x_1, x_2, x_3 orthogonal coordinate system (x_3 is normal to the middle surface of the panel)

$\{\mathbf{Z}\}$ response vector of the panel

α_c coefficient of thermal expansion of the core material

α_{1f}, α_{2f} coefficients of thermal expansion of the fibers in the longitudinal and transverse directions

α_L, α_T effective coefficients of thermal expansion of the individual layers of the face sheets in the direction of the fibers and normal to it, respectively

α_m coefficient of thermal expansion of the matrix material

$\{\alpha\}^{(\ell)}$ vector of coefficients of thermal expansion of the ℓth layer of the panel (referred to the x_1, x_2, x_3 coordinate system)

$\{\gamma\}$ vector of transverse shear strain components of the panel, see Eqs. A.1 - Appendix A

$\{\varepsilon\}$	vector of extensional strain components of the panel, see Eqs. A.1 - Appendix A
$\{\varepsilon_T\}$	thermal strain subvector, see Eqs. B.5 - Appendix B
θ	fiber orientation angles of the individual face sheet layers
$\{\kappa\}$	vector of bending strain components of the panel, see Eqs. A.1 - Appendix A
λ	typical panel, effective layer or micromechanical parameter
$\ell_{1c}, \ell_{2c}, t_c, \theta_c$	characteristic lengths, thickness and angle of a typical hexagonal honeycomb cell
ν_{12f}, ν_{23f}	Poisson's ratios of the fibers
ν_{LT}	effective major Poisson's ratio of the individual face sheet layers
ν_m	Poisson's ratio of the matrix
ν_c	Poisson's ratio of the core material
$\nu_{12c}, \nu_{13c}, \nu_{23c}$	effective Poisson's ratios of the core
ϕ_1, ϕ_2	rotation components of the middle surface of the panel

Subscripts

$\bar{I}, \bar{J} = 1$ to the total number of degrees of freedom (free nodal displacements and stress-resultant parameters) in the model

$I' = 1$ to the total number of stress-resultant parameters in the model (components of the vector $\{\mathbf{H}\}$)

$I, J = 1$ to the total number of free nodal displacement components in the model (components of the vector $\{\mathbf{X}\}$)

L = direction of fibers

$\ell = 1$ to the total number of layers, NL

$i = 1$ to the total number of panel parameters

$j = 1$ to the total number of layer parameters

$k = 1$ to the total number of micromechanical parameters

f = fiber

m = matrix

T = transverse direction

T = thermal

$\beta = 1, 2$

Superscripts

ℓ	denotes layer
m	denotes micromechanical property
p	denotes panel property
t	denotes transposition

Introduction

In recent years considerable work has been devoted to the study of thermomechanical nonlinear and postbuckling responses of composite and sandwich plates and shells. Attempts have been made to identify the differences between the isothermal and thermal responses. Reviews of recent contributions are contained in four survey papers (Refs. 1-4) and four monographs (Refs. 5-8). Only a few of the reported studies considered the nonlinear response of curved panels subjected to temperature gradient through-the-thickness (see, for example, Refs. 9 and 10), and to the authors' knowledge, none considered sandwich panels with composite face sheets, or boundary conditions other than simple supports. Since curved sandwich panels have many applications in aircraft structures, including fuselage, wing and empennage components of high-speed aircraft, an understanding of their nonlinear response when subjected to a temperature gradient through-the-thickness combined with a mechanical loading is desirable. Moreover, a study of the sensitivity of the nonlinear response to variations in the material, lamination and geometric parameters of these panels is needed to provide an indication of the effects of changes in these parameters on the structural response.

The present study focuses on understanding the detailed nonlinear response characteristics of cylindrical sandwich panels with composite face sheets subjected to a temperature gradient through-the-thickness combined with mechanical loadings. Sensitivity coefficients are evaluated which measure the sensitivity of the various response quantities to variations in the panel stiffnesses, the effective material properties of the individual face sheet layers and core, and the micromechanical parameters.

The sandwich panels considered in the study consist of a number of perfectly bonded composite face sheet layers, and a honeycomb core. The layers of the top and bottom face sheets are

symmetrically distributed with respect to the middle surface. The individual layers of the face sheets and the core are assumed to be homogeneous and anisotropic. A plane of thermoelastic symmetry exists at each point of the panel, parallel to the middle surface. The loading is selected to simulate that of a typical fuselage panel of a high-speed aircraft.

Mathematical Formulation

Finite Element Equations Governing the Panel Response

The analytical formulation is based on a first-order shear-deformation Sanders-Budiansky type shell theory with the effects of large displacements, moderate rotations, average transverse shear deformation through-the-thickness, and laminated anisotropic material behavior included. For simplicity, a linear Duhamel-Neumann type constitutive model is used and the material properties are assumed to be independent of temperature. The constitutive relations for the panel are given in Appendix A. A total Lagrangian formulation is used and the panel deformations, at different values of the applied loading, are referred to the original undeformed configuration. The panel is discretized by using two-field mixed finite element models. The fundamental unknowns consist of the nodal displacements and the stress resultant parameters. The stress resultants are allowed to be discontinuous at interelement boundaries in the model. The sign convention for the generalized displacements and the stress resultants for the model are shown in Fig. 1. The external loading consists of a uniform pressure loading p; monotonically increasing edge displacement q_e (either normal or tangential to the edge); and a temperature gradient through-the-thickness q_T (linear through-the-thickness temperature variation, $q_T = (T_t - T_b)/h$, where T_t and T_b are the changes in the top and bottom surface temperatures, see Fig. 2).

The governing finite element equations describing the nonlinear and postbuckling responses of the sandwich panel can be written in the following compact form:

$$\{\mathbf{f}(\mathbf{Z})\} = [\mathbf{K}]\{\mathbf{Z}\} + \{\mathbf{G}(\mathbf{Z})\} - p\{\mathbf{Q}^{(1)}\} - q_e\{\mathbf{Q}^{(2)}\} - q_T\{\mathbf{Q}^{(3)}\} = 0 \tag{1}$$

where $[\mathbf{K}]$ is the global linear structural matrix which includes the flexibility and the linear strain-displacement matrices; $\{\mathbf{Z}\}$ is the response vector which includes both unknown (free) nodal displacements and stress-resultant parameters; $\{\mathbf{G}(\mathbf{Z})\}$ is the vector of nonlinear terms; p, q_e and q_T are the magnitudes of the internal pressure, applied edge displacement and temperature gradient through-the-thickness; $\{\mathbf{Q}^{(1)}\}, \{\mathbf{Q}^{(2)}\}, \{\mathbf{Q}^{(3)}\}$ are normalized vectors corresponding to unit values of p, q_e and q_T. The form of the arrays $[\mathbf{K}], \{\mathbf{G}(\mathbf{Z})\}, \{\mathbf{Q}^{(2)}\}$ and $\{\mathbf{Q}^{(3)}\}$ is given in Appendix B.

The standard approach for the solution of Eqs. 1 is to fix the value of two of the three parameters p, q_e and q_T and to vary the third, or to choose a functional relationship between the three parameters which is dependent on a single parameter q. In either case, the solution corresponding to the chosen combination of p, q_e and q_T (which is effectively dependent on a single parameter) constitutes a curve on the equilibrium surface of the panel.

Governing Equations for the Sensitivity Coefficients

The sensitivity coefficients are the derivatives of the various response quantities with respect to the different material, lamination and geometric parameters of the panel. They can be used to study the sensitivity of the nonlinear and postbuckling responses to variations in the different parameters. The governing equations for the sensitivity coefficients are obtained by differentiating Eqs. 1 with respect to a typical parameter λ. The resulting linear algebraic equations have the following form:

$$\left[[\mathbf{K}] + \left[\frac{\partial \mathbf{G}_{\bar{I}}}{\partial \mathbf{Z}_{\bar{J}}}\right]\right]\left\{\frac{\partial \mathbf{Z}}{\partial \lambda}\right\} = -\left[\frac{\partial \mathbf{K}}{\partial \lambda}\right]\{\mathbf{Z}\} + q_T\left\{\frac{\partial \mathbf{Q}^{(3)}}{\partial \lambda}\right\} \tag{2}$$

where the range of the indices $\bar{I}$ and $\bar{J}$ is 1 to the total number of degrees of freedom in the model; and $\{\mathbf{Q}^{(1)}\}$ and $\{\mathbf{Q}^{(2)}\}$ are assumed to be independent of λ. Note that the matrix on the left-hand-side of Eqs. 2 is identical to that used in the Newton-Raphson iterative process. Therefore, if

the Newton-Raphson technique is used in generating the nonlinear response, the evaluation of the sensitivity coefficients requires the generation of the right-hand side of Eqs. 2, and a forward-reduction/back-substitution operation only (no decomposition of the left-hand-side matrix is required).

Evaluation of the Transverse Shear Stresses

The transverse shear stresses are evaluated by using piecewise integration, in the thickness direction, of the three-dimensional equilibrium equations. For optimum accuracy, the transverse shear stresses are computed at the numerical quadrature points and then interpolated to the center of the element. The same procedure is used for evaluating the thickness distributions of the sensitivity coefficients of the transverse shear stresses.

Hierarchical Sensitivity Coefficients

The nonlinear and postbuckling response characteristics of sandwich panels are dependent on a hierarchy of interrelated parameters including panel, effective layer and micromechanical parameters. A study of the sensitivity of the response to variations in each of these parameters provides insight into the importance of the parameters and helps in the development of materials to meet certain performance requirements.

Three sets of sandwich parameters are considered herein; namely, panel, effective layer and micromechanical parameters. The panel parameters include the extensional, bending-extensional, bending and transverse shear stiffnesses (components of the matrices $[\mathbf{A}],[\mathbf{B}],[\mathbf{D}]$ and $[\mathbf{A}_s]$- see Eqs. A.10 and A.11, Appendix A); and the vectors of thermal effects $\{\mathbf{N}_T\}$ and $\{\mathbf{M}_T\}$ - see Eq. A.12, Appendix A. The layer parameters include the individual face sheet layer properties: elastic moduli E_L, E_T; shear moduli G_{LT}, G_{TT}; major Poisson's ratio ν_{LT}; coefficients of thermal expansion α_L, α_T; fiber-orientation angle $\theta^{(\ell)}$; layer thickness $h^{(\ell)}$, where subscripts L and T refer to the longitudinal (fiber) and transverse directions, respectively. The parameters also include the effective core properties: elastic moduli E_{1c}, E_{2c}; shear moduli $G_{12c}, G_{13c}, G_{23c}$; Poisson's ratios $\nu_{12c}, \nu_{13c}, \nu_{23c}$; coefficient of thermal expansion α_c and core thickness $h^{(c)}$. The micromechanical parameters refer to the fiber, matrix and core material moduli $E_{1f}, E_{2f}, E_m, E_c, G_{12f}, G_m, G_c$; Poisson's ratios $\nu_{12f}, \nu_{23f}, \nu_m, \nu_c$; coefficients of thermal expansion $\alpha_{1f}, \alpha_{2f}, \alpha_m, \alpha_c$; the fiber volume fraction ν_f of the face sheet layers; and the geometric parameters of the core $\ell_{1c}, \ell_{2c}, t_c, \theta$. The subscripts f, m and c denote the fiber, matrix and core property, respectively. The three sets of parameters will henceforth be referred to as $\lambda_i^{(p)}, \lambda_j^{(\ell)}, \lambda_k^{(m)}$ where superscripts p, ℓ and m refer to the panel, effective layer and micromechanical parameters, respectively; and the indices i, j and k range from 1 to the number of parameters in each category.

The computational procedure consists of evaluating the sensitivity coefficients with respect to each of the panel parameters $\left\{\frac{\partial \mathbf{Z}}{\partial \lambda_i^{(p)}}\right\}$ using Eqs. 2. The sensitivity coefficients with respect to the effective layer and micromechanical parameters are then obtained by forming the following linear combinations:

$$\left\{\frac{\partial \mathbf{Z}}{\partial \lambda_j^{(\ell)}}\right\} = \sum_i a_{ij} \left\{\frac{\partial \mathbf{Z}}{\partial \lambda_i^{(p)}}\right\} \tag{3}$$

and

$$\left\{\frac{\partial \mathbf{Z}}{\partial \lambda_k^{(m)}}\right\} = \sum_j b_{jk} \left\{\frac{\partial \mathbf{Z}}{\partial \lambda_j^{(\ell)}}\right\} = \sum_i c_{ik} \left\{\frac{\partial \mathbf{Z}}{\partial \lambda_i^{(p)}}\right\} \tag{4}$$

where

$$a_{ij} = \left\{\frac{\partial \lambda_i^{(p)}}{\partial \lambda_j^{(\ell)}}\right\} \tag{5}$$

$$b_{jk} = \left\{\frac{\partial \lambda_j^{(\ell)}}{\partial \lambda_k^{(m)}}\right\} \tag{6}$$

$$c_{ik} = \left\{\frac{\partial \lambda_i^{(p)}}{\partial \lambda_k^{(m)}}\right\} = \sum_j a_{ij} b_{jk} \tag{7}$$

The a_{ij} coefficients relate the panel stiffnesses to the effective properties of the individual layers and

are obtained from the lamination theory. The b_{jk} coefficients relate the effective layer properties to the constituent properties and are obtained from the micromechanical and core models; and the c_{ik} coefficients relate the panel stiffnesses to the micromechanical properties (see Fig. 2). If the panel stiffnesses are uniform, and the constitutive relations of the panel, layer, and the constituents are linear, then the a_{ij}, b_{jk}, c_{ik} coefficients are constants and need to be generated only once for each panel, even when the response is nonlinear.

Numerical Studies

Numerical studies were performed to determine the effects of variations in the loading, the panel aspect ratio, and the stacking sequence of the face sheet layers on the nonlinear response and the sensitivity coefficients of cylindrical sandwich panels. The panels considered have composite, eight-layer quasi-isotropic face sheets and a titanium honeycomb core with hexagonal cells. The material properties and geometric characteristics for the panels considered in the present study are given in Fig. 1. The material properties, the fiber orientation and the stacking sequences selected are those typical of sandwich panels considered for high-speed aircraft applications. The loading on the panels consisted of a sequence of mechanical and thermal loadings: uniform pressure loading p = 6.894×10^4 Pa., followed by monotonically increasing edge displacemen t q_e, and then a temperature gradient through-the-thickness q_T (linear through-the-thickness temperature variation, $q_T = (T_t - T_b)/h$, where T_t and T_b are the changes in the top and bottom surface temperatures). The value of T_b was zero and T_t was increased to 137.8°C. Three different types of edge displacements were applied, namely, edge shortening, edge extension and edge shear. The boundary conditions selected for the cases of edge shortening or extension and edge shear are shown in Fig. 2. In each loading case, the maximum value of q_e was selected in such a way that the maximum principal strains on the surfaces do not exceed 0.005. Three different values of the panel aspect ratio are considered; namely, $L_1/L_2 = 1, 3$ and 1/3. For each problem, hierarchical sensitivity coefficients are evaluated (see Fig. 3). The hierarchical sensitivity coefficients are the derivatives of the different response quantities with respect to panel stiffnesses, material parameters and fiber angles of the individual face sheet layers; effective and actual properties of the core; and micromechanical parameters of the face sheet layers.

Mixed finite element models were used for the discretization of each panel. Biquadratic shape functions were used for approximating each of the generalized displacements, and bilinear shape functions were used for approximating each of the stress resultants. The characteristics of the finite element model are given in Ref. 11. For each panel, the multiple parameter reduction methods described in Refs. 12-14 were used in generating the nonlinear and postbuckling responses, and evaluating the sensitivity coefficients. Typical results are presented in Figs. 4-8 for the response studies and in Figs. 9-17 for the sensitivity studies, and are described subsequently.

Response Studies

The responses of the sandwich panels considered are shown in Figs. 4-8. Plots of the total axial force $\overline{N}_t$ versus the applied end shortening or extension q_e, the transverse displacement w_c, and the total strain energy, U, are shown in Fig. 4 for panels with $L_1/L_2 = 1, 3$ and $1/3$. Similar plots of the total edge shear force $\overline{N}_s$ (at $x_1 = 0, L_1$) versus the applied edge shear q_e, w_c, and U are shown in Fig. 5. Normalized contour plots for the transverse displacement w, the total strain energy density $\overline{U}$ and the transverse shear strain energy density $\overline{U}_{sh}$ at the end of the loading stage $p + q_e + q_T$, are shown in Figs. 6 and 7 for the panels with $L_1/L_2 = 1, 3$ and $1/3$. The effect of loading and aspect ratio on the distribution of the transverse shear strain energy density $\hat{U}_{sh}$, at the location of maximum $\overline{U}_{sh}$, is shown in Fig. 8. The nonlinear response studies can be summarized as follows:

1) The stacking sequence of the face sheet layers (i.e., the relative locations of the +45° and -45° layers) has no noticeable effect on the global response characteristics of the panel.

2) For all the panels considered, the pressure loading p had the least effect on the global response characteristics, and the edge displacement q_e had the most effect on the global response. By contrast, the edge shear q_e had the least effect on the transverse shear strain energy density $\hat{U}_{sh}$, at the location of maximum $\overline{U}_{sh}$.

3) For all the panels considered, no mode change occurs from the first to the second and third

loading stages $(p, p+q_e, p+q_e+q_T)$. However, the distribution of the strain energy density $\overline{U}$ in the panel changes significantly from being nonuniform after application of p to nearly uniform after the application of $p+q_e$ and remains nearly uniform after the application of q_T.

4) For the case of edge shear, relaxing the constraint $\phi_1 = 0$ at $x_1 = 0$, L_1 has no noticeable effect on the in-plane shear stiffness or on the total strain energy of the panels. However, it results in increasing the center displacement w_c, particularly for panels with $L_1 / L_2 = \leq 1$.

5) For the case of edge shear q_e, the location of the maximum strain energy density $\overline{U}$ was different in each loading stage. By contrast, for the case of edge extension, the location of maximum $\overline{U}$ was the same after the application p as after $p+q_e$, but was different after $p+q_e+q_T$; and for the case of edge compression, only the panels with $L_1 / L_2 = 1$ had the location of maximum $\overline{U}$ after p the same as that after $p+q_e+q_T$ but different from the location of maximum $\overline{U}$ after $p+q_e$.

Sensitivity Studies

Sensitivity studies were conducted to identify which of the panel parameters, effective face sheet and core properties, and micromechanical parameters most affect the nonlinear response. For the case of edge shortening or extension, typical results showing the sensitivity of the total strain energy U with respect to the extensional, bending, transverse shear stiffnesses, and the thermal forces and moments in the panel are presented in Fig. 9. Sensitivity coefficients of U with respect to effective material properties of individual face sheet layers are shown in Fig. 10; with respect to effective and actual core parameters are presented in Fig. 11; and with respect to micromechanical parameters of the face sheet layers are shown in Fig. 12. Corresponding results for the case of edge shear are shown in Figs. 13-16. For all the loading cases and the panels considered, the stacking sequence of the face sheet layers has no noticeable effect on the sensitivity coefficients. Normalized contour plots for the largest sensitivity coefficients of the total strain energy density $\overline{U}$ with respect to panel, core and face sheet parameters at the end of each loading stage (p only, $p+q_e$ and $p+q_e+q_T$) are shown in Fig. 17. An examination of Figs. 9-17 reveals:

Case of Edge Shortening or Extension:

1) The total strain energy U is considerably more sensitive to variations in A_{11} than to variations in the other extensional stiffnesses. For the panels with $L_1 / L_2 = 1$, U is more sensitive to variations in D_{11} and D_{22} than to variations in the other bending stiffnesses. For the panels with $L_1 / L_2 = 3$, U is more sensitive to variations in D_{22} than to variations in the other bending stiffnesses, and for panels with $L_1 / L_2 = 1/3$, U is more sensitive to variations in D_{11}.

2) The sensitivity of U to variations in A_{11} increases with an increase in q_e. For the case of edge shortening, the addition of the temperature gradient does not change the sensitivity with respect to A_{11}, but increases the sensitivity with respect to D_{11} (and with respect to D_{22} for the panels with $L_1 / L_2 \geq 1$). For the case of edge extension, the addition of temperature gradient does not change the sensitivity with respect to A_{11}, but decreases the sensitivity with respect to D_{11}, (and with respect to D_{22} for the panels with $L_1 / L_2 \geq 1$).

3) The total strain energy is considerably more sensitive to variations in the following parameters than to each of the other parameters in the same category: a) the effective elastic modulus of the face sheets E_L; b) the fiber angles +45° and -45°; c) effective core properties $\nu_{12c}, E_{1c}, E_{2c}$; d) the four core parameters θ_c, ℓ_{1c}, E_c and t_c; and e) micromechanical parameters of the face sheets $\nu_f, E_{1f}, E_m, \nu_m$ and α_m. The sensitivity of U to variations in each of the parameters listed increases with the increase in q_e. For the edge shortening, the addition of q_T increases the sensitivity of U to variations in $\nu_{12c}, E_{1c}, E_{2c}, \theta_c, \ell_{1c}, E_c, t_c, E_m$, ν_m and α_m; slightly decreases the sensitivity to variations in E_L, fiber angles +45°, -45°, E_{1f} and ν_f. For the edge extension case, the addition of q_T has an opposite effect to that described for edge shortening.

4) The distribution of the sensitivity coefficients of the strain energy density $\overline{U}$ with respect to all the parameters considered becomes nearly uniform throughout the panel after the application of $p+q_e$. Exceptions to that are the sensitivity coefficients of $\overline{U}$ with respect to D_{11} and the fiber angles +45° and -45°.

Case of Edge Shear:

1) The total strain energy U is considerably more sensitive to variations in the following parameters than to each of the other parameters in the same category: a) extensional stiffness A_{66}, and bending stiffness D_{11} (for the panels with $L_1 / L_2 \leq 1$); b) the effective modulus of the face sheets E_L; c) fiber angles 0° and 90° (after the application of q_T); d) effective core parameters $\nu_{12c}, E_{1c}, E_{2c}$ (after the application of q_T); e) core parameters $t_c, \alpha_c, E_c, \ell_{1c}$ and θ_c; and f) micromechanical parameters of the face sheets ν_f, E_{1f}, E_m and α_m.

2) The sensitivity of U to variations in $A_{66}, E_L, t_c, \theta_c, E_c, \ell_{1c}, \nu_f, E_{1f}$ and E_m increases with the increase of q_e. The sensitivity of U to variations in the other parameters listed in (1) does not change with changes in q_e. The addition of q_T significantly changes the sensitivity of U to variations in D_{22}, fiber angles 0°, 90° and the parameters $\nu_{12c}, E_{1c}, E_{2c}, \ell_{1c}, t_c, E_c, \alpha_c, E_m$ and α_m.

3) The distribution of the sensitivity coefficients of the strain energy density $\overline{U}$ with respect to A_{66}, E_L and ν_f becomes nearly uniform after the application of $p+q_e$, and remains uniform after the addition of q_T.

Concluding Remarks

A study is made of the nonlinear response of curved sandwich panels with composite face sheets subjected to a temperature gradient through-the-thickness combined with mechanical loadings. The panels are composed of perfectly bonded layers (face sheet layers and core), and the core is replaced by an equivalent homogeneous anisotropic layer. The analysis is based on a first-order shear deformation Sanders-Budiansky type theory with the effects of large displacements, moderate rotations, average transverse shear deformation through the thickness, and laminated anisotropic material behavior included. A linear, Duhamel-Neumann type constitutive model is used and the material properties are assumed to be independent of temperature. The panels are discretized by using two-field mixed finite element models with the fundamental unknowns consisting of the nodal displacements and stress resultant parameters. The stress resultants are allowed to be discontinuous at interelement boundaries.

Both the nonlinear response of the panel as well as the hierarchical sensitivity coefficients are generated. The hierarchical sensitivity coefficients measure the sensitivity of the different response quantities to variations in three sets of interrelated parameters; namely, panel stiffnesses, effective properties of the face sheet layers and the core, and micromechanical parameters of the face sheet layers and the core. An efficient multiple-parameter reduction method is used for generating the nonlinear response and evaluating the sensitivity coefficients.

The computational procedure for evaluating the hierarchical sensitivity coefficients consists of evaluating the sensitivity coefficients with respect to each of the panel stiffnesses, and then generating the sensitivity coefficients with respect to the effective layer and micromechanical parameters as linear combinations of the sensitivity coefficients with respect to the panel parameters. Hierarchical sensitivity coefficients can be used to assess the effects of variations in the panel, face sheet layers, core and micromechanical parameters on the nonlinear response. They can also help relate structural design and material development.

Numerical studies are presented which show the effects of variations in the loading, the panel aspect ratio, and in the stacking sequence of the face sheet layers on the nonlinear response and the sensitivity coefficients of cylindrical sandwich panels with eight-layer quasi-isotropic face sheets and titanium honeycomb core with hexagonal cells. The loading on the panels consisted of a sequence of mechanical and thermal loadings: uniform pressure loading, monotonically increasing edge displacement, and then a temperature gradient through the thickness. Three types of edge displacements were considered; namely, edge shortening, edge extension, and edge shear. In all cases considered, the stacking sequence of the face sheet layers did not have a noticeable effect on either the nonlinear response or the sensitivity coefficients; and the edge displacement had the most pronounced effect on the response.

Acknowledgments

This work was partially supported by NASA Grant No. NAG-1-1162 and AFOSR Grant No. F49620-96-1-0462. The numerical studies were performed on the CRAY C-90 computer at NASA Ames Research Center. The authors acknowledge the assistance of Thea Ganoe of the University of

Virginia in preparing the final manuscript and improving the figures.

References

1. Noor, A. K. and Burton, W. S., "Computational Models for High-Temperature Multilayered Composite Plates and Shells," *Applied Mechanics Reviews*, ASME, Vol. 45, No. 10, Oct. 1992, pp. 419-446.
2. Noor, A. K. and Peters, J. M., "Finite Element Buckling and Postbuckling Solutions for Multilayered Composite Panels," *Finite Elements in Analysis and Design*, Vol. 15, 1994, pp. 343-367.
3. Bert, C. W., "Shear Deformation and Sandwich Configuration, " in *Buckling and Postbuckling of Composite Plates*, Turvey, G. J. and Marshall, I. H. (eds.), Chapman and Hall, London, 1995, pp. 157-189.
4. Noor, A. K., Burton, W. S. and Bert, C., "Computational Models for Sandwich Panels and Shells," *Applied Mechanics Reviews*, ASME, Vol. 49, No. 3, March 1996, pp. 155-199.
5. Hoff, N. J., *Monocoque, Sandwich, and Composite Aerospace Structures*, Technomic, Lancaster, PA, 1986.
6. Noor, A. K., "Buckling and Postbuckling of Composite Structures," *Proceedings of the Symposium on Buckling and Postbuckling of Composite Structures*, ASME International Mechanical Engineering Congress and Exposition, Chicago, IL, Nov. 6-11, 1994, AD Vol. 41/PVP Vol. 293, 1994.
7. Zenkert, D., *An Introduction to Sandwich Construction*, Chameleon Press, London, 1995.
8. Turvey, G. J. and Marshall, I. H. (eds.), *Buckling and Postbuckling of Composite Plates*, Chapman and Hall, London, 1995.
9. Librescu, L. and Souza, M. A., "Postbuckling of Geometrically Imperfect Shear-Deformable Flat Panels Under Combined Thermal and Compressive Edge Loadings," *Journal of Applied Mechanics*, Vol. 60, June 1993, pp. 526-533.
10. Librescu, L., Lin, W., Nemeth, M. P. and Starnes, J. H., "Thermomechanical Postbuckling of Geometrically Imperfect Flat and Curved Panels Taking into Account Tangential Edge Constraints," *Journal of Thermal Stresses*, Vol. 18, 1995, pp. 465-482.
11. Noor, A. K. and Andersen, C. M., "Mixed Models and Reduced/Selective Integration Displacement Models for Nonlinear Shell Analysis," *International Journal for Numerical Methods in Engineering*, Vol. 18, 1982, pp. 1429-1454.
12. Noor, A. K. and Peters, J. M., "Multiple-Parameter Reduced Basis Technique for Bifurcation and Postbuckling Analyses of Composite Plates," *International Journal for Numerical Methods in Engineering*, Vol. 19, 1983, pp. 1783-1803.
13. Noor, A. K. and Peters, J. M., "Recent Advances in Reduction Methods for Instability Analysis of Structures," *Computers and Structures*, Vol. 16, No. 1-4, January 1983, pp. 67-80.
14. Noor, A. K. and Peters, J. M., "Reduced Basis Technique for Calculating Sensitivity Coefficients of Nonlinear Structural Response," *AIAA Journal*, Vol. 30, No. 7, July 1992, pp. 1840-1847.
15. Aboudi, J., *Mechanics of Composite Materials: A Unified Micromechanical Approach*, Elsevier, Amsterdam, 1991.
16. Gibson, L. J. and Ashby, M. F., *Cellular Solids, Structures and Properties*, Pergamon Press, Oxford, 1988.
17. Burton, W. S. and Noor, A. K., "Assessment of Continuum Models for Sandwich Panel Honeycomb Cores," *Computer Methods in Applied Mechanics and Engineering* (to appear).
18. Jones, R. M., *Mechanics of Composite Materials*, McGraw Hill, New York, 1975.
19. Tsai, S. W. and Hahn, H. T., *Introduction to Composite Materials*, Technomic Publishing Co., Westport, CT, 1980.
20. Padovan, J., "Anisotropic Thermal Stress Analysis," in *Thermal Stresses I*, Hetnarski, R. B. (ed.), Elsevier Science, Amsterdam, 1986, pp. 143-262.
21. Bert, C. W., "Analysis of Plates," Vol. 7 - Structural Design and Analysis, Part I, Chamis, C. C. (ed.), *Composite Materials*, Academic, New York, 1975, pp. 149-206.
22. Noor, A. K., Starnes, Jr., J. H. and Peters, J. M., "Thermomechanical Buckling of Multilayered Composite Panels with Cutouts," *Journal of Composite Structures*, Vol. 23, 1993, pp. 233-251.
23. Noor, A. K. and Tenek, L. H., "Stiffness and Thermal Coefficients for Composite

Laminates," *Journal of Composite Structures*, Vol. 21, No. 1, 1992, pp. 57-66.

Appendix A - Thermoelastic Constitutive Relations for the Panel

The thermoelastic model used in the present study is based on the following assumptions:

1) The panels are composed of a number of perfectly bonded layers (face sheet layers and core).

2) A honeycomb core with hexagonal cells is used.

3) The Aboudi cell method is used to evaluate the effective properties of the face sheet layers (see Ref. 15) and an upper-bound energy approach is used to evaluate the effective core properties (see Refs. 16 and 17).

4) Every point of the panel is assumed to possess a single plane of thermoelastic symmetry parallel to the middle surface of the panel.

5) The material properties are independent of temperature.

6) The constitutive relations for the panel are described by the lamination theory, and can be written in the following compact form:

$$\begin{Bmatrix}\mathbf{N}\\ \mathbf{M}\\ \mathbf{Q}\end{Bmatrix}=\begin{bmatrix}[A] & [B] & \mathbf{0}\\ [B]^t & [\mathbf{D}] & \mathbf{0}\\ \mathbf{0} & \mathbf{0} & [A_s]\end{bmatrix}\begin{Bmatrix}\varepsilon\\ \kappa\\ \gamma\end{Bmatrix}-\begin{Bmatrix}\mathbf{N_T}\\ \mathbf{M_T}\\ \mathbf{0}\end{Bmatrix} \quad \text{(A.1)}$$

where $\{\mathbf{N}\},\{\mathbf{M}\},\{\mathbf{Q}\},\{\varepsilon\},\{\kappa\},\{\gamma\},\{\mathbf{N_T}\},\{\mathbf{M_T}\}$ are the vectors of extensional, bending and transverse shear stress resultants, strain components and thermal effects of the panel and are given by:

$$\{\mathbf{N}\}^t=[N_1 \quad N_2 \quad N_{12}] \quad \text{(A.2)}$$

$$\{\mathbf{M}\}^t=[M_1 \quad M_2 \quad M_{12}] \quad \text{(A.3)}$$

$$\{\mathbf{Q}\}^t=[Q_1 \quad Q_2] \quad \text{(A.4)}$$

$$\{\varepsilon\}^t=[\varepsilon_1 \quad \varepsilon_2 \quad 2\varepsilon_{12}] \quad \text{(A.5)}$$

$$\{\kappa\}^t=[\kappa_1 \quad \kappa_2 \quad 2\kappa_{12}] \quad \text{(A.6)}$$

$$\{\gamma\}^t=[2\varepsilon_{31} \quad 2\varepsilon_{32}] \quad \text{(A.7)}$$

$$\{\mathbf{N_T}\}^t=[N_{T1} \quad N_{T2} \quad N_{T12}] \quad \text{(A.8)}$$

and

$$\{\mathbf{M_T}\}^t=[M_{T1} \quad M_{T2} \quad M_{T12}] \quad \text{(A.9)}$$

The matrices $[\mathbf{A}],[\mathbf{B}],[\mathbf{D}]$ and $[\mathbf{A}_s]$ contain the extensional, coupling, bending and transverse shear stiffnesses of the panel which can be expressed in terms of the effective layer stiffnesses as follows:

$$[[\mathbf{A}][\mathbf{B}][\mathbf{D}]]=\sum_{\ell=1}^{NL}\int_{h_{\ell-1}}^{h_\ell}\left[\overline{\mathbf{Q}}^{(\ell)}\right]\left[[\mathbf{I}] \;\; x_3[\mathbf{I}] \;\; (x_3)^2[\mathbf{I}]\right]dx_3 \quad \text{(A.10)}$$

$$[\mathbf{A}_s]=\sum_{\ell=1}^{NL}\int_{h_{\ell-1}}^{h_\ell}\left[\overline{\mathbf{Q}}_s\right]^{(\ell)}dx_3 \quad \text{(A.11)}$$

where $\left[\overline{\mathbf{Q}}\right]^{(\ell)}$ and $\left[\overline{\mathbf{Q}}_s\right]^{(\ell)}$ are the extensional and transverse shear stiffnesses of the ℓth layer (referred to the x_1,x_2,x_3 coordinate system); $[\mathbf{I}]$ is the identity matrix; h_ℓ and $h_{\ell-1}$ are the distances from the top and bottom surfaces of the ℓth layer to the middle surface; and NL is the total number of layers in the laminate. The expressions for the different coefficients of the matrices $\left[\overline{\mathbf{Q}}\right]^{(\ell)}$ and $\left[\overline{\mathbf{Q}}_s\right]^{(\ell)}$ in terms of the material and geometric properties of the constituents of the composite face sheets (fiber and matrix) are given in Refs. 18 and 19 and for the core are given in Refs. 16 and 17.

The vectors of thermal effects, $\{\mathbf{N_T}\}$ and $\{\mathbf{M_T}\}$, are given by:

$$[\{\mathbf{N_T}\} \;\; \{\mathbf{M_T}\}]=\sum_{\ell=1}^{NL}\int_{h_{\ell-1}}^{h_\ell}\left[\overline{\mathbf{Q}}\right]^{(\ell)}\{\alpha\}^{(\ell)}[1 \quad x_3]Tdx_3 \quad \text{(A.11)}$$

where $\{\alpha\}^{(\ell)}$ is the vector of coefficients of thermal expansion coefficients of the ℓth layer (referred to the coordinates - x_1,x_2,x_3; see, for example, Refs. 20 and 21).

Appendix B - Form of the Arrays in the Governing Discrete Equations of the Panel

The governing discrete equations of the panel, Eqs. 1, consist of both the constitutive relations and the equilibrium equations.

The response vector $\{\mathbf{Z}\}$ can be partitioned into subvectors of stress-resultant parameters $\{\mathbf{H}\}$, and free (unconstrained) nodal displacements $\{\mathbf{X}\}$, as follows:

$$\{\mathbf{Z}\}=\begin{Bmatrix}\mathbf{H}\\ \mathbf{X}\end{Bmatrix} \quad \text{(B.1)}$$

The different arrays in Eqs. 1 and 2 can be partitioned as follows:

$$[\mathbf{K}]=\begin{bmatrix}\mathbf{F} & \mathbf{S}_1\\ \mathbf{S}_1^t & \mathbf{0}\end{bmatrix} \tag{B.2}$$

$$\{\mathbf{G}(\mathbf{Z})\}=\begin{Bmatrix}\mathbf{M}(\mathbf{X},\overline{\mathbf{X}}_e)\\ \mathbf{N}(\mathbf{H},\mathbf{X},\overline{\mathbf{X}}_e)\end{Bmatrix} \tag{B.3}$$

$$\{\mathbf{Q}^{(2)}\}=\begin{Bmatrix}-[\mathbf{S}_2]\{\overline{\mathbf{X}}_e\}\\ \mathbf{0}\end{Bmatrix} \tag{B.4}$$

$$\{\mathbf{Q}^{(3)}\}=\begin{Bmatrix}\varepsilon_T\\ \mathbf{0}\end{Bmatrix} \tag{B.5}$$

$$\left[\frac{\partial \mathbf{G}_{\bar{I}}}{\partial \mathbf{Z}_{\bar{J}}}\right]=\begin{bmatrix}\mathbf{0} & \dfrac{\partial \mathbf{M}_{I'}}{\partial \mathbf{X}_J}\\ \text{Sym} & \dfrac{\partial \mathbf{N}_I}{\partial \mathbf{X}_J}\end{bmatrix} \tag{B.6}$$

$$\left[\frac{\partial \mathbf{G}_{\bar{I}}}{\partial \mathbf{Z}_{\bar{J}}}\right]=\begin{bmatrix}-\left[\dfrac{\partial \mathbf{F}}{\partial \lambda}\right] & \mathbf{0}\\ \mathbf{0} & \mathbf{0}\end{bmatrix} \tag{B.7}$$

$$\left[\frac{\partial \mathbf{Q}^{(2)}}{\partial \lambda}\right]=\begin{Bmatrix}\dfrac{\partial \varepsilon_T}{\partial \lambda}\\ \mathbf{0}\end{Bmatrix} \tag{B.8}$$

where $[\mathbf{F}]$ is the linear flexibility matrix; $[\mathbf{S}_1]$ and $[\mathbf{S}_2]$ are the linear strain-displacement matrices associated with the free nodal displacements $\{\mathbf{X}\}$, and the constrained (prescribed nonzero) edge displacements $q_e\{\overline{\mathbf{X}}_e\}$; $\{\mathbf{M}(\mathbf{X},\overline{\mathbf{X}}_e)\}$ and $\{\mathbf{N}(\mathbf{H},\mathbf{X},\overline{\mathbf{X}}_e)\}$ are the subvectors of nonlinear terms; $\{\varepsilon_T\}$ is the subvector of normalized thermal strains; $\mathbf{0}$ is a null matrix or vector; and superscript t denotes transposition. The explicit form of $\{\varepsilon_T\}$ is given in Ref. 22.

For the purpose of obtaining analytic derivatives with respect to lamination parameters (e.g., fiber orientation angles of different layers), it is convenient to express $\dfrac{\partial[\mathbf{F}]}{\partial\lambda}$ in terms of $\dfrac{\partial[\mathbf{F}]^{-1}}{\partial\lambda}$ as follows:

$$\frac{\partial[\mathbf{F}]}{\partial\lambda}=-[\mathbf{F}]\frac{\partial[\mathbf{F}]^{-1}}{\partial\lambda}[\mathbf{F}] \tag{B.9}$$

The explicit forms of $\dfrac{\partial[\mathbf{F}]^{-1}}{\partial\lambda}$ and $\left\{\dfrac{\partial\varepsilon_T}{\partial\lambda}\right\}$ are given in Ref. 22.

Analytic expressions are given in Ref. 23 for the laminate stiffnesses $[\mathbf{A}],[\mathbf{B}],[\mathbf{D}]$ and $[\mathbf{A}_s]$; the vectors of thermal effects $\{\mathbf{N}_T\}$ and $\{\mathbf{M}_T\}$; and their derivatives with respect to each of the material properties of the individual layers and fiber orientation angles.

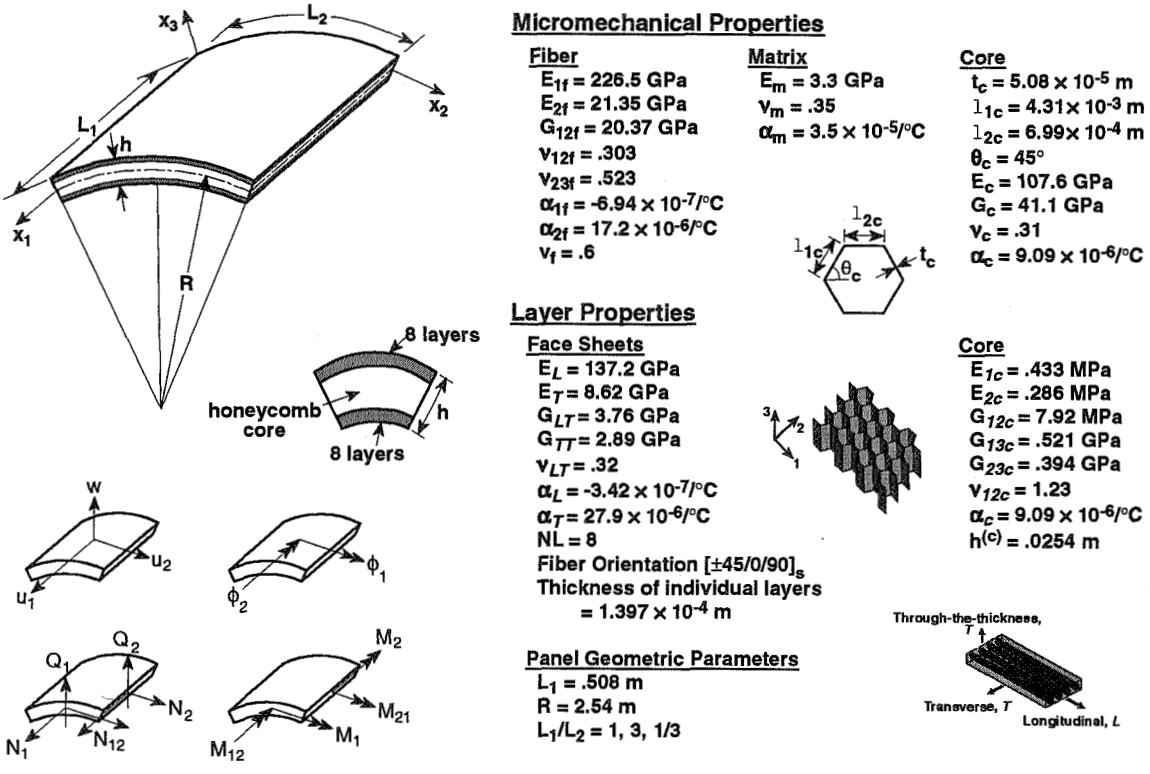

Figure 1. Panels considered in the present study and sign convention for generalized displacements and stress resultants.

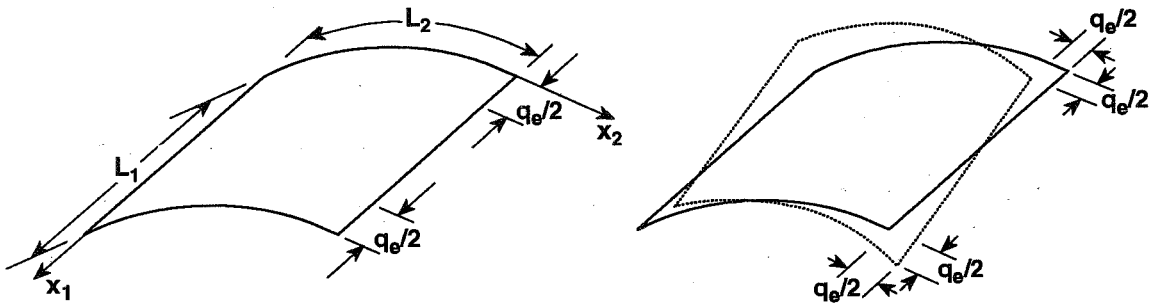

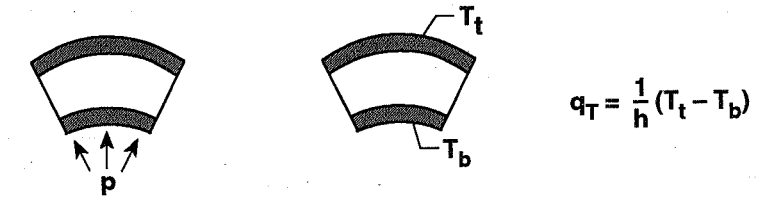

edge shortening:

At $x_1 = 0, L_1$
$u_1 = \pm\, q_e/2$ (shortening)
$= m\ q_e/2$ (extension)
$u_2 = w = \phi_1 = \phi_2 = 0$

At $x_2 = 0, L_2$
$u_2 = w = \phi_1 = \phi_2 = 0$

edge shear:

At $x_1 = 0, L_1$
$u_2 = m\ q_e/2$
$w = \phi_1 = \phi_2 = 0$

At $x_2 = 0, L_2$
$u_1 = m\ q_e/2$
$w = \phi_1 = 0$

Figure 2. Loadings and boundary conditions considered in the numerical studies.

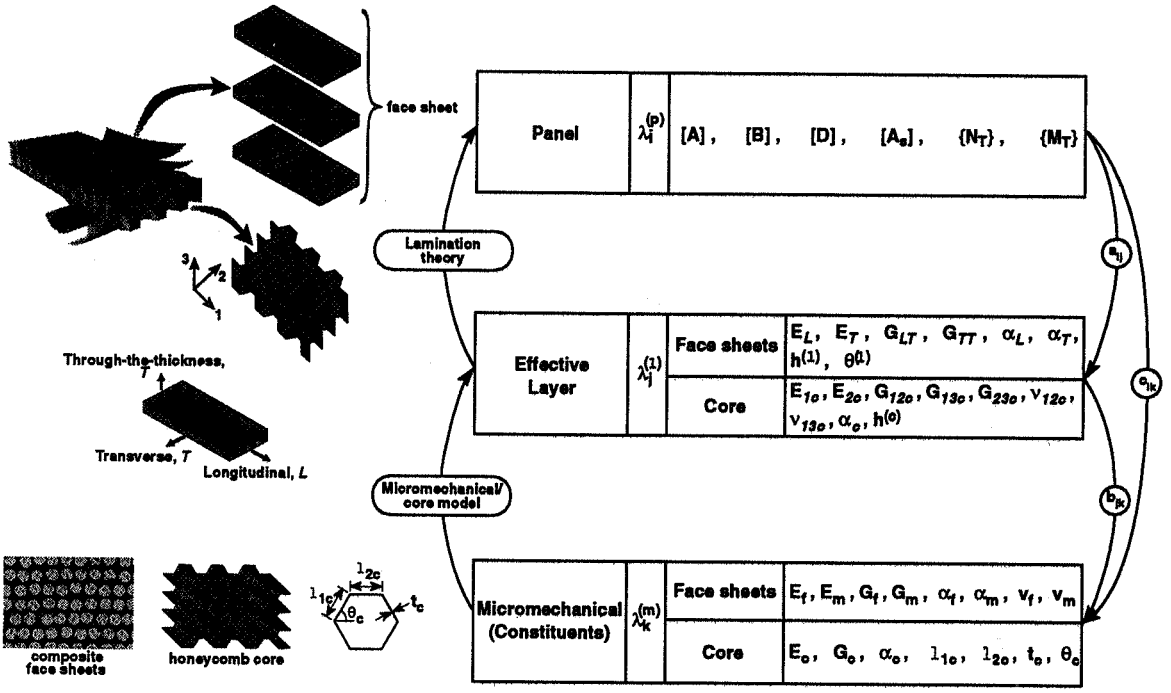

Figure 3. Hierarchical sensitivity coefficients for sandwich panels with composite face sheets.

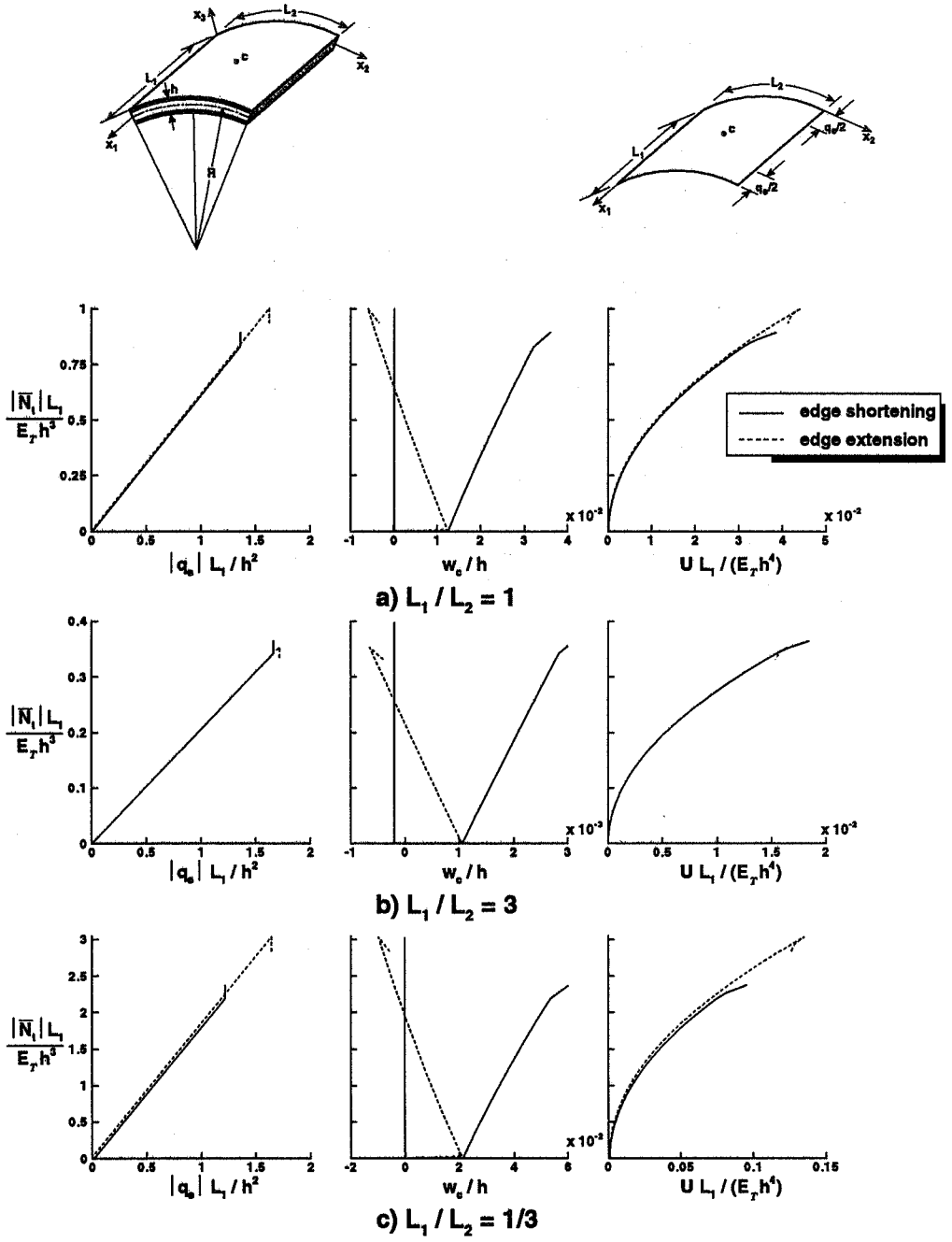

Figure 4. Effect of loading and aspect ratio on the nonlinear response of cylindrical sandwich panels with honeycomb core and composite eight-layer face sheets subjected to combined pressure loading, edge shortening or extension and temperature gradient through the thickness.

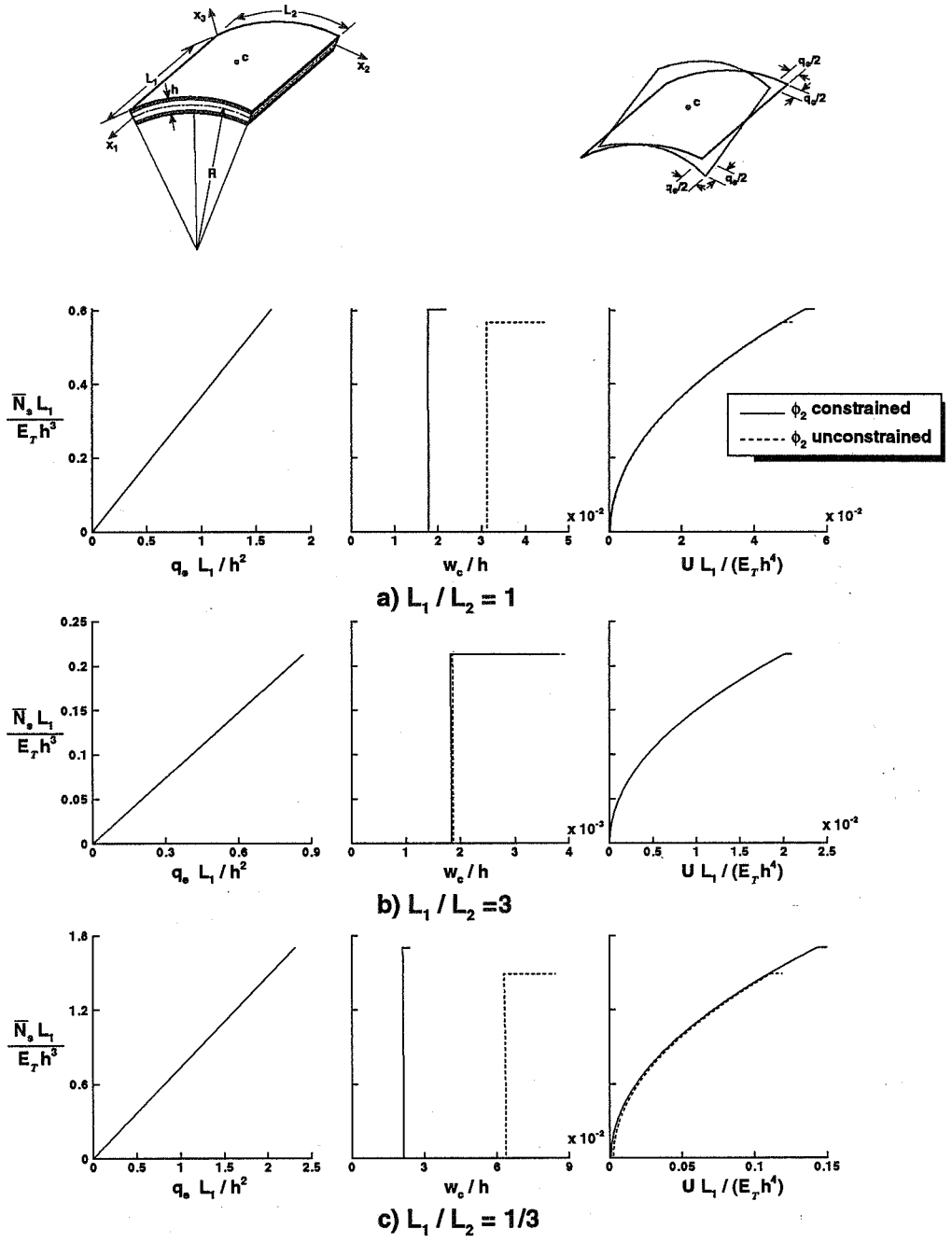

Figure 5. Effect of loading and aspect ratio on the nonlinear response of cylindrical sandwich panels, with honeycomb core and composite eight-layer face sheets, subjected to combined pressure loading, edge shear and temperature gradient through the thickness.

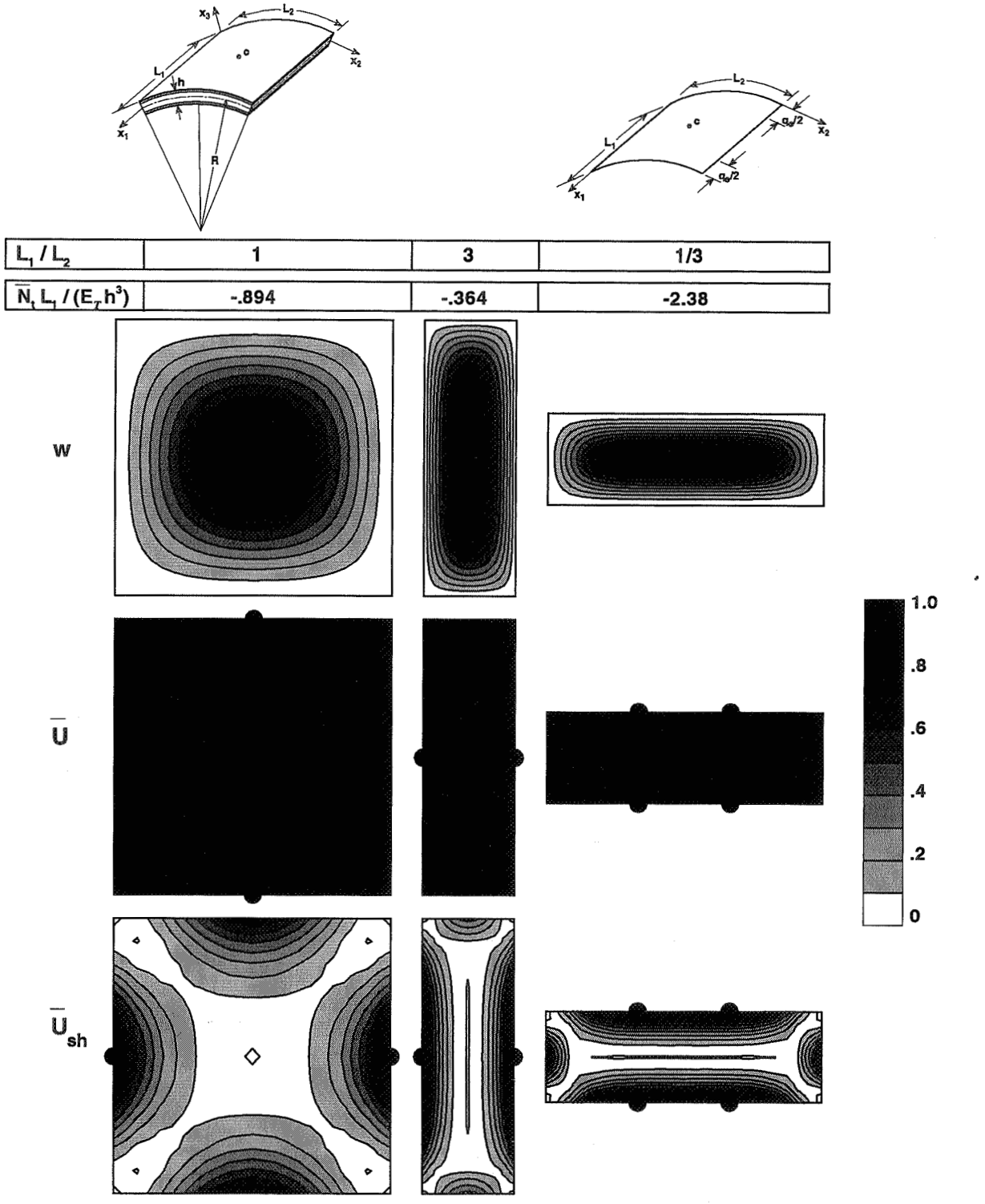

Figure 6. Normalized contour plots depicting the effect of aspect ratio on the transverse displacement w, the total strain energy density $\overline{U}$ and the transverse shear strain energy density $\overline{U}_{sh}$ for cylindrical panels, with honeycomb core and composite eight-layer face sheets, subjected to combined pressure loading, edge shortening and temperature gradient through the thickness. Location of maximum values identified by a small solid circle.

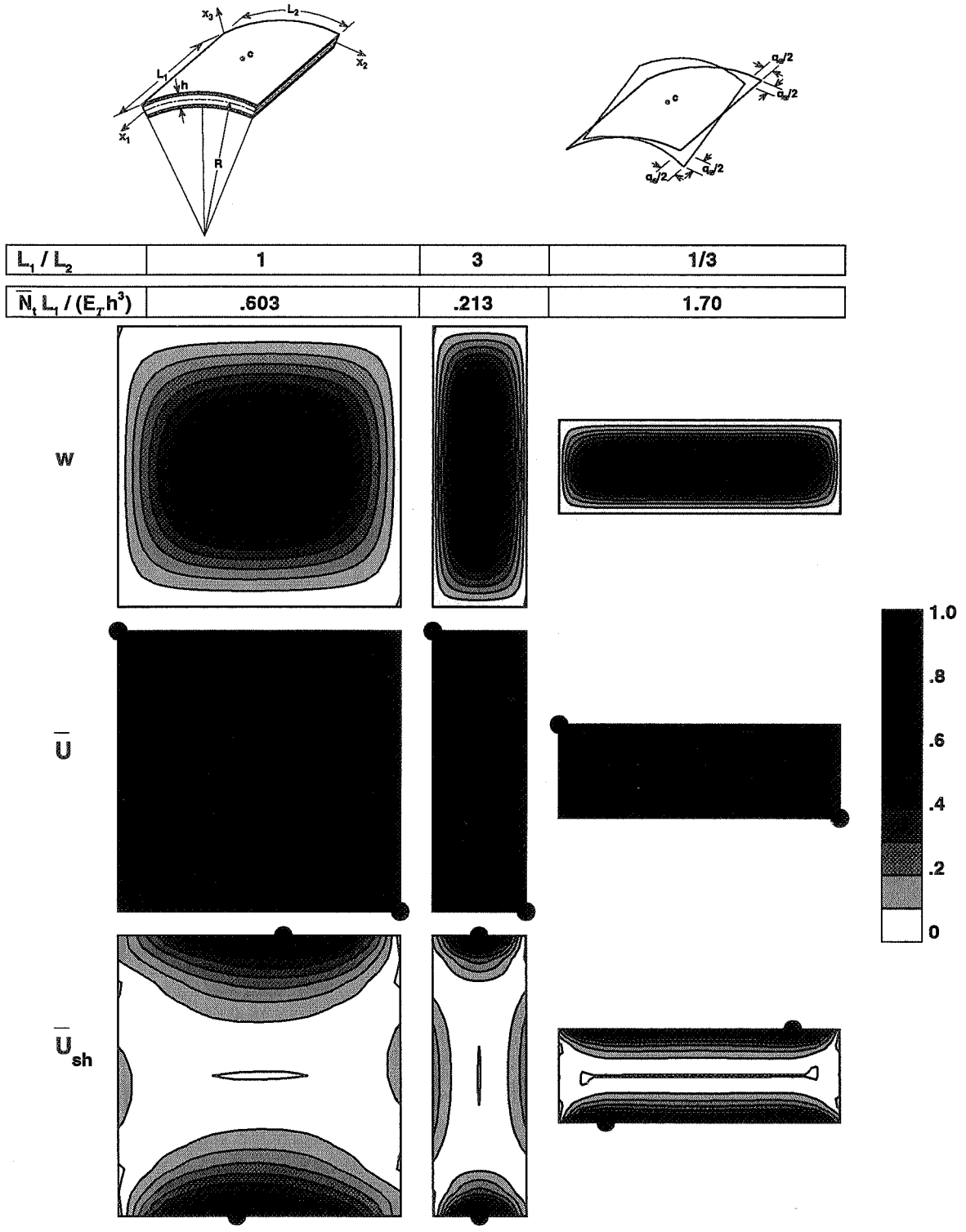

Figure 7. Normalized contour plots depicting the effect of aspect ratio on the transverse displacement w, the total strain energy density $\overline{U}$ and the transverse shear strain energy density $\overline{U}_{sh}$ for cylindrical panels, with honeycomb core and composite eight-layer face sheets, subjected to combined pressure loading, edge shear and temperature gradient through the thickness. Location of maximum values identified by a small solid circle.

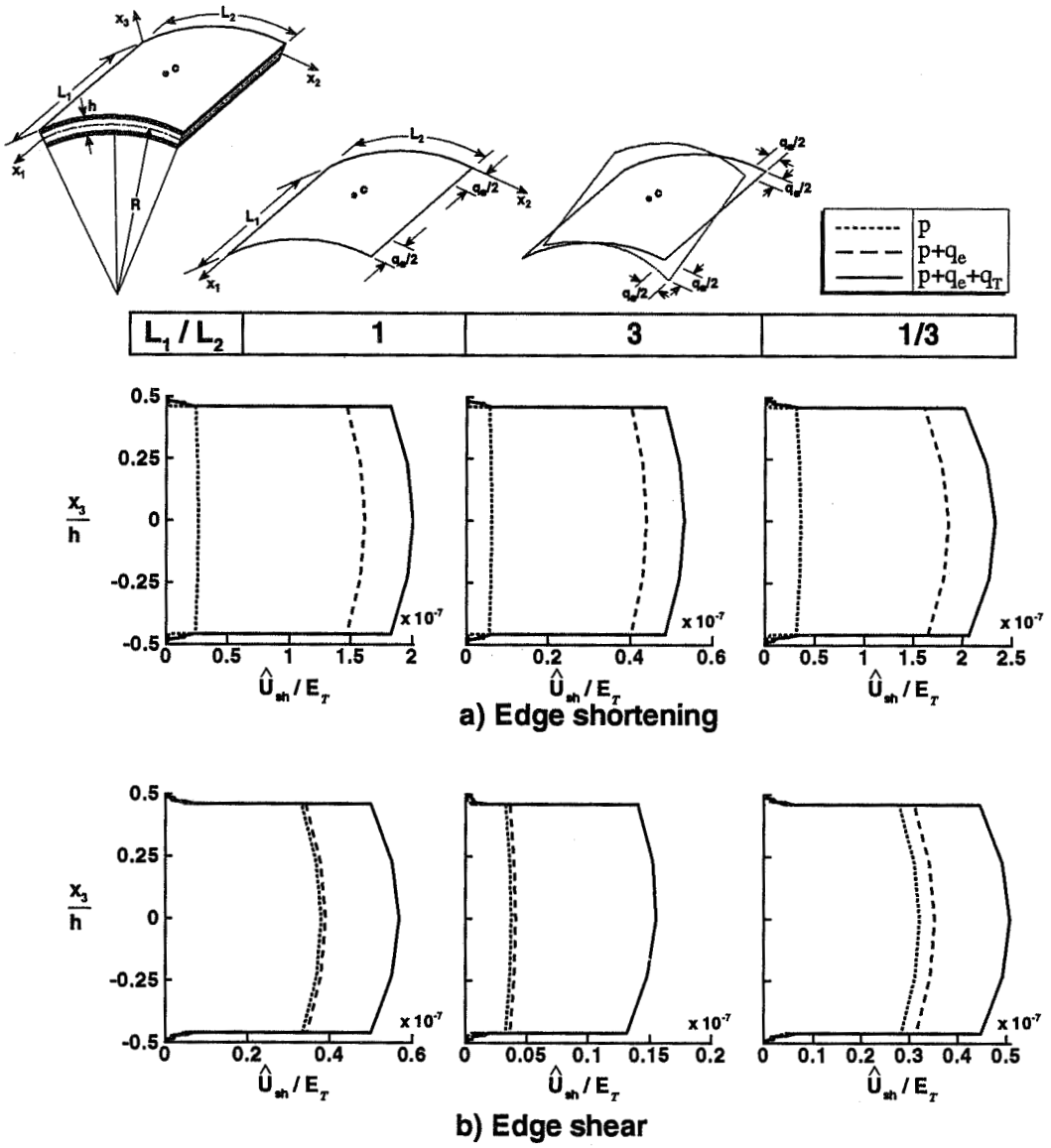

Figure 8. Effect of loading and aspect ratio on the distribution of transverse shear strain energy density $\hat{U}_{sh}$, through the thickness, at the point of maximum transverse shear strain energy density $\overline{U}_{sh}$ (see Fig. 6). Cylindrical sandwich panels, with honeycomb core and composite eight-layer face sheets, subjected to combined pressure loading, prescribed edge displacement and temperature gradient through the thickness.

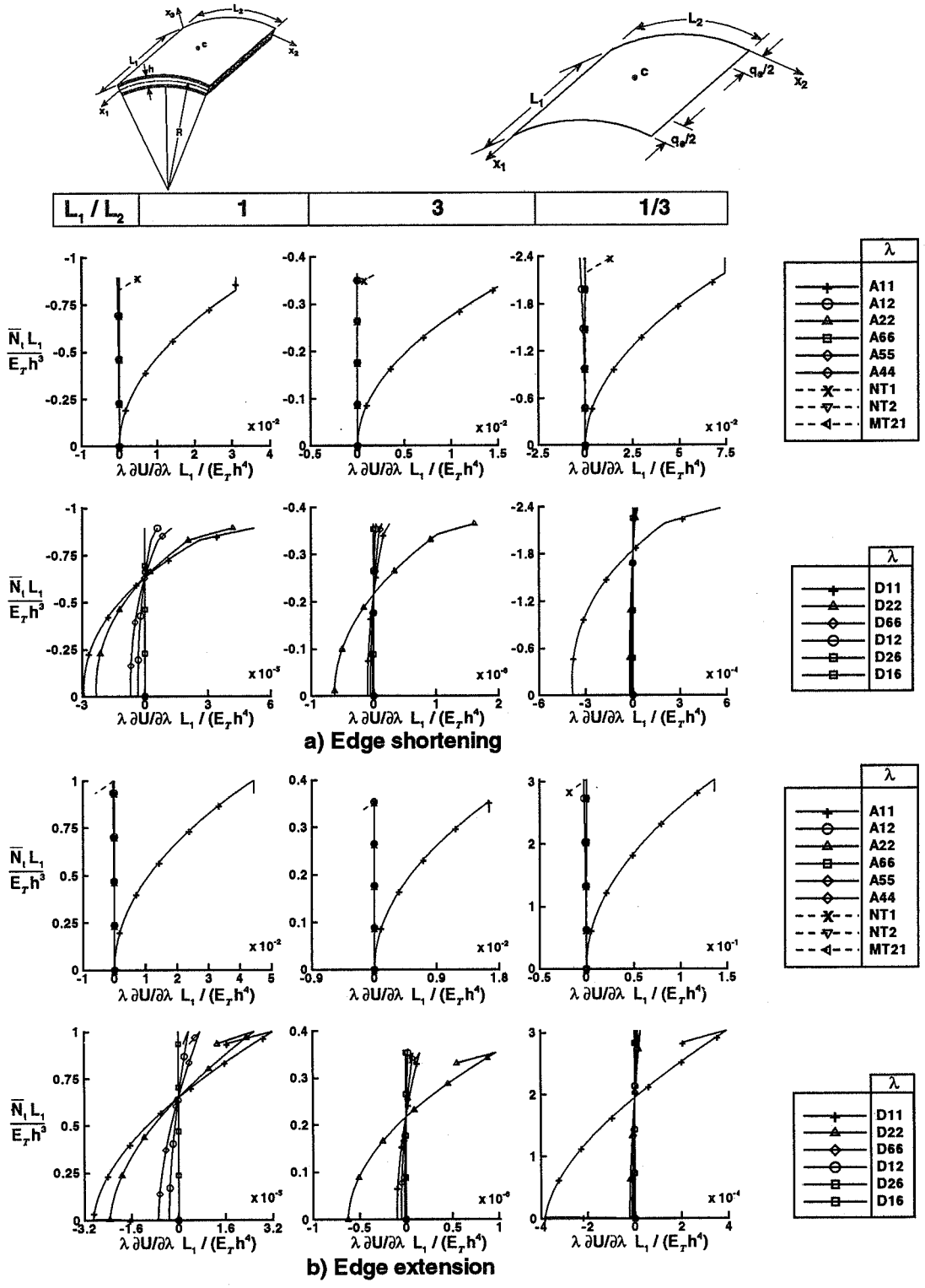

Figure 9. Effect of loading and aspect ratio on the normalized sensitivity coefficients of the total strain energy U with respect to panel stiffnesses. Cylindrical sandwich panels, with honeycomb core and composite eight-layer face sheets, subjected to combined pressure loading, edge shortening and temperature gradient through the thickness.

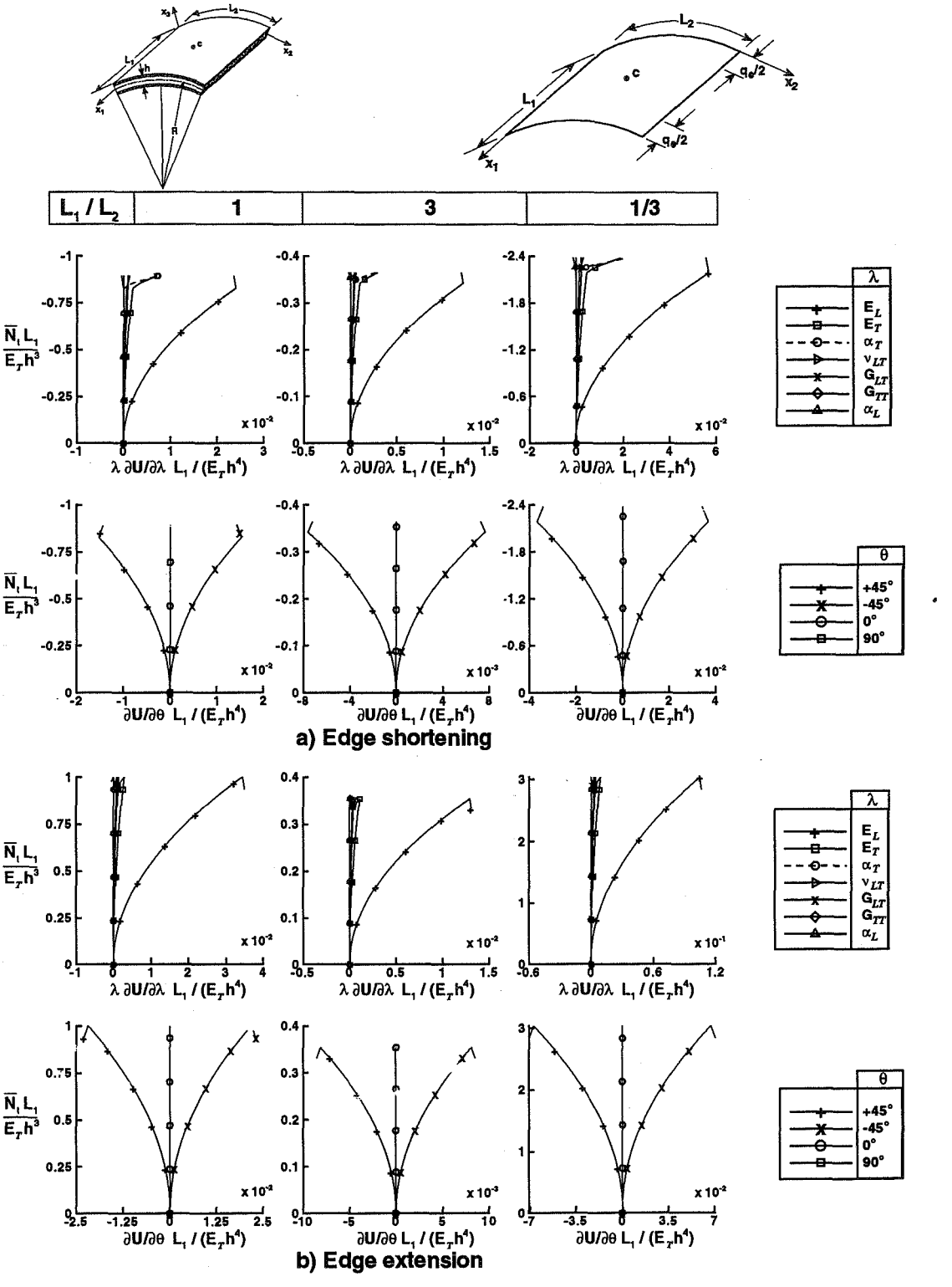

Figure 10. Effect of loading and aspect ratio on the normalized sensitivity coefficients of the total strain energy U with respect to effective face sheet layer properties. Cylindrical sandwich panels, with honeycomb core and composite eight-layer face sheets, subjected to combined pressure loading, edge shortening and temperature gradient through the thickness.

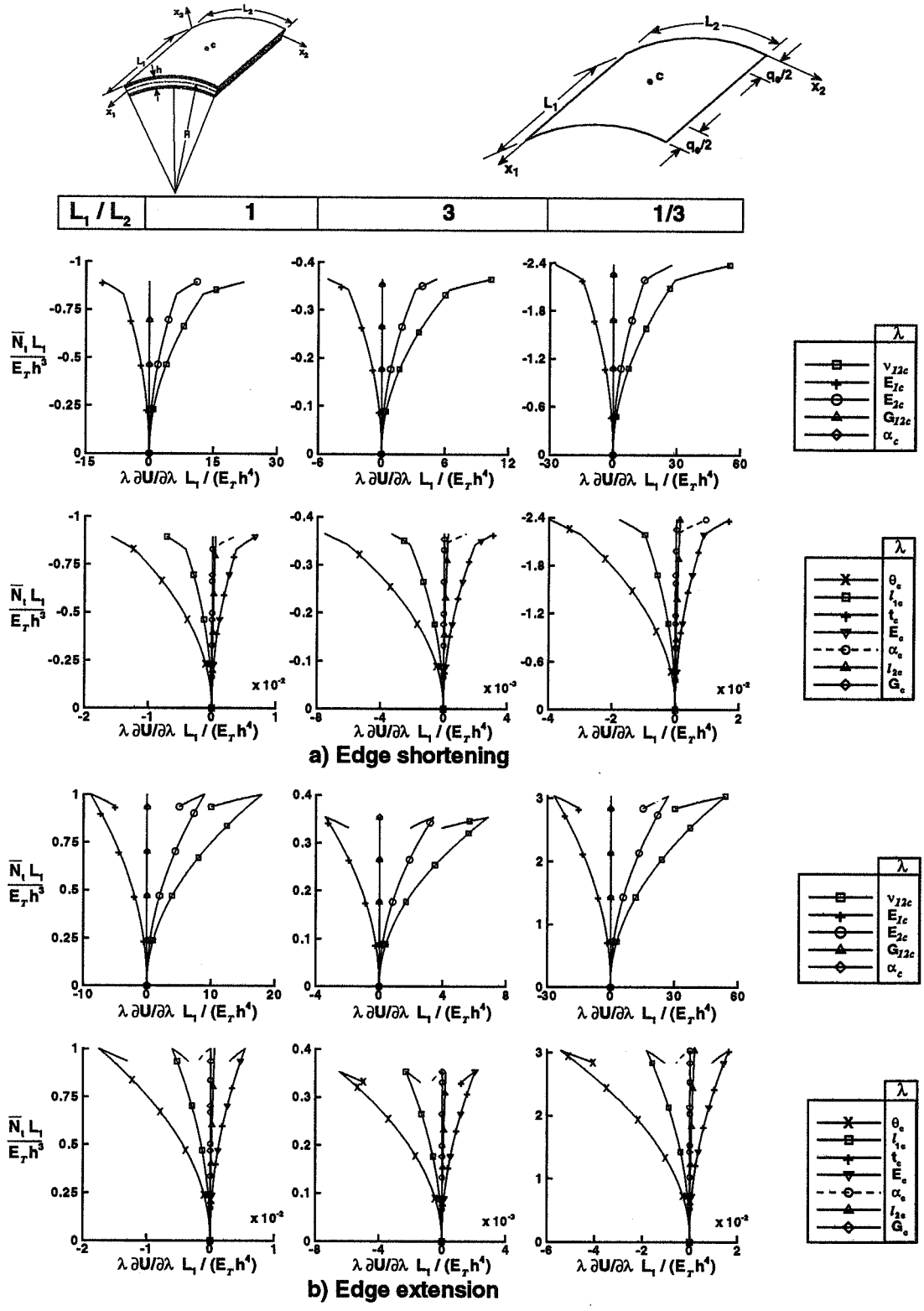

Figure 11. Effect of loading and aspect ratio on the normalized sensitivity coefficients of the total strain energy U with respect to core properties. Cylindrical sandwich panels, with honeycomb core and composite eight-layer face sheets, subjected to combined pressure loading, edge shortening and temperature gradient through the thickness.

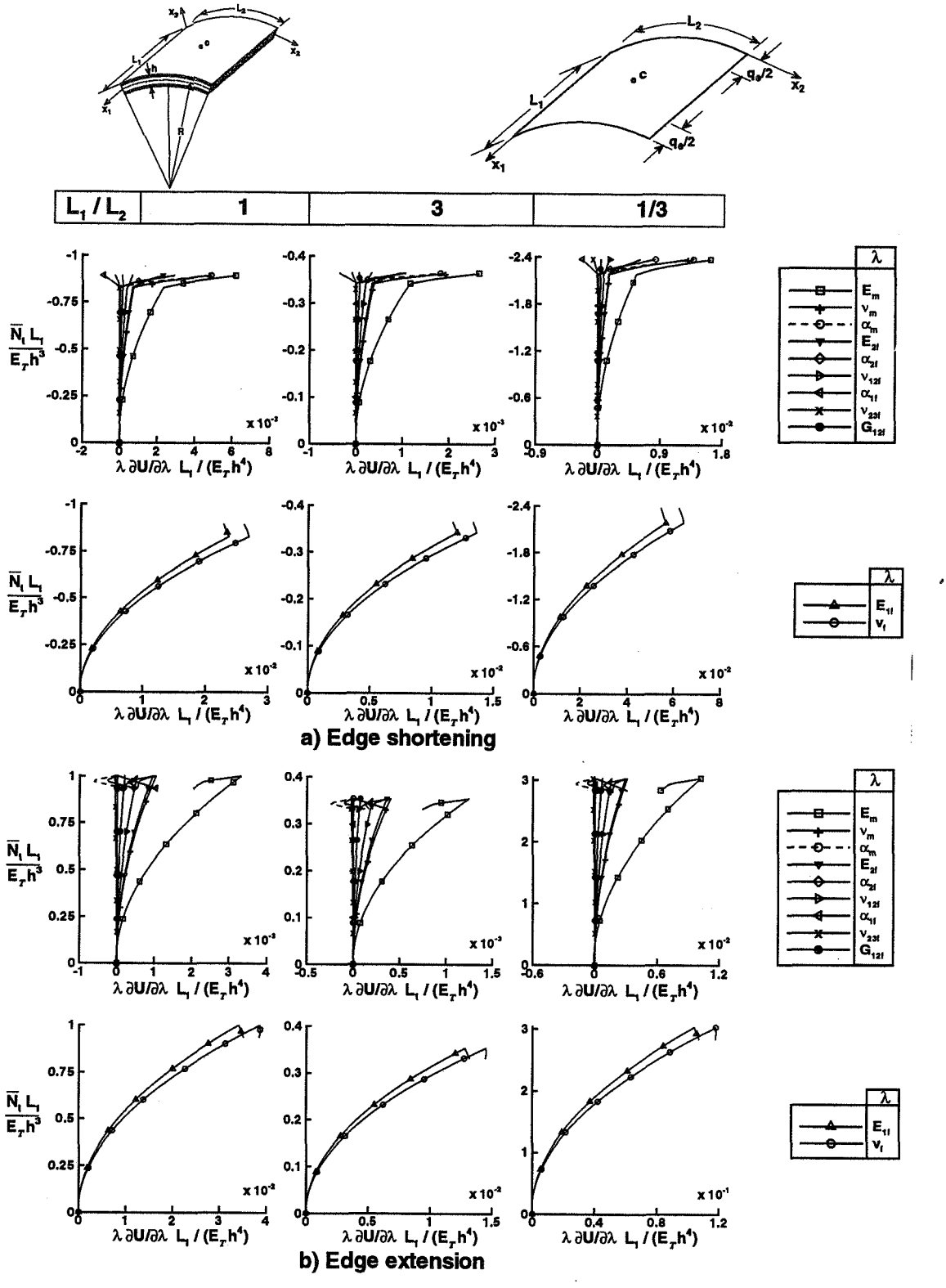

Figure 12. Effect of loading and aspect ratio on the normalized sensitivity coefficients of the total strain energy U with respect to micromechanical properties of the face sheet layers. Cylindrical sandwich panels, with honeycomb core and composite eight-layer face sheets, subjected to combined pressure loading, edge shortening and temperature gradient through the thickness.

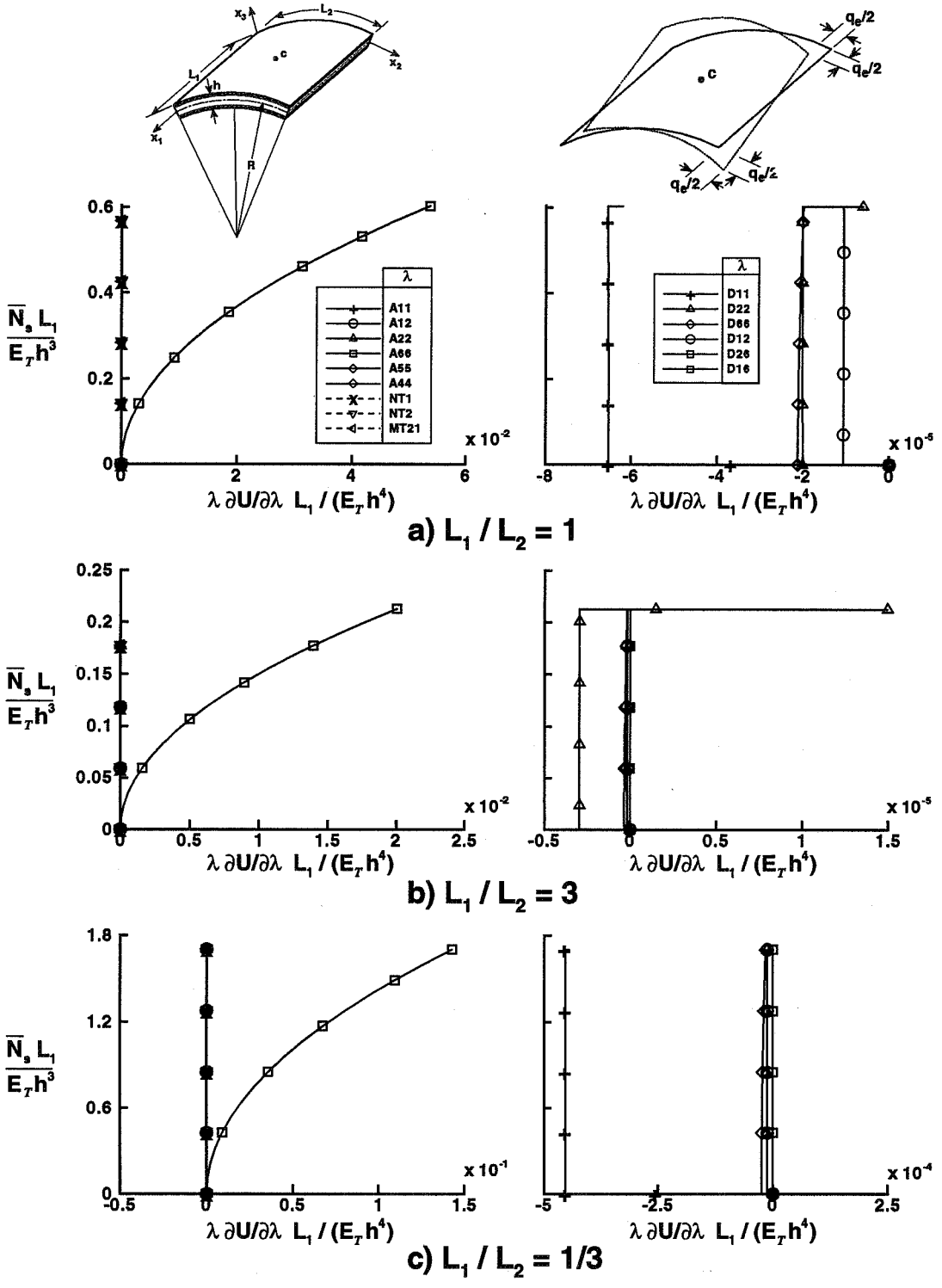

Figure 13. Effect of loading and aspect ratio on the normalized sensitivity coefficients of the total strain energy U with respect to panel stiffnesses. Cylindrical sandwich panels, with honeycomb core and composite eight-layer face sheets, subjected to combined pressure loading, edge shear and temperature gradient through the thickness.

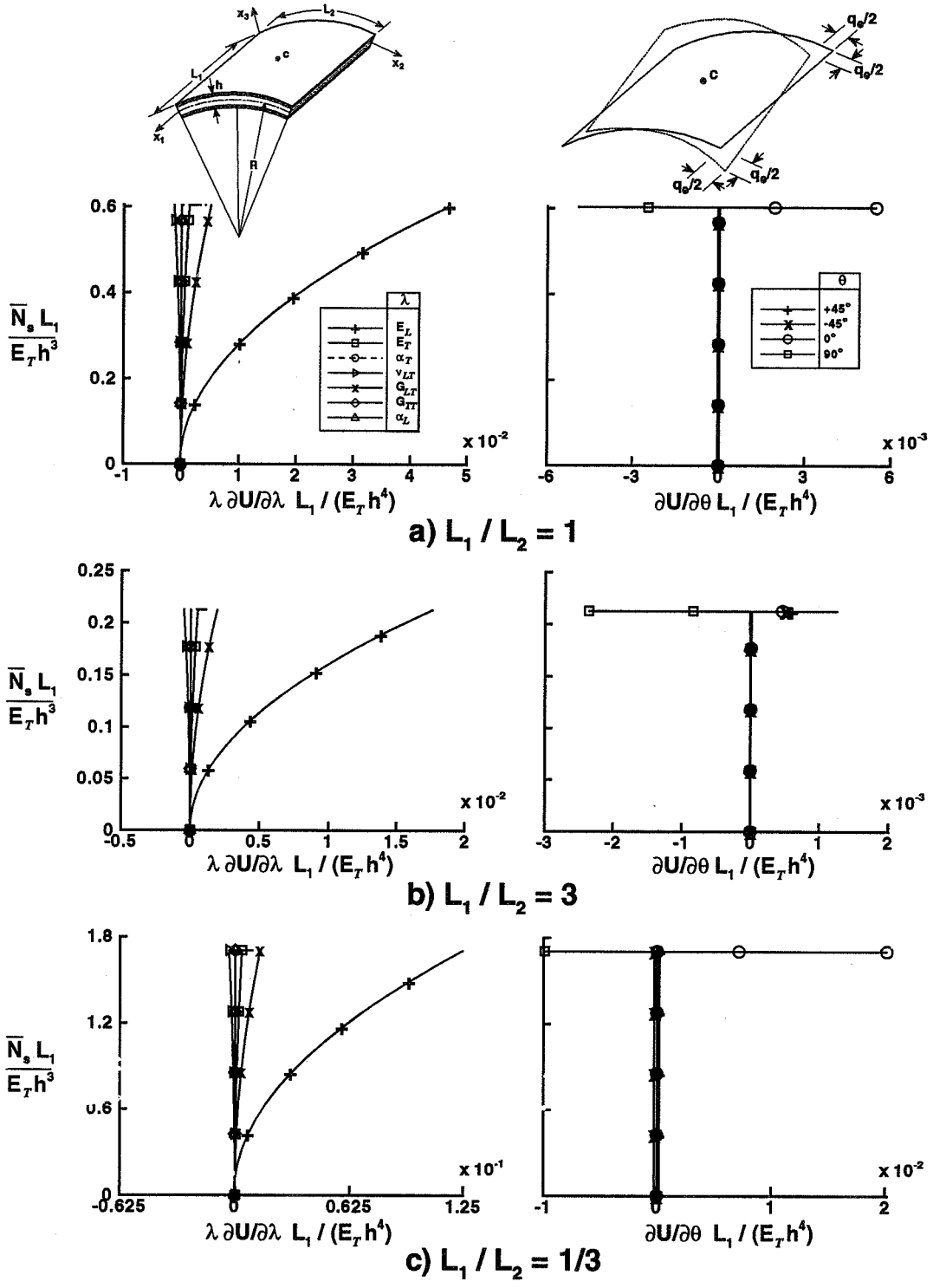

Figure 14. Effect of loading and aspect ratio on the normalized sensitivity coefficients of the total strain energy U with respect to effective face sheet layer properties. Cylindrical sandwich panels, with honeycomb core and composite eight-layer face sheets, subjected to combined pressure loading, edge shear and temperature gradient through the thickness.

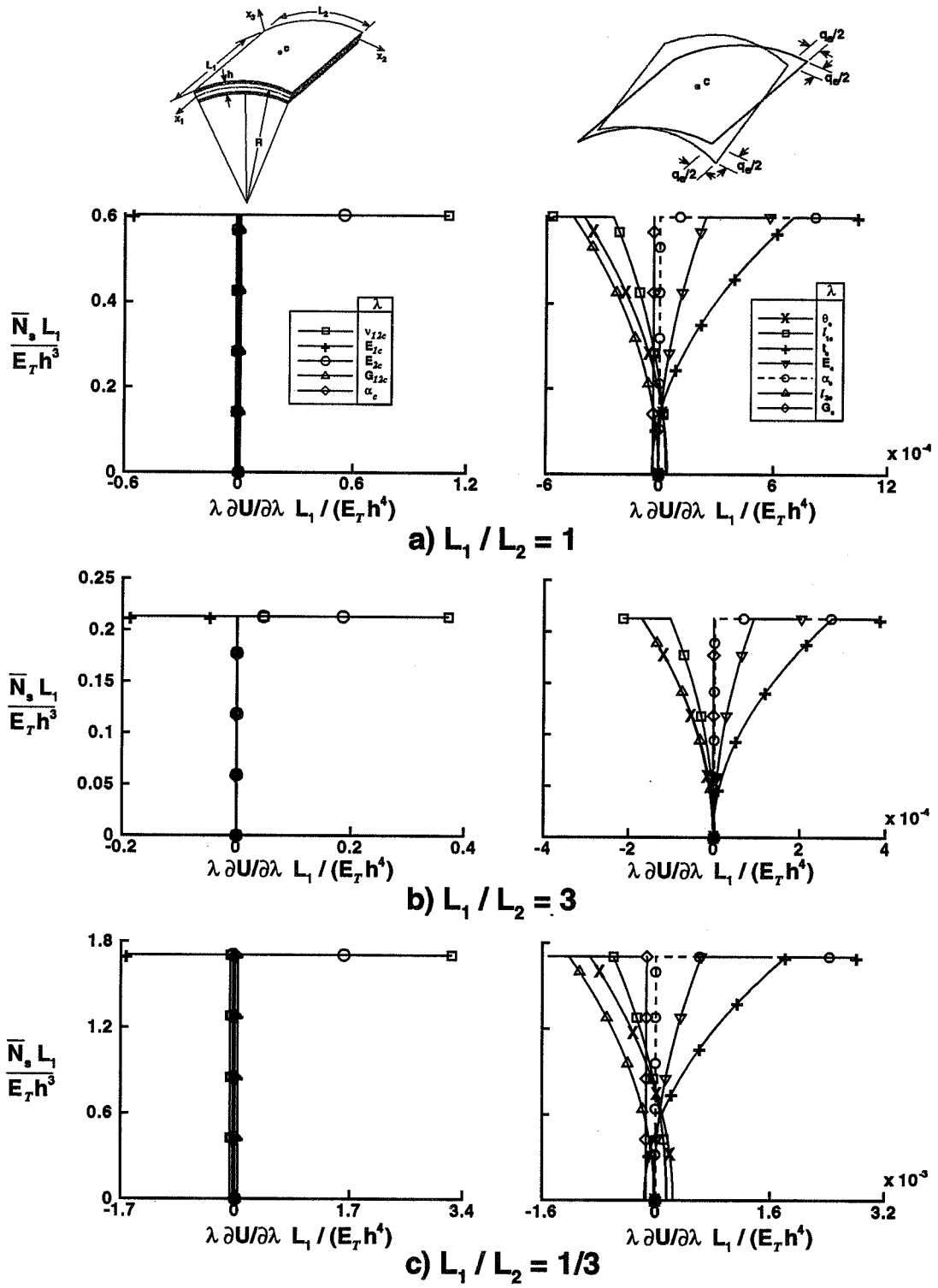

Figure 15. Effect of loading and aspect ratio on the normalized sensitivity coefficients of the total strain energy U with respect to core properties. Cylindrical sandwich panels, with honeycomb core and composite eight-layer face sheets, subjected to combined pressure loading, edge shear and temperature gradient through the thickness.

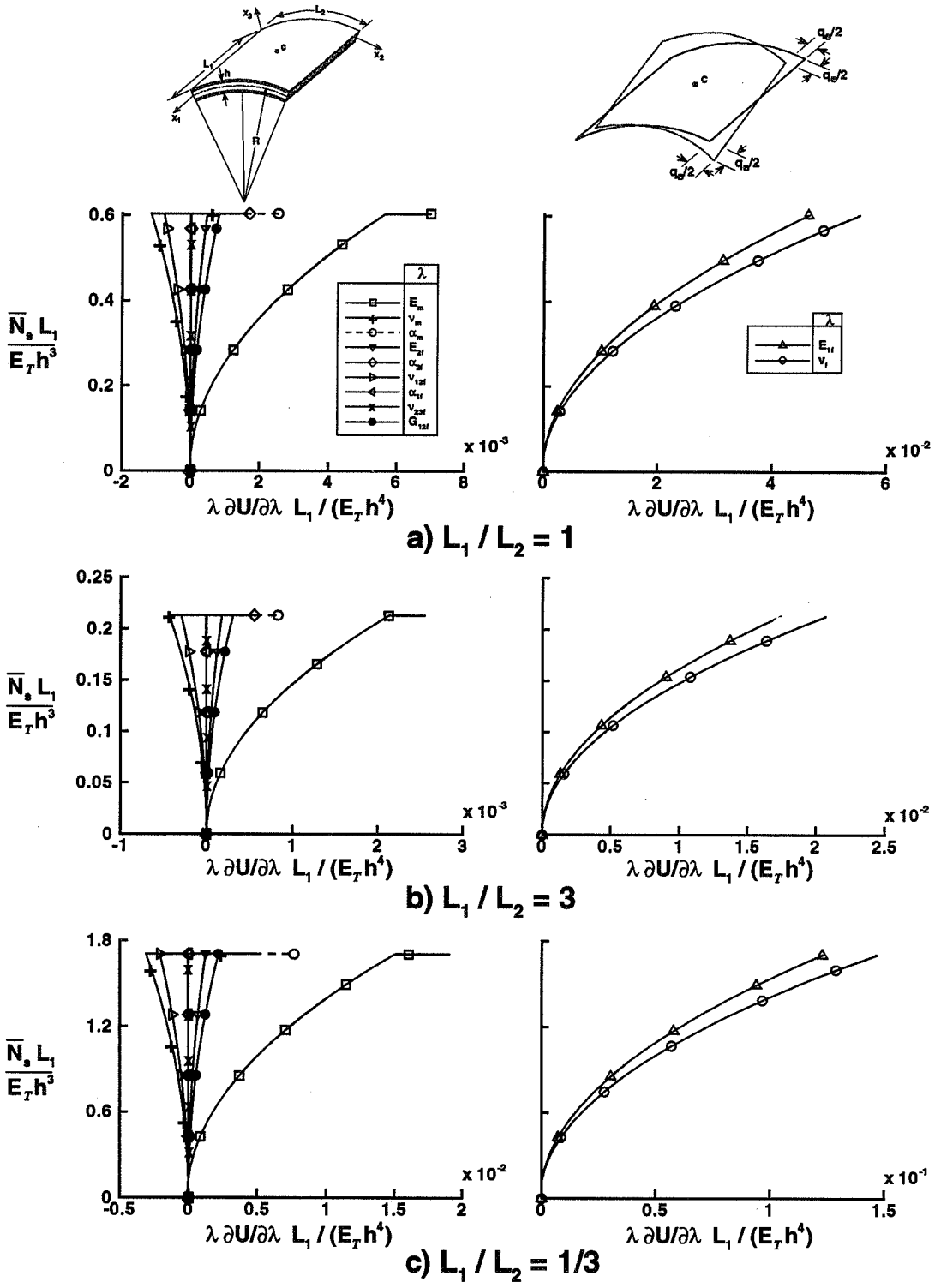

Figure 16. Effect of loading and aspect ratio on the normalized sensitivity coefficients of the total strain energy U with respect to micromechanical properties of the face sheet layers. Cylindrical sandwich panels, with honeycomb core and composite eight-layer face sheets, subjected to combined pressure loading, edge shear and temperature gradient through the thickness.

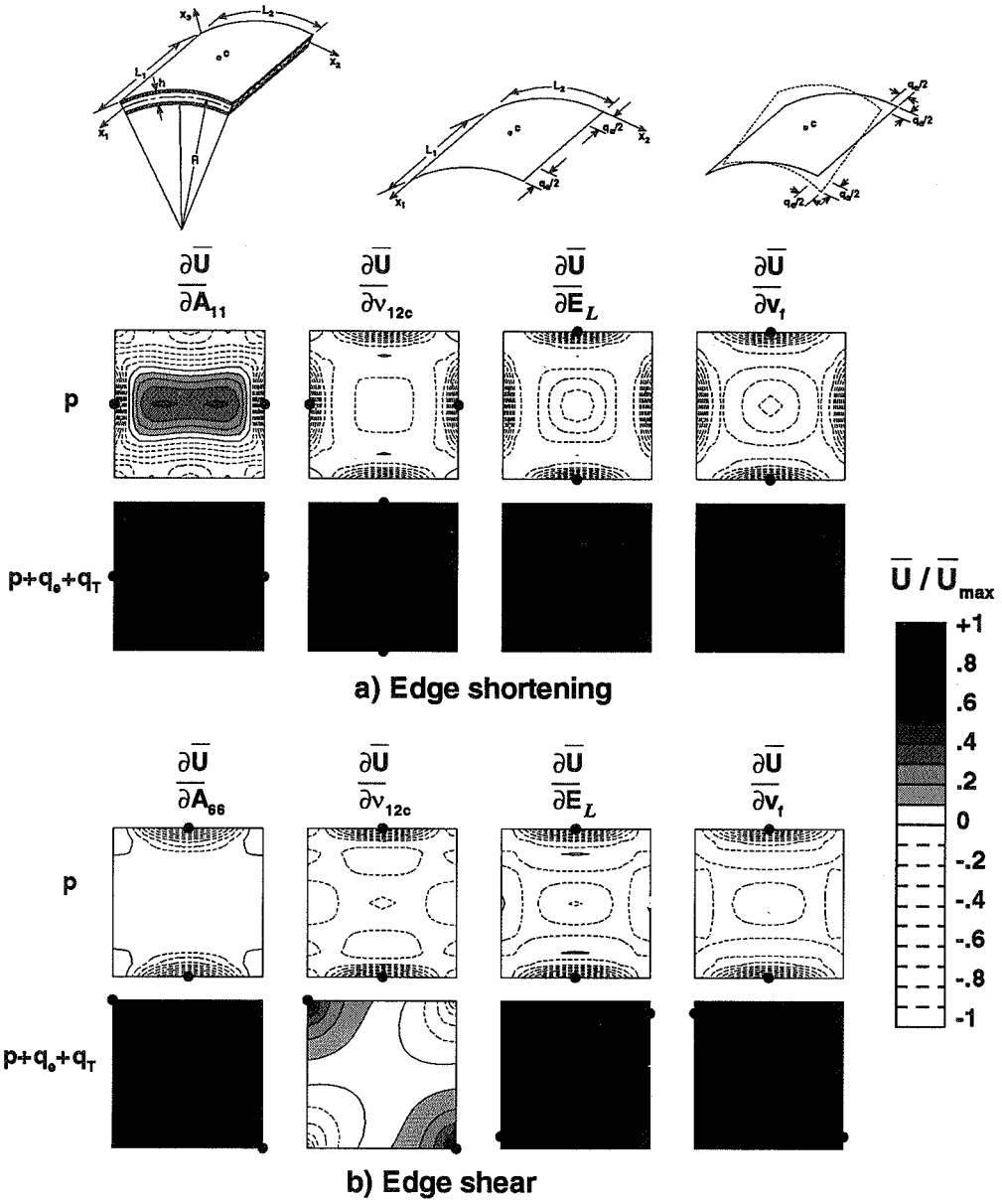

Figure 17. Normalized contour plots depicting the effect of loading on the largest sensitivity coefficients of the total strain energy density $\overline{U}$. Cylindrical sandwich panels, with honeycomb core and composite eight-layer face sheets, subjected to combined pressure loading, prescribed edge displacement and temperature gradient through the thickness. Location of maximum values identified by a small solid circle.

THERMAL AND MECHANICAL BUCKLING AND POSTBUCKLING RESPONSES OF SELECTED CURVED COMPOSITE PANELS

N. L. Breivik* and M. W. Hyer†
Virginia Polytechnic Institute and State University
Blacksburg, VA 24061-0219

J. H. Starnes, Jr.‡
NASA Langley Research Center
Hampton, VA 23681-0001

Abstract

The results of an experimental and numerical study of the buckling and postbuckling responses of selected unstiffened curved composite panels subjected to mechanical end shortening and a uniform temperature increase are presented. The uniform temperature increase induces thermal stresses in the panel when the axial displacement is constrained. An apparatus for testing curved panels at elevated temperature is described. Numerical results generated by using a geometrically nonlinear finite element analysis code are presented. Several analytical modeling refinements that provide more accurate representation of the actual experimental conditions, and the relative contribution of each refinement, are discussed. Experimental results and numerical predictions are presented and compared for three loading conditions including mechanical end shortening alone, heating the panels to 250°F followed by mechanical end shortening, and heating the panels to 400°F. Changes in the coefficients of thermal expansion were observed as temperature was increased above 330°F. The effects of these changes on the experimental results are discussed for temperatures up to 400°F.

Introduction

The buckling and postbuckling responses of unstiffened, curved composite panels subjected to thermal loading conditions are of interest for future high-speed aircraft which are expected to operate in an elevated temperature environment. Although experimental and analytical studies have provided an understanding of the response of curved composite panels subjected to mechanical axial compression loads, only analytical results are available for panels subjected to thermal loads. Knight and Starnes,[1] for example, conducted room-temperature tests of curved composite panels subjected to mechanical axial compression loads, and compared the test results with numerical results from a nonlinear finite element code which included the effects of measured geometric imperfections. The response of curved composite panels to thermal loading conditions has been studied analytically by a number of investigators[2-8] for panels both with and without cutouts, but these results were not correlated with experimental results.

The present paper presents the results of an experimental and numerical study of curved composite panels subjected to a uniform temperature change and a mechanical axial compression load. The response of the panels due to the thermal stresses caused by boundary condition constraints are described. Comparisons of the results of panels loaded in axial compression and panels subjected to a uniform temperature change with restricted axial displacement are made to help explain their complex behavior. Numerical results were generated using the geometrically nonlinear finite element code STAGS,[9] which accounts for large rotations and allows solutions along an unstable postbuckling path.

Experiments

Test Specimens

Test specimens were fabricated from unidirectional layers of IM7/5260 graphite-bismaleimide preimpregnated tape using the resin manufacturer's recommended processing procedure. The resulting test panels are 8-plies thick and have a $[\pm 45/0/90]_s$ quasi-isotropic lamination. The test panels are 10-in. long, 10-in. wide, and have a 60-in. radius. The mechanical properties of the material are given in Table 1. The laminate coefficients of thermal expansion are obtained from the properties in Table 1, and the values $\alpha_x = \alpha_y = 1.136 \times 10^{-6}$/°F indicate that the thermal expansion in the axial and circumferential directions are equal when the panel is subjected to elevated temperatures. Panel geometry and analytical

*Graduate Research Assistant, Dept. of Engineering Science and Mechanics

†Professor, Dept. of Engineering Science and Mechanics, Associate Fellow AIAA

‡Head, Structural Mechanics Branch, Fellow AIAA

boundary conditions are shown in fig. 1.

Initial geometric imperfections were measured on both the inner and outer surfaces of each panel. Measurements were taken every 0.125 in. along the axial and circumferential directions. The panel thickness was determined by taking the difference between the measurements for the inner and outer surfaces. The initial radial geometric imperfections were found by averaging the inner and outer surface measurements to obtain a contour of the midsurface geometric imperfections.

Panels were instrumented with back-to-back pairs of strain gages and thermocouples. Eighteen thermocouples were used to determine the uniformity of the applied temperature for each panel. Forty-two strain gages were used to measure of the strain in each panel. Two additional strain gages were attached to a piece of quartz with a near zero coefficient of thermal expansion and were used to compensate for the thermal expansion of the strain gages used for each test. The instrumented quartz was placed in the insulated heated enclosure along with the test panel, and the resulting strain gage readings indicated a measure of the gages' apparent strain. Strain gage readings from the panel were corrected for the thermal expansion of the strain gages so that the resulting values represented only the change in length of the panel per initial unit of length.

Test Apparatus and Procedure

Panels were supported with curved end fixtures along the curved ends to provide clamped boundary conditions, and with knife-edge supports along the straight edges to prevent radial displacements. All support fixtures were fabricated from stainless steel. Panels tested at room temperature were painted white on one side to allow the use of the shadow moiré technique to observe radial deformations. Room temperature testing was conducted with a 120-kip-capacity hydraulic testing machine. End shortening was measured by three direct-current differential transformers (DCDT's) located at three corners of the load-frame platens.

The experimental study of the thermal response of the panels required both a load frame to restrict axial end shortening and an insulated, heated enclosure to provide a uniformly distributed temperature increase. The experimental apparatus for this study is shown in figs. 2 and 3. Primary heating is provided by coil resistance heaters with a fan (not shown) at the back of the enclosure to circulate the heated air. Additional heating of the curved end fixtures was provided by heated platens that consist of eight cartridge heaters embedded in a 0.75-in.-thick piece of stainless steel. By including the heated platens as an additional heat conduction source, the temperature increase of the curved end fixtures can be controlled to be the same as the air temperature increase, rather than lagging behind the air temperature increase due to the substantial mass of the stainless steel. Two layers of Mycroy/Mycalex Ceramics, grade 500 Supra Mica insulation were used between the heated platens and the load-frame platens to provide thermal isolation. Because a single, large piece of ceramic insulation tends to warp out-of-plane when heated, the insulation was cut into small blocks measuring 2-in. long by 2.5-in. wide by 0.75-in. thick, with 0.5-in. deep grooves cut in a 0.5-in. grid pattern. Measurement of the deflection of the ceramic insulation at elevated temperatures up to 450°F indicated that the ceramic insulation blocks deflect from their flat and parallel shape by less than the machining tolerances of ±0.003 in.

To accommodate the size of the heated enclosure within the load-frame platens, elevated temperature tests were conducted in a 300-kip-capacity hydraulic testing machine. End shortening was measured by using a combination of two linear variable differential transformers (LVDT's) located inside of the heated enclosure and one DCDT outside of the enclosure. The LVDT's were not thermally compensated, and only provided a relative measure of end shortening after a constant elevated temperature had been established.

Temperature was controlled using four separate control loops that controlled the temperature of the top heated platen, the bottom heated platen, the side cartridge heaters, and the air, which was heated primarily by convection from the combination of the resistance heaters and the air circulating fan. Temperature was increased slowly to insure that the panel maintained a nearly uniform temperature distribution and to eliminate transient thermal effects. Heating a panel from room temperature to 400°F took approximately two hours. The resulting thermal gradients in the panel were well established when the temperature reached 150°F and remained relatively constant up to 400°F.

Analysis

Numerical analyses were conducted using the STAGS geometrically nonlinear finite element analysis code.[9] The curved panels were modeled with eight-node quadrilateral faceted shell elements formulated according to the Kirchhoff-Love hypothesis with Lagrangian nonlinear strain-displacement relations. Each node is allowed six degrees of freedom, comprised of three translations and three rotations, as illustrated in fig. 1.

The response of interest in the present study is the relationship between load and axial strain. The axial

strain due to end shortening can be found by dividing the change in panel length by the original length, $\Delta u/a$. For thermal loading, the axial strain is given by the change in temperature multiplied by the negative of the axial coefficient of thermal expansion, $-\alpha_x \Delta T$.

Preliminary nonlinear analyses were performed assuming an ideal geometry, a laminate thickness of 0.04 in., and a completely uniform temperature distribution. Boundary conditions were applied along the edges of the 10-in.-long by 10-in.-wide panels. The panels were loaded either by axial end shortening, Δu, or by a uniform temperature change, ΔT. When a temperature change was applied, the end shortening of the panel was restrained by setting $\Delta u = 0$. The nonlinear load-strain response for this ideal model are compared to results for more refined models in figs. 4-9 and in Table 2. As indicated in Table 2, the buckling load due to a uniform temperature change is P_{cr}=-1530 lbs. for the ideal model, which is approximately 13% greater than the buckling load of P_{cr}=-1360 lbs. due to axial end shortening.

Experimental Boundary Conditions

Since the curved end fixtures provide support over 0.375 in. of the panel length at each end, and the knife edge supports are applied 0.125 in. in from the straight edges, the analytical boundary conditions required modification from those used for the ideal model to represent the experimental boundary conditions. The constraint on the radial displacement, $w = 0$, was moved in 0.125 in. from the straight edges, and a constraint on the radial displacement 0.375 in. from the curved ends was added to the clamped boundary conditions. The effect of these experimental boundary conditions on the analytical results are shown in fig. 4. The analytical buckling loads are 6% and 9% greater for end shortening and thermal loading, respectively, and the postbuckling stiffnesses are similar. The postbuckling loads are higher for the experimental boundary conditions than for those of the ideal model.

Measured Thickness

Average measured panel thickness, determined from the inner and outer surface measurements, was calculated for each panel and analyses were conducted by assuming this average value as the constant panel thickness. The measured thickness is approximately 8% greater than the thickness assumed for the ideal model. The effects of measured thicknesses on the nonlinear response are shown in fig. 5. The prebuckling stiffnesses and the buckling loads are substantially increased, but the postbuckling stiffness is relatively unaffected, compared to results for the thinner ideal model. Assuming that the buckling load is proportional to the thickness cubed, it is expected that an 8% increase in thickness would result in a 26% increase in the buckling load. The results in Table 2 suggest that this calculation provides a good approximation for the buckling load.

Initial Geometric Imperfections

The measurements for the initial geometric imperfections were sensitive to the surface irregularities of the panels. The panel outer-surface roughness was caused by a porous release cloth that was used during specimen fabrication. The resulting imperfection measurements required some smoothing to separate the midsurface variations in radial displacements from the surface irregularities associated with the outer surface layer. A Fourier series approximation of the midsurface radial imperfection data was calculated using a trapezoid rule for numerical integration of the form

$$\bar{w}(x,\theta) = \sum_{n=0}^{n_{max}} \sum_{m=0}^{m_{max}} A_{mn} \cos\left(\frac{m\pi x}{a}\right) \cos\left(\frac{n\pi\theta}{\beta}\right). \quad (1)$$

Due to the relatively large finite element size, approximately 0.45-in. square, used in the analysis compared to the 0.125-in. grid of measurement points, too much accuracy in the Fourier representation could result in a choppy or discontinuous finite element representation. A series with $n_{max} = 6$ and $m_{max} = 14$ was found to give satisfactory results, based on an error calculation given by

$$error = \sqrt{\frac{\sum (w_{measured} - \bar{w})^2}{\sum (w_{measured})^2}} \quad (2)$$

where the summation is taken over the total number of measurement points. The error showed little improvement when additional terms were added to the Fourier approximation.

The Fourier approximation for a typical initial geometric imperfection is shown in fig. 6, where the radial imperfection $\bar{w}$ is normalized by the nominal layer thickness of 0.005 in. The magnitude of the maximum imperfection is on the order of two layer thicknesses, or 25% of the total panel thickness.

The nonlinear response presented in fig. 7 includes the measured initial geometric imperfections of fig. 6. Compared to the results for the ideal model, including the initial geometric imperfections has little effect on the panel stiffness. The bucking loads are decreased by 12% and 5% for the mechanical loading and thermal loading cases, respectively, as shown in Table 2.

Thermal Gradients

Temperature was measured during testing using nine equally spaced thermocouples on each surface of the panel. The thermocouple data were approximated by a second-order-polynomial function which allows continuous temperature gradients to be calculated for the inner and outer surfaces. The temperature gradient over one surface is given by

$$T(x,\theta) = C_1x^2\theta^2 + C_2x^2\theta + C_3x^2 + C_4x\theta^2 + C_5x\theta + C_6x + C_7\theta^2 + C_8\theta + C_9 \quad (3)$$

where C_1-C_9 are constants determined by the nine thermocouple readings for that surface. This approximation is repeated for the other surface.

A typical temperature gradient approximation is shown in fig. 8. The maximum temperature difference along one surface of the panel is approximately 20°F, while the maximum temperature difference between inner and outer surfaces is approximately 4°F.

The nonlinear response shown in fig. 9 includes the temperature gradient represented in fig. 8. These temperature gradient appear to have little effect on the load-strain response. The buckling load is decreased about 4% compared to the buckling load of the ideal model as shown in Table 2. These results suggest that the level of temperature uniformity obtained with the experimental apparatus is sufficient for studies focusing on the effects of uniform elevated temperatures.

Fully Refined Model

When the effects of experimental boundary conditions, measured thicknesses, initial geometric imperfections, and thermal gradients are considered together, the nonlinear response varies significantly from the response of the ideal model, as shown in fig. 10. The effects of the modeling refinements on the end-shortening response tend to cancel each other out as shown in Table 2, so that the overall difference between the results for the ideal model and the results for the refined model is small. However, the thermal loading response showed greater sensitivity to boundary condition and thickness refinements, which tend to increase the buckling load, and less sensitivity to initial imperfections, which tend to lower the buckling load. Including all of the modeling refinements causes a greater change in the ideal model results for a thermal load than for a mechanical load, as compared to the refined model results.

Experimental Results and Discussion

Δu Loading

Room-temperature tests were conducted with a test specimen to establish a baseline for comparison to thermal loading results. This specimen has the same panel geometry and $[\pm45/0/90]_s$ lamination as the other specimens. The nonlinear response results from the experiment and from the numerical predictions with the STAGS finite element code are shown in fig. 11. The discontinuity in the experimental data points indicates that the panel collapses from a maximum or buckling load to a lower load, and that the stiffness associated with the postbuckling response is reduced. The finite element model incorporates the refinements discussed previously, namely experimental boundary conditions, measured thickness, and measured initial geometric imperfections. The value of the experimentally established bucking load is between the values of the buckling load predicted by the model incorporating initial imperfections and the buckling load predicted by the model without initial imperfections, as indicated in Table 3. A possible explanation for this discrepancy is that a constant thickness was assumed along with a midsurface geometric imperfection, while the actual measured imperfections may have included both midsurface imperfections and local thickness variations.

The deformation mode shape of the postbuckling response is indicated by the photograph of the shadow moiré fringe pattern shown in fig. 12 along with the predicted response from STAGS. The two deformation shapes qualitatively agree, with both indicating a single buckle pattern in the center of the panel.

ΔT to 250°F Followed by Δu Loading

To determine the response of a $[\pm45/0/90]_s$ panel at an elevated temperature of 250°F, the panel was slowly heated while data were collected from the strain gages, the thermocouples, the external DCDT, and the load cell. The original test plan was to hold the end shortening constant during heating, but this was not possible due to two opposing factors. First, the 300-kip load frame was designed to apply end shortening by raising or lowering the lower load-frame platen. When an attempt was made to hold the end shortening at a constant value, a slow leak in a hydraulic valve caused the lower load-frame platen to drift slowly downward. This drift resulted in the axial expansion of the curved test panel. Secondly, the steel end fixtures and steel heated platens, which were heated along with the panel, expanded due to the elevated temperatures. Together, these steel components were 2.0-in. thick between the curved ends of the test panel and the load-frame platens.

The steel expanded with a coefficient of thermal expansion of $\alpha = 6.0 \times 10^{-6}/°F$ and exerted a compressive axial displacement on the curved test panel. The superposition of the lower-platen drift and the steel expansion resulted in a known net axial expansion of the panel during thermal loading.

The known expansion of the panel as a function of temperature was included in the finite element model, so that the actual loading of the panel can be described as combined thermal and mechanical loading, followed by mechanical loading alone. The experimental and predicted nonlinear responses for this loading sequence are shown in fig. 13. The portion of the response curve in the upper part of the figure indicates that a positive or expanding end shortening occurs during the application of the elevated temperature. This response corresponds to the portion of the response curve in the lower part of the figure with an increasing load and a compressive thermal strain. When the thermal strain reaches a constant level, $-\alpha_x \Delta T = -0.0002$, the loading is due to end shortening alone. The numerically predicted nonlinear response due to the combination of thermal and mechanical loads is not as accurate as the numerical prediction for mechanical loads alone, e.g., see fig. 11. The finite element model predicts a slight nonlinearity in the load-strain response before buckling, which was not observed experimentally. Also, the value of the buckling load obtained experimentally is greater than the values of the predicted buckling loads obtained either by including or not including initial geometric imperfections.

The value of the buckling load for a panel loaded by end shortening at 250°F is greater than the value of the buckling load obtained for the panel tested at room temperature, as indicated in Table 3. The experimental results indicate that there is an approximately 15% increase in value of the buckling load for the panel tested at 250°F compared to results for the panel tested at room temperature. The analytical results indicate the same trend, although the increase in the value of the buckling load is only 4 to 7%, depending on whether or not initial geometric imperfections are included in the analyses.

ΔT Loading

The buckling response of the $[\pm 45/0/90]_s$ panel subjected to only thermal loading cannot be studied experimentally due to the thermal limitations of the material. However, interesting insight into the prebuckling response was obtained by heating a panel to 400°F while taking data from the strain gages, thermocouples, and external DCDT. Experimental results and numerical predictions for this loading condition are shown in fig. 14. Again there was drift of the lower load platen and thermal expansion of the steel fixture and heated platen. Because the rate of drift of the lower load platen varied from test to test, the slope of the load-strain response curves also varied from test to test. At a temperature of 300°F, the panel experiences a compressive load of -590 lbs., equal to more than one third of the mechanical buckling load of the panel. At a temperature of approximately 330°F, the response of the panel changes, and the load does not increase with increasing temperature. The finite element numerical prediction did not indicate this behavior, suggesting that a change in material properties may have occurred above 330°F.

Free Thermal Expansion

To examine the material properties above 330°F, the free thermal expansion of an IM7/5260 panel was studied by heating the panel to a temperature of 400°F. The only panel for which these data are available has a $[\pm 45/0_2]_s$ stacking sequence, however, the trends in properties are a function of the material and are independent of the particular stacking sequence. The relationship between strains from axial and circumferential strain gages located at the center of the panel and the temperature change is shown in fig. 15. The slopes $\varepsilon/\Delta T$ of the curves are the coefficients of thermal expansion. At temperatures below 330°F, an increase in temperature produces a positive strain in the circumferential direction, indicating circumferential expansion, and a negative strain in the axial direction, indicating axial contraction or shrinking. The corresponding coefficients of thermal expansion are positive in the circumferential direction and negative in the axial direction. Above a temperature of 330°F, the panel begins to contract in the circumferential direction and to expand in the axial direction, as indicated by the changing slopes in fig. 15. This change in slope implies a change in the sign of the coefficients of thermal expansion. At approximately 330°F, the coefficient of thermal expansion in the circumferential direction changes from positive to negative, while the coefficient of thermal expansion in the axial direction changes from negative to positive.

These changes in the coefficients of thermal expansion, coupled with a likely change in the material stiffness properties, could be an explanation for the loss of stiffness of the $[\pm 45/0/90]_s$ panel when it was heated to 400°F. Thus, the loss of stiffness that occurred at 330°F may be due to a change in material properties of the IM7/5260 material as opposed to a structural phenomenon.

Concluding Remarks

The results of an experimental and numerical study of the buckling and postbuckling responses of selected unstiffened curved graphite-bismaleimide composite panels subjected to mechanical end shortening and a uniform temperature increase are presented. The effect of various experimental conditions on the load-strain response of the panels was studied analytically using a geometrically nonlinear finite element analysis code, and the results of the study indicate which conditions affect the panel response. The magnitude of the panel thickness, initial geometric imperfections, and experimental boundary conditions affected the analytically predicted buckling load, but the small experimentally determined thermal gradients associated with the tests had little effect on the predicted results.

The numerically predicted results for a panel subjected to a mechanical end-shortening load correlated well with the room-temperature test results. The numerically predicted results for panels subjected to elevated temperatures and a mechanical end-shortening load correlated well with the test results when the effects of displacements associated with the test apparatus were included in the analysis The results indicate that it is necessary to include the changes in the load platen displacements caused by a small leak in a test-machine hydraulic valve and the thermal expansion of the end fixtures and heated platen to obtain acceptable correlation of the test and analytical results.

The results indicate that the coefficients of thermal expansion of the material were affected by temperature. It was found that the coefficients of thermal expansion in the axial and circumferential directions change sign for temperatures above 330°F, and the resulting changes in properties affect the correlation between the experimental and analytical result.

References

[1]Knight, N. F., Jr. and Starnes, J. H., Jr., "Postbuckling Behavior of Selected Graphite-Epoxy Cylindrical Panels Loaded in Axial Compression," *Proceedings of the 27th AIAA/ASME/ASCH/AHS Structures, Structural Dynamics and Materials Conference*, San Antonio, TX, 1986, pp. 142-158.

[2]Chen, L. W. and Chen, L. Y., "Thermal Buckling Analysis of Laminated Cylindrical Plates by the Finite Element Method," *Computers and Structures*, Vol 34, No. 1, 1990, pp. 71-78.

[3]Chang, J. S. and Chui, W. C., "Thermal Buckling Analysis of Antisymmetric Laminated Cylindrical Shell Panels," *International Journal of Solids and Structures*, No. 27, No. 1, 1991, pp. 1295-1309.

[4]Huang, N. N. and Tauchert, T. R., "Large Deflections of Laminated Cylindrical and Doubly-Curved Panels Under Thermal Loading," *Computers and Structures*, Vol. 41, No. 2, 1991, pp. 303-312.

[5]Librescu, L., Lin, W., Nemeth, M. P. and Starnes, J. H., Jr., "Thermomechanical Postbuckling of Geometrically Imperfect Flat and Curved Panels Taking Into Account Tangential Edge Constraints," *Journal of Thermal Stresses*, Vol. 18, 1995, pp. 465-482.

[6]Madenci, E. and Barun, A., "Thermal Postbuckling Analysis of Cylindrically Curved Composite Laminates with a Hole," *International Journal for Numerical Methods in Engineering*, Vol. 37, 1994, pp. 2073-2091.

[7]Noor, A. K and Starnes, J. H., Jr., "Nonlinear and Postbuckling Responses of Curved Composite Panels with Cutouts," *Proceedings of the 36th AIAA/ASME/ASCE/AHS/ASC Structures, Structural Dynamics, and Materials Conference*, New Orleans, LA, 1995, pp. 2116-2144.

[8]Breivik, N. L. and Hyer, M. W., "Buckling and Postbuckling Behavior of Curved Composite Panels Due to Thermal and Mechanical Loading," *Proceedings of the American Society for Composites 11th Technical Conference*, Atlanta, GA, 1996, pp. 80-89.

[9]Brogan, F. A., Rankin, C. C., and Cabiness, H. D., *STAGS User Manual*, LMSC PO32594, Lockheed Palo Alto Research Laboratory, Palo Alto, CA, March, 1994.

Table 1. IM7/5260 Material Properties.

$E_1 = 22.1$ Msi
$E_2 = 1.457$ Msi
$\nu_{12} = 0.258$
$G_{12} = 0.860$ Msi
$\alpha_1 = 0.01250 \times 10^{-6}$ /°F
$\alpha_2 = 14.91 \times 10^{-6}$ /°F

Table 2. Buckling loads for refined analytical models.

	Δu loading P_{max}/P_{cr} P_{cr}=-1360 lbs.	ΔT loading P_{max}/P_{cr} P_{cr}=-1530 lbs.
Ideal model	1.00	1.00
Experimental boundary conditions	1.06	1.09
Measured thickness	1.21	1.28
Initial geometric imperfections	0.88	0.95
Temperature gradient		0.96
All refinements	1.07	1.32

Table 3. Buckling load, experiment and predictions.

	Δu loading P_{max}, lbs.	ΔT to 250°F, then Δu P_{max}, lbs.
Experiment	-1670	-1920
Nonlinear analysis	-1460	-1560
Nonlinear analysis without imperfections	-1750	-1820

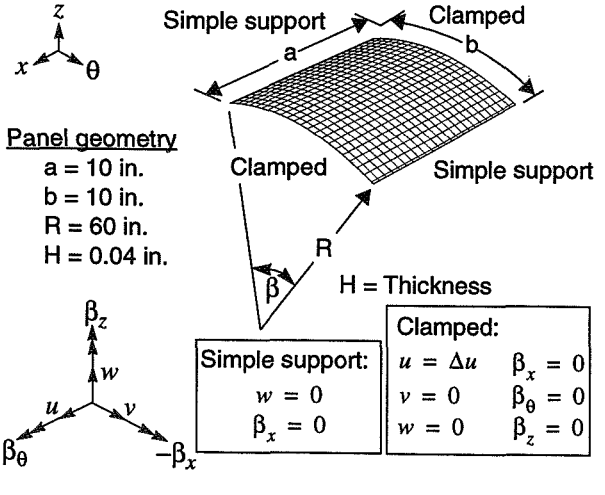

Fig. 1 - Panel geometry and boundary conditions.

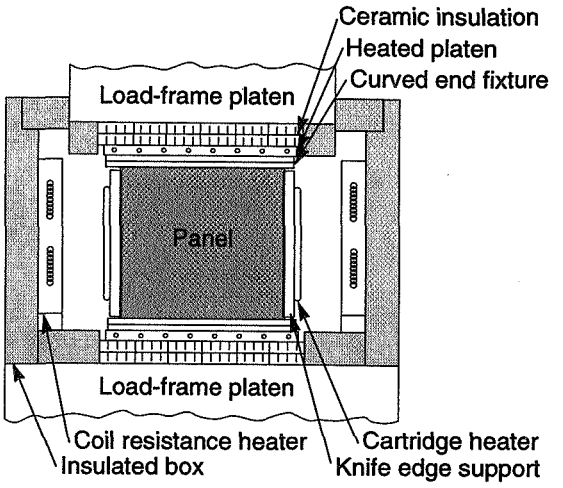

Fig. 2 - Elevated temperature testing apparatus.

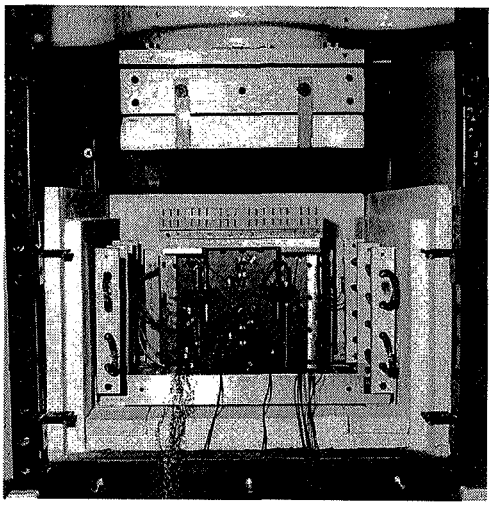

Fig. 3 - Photograph of experimental set-up.

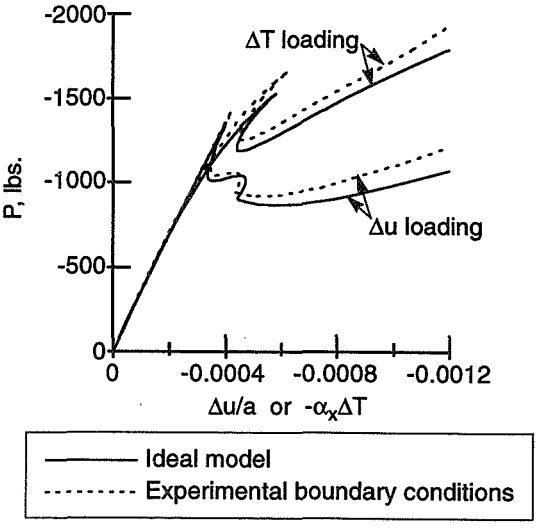

Fig. 4 - Effect of experimental boundary conditions.

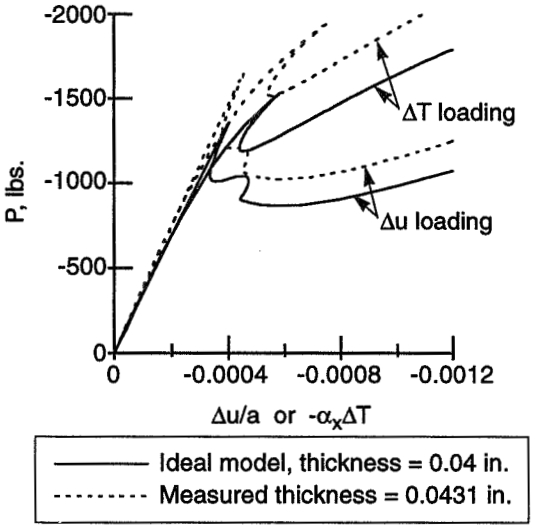

Fig. 5 - Effect of measured thickness.

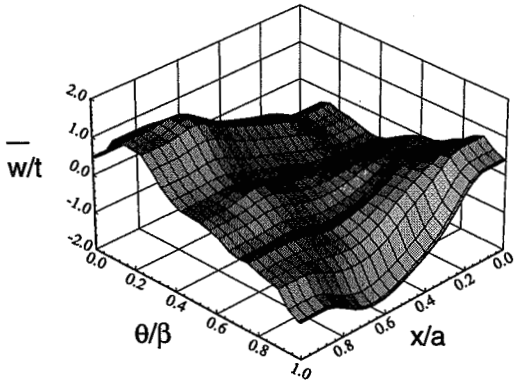

t = Ideal layer thickness = 0.005 in.

Fig. 6 - Typical initial geometric imperfection.

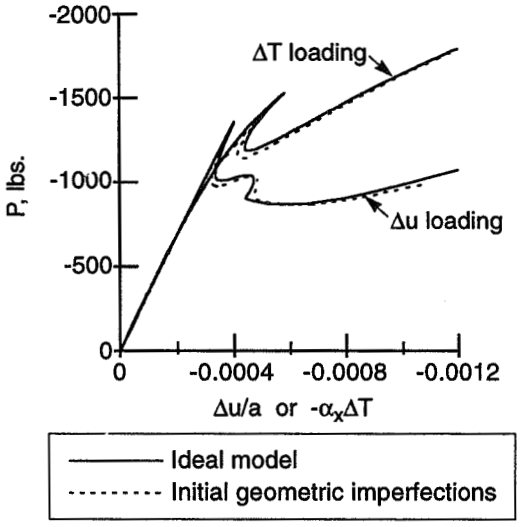

Fig. 7 - Effect of initial geometric imperfection.

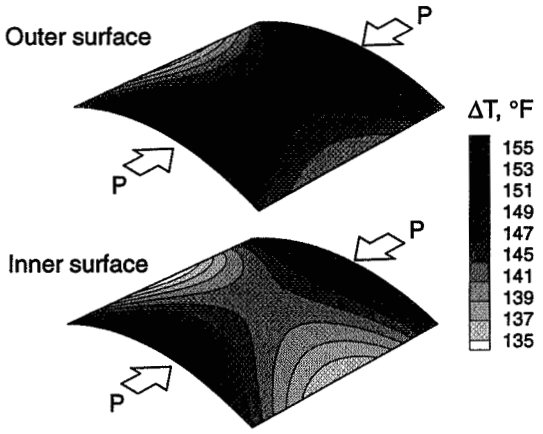

Fig. 8 - Typical temperature gradient.

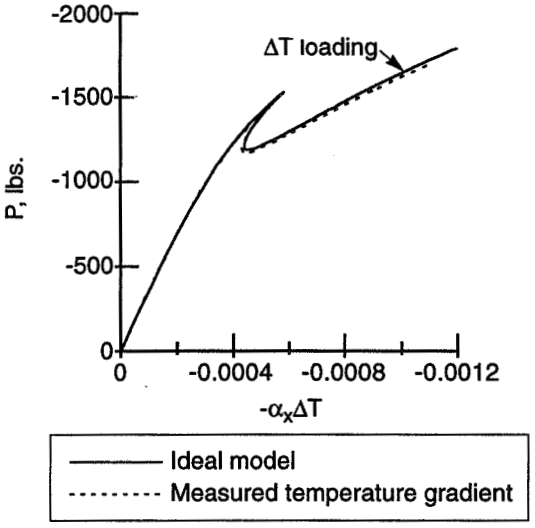

Fig. 9 - Effect of measured temperature gradient.

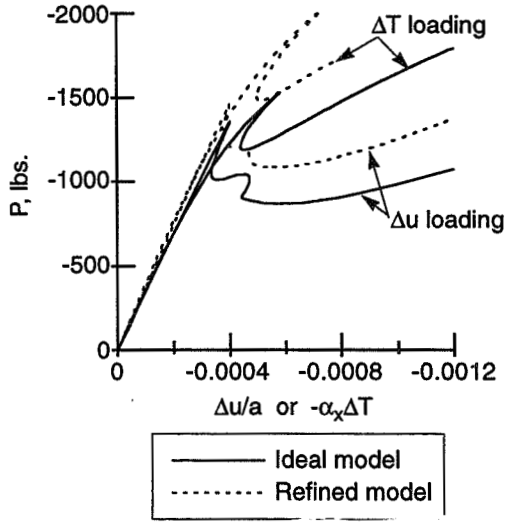

Fig. 10 - Effect of all model refinements together.

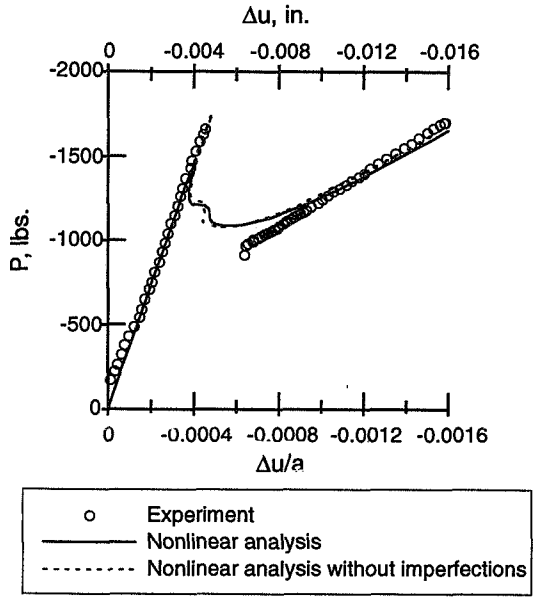

Fig. 11 - Response for Δu loading.

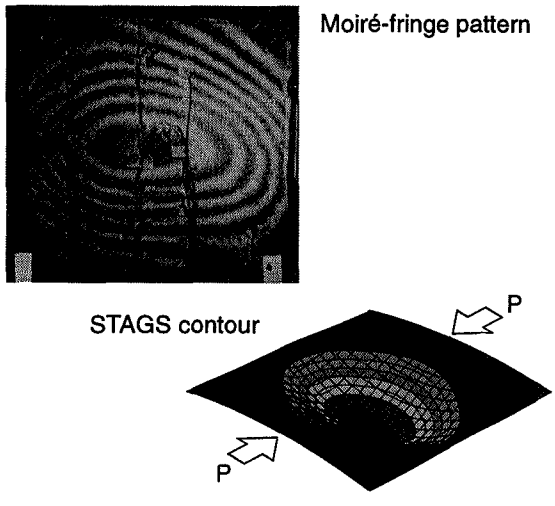

Fig. 12 - Postbuckling deformations for Δu loading.

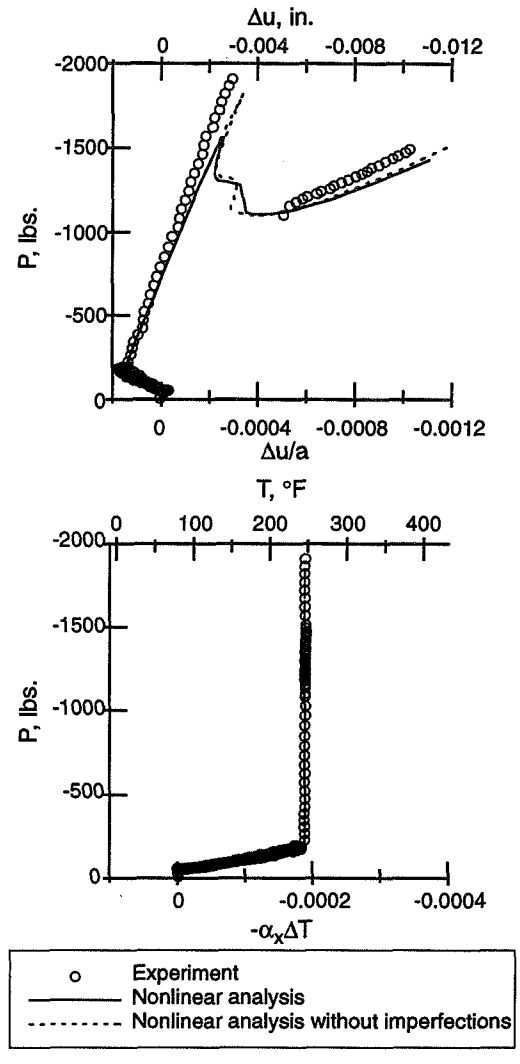

Fig. 13 - Response due to ΔT loading to 250°F and then Δu loading.

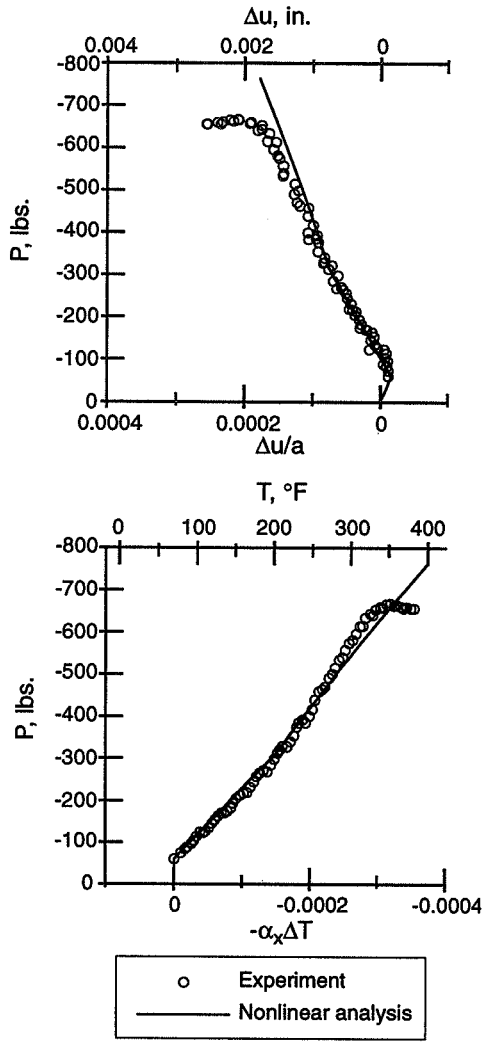

Fig. 14 - Response due to ΔT loading to 400°F.

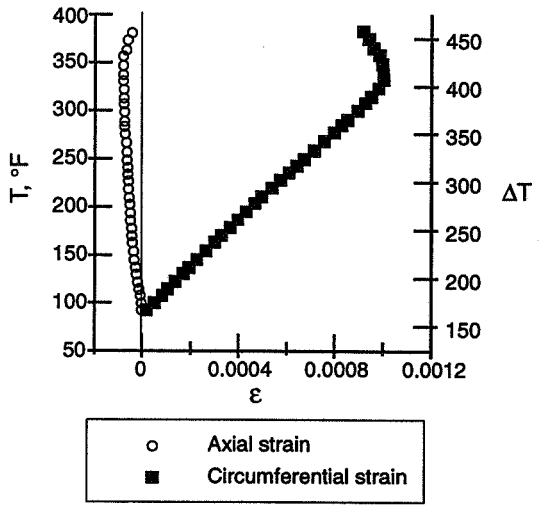

Fig. 15 - Free thermal expansion for a $[\pm 45/0_2]_s$ laminate.

Scaled Down Imperfection Sensitive Composite Cylindrical Shells Under Axial Compression and Lateral Pressure

A. Tabiei and G. J. Simitses*
Department of Aerospace Engineering and Engineering Mechanics
University of Cincinnati, Cincinnati, OH 45221-0070

Abstract

The study reported herein includes assesment of imperfection sensitivity of scaled down models. Understanding the relationship between model and prototype behavior is essential in designing scaled down models. This study investigates problems associated with establishing similarity among symmetric laminated cross-ply cylindrical shells subjected to axial compression and lateral pressure. Particular emphasis is placed on the imperfection sensitivity of scaled down models and prototypes. Such a study is important since it provides the necessary scaling laws and scale factors which affect the accuracy of the predicted response. The results presented herein indicate that, for elastic response of a cross-ply cylindrical shell, based on structural similitude, a set of scaling laws can be found to establish similarity among a large number of cylinders with different number of plies, stacking sequence, and geometries.

Nomenclature

A_{ij}	*laminate extensional stiffnesses*
B_{ij}	*laminate coupling stiffnesses*
D_{ij}	*laminate flexural stiffnesses*
K_{yy}	*non-dimensional load*
L	*cylinder length*
N_{xx}, P	*critical loads(limit point)*
N_{xxcr}, P_{cr}	*buckling load(bifurcation point)*
R	*cylinder radius*
t	*total laminate thickness*
Z	*curvature parameter* L^2/Rt
λ_i	*scale factors*
ξ	*imperfection amplitude coefficient*

Subscripts

m	*model*
p	*prototype*
pr.	*predicted*
th.	*theoretical*

Introduction

A scaled-down model, *scale model*, which can predict the structural behavior of the full-scale system, *prototype*, has been proven[1,2,3] to be an extremely beneficial tool. This possible development must be based on the existence of certain structural parameters that control the behavior of the structural system when acted upon by static and/or dynamic loads. Understanding the relationship between model and prototype behavior is essential in designing scaled down models. In order to better understand the applicability of these models in designing laminated composite structures, an analytical investigation was undertaken to assess the feasibility of their use. Such a study is important since it provides the necessary scaling laws and scale factors which affect the accuracy of the predicted response.

However, scaled down models are not widely used because of the uncertainty associated with scaling down a laminated structure. Before scaled down models can be used, the following technical barriers must be overcome: 1) the determination of the proper scale factors of the structural geometry parameters, 2) establishing the necessary conditions which relate the

*Assistant Professor and Professor respectively.

response behavior of the scaled down model to the original system, 3) the determination of the sensitivity of the scaled down models to initial imperfections, and 4) understanding the effect of scaling (scale effect) on accuracy of the models in replicating the prototype behavior. The last item has received much attention from researchers in recent years and was focused on initially, because most studies were experimental in nature. This issue is important especially for model testing which involves failure or inelastic behavior[4,5,6]. In these studies, the variation of scale factors of parameters are limited to the number of experiments. First and second items have been investigated in previous papers[1,2].

In previous studies[1,2,3], it was assumed that the shells are perfect. However, laminated cylinders contain several imperfections and defects, namely initial geometric imperfections, and structural or material defects. It is assumed that the prototype and its models are free of any defects in material or construction. The initial geometric imperfections can be classified as initial shape imperfections or load eccentricities[7]. In order to include the effects of these imperfections in the analysis, there is a need to have a complete knowledge of the imperfections, which is virtually impossible. A practical way to consider these effects in scaled down model design, is to use the scaling laws which have been derived based on classical theory, by assuming that imperfections have the same effect on both the prototype and its model. To do so, the designer has to have a good knowledge of imperfection sensitivity of the structures which are under investigation. This type of information is necessary for both complete similarity(ply-level scaling) and partial similarity. To design an accurate scaled down model, it is crucial to know exactly how imperfections affect the cylinder behavior, for the following cases:

- Distortion in the number of plies: (a) ply-level scaling, (b) sublaminate-level scaling, and (c) general scaling.
- Distortion in stacking sequences
- Distortion in geometry: (a) distortion in length(L), (b) distortion in radius(R), and (c) distortion in total thickness(t).

Based on this information, the designer can choose models which have identical, or at least similar, imperfection sensitivity with their prototype.

The main objective of this study is to investigate the applicability of similitude theory in designing scaled down models with initial imperfections. Particular emphasis is placed on the imperfection sensitivity of symmetric laminated cross-ply cylindrical shells subjected to axial compression and lateral pressure.

Scaling Laws for Perfect Cylinders

Previous results[2] indicated that, for elastic response of a cross-ply cylindrical shell, based on structural similitude, a set of scaling laws can be found to establish similarity among large number of cylinders with different number of plies, stacking sequence, and geometries. Both models with partial and complete similarity were presented. Similitude theory is employed to develop the necessary similarity conditions(scaling laws) from the governing equations of symmetric laminated cylindrical shells(for detail see Ref. 2).

$$(\frac{\lambda_\eta}{\lambda_\xi})^4 = \frac{\lambda_{A_{22}}}{\lambda_{A_{11}}} \tag{1}$$

$$(\frac{\lambda_\eta}{\lambda_\xi})^2 = \frac{\lambda_{A_{22}}}{\lambda_{A_{66}}} \tag{2}$$

$$(\frac{\lambda_\eta}{\lambda_\xi})^2 = \frac{\lambda_{A_{66}}}{\lambda_{A_{11}}} \tag{3}$$

$$(\frac{\lambda_\eta}{\lambda_\xi})^2 = \frac{\lambda^2_{A_{12}}}{\lambda_{A_{11}}\lambda_{A_{66}}} \tag{4}$$

$$\lambda_{K_{yy}} = \lambda^2_\eta \lambda^2_L \tag{5}$$

$$\lambda_{K_{yy}} = \frac{\lambda_{D_{12}}}{\lambda_{D_{11}}}\lambda^2_\xi \lambda^2_L \tag{6}$$

$$\lambda_{K_{yy}} = \frac{\lambda_{A_{22}}}{\lambda_{D_{11}}}\frac{\lambda^2_L}{\lambda^2_R \lambda^2_\eta} \tag{7}$$

$$\lambda_{K_{yy}} = \frac{\lambda^2_{A_{12}}}{\lambda_{A_{11}}\lambda_{D_{11}}}\frac{\lambda^2_L}{\lambda^2_R \lambda^2_\eta} \tag{8}$$

$$\lambda_{K_{yy}} = \frac{\lambda_{D_{22}}}{\lambda_{D_{11}}}\frac{\lambda^4_\xi \lambda^2_L}{\lambda^2_\eta} \tag{9}$$

where $K_{yy} = \frac{\bar{N}_{yy} L^2}{D_{11} \pi^2}$, and $\lambda_x = \lambda_L$ and $\lambda_\alpha = \frac{\alpha_p}{\alpha_m}$ denotes the scale factor of parameter α.

Conditions depicted by Eqs.(5)-(9) and the conditions that relate structural geometries and mode shapes, Eqs.(1)-(4), are the necessary scaling laws for symmetric, cross-ply, laminated cylinders subjected to lateral pressure. For the case of axial compression the scaling laws are the same as in equations (1)-(9) if the non-dimensional load K_{yy} is replaced by K_{xx}.The derived scaling laws, Eqs.(5)-(9), relate the response behavior of a scaled down model to that of the prototype. They can be used in designing scaled down models for a specific prototype or vice versa. As is apparent, the scaling laws are arranged in the form of different scale factor for buckling load (K_{yy}). It is necessary to state that, the presented form of arranging the scaling laws is not unique.

So far, the necessary scaling laws for cross-ply cylinders subjected to axial compression and lateral pressure have been established.

In designing the scaled down models the following assumptions are made:

- Model and prototype have classical simply supported boundary conditions (SS-3).
- Models have the same material properties as their prototype ($\lambda_{E_{ij}} = \lambda_{\nu_{ij}} = \lambda_{G_{ij}} = 1$). The material of each ply is a high modulus Graphite/Epoxy (AS4/3502).
- Two configurations are considered for prototype geometry $(0_{10}/90_{10})_s$ and $(0/90)_{10s}$ with $L_p = 42in$ and $R_p = 14in$.
- The thickness of each layer is assumed to be constant ($h = 0.007in$) for all cylinders(models and prototypes).

Different possibilities of scaled down models, i.e. scaling of the number of plies and geometrical parameters(L and R) are considered. There are three ways to scaled down the number of plies in a laminate (see Figure 1): 1) Ply-Level scaling: by eliminating the repeated plies $[(+\theta_n/-\theta_n)_s, n = 1, 2, 3, \cdots]$. 2) Sublaminate-Level scaling[5]: by eliminating the repeated group of plies $[(+\theta/-\theta)_{ns}, n = 1, 2, 3, \cdots]$. 3) General scaling: by reducing the number of plies arbitrary i.e. $[(+\theta_n/-\theta_n/+\theta_n)]$.

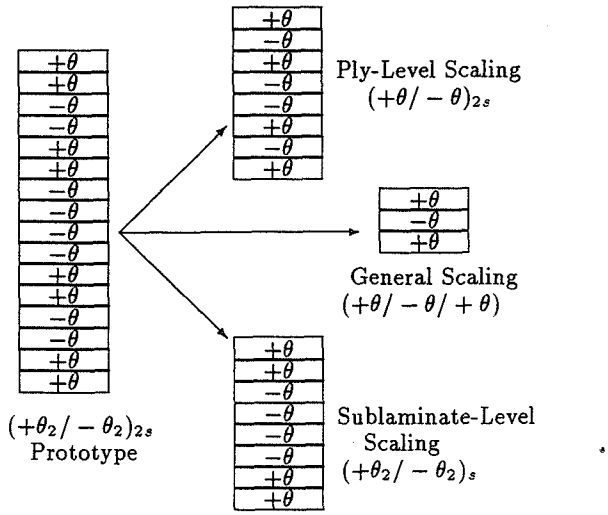

Figure 1: *Different possibilities for distortion of the number of plies.*

Models with Complete Similarity

Using ply-level scaling, $[(+\theta_n/-\theta_n)_s, n = 1, 2, 3, \cdots]$, all scaling laws are satisfied, providing geometrical similitude between model and prototype. In other words model and prototype must have the same curvature parameter $Z = L^2/Rt$. Note that $\lambda_Z = 1$ is a necessary but not a sufficient condition for complete similarity. This requires that the scale factors of geometric parameters (length, radius, and thickness or number of plies) of both model and prototype be the same (this yield $\lambda_L = \lambda_R = \lambda_t = \lambda_N$ *or* λ_P).

Note that $\lambda_Z = 1$ can also be achieved by choosing different scale factors for geometric parameters ($\lambda_L \neq \lambda_R \neq \lambda_N$). Prototype $(0_{10}/90_{10})_s$ can be ply level scaled down, but prototype $(0/90)_{10s}$ cannot. However, prototype $(0/90)_{10s}$, can have sublaminate level and/or general scaled down models. These type of ply reductions yield distorted models with partial similarity which is considered next.

Distorted Models

Complete similarity is very useful if there is freedom in designing scaled down models. In many cases it is impossible to satisfy complete similarity between model and prototype due to the size, shape, material properties, boundary conditions of prototype. When at least one scaling law cannot be satisfied, distorted models with partial similarity are achieved.

In the present studies, the material behavior is assumed to be linearly elastic. Therefore, scale effects are not present. Furthermore, it is assumed that the prototype and its scaled down models are free of imperfections or imperfections have the same effect on both the prototype and its small scale model. Since imperfection sensitivity of cylindrical shells varies with structural geometry parameters, models might be more sensitive to geometric imperfections than the prototype.

Imperfection Sensitivity of Models

In the previous section, it was assumed that the shells are perfect. However, thin laminated cylinders contain initial geometric imperfections. In order to include the effects of these imperfections in the analysis, there is a need to have a complete knowledge of the effect of initial imperfections on buckling behavior of both scaled down models and prototypes.

Numerical results are generated by employing the ABAQUS[8] finite element software. Mesh convergence study for $(0/90)_{10s}$ (the largest cylinder) and $(0/90)_s$ (the smallest cylinder)indicates that using 80-100 elements in circumferential by 20-30 elements in longitudinal direction yields an acceptable convergent state. The ABAQUS four nodded shell element (SR4) is used for this investigation. Using ABAQUS, first three eigenvalues and corresponding eigenvectors are obtained for each cylinder. The lowest eigenvalue represent either the axial compression buckling load or the lateral pressure buckling load for a perfect cylinder. The initial geometric imperfection were given by superimposing a small imperfection in the form of the weighted sum of several buckling modes(eigenvectors) on the initial geometry. In generating results two type of imperfection shapes are considered with different imperfection amplitude coefficients(ξ). Three amplitude coefficients (ξ= 0.1, 0.5 and 1.0) are considered. Imperfection sensitivity of ply-level scaling of laminates for the case of axial compression are presented in Figure 3. This figure shows that, ply-level scaled models have almost the same imperfection sensitivity regardless of the number of plies.

Figure 4 shows the normalized critical end-shortening for the ply-level scaled models. It is clear that despite the scalibility of imperfection sensitivity, the end-shortening can not be scaled for the case of axial compression. Figure 5 shows the effect of imperfections on critical axial compression loads for sublaminate-level scaled models. Cylinders with 4,8,12, and 16 layers with sublaminate-level scaling has roughly the same imperfection sensitivity.

Figure 6 shows the normalized post-buckling behavior for ply-level completely similar cylindrical shells under lateral pressure. We can see that the limit point in this case can be scaled and equ. 6 can be used to predict the limit point of prototype using results of model. For this case the post buckling behavior can also be scaled as depicted in figure 7 once the end shortening is normalized with respect to the thickness of the shell. Imperfection sensitivity of ply-level scaling of laminates for the case of lateral pressure are presented in figure 8. This figure shows that, ply-level scaled models have the same imperfection sensitivity regardless of the number of plies. Next, partial similarity is considered in which two distortions are analyzed. The normalized post-buckling behavior of cylindrical shells under lateral pressure with distortions in the length and thickness for two different imperfection amplitude are presented in figures 9 and 10. Also, similar results are presented for distortions in length and radii of the shell in figure 11. From these results, one can observe that limit points can be predicted using scaling laws, however, post-buckling do not obey similarity conditions derived from the linearized buckling equations.

Based on this information, the designer can choose

models which have identical, or at least similar, imperfection sensitivity with their prototype.

Discussion

The results presented herein indicate that, for buckling response of laminated cylindrical shells subjected to axial compression and lateral pressure, based on structural similitude, a set of scaling laws can be found which are used to develop design rules for designing small scale models. For simplicity the linear form of governing equations of the system can be used to developed the necessary scaling laws. These scaling laws can be used to design or investigate the available scaled down models. Later, a more complex non-linear analysis(with initial imperfection) can be used to investigate the effect of non-linearity on the prototype and its models behavior. If the model structural geometry parameters are chosen carefully, a set of models with the same imperfection sensitivity can be found which are capable of predicting the prototype behavior. When model and its prototype have the same material properties, through ply-level and sublaminated-level scaling of the prototype a wide range of models can be found which predict accurately the prototype behavior. However, models must be geometrically scaled down and have the same material properties as their prototype (complete similarity).

Conclusions and Recommendations

Understanding the relationship between model and prototype behavior is essential in designing scaled down models. With a view of better understanding the applicability of these models in designing laminated composite structures, an analytical investigation was undertaken to assess the feasibility of their use. This study investigates problems associated with establishing similarity among symmetric laminated cross-ply cylindrical shells subjected to axial compression and lateral pressure. Such a study is important since it provides the necessary scaling laws and scale factors which affect the accuracy of the predicted response. The results presented herein indicate that, for elastic response of a cross-ply cylindrical shell with initial geometric imperfections, based on structural similitude, a set of scaling laws can be found to establish similarity among a large number of cylinders with different number of plies, stacking sequence, and geometries. Both models with partial and complete similarity are presented.

Some recommendations for future research include (*a*) develop a set of scaling laws for nonlinear governing equations with the effect of geometric imperfections. (*b*) study of the effect of boundary conditions, configurations and (*c*) initiation of an experimental program for validation.

Acknowledgments

The work reported herein was supported by the Office of Naval Research under Grant ONR- N00014-95−1−0597. The ONR technical officer is Dr. Yapa D. S. Rajapakse. Their encouragement are appreciated. The financial support provided by ONR is gratefully acknowledged. The authors also wish to thank NCSA(National Center for Super computing Applications) at University of Illinois at Urbana Champaign for allowing the authors to use their SGI super computer, under grant MSS960005N.

References

[1]Simitses, G. J. and Rezaeepazhand, J., Structural Similitude for Laminated Structures, *Composites Engineering*, Vol.3, Nos 7-8. Pp. 751-765, 1993.

[2]Simitses, G. J. and Rezaeepazhand, J., and Sierakowski, R. L., Scaled Models for Laminated Cylindrical Shells Subjected to External Pressure, *Proceedings of 7th Japan-US Conference on Composite Materials*, Kyoto, Japan, June, 1995, pp. 459-466.

[3]Tabiei, A., Sun, J., and Simitses. G., J.,On The Scaling Laws of Cylindrical shells Under lateral pressure, *AIAA Jo.*, (Submitted for Publication).

[4]Jackson, K. E., "Scaling Effect in the Static and Dynamic Response of Graphite-Epoxy Beam-Columns," *Ph.D. Dissertation*, Virginia Polytechnic Institute and State University, Department of Engineering Mechanics, 1990.

[5]Kellas, S. and Morton, J., "Strength Scaling in Fiber Composites," *AIAA Journal* , Vol. 30, No.4, 1992, pp. 1074-1080.

[6]Qian, Y., Swanson, S. R., Nuismer, R. J., and Buciell, R. J., "An Experimental Study of Scaling Rules for Impact Damage in Fiber Composites," *Journal of Composite Materials*, Vol. 24, 1990, pp. 559 - 570.

[7]Simitses, G. J. ,"Buckling and Postbuckling of Imperfect Cylindrical Shells: A Review," *Applied Mechanic Review*, Vol. 39, No. 10, pp. 1517 - 1524, 1986.

[8]Hibbitt, Karlsson, and Sorensen Inc., ABAQUS User Mannual, Ver. 5.5, 1995.

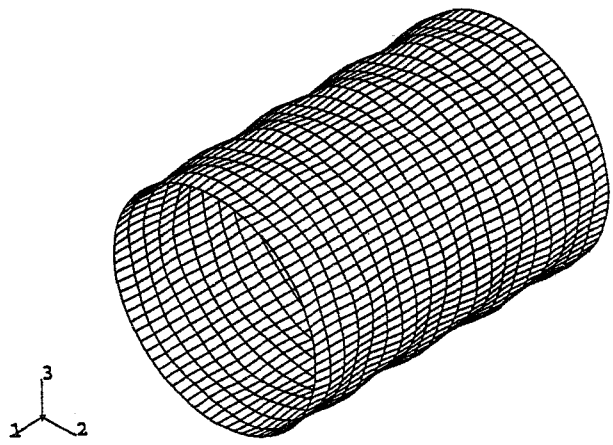

Figure 2: *Shell geometry with initial geometric imperfections.*

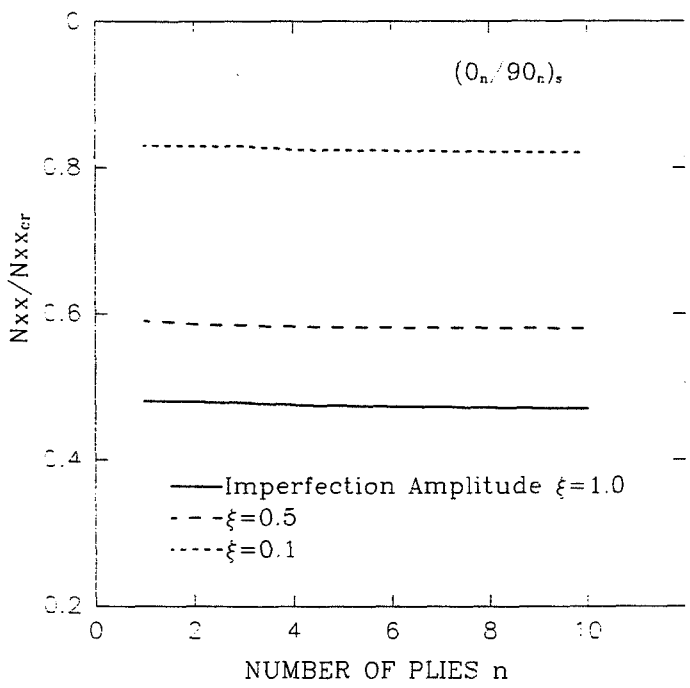

Figure 3: *Normalized Axial Critical Loads for Ply-Level Scaled Laminates.*

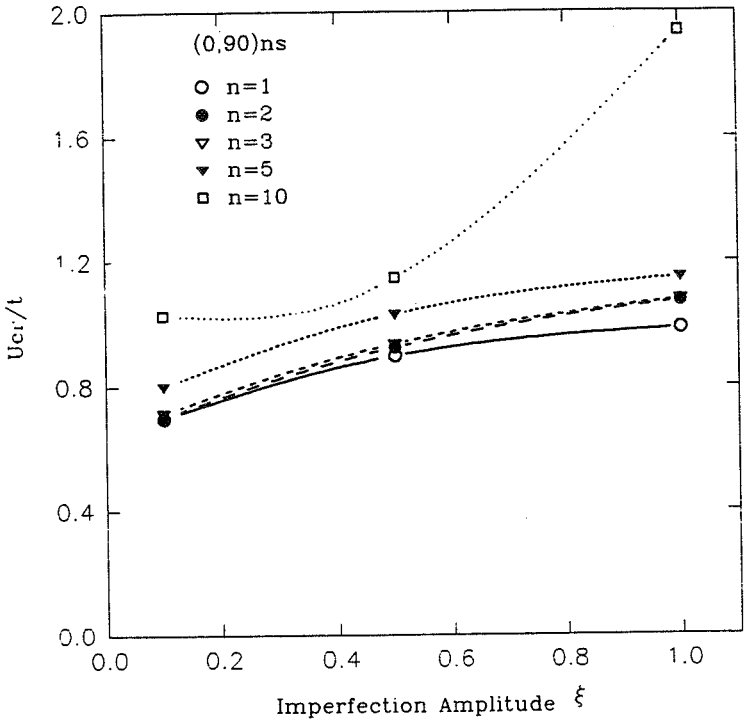

Figure 4: *Normalized Critical End-Sortning for Ply-Level Scaled Laminates.*

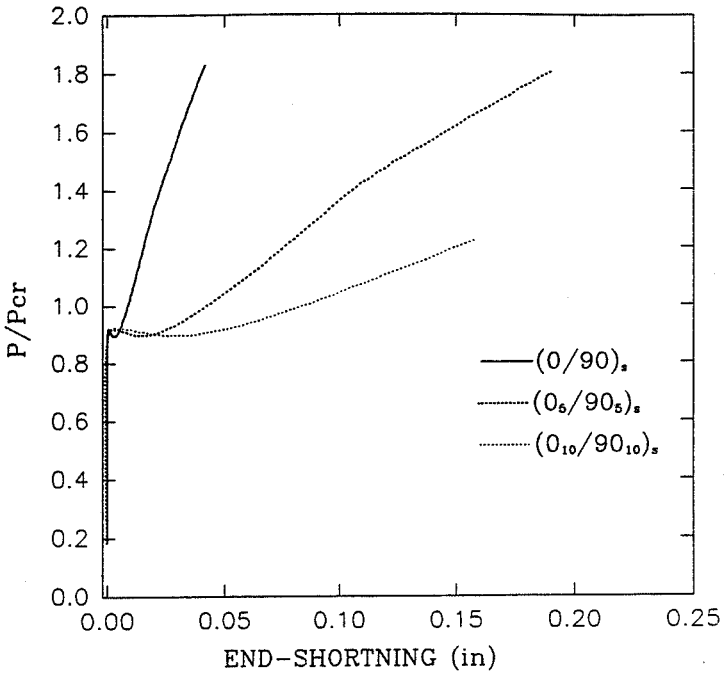

Figure 6: *Normalized Critical Lateral Pressure For Ply-Level Scaled Laminates.*

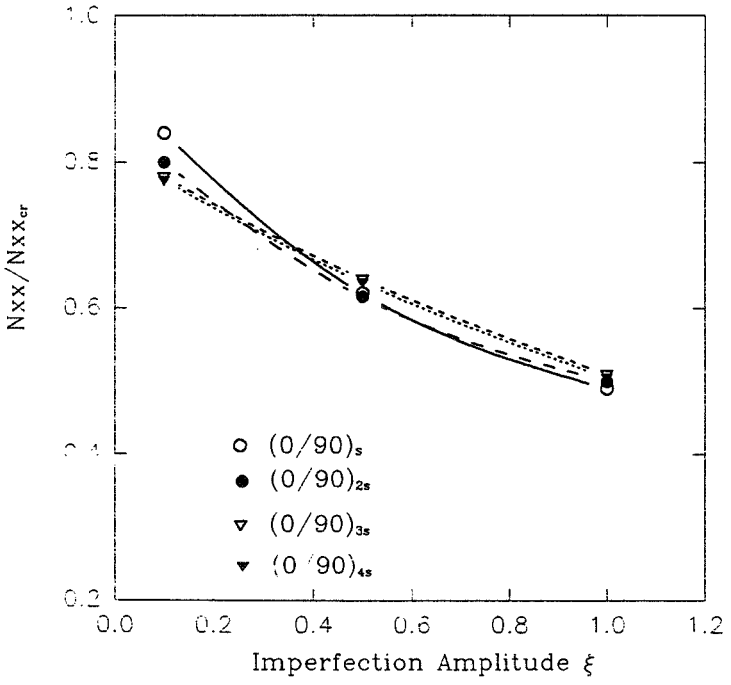

Figure 5: *Normalized Axial Critical Loads for Sublaminate-Level Scaled Laminates.*

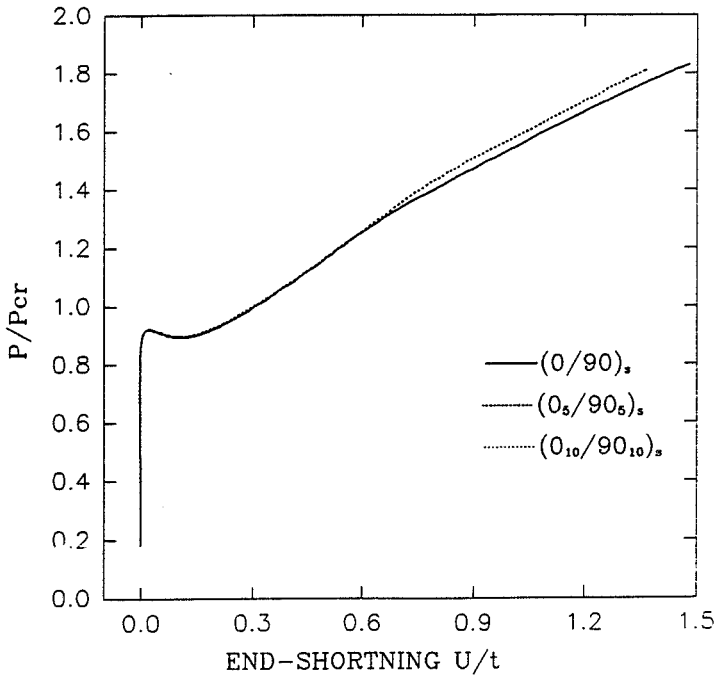

Figure 7: *Normalized Critical Lateral Pressure for Ply-Level Scaled Laminates.*

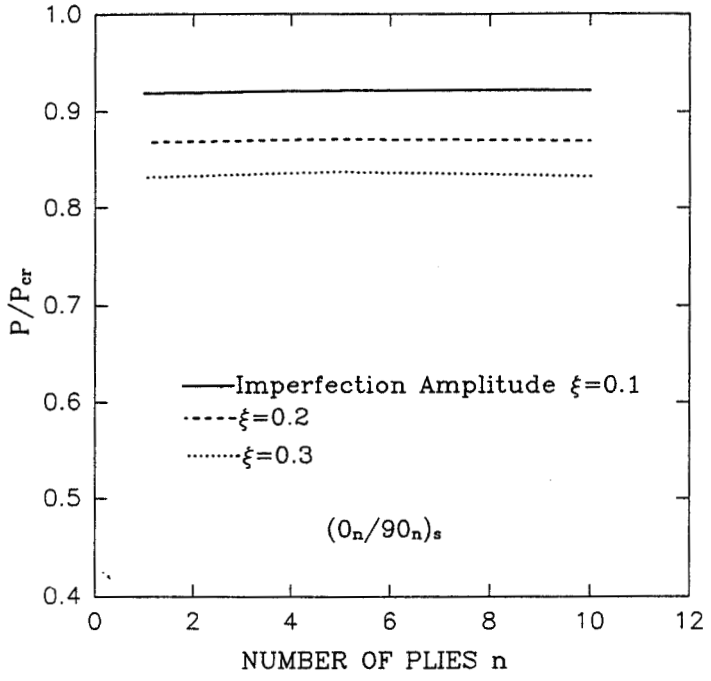

Figure 8: *Normalized Critical Lateral Pressure for Ply-Level Scaled Laminates.*

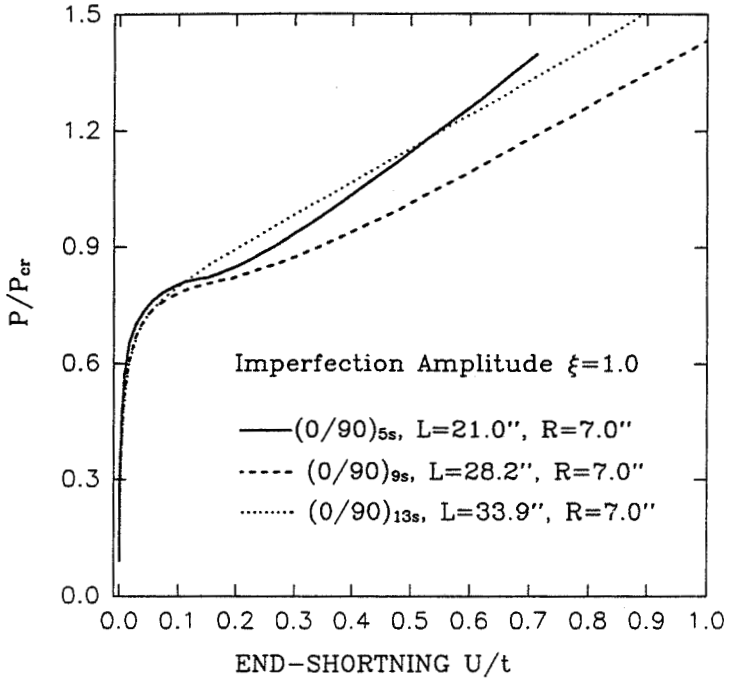

Figure 10: *Normalized Critical Lateral Pressure for Cylinders with Distortion in Thickness and Length.*

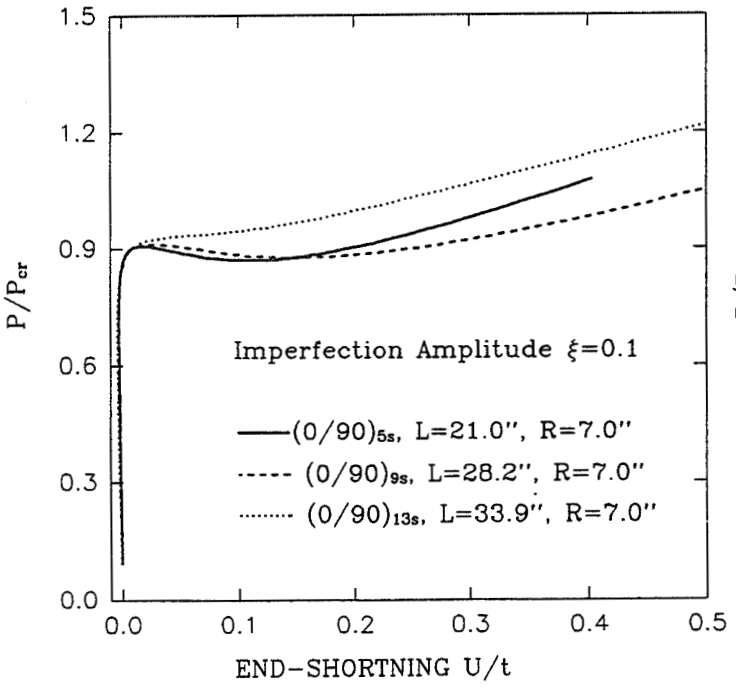

Figure 9: *Normalized Critical Lateral Pressure for Cylinders with Distortion in Thickness and Length.*

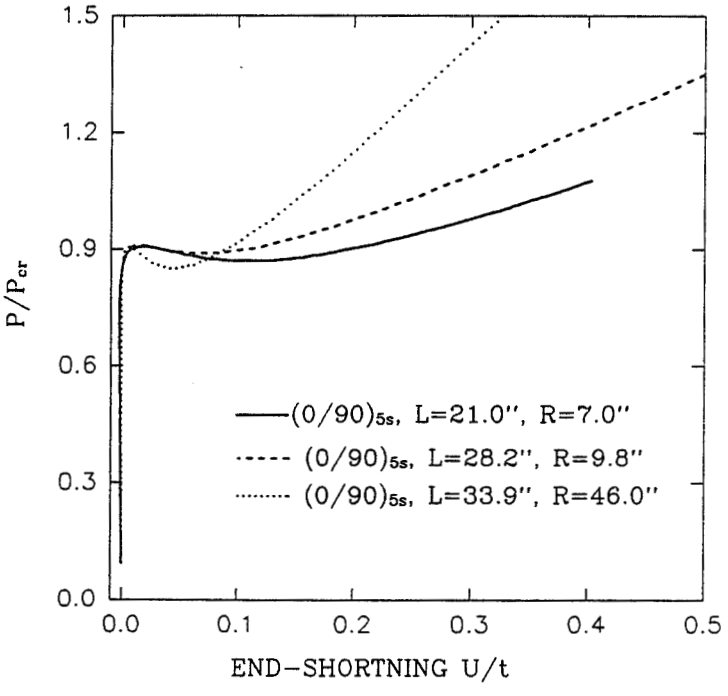

Figure 11: *Normalized Critical Lateral Pressure for Cylinders with Distortion in Length and Radii.*

OPTIMAL DESIGN OF GENERAL STIFFENED COMPOSITE CIRCULAR CYLINDERS FOR GLOBAL BUCKLING WITH STRENGTH CONSTRAINTS

Navin Jaunky* and Norman F. Knight, Jr.†
Old Dominion University
Norfolk, VA 23529-0247

Damodar R. Ambur‡
NASA Langley Research Center
Hampton, VA 23681-0001

ABSTRACT

A design strategy for optimal design of composite grid-stiffened cylinders subjected to global and local buckling constraints and, strength constraints is developed using a discrete optimizer based on a genetic algorithm. An improved smeared stiffener theory is used for the global analysis. Local buckling of skin segments are assessed using a Rayleigh-Ritz method that accounts for material anisotropy. The local buckling of stiffener segments are also assessed. Constraints on the axial membrane strain in the skin and stiffener segments are imposed to include strength criteria in the grid-stiffened cylinder design. Design variables used in this study are the axial and transverse stiffener spacings, stiffener height and thickness, skin laminate stacking sequence, and stiffening configuration, where herein stiffening configuration is a design variable that indicates the combination of axial, transverse, and diagonal stiffener in the grid-stiffened cylinder. The design optimization process is adapted to identify the best suited stiffening configurations and stiffener spacings for grid-stiffened composite cylinder with the length and radius of the cylinder, the design in-plane loads, and material properties as inputs. The effect of having axial membrane strain constraints in the skin and stiffener segments in the optimization process is also studied for selected stiffening configurations.

Nomenclature

a	Axial stiffener spacing
b	Transverse stiffener spacing
h	Stiffener height
t	Skin laminate thickness
t_s	stiffener thickness
N_1	Axial design load
$LAMI$	Design variable for stacking sequence of skin laminate
$ICON$	Design variable for stiffening configuration
λ_G	Global buckling load factor
λ_{sk}	Buckling load factor of skin segment
λ_1, λ_2, λ_3	Crippling load factor of axial transverse, and diagonal stiffener segment
S_{sk}	Strain level factor for skin segment
S_1, S_2, S_2	Strain level factor for axial transverse, and diagonal stiffener segment

Introduction

An aircraft or a launch vehicle in flight is subjected to loads associated with all flight conditions. These external loads are resisted by the structure, and an internal load distribution is established based on the structural layout and external loads. The internal loads, which depend

*Post-Doctoral Research Associate, Department of Aerospace Engineering,
†Professor, Department of Aerospace Engineering.
‡Assistant. Head, Structural Mechanics Branch,

on the location in the aerospace vehicle, may cause either overall buckling of the stiffened fuselage/fuel tank structure, buckling of the skin segment between stiffeners, or crippling of stiffener segment. A stiffened circular cylindrical shell is a widely used structural configuration for an aircraft fuselage or a launch vehicle fuel tank. An efficient and accurate analysis method is needed for developing a buckling-resistant design of general grid-stiffened composite circular cylindrical shell and to identify the most effective stiffening configurations and stiffener spacings for shells subjected to combined in-plane loading conditions. The identification of structurally efficient stiffening configurations and stiffener spacings also requires integration of optimization techniques with accurate structural analysis methods.

The optimum design of stiffened panels or shells that satisfy buckling constraints along with or without strain constraints have been of considerable interest to researchers since aircraft and launch vehicle structures consist mostly of stiffened panels or shells. Researchers have used gradient-based optimizer, discrete optimizer, and the simplex method. Gradient-based optimizer has been used in References [1] - [8]. Discrete optimizer has been used in References [9] - [13]. The simplex method has been used in References [14] and [15].

A literature survey of optimal design of stiffened panels and shells is presented in Reference [13]. The survey deals with the type of optimizers that used has been used, the type of buckling analysis, and the type of stiffened panel or shell that has been optimized. Type of stiffened panel or shell herein refers to whether the panel or shell is stiffened axially, orthogonally or in multiple directions (e.g grid-stiffened panel or shell). According to the review, optimization of panels or shells stiffened in multiple directions have been considered in Reference [5, 6, 8] and [16]. Grid-stiffened cylinders was considered in Reference [6, 8] and [16]. Geodesically stiffened flat panels were considered in Reference [5] and recently grid-stiffened curved panel were considered in Reference [13].

The survey also shows that the stiffener spacing is treated as a design variable in References [1, 2, 7, 8, 14] and [15]. Gradient-based optimizer was used in References [1, 2, 7] and [8], whereas the simplex method ([17]) was used in References [14] and [15]. The stiffener spacing is a discrete variable since it can be a certain multiple of the length or width of the panel or shell. Both gradient-based optimizer and the simplex method assume continuous variables and in addition the gradient-based optimizers require derivative information. Therefore as discussed in Reference [13] rigorous optimization with respect to stiffener spacing as a design variable is best achieved using a discrete optimizer such as the genetic algorithm ([11]).

Reddy et. al. ([16]) studied the buckling response of isogrid and orthogrid cylinders with various stiffener spacings using global and local analyses and concluded that isogrid cylinders are in general more efficient than orthogrid cylinders. It is also shown in Reference [7] that optimizing axially stiffened panels for different fixed stiffener spacings using gradient-based optimizer can be a good strategy. For panels or shells stiffened in multiple directions, this approach is tedious since one has to consider too many starting points in the optimal design process. The stiffener spacings and stiffening configurations can be treated as design variables in an optimization process provided a discrete optimizer is used. A discrete optimizer such as the genetic algorithm ([11]) has been used in References [9] - [13] in optimizing unstiffened or axially stiffened composite panels, and in Reference [18] for other engineering problems. Haftka et. al. (Ref. [9] - [12]) showed the efficiency of the genetic algorithm in dealing with discrete design variables for optimizing composite panels. They treated the skin and/or stiffener laminate as discrete variables since in practical applications, the ply orientations are limited to 0, 90 or ± 45 degrees and, the laminate thickness can only be integer multiples of commercially available ply thickness. Jaunky et. al. ([13]) optimized flat and curved grid-stiffened panels with stiffener height and thickness, skin laminate, stiffener spacings, and stiffening configuration as design variables with a global buckling constraint only and showed that the efficiency of the genetic algorithm in dealing with all these discrete design variables that affect the buckling response of grid-stiffened panels.

The literature survey in Reference [13] also comments about the buckling analyses that have been used. Finite element analysis (e.g. Ref. [6]), discrete analysis (e.g. Ref. [5]), PASCO ([19]) type analysis (e.g. [3]), and global and local analyses. The merits of these type of analyses are discussed in Reference [13]. Most researchers have used global and local analyses and local analyses.

Examples are References [1, 2, 7, 8, 14, 15, 16] and [13]. Global and local analyses can be made computationally very efficient. Researchers have neglected the anisotropic properties of skin segments in the local buckling analysis, and also the curvature of the skin segments. Restrictions on the geometry of the skin segment and loading were imposed in order to obtain closed-form solution for the buckling response. In some cases the eccentricities of the stiffener were even neglected. The main problem of assessing the local buckling of the skin segment was the non-availability of computationally efficient and accurate buckling analyses for curved skin segments with anisotropic material properties, and different planform geometry (e.g. general triangular and arbitrary quadrilateral geometry). In Reference [13] accurate buckling analyses (Ref. [21, 22] and [23]) were used for global and local analyses, and the occurrence of non-simultaneous of global and local failure were used as this condition leads to design that are less sensitive to imperfections as discussed in Reference [15].

The present paper will present the analysis and weight optimization strategy for grid-stiffened composite circular cylindrical shells subjected to axial load and a global buckling design constraint as well as strength constraints using the genetic algorithm. Design variables are the stiffener height and thickness, skin laminate, stiffener spacings, and stiffening configuration. It is intended at developing a design tool that can be used at a preliminary design stage for grid-stiffened cylinders for aircraft fuselage or launch vehicle application. To the authors' opinion such a tool for cylinders stiffened in multiple directions is lacking. Results will be presented and discussed for cylinder designs with and without strength or strain constraints which explains the damage tolerant characteristics of grid-stiffened structures [20].

Shell Buckling Analysis

The buckling analysis of grid-stiffened composite shells subjected to combined loads requires several key steps. In the present study, acceptable designs are those which buckle globally and do not exhibit any local skin buckling or stiffener crippling. The first step in the design process is to assess the global buckling response of a grid-stiffened shell. Once this global buckling response is determined, the second step is to determine the local skin buckling response for the quadrilateral and/or triangular skin segments between the stiffeners. The third step is to determine whether stiffener buckling or stiffener crippling has occurred at this global buckling load level.

The global buckling analysis is based on a Rayleigh-Ritz method using a first-order, shear-deformation theory and the improved smeared-stiffener modeling approach discussed in [21] that accounts for skin-stiffener interactions. It is shown in Reference [21] that buckling loads for stiffened panels with different stiffening configurations obtained using the improved smeared stiffener theory are in good agreement with results obtained using detailed finite element analysis. The cylinder is assumed to be simply supported and hence, the Rayleigh-Ritz method for the global analysis assumes the following mode shape for the transverse deflection w:

$$w = \sum_{i=1}^{N} (A_{m_i n_i} sin\frac{n_i y}{R} + B_{m_i n_i} cos\frac{n_i y}{R}) sin\frac{m_i \pi x}{L} \quad (1)$$

where L and R are the length and radius of the cylindrical shell, respectively, and N is the number of terms in the Fourier series. The coordinate system for the cylinder is shown in Figure 1.

The buckling analysis of local skin-segments is also based on a Rayleigh-Ritz analysis using a first-order, shear-deformation theory and accounts for material anisotropy. Boundary restraints on the skin segments are provided by the stiffeners and hence, the analysis must be capable of accommodating a variety of boundary conditions and a variety of skin-segment shapes [22, 23]. In most cases, the skin segments for grid-stiffened panels will have either a general parallelogram-shaped or a general triangular-shaped planform. The skin segments are assumed to have simply supported boundary conditions in the present study. It is shown in References [22] and [23] the buckling analyses presented for arbitrary anisotropic quadrilateral plates and general triangular anisotropic plates can accommodate different boundary conditions, and provide buckling loads that are in very good agreement with finite element analysis and existing solutions. The Rayleigh-Ritz buckling analysis method for the global and local analysis makes use of the Sanders-Koiter shell theory [24, 25]. This shell theory provides buckling loads that are in good agreement with finite element analysis compared

to other shell theories as shown in Refences [26] and [27].

In addition to analyzing the local skin segment for buckling, the local stiffener segments must be analyzed to determine whether stiffener crippling will occur. Reference [16] provides a method for determining the crippling load of a stiffener segment. Accordingly, the stiffener segment is assumed to be clamped at the nodes or intersection points of the stiffeners while the edge of the stiffener along the stiffener-skin attachment line is assumed to be a simply supported.

The global buckling load is assumed to be a scalar multiple of the design load and has the form

$$N_x = \lambda_G N_1 \tag{2}$$

where N_1 is the applied prebuckling axial load and represents the design load. Once the global buckling load factor (λ_G) has been determined using the improved smeared stiffener theory, the loads acting on the stiffener and skin segments have to be determined by distributing the loads based on the extensional stiffness of the skin and the stiffener. The procedure for distributing the applied loads for a general grid-stiffened panel is discussed in References [5] and [26] and is the same for a general grid-stiffened circular cylindrical shell. The loads acting on the skin and stiffener segments are computed based on a global load of $N_x = \lambda_G N_1$ and these loads are used to determine the local buckling load factor of the skin, (λ_{sk}), local crippling factors of axial stiffener segment, (λ_1), transverse stiffener segment, (λ_2) and diagonal stiffener segment, (λ_3). The local buckling load factors of each stiffener segment type and skin segment is

$$\lambda_i = \frac{critical\ \ load\ \ of\ \ local\ \ segment}{load\ \ in\ \ local\ \ segment\ \ due\ \ to\ \ \lambda_G \times N_1} \tag{3}$$

where i = 1, 2, 3 and sk. These local buckling and crippling load factors describe the buckling characteristics of the stiffened cylinder and is as follows

- For $\lambda_{sk}, \lambda_1, \lambda_2, \lambda_3 \geq 1.0$, then the cylinder buckles globally at an axial load of $\lambda_G N_1$, i.e., $\lambda_{cr} = \lambda_G$.
- If one of λ_{sk}, λ_1, λ_2, $\lambda_3 < 1.0$, then the stiffened cylinder buckles locally. If $\lambda_{sk} <$ 1.0, then skin buckling occurs, and if λ_1 < 1.0 then crippling of the axial stiffener occurs. For this case, $\lambda_{cr} = \lambda_i \times \lambda_G$ where λ_i is < 1.0, and subscript i can be any one of sk, 1, 2 or 3.
- If more than one of λ_{sk}, λ_1, λ_2 and λ_3 are < 1.0, then local buckling of the stiffened cylinder occurs and $\lambda_{cr} = \lambda_i \times \lambda_G$ where λ_i is the minimum of any of λ_{sk}, λ_1, λ_2 or λ_3 with values < 1.0.

Strain Analysis

The critical buckling load of the stiffened cylinder is $\lambda_{cr} N_1$ where λ_{cr} takes on values as discussed previously and based on this load value the loads acting on the skin and stiffeners segments are obtained [5, 26]. For an axial load in the skin segment of N_{xsk}, and the loads in axial, transverse and diagonal stiffener segments of N_{x1}, N_{x2} and N_{x3}, respectively, the axial membrane strain in the skin and stiffener segments are

$$\begin{aligned}
\epsilon^0_{xsk} &= a^{(sk)}_{11} N_{xsk} + a^{(sk)}_{12} N_{ysk} + a^{(sk)}_{16} N_{xysk} \\
\epsilon^0_{x1} &= a^{(1)}_{11} N_{x1} \\
\epsilon^0_{x2} &= a^{(2)}_{11} N_{x2} \\
\epsilon^0_{x3} &= a^{(3)}_{11} N_{x3}
\end{aligned} \tag{4}$$

where ϵ^0_{xsk}, ϵ^0_{x1}, ϵ^0_{x2} and ϵ^0_{x3} are the axial membrane strains in the skin segment, axial, transverse, and diagonal stiffener segments respectively. The quantities $a^{(sk)}_{ij}$, $a^{(1)}_{11}$, $a^{(2)}_{11}$, and $a^{(3)}_{11}$ are axial flexibilities of the skin, axial, transverse, and diagonal stiffeners respectively.

The strain level factors for the skin, axial, transverse, and diagonal stiffener segment are

$$\begin{aligned}
S_{sk} &= (\epsilon^0_{xsk})_{al} \,/\, \epsilon^0_{xsk} \\
S_1 &= (\epsilon^0_{xst})_{al} \,/\, \epsilon^0_{x1} \\
S_2 &= (\epsilon^0_{xst})_{al} \,/\, \epsilon^0_{x2} \\
S_3 &= (\epsilon^0_{xst})_{al} \,/\, \epsilon^0_{x3}
\end{aligned} \tag{5}$$

where $(\epsilon^0_{xsk})_{al}$ and $(\epsilon^0_{xst})_{al}$ are the allowable axial membrane strains in the skin and stiffeners, respectively. The values for $(\epsilon^0_{xsk})_{al}$ and $(\epsilon^0_{xst})_{al}$ are taken from Reference [28].

These global and local buckling analysis methods and the strain analysis have been integrated into a computer code to provide a computationally efficient tool for predicting the buckling load and the strain level factors of grid-stiffened composite circular cylindrical shells subjected to axial compression.

Shell Design Procedure

The design variables for a grid-stiffened composite shell are the axial and transverse stiffener spacings (a, b), the stiffening configuration ($ICON$), which is the combination of axial, transverse and diagonal stiffeners, the skin laminate ($LAMI$), and the height (h), and thickness (t_s) of the stiffener. Except for the height of the stiffener, these design variables take on discrete values. Hence gradient-based optimization methods are not suitable for optimal design grid-stiffened shells. Furthermore, due to manufacturing constraints a "family" of good designs is needed rather than a single point design.

The genetic algorithm is a method for "evolving" a given design problem to a family of near-optimum designs (e.g., see References [10], [11], [13] and [18]). Stochastic processes are used to generate an initial population of individual designs and the process then applies principles of natural selection and survival of the fittest to find improved designs. Furthermore, since the discrete design procedure works with a population of designs it can explore a large design space and climb different hills. This is a major advantage as the converged solution may contains many optima of comparable performance. The cost of having a large number of function evaluations is offset by the fact that a large number of optimum solutions are now available. The population or family of good designs produced by using the genetic algorithm may include the global optimal design, rather than a single design. Hence, it is an appropriate tool for designing general grid-stiffened composite shells.

Design Problem Definition

The present design problem is to minimize the weight of a grid-stiffened composite circular cylindrical shell given the design loading condition, the length and radius of the cylinder, and the material properties for the skin and stiffeners. The design variables include stiffener spacings (a, b), the stacking sequence of the skin, stiffener layout, stiffener thickness (t_s), and stiffener height (h) as shown in Figure 1. All stiffeners are assumed to be of the same height and thickness for manufacturing and assembly reasons. The design sought here is a cylinder of minimum weight in a certain design space which buckles globally at the design loads while the axial membrane strain in the skin and the stiffener segments do not exceed the allowable axial membrane strain $(\epsilon^0_{xsk})_{al}$ and $(\epsilon^0_{xst})_{al}$ respectively. This design problem can be defined by setting up the optimization procedures in the following way. First, the global buckling load is assumed to be a scalar multiple of design loads and has the form

$$N_x = \lambda_G N_1, \tag{6}$$

where N_1 is the applied in-plane prebuckling load. This values represent the design loads for the grid-stiffened cylinder. Second, the design constraints imposed on panel include

1. The critical buckling load should be greater than or equal to the design loads, that is, $\lambda_G \geq 1$.
2. Skin segments should not buckle at the critical buckling load, that is, $\lambda_{sk} \geq 1$.
3. Stiffener segments should not cripple at the critical buckling load, that is, $\lambda_1,\ \lambda_2,\ \lambda_3 \geq 1$.
4. The axial membrane strain in the skin segment should be greater than or equal $(\epsilon^0_{xsk})_{al}$, that is, $S_{sk} \geq 1$.
5. The axial membrane strain in the stiffener segment should be greater than or equal $(\epsilon^0_{xst})_{al}$, that is, $S_1,\ S_2,\ S_3 \geq 1$.

The general form of each constraint equation is written as

$$g_j = \begin{cases} (\frac{1}{\lambda_j} - 1) \leq 0.0 \\ (\frac{1}{S_j} - 1) \leq 0.0 \end{cases} \quad j = 1, ..., N_c \tag{7}$$

Finally, the "Fitness" expression based on exterior penalty function approach is

$$\text{Fitness} = \quad (\frac{Q}{F(\mathbf{X}, r_i)}) = \text{Max} \frac{Q}{W(\mathbf{X}) + r_i \sum_j^{N_c} \ [|g_j(\mathbf{X})| + g_j(\mathbf{X})]^2} \tag{8}$$

where $\mathbf{X}$ = design variable vector
$F(\mathbf{X}, r_i)$ = Modified objective function
$W(\mathbf{X})$ = weight of panel per unit area
$r_i \sum_j^{N_c} \ [|g_j(\mathbf{X})| + g_j(\mathbf{X})]^2$ = penalty function
Q = normalizing constant
N_c = Number of design constraints
r_i = penalty parameter
i = generation or iteration cycle in the optimization procedure.

Design Process Based on Genetic Algorithm

Implementation of the genetic algorithm ([11]) is shown schematically in Figure 2. The design process begins with a random selection of a specified number of designs which comprise the initial population (i.e., first generation) for the genetic algorithm. Material properties, radius and length of the cylinder, boundary conditions of the skin segment, and design loadings are input to the analysis processor routine. The buckling analysis is performed which provides the critical eigenvalues for the global buckling response of the grid-stiffened cylinder, the local buckling response of the skin and stiffener segments, and the strain level factors of the skin and stiffener segments. The weight of the grid-stiffened cylinder is also computed. This procedure is repeated for each design configuration in the population. The "fitness" processor then evaluates the "fitness" of each design using Equation (8) and assigns a rank based on the fitness expression or objective function. The current population of design configurations is then processed by the genetic operators (crossover, mutation, and permutation) to create a new population of design configurations for the next generations which combines the most desirable characteristics of previous generations. Designs from previous generations may be replaced by new ones (i.e., children) except for the "most fit" designs (i.e., parents) which are always included in the next generation. The process is repeated until design convergence is obtained, which is defined herein by specifying a maximum number of generations ($NSTOP$) that may occur without improvement in the best design. The design procedure will now be demonstrated on grid-stiffened cylinders with and without the axial membrane strain constraint in the skin and stiffener segments to study the influence of constraints on the axial membrane strain on the optimal designs.

Numerical Results for Grid-stiffened Cylinders

Results are presented for composite grid-stiffened cylinders subjected to axial compression in order to demonstrate the changes in optimal designs due to constraints on the axial membrane strain. These changes will depend on the loading, stiffening configuration ($ICON$), and stiffener spacings (a, b), and the skin laminate ($LAMI$). The cylinders studied in examples 1 and 2 are 291.0-in.-long and have a radius of 95.5 in. and have blade stiffeners made of unidirectional materials [16]. The nominal ply mechanical properties are: E_{11} = 18.500 Msi; E_{22} = 1.640 Msi; G_{12}=G_{13}=G_{23} = 0.870 Msi and ν_{12} = 0.300. The mass density of the material ρ, is 0.057 lbs/in^3. The probabilities used for crossover, mutation, and permutation are 1.0, 0.10 and 0.95, respectively, and the number of discrete values that each design variable can accommodate is eight which is a limitation of the FORTRAN code being used. The design variables $ICON$ and $LAMI$ are described in Table 1.

Example 1

The first example is a cylinder subjected to an axial load of N_1 = 1000 lbs/in. which represents a cylinder case studied in Ref. [16]. The design variables are the axial and transverse stiffener spacings, the height and thickness of the stiffeners, the stiffening configuration ($ICON$), and the skin laminate ($LAMI$). The thickness of each ply of the skin laminate for this example is 0.006 in. The design space for a, b, h, and t_s is shown in Table 2. The height and thickness of the stiffener is chosen such that the aspect ratio (h/t), of the stiffener is between 4 and 10, and the stiffener thickness is an integer multiple of 0.006 in. due to manufacturing constraints. The minimum values of the stiffener spacings are also due to manufacturing constraints. A population size of 20 is used $NSTOP$ = 15, and the penalty parameter r_i = 100,000 at any iteration. The allowable strains $(\epsilon^0_{xsk})_{al}$ and $(\epsilon^0_{xst})_{al}$ are 2428μ in./in. and 1092μ in./in., respectively ([28]).

The results from design optimization with and without strain constraints are shown in Table 3. The minimum weight for this cylinder is 1061.6 lbs compared to the weights of 1058 lbs for an isogrid cylinder and 1053 lbs for an orthogrid cylinder presented in Ref. [16]. Only three optimal designs are identify here and they all buckle globally at their respective λ_G values since λ_{sk} and λ_3 values are greater than 1. For this case, the optimal designs have $ICON$ = 6, that is the stiffening configuration has transverse and diagonal stiffeners only, and $LAMI$ = 4, which corresponds to a skin laminate which a stacking sequence of $[\pm 45/0_2]_{2s}$, h = 0.4 in., and t_s = 0.048 in. In this case, the optimal designs without strain constraints are the same as the optimal design with strain constraints. The buckling-resistant design for this load case results in in-plane stiffness values that provide large strain level factors. This

analysis suggests that the cylinder design satisfies both buckling and strength requirement. Convergence is obtained after 49 generations for the case without strain constraints and after 77 generations for the case with strain constraints.

Example 2

The second example is for a grid-stiffened cylinder as in Example 1 but subjected to an axial load of $N_1 = 1800$ lbs/in. For this case, the stiffening configuration with axial and diagonal stiffeners only ($ICON$)has been selected. The design variables are the axial and transverse stiffener spacings, the height and thickness of the stiffeners, and the skin laminate with each ply being 0.008-in. thick. The design space for the skin laminate is the same as shown in Table 1, and the design space for a, b, h and t_s is shown in Table 2. The material properties, the genetic parameters and the strain allowables for Example 2 are same as in Example 1. The optimal designs without strain constraints are shown in Table 4, whereas the optimal designs with strain constraints are shown in Table 5. Only three optimal designs are shown here for each case.

All the designs in Tables 4 and 5 buckle globally since λ_{sk}, λ_1 and λ_3 are all greater than one. The optimal designs obtained with constraints on the axial strain are about 9 to 14 lbs heavier than the optimal designs obtained without constraints on the axial strain for approximately the same global buckling load. The designs in Table 5 have larger axial stiffener spacing (a) than the second and third designs in Table 4. For the designs in Table 5, the strain level factors of the axial stiffeners (S_1), are very close to unity whereas the strain factors for the diagonal stiffeners (S_1) are much larger. The increase in structural weight of the optimums design for this case over the designs in Example 1 is due to the increase in load and the choice of stiffening configuration. Even for this load condition, imposing strain constraints does not result in a significant increase in weight. Convergence is obtained after 18 generations for the case without strain constraints and after 41 generations for the case with strain constraints.

Example 3

The third example is a grid-stiffened cylinder subjected to an axial load of $N_1 = 2000$ lbs/in. This represents a generic, wide body transport aircraft fuselage section between two frames. The radius of the cylinder is 95.5-in. and the length is 22-in. The design variables are the transverse stiffener spacing, the height and thickness of the stiffeners, and the skin laminate with each ply being 0.009-in. thick. The optimization is performed with the stiffening configuration selected to $ICON = 1$ and $ICON = 5$. For the case when $ICON = 5$, the axial stiffener spacing is 6.2857 in. The design space for the skin laminate is the same as shown in Table 1. and the design space for b, h and t_s is shown in Table 6. The material properties and the genetic parameters for Example 3 is same as in Example 1. Three optimal designs obtained with strain constraints are shown in Table 7 for the axially stiffened cylinders and in Table 8 for the cylinders stiffened with axial and diagonal stiffeners. For axially stiffened cylinders convergence is obtained at 38 generations, while for the cylinders with axial and diagonal stiffeners, convergence is obtained at 20 generations.

All the optimal designs in Tables 7 and 8 buckle globally and do not violate any strain constraint. However, the optimal designs with $ICON$=5 are slightly heavier than the optimal designs with $ICON$=1. The buckling behavior of the first design in Table 7 and Table 8 subjected to an axial load of $N_x = 2000$ lbs/in. and combined transverse compression (N_y), and shear (N_{xy}) is sought to determine their capability to support additional in-plane loads. A load combination for $N_x = 2000$ lbs/in., N_y and N_{xy} is sought in such a way that the cylinder can still support an axial load of $N_x = 2000$ lbs/in., i.e., $\lambda_{cr} \geq 1$ and $\lambda_{cr} \approx 1$. The results are shown in Table 9 for the axially stiffened cylinder and in Table 10 for the grid-stiffened cylinder with $ICON = 5$. It is seen that the grid-stiffened cylinder can support up to 400 lbs/in. of transverse compression and 400 lbs/in. in shear whereas the axially stiffened cylinder can only support additional loads of 20 lbs/in. in transverse compression and 220 lbs/in. in shear without exceeding the strain allowables. It is assumed here that the strains ϵ_y, and γ_{xy} due to N_y and N_{xy} do not produce strains large enough to create failure since N_y and N_{xy} are small compared to N_x. For these loading combinations, both cylinders buckle globally and the constraint on the axial membrane strains in the skin and stiffener are not violated. Hence the grid-stiffened cylinder can sustain larger magnitudes of additional transverse compression and shear loads than the axially stiffened cylinder.

Concluding Remarks

A minimum-weight design optimization tool with global buckling constraint and constraint on the axial membrane strain in the skin and stiffener segments has been developed for grid-stiffened cylinders using global and local buckling analyses and a genetic algorithm. Design variables used are axial and transverse stiffener spacing, stiffener height and thickness, skin-laminate stacking sequence, and stiffening configuration. The present design optimization procedure has been validated by comparing with existing results. Results for grid-stiffened cylinders subjected to axial compression indicate that there is no significant difference in weight between optimal designs obtained with and without strain constraints for simply supported cylinders that buckle globally. It is also shown that a grid-stiffened cylinder optimized for axial load has a larger additional load capacity for combined loading than for a conventional axially stiffened cylinder. This additional load capability permits load redistribution in the event of structural damage and suggests that a grid-stiffened cylinder is more damage tolerant than an axially stiffened cylinder.

Acknowledgement

The work of the first two authors was supported by NASA Grant NAG-1-1588 and is gratefully acknowledged.

References

[1] Schmit L., A., Kicher T., P., and Morrow W., M., "Structural Synthesis Capability for Integrally Stiffened Waffle Plates," *AIAA Journal*, Vol. 1, No. 12, 1963, pp. 2820-2836.

[2] Jones, R., T., and Hague D., S., "Application of Multivariable Search Techniques to Structural Design Optimization," NASA CR-2038, June 1972.

[3] Stroud W. J., "Optimization of Composite Structures," IUTAM Proceedings for Mechanics of Composite Materials-Recent Advances, Hashin and Harakovich (Editors), 1982.

[4] Yung S. Shin, Haftka, R. T., Watson L. T., and Plaut R. H., "Design of Laminated Plates for Maximum Buckling Load," *Journal of Composite Materials*, Vol. 23, April 1989, pp. 348-369.

[5] Phillips, J. L. and Gurdal, Z., "Structural Analysis and Optimum Design of Geodesically Stiffened Composite Panels," Report CCMS-90-05, Center for Composite Materials and Structures, Virginia Polytechnic Institute and State University, Blacksburg, VA, July 1990.

[6] Gendron, G., and Gurdal, Z., "Optimal Design of Geodesically Stiffened Composite Cylindrical Shell," Proceedings of the 33rd AIAA/ASME/ASCE/AHS/ASC Structures, Structural Dynamics, and Materials Conference, Dallas, TX, AIAA Paper No. 92-2306-CP, April 13-15, 1992, pp. 2431-2441.

[7] Bushnell, D., and Bushnell, W. D., "Approximate Method for Optimum Design of Ring and Stringer Stiffened Cylindrical Panels and Shells with Local, Interring, and General Buckling Modal Imperfections," *Computers and Structures*, Vol. 59, No. 3, 1996, pp. 489-527.

[8] Bushnell, D., "Recent Enhancements to PANDA2," Proceedings of the 37^{th} AIAA/ASME/ASCE/AHS/ASC Structures, Structural Dynamics, and Materials Conference, Salt Lake City, UT, AIAA Paper No. 96-1337-CP, April, 15-17, 1996, pp. 126-182.

[9] Nagendra, S., Haftka, R. T., and Gurdal, Z., "Stacking Sequence Optimization of Simply Supported Plates with Stability and Strain Constraints," *AIAA Journal*, Vol. 30. No. 8, August 1992, pp. 2132-2137.

[10] Nagendra, S., Haftka, R. T., and Gurdal, Z., "Design of a Blade Stiffened Composite Panel by Genetic Algorithm," Proceedings of the 34th AIAA/ASME/ASCE/AHS/ASC Structures, Structural Dynamics and Materials Conference, AIAA Paper No. 93-1584-CP, April 1993, La Jolla, CA, pp. 2418-2436.

[11] Leriche, R., and Haftka, R. T., "Optimization of Laminate Stacking Sequence for Buckling Load Maximization by Genetic Algorithm," *AIAA Journal*, Vol. 31, No. 5, May 1993, pp. 951-956.

[12] Harrison, P., N., Leriche, R., and Haftka, R., T., " Design of Stiffened Panels by Genetic Algorithm and Response Surface Approximations," Proceedings of 36^{th} AIAA/ ASME/ASCE/AHS/ASC Structures, Structural Dynamics, and Materials Conference, New Orleans, LA, AIAA Paper No. 95-1163-CP, April 10-13, 1995, pp. 58-68.

[13] Jaunky, N., Knight, N. F. and Ambur, D. R., "Optimal Design of Grid-stiffened Composite Panels Using Global and Local Buckling Analyses," To appear in *Journal of Aircraft.*

[14] Simites G. J., and Ungbhakorn V., "Minimum-Weight Design of stiffened Cylinders Under Axial Compression," *AIAA Journal*, Vol. 13, No. 6, 1975. pp. 750-755.

[15] Simitses, G. J., "Optimization of Stiffened Cylindrical Shells Subjected to Destabilizing Loads," *Structural Optimization: Status and Promise*, Progress in Astronautics and Aeronautics, Volume 150, Manohar P. Kamat (editor), A. R. Seebass (Editor-in-Chief), Published by the American Institute of Aeronautics and Astronautics, Inc., 1992, pp. 663-704.

[16] Reddy, A. D., Valisetty, Rao R., and Rehfield, L. W., "Continuous Filament Wound Composite Concepts for Aircraft Fuselage Structures," *Journal of Aircraft*, Vol. 22, No. 3, March 1985, pp. 249-255.

[17] Nelder, J. A., and Mead, R., "A Simplex Method for Function Minimization ," *Computer Journal*, Vol. 7, 1964, pp. 308-313.

[18] Whitney, S. A., "Formulation of Genetic Algorithm for Solution of Engineering Designs," Old Dominion University, Norfolk, VA, Master's Thesis, May 1995.

[19] Anderson, M. S., Stroud, W. J., Durling, B. J., and Hennessy, K. W., "PASCO: Structural Panel Analysis and Sizing Code. User's Manual," NASA TM 80182, November 1981.

[20] Rouse, M., and Ambur, D. R., "Damage Tolerance and Failure Analysis of a Geodesically Stiffened Structure Loaded in Axial Compression," AIAA Paper No. 94-1534, Proceedings of the 35th AIAA/ASME/ ASCE/AHS/ASC Structures, Structural Dynamics, and Materials Conference, Hilton Head, SC, April 18-21, 1994, pp. 1691-1698.

[21] Jaunky, N., Knight, N. F. and Ambur, D. R., "An Improved Smeared Theory for Buckling Analysis of Grid-Stiffened Composite Panels," *Composite: Part B* (formerly *International Journal for Composite engineering*), Vol. 27B, No. 5, 1996, pp. 519-526.

[22] Jaunky, N., Knight, N. F. and Ambur, D. R., "Buckling of Arbitrary Quadrilateral Anisotropic Plates," *AIAA Journal*, Vol. 33, May 1995, pp. 938-944.

[23] Jaunky, N., Knight, N. F. and Ambur, D. R., "Buckling Analysis of General Triangular Anisotropic Plates using Polynomials," *AIAA Journal*, Vol. 33, December 1995, pp. 2414-2417.

[24] Sanders, J. L. Jr., "An Improved First Approximation Theory for Thin Shells," NASA Report R-24, 1959.

[25] Koiter, W. T., "A Consistent First Approximation in General Theory of Thin Elastic Shells," The Theory of Thin Elastic Shells, Proceedings IUTAM Symposium, Delft, pp. 12-33, 1960, Amsterdam, the Netherlands, North-Holland Publishing Company.

[26] Jaunky, N., "Buckling Analysis and Optimum Design of Multidirectionally Stiffened Composite Curved Panel," Old Dominion University, Norfolk, VA, Ph. D. Dissertation, December 1995.

[27] Yi-Wei Li, Isaac Elishaoff, James H. Starnes, and David Bushnel, "Effect of the Thickness Variation and Initial Imperfection on Buckling of Composite Cylindrical Shells: Asymptotic Analysis and Numerical Results by BOSOR4 and PANDA2", To appear in the International Journal of Solids and Structures.

[28] Personal Communications with Dr. Damodar R. Ambur, Structures Division, NASA Langley Research Center.

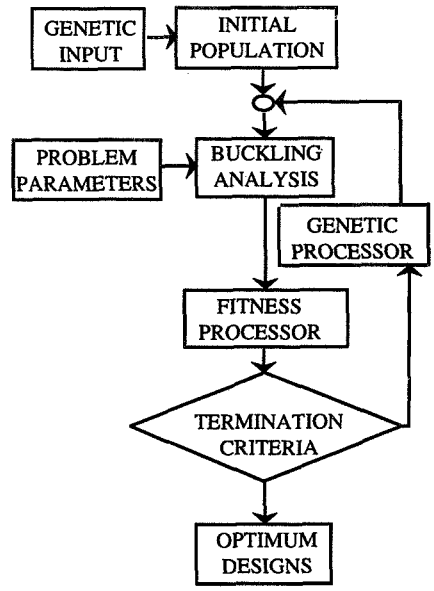

Figure 2 Flow chart for the optimization procedure using the genetic algorithm

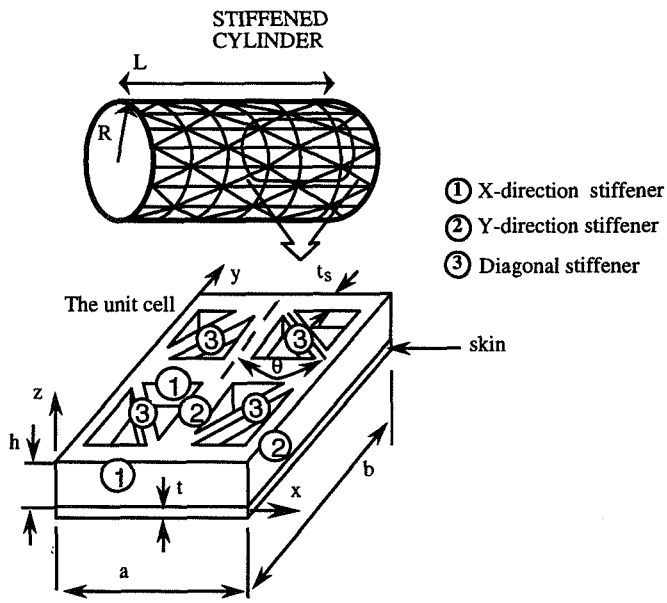

Figure 1 Unit cell of a grid-stiffened cylinder showing design variables

Table 1 Design space for design variables $ICON$ and $LAMI$.

Integer value	$LAMI$	$ICON$
1	$[\pm 45/0]_{2s}$	axial stiffeners
2	$[\pm 45/90]_{2s}$	axial stiffeners
3	$[\pm 45/0/90]_{2s}$	axial and transverse stiffeners
4	$[\pm 45/0_2]_{2s}$	diagonal stiffeners
5	$[\pm 45/90_2]_{2s}$	axial and diagonal stiffeners
6	$[\pm 45/0_2/90]_{2s}$	transverse and diagonal stiffeners
7	$[\pm 45/0/90_2]_{2s}$	axial, transverse and diagonal stiffeners
8	$[\pm 45/0_2/90_2]_{2s}$	no stiffeners

Table 2 Design space for a, b, h, and t_s for Example 1 and 2.

a, in.	8.559	8.314	8.083	7.864	7.657	7.461	7.275	7.097
b, in.	20.689	20.000	19.355	18.750	18.182	17.143	17.647	16.667
h, in.	0.400	0.4125	0.4250	0.4375	0.4500	0.4625	0.4750	0.4875
t_s, in.	0.048	0.054	0.060	0.066	0.072	0.078	0.084	0.090

Table 3 Best designs obtained by genetic algorithm for grid-stiffened cylinders (N_x = 1000 lbs/in).

Design variables (in.)	Weight (lbs)	λ_i	S_i
$a = 7.461$, $b = 20.689$	1061.6	$\lambda_G = 1.008$	$S_{sk} = 2.68$
$h = 0.4$, $t_s = 0.048$		$\lambda_{sk} = 1.009$	$S_3 = 105.1$
$LAMI$= 4, $ICON = 6$		$\lambda_3 = 55.1$	
$a = 7.461$, $b = 19.355$	1062.0	$\lambda_G = 1.025$	$S_{sk} = 2.63$
$h = 0.4$, $t_s = 0.048$		$\lambda_{sk} = 1.011$	$S_3 = 81.7$
$LAMI$= 4, $ICON = 6$		$\lambda_3 = 43.4$	
$a = 7.461$, $b = 18.75$	1062.3	$\lambda_G = 1.034$	$S_{sk} = 2.61$
$h = 0.4$, $t_s = 0.048$		$\lambda_{sk} = 1.012$	$S_3 = 72.6$
$LAMI$= 4, $ICON = 6$		$\lambda_3 = 38.8$	

Table 4 Best designs obtained by genetic algorithm for grid-stiffened cylinder with no constraints on strain and $ICON$= 5, (N_x = 1800 lbs/in).

Design variables (in.)	Weight (lbs)	λ_i
$a = 8.559, b = 16.667$	1397.9	$\lambda_G = 1.0088$
$h = 0.4500, t_s = 0.072$		$\lambda_{sk} = 1.078$
$LAMI$= 4		$\lambda_1 = 1.11, \lambda_3 = 24.6$
$a = 7.657, b = 17.143$	1399.6	$\lambda_G = 1.0447$
$h = 0.4000, t_s = 0.078$		$\lambda_{sk} = 1.051$
$LAMI$= 3		$\lambda_1 = 1.04, \lambda_3 = 35.3$
$a = 7.657, b = 16.667$	1401.1	$\lambda_G = 1.0541$
$h = 0.4000, t_s = 0.078$		$\lambda_{sk} = 1.077$
$LAMI$=3		$\lambda_1 = 1.04, \lambda_3 = 32.1$

Table 5 Best designs obtained by genetic algorithm for grid-stiffened cylinder with constraints on strain and $ICON$= 5, (N_x = 1800 lbs/in).

Design variables (in.)	Weight (lbs)	λ_i	S_i
$a = 8.314, b = 16.667$	1406.6	$\lambda_G = 1.0113$	$S_{sk} = 2.07$
$h = 0.4375, t_s = 0.078$		$\lambda_{sk} = 1.101$	$S_1 = 1.08$
$LAMI$= 4		$\lambda_1 = 1.36, \lambda_3 = 32.9$	$S_3 = 27.2$
$a = 8.0833, b = 16.667$	1408.7	$\lambda_G = 1.0100$	$S_{sk} = 2.08$
$h = 0.4375, t_s = 0.078$		$\lambda_{sk} = 1.126$	$S_1 = 1.08$
$LAMI$= 4		$\lambda_1 = 1.38, \lambda_3 = 36.2$	$S_3 = 29.8$
$a = 8.314, b = 16.667$	1414.2	$\lambda_G = 1.0600$	$S_{sk} = 1.99$
$h = 0.4625, t_s = 0.078$		$\lambda_{sk} = 1.053$	$S_1 = 1.03$
$LAMI$= 4		$\lambda_1 = 1.19, \lambda_3 = 28.9$	$S_3 = 26.0$

Table 6 Design space for b, h, t_s for Example 3.

Axially stiffened cylinder, $ICON$= 1								
b, (in.)	8.5590	8.3140	8.0833	7.8640	7.6570	7.4610	7.2750	7.0970
h, (in.)	0.6375	0.6500	0.6625	0.6750	0.6875	0.7000	0.7125	0.7250
t_s, (in.)	0.102	0.108	0.114	0.120	0.126	0.132	0.138	0.144
Grid-stiffened cylinder, $ICON$= 5								
b, (in.)	12.7669	12.5609	12.2458	12.0000	11.7656	11.5393	11.3216	11.1119
h, (in.)	0.525	0.5375	0.5500	0.5625	0.5750	0.5875	0.6000	0.6125
t_s, (in.)	0.066	0.072	0.078	0.084	0.090	0.096	0.102	0.108

Table 7 Best designs obtained by genetic algorithm for axially cylinder with constraints on strain, (N_x = 2000 lbs/in).

Design variables (in.)	Weight (lbs)	λ_i	S_i
$b = 8.559$, $h = 0.6500$ $t_s = 0.102$, $LAMI = 4$	120.1	$\lambda_G = 1.0177$ $\lambda_{sk} = 2.803$, $\lambda_1 = 1.025$	$S_{sk} = 2.310$ $S_1 = 1.200$
$b = 8.314$, $h = 0.6375$ $t_s = 0.102$, $LAMI = 4$	120.2	$\lambda_G = 1.0079$ $\lambda_{sk} = 3.004$, $\lambda_1 = 1.073$	$S_{sk} = 2.335$ $S_1 = 1.213$
$b = 8.314$, $h = 0.6500$ $t_s = 0.102$, $LAMI = 4$	120.4	$\lambda_G = 1.0285$ $\lambda_{sk} = 2.952$, $\lambda_1 = 1.018$	$S_{sk} = 2.295$ $S_1 = 1.192$

Table 8 Best designs obtained by genetic algorithm for grid-stiffened cylinder with constraints on strain, $ICON$= 5 (N_x = 2000 lbs/in).

Design variables (in.)	Weight (lbs)	λ_i	S_i
$b = 12.5609$, $h = 0.5250$ $t_s = 0.078$, $LAMI = 4$	123.0	$\lambda_G = 1.0368$, $\lambda_{sk} = 2.341$ $\lambda_1 = 1.068$, $\lambda_3 = 24.6$	$S_{sk} = 2.08$ $S_1 = 1.08$, $S_3 = 27.0$
$b = 12.2458$, $h = 0.5250$ $t_s = 0.078$, $LAMI = 4$	123.2	$\lambda_G = 1.0490$, $\lambda_{sk} = 2.387$ $\lambda_1 = 1.057$, $\lambda_3 = 22.79$	$S_{sk} = 2.064$ $S_1 = 1.072$, $S_3 = 24.67$
$b = 12.0000$, $h = 0.5250$ $t_s = 0.078$, $LAMI = 4$	123.4	$\lambda_G = 1.0595$, $\lambda_{sk} = 2.424$ $\lambda_1 = 1.049$, $\lambda_3 = 21.44$	$S_{sk} = 2.048$ $S_1 = 1.064$, $S_3 = 22.96$

Table 9 Buckling load factors and strain level factors for axially stiffened cylinder

Loading (lbs/in.)	N_x=2000, N_y=20, N_{xy}=0	N_x=2000, N_y=15, N_{xy}=55	N_x=2000, N_y=5, N_{xy}=165	N_x=2000, N_y=0, N_{xy}=220
λ_i	λ_G=1.0085 λ_{sk}=2.710 λ_1=1.034	λ_G=1.0108 λ_{sk}=2.725 λ_1=1.032	λ_G=1.0108 λ_{sk}=2.757 λ_1=1.032	λ_G=1.0087 λ_{sk}=2.774 λ_1=1.034
S_i	S_{sk}=2.349 S_1= 1.211	S_{sk}=2.339 S_1= 1.208	S_{sk}=2.330 S_1= 1.208	S_{sk}=2.330 S_1= 1.211

Table 10 Buckling load factors and strain level factors for grid-stiffened cylinder

Loading (lbs/in.)	N_x=2000, N_y=400, N_{xy}=0	N_x=2000, N_y=300, N_{xy}=100	N_x=2000, N_y=100, N_{xy}=300	N_x=2000, N_y=0, N_{xy}=400
λ_i	λ_G=1.0899 λ_{sk}=1.930 λ_1=1.192 λ_3=2.958	λ_G=1.0899 λ_{sk}=1.991 λ_1=1.191 λ_3=2.929	λ_G=1.0898 λ_{sk}=2.111 λ_1=1.192 λ_3=2.873	λ_G=1.0897 λ_{sk}=2.169 λ_1=1.192 λ_3=2.846
S_i	S_{sk}=2.240 S_1= 1.036 S_3= 2.779	S_{sk}=2.173 S_1= 1.036 S_3= 2.752	S_{sk}=2.050 S_1= 1.036 S_3= 2.699	S_{sk}=1.994 S_1= 1.036 S_3= 2.673

THE NASA MONOGRAPHS ON SHELL STABILITY DESIGN RECOMMENDATIONS - A REVIEW AND SUGGESTED IMPROVEMENTS

Michael P. Nemeth* and James H. Starnes, Jr.†
NASA Langley Research Center
Hampton, Virginia 23681-0001

Abstract

A summary of existing NASA design criteria monographs for the design of buckling-resistant thin-shell structures is presented. Subsequent improvements in the analysis for nonlinear shell response are reviewed, and current issues in shell stability analysis are discussed. Examples of nonlinear shell responses that are not included in the existing shell design monographs are presented, and an approach for including reliability based analysis procedures in the shell design process is discussed. Suggestions for conducting future shell experiments are presented, and proposed improvements to the NASA shell design criteria monographs are discussed.

Introduction

In the 1960's, NASA experience with spacecraft development indicated a need for uniform design criteria. This need led to the development of a series of monographs that provide design information and recommendations in the areas of environment; material properties and processes; stability, guidance, and control; chemical propulsion; and structures. One of the structures monographs published in 1965, and revised in 1968, provides recommendations for the design of buckling-resistant circular cylindrical shell structures. This monograph is known throughout the aerospace industry as NASA SP-8007.[1] This monograph was followed in 1968 by NASA SP-8019[2], which gives recommendations for the design of conical shells, and in 1969 by NASA SP-8032[3] ,which gives recommendations for the design of doubly curved shells. These monographs emphasize primarily the behavior of thin-walled metallic shells subjected to axial compression, torsion, pressure, and bending loads, and to various combinations of these loads. Prior to the publication of these monographs, one of the most comprehensive collections of shell stability information available was the series of structural stability handbooks written by Gerard and Becker.[4, 5, 6] The NASA monographs used and expanded the information provided in these handbooks.

The NASA structural stability monographs remain popular among designers primarily because they address one of the most important concerns associated with designing shells to satisfy stability requirements. Experience has shown that large discrepancies often occur between the classical shell stability analysis predictions for geometrically perfect shells and corresponding results from experiments. The NASA monographs provide a reliable, but often overly conservative, means of designing shells using simple, linear analytical models and an empirical correction factor, referred to herein as a "knockdown factor." The format of the monographs was intended to satisfy the requirements of engineers and project managers concerned with the preliminary design of spacecraft. However, the amount of information presented in the NASA monographs is somewhat limited and, as a result, their range of applicability to the design of high-performance shell structures, such as those made of fiber-reinforced composite materials, is small.

Continued use of these NASA monographs by structural designers and technical specialists, and recent NASA experience with the development of launch vehicles and aircraft structures have indicated that the monographs on shell stability need to be updated and expanded. For example, the original NASA monographs contain practically no design information for lightweight, high-strength laminated composite shells subjected to mechanical or thermal loads. Such information could be used in the preliminary design of a high-speed civil transport aircraft or a single-stage-to-orbit reusable launch vehicle. The interest in updating the monographs is also influenced by the many advances in the state of the art of shell stability analysis that have taken place since the original monographs were published. Significant advances in computer technology and computational analysis tools since the late 1960's have made it possible to use much more sophisticated analytical models of nonlinear shell response. These tools have also enabled in-depth investigations of the effects of complicating structural details such as cutouts and other discontinuities on the buckling of shells, and on their nonlinear behavior. In addition to advancements in analytical tools, many advancements have been made in experimental methods

---

* Senior Research Engineer, Structural Mechanics Branch. Senior Member, AIAA.

† Head, Structural Mechanics Branch. Fellow, AIAA.

and techniques. For example, technology is now available to measure accurately the initial geometric imperfections of shell test specimens, and new combined-load test capabilities have been developed and used to provide more carefully controlled experiments and higher-fidelity test results. Because of these technological advances and the large body of experimental data that has been amassed since the late 1960's, the development of modern versions of the shell stability monographs is being considered at the NASA Langley Research Center.

The present paper begins with a discussion of the approach commonly used to design buckling-resistant, thin-walled shells and how it evolved. Then, an overview of the NASA monographs on shell stability is given. Next, a discussion of some important issues that are presently confronting designers is presented, and then two examples that illustrate some of these issues are described. The first example is the Space Shuttle superlightweight external LO_2 tank. This contemporary thin-walled spacecraft structure was partially designed using NASA SP-8007. The second example is a basic example that illustrates the effect of cutout size on the buckling behavior of a compression-loaded curved panel. Both of these examples illustrate shell behavior that is not addressed in the NASA monographs. The present paper includes a brief discussion of a state-of-the-art nonlinear shell analysis code and how it could be used to obtain a wide range of design information. In addition, a discussion of how to address design uncertainties and reliability in shell design is presented, and some suggestions for conducting future high-fidelity experiments are given. Finally, potential improvements to the NASA monographs on shell stability are discussed

Common Approach to Stability Design

Prior to the late 1970's, the use of sophisticated analytical methods, such as the finite-element method, was not widespread and shell stability calculations were done primarily with simple, specialized analytical models. These analytical models were typically formulated for regular geometries with uniform properties, uniform loading conditions, and uniform boundary conditions, and certain aspects of the response were neglected in order to obtain linear partial differential equations that could be readily solved. The simple analytical models typically neglected nonlinear prebuckling deformations, and simply supported boundary conditions were often used to reduce the computational effort needed to conduct parametric studies. This linear modeling approach, referred to more accurately as a linear bifurcation buckling analysis, came into use not only because of the computational considerations mentioned above, but also as the natural extension of the linear bifurcation buckling approach that had been used successfully for modeling columns and plates. Over the course of time, scientists and engineers learned that the buckling behavior of shells is fundamentally different from that of columns and plates.

The fundamental difference between the buckling behavior of columns and plates and the buckling behavior of shells was identified by von Kármán and Tsien[7] and clarified by Donnell and Wan[8] and by Koiter.[9] These references show that a major reason for the large discrepancy between the analytical predictions of shell buckling behavior and the corresponding experimental results is a sensitivity of shell buckling to initial geometric imperfections. This sensitivity was shown to be a consequence of the fact that shells are typically unstable at load levels equal to the bifurcation load. Because of the practical limitations of the analytical models and the sensitivity of shells to geometric imperfections, a stability design process evolved in which empirical "knockdown factors" were introduced to compensate for the differences observed between the results of theory and experiments. As a part of this design process, a designer was faced with the need to conduct expensive experiments.

The NASA Monographs on Shell Stability

By 1960, many buckling tests of isotropic cylinders and curved panels had been conducted (e.g., see Refs. 4, 5, and 6) as part of an effort by the technical community to establish a rational, practical approach for designing buckling-resistant shells. NASA conceived the shell stability monographs at that time to make available to the aerospace structural design community the results of these tests and many proposed tests for other shell geometries, and to establish practical design recommendations. The development of these monographs was a combined effort by members of industry, academia, and the NASA Langley Research Center. Much of the information given in these monographs is based on the research conducted by Seide, Weingarten, and Morgan.[10] The initial emphasis on cylinders and cones, and the format of the monographs, were originally intended to satisfy the needs of engineers and project managers concerned with the preliminary design of launch vehicles and spacecraft. However, over time, it became evident that the monographs were also of great interest to structural stability specialists. The use of NASA SP-8007 was recently demonstrated in the shell analysis textbook by Vinson.[11]

The NASA monographs provide design information in the form of empirical knockdown factors (referred to in the monographs as correction factors) and design recommendations for isotropic, orthotropic, ring- and stringer-stiffened, and sandwich shells. The important characteristics of various shell design problems, the sources of the design recommendations and their limitations, and discussions of how to proceed for cases with little known analytical and experimental data are also

presented. In most cases, the knockdown factors are defined as empirical corrections to linear bifurcation buckling solutions for primarily elastic, simply supported shells. The knockdown factors are lower bounds to experimental data that were available at that time, and are used to account for the large amount of scatter in the data. They consist of corrections that account primarily for initial geometric imperfections, nonlinear prebuckling effects associated with edge supports, and plasticity in some cases. The effects of edge boundary restraints (e.g., a simply supported versus a clamped boundary condition) are included in the knockdown factors so that edge restraints are treated as a random effect, in addition to the initial geometric imperfections. Plasticity correction factors are given only for cases where there was a sufficient amount of data to characterize the behavior in a conservative manner. The basic recommendation given in the monographs is that any knockdown factor used for a design be substantiated by experiments. This recommendation applies for shell designs in which the restraint or boundary conditions are to be accounted for more accurately, or for designs with unusual surface geometries, modal interaction associated with optimization, cutouts, joints, or other irregularities, or where there are little or no test data and analytical results. A brief overview of the contents of each monograph follows.

NASA SP-8007 (1968 Revision)

The 1968 revision of NASA SP-8007 consists primarily of discussions of research studies and design recommendations for elastic, isotropic, cylindrical shells. However, some information is provided for orthotropic and sandwich cylinders. Design recommendations are presented for isotropic cylinders subjected to axial compression, pure bending, uniform lateral pressure, uniform hydrostatic pressure, torsion, and combined loading conditions. The uniform lateral pressure loading condition does not include the compressive axial load caused by pressure acting at the ends of a cylinder. In contrast, the uniform hydrostatic pressure loading condition includes the lateral pressure load and the compressive axial load. Design recommendations for cylinders that are subjected to combined loading conditions are limited almost entirely to isotropic shells. The combined loading conditions consist of axial compression and pure bending; axial compression and lateral pressure or hydrostatic pressure; axial compression and torsion, internal pressure and axial compression; internal pressure and pure bending; and internal pressure, axial compression, and pure bending loads.

Design recommendations and buckling formulas that are lower bounds to experimental data for a wide range of radius-to-thickness ratios are given for isotropic cylinders subjected to axial compression or pure bending loads. For cylinders loaded by lateral or hydrostatic pressure, a single knockdown factor, that is a lower bound to the corresponding experimental data, is given for shells that buckle with more than two circumferential waves. An additional empirical knockdown factor is given for long shells that buckle into a one-half-wave oval shape. For torsion loads, a single knockdown factor that is a lower bound to the corresponding experimental data is given for moderately long cylinders. Because of limited experimental verification, design recommendations are given in the form of conservative, linear buckling interaction equations for shells subjected to combined axial compression and pure bending loads, combined axial compression and lateral pressure loads or hydrostatic pressure loads, and combined axial compression and torsion loads. For shells subjected to combined internal pressure and axial compression or combined internal pressure and pure bending loads, the buckling load is expressed as a combination of the load caused by the internal pressure, the buckling load for the unpressurized shell (including the appropriate knockdown factor), and an increase in the buckling load associated with the reduction in imperfection sensitivity caused by the internal pressure. Empirically determined increases in the buckling load, that are associated with the reduced imperfection sensitivity, are given for moderate ranges of internal pressures and radius-to-thickness ratios. Conservative, linear buckling interaction equations are also given for shells subjected to combined internal pressure, axial compression, and pure bending loads.

Results are also presented in NASA SP-8007 for elastic, orthotropic cylindrical shells subjected to axial compression, pure bending, uniform hydrostatic pressure, uniform lateral pressure, or torsion loads, and to combined axial compression and bending loads. The term "orthotropic" is used to indicate single-layer and multi-layer composite monocoque shell wall constructions and stiffened shell wall constructions for which the rings and stringers are perpendicular. These results consist primarily of design recommendations because of the small amount of experimental data for orthotropic cylinders that was available at the time. Formulas for computing homogenized (or "smeared") elastic, orthotropic stiffnesses for multi-layered stiffened cylinders, isotropic stiffened cylinders, and ring-stiffened corrugated cylinders are presented.

An empirical formula for knockdown factors is presented for monocoque orthotropic cylinders loaded by axial compression. This formula is based on a small amount of experimental data and has a very limited range of validity. A similar formula is given for cylinders loaded by pure bending. A single knockdown factor, that is based on a small amount of experimental data, is given for cylinders subjected to axial compression or pure bending loads and with closely spaced, moderately large stiffeners. A single knockdown factor that is also based on a small amount of experimental data is suggested for

cylinders loaded by lateral or hydrostatic pressure, or by torsion loads. In addition, because of a small amount of experimental data, a conservative, linear buckling interaction formula is suggested for use with cylinders loaded by combined axial compression and pure bending loads.

Design recommendations for sandwich cylinders with isotropic face sheets and with either an isotropic or an orthotropic core are also presented in NASA SP-8007. Design recommendations are given for shells loaded by axial compression, pure bending, uniform lateral pressure, or torsion loads. Knockdown factors are given only for shells with cores that have high transverse shear stiffness, and practically no experimental validation is described.

Analytical results and design recommendations are also presented in NASA SP-8007 for isotropic cylindrical shells with an elastic core and that are subjected to axial compression, uniform lateral pressure, or torsion loads, or to combined axial compression and lateral pressure loads. The knockdown-factor formula given for compression-loaded cylinders without an elastic core is recommended for use for cylinders with an elastic core, based on experimental data. For cylinders loaded by lateral pressure, a single knockdown factor is given that is a lower bound to the corresponding experimental data. For the cylinders loaded by torsion, only design recommendations are given. Similarly, a conservative linear buckling interaction formula is recommended for cylinders loaded by combined axial compression and lateral pressure loads.

NASA SP-8019

NASA SP-8019 consists primarily of design recommendations for elastic, isotropic, conical shells subjected to axial compression, pure bending, uniform hydrostatic pressure, torsion, or combined loads. The design recommendations for cones subjected to combined loads are given for isotropic shells only. The combined loads consist of internal pressure and axial compression; internal pressure and pure bending; axial compression and pure bending; internal pressure, axial compression, and pure bending; uniform hydrostatic pressure and axial compression; torsion and uniform hydrostatic pressure; and torsion and axial compression.

Design recommendations and a single empirical knockdown factor that is a lower bound to experimental data are given for each of the single-component loading conditions. Only conservative design recommendations based on rational arguments are given for loading conditions that consist of combined internal pressure and axial compression, and combined internal pressure and pure bending, because of the very small amount of experimental data and the lack of analytical results that were available at the time. Conservative, linear buckling interaction equations based on experimental results are given for all the other combined load conditions.

Results are also presented in NASA SP-8019 for elastic, orthotropic conical shells (constant-thickness orthotropic material and stiffened shells) subjected to uniform hydrostatic pressure or to torsion loads. These results consist primarily of design recommendations because of the very small amount of experimental data that were available at the time. Similarly, only design recommendations are given for sandwich cones with isotropic or orthotropic face sheets and with either an isotropic or orthotropic core.

NASA SP-8032

NASA SP-8032 consists primarily of discussions of research studies and results for elastic, isotropic, doubly curved shells. Design recommendations are given for spherical caps that are loaded by uniform external pressure, by a concentrated load at the apex, or by a combination of these loads. Buckling formulas that are lower bounds to experimental data are given for clamped spherical caps that are loaded by uniform external pressure or by a concentrated load at the apex. A lower-bound, empirical buckling formula is given for spherical caps that are loaded by a concentrated load at the apex and that have edges that are free to rotate and expand in the direction perpendicular to the axis of revolution. No conclusive experimental results are given for spherical caps that are loaded by combined uniform external pressure and a concentrated load at the apex.

Design recommendations are also discussed for complete prolate and oblate spheroidal shells subjected to uniform external pressure, and for complete oblate spheroidal shells subjected to uniform internal pressure. A single knockdown factor is given for the prolate spheroidal shells, and a lower-bound, empirical buckling formula is given for the oblate spheroidal shells. No experimental validation is given for the results for the oblate spheroidal shells subjected to uniform internal pressure. Design recommendations are also discussed for oblate spheroidal and torispherical bulkheads that are subjected to uniform internal pressure and that have clamped edges. An empirical knockdown factor is given for the torispherical bulkheads; however, no experimental validation is given for the oblate spheroidal bulkhead.

Design recommendations are discussed and results are given for complete circular toroidal shells subjected to uniform external pressure, and for shallow, equatorial segments of complete toroidal shells. The toroidal shell segments, which consist of barrel-like shells that are bowed outward from the axis of revolution (positive Gaussian curvature) and waisted shells that are bowed inward (negative Gaussian curvature), are subjected to axial tension, uniform lateral pressure, or uniform hydrostatic pressure loads. Experimentally verified analytical results are given for complete circular toroidal shells for

a small range of geometric parameters. Similarly, an experimentally verified knockdown factor is given only for equatorial segments of toroidal shells that are loaded by axial tension and that are truncated hemispheres.

Essentially no experimentally validated design information is given for orthotropic shells or sandwich shells that are doubly curved. Rational arguments are used to present design recommendations for specially orthotropic shells due to the absence of experimental data. No design recommendations are given for sandwich shells.

Shell Stability Issues

There are several important shell stability issues. most of which are not addressed in the NASA monographs, that designers must understand in order to design adequately a lightweight, thin-walled shell structure to be buckling resistant. Some of these issues are listed in Table 1 and a few are discussed subsequently.

Table 1 Shell stability issues

Initial geometric imperfections
Nonlinear prebuckling deformations
Cutouts and joints
Boundary conditions
Load introduction effects
Thickness variations
Variation in material properties
Stiffener spacing
Local reinforcement
Combined loads
Variation of loads with time
Small vibrations
Laminate construction
Transverse shear deformation
Sandwich construction
Inelasticity and damage
Local eccentricities

Initial Geometric Imperfections

Two major issues in the design of isotropic shells are sensitivity to initial geometric imperfections and the effects of nonlinear prebuckling deformations. Experience has shown that initial geometric imperfections with a maximum amplitude on the order of one wall thickness can cause a reduction in the buckling load of a shell that is on the order of 60% of the buckling load calculated for the corresponding geometrically perfect shell. Thus, designing a minimum mass shell structure to be buckling resistant is a difficult task because a designer usually does not know the initial geometric imperfection shape and amplitude in advance. As a result of this lack of knowledge, an assumed imperfection shape must be used to determine analytically a knockdown factor, or the design must be based on a knockdown factor that corresponds to the lower bound to the known relevant experimental data. Often, these data do not exist. In some cases, however, the shell manufacturing process may consistently produce a known imperfection shape with a known maximum amplitude. If so, this information can be used to determine a knockdown factor analytically.

Nonlinear Prebuckling Deformations

Nonlinear prebuckling deformations of shells are generally caused by the interaction between the compressive stresses in a shell and any localized bending deformations that arise, for example, from support conditions, or discontinuities in stiffness that are caused by abrupt changes in thickness, or joints. The significance of the nonlinear prebuckling deformations was first identified by Stein for compression-loaded isotropic cylinders.[12, 13] As an isotropic cylindrical shell is compressed axially, it expands outward radially. At the supported edges, however, the radial expansion is restrained which produces local bending deformations whose extent along a generator depends on the cylinder radius and thickness. A similar condition exists for compression-loaded isotropic truncated conical shells where the extent of local bending deformations along a generator also depends on the vertex angle. Generally, as a cone gets flatter, the extent of the boundary bending deformations grows. Another example of nonlinear prebuckling deformations is the local bending deformations that occur around a relatively large cutout in a compression-loaded cylinder or curved panel. These bending deformations are manifested by the coupling between the in-plane and out-of-plane displacements in the strain-displacement relations for curved panels or shells.

A very important consequence of substantial nonlinear prebuckling deformations is that a linear bifurcation solution and a knockdown factor may be inadequate and uncharacteristic of the actual nonlinear response. One simple example of this deficiency is illustrated by the behavior of a ring-stiffened cylindrical shell loaded by axial compression or by external pressure.[14, 15] For these shells, a linear bifurcation analysis may not only overpredict the buckling load, but may also predict an incorrect buckling mode. Another, more complicated example is presented in Ref. 16 for the Space Shuttle superlightweight LO_2 tank shown in Fig. 1 and is discussed in the section entitled, "Examples," of the present paper.

Cutouts

The effects of a cutout on the buckling behavior of a shell is another important shell stability issue for designers. The presence of a cutout may alter significantly the prebuckling stress distribution in a shell, depending on the type of loading and the cutout size, and reduce its buckling load significantly. In addition, nonlinear preb-

uckling deformations, that are local bending deformations near the cutout, may be present that can affect significantly the characteristics of the buckling behavior. A cutout may also have a significant effect on the imperfection sensitivity of a shell because as the cutout size increases the amount of material removed by the cutout region, where imperfections may be very important, is reduced. Some of the effects of cutouts on the behavior of compression-loaded curved panels are also discussed in the section entitled, "Examples," of the present paper.

Laminate Construction

Approximately twenty-five years ago, it was realized that there is a great potential for reducing structural weight by using fiber-reinforced composite materials for structures. The increased use of composite materials for shell structures has led to additional shell stability issues for designers. For example, the effects of laminate construction (including sandwich construction) and transverse shear deformations on imperfection sensitivity are not well understood. Transverse shear flexibility tends to reduce the effective stiffness of a structure and can reduce its buckling load. It is also known that laminated shell wall construction can greatly affect the attenuation length of bending deformations, which implies that the effects of nonlinear prebuckling deformations may be severe for some laminate constructions.

Examples

The common approach to stability design described previously in the present paper is often used by industry in the preliminary design of shell structures. However, in some cases, the results of a linearized stability problem may not represent adequately the underyling physics of the actual response. Two examples that illustrate this potential pitfall are presented in this section. The first example is the Space Shuttle superlightweight LO_2 tank. This example of a contemporary thin shell structure that is subjected to combined loads illustrates complex nonlinear behavior that is dominated by local bending deformations. The second example is a much simpler "subcomponent-level" example; that is, a compression-loaded curved panel with a cutout. Because cutouts appear in nearly every kind of aerospace vehicle structure, properly designing for their effects on the buckling resistance of shells is very important. These two examples illustrate some physical behaviors that are not commonly understood and are representative of problems that are dominated by effects that are currently not addressed in the NASA monographs.

Space Shuttle Superlightweight LO_2 Tank

The Space Shuttle consists of the Orbiter, two Solid Rocket Boosters (SRBs), and the External Tank (ET), as shown in Fig. 1. The External Tank consists of a liquid

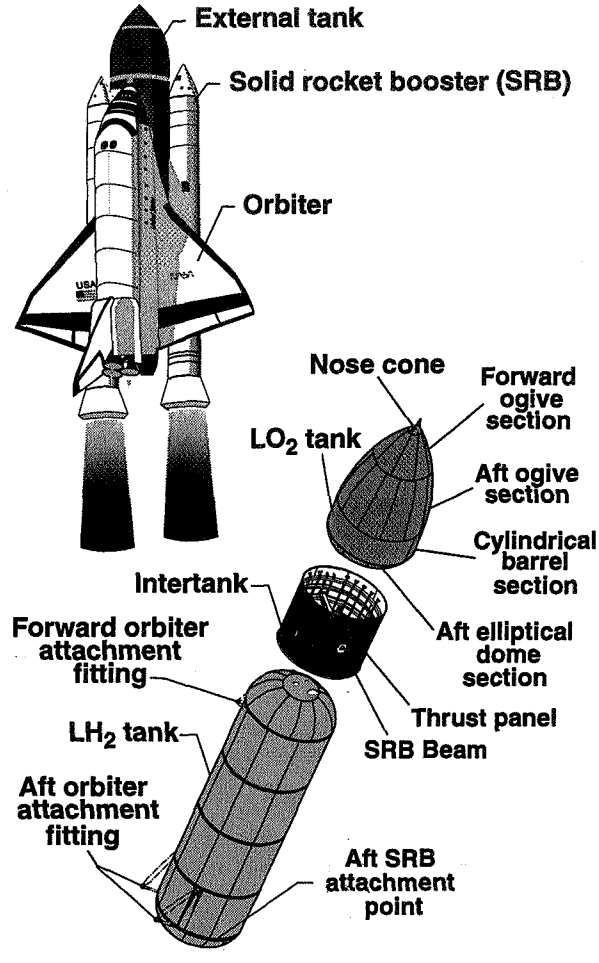

Fig. 1 Space Shuttle External Tank components.

oxygen (LO_2) tank, a liquid hydrogen (LH_2) tank, and an intermediate structure called the Intertank (see Fig. 1). Currently, NASA is engaged in the flight certification of a newly designed LO_2 tank that is referred to as the superlightweight LO_2 tank. This new LO_2 tank is significantly lighter than the one presently in service, and a significant concern in its design is its buckling behavior. The superlightweight LO_2 tank is a thin-walled monocoque shell that is made primarily of 2195 aluminum-lithium alloy. It consists of a nose cone, a forward ogive section, an aft ogive section, a cylindrical barrel section, and an aft elliptical dome section, as shown in Fig. 1. The Intertank (see Fig. 1) is a right circular cylinder that is made from 2090 and 7075 aluminum alloys. Details and dimensions of the LO_2 tank, the LH_2 tank and the Intertank are given in Ref. 16.

An important loading condition that is illustrated by this example is the prelaunch loading condition for which the LH_2 and LO_2 tanks are full. Compressive stresses are present in the ogive sections of the (mono-

coque) LO_2 tank directly above the solid rocket booster attachment points for this loading condition. These compressive stresses are caused by the weight of the filled LH_2 and LO_2 tanks that is reacted at the two SRB attachment points. Both linear bifurcation and nonlinear analyses are presented in detail in Ref. 16. These results, which were obtained by using the Structural Analysis of General Shells (STAGS) nonlinear structural analysis code,[17] are described briefly as follows.

The linear bifurcation solution yields a critical buckling load factor of $p_a = 3.78$, where a value of $p_a = 1.0$ corresponds to the magnitude of the operational loads. The corresponding buckling mode is shown in Fig. 2 and consists of a short-wavelength buckle in the forward part of the aft ogive that is essentially a wrinkle in the skin. The shortness of the wavelength is caused by the hoop tension that resists the LO_2 pressure.

Results of nonlinear analyses presented in Ref. 16 are reproduced in Figs. 3 and 4. The solid lines shown in Fig. 3 represent the normal displacements along the length of the aft ogive shell wall for values of the applied load factor p_a approximately equal to 3.0, 4.0, and 5.0. Overall, negative values of the normal displacements are indicated by the left-hand-side ordinate for these three lines because of contraction of the aft ogive that is caused primarily by the LO_2 thermal load. The linear bifurcation mode is represented in the figure by the dashed line with the normalized amplitude given by the right-hand ordinate of the figure. The solid lines shown in Fig. 3 indicate a short-wavelength bending response in the aft ogive over the SRB attachment point (figure 2) that is similar in shape to the corresponding linear bifurcation mode shape. The overall slope of the solid lines (obtained by fitting a straight line to each curve) is a result of outward displacements of the shell wall (indicated by less negative values) that are caused by the internal pressure and that are represented by a nonlinear analysis. This effect is not represented in the prebuckling stress state that is used in a linear bifurcation buckling analysis and, as a result, does not affect the overall slope of the dashed line.

The results presented in Fig. 3 predict a stable nonlinear response at load levels greater than the buckling load predicted by a linear bifurcation analysis. As the applied load increases, substantial bending deformations (indicated by the waviness of the curves) develop and grow in the shell wall. These bending deformations reduce the apparent meridional stiffness of the aft ogive. The nonuniformity of the bending deformations is caused by thickness variations in the ogive and the presence of circumferential weld lands. Similar results are presented in Ref. 16 which indicate that a geometric imperfection with a small negative amplitude and with the shape of the linear bifurcation mode greatly increases the severity of the stable bending deformations. This imperfection causes the growth of the bending deformations to begin at much lower load levels than the linear bifurcation buckling load.

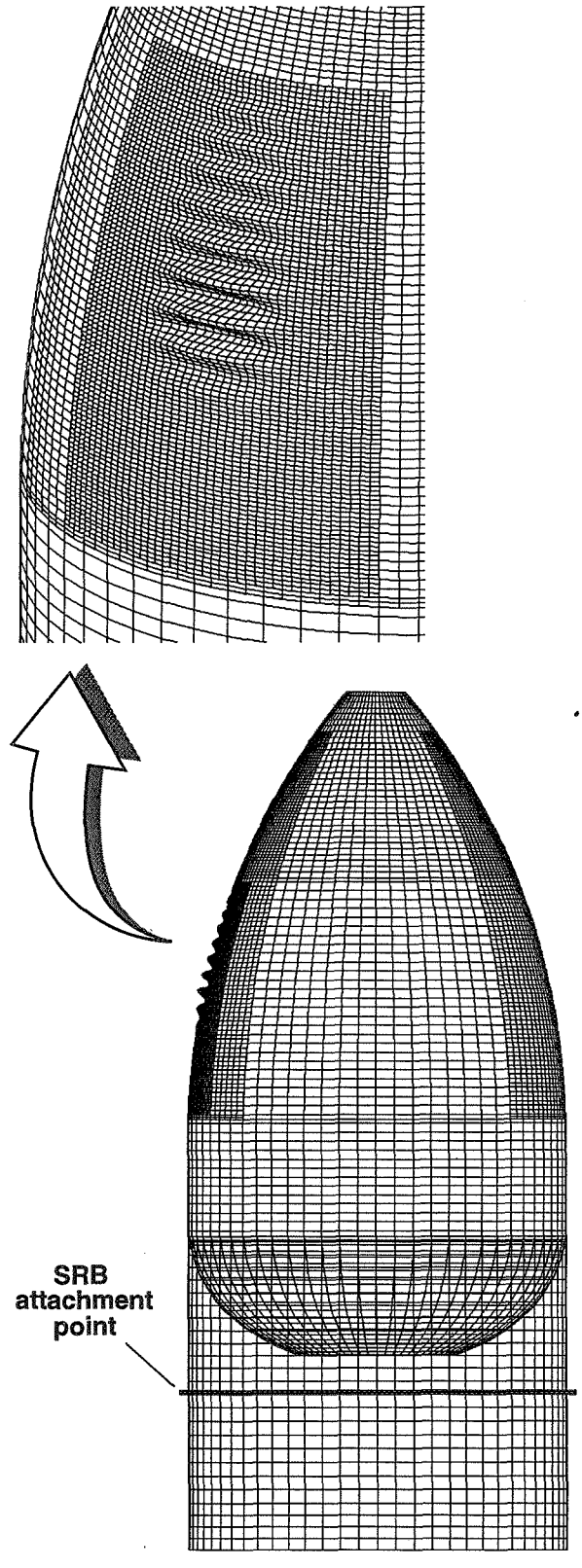

Fig. 2 Linear bifurcation buckling mode for a 99,000 degree-of-freedom model. ($p_a = 3.78$).

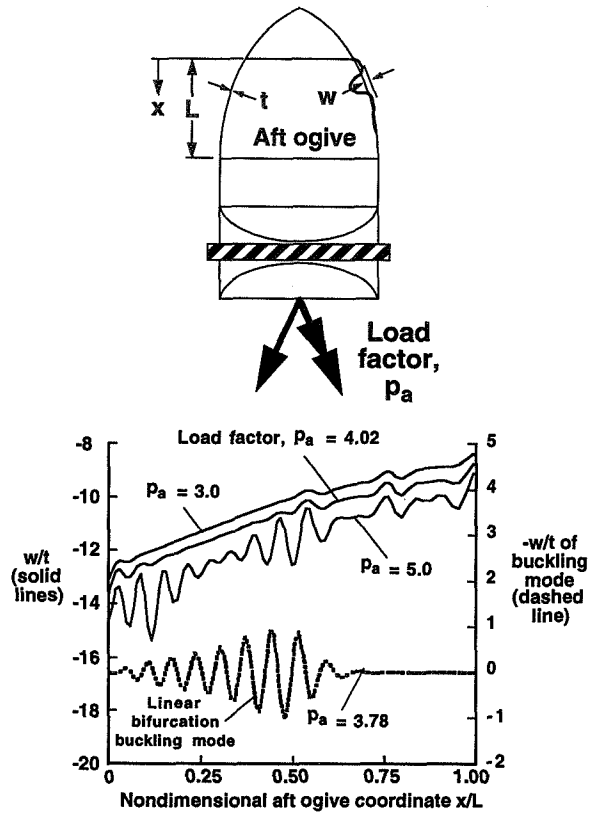

Fig. 3 Predicted nondimensional normal displacement w/t of the aft ogive of a geometrically perfect shell for inceasing LH_2 interface loads.

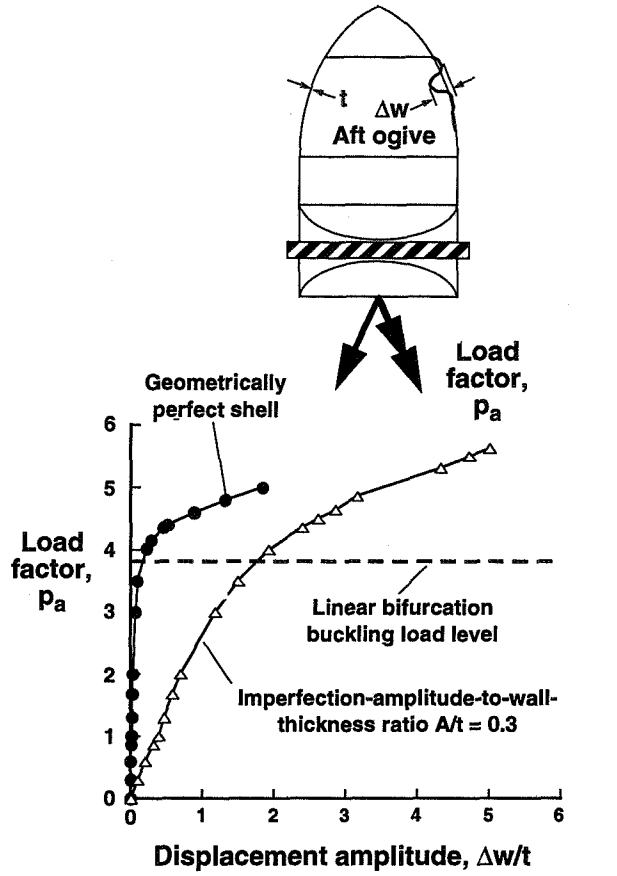

Fig. 4 Predicted local nondimensional displacement amplitude Δw/t of the aft ogive surface for inceasing LH_2 interface loads; geometrically perfect and geometrically imperfect shells.

The reduction in the apparent meridional stiffness of the aft ogive is shown more explicitly in Fig. 4. In this figure, the intensities of the largest bending deformations (indicated by the largest magnitude of the normal displacement amplitude) for the geometrically perfect shell and a geometically imperfect shell are given as a function of the load factor p_a. The amplitude Δw shown in Fig. 4 is the distance from the maximum value of the shell-wall displacement to the adjacent minimum value and represents the intensity of the local bending deformation in the response. The filled circles in the figure correspond to results for a geometrically perfect shell and the unfilled triangles correspond to results for geometrically imperfect shells with imperfection-amplitude-to-wall-thickness ratio of A/t = 0.3 (t = 2.540 mm (0.100 in.)). The horizontal dashed line in the figure represents the linear bifurcation buckling load level.

The results presented in Fig. 4 indicate that the amplitude of the greatest local bending deformation grows with increasing load, and that the amount of growth increases substantially with increasing geometric imperfection amplitude. The results predict that the shell can support loads greater than the critical buckling load predicted by the linear bifurcation analysis. Most importantly, the results show that the linear bifurcation analysis does not accurately represent the mechanics of the actual shell response. Moreover, a design based on the linear bifurcation analysis and a knockdown factor that was arrived at using an intuitive approach would likely be overly conservative.

Compression-Loaded Curved Panel With a Cutout

Several tests of compression-loaded 6061-T6 aluminum singly curved panels with a central circular cutout were conducted at the NASA Langley Research Center. The panels had a nominal radius of curvature of R = 152.4 cm (60 in.) and a nominal thickness of t = 2.54 mm (0.10 in.). The length and arc-width of the panels were approximately 37.47 cm (14.75 in.) and 36.83 cm (14.5 in.), respectively. The panels were loaded slowly in axial compression by uniformly displacing the two opposite curved edges with a 1334-kN (300-kip)-capacity hydraulic testing machine. The loaded ends of a panel were clamped and the unloaded edges were simply supported by a test fixture. The length and arc-width of the panels between the inside edges of the test fixture (unsupported area) were both 35.56 cm (14.0 in.). Electrical resistance

strain gauges were used to measure strains, and direct-current differential transformers were used to measure axial displacements and displacements normal to the panel surface. Shadow moiré interferometry was also used to monitor displacements normal to the panel surface.

Experimental results for load versus end shortening are presented in Fig. 5. The load is nondimensionalized

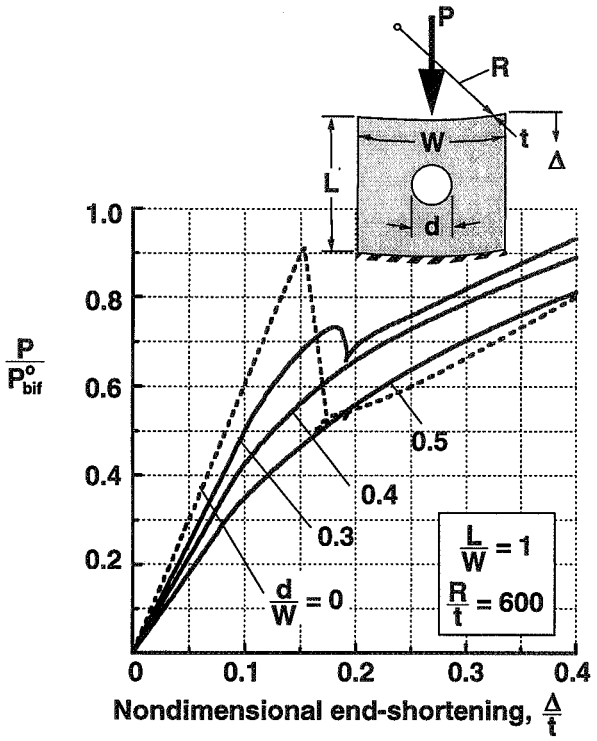

Fig. 5 Nondimensional load versus end-shortening curves for aluminum curved panels with a central circular cutout.

by the linear bifurcation buckling load for a panel without a cutout P^{o}_{bif} = 62,988 N (14,161 lbs) that was obtained from STAGS. This buckling load is based on a length L = 35.56 cm (14.0 in.), an arc-width W = 35.56 cm (14.0 in.), a nominal thickness of t = 2.54 mm (0.1 in.), a Young's modulus of E = 72.4 GPa (10.5 x 10^6 psi), and a Poisson's ratio of ν = 0.33. The end-shortening Δ is nondimensionalized by the nominal panel thickness t. The dashed line in the figure corresponds to a panel without a cutout and the solid lines correspond to panels with cutout-diameter-to-panel-width ratios d/W = 0.3, 0.4, and 0.5.

The experimental results presented in Fig. 5 indicate that the character of the nonlinear response of a panel changes significantly as the cutout size increases. For example, the results indicate that the panels with d/W = 0 and 0.3 exhibit buckling behavior that involves a dynamic change from one stable equilibrium configuration to another. Similar results, not shown in the figure, were obtained for panels with d/W = 0.1 and 0.2. The results in Fig. 5 also indicate that the panels with d/W = 0.4 and 0.5 do not exhibit this type of behavior, but exhibit stable, monotonically increasing nonlinear responses. The results show that the intensity of the dynamic buckling process decreases substantially as d/W increases from a value of zero to 0.3. The intensity of the dynamic buckling response is indicated by the difference between the buckling load and the lowest stable postbuckling load.

The results presented in Figs. 6 through 9 provide additional insight into the effect of cutout size on the character of the nonlinear response. The results in these figures are shadow moiré patterns on the convex or outer surface of the panels. The shadow moiré patterns for the panel without a cutout are shown in Fig. 6 for values of P/P^{o}_{bif} = 0.86 (just before buckling) and 0.57 (just after buckling). The top pattern in Fig. 6 indicates that no sig-

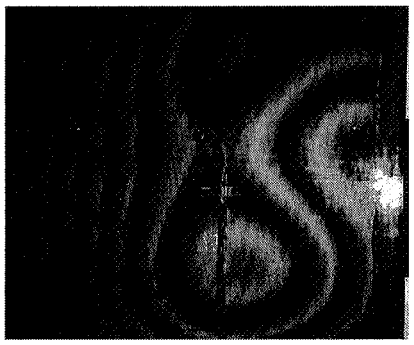

$\frac{P}{P^{o}_{bif}}$ = 0.86 (before buckling)

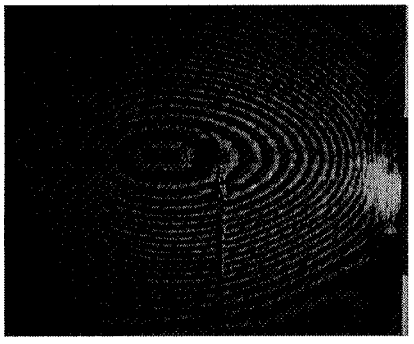

$\frac{P}{P^{o}_{bif}}$ = 0.57 (after buckling)

Fig. 6 Shadow moiré patterns for aluminum curved panels without a cutout.

nificant nonlinear prebuckling deformations are present, which is consistent with the straightness of the initial portion of the dashed line shown in Fig. 5. The bottom pattern in Fig. 6 indicates that the stable postbuckling mode shape consists of a single half-wave along the panel length and across the panel width. The radial displace-

ments of this postbuckling mode shape are inward.

Shadow moiré patterns for the panel with a cutout with d/W = 0.3 are shown in Fig. 7 for values of P/P^{o}_{bif} = 0.72 (just before buckling) and 0.67 (just after buckling).

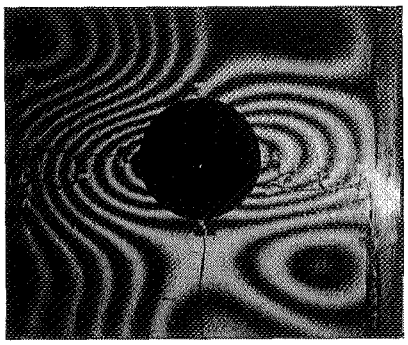

$\frac{P}{P^{o}_{bif}}$ = 0.72 (before buckling)

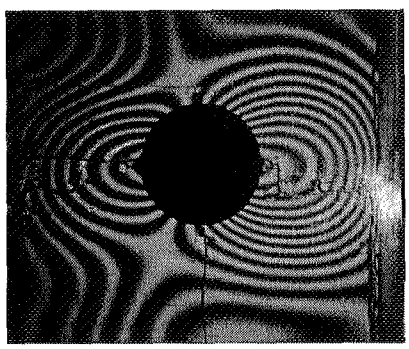

$\frac{P}{P^{o}_{bif}}$ = 0.67 (after buckling)

Fig. 7 Shadow moiré patterns for aluminum curved panels with a central circular cutout (d/W = 0.3).

The top pattern in Fig. 7 indicates that significant nonlinear prebuckling deformations occur around the cutout, which is consistent with the deviation from straightness of the initial portion of the solid line shown in Fig. 5 for d/W = 0.3. The radial deformations around the cutout are outward. The bottom pattern in Fig. 7 indicates that the stable postbuckling mode shape consists of an outward deformation pattern on the left-hand-side of the cutout, similar to the nonlinear prebuckling deformation pattern shown on the left side of the top pattern in the figure, and an inward buckle on the right-hand-side of the cutout. This buckle consists of, approximately, a single half-wave along the panel length and across the panel half-width.

Shadow moiré patterns for the panel with a cutout with d/W = 0.4 are shown in Fig 8 for values of P/P^{o}_{bif} = 0.46 and 0.71. The patterns in Fig. 8 and the corresponding curve in Fig. 5 indicate that significant outward non-

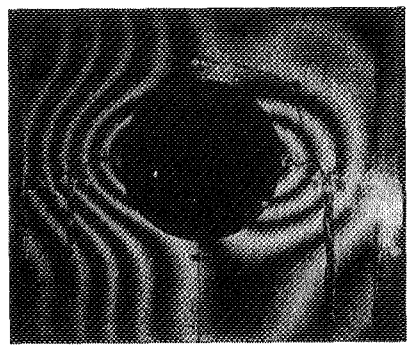

$\frac{P}{P^{o}_{bif}}$ = 0.46

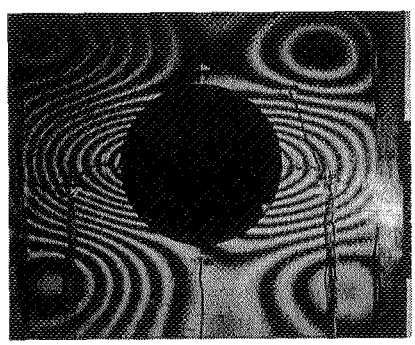

$\frac{P}{P^{o}_{bif}}$ = 0.71

Fig. 8 Shadow moiré patterns for aluminum curved panels with a central circular cutout (d/W = 0.4).

linear prebuckling deformations around the cutout dominate the response. There is no dynamic buckling response for this panel. Similarly, the shadow moiré patterns for the panel with a cutout with d/W = 0.5 are shown in Fig. 9 for values of P/P^{o}_{bif} = 0.50 and 0.70, and the corresponding curve in Fig. 5 supports the same conclusion about the response.

In summary, this simple example illustrates a response for compression-loaded curved panels that is typically not well understood, not considered by designers, and that is not addressed in the NASA monographs. The response trends change with loading, boundary conditions, and material systems, such as a laminated composite system. How these trends affect the cutout size at which the response changes its character is generally unknown. Information of this kind would be a valuable contribution to an updated shell design monograph.

Concept for New Design Recommendations

New, expanded versions of the NASA monographs are now possible to develop because of significant technological advances and advances in the understanding of

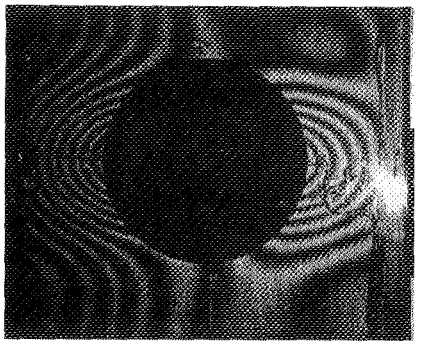

$\frac{P}{P^{o}_{bif}} = 0.50$

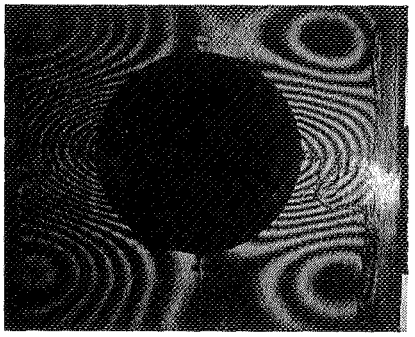

$\frac{P}{P^{o}_{bif}} = 0.70$

Fig. 9 Shadow moiré patterns for aluminum curved panels with a central circular cutout (d/W = 0.5).

shell stability. In particular, advances in computers and analysis tools have increased greatly the ability to solve complex shell stability problems. Thus, a brief description of the capabilities of an advanced, state-of-the-art analysis tool that could be used to obtain a wide range of analytical results that could be included in expanded versions of the NASA monographs is presented in this section.

Before embarking on an endeavor to revise the NASA monographs, a two-part question remains to be addressed; that is, "What kind of an approach to stability design should be used, and how should problem uncertainties be addressed?" A basic, first-approximation answer to this question is suggested below. The approach is based on the premises that many of the shell response parameters are not necessarily probabilisitic in nature, and that a completely probabilistic approach may tend to obscure the physical understanding of behavior. Thus, a hybrid approach to shell stability design is under consideration and will be discussed briefly in this section.

Another major consideration in the formulation of new design recommendations for a revised set of NASA monographs is experimental testing. With shell buckling behavioral trends established analytically, selective experiments can be identified and conducted to establish credible design recommendations. This selective testing approach, made possible by advanced analysis tools, is particularly important when considering the costs of conducting experiments and the costs of test specimens such as those made of fiber-reinforced composite materials. Moreover, to establish the best possible design recommendations, it is imperative to use high-fidelity experimental results. This step is necessary to prevent the introduction of excessive conservatism through the use of poor-quality experimental results. Some suggestions on how to obtain high-fidelity experimental results are also given in this section. Finally, some specific suggestions for improving the NASA monographs are presented.

Capabilities of an Advanced Analysis Tool

Advances in the finite-element method during the last fifteen years have improved the capability for analyzing complex nonlinear shell problems and to obtain accurate buckling and nonlinear response predictions. For example, an advanced, state-of-the-art structural analysis code has been used to conduct in-depth nonlinear analyses of the Space Shuttle superlightweight LO_2 tank.[16] This code was chosen for analyzing this problem because of its robust state-of-the-art nonlinear-equation solution algorithms and its general user-input capability that is convenient for modeling branched shells typically used for launch vehicles. It uses both the full and modified Newton methods to obtain an accurate nonlinear solution, and large rotations in a shell are represented by a co-rotational algorithm at the element level. The Riks arc-length projection method is used to continue a solution past limit points, and the Thurston[18] equivalence transformation processor is used for solution-branch switching in the vicinity of a bifurcation point. The code also permits complex geometries, loading conditions, boundary conditions and initial geometric imperfections to be modeled in a direct manner by the use of user-written subroutines. These subroutines are essentially independent of the mesh discretization, and provide analysts with a great deal of flexibility for modeling complex structural configurations (e.g., see Ref. 16) and conducting mesh refinement studies.

Advanced analysis tools with the capabilities mentioned above make it possible to determine accurate analytical estimates of the sensitivity of a shell buckling load to initial geometric imperfections or other destabilizing irregularities. Thus, state-of-the-art nonlinear shell analysis codes can be used to establish shell buckling behavioral trends deterministically for a wide range of system parameters, and to identify any unusual, possibly unexpected nonlinear behavior that designers should consider.

Basic Approach to Stability Design

Modern, high-fidelity nonlinear shell analysis codes, such as STAGS, have enabled accurate predictions of the nonlinear response and buckling loads of thin shell structures. The response of a shell can be determined accurately when its dimensions and properties are known to sufficient precision. For example, the effects of initial geometric imperfections can be dealt with by measuring the true shape of the shell and modifying the shell analysis model to represent the true measured geometry. Such deterministic analyses are valuable for identifying and isolating important contributions to the nonlinear response, and for systematically quantifying the effects of changes in structural and material design parameters.

The reliability of current shell design procedures can be improved by using these more accurate deterministic tools, provided that accurate information on the dimensions and material properties is available. If some dimensions and properties are not well known, however, it should be possible to modify the design process to include such uncertainties. By coupling a probabilistic representation of uncertain dimensions, tolerances, and material properties with a deterministic analysis that incorporates the better-known parts of the design problem, a hybrid design process could be developed. A typical result of the process might be a stiffened shell with a prescribed buckling load complete with a rationally obtained confidence interval. The hybrid approach could also serve as the basis for a reliability-based design procedure.

Suggestions for Future Experiments

The determination of meaningful knockdown factors for shell buckling depends greatly on high-fidelity experimental results. Some of the scatter in the post-1930's test data for buckling loads of isotropic cylindrical shells can be attributed to nonuniform load introduction or a poor simulation of the boundary conditions by the test fixture. When questionable test results are used to determine knockdown factors from lower bound curve fit approximations to the test data, the knockdown factor is likely to be overly conservative. Thus, it is very important to know the pedigree of a given set of test data.

To obtain high-fidelity experimental results, several issues must be addressed and several tasks must be performed. Prior to conducting an experiment, initial geometric imperfections of the shell surface, the wall thickness distribution, unevenness of the loaded edges, and the material properties should be measured. Knowledge of these quantities is extremely important for obtaining good correlation between theory and experiment. The instrumentation for a test should be planned adequately to facilitate the correlation between theory and experiment, and to provide enough data to help understand the expected behavior. The data sampling rate should be high enough to represent the shell response. The instrumentation should include back-to-back strain gages for monitoring bending strains and local nonlinear deformations; direct-current differential transformers (DCDT's), or other similar devices, for monitoring displacements normal to the shell surface; and shadow moiré interferometry for qualitatively monitoring buckle patterns. In many cases, the amount and type of instrumentation needed can be determined from preliminary analyses. It is important to reiterate that for some shell stability problems, a linear bifurcation analysis may not represent adequately the shell behavior, and as a result, may be inadequate for planning instrumentation. For experiments that involve load introduction by displacing a platen of a loading machine, proper alignment of the platens should be verified, and DCDT's, or other similar devices, should be used to define the plane of the loading platen and to detect any load introduction anomaly. The loaded edges of compression-loaded shells should be measured to ensure that the edges are as close to flat and parallel as possible. A loading rate that is consistent with the goals of the test should be selected. Details of the test fixture, and its relationship to the desired boundary conditions, should be clearly defined when reporting test data, and the locations of all instrumentation that correspond to the reported results should be clearly indicated.

For experiments that involve thermal loading, or combined mechanical and thermal loading, additional issues must be considered. An in-depth discussion of several of these issues has been presented by Blosser[19] and some of the information needed to characterize experimental results adequately is summarized as follows. First, the temperature distribution of the structure and its test fixture and the heat flux at all of the surfaces need to be recorded adequately to facilitate the correlation between theory and experiment. In addition, any difference in coefficient of thermal expansion of the specimen and the test fixture, any heating of the loading platens, and all locations of insulated surfaces and heat conduction paths should be recorded. Complete descriptions of the thermal test fixture components, including coolant passages and cavities, should be given and any interaction of the thermal components with the components used to introduce mechanical load should be identified. Other important details that should be recorded are the air temperature in the area surrounding the test specimen, the method of heating or cooling used for the specimen and test fixture, and changes in material properties of the specimen and test fixture with temperature.

Potential Improvements to the NASA Monographs

Certainly one of the most signficant improvements to the NASA monographs would be the inclusion of design recommendations for laminated composite shells

that are based on the analytical and experimental studies that have been conducted over the past twenty-five years. Another improvement would be to base knockdown factors on accurate analytical models of "nominally perfect" shells (shells free of initial geometric imperfections, material variances, etc.) that include the proper boundary conditions (as opposed to only simply supported boundary conditions which are used to a large extent in the current monographs) and possibly the effects of nonlinear prebuckling deformations. These tasks can be done for a wide range of parameters using specialized codes such as BOSOR4 and DISDECO, that compute bifurcation buckling loads that include the effects of nonlinear prebuckling deformations and various boundary conditions by solving a nonlinear eigenvalue problem.[20, 21] Isolating the effects of nonlinear prebuckling and boundary conditions are essential steps to understanding the shell behavior and to obtaining reliable knockdown factors that are not overly conservative.

Another significant improvement to the NASA monographs would be to establish practical nondimensional parameters that contain the appropriate geometric and material variables and that enable concise representations of behavioral trends and sensitivity of the response to variations of the parameters (e.g., see Ref. 22). Guidelines for including damage tolerance and the sensitivity of a design to load introduction effects would be valuable additions to the monographs. One of the most significant improvements that can be made immediately is to provide insight into, and quantitative results for, the true nonlinear interaction of combined loads that has been treated very conservatively in the NASA monographs as a linear interaction. Furthermore, providing design recommendations for thermal loads and for combined mechanical and thermal loads would be a significant improvement.

Another issue that must be addressed in order to obtain a new set of useful and practical design monographs is design uncertainties. A significant contribution to this area can be made by providing guidelines for determining which shell stability issues are handled more adequately in a deterministic rather than a probabilistic manner. From a practical viewpoint, this information indicates approximately the number of experiments and analyses needed to establish meaningful design recommendations and reliable, but not overly conservative, knockdown factors. Ultimately, the improvements to the NASA monographs should be focused on the practical needs of industry structural designers and chief engineers, and should reflect the scientific advances that have been made over the last twenty-five years. The end result of such an effort would be a collection of scientifically based knockdown factors and design recommendations.

Concluding Remarks

A summary of existing NASA monographs for the design of buckling resistant thin shell structures has been presented. Improvements in the analysis of nonlinear shell response were reviewed, and current issues in shell stability analysis were discussed. Examples of nonlinear shell responses that are not included in existing NASA shell design monographs have been presented, and an approach for including reliability-based analysis procedures in the shell design process was discussed. Suggestions for conducting future shell experiments to obtain high-fidelity results have been presented, and proposed improvements to the NASA shell design criteria monographs have been discussed.

Acknowledgements

The authors would like to express their thanks to Mrs. Vicki O. Britt, formerly of the NASA Langley Research Center, who conducted the experiments on the compression-loaded curved panels, and to Professor Johann Árbocz of Delft University of Technology, for many useful discussions on the topic of this paper.

References

[1]Anon., "Buckling of Thin-Walled Circular Cylinders," NASA Space Vehicle Design Criteria, NASA SP-8007, September 1965.

[2]Anon., "Buckling of Thin-Walled Truncated Cones," NASA Space Vehicle Design Criteria, NASA SP-8019, September 1968.

[3]Anon., "Buckling of Thin-Walled Doubly Curved Shells," NASA Space Vehicle Design Criteria, NASA SP-8032, August 1969.

[4]Gerard, G. and Becker, H., Handbook of Structural Stability, Part III - Buckling of Curved Plates and Shells, NACA TN 3783, August 1957.

[5]Becker, H., Handbook of Structural Stability, Part VI - Strength of Stiffened Curved Plates and Shells, NACA TN 3786, 1958.

[6]Gerard, G., Handbook of Structural Stability, Supplement to Part III - Buckling of Curved Plates and Shells, NASA TN D-163, 1959.

[7]von Kármán, T. and Tsien, H. S., "The Buckling of Thin Cylindrical Shells Under Axial Compression," *Journal of the Aeronautical Science*, Vol. 8, No. 8, June 1941, pp. 303-312.

[8]Donnell, L. H. and Wan, C. C., "Effect of Imperfections on Buckling of Thin Cylinders and Columns Under Axial Compression," *Journal of Applied Mechanics*, Vol. 17, No. 1, March 1950, pp. 73-83.

[9]Koiter, W. T., *On the Stability of Elastic Equilibrium*, (in Dutch), H. J. Paris, Amsterdam, Holland, 1945; translation available as AFFDL-TR-70-25, February, 1970, Wright-Patterson Air Force Base.

[10]Seide, P., Weingarten, V. I., and Morgan, E. J., "The Development of Design Criteria for Elastic Stability of Thin Shell Structures," STL/TR-60-0000-19425 (AFBMD/TR-61-7), Space Technology Laboratories, Inc., December 31, 1960.

[11]Vinson, J. R., The Behavior of Shells Composed of Isotropic and Composite Materials, Kluwer Academic Publishers, 1993.

[12]Stein, M., "The Effect on the Buckling of Perfect Cylinders of Prebuckling Deformations and Stresses Induced by Edge Support," Collected Papers on Instability of Shell Structures, NASA TN D-1510, December 1962, pp. 217-227.

[13]Stein, M., The Influence of Prebuckling Deformations and Stresses on the Buckling of Perfect Cylinders, NASA TR R-190, 1964.

[14]Árbocz, J., "Comparison of Level-1 and Level-2 Buckling and Postbuckling Solutions," Faculty of Aerospace Engineering, Report LR-700, Delft University of Technology, Delft, The Netherlands, November 1992.

[15]Sridharan, S. and Alberts, J., "Numerical Modeling of Buckling of Ring-Stiffened Cylinders," *AIAA Journal*, Vol. 35, No. 1, January 1997, pp. 187-195.

[16]Nemeth, M. P., Britt, V. O., Collins, T. J., and Starnes, J. H., Jr., "Nonlinear Analysis of the Space Shuttle Super-Lightweight External Fuel Tank," NASA TP 3616, December 1996.

[17]Brogan, F. A., Rankin, C. C., and Cabiness, H. D., "STAGS User Manual," Lockheed Palo Alto Research Laboratory, Report LMSC P032594, 1994.

[18]Thurston, G. A., Brogan, F. A., and Stehlin, P., "Postbuckling Analysis Using a General-Purpose Code," *AIAA Journal*, Vol. 24, No. 6, June 1986, pp. 1013-1020.

[19]Blosser, M. L., "Boundary Conditions for Aerospace Thermal-Structural Tests," Aerospace Thermal Structures and Materials for a New Era, E. A. Thornton, ed., Vol. 168, Progress in Astronautics and Aeronautics, 1995, pp. 119-144.

[20]Bushnell, D., "Stress, Stability, and Vibration of Complex Branched Shells of Revolution, Analysis and User's Manual for BOSOR4," LMSC-D243605, Lockheed Missles and Space Co., Inc., Sunnyvale, Ca., March 1972.

[21]Árbocz, J. and Hol, J. M. A. M., "Koiter's Stability Theory in a Computer-Aided Engineering (CAE) Environment," *International Journal of Solids and Structures*, Vol. 26, No. 9/10, 1990, pp. 945-973.

[22]Nemeth, M. P., "Nondimensional Parameters and Equations for Buckling of Anisotropic Shallow Shells," *Journal of Applied Mechanics*, Vol. 61, September 1994, pp. 664-669.

Design and Evaluation of Composite Fuselage Panels Subjected to Combined Loading Conditions

Damodar R. Ambur* and Marshall Rouse†
NASA Langley Research Center
Hampton, VA 23681-0001

Abstract

Methodologies used in industry for designing transport aircraft composite fuselage structures are discussed. Several aspects of the design methodologies are based on assumptions from metallic fuselage technology which requires that full-scale structures be tested with the actual loading conditions to validate the designs. Composite panels which represent crown and side regions of a fuselage structure are designed using this approach and tested in biaxial tension. Descriptions of the state-of-the-art test facilities used for this structural evaluation are presented. These facilities include a pressure-box test machine and a D-box test fixture in a combined loads test machine which are part of a Combined Loads Test System (COLTS). Nonlinear analysis results for a reference shell and a stiffened composite panel tested in the pressure-box test machine with and without damage are presented. The analytical and test results are compared to assess the ability of the pressure-box test machine to simulate a shell stress state with and without damage. A combined loads test machine for testing aircraft primary structures is described. This test machine includes a D-box test fixture to accommodate curved stiffened panels and the design features of this test fixture are presented. Finite element analysis results for a curved panel to be tested in the D-box test fixture are also discussed.

Introduction

The potential for cost and weight reductions still exists for aircraft structures made of polymeric composite materials despite recent material and manufacturing advances for metallic materials. This potential can be realized in aircraft fuselage structures by judicial integration of materials, structural design and analysis practices, and manufacturing processes. Assessing the advantages of using different materials and material forms, and understanding the response of aircraft structures subjected to combined loading conditions are important aspects of designing aircraft structures. Current composite structural designs are based on metallic structural experience-based approximations for design loads and individual panel analysis and sizing techniques. Such a metals-based design approach can result in a composite structural design with inadequate margins of safety. Structures are analyzed at the local level to satisfy damage tolerance and durability requirements. Existing tension-fracture and impact-damage data from flat laminates are currently used to design stiffened-skin and sandwich shell structures which could result in very conservative structural designs. A very limited amount of information currently exists for curved stiffened panels subjected to combined loading conditions to support the design of composite fuselage structures with large-size damage. Since composite structures have more material design variables than metallic structures, better design and analysis approaches are necessary to design efficient structures and to assess properly the advantages of using composite structures to replace metallic structures. Testing composite structures is likely to be an integral part of developing and validating designs for composite structures in the future.

Analytical and experimental work on composite fuselage crown and side panels is currently being conducted at NASA Langley Research Center to help study issues related to the nonlinear response, tensile fracture, damage tolerance, and residual strength of composite structures. New facilities are being developed to test new structural concepts subjected to combined internal pressure and mechanical loads. A pressure-box test machine and a combined loads test system with a D-

* Assistant Head, Structural Mechanics Branch. Associate Fellow, AIAA.
† Senior Aerospace Engineer, Structural Mechanics Branch. Member, AIAA.

box test fixture have been designed and fabricated to test structural panels with boundary conditions that simulate the actual stress states for panels in a fuselage shell structure. These new test facilities are designed to test damaged and undamaged panels subjected to actual flight load conditions.

The present paper presents an integrated approach for designing structures to satisfy performance, producibility and cost requirements. The paper describes the pressure-box test machine and the D-box test fixture for a combined loads test machine, and describes how these new facilities are being used to simulate the actual stress states in a fuselage shell. Analytical and experimental results are presented and compared for two composite curved panels tested in the pressure-box test machine. Analytical results are also presented that relate test results for panels subjected to combined loads to fuselage shell results. The need to include nonlinear effects in the analysis and design of pressurized composite structures is also discussed.

Design Methods for Fuselage Structure

The current approach for designing fuselage shell structures is based on designing individual panels based on the fuselage load distribution and manufacturing considerations. A fuselage barrel section divided into three different panels is shown in Figure 1, and the panels represent the crown, side and keel panels for the section. Each panel is further sub-divided into smaller-sized panels with approximately uniform stress states and analyzed and sized to satisfy stability and strength requirements. Since manufacturing procedures and cost are important elements in developing a transport composite fuselage, an integrated design approach is used that includes all structures and manufacturing disciplines in the design process for sizing the smaller-sized panels.

This integrated design approach includes the traditional structural design, structural analysis, weights, cost and manufacturing disciplines. The internal load distribution is determined from a finite element analysis model. Manufacturing processes that are appropriate for the structural concepts and material forms are selected to assure cost-effective fabrication of the structural parts, and the material strength, stiffness properties and design and manufacturing cost centers are identified. Structural design constraints including stability, strength, skin-to-stringer and skin-to-frame stiffness ratios, minimum skin gage, stringer spacing, ply layup, stringer height, minimum stringer flange width, stringer web angle, etc. are used for the structural analysis and sizing of the smaller-size panels. Additional constraints are imposed for damage tolerance and durability. A panel blending algorithm is used to optimize and assemble all the smaller-size panels into a larger panel design such that structural continuity is maintained for the skin, stringers, and frames. Design rules based on empirical and semi-empirical data are defined for blending the designs of several skin laminates, stringers, and frames. The designer identifies one or more sub-divided panels with regions of high stress concentrations to assure that the blending variables in non-critical areas of the panel are controlled by those for the critical areas, and a preliminary design for the fuselage shell is generated. Since the structural definition is usually completed to the 70 to 80 percent level of the final structural configuration during the preliminary design phase, it is important to use accurate structural analysis methods for this part of the design process. Finite element analyses are performed using the preliminary design as a starting point to arrive at a final design.

Evaluation of Fuselage Panels Subjected to Combined Loads

A common approach for studying the damage tolerance characteristics of pressure-loaded stiffened panels is to test flat panels with combinations of tension and compression loads in the longitudinal and lateral directions. These tests are relatively easy to perform, but the data generated from such tests are not directly applicable to the design of pressure-loaded curved panels since the bending gradients in the skin and the resulting nonlinear effects are not represented by the simpler tests. The best approach for determining the effect of these nonlinear response phenomena is to perform tests on a cylindrical shell to generate the required structural response information. Another approach for testing curved panels with combined compression, internal pressure, and inplane shear loading conditions is to mount a test panel in a cylindrical shell test fixture that has a cutout to accommodate the test panel. The panel is then subjected to the intended combined loading conditions by loading the cylindrical shell test fixture. The correct boundary conditions can be imposed on the test specimen more readily using this approach. This approach is useful unless it is necessary to test panels with different radii than the radius of the cylindrical shell test fixture. To avoid the expense of building a series of cylindrical shell test fixtures with different radii, a pressure-box test machine and a D-box test fixture have been developed for testing curved stiffened panels of different radii and frame spacings. The pressure-box test machine is used to test curved stiffened panels subjected to internal pressure and biaxial

tension loading conditions, and the D-box test fixture has been developed for testing curved stiffened panels subjected to combined internal pressure, compression, and shear loads compression by using a combined loads test machine. Analytical and test results for two typical fuselage panels tested in the pressure-box test machine, and analytical results that supported the design and development of the D-box test fixture are presented in the next section.

Biaxial Tension Loading Conditions

A photograph of the pressure-box test machine for testing curved stiffened panels subjected to internal pressure and biaxial tension loads is shown in Figure 2. This pressure-box test machine was designed to ensure that the appropriate boundary conditions are imposed on a pressurized curved panel to develop a stress state in the panel that is representative of a fuselage shell. This design requirement is particularly important when investigating failure of curved panels and for damage propagation studies. For both the undamaged and damaged states of the panels investigated using this test machine, It is possible to develop the proper stress magnitudes and gradients in a curved panel that are representative of the stress state in a shell with the corresponding loading conditions. A detailed description of this test machine is presented in Ref. 1.

Fuselage Crown Panel Evaluation. A stiffened graphite-epoxy fuselage crown panel shown in Figure 3 was tested in the pressure-box test machine to study its response characteristics. The panel has a 122-in. radius, a 72-in. length, and a 63-in. arc width. The material type and material properties for this panel are presented in Ref. 1. The panel skin is tow-placed using a fiberglass-graphite-epoxy hybrid material system to improve the damage tolerance characteristics of the panel. The panel frames are made of triaxially braided graphite fiber preform impregnated with an epoxy resin and cured using a Resin Transfer Molding process. The stringers pass through cutouts machined into the frames and no clips are used to attach the stringers to the frames. This design detail reduces the structural part count and the cost associated with panel fabrication.

The crown panel was analyzed using a nonlinear finite element code to determine the hoop-load reaction forces needed for the panel to simulate the stress state in the corresponding shell, and to provide analysis results to correlate with the test data for the damaged and undamaged test specimen. The hoop-load reaction forces are generated by adjusting a series of turnbuckles that attach the skin and the frames to the load reaction frame of the test machine. Finite element models for the cylindrical shell and the test panel in the pressure-box test machine were generated using PATRAN (Ref. 2). Nonlinear structural analyses for both the shell and the test panel were performed using STAGS (Ref. 3).

The finite element models for the test panel and the shell are shown in Figure 4. The quarter model for the panel shown in Figure 4(a) has approximately 10,000 shell, rod, and beam elements and 62,000 degrees of freedom. The load introduction structure, the turnbuckles, and actuator rods for the axial hydraulic jacks are modeled to account for rigid-body displacements and flexibilities at the panel boundaries. The shell reference model is shown in Figure 4(b). The model has symmetry boundary conditions, 16,686 shell and beam elements, and 100,000 degrees of freedom. Analytical hoop stress resultant results for the test panel subjected to 18 psi of internal pressure are compared with analytical shell results in Figure 5. The nonlinear analysis results for the panel with the turnbuckle loads adjusted to the required magnitude indicate that the boundaries influence the stress state in the load introduction region, but the stress states in the interior of the panel compare very well with the stress states for the shell structure. The hoop stress gradients for the reference shell and the panel in the pressure box with a 22-in.-long notch are compared in Figure 6. The location of the maximum value for the hoop stress resultant for both models is at the notch tip. The magnitudes for the hoop stress resultants also compare well with one another in the interior of the panel, but there are some differences in the results due to the load introduction effects at the boundaries of the curved panel. The undamaged test panel was subjected to an internal pressure of 18.2 psi and an axial load of 1,110 lb/in. This pressure value corresponds to twice the operating pressure, the design limit load condition, for the fuselage structure. Analytical and experimental hoop strain results are compared for the panel in Figure 7, and the strain gage locations are defined in the figure. The results correlate very well for the 5-psi and 18-psi internal-pressure load conditions shown in the figure. After the undamaged panel test was completed, a notch was cut into the panel skin to study the damage tolerance characteristics of the panel. Damage growth initiated at the notch tips for an internal pressure of 6.3 psi, and grew along a curved trajectory at approximately 11.2 psi of internal pressure. The details of the experimental results for the damaged panel are presented in Ref. 1. These results illustrate that the pressure-box test machine can be used to simulate a shell stress state in a test panel. The test panel exceeded its design requirements for the design burst pressure condition (twice the design limit load condition) in the undamaged

state, and satisfied the design limit load condition with damage.

Sandwich Fuselage Side Panel Evaluation. Sandwich fuselage side panels with window cutouts have also been evaluated using the pressure-box test machine. One of the sandwich panels is shown in Figure 8(a) and has three frames, a 122-in. radius, a 72-in. length, and a 63-in. arc width. The panel has two window cutouts located midway between the center frame and each of the outer frames. The elliptical window cutouts are 19.92-in. long in the fuselage circumferential direction and 15.30-in. long in the fuselage longitudinal direction. The sandwich panel facesheets were fabricated from the Hercules, Inc. AS4-8552 graphite-epoxy material system, and the core is a Korex honeycomb core material. The facesheets were made from tow-placed material for the inner plies and fabric material for the outer plies. The fuselage frames and window frames were fabricated from fiber preforms consisting of triaxially braided AS4 graphite fibers impregnated with PR500 epoxy resin and cured by using a Resin Transfer Molding (RTM) process. The sandwich skin and the three precured frames were cocured in a single cure stage. Typical material properties for the tow placed, fabric, and triaxially braided AS4-8552 and AS4-PR500 graphite-epoxy material systems are presented in Table 1. A photograph of the finished test panel assembled in the pressure-box test machine is shown in Figure 8(b). One of the objectives of this effort was to determine whether the structure designed with a three-frame configuration could be used with an increased frame spacing to demonstrate additional potential for aircraft structural weight reductions. A two-frame panel configuration was developed from the tested three-frame panel by removing its center frame.

A finite element model of the sandwich panel in the pressure-box test machine is shown in Figure 9. The sandwich panel is modeled using the ABAQUS finite element program (Ref. 4) with 4-node isoparametric elements for the face sheets and three 8-node solid elements through-the-thickness to represent the honeycomb core. The circumferential frames and the window frames are also modeled using the 4-node shell elements. The window glazing is also modeled using shell elements. The hoop and axial load introduction plates are modeled with shell elements. Symmetry boundary conditions are assumed at the axial and hoop centerlines which allows a quarter of the structure to be modeled and analyzed. The quarter model of the test panel in the pressure box has a total of 5,343 elements and approximately 26,650 degrees of freedom. This test panel was evaluated in the three-frame and two-frame configurations for two combined loading conditions: an 18.2-psi burst-pressure condition with 1,110 lb/in. of axial tension and a 13.65-psi design ultimate-pressure condition with 2,450 lb/in. of axial tension. Finally, the panel with the two-frame configuration was damaged with a cut along the panel hoop direction at the window cutout and tested to the design limit load condition of 8.85 psi of internal pressure and 1,630 lb/in. of axial tension.

The analytical hoop and axial strain results for the panel with three frames subjected to the design ultimate loading condition are presented in Figure 10. The design ultimate loading condition includes 13.65 psi of internal pressure and 2,450 lb/in. of axial tension. This loading condition causes high tensile forces in both the panel axial and hoop directions. The stress concentration factors are 2.88 and 2.05 for the hoop and axial stresses, respectively, at the edge of the cutout. The trends of the experimental results agree very well with the finite element analysis results. The experimentally measured strains on the panel outer surface in the hoop direction vary from 1,150 μin./in. to -900 μin./in. and the finite element analysis results which vary from 937 μin./in. to -949 μin./in. The measured strains in the axial direction vary from 4,000 μin./in. to -775 μin./in. and the corresponding results from the finite element analysis vary from 3,540 μin./in. to -815 μin./in.

The next set of loading conditions imposed on the panel with the center frame removed include 13.65 psi of internal pressure and 2,450 lb/in. of axial tension load. The panel outer surface hoop and axial strain results from the finite element analysis for this loading condition are very similar to the results presented in Figure 10 with the center frame loads redistributing in the sandwich skin. The experimental strain results for the two-frame panel are compared with the three-frame panel results in Figure 11. Strain gage locations around the panel cutout are illustrated in Figure 11(a). The maximum axial strain results at the cutout for the two-frame panel varies from -850 μin./in. to 4,000 μin./in. compared to the analytical results which vary from -540 μin./in. to 3,860 μin./in. These strain magnitudes are comparable to the axial strains for the three-frame panel for the same load condition.

This configuration was also tested with damage. A maximum value for the axial strain of the undamaged test panel occurs at the edge of the elliptical cutout at its major axis. The magnitude of this strain is 3,860 μin./in. for 13.65 psi of internal pressure and 2,450 lb/in. of axial tension. A 1-in.-long notch was cut into the panel at this critical location to study the damage tolerance characteristics of this sandwich panel concept. The notch was machined into the panel to extend in the panel hoop direction slightly beyond the

window frame edge. A combined loading condition with 8.85 psi of internal pressure and 1,630 lb/in. of axial load was applied to the panel. This loading condition corresponds to 2/3 of the design ultimate load condition. The panel outer surface hoop and axial strain results from the finite element analysis are presented in Figure 12 for this combined loading condition. The hoop varies from -1,100 μin./in. at q=90° to 1,900 μin./in. at q=0°. These strain magnitudes are 150% higher than for the hoop strain results presented in Figure 12 for 13.65 psi of internal pressure and 2,450 lb/in. of axial tension. This increase in strain for this test case is due to the increased bending in the skin between the two cutouts caused by the notch. The finite element results for the axial strain at the outer surface along the cutout indicate that the maximum strain of approximately 5,200 μin./in. occurs at the tip of the machined notch. The experimental strain results for this load case are presented in Figure 13(a). The test results indicate that the axial strains -500 μin./in. to 5,800 μin./in. and compare very well with the analysis results. No growth was observed in the notch length during the test. The experimental hoop strain results along the x-axis for the three-frame panel, for the two-frame panel, and for the two-frame panel with a notch at the window cutout are compared in Figure 13(b). These results suggest that the far field strains in the hoop direction are influenced more by the removal of the frame than by the introduction of the notch. The increase in the panel strain state due to the introduction of the notch is local and does not result in any significant load redistribution. These results illustrate that the panel configuration with three- and two-frames respond in a predictable manner and the strain are well within the failure strain allowables for this loading condition. The results on the three- and two-frame sandwich side panel suggest that additional structural weight savings are possible by increasing the frame spacing to 40 inches.

Combined Axial Compression and Internal Pressure Loading Conditions

Combined Loads Test Machine and D-Box Test Fixture

The combined loads test machine and D-box test fixture configurations are illustrated in Figure 14. The details of the combined loads test machine are summarized in Ref. 5. The D-box test fixture has been designed to ensure that appropriate boundary conditions are imposed on a curved panel to provide a stress state that is representative of a shell. This requirement is particularly important when investigating the failure of a curved panel and in damage propagation studies. Analytical studies have been performed on a D-box test fixture with a full-scale stiffened aluminum fuselage panel.

The D-box test fixture shown in Figure 15(a) must have adequate radial stiffness to support the pressure load but have a small axial stiffness compared to the test panel. The small axial stiffness of the D-box test fixture allows a test panel to experience most of the applied axial load and minimizes the shift in the center-of- pressure of the assembly if the test panel buckles. The low axial stiffness of the D-box test fixture is the result of an assembly of curved I-beams with the cross-section shown in the inset. The I-beam sections are 8.0 inches deep and 15 of these sections are used for the D-box test fixture. The axial stiffness of the D-box test fixture is designed to be 5 percent of a typical curved stiffened panel and D-box test fixture. The axial stiffness of the curved panel is assumed to be 1.1×10^6 lb/in., which is representative of the stiffness of a typical fuselage shell. This D-box test fixture is designed to test curved panels with 60 to 130 inch radii and 20 to 22 inch frame spacings. The panels are attached to the D-box test fixture with the hinge fittings as indicated in Figure 15(b). A cross-section of the D-box test fixture is presented in Figure 15(b) that shows the details of the hinge fittings. Thirteen of these hinge fittings are provided between the I-beams for this purpose. When the D-box assembly is internally pressurized, the assembly expands in a manner that causes the hinge supports to move inward. This deformation will cause the test panel to bend in a way that is not representative of the response of an internally pressurized shell. To prevent this undesirable deformation, cross bars are mounted between the hinge points as shown in the figure such that the distance between the hinge points can be held constant or adjusted as needed to induce the appropriate stress state in the test panel.

Description of Finite Element Models

Two important design details significantly influence the stress state in a curved stiffened panel tested in a D-box test fixture. The first design detail is the load introduction region that attaches the curved panel to the D-box test fixture. If the hoop load in the panel from internal pressure of the D-box assembly is only reacted at the panel boundary by the skin, the panel will be subjected to bending moments at the hinge attachment point. Part of the hinge fitting that attaches the test panel to the D-box test fixture is designed to react load through the frames as well as the skin. The analytical results used to select a hinge fitting design are

presented in Ref. 5. The second design detail is the support conditions along the two straight edges of the panel. Appropriate boundary conditions must be imposed on the panel so its response compares with the corresponds shell response for a given loading condition. The cross bars have to be designed to apply forces that prevent unwanted radial displacements that would bend the panel at the hinge locations. These design details have been studied using the results of finite element analyses. The finite element models for a cylindrical shell and the D-box test fixture with a corresponding test panel were generated using PATRAN (Ref. 2) and linear and nonlinear structural analyses were performed using NASTRAN (Ref. 6). The nonlinear analyses for the pressure and the combined pressure and axial load cases have been performed for the cylindrical shell case to understand nonlinear effects.

The shell is modeled using quadrilateral plate elements and has 25,973 degrees of freedom. The D-box test fixture assembly with the curved panel is modeled with plate, bar, beam, and spring elements totaling 6,773 elements and 33,130 degrees of freedom. To simulate the cylindrical shell subjected to internal pressure, the curved panel for the D-box test fixture is analyzed with boundary conditions that only permit radial displacements along the straight. To simulate the 20-in.-long longitudinal crack in the panel, two rows of coincident nodes are generated along the panel centerline which were disconnected along the 20-in. length.

Curved Panel and Shell - Linear Analyses

Finite element analysis results for internal pressure load cases and a combination of internal pressure and axial compression loads are presented herein for both undamaged and damaged curved panels. The entire hoop load developed in a pressurized panel must be supported by the D-box test fixture without introducing undesirable boundary effects. When a stiffened curved panel is tested in a D-box test fixture, the test fixture should provide proper support conditions to the panel and induce a stress state that is representative of the corresponding shell structure. Cylindrical shell results are compared with the corresponding curved panel results for internal pressure load cases with and without an axial compression load to study these issues. The panel used for the analytical studies is a full-scale aluminum panel which is planned to be tested as a proof-test article for the D-box test fixture which will be loaded in the combined loads test machine. The frame spacing for the panel is 20 inches and the stringer spacing is 6.85 inches. The panel is 96 inches wide and 120 inches long, and has a radius of 120 inches. A 20-in.-long longitudinal crack through the skin and the frame at the mid-length is used to represent penetration damage in an aircraft fuselage. The response of the panel with this damage condition will be studied with the panel tests.

Internal Pressure Loads. Two specimen and pressure combinations are considered for the internal pressure load cases. The first combination is the undamaged panel subjected to 18 psi internal pressure condition that is representative of the burst pressure (ultimate load) condition in a transport aircraft fuselage. The second combination is a panel with 20-in.-long penetration damage and subjected to the limit load condition of approximately 9 psi internal pressure. The panel also has a severed frame to simulate penetration damage.

Linear finite element analysis results for the panel in the D-box test fixture subjected to 18 psi of internal pressure and the results for the corresponding cylindrical shell are shown in Figure 16. The resulting hoop stresses in the shell (Fig. 16(a)) are uniform in the skin and frame regions. The load distribution between and the skin and frames is 46 percent and 54 percent of the total load, respectively. The maximum hoop stress resultant of 3500 lb/in. occurs on the skin surface opposite to the frame location, the hoop stress resultants for the inside flange of the frame is 1600 lb/in. The corresponding stress state in the curved panel supported in the D-box test fixture with rigid cross bars to prevent relative displacement between the hinge points is shown in Figure 16(b). The load is not uniformly distributed in the panel skin bays. The load distribution between the frame and the skin is 47 and 53 percent of the total load, respectively. The load in the middle of the panel has a bending component in addition to the membrane tension component. This undesirable bending moment can be corrected by applying a compressive preload to the cross bars which generates in a bending moment in the opposite direction. This correction is accomplished in the analysis by applying a uniform temperature to the cross bars. The cross bars apply an equal and opposite bending moment to the test panel and provide a uniform membrane stress state between the skin bays for a temperature of 150°F. The load distribution between the frames and the skin are also comparable to that of the cylindrical shell case for this 18-psi internal pressure condition as shown in Figure 16(c).

Analytical results for a panel with a 20-in.-long longitudinal crack extending from the center of one skin bay and with a severed frame are shown in Figure 17. The applied pressure load is 9 psi for this damage condition, which is the design limit pressure for the

fuselage. The load distribution for the shell is shown in Figure 17(a) and indicates that there is a 25 percent increase in the stress level in the undamaged frames compared to the undamaged panel results. This loading condition can be simulated in a curved panel in the D-box test fixture and the results of an analysis for this configuration are shown in Figure 17(b).

Combined Internal Pressure and Axial Compression Load Case. Linear analysis has been performed on the shell and the curved panel in the D-box test fixture to determine the loads that need to be applied through the cross bars to simulate the stress state in a shell by the stress state in the curved panel in the D-box test fixture. The results for the undamaged panel are summarized in Ref. 5. The hoop stress results for a shell with a 20-in.-long longitudinal crack and loaded with 2350 lb/in. of axial compression and 9 psig of internal pressure are compared with a corresponding case for the damaged curved panel in Figure 18. The stress resultant distributions for the two surfaces are comparable as shown in this figure when the appropriate cross bar forces are applied for this load case. The results indicate that the influence of a 20-in.-long longitudinal crack or an axial compression load is approximately the same on the loads in the cross bars. The crossbar forces are minimally affected by the above two conditions.

Axial Compression Load Case - Nonlinear Cylindrical Shell Analysis

The proof test of the panel for the combined loads test machine will be loaded in compression to levels beyond buckling. Reductions in curved panel stiffness in the postbuckling load range are determined from a nonlinear analysis to understand the panel response and the associated boundary conditions that must be imposed on the test panel in the D-box test fixture. The internal pressure causes nonuniform skin displacements that cause nonlinear interactions between skin and stringers and this response must be understood. Shell analyses have been performed for internal pressure and combined pressure and axial loading conditions to help understand the influence of these nonlinear effects on structural response. A representative shell segment is used for these analyses. The relatively small model size minimizes the computational times associated with the nonlinear analysis. Since the structure will be loaded beyond buckling, the dimensions of this shell segment need to be determined so that the model represents the shell response for compression loads. The cyclic symmetry technique in MSC/NASTRAN (Ref. 6) was used for a linear buckling analysis study to determine the size of this shell segment. The lowest eigenvalue for the shell segment was determined to be for a skin buckling mode with the skin between frames buckling along the shell circumference into 48 half-waves at a total load of 773 lb/in. A shell segment with two stringer spacings was chosen to correspond to this harmonic result. The length of the shell segment was chosen to include three frames to facilitate studies of shell response with a 20-in.-long longitudinal crack in the skin and with a failed mid-frame. Interactions from the boundaries of the shell segment on the internal stress states are expected to be a minimum for this structural size.

The hoop stresses for the damaged shell with the combined load case with 9 psi of internal pressure and 1,600 lb/in. of axial compression are presented in Figure 19. The nonlinear analysis results indicate significantly larger out-of-plane deformations for the damaged shell. The maximum values for the out-of-plane deflection occur in the vicinity of the crack tip. The magnitudes of these deflections are 0.26 in. and 0.59 in. for the linear and nonlinear analyses, respectively. The maximum hoop stress values for the nonlinear analysis results (Figure 19(b)) are twice the values for the linear analysis results. The load distributions between the skin and the frames obtained from nonlinear analysis results for both the undamaged and damaged shell models suggest that the stiffening of the skin due to large deformations enables the skin to support greater loads. The nonlinear analysis results for this axial load condition suggest that the skin supports 50 percent of the total load in the damaged state compared to 35 percent for the linear analysis results.

The differences between the load carrying capability of the skin with and without damage as obtained form the results from linear and nonlinear analyses for the combined pressure and axial load cases are explained by means of Figure 19(c). The change in stiffness of the skin is summarized in this figure as the end-shortening corresponding to an axial compression load is increased for the pressure loaded panel. Both the linear and nonlinear analysis results suggest that as the compression load is increased, stiffness reduction for the skin in the undamaged state is more than that for the skin in the damaged state. The nonlinear results suggest that for end-shortening values greater than 0.070 in. and 0.055 in. for the undamaged and damaged panels, respectively, the skin exhibits a stiffening behavior that results in the skin carrying more load compared to the value obtained from the linear analysis.

These analysis results suggest that curved panels subjected to internal pressure and axial compression can be tested in the D-box test fixture to study the response of full-scale shell structures.

Concluding Remarks

A design approach for fuselage shell structures has been summarized which takes performance, producibility and cost of the structure into consideration during the preliminary design phase. The quality of the preliminary design depends on the accuracy of the structural analysis methods that are available for this part of the design cycle. The approximations and simplifications that are currently being made during this design phase require that experiments be conducted on full-scale structure to validate the designs. A pressure-box test machine and a D-box test fixture can be used to simulate the shell stress state test panels such that the shell response can be assessed in a relatively inexpensive manner for both in undamaged and damaged structures. The comparison of experimental and analytical results re-emphasize the importance of performing geometrically nonlinear analyses to evaluate the response of thin-walled structures subjected to combined mechanical and pressure loading conditions.

References

[1]Rouse, M., and Ambur, D. R., "Fuselage Response Simulation of Stiffened Panels Using a Pressure-box Test machine," AIAA-95-1362-CP, April 1995.

[2]Anon., "PATRAN Plus User Manual - Release 2.4." PDA Engineering, Publication Number 2191023, September 1989.

[3]Brogan, F. A., Rankin, C. C., and Cabiness, H. D., "STAGS User Manual," Lockheed Palo Alto Research Laboratory, Report LMSC P032594, 1994.

[4]Anon., "ABAQUS Finite Element Code," Hibbitt Carlson and Sorenson, Inc., Vol 1-2, 1995.

[5]Ambur, D. R., Cerro, J. A., and Dickson, J. N., "Analysis of a D-box Fixture for Testing Stiffened Panels in Compression and Pressure," *Journal of Aircraft*, Vol. 32, No. 6, November-December 1995, pp. 1382-1389.

[6]Anon., "MSC/NASTRAN Handbook for Linear Analysis - Version 64," The MacNeal-Schwendler Corporation, August 1985.

Table 1. Typical material properties for graphite-epoxy materials used to manufacture the sandwich fuselage side panel.

Property	Tow AS4/8552	Fabric AS4/8552	Triaxial braid AS4/PR500	Korex core
Longitudinal modulus, E_1, Msi	18.30	9.20	7.50	0.00001
Transverse modulus, E_2, Msi	1.36	9.20	7.50	0.00001
Lateral modulus, E_3, Msi	1.36	1.30	----	0.0340
In-plane shear modulus, G_{12}, Msi	0.76	0.72	0.57	0.00001
Transverse shear modulus, G_{23}, Msi	0.52	0.50	0.40	0.0136
Transverse shear modulus, G_{13}, Msi	0.76	0.50	0.57	0.0326
Major Poisson's ratio, ν_{12}	0.32	0.04	0.29	0.30

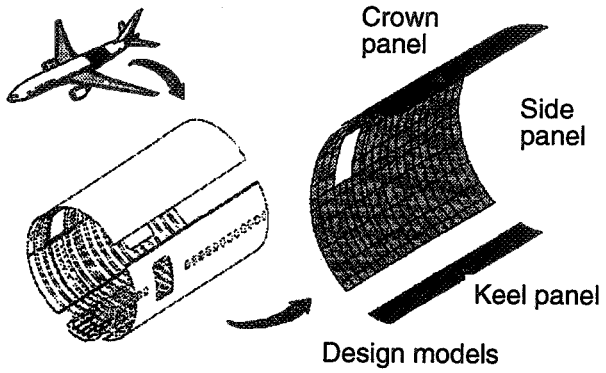

a. Hierarchy of design models.

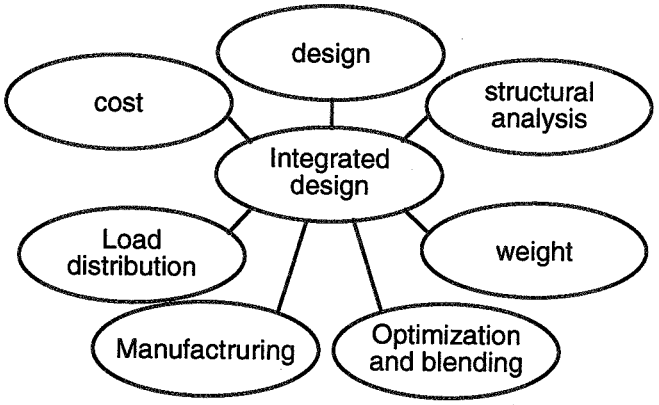

b. Interactions between major disciplines.

Figure 1. Summary of an integrated structural design approach.

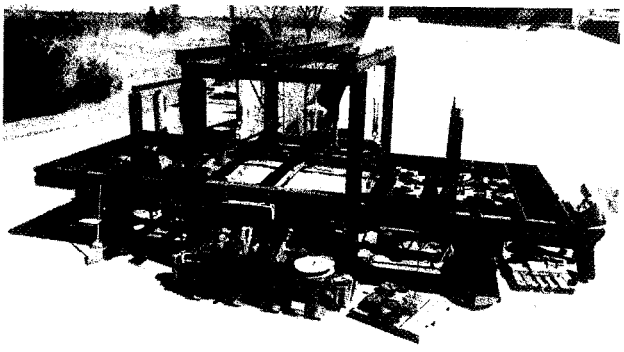

Figure 2. Pressure-Box Test machine.

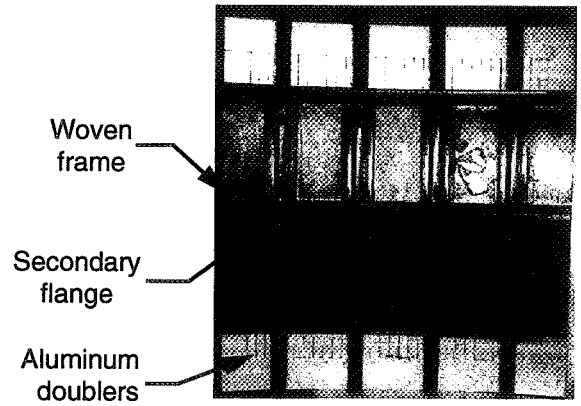

Figure 3. Composite fuselage panel.

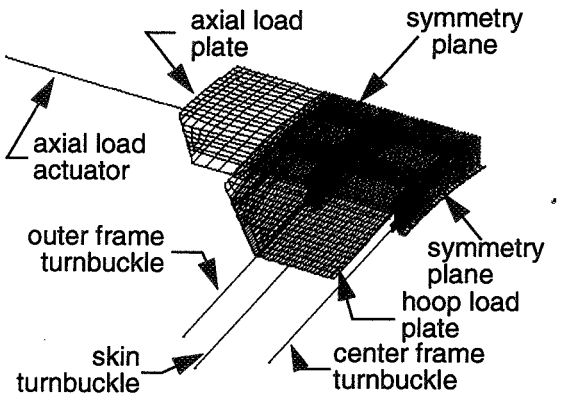

a. Curved panel in the pressure-box test machine..

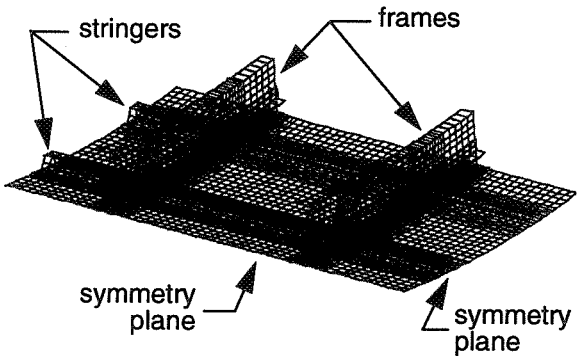

b. Cylindrical shell.

Figure 4. Finite element models.

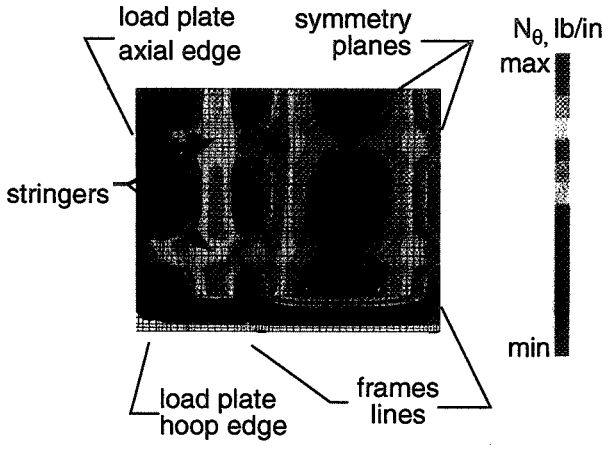

a. Curved panel in the pressure-box test machine.

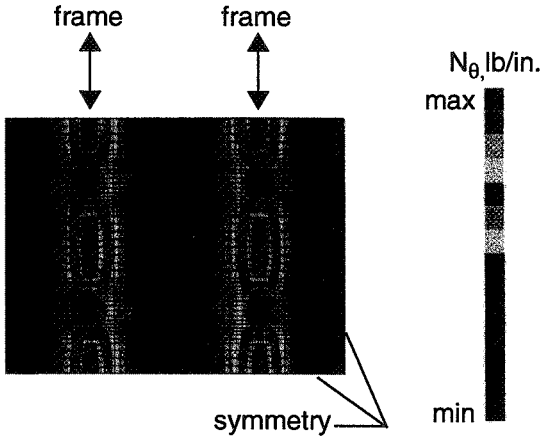

b. Cylindrical shell.

Figure 5. Typical hoop stress contour results.

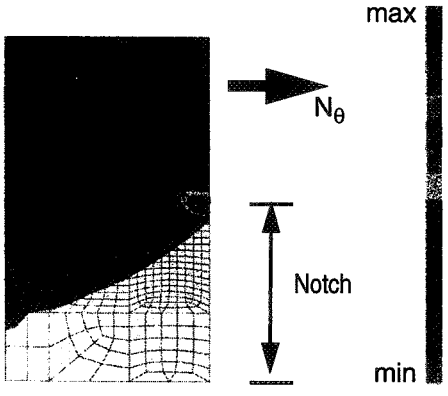

a. Curved panel in the pressure-box test machine..

Figure 6. Continued.

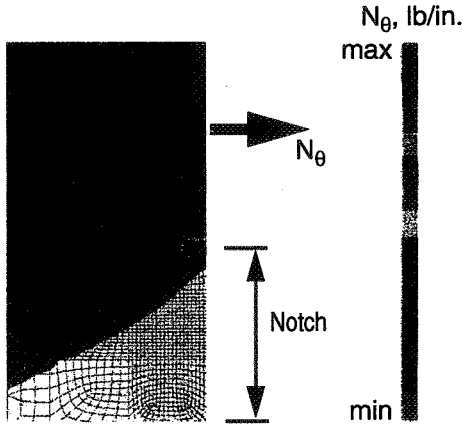

b. Cylindrical shell.

Figure 6. Typical hoop stress contour results at notch tip.

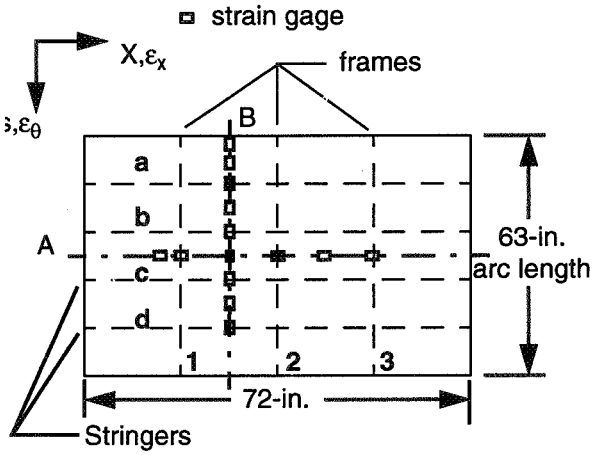

a. Strain gage locations.

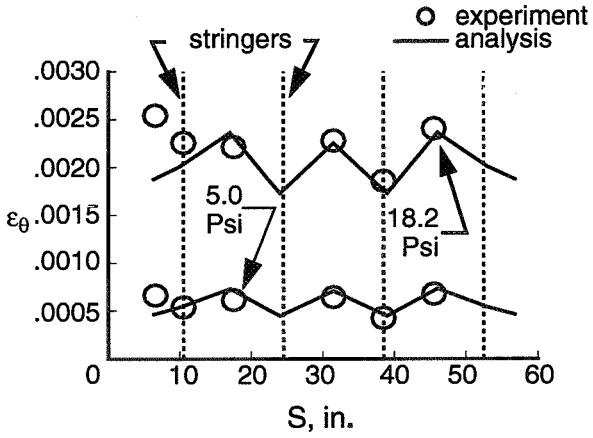

b. hoop strains along Line B

Figure 7. Comparison of experimental and analytical hoop strain results.

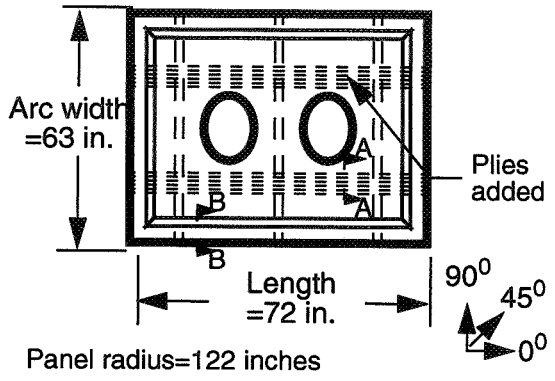

a. Plan view of panel design.

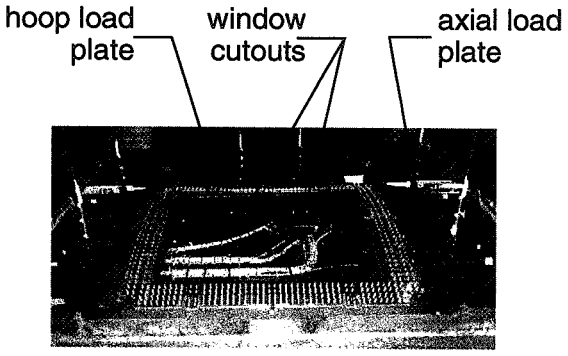

b. Photograph of sandwich panel in pressure-box test machine.

Figure 8. Details for the sandwich panel.

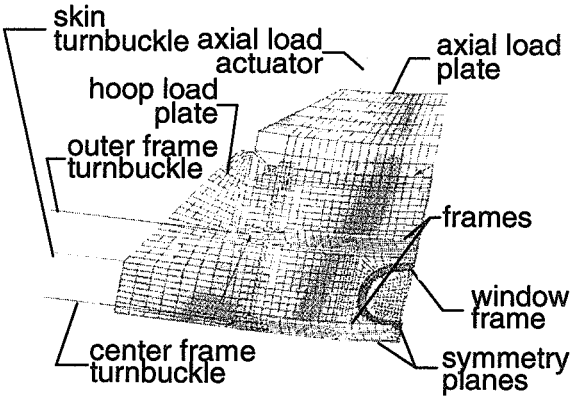

Figure 9. Finite element model of the sandwich panel.

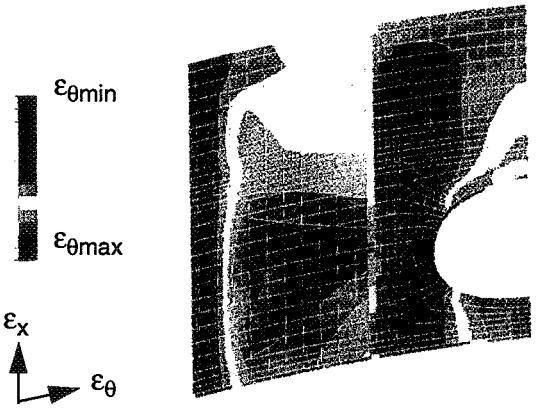

a. Hoop strain contour.

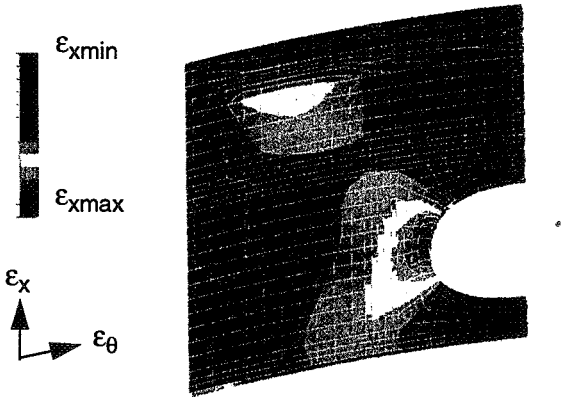

b. Axial strain contour.

Figure 10. Finite element analysis results for strain contours on the panel outer surface for a combined 13.65 psi internal pressure and 2,450 lb/in. axial loading condition.Concluded

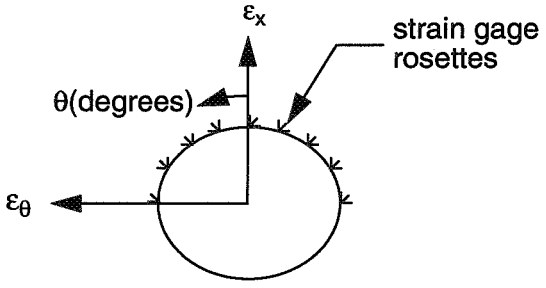

a. Strain gage locations on the cutout edge.

Figure 11. Experimental strain results on the two-frame panel outer surface for a combined 13.65 psi internal pressure and 2,450 lb/in. axial loading condition..

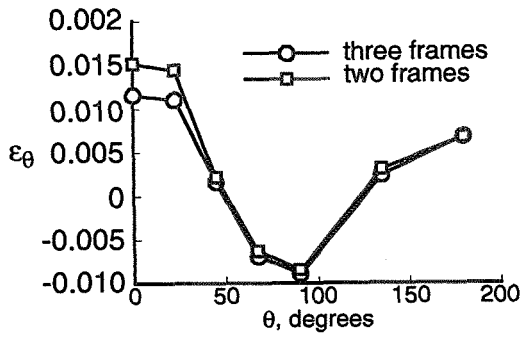

b. Hoop strain.

Figure 11. Continued.

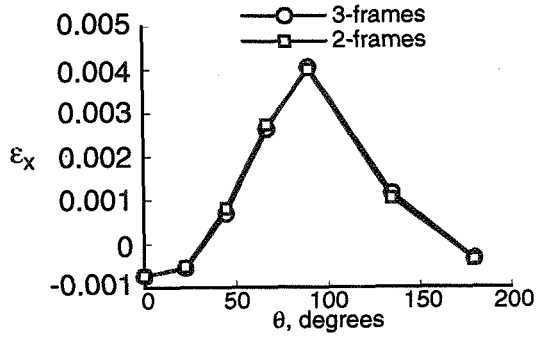

c. Axial strain.

Figure 11. Concluded.

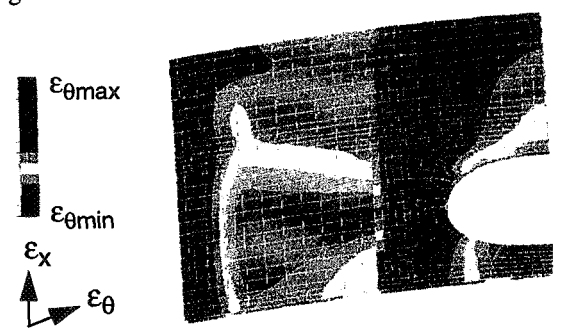

a. Hoop strain.

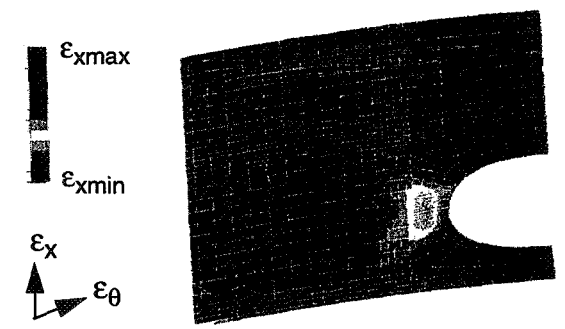

b. Axial strain.

Figure 12. Finite element analysis results for strains on the notched two-frame panel outer surface for a combined 8.85 psi internal pressure and 1,630 lb/in. axial loading condition.

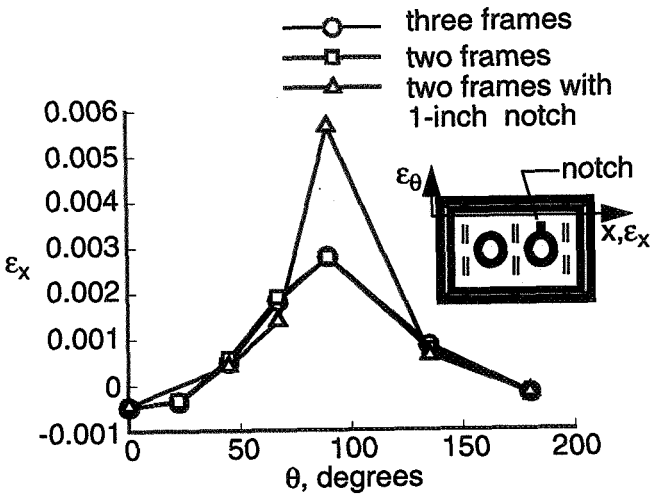

a. Axial strain around cutout.

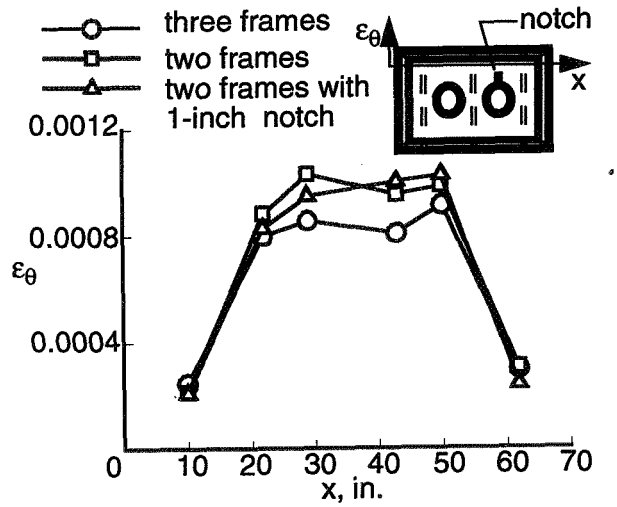

b. Hoop strain.

Figure 13. Comparison of experimental strain results on the three-frame, two-frame, and notched two-frame panel outer surface for a combined 8.85 psi internal pressure and 1,630 lb/in. axial loading condition.

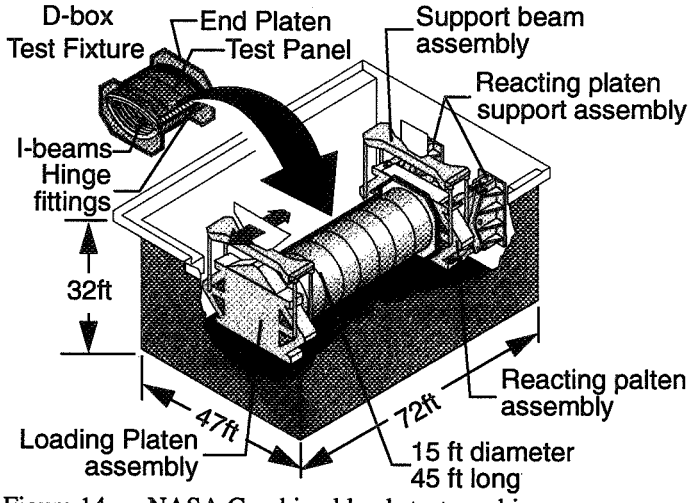

Figure 14. NASA Combined loads test machine.

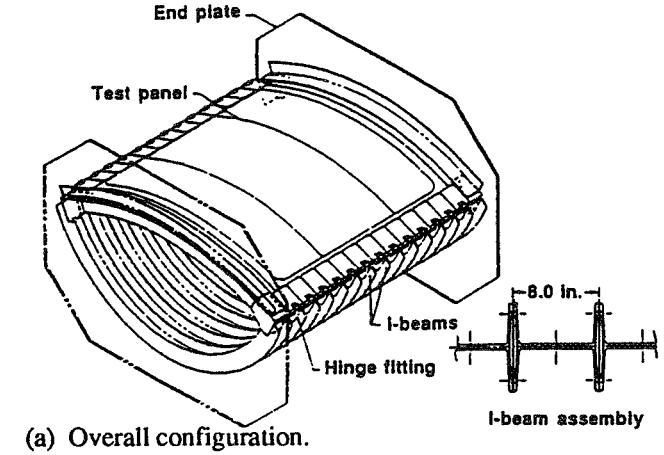

(a) Overall configuration.

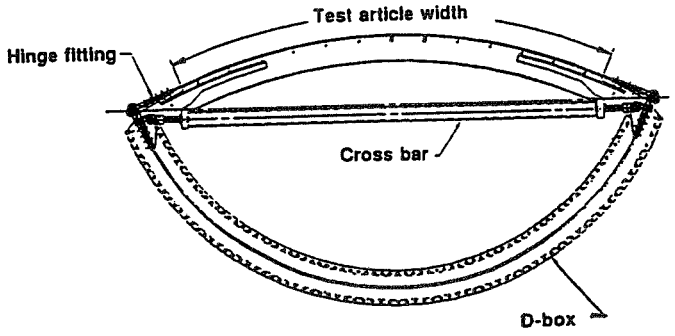

(b) Cross-sectional view.

Figure 15. D-box test fixture for testing curved stiffened panels.

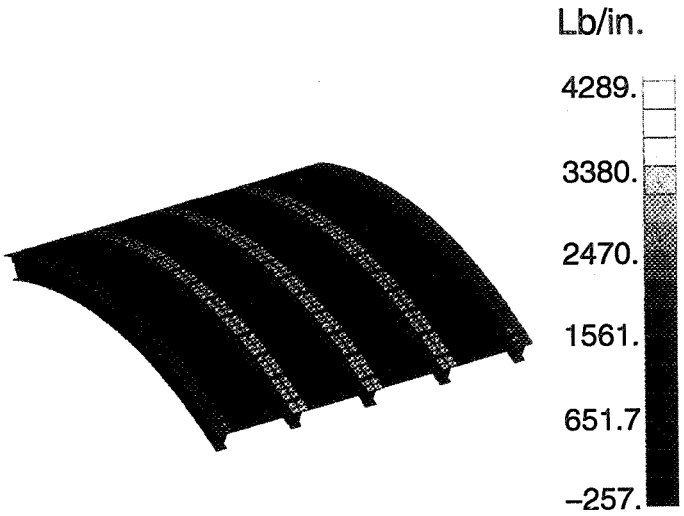

a. Cylindrical shell.

Figure 16. Comparison of hoop stress resultant distributions for the cylindrical shell and the curved stiffened panel for an internal pressure of 18 psi.

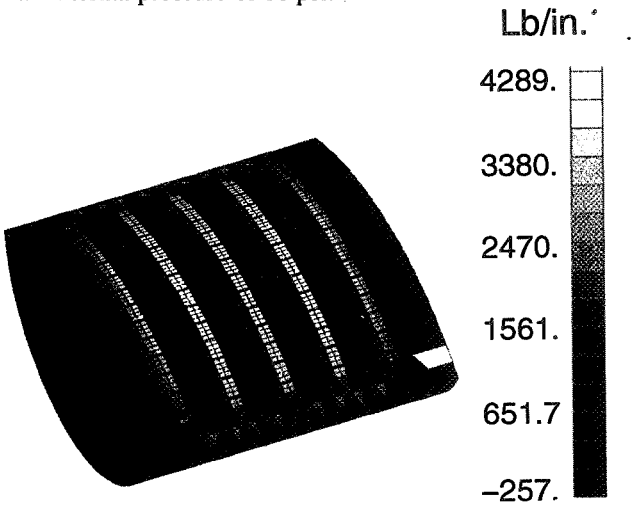

b. Curved panel in the D-box test fixture with rigid cross bars.

Figure 16. Continued.

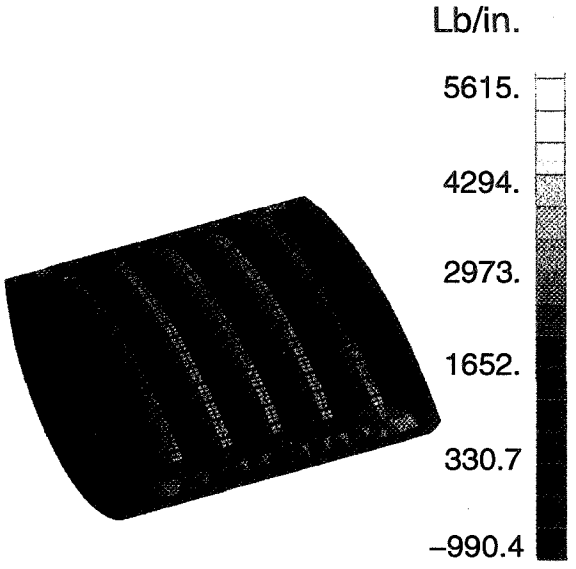

c. Curved panel in the D-box test fixture with preloaded cross bars.

Figure 16. Concluded.

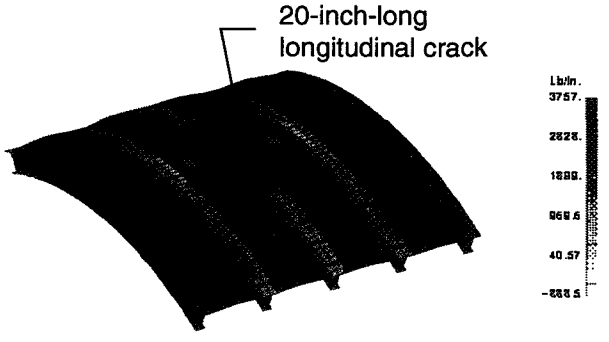

a. Cylindrical shell.

Figure 17. Continued.

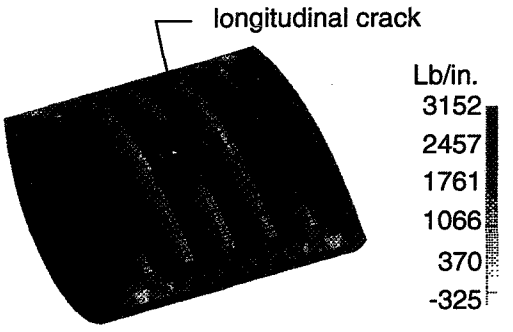

b. Curved panel in the D-box test fixture with loaded cross bars.

Figure 17. Comparison of hoop stress resultants contours for the cylindrical shell with 20-inch-long longitudinal crack for 9 psi internal pressure.

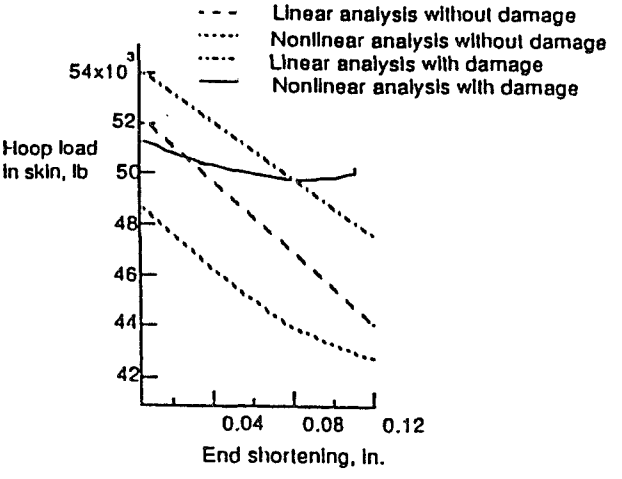

a. Cylindrical shell.

Figure 18. Comparison of hoop stress resultant distributions for the cylindrical shell and curved stiffened panel for a combined internal pressure of 9 psi and an axial loading of 2,350 lb/in.

MODELING TECHNIQUES FOR BIFURCATION AND COLLAPSE ANALYSIS OF RING-STIFFENED CYLINDERS : A COMPARATIVE STUDY

Srinivasan Sridharan, Member, A.I.A.A.
Professor of Civil Engineering, Washington University in St.Louis, MO 63130

ABSTRACT

The questions regarding the most effective technique of modelling stiffened shells persist despite the extensive literature available on them. In this study, ring stiffened cylinders having widely varying radius to thickness ratios are analyzed using alternative approaches for the determination of their buckling strength under pressure. The approaches considered here are : (i) Linear stability analysis using a two- dimensional model (ii) Linear stability analysis using a three dimensional model (iii) Nonlinear bifurcation analysis using a two dimensional model and (iv) Nonlinear bifurcation analysis using a three dimensional model. In-house computer programs based on p-version ring elements have been developed for these approaches. It is found that for thin shells linear stability analysis can significantly overestimate the buckling capacity. For moderately thick shells the linear and nonlinear approaches give close results for overall buckling, but can differ significantly for local buckling. This is largely due to end effects where the buckling mode is localized. For two dimensional models, the precise manner of connecting the shell and stiffener seems to be important. Asymptotic approach can predict the collapse load with an accuracy often sufficient for initial design, but not if there is a possibility of modal interaction.

INTRODUCTION

Ring-stiffened cylinders have been a subject of detailed study by several investigators in the past (see for example ref. 1-5). The problem is revisited in the present work, and ring-stiffened cylinders under hydrostatic pressure investigated for buckling and collapse by several alternative modeling techniques in order to gain an insight into the limitations and the range of applicability . To this end , in-house programs have been developed using ring elements with p-version type shape functions. Both "live" and "dead" normal pressures are treated.

In the context of bifurcation analysis, the paper focusses attention on two specific points :
(i) Accuracy of the classical linear stability analysis in comparison to that of nonlinear bifurcation analysis ,
(ii) various 2-D formulations in comparison to a rigorous 3-D formulation.

We note that, of these the former has been explored in detail by Arbocz [2-3] and his coworkers, but the latter has not received sufficient attention.

In general, for structures for which a single mode of buckling is identified to be the dominant one, one can use Koiter's asymptotic approach for the determination of the maximum load . The asymptotic approach is discussed in several treatises starting with Koiter's thesis[6]. In the context of ring-stiffened cylinders this is discussed in a recent paper by Kasagi and Sridharan[5]. There is often a question of how accurate is this prediction even in the context of a single dominant mode of buckling. Noting that the asymptotic approach is often used in conjunction with a linear prebuckling analysis, there arises the question if indeed the buckling mode thus generated is the critical mode of imperfection. Obviously there is a more realistic alternative, namely the buckling mode generated by a nonlinear bifurcation analysis, which entails significantly greater computational effort.

In this study, the results of collapse loads given by the asymptotic approach are compared with those obtained using full-fledged nonlinear analysis . For the latter too, ring elements are employed with harmonic shape functions. In the examples considered the number of participating harmonics is not too many as there is only a single dominant mode of buckling,.Thus not-withstanding the coupling of harmonics that occurs, the ring- elements are found to be a viable tool for the analysis. Further the harmonics are decoupled in the solution process, so that the governing equations are of the block-diagonal form as in the linear analysis[7].

In the context of prediction of collapse , the paper addresses two specific issues: (i) the accuracy of the asymptotic prediction of the maximum load and (ii) the sensitivity to imperfections in the shape of buckling modes given respectively by the linear and nonlinear bifurcation analysis.

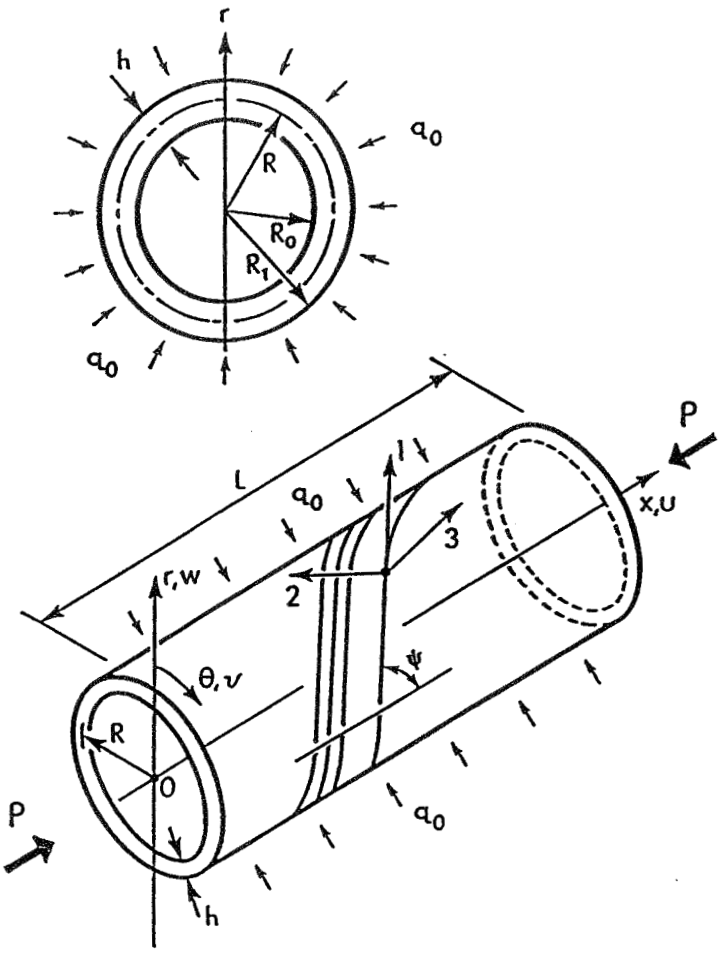

Fig.1 Cylinder with the Coordinate Systems, Key Dimensions and Loading

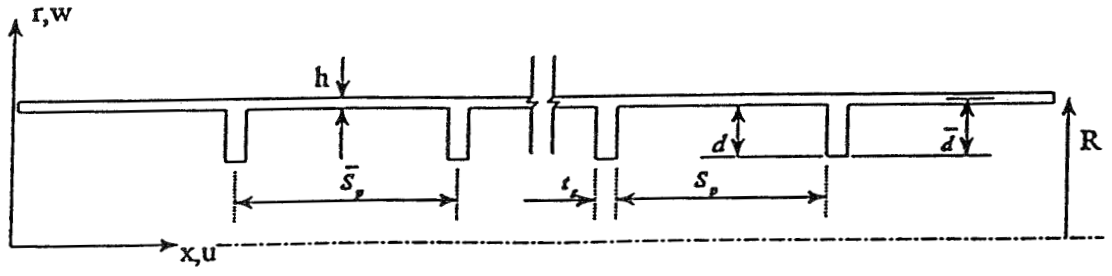

Fig.2 Longitudinal Section of the Cylinder

Geometry, Loading and Discretization

Fig.1 shows the coordinate axes and the loading of the cylinder. The longitudinal section of the cylinders which carry internal ring-stiffeners is shown in Fig.2 In-house computer programs employ ring elements with harmonic description of displacement variation in the circumferential direction. p-version type shape functions are utilized in the x-direction for 2-D models and x- and thickness direction for 3-D models.

Bifurcation Buckling

The following approaches are considered for comparative evaluation:

(i) 2-D Classical Linear Stability Analysis (LIN2D) which employs Sander's shell theory modified to capture the first order shear deformation effects. Stiffeners are treated by the Reissner-Mindlin plate theory. The classical lamination theory is used to treat the layered composite shells. The shell and the stiffeners are assumed to be connected at their middle surfaces. A linear prebuckling analysis generates the stress- distribution and the effect of prebuckling displacements are neglected in the buckling analysis.

(ii) 2-D Nonlinear Bifurcation Analysis (NONLIN2D) : The formulation is similar to LIN2D, but the prebuckling analysis is nonlinear and the critical pressures are obtained as bifurcation from the nonlinear prebuckling path. At the end of each loading step, a locally linear analysis is performed which extends the equilibrium path along the tangent at the current equilibrium state. At any point along this projected path, the displacements, the stresses and the strains are all given in terms of a single variable λ , the increment in the loading parameter from that of the equilibrium state. A linear eigen-value problem is then set up to compute the critical value of λ . Better and better approximations of the critical pressures are obtained as the equilibrium state approaches the bifurcation point, i.e. as $\lambda \to 0$.

(iii) 3-D Classical Linear Stability Analysis (LIN3D) : Three dimensional elasticity theory is employed to model the structure which is discretized into three types of elements, viz., shell, stiffener and junction. It is presumed that each of the constituent laminates is made up of a number of repetitive multi-ply units, so that for elastic analysis the layered material can be homogenized. As in LIN2D, the effect of pre-buckling displacements is neglected in the determination of bifurcation pressures.

(iv) 3-D Nonlinear Bifurcation Analysis (NONLIN3D) : The formulation is based on three dimensional elasticity but otherwise similar to NONLIN2D. The homogenization technique is employed as in LIN3D. This is the most rigorous of the four approaches to the bifurcation analysis mentioned in the foregoing.

Benchmark Problems

Ring stiffened cylinders having the following description are studied and the results obtained are compared to results obtained by using generally accepted computer codes, whenever available.

(i) An isotropic, thin, (R/t = 173.4) cylinder carrying six ($N_s = 6$) stiffeners. These were investigated by Moradi and Parsons[8] using a variety of commercial codes.

(ii) Moderately thick isotropic cylinder (R/t =50) carrying 12 ($N_s = 12$) stiffeners, investigated by Arbocz using BOSOR and EPAC at Delft University of Technology (Arbocz, Private Communication, 1992). These cylinders were analyzed with alternative depths of rings.

(iii) The last cylinder studied is a layered composite ring stiffened cylinder composed of a large number of [90/0] units, with R/t = 100 and 10 stiffeners ($N_s = 10$). When composed of a single unit of plies, this was analyzed by Kasagi and Sridharan[5] using INSTACC[4] and investigated for interactive buckling.

The key dimensions of the 3-D and 2-D models respectively are shown in Fig.2. In all the calculations symmetry with respect to center line (x = L/2) was exploited and only half the cylinder was modelled. The simply supported boundary conditions applied to the cylinder for each analysis :

At $x = 0, L$, $v_o = w_o = \beta = 0$ (2-D analysis) ; $v = w = 0$ (3-D analysis)

By virtue of symmetry at $x = L/2$, $u_o = \alpha = 0$ (2-D analysis) and $u = 0$ (3-D analysis).

Thin, Isotropic Cylinder (Moradi/Parsons)

The first cylinder studied is an isotropic cylinder with six ring stiffeners. A thorough study of this shell was completed by Moradi and Parsons[8], and this study provides a benchmark to compare current results with.

Geometric Data : $L = 2.38$ in ; $R = 3.9885$ in ; ($R_1 = 4$ in) $h = 0.023$ in ; $N_s = 6$; $t_s = 0.017$ in ; $S_p = 0.34$ in . The ratio of volume of stiffener materia material to that of cylinder is 0.24, based on center line dimensions, so that

the stiffener depth (measured from the centerline of the shell) d = 0.1288 in. The geometry of the 3-D models (LIN3D, NONLIN3D, INSTACC) is derived from the centerline dimensions given above. (All bays of 2-D model are of equal length whereas the end bays of 3-D models differ from the interior ones by $t_s/2$.)
The material properties are: E = 10,400 ksi, $\nu = 0.3$ The cylinder was subjected to hydrostatic pressure in the form of radial loading.

TABLE 1
Buckling pressures of Moradi-Parson Cylinder

Program used	Linear q_{cr}, psi	Nonlinear q_{cr}, psi
Abaqus S4R5	298	261
Abaqus STR15	309	***
Abaqus S8R5	303	265
Abaqus C3D20	307	274
BOSOR4	302	265
INSTACC	302	***
LIN2D	301	***
NONLIN2D	***	265
LIN3D	302	***
NONLIN3D	***	262

The buckling loads obtained by Moradi and Parsons using different types of elements and formulations[8] are presented in Table 1 along with the current results. The results shown are buckling pressures for the overall mode of buckling, with seven waves in the circumferential direction.

Table 1. demonstrates:
(i) The close agreement of the current results shown in the bottom half of the table with previous results shown in the top half of the table which were obtained by standard software such as ABAQUS and BOSOR4.
(ii) The importance of a nonlinear prebuckling analysis. The table shows a fairly large discrepancy between the loads obtained by the linear prebuckling analysis and those obtained by the nonlinear prebuckling analysis.
(iii) Both 2-D and 3-D analyses give essentially the same results for the shell.

In general, for thin cylinders the buckling pressure produced by the nonlinear bifurcation analysis is significantly less than that produced by the linear bifurcation analysis. This appears to have been caused essentialy by the prebuckling deformation which alters the longitudinal profile of shell at the ends of the cylinder. This becomes evident upon an inspection of the prebuckling response which shows marked nonlinearities with significant deflections developing in the first bay. This effect is missed in the linear bifurcation analysis.

It is also important to note that the overall buckling mode as generated by the linear prebuckling analysis differs greatly from that generated by the nonlinear prebuckling analysis.This can be seen in Fig. 3(a) , which shows the overall buckling modes generated by LIN2D and NONLIN2D. For the nonlinear bifurcation analysis, the maximum radial displacement occurs near the edge of the cylinder and for the linear bifurcation analysis the maximum radial displacement occurs at the center of the cylinder.

Only the overall buckling pressures are shown in Table1 as this cylinder was studied for purposes of comparison, and there was no previously obtained data in on local buckling pressures. As a matter of interest, the local buckling pressure determined by LIN2D was 578 psi (m =17) in the circumferential direction. The local buckling modes as determined by LIN2D and NONLIN2D are shown in Fig. 3(b). Once again, it is demonstrated that the buckling mode generated by the linear bifurcation analysis differs greatly from that of the nonlinear bifurcation analysisis. It is seen that the maximum modal radial displacement generated by the linear bifurcation analysis is near the center, and the maximum modal radial displacement generated by the nonlinear bifurcation analysis is near the edge of the cylinder.

Note that the application of live pressure as against dead pressure does not change the results by more than a fraction of percent. This is due to the relatively large number of waves associated with buckling (m = 7).

Stiffened, Moderately Thick, Isotropic (Arbocz) Cylinders

These two cylinders, designated as Case 1. and Case 2 Arbocz cylinders , are moderately thick, isotropic cylinders with twelve stiffeners. Both the Arbocz cylinders have the same goemetry, with the only difference being that the Case 1 cylinder has a greater depth of the stiffener than

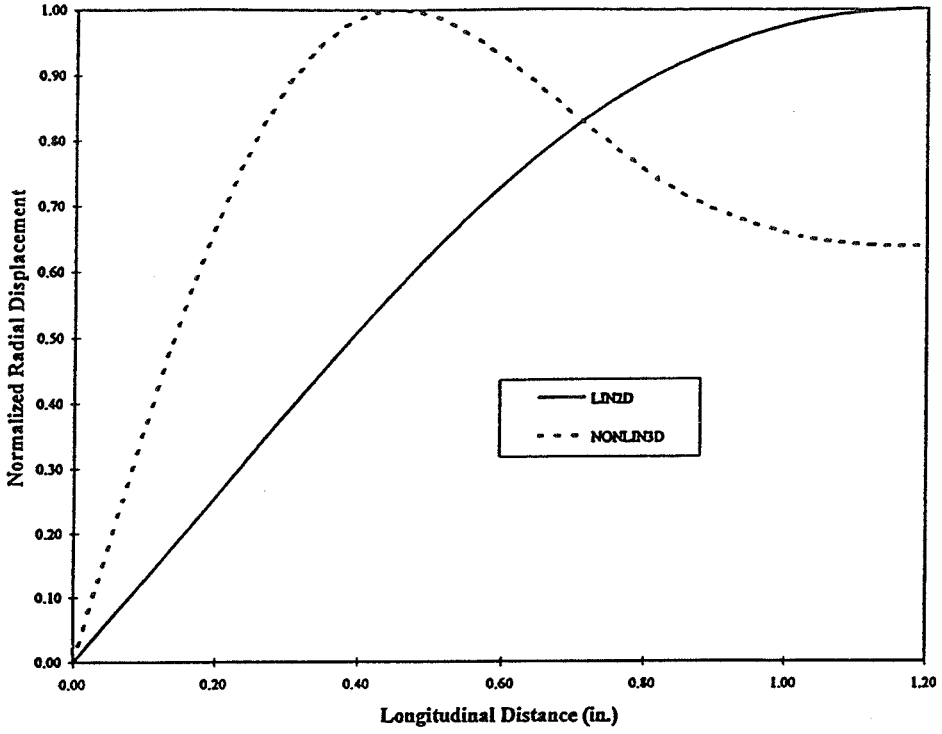

Fig.3(a) Overall Buckling Mode of Moradi-Parson Cylinder

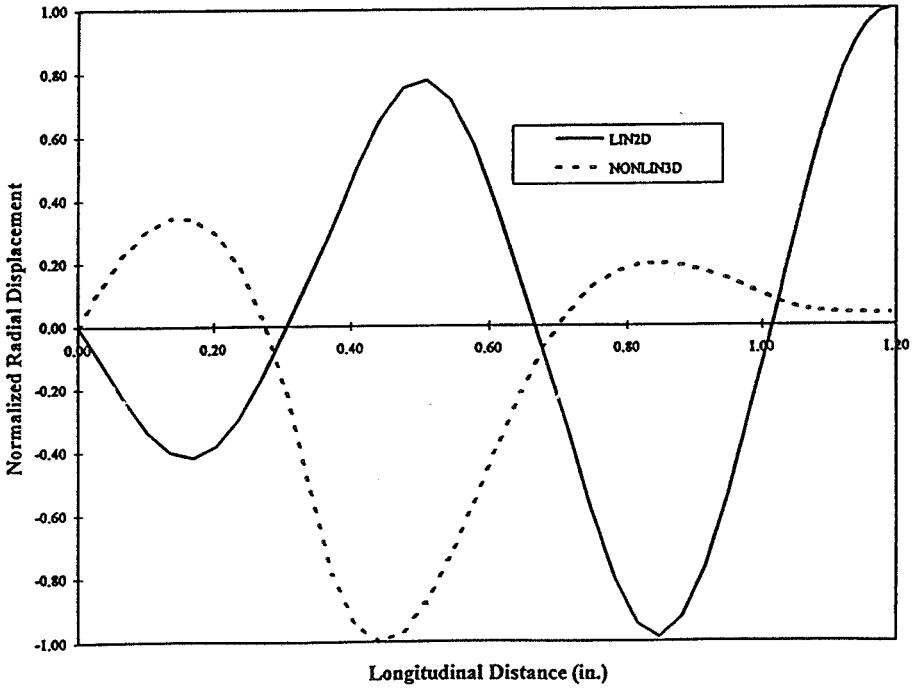

Fig.3(b) Local Buckling Mode of Moradi-Parson Cylinder

Case 2. The dimensions of both the cases are listed in Table 2. All the bays are of equal length in the 3-D model. Poisson's ratio is taken as 0.3 . The cylinders were subjected to both live and dead pressures.

Table 2. Dimension of the Arbocz Cylinders

Dimension	Case 1	Case 2
t_s/h	1.0	1.0
R/h	50.0	50.0
S_p/h	20.0	20.0
d/h	7.6	3.0
S_p/h	21.0	21.0
d/h	8.1	3.5

Tables 3(a-b) and 4 (a-b) show the buckling pressure predictions for for overall and local buckling respectively. Two cases are considered viz. Case 1 and Case 2 with alternative depths of stiffeners. The buckling pressures are given in the non-dimensional form of the ratio of the buckling pressure to the elastic modulus. **n** and **m** indicates the number of waves in the circumferential direction for overall and local buckling respectively.

Overall Buckling Results

The most significant observation from Table 3(a) is that both EPAC and BOSOR5 overestimate the buckling pressures in comparison to the bench mark result of NONLIN3D which makes no assumptions other than linear elastic material response. The error (which is about 15% or more) is the combined result of approximations in the formulation and the manner in which stiffener is modelled. The BOSOR program (i) models the shell and stiffeners by thin shell approximations , (ii) treats the stiffeners as connected to the inside of the shell , and (iii) assumes that the junction region behaves as a thin shell. In contrast , the present 2-D treatment accounts for the first order shear deformation effects and assumes the shell and stiffener as connected at the center of the shell. With respect to the connection of the stiffener with the shell, neither the BOSOR nor the present treatment can be claimed to be satisfactory for thicker shells. However for the Case 1, the present 2-D analyses produce results that are in better agreement with those given by the 3-D models. The errors associated with the present 2-D classical linear stability analysis (LIN2D) and 2-D nonlinear bifurcation analysis (NONLIN2D) are about 7% and 2% respectively .

Table 3(a) Overall Buckling Pressures of Arbocz Cylinders (n = 2)

Analysis Program	$\{q_{cr}/E\} \times 10^4$	
	Dead	Live
EPAC	2.784	2.208
BOSOR5	------	2.254
NONLIN2D	2.301	1.913
NONLIN3D	2.286	1.939
INSTACC	2.158	1.796
LIN2D	2.157	1.827
LIN3D	2.156	1.861

Table 3(b) Overall Buckling Pressures of Arbocz Cylinders (n = 2)

Analysis Program	$\{q_{cr}/E\} \times 10^4$	
	Dead	Live
EPAC	5.527	4.929
BOSOR5	------	4.981
NONLIN2D	5.207	4.724
NONLIN3D	5.201	4.809
INSTACC	5.208	4.775
LIN2D	5.070	4.600
LIN3D	5.206	4.814

Local Buckling Results:

Table 4(a) and 4(b) summarize the critical pressures associated with local buckling for the two Arbocz cylinders. m is found to be 9 in all but one result. This is the BOSOR5 result of case 2 where m = 8. The point of major interest in these results is the significant difference between the critical pressures as given by the nonlinear bifurcation analysis on the one hand and the linear bifurcation analysis on the other. The buckling modes are strongly localized near the ends due to significant prebuckling deformation near the supports - a phenomenon not picked up by the linear programs LIN2D, LIN3D and INSTACC. BOSOR5 and EPAC results are now in better agreement with the bench mark result (of NONLIN3D) than NONLIN2D.

Stiffened Composite Cylinder

The results for a carbon-epoxy stiffened shell $[90/0]_n$ (n is very large) as obtained using various approaches are shown in Table 5. The geometric parameters (ref. Fig.1) are :
$L/h = 262$, $R/h = 100$, N_s (number of stiffeners) = 10,
$S_p/h = 22$, $t_s/h = 2.0$, $d/h = 5.422$.
The shell is subjected to hydrostatic pressure and is simply supported at its ends. For calculations employing INSTACC the number of layers were increased till the results converged. A homogenization procedure[9] was adopted to obtain the effective elastic constants for LIN3D and NONLIN3D.

As can be seen, there are considerable differences between the predictions of the various approaches. The differences are accentuated in this case where shear deformation, the actions of shell-stiffener junctions and the tendency for localization of the buckling mode all become important.

For thin shells, the nonlinear bifurcation pressures significantly differ from those given by linear stability analysis. The buckling displacements as given by the nonlinear bifurcation analysis tend to be concentrated near the ends of the shell. For thicker shells, considerable differences can arise in the predictions of 2-D and 3-D models. This is the combined result of shear-deformation of the shell, the 3-D action at the junctions and the significant difference between the inner and outer radii of the shell.

Table 4(a) Local Buckling Pressures of Arbocz Cylinders (m= 9) : Case 1

Analysis Program	$\{q_{cr}/E\} \times 10^4$	
	Dead	Live
EPAC	1.545	1.534
BOSOR5	------	1.546
NONLIN2D	1.496	1.492
NONLIN3D	1.553	1.582
INSTACC	1.866	1.880
LIN2D	1.776	1.769
LIN3D	1.867	1.910

Table 4(b) : Local Buckling Pressures of Arbocz Cylinders (m = 9) : Case 2

Analysis Program	$\{q_{cr}/E\} \times 10^4$	
	Dead	Live
EPAC	1.543	1.501
BOSOR5	------	1.476 (m=8)
NONLIN2D	1.450	1.445
NONLIN3D	1.495	1.523
INSTACC	1.758	1.772
LIN2D	1.684	1.677
LIN3D	1.759	1.798

Prediction of Collapse :Nonlinear Analysis

In order to determine the imperfection-sensitivity and collapse strengths both asymptotic and full-blown nonlinear analyses are employed and the results studied in comparison. The nonlinear analysis employs ring elements with displacement functions in the form of multiple harmonics in the circumferential direction and p-version polynomials in the longitudinal direction. A preconditioned conjugate gradient scheme is employed to uncouple the harmonics in the solution process.

Table 5 (a) : Overall Buckling Pressures of Composite Cylinder (n = 3)

Analysis Program	$\{q_{cr}/E\} \times 10^4$	
	Dead	Live
NONLIN2D	2.2687	2.0975
NONLIN3D	2.1123	1.9786
INSTACC	2.1016	1.9470
LIN2D	2.2530	2.0626
LIN3D	2.0976	1.9676

Table 5 (b) : Local Buckling Pressures of Composite Cylinder (m = 10)

Analysis Program	$\{q_{cr}/E\} \times 10^4$	
	Dead	Live
NONLIN2D	2.3011	2.3063
NONLIN3D	2.0269	2.0532
INSTACC	2.2783	2.2815
LIN2D	2.5081	2.4970
LIN3D	2.2783	2.2956

Prediction of Collapse: Asymptotic Procedure

Asymptotic procedure which is an order of magnitude simpler offers itself as a viable alternative to nonlinear analyses . The simplest version of such a procedure is based on the extraction of the buckling load by a linear stability analysis and the calculation of a second order field. The problem is converted to one of single degree of freedom in which it is possible to incorporate the effect of initial imperfections in the form of the buckling mode.

Both these types ofcalculations, i.e. the asymptotic and the fully nonlinear , have been performed for the Moradi -Parson cylinder and the results obtained are plotted in Fig.4. The following cases are studied :

following cases:

(i) Asymptotic procedure with imperfection in the form of buckling mode as given by the linear stability analysis (LB) with amplitudes repectively of 0.25h and 0.5h at the center of the shell.

(ii) Full-blown nonlinear analysis with the same levels of imperfection as in (i) above, and finally

(iii) Full-blown nonlinear analysis with imperfections in the form of the buckling mode as given by the nonlinear bifurcation analysis (NLB) with maximum amplitudes of imperfection of 0.25h and 0.50h (near the first bay) respectively.

The asymptotic procedure results are higher than the corresponding nonlinear analysis results by 7% and 5% for the two levels of imperfections. This is because the asymptotic procedure does not account for prebuckling axisymmetric deformation. As discussed earlier, the prebuckling nonlinearities tend to precipitate buckling Further in the nonlinear analysis there is some scope for a freer readjustment of the deformations in the longitudinal direction in comparison to the asymptotic analysis. Nevertheless, the latter gives a quick estimate of the maximum load albeit with some sacrifice of accuracy.

Comparing the results of nonlinear analysis with imperfections in Mode LB and Mode NLB respectively, it is seen that the latter imperfection is more critical. The discrepancies are of the order of 7%. Furthermore, the analysis employing Mode LB as the imperfection shape fails to identify the region of the shell structure where failure would initiate.

However, there are cases when the asymptotic analysis would underestimate the maximum capacity of the shell. This happens because the second order field is evaluated at the critical load which is significantly greater than the maximum load carried by the structure. This tends to overestimate the second order deformations and thus exaggerate their destabilizing influence.

All the foregoing pertains to situations where a single buckling mode plays the dominant role. Ofcourse, if there is modal interaction especially between a local mode and an overall mode, the maximum load can be significantly lower. The problem of modal interaction in stiffened cylinders has been studied in detail by Kasagi and Sridharan[5]. It turns out that this is a highly imperfection-sensitive phenomenon and must be considered in any near-optimal design of stiffened shells.

CONCLUSION

1. For thin shells (R/h > 150) carrying ring stiffeners, linear stability analysis not only overestimates the buckling pressures, but also fails to capture the correct buckling mode. Even for moderately thick shells, linear bifurcation analysis is found to be unsatisfactory when the governing mode is local. The nonlinear bifurcation analysis captures the effect of prebuckling bending deformation in the vicinity of the supports and a buckling mode which is localized near the ends . In all these cases nonlinear bifurcatiion analysis must be used. For thicker shells which tend to buckle in the overall mode, the linear stability analysis can give an acceptable estimates for practical design.

2. For moderately thick stiffened cylinders the precise modeling of the stiffener and shell connection is important. A simple approach in which the stiffener and the shell are both represented by their centerlines and assumed to be connected at the point of intersection was found to be effective and produced results within 2% of the corresponding 3-D result for thin shells. For shells with stocky stiffeners, 2-D approaches give poor results especially for local buckling.

3.In general, the asymptotic procedure can either underestimate or overestimate the maximum load. In thin shells with R/t > 150, the prebuckling nonlinearities play a significant role in causing a reduction of the maximum load carrying capacity - an effect not considered by the asymptotic procedure. On the other hand, for moderately thick shells the prebuckling nonlinearities may enhance the buckling capacity and in such cases the asymptotic procedure underestimates the maximum load. Further if the second order contributions are often exaggerated in asymptotic analysis leading to an underestimate of the maximum load.

4. The 3-D homogenization procedure for composite shells consisting of a large number of repeating group of plies (n) was found to yield accurate results for n >20.

Acknowledgement :
The work reported herein was supported by an ONR grant (No. N00014-91-J1637). The constant interest and encouragement of the Program monitor Dr.Yapa D.S. Rajapakse is greatly appreciated.

REFERENCES

1. Bushnell, D., " Computerized Buckling Analysis of Shells", Kluwer Academic Publishers, 1985.

2. Arbocz, J. "The effect of Initial Imperfections on Shell Stability - An Updated Review", Report LR-695, Delft University of Technology, Faculty of Aerospace Engineering, The Netherlands, September,1992

.3. Arbocz, J. and Hol, J.M.A.M., "On the Reliability of Buckling Load Predictions" The 35th AIAA/ASME/ ASCE/AHS/ASC Structures, Structural Dynamics and Materials Conference, Hilton Head , SC, April 18-20,1994, pp.514-521.

4. A.Kasagi, S.Sridharan and A.Schokker, INSTACC User Manual, Department of Civil Engineering, Washington University in St.Louis, 1994.

5. A.Kasagi and S.Sridharan, " Modal Interaction in Composite Cylinders Under Hydrostatic Pressure", International Journal of Solids and Structures, Vol.32, No.10, pp.1349-1369, 1995.

6. Koiter, W.T., "On the Stability of Equilibrium", Dissertation, Delft,Holland, 1945, English Translation : NASA Tech.Trans., F-10, 833, 1967.

7. Wunderliche,W., Cramer, H. and Obrecht, H., "Application of Ring-Elements in the Nonlinear Analysis of Shells of Revolution Under Nonaxisymmtric Loading", Computer Methods in applied Mechanics and Engineering, Vol.51, pp.259-275, 1985.

8. Moradi, B. and Parsons, I.O., "A Comparison of the Modeing Techniques for the Buckling of Stiffened Shells", ASCE Engineering Mechanics Conference Proceedings, Columbus, Ohio, pp.856-860, 1991.

9. S.Sridharan and J.Alberts, "Numerical Modeling of Buckling of Ring-Stiffened Cylinders", AIAA Journal, Vol.35, No.1, pp.187-195, 1997.

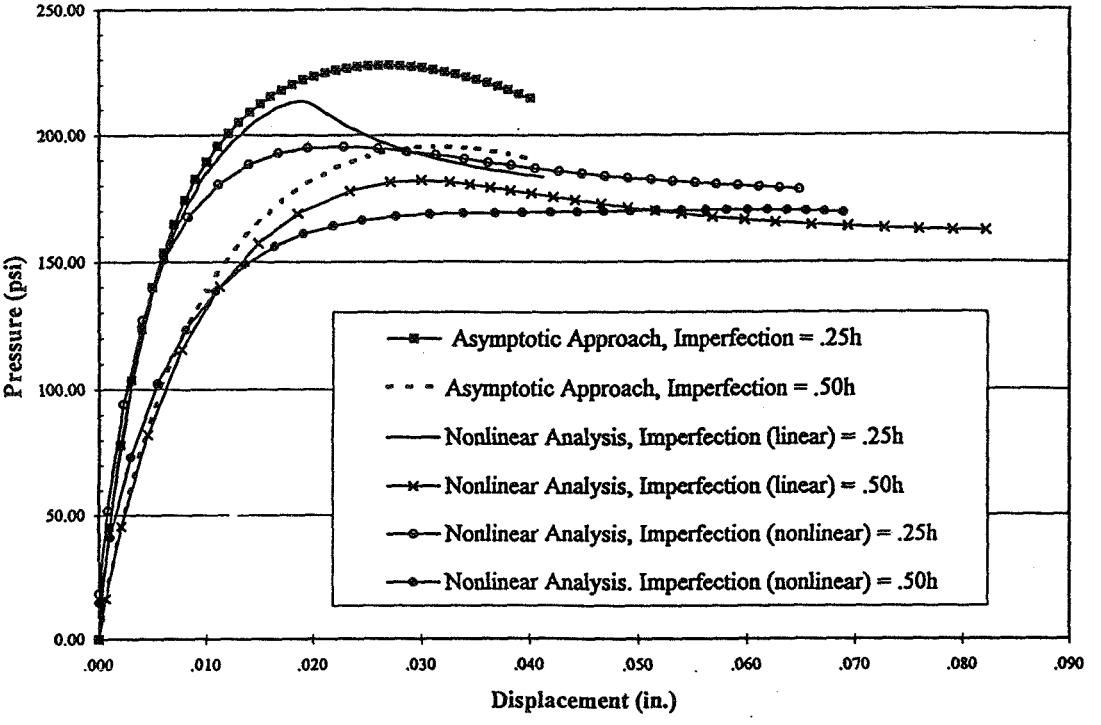

Fig.4 Pressure vs Maximum Displacement Plots For Moradi-Parson Cylinder

DEVELOPMENT OF CURVED-PLATE ELEMENTS FOR THE EXACT BUCKLING ANALYSIS OF COMPOSITE PLATE ASSEMBLIES INCLUDING TRANSVERSE SHEAR EFFECTS

David M. McGowan*
NASA Langley Research Center
Hampton, VA 23681-0001

and

Melvin S. Anderson**
Eagle Aeronautics, Inc.
Newport News, VA 23606

Abstract

The analytical formulation of curved-plate non-linear equilibrium equations that include transverse-shear-deformation effects is presented. A unified set of non-linear strains that contains terms from both physical and tensorial strain measures is used. Using several simplifying assumptions, linearized, stability equations are derived that describe the response of the plate just after bifurcation buckling occurs. These equations are then modified to allow the plate reference surface to be located a distance z_c from the centroidal surface which is convenient for modeling stiffened-plate assemblies. The implementation of the new theory into the VICONOPT buckling and vibration analysis and optimum design program code is described. Either classical plate theory (CPT) or first-order shear-deformation plate theory (SDPT) may be selected in VICONOPT. Comparisons of numerical results for several example problems with different loading states are made. Results from the new curved-plate analysis compare well with closed-form solution results and with results from known example problems in the literature. Finally, a design-optimization study of two different cylindrical shells subject to uniform axial compression is presented.

List of Symbols

A	extensional stiffness matrix
a	upper half of the eigenvectors of matrix **R**, associated with displacements
B	coupling stiffness matrix
$\underline{B}$, $\underline{C}$, $\underline{E}$, $\underline{F}$, $\underline{G}$, $\underline{H}$	coefficients used to select physical or tensorial strains
b	lower half of the eigenvectors of matrix **R**, associated with forces
b	plate width (arc length)
c	single eigenvector of matrix **R**
D	bending stiffness matrix
d	vector of displacement amplitudes at the two edges of a plate
E_{ii}	Young's modulus in the i-direction
E	matrix used to define vector **d**
F	matrix used to define vector **f**
f	vector of force amplitudes at the two edges of a plate
G_{ij}	shear stiffness associated with i-j direction
I	identity matrix
i	imaginary number, square root of -1
K	plate stiffness matrix
k	transverse shear compliance matrix
M_{11}, M_{22}, M_{12}	applied (prebuckling) moment resultants
m_{11}, m_{22}, m_{12}	perturbation values of moment resultants just after buckling has occurred
$\tilde{m}_{11}, \tilde{m}_{22}, \tilde{m}_{12}$	moment resultants
N_{11}, N_{22}, N_{12}	applied (prebuckling) stress resultants
n_{11}, n_{22}, n_{12}	perturbation values of stress resultants just after buckling has occurred
$\tilde{n}_{11}, \tilde{n}_{22}, \tilde{n}_{12}$	stress resultants
$\hat{n}_{22}, \hat{n}_{12}$	effective forces per unit length at an edge ξ_2 = constant
n_l	number of layers in a general curved laminate
P	coefficient matrix of the set of first-order plate differential equations
$\overline{\mathbf{Q}}$	lamina reduced transformed stiffness matrix
Q_1, Q_2	applied (prebuckling) shear stress resultants
q_1, q_2,	perturbation values of shear stress resultants just after buckling has occurred
$\tilde{q}_1, \tilde{q}_2$	shear stress resultants
$\hat{q}_2$	effective transverse shear force per unit length at an edge ξ_2 = constant
R	matrix whose eigenvalues are the characteristic roots of the plate differential equations
R_1, R_2	radii of lines of principal curvature
T	coefficient matrix of the set of first-order plate differential equations
t	plate thickness
U_1, U_2	prebuckling displacements
u_1, u_2	perturbation values of displacements just after buckling has occurred
w	normal displacement in the ξ_3-direction
Z	vector of the forces and displacements in the plate
z	vector of the amplitudes of the forces and

* Aerospace Engineer, Structural Mechanics Branch, Structures Division. Senior Member, AIAA.

** Research Engineer. Associate Fellow, AIAA.

displacements in the plate assuming a sinusoidal variation in the ξ_1-direction

z_c distance from the plate centroidal surface to the plate reference surface

z_k distance from laminate reference surface to the kth layer in the laminate

Greek

α_1, α_2 Lamé parameters

β angle included by a curved plate

ε vector containing strains ε_{11}, ε_{22}, and γ_{12}

$\varepsilon_{11}, \varepsilon_{22}$ in-plane direct strains

$\varepsilon_{12}, \gamma_{12}$ in-plane shear strains

$\varepsilon_{13}, \gamma_{13}$

$\varepsilon_{23}, \gamma_{23}$ transverse shear strains

ϕ_1, ϕ_2 rotations

ϕ_n rotation about the normal to the plate middle surface

k vector containing curvatures κ_{11}, κ_{22}, and κ_{12}

κ_{11}, κ_{22} middle surface changes in curvature

κ_{12} middle surface twisting curvature

λ half wavelength of buckling mode

ν Poisson's ratio

θ_k angular orientation of ply k in a laminate with respect to the laminate coordinate system

ρ density

σ vector containing stresses σ_{11}, σ_{22}, and τ_{12}

σ_{11}, σ_{22} in-plane direct stresses

τ_{12} in-plane shear stress

ξ_1, ξ_2, ξ_3 coordinate measures in the 1, 2, and 3-directions, respectively

Subscripts and Superscripts

cr critical value for buckling

k kth layer in a laminated composite plate

n normal to middle surface

1, 2, 3 1, 2, and 3-directions, respectively

° value at centroidal surface

Introduction

Longitudinally stiffened plate structures occur frequently in aerospace vehicle structures. Thus, analysis and optimization capabilities that can be used economically for their design are of great importance. One approach to modeling these structures is to represent the stiffened panel mathematically by long, thin, flat or curved-plate elements that are rigidly connected along their longitudinal edges as shown in Figure 1. Furthermore, the designs for these structures often exploit the increased structural efficiency that can be obtained by the use of advanced composite materials. Therefore, any analysis tool used to design these structures must include the effects of anisotropy and through-the-thickness or transverse-shear deformation. The transverse-shear deformation capability is especially important when the plate elements are thick compared to their width or are made of compliant lamina. Additionally, to satisfy the current demands for more cost-effective and structurally efficient aerospace vehicles, these structures are frequently optimized to obtain minimum-mass designs that satisfy a wide range of constraints. Two particularly important phenomena that must be accounted for when performing a design optimization of a stiffened-plate structure are buckling and vibration. Constraints on buckling loads, vibration frequencies, or a combination of both usually appear as design criteria in the design-optimization process. Therefore, an analytical tool that is economical and predicts accurately the structural response of stiffened-plate structures is highly desirable. One such analytical tool is the VICONOPT computer code [1].

The VICONOPT computer code is an analysis and design-optimization code for the buckling and vibration analyses of prismatic assemblies of flat- or curved-plate elements subjected to in-plane-loads. The code includes the capability to model anisotropic stiffened-plate structures that have fully populated **A**, **B** and **D** stiffness matrices. The user can select either classical plate theory (CPT) or first-order transverse-shear-deformation plate theory (SDPT) [2]. The SDPT used in VICONOPT and in the present study uses the usual first-order assumption that straight material lines that are originally normal to the centroidal surface of a plate remain straight and inextensional during deformation of the plate, but not necessarily normal to the centroidal surface. The formulation used in VICONOPT to model plate elements is referred to herein as an exact finite-strip method (FSM) [3] because it uses the exact solution to the differential equations that describe the behavior of a plate element to formulate the corresponding stiffness matrices. Examples of other exact FSM analyses of curved plates are given in Refs. [4, 5, and 6]. Other FSM analyses that formulate the stiffness matrices from a variational approach are referred to as approximate FSM's. Examples of approximate FSM analyses of curved plates are given in Refs. [7 and 8].

As the use of advanced composite materials has increased in the design of aerospace vehicles, stiffened-plate structures with one or more curved-plate elements have become more common. Currently, the VICONOPT code approximates the geometry of a curved plate by subdividing or discretizing it into a series of flat-plate elements that are joined to form the complete curved plate as shown in Figure 2. Thus, the analyst must ensure that an adequate number of flat-

plate elements is used in the analysis. This procedure is analogous to the discretization approach used in finite element analysis, and it is referred to herein as the segmented-plate analysis in the VICONOPT code. Although this approach it not very difficult, it would be more efficient to have an exact method for modeling curved-plate elements within VICONOPT.

The present paper describes an analysis method for modeling curved-plate elements exactly that has been implemented into the VICONOPT code. This new analysis capability is referred to herein as the curved-plate analysis in VICONOPT. Several features accompanying this analysis that have been added to the VICONOPT code are described in the present paper. The current version of VICONOPT only analyzes flat-plate elements based on a tensorial strain-displacement relation. However, the choice of strain-displacement relations can affect the magnitude and distribution of prebuckling stresses in curved plates. Therefore, a unified set of nonlinear strain-displacement relations that contains terms from both physical and tensorial strain measures is used to derive the curved-plate equilibrium equations. This unified set of strains is used throughout the derivation of the equilibrium equations, and the selection of either physical or tensorial strains is achieved by setting appropriate coefficients in the equilibrium equations equal to one or zero. Another addition to the code is the option to include the effects of in-plane transverse loads that act perpendicular to the longitudinal edges of a plate element and in-plane shear loads in the in-plane equilibrium equations. These effects are currently ignored in the VICONOPT code (see [1]). All of these features have been implemented such that they are available for use in the analysis of both flat and curved-plate elements. The methodology used to accomplish this enhancement of the code and results obtained using this new capability are presented.

Analytical Formulation

The analytical formulation of the present theory is described. The geometry, loadings, and sign conventions used in the present study are described first. The unified set of strain-displacement relations used in the present theory is then presented. Next, the derivation of a set of non-linear equilibrium equations and linearized stability equations is described. The stability equations are then modified such that they describe the response of the curved-plate segment with respect to a reference surface which may be offset from the centroidal surface of the plate. These modified stability equations are needed to simplify the numerical procedure used to implement the present analysis into the VICONOPT code.

Geometry, Loadings, and Sign Conventions

The geometry of the basic curved-plate element this is being studied in this section is given in Figure 3. This figure depicts the orthogonal curvilinear coordinate system (ξ_1, ξ_2, ξ_3) used in the analysis. The ξ_1- and ξ_2-axes shown in the figure are along lines of principal curvature and they have radii of curvature R_1 and R_2, respectively. Lines of principal curvature coordinates are sufficient for the analysis because twist of the curved-plate reference surface is absent in prismatic curved-plate assemblies. The reference surface for a curved-plate element used herein is its middle surface, and the corresponding first fundamental form is given by

$$ds^2 = \alpha_1^2 d\xi_1^2 + \alpha_2^2 d\xi_2^2 \qquad (1)$$

where α_1 and α_2 are the Lamé parameters. The coordinates ξ_1 and ξ_2 are measured as arc lengths along the ξ_1- and ξ_2-axes, respectively. The result of measuring the coordinates in this manner is $\alpha_1 = \alpha_2 = 1$. The sign conventions for buckling displacements, moments, rotations, and stress resultants are also shown in Figure 3. The sign convention for the applied in-plane loadings and the relationship of the reference surface of the plate to the centroidal surface of the plate are shown in Figure 4. The centroidal surface is defined to be located at the centroid of the face of the panel that is normal to the ξ_1-axis. Observe that the centroidal surface can be offset from the reference surface by a distance z_c. This offset is useful in maintaining a smooth outer-surface mold line when plates of different thicknesses are linked together (as in the analysis of a stringer-stiffened panel). The loading N_{22} shown in Figure 4 is referred to in the present paper as an in-plane transverse loading.

Strain-Displacement Relations

The unified set of nonlinear strain-displacement relations used for the present study for small strains are given by

$$\varepsilon_{11} = u_{1,1} + \frac{w}{R_1} + \frac{1}{2}\left[w_{,1} - \frac{u_1}{R_1}\right]^2 + \frac{\overline{B}}{2}\left(u_{2,1}\right)^2 + \frac{\overline{C}}{2}\left[u_{1,1} + \frac{w}{R_1}\right]^2 \qquad (2a)$$

$$\varepsilon_{22} = u_{2,2} + \frac{w}{R_2} + \frac{1}{2}\left[w_{,2} - \frac{u_2}{R_2}\right]^2 + \frac{\underline{E}}{2}\left(u_{1,2}\right)^2 + \frac{\underline{F}}{2}\left[u_{2,2} + \frac{w}{R_2}\right]^2 \tag{2b}$$

$$2\varepsilon_{12} = \gamma_{12} = u_{1,2} + u_{2,1} + w_{,1}w_{,2} - w_{,1}\frac{u_2}{R_2} - w_{,2}\frac{u_1}{R_1} + \frac{u_1 u_2}{R_1 R_2} - \underline{G}\left[u_{1,2}u_{2,2} + u_{2,1}u_{1,1} + u_{1,2}\frac{w}{R_2} + u_{2,1}\frac{w}{R_1}\right] + \underline{H}\left[u_{1,2}u_{1,1} + u_{2,1}u_{2,2} + u_{1,2}\frac{w}{R_1} + u_{2,1}\frac{w}{R_2}\right] \tag{2c}$$

$$2\varepsilon_{13} = \gamma_{13} = w_{,1} - \frac{u_1}{R_1} - \phi_1 \tag{2d}$$

$$2\varepsilon_{23} = \gamma_{23} = w_{,2} - \frac{u_2}{R_2} - \phi_2 \tag{2e}$$

where the following notation for partial derivatives is used: $\frac{\partial u_i}{\partial \xi_i} \equiv u_{,i}$. The displacement quantities in Eqs. (2a)-(2e) are displacements of the centroidal surface of the curved-plate element. The constants $\underline{B}$, $\underline{C}$, $\underline{E}$, $\underline{F}$, and $\underline{H}$ are set equal to one and $\underline{G}$ is set equal to zero in Eqs. (2a)-(2c) to obtain tensorial strain measures. The constants $\underline{B}$, $\underline{E}$, and $\underline{G}$ are set equal to one and $\underline{C}$, $\underline{F}$, and $\underline{H}$ are set equal to zero to obtain physical strain measures. Note that the linear portions of the tensorial and physical strain measures are identical. The tensorial strain measures are those of Novozhilov [9]. The physical strains used in the present thesis are derived in a manner similar to that presented by Stein in [10] and they were communicated to the first author in terms of lines of curvature coordinates by Dr. Michael P. Nemeth[1].

The definitions for the changes in curvature of the centroidal surface in terms of surface rotations used for both theories are

$$\kappa_{11} = -\phi_{1,1} \tag{3a}$$

$$\kappa_{22} = -\phi_{2,2} \tag{3b}$$

$$\kappa_{12} = -\left(\phi_{1,2} + \phi_{2,1}\right) \tag{3c}$$

These changes in curvatures are equivalent to those given by Sanders in [11] with the terms involving rotations about the normal neglected to simplify the analysis.

Derivation of Stability Equations

The nonlinear equilibrium equations for the curved plate illustrated in Figure 3 are derived using the principle of virtual work [12]. The present derivation uses the principle of virtual work in the manner of Sanders [13] that is written in the following form

$$\iint_{\text{area}} \begin{bmatrix} \tilde{n}_{11}\delta\varepsilon_{11} + \tilde{n}_{22}\delta\varepsilon_{22} + 2\tilde{n}_{12}\delta\varepsilon_{12} \\ +\tilde{m}_{11}\delta\kappa_{11} + \tilde{m}_{22}\delta\varepsilon_{22} + 2\tilde{m}_{12}\delta\kappa_{12} \\ +\tilde{q}_1\delta\gamma_{13} + \tilde{q}_2\delta\gamma_{23} \end{bmatrix} d\xi_1 d\xi_2 + \oint_c \begin{bmatrix} N_{11}\delta u_1 + N_{12}\delta u_2 + Q_1\delta w - M_{11}\delta\phi_1 \\ -M_{12}\delta\phi_2 \end{bmatrix} d\xi_2 - \oint_c \begin{bmatrix} N_{12}\delta u_1 + N_{22}\delta u_2 + Q_2\delta w - M_{12}\delta\phi_1 \\ -M_{22}\delta\phi_2 \end{bmatrix} d\xi_1 = 0 \tag{4}$$

The terms $\tilde{n}_{12}$ and $\tilde{m}_{12}$ are the effective membrane-shear and bending stress measures, respectively, defined by Sanders in [13]. The terms $\tilde{q}_1$ and $\tilde{q}_2$ are the effective transverse-shear stress measures defined by Cohen in [14]. The uppercase terms in Eq. (4) are the applied loads on the boundary of the plate.

In order to derive a set of non-linear equilibrium equations that adequately models the behavior of an assembly of curved or flat-plate elements, the issue of continuity of rotations at a plate junction must be examined. When two plates are joined together such that one cross-section is oriented at an arbitrary angle, α, to the other, rotations about the normals to the centroidal surfaces of the two plates must be included to satisfy continuity of rotations. However, this rotation, ϕ_n, has been neglected in the kinematic equations used in the present paper. To account for this effect, a procedure to maintain continuity of rotations that was developed by Cohen in [15] is used in the present study and in VICONOPT. This procedure introduces the shear strain, γ_{13}, as a fundamental displacement variable instead of the rotation, ϕ_1 by replacing ϕ_1 with the expression $w_{,1} - \frac{u_1}{R_1} - \gamma_{13}$ in the boundary integral over ξ_2 in Eq. (4). Although a detailed discussion of this topic is given in reference [16], a brief discussion of the justification for using this approach is presented subsequently. As shown in reference [16] the equations for continuity of rotations at a plate junction will be satisfied if the transverse shear strain, γ_{13}, equals zero for any non-zero value of the angle α. Therefore, if γ_{13} is a fundamental displacement variable, it may easily be set equal to zero

[1] Structures Division, Structural Mechanics Branch, NASA Langley Research Center, Hampton, Virginia, 23681-0001

by simply striking out the appropriate rows and columns in the stiffness matrix of the plate. The equations of continuity of rotations at a plate junction presented in reference [16] also indicate that for $\alpha = 0$, the values of γ_{13} in each plate are equal.

To derive a set of nonlinear equilibrium equations, the variations of Eqs. (2) and (3) are substituted into Eq. (4) and the resulting equation is integrated by parts to yield an integral equation that consists of an area integral and two line integrals. This integral equation is given in reference [16]. Recall that, per Cohen's procedure, ϕ_1 is replace with the expression $w_{,1} - \frac{u_1}{R_1} - \gamma_{13}$ in the boundary integral over ξ_2 in Eq. (4). For arbitrary displacements u_1, u_2, w, ϕ_1, and ϕ_2, the coefficients of the displacements in the area integral are the five equilibrium equations. The coefficients of the displacement variables in the line integrals are the natural or force boundary conditions for the edges ξ_1=constant and ξ_2=constant.

A set of linear perturbation equilibrium equations that govern the stability of the plate, referred to herein as the stability or linear bifurcation buckling equations, is obtained by taking the difference between the equilibrium equations evaluated for a stable equilibrium state just prior to bifurcation buckling and an adjacent (perturbed) equilibrium state (not necessarily stable) just after bifurcation buckling has occurred. The prebuckling state is represented herein by:

$$\begin{aligned} &\tilde{n}_{11} = -N_{11},\ \tilde{n}_{22} = -N_{22},\ \tilde{n}_{12} = -N_{12}, \\ &\tilde{m}_{11} = -M_{11},\ \tilde{m}_{22} = -M_{22},\ \tilde{m}_{12} = -M_{12}, \\ &\tilde{q}_1 = -Q_1,\ \tilde{q}_2 = -Q_2,\ U_1,\ U_2,\ W \end{aligned} \tag{5}$$

where the minus signs in the loading terms reflect the sign convention used in which the applied loads are opposite in direction to the loads that develop after buckling. The adjacent equilibrium state just after bifurcation buckling has occurred is represented herein by:

$$\begin{aligned} &\tilde{n}_{11} = n_{11} - N_{11},\ \tilde{n}_{22} = n_{22} - N_{22}, \\ &\tilde{n}_{12} = n_{12} - N_{12},\ \tilde{m}_{11} = m_{11} - M_{11}, \\ &\tilde{m}_{22} = m_{22} - M_{22},\ \tilde{m}_{12} = m_{12} - M_{12}, \\ &\tilde{q}_1 = q_1 - Q_1,\ \tilde{q}_2 = q_2 - Q_2,\ u_1 + U_1, \\ &u_2 + U_2,\ w + W \end{aligned} \tag{6}$$

where the lower-case variables are perturbation variables. Taking the difference between the two equilibrium states represented by Eqs. (5) and (6), linearizing the resulting equations with respect to the perturbation variables, and applying several simplifying assumptions yields the set of five stability equations and two sets of boundary conditions given in reference [16]. These assumptions are:

1) Prebuckling deformations, moments and transverse shear stress are negligible
2) The in-plane prebuckling stress state is uniform

The form of the stability equations used herein is a form that describes the response of the curved plate with respect to a reference surface of the plate that is located a distance z_c from the centroidal surface shown in Figure 4. To obtain this form of the stability equations, the following information is used:

1) The relationships of the displacements at the centroidal surface, u_1^o and u_2^o, to the displacements at the reference surface, u_1 and u_2 are:

$$u_1^o = u_1 - z_c\phi_1 \tag{7a}$$

$$u_2^o = u_2 - z_c\phi_2 \tag{7b}$$

2) The relationships of the moments at the centroidal surface, m_{11}^o, m_{22}^o, and m_{12}^o, to the displacements at the reference surface, m_{11}, m_{22}, and m_{12} are:

$$m_{11}^o = m_{11} - z_c n_{11} \tag{8a}$$

$$m_{22}^o = m_{22} - z_c n_{22} \tag{8b}$$

$$m_{12}^o = m_{12} - z_c n_{12} \tag{8c}$$

3) The following quantities do not vary through the thickness (with ξ_3):

N_{11}, N_{22}, N_{12}, n_{11}, n_{22}, n_{12}, q_1, q_2, and w

4) The applied in-plane stress resultants, N_{11}, N_{22}, and N_{12} act at the centroidal surface.

Substitution of Eqs. (7) and (8) into the original linear stability equations yields the following modified linear stability equations:

$$\begin{aligned} &n_{11,1} + \hat{n}_{12,2} + \frac{q_1}{R_1} - \frac{N_{11}}{R_1}\left(w_{,1} - \frac{u_1 - z_c\phi_1}{R_1}\right) \\ &- \frac{N_{12}}{R_1}\left(w_{,2} - \frac{u_2 - z_c\phi_2}{R_2}\right) - \underline{C}N_{11}\left(\frac{w}{R_1} + u_{1,1} - z_c\phi_1\right)_{,1} \\ &+ \underline{G}N_{12}[u_2 - z_c\phi_2]_{,11} - \underline{H}N_{12}[u_1 - z_c\phi_1]_{,12} = 0 \end{aligned} \tag{9a}$$

$$\begin{aligned} &n_{12,1} + \hat{n}_{22,2} + \frac{q_2}{R_2} - \frac{N_{22}}{R_2}\left(w_{,2} - \frac{u_2 - z_c\phi_2}{R_2}\right) \\ &- \frac{N_{12}}{R_2}\left(w_{,1} - \frac{u_1 - z_c\phi_1}{R_1}\right) - \underline{B}N_{11}(u_2 - z_c\phi_2)_{,11} \\ &+ \underline{G}N_{12}\left(\frac{w_{,1}}{R_1} + [u_1 - z_c\phi_1]_{,11}\right) \\ &- \underline{H}N_{12}\left(\frac{w_{,1}}{R_2} + [u_2 - z_c\phi_2]_{,12}\right) = 0 \end{aligned} \tag{9b}$$

$$q_{1,1}+\hat{q}_{2,2}-\frac{n_{11}}{R_1}-\frac{\hat{n}_{22}}{R_2}-N_{11}\left(w_{,1}-\frac{u_1-z_c\phi_1}{R_1}\right)_{,1}$$
$$-N_{12}\left(w_{,2}-\frac{u_2-z_c\phi_2}{R_2}\right)_{,1}$$
$$+\frac{\underline{C}N_{11}}{R_1}\left(\frac{w}{R_{,1}}+\left[u_1-z_c\phi_1\right]_{,1}\right) \qquad (9c)$$
$$+\frac{\underline{G}N_{12}\left[u_2-z_c\phi_2\right]_{,1}}{R_1}+\frac{\underline{H}N_{12}\left[u_1-z_c\phi_1\right]_{,2}}{R_1}=0$$

$$m_{11,1}+m_{12,2}-z_c\left(n_{11,1}+n_{12,2}\right)-q_1=0 \qquad (9d)$$
$$m_{12,1}+m_{22,2}-z_c\left(n_{12,1}+n_{22,2}\right)-q_2=0 \qquad (9e)$$

As will be discussed subsequently, a sinusoidal variation of the displacements and forces in the ξ_1-direction will be assumed to simplify the analysis by reducing the linear stability equations to a system of ordinary differential equations. Therefore, the boundary conditions for an edge ξ_1 = constant are ignored. The remaining natural boundary conditions for an edge ξ_2 = constant are

$$\hat{n}_{12}=n_{12}-\underline{E}N_{22}\left[u_1-z_c\phi_1\right]_{,2}$$
$$+\underline{G}N_{12}\left(\left[u_2-z_c\phi_2\right]_{,2}+\frac{w}{R_2}\right) \qquad (10a)$$
$$-\underline{H}N_{12}\left(\left[u_1-z_c\phi_1\right]_{,1}+\frac{w}{R_1}\right)=0$$

$$\hat{n}_{22}=n_{22}-\underline{F}N_{22}\left(\left[u_2-z_c\phi_2\right]_{,2}+\frac{w}{R_2}\right)$$
$$+\underline{G}N_{12}\left[u_1-z_c\phi_1\right]_{,2} \qquad (10b)$$
$$-\underline{H}N_{12}\left[u_2-z_c\phi_2\right]_{,1}=0$$

$$\hat{q}_2=q_2-N_{12}\left(w_{,1}-\frac{\left[u_1-z_c\phi_1\right]}{R_1}\right)$$
$$-N_{22}\left(w_{,2}-\frac{\left[u_2-z_c\phi_2\right]}{R_2}\right)+\left[m_{12}-z_cn_{12}\right]_{,1} \qquad (10c)$$

$$m_{12}-z_cn_{12}=0 \qquad (10d)$$
$$m_{22}-z_cn_{22}=0 \qquad (10e)$$

where the terms with a caret (^) are forces per unit length at an edge ξ_2=constant that are aligned with the original (undeformed) coordinates. These forces have been introduced herein because of the fact that the stiffness matrix of a finite-strip element must relate the forces along the longitudinal edges of the plate in the original coordinate directions to the corresponding displacements along those edges. Note that the term $m_{12,1}$ which appears in the Kirchhoff shear term of CPT also appears in the expression for $\hat{q}_2$ for SDPT when γ_{13} is used as a fundamental displacement quantity.

Modified expressions for the last two stability equations are obtained by substituting expressions for the quantities $\left(n_{11,1}+n_{12,2}\right)$ and $\left(n_{12,1}+n_{22,2}\right)$ that are obtained by using Eqs. (9a) and (10a), and Eqs. (9b) and (10b) in the appropriate places in Eqs. (9d) and (9e), respectively. The definitions for the effective forces given in Eqs (10a)-(10c) are needed since the terms n_{12} and n_{22} that appear in the quantities in parentheses above are the perturbation values, not the effective forces. Substitution of the expressions for the two quantities in parentheses above into Eqs. (9d) and (9e), respectively, yields the final form of the last two stability equations

$$m_{11,1}+m_{12,2}-q_1+z_c\left[\frac{q_1}{R_1}-\right.$$
$$\frac{N_{11}}{R_1}\left(w_{,1}-\frac{u_1-z_c\phi_1}{R_1}\right)-\frac{N_{12}}{R_1}\left(w_{,2}-\frac{u_2-z_c\phi_2}{R_2}\right)$$
$$-\underline{C}N_{11}\left(\frac{w}{R_1}+u_{1,1}-z_c\phi_1\right)_{,1}-\underline{E}N_{22}\left(u_1-z_c\phi_1\right)_{,22} \qquad (11a)$$
$$+\underline{G}N_{12}\left(\frac{w_{,2}}{R_2}+\left[u_2-z_c\phi_2\right]_{,11}+\left[u_2-z_c\phi_2\right]_{,22}\right)$$
$$\left.-\underline{H}N_{12}\left(\frac{w_{,2}}{R_1}+2\left[u_1-z_c\phi_1\right]_{,12}\right)\right]=0$$

$$m_{12,1}+m_{22,2}-q_2$$
$$+z_c\left[\frac{q_2}{R_2}-\frac{N_{22}}{R_2}\left(w_{,2}-\frac{u_2-z_c\phi_2}{R_2}\right)\right.$$
$$-\frac{N_{12}}{R_2}\left(w_{,1}-\frac{u_1-z_c\phi_1}{R_1}\right)-\underline{B}N_{11}\left(u_2-z_c\phi_2\right)_{,11}$$
$$-\underline{F}N_{22}\left(\frac{w_{,2}}{R_2}+\left[u_2-z_c\phi_2\right]_{,22}\right) \qquad (11b)$$
$$+\underline{G}N_{12}\left(\frac{w_{,1}}{R_1}+\left[u_1-z_c\phi_1\right]_{,11}+\left[u_1-z_c\phi_1\right]_{,22}\right)$$
$$\left.-\underline{H}N_{12}\left(\frac{w_{,1}}{R_2}+2\left[u_2-z_c\phi_2\right]_{,12}\right)\right]=0$$

These modified equations are used to simplify the numerical procedure used to implement the present analysis into the VICONOPT code. The stability equations in the form given in Eqs. (9a)-(9c) and Eqs.

(11a)-(11b) are those implemented into the VICONOPT code.

Constitutive Relations

The through-the-thickness geometry and the geometry of an arbitrary lamina of a general, curved laminate is given in Figure 5. The number of layers in the laminate is n_l, and as shown in the figure, the arc-width of the laminate is b. The ξ_1-- and ξ_2-axes are the principal material axes of the kth specially orthotropic lamina that makes an angle θ_k with the ξ_1-axis in the middle surface tangent plane at a given point of the plate. The laminate ξ_1-axis is aligned with the longitudinal edges of the plate. The overall isothermal constitutive relations for a thin, elastic laminated composite shell are defined in reference [17] as

$$\begin{Bmatrix} \mathbf{N} \\ \mathbf{M} \end{Bmatrix} = \begin{bmatrix} \mathbf{A} & \mathbf{B} \\ \mathbf{B} & \mathbf{D} \end{bmatrix} \begin{Bmatrix} \varepsilon \\ \kappa \end{Bmatrix} \tag{12}$$

The stress and moment resultants acting on the laminate, {**N**} and {**M**}, respectively, are defined as

$$\begin{Bmatrix} N_{11} \\ N_{22} \\ N_{12} \end{Bmatrix} = \sum_{k=1}^{n_l} \int_{z_{k-1}}^{z_k} \begin{Bmatrix} \sigma_{11} \\ \sigma_{22} \\ \tau_{12} \end{Bmatrix} d\xi_3 \tag{13}$$

$$\begin{Bmatrix} M_{11} \\ M_{22} \\ M_{12} \end{Bmatrix} = \sum_{k=1}^{n_l} \int_{z_{k-1}}^{z_k} \begin{Bmatrix} \sigma_{11} \\ \sigma_{22} \\ \tau_{12} \end{Bmatrix} \xi_3 \; d\xi_3 \tag{14}$$

The extensional, coupling, and bending stiffness matrices, **A**, **B**, and **D**, respectively, are defined as

$$(\mathbf{A},\ \mathbf{B},\ \mathbf{D}) = \sum_{k=1}^{n_l} \int_{z_{k-1}}^{z_k} \left[\overline{\mathbf{Q}}^k\right] \left(1,\ \xi_3,\ \xi_3^2\right) d\xi_3 \tag{15}$$

The constitutive relations for transverse shear used in VICONOPT are those presented by Cohen in [14]. The constitutive relations for transverse shear are written in inverted form as

$$\begin{Bmatrix} \gamma_{13} \\ \gamma_{23} \end{Bmatrix} = \begin{bmatrix} k_{11} & k_{12} \\ k_{12} & k_{22} \end{bmatrix} \begin{Bmatrix} q_1 \\ q_2 \end{Bmatrix} \tag{16}$$

where [**k**] is a symmetric 2-by-2 transverse shear compliance matrix whose terms are defined in [14].

Implementation into VICONOPT

The implementation of the present theory into the VICONOPT code is described in this section. Several simplifications made to the present theory are described first. Then the derivation of the curved-plate stiffness matrix based upon the analysis of the present study is presented. The implementation of the present curved-plate theory into VICONOPT follows very closely the procedure described in [2]. Therefore, for convenience, the following discussion is presented in a form similar to that in [2].

Simplifications to the Theory

The theory implemented into the VICONOPT code is for structures that are prismatic in the longitudinal direction. Therefore, for the curved-plate elements that are considered in the present paper, the radius of curvature in the longitudinal direction, R_1, is infinite; i.e., any terms involving the quantity $\frac{1}{R_1}$ are zero. Although these terms are set equal to zero in the calculation of the terms of the stiffness matrix, they have been retained for completeness of the theory presented herein. Another simplification to the theory involves limiting the capability to locate the reference surface a distance z_c from the centroidal surface. This capability has only been implemented for the case where the effects of N_{22} and N_{12} loads in the in-plane stability equations are neglected. The expressions for the stiffness terms that result when N_{22} and N_{12} are included in the in-plane stability equations are prohibitively long. Therefore, in the derivation of the stiffness matrix that follows, only the following two cases are included:

1) N_{22} and N_{12} are included in the in-plane stability equations and z_c is zero (i.e., reference surface is coincident with the centroidal surface)

2) N_{22} and N_{12} are neglected in the in-plane stability equations and z_c is non-zero (i.e., reference surface may be shifted from the centroidal surface)

Derivation of the Curved-Plate Stiffness Matrix

Throughout this section, reference is made to force quantities. Although these quantities are force per unit length, they are designated forces herein for convenience. The first step in implementing the present theory into VICONOPT is to derive a stiffness matrix that relates the force quantities along the two longitudinal edges (referred to herein as simply forces), $\xi_2 = \pm\frac{b}{2}$, to the displacements along those edges. The desired force and displacement quantities are in the direction of the original (undeformed) coordinates. The displacement and force variables are

$$\mathbf{d} = \begin{Bmatrix} i\ u_1 \\ u_2 \\ w \\ \phi_2 \\ i\ \gamma_{13} \end{Bmatrix} \quad \text{and} \quad \mathbf{f} = \begin{Bmatrix} i\ \hat{n}_{12} \\ \hat{n}_{22} \\ \hat{q}_2 \\ m_{22} \\ i\ m_{12} \end{Bmatrix} \tag{17}$$

where the shear strain, γ_{13}, has been introduced as a fundamental displacement quantity instead of the rotation, ϕ_1. Note that the effective forces per unit length at the boundaries, defined by Eqs. (10a)-(10c), are used as forces since they are equal to forces in the direction of the original (undeformed) coordinates.

The curved-plate element equations may now be reduced to ordinary differential equations in ξ_2 by assuming that the response of the plate in the longitudinal ξ_1-direction varies sinusoidally. For isotropic or orthotropic plate assemblies without shear loading, a sinusoidal response in the ξ_1-direction is exact for simply supported end conditions. A series of sinusoidal modes is used with a Lagrangian multiplier technique to obtain results for other loadings and end conditions [2]. Applying the assumption of a sinusoidal variation in the ξ_1-direction, the variables of Eqs. (17) may be written as

$$\mathbf{Z}(\xi_1,\xi_2)=\exp\left(\frac{i\ \pi\ \xi_1}{\lambda}\right)\mathbf{z}(\xi_2),\qquad \mathbf{z}=\begin{Bmatrix}\mathbf{d}\\ \mathbf{f}\end{Bmatrix} \tag{18}$$

where λ is the half-wavelength of the response in the ξ_1-direction. Since a sinusoidal variation in the ξ_1-direction is assumed, the vector $\mathbf{z}$ will involve the amplitudes of the displacement and forces. The imaginary number, i, has been used in Eqs. (17) to account for the spatial phase shift that occurs between the displacement and force quantities when an in-plane shear loading is present and to result in real plate stiffnesses when using the exponential expression of Eq. (18).

The next step in the derivation is to express all unknowns in terms of $\mathbf{z}$. A partially inverted form of the constitutive relations is used to express the required quantities as functions of the fundamental variables in $\mathbf{d}$ and $\mathbf{f}$, or terms that may be derived from the fundamental variables. The partially inverted constitutive relations are given in reference [2].

Another requirement of the present derivation is to express the relationship between q_2 and $\hat{q}_2$ without any ξ_2-derivatives so that a first-order system of differential equations is maintained. This expression is

$$q_2=\frac{\begin{pmatrix}\hat{q}_2+N_{12}\left(w_{,1}-\dfrac{[u_1-z_c\phi_1]}{R_1}\right)\\ +N_{22}(\phi_2-h_{78}\gamma_1)+[m_{12}-z_c n_{12}]_{,1}\end{pmatrix}}{1-N_{22}h_{88}} \tag{19}$$

where h_{78} and h_{88} are terms from the partially inverted constitutive relations given in reference [2]. As with the stability equations, only the linear portion of the strain-displacement relations (Eqs. (2c), (2b), (2e), (3b), and (3c)) are considered in the present derivation. The expression for κ_{12} is re-written after substituting expressions obtained for ϕ_1 and ϕ_2 from Eqs. (2d) and (2e) and using the linear portion of ε_{12}, that is,

$$\kappa_{12}=-\left[\gamma_2+\left(\frac{1}{R_1}+\frac{1}{R_2}\right)u_2+2\phi_2\right]_{,1} +\frac{\varepsilon_{12}}{R_1}+\gamma_{1,2} \tag{20}$$

Using the partially inverted constitutive relations and Eq. (19), the strain displacement equations, Eqs. (2c), (2b), (2e), (3b), and (3c), and the stability equations, Eqs. (9a)-(9c) and Eqs. (11a) and (11b) are written in terms of the elements of $\mathbf{z}$ as

$$\mathbf{T}\,\mathbf{z}'=\mathbf{P}\,\mathbf{z}\qquad\text{or}\qquad \mathbf{z}'=\mathbf{T}^{-1}\mathbf{P}\,\mathbf{z} \tag{21}$$

where a prime denotes differentiation with respect to ξ_2. The square matrix $\mathbf{T}$ appears in the present study as a result of the inclusion of the effects of N_{22} and N_{12} in the in-plane stability equations. When these terms are neglected, this matrix is shown to be the identity matrix in reference [2]. The use of the modified stability equations given in Eqs. (11a) and (11b) is also required for $\mathbf{T}$ to be the identity matrix. The presence of off-diagonal terms in $\mathbf{T}$ is a fundamental difference between the present theory and that presented in reference [2].

The elements of $\mathbf{z}$ are now assumed to be given by

$$z_j=c_j\exp\left(\frac{i\ \beta\ \xi_2}{b}\right) \tag{22}$$

where β is a characteristic root of the system of differential equations. The number of values of β is equal to the order of the differential equation system. Substituting Eq. (22) into Eq. (21) results in the following equation

$$(\mathbf{R}-\beta\mathbf{I})\,\mathbf{c}=0,\qquad\text{where}\qquad \mathbf{R}=b\mathbf{T}^{-1}\mathbf{P} \tag{23}$$

where $\mathbf{I}$ is the identity matrix. The vector $\mathbf{c}$ consists of the c_j of Eq. (22). The eigenvalues of the matrix $\mathbf{R}$ are the characteristic roots of the differential equation. This matrix is not symmetric; however, it can be made real by multiplication or division of appropriate rows and columns by the imaginary number, i. The elements of the matrices $\mathbf{T}$ and $\mathbf{P}$ are given in reference [16]. For each eigenvalue of $\mathbf{R}$, there exists an eigenvector, $\mathbf{c}$. The upper half of each eigenvector, denoted $\mathbf{a}$, is associated with displacements, and the lower half, denoted $\mathbf{b}$, is associated with forces.

The next step in the derivation is to determine the amplitudes of the displacements and forces at the two edges of the plate. Quantities evaluated at $\xi_2=-\frac{b}{2}$ are identified with a superscript 1 and quantities

evaluated at $\xi_2 = +\frac{b}{2}$ are identified with a superscript 2 as follows:

$$d_j^1 = \sum_{k=1}^{N} a_{jk} r_k \exp\left(\frac{-i\ \beta_k}{2}\right) \tag{24a}$$

$$d_j^2 = \sum_{k=1}^{N} a_{jk} r_k \exp\left(\frac{i\ \beta_k}{2}\right) \tag{24b}$$

$$f_j^1 = \sum_{k=1}^{N} b_{jk} r_k \exp\left(\frac{-i\ \beta_k}{2}\right) \tag{24c}$$

$$f_j^2 = \sum_{k=1}^{N} b_{jk} r_k \exp\left(\frac{i\ \beta_k}{2}\right) \tag{24d}$$

where the r_k are constants determined from the edge values and N is the order of the system of differential equations. Equations (24a)-(24d) may be written in matrix form as

$$\begin{Bmatrix} \mathbf{d}^1 \\ \mathbf{d}^2 \end{Bmatrix} = \mathbf{E}\,\mathbf{r} \qquad \text{and} \qquad \begin{Bmatrix} \mathbf{f}^1 \\ \mathbf{f}^2 \end{Bmatrix} = \mathbf{F}\,\mathbf{r} \tag{25}$$

Eliminating $\mathbf{r}$ from Eqs. (25) yields

$$\begin{Bmatrix} \mathbf{f}^1 \\ \mathbf{f}^2 \end{Bmatrix} = \mathbf{K} \begin{Bmatrix} \mathbf{d}^1 \\ \mathbf{d}^2 \end{Bmatrix} \tag{26}$$

where $\mathbf{K}$ is the stiffness matrix given by

$$\mathbf{K} = \mathbf{F}\,\mathbf{E}^{-1} \tag{27}$$

For CPT, $\mathbf{K}$ is real and symmetric. For SDPT, $\mathbf{K}$ is real and symmetric for orthotropic plates without in-plane shear loading, and it is Hermitian otherwise. Reference [2] presents a discussion of techniques used to ensure that accurate numerical results for $\mathbf{K}$ are obtained from Eq. (27). The stiffness matrix $\mathbf{K}$ is a transcendental function of the load factor and half wavelength of the buckling modes of the structure. Therefore, the eigenvalue problem for determining bifurcation buckling load factors is transcendental. The iterative analysis procedure used in VICONOPT to solve this eigenvalue problem is based upon the Wittrick-Williams eigenvalue algorithm described in [18]. This algorithm will not be discussed in the present paper.

Numerical Results

Numerical results are presented in this section that were obtained using the new curved-plate analysis derived herein that has been implemented into the VICONOPT code. Results for several known example problems are presented to verify the results obtained with this new capability. Comparisons of analyses that use both physical and tensorial strain measures are made for selected examples, and, where appropriate, results based upon CPT and SDPT are compared. The positive sense of the applied loadings for all of the following examples is given in Figure 6.

Convergence of the Segmented-Plate Approach

The convergence of bifurcation buckling results obtained using the segmented-plate analysis in VICONOPT is examined for the long, compression-loaded aluminum cylinder illustrated in Figure 7. The values of the material properties used for this example are E = 10.0 x 10^6 psi and ν_{12} = 0.33. The wall thickness, t, is 0.1 in., and the radius, R_2 is 60 in. As shown in Ref. [19], the critical value for the applied stress resultant, $(N_{11})_{cr}$, for the axisymmetric buckling of a long isotropic cylindrical shell is

$$(N_{11})_{cr} = \frac{Et^2}{R_2\sqrt{3(1-\nu^2)}} = 1019.354 \text{ lb/in.} \tag{28}$$

and the corresponding critical half wavelength, λ_{cr}, is

$$\lambda_{cr} = \pi \sqrt[4]{\frac{R_2^2 t^2}{12(1-\nu^2)}} = 1.74\sqrt{R_2 t} = 4.255 \text{ in.} \tag{29}$$

Results that illustrate the convergence of the VICONOPT segmented-plate results for $(N_{11})_{cr}$ as a function of the number of flat-plate elements used to approximate the cylinder are shown in Figure 8. In this figure, the results of the segmented-plate analysis are shown as the solid curve. The theoretical value obtained from Ref. [19] is shown as the dashed horizontal line. The value obtained by using the present curved-plate analysis is shown as the open symbol. All results in this figure were calculated for the value of λ_{cr} given in Eq. (29). The VICONOPT results presented in this figure were obtained using CPT with tensorial strain measures. As shown in Figure 8, the segmented-plate results converge to the theoretical value of 1019.354 lb/in. when 120 flat-plate elements are used. Therefore, to ensure that converged results are obtained when the segmented-plate approach is used to analyze the remaining example problems, sixty elements will be used when analyzing curved plates with an included angle of 180 degrees or less, and 120 elements will be used when analyzing full cylinders.

Buckling of an Unsymmetrically Laminated Curved Plate

This example problem includes the effect of bending-stretching coupling and shear-extension coupling on the buckling of an unsymmetrically laminated curved plate with simply supported

longitudinal edges (i.e., $u_1 = w = m_{22} = 0$). The pre-buckling deformations associated with bending-stretching coupling are neglected in the analysis. The geometry of the curved plate is shown in Figure 9. To allow for direct comparison of results with those presented in [6], SI units are used. As shown in the figure, the laminate that is being studied consists of a 0.508-cm.-thick layer of 2024 aluminum that is reinforced on the inner surface with pairs of ±45° boron/epoxy plies. The material properties for a boron/epoxy lamina and 2024 aluminum are given in Table 1. For this example, the number of pairs of ±45° boron/epoxy plies is increased from one to seven. Both physical and tensorial strains are used with the new curved-plate analysis, while only physical strains are used with the segmented-plate analysis. The analysis of [6] uses physical strains. All analyses use CPT. Eight curved-plate elements are used for the curve-plate analyses, and 60 flat-plate elements are used for the segmented-plate analysis. The critical value of the applied stress resultants N_{11} and N_{12} at buckling are plotted as a function of the number of boron/epoxy plies used in the laminate in Figure 10 and Figure 11, respectively. The agreement between all the analyses is very good. As shown in the figures, there is no appreciable difference in the results obtained using physical and tensorial strains.

Design Optimization of a Cylindrical Shell Subject to Uniaxial Compression

The final example utilizes the new curved-plate analysis with the design optimization capability of VICONOPT to perform a structural optimization of two different cylindrical shell concepts subject to uniform axial compression (N_{11} loading). The two concepts are solid-wall construction and honeycomb-sandwich-wall construction. The geometry of this example problem is shown in Figure 12. As shown in the figure, the facesheets of the honeycomb-sandwich-wall concept are aluminum, and the core is Korex™ aramid paper honeycomb core [20]. The solid-wall concept is aluminum. The material properties used for the facesheets and core are presented in Table 2. Tensorial strains are used for the analysis.

The design variables for the structural optimization are the thicknesses of the facesheets and the core for the sandwich concept and the wall thickness for the solid-wall construction. There is no minimum gage restriction on these design variables. The nominal values for these variables are 0.1 in., 0.5 in., and 0.1 in., respectively. The design constraints are that the strain in the facesheets or the solid wall cannot exceed 0.005 in/in and that the stress in the core cannot exceed 115 psi in the ξ_1 direction and 55 psi in the ξ_2 direction.

The results of this study, including the mass of the optimized cylinder and the final values of the design variables are given in Table 3 for the honeycomb-sandwich-wall concept and in Table 4 for the solid-wall concept. Results obtained using both CPT and SDPT with tensorial strains are given in these tables. The optimized mass values are also plotted as a function of the applied loading in Figure 13. As seen in the tables and the figure, the values of the optimized mass obtained using CPT are slightly less than those for SDPT for the honeycomb-sandwich-wall cylinder as the applied loading is increased. However, the values of the core thickness obtained using CPT become significantly less than those for SDPT as the loading is increased. This trend is expected because CPT results in an overly stiff approximation since transverse-shear flexibility is neglected. This overly stiff approximation results in higher buckling loads for a given core thickness. Therefore, the core thickness and the optimum mass obtained using CPT is less than that obtained using SDPT. The optimized mass values for the solid-wall construction are much greater than those for the honeycomb sandwich construction. The results for CPT and SDPT are nearly identical for the solid-wall construction with $R_2/t = 600$, as expected.

Concluding Remarks

The VICONOPT computer code is an exact analysis and optimum design program that includes the buckling and vibration analyses of prismatic assemblies of flat, in-plane-loaded anisotropic plates. In the present paper, the capability to analyze structures by using curved-plate elements has been described, and this capability has been added to the VICONOPT code. Non-linear curved-plate equilibrium equations have been formulated, and linearized stability equations were derived following the application of several simplifying assumptions. Modifications to these equations were then made to allow the reference surface of the plate to be located at a distance z_c from the centroidal surface.

The analysis described in the present paper improves upon the analysis existing previously in the VICONOPT code which required that curved-plate geometries be subdivided into several flat-plate elements that are joined along their longitudinal edges to approximate the curved-plate geometry. The new analysis formulation includes either classical plate theory (CPT) and first-order shear-deformation plate theory (SDPT), and anisotropic laminates with fully populated **A**, **B**, and **D** stiffness matrices can be analyzed.

The option to use plate elements (flat or curved) that are based upon nonlinear strain-displacement

relations that contain terms from either physical or tensorial strain measures has also been added to the VICONOPT code. The option to include the effect of terms associated with in-plane transverse and in-plane shear loading in the in-plane stability equations has been added as well.

Results from the present curved-plate analysis capability compare very well with a closed-form solution and the existing segmented-plate analysis for the linear bifurcation buckling of a long isotropic cylinder subjected to uniaxial compression. Results from the present analysis also compare well with results for unsymmetrically laminated plates that include the effect of extension-bending and shear-extension coupling. No appreciable effects of using tensorial versus physical strains were noted in these examples.

Finally, the present curved-plate analysis was used to conduct a design-optimization study of two cylindrical shells subject to uniform axial compression. One shell was constructed with a honeycomb-sandwich-wall, and the other was a solid-wall construction. The values of mass for the optimized solid-wall design were much higher than those for the honeycomb-sandwich-wall construction. There was no difference between results using CPT and SDPT for the solid-wall cylinder. However, the values of core thickness and mass for the optimized honeycomb-sandwich-wall cylinder using CPT were less than those for SDPT as the applied loading was increased. This result occurred because CPT overestimates the wall stiffness by neglecting transverse-shear flexibility which results in higher buckling loads and a lower optimum mass.

References

1. Williams, F. W., Kennedy, D., Anderson, M. S., and Edwards, D. A., "User Manual for VICONOPT," Release 1.3, April 1996.
2. Anderson, M. S., and Kennedy, D., "Inclusion of Transverse Shear Deformation in the Exact Buckling and Vibration Analysis of Composite Plate Assemblies," Presented at the AIAA/ASME/ASCE/AHS/ACE 32nd Structures, Structural Dynamics and Materials Conference, Dallas, Texas, April 13-15, 1992. AIAA Paper No. 92-2287.
3. Cheung, Y. K., *The Finite Strip Method in Structural Analysis*, Pergamon Press, Oxford, England, 1976.
4. Viswanathan, A. V., and Tamekuni, M, "Elastic Buckling Analysis For Composite Stiffened Panels and other Structures Subjected to Biaxial Inplane Loads," NASA CR-2216, 1973.
5. Viswanathan, A. V., Tamekuni, M., and Tripp, L. L., "Elastic Stability of Biaxially Loaded Longitudinally Stiffened Composite Structures," Proceedings of the AIAA/ASME/SAE 14th Structures, Structural Dynamics, and Materials Conference, Williamsburg, VA, March 20-22, 1973. AIAA Paper No. 73-367.
6. Viswanathan, A. V., Tamekuni, M., and Baker, L. L., "Elastic Stability of Laminated, Flat and Curved, Long Rectangular Plates Subjected to Combined Loads," NASA CR-2330, 1974.
7. Dawe, D. J., "Finite Strip Buckling Analysis of Curved Plate Assemblies Under Biaxial Loading," *International Journal for Numerical Methods in Engineering*, Vol. 13, 1977, pp. 1141-1155.
8. Morris, I. R., and Dawe, D. J., "Free Vibration of Curved-Plate Assemblies With Diaphragm Ends," *Journal of Sound and Vibration*, Vol. 73, 1980, pp. 1-17.
9. Novozhilov, V. V., *Foundations of the Nonlinear Theory of Elasticity*, Graylock Press, Rochester, New York, 1963.
10. Stein, M., "Nonlinear Theory for Plates and Shells Including the Effects of Transverse Shearing," *AIAA Journal*, Vol. 24, No. 9, September 1986, pp. 1537-1544.
11. Sanders, J. L., Jr., "Nonlinear Theories for Thin Shells," *Quarterly of Applied Mathematics*, Vol. 21, 1963, pp. 21-36.
12. Shames, I. H., and Dym, C. L., *Energy and Finite Element Methods in Engineering Mechanics*, Hemisphere Publishing Corporation, New York, New York, 1985.
13. Sanders, J. L., Jr., "An Improved First-Approximation Theory For Thin Shells," NASA TR R-24, 1959.
14. Cohen, G. A., "Transverse Shear Stiffness of Laminated Anisotropic Shells," *Computer Methods in Applied Mechanics and Engineering*, Vol. 13, 1978, pp. 205-220.
15. Cohen, G. A., "FASOR - A Second Generation Shell of Revolution Code," *Computers & Structures*, Vol. 10, 1979, pp. 301-309.
16. McGowan, D. M., "Development Of Curved-Plate Elements For The Exact Buckling Analysis Of Composite Plate Assemblies Including Transverse Shear Effects," M.S. Thesis, Old Dominion University, Norfolk, VA, to appear May, 1997.
17. Jones, R. M., *Mechanics of Composite Materials*, Hemisphere Publishing Corp., New York, New York, 1975.

18. Wittrick, W. H., and Williams, F. W., "An Algorithm for Computing Critical Buckling Loads of Elastic Structures," *Journal of Structural Mechanics*, Vol. 1, 1973, pp. 497-518.
19. Timoshenko, S. P., and Gere, J. M., *Theory of Elastic Stability, Second Edition*, McGraw-Hill Book Company, New York, New York, 1961.
20. Anonymous, DuPont KOREX™ Honeycomb Core for High Performance Applications, DuPont Technical Data Specification Sheet.

Table 1. Material properties for boron/epoxy plies and 2024 aluminum (SI units).

Material	$E_{11}x10^{-10}$, N/m^2	$E_{22}x10^{-10}$, N/m^2	$G_{12}x10^{-10}$, N/m^2	ν_{12}	ρ, kg/m^3
Boron/epoxy	20.69	1.86	0.48	0.21	2006.8
Aluminum 2024	7.38	7.38	2.76	0.33	2768.0

Table 2. Material properties for aluminum and Korex™ honeycomb core (English Engineering units).

Material	$E_{11}x10^{-6}$, lb/in^2	$E_{22}x10^{-6}$, lb/in^2	$G_{12}x10^{-6}$, lb/in^2	$G_{13}x10^{-6}$, lb/in^2	$G_{23}x10^{-6}$, lb/in^2	ν_{12}	ρ, lb/in^3
Aluminum	10.0	10.0	3.846	3.846	3.846	0.3	0.1
Korex™ H/C core	0.0001	0.0001	0.0001	0.012	0.004	0.3	0.00116

Table 3. Design-optimization results for a honeycomb sandwich cylinder subjected to N_{11} loading.

N_{11},	Classical plate theory (tensorial strains)			Transverse shear plate theory (tensorial strains)		
lb/in.	t_{fs}, in.	t_{core}, in.	mass, lb_m	t_{fs}, in.	t_{core}, in.	mass, lb_m
1,000	0.010	0.310	213.53	0.010	0.313	213.85
2,000	0.020	0.334	397.00	0.020	0.338	397.43
3,000	0.030	0.324	576.88	0.030	0.331	577.64
4,000	0.040	0.280	753.17	0.040	0.349	760.47
5,000	0.050	0.270	933.02	0.050	0.367	943.44
10,000	0.100	0.250	1,835.8	0.100	0.606	1,873.2
15,000	0.150	0.194	2,734.7	0.150	0.909	2,809.7
20,000	0.200	0.135	3,633.3	0.200	1.212	3,746.3

Table 4. Design-optimization results for a solid-wall cylinder subjected to N_{11} loading.

N_{11},	Classical plate theory (tensorial strains)		Transverse shear plate theory (tensorial strains)	
lb/in.	t_{wall}, in.	mass, lb_m	t_{wall}, in.	mass, lb_m
1,000	0.102	924.68	0.102	924.69
2,000	0.143	1,296.8	0.143	1,296.8
3,000	0.179	1,622.0	0.179	1,622.0
4,000	0.207	1,873.8	0.207	1,873.9
5,000	0.230	2,082.1	0.230	2,082.2
10,000	0.324	2,931.8	0.324	2,931.9
15,000	0.409	3,697.5	0.409	3,697.7
20,000	0.474	4,291.3	0.474	4,291.6

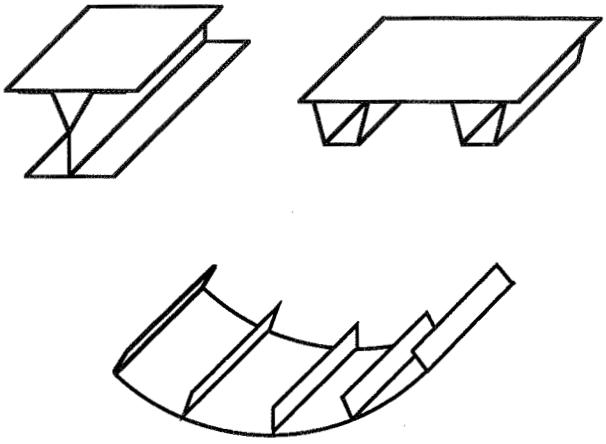

Figure 1. Typical longitudinally stiffened plate structures.

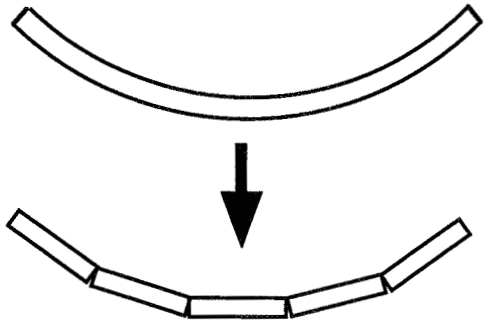

Figure 2. Segmented representation of curved-plate geometry currently used by VICONOPT.

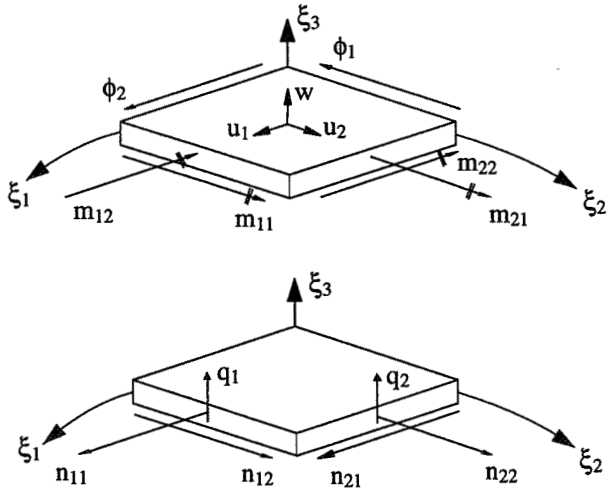

Figure 3. Curved-plate geometry and sign convention for buckling displacements, rotations, moments, and forces.

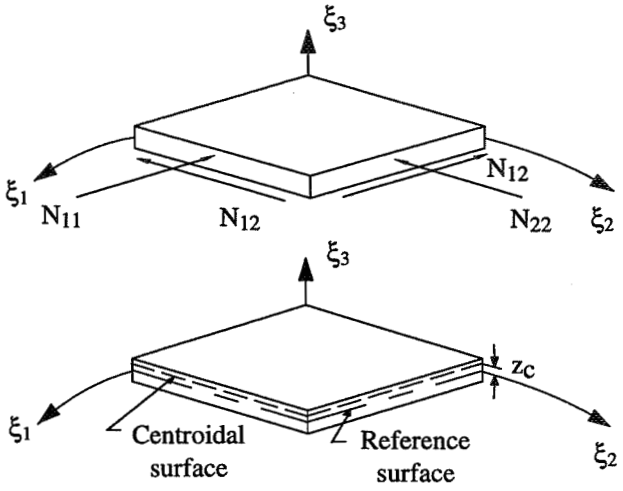

Figure 4. Sign convention for applied in-plane loads and relation of reference surface to centroidal surface.

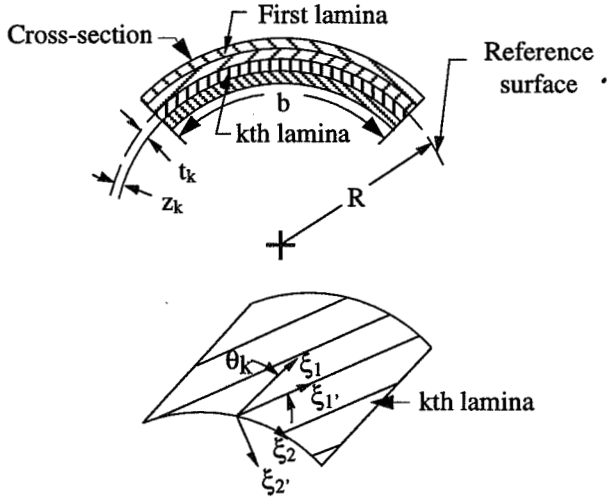

Figure 5. Curved-laminate geometry.

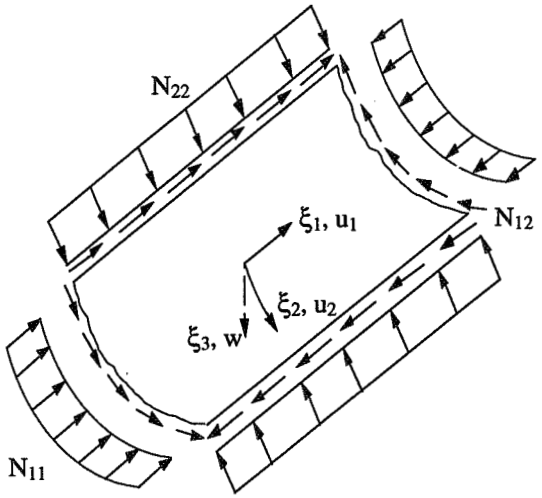

Figure 6. Positive applied in-plane loads on a long curved plate.

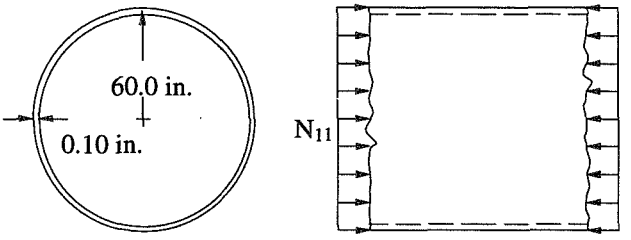

$E = 10.0 \times 10^6$ psi
$\nu_{12} = 0.33$
$\rho = 0.1$ lb/in^3

Figure 7. Long isotropic (aluminum) cylinder subjected to uniaxial compression.

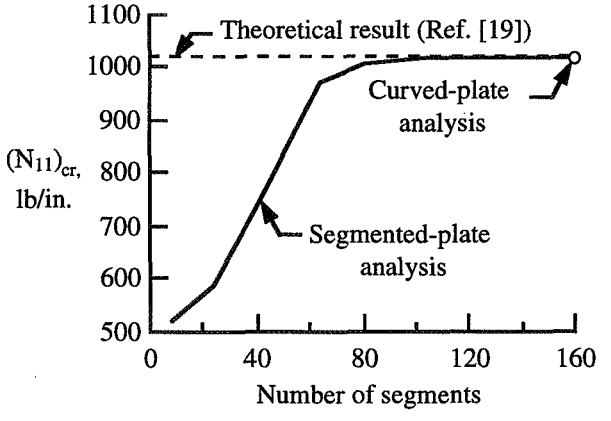

Figure 8. Convergence of VICONOPT segmented-plate results as a function of the number of elements used in the approximation.

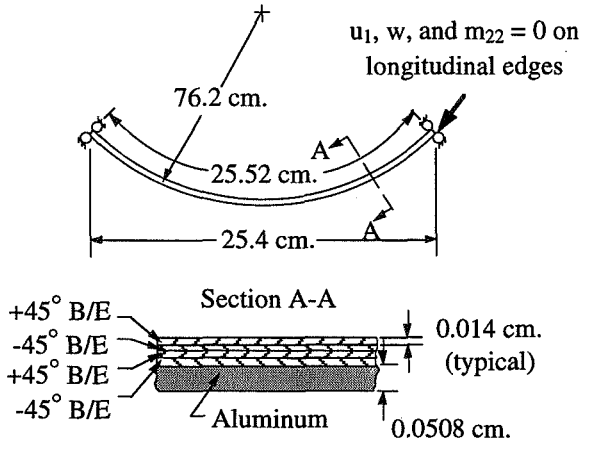

Figure 9. Unsymmetrically laminated curved plate with simply supported edges subjected to applied in-plane loads.

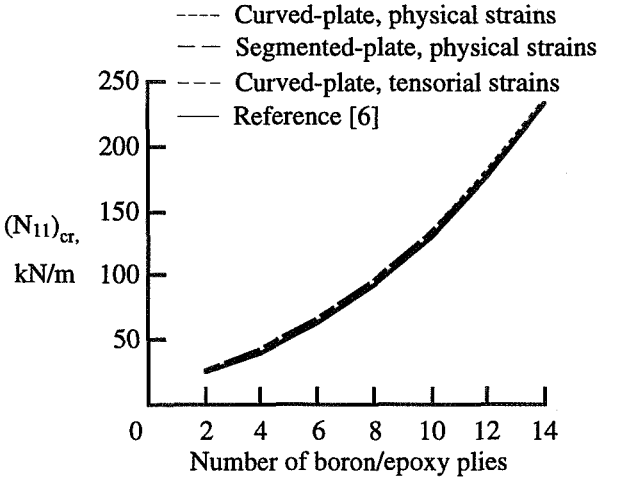

Figure 10. Critical value of N_{11} for buckling of an unsymmetrically laminated curved plate with simply supported longitudinal edges.

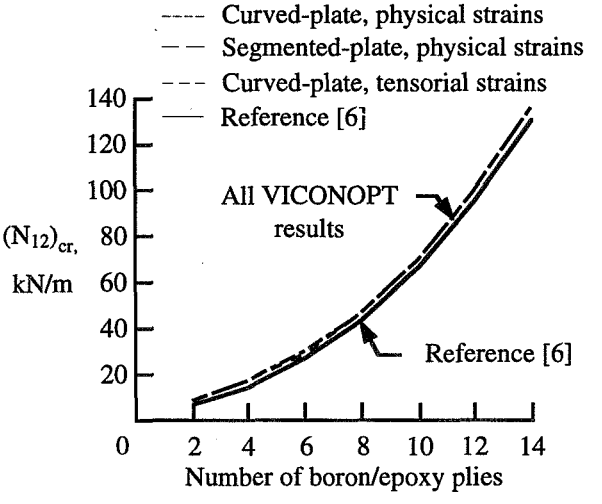

Figure 11. Critical value of N_{12} for buckling of an unsymmetrically laminated curved plate with simply supported longitudinal edges.

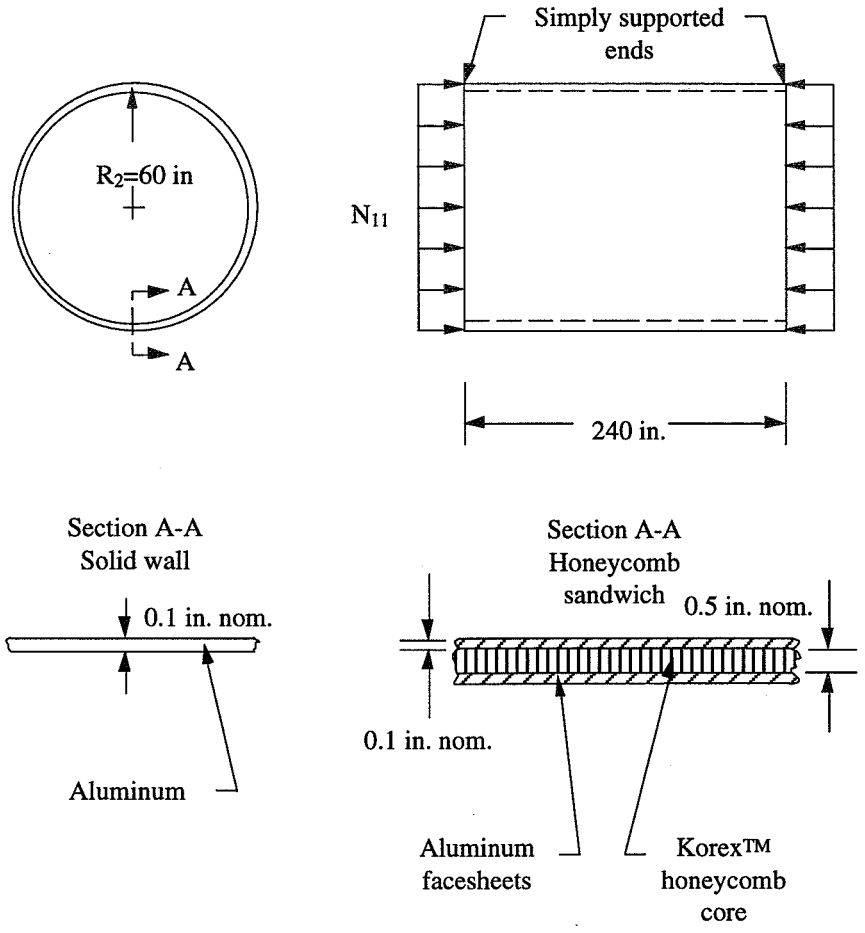

Figure 12. Cylindrical shell subjected to uniform axial compression (N_{11} loading).

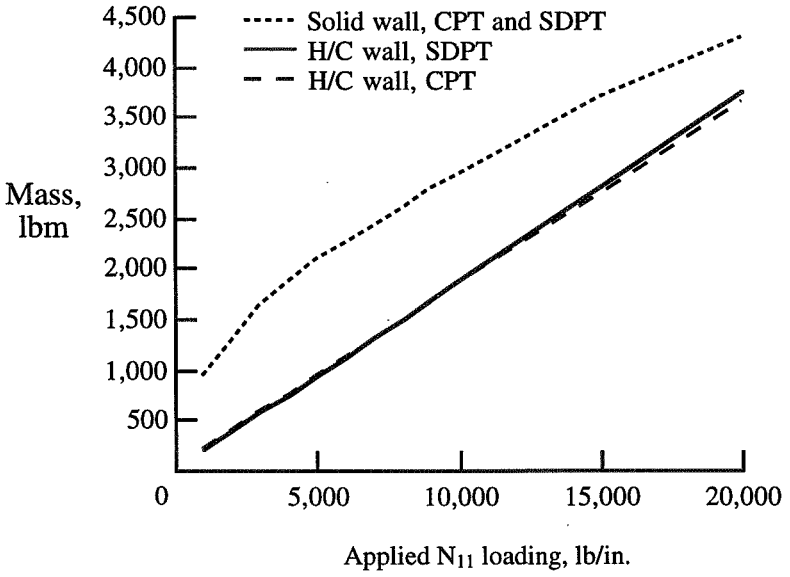

Figure 13. Optimized cylinder mass as a function of the applied loading for a cylindrical shell.

ACCURATE MODELING OF THE POSTBUCKLING RESPONSE OF COMPOSITE PANELS WITH SKEWED STIFFENERS

Richard D. Young*
Lockheed Martin Engineering and Science Services
Hampton, Virginia 23681-0001

Michael W. Hyer†
Virginia Polytechnic Institute and State University
Blacksburg, Virginia 24062

Abstract

Modeling procedures which predict accurately the postbuckling response of composite panels with skewed stiffeners are presented. A particular experimental program is considered and detailed finite element models are created to represent the conditions in the experiment. First, a simple baseline model with minimal detail is defined. Then, a number of modeling refinements that improve the accuracy of the model are identified. These refinements are applied individually to the baseline model to assess the effect of each refinement on the predicted response. The individual refinements are then combined to create an advanced finite element model. In addition to model refinements which affect the overall panel response, a modeling procedure for simulating nonuniform initial load introduction that is specific to an particular experiment is described and demonstrated.

By implementing a number of modeling refinements, a finite element model is developed which improves the correlation between the measured and predicted responses. The skewed stiffener detail and anisotropic skin in the selected problem create axial-shear stiffness coupling which makes this problem sensitive to the constraint on the shear displacement. The remainder of the modeling refinements considered are applicable to general structural configurations. The results presented may be used to guide future efforts to improve correlation between predicted and measured responses for postbuckled stiffened panels.

Introduction

Stiffened laminated composite panels are finding an increased number of applications in structural design. Stiffened panels, generally consisting of beam-like members adhesively bonded or mechanically fastened to a thin laminate, or skin, are typically utilized because of their structural efficiency and their ability to carry additional load after the skin has buckled. The use of laminated fiber-reinforced composites has grown due to their high strength-to-weight and stiffness-to-weight ratios, and the ability to tailor laminate properties for specific applications.

Since experimental studies have shown that composite stiffened panels can exhibit substantial postbuckling strength (see Refs. 1 and 2, for example), some design practices allow the skin of certain stiffened components to buckle at load levels below design ultimate load conditions. Starnes, et al.[1] presented the results of an experimental and numerical study of postbuckled compression loaded panels with four I-shaped longitudinal stiffeners. In the experiments some panels supported as much as three times their initial buckling loads before failing.

In some aerospace applications, stiffened panels have been structurally tailored by introducing axial-shear stiffness coupling to control aeroelastic deformations in order to improve structural performance (see Refs. 3 and 4, for example). Two techniques have been applied for structural tailoring of stiffened panels. Axial-shear stiffness coupling has been incorporated in metallic stiffened panels by utilizing skewed stiffeners, i.e., stiffeners not aligned with the primary direction of loading. In stiffened panels with laminated composite skins, axial-shear stiffness coupling has been generated by rotating the principal direction of orthotropy of the laminated skin relative to the principal direction of loading. A recent experimental and numerical study conducted by the authors has reported on the effects of tailoring both skin laminate anisotropy and stiffener orientation on the prebuckling and postbuckling response of stiffened composite panels subjected to an end shortening displacement. Preliminary results from this study were presented by Young, et al.[5] and the entire study was documented in Ref. 6. The structural configurations considered in Refs. 5 and 6 were adopted by Noor et al.[7] in a numerical study which included thermal loads and introduced hierarchi-

*Aerospace Engineer, Acoustics and Structures Department.
†Professor, Department of Engineering Science and Mechanics. Associate Fellow, AIAA.

cal sensitivity coefficients to characterize the structural response.

When conducting an experimental and numerical study, efforts are made to create good correlation between experimental and predicted responses. If good correlation is achieved, the numerical results can provide detailed information useful in interpreting the experimental behavior. Furthermore, the experiments can verify the model accuracy so that the models can be used with confidence to study other configurations and conditions without the need to always conduct confirming experiments. The current paper presents the results of an investigation to determine the level of detail in a finite element model that is necessary to simulate accurately the postbuckling response of a composite panel with skewed stiffeners. This investigation was conducted as part of the experimental and numerical study reported in Ref. 6 mentioned above. A single test panel from Ref. 6 is considered and the effects of several modeling details on the correlation of the experimental and predicted postbuckling responses are assessed. By carefully considering the details of the experiment, finite element modeling procedures which correctly represent the conditions in the experiment are defined. The current paper presents results which demonstrate the effect of individual modeling refinements on the predicted response, and also demonstrate the improvement in correlation between the experimental and predicted responses resulting from modeling refinements. The skewed stiffener detail in the selected problem creates axial-shear stiffness coupling which raises additional response and modeling issues. The results provide insight into modeling procedures which specifically address panels with stiffness coupling, although the majority of the results are also applicable to general structural configurations.

Structural Configuration

The structural configuration considered in Refs. 5 - 7 consisted of a rectangular graphite-epoxy laminated panel with a single centrally located I-shaped graphite-epoxy stiffener. Axial-shear stiffness coupling was introduced by rotating the orientation of the stiffener or the principal direction of orthotropy of the skin, or both. The structural parameters varied are shown in Fig. 1. The stiffener orientation is represented by the angle α, and the orientation of the principal direction of orthotropy of the skin laminate is represented by the angle β, both measured relative to the axial, or x, direction. A uniform end shortening displacement u is applied to the upper end of the panel in the axial direction, and the axial displacement of the lower end is restrained. The upper and lower ends are clamped and the unloaded sides are simply supported. The axial compressive force corresponding to the applied end shortening is represented by P_x, and the shear force reaction generated by the axial-shear stiffness coupling is represented by P_{xy}. If the upper end of the panel is free to shear in the lateral, or y, direction, then the lateral displacement associated with shear is represented by v.

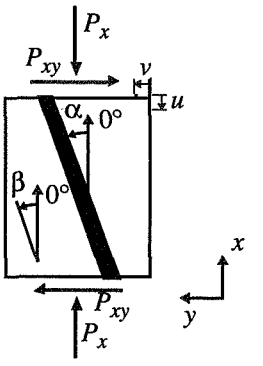

Fig. 1. Structural parameters studied in Refs. 5 - 7

Test Panel

The panels tested by Young[5,6] were fabricated from Hercules, Inc. AS4-3502 graphite-epoxy unidirectional preimpregnated tape (pre-preg). The panels were sized so that the unsupported panel was 21.0 in. long and 16.0 in. wide. All components were constructed from 16-ply laminates. The stacking sequence for the unrotated skin laminate was $[\pm 45/\mp 45/0_3/90]_s$. The stiffener was an open-section I-stiffener with all sections made with a $[\pm 45/0/90]_{2s}$ laminate. The stiffener geometry is shown schematically in Fig. 2(a). Five panel configurations with various combinations of skin and stiffener orientation were tested. The single configuration considered in the current paper has both the skin laminate and the stiffener orientation rotated by 20° relative to the axial direction, i.e., $\alpha = 20°$ and $\beta = 20°$. Photographs of this test panel are shown in Figs. 2(b) and 2(c).

Approach for Model Development

Experimental results[6] for the panel with the stiffener and skin rotated 20° are compared with numerical results obtained from the STAGS finite element code.[8] The approach applied in this paper is as follows. First, a simple baseline finite element model is defined. When the panel response predicted by this model is shown to poorly correlate with the experimental results, a list of possible modeling refinements is developed that could possibly make the model more closely resemble the test panel. The effect of each modeling refinement is assessed by creating additional models, each model introducing only one refinement to the baseline model, and comparing the response of each new model to the baseline model. After each modeling refinement is assessed

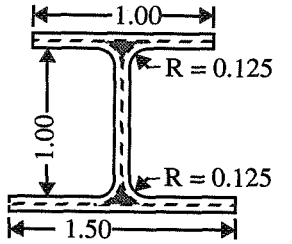

(a) Stiffener geometry, dimensions in inches.

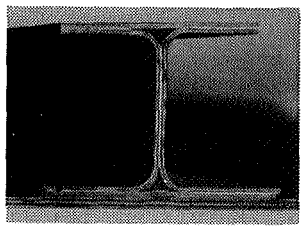

(b) Stiffener-skin cross section.

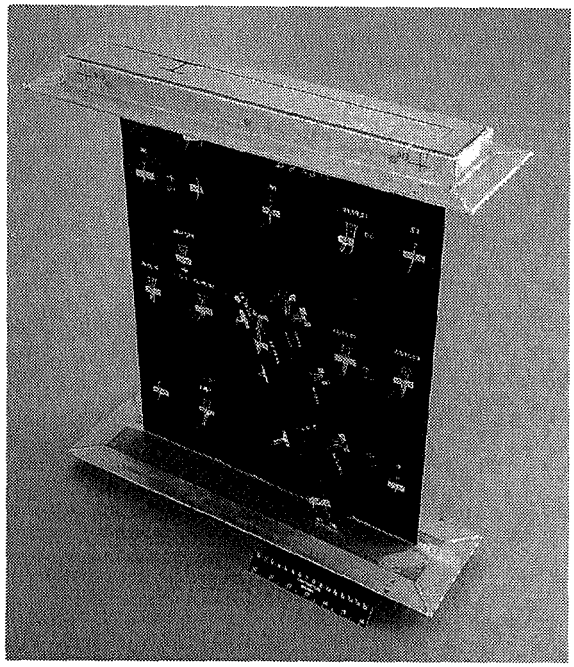

(c) Potted panel: stiffener rotated, $\alpha = 20°$.

Fig. 2. Test panel

independently, a model is assembled that incorporates all of the refinements. The predicted response of this model is then compared to the baseline model and the experimental data. Linear buckling and nonlinear postbuckling analyses are conducted for each model. The panel's global response is reflected in the predicted linear buckling load and nonlinear load vs. end shortening response. These results are presented for each model as a guide to the overall predicted behavior. The experimental buckling load for this panel was $(P_x)_{cr}^{exp} = 5.12$ kips. In this paper, load vs. end shortening results for loads up to 15 kips are considered.

The Baseline Model

The baseline model, which is the starting point for model development and is shown in Fig. 3(a), represents only the unsupported section of the panel, i.e., the 21.0 in. length between the potted ends and the 16.0 in width between the knife edge supports. The panel is assumed to

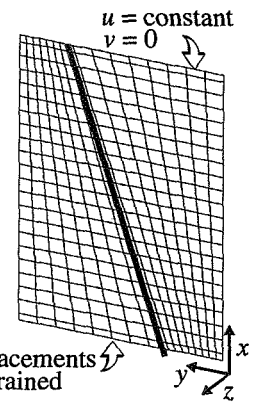

(a) Baseline model

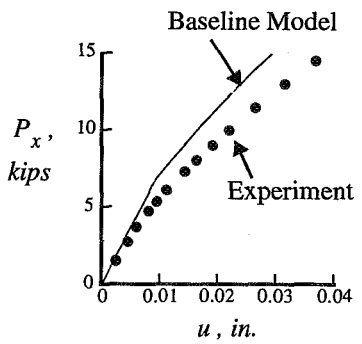

(b) Axial load vs. end shortening response

Fig. 3. Baseline model and experiment

be perfectly flat. The boundary conditions are typical of a clamped-clamped—simply-supported–simply-supported panel with a uniform end shortening:

- Top edge: u = constant, $(v, w, Ru, Rv, Rw) = 0$.
- Bottom edge: $(u, v, w, Ru, Rv, Rw) = 0$.
- Sides: $(w, Rv) = 0$,

where Ru, Rv, and Rw are rotations about the x, y and z axes, respectively.

The stiffener is modeled as a discrete beam stiffener, rotated 20° from the x-axis, and located with an eccentricity relative to the reference plane of the skin. The nominal material properties in Table 1 are used in the baseline model.

A linear buckling analysis using the baseline model predicts $(P_x)_{cr} = 6.52$ kips, as compared to $(P_x)_{cr}^{exp} = 5.12$ kips. The axial load vs. end shortening response for the baseline model and the experiment are compared in Fig. 3(b). The results from the baseline model do not correlate well with the experimental response. The baseline model over-predicts the stiffness and the buckling load of the panel. Below is a list of modeling refinements that are employed to make the baseline model more closely simulate the response of the test panel:

1. The discrete beam stiffener is replaced with a branched shell model.
2. The length of the panel in the potted sections on each end is included in the model.
3. The width of the panel outside the knife edge supports is included in the model.
4. The material properties adjusted for the as-fabricated test panels are used.
5. The top edge of the model is allowed to translate uniformly in the y-direction.
6. Initial geometric imperfections are introduced.

Table 1 Typical Material Properties: Hercules AS4-3502 Graphite-Epoxy[9]

E_1	19.40 Msi
E_2	1.48 Msi
G_{12}	0.82 Msi
ν_{12}	0.30
V_f	0.62
t_{ply}	0.0055 in.

Incremental Modifications to the Baseline Model

Each of the model refinements mentioned above is independently introduced into the baseline model to show how each model refinement alters the predicted response.

Branched Shell Stiffener Model

The discrete beam stiffener in the baseline model is replaced with a branched shell model as shown in Fig. 4(a). The cap, web, and attachment flanges of the stiffener geometry shown in Fig. 2(a) are modeled with plate elements. A linear buckling analysis of the model with the branched shell stiffener predicts $(P_x)_{cr} = 7.06$ kips. The axial load vs. end shortening response for this model and the baseline model are compared in Fig. 4(b). As can be seen in the figure, the prebuckling response of the two models are the same, but the model with the branched-shell stiffener has a higher buckling load and higher postbuckling stiffness. The buckling load and postbuckling stiffness are higher because the attachment flange of the branched shell stiffener provides out-of-plane and in-plane stiffness to the panel skin over a finite width, rather than along a line.

Extended Length in Potting

The test panels had a total length of 24.0 in. The top and bottom edges were potted in 1.5 in. of casting compound. While the baseline model includes only the 21.0 in. length of unsupported panel between the potted ends, the model shown in Fig. 5(a) uses an extended length to represent the potted portion of the panel. The uniform end shortening is still applied at the top edge of the model. The dashed lines on the model indicate the sections of the model located within the potting. It is assumed that the potting provided support perpendicular to the panel components. This support is modeled by setting $w = 0$ for nodes within the potting and constraining the u- and v-displacements such that the beam stiffener exits the potted regions at a constant 20°. A linear buckling analysis of the model with the extended length predicts $(P_x)_{cr} = 6.47$ kips. The axial load vs. end shortening response for this model and the baseline model are compared in Fig. 5(b). The buckling loads from the two models are similar, but the extended length model is less stiff for all loads. This is the case because axial strain is allowed to occur within the potted ends of the extended length model. For a given amount of end shortening, the longer model has a lower strain, and therefore, a lower axial load.

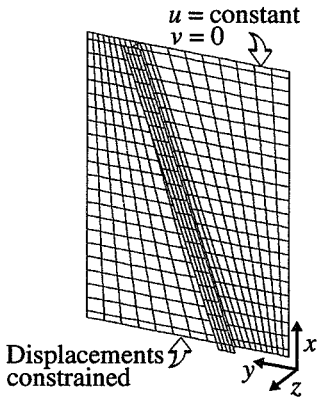

(a) Model with branched shell stiffener

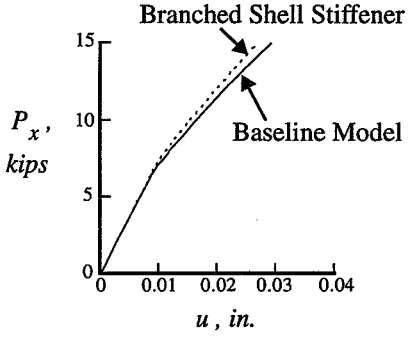

(b) Axial load vs. end shortening response

Fig. 4. Branched shell stiffener

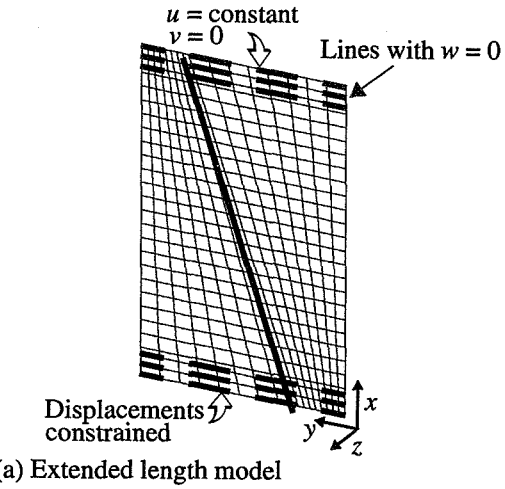

(a) Extended length model

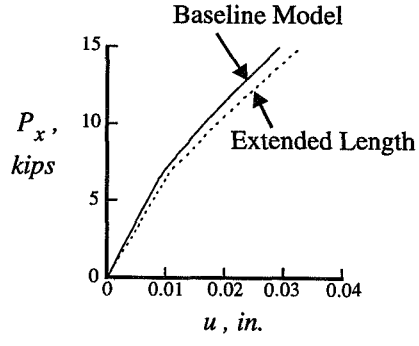

(b) Axial load vs. end shortening response

Fig. 5. Extended length in potting

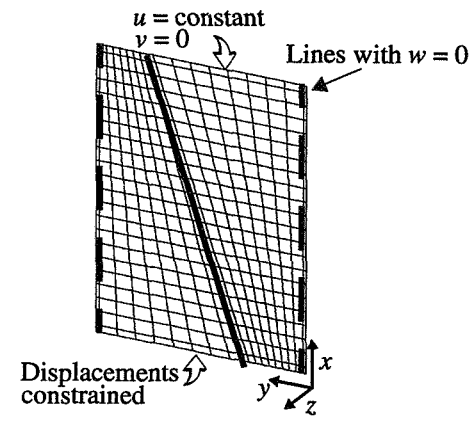

(a) Extended width model

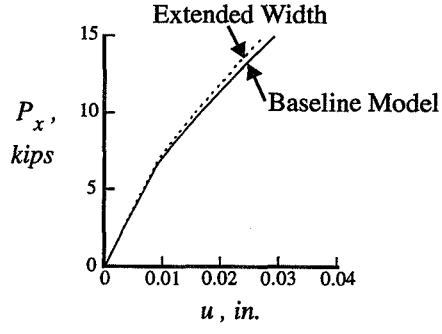

(b) Axial load vs. end shortening response

Fig. 6. Extended width outside knife-edge supports

Extended Width Outside Knife-Edge Supports

The panels had a total width of 16.5 in. The unloaded edges had knife-edge supports located 0.25 in. from the panel edges. While the baseline model included only the 16.0 in. width of panel between the knife-edge supports, the model shown in Fig. 6(a) represents an extension to include the entire width. The dashed lines on the model indicate where the $w = 0$ constraint was imposed. A linear buckling analysis of the model with the extended width predicted $(P_x)_{cr} = 6.74$ kips. The axial load vs. end shortening response for this model and the baseline model are compared in Fig. 6(b). The buckling loads from the two models were similar, but the extended width model was stiffer for all loads. The difference in stiffness increased in the postbuckling response, as the buckled skin transferred load into the stiffener and the region of the skin supported by the knife-edges.

Modified Material Properties

In Ref. 6, experimental results were used to define modified material properties for the as-fabricated panels. The ply thickness and fiber volume fraction were altered to provide better correlation between the load cell data and the axial load obtained by integrating the stress resultants computed from strain gage data. The modified material properties that were obtained are shown in Table 2. A linear buckling analysis of the model which uses the modified material properties predicts $(P_x)_{cr} = 4.97$ kips. The axial load vs. end shortening response for this model and the model with nominal material properties are compared in Fig. 7. Using the modified material properties reduces the prebuckling panel stiffness by only 4.4%, but reduces the buckling load by 31%. The large reduction in the buckling load reflects the loss of local bending stiffness caused by reducing the ply thickness by 11%.

Table 2 Modified Material Properties: Hercules AS4-3502 Graphite-Epoxy

E_1	20.9 Msi
E_2	1.578 Msi
G_{12}	0.886 Msi
ν_{12}	0.297
V_f	0.660
t_{ply}	0.00490 in.

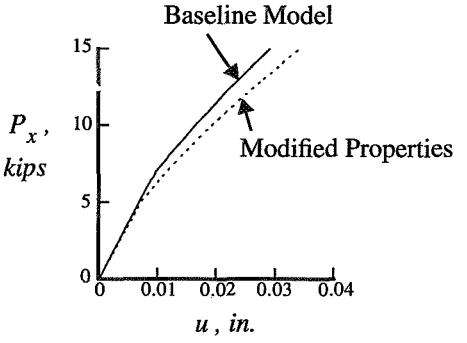

Fig. 7. Modified material properties: axial load vs. end shortening response

Unspecified v-displacement on the Top Edge

When a panel with axial-shear stiffness coupling is subjected to a uniform axial end shortening, the type of coupling exhibited depends on the boundary condition on the v-displacement. Two ideal boundary conditions are considered in Fig. 8. The first case assumes that $v = 0$ and is represented in Fig. 8(a). In this situation an axial end shortening induces both axial and shear force reactions. This case represents pure force coupling with the amount of force coupling defined by the ratio P_{xy} to P_x. The second case considered assumes that v is uniform, but is unspecified, and the net shear force is equal to zero. As shown in Fig. 8(b), instead of a shear force reaction, an axial end shortening induces a shear displacement. This case represents pure displacement coupling with the amount of displacement coupling defined by the ratio v to u. The experimental response was bounded by these two ideal cases.

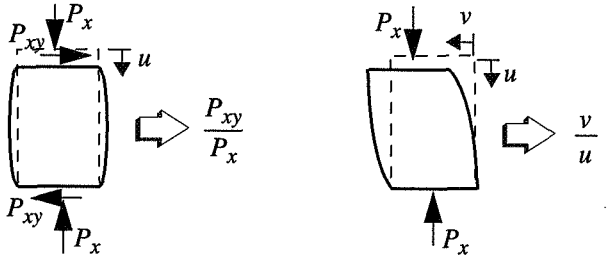

(a) Pure force coupling ($v = 0$, $P_{xy} \neq 0$)

(b) Pure displacement coupling ($v \neq 0$, $P_{xy} = 0$)

Fig. 8. Axial-shear force and displacement coupling: boundary condition on v

The baseline model had $v = 0$ on both of the loaded edges and thus represented the pure force coupling case. The pure displacement coupling case is created by allowing a v-displacement of the top edge which is uniform and unspecified. A linear buckling analysis of a model which has the v-displacement unspecified predicts $(P_x)_{cr} = 5.83$ kips. The axial load vs. end shortening responses for this model and the baseline model are compared in Fig. 9(a). Releasing the constraint of the

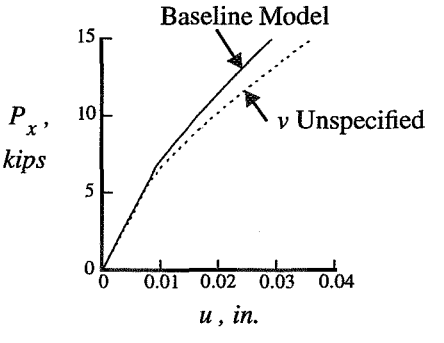

(a) Axial load vs. end shortening response

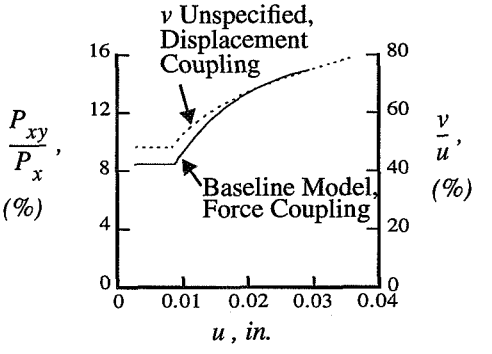

(b) Force coupling and displacement coupling

Fig. 9. Unspecified v-displacement

v-displacement lowers the buckling load and reduces the axial stiffness. The displacement coupling (v/u) for this model and the force coupling (P_{xy}/P_x) for the baseline model are compared in Fig. 9(b). Although the magnitude of the coupling response differs for the two cases, the behavior of the response is very similar. In both cases, the coupling response is constant in prebuckling and increases substantially in postbuckling. The experimental results[6] for this test panel demonstrated a mixture of force coupling and displacement coupling, each to a lesser degree than shown in Fig. 9(b).

Initial Geometric Imperfections

Prior to testing, the surface shape of the panel skin was measured. A contour plot of the measured surface shape normalized by the thickness of the panel skin is shown in Fig. 10(a). The flat baseline model is modified by introducing an initial out-of-plane geometric imperfection defined by a Fourier series representation of the measured surface shape. The axial load vs. end shortening response for the imperfect model and the baseline model are compared in Fig. 10(b). The measured imperfection shape for this panel has very little affect on the overall stiffness of the model. The imperfection does remove the bifurcation behavior observed with the baseline model and increases the likelihood that the predicted and experimental deformations will be in the same direction.

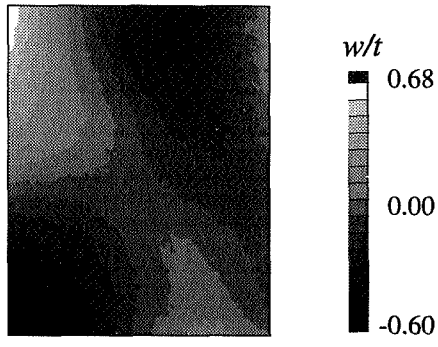

(a) Measured surface shape, *w/t*

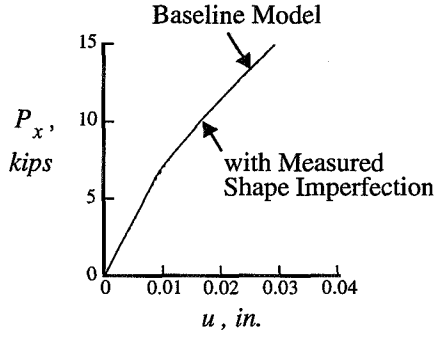

(b) Axial load vs. end shortening response

Fig. 10. Initial geometric imperfection

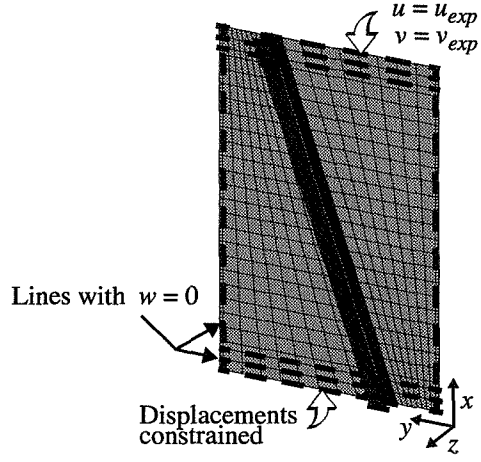

(a) Advanced model

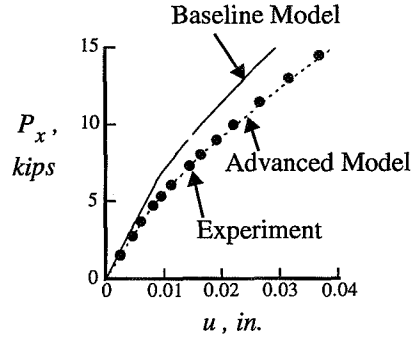

(b) Axial load vs. end shortening response

Fig. 11. Advanced model and experiment

The Advanced Model

Based on the individual model refinements, an advanced finite element model was developed to simulate the response of the test panel. This model is shown in Fig. 11(a). The stiffener is represented by branched plates, the entire length and width of the panel is included in the model, and the modified material properties are used. Measured shape data is applied as an initial geometric imperfection. The mixture of force coupling and displacement coupling observed in the experiment is addressed by specifying that the *u*- and *v*-displacement of the top edge be defined by measured experimental data u_{exp} and v_{exp}.

A nonlinear postbuckling analysis of the advanced model was conducted. The axial load vs. end shortening response for the baseline model, advanced model, and the experiment are compared in Fig. 11(b). The advanced model accurately simulates the all response of the panel in the prebuckling and postbuckling range of loading.

Local Panel Response

The previous refinements to the finite element model were directed toward accurately predicting the overall response of a panel. Considering the local panel response, one more modification is introduced to the finite element model to simulate the nonuniform initial load introduction that was evident in the experiments. During testing, load introduction into the panel skin was monitored by strain gages located across the panel width, 4.0 in. from the top and bottom potting, and load introduction into the stiffener was monitored by strain gages located on the stiffener cap near the potted ends. Experimental strain readings were highly nonlinear and nonuniform during initial loading, and became nearly linear when $u \approx 0.25u_{cr}$. For the panel under consideration u_{cr} was 8.38 mil.

For $u = 0.25u_{cr}$, numerically-predicted strains obtained using the advanced finite element model are compared to the measured strains in Fig. 12. The strains shown are normalized by the strain at buckling, i.e., $\varepsilon_x^* = \varepsilon_x / (u_{cr}/24)$. Note that with this normalization, compressive strains are positive. The measured strain values in the skin were low in the center of the panel. The measured strain values in the stiffener cap indicated bending, with the gages on the cap near the top potting showing a negative normalized strain, i.e., the stiffener cap was in tension when the remainder of the panel was in compression.

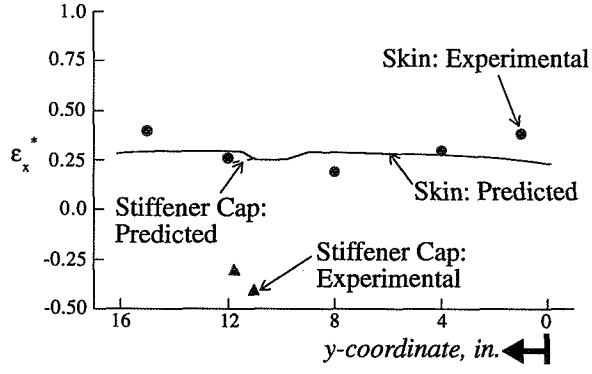

(a) Strains across width near top potting

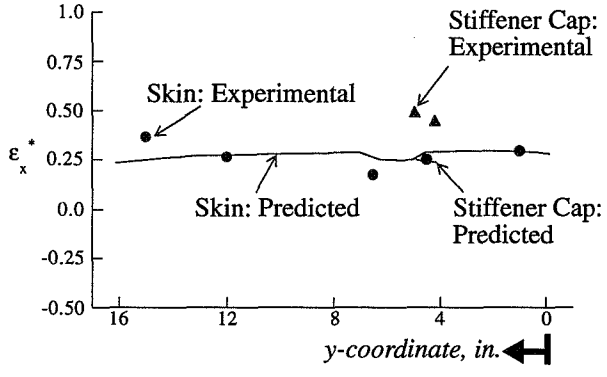

(b) Strains across width near bottom potting

Fig. 12. Experimental and predicted strains near loaded ends: advanced model

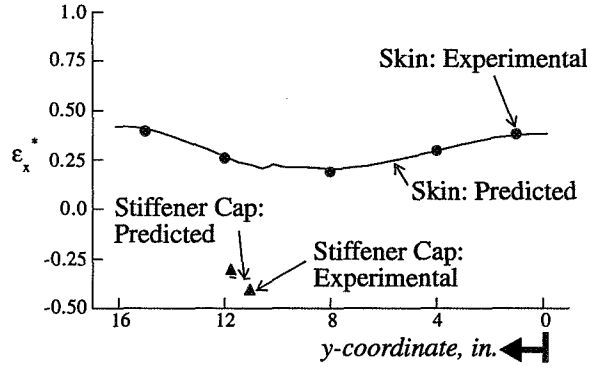

(a) Strains across width near top potting

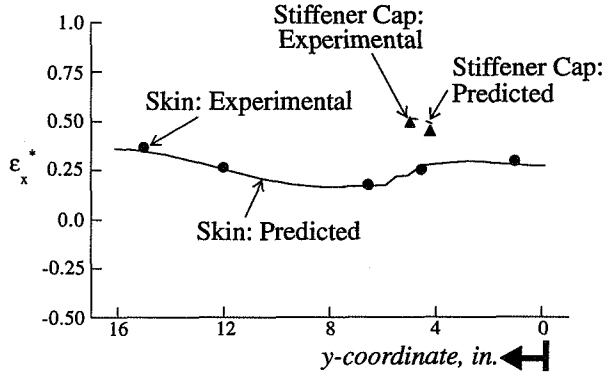

(b) Strains across width near bottom potting

Fig. 13. Experimental and predicted strains near loaded ends: nonuniform initial displacement

To better simulate the experimental load introduction, a nonuniform initial displacement on each end of the model and superimposed on the uniform end shortening. The nonuniform initial displacement consists of a nonuniform u-displacement and a rotation about the y-axis and is defined based on the experimental data for a uniform endshortening $u = 0.25u_{cr}$. Experimental data from strain gages on the skin are used to infer the shape of the nonuniform u-displacement, while data from strain gages on the stiffener cap are used to infer the end rotations. The nonuniform initial displacement is adjusted iteratively until the discrepancies between the predicted and measured strains for $u = 0.25u_{cr}$ are minimized. The predicted strains obtained with the nonuniform initial displacement model are compared to the experimental strains in Fig. 13. The magnitude of the nonuniform initial displacement in less than 3.0 mil. Although this value is within the tolerance allowed for machining and fixturing test specimens, 3.0 mil. does represent a significant percentage of the end shortening at buckling, and thus nonuniform initial loading is important when considering local response values.

To conduct analyses at higher loads, the nonuniform initial displacement is held constant, and a uniform end shortening is added. The axial load vs. end shortening response for the advanced model, the nonuniform initial displacement model, and the experiment are compared in Fig. 14. The results in Fig. 14 indicate that the nonuniform initial displacement which has a substantial effect on the local strain distribution has very little effect on the overall panel response.

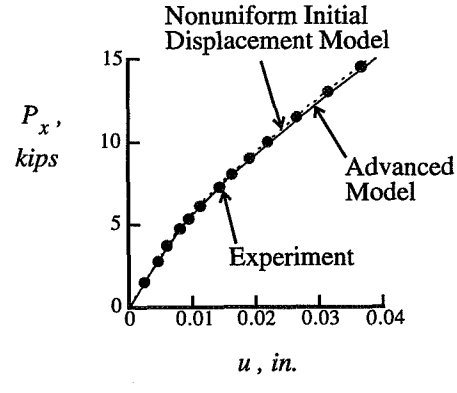

Fig. 14. Advanced model, nonuniform initial displacement model, and experiment: axial load vs. end shortening response

A contour plot of the out-of-plane skin displacement predicted by the nonuniform initial displacement

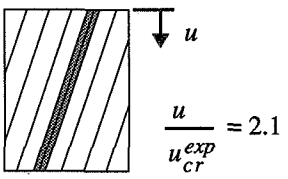

(viewed from unstiffened side)

(a) Moiré-fringe pattern

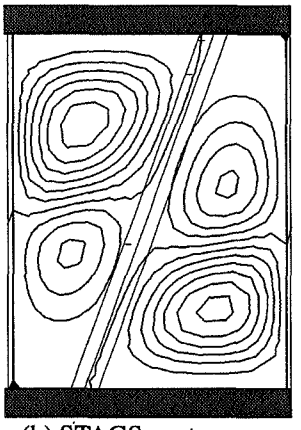

(b) STAGS contour nonuniform initial displacement model

Fig. 15. Comparison of experimental and predicted out-of-plane skin displacement contours in the postbuckled state

model and a moiré-fringe pattern from the experiment are compared in Fig. 15 for an applied end shortening $u = 2.1u_{cr}^{exp}$. The shape, sign, and amplitude of the experimental and predicted out-of-plane skin displacements in the postbuckling equilibrium state correlate well.

Summary and Conclusions

Results of a study conducted to define modeling procedures which simulate accurately the postbuckling response of composite panels with skewed stiffeners have been presented. A particular experimental program was considered carefully and detailed finite element models were created to represent the conditions in the experiment.

To initiate the study, a simple baseline model with minimal detail was defined. A number of modeling refinements that could improve the accuracy of the model were identified. These refinements were applied individually to the baseline model and the effect of each refinement on the predicted response is summarized below. Compared to the baseline model:

- Modeling the stiffener with branched shell elements increased the buckling load and postbuckling stiffness because the attachment flange's finite width provided greater support to the panel skin. This would not be the case if the attachment flange was very thin.
- Modeling the extended length in the potting reduced the panel stiffness since a given end shortening caused lower strains.
- Modeling the extended width outside the knife-edge supports increased the effective width and thus increased the increased the buckling load and postbuckling stiffness.
- Using the modified material properties for the as-fabricated test panels substantially reduced the buckling load and postbuckling stiffness.
- Releasing the constraint on the transverse displacement altered the type of coupling response predicted lowered the buckling load and substantially reduced the postbuckling stiffness.
- Initial geometric imperfection had little effect on the predicted response.

The individual refinements were then combined to create an advanced finite element model. In addition to model refinements which affect the overall panel response, a modeling procedure for simulating nonuniform initial load introduction that is specific to an experiment were described and demonstrated. In the case considered, the nonuniform initial loading affected the local panel response primarily and had little affect on the overall panel response. In other situations, a local panel response may cause perturbations which influence the panel's overall response.

Efforts to improve the correlation between the measured and predicted response were successful. By implementing a number of modeling refinements, a finite element model was developed which represented the physics of the response. The skewed stiffener detail and rotated skin orientation in the selected problem created axial-shear stiffness coupling which made this problem sensitive to the constraint on the v-displacement. The remainder of the modeling refinements considered were applicable to general structural configurations.

The results of this paper are considered quite important to researchers interested in correlating predicted responses with experimental results for structural level tests. Inaccurate modeling assumptions and anomalies in the test, i.e., the support fixtures, the loading frame, the load introduction or the test specimen, can cause the predicted response and the measured response to differ substantially. To have credible predicting capability, the differences must be thoroughly understood. This paper represents a step in that direction.

Acknowledgments

This work was supported by the Acoustics and Structures Department of Lockheed Martin Engineering and Science Services Company and the Structural Mechanics Branch of NASA Langley Research Center. The authors would like to express their thanks to Dr. James H. Starnes, Jr., Dr. M. P. Nemeth and the late Dr. M. Stein of NASA Langley Research Center for their technical guidance and insightful discussions on the buckling and postbuckling behavior of plates and the influence of anisotropy.

References

[1]Starnes, J. H., Jr., Knight, N. F., Jr., and Rouse, M., "Postbuckling Behavior of Selected Flat Stiffened Graphite-Epoxy Panels Loaded in Compression," *AIAA Journal*, Vol. 23, No. 8, August 1985, pp. 1236-1246.

[2]Dickson, J. N., Biggers, S. B., and Starnes, J. H., Jr., "Stiffener Attachment Concepts for Graphite-Epoxy Panels Designed for Postbuckling Strength," AFWAL-TR-85-3094, June 1985, pp. v(a)95-v(a)109.

[3]Gimmestad, D., "An Aeroelastic Optimization Procedure for Composite High Aspect Ratio Wings," Proceedings of the 20th Structures, Structural Dynamics, and Material Conference, St. Louis, MO, April 1979. AIAA Paper No. 79-0726.

[4]Mansfield. E. H., "Some Structural Parameters for Aero-Isoclinic Wings," *Aircraft Engineering*, Vol. 24, No. 283, September 1952, pp. 263-264.

[5]Young, R. D., Starnes, J. H., Jr. and Hyer, M. W., "Effects of Skewed Stiffeners and Anisotropic Skins on the Response of Compression-Loaded Composite Panels," Proceedings of the Tenth DoD/NASA/FAA Conference of Fibrous Composites in Structural Design, Hilton Head Island, SC, Nov. 1-4, 1993, Naval Air Warfare Center Report No. NAWACADWAR-94096060, Vol. 1, April 1994, pp. II-109 to II-123.

[6]Young, R. D., "Prebuckling and Postbuckling Behavior of Stiffened Composite Panels with Axial-Shear Stiffness Coupling," Ph.D. Dissertation in Engineering Mechanics, Virginia Polytechnic Institute and State University, Blacksburg, VA, July 1996.

[7]Noor, A. K., Starnes, J. H., Jr. and Peters, J. M., "Thermomechanical Buckling and Postbuckling Responses of Composite Panels with Skewed Stiffeners," AIAA Paper No. 96-1636-CP, April, 1996.

[8]Brogan, F. A., Rankin, C. C., Cabiness, H. D., and Loden, W. A., "STAGS Users Manual," Lockheed Martin Missiles and Space Co., Report LMMS P032594, 1996.

[9]Sensmeier, M. D., Griffin, O. H., Jr., and Johnson, E. R., "Static and Dynamic Large Deflection Response of Graphite-Epoxy Beams," NASA CR-4118, 1988.

FINITE ELEMENT INVESTIGATION OF THE SNAP PHENOMENON IN BUCKLED PLATES

Frederick Stoll* and Steven E. Olson†
University of Dayton Research Institute Dayton, OH, USA 45469-0110

Abstract

Finite element analysis was used to study a compressively loaded plate with supported edges which exhibits a secondary instability in the postbuckling regime. The instability initiates a dynamic snap from one waveform to another with an increase in the number of buckles along the load axis. The analysis simulated a plate configuration tested by Dr. Manuel Stein in 1959. Both clamped and simple support of the loaded ends were modeled, and dynamic analyses of the snap were performed. Good agreement with Stein's data was obtained with the clamped-end model, and major differences in snap behavior for the two different end-support conditions are examined in detail. Material stresses during the dynamic snap were found to exceed the pre-snap stresses by as much as 17%. An explanation is given for the inaccuracies of a previously used analytical approach.

1. Introduction

Axially compressed thin rectangular plates with supported edges are capable of withstanding loads in excess of initial buckling loads. This postbuckling strength is used to advantage in obtaining the ultimate compressive strength of stiffened panels found in aircraft fuselage and wing structures. When loaded into the postbuckling regime, some plate configurations encounter a secondary instability which initiates a dynamic snap to a different waveform, resulting in an increase in the number of buckles along the load axis. Observations of this phenomenon have been reported for metallic plates,[1,2] symmetrically and unsymmetrically laminated composite plates,[3-5] a one-edge-free composite plate,[6] a composite channel section,[6] and a composite plate with a hole,[7] to name a few.

Stein studied the snap phenomenon both experimentally and analytically.[1,8,9] Stein tested in uniaxial compression a rectangular aluminum plate which was supported against out-of-plane deflection by a series of 12 evenly spaces knife edges running the length of the plate.[1,8] Eleven bays were thus formed, each with a length-to-width ratio of 5.4 and a width-to-thickness ratio of 67. The plate was flat-end loaded, which resulted in "almost complete clamping of the loaded edges."[1] The test configuration is depicted in Figure 1. The plate buckled initially with 5 buckles along the length. Further increases in the end displacement produced snaps to 6, then 7, then 8 buckles along the length, with the first snap occurring in the elastic range of the material, and the second and third snaps occurring after some plastic deformation had occurred. The snaps occurred "in a violent manner".[1]

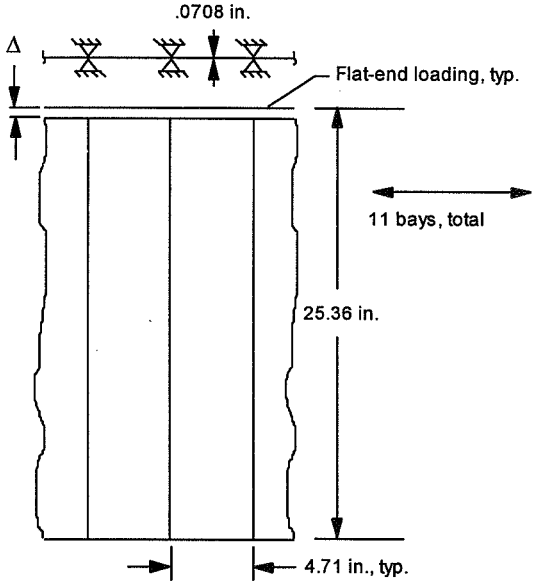

Figure 1. Aluminum plate configuration tested by Stein.[1]

Stein analyzed an axially compressed infinite-length isotropic plate strip with side edge support conditions simulating those of a typical bay of the test panel.[1] The plate strip buckles with a longitudinal halfwave length equal to the plate width, but as additional load is applied, the halfwave length decreases. For example, at twice the initial buckling load, the halfwave length is slightly less than 70% of the width. Stein also studied the snap phenomenon using a simplified structural model possessing two

* Associate Research Engineer, Member AIAA
† Associate Research Engineer, Member AIAA

lateral degrees of freedom. He determined the complete topology of the equilibrium solution paths and the stability of the equilibrium along those paths. The model qualitatively duplicated plate buckling and snap behavior, thereby providing insight into the snap phenomenon with respect to potential energy and stability considerations. However, the full analytical characterization of the snap phenomenon in compressively loaded rectangular plates has remained elusive to date.

Previous efforts[2,5,10-23] related to the analysis of the snap phenomenon in buckled rectangular plates were reviewed by Stoll.[24] In all of these studies equilibrium behavior was analyzed, and in most, though not all, stability principles were employed to predict the onset of a snap. In none was the snap simulated dynamically. The majority of these studies[10-19,21-23] include analyses of plates with simple support on all edges, with out-of-plane displacements represented using terms of a double Fourier series. The Fourier coefficients serve as generalized coordinates. In this approach, the equilibrium equations for von Karman nonlinear plate theory reduce to a coupled set of algebraic equations in terms of a load parameter and the generalized coordinates. The double Fourier series provides a complete set of shape functions which also correspond to buckling mode shapes, and simple postbuckling behavior can be analyzed accurately with only a few degrees of freedom.[25]

Nakamuro and Uetani systematically identified the consistent sets of shape functions required to accurately predict initial postbuckling, secondary bifurcation, and initial post-secondary-bifurcation equilibrium behavior for simply supported isotropic plates.[19] Plates with length-to-width ratios between 1.4 and 8 were considered, and it was demonstrated that the snap phenomenon can occur for all plates within (but not limited to) that range. It was found that a large number of appropriately selected shape functions must be incorporated to accurately analyze some regimes of behavior. Judged in the context of the rigorous approach of Nakamuro and Uetani, all other studies noted which employed global shape functions used inadequate sets of functions for accurately analyzing the secondary instability which initiates a snap. This has resulted in conclusions which were both quantitatively and qualitatively incorrect. For example, in several studies[11,12,21,22] it was erroneously concluded that various simply supported plates in the category considered by Nakamuro and Uetani will not exhibit a snap.

When applied to the plate geometry tested by Stein, the results of Nakamuro and Uetani do not accurately predict the observed snap initiation load. The fundamental difference between the analysis and experiment was the simple supported ends for the former versus the effectively clamped ends for the latter. Uemura and Byon[2] performed static finite element analyses of rectangular plates with length-to-width ratios ranging from 1 to 2, and found a strong influence of the loaded-end support condition on the secondary instability load. Stoll[24] investigated the importance of the end support condition for the Stein plate geometry by performing static analyses using global shape functions with clamped-end boundary conditions. Stoll obtained analytical predictions for the snap initiation load which agree relatively well with the experiment. It was found that while the end support condition only slightly affects the initial buckling load and mode shapes, it has a large affect on both the load at which the secondary instability occurs, and on the mode shape of the secondary instability.

The set of ten global shape functions used by Stoll[24] was not selected using a rigorous basis, and therefore, the results are not conclusive. Furthermore, the actual transition from one buckled waveform to another has never been analyzed as the dynamic event which it is. Consequently there remain questions about some aspects of the snap phenomenon.

This paper seeks to fill gaps in the understanding of the snap phenomenon through the use of a general purpose finite element (FE) analysis code. Results from static and dynamic FE analyses of the plate configuration tested by Stein are presented. The specific goals of the paper are: 1) to verify the conclusions presented in Ref. 24 regarding the importance of boundary conditions at the loaded edges, 2) to investigate the characteristic stress levels induced during the dynamic snap, and 3) to explore some issues surrounding the analytical approaches that have been used to study the snap phenomenon. Section 2 presents a discussion of the FE code, FE models, and analysis procedures used. FE analysis results are presented and discussed in Section 3, and conclusions are presented in Section 4.

2. Finite Element Analysis Approach

The FE analyses reported herein were performed using ABAQUS/Standard Version 5.5 (ABAQUS), by Hibbitt, Karlsson, and Sorensen Inc. ABAQUS is a general purpose finite element code capable of both linear and nonlinear static and dynamic analysis. Pre- and post-processing of the FE model and results were

performed using MSC/PATRAN Version 5.0 by the MacNeal-Schwendler Corp. Analyses were run on a Silicon Graphics Indigo 2 computer with an R8000 processor.

The FE model geometry represented a single bay of the plate tested by Stein.[1] The geometry modeled was a plate 25.36 inches in length, 4.71 inches in width, and 0.0708 inches thick, providing a length-to-width ratio of 5.4 and a width-to-thickness ratio of 67. One longitudinal edge was fixed from translating out-of-plane or in the width direction. The second longitudinal edge was fixed from translating out-of-plane, but was free to move in the width direction provided the entire edge translated the same amount. Multiple-point constraints (MPCs) were used to enforce this condition. The longitudinal edges thus were simply supported, and were constrained to remain straight while carrying no net edge-normal load. Two different sets of end support conditions were used for the analyses: simply supported, and clamped. End-shortening was imposed by fixing one end of the plate and controlling displacements at the opposite end. MPCs were used such that uniform axial displacement of the entire end of the plate could be controlled by imposing the displacement at a single node. The end load was then obtained as the reaction force at this key node. The plate was given typical properties of aluminum, including an elastic modulus of 10.0×10^6 psi, a density of 0.100 lbm/in^3, and a Poisson's ratio of 0.33. The analyses were limited to elastic material response.

A baseline FE model used for most of the reported analyses consisted of 459 nodes and 400 four-node shell elements (ABAQUS type S4R5), with 50 elements down the length of the model and 8 elements through the width. A refined-mesh model, with 200 elements down the length and 32 element through the width, was used to check convergence with respect to FE discretization. Geometrically imperfect models for both end-support conditions were used for some analyses. The basic imperfect model for each end-support condition was created by adding imperfections with amplitudes of 0.1% of the plate thickness in the shapes of each of the first and second buckling modes.

Several different solution strategies were employed during the investigation, and these are briefly described here. Initial bifurcation buckling analyses were performed with the geometrically perfect models. Nonlinear static analyses were performed using both controlled end-shortening, and a modified Riks method for arc-length control. The modified Riks method was used to trace equilibrium solution paths for the geometrically imperfect models. Nonlinear dynamic transient analysis was used to simluate the snap event. Numerical damping was included in the dynamic analyses, so that the post-snap equilibrium path could be located. The effective degree of damping used was relatively low, as discussed in Section 3.

3. Analytical Results

All end-load values, P, and end-shortening values, Δ, reported in this section are nondimensionalized by the following reference load and end-shortening values:

$$P_{ref} = \frac{\pi^2 E h^3}{3(1-\nu^2)b}$$

$$\Delta_{ref} = \varepsilon_{ref} L$$

where E is Young's modulus, ν is Poisson's ratio, h is the plate thickness, b is the plate width, and ε_{ref} is the reference value of longitudinal compressive strain, given by

$$\varepsilon_{ref} = \frac{\pi^2 h^2}{3(1-\nu^2)b^2}$$

P_{ref} and ε_{ref} are the thin-plate-theory theoretical values of end load and axial strain, respectively, for initial buckling of both a uniaxially loaded square plate with simple support on all edges, and a uniaxially loaded infinite-length plate strip with simply supported edges. The numerical values of the parameters used in the current study are summarized in Table 1.

Table 1. Reference Parameter Values

b	4.71 in	ν	0.33
h	0.0708 in	P_{ref}	2782 lb
L	25.36 in	ε_{ref}	.0008342
E	10×10^6 psi	Δ_{ref}	0.02116 in

3.1 Initial Buckling

The initial thin-plate buckling problem for both the clamped-end plate and the simply supported plate can be solved analytically. Buckling eigenvalues and eigenfunctions so obtained were reported by Stoll.[24] The profiles of the buckling eigenfunctions along the load axis are plotted in Figure 2. All eigenfunctions feature a half sine wave profile across the plate width. Although the numbers of buckles along the length are the same for both end support conditions (five for the first mode, six for the second), there is a distinct

influence of the end support condition on the buckling eigenfunctions.

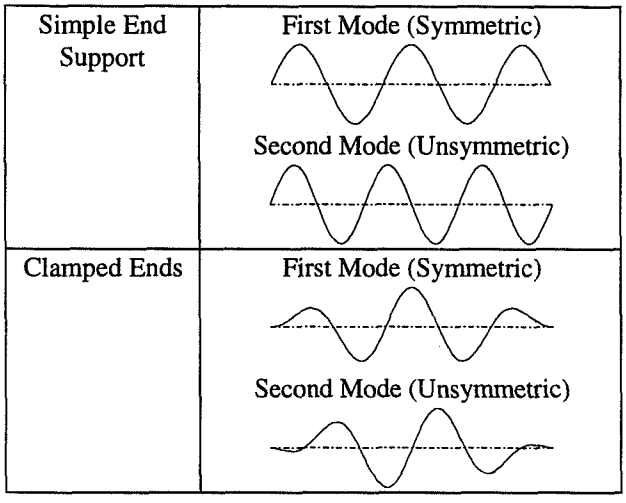

Figure 2. Profiles of buckling eigenfunctions along the load axis.

The analytic buckling eigenvalues are summarized in Table 2 along with the eigenvalues for the baseline and refined-mesh FE models. It can be seen that the first and second eigenvalues for each end-support condition are very close, differing by 0.6% for simple support, and by 0.7% for clamped, according to the analytic solutions. The primary eigenvalue for clamped ends is 2.5% greater than the primary eigenvalue for simple end support. The buckling eigenvalues for the baseline FE model follow these trends very closely, except that they run 2.1% to 2.3% higher than the analytic values. The refined-mesh FE model results follow closely the trends of the first two results sets, but are approximately 0.5% below the analytic values and 2.7% less than the baseline-mesh values.

Table 2. Normalized Buckling Eigenvalues, P_{cr}/P_{ref}

End Support	Analysis	First	Second
Simple	Analytic	1.009	1.015
	FE, baseline mesh	1.031	1.036
	FE, refined mesh	1.004	1.010
Clamped	Analytic	1.034	1.043
	FE, baseline mesh	1.057	1.066
	FE, refined mesh	1.029	1.037

It is not clear why the refined-mesh eigenvalues fall slightly below the analytic values. Barring numerical error, the FE results should converge from above to the analytic values. The discrepancy is small however, and is not considered important to the conclusions presented in this paper. While the baseline-model eigenvalues run 2.7% higher than the values for the refined mesh model, the consistency of the eigenvalue trends between the different mode shapes gives some confidence in the use of the baseline FE model.

3.2 Postbuckling Response of Clamped End Plate

A static analysis of the geometrically imperfect plate was performed using arc-length control to obtain a quick characterization of the clamped-end plate behavior. This approach avoids the difficulties of controlling path switching at the bifurcation points that are encountered with a geometrically perfect plate, while providing a good estimate of the perfect-plate secondary instability load due to the small amplitude of the imperfections. The end-load versus end-shortening curve generated using this approach is plotted in Figure 3. The initial postbuckling path represents stable equilibrium with five buckles along the length. The first load reversal on the postbuckling path corresponds to a change to unstable equilibrium. The second load reversal constitutes a return to stable equilibrium with six buckles along the plate length. The sharp reversal of the load/displacement curve for the first load reversal indicates that the loss of stability occurs at essentially the same point for either controlled end shortening or controlled load. The post-buckling instability occurs at normalized load and end-shortening values of $P/P_{ref}=1.90$ and $\Delta/\Delta_{ref}=2.61$, respectively. The postbuckling instability load correlates well with the experimentally observed value of $P/P_{ref}=1.84$.[1]

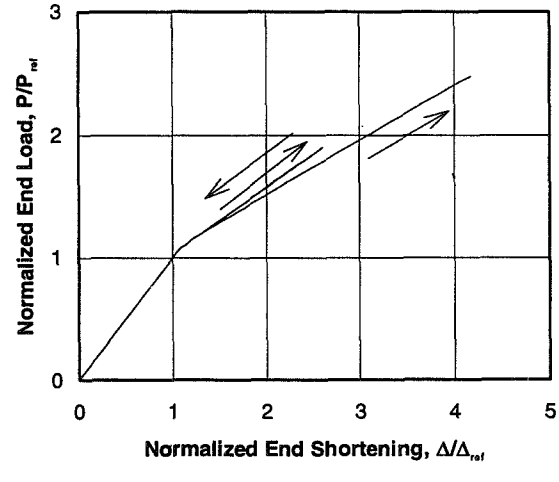

Figure 3. Load/end-shortening curve for the static response of the geometric imperfect clamped-end plate, computed using arc-length control.

using controlled end shortening. This analysis was continued to 99.5% of the critical value for the postbuckling instability, or Δ/Δ_{ref} =2.5945. From this point, a dynamic analysis was performed simulating 0.679 seconds while Δ/Δ_{ref} was increased at a rate of approximately 0.1 per second. The snap initiated between 0.382 sec and 0.387 sec elapsed time. Because the slight geometric imperfections cause the postbuckling instability to occur at a limit point rather than a symmetric bifurcation point, this analysis approach was adequate to initiate the simulated dynamic snap, since the solution was forced off the quasi-equilibrium solution path at the limit point. The automatic time step control option of ABAQUS was used, and the analysis was performed in 5000 non-uniform time steps. Analysis results were saved for postprocessing at every 10th time step

Exaggerated-displacement images of the deformed FE model at key time steps in the dynamic analysis are presented in Figure 4. Figure 4(a) corresponds to the last results set before snap initiation, at which point the maximum von Mises stress was 33.2 ksi. Figure 4(b) is the instability mode shape corresponding to the perturbation buckling analysis performed with respect to the starting solution of the dynamic analysis. Figure 4(c) is the state for the first results set after snap initiation. Figure 4(d) is the state at which the maximum von Mises stress value for all time steps, 38.3 ksi, was computed. This peak stress value is 15% greater than the maximum stress before the snap. Figure 4(e) is the state at the end of the dynamic analysis, at which time most of the motion was numerically damped out. At the end of the dynamic analysis, the maximum von Mises stress was oscillating between 33.4 and 34.1 ksi, or about 1.01 to 1.025 times the pre-snap level. It can be seen in the figures that the dynamic snap produced a change from five buckles to six, which correlates with the initial snap in Stein's experiment.[1] The intermediate states depicted in Figures 4(c-d) also feature six buckles, but the peaks are shifting along the length of the plate. An inspection of displacement and stress results revealed that the back-and-forth wave motion had a period of approximately 0.008 sec. The dynamic simulation continued approximately 0.29 sec after snap initiation, or about 36 cycles of the dominant motion. During this interval, the short-term dynamic fluctuations in the maximum von Mises stress decreased from about 15% to about 1.4%. These performance numbers give an idea of the level of numerical damping.

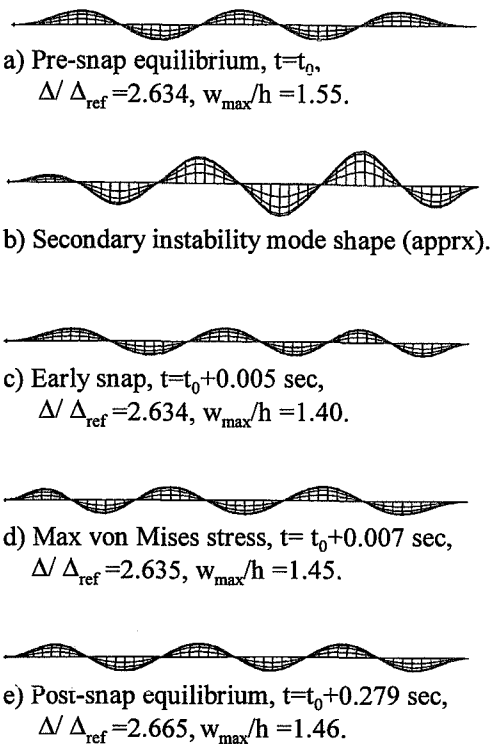

a) Pre-snap equilibrium, $t=t_0$, Δ/Δ_{ref} =2.634, w_{max}/h =1.55.

b) Secondary instability mode shape (apprx).

c) Early snap, $t=t_0+0.005$ sec, Δ/Δ_{ref} =2.634, w_{max}/h =1.40.

d) Max von Mises stress, $t= t_0+0.007$ sec, Δ/Δ_{ref} =2.635, w_{max}/h =1.45.

e) Post-snap equilibrium, $t=t_0+0.279$ sec, Δ/Δ_{ref} =2.665, w_{max}/h =1.46.

Figure 4. Exaggerated-displacement images of FE results from dynamic and perturbation-buckling analyses of the clamped-end plate.

The approximate instability mode shape depicted in Figure 4(b) is similar to that computed in Ref. 24, except that in the latter, the mode shape was exactly anti-symmetric since the model was free of imperfections. It can be seen that the secondary instability causes a new buckle to grow at one end of the plate as the bending curvature at that end changes direction. The maximum von Mises stress occurs at the left end of the plate in Figure 4(d) due to extreme bending curvature.

3.3 Postbuckling Response of Simply Supported Plate

A static analysis of the simply supported plate with geometric imperfections was performed using arc-length control. The load versus end-shortening curve generated using this approach is plotted in Figure 5. The initial postbuckling path represents stable equilibrium with five buckles along the length. As with the clamped-end plate, the first load reversal corresponds to a change to unstable equilibrium. However, following the second load reversal the equilibrium remains unstable and the equilibrium path exhibits a steeper slope than the initial postbuckling path. In either a constant-end-load or constant-end-shortening jump from the limit point to the upper path,

path. In either a constant-end-load or constant-end-shortening jump from the limit point to the upper path, the total potential energy increases, indicating that the upper path cannot be reached in an energy-dissipating snap.

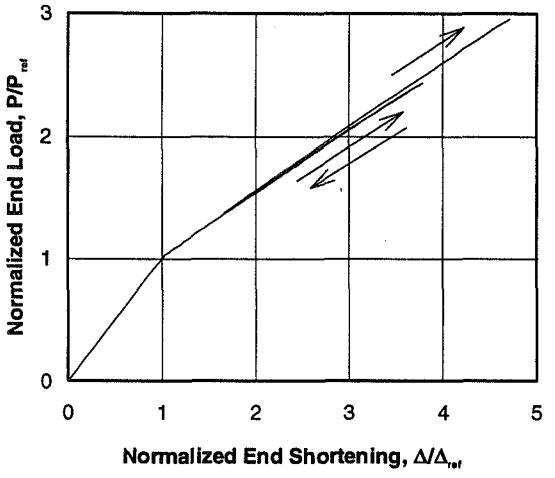

Figure 5. Load/end-shortening curve for the static response of the geometric imperfect simply supported plate, computed using arc length control.

The equilibrium solution path computed using arc-length control demonstrates that when arc-length control is used on a limit-point problem, it does not always guide an analysis to the proper post-snap equilibrium solution. This type of behavior has also been observed in a nonlinear plate analysis which used a series solution approach.[26] Analysts should thus be aware that while arc-length control can be used to analyze some limit-load problems in terms of equilibrium behavior, it does not provide a fool-proof method to locate a physically meaningful post-snap equilibrium solution path for all problems.

The post-buckling instability with simple end support occurs at normalized load and end-shortening values of P/P_{ref}=2.44 and Δ/Δ_{ref}=3.78. This critical load significantly exceeds the value predicted for the clamped-end plate (P/P_{ref}=1.90), but agrees fairly well (considering that imperfections are present) with the value P/P_{ref}=2.53 taken from the charts of Nakamuro and Uetani.[19]

A second, multi-leg analysis of the geometrically imperfect simply supported plate was performed to study the dynamic snap and post-snap behavior. A static analysis was performed using controlled end-shortening, which was increased to 99.5% of the critical value for postbuckling instability, or Δ/Δ_{ref}=3.763. From this point, a dynamic analysis was performed simulating 2.183 seconds while Δ/Δ_{ref} was increased at a rate of 0.1 per second. The snap initiated between 0.366 sec and 0.373 sec elapsed time. The automatic time step control option of ABAQUS was used, and the analysis was performed in 388 non-uniform time steps. The last couple of time steps were very large (0.72 and 0.79 sec) revealing that the simulated dynamic motion had been almost completely damped out. Analysis results were saved for postprocessing every 10th time step. A static analysis using controlled end-shortening was resumed starting at the final solution point from the dynamic analysis. The composite load versus end-shortening curve thus formed is discussed in Section 3.4.

Exaggerated-displacement images of the deformed FE model at key time steps during the dynamic analysis are presented in Figure 6. Figure 6(a) corresponds to the last results set before snap initiation, at which point the maximum von Mises stress was 44.8 ksi. Figure 6(b) is the instability mode shape corresponding to the perturbation buckling analysis performed with respect to the starting solution for the dynamic analysis. Figure 6(c) corresponds to the first results step after snap initiation. Figure 6(d) corresponds to the time at which the maximum value of von Mises stress, 52.3 ksi, was computed. This peak stress value is 17% greater than the maximum von Mises stress at the time step before the snap. Figure 6(e) depicts the deflection state at the end of the dynamic analysis, at which point the motion was essentially damped out.

While the critical snap-initiation load from FE analysis agrees fairly well with the series-solution results of Nakamuro and Uetani,[19] the instability mode shape of Figure 6(b) is very different. The shape computed by Nakamuro and Uetani was symmetric with respect to the mid-length. As a check of the mode shape shown in Figure 6(b), a second series of FE analyses leading up to the perturbation buckling solution was performed which differed from the first in that the FE model had imperfections only in the shape of the first buckling mode. This provides a perturbation buckling solution which is very close to the solution for a perfect plate. The secondary instability mode shape was qualitatively the same as the one in Figure 6(b) except that it was purely anti-symmetric. This result suggests that despite the meticulous effort of Nakamuro and Uetani,[19] they may have failed to identify the most-critical secondary instability mode shape in their series-solution approach.

a) Pre-snap equilibrium, $t=t_0$, $\Delta/\Delta_{ref}=3.801$, $w_{max}/h=2.05$.

b) Secondary instability mode shape (apprx).

c) Early snap, $t=t_0+0.007$ sec, $\Delta/\Delta_{ref}=3.802$, $w_{max}/h=1.86$.

d) Max von Mises stress, $t=t_0+0.009$ sec, $\Delta/\Delta_{ref}=3.802$, $w_{max}/h=1.78$.

e) Post-snap equilibrium, $t=t_0+1.817$ sec, $\Delta/\Delta_{ref}=3.988$, $w_{max}/h=1.75$.

Figure 6. Exaggerated-displacement images of FE results from dynamic and perturbation-buckling analyses of the simply supported plate.

It can be seen in the Figure 6 that the dynamic snap produced an increase of two in the number of buckles, from five buckles to seven, in contrast to the clamped-end case in which the number of buckles increased by one. An explanation can be found by inspecting the secondary instability mode shapes. For the clamped end case, the instability manifests itself with a change in curvature at one end of the plate. The slope at the ends is zero, so no end rotation need occur for the buckle at one end to reverse direction. With simple end support, the ends are highly rotated before the snap, and there is apparently not enough strain energy available to produce through-rotation of an end.

The displacement form early in the snap (Figure 6(c)) is rather complex, and defies easy characterization in terms of waveform. However a short time later (Figure 6(d)) the displacement form is qualitatively similar to the final rest state (Figure 6(e)), although the buckle peaks are shifted toward one end of the plate. An inspection of displacement and stress results revealed that the back-and-forth wave motion had a period of approximately 0.0065 sec. Approximately 0.3 sec simulated time after snap initiation, the motion was largely damped out, and the peak von Mises stress was approximately equal the pre-snap value.

3.4 Discussion of Results

Composite load/end-shortening curves formed from the results of FE analyses described in Section 3.2 and 3.3 are compared with the experimental results of Stein[8] in Figure 7. The experimental results presented in Ref. 8 reflect a correction to the results originally reported in Ref. 1. The measured value of end-shortening at the initial buckling point is in err due to deformation of the load plattens which prevented accurate determination of the end-shortening value.[8] The declining slope in the experimental results following the first snap is due to yielding of the aluminum material.[1] It can be seen that the clamped-end analysis results agree well with the experimental results with respect to the initiation load for the first snap. The drop in end load due to the snap in the simply supported plate is much greater than the drop in the clamped-end plate.

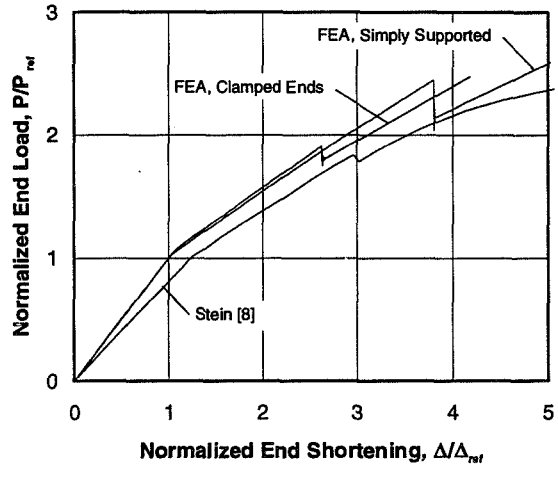

Figure 7. Comparison of load/end-shortening curves from analysis and experiment.

There is some uncertainty in the comparison of analysis and test results because of the sensitivity of the snap initiation load to imperfections.[24] For example, even with the small initial imperfections used in the clamped-end plate FE analysis (contributions of 0.1% of the plate thickness in the shape of each of the first two buckling modes) previous analytical results[24] indicate that the snap initiation load is reduced by about 3.5%. The effective imperfections for the test plate are not known.

FE discretization also adds error in the form of an artificial increase in the computed snap initiation load. The refined-mesh FE model was used to compute the

snap initiation load of the imperfect simply supported plate. The resulting critical load was P/P_{ref}=2.33, compared to 2.44 for the baseline mesh, a decrease of 4.6%. (The decrease in the initial buckling load due to mesh refinement was 2.7%.)

The FE results presented here provide confirmation of themes put forth in Ref. 24 regarding the postbuckling behavior of uniaxially loaded plates with supported edges with length-to-width ratios significantly greater than unity. Specifically, despite the relative insensitivity of both the initial buckling load and initial postbuckling stiffness to the end-support condition, the snap initiation load is much higher for simple end support than for clamped end support.

A new result from the current study is that for the specific plate aspect ratio considered, the clamped-end plate snaps to the next higher buckle number (from five to six) whereas the simply supported plate snaps from five to seven buckles, retaining the direction of end rotation at both ends. Furthermore, the maximum von Mises stress in this isotropic plate achieves peak values during the dynamic snap which are significantly higher than the pre-snap and post-snap values (15% to 17% higher, depending on the end-support condition). This is important because it shows that plates designed only with a consideration of static postbuckling stresses may be underdesigned if a snap can occur within the design load range.

Numerous researchers have used a two-term series solution or a two-term perturbation analysis to study the snap phenomenon. [10-13,21-23] As discussed in the Introduction, two-term solution approaches have provided results which are both quantitatively and qualitatively inaccurate. The two-term perturbation approach was developed by Koiter[27] to analyze buckling mode interaction in, and predict the imperfection sensitivity of, structures such as axially compressed weight-minimized buckling-critical cylindrical shell designs. For such configurations, fundamentally different buckling mode shapes (short wavelength versus long wavelength) having identical buckling eigenvalues interact in the vicinity of the initial buckling point. In retrospect, the plate snap problem has deceived many researchers because the snap involves a change of state between two waveforms which are associated with two buckling mode shapes that can have close or identical eigenvalues. This has led to the perception of the problem as a "modal interaction" problem in the same sense as the cylindrical shell. For buckled plates, however, the instability which initiates the snap occurs not in the vicinity of the initial buckling point, but instead deep in the postbuckling regime.

4. Conclusions

Finite element simulations were performed using a general purpose finite element code to simulate the postbuckling snap or "mode change" phenomenon in a uniaxially compressed plate configuration with supported edges. The 5.4 aspect ratio plate configuration was one for which experimental results were available in the literature. Analytical simulations included initial buckling, tracing of stable and unstable equilibrium paths in the geometrically nonlinear regime, and geometrically nonlinear dynamic simulations. The plate was isotropic, and linear elastic material behavior was modeled in the analysis. The following conclusions were reached based on the results obtained.

1. For the 5.4 aspect ratio plate modeled with finite elements, the difference between clamped and simple support at the loaded ends was found to have a large effect on the postbuckling snap behavior. The clamped-end plate with slight shape imperfections initiated a dynamic snap at a normalized load of 1.90, correlating well with the experimentally observed value of 1.84, whereas the simply supported plate with slight shape imperfections initiated a dynamic snap at a normalized load of 2.44. The clamped-end plate snapped from five to six buckles whereas the simply supported plate snapped from five to seven buckles.
2. Peak values of the von Mises stress during the dynamic snap were 15% to 17% higher, depending on the end-support condition, than pre-snap or post-snap stress values. This suggests that plates and panels designed based on static postbuckling stress levels may be under-designed if a snap occurs within the design operation range.
3. While the plate snap phenomenon has the appearance of a classic "modal interaction" problem, the initial buckling modes do not interact in the vicinity of the initial buckling point. The snap instability generally occurs deep in the postbuckling regime. For this reason, series solutions or perturbation analyses which, in the spirit of Koiter's perturbation approach, use only two buckling modes to represent out-of-plane displacements are fundamentally inadequate for analyzing the plate snap problem.

4. One arc-length control plate analysis failed to return to a stable equilibrium path after completing two load reversals in the postbuckling regime. This phenomenon has also been observed in series-solution analyses of geometrically nonlinear plate problems. Analysts should thus be aware that while arc-length control can be used to analyze some limit-load problems in terms of equilibrium behavior, it does not provide a fool-proof method to locate a physically meaningful post-snap equilibrium solution path for all problems.

Acknowledgments

The authors gratefully acknowledge the use of the Computational Mechanics Laboratory of the University of Dayton Research Institute, Dayton, Ohio.

References

1. Stein, M., Loads and Deformations of Buckled Rectangular Plates, NASA TR R-40 (1959).
2. Uemura, M., and Byon, O., Secondary Buckling of a Flat Plate under Uniaxial Compression, Part 2: Analysis of Clamped Plate by F.E.M. and Comparison with Experiments, *Int. J. Non-Linear Mechanics*, **13**, 1-14 (1978).
3. Jeffrey, G.L., Postbuckling of Laminated Anisotropic Panels, NASA-TM-100509 (1987).
4. Jensen, D.W., and Lagace, P.A., Influence of Mechanical Couplings on the Buckling and Postbuckling of Anisotropic Plates, *AIAA Journal*, **26**, 1269-1277 (1988).
5. Minguet, P.J., Dugundji, J., and Lagace, P.A., Postbuckling Behavior of Laminated Plates using a Direct Energy-Minimization Technique, *AIAA Journal*, **27**, 1785-1792 (1989).
6. Spier, E.E., Postbuckling Fatigue Behavior of Graphite-Epoxy Stiffeners, AIAA-82-0779; in *Proceedings, AIAA 23rd Structures, Structural Dynamics and Materials Conference, New Orleans, LA*, 511-527 (1982).
7. Lee, H.H., and Hyer, M.W., Postbuckling Failure of Composite Plates with Holes, *AIAA Journal*, **31**, 1293-1298 (1993).
8. Stein, M., Postbuckling of Eccentric Open-Section Stiffened Composite Panels, AIAA-88-2215 (1988).
9. Stein, M., The Phenomenon of Change in Buckle Pattern in Elastic Structures, NASA TR R-39 (1959).
10. Dombourian, E.M., Smith, C.V. Jr., and Carlson, R.L., A Perturbation Solution to a Plate Postbuckling Problem, *Int. J. Non-Linear Mechanics*, **11**, 49-58 (1976).
11. Hlavacek, I., Einfluss der Form der Anfangskrummung auf das Ausbeulen der Gedruckten Rechteckigen Platte, *Acta Technica Csav*, **2**, 174-206 (1962).
12. Supple, W.J., Changes of Wave-Form of Plates in the Post-Buckling Range, *Int. J. Solids and Structures*, **6**, 1243-1258 (1970).
13. Wicks, P.J., A Classification of Behavior in Doubly-Symmetric Compound Branching, *Int. J. Mech. Sci.*, **30**, 821-833 (1988).
14. Stroebel, G.J., and Warner, W.H., Stability and Secondary Bifurcation for von Karman Plates, *J. of Elasticity*, **3**, 185-202 (1973).
15. Uemura, M., and Byon, O., Secondary Buckling of a Flat Plate under Uniaxial Compression, Part 1: Theoretical Analysis of Simply Supported Flat Plate, *Int. J. Non-Linear Mechanics*, **12**, 355-370 (1977).
16. Shin, D.K., Griffin, O.H. Jr., and Gurdal, Z., Postbuckling Response of Laminated Plates under Uniaxial Compression, *Int. J. Non-Linear Mechanics*, **28**, 95-115 (1993).
17. Shen, H.S., and Zhang, J.W., Perturbation Analyses for the Postbuckling of Simply Supported Rectangular Plates under Uniaxial Compression, *Applied Mathematics and Mechanics* (English Edition, Shanghai, China), **9**, 793-804 (1988).
18. Shen, H.S., Postbuckling Behavior of Rectangular Plates under Combined Loading, *Thin-Walled Structures*, **8**, 203-216 (1989).
19. Nakamura, T., and Uetani, K., The Secondary Buckling and Post-Secondary-Buckling Behaviors of Rectangular Plates, *Int. J. Mech. Sci.*, **21**, 265-286 (1979).
20. Carnoy, E.G., and Hughes, T.J.R., Finite Element Analysis of the Secondary Buckling of a Flat Plate under Uniaxial Compression, *Int. J. Non-Linear Mechanics*, **18**, 167-175 (1983).
21. Schaeffer, D., and Golubitsky, M., Boundary Conditions and Mode Jumping in the Buckling of a Rectangular Plate, *Communications of Mathematical Physics*, **69**, 209-236 (1979).
22. Maaskant, R., and Roorda, J., Mode Jumping in Biaxially Compressed Plates, *Int. J. Solids Structures*, **29**, 1209-1219 (1992).
23. Suchy, H., Troger, H., and Weiss, R., Numerical Study of Mode Jumping of Rectangular Plates, *Zeitchrift fur Angewandte Mathematik und Mechanik*, **65**, 71-78 (1985).

24. Stoll, F., Analysis Of The Snap Phenomenon In Buckled Plates, *Int. J. Non-linear Mech.* **29,** 123-138, 1994.
25. Levy, S., Bending of Rectangular Plates with Large Deflections, NACA Rept. 737, (1942).
26. Stoll, F., An Implementation of Solution Strategies for the Analysis of Complex Nonlinear Equilibrium Behavior, *Int. J. Non-linear Mech.* **29,** 109-122, 1994.
27. Koiter, W.T., On the Stability of Elastic Equilibrium, Doctoral Thesis, Polytechnic Institute of Delft, 1945 (English translation: NASA TT F-10,833, March, 1973.)

REPORT DOCUMENTATION PAGE

Form Approved
OMB No. 0704-0188

1. AGENCY USE ONLY (*Leave blank*)	2. REPORT DATE	3. REPORT TYPE AND DATES COVERED
	January 1998	Conference Publication

4. TITLE AND SUBTITLE
Stability Analysis of Plates and Shells: A Collection of Papers in Honor of Dr. Manuel Stein

5. FUNDING NUMBERS
522-11-41-02

6. AUTHOR(S)
Norman F. Knight, Jr., and Michael P. Nemeth (Compilers)

7. PERFORMING ORGANIZATION NAME(S) AND ADDRESS(ES)
NASA Langley Research Center
Hampton, VA 23681-2199

8. PERFORMING ORGANIZATION REPORT NUMBER
L-17659

9. SPONSORING / MONITORING AGENCY NAME(S) AND ADDRESS(ES)
National Aeronautics and Space Administration
Washington, DC 20546-0001

10. SPONSORING / MONITORING AGENCY REPORT NUMBER
NASA/CP-1998-206280

11. SUPPLEMENTARY NOTES
Compilation of papers presented at special sessions honoring Dr. Manuel Stein during the 38th AIAA/ASME/ASCE/AHS/ASC Structures, Structural Dynamics, and Materials Conference.

12a. DISTRIBUTION / AVAILABILITY STATEMENT
Unclassified - Unlimited
Subject Category 39
Distribution: Standard
Availability: NASA CASI (301) 621-0390

12b. DISTRIBUTION CODE

13. ABSTRACT (*Maximum 200 words*)

This special publication contains the papers presented at the special sessions honoring Dr. Manuel Stein during the 38th AIAA/ASME/ASCE/AHS/ASC Structures, Structural Dynamics, and Materials Conference held in Kissimmee, Florida, April 7-10, 1997. This volume, and the SDM special sessions, are dedicated to the memory of Dr. Manuel Stein, a major pioneer in structural mechanics, plate and shell buckling, and composite structures. Many of the papers presented are the work of Manny's colleagues and co-workers and are a result, directly or indirectly, of his influence.

Dr. Stein earned his Ph.D. in Engineering Mechanics from Virginia Polytechnic Institute and State University in 1958. He worked in the Structural Mechanics Branch at the NASA Langley Research Center from 1943 until 1989. Following his retirement, Dr. Stein continued his involvement with NASA as a Distinguished Research Associate.

14. SUBJECT TERMS
stability
buckling
composites

15. NUMBER OF PAGES
453

16. PRICE CODE
A20

17. SECURITY CLASSIFICATION OF REPORT	18. SECURITY CLASSIFICATION OF THIS PAGE	19. SECURITY CLASSIFICATION OF ABSTRACT	20. LIMITATION OF ABSTRACT
Unclassified	Unclassified	Unclassified	